

Mahdi O. Karkush  
Deepankar Choudhury *Editors*

# Geotechnical Engineering and Sustainable Construction

Sustainable Geotechnical Engineering

 Springer

# Geotechnical Engineering and Sustainable Construction

Mahdi O. Karkush · Deepankar Choudhury  
Editors

# Geotechnical Engineering and Sustainable Construction

Sustainable Geotechnical Engineering

 Springer

*Editors*

Mahdi O. Karkush  
Department of Civil Engineering  
University of Baghdad  
Baghdad, Iraq

Deepankar Choudhury  
Department of Civil Engineering  
Indian Institute of Technology Bombay  
Mumbai, Maharashtra, India

ISBN 978-981-16-6276-8

ISBN 978-981-16-6277-5 (eBook)

<https://doi.org/10.1007/978-981-16-6277-5>

© The Editor(s) (if applicable) and The Author(s), under exclusive license to Springer Nature Singapore Pte Ltd. 2022

This work is subject to copyright. All rights are solely and exclusively licensed by the Publisher, whether the whole or part of the material is concerned, specifically the rights of translation, reprinting, reuse of illustrations, recitation, broadcasting, reproduction on microfilms or in any other physical way, and transmission or information storage and retrieval, electronic adaptation, computer software, or by similar or dissimilar methodology now known or hereafter developed.

The use of general descriptive names, registered names, trademarks, service marks, etc. in this publication does not imply, even in the absence of a specific statement, that such names are exempt from the relevant protective laws and regulations and therefore free for general use.

The publisher, the authors and the editors are safe to assume that the advice and information in this book are believed to be true and accurate at the date of publication. Neither the publisher nor the authors or the editors give a warranty, expressed or implied, with respect to the material contained herein or for any errors or omissions that may have been made. The publisher remains neutral with regard to jurisdictional claims in published maps and institutional affiliations.

This Springer imprint is published by the registered company Springer Nature Singapore Pte Ltd. The registered company address is: 152 Beach Road, #21-01/04 Gateway East, Singapore 189721, Singapore

# Contents

<b>Development in Geotechnical Engineering</b>	
<b>Improving the Gypseous Soil Bearing Capacity Using Geotextile Reinforcement Under Dry Condition</b> .....	3
Makki K. Mohsen, Qasim A. Al-Obaidi, and Ayad O. Asker	
<b>Numerical Modeling of Circular Tunnel Alignment Under Seismic Loading</b> .....	15
Hayder A. Al-Mirza and Mahdi O. Karkush	
<b>Triaxial Compression Behavior of Sandy Soil Polluted with Crude Oil</b> .....	29
Farman K. Ghaffoori, Mohamed M. Arbili, Hanifi Çanakcı, and Talib K. Ibrahim	
<b>Isotropic and Cross-Anisotropic Stiffness Parameters for Unsaturated Soils Using Conventional and Bishop's Stress State Variables</b> .....	41
Ahmed Mohammed Hasan	
<b>The Effect of Electric Field on the Settlement Behavior to Improve Gypseous Soil</b> .....	53
Methaq A. Talib and Qasim A. Aljanabi	
<b>Tsunami Waves, Causes and Its Implications: A Review</b> .....	63
Hiba A. Bachay, Asad H. Aldefae, Salah L. Zubaidi, Wissam H. Humaish, and Evgeny K. Sinichenko	
<b>The Scale Effects on the Shear Strength Behavior of Silty Sand Soil in Direct Shear Tests</b> .....	79
Omar H. Al-Emami and Ammar A. Al-Sultan	
<b>Tunnel-Soil-Structure Interaction Under Seismic Load</b> .....	91
Zaid F. Al-Farhan, Moataz A. Al-Obaydi, and Qutayba N. Al-Saffar	

<b>Effect of Microbial Induced Calcite Precipitation on Shear Strength of Gypseous Soil in Dry and Soaking Conditions</b> .....	103
Alaa D. Salman, Mahdi O. Karkush, and Hussein H. Karim	
<b>Suction—Resistivity Relationship in Unsaturated Gypseous Soil</b> .....	115
Qasim A. Al-Obaidi and Ali A. Al-Shamoosi	
<b>Assessment of Effect of Tidal Level and Footing Proximities on Retaining Wall-Grain Interactions Using Finite Element Method</b> ....	125
Zuhair Kadhim Jahanger, Qais K. Jahanger, and S. Joseph Antony	
<b>Evaluation of Dam Breach Parameters Using Different Approaches for Earth-Fill Dam</b> .....	135
Israa Dheyaa Abdulrazzaq, Qassem H. Jalut, and Jasim M. Abbas	
<b>Manufacturing of Small-Scale Flume to Assess the Riverbank’s Settlement</b> .....	145
Asad H. Aldefae, Rusul A. Al-Khafaji, Wissam H. Humaish, and Evgeny K. Sinichenko	
<b>Groundwater Analysis Based on the Hydrogeological Model of Taichung Basin, Taiwan</b> .....	159
K. J. Shou and C. C. Pan	
<b>Design and Manufacturing of Rainfall Simulator Machine for the Soil Erosion Investigation</b> .....	177
Shereen A. Alzamly, Asad H. Aldefae, Wissam H. Humaish, Evgeny K. Sinichenko, and Salah L. Zubaidi	
<b>Numerical Analysis of Water and Crude Oil Flux from Clayey Soil by GeoStudio-SEEP/W</b> .....	191
Amina Hamid Alwan and Aqeel Al-Adili	
<b>Evaluation of the Efficiency of a Selected Section of the Mosul Dam Grout Curtain</b> .....	207
Mohammed Khalid Ibrahim and Suhail Idrees A. Khattab	
<b>Stability of Slopes Under Unsaturated Conditions Using a Modified Upper Bound Theorem</b> .....	221
Bestun J. Shwan	
<b>Monitoring of the Western Breakwater of Al-Faw Grand Port-South of Iraq Using Differential InSAR-ISBAS Technique</b> .....	229
Lubna Alshammari and Omar Natiq Mohammed	
<b>Numerical Modelling of Surface Runoff in Watershed Areas Related to Bahr AL-Najaf</b> .....	241
Ataa A. Farhan and Basim Sh. Abed	

**Challenges in Foundation Engineering**

**Bearing Capacity of Model Strip Footing on Unsaturated Very Loose Sand** ..... 255  
 Khashayar Nikoonejad and Reza Imam

**Overall Static and Seismic Stability of Oil Tank Resting on Shallow Foundation: A Case Study** ..... 269  
 Chaidul Haque Chaudhuri, Rana Acharyya, Milind Patil, and Deepankar Choudhury

**Numerical Modeling of Screw Piles Performance Under Static and Seismic Loads in Soft Soils** ..... 291  
 Ahmed D. Alkaby and Mahdi O. Karkush

**Numerical Simulation of Driven Piles Under Static Axial Compressive Load Testing Using Finite Element Model** ..... 305  
 Hazim AlKhafaji and Meysam Imani

**Experimental Investigation of Pullout Capacity of Screw Piles in Soft Clayey Soil** ..... 315  
 Asaad A. Hussein and Mahdi O. Karkush

**Effect of Embankment on the Behavior of Rigid Passive Pile Group in Sandy Soil** ..... 329  
 Mahdi O. Karkush, Majeed R. Sabaa, Ghofran S. Jaffar, and Omar K. Al-Kubaisi

**Effect of River Water Level on the Shallow Foundation Behavior with Two Slopes of Riverbank** ..... 343  
 Noor Salim Atia, Qassun S. Mohammed Shafiqu, and Asma Thamir Ibraheem

**Numerical Modeling of Sheet Pile Quay Wall Performance Subjected to Earthquake** ..... 355  
 Mahdi O. Karkush, Shahad D. Ali, Naghm M. Saidik, and Alaa N. Al-Delfee

**Effect of Wing Ratio of Single Helix Screw Pile on Ultimate Compression Capacity Embedded in Cohesionless Soil** ..... 367  
 Hiba D. Saleem, Asad H. Aldefae, and Saleem M. Mearek

**Numerical Analysis of Piles Group Surrounded by Grouting Under Seismic Load** ..... 379  
 Mahdi O. Karkush, Abeer H. Mohsin, Husam M. Saleh, and Bilal J. Noman

<b>Effect of Spacing Ratio on the Pull-Out Capacity of Double Helix Pile in Organic Soil</b> .....	391
Majid Hamed, Waleed Mohammed, Hanifi Canakci, and Abdalkhaliq Mijwel	
<b>Comparative Analysis of Static and Dynamic Pile Tests at the Site of the Astana Medical University Hospital in Nur-Sultan, Kazakhstan</b> .....	401
A. Zh. Zhussupbekov, A. U. Yessentayev, B. G. Abdrakhmanova, and V. N. Kaliakin	
<b>Vertical Displacement Analysis of Embedded Square Foundation Under Vertical Dynamic Load</b> .....	409
Abdulrahman Ahmed Najm, Bayar J. AL-Sulayvani, and Mohammed N. Jaro	
<b>Investigation of Laterally Loaded Pile Response and CohesionLess Soil Deformation Pattern Using PIV Technique</b> .....	423
Mohammed A. Al-Neami, Mohammed H. Al-Dahlaki, and Aya H. Al-Majidy	
<b>An Experimental Investigation the Response of Pile Groups to Inclined Cyclic Loading in Sandy Soil</b> .....	435
Reyah D. Khurshed and Jasim M. Abbas	
<b>Numerical Modeling of Under Reamed Piles Behavior Under Dynamic Loading in Sandy Soil</b> .....	447
Ahmed M. Najemalden, Mustafa M. Jasim, and Ansam A. Al-Karawi	
<b>Merges in Structural Engineering and Construction Materials</b>	
<b>Exploring Biochar as Stable Carbon Material for Suppressing Erosion in Green Infrastructure</b> .....	461
Yuan-Xu Huang, Xia Bao, He Huang, Ankit Garg, Wei-Ling Cai, and Askar Zhussupbekov	
<b>Dynamic Response of Slender Reinforced Concrete Columns Strengthened by Using CFRP and Circularization Subjected to Seismic Excitation</b> .....	469
Zena H. Abdulghafoor and Hayder A. Al-Baghdadi	
<b>Experimental and Numerical Study of the Influence of Various Parameters on the Development of Deformations in Reinforced Base</b> ...	481
V. M. Antonov and I. A. Al-Naqdi	
<b>Human-Induced Vibration on Light-Gauge Steel Lightweight Concrete Composite Floors</b> .....	495
Tiba H. Saadi and Salah R. Al-Zaidee	



**Evaluating Nonlinear Behavior of a Reinforced Concrete Building with Shear Walls and Centric Steel Bracings** ..... 511  
 Anwar Jabar Qadesheen, Esra Mete Güneysi, and Halmat Ahmed Awla

**Yield Line Model for Estimation Shear Strength UHPC Non-prismatic Beams** ..... 523  
 Nasser H. Tu'ma and Abdulmuttalib I. Said

**Evaluation of Live Load Distribution Factors of a Highway Bridge** ..... 531  
 Abbas A. Allawi, Abdulmuttalib I. Said, Mohannad H. Al-Sherrawi, Amjad Albayati, Mohammed Al Gharawi, and Ayman El-Zohairy

**Numerical Analysis of Historical Masonry Minaret Subjected to Wind Load** ..... 545  
 Alaa Hussein Al-Zuhairi, Ammar R. Ahmed, and Salah R. Al-Zaidee

**Accuracy Assessment of Shell Finite Elements for Considering to Masonry Structures Under Seismic Loading** ..... 557  
 Halmat Ahmed Awla and Mohamed M. Arbili

**Stability and Seismic Performance of Tall Steel Structures with Hybrid Energy Absorbers Including P-Delta Effect** ..... 569  
 Rafea M. Abbas and Ameer J. Abdulkareem

**Estimations the Combined Flexural-Torsional Strength for Prestressed Concrete Beams Using Artificial Neural Networks** ..... 583  
 Hend S. Zayan and Akram S. Mahmoud

**Theoretical Evaluation of Sand Subgrade Behavior Underneath the Asphalt Pavement with Rutting Deformation** ..... 597  
 Saad F. I. Al-Abdullah, Zaman T. Teama, Suha Aldahwi, and Maysaloon Zaidn

**Large Scale Laboratory Setup for Testing Structural Performance of Slender High-Strength Concrete Columns Subjected to Axial Load and Fire: A Preliminary Study** ..... 611  
 Muyasser M. Jomaa'h, Ali I. Salahaldin, Qahtan A. Saber, and Aram M. Raheem

**Experimental Investigation of Masonry Arches Strengthened with Carbon Fiber Composites CFRP** ..... 627  
 Juman E. M. ALTemimi, Abdulmuttalib I. Said, and R. Al-Mahaidi

**Mechanical Properties of Normal Strength Concrete Covered with Gypsum Layers and Exposed to High Temperatures (Fire Flame)** ..... 641  
 Raid S. Warwar and Abdulmuttalib I. Said

<b>Performance of Self-compacting Geopolymer Concrete with and Without Portland Cement at Ambient Temperature</b> .....	657
Alaa Mohammedameen, Khaleel H. Younis, Radhwan Alzebaree, Mohamed Moafak Arbili, and Talib K. Ibrahim	
<b>Construction Management and Sustainability</b>	
<b>Cost Prediction of Roads Construction Projects Using OLS Regression Method</b> .....	671
Ruqayah H. Rasheed and Sedqi E. Rezouki	
<b>Modeling of Variation Orders in Cost and Time Using System Dynamics in Iraqi Construction Projects</b> .....	681
Wissam A. Ismaeel, Hafth I. Naji, and Raquim N. Zehawi	
<b>Evaluating the Performance of Iraq Construction Projects Using Building Information Modelling Technique</b> .....	691
Noor H. Kadume and Hafeth I. Naji	
<b>The Priorities for the Distribution of Primary School Projects According to the Spatial Gap Criterion at Baghdad/Iraq</b> .....	701
Yaqdhan A. Kamil and Sedqi E. Rezouki	
<b>Regulation of Supplier Standards in Iraq: Through Sustainability Standards</b> .....	715
Bariq W. Abdulmajeed and Meervat R. Altaie	
<b>Assessment of Standard Request for Proposal for the Selection of Consultants in Iraq</b> .....	727
Noor A. Ramadhan and Sawsan R. Mohammed	
<b>An Optimization Model to Estimate the Construction Costs of Highways Projects: Al-Rihab Highway as a Case Study</b> .....	739
Abbas M. Burhan	
<b>Determine the Most Common Geotechnical Risks and Their Impacts on the Cost and Time Schedule for Implementing Water Treatment Plants in Iraq</b> .....	749
Ahmed J. Kadhom and Meervat R. Altaie	
<b>Mapping and Analyzing Flood Hazard Using Remote Sensing and GIS Techniques in Diyala River Basin, Iraq</b> .....	759
Hussain Muhamed, Mustafa N. Hamoodi, and Abd Alrazzak T. Ziboon	
<b>Towards Sustainable Local Tourism to Conserve the Natural Environment: Foundations of Sustainable Ecolodge Design</b> .....	769
Zahraa Sabah Salih and Zaynab Radi Abaas	

<b>Using Infrared Spectroscopy to Examine the Influences of Stabilizers on the Molecular Structure of Stabilized Contaminated Clay Soils</b> .....	781
Khitam Abdulhussein Saeed and Sabah Hassan Fartosy	
<b>Spatial Analysis of Archaeological and Heritage Sites Using Geographic Information System Techniques: A Case Study of Wasit Province, Iraq</b> .....	793
Ali Hussein Alwan and Hussein Sabah Jaber	
<b>Future Cities and Reality: Analytical Preview of the Different Theories from Information Cities, Smart Cities, to Liveable Cities</b> .....	805
Hussaen Ali Hasan Kahachi	

# **Development in Geotechnical Engineering**

# Improving the Gypseous Soil Bearing Capacity Using Geotextile Reinforcement Under Dry Condition



Makki K. Mohsen, Qasim A. Al-Obaidi, and Ayad O. Asker

**Abstract** Gypseous soil is one of the problematic soils and greatly affects the stability of the engineering structures, especially in Iraq. The main geotechnical problem of this soil is the significant reduction of its bearing capacity upon loading and/or wetting processes due to the dissolution of gypseous cementing bonds. This study aims to improve the soil's bearing capacity by using geosynthetic material in single, double, and triple distribution patterns. The gypseous soil samples were brought from a site near Sawa Lake by coordinates (31°18'42.83" N, 45°00'49.36" E) in Al-Muthanna Governorate with gypsum content of 37.35% forms about 3.0 m high under the ground surface. The Soil-Model apparatus of dimensions (60 × 60 × 50) cm is used, while the proposed square footing dimensions are (10 × 10) cm. The main test program investigates the bearing capacity before and after the soil reinforcement with the geotextile layers. The results showed a considerable increase in bearing capacity and the increase of volume change when using the triple phase pattern with the allowable bearing capacity increase for reinforced gypseous soil, especially with the increasing reinforcement layers at the triple reinforcement pattern. The depth of the geotextile layer with the soil mass has a significant effect on the magnitude of the bearing capacity and decreases the settlement. The improvement proportion of soil bearing capacity using Geotextile Reinforcement at dry state is ranged 20–90% for relative densities 30 and 60% and different reinforcement patterns.

**Keywords** Gypseous soil · Collapse · Improvement · Bearing capacity · Geotextile

---

M. K. Mohsen · Q. A. Al-Obaidi (✉) · A. O. Asker  
Civil Engineering Department, University of Technology, Baghdad, Iraq  
e-mail: [Qasim.A.Jassim@uotechnology.edu.iq](mailto:Qasim.A.Jassim@uotechnology.edu.iq)

M. K. Mohsen  
e-mail: [40139@uotechnology.edu.iq](mailto:40139@uotechnology.edu.iq)

A. O. Asker  
e-mail: [bce.19.60@grad.uotechnology.edu.iq](mailto:bce.19.60@grad.uotechnology.edu.iq)

## 1 Introduction

Collapsible soil is known as any unsaturated soil that passes into a radical changing of particles positions related to loss of volume upon wetting with or without extra load [1, 2]. Gypseous soils cover numerous districts in the world, particularly in parched and semi-arid locales, where the yearly amount of water is inadequate for filtering the gypsum from these soils [3]. Gypseous soil presents a wide collapse potential as a result of its metastable structure. It has weakly dry and damp content in its normal state due to the existence of cementation bonds and an open gypsum structure, especially at unsaturated states or in bone-dry or semi-arid districts. Additionally, change in volume, quick settlement, and a high lowering within the void proportion of a metastable soil structure can happen. Huge volume changes and sudden collapses occur when the soil is immersed in the water beneath steady vertical pressure. Soil distortion happens as a result of the disintegration of the cemented gypsum bonds causes an articulated increment within the compressibility of the soil [4]. The chemical composition of the gypseous soil is  $(\text{CaSO}_4 \cdot 2\text{H}_2\text{O})$ . According to Barzanji [5], the soil is considered as slightly gypseous soil if the gypsum amount (3–10%) and highly gypseous soil if the gypsum amount is (25–50%). The collapse potential (CP) of gypseous soil can be estimated in the lab from single or double Oedometer tests where the soil considers as trouble or severe trouble when the collapse potential (CP) exceeds the value of 5% [4, 6, 7]. Geotextiles are considered to have the bearing capacity or have high tensile strength, while soils, in general, are considered low-stress materials and have high compressive strength. Therefore, geotextiles are the ideal material for improving and increasing the efficiency of the soil and thus increasing structural stability. To protect the soil from collapse [8, 9].

## 2 Material, Equipment, and Test Setup

**Soil.** The undisturbed soil sample is brought from a site near Sawa Lake, Al-Muthanna Governorate, from a depth of (3.0) m. This region is considered an arid area, and the soil can be defined as the medium to dense light brown silty SAND with white traces of gypsum particles. The soil classification is (SP-SM) according to the Unified Soil Classification System (USCS). The physical and chemical properties of the soil are shown in Table 1.

**Geotextile Material.** Geotextile soil fabrics or knitting warp is considered one of the successful practical solutions to some problems arising from the nature of the soil. Geotextile is used in road, and railway soil steady on waterways and beach corrosion control, asphalt pavement overlap crack relief, subsurface drainage systems, waterproofing membrane defend on, landfill, landscaping, etc. Its multiple-use functions include Separation, Filtration, Reinforcement and stabilization function, and drainage [8, 9]. The geotextile reinforcement used in this study is displayed in Fig. 1 and Table 2.

**Table 1** Physical and Chemical properties of the soil sample

Property	Value	Standard
<i>Physical properties</i>		
Initial water content (%)	6.1	ASTM D 2216
Liquid, plastic and plasticity index (%)	38, 33, 5	ASTM D 4318
Passing sieve No.200 (%)	9.2	ASTM D 422
D10 (mm)	0.08	ASTM D 422
D30 (mm)	0.115	ASTM D 422
D60 (mm)	0.31	ASTM D 422
Cu	3.87	ASTM D 422
Cc	0.53	
Specific gravity (Gs)	2.37	ASTM D 854
Max. dry density (g/cm <sup>3</sup> )	1.62	ASTM D 4253
Opt. moisture content (%)	13.5	ASTM D 4254
<i>Cohesion (kPa)</i>		
For RD = 30%	4	ASTM D3080
For RD = 60%	5.3	
<i>Angle of friction (°)</i>		
For RD = 30%	28.5	For RD = 60%
For RD = 60%	30	
<i>Chemical properties</i>		
Gypsum content (%)	37.3	
Total sulphate content (SO <sub>3</sub> ) (%)	17.8	
Total soluble salts (TSS) (%)	12.4	

**Fig. 1** Geotextile reinforcement was used in this study

**Table 2** Geotextile properties

Property	Value	Standard	Property	Value	Standard
Type of geotextile	Nonwoven		Grab tensile strength	750 N	ASTM D4632
Type of fiber	Polypropylene		Wide width tensile strength	13 kN/m	ASTM D4595
Trade name	Prime geo 200		Puncture strength (CBR)	2200 N	ASTM D6241
Weight	200 gm/m <sup>2</sup>	ASTM D 5261	Trapezoidal tear strength	280 N	ASTM D4533
Pore size	80 microns	ASTM D 4751	Permittivity	1.6 S <sup>-1</sup>	ASTM D4491

**Soil-Model Apparatus.** The Soil-Model Apparatus is made from rigid steel with inner dimensions of the model box are (60 × 60 × 50) cm length, width, and height, the plate thickness of 0.5 cm with square footing (10 × 10 × 1 cm) of rigid steel. The Soil-Model Apparatus consists of several mechanical and electronic parts: Steel load frame, Axial loading system, hydraulic jack, Load cell, a data logger (Adriano), dial gauges, computer software plate, as explained in Figs. 2 and 3.

**Sample Preparation.** The soil samples are prepared in a test box with a relative density of (30% and 60%). In order to achieve the required dry density, the box is distributed into layers with 50 mm height for every layer and an area of (60 × 60) cm till the full height of 50 cm is reached. The whole number of layers is 10

**Fig. 2** Soil-model apparatus during test



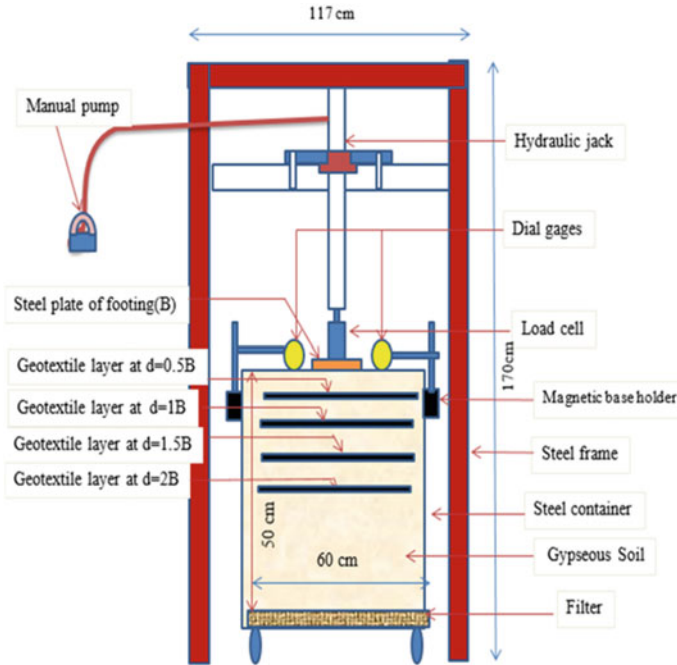


Fig. 3 Diagram of loading system

layers, and the weight of the sandy soil for every layer was (23.11 and 25.36) kg for relative densities 30 and 60%, respectively. Every layer is a store with a level plane and leveled from at that point utilizing the manual compactor instrument until the required density is gotten for all layers as appeared in Fig. 2.

**Test Procedure.** The compression (i.e., bearing capacity) test is showed by following method nonrepetitive static plate load technique according to the test process mentioned in ASTM D1194-94. The bearing capacity is measured for several layers of geotextile reinforcement with dry conditions of the gypseous soil model. In every case of test, the gypseous soil was put in layers with 5 cm depth. The raining technique measured the position of density. The gypseous soil was placed guardedly on two opposite sides to guarantee a matching density. After setting the final layer, leveled the surface carefully within the straight edge. At that point, the foundation was settled within the center of the test box in x and y trends in unpredictable loading, and after that, the two attractive holders utilizing dial gages within the edge of the box were associated. By the hydraulic jack starts applied the load constantly. The applied load was got from the load cell while the dial gauges determined the settlement. The application of load continuously until to reach the failure. The failure was exposed by the rise of settlement at a constant value of load amount. The diagram of the test setup is shown in Fig. 3.

### 3 Results and Discussion

To analyze and discuss the effect of using geotextile reinforcement in the gypseous soil under the footing, 20 model tests were carried out consisting of different patterns at the dry state of the soil. For the model tests, the soil bed was prepared with a dry unit weight of 12.84 and 14.1 kN/m<sup>3</sup> identical to a relative density of 30 and 60%, respectively. The bearing capacity tests are divided into two main groups: untreated and treated soil tests. The treated and treated soil tests involve three different categories of soil sample conditions as follows: (10) model tests using a single geotextile layer, (6) model tests using double geotextile layers, and (4) model tests using triple geotextile layers.

**Load-Settlement Results.** These results display that the performance of load–settlement relations sound to be like the general shear failure relation and refer to the soil failure. The reinforcement geotextile layers were placed at a different depth such as (0.5 B, 1B, 1.5B, and 2B) when B represented the width of footing for all model tests. The results are shown in Figs. 4 and 5 with a relative density of 30 and 60%.

#### Ultimate Bearing Capacity of Dry Gypseous Soil at Relative Density (30%).

Figures 6 explains the experimental work to determine the value of ultimate bearing capacity [untreated] at relative density (30%) by two tangent intersection methods under the square footing.

#### Ultimate Bearing Capacity of Dry Gypseous Soil at Relative Density (60%).

Figures 7 explains the experimental results for determining the values of ultimate bearing capacity [untreated] at relative density (30%) by two Tangent Intersection Method under the square footing.

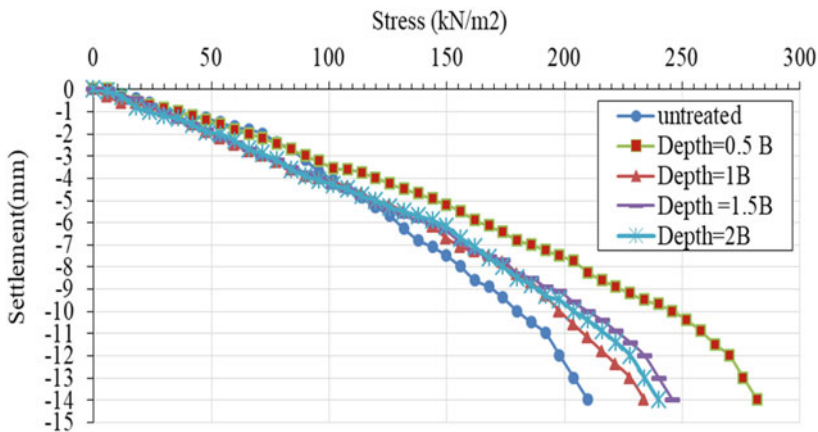


**Fig. 4** The relation between the stress and the settlement for gypseous soil in a dry state (reinforced) experimental model (single layer) at RD = 30%

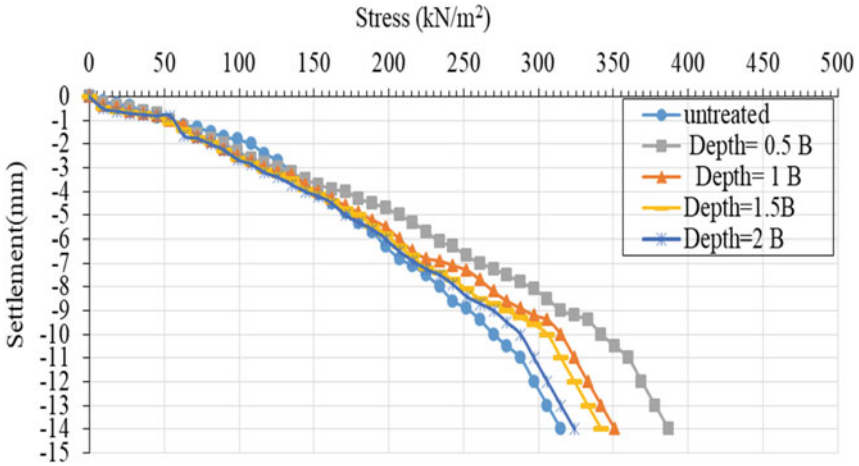


**Fig. 5** The relation between the stress and the settlement for gypseous soil in a dry state (reinforced) experimental model (single layer) at RD = 60%

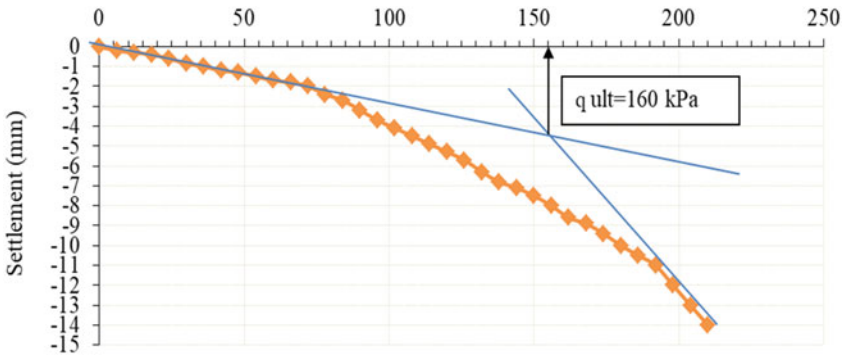


**Fig. 6** The relation between the stress and the settlement for gypseous soil in dry State experimental model Result at RD = 30% (untreated)

**Comparison of Allowable Bearing Capacity and Relative Density 30 and 60% for Dry Gypseous Soil.** Figure 8 explains the relation between allowable bearing capacity and relative density for dry gypseous soil using single-layer geotextile reinforcement. Figure 9 explains the relationship between allowable bearing capacity and relative density for dry gypseous soil when using double-layer geotextile reinforcement. Figure 10 explains the relation between allowable bearing capacity and relative density for dry gypseous soil using triple-layer geotextile reinforcement.

Tables 3 shows the results of experimental work and explains the improvement of using geotextile reinforcement on the bearing capacity of gypseous soil. The geotextile has proved it's effective in improving the bearing capacity and lowering the settlement values, see Figs. 4 and 5. Figures 8, 9 and 10 show a comparison of

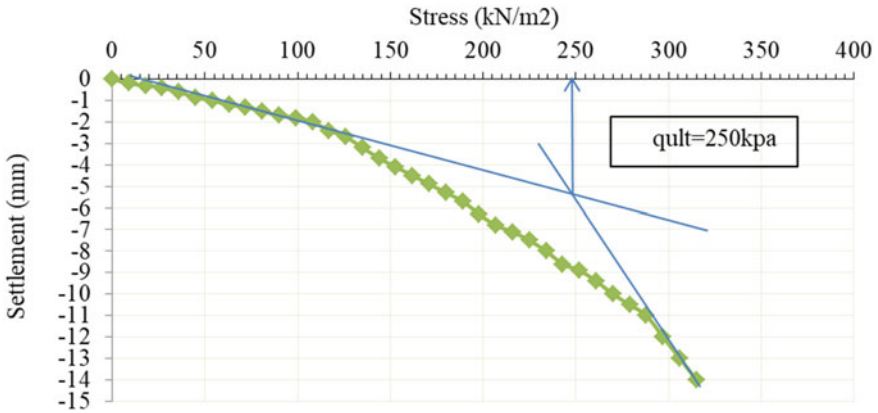


Fig. 7 The relation between the stress and the settlement for gypsum soil in dry State experimental model Result at RD 60% [untreated]

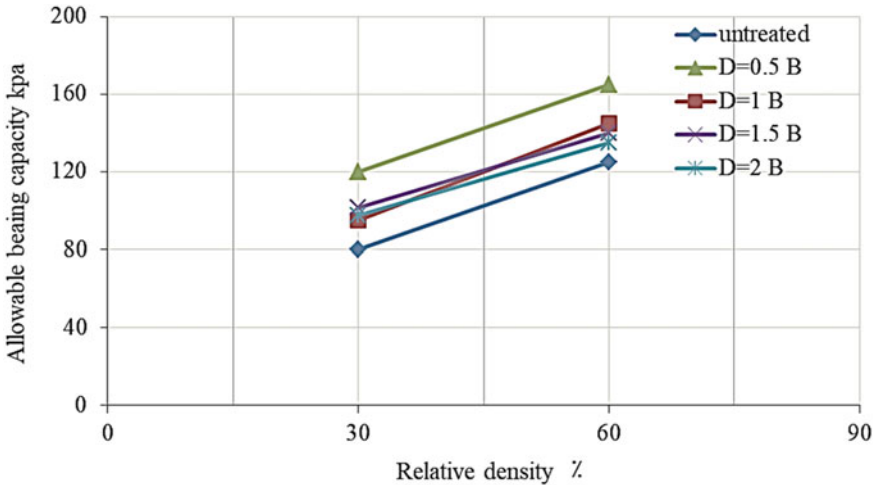
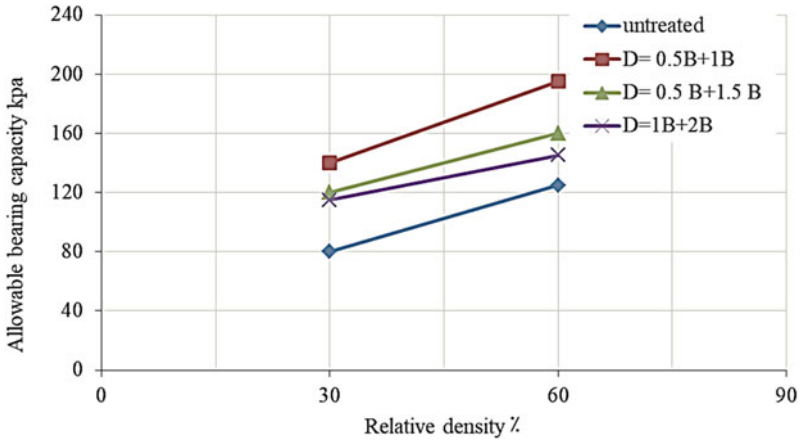
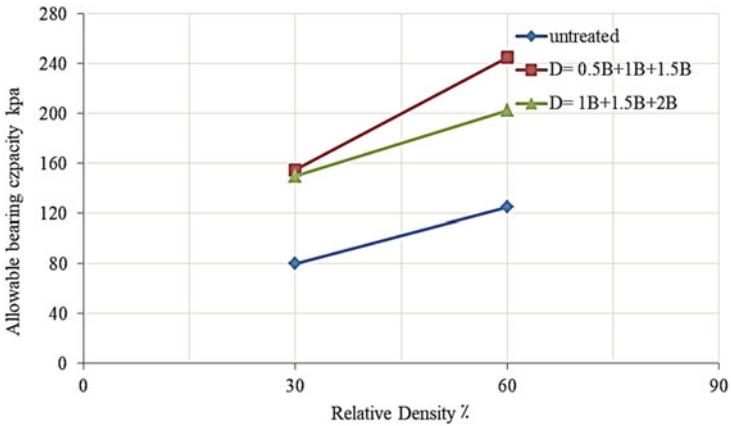


Fig. 8 Allowable bearing capacity and relative density at 30 and 60% relationship (when the dry gypsum soil model samples is treated by single layer of geotextile reinforcement)

allowable bearing capacity and relative density 30 and 60% for dry gypsum soil, the triple-layer phase pattern of geotextile reinforcement at depth (0.5B + 1B + 1.5B) gives a higher value of allowable bearing capacity equal to 155 kPa at RD (30) while equal to 245 kPa at RD (60).



**Fig. 9** Allowable bearing capacity and relative density at 30 and 60% relationship (when a double layer treats the dry gypseous soil model samples of geotextile reinforcement)



**Fig. 10** Allowable bearing capacity and relative density at 30 and 60% relationship (when a triple layer treats the dry gypseous soil model samples of geotextile reinforcement)

## 4 Conclusions

The following points can be concluded from the results of this study:

- The allowable bearing capacity of gypseous soil increase with the increase of relative density and reinforcement layers, where the allowable bearing capacity was 80 and 125 kPa at relative density 30 and 60%, respectively.

**Table 3** The values of ultimate bearing capacity for dry gypsum soil models by two tangent intersection method under square footing in the dry state at RD = 30% and 60%

Test no	Pattern	Depth of placement	RD = 30%		RD = 60%	
			q <sub>ult</sub> (kN/m <sup>2</sup> )	q <sub>all</sub> (kN/m <sup>2</sup> )	q <sub>ult</sub> (kN/m <sup>2</sup> )	q <sub>all</sub> (kN/m <sup>2</sup> )
1	Untreated	-	160	80	250	125
2	Single layer geotextile reinforcement	D = 0.5B	240	120	330	165
3		D = 1B	190	95	290	145
4		D = 1.5B	203	101.5	280	140
5		D = 2B	195	97.5	270	135
6		Double layer geotextile reinforcement	D = 0.5B + 1B	280	140	390
7	D = 0.5B + 1.5B		240	120	320	160
8	D = 1B + 2B		230	115	290	145
9	Triple layer geotextile reinforcement	D = 0.5B + 1B + 1.5B	310	155	490	245
10		D = 1B + 1.5B + 2B	300	150	405	202.5

- The reinforcement pattern, depth (i.e., position), and a number of the reinforcement geotextile layer have a large effect on the allowable bearing capacity of gypseous soil.
- For a single geotextile layer model, the maximum value of allowable bearing capacity when the reinforcement is at depth (0.5B) with  $q_{all}$  was 165 kPa at relative density 60%, while the minimum value of allowable bearing capacity when the reinforcement is at depth (1 B) with  $q_{all}$  was 95 kPa at relative density 30%.
- For the double geotextile layer model, the maximum value of allowable bearing capacity when the reinforcement is at depth (0.5 B + 1 B) with  $q_{all}$  was 195 kPa at relative density 60%, while the minimum value of allowable bearing capacity when the reinforcement is at depth (1B + 2B) with  $q_{all}$  was 115 kPa at relative density 30%.
- For the triple geotextile layer model, the maximum value of allowable bearing capacity when the reinforcement is at depth (0.5 B + 1 B + 1.5 B) with  $q_{all}$  was 245 kPa at relative density 60% while the minimum value of allowable bearing capacity when the reinforcement is at depth (1 B + 2 B) with  $q_{all}$  was 150 kPa at relative density 30%.

## References

1. Ahmad, F., Said, M. A., & Najah, L. (2012). Effect of leaching and gypsum content on properties of gypseous soil. *International Journal of Scientific and Research Publications*, 2(9), 1–5.
2. Al-Obaidi, Q. A., Ibrahim, S. F., & Schanz, T. (2013). Evaluation of collapse potential investigated from different collapsible soils. In *Multiphysical testing of soils and shales* (pp. 117–122) Berlin, Heidelberg: Springer.
3. Fattah, M. Y., Obead, I. H., & Omran, H. A. (2019). A study on leaching of collapsible gypseous soils. *International Journal of Geotechnical Engineering*, 1–11.
4. Al-Obaidi, Q. A., Karim, H. H., & Al-Shamoosi, A. A. (2020, February). Collapsibility of gypseous soil under suction control. In *IOP Conference Series: Materials Science and Engineering* (Vol. 737, No. 1, p. 012103). IOP Publishing.
5. Jha, A. K., & Sivapullaiah, P. V. (2017). Unpredictable behaviour of gypseous/gypsiferous soil: An overview. *Indian Geotechnical Journal*, 47(4), 503–520.
6. Al-Saoudi, N. K., Al-Khafaji, A. N., & Al-Mosawi, M. J. (2013). Challenging problems of gypseous soils in Iraq. In *Proceedings of the 18th International Conference on Soil Mechanics and Geotechnical Engineering* (pp. 479–482).
7. Fattah, M. Y., Joni, H. H., & Al-Dulaimy, A. S. (2016). Compaction and collapse characteristics of dune sand stabilized with lime-silica fume mix. *Earth Sciences Research Journal*, 20(2), 1–8.
8. Koerner, R. M. (2005). *Designing with geosynthetic*. 5th edn. (P. 796) USA: Pearson Prentice Hall.
9. Tawfeeq, S. S. (2009). *Performance of geosynthetics to improve gypseous soils*. Thesis, Civil Engineering Department, University of Tikrit, Iraq.

# Numerical Modeling of Circular Tunnel Alignment Under Seismic Loading



Hayder A. Al-Mirza and Mahdi O. Karkush

**Abstract** The continuous increase in population has led to the development of underground structures like tunnels to be of great importance due to several reasons. One of these reasons is that tunnels do not affect the living activities on the surface, nor they interfere with the existing traffic network. More importantly, they have a less environmental impact than conventional highways and railways. This paper focuses on using numerical analysis of circular tunnels in terms of their behavior during construction and the deformations that may occur due to overburden and seismic loads imposed on them. In this study, the input data are taken from an existing Cairo metro case study; results were found for the lateral and vertical displacements, the Peak Ground Acceleration (PGA), Arias Intensity ( $I_A$ ), and the Fourier amplitude spectrum. It was found that the vertical displacement was 26.2 mm under overburden pressure and reached 28 mm under seismic loading. These results were discussed and compared to other information and given a logical explanation based on the findings.

**Keywords** Tunnels · Alignment · Seismic loading · Numerical modeling · PLAXIS 3D

## 1 Introduction

In the middle and southern parts of Iraq, natural soil characteristics from an engineering perspective are inadequate and require additional precautions when building a superstructure or an underground structure. Recently, Baghdad has witnessed some earthquakes, so with this problem comes the necessity to do thorough studies regarding soil behavior in such conditions. The reason for that is because, in the future, one should be prepared for worst-case scenarios when designing an underground structure in such relatively weak soils. On the other hand, transportation

---

H. A. Al-Mirza (✉) · M. O. Karkush  
Department of Civil Engineering, University of Baghdad, Baghdad, Iraq  
e-mail: [h.almirza1901m@coeng.uobaghdad.edu.iq](mailto:h.almirza1901m@coeng.uobaghdad.edu.iq)

M. O. Karkush  
e-mail: [mahdi\\_karkush@coeng.uobaghdad.edu.iq](mailto:mahdi_karkush@coeng.uobaghdad.edu.iq)



infrastructures like highways, railways, and tunnels used for sanitation purposes have become a challenging topic over the years due to advancements in this field. In recent decades, there have been numerous studies on tunnels under seismic loadings, and it became more accessible with the development of software that evaluates the load-deformation of tunnels along with other parameters. Tunnels' resistance to static and seismic damage is generally dependent on a variety of factors: the overburden and seismic response of surrounding ground. In order to ensure the safety and serviceability of the underground structure, detailed design and construction procedures have to be carried out, taking into account all possible outcomes.

Although tunnels are considered a crucial part of the transportation infrastructure today, there are many problems related to the tunneling process, whether about the construction itself and its effect on the surrounding buildings or the post-construction long-term impact on tunnel parts. Most studies have showed interest in this topic whether regarding the tunnel face stability [1] or the behavior of a tunnel under deformation [2]. On the other hand, a case study of the Cairo Metro used PLAXIS 3D numerical analysis, which assumed a hardening soil model and evaluated the lateral and vertical displacements under static loading [3]. Also, a database has been created for earthquakes worldwide, documenting the effect on different tunnels and the different levels of damage from which they have suffered. Evidently, the seismic loading can really have a detrimental influence on the tunnel lining, and many factors can contribute to this, such as frequency, amplitude, and magnitude, and this influence is governed by the tunnel length, thickness, and other structural parts. Based on the previous literature, one should simulate a model and study the aforementioned factors numerically so as to evaluate this model under conditions similar to actual cases. The proposed research paper will focus on the response of tunnels under overburden and seismic loading conditions by creating finite element models of a circular tunnel, Cairo tunnel. The variables that will be assessed, as mentioned earlier, include the tunnel face stability during construction and the magnitude of the earthquake, its amplitude and frequency, and their effect on circular tunnels. This paper will consist of the impact of vertical propagation of seismic waves and the overburden loadings on the tunnel. The resulting displacement from these loadings will also be discussed in detail in the following sections.

## **2 Alignment of Tunneling**

According to King and Kuesel [4], the governing factors that determine the tunnel's feasibility and route include the soil's geological conditions, cost, and construction time. The types of tunnels can be classified based on purpose, alignment, and shape. The geometry is different from one tunnel to another based on its purpose as prescribed by the American Association of State Highway and Transportation Officials (AASHTO). A two-lane highway tunnel should be 3.5 m wide each, while the right shoulder should provide a sufficient area for disabled vehicles and the left

one should provide a space for motorists. Additionally, trunk highway tunnel’s clearance should be at least 4.5 m with additional vertical clearance for traffic lights and signs, ventilation systems, and lighting. Table 1 shows the relationship between the construction method and the tunnel shape [5].

**Tunnel Face Stability.** One of the most crucial factors that should be looked into when constructing a tunnel in weak soils is the tunnel face’s stability. According to Broere [6], despite the support type used in the process, the boring machine chamber pressure should be kept at a certain level to ensure stable working conditions. This means that the pressure should not be so high that deformation happens in the soil, nor should it be so low that uncontrolled collapse occurs. During the process of validating the failure assumptions, Broere [6] has carried out laboratory tests to distinguish the failure mechanisms in clay and sand, and the finding was so distinct because, in the sand, the failure takes the shape of a chimney while in clay it is much larger and broader.

**Time and Cost-Related Problems.** One of the main problems related to tunnel construction projects is that they substantially cost more than open highways or railways because these kinds of projects require extensive investigations and design criteria. Paraskevopoulou and Benardos [7] have investigated 258 projects in 20 countries, and they have found that one major problem in these projects is the cost underestimation and that 90% of these projects have exceeded their initial estimation regarding the cost. When it comes to time consumption, these projects during their various stages will consume time because each stage requires additional work due to many uncertainties to achieve the required goal instead of conventional projects.

**Tunnel Convergence.** Advancing in tunnel excavation will create pressure on the surrounding soil, and this soil will undergo deformation due to this advancement. This phenomenon is called "convergence" and it requires field and numerical analyses to be fully understood.

**Squeezing Ground.** According to Schubert and Radonicic [8], the term "squeezing ground" refers to the deformation occurring in zones with high overburden pressure, which is generally encountered either during the construction of the tunnel or afterward. Whether the tunnel is constructed in rock or weaker soils, the lining should be allowed for specific strains. Due to the difficulty of predicting the ground conditions,

**Table 1** Tunnel type versus construction method

Construction Method	Rectangular	Circular	Horseshoe	Oval
Shield-driven	*	*		
Cut-and-cover	*			
Immersed Tube	*			
Drilling and Blasting			*	*
Sequential Excavation			*	*

it is imperative to adjust the excavation process and support method by using monitoring techniques for the displacement to understand better the mechanical processes happening around the tunnel.

### 3 Seismic Loading

This field of study is a crucial part of geotechnical engineering and plays an essential role in civil infrastructure nowadays because it involves studying the design for overburden loads and seismic conditions as an additional load. With the increasing population rate, tunnels have become an essential aspect where they are used for transportation means. Until recently, the soil-structure interaction was not considered a significant problem and was not given the needed attention because, in general, the embedded structures have performed well under seismic conditions compared to superstructures. But post-earthquake investigations have shown that tunnels tend to be susceptible during earthquakes or even collapse if seismic design requirements are not met. To better comprehend tunnels stability, one should assess the factors that include peak acceleration and velocity, magnitude and duration of the earthquake, the shape of the tunnel, overburden pressure, and soil type. Underground structures behavior is quite different from that of above-ground structures because the former suffers from kinematic loads of ground rather than the underground structure's inertial loads. As previous earthquakes have proven, tunnels seismic response is highly dependent on the soil-structure interaction (SSI). This leads to the conclusion that the depth, shape, and dimensions of the tunnel, relative stiffness of soil to the tunnel, properties of the ground itself and its seismic response, and the interface, play a significant role in the seismic design of tunnels. Concerning the intensity of earthquakes near Baghdad, Al-Taie and Albusoda [9] investigated the Halabja earthquake case study. They found that some earthquakes have been observed in the last few decades in Baghdad that have caused some damages to structures in the vicinity, as shown in Table 2.

**Table 2** Earthquake intensity in Baghdad and the vicinity

Year	Earthquake Richter scale	Observations
1960	Max. 6.7	Caused damages in Halabja and felt in Baghdad
1967	6.1	Observed 100 km south of Halabja
2013	5.1 and 5.8	The two earthquakes were 60 km south of Halabja
2017	7.3	30 km south of Halabja with a maximum earthquake magnitude of 7.3
2018	Max. 4.5	Maximum magnitude was 4.5 in the Northeastern part of Baghdad
2021	4.9	Recorded in Baghdad. (Source: earthquaketrack.com)

## 4 Numerical Modeling

Because soil-structure interaction representation in an underground structure is somewhat complex and requires a substantial amount of money and time, numerical modeling was always used for this purpose. There are plenty of methods to analyze a tunnel to get the needed relationships, whether regarding the tunnel's deformed shape or the stresses and displacements. These methods include the finite element (FEM), discrete element (DEM), boundary element (BEM), and finite difference method (FDM). FEM is used extensively in engineering applications and can be represented either by using 2-dimensional or 3-dimensional software, and this representation takes the body as elements and analyzes them accordingly. According to Pradhan and Chakraverty [10], it is used for various applications, whether for structural analyses or soil modeling. Hutton [11] defines it as a computational method whose purpose is to find an approximate solution in boundary value problems. To simplify it even further, it allows the continuum to be modeled and separated into a finite number of elements, studies their characteristics, and then assembles these elements to estimate the continuous domain's properties. The implementation of FEM has been developed over the years and is being used rigorously in engineering and applied sciences applications [12]. In this paper, an FE model for the soil and the circular tunnel was created using PLAXIS 3D software, and overburden and seismic loading states were simulated. First, the soil body was defined with 60 m width, 10 m length, and 35 m depth, and a borehole was created in four different layers, each with distinct soil characteristics and depth [3].

It is worth mentioning that the tunnel lining was given properties equivalent to the adjacent soil, and the cohesion for the 4th soil layer was given a value so that the tunnel would not collapse during the tunneling process (see Table 3). The second step was creating the tunnel at a depth of 10 m using the tunnel designer tool in the software with a diameter of 9.4 m, and properties were given for TBM shield as shown in Table 4. The interface between the soil and structure was also created and given a virtual thickness factor of 0.1 for the tunnel lining to assume a case of full-slip boundary conditions in order to consider an infinite domain. After that, the trajectory was defined at 10 m segment length with slices of 1 m each and using the TBM excavation method; four steps were created for tunnel crown and invert excavation process and lining application. Also, the seismic load was applied in the x and z directions with a load multiplier of frequency of 5 Hz as stated in El-Naggar and Bentley [13]. Moreover, a finely distributed element mesh was generated, and the water table was set at 2 m below the surface as assumed by El-Nahhas et al. [3] (see Fig. 1).

Using Python script as the tunnel advancement tool, the tunnel took 12 phases for the excavation and TBM shield installment using TBM sequence, and during this advancement the failure criterion was the soil collapse potential. Moreover, one additional phase was added for applying the seismic load in the x-direction and one phase for the same load in the z-direction. The seismic load was simulated in phases 13 and 14 with 0.5 s dynamic time interval, and the displacement was dependent on

**Table 3** Soil properties in HS material model

Parameter	1st layer	2nd layer	3rd layer	4th layer	Unit
Material model	HS	HS	HS	HS	–
Material behavior	Drained	Drained	Drained	Drained	–
Depth	3	1.5	5	25.5	m
Unsaturated unit weight	17	18	19	20	kN/m <sup>3</sup>
Saturated unit weight	17	18	19	20	kN/m <sup>3</sup>
Cohesion	0	80	0	25	kPa
Internal friction	15	0	30	37	°
Secant triaxial test stiffness	7230	9100	20,310	35,430	kPa
Tangent stiffness	7230	9100	20,310	35,430	kPa
Unreload/reload stiffness	21,680	27,300	60,930	106,290	kPa
Shear modulus at small strain	37,500	59,340	116,210	170,590	kPa
Shear strain at $G_s = 0.722G_o$	1.61E-04	5019E-04	2.79E-04	4.52E-04	–
Power for stress law	0.5	1	0.5	0.5	–
Reference stress	100	100	100	100	kPa
Poisson's ratio	0.2	0.2	0.2	0.2	–
Coefficient of lateral stress	0.74	1	0.5	0.4	–
Failure ratio	0.7	0.75	0.8	0.8	–
Interface strength	Rigid	Rigid	Rigid	Rigid	–

**Table 4** TBM shield material properties

Parameter	TBM	Unit
Thickness	0.14	m
Unit weight	70	kN/m <sup>3</sup>
Elasticity modulus	$26 \times 10^7$	kPa
Poisson's ratio	0.3	–
Shear modulus	$10^8$	kPa

the tunneling process's previous phases. The model used for analysis was Paradiso multicore direct with maximum cores of 256, 1000 maximum number of steps, and 60 maximum number of iterations allowed with 0.01 tolerated error. The results of settlement under the overburden, excavation, and the seismic pressures will be discussed in the next section.

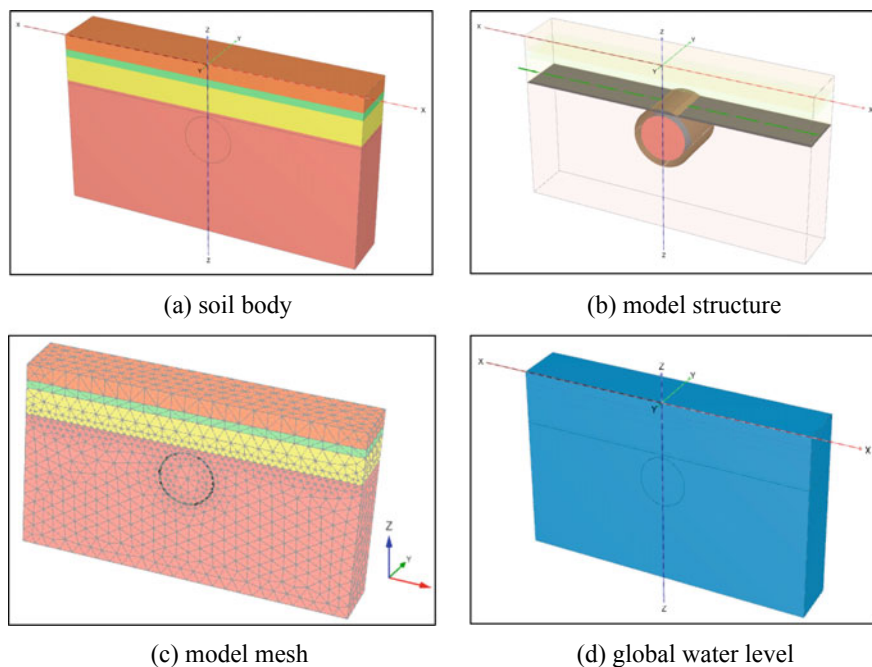


**Fig. 1** PLAXIS 3D FE model of the case study

## 5 Results and Discussion

Starting with Phase 1 to excavate the upper half of the tunnel portal in the first slice, the total displacement was approximately 8.5 mm at the tunnel portal crown. When the lower half of the first slice was excavated the settlement almost doubled and reached 15.5 mm. The tunneling process started to increase until Phase 12, where the settlement reached a maximum of 26.2 mm at the same location. This phase was verified with the Cairo metro [3], a maximum vertical displacement of about 20 mm. Also, this phase was the end of the tunneling process and the applied overburden pressure on the tunnel and can be represented in Fig. 2.

The next phase which is additional to the research this paper was verified with included the seismic load in the x-direction resulted in a maximum of 1.35 mm and minimum -0.55 mm lateral displacements at the tunnel portal crown. On the other hand, the last phase was applying the load in the z-direction, and the maximum vertical displacement was 28 mm. Figures 3 and 4 show the lateral and vertical displacements versus the portal's dynamic time, 2.5 m and 5 m away from the portal on the upper part of the tunnel shield during Phases 13 and 14, respectively. The negative and positive values represent the direction of the lateral displacements during seismic loading.

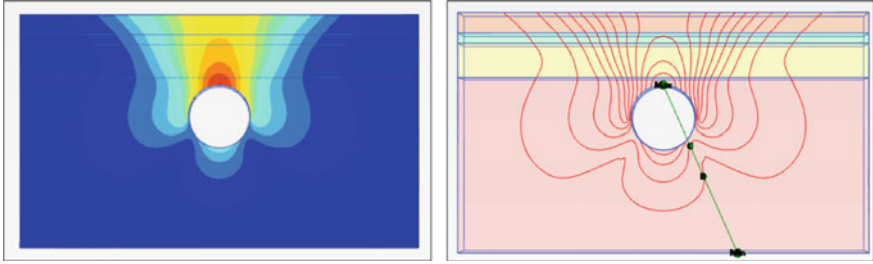


Fig. 2 Vertical displacement in phase 12

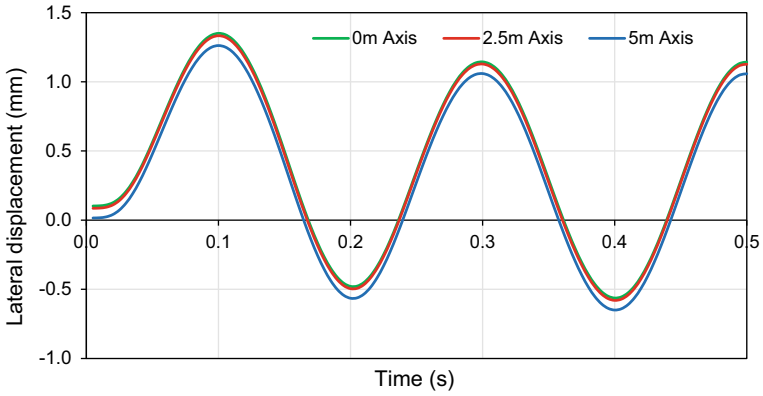


Fig. 3 Variation of lateral displacement with time at tunnel axis

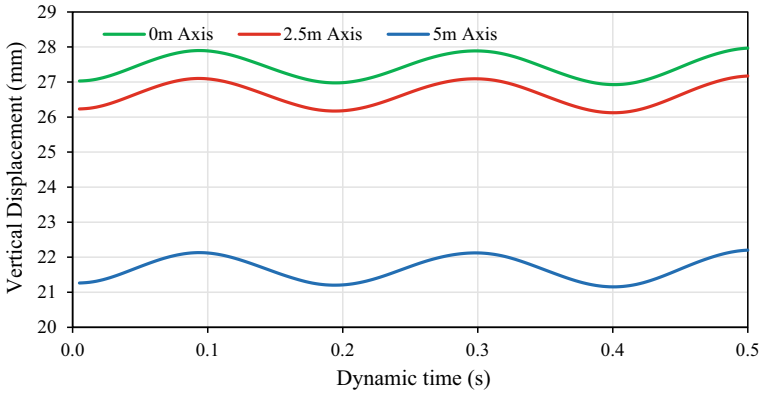


Fig. 4 Variation of vertical displacement with time at tunnel axis

It can be observed that the displacements in the x-direction along the tunnel were approximately the same, while the displacements in the z-direction are at their peak at the tunnel portal and keep decreasing until reaching the end of the tunnel. Furthermore, Figs. 5 and 6 depict the displacements on the tunnel shield's side with the same distances as before.

By comparison with Figs. 3 and 4, one can see that the lateral displacements increase on the tunnel side to reach approximately 8.46 mm while the vertical displacements decreased to reach 18 mm on the side compared to 28 mm on the top. Concerning the PGA, the highest observed value in Phase 13 was 0.45 g, while in Phase 14, it was 0.553 g at node 13,059 on the surface of the first soil layer, but it decreases with increasing the depth of the soil layers (see Fig. 7). Furthermore, Figs. 8 and 9 were obtained at the top of the acceleration tunnel in terms of gravitational acceleration versus the dynamic time ranging (0–0.5 s). It can be observed that

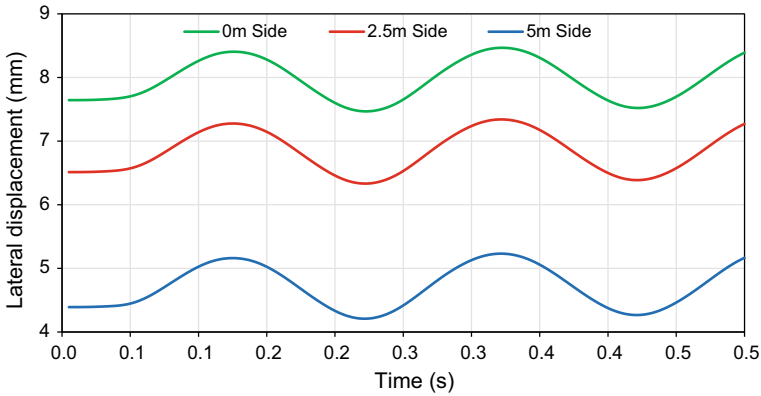


Fig. 5 Variation of lateral displacement with time on tunnel side

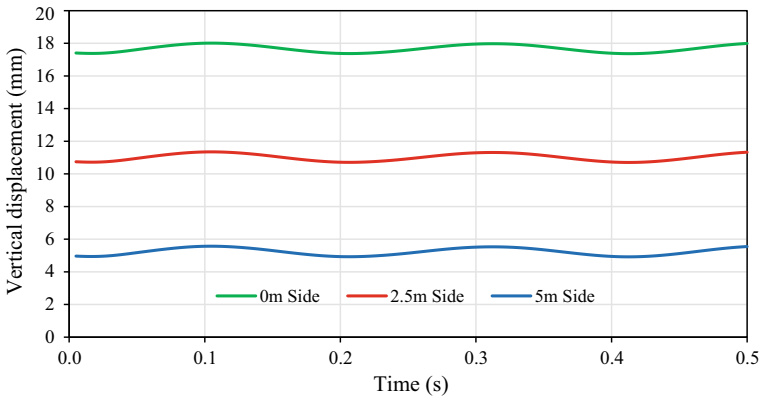


Fig. 6 Variation of vertical displacement with time on tunnel side



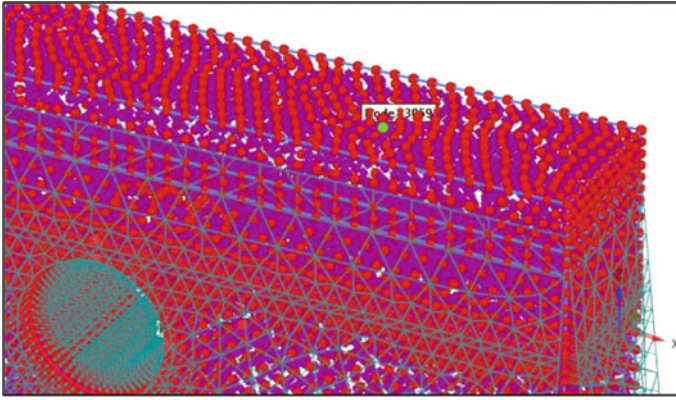


Fig. 7 PGA at Node 13,059 on the soil surface

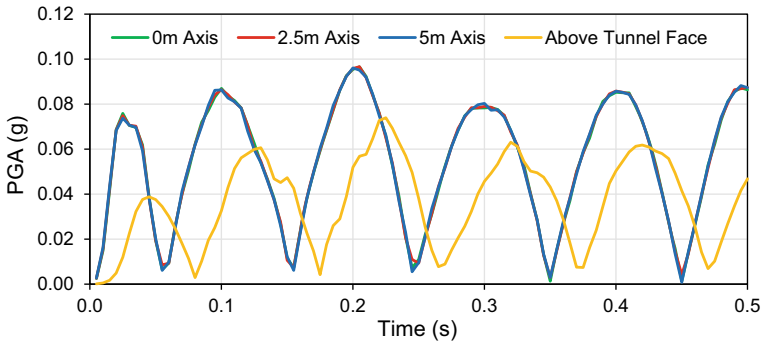


Fig. 8 Variation of PGA with time on tunnel axis Phase 13

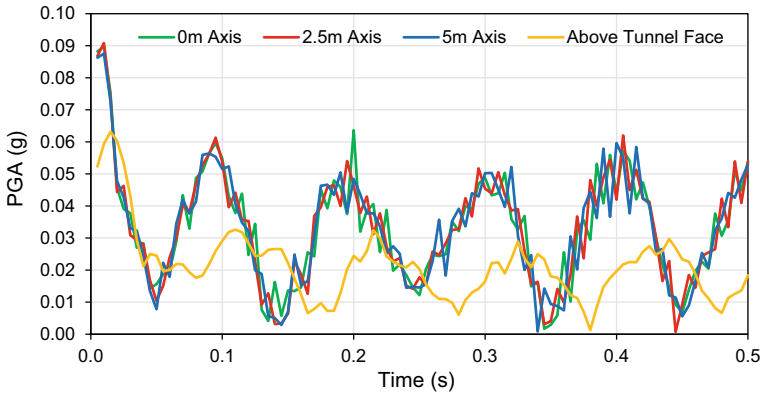
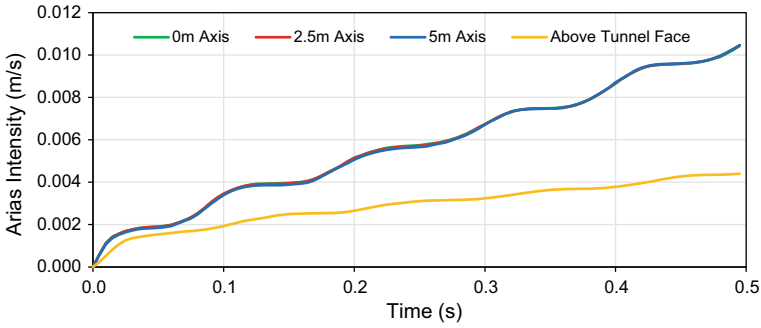


Fig. 9 Variation of PGA with time on tunnel axis Phase 14



**Fig. 10** Variation of Arias intensity with time on tunnel axis

the acceleration reaches its peak value at the portal crown and begins to decrease in other sections along the tunnel.

To check the intensity of the ground motion in the FE model using seismic parameters, the Arias intensity ( $I_A$ ) was obtained as shown in Fig. 10.

According to (Earthquaketrack.com), there was only one recorded earthquake activity in the Mayoralty of Baghdad for the first three months in 2021 on a moment magnitude scale ( $M_w$ ) of 4.9. When comparing the obtained Arias Intensity data with the Levkaz Island earthquake in 1992, which has recorded ( $M_w = 4.6$ ), the same result for ( $I_A = 0.0105$  m/s) has been obtained. On the other hand, the Fourier amplitude spectrum for the seismic phases was also obtained, and the following amplitude versus frequency curves was generated. These curves show that the highest amplitude observed in terms of acceleration was (0.652) at zero frequency for the nodes along the tunnel top. However, the amplitude was (0.422) for the node above the tunnel face for the same frequency, and all curves start to decrease as the frequency increases, as shown in Fig. 11.

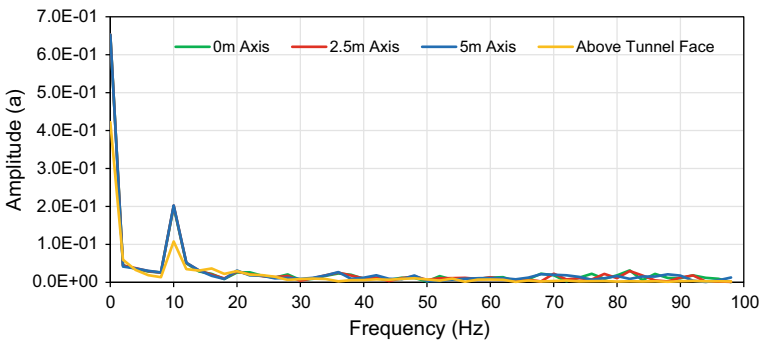


**Fig. 11** Fourier amplitude spectrum

## 6 Conclusions

Numerical analysis using the finite element model was carried out in order to understand the behavior of a circular tunnel under the overburden and seismic loads. The results were obtained from this analysis, including the lateral and vertical displacements, PGA of the seismic case, Arias Intensity, and the Fourier amplitude spectrum. The findings were as follows:

- As the tunneling process commences, the vertical displacement was 8.5 mm and kept increasing until it reaches 26.2 mm at the end of this process.
- The tunnel face stability was maintained during the tunneling process since there was no soil collapse nor there was load advancement failure.
- The lateral displacement in Phase 13 had a maximum value of 1.35 mm and a minimum value of -0.55 mm while the vertical displacement was 28 mm maximum.
- The highest PGA was 0.45 g in Phase 13 and 0.55 g in Phase 14 on the first layer's surface, and it was at its highest at the first slice concerning the tunnel.
- The obtained Arias intensity was 0.0105, which is typical compared to the seismic activity in Baghdad.
- The Fourier amplitude spectrum showed a maximum value at the tunnel top 0.652 and 0.422 at a node above the tunnel face.

## References

1. Zhang, F., Gao, Y., Wu, Y., & Wang, Z. (2018). Face stability analysis of large-diameter slurry shield-driven tunnels with linearly increasing undrained strength. *Tunneling and Underground Space Technology*, 78, 178–187.
2. Paternesi, A., Schweiger, H. F., & Scarpelli, G. (2017). Numerical analyses of stability and deformation behavior of reinforced and unreinforced tunnel faces. *Computer and Geotechnics*, 88, 256–266.
3. El-Nahas, F. M., El-Mossallamy, Y. M., & El-Shamy, A. A. (2015). 3D analysis of ground settlement induced by mechanized tunnelling. In *14th International Conference on Structural and Geotechnical Engineering*, Ain Shams University, Egypt.
4. King, E. H., & Kuesel, T. R. (1996). *Tunnel layout BT—Tunnel engineering handbook* (pp. 4–12). Springer.
5. Balasubramanian, A. (2014). *Tunnels-types and importance. Technical report*. Centre for Advanced Studies in Earth Science, University of Mysore, March.
6. Broere, W. (2002). *Tunnel face stability and new CPT applications*.
7. Paraskevopoulou, C., & Benardos, A. (2013). Assessing the construction cost of Greek transportation tunnel projects. *Tunnelling and Underground Space Technology*, 38, 497–505.
8. Schubert, W., & Radonic, N. (2015). Tunnelling in "squeezing" ground conditions—problems and solutions. In *13th ISRM International Congress of Rock Mechanics. International Society for Rock Mechanics and Rock Engineering*.
9. Al-Taie, A. J., & Albusoda, B. S. (2019). Earthquake hazard on Iraqi soil: Halabjah earthquake as a case study. *Geodesy and Geodynamics*, 10(3), 196–204.
10. Pradhan, K. K., & Chakraverty, S. (2019). Chapter four—Finite element method. In *Computational structural mechanics* (pp. 25–28). Academic Press.

11. V Hutton, D. (2003). *Fundamentals of finite element analysis*. McGraw-Hill Education.
12. Rao, S. S. (2017). *The finite element method in engineering*. Butterworth-Heinemann.
13. El-Naggar, M. H., & Bentley, K. J. (2000). Dynamic analysis for laterally loaded piles and dynamic p-y curves. *Canadian Geotechnical Journal*, 37(6), 1166–1183.

# Triaxial Compression Behavior of Sandy Soil Polluted with Crude Oil



Farman K. Ghaffoori, Mohamed M. Arbili, Hanifi Çanakcı,  
and Talib K. Ibrahim

**Abstract** This study aims to use a series of laboratory tests to analyze the geotechnical behavior of oil-contaminated sandy soil, including compaction and triaxial compression tests. In assessing an engineering problem, shear strength can be seen as a geotechnical property of soil. Therefore, the purpose of using the triaxial test on the polluted soil is to investigate the shear strength of the soil due to the appearance of the crude oil contaminated. Polluted samples were prepared with the addition of 0, 4, 8, 12, and 16 percent of crude oil and tested after 14 days. The series contains clean and contaminated soils that have been compacted at optimum moisture content. Results show that shear strength decreased with an increased percentage of crude oil. The maximum value of cohesion obtained at 8% was 62 kPa.

**Keywords** Contamination · Triaxial test · Compaction · Crude oil · Sandy soil

## 1 Introduction

Soil pollutes by leaking crude petroleum affects the mechanical and physical properties of soil. [1, 2] observed the influence of crude oil pollution on the geotechnical characteristic of soils and showed that the soil's plasticity index and compression parameters decreased when its strength increased.[3] have shown that the fraction of

---

F. K. Ghaffoori  
Ministry of Municipality and Tourism, Erbil, Kurdistan Region, Iraq

M. M. Arbili (✉)  
Department of Information Technology, Choman Technical Institute, Erbil Polytechnic  
University, Erbil, Iraq  
e-mail: [mohamed.arbili@epu.edu.iq](mailto:mohamed.arbili@epu.edu.iq)

H. Çanakcı  
Department of Civil Engineering, Hasan Kalyoncu University, Gaziantep, Turkey  
e-mail: [hanifi.canakci@hku.edu.tr](mailto:hanifi.canakci@hku.edu.tr)

T. K. Ibrahim  
Department of Petroleum Engineering, College of Engineering, Knowledge University, Kurdistan  
Region, Iraq  
e-mail: [talib.ibrahim@knu.edu.iq](mailto:talib.ibrahim@knu.edu.iq)

clay tends to be higher in heavily polluted specimens when their liquid limits have increased with increased oil contamination. Depending on the triaxial test, the parameters of shear strength (cohesion  $c$  and internal friction angle  $\phi$ ) can be obtained and is the most common test technique used to evaluate oil-polluted sands' mechanical properties. Khamehchiyan et al. [4] studied two cases of initial relative density for the sandy soil sample (dense and loose) as well as two liquids for saturation (oil and water). All samples were consolidated and sheared under triaxial compression conditions up to approximately 20% of the axial strain. Rahman et al. [5] observed triaxial compression tests using a constant relative density of 60 percent in all tests, and oil saturation in the specimens was equivalent to soil contaminated with 6 percent of heavy crude oil.

Ghadyani et al. [6] used an undrained triaxial test on contaminated quartzite containing 60 g/kg of heavy petroleum at different temperatures and on non-polluted quartzite at room temperature, utilizing a triaxial cell to enhance the testing procedure at controlled temperatures. The soil samples were prepared in the triaxial cell on a rubber diaphragm stretched thinly on a mold and compacted to the optimum dry density using vibrations under a surcharge. Many researchers dealt with utilized mixtures of mica and sand and showed the enormous effect of particle shape on the mechanical properties. Ratnaweera and Meegoda [7] conducted various fines content with its effects on triaxial behavior of a coarse Leighton Buzzard sand. It could be useful in many geotechnical and geoenvironmental engineering problems.

## 2 Materials and Preparation of Samples

The soil used in this investigation was sandy soil and obtained from Erbil Province. The most common type of sand occurring in non-tropical and tropical environments is silica in quartz [8]. Calcium carbonate (aragonite), the second most common variety, was formed around half a billion years ago by organisms including shellfish and coral. A hydrometer and sieve analysis was used to analyze sand's particle size distribution (ASTM D421-58 and ASTM D422-63). Figure 1 shows the sand's grain size distribution curve. The sand sample had a specific gravity of 2.619 (Gs). According to the USCS classification system, the soil was categorized as SM.

Crude oil was polluted in this study. It is a liquid form of petroleum that occurs naturally and is derived from the earth in its liquid state. It is mainly made up of hydrocarbon compounds. Based on the most available category of hydrocarbons present, crude petroleum may be classified as naphthenes base, paraffin base, or mixed base. The crude oil used in this analysis came from the refinery of the Kar in the oilfield of Khurmala in Erbil province. Table 1 shows the characteristics of crude oil.

**Preparation of Specimen.** The samples were of sandy soil. It was gotten from a 50 cm depth from the upper layers to eliminate the mixing of specimens. Firstly, soil samples were collected and passed through a sieve of 4.75 mm diameter (#4). After

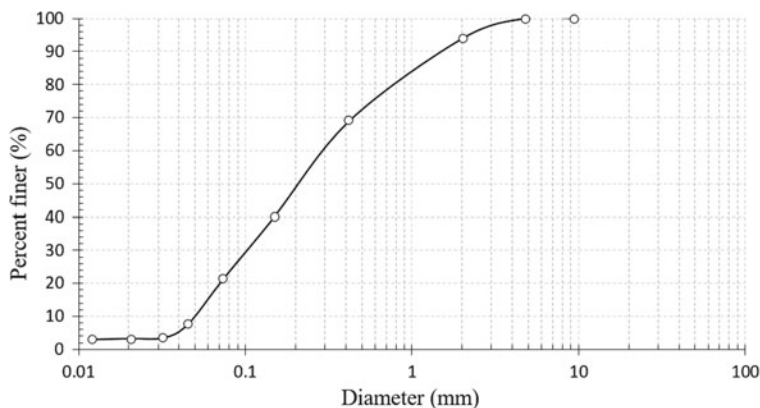


**Fig. 1** The grain size distribution curve

**Table 1** Crude oil properties

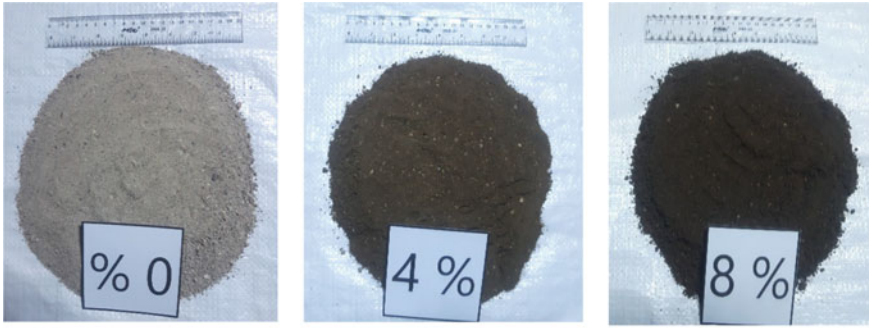
#	API°	Flash point °C	Viscosity (Cp)	Density @ 25 °C (g/cm <sup>3</sup> )
Refinery (kar)	23.26	52.9	18.21	0.8489

that, the soil samples dried in the oven, and then the specimens were mixed with crude oil by the following percentages of their dry weight 4, 8, 12, and 16% put in the closed container for 14 days. All the contaminated and clean soil samples were demonstrated in Fig. 2a, b. This whole exercise was done in the laboratory.

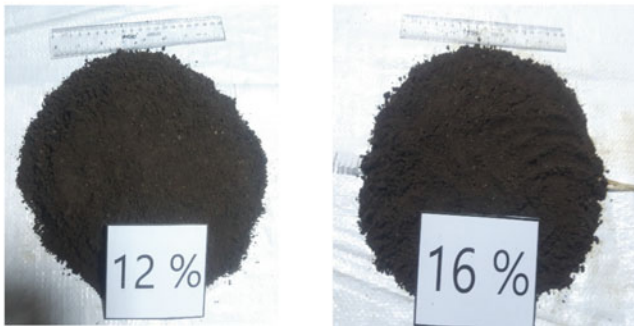
### 3 Experimental Work

**Compaction.** A compaction test was applied on the soil samples to obtain the maximum moisture content and maximum dry density. A Proctor test was used to find the properties of the compacted material. This test was created by Proctor in 1993 and was linked to the construction of earth-fill dams in California [9]. The agreed sizes of the equipment used in this investigation were determined using Method-A of ASTM D-1557. The soil was blended with normal water content, and the mixture was then put in a compaction specimen with a capacity of  $9.438 \times 10^{-4} \text{ m}^3$ . The mold was filled in five layers and then compacted each layer with a sheet receiving 25 blows from a height of 457 mm with a 44.5 N hammer.

**Triaxial Tests.** To find the shear strength of the soil specimen for this study by utilizing the UU unconsolidated undrained triaxial test. UU triaxial compression tests were carried out on contaminated and uncontaminated sand specimens prepared according to the procedures outlined in the preceding section to determine the shear



(a) soil sample with ( 0%, 4, and 8%) crude oil.



(b) soil sample with ( 12 and 16%) crude oil.

**Fig. 2** Sandy soil with different percentages of oil

behavior of the sand. The drainage valve to the specimen was closed for undrained tests. The loading ram has been brought into just above the specimen, then zero of the external LDS and proving ring were set. The compressive load was applied using a strain-controlled load frame. The rate of loading of 0.15 mm/min for unconsolidated undrained tests was used. Figures 3 and 4 showed the sketch of the triaxial testing system setup. The specimen is contaminated, and the container tension ( $\sigma_3$ ) is utilized without draining or consolidation (drains were closed for the entire test duration). The confining pressures used for the tests were (50, 100, and 200) kPa. The degree of saturation on the triaxial test samples in compacted specimens was less than 100%. During the shear test, the data was governed by ten second-logging rates. For each logging, the measurements of deviatoric load, external axial deformation and volume change were recorded. Triaxial specimens were sheared until an axial strain of 15% had been reached.



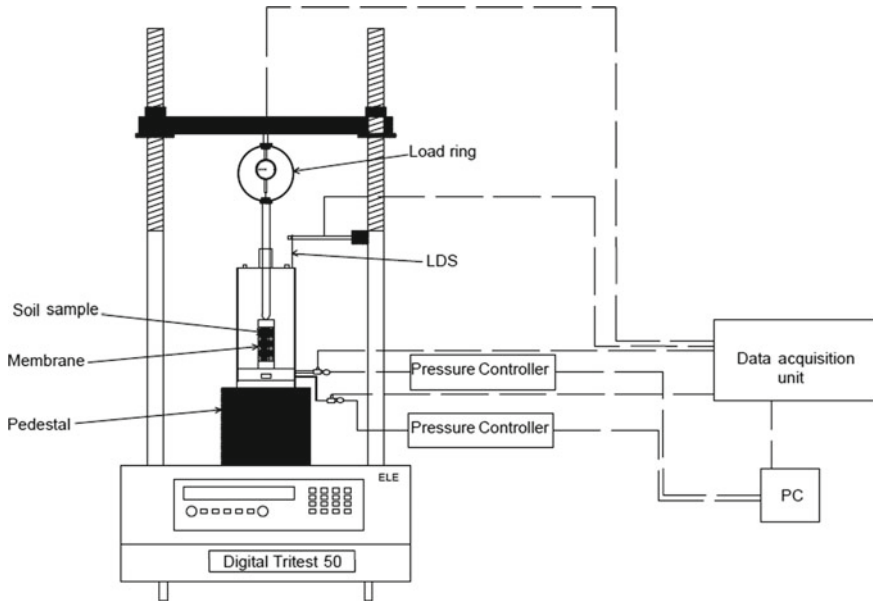


Fig. 3 Triaxial testing system setup sketch

## 4 Results and Discussion

Compaction is the method of using mechanical energy, such as vibration, tamping, and rolling, to maximize soil density by reducing air voids. Compaction is used to improve the engineering characteristics of the soil. The key criteria for compaction properties of soil are optimum moisture content and maximum dry density. Artificially processed specimens with a crude oil content of (0, 4, 8, 12, and 16%) were subjected to compaction checks. Figure 5 shows the impact of the polluted (crude oil) on the compaction parameters.

The overall dry density decreases as the proportion of crude oil content increases, as seen in Fig. 5. Since the pore spaces in sand soil samples are wider, crude oil could flow in the soil particles at a similar rate as water and has the same lubricating impact. The capillary tension effect [4] can be due to the reduction in dry unit weight with an increase in oil content. Capillary tension in the water reduces the ability of soil particles to move about and be tightly compacted. The surface tension of electrolytes and the angle of contact have a significant impact on capillary tension. Since oil has a hydrophobic property, it prevents water from coming into contact with soil particles. As a result, as the crude oil content of soil samples increases, the capillary tension force decreases [10]. This is due to the lubricating effect of the oil, which aids compaction and reduces the volume of water needed to achieve optimum density. Another cause may be crude oil's waste of compaction capacity. Since crude oil has a higher viscosity than water, it needs more compaction energy to increase



Fig. 4 The triaxial cell and was assembled and filled with water

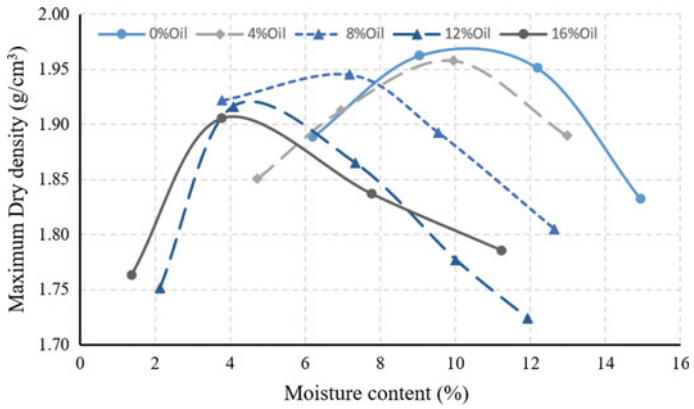


Fig. 5 Curves of compaction for soil samples

the strain between the molecules. As a result, it consumes more steam, allowing the soil texture to increase.

The stress path space graph of the uncontaminated sand specimen's in UU condition for sand specimens in three confining pressures is illustrated in Fig. 6. In this Figure,  $q$  represents the deviatoric stress, and  $p$  represents mean effective stress. It is observed that the change in the confining pressure significantly influences the behavior of the clean sandy soil samples. Figure 6 shows the variation of the stiffness of uncontaminated sand specimens with the axial strain for specimens sheared under different confining pressure. In general, the uncontaminated sand stiffness

**Fig. 6** Stress–strain behavior of sandy soil with different ratios of crude oil in three different confining pressures

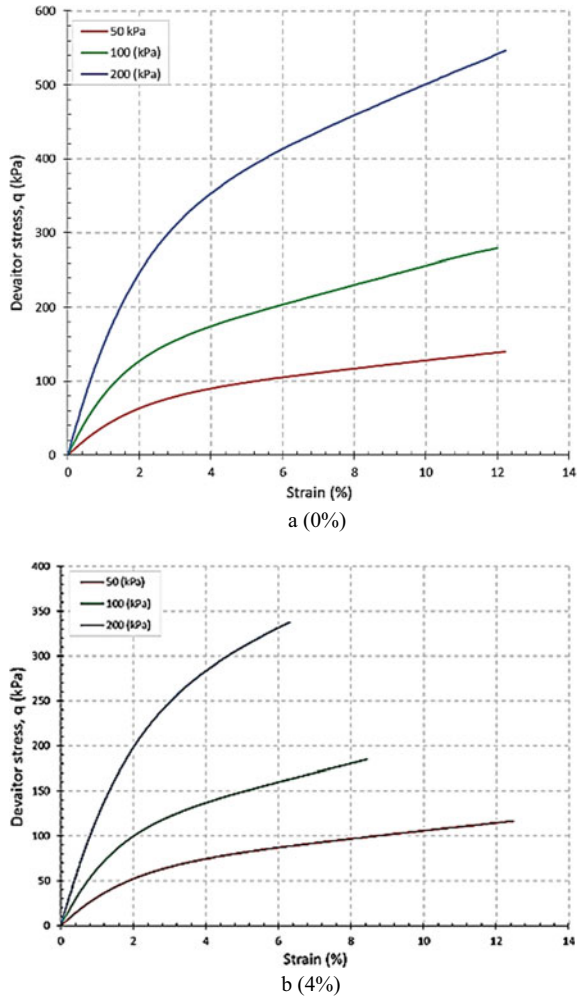
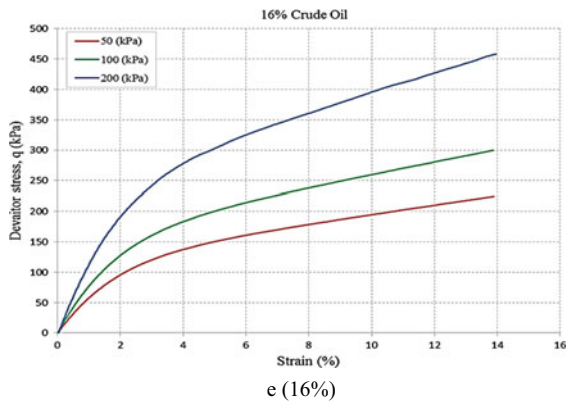
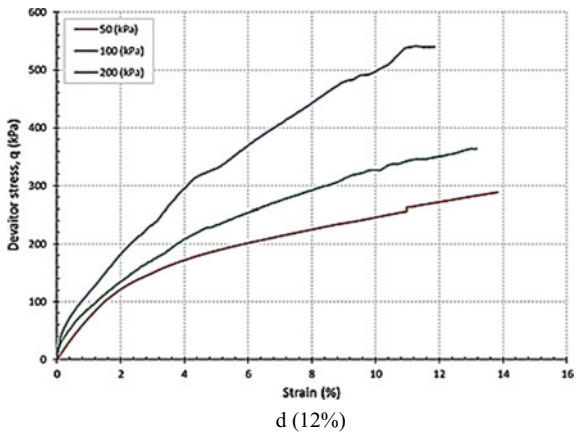
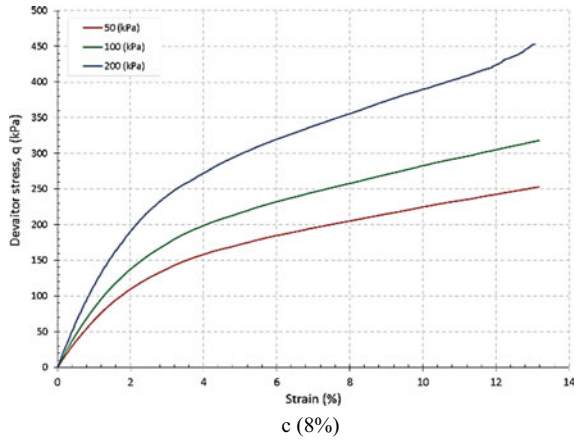


Fig. 6 (continued)



**Table 2** The angle of internal friction and cohesion values from the triaxial test with different crude oil content ratios of sandy soil sample

% Crude oil	c (kPa)	$\varphi$ (degree)
0	0	36.2
4	19	23.9
8	62	23.7
12	61	27.4
16	43	26.6

was degraded as the axial strain increases. The specimens that were sheared at high confining pressure have higher stiffness values than the specimens at low confining pressure. The Mohr circles and failure envelopes of the uncontaminated sands are presented in Fig. 6. The failure envelope and angle of the internal friction were determined for specimens in UU condition based on total stress. However, in the results based on total stress, no value for the cohesion appeared. The results showed that the value of the angle of internal friction equal to 36.2°. Similar observations were made by many researchers [11–16].

The influence of the crude oil on the Mohr circle and the parameters of shear strength are based on total stresses. Contamination of sand specimens with different percentages of crude oil influences the Mohr circles and their parameters. The samples were mixed artificially with crude oil in the amount of (4, 8, 12, and 16%) by dry weight of the soil samples. A series of unconsolidated undrained triaxial tests were aimed from one hand to find the angle of internal friction and cohesion of contaminated soil specimens. On the other hand, the tests were directed to compare the results with different percentages of crude oil content. Results (as shown in Table 2) exhibit increase cohesion to the peak value in 8 percentage crude oil content after that cohesion of the contaminated samples become lower. The angle of internal friction decrease with increases in oil content. Similar results were found by [17], who determined strength parameters for clean and contaminated sands angle of internal friction and cohesion. It demonstrated a decrease in the friction angle due to oil contamination.

## 5 Conclusions

The outcome obtained from this research listed as below:

- The viscosity of the crude oil higher than of water requires more effort of compaction energy to increase the strain between the molecules. As a result, it consumes more steam, allowing the soil texture to increase.
- Under increasing levels of crude oil pollution, the maximum dry density indicates a decreasing pattern. The difference in maximum dry density between soil samples and pollution levels is negligible.

- Oil plays a similar function to water in that it raises the risk of inter-particle slippage, lowering the shear strength of polluted soils.
- The findings explicitly demonstrated that oil contamination of the soil environment had affected the sandy soil's geotechnical properties.
- The cohesion improved dramatically with up to 8% oil contamination and then declined when increased the percentage of crude oil.
- The angle of internal friction of sandy soil particles decreases with contamination crude oil in a small resulted due to inter-grain lubrication.

## References

1. Arbili, M. M., & Karpuzcu, M. (2018). Effect of crude oil contamination on physical and chemical properties of soil of Tarjan refineries Erbil province-North of Iraq. *Polytechnic Journal*, 8(2), 159–170.
2. Karpuzcu, M. (2018). Influence of oil contamination on geotechnical properties of sandy soil. *Polytechnic Journal*, 8(2), 129–141.
3. Ghaffoori, F. K. M. (2019). Effects of mineral admixtures on some properties of crude oil polluted sand.
4. Khamehchiyan, M., Charkhabi, A. H., & Tajik, M. (2007). Effects of crude oil contamination on geotechnical properties of clayey and sandy soils. *Engineering Geology*, 89(3–4), 220–229.
5. Rahman, Z. A., Hamzah, U., Taha, M. R., Ithnain, N. S., & Ahmad, N. (2010). Influence of oil contamination on geotechnical properties of basaltic residual soil. *American Journal of Applied Sciences*, 7(7), 954.
6. Ghadyani, M., Hamidi, A., & Hatambeigi, M. (2019). Triaxial shear behaviour of oil contaminated clays. *European Journal of Environmental and Civil Engineering*, 23(1), 112–135.
7. Ratnaweera, P., & Meegoda, J. N. (2006). Shear strength and stress-strain behavior of contaminated soils. *Geotechnical Testing Journal*, 29(2), 133–140.
8. Nelson, C. S., Harris, G. J., & Young, H. R. (1988). Burial-dominated cementation in non-tropical carbonates of the Oligocene Te Kuiti Group, New Zealand. *Sedimentary Geology*, 60(1–4), 233–250.
9. Das, B. M. (2019). *Advanced soil mechanics*. CRC Press.
10. Khosravi, E., Ghasemzadeh, H., Sabour, M. R., & Yazdani, H. (2013). Geotechnical properties of gas oil-contaminated kaolinite. *Engineering Geology*, 166, 11–16.
11. Ghaffoori, F. K., & Arbili, M. M. (2019). Effects of fly ash and granulated ground blast furnace slag on stabilization of crude oil contamination sandy soil. *Polytechnic Journal*, 9(2), 80–85.
12. Hamed, M., Sidik, W. S., Canakci, H., Celik, F., & Georgees, R. N. (2020). Characterization of shear strength and interface friction of organic soil. In *Key engineering materials* (Vol. 857, pp. 203–211). Trans Tech Publications Ltd.
13. Botero, E., Ossa, A., Sherwell, G., & Ovando-Shelley, E. (2015). Stress–strain behavior of a silty soil reinforced with polyethylene terephthalate (PET). *Geotextiles and Geomembranes*, 43(4), 363–369.
14. Abousnina, R. M., Manalo, A., Shiau, J., & Lokuge, W. (2015). Effects of light crude oil contamination on the physical and mechanical properties of fine sand. *Soil and Sediment Contamination: An International Journal*, 24(8), 833–845.
15. Hosseini, F. M. M., Hosseini, S. M. M. M., Ebadi, T., & Eslami, A. (2019). Elasto-plastic characteristics of clayey soils contaminated by gasoil using cyclic triaxial apparatus. *Arabian Journal of Geosciences*, 12(6), 1–10.

16. Tong, F., Ma, Q., & Hu, X. (2019). Triaxial shear test on hydrochloric acid-contaminated clay treated by lime, crushed concrete, and super absorbent polymer. *Advances in Materials Science and Engineering*, 2019.
17. Naeini, S. A., & Shojaedin, M. M. (2014). Effect of oil contamination on the liquefaction behavior of sandy soils. *International Journal of Environmental, Chemical, Ecological, Geological and Geophysical Engineering*, 8, 289–292.

# Isotropic and Cross-Anisotropic Stiffness Parameters for Unsaturated Soils Using Conventional and Bishop's Stress State Variables



Ahmed Mohammed Hasan

**Abstract** This paper aims to examine the ability of conventional unsaturated stress state variables (i.e., net stress,  $\bar{\sigma}$  and suction,  $s$ ) and alternative unsaturated stress state variables (i.e., Bishop's stress,  $\sigma^*$  and modified suction,  $s^*$ ) in demonstrating isotropic and cross-anisotropic stiffness parameters for unsaturated soils in the formulation of stiffness matrices and compliance matrices. To do this, a Matlab code was generated to give outputs of the formulation of the stiffness matrices. The bulky outputs of the code were simplified. To check whether the conventional or alternative unsaturated stress state variables produce less complex outputs, a comparison between them was performed in the form of the stiffness matrices and compliance matrices under isotropic and cross-anisotropic unsaturated conditions. For isotropic unsaturated soils, the comparison showed that the stiffness and compliance matrices could be demonstrated in a similar level of complexity using both conventional and alternative unsaturated stress state variables. For cross-anisotropic unsaturated soils, alternative unsaturated stress state variables successfully formed a manageable level of complexity in formulating the stiffness matrix and uncoupling between the mechanical response and water retention behavior in the formulation of a compliance matrix. Conversely, conventional unsaturated stress state variables could not demonstrate these two key features of the matrices.

**Keywords** Stiffness parameters · Unsaturated soils · Net stress · Bishop's stress

## 1 Introduction

Small strain elastic behavior of isotropic and cross-anisotropic unsaturated and saturated soils is crucial to predict settlement in many geotechnical projects such as deep excavations, tunnels etc. The effective stress,  $\sigma'$  alone is satisfactorily enabled to describe stress-strain behavior of fully saturated soils which introduced by Terzaghi [1]:

---

A. M. Hasan (✉)

Civil Engineering Department, College of Engineering, Salahaddin University-Erbil, Erbil, Iraq  
e-mail: [ahmed.hasan@su.edu.krd](mailto:ahmed.hasan@su.edu.krd)



$$\sigma' = \sigma - u \quad (1)$$

where  $\sigma$  is total stress, and  $u$  is the pore water pressure. Using only  $\sigma'$  is unsatisfactory to properly describe the mechanical behavior of unsaturated soils. Therefore, Bishop and Blight [2] introduced two independent stress state variables: net stress  $\bar{\sigma}$  and suctions. The  $\bar{\sigma}$  is defined by:

$$\bar{\sigma} = \sigma - u_a \quad (2)$$

where  $u_a$  is the pore air pressure and  $s$  is defined by:

$$s = u_w - u_a \quad (3)$$

The  $\bar{\sigma}$  and  $s$  have been used as two independent stress state variables by many researchers to describe both large strain plastic behavior [3–5] and small strain elastic behavior for unsaturated soils [6–8]. Alonso, Gens, and Josa [9] developed the first constitutive model for unsaturated soils called Barcelona Basic Model (BBM), employing  $\bar{\sigma}$  and  $s$  as the two independent stress state variables. Bishop's stress,  $\sigma^*$  and modified suction  $s^*$  are the two alternative stress state variables to the conventional ones that many researchers have investigated to describe together the mechanical behavior and hysteresis of hydraulic in unsaturated soils for plastic behavior [10–12] and elastic behavior [13–15]. The  $\sigma^*$  and  $s^*$  can be defined by:

$$\sigma^* = \sigma - S_r u_w - (1 - S_r) u_a = \bar{\sigma} + S_r s \quad (4)$$

and

$$s^* = ns \quad (5)$$

where  $S_r$  represents the pressure of water in the pores and  $(1 - S_r)$  refers to air pressure in the pores in Eq. (4). These two pressures work in the volume of total voids. The pressure of water in the pores comes from the bulk water; whereas, the pressure of air in the pores usually comes from the atmospheric pressure.  $n$  is the porosity. Houlsby [16] developed a constitutive equation for work input decrement of unsaturated soil by:

$$dW = \sigma_{ij}^* d\epsilon_{ij} - n(u_a - u_w) dS_r \quad (6)$$

where  $d\epsilon_{ij}$  represents an increment of strain, and  $dS_r$  is the decrement of the degree of saturation. when  $\sigma_{ij}^*$  and  $s^*$  used as two applied stresses, Eq. 6 suggests that suitable increment of strain and— $dS_r$  are the most proper selected ones, respectively. In their BBM model for soils under unsaturated conditions, Alonso, Gens and Josa [9]

employed  $\bar{\sigma}$  and  $s$  to capture the change of elastic volumetric strain, the response of shear and post-yielding responses. In contrast, Wheeler, Sharma and Buisson [17] developed a model for soils under unsaturated conditions, which is called Glasgow Coupled Model (GCM) to capture hydromechanical response of partially saturated soils. The GCM model uses  $\sigma^*$  and  $s^*$ . In the model, the  $s^*$  has involved only the change of degree of saturation, which only influences the yielding behavior (plastic change of degree of saturation) within the mechanical response. In the GCM, the change of elastic volumetric strain and shear behavior (i.e., a large part of mechanical behavior) solely depends on  $\sigma^*$ .

Experimentally proved that unsaturated soils' small strain elastic behavior could be captured by only Bishop's stress [18]. Therefore, using only  $\sigma^*$  is sufficient to describe the mechanical retention behavior of isotropic and cross-anisotropic unsaturated soils in small strain levels. The main objectives of this investigation are to prove whether the conventional and/or alternative unsaturated stress state variables would be able to: (1) provide compliance matrices in the form of uncoupling of mechanical response and water retention behavior and (2) to produce compliance matrices in terms of manageable size and complexity. From the practical point of view, it is crucial in the geotechnical laboratory testing to have uncoupling formulation of constitutive equation relationships or compliance matrices that separate between volumetric and distortional behavior. This helps researchers to investigate the effect of an individual variable on a particular response of soils properly.

## 2 Theoretical Background

If material is assumed to be elastic, the stress-strain behavior is reversible. Elastic behavior can be either linear or non-linear. In the latter case, elastic stiffness parameters vary with stress or strain. Based on the Hook's law for isotropic saturated soils, which is independent of direction, to fully describe the minimal strain elastic behavior, Young's modulus  $E$  and Poisson's ratio  $\nu$  are the two independent variables that can be employed [19]. Compliance matrix can be formulated for isotropic saturated soils in accordance to Hooke's law by:

$$\begin{bmatrix} d\epsilon_x \\ d\epsilon_y \\ d\epsilon_z \\ d\gamma_{xy} \\ d\gamma_{yz} \\ d\gamma_{zx} \end{bmatrix} = \begin{bmatrix} \frac{1}{E} & -\frac{\nu}{E} & -\frac{\nu}{E} & 0 & 0 & 0 \\ -\frac{\nu}{E} & \frac{1}{E} & -\frac{\nu}{E} & 0 & 0 & 0 \\ -\frac{\nu}{E} & -\frac{\nu}{E} & \frac{1}{E} & 0 & 0 & 0 \\ 0 & 0 & 0 & \frac{2(1+\nu)}{E} & 0 & 0 \\ 0 & 0 & 0 & 0 & \frac{2(1+\nu)}{E} & 0 \\ 0 & 0 & 0 & 0 & 0 & \frac{2(1+\nu)}{E} \end{bmatrix} \begin{bmatrix} d\sigma'_x \\ d\sigma'_y \\ d\sigma'_z \\ d\tau_{xy} \\ d\tau_{yz} \\ d\tau_{zx} \end{bmatrix} \quad (7)$$

where  $z$  is the vertical direction and  $x, y$  are the horizontal direction,  $d\sigma'_x, d\sigma'_y$  and  $d\sigma'_z$  are the effective stress increments,  $d\epsilon_x, d\epsilon_y$  and  $d\epsilon_z$  are the corresponding strain

increments,  $d\tau_{xy}$ ,  $d\tau_{yz}$  and  $d\tau_{zx}$  are the shear stress increments and  $d\gamma_{xy}$ ,  $d\gamma_{yz}$  and  $d\gamma_{zx}$  are the corresponding shear strain increments. Equation 7 can be expressed in stiffness matrix as inverted:

$$\begin{bmatrix} d\sigma'_x \\ d\sigma'_y \\ d\sigma'_z \\ d\tau_{xy} \\ d\tau_{yz} \\ d\tau_{zx} \end{bmatrix} = A \begin{bmatrix} (1-\nu) & \nu & \nu & 0 & 0 & 0 \\ \nu & (1-\nu) & \nu & 0 & 0 & 0 \\ \nu & \nu & (1-\nu) & 0 & 0 & 0 \\ 0 & 0 & 0 & \frac{(1-2\nu)}{2} & 0 & 0 \\ 0 & 0 & 0 & 0 & \frac{(1-2\nu)}{2} & 0 \\ 0 & 0 & 0 & 0 & 0 & \frac{(1-2\nu)}{2} \end{bmatrix} \begin{bmatrix} d\epsilon_x \\ d\epsilon_y \\ d\epsilon_z \\ d\gamma_{xy} \\ d\gamma_{yz} \\ d\gamma_{zx} \end{bmatrix} \quad (8)$$

where  $A = \frac{E}{(1-2\nu)(1+\nu)}$ .

For cross-anisotropic saturated soils, elastic behavior can be fully described using five elastic parameters such as  $E_v$ ,  $E_h$ ,  $\nu_{vh}$ ,  $\nu_{hh}$  and  $G_{hv}$  [20, 21], where  $E_v$  and  $E_h$  are Young's moduli in horizontal and vertical directions respectively,  $\nu_{vh}$  is the Poisson's ratio when lateral stress is applied in the horizontal direction to produce a ratio of vertical strain to horizontal strain,  $G_{hv}$  is the shear modulus in the vertical plane (which is equal to  $G_{vh}$ ). Therefore, it is possible to express the compliance matrix of cross-anisotropic saturated soils by:

$$\begin{bmatrix} d\epsilon_x \\ d\epsilon_y \\ d\epsilon_z \\ d\gamma_{xy} \\ d\gamma_{yz} \\ d\gamma_{zx} \end{bmatrix} = \begin{bmatrix} \frac{1}{E_h} & -\frac{\nu_{hh}}{E_h} & -\frac{\nu_{vh}}{E_v} & 0 & 0 & 0 \\ -\frac{\nu_{hh}}{E_h} & \frac{1}{E_h} & -\frac{\nu_{vh}}{E_v} & 0 & 0 & 0 \\ -\frac{\nu_{vh}}{E_v} & -\frac{\nu_{vh}}{E_v} & \frac{1}{E_v} & 0 & 0 & 0 \\ 0 & 0 & 0 & \frac{1}{G_{hv}} & 0 & 0 \\ 0 & 0 & 0 & 0 & \frac{1}{G_{hv}} & 0 \\ 0 & 0 & 0 & 0 & 0 & \frac{2(1+\nu_{hh})}{E_h} \end{bmatrix} \begin{bmatrix} d\sigma'_x \\ d\sigma'_y \\ d\sigma'_z \\ d\tau_{xy} \\ d\tau_{yz} \\ d\tau_{zx} \end{bmatrix} \quad (9)$$

The inverted form of Eq. 9 can be expressed by:

$$\begin{bmatrix} d\sigma'_x \\ d\sigma'_y \\ d\sigma'_z \\ d\tau_{xy} \\ d\tau_{yz} \\ d\tau_{zx} \end{bmatrix} = \begin{bmatrix} (E_v - E_h\nu_{vh}^2) & (E_h - \nu_{vh}^2 + E_v\nu_{hh}) & -E_v\nu_{vh}(\nu_{hh} + 1) & 0 & 0 & 0 \\ (E_h - \nu_{vh}^2 + E_v\nu_{hh}) & (E_v - E_h\nu_{vh}^2) & -E_v\nu_{vh}(\nu_{hh} + 1) & 0 & 0 & 0 \\ -E_v\nu_{vh}(\nu_{hh} + 1) & -E_v\nu_{vh}(\nu_{hh} + 1) & -\frac{(\nu_{hh}^2 - 1)E_v^2}{E_h} & 0 & 0 & 0 \\ 0 & 0 & 0 & LG_{hv} & 0 & 0 \\ 0 & 0 & 0 & 0 & LG_{hv} & 0 \\ 0 & 0 & 0 & 0 & 0 & N \end{bmatrix} \begin{bmatrix} d\epsilon_x \\ d\epsilon_y \\ d\epsilon_z \\ d\gamma_{xy} \\ d\gamma_{yz} \\ d\gamma_{zx} \end{bmatrix} \quad (10)$$

where

$$J = -\frac{E_h}{(\nu_{hh} + 1)(2E_h\nu_{vh}^2 - E_v + E_v\nu_{hh})}, \quad L = -\frac{(\nu_{hh} + 1)(2E_h\nu_{vh}^2 - E_v + E_v\nu_{hh})}{E_h}$$

and

$$N = -\frac{(2E_h\nu_{vh}^2 - E_v + E_v\nu_{hh})}{2}$$

Equation 10 is the output of a MATLAB code generated in the current study.

### 3 MATLAB Code

A MATLAB code was written to generate compliance and stiffness matrices for both isotropic and cross-anisotropic unsaturated soils involving both conventional and alternative stress state variables. Under isotropic, cross-anisotropic, and unsaturated conditions, when the stress state variables govern by the conventional ones (i.e.,  $\bar{\sigma}$  and  $s$ ), in Eq. 7, the  $\sigma'$  changed by the  $\bar{\sigma}$ . In addition, matric suction,  $s$  was added to stresses in the compliance matrix. The suction stress increment,  $ds$  lead to corresponding volumetric water content strain increments,  $d\epsilon_{vw}$ . Similarly, when the stress state variables govern by the alternative ones ( $\sigma^*$  and  $s^*$ ), in Eq. 7, the  $\sigma'$  changed by the  $\sigma^*$  and a scalar stress state (i.e.,  $s^*$ ) was added to stresses in the compliance matrix. The modified suction stress increment ( $ds^*$ ) causes a corresponding decrement of the degree of saturation –  $dS_r$  as explained in the following paragraphs. The formulation of compliance and stiffness matrices of unsaturated soils are:

**Isotropic Elastic Behavior.** Isotropic elastic responses of unsaturated soils are possible to be presented in terms of compliance matrix as below when net stresses,  $\bar{\sigma}$  and suction,  $s$  are considered as the governing stress variables:

$$\begin{bmatrix} d\epsilon_x \\ d\epsilon_y \\ d\epsilon_z \\ d\gamma_{xy} \\ d\gamma_{yz} \\ d\gamma_{zx} \\ d\epsilon_{vw} \end{bmatrix} = \begin{bmatrix} \frac{1}{E} & -\frac{\nu}{E} & -\frac{\nu}{E} & 0 & 0 & 0 & \frac{1}{H} \\ -\frac{\nu}{E} & \frac{1}{E} & -\frac{\nu}{E} & 0 & 0 & 0 & \frac{1}{H} \\ -\frac{\nu}{E} & -\frac{\nu}{E} & \frac{1}{E} & 0 & 0 & 0 & \frac{1}{H} \\ 0 & 0 & 0 & \frac{2(1+\nu)}{E} & 0 & 0 & 0 \\ 0 & 0 & 0 & 0 & \frac{2(1+\nu)}{E} & 0 & 0 \\ 0 & 0 & 0 & 0 & 0 & \frac{2(1+\nu)}{E} & 0 \\ \frac{1}{H} & \frac{1}{H} & \frac{1}{H} & 0 & 0 & 0 & \frac{1}{R^*} \end{bmatrix} \begin{bmatrix} d\bar{\sigma}_x \\ d\bar{\sigma}_y \\ d\bar{\sigma}_z \\ d\tau_{xy} \\ d\tau_{yz} \\ d\tau_{zx} \\ ds \end{bmatrix} \quad (11)$$

where  $d\epsilon_{vw}$  is the increment of water volumetric strain and equals to  $d\epsilon_{vw} = \frac{dv_w}{v}$ ,  $v$  is the specific volume ( $1 + e$ ) and  $v_w$  is the quantity ( $1 + S_r e$ ) defined by Wheeler [22].  $H$  is Young's modulus for the soil regarding matric suction change and  $R^*$  is water volumetric (bulk) modulus associated with a matric suction change [23]. In Eq. 11 two extra elastic constants (i.e.,  $H$  and  $R^*$ ) have been added due to adding the effect of  $ds$ . The three components of shear stress in stiffness and compliance matrices do not change for both saturated and unsaturated conditions because the effect of the pore water pressure is canceled [19, 24]. The Young's modulus ( $E$ ) in Eq. 11, is defined concerning a change of the net stress,  $\bar{\sigma}$ . It is also possible to apply the above stiffness matrix to non-linear elastic soil behavior [23]. It can be

noticed from Eq. 11 that one scalar stress variable,  $ds$  added to the 6 tensorial stress variables resulting in the seventh corresponding strain variables. The scalar  $ds$  cause elastic swelling strain in wetting and elastic shrinkage strain on drying due to matric suction changes [9, 17]. To know the elastic straining in swelling and drying, the soil's water retention behavior is essential. From Eq. 11, it can also be noticed that the first six stress and strain relations give the all-mechanical response; whereas, the last row of the stiffness matrix gives the change of the elastic water volumetric behavior due to change in the water retention behavior [9]. The stiffness matrix of the above compliance matrix can be expressed as:

$$\begin{bmatrix} d\bar{\sigma}_x \\ d\bar{\sigma}_y \\ d\bar{\sigma}_z \\ d\tau_{xy} \\ d\tau_{yz} \\ d\tau_{zx} \\ ds \end{bmatrix} = B \begin{bmatrix} \left(\nu - 1 + \frac{2ER^*}{H^2}\right) & \left(\nu + \frac{ER^*}{H^2}\right) & \left(\nu + \frac{ER^*}{H^2}\right) & 0 & 0 & 0 & \frac{(1+\nu)R^*}{H} \\ \left(\nu + \frac{ER^*}{H^2}\right) & \left(\nu - 1 + \frac{2ER^*}{H^2}\right) & \left(\nu + \frac{ER^*}{H^2}\right) & 0 & 0 & 0 & \frac{(1+\nu)R^*}{H} \\ \left(\nu + \frac{ER^*}{H^2}\right) & \left(\nu + \frac{ER^*}{H^2}\right) & \left(\nu - 1 + \frac{2ER^*}{H^2}\right) & 0 & 0 & 0 & \frac{(1+\nu)R^*}{H} \\ 0 & 0 & 0 & C & 0 & 0 & 0 \\ 0 & 0 & 0 & 0 & C & 0 & 0 \\ 0 & 0 & 0 & 0 & 0 & C & 0 \\ \frac{(1+\nu)R^*}{H} & \frac{(1+\nu)R^*}{H} & \frac{(1+\nu)R^*}{H} & 0 & 0 & 0 & D \end{bmatrix} \begin{bmatrix} d\epsilon_x \\ d\epsilon_y \\ d\epsilon_z \\ d\gamma_{xy} \\ d\gamma_{yz} \\ d\gamma_{zx} \\ d\epsilon_{vw} \end{bmatrix} \quad (12)$$

where

$$B = \frac{EH^2}{(1+\nu)(2\nu H^2 - H^2 + 3ER^*)}, C = \frac{(2\nu H^2 - H^2 + 3ER^*)}{2H^2} \text{ and} \\ D = \frac{(1+\nu)(2\nu - 1)R^*}{E}$$

The stiffness matrix in Eq. 12 is an output of the Matlat code in the current study. It is clear from Eqs. 11 and 12 that the compliance matrix is simpler than the stiffness matrix. If the isotropic elastic behavior of unsaturated soils is expressed under Bishop's stress and modified suction as the governing stress variables, Eq. 11 would include just a single elastic constant (X):

$$\begin{bmatrix} d\epsilon_x \\ d\epsilon_y \\ d\epsilon_z \\ d\gamma_{xy} \\ d\gamma_{yz} \\ d\gamma_{zx} \\ -dS_r \end{bmatrix} = \begin{bmatrix} \frac{1}{E} & -\frac{\nu}{E} & -\frac{\nu}{E} & 0 & 0 & 0 & 0 \\ -\frac{\nu}{E} & \frac{1}{E} & -\frac{\nu}{E} & 0 & 0 & 0 & 0 \\ -\frac{\nu}{E} & -\frac{\nu}{E} & \frac{1}{E} & 0 & 0 & 0 & 0 \\ 0 & 0 & 0 & \frac{2(1+\nu)}{E} & 0 & 0 & 0 \\ 0 & 0 & 0 & 0 & \frac{2(1+\nu)}{E} & 0 & 0 \\ 0 & 0 & 0 & 0 & 0 & \frac{2(1+\nu)}{E} & 0 \\ 0 & 0 & 0 & 0 & 0 & 0 & \frac{1}{X} \end{bmatrix} \begin{bmatrix} d\sigma_x^* \\ d\sigma_y^* \\ d\sigma_z^* \\ d\tau_{xy} \\ d\tau_{yz} \\ d\tau_{zx} \\ ds^* \end{bmatrix} \quad (13)$$

where X is the water volumetric (bulk) modulus related to the change of  $s^*$ . As stated above that the appropriate work-conjugate strain increment variable is the decrement of the degree of saturation,  $-dS_r$  for the increment stress variable  $ds^*$ . It is clear from Eq. 13, that the form of the compliance matrix is the same as that

in Eq. 7 for saturated soils and the only difference is that the Bishop's stress,  $\sigma^*$  is changed by effective stress,  $\sigma'$ . In Eq. 7, uncoupling is achieved between volumetric and distortional response for isotropic elastic saturated soils [24]. Similarly, Eq. 13 which is proposed in the current work, provides uncoupling between the volumetric and distortional effect for isotropic elastic unsaturated soils. In addition, Eq. 13 also provides an uncoupling between mechanical response and water retention behavior. This proves that  $\sigma^*$  and  $s^*$  produce a very simple form of compliance matrices compared to the  $\bar{\sigma}$  and  $s$ . The inverted version of the above equation is:

$$\begin{bmatrix} d\sigma_x^* \\ d\sigma_y^* \\ d\sigma_z^* \\ d\tau_{xy} \\ d\tau_{yz} \\ d\tau_{zx} \\ ds^* \end{bmatrix} = F \begin{bmatrix} (\nu - 1) & -\nu & -\nu & 0 & 0 & 0 & 0 \\ -\nu & (\nu - 1) & -\nu & 0 & 0 & 0 & 0 \\ -\nu & -\nu & (\nu - 1) & 0 & 0 & 0 & 0 \\ 0 & 0 & 0 & (2\nu - 1) & 0 & 0 & 0 \\ 0 & 0 & 0 & 0 & (2\nu - 1) & 0 & 0 \\ 0 & 0 & 0 & 0 & 0 & (2\nu - 1) & 0 \\ 0 & 0 & 0 & 0 & 0 & 0 & \frac{X}{F} \end{bmatrix} \begin{bmatrix} d\epsilon_x \\ d\epsilon_y \\ d\epsilon_z \\ d\gamma_{xy} \\ d\gamma_{yz} \\ d\gamma_{zx} \\ -dS_r \end{bmatrix} \quad (14)$$

$$\text{where } F = \frac{E}{(2\nu - 1)(1 + \nu)}.$$

**Anisotropic Elastic Behavior.** When net stresses,  $\bar{\sigma}$  and suction,  $s$  are considered as the governing stress variables, the compliance matrix of anisotropic elastic behavior can be expressed by:

$$\begin{bmatrix} d\epsilon_x \\ d\epsilon_y \\ d\epsilon_z \\ d\gamma_{xy} \\ d\gamma_{yz} \\ d\gamma_{zx} \\ d\epsilon_{vw} \end{bmatrix} = \begin{bmatrix} \frac{1}{E_h} & -\frac{\nu_{hh}}{E_h} & -\frac{\nu_{vh}}{E_v} & 0 & 0 & 0 & \frac{1}{H} \\ -\frac{\nu_{hh}}{E_h} & \frac{1}{E_h} & -\frac{\nu_{vh}}{E_v} & 0 & 0 & 0 & \frac{1}{H} \\ -\frac{\nu_{vh}}{E_v} & -\frac{\nu_{vh}}{E_v} & \frac{1}{E_v} & 0 & 0 & 0 & \frac{1}{H} \\ 0 & 0 & 0 & \frac{1}{G_{hv}} & 0 & 0 & 0 \\ 0 & 0 & 0 & 0 & \frac{1}{G_{hv}} & 0 & 0 \\ 0 & 0 & 0 & 0 & 0 & \frac{2(1 + \nu_{hh})}{E_h} & 0 \\ \frac{1}{H} & \frac{1}{H} & \frac{1}{H} & 0 & 0 & 0 & \frac{1}{R^*} \end{bmatrix} \begin{bmatrix} d\bar{\sigma}_x \\ d\bar{\sigma}_y \\ d\bar{\sigma}_z \\ d\tau_{xy} \\ d\tau_{yz} \\ d\tau_{zx} \\ ds \end{bmatrix} \quad (15)$$

In terms of the stiffness matrix of Eq. 15, the MATLAB code in the current study produced an extremely complex and very long stiffness matrix. Therefore, the matrix could not be expressed here. This is a drawback of using conventional stress state variables as the governing stress variables. When Bishop's stress and modified suction are considered as the governing stress variables (with elastic straining solely dependent on Bishop's stresses) a similar compliance matrix for saturated soil is produced by:

$$\begin{bmatrix} d\epsilon_x \\ d\epsilon_y \\ d\epsilon_z \\ d\gamma_{xy} \\ d\gamma_{yz} \\ d\gamma_{zx} \\ -dS_r \end{bmatrix} = \begin{bmatrix} \frac{1}{E_h} & -\frac{\nu_{hh}}{E_h} & -\frac{\nu_{vh}}{E_v} & 0 & 0 & 0 & 0 \\ -\frac{\nu_{hh}}{E_h} & \frac{1}{E_h} & -\frac{\nu_{vh}}{E_v} & 0 & 0 & 0 & 0 \\ -\frac{\nu_{vh}}{E_v} & -\frac{\nu_{vh}}{E_v} & \frac{1}{E_v} & 0 & 0 & 0 & 0 \\ 0 & 0 & 0 & \frac{1}{G_{hv}} & 0 & 0 & 0 \\ 0 & 0 & 0 & 0 & \frac{1}{G_{hv}} & 0 & 0 \\ 0 & 0 & 0 & 0 & 0 & \frac{2(1+\nu_{hh})}{E_h} & 0 \\ 0 & 0 & 0 & 0 & 0 & 0 & \frac{1}{\bar{\chi}} \end{bmatrix} \begin{bmatrix} d\sigma_x^* \\ d\sigma_y^* \\ d\sigma_z^* \\ d\tau_{xy} \\ d\tau_{yz} \\ d\tau_{zx} \\ ds^* \end{bmatrix} \quad (16)$$

The stiffness matrix of the above compliance matrix can be expressed as:

$$\begin{bmatrix} d\sigma_x^* \\ d\sigma_y^* \\ d\sigma_z^* \\ d\tau_{xy} \\ d\tau_{yz} \\ d\tau_{zx} \\ ds^* \end{bmatrix} = J \begin{bmatrix} (E_v - E_h \nu_{vh}^2) & (E_h - \nu_{vh}^2 + E_v \nu_{hh}) & -E_v \nu_{vh} (\nu_{hh} + 1) & 0 & 0 & 0 & 0 \\ (E_h - \nu_{vh}^2 + E_v \nu_{hh}) & (E_v - E_h \nu_{vh}^2) & -E_v \nu_{vh} (\nu_{hh} + 1) & 0 & 0 & 0 & 0 \\ -E_v \nu_{vh} (\nu_{hh} + 1) & -E_v \nu_{vh} (\nu_{hh} + 1) & -\frac{(\nu_{hh}^2 - 1)E_v^2}{E_h} & 0 & 0 & 0 & 0 \\ 0 & 0 & 0 & LG_{hv} & 0 & 0 & 0 \\ 0 & 0 & 0 & 0 & LG_{hv} & 0 & 0 \\ 0 & 0 & 0 & 0 & 0 & N & 0 \\ 0 & 0 & 0 & 0 & 0 & 0 & LX \end{bmatrix} \begin{bmatrix} d\epsilon_x \\ d\epsilon_y \\ d\epsilon_z \\ d\gamma_{xy} \\ d\gamma_{yz} \\ d\gamma_{zx} \\ -dS_r \end{bmatrix} \quad (17)$$

where

$$J = -\frac{E_h}{(\nu_{hh} + 1)(2E_h \nu_{vh}^2 - E_v + E_v \nu_{hh})}, \quad L = -\frac{(\nu_{hh} + 1)(2E_h \nu_{vh}^2 - E_v + E_v \nu_{hh})}{E_h}$$

$$\text{and } N = -\frac{(2E_h \nu_{vh}^2 - E_v + E_v \nu_{hh})}{2}.$$

Equation 17 is the stiffness matrix for unsaturated soils and Eq. 10 is the stiffness matrix for saturated soils both under cross-anisotropic conditions. Comparison of Eq. 10 and Eq. 17 shows that these two equations are very similar in terms of the level of complexity, even though the latter is for unsaturated soils, which had a more complex form. This is confirming that using  $\sigma^*$  and  $s^*$  is much better than using  $\bar{\sigma}$  and  $s$  in terms of formulation matrices regarding complexity. As mentioned above the stiffness matrix of Eq. 15 has not presented here because the matrix was very complex.

## 4 Interpretations and Discussion

Investigation of Eqs. 11 and 13 shows that any change of  $s$  and  $s^*$ , respectively, produces similar changes in stresses in  $x$ ,  $y$  and  $z$  directions due to isotropic conditions; however, this is not true in cross-anisotropic conditions. In Eqs. 15 and 16, the compliance matrices' formulations can be compared when conventional and alternative stress state variables are used. In Eq. 16, the water retention behavior can be

linked by only one constitutive equation (i.e.,  $dS_r = ds^*/X$ , the last row of the compliance matrix), which is totally separated from the mechanical response of the elastic behavior. In contrast, in Eq. 15, there is a strong relation (coupling) between the mechanical response and the water retention behavior because any change in suction will produce changes in the net stresses. For example, in Eq. 15, when suction is changed by a certain amount while keeping the net stresses ( $\bar{\sigma}_x, \bar{\sigma}_y, \bar{\sigma}_z$ ) constant, this will produce changes in the values of  $\bar{\sigma}_x, \bar{\sigma}_y,$  and  $\bar{\sigma}_z$  by a different amount because of different constants ( $1/E_h, -v_{hh}/E_h, -v_{vh}/E_{hh}$ , respectively) in different directions [24, 25]. In contrast, when  $s^*$  is changed in Eq. 16, while keeping the values of  $\bar{\sigma}_x, \bar{\sigma}_y,$  and  $\bar{\sigma}_z$  constant, the values of the  $\bar{\sigma}_x, \bar{\sigma}_y,$  and  $\bar{\sigma}_z$  will not change when  $s^*$  changes because the elastic response of unsaturated soils solely depends on Bishop's stress not modified suction,  $s^*$  (i.e., uncoupling between mechanical response and water retention behavior) [18]. It can be deduced that Eq. 16 is a better representation of real behavior in terms of elastic behavior in anisotropic unsaturated soils, and it is also simpler than Eq. 15 in terms of the number of elastic constants. It can be noted that the forms of Eqs. 4 and 5 (i.e., alternative stress variables  $\sigma^*$  and  $s^*$ ) are clearly more complex than the traditional stress state variables of net stress  $\bar{\sigma}$  and suction,  $s$  (see, Eqs. 2 and 3).

## 5 Conclusions

From the above interpretations and discussions, several important points could be concluded as follow:

- For elastic behavior of anisotropic unsaturated soils, conventional stress state variables ( $\bar{\sigma}$  and  $s$ ) cannot produce a stiffness matrix with manageable size and complexity, whereas the alternative stress state variables ( $\sigma^*$  and  $s^*$ ) can.
- Bishop's stress can represent the elastic behavior of isotropic and cross-anisotropic unsaturated soils, which cannot be performed by net stress and suction due to strong relations between mechanical response and water retention behavior.
- The elastic behavior of isotropic and anisotropic unsaturated soils solely depends on the  $\sigma^*$ .

## References

1. Terzaghi, K. V. (1936). The shearing resistance of saturated soils and the angle between the planes of shear. In *First international conference on soil Mechanics* (Vol. 1, pp. 54–59).
2. Bishop, A. W., & Blight, G. E. (1963). Some aspects of effective stress in saturated and partly saturated soils. *Geotechnique*, 13(3), 177–197.
3. Fredlund, D. G., Morgenstern, N. R., & Widger, R. A. (1978). The shear strength of unsaturated soils. *Canadian Geotechnical Journal*, 15(3), 313–321.



4. Alonso, E. E., Romero, E., Hoffmann, C., & García-Escudero, E. (2005). Expansive bentonite-sand mixtures in cyclic controlled-suction drying and wetting. *Engineering Geology*, 81(3), 213–226.
5. Abeyrathne, A., Sivakumar, V., & Kodikara, J. (2019). Isotropic volumetric behavior of compacted unsaturated soils within specific volume, specific water volume, mean net stress ( $v$ ,  $vw$ ,  $p$ ) space. *Canadian Geotechnical Journal*, 56(12), 1756–1778.
6. Khosravi, A., Rahimi, M., Gheibi, A., & Mahdi Shahrabi, M. (2018). Impact of plastic compression on the small strain shear modulus of unsaturated silts. *International Journal of Geomechanics*, 18(2), 04017138.
7. Ng, C. W. W., Zheng, G., Ni, J., & Zhou, C. (2020). Use of unsaturated small-strain soil stiffness to the design of wall deflection and ground movement adjacent to deep excavation. *Computers and Geotechnics*, 119, p. 103375.
8. Ngoc, T. P., Fatahi, B., & Khabbaz, H. (2019). Impacts of drying-wetting and loading-unloading cycles on small strain shear modulus of unsaturated soils. *International Journal of Geomechanics*, 19(8), 04019090.
9. Alonso, E. E., Gens, A., & Josa, A. (1990). A constitutive model for partially saturated soils. *Géotechnique*, 40(3), 405–430.
10. Santagiuliana, R., & Schrefler, B. A. (2006). Enhancing the Bolzon-Schrefler-Zienkiewicz constitutive model for partially saturated soil. *Transport in porous media*, 65(1), 1–30.
11. Loret, B., & Khalili, N. (2000). A three-phase model for unsaturated soils. *International Journal for Numerical and Analytical Methods in Geomechanics*, 24(11), 893–927.
12. Vecchia, G. D., & Romero, E. (2013). A fully coupled elastic-plastic hydromechanical model for compacted soils accounting for clay activity. *International Journal for Numerical and Analytical Methods in Geomechanics*, 37(5), 503–535.
13. Biglari, M., Mancuso, C., d’Onofrio, A., Jafari, M. K., & Shafiee, A. (2011). Modelling the initial shear stiffness of unsaturated soils as a function of the coupled effects of the void ratio and the degree of saturation. *Computers and Geotechnics*, 38(5), 709–720.
14. Zhou, C. (2014). Experimental study and constitutive modelling of cyclic behavior at small strains of unsaturated silt at various temperatures (Doctoral dissertation, Hong Kong University of Science and Technology).
15. Wong, K. S., Mašín, D., & Ng, C. W. W. (2014). Modelling of shear stiffness of unsaturated fine grained soils at very small strains. *Computers and Geotechnics*, 56, 28–39.
16. Houlby, G. T. (1997). The work input to an unsaturated granular material. *Géotechnique*, 47(1), 193–196.
17. Wheeler, S. J., Sharma, R. S., & Buisson, M. S. R. (2003). Coupling of hydraulic hysteresis and stress-strain behavior in unsaturated soils. *Géotechnique*, 53(1), 41–54.
18. Hasan, A. M. (2016). Small strain elastic behavior of unsaturated soil investigated by bender/extender element testing (Doctoral dissertation, University of Glasgow).
19. Cassidy, M.J., Houlby, G.T., Hoyle, M. and Marcom, M.R., 2002, January. Determining appropriate stiffness levels for spudcan foundations using jack-up case records. In *International Conference on Offshore Mechanics and Arctic Engineering* (Vol. 36142, pp. 307–318)
20. Graham, J., & Houlby, G. T. (1983). Anisotropic elasticity of a natural clay. *Géotechnique*, 33(2), 165–180.
21. Braun, P., Ghabezloo, S., Delage, P., Sulem, J., & Conil, N. (2021). Transversely isotropic poroelastic behavior of the Callovo-Oxfordian claystone: A set of stress-dependent parameters. *Rock Mechanics and Rock Engineering*, 54(1), 377–396.
22. Wheeler, S. J. (1996). Inclusion of specific water volume within an elasto-plastic model for unsaturated soil. *Canadian Geotechnical Journal*, 33(1), 42–57.
23. Borden, R. H., Gabr, M. A., Lee, J., Tang, C. T., & Wang, C., (2016). Design of temporary slopes and excavations in NC residual soils (No. FHWA/NC/2013–07). North Carolina. Department of Transportation.
24. Wood, D. M. (2003). Geotechnical modelling (Vol. 1). CRC press.

25. Atkinson, J. H., Richardson, D., & Stallebrass, S. E. (1990). Effect of recent stress history on the stiffness of overconsolidated soil. *Géotechnique*, 40(4), 531–540.
26. Lings, M. L., Pennington, D. S., & Nash, D. F. T. (2000). Anisotropic stiffness parameters and their measurement in a stiff natural clay. *Géotechnique*, 50(2), 109–125.

# The Effect of Electric Field on the Settlement Behavior to Improve Gypseous Soil



Methaq A. Talib and Qasim A. Aljanabi

**Abstract** There are many techniques to improve gypseous soil, one of these is used electrical field (Electro-osmotic consolidation), which is the technology of transferring water and positively charged ions by directing the electric field from the anode to the cathode. This application has many successful applications in geotechnical engineering, such as dewatering, electrostatic filling. The present study attempts to verify the effect of electric field on behavior settlement of gypseous soils by the experimental model. This experimental model represents the primary load applied on a gypseous soil experiencing a water rise and collapses. In this study, the soil has 30% gypsum content and is treated with electroosmosis. Two intensities of loads were applied on the soil, equals to 20 and 28 T/m<sup>2</sup>. The test was performed using Dc voltage on the soil; the results from this test were compared with the soil without Dc voltage. The results showed the soil response for the electroosmosis technique, which improves the settlement of soil. The optimum voltage level is reported to be between 15 and 20 V DC voltage. The maximum reported degree of improvement for 15 V was 70%, while in 20 V, such level may reach 80% in some stations within the testing time. Further studies can be achieved by changing the gypsum content, the type of electrodes used, and changing the device's dimensions.

**Keywords** Gypseous soil · Gypsum content · Electroosmosis · DC voltage · Settlement

## 1 Introduction

In general, soil improvement techniques are procedures that geotechnical engineers can follow to enhance soils' properties or behavior that inherently lack a considerable problem in their performance, such as gypseous soil. Gypseous soils speared in many regions of the world, particularly in arid and semi-arid areas, where the annual quantity of rainfall is not enough for leaching the gypsum from these soils [1]. In Iraq, this soil is found with different gypsum content ranging from 10–70% and

---

M. A. Talib (✉) · Q. A. Aljanabi  
Civil Engineering Department, University of Diyala, Baqubah, Diyala, Iraq

covers about 31.7% [2]. Gypseous soils are soils that have enough gypsum content to change or affect their engineering properties. Gypsum (calcium sulfate dehydrate) can have a detrimental effect on buildings, pavements, and earth structures because it is moderately soluble salts. Gypsum dissolves with water and generates caves and progressive settlements, accelerating seepage flows and the accompanying deterioration in foundations [3]. In addition, gypseous soils have enough gypsum amount to vary or affect engineering properties. Gypsum (hydrated calcium sulfate) can injure buildings, earth structures, and pavements because it is one of the solubility moderate salts. There are many techniques to improve gypseous soil, one of these using electrical field (Electro-osmotic consolidation), a method in which the pore-water migrated from anode under in the electrical field the existing soils [4]. The first contribution that included the first set up of an apparatus for electroosmosis consolidation was proposed by Reuss when the wires used as electrodes, and no-load was applied, and the water transport was observed qualitatively during that study [5]. Additionally, Casagrande used the same setup, but the solid electrodes were used instead [6]. After that time, many attempts were made to explore improvement for different soil types and other criteria, including some of the successful case histories. Since that date, the electroosmosis technique has taken a trend to be a unique option for cost and environmental purposes.

Furthermore, this technique's procedural purpose is to increase the shear strength of soil through rapid consolidation, which is very useful in some site cases when preloading is not possible, like slope soil stabilization. In addition, electroosmosis was also used successfully in many dewatering applications, including volume reduction of hazardous materials such as biosolids, mining applications, and groundwater recharge [7]. Such a promising technique is considered an excellent alternative to treat problematic soils and used in many applications like excavations, slopes/embankment stabilization, pile capacity increasing, clays' strength, dewatering sludge/tailings, and controlling groundwater flow [4]. Hamir et al. [8] proposed an electroosmosis cell and applied higher order of load in parallel with electrical voltage. Porewater pressure, the electrical water flow rate, and the soil-electrode zone potential drop were measured during that program [8]. Wu and Hu [9] proposed analytical and numerical solutions for vacuum preloading in combination with electroosmosis. Two models were presented, the first was one-dimensional, and the other is axisymmetric. The results showed good agreement between the analytical and the numerical solution [9]. Karkush and Ali [10] studied the clay soil polluted with lead nitrate has been investigated by using the electrokinetic technique enhanced by using mid compartment, purging solutions, and washing technique. The result showed that an increment of the lead causes increases the electrical current generated during the treatment process, and the washing process is found beneficial in decreasing the period of remediation but does not influence the removal efficiency [10]. Karkush and Ali [11] use of electrical kinetic technology to treat clay soil contaminated with copper in two ratios and the results showed that increment the concentricity of copper causes an increment in the electric current generated during the treatment process [11]. This study is an attempt to verify and improve the gypseous soil using the electroosmosis technique with different applied voltage levels and the possibility of

**Table 1** Results of chemical properties of gypseous soil

Properties	Value	Properties	Value
Total soluble salts (TSS) (%)	33	Organic matter (OM) %	0.22
Gypsum contents (%)	30	Chloride contents (Cl) %	0.056
Sulphate content (SO <sub>3</sub> ) (%)	13.89	pH value	7

knowing the gypseous soil's response to the best electrical voltage and reduce the soil settlement that happened.

## 2 Soil Sampling and Geotechnical Properties

The gypseous soil was brought from Tikrit, Salah al-Din city center to use in this study. This city is located in the middle of Iraq and north of Baghdad by 180 km, with a gypsum content of 30%. The existence of several industrial areas as well as the future projects which were proposed. The disturbed samples are taken from depths ranging from (0.75–1.5) m under the natural ground level. Then, soil samples are packed in bags of double nylon, labeled, and imparted to the soil mechanics laboratory at the University of Diyala to carry on the required testing. During the conducted experimental program, gypseous soil is air-dried and crushed with a rubber hammer to make it as uniform as possible and sieved with No. 4 (4.75 mm diameter of sieve) to extract unwanted impurities. The soil is mixed well together to attain a homogenous condition as much as possible. The soil was used to study soil properties' improvement. The chemical and physical properties of the gypseous soil are illustrated in Tables 1 and 2. The results of particle size distribution curve and collapse test are shown in Figs. 1 and 2. The relative density of the test is not applicable for this soil (ASTM D4254), the temperature used for the procedure the initial water content test (40–50) °C to avert the loss of the gypseous crystals [12]. Gypseous soil is classified as a medium to medium hazard (ASTM D 5533).

## 3 Experiential Work

The tests are procedure in the Civil Engineering Laboratory in the College of Engineering at the University of Diyala using an experimental model. The plywood box was utilized together with dimensions (30 × 30 × 30) cm inside a steel tank with dimensions (50 × 50 × 35) cm, is filled with water. The voltage was applied using DC volts, and the device was designed so that the load is applied through the loading arm.

**Table 2** Results of physical properties of gypseous soil

Properties		Value	Specification
Grain size analysis	D10 (mm)	0.06	ASTM D422
	D 30 (mm)	0.07	
	D 60 (mm)	0.18	
	Uniformity coefficient, Cu	3.12	
	Curvature coefficient, Cc	0.453	
	Passing sieve No.200 (%) (using kerosene)	37.2	
Soil classification based on (USCS)		SM	
Specific gravity, Gs		2.48	ASTM D 854
Atterberg's limits	Liquid limit (LL) (%)	22	ASTM D4316
	Plastic limit (PL) (%)	NP	
Direct shear test	Angle of internal friction ( $\phi$ ) in dry condition	34.4	ASTM D 3080
	Angle of internal friction ( $\phi$ ) in soaking condition	31	
	Soil cohesion (c) (kN/m <sup>2</sup> ) in dry	9	
	Soil cohesion (c) (kN/mm <sup>2</sup> ) after soaked	4	
Dry unit weight	Maximum dry unit weight (kN/m <sup>3</sup> )	16.75	
	Minimum dry unit weight (kN/m <sup>3</sup> )	12.54	
	Relative density, Dr (%)	70	
	Dry weight test at a relative density of 70% (kN/m <sup>3</sup> )	15.22	
Field unit weight (kN/m <sup>3</sup> )		15	ASTM D1556
Initial void ratio		0.64	
Water content (%)		0.81	ASTM D2216
Compaction characteristics	Maximum dry unit weight (kN/m <sup>3</sup> )	17.95	ASTM 698
	Optimum moisture content (%)	14.13	
	Dry unit weight at a relative density of 85% (kN/m <sup>3</sup> )	15.26	
Collapse potential, %		5	ASTM D5533

**Apparatuses of Model.** The apparatus and equipment used in tests are listed below. Figure 3 explains a sketch of the laboratory model used in tests.

(1) Load arm; (2) Rigid footing (5 × 5) cm; (3) Anode; (4) Soil sample (30 × 30 × 25) cm; (5) Cathode; (6) Plywood box (30 × 30 × 30) cm; (7) Steel water tank (50 × 50 × 35) cm; and (8) Dial gauge.

In this study, five levels of voltage were applied by the DC voltage (5, 10, 15, 20, and 25 V). A subject load (20 and 28) T/m<sup>2</sup> was applied. The 3 mm commercial

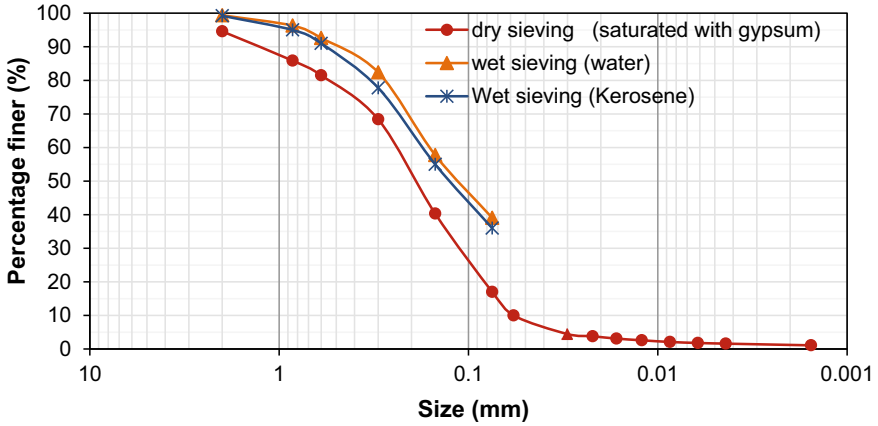


Fig. 1 Grains size distribution curve of gypseous soil

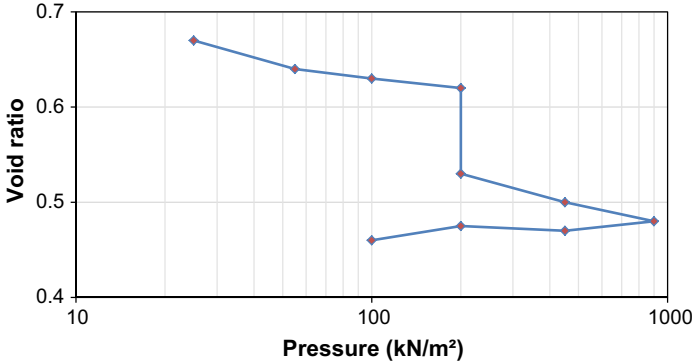


Fig. 2 Result of collapse test (odometer test) for gypseous soil

aluminum plate was used to fabricate both anode and cathode, and the used foundation is made in the form of a steel plate (5 × 5) cm and a thickness of 3 mm. A (30 × 30 × 30) cm plywood box is manufactured to include the soil sample. The bottom of this box was perforated to facilitate the exit of water into the soil sample. The steel box was built with dimensions (50 × 50 × 35) cm to contain water, as illustrated in Fig. 4.

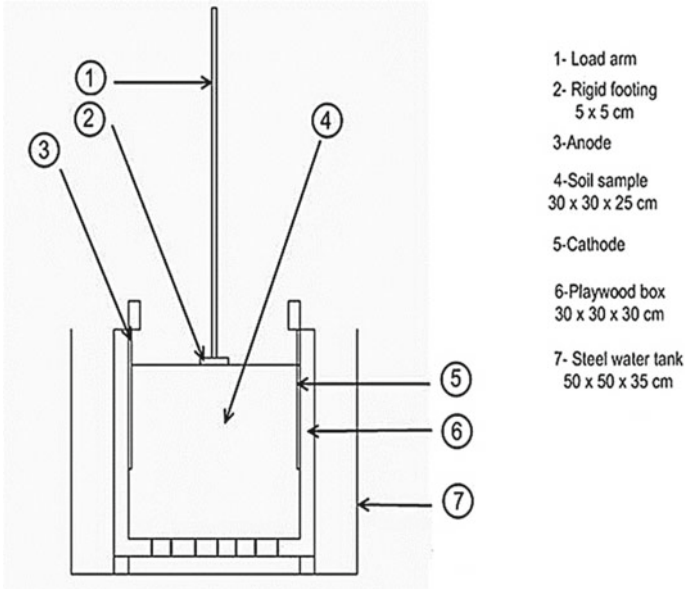
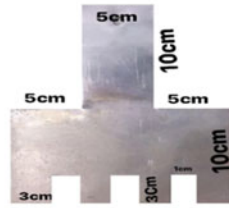


Fig. 3 Schematic diagram of the testing setup



The Dc voltage regulator



The aluminum electrodes



The plywood box



The steel tank

Fig. 4 Main parts of the testing setup



## 4 Testing Procedures

The gypseous soil utilized in this study is dried in a sufficient quantity to fill the wooden box ( $30 \times 30 \times 25$ ) cm. It is divided into two layers. Each layer has dimensions of ( $15 \times 15 \times 12.5$ ) cm. By depending on the dry unit weight of soil ( $15.22 \text{ kN/m}^3$ ), the weight of the total volume of soil is calculated. A hammer is used to obtain the soil's required density where a steel plate with dimensions ( $200 \times 200$ ) mm and a thickness of 5 mm is installed in the front. Several tests are outright to ensure the adjustment process is controlled, achieve the test optimally's required density, and avoid any difference in the density values between one test and another to ensure accurate results. After the soil preparation operation, the rest of the device is installed, where the water tap is opened to fill the steel box until it reaches the level of the soil sample, and the loads and voltages are applied by the DC voltage current. The readings are taken by the dial gauge, where these readings are taken every half hour during the 600 min until a soil collapse occurs, where the rest readings are ignored.

## 5 Results and Discussion

During the current study, the applied voltage levels are 5, 10, 15, 20, and 25 V. The soil was embedded in (30% gypsum), two levels of applied load were used to simulate the heavy load accumulated for the superstructure (20 and  $28 \text{ T/m}^2$ ). This study is characterized by the ratio (the difference between the reference settlement and the improved soil on the reference soil level). At the outset, the overall settlement outreach is presented and discussed. Next, the suitability of the improvement is considered to gain a better understanding of the intended role. In general, the settlement propagation method versus time is equivalent to both reference, and improved soils are shown in Figs. 5 and 6. The failure time is taken into account when suddenly the soil collapses. The dial gauge reading is not recognized. However, it has been reported that the time of this collapse is 600 min for soil. In addition, at a low voltage level (5 V), there are not enough negative electrons that can play the optimum role in the movement of the water dipole towards the cathode.

On the other hand, when the voltage level is high (25 V), the excessive negative electrons dictate the dipoles' turbulent motion, revealing a decrease in performance. Also, it is not possible to determine the optimum voltage level throughout the entire test period, but it is clear that this value is between 15 and 20 V for these soils and the applied loads. Table 3 shows the degree of improvement monitored at the fourth quarter of total failure time in soil, and the applied load was  $20 \text{ T/m}^2$ .

Due to the above, it can be observed that there is no recognized context to the variation of the degree of improvement due to the time of testing progress in this way. The Pearson correlation factor is used to understand the degree of dependency between the degree of improvement and time testing stations. This factor is represented by a

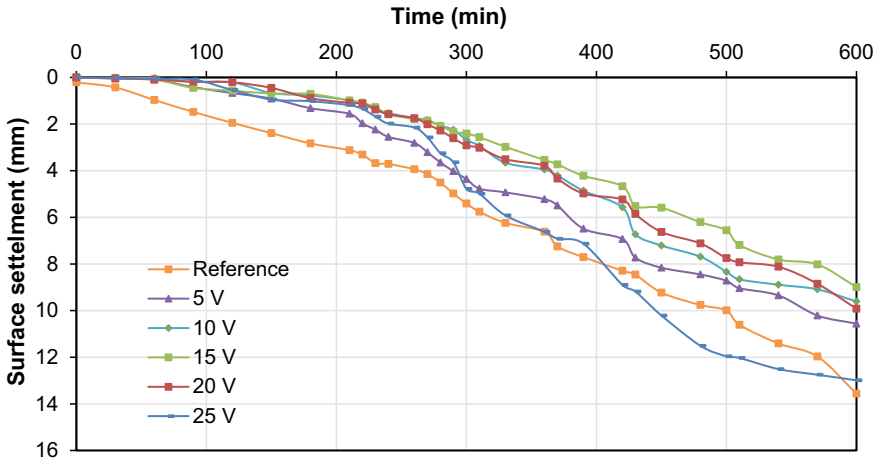


Fig. 5 Effect of voltage level on time-settlement behavior, 20 T/m<sup>2</sup>

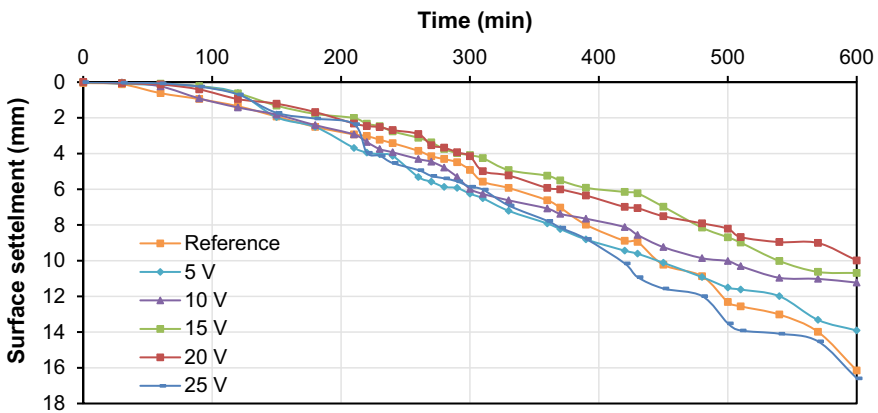


Fig. 6 Effect of the voltage level on time-settlement behavior, 28 T/m<sup>2</sup>

single number that ranges from  $-1$  to  $+1$  in the correlation test to characterize the required degree of relevancy. This test was conducted to the complete set of variables by utilizing the statistic software package (SPSS) whose description is provided in this section. The result of the correlation test is listed in Table 4. When the degree of correlation is negative, the electroosmosis technique has more effectiveness in the initial stages than in the final ones and vice versa. More precisely, in the soil with  $20 \text{ T/m}^2$ , the Dc voltage depletes the vast majority of improvement potential at the first stages because the foundation stress does not confine dipolar movement towards the cathode. This behavior was inverted in  $28 \text{ T/m}^2$  when the stress determines such movement till 25 V, which can break this role due to the excessive applied potential.

**Table 3** Degree of improvement of soil

Load	Time station (%)	Degree of improvement				
		5 V	10 V	15 V	20 V	25 V
20 T/m <sup>2</sup>	25	61.92	71.97	71.13	81.17	60.25
	50	19.41	50.65	55.45	46.03	11.65
	75	11.59	21.89	39.44	28.17	-10.62
	100	22.12	29.13	33.70	26.84	4.20
28 T/m <sup>2</sup>	25	-2.07	5.69	31.61	37.31	10.88
	50	-27.03	-21.54	16.89	15.65	-19.11
	75	1.07	9.68	31.77	26.59	-13.00
	100	13.87	30.46	33.81	38.14	-2.72

**Table 4** The pearson correlation factor for soil

Load	Standard	5 V	10 V	15 V	20 V	25 V
20 T/m <sup>2</sup>	Pearson factor	-0.728	-0.898	-0.898	-0.923	-0.801
	Degree	Moderate negative	Strong negative	Strong negative	Strong negative	Strong negative
28 T/m <sup>2</sup>	Pearson factor	0.573	0.637	0.355	0.164	-0.342
	Degree	Weak positive	Moderate positive	Weak positive	Weak positive	Weak negative

## 6 Conclusion

The main conclusion that can be express throughout this study are as follows:

- Applying DC voltage to the gypseous enhances the surface settlement versus time behavior of such soils.
- The optimum level of DC voltage is located between 15 and 20 V.
- The maximum reported degree of improvement for 15 V was 70%, while in 20 V, such level may reach 80% in some stations within the testing time.
- There is no recognized context to the variation of the degree of improvement due to the time of testing progress.
- The excessive negative charged electrons dictate dipoles' disconcerted movement, which reveals soil agitation and low electro osmoses performance.
- Increasing the applied loads causes a consequent increase in the electroosmosis deflection response due to excessive stress.

## References

1. Al-Emami, O. H. (2007). *Collapsibility of gypseous soil under fluctuation of groundwater table*. Ph.D. Thesis, University of Technology, Iraq.
2. Razouki, S. S., Al-Omari, R. R., Nashat, I. H., Razouki, H. F., & Khalid, S. (1994). The problem of gypsiferous soils in Iraq. In *Proceeding of the symposium on gypsiferous soils and their effect on structures* (pp. 7–33). NCCL.
3. Subhi, H. M. (1988). *The properties of salt contaminated soils and their influence on the performance of roads in Iraq*. Doctoral dissertation, Queen Mary, University of London.
4. Hu, L., Wu, H., & Wen, Q. B. (2013). Electro-osmotic consolidation: Laboratory tests and numerical simulation. In *The 18th international conference on soil mechanics and geotechnical engineering, Paris* (pp. 231–234).
5. Wall, S. (2010). The history of electrokinetic phenomena. *Current Opinion in Colloid & Interface Science*, 15(3), 119–124.
6. Casagrande, I. L. (1949). Electro-osmosis in soils. *Geotechnique*, 1(3), 159–177.
7. Jones, C. J., Lamont-Black, J., & Glendinning, S. (2011). Electrokinetic geosynthetics in hydraulic applications. *Geotextiles and Geomembranes*, 29(4), 381–390.
8. Hamir, R. B., Jones, C. J. F. P., & Clarke, B. G. (2001). Electrically conductive geosynthetics for consolidation and reinforced soil. *Geotextiles and Geomembranes*, 19(8), 455–482.
9. Wu, H., & Hu, L. (2011). Theoretical analysis and numerical simulation of vacuum preloading in combination with electro-osmosis consolidation. In *Geo-frontiers 2011: Advances in geotechnical engineering* (pp. 605–615).
10. Karkush, M., & Ali, S. (2019). Remediation of clay soil contaminated with lead nitrate using washing-enhanced electrokinetic technique. *Journal of Electrochemical Science and Engineering*, 9(1), 63–73.
11. Karkush, M. O., & Ali, S. D. (2019). Remediation of clayey soil contaminated with copper sulfate using washing-enhanced electrokinetics technique. *Russian Journal of Electrochemistry*, 55(12), 1381–1390.
12. Al-Muftay, A. A., & Nashat, I. H. (2000). Gypsum content determination in gypseous soils and rocks. In *Proceedings of the 3rd Jordanian international mining conference, Amman*, vol. 2 (pp. 485–492).

# Tsunami Waves, Causes and Its Implications: A Review



Hiba A. Bachay, Asad H. Aldefae, Salah L. Zubaidi, Wissam H. Humaish, and Evgeny K. Sinichenko

**Abstract** This paper reviews the basic theoretical information needed to understand the tsunami wave's phenomenon, causes, and implications on coastal cities. The first part describes the basic knowledge of the tsunami waves and some experimental and large and small physical modeling performed to understand the Tsunami and take care of its effect in the future. The influence of climate changes and global warming on the rise of water level and its effect on the Arab Gulf and Iraq are also presented. Then the principles of tsunami generation, involving earthquakes, landslides, and volcanic will be discussed. The tsunami propagation, inundation, and interaction with the coastal structures will be reviewed in brief. Also, the paper reviews some previous studies on tsunami simulation.

**Keywords** Tsunami · Earthquake · Wavelength · Inundation · Wave propagation

## 1 Introduction

Due to the recent phenomena in the Indian Ocean and Japan, humanity is afraid of the risk imposed by tsunamis after earthquakes. Tsunamis can be created by a sudden huge-scale disruption of a quantity of ocean water. This displaces the surface of the ocean and generates waves series that branched from the occurred disturbance. The

---

H. A. Bachay (✉) · A. H. Aldefae · S. L. Zubaidi  
Civil Engineering Department, Wasit University, Wasit, Iraq  
e-mail: [hibab301@uowasit.edu.iq](mailto:hibab301@uowasit.edu.iq)

A. H. Aldefae  
e-mail: [asadaldefae@uowasit.edu.iq](mailto:asadaldefae@uowasit.edu.iq)

S. L. Zubaidi  
e-mail: [salahlafta@uowasit.edu.iq](mailto:salahlafta@uowasit.edu.iq)

W. H. Humaish · E. K. Sinichenko  
Hydraulic and Engineering Hydrology, Peoples' Friendship University (RUDN), Moscow, Russia  
e-mail: [whumaish@uowasit.edu.iq](mailto:whumaish@uowasit.edu.iq)

E. K. Sinichenko  
e-mail: [csinichenko-ek@rudn.ru](mailto:csinichenko-ek@rudn.ru)

magnitude of these earthquakes is higher than 6.5 on the scale of Richter and their central depth of approximately 60 km [1]. The great part of the tsunamis (about 88%) in the Database of Global Historical Tsunami, DGHT (since 1900 A.D), has been triggered by landslides or earthquakes. The essential reason for a tsunami occurrence is an enormous earthquake under the ocean floor [2]. Earthquakes do not always produce tsunamis. It depends on key features such as its location, magnitude, whether an earthquake generates a tsunami [3]. The displacement value of the ocean bed, the extent of the area that the earthquake covers and the water height above it are the major factors that govern the tsunami size.

Furthermore, earthquakes may also produce tsunami-generating landslides [2]. Landslide is a general term relating to tsunami generation that describes various ground displacement forms, involving rocks and slope collapses, falls, flows of debris, and slumps. Tsunamis are produced due to the displacements of the water from below (submarine) or above (subaerial) by the effect of a landslide. The generation of tsunamis is governed by the number of landslide materials that move the water, the velocity, and the depth at which it travels shifts, respectively [2].

A group of researchers works to study an unusual type of Tsunami generated by large underwater landslips and determine if their occurrence may be affected by climate change. It has been suggested that climate change could increase the frequency of slides in two ways. The first is methane hydrate dissociation (the methane gas release from a priorly stable condition in the sediment) that is able to cause structural impairment and generate a slip [3]. The other way is the crustal rebound, where the ice sheet's removal causes a pressure releasing from the Earth's crust, so it returns to a new equilibrium place [3]. Independent of ETTs (earthquake-triggered tsunamis), global warming, which is a long-term phenomenon, is predictable to result in an accelerated increase in SLR (sea level rise). This may contribute to a higher risk of low-lying coastal areas being inundated. As a result, damage due to coastal flooding is projected to increase dramatically throughout and beyond the twenty-first century as the sea level increases, making socio-economic damage more prevalent in coastal regions [4]. In the last two decades, numerous studies have been undertaken to assess, understand and improve management techniques and risk adaptation measures due to SLR (sea level rise) [4]. There has been a surge in research in recent years regarding force and pressure measurements of waves on structures. Physical simulations and experimental tests have previously extensively studied the effects of tsunami loads on coastal structures. Generally, numerical modeling is used to investigate the impact of these loads on structures. It normally integrates sufficient validated hydrodynamic equations. Usually, it is used to analyze certain features of a system exposed to tsunami wave forces.

Solitary waves have been used as an estimated waveform for tsunami representation in many hydraulic studies [5]. However, a new wave generation method (pneumatic wave generator) to regenerate tsunami waves that seismically produced in a laboratory has been presented by Rossetto et al. [5]. A wave creator can regenerate scaled waves uses this new design. The wave generator can be used for broad wavelength reproductions of solitary waves and N-waves. Experimental research was performed by Farahmandpour et al. [6] to study the relationship between an onshore

building and a tsunami surge. A new dam-break model was used to produce the tsunami surge. For each tsunami surge, the ratio between impulsive and hydrodynamic forces was determined to be about 2.40. With regard to those assessed using the 'Federal Emergency Management Agency' FEMA P646 guidelines, the hydrodynamic forces were found to be higher, while they were roughly in accordance with those obtained by FEMA 55. Also, the results indicated that the 'Structural Design Method of Building for Tsunami Resistance' overestimates the impulsive energy.

Another experimental study to examine the effect of the tsunami loads on the coastal building is carried out [7]. An experimental investigation was explicitly initiated for studying the influence of the tsunami loads on a square-shaped prism model. It was concluded that the pressure distribution differed in the experiment depending on the system's orientation in terms of flow direction. In addition, the Tsunami bore velocity has been found to have a greater significant impact on the tsunami intensity rather than the height of the wave. Onshore buildings that are influenced at the immersion stage by tsunami loads are largely due to the water's unsteady movement around the constructed building. A combination of several tsunami forces can be measured as a phenomenon, such as drag, hydrostatic and inertia forces. Therefore, a study to explore the influences of unstable flow on houses of rectangular shape, where the unstable flows are mostly according to trough-led (N-waves) and solitary wave, is performed by Foster et al. [8]. According to the obtained results, the water height attained approximately 10–90% of the height of the obstacle. Thus, it was inferred that the high-water measurement was proportioned with the blocking fractions in the obstacles' face. Both experimental and numerical models to show the Tsunami bore effect on the building structure are done [9]. Numerical simulation was performed with the recently improved semi-implicit three-dimensional moving particle (3D-MPS) method to verify the physical experimental results and equate them with the original MPS method. The newly enhanced 3D-MPS system demonstrates strong qualitative and quantitative agreement with the pressure and height recorded experimentally. The Tsunami bore effect strength depends on the initial height of the Tsunami. Compared to the upper floors of the structure, the building's base faces a considerable impact. The improved numerical simulation method shows more significant agreement than that of the original with the experimental results. The changes in impact pressure on the structure of the building model are due to the variations in Tsunami bore height and velocity across the structure of the building model.

An extensive experimental program focused on severe hydrodynamic forces on structural models created by a turbulent hydraulic bore [10]. The results indicated that the basis shear force in flow directed by experimental testing was higher than predicted using document FEMA P646, while the Structural Design Building Method for Tsunami Resistance (SMBTR) overestimated the base shear force. Using the wave tank model, the subjected tsunami loads on buildings were explored by Thusyanthan and Gopal Madabhushi [11]. A rectangular block was projecting inside the water at the tank's deepest side. The model tsunami wave was formed. Test results showed that 5.1 kPa was the maximum pressure at the house's front wall, representing 127.5 kPa due to scaling of Froude number ( $5.1 \times 25$ ) for prototype scale with 5 m/s tsunami

wave velocity. Finally, numerical modeling can generate several tsunami scenarios and magnitude that significantly affect tsunami events. While physical modeling predominantly focuses on worst-case scenarios.

## 2 Climate Change

The increase in the temperature of the earth from the pre-industrial period to the present is  $\sim 1$  °C. Projections for rises in sea-level rise and climate changes from global warming for a global average surface temperature rise of 1.5 °C with more estimated 2.0 °C conditions and coastal implications. Therefore, port cities may be at risk and vulnerable to natural and anthropogenic hazards unrelated to or indirectly linked to global warming/climate change (i.e., earthquakes, exposure to pollution) [12]. Iraq is situated along the convergent tectonic border between the Eurasian and Arab plates, in the northeastern portion of the Arabian plate (see Fig. 1a). Here, the Bitlis-Zagros Fold and Thrust Belt produce severe earthquake activity, including Mw7.3 in November 2017, in northern and eastern Iraq. The remainder of Iraq, away from significant plate boundaries and prone to less regular seismicity, is situated mainly on the Arab Platform [13]. Iraq has a limited coastline on the Arabian Gulf. However, due to its depressed altitude relative to the sea level, the Iraqi coastline can be considered a vulnerable zone in our local region. Even with a 1 m altitude, the areas of low elevation stretch across Al-Basra City [14]. Onshore, Al-Faw, and Um Qasr cities, which facilitate exports, trade, and different undertakings and various industrial processes (involving the oil production and storage), are susceptible to

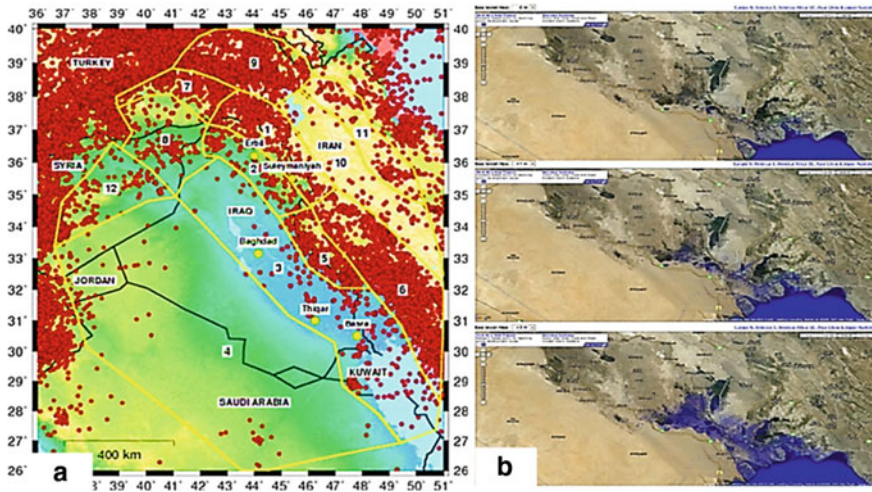


**Fig. 1** a Clarification of seismic regions in Iraq [13] and b sea level raise in Iraq represented by three scenarios et al. Basrah city [14]



**Table 1** Some of the coastal cities at danger due to the natural risks and global warming [12]

Urban area	Urban population	Urban area	Urban population
Odessa, Ukraine	1,100,000	Wahran, Algeria	1,040,000
Bucaramanga Colombia	1,090,000	Da Nang, Vietnam	1,040,000
Basrah, Iraq	1,085,000	Maceio, Brazil	1,025,000
Cartagena, Colombia	1,060,000	Oslo, Norway	1,025,000
Pointe Noire, Congo	1,045,000	Antwerp, Belgium	1,020,000

increment of the sea levels and evolving the patterns of weather, which can maximize the shore’s natural features and infrastructures. They a pretty low elevation, as shown in Fig. 1b, and they are susceptible to any increase in water elevation. Furthermore, they are subjected to marine and coastal sediment redistribution due to the intensive storm phenomena [14]. Table 1 shows many littoral areas that their population is a million or more. They are threatened by the effects of global warming, such as the change of climate and natural risks [12].

### 3 Tsunami Occurrence Factors

As explained in the introduction, there are many factors that directly affect tsunami occurrence. It can be explained in details as follow:

**Earthquakes.** Earthquakes may cause a sudden rising or fall in the bedrock of the ocean. The abrupt normal movement of the ocean bed makes a tsunami in motion. When the surface of the ocean rises or drops, the water body above it often does so. When the water goes up and down, the tsunami waves radiate out in all directions, trying to recover their balance. The displacement value of the ocean bed, the extent of the area that the earthquake covers, and the water height above it are the major factors that govern the tsunami size. Furthermore, earthquakes may also produce tsunami-generating landslides [2]. In plate tectonics terms, the bulk of earthquakes can be clarified. The basic idea is that many large and reasonably durable slabs of solid and relatively rigid rock, called plates, consist of the outermost part of the Earth. These plates shift (very slowly) continuously and brush against each other along the edges of the plate, which are often called faults. Therefore, along these faults, stress and strain build up, and gradually they become too heavy to bear, and the plates shift suddenly such that the stress and strain are released, causing an earthquake. The greatest of tsunamigenic earthquakes occur in subduction zones. Along subduction margins, there are distinct forms of faults. The inter-plate fault usually accommodates a broad relative motion between two tectonic plates, and the

overlying plate is typically driven upward. This upward movement is impulsive; it happens in a few seconds, very quickly. The ocean water surface reacts instantly to the upward motion of the seafloor, and the profile of the ocean surface typically resembles the seafloor displacement, as shown in Fig. 2 [15].

Vertical movement in an earthquake source system itself is not always needed to generate a tsunami. In the case of sub-aerial and sub-marine landslides (sometimes defined as sub-marine mass failures), local ground movement from an earthquake of any type may cause unstable material on a slope to slide into or under the sea [16]. Tsunamis can be caused by only three types of earthquakes: a vertical fault strike-slip earthquake, a vertical fault dip-slip earthquake, and earthquakes in the dipping plan thrust (see Fig. 3). If the magnitude of the earthquake increases, the previous scales suggest that the intensity of a tsunami should increase. This applies to most Pacific Ocean seismic tsunamis, but it was understood that several earthquakes of weak and medium seismic moments may cause massive, destructive tsunamis. Both are

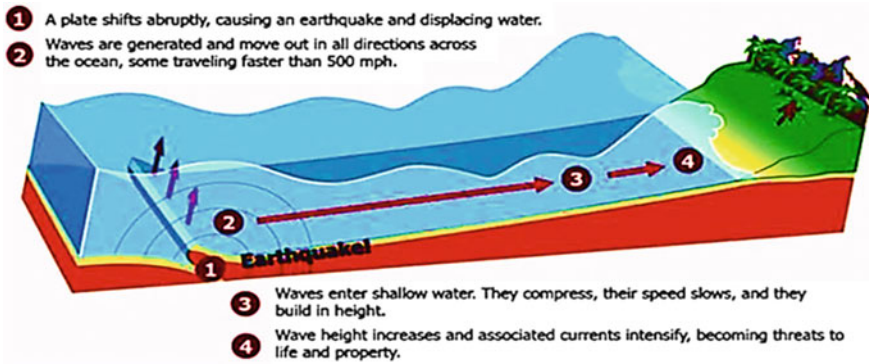
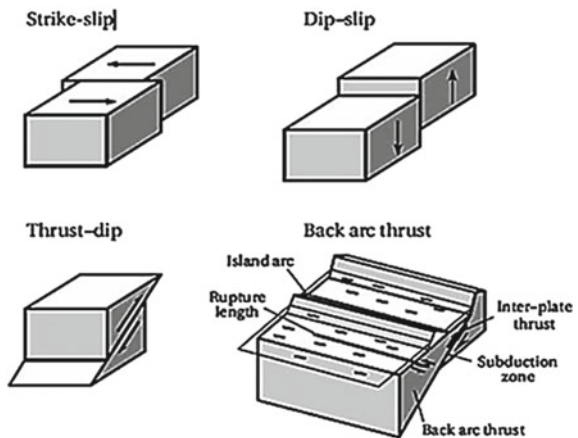
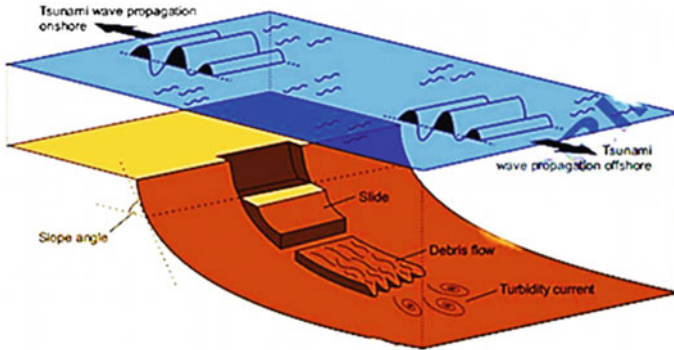


Fig. 2 Tsunami formation, triggered by a massive undersea earthquake [2]

Fig. 3 Fault types giving Tsunami generation [16]





**Fig. 4** Tsunami generation due to landslide [17]

the Great Meiji Sanriku and the Alaskan earthquake in 1896 and 1946, respectively [16].

**Landslides.** Submarine gravitational mass wasting is more effective in creating essential tsunamis in the far-field. This can be attributed to the effective transfer of energy to the body of water and the greater volume and mass typically shifted within the waste of submarine mass. This is especially valid with regard to submarine landslides (i.e., unconsolidated downslope sliding material) which can range from 1000 to 20,000 km<sup>3</sup>. Compared to subaerial mass wasting, the vast number of submarines is primarily covered by unconsolidated sediments due to the seafloor. This is likely to cause gravity mass wastage in the marine climate, combined with the lack of vegetation, increased pore water pressure, and high relief energy along continental margins, deep-sea trenches, mid-ocean ridges, volcanoes, seamounts, or guyots. In addition to unconsolidated material, submarine mass wastage is also associated with submarine rock, particularly when stratified parallel to the slope (i.e., Fig. 4) [17].

Landslide pushes the water forward when it reaches the water body, and a positive seaward radiating wave is produced. The water is initially depressed by creating a trailing wave until the landslide is fully submerged. Strong offshore free surface gradients occur in the generation field, resulting in converging flows that converge and rebound along the landslide centerline. The rebound is responsible for radiating offshore with a significant positive wave [18]. Both larger temporal and smaller spatial scale displacements may occur for either subaerial or underwater landslides. The distortions are of the order of hundreds of meters, and the waves produced are very different from those caused by submarine earthquakes. Landslide tsunamis, therefore, appear to be a local phenomenon, although extreme. Submarine failures have been associated with “sea waves without earthquake” for two centuries ago [18]. Examples of tsunamis caused by landslides include: October 11, 1918, Puerto Rico-An earthquake with an intensity of 7.3 triggered a submarine landslide that created a tsunami [2].

**Volcanic.** Historically, volcanic eruptions have been another cause of tsunamis. A range of processes, including slope instability, earthquakes of volcano-tectonic,

shock waves, pyroclastic flows, caldera collapse, and underwater blasts, produce volcanic tsunamis [19]. The eruptive origin tsunamis take place when a magnitude of the released energy during the eruption indirectly or directly transmits to the sea, producing impulsive waves by the water displacement. Although this phenomenon is understood, its precise nature and processes and dynamics interactions that generate waves throughout the eruptions are not fully grasped. The production of volcanic tsunamis involves up to eight mechanisms, they are underwater blasts, lahars entering the ocean, flows of pyroclastic, and flank failure (from the falls of rock to massive debris collapse), earthquakes during or preceding a volcanic eruption, the coastal lava bench collapse, caldera collapse (leading to a quick drop of the seafloor) and shock wave [20]. If an explosive submarine eruption occurs, as in the event of a blast of a sub astral active volcano, volcanic materials are blown out. Conversely, if, according to an eruption of submarine volcanic, any magma is emitted from a chamber, a ground drop occurs, resulting in the formation of a caldera. The water of the sea that touches raised temperature magma in the neighborhood of seafloor during the submarine phreatomagmatic explosion process, after which the water of the sea evaporates with a blast rise in its volume, leading to a tsunami-generating displacement of the water surface [21].

## 4 Tsunami Propagation

In a tsunami event, the potential energy obtained during the generation process is converted to kinetic energy once the water body has been displaced from its equilibrium location in its source field [22]. Particles of water are induced to oscillate when gravity acts against this motion as a restoring force. Tsunamis are therefore defined as waves of gravity [17]. The main parameters that characterize tsunami waves are length, duration, phase velocity, and wave height. In addition, tsunamis can be caused by refraction and diffraction, like wind-generated waves, and when reaching the coast, they undergo shoaling and fracturing [1]. The period of a tsunami will range from 10 to 120 min, and the length of the wave may reach 500 km [23]. Their wavelengths, largely more than 3000 m, are far greater than the seawater depth. Tsunamis tend to travel like shallow waves of water. The waves of shallow water fulfill the condition ( $d < L/20$ ) where  $d$  is the depth of the water (m), and  $L$  can be defined as the length of the wave m [17]. The distance between two crests of tsunami waves barely drops below 10 km, even in coastal areas. This enables tsunamis to stand out from the waves generated by wind because of their shorter wavelength, only impacting the upper water column. The following equation represents the speed or velocity of the waves of shallow water and tsunamis [1]:

$$c = \sqrt{gd} \quad (1)$$

where  $c$  represents the phase celerity or velocity of the wave (m/s), while  $g$  refers to the gravitational acceleration ( $9.81 \text{ m/s}^2$ ), as a result, the tsunami waves' phase,

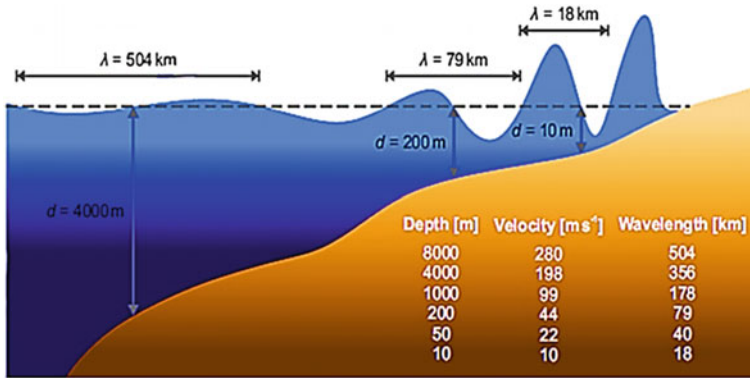


**Fig. 5** Shoaling of the tsunami wave. The wavelengths are determined based on a typical tsunami wave with a period of 30 min;  $\lambda$  represents the wavelength (L) [17]

velocity is directly related with the depth of gravity and water, as shown in Fig. 5, while it is independent of the wavelength and height of the wave [17].

In general, during the propagation of the Tsunami into the ocean, the magnitude of the Tsunami will decrease since the energy of the wave is distributed throughout a wider area [15]. The wavelength of a tsunami is very large. As it propagates, it loses a very small amount of energy. Thus, in quite deep water, a tsunami can move at raised speeds without energy loss. For instance, a tsunami travels around 890 km/h when the ocean is 6100 m deep. Thus, it requires less than 24 h to travel through the Pacific Ocean. A transformation occurs as a tsunami passes the sea’s deep water and enters the deeper waters near the shore [23]. As a tsunami spreads into the shallow water, it undergoes a rapid transformation as a tsunami propagates into shallower waters of the coast. The Tsunami’s velocity minimizes as it arrives at the shallower water, while the Tsunami’s height increases. Because of the shoaling effect, a tsunami that was insignificant in the ocean may magnify to reach a height of meters or more [15]. Onshore, the water level will increase by many meters. In the most severe conditions, the water elevation may increase to higher than 20 m for distant tsunamis and higher than 30 m for those near the quake’s epicenter. Basically, in the series of waves, the first one may not always be the greatest. The most important characteristic of tsunami wave during propagation represented by:

**Diffraction.** It is defined as the process that transmits the wave’s energy laterally along the crest of the wave into a sheltered position. The exposed reefs and the islands of limited area are the most that produced a protected area behind them [24].

**Refraction.** It can be defined as (i) The process that changes the moving direction of the wave in shallow water at a small angle of contour; the section of the wave crest passing in deeper water moves quicker than that which passes in shallower water. (ii) The currents are bending by the crests of the wave [24].

**Shoaling.** It can be defined as the mechanism whereby the velocity, length, height, and other wave characteristics alter while moving from deep to shallow water [24]. Shoaling can be divided into two stages: (i) the offshore Tsunami wave water rises

due to the disadvantage, and (ii) the Tsunami wave water breaks, resulting in a large flood of water to the shoreline on the dry seabed. As tsunami waves hit the ocean shoreline, seawater first withdraws, and the drawback is created by water rushing into the sea. The amount of drawback water could exceed 1 million cubic meters or 1 million tons of seawater [25].

## 5 Run up and Inundation

The maximum vertical height in which the water waves are observed referred to the runup concerning sea level. Simultaneously, inundation refers to the maximum horizontal distance reached by a tsunami [23]. Tsunamis are famous for their spectacular runup elevations; they usually are 2 or more times higher than the elevation of the Tsunami arriving at the coast. For example, 41 tsunamis have produced wave runup heights in the Pacific Ocean region in excess of 6 m since 1900. A runup height of 10 m was developed by the quake offshore from Gisborne, New Zealand, in 1947. Usually, runup heights like that are localized. This magnitude was constant along a coastal distance of 13 km [16]. Runup is the local feature of the inland wave flow. Compared to other wave characteristics, runup is commonly used to measure wave potential for inundation and coastal effects [26].

Runup is the final stage of tsunami life. As the incoming tsunami shoals to an amplitude approximately equal to the depth of the ocean, the runup process begins, and the wave starts to break. It also involves the inundation process in which the water flows overland and achieves its full excursion above sea level [27]. Based on the sea floor's topography, the wave starts to slow down and increase in height. The wave of Tsunami moves through a fresh near-field phase of extinguishing and runup of the wave of Tsunami and land immersion approaching the coast from a specific reference point. Large Tsunami waves move as spill breakers ashore in the runup; this is a nonlinear process. The techniques for predicting such processes are highly complex; they depend on the height of the incoming wave, the natural, man-made landscape; and they are challenging to model [28].

Nevertheless, the incoming wave approaches much the same as the incoming tide on a much faster scale. After runup process tsunami wave induced to the coasts. Hydrodynamic loading on structural components, floating debris impact loading, and scouring around foundations resulted in tsunami flooding of coastal towns and cities, significantly as the inundating water receded during the drawdown time. Timber-framed houses and unreinforced or poorly strengthened masonry structures have typically been badly damaged or demolished by hydrodynamic loads [29].

## 6 Tsunami Wave-Structure Interaction

A Tsunami's broken waves moving toward the shores create forces in its direction that affect structures. Three essential factors must be relied on to define the value and application of these forces; the depth of immersion, the velocity of flow, and flow direction. Tsunami bores govern forces involve the debt, buoyant force, hydrodynamic (drag) force, hydrostatic force, and surge force [30]. The factors majorly rely on the period and height of the tsunami wave, the shore's topography, and the inland shore's roughness [30]. Using different scenarios of the probable Tsunami (direction and magnitude) and modeling littoral immersion accordingly, the range of the littoral flood induced by a tsunami and its depth at a particular position is calculated. The evaluation of flow direction and velocity, however, is typically complex. The velocities are ranging from zero to considerably large velocities, while the direction varies based on the local topographic properties onshore, obstacles, and soil cover [31]. The possibility of tsunami occurrences is low. However, the damages triggered during the last two tsunamis (the year 2004 Indian Ocean tsunami and the year 2011 Japan tsunami) have prompted scientists and engineers to consider elements of Tsunami robust in the design of coastal structures for the protection of coastal communities. Several researchers have discussed modeling inundation over terrain with variable roughness, and standard commercial and academic codes typically perform well. The interaction may be considered as a special case of the flooding process. However, the distinction that is made regarding the effects that buildings have on the flow and how the physics found in the models discussed so far do not sufficiently capture this. The substantial forces that developed due to Tsunami can be summarized as:

**Hydrostatic Force.** The buoyant force is the vertical force that works through a submerged body's center of mass. Its magnitude is equal to the weight of the water volume displaced by the body being submerged (see Eq. 2).

$$F_B = \rho gV \quad (2)$$

where  $V$  the water volume displaced by submerged structure,  $\rho$  is the water unit weight, and  $g$  is ground acceleration.

**Hydrodynamic (Drag) Force.** Structures are exposed to hydrodynamic forces caused by drag as the Tsunami bore travels inland at moderate to high velocity. For this force, the general expression is shown in Eq. 3. Current codes use the same expression, but the drag coefficient values ( $C_D$ ) are different:

$$F_D = \frac{\rho C_D A u^2}{2} \quad (3)$$

where  $F_D$  is the drag force acting in the flow direction,  $A$  is the projected area of the body normal to the flow direction, and  $u$  is the velocity of the Tsunami bore. Drag Coefficient ( $C_D$ ) values differ between FEMA 55 and CCH. FEMA allows the

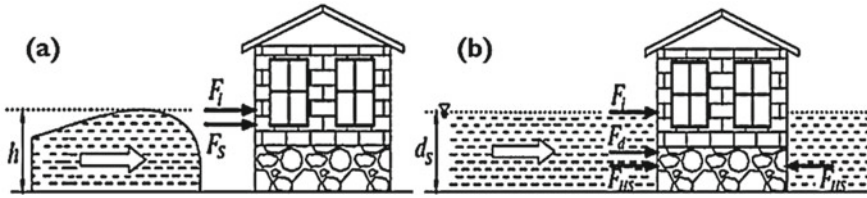


Fig. 6 Proposed conditions for loading: **a** impact point; and **b** post impact [32]

hydrodynamic force to be transformed to an equivalent hydrostatic force for flood speeds that do not exceed approximately 3.05 m/s (10 ft/s).

**Surge Force.** The surge force is created by the impingement of a tsunami bore’s advancing waterfront on a structure. The measurement of the surge force exerted on a structure is subject to considerable uncertainty because of the absence of extensive experiments directly relevant to tsunami bores running up the shoreline. CCH suggests using Eq. 4 with Dames and Moore as its basis:

$$F_s = 4.5\rho gh^2 \tag{4}$$

where  $F_s$  the surge force per unit width of wall and  $h$  the height of surge.

**Debris Impact Force.** A high-speed tsunami bears debris such as floating vehicles, floating building parts, driftwood, boats, and ships bore moving inland. The effect of floating debris on a building can cause significant forces, resulting in structural damage or collapse. Using the same method, both FEMA 55 and CCH codes reliably account for debris impact forces and suggest using Eq. 5 for calculating the impact force of debris:

$$F_i = m_b \frac{d_{ub}}{dt} = m \frac{u_i}{\Delta t} \tag{5}$$

where  $F_i$  is the impact force,  $m_b$  is the mass of the body affecting the structure,  $d_{ub}$  is the velocity of the impacting body (assumed equal to the flow velocity),  $u_i$  is the approach velocity of the impacting body (assumed equal to the flow velocity), and  $\Delta t$  is the period of impact taken equal to the time between the floating body’s initial contact with the construction and the maximum impact force. Proposed condition loading is shown in Fig. 6 [32].

## 7 Tsunami and Geo-Earth Structure Failure

The world witnessed one of the fifth largest earthquakes in more than ten decades in March 2011. 9 MW earthquake hit the pacific coast of east of Japan. Serious damages are recorded in infrastructures in the Tohoku district, and the failure of the



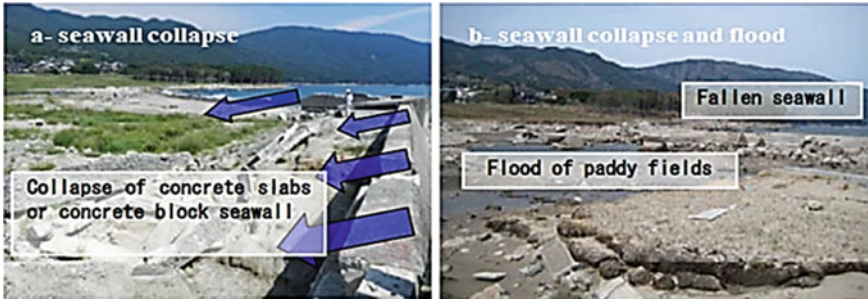


Fig. 7 See wall collapse in Yoshihama [33]

geotechnical-earth structure (i.e., the coastal protection structures) are distinguishable. Extensive field surveys are performed in the Yoshihama and Okirai areas of Ofunato district, Iwate. The coastal dike at the mouth of the Yoshihama River (i.e., the sea wall) was completely destroyed across a large wide due to the earthquake and Tsunami that resulted, with a total collapse of concrete slabs and concrete blocks (Fig. 7a). The sea wall has shifted by more than 30 m in some places (Fig. 7b). Unlike several other sea walls weakened by the Tsunami in the Tohoku region's coastal area, the damage to this sea wall in Yoshihama was not caused by scouring or erosion [33].

## 8 Conclusions

The paper presents the basic principles for studying the Tsunami phenomenon and its interaction with coastal structures and its causes. The conclusions are:

- Several factors contribute to the generation of Tsunami waves, which include earthquakes, landslides, and volcanic.
- Climate change and global warming are causing sea level water-raising, which may cause the flooding of coastal cities and Tsunami threatening.
- Tsunami propagation, inundation, and interaction with the coastal structure are well understood, but it is not easy to calculate. Previous researchers developed experimental and theoretical methods to simulate different scenarios of tsunami waves and their effect on the structures with other methods.
- The importance of the study of tsunami wave simulation is to understand the reasons that led to causing Tsunami and its influence on the coastal cities and thus to identify the necessary treatment that is compatible with the hydraulic requirements to prevent the recurrence of failure, also that to design structures that resist these waves.

## References

1. Sorensen, R. M. (2005). *Basic coastal engineering* (vol. 10). Springer Science & Business Media.
2. González, F. I., Bernard, E. N., Meinig, C., Eble, M. C., Mofjeld, H. O., & Stalin, S. (2005). The NTHMP tsunameter network. *Natural Hazards*, 35(1), 25–39.
3. Waves on the horizon. (2013). *Nature Clim Change*, 3, 179. <https://doi.org/10.1038/nclimate1815>
4. Yavuz, C., Kentel, E., & Aral, M. M. (2020). Climate change risk evaluation of Tsunami hazards in the Eastern Mediterranean sea. *Water*, 12(10), 2881.
5. Rossetto, T., Allsop, W., Charvet, I., & Robinson, D. I. (2011). Physical modelling of Tsunami using a new pneumatic wave generator. *Coastal Engineering*, 58(6), 517–527.
6. Farahmandpour, O., Marsono, A. K., Forouzani, P., Tap, M. Md., & Abu Bakar, S., (2020). Experimental simulation of tsunami surge and its interaction with coastal structure. *International Journal of Protective Structures*, 11(2), 258–280.
7. Shafiei, S., Melville, B. W., & Shamseldin, A. Y. (2016). Experimental investigation of Tsunami bore impact force and pressure on a square prism. *Coastal Engineering*, 110, 1–16.
8. Foster, A. S. J., Rossetto, T., & Allsop, W. (2017). An experimentally validated approach for evaluating tsunami inundation forces on rectangular buildings. *Coastal Engineering*, 128, 44–57.
9. Rahman, M. M., & Nakaza, E. (2016). Experimental and numerical simulation of Tsunami bore impact on a building. *International Journal of Civil Engineering and Technology*, 7(4).
10. Al-Faesly, T., Palermo, D., Nistor, I., & Cornett, A. (2012). Experimental modeling of extreme hydrodynamic forces on structural models. *International Journal of Protective Structures*, 3(4), 477–505.
11. Thusyanthan, N. I., & Gopal Madabhushi, S. P. (2008). Tsunami wave loading on coastal houses: a model approach. In *Proceedings of the institution of civil engineers-civil engineering* (vol. 161, no. 2, pp. 77–86). Thomas Telford Ltd.
12. Siegel, F. R. (2019). *Adaptations of coastal cities to global warming, sea level rise, climate change and endemic hazards*. Springer.
13. Du, W., & Pan, T. C. (2020). Probabilistic seismic hazard assessment for Singapore. *Natural Hazards*, 103(3), 2883–2903.
14. El-Askary, H. M., El-Hattab, M., El-Raey, M., & Kafatos, M. (2009). Impact of sea level rise on the low land area South East of Alexandria, Egypt. In *AGU fall meeting abstracts* (vol. 2009, pp. NH11A-1097).
15. Koshimura, S. (2019). Tsunami. In *Encyclopedia of ocean sciences* (pp. 692–701). Elsevier.
16. Bryant, E. (2014). *Tsunami: The underrated hazard*. Springer.
17. Röbbke, B. R., & Vött, A. (2017). The tsunami phenomenon. *Progress in Oceanography*, 159, 296–322.
18. Di Risio, M., De Girolamo, P., & Beltrami, G. M. (2011). Forecasting landslide generated tsunamis (pp. 81–106).
19. Paris, R. (2015). Source mechanisms of volcanic tsunamis. *Philosophical Transactions of the Royal Society A: Mathematical, Physical and Engineering Sciences*, 373(2053), 20140380.
20. Paris, R., Switzer, A. D., Belousova, M., Belousov, A., Ontowirjo, B., Whelley, P. L., & Ulvrova, M. (2014). Volcanic Tsunami: A review of source mechanisms, past events and hazards in Southeast Asia (Indonesia, Philippines, Papua New Guinea). *Natural Hazards*, 70(1), 447–470.
21. Kakinuma, T. (2016). Tsunami generation due to a landslide or a submarine eruption. In *Tsunami* (pp.35–58). InTech.
22. Power, W., Downes, G., & Stirling, M. (2007). Estimation of tsunami hazard in New Zealand due to South American earthquakes. In *Tsunami and its hazards in the Indian and Pacific oceans* (pp. 547–564). Birkhäuser Basel.
23. Helal, M. A., & Mehanna, M. S. (2008). Tsunamis from nature to physics. *Chaos, Solitons & Fractals*, 36(4), 787–796.

24. Gourlay, M. R. (2011). Waves and wave-driven currents.
25. De Wilde, P., & Carlomagno, G. M. (Eds.). (2019). *Computational methods and experimental measurements XIX and earthquake resistant engineering structures XII*. WIT Press.
26. Charvet, I., Eames, I., & Rossetto, T. (2013). New tsunami runup relationships based on long wave experiments. *Ocean Modelling*, 69, 79–92.
27. Ward, S. N. (2010). The 1889 Johnstown, Pennsylvania Flood. A physics-based simulation. In *The Tsunami threat: research and technology* (pp.447–466).
28. Eliasson, J. (2019). Earthquake-generated landslides and tsunamis. In *Earthquakes-impact, community vulnerability and resilience*. InTech Open.
29. Robertson, I., Chock, G., & Morla, J. (2012). Structural analysis of selected failures caused by the 27 February 2010 Chile tsunami. *Earthquake Spectra*, 28(1\_suppl1), 215–243.
30. Kim, Y. C. (2010). *Handbook of coastal and ocean engineering*. World Scientific.
31. Nistor, I., Palermo, D., Cornett, A., & Al-Faesly, T. (2011). Experimental and numerical modeling of tsunami loading on structures. *Coastal Engineering Proceedings*, 32, 2–2.
32. Govindasamy, N., Mardi, N. H., & Malek, M. A. (2018). Modelling of tsunami forces on coastal structures: A review.
33. Hazarika, H., Okada, H., Hara, T., Ueno, M., Ohsumi, T., Yamanaka, M., Yamazaki, T., Kosaka, N., Minowa, H., & Furuichi, H. (2012). Case studies of geotechnical damage by the 2011 off the Pacific Coast of Tohoku Earthquake and Tsunami in Japan. In *Proceedings of the 15th world conference on earthquake engineering, Lisbon, Portugal, Paper (No. 4796)*.

# The Scale Effects on the Shear Strength Behavior of Silty Sand Soil in Direct Shear Tests



Omar H. Al-Emami and Ammar A. Al-Sultan

**Abstract** The direct shear test is widely used in geomechanics investigation to obtain the shear strength properties of soils. The simplicity and repeatability of the results presented by this apparatus have kept the direct shear tests in use for more than 60 years. An effort has been made to study the effect of two various sizes of the shear box ( $60 \times 60$  and  $300 \times 300$  mm) on the shear strength characteristics of silty sand soil used in this research and to evaluate the effect of test condition (saturated and wet conditions) on the experimental results of this test. The disturbed samples are almost prepared at an initial water content of  $(8 \pm 1\%)$  and two different initial dry unit weights ( $1.662$  and  $1.330 \text{ Mg/m}^3$ ). The results from two apparatuses appear that the internal angle of friction obtained from small shear box is higher ( $1\text{--}2^\circ$ ) compared to the big shear box. Also, the samples sheared under unsaturated conditions exhibited higher shear strength corresponding to those tested under saturated conditions. The results indicate that an increasing the specimen density caused an increase in the maximum shear strength in each of two shear box sizes.

**Keywords** Scale effects · Direct shear · Peak shear strength · Silty sand · Density · Test condition

## 1 Introduction

In geotechnical engineering, it is well known that the values of shear strength parameters, angle of friction, and cohesion are adopted to solve many tasks in the construction field, such as retaining walls, pile foundations, and shallow footings. There are two kinds of tests to obtain those parameters laboratory tests and in-situ testing. One of the common tests used in the study of shear strength characteristics is the direct shear experiments, as it is simple and gives reliable results. In the middle of

---

O. H. Al-Emami (✉) · A. A. Al-Sultan  
Civil Engineering Department, University of Technology, Baghdad, Iraq  
e-mail: [40118@uotechnology.edu.iq](mailto:40118@uotechnology.edu.iq)

A. A. Al-Sultan  
e-mail: [40321@uotechnology.edu.iq](mailto:40321@uotechnology.edu.iq)

the last century, the shear strength behavior's sample size effects have been investigated experimentally by Parsons [1]. The author performed a series of different sizes of shear boxes ( $60 \times 60$  mm,  $120 \times 100$  mm, and  $120 \times 200$  mm) direct shear tests on crushed quartz and Ottawa clean uniform sandy soil. The laboratory results revealed that the friction angle slightly decreased with increasing the shear cell dimensions. It was shown that the friction angle of Ottawa sand ranged from  $28.5^\circ$  to  $31.0^\circ$  and the friction angle resulted from testing the crushed quartz ranged from  $30.7^\circ$  to  $31.5^\circ$ . Cerato et al. [2] examined the scale effects of three-square shear boxes (60 mm, 101.6 mm, and 304.8 mm) on the shearing behavior of five sands with different relative densities (loose, medium, and dense). The authors indicated a noticeable dependency of friction angle on the sample size, and the effect of sample dimensions is also a function of the sand type and relative density. A similar trend of behavior was observed by other researchers, such as [3–5]. Recently, Shakri et al. [6] performed a series of direct shear tests of two shear box sizes ( $60 \times 60$  mm and  $300 \times 300$  mm) on modified sand-column (PFA-sand mixture) and soft soil.

Their test results revealed that as the shear cell's dimensions increased, a decrease in the shear strength was observed. Conversely, Palmeira and Milligan [5] reported no significant difference in frictional angle with the increasing the size of the shear box. The authors obtained their results by performing several laboratory tests on dense Leighton Buzzard Sand using three different shear boxes (small, medium, and large). In the current study, in continuation of previous research, soil specimens with two densities were adopted and tested under saturated and unsaturated conditions to examine the effect of two various shear box sizes ( $60 \times 60$  mm and  $300 \times 300$  mm) on the shear strength of silty sand soil. It is noteworthy to mention here that the term "unsaturated condition" used in this study indicates that the soil samples tested in the direct shear apparatus under two stages consolidation and shearing (i.e. without saturation stage).

## 2 Experimental Program

**Direct shear apparatus.** Consolidated-drained direct shear experiments were performed on silty sand soil samples based on the ASTM D3080 (2011) [7]. According to this specification, several requirements related to the ratio of particle dimensions to the box dimensions should be considered when preparing samples for testing. It is recommended that the minimum specimen width should not be less than 10 times the maximum particle-size diameter, and the minimum initial specimen thickness should not be less than 6 times the maximum particle diameter. In addition, the ratio of minimum specimen width to thickness is required to be 2 [2, 8]. Two types of direct shear apparatus were taken for this research, as shown in Fig. 1. The first apparatus has a square shear box having dimensions  $60 \times 60 \times 20$  mm. The normal load is applied on the tested samples using a lever arm frame. The small-sized shear box apparatus is equipped with two displacement transducers to gauge the horizontal displacement and vertical deformation and load cell for horizontal shear

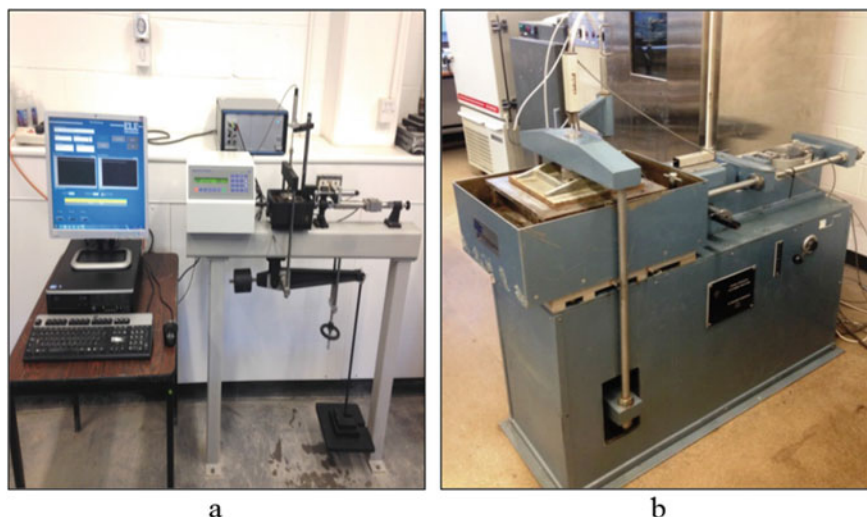


**Fig. 1** Direct shear test apparatus: **a** small shear box, **b** large-shear box

force measurement. The second apparatus has a square cross-section of 300 mm by 300 mm and a thickness of 140 mm. In this apparatus, the vertical pressure for consolidating the sample is applied and controlled by an automatically closed-loop hydraulic system. The soil samples were tested under four vertical stress values (50, 100, 200, and 400 kPa). Whereas, in the large-dimensioned shear box, tests were done under three different normal stresses (100, 200, and 400 kPa). For each shear box size, the samples were subjected to saturated and unsaturated conditions for the selected dry density.

#### **Properties of the Tested Material.**

The soil used for the experimental investigations in this research is classified as Silty sand (SM) based on the Unified Soil Classification System (USCS). The soil was collected from a depth ranging from 16.5–25 m below the natural ground level. The particle size distribution of the tested material is presented in Fig. 2. The soil consists of 0.6% gravel, 77.3% sand, 20.1% silt, and 2% clay. The mean particle size ( $D_{50} = 0.23$  mm) and specific gravity ( $G_s = 2.67$ ) were determined from the sieve analysis and particle density tests. In addition, the used material was found non-plastic. The laboratory compaction characteristics of the silty sand samples, maximum dry unit weight ( $1.629$  Mg/m<sup>3</sup>), and optimum moisture content (11.25%) were measured following ASTM standard procedure D1557-09 [9].

**Sample Preparation and Testing Procedure.** All direct shear samples were prepared at an initial water content of  $8 \pm 1\%$ . In small and large sizes of shear boxes, the required amount of soil mixture to achieve the targeted dry unit weight (i.e., 1.662 and 1.330 Mg/m<sup>3</sup>) is compacted inside the shear box in four layers. After completing the compaction, the samples were allowed to soak water for 24 h for

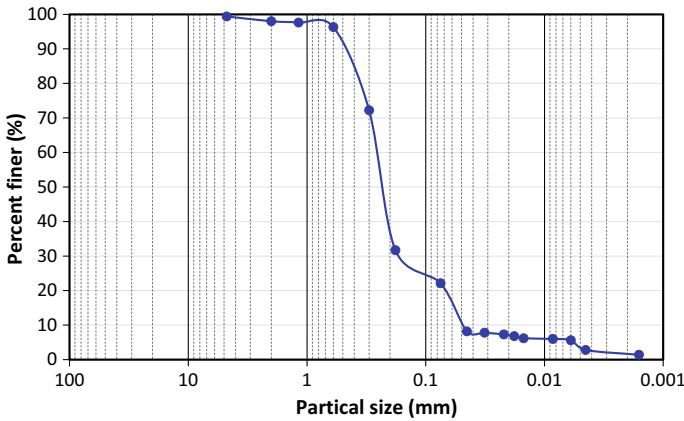


Fig. 2 Particle size distribution curve for the tested soil

saturated tests. A pre-calculated vertical load corresponding to the targeted vertical stress was applied during the consolidation stage. After attaining the consolidation, the tested specimen was subjected to constant vertical stress and constant horizontal shear rate. Considering the previous studies, the saturated samples were sheared at a constant rate of shear displacement of 0.04 mm/min. In contrast, the samples conducted under unsaturated conditions were directly consolidated after completing the compaction process and then sheared at 0.0095 mm/min shear rate displacement.

### 3 Results and Discussion

**Effect of the shear cell dimensions on the shearing behavior.** Typical direct shear exam results are best showed through the plots of shear strength versus horizontal displacement. Figures 3 and 4 show these relationships for silty sand samples having an initial dry unit weight of 1.662 and 1.330 Mg/m<sup>3</sup> and tested in two different shear box sizes under saturated conditions. Generally, at any given value of soil density, the shear strength increased with increasing the level of applied vertical stress. However, at any stress level, the denser samples showed higher shear strength than the looser samples. A similar trend of behavior has been reported by previous researchers [e.g., 1, 10, 11]. The shear strength plots presented in Figs. 3 and 4 revealed two differentiated patterns: strain-softening pattern (peak pattern) and strain-hardening pattern (non-peak pattern). Denser samples ( $\rho_{dmax} = 1.662 \text{ Mg/m}^3$ ) exhibited peak patterns, whereas looser samples ( $\rho_{dmax} = 1.330 \text{ Mg/m}^3$ ) exhibited non-peak patterns. Also, the horizontal displacement corresponding to the peak and/or maximum shear strength increased with increasing applied vertical stress, as shown in Table 1.

Similar to saturated tests, the results of soil samples tested under unsaturated conditions showed a similar trend of behavior, in the sense that the shear strength

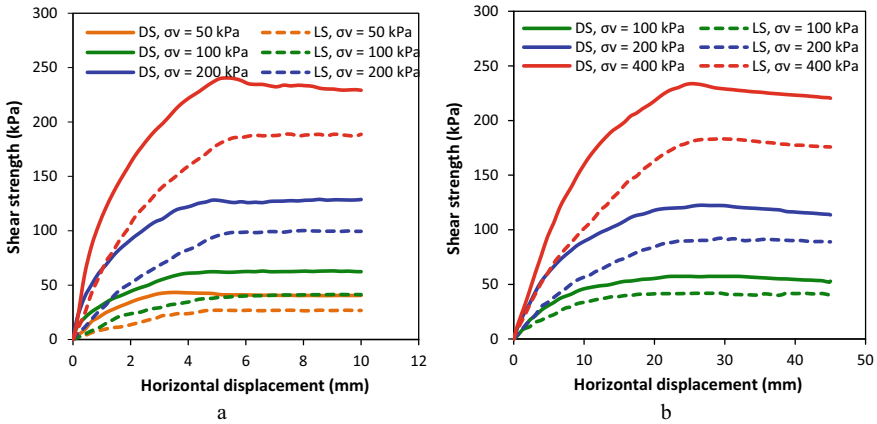


**Fig. 3** Shear strength versus horizontal displacement for dense and loose samples tested in **a** small-sized box and **b** large-sized box under saturated condition

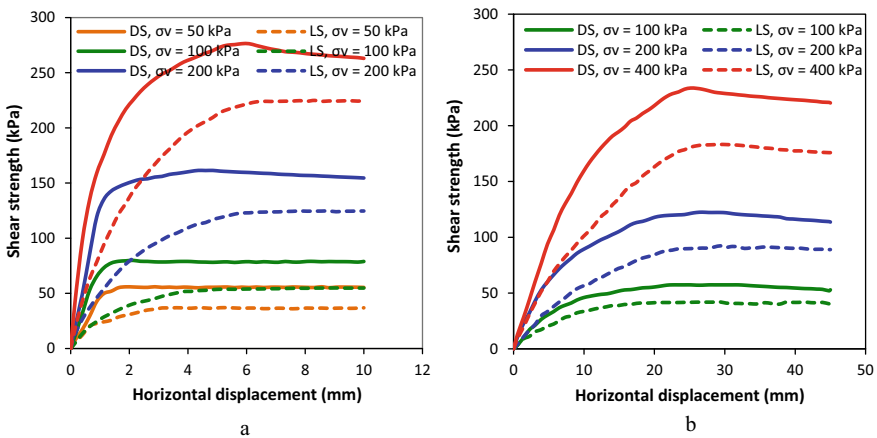


**Fig. 4** Shear strength versus horizontal displacement for dense and loose specimens tested in **a** small-sized box and **b** large-sized box under unsaturated condition

increased with increasing the level of applied stresses. From the observation of Figs. 3 and 4, the obtained shear strength of samples tested under constant water content is distinctly more significant than those obtained from saturated samples and all levels of vertical stress. The latter phenomenon is attributed to the fact that the meniscus around particle contact points tends to attract the particle together, which causes the increase of soil skeleton stiffness resulting in greater resistance during shearing, and consequently, the shear strength is increased [6, 11, 12]. For dense samples, a noticeable strain-softening behavior was observed after the peak shear strength (peak pattern). In contrast, looser samples exhibited non-peak patterns (little to no strain



**Table 1** Values of horizontal displacement corresponding to the peak/maximum shear strength for samples with different densities tested under (saturated and unsaturated) conditions

Test condition	Shear box sizes, (mm)	Vertical stress, $\sigma$ (kPa)	$\rho_{dry} = 1.662$ (Mg/m <sup>3</sup> )	$\rho_{dry} = 1.330$ (Mg/m <sup>3</sup> )	Horizontal dis. at peak shear strength, $\delta_h$ (mm)	
			$\tau_{peak/maximum}$ (kPa)	$\tau_{peak/maximum}$ (kPa)	$\rho_{dry} = 1.662$ (Mg/m <sup>3</sup> )	$\rho_{dry} = 1.330$ (Mg/m <sup>3</sup> )
Saturated	60 × 60	50	43.18	27.23	3.36	3.11
		100	61.31	38.86	3.61	4.35
		200	128.17	98.70	4.84	5.09
		400	240.48	187.58	5.58	5.58
	300 × 300	100	59.07	41.05	20.04	14.04
		200	122.22	91.83	23.43	21.76
		400	233.73	182.65	25.98	25.15
Unsaturated	60 × 60	50	52.81	38.24	1.63	2.98
		100	77.49	52.48	1.91	3.61
		200	160.60	117.02	4.10	4.84
		400	276.29	220.36	6.08	5.83
	300 × 300	100	74.31	52.05	21.76	13.26
		200	156.40	118.16	25.15	20.92
		400	277.92	217.29	28.53	23.43

hardening–softening behavior). Figure 3 that the different patterns of behavior in the post-peak shear strength region indicate that the soil suction is less significant, whereas the soil suction contributes clearly to the peak shear strength. This behavior agrees with that found by [10, 13, 14].

Examining Table 1 closely, it can be seen that the peak and/or maximum shear strength of the tested samples slightly decreased (2–8 kPa) as the size of the shear box increase. This behavior is consistent with many previous researchers' observations [e.g., 5, 11, 15]. Wu et al. [15] attributed the decrease in the peak shear strength of the dense Toyoura sandy soil with an increase in the ratio  $L/D_{50}$  to two reasons: (i) a decrease in the influence of mechanical boundary restraint on the free development of the shear band, and (b) increasing in the effect of the gradual failure with an increase in length specimen of relative to the size of the sand particles. Figures 3 and 4, in conjunction with Table 1 revealed that the horizontal displacement corresponding to the peak and/or maximum shear strength is not consistent for the two shear box sizes. Hence, the comparison between the results is difficult. The shear strength is plotted against relative lateral strain (horizontal displacement/shear box length) instead of horizontal displacement to overcome this problem.

Figures 5 and 6 show that the same results shown in Figs. 3 and 4 are redrawn but plotting the x-axis as a relative lateral strain. The results showed that the peak and/or

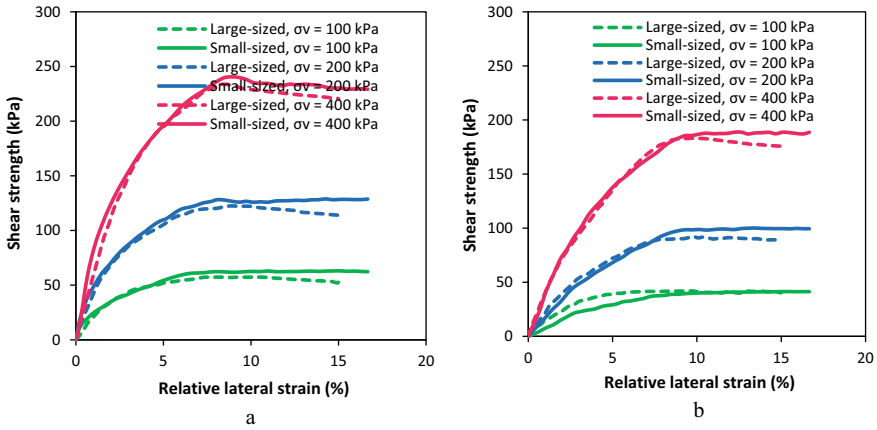


**Fig. 5** Comparison of the shear strength curves using two different shear box sizes under saturated condition **a** dense samples and **b** loose samples

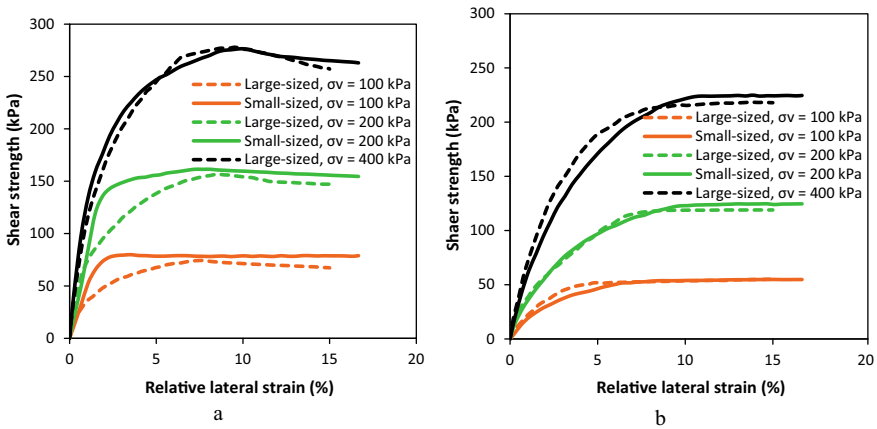


**Fig. 6** Comparing the shear strength curves using two different shear box sizes under unsaturated conditions **a** dense samples and **b** loose samples

maximum shear strength achieved approximately similar relative lateral strain. In addition, the peak/maximum shear strength slightly decreased as the size of the shear box increased (Table 1). This trend was mostly observed for all the tested samples performed under saturated and unsaturated conditions. The researchers [e.g., 3, 8] attributed this behavior to the different heights of samples that influence the vertical stress distribution of the sample shear plane, caused by the moment of shear force applied to the upper half of the shear box, which is transferred to the specimen. The researchers have found that the thickness of the specimen and the shear box's adequate length is necessary to consider to allow fully generation of the shear zone.

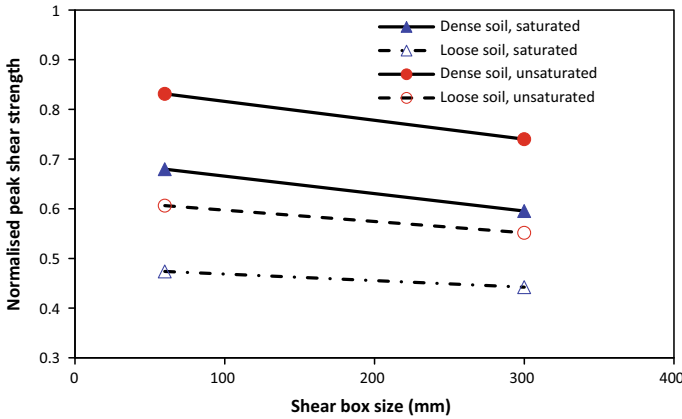


**Fig. 7** Influence of shear box size on the average of normalized shear strength for saturated and unsaturated silty sand samples

The average values of the normalized peak and/or maximum shear strength ( $\tau_{\text{peak}/\text{maximum}}/\sigma_v$ ) of the tested samples are plotted against the shear box's width, as shown in Fig. 7. Test results of saturated and unsaturated samples presented in this figure showed that the shear box's size influences the values of ( $\tau_{\text{peak}/\text{maximum}}/\sigma_v$ ), which is generally decreased with increasing the specimen's length. This agrees with the observations obtained by other researchers [5, 15, 16]. The authors attributed this behavior to the matter that the shear region in a small-sized shear box may not be fully developed, leading to a higher angle of friction. Moreover, Fig. 6 reveals a noticeable correlation between ( $\tau_{\text{peak}/\text{maximum}}/\sigma_v$ ) and the initial dry unit weight of the tested material. For both saturated and unsaturated test conditions, denser samples appeared greater ( $\tau_{\text{peak}/\text{maximum}}/\sigma_v$ ) than looser samples.

**Effect of the Shear Cell Dimensions on Shear Strength Parameters.** Plots of peak and/or maximum shear strength versus vertical stress corresponding to failure for dense and loose samples performed under saturated and unsaturated conditions are shown in Figs. 8 and 9, respectively. These figures showed clearly that the shear strength envelopes showed good linearity over the vertical stress range of 50 to 400 kPa. It can be seen from these figures, as expected, that the shear strength envelopes shifted upward with increasing the initial dry unit weight of the tested samples. The soil shear strength parameters are calculated from Figs. 8 and 9 and tabulated in Table 2. Also, the shear envelopes' R-square values are indicated in this table to verify the linearity of the relations. A very little scattering was noticed regarding the R-square values of the first order failure envelope lines of different void ratios samples for soil and interfaces, ranging from 0.9937 to 0.9992. This can be attributed to many factors, such as the accuracy adopted during the tested samples' preparation method and performing the laboratory tests under controlled conditions to some extent.

**Fig. 8** Failure envelopes corresponding to different unit weights under saturated conditions

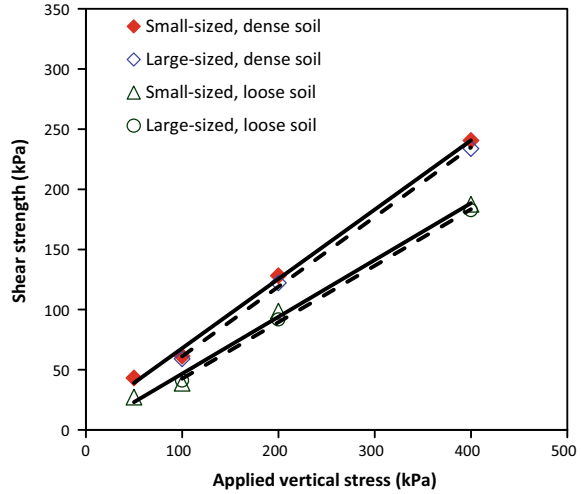


**Fig. 9** Failure envelopes corresponding to different unit weights under unsaturated conditions

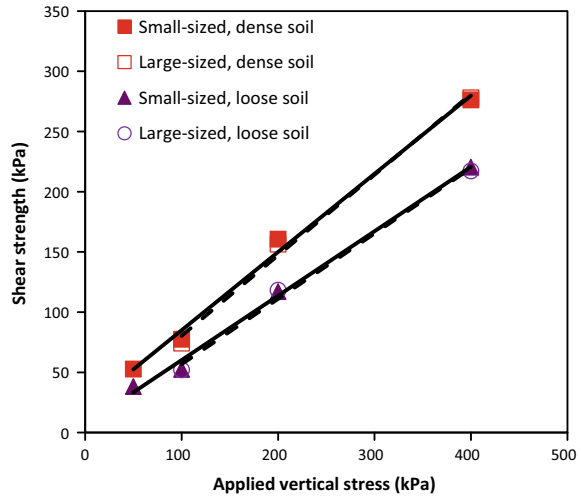


Figure 8 and Table 2 indicate that the friction angle,  $\phi'$  slightly decreases ( $1.5^\circ$ ) with the increase of the shear box size. The test results were found to agree with other researchers' findings [e.g., 1–3]. Also, it can be noted that only the failure envelopes of the dense samples tested under saturated conditions passed a little above the point of origin on the abscissa. Similar trends have been reported by Yokoi [17] after studying the relationship between shear strength and soil cohesion of Kibushi and Kashima soils. The author attributed this behavior to the matter that the absolute value of soil cohesion cannot be evaluated owing to the effective angle of extreme edge; soil cohesion measured by the metal-wedge method is closely related to the applied initial stress. Hence, it is probable that soil cohesion acts as compressive stress to

**Table 2** Shear strength parameters of samples with different densities tested under (saturated and unsaturated) conditions

Shear box sizes (mm)	Initial density, $\gamma_{dry}$ (kN/m <sup>3</sup> )	Test condition	$\phi'$ (Degree)	$c'$ (kPa)	$R^2$
60 × 60	16.62	Saturated	32.5	7.5	0.9972
	13.30		28.0	0.0	0.9937
300 × 300	16.62	Saturated	31.0	5.5	0.9990
	13.30		26.5	0.0	0.9992
60 × 60	16.62	Unsaturated	36.5	21.0	0.9940
	13.30		31.0	4.5	0.9955
300 × 300	16.62	Unsaturated	36.0	16.0	0.9938
	13.30		29.0	3.0	0.9943

the corresponding shear cohesion. In addition, it is found that the cohesionless soils under saturated conditions have little soil cohesion.

Similar to saturated tests, at any dry unit weight used in this study, the value of  $\phi'$  obtained from unsaturated samples exhibits decrease (0.5° to 2°) with increasing the size of the shear box. The test results presented in Fig. 9 and Table 2 showed that the soil suction mainly influences the shear strength parameters. More specifically, the values of soil cohesion,  $c'$  presented in Table 2 of the dense samples increased by twofold when performed at the unsaturated condition compared to those tested under saturated condition. Likewise, a slight increase in the value of effective cohesion was observed for loose samples. It can also be noticed from Table 2 that there is a noticeable dependency of the effective friction angle on the test conditions (saturated or unsaturated). Similar to  $c'$ , the friction angle values obtained from unsaturated samples are higher than saturated samples, as expected. These results match those observed in studies [e.g., 5, 10, 13, 14].

## 4 Conclusions

A laboratory testing program was designed to examine the sample size effect on the shearing behavior of silty sand soil with different initial dry unit weights and test conditions. The samples were tested in a large-sized (300 × 300 mm) and small-sized (60 × 60 mm) direct shear apparatus. Tests results presented in this research revealed the followings:

1. Based on the results, soil suction plays a considerable influencing role in increasing the tested samples' shear strength. However, this role is less significant beyond the peak and/or maximum shear strength.
2. The test results obtained from two different shear box sizes appeared that there is no remarkable difference in shear strength's measured values (2–8 kPa). Also,

- the effect of samples size and the dry unit weight on the residual shear strength of the samples can be considered insignificant.
3. The angle friction angle values obtained from the small-sized shear box are slightly higher ( $1^\circ$  to  $2^\circ$ ) than those obtained from the large-sized shear box. The decrease in the friction angle increased with decreasing the initial dry unit weight of the tested samples.
  4. The soil cohesion of dense samples performed under saturated conditions slightly reduces with increasing the shear box size. Simultaneously, an increase in sample size had a negligible effect on the soil cohesion of loose samples. Similarly, all large samples tested under unsaturated conditions showed a lower value of apparent cohesion than small samples.
  5. Test results of saturated and unsaturated samples exhibited that the shear box's size influences the average values of the normalized peak and/or maximum shear strength ( $\tau_{\text{peak/maximum}}/\sigma_v$ ), which is generally decreased with increasing the length of the samples. Also, denser samples appeared greater values of ( $\tau_{\text{peak/maximum}}/\sigma_v$ ) compared with looser samples.

## References

1. Parsons, J. D. (1936). Progress report on an investigation of the shearing resistance of cohesionless soils. In *Proceedings of the 1st International Conference on Soil Mechanics and Foundation Engineering* (Vol. 2, pp. 133–138).
2. Cerato, A., David, L. S., Sheahan, T., & Lutenegeger, A. (2006). Specimen size and scale effects of direct shear box tests of sands. *Geotechnical Testing Journal*, 29(6). <https://doi.org/10.1520/gtj100312>
3. Dadkhah, R., Ghafoori, M., Ajalloeian, R., & Lashkaripo, G. R. (2010). The effect of scale direct shear test on the strength parameters of clayey sand in Isfahan city, Iran. *Journal of Applied Science*, 10(18), 2027–2033. <https://doi.org/10.3923/jas.2010.2027.2033>
4. Matsushima, K., Suits, L. D., Sheahan, T. C., Wu, P.-K., & Tatsuoka, F. (2008). Effects of specimen size and some other factors on the strength and deformation of granular soil in direct shear tests. *Geotechnical Testing Journal*, 31(1). <https://doi.org/10.1520/gtj100773>
5. Palmeira, E. M., & Milligan, G. W. E. (1991). Scale effects in direct shear tests on sand. *International Journal of Rock Mechanics and Mining Science and Geomechanics*, 28(6). [https://doi.org/10.1016/0148-9062\(91\)91203-4](https://doi.org/10.1016/0148-9062(91)91203-4)
6. Shakri, M. S., Md. Noor, M. G., Nazaruddin, A. T., & Hafez, M. A. (2017). Effects of shear box size on shear strength between modified sand-column (PFA-Sand Mixture) and soft soil. *International Journal of Structural and Civil Engineering Research*, 6(1).
7. ASTM D 3080. (2011). Standard test method for direct shear test of soils under consolidated drained conditions ASTM international West Conshohocken PA. [https://doi.org/10.1520/D3080\\_D3080M](https://doi.org/10.1520/D3080_D3080M)
8. Hight, D. W., & Leroueil, S. (2003). Characterisation of soils for engineering purpose. In *Proceedings of the Characteristics and Engineering Properties of Natural Soils*, (Vol. 1, pp. 255–360).
9. ASTM D 1557. (2009). Standard test methods for laboratory compaction characteristics of soil using modified effort. ASTM international West Conshohocken PA. <https://doi.org/10.1520/D1557-09>

10. Hossain, M. A., & Yin, J.-H. (2010). Shear strength and dilative characteristics of an unsaturated compacted completely decomposed granite soil. *Canadian Geotechnical Journal*, 47(10), 1112–1126. <https://doi.org/10.1139/t10-015>
11. Wang, L. C., Long, W., & Gao, S. H. (2014). Effect of moisture content, void ratio and compacted sand content on the shear strength of remolded unsaturated clay. *Electrical Journal of Geotechnical Engineering*, 19(2), 4413–4426.
12. Larson, W. E., & Gupta, S. C. (1980). Estimating critical stress in unsaturated soils from changes in pore water pressure during confined compression. *Soil Science Society of America Journal*, 44(6), 1127. <https://doi.org/10.2136/sssaj1980.03615995004400060001x>
13. Borana, L.Y.J.-H., Singh, D. N., & Shukla, S. K. (2015). A modified suction-controlled direct shear device for testing unsaturated soil and steel plate interface. *Marine Georesources and Geotech.*, 33(4), 289–298. <https://doi.org/10.1080/1064119x.2013.843045>
14. Hamid, T. B., & Miller, G. A. (2008). A constitutive model for unsaturated soil interfaces. *International Journal for Numerical and Analytical Methods in Geomechanics*, 32(13), 1693–714. <https://doi.org/10.1002/nag.692>
15. Wu, P. K., Matsushima, K., & Tatsuoka, F. (2007). Effects of test conditions on shear behaviour of composite soil. *Geotechnical Testing Journal*, 31(1), 45–64.
16. Wang, J., & Gutierrez, M. (2010). Discrete element simulations of direct shear specimen scale effects. *Géotechnique*, 60(5), 395–409. <https://doi.org/10.1680/geot.2010.60.5.395>
17. Yokoi, H. (1968). Relationship between soil cohesion and shear strength. *Soil Science and Plant Nutrition*, 14(3), 89–93. <https://doi.org/10.1080/00380768.1968.10432750>

# Tunnel-Soil-Structure Interaction Under Seismic Load



Zaid F. Al-Farhan, Moataz A. Al-Obaydi, and Qutayba N. Al-Saffar

**Abstract** The soil-structure interaction is significant in analyzing and designing structures, especially the high-rise buildings under dynamic loads. In many cities, there are tunnels under the buildings. Therefore, this study took into account the interaction between the tunnel, structure, and the soil. This interaction is valued on the behavior of a high-rise building consisting of 15 floors that are exposed to an earthquake underneath by a tunnel of 10 m diameter ( $D$ ). Several parameters have been considered using numerical analysis using PLAXIS 2D software, comprising the horizontal distance ( $X$ ) between the tunnel and the center of the building as ratios ( $X/D = 0, 1, 2, 3,$  and  $4$ ), as well as the effect of the vertical distance ( $H$ ) between the foundation base and the crown of the tunnel as ratios ( $H/D = 1, 2, 3$  and  $4$ ). Results showed a significant influence on the interaction between the tunnel, soil, and structure. The horizontal displacement of the building increased under the seismic load when the axis of the building coincided with the tunnel ( $X/D = 0$ ), and the maximum displacement was obtained at a distance ( $X/D = 1$ ). The horizontal displacement decreased with the increase in the horizontal distance. Besides, the Inter-story drift increased more than 1.5% at a distance ( $X/D = 0$ ), meaning that the building began to collapse, and the effect of the tunnel decreased as it became away from the building. The differential settlement increased with the presence of the tunnel, reaching the highest increase by 240% at ( $X/D = 1$ ). On the other hand, the influence of tunnel depth showed through an increase in the horizontal displacement and the inter-story drift when the tunnel is shallow ( $H/D = 1$  and  $2$ ). The differential settlement increased by 200% at ( $H/D = 1$ ) and decreased with increasing the depth of the tunnel. The effect of the tunnel disappeared at a depth greater than  $4D$ .

---

Z. F. Al-Farhan · M. A. Al-Obaydi (✉) · Q. N. Al-Saffar  
Department of Civil Engineering, College of Engineering, University of Mosul, Mosul, Iraq  
e-mail: [dralobaydi@uomosul.edu.iq](mailto:dralobaydi@uomosul.edu.iq)

Z. F. Al-Farhan  
e-mail: [zaid.enp154@student.uomosul.edu.iq](mailto:zaid.enp154@student.uomosul.edu.iq)

Q. N. Al-Saffar  
e-mail: [dr.qutayba@uomosul.edu.iq](mailto:dr.qutayba@uomosul.edu.iq)



**Keywords** Soil-structure interaction · Seismic load · Tunnel · Finite element method

## 1 Introduction

Urban growth is continuously increasing leads to a lack of places and transportation facilities. Therefore, it is a need for high-rise buildings to exploit areas and the underground facilities. This crowding in different structures creates the interaction between them and how others influence each one, especially under dynamic load. The construction of a tunnel can be a significant influence factor to the damage of surfaces building. For example, Dublin Port Tunnel created 334 claims of building damage like cracks and damage of windows [1]. The active seismicity zones should also pay attention to the seismic performance of both the ground and underground surfaces in design. This performance is impacted by the dynamic interaction between superstructure and underground within the soil, i.e., the impact of a tunnel on the soil-structure interaction.

For many years, the underground tunnels were thought to be safe constructions from the impact of earthquakes. Recently, many failures have been reported in this type of construction under the influence of earthquakes [2–4], especially in the shallow tunnels which are near the ground surface. Also, the researchers noted that the failure and destruction of the superstructures occurred due to the influence of the earthquake as a result of the wave's amplification when it reaches the surface. In this regard, several studies have been made [5–12], all stated that soil-structure interaction could increase the lateral deformation and inter-story drifts of the structure, which imposing the structure to behave in the range of inelastic and leading to damage of the structure. The effect of a circular tunnel on structures was investigated analytically, and it was found that the presence of the tunnel changes the acceleration reaching the surface of the earth [13–15]. The soil and structure response due to the presence of the tunnel in different locations under the structure is found through the change in the acceleration due to variation in the earthquake frequency [16, 17].

Stefania [18] studied the effect of underground openings on the amplification of the ground motion on the free surface of a hilly area. The presence of many shallow openings affects the amplification of the ground and, therefore, cannot be omitted. Rostami [19] examined the changes in seismic velocity at the ground surface, Fourier spectrum, and structural response spectrum by excavating a circular tunnel. The excavated shallow tunnel caused a change in the recording of the profile of the earthquake. With the aid of laboratory and numerical models, Baziar et al. [20] found that constructing a rectangular tunnel increased the maximum earthquake acceleration more than the situation without the tunnel. Sun and Wang [21] examined the acceleration of the ground surface of the free-field conditions in the existence of underground structures. The results indicated that the underground structures have a significant effect on the response spectrum and PGA. Hamed and Reza [22] examined the impact of the existing tunnel numerically with different system frequencies on

the ground surface’s acceleration. Rostami [23] studied the effect of tunneling with the excavation stages (neglecting the concrete membrane of the tunnel) and at several distances and depths on a steel structure and a certain soil.

All the previous studies focused on the effect of tunnel on the change of acceleration and the change of the earth’s surface response to an earthquake, ignoring the presence of structure. Few studies have investigated the coupled interaction between tunnel and structure with soil under seismic load. In this study, the direct method was adopted to simulate the Tunnel-Soil-Structure model with the aid of PLAXIS 2D software. This code can simulate the complexity of geometry and coupled interaction between Tunnel-Soil-Structure under the dynamic load.

## 2 Methodology and Numerical Model

There are two methods to study the behavior of the coupled soil-structure interaction that direct and indirect methods [24]. In this study, the direct method has been used to simulate the whole soil, structure, and tunnel (Fig. 1). The PLAXIS 2D software based on the finite element method was used to model the Tunnel-Soil-Structure-Interaction (TSSI) systems to analyze complex geometric equations and boundary conditions.

**Numerical Model.** Two-dimensional plane strain dynamic finite element has been carried out with domain dimensions of  $140 \times 70$  m, as shown in Fig. 2. It was considered the recommendation is given by Al-Rayhani and Naggar [25] on the minimum horizontal limits and depth of the bedrock, take into account the condition of the present study. The soil media simulated using a 15-node triangle element. All

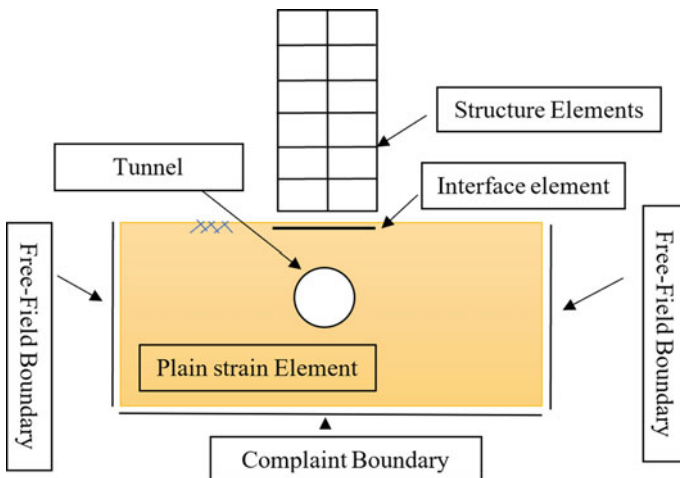
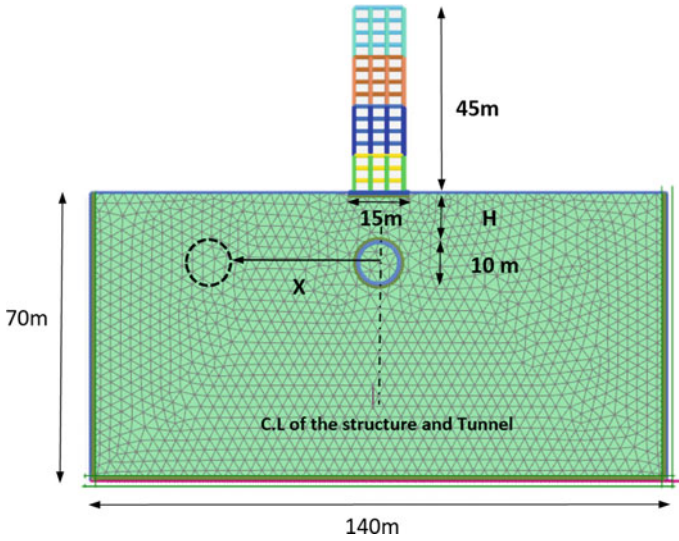


Fig. 1 Component of Soil-Tunnel-Structure Model



**Fig. 2** Meshed model with geometry dimension of system by PLAXIS 2D

structure and lining elements simulated as a 5-node plate element with three degrees of freedom per node. For the earthquake analysis problem, a free-field boundary at vertical sides considered consists of two dashpots in the normal and shear direction. The compliant base boundary has been used at the bedrock [26]. The contact zone between the foundation and soil as well as the zone between the tunnel and soil are simulated by interface elements (Fig. 1). The interface shear strength between soil and foundation defined by Mohr–Coulomb failure criteria.

**Soil Strata.** The soil media proposed in the numerical model is clayey soil with properties presented in Table 1. The dynamic properties of soil have been modeled by using Hardening soil with a small-strain stiffness model, which considers the stiffness reduction curve.

**Structural Element Properties.** The structural model proposed in this study is a reinforced concrete building with a raft foundation of 1.48 m thickness were designed by Tabatabaiefar [11]. The proposed RC building consists of 15 floors, each floor 3 m height with a total building height of 45 m and 3 bays. Each bay width is 4 m with the section properties presented in Table 2. The density, compressive strength, and modulus of elasticity of concrete are  $25 \text{ kN/m}^3$ , 25 MPa, and 28,600 MPa, respectively. The diameter of the proposed tunnel is 10 m with a shotcrete lining of a thickness of 250 mm. The elastic modulus of lining is  $E_c$  is  $10 \times 10^3$  MPa, and the Poisson's ratio is 0.2.

**Earthquake Motion.** EL-Centro 1940 earthquake has been chosen for analysis. The magnitude of the earthquake was 6.9 on the Richter scale. The peak ground acceleration (PGA) of this earthquake is 0.4 g with a maximum frequency of 1.5 Hz from

**Table 1** Engineering properties of soil stratum

Parameter	Symbol	Unit	Clay
Material model	model	–	HS small
Type	–	–	Drained
Unsaturated unit weight	$\gamma_{\text{unsat}}$	kN/m <sup>3</sup>	16
Saturated unit weight	$\gamma_{\text{sat}}$	kN/m <sup>3</sup>	20
Secant stiffness in standard drained triaxial test	$E_{50}^{\text{ref}}$	kN/m <sup>2</sup>	2.0E4
Tangent stiffness for primary odometer loading	$E_{\text{oed}}^{\text{ref}}$	kN/m <sup>2</sup>	2.561E4
Unloading/reloading stiffness	$E_{\text{ur}}^{\text{ref}}$	kN/m <sup>2</sup>	9.484E4
Power for stress-level dependency of stiffness	m	–	0.5
Effective cohesion	$c'_{\text{ref}}$	kN/m <sup>2</sup>	10
Effective angle of internal friction	$\varphi'$	°	18
Angle of dilatancy	$\psi$	°	0
Shear strain at which $G_s = 0.722G_0$	$\gamma_{0.7}$	–	1.2E-04
Shear modulus at very small strain	$G_0^{\text{ref}}$	kN/m <sup>2</sup>	2.7E5
Poisson's ratio for unloading–reloading	$\nu'_{\text{ur}}$	–	0.2
Shear wave velocity	$V_s$	m/s	410

**Table 2** Section details of the building

Reference name code	Floor	Columns		Beams		Raft foundation	
S15	1–3	EA	EI	EA	EI	EA	EI
		9.0E6	2.3E5	6.0 E6	1.0E5		
	4–7	7.5E6	1.6E5	4.8E6	0.6E5		
	8–11	6.0E6	1.0E5	3.6E6	0.37E5		
12–15	4.8E6	0.6E5	2.7E6	0.2E5			

the Fourier amplitude spectrum curve. The earthquake was simulated by horizontal prescribed displacement at the bedrock at depth 70 m from the surface.

**Dynamic Analysis.** Two stages of analyses have been conducted, the static analysis stage and the completely nonlinear time history analysis stage (dynamic) under the EL-Centro earthquake. It should be noted that the mesh was automatic generation based on a triangulation method. The dimension of the triangular elements needs to be controlled, and the mesh refinement allows to get a specific value for the average length of the element side. Kuhlmeier and Lysmer [27] recommended an average size of the element should be less than or equal to one-eighth of the wavelength related to the maximum frequency component  $f_{\text{max}}$  of the select wave (i.e. the palpable energy associated with the highest frequency component).

**Parametric Study.** To investigate the effect of the tunnel on soil-structure-interaction (TSSI), different horizontal distances of the tunnel from the center of the building

were studied. Moreover, the existence of the tunnel at different depths from the ground surface was also studied individually. The horizontal distances ( $X$ ) are 0, 10, 20, 30, and 40 m from the center axis of the building to the center of the tunnel. These distances are taken as a ratio to the tunnel ( $D$ ) diameter and refer to as  $X/D = 0, 1, 2, 3,$  and  $4,$  respectively. Different models for various tunnel depths ( $H$ ) are conducted at 10, 20, 30, and 40 m depth from the base of the foundation and refer to  $H/D = 1, 2, 3,$  and  $4,$  respectively. In the modeling, a complete nonlinear time history analysis was adopted to assess the response of the reinforced concrete building due to Tunnel-Soil-Structure-Interaction. The building response and foundation concerning the horizontal displacement, inter-story drift, and differential settlement of the foundation have been studied. Nine models have been conducted (4 depth modes and 5 horizontal modes) to investigate the Tunnel-Soil-Structure-Interaction. The drift amount is calculated according to the standard formula (1) [28]:

$$\text{Drift} = (d_{i+1} - d_i)/h \quad (1)$$

which  $d_{i+1}$  is the floor displacement in the  $(i + 1)$  floor and  $d_i$  is the floor displacement in the  $(i)$  floor and  $h$  is the floor height.

### 3 Results and Discussion

**Variation of Tunnels' Location Horizontally.** The effect of moving the tunnel horizontally away from the center of the building at different distances ( $X/D = 0, 1, 2, 3,$  and  $4$ ) shown in Fig. 3. The presence of a tunnel has a direct impact on the horizontal displacement of the building. It can be shown that when the tunnel is not present, the horizontal displacement is 490 mm at the uppermost of the building. When the tunnel is located at the center of the building axis ( $X/D = 0$ ), the displacement increased to 550 mm. Further, increase the horizontal displacement of the building to the maximum value of 610 mm when the tunnel is located at 10 m away from the center of the building axis ( $X/D = 1$ ). Thereafter, the displacement decreases with the increase in the distance between the tunnel and the axis of the building. At a distance of 40 m ( $X/D = 4$ ), the presence of the tunnel is no longer affect. Therefore, the maximum magnification of the amplitude of the seismic waves when the tunnel is located at 10 m away from the building axis, i.e., under the corner of the foundation directly, produced a 25% increase in the horizontal displacement.

Figure 4 shows the variation in the inter-story drift with the floor number. It was found that the existence of a tunnel has a pronounced effect on the inter-story drift of the building. The maximum increase in the inter-story drift was obtained when the axis of both tunnel and building coincided ( $X/D = 0$ ). When the tunnel present at ( $X/D = 0$ ), the inter-story drift increased from 1.5 to 1.75%, while it is increased from 1.5 to 1.7%. When the tunnel away 10 m from the center axis of the building ( $X/D = 1$ ). Beyond the horizontal distance ( $X/D > 1$ ), the floors show the same

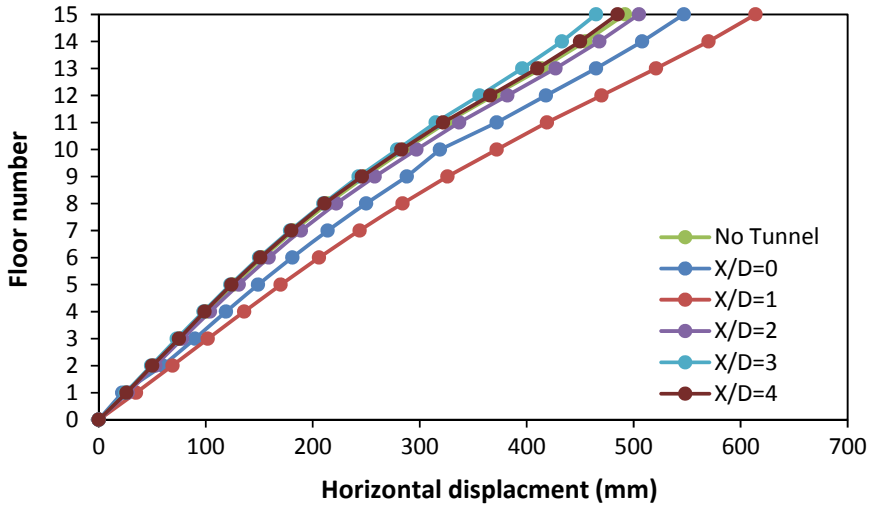


Fig. 3 Horizontal displacement of the building set on clayey soil with the horizontal location of the tunnel

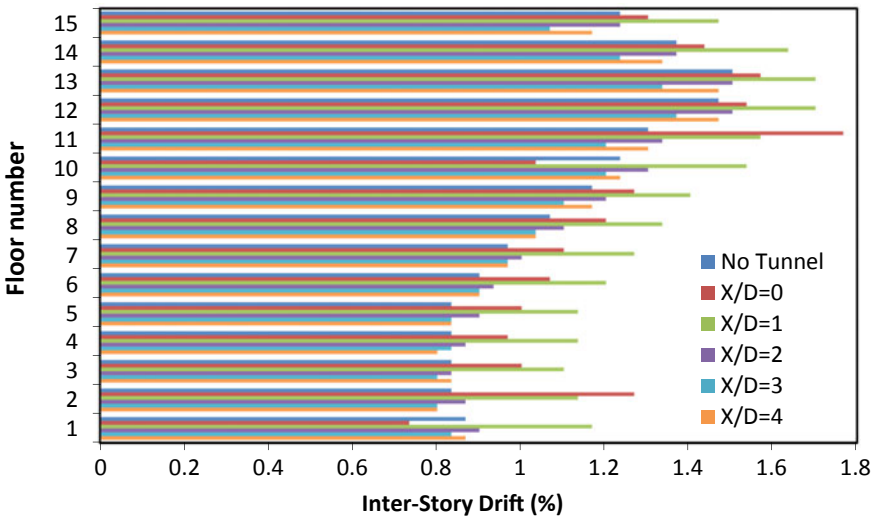
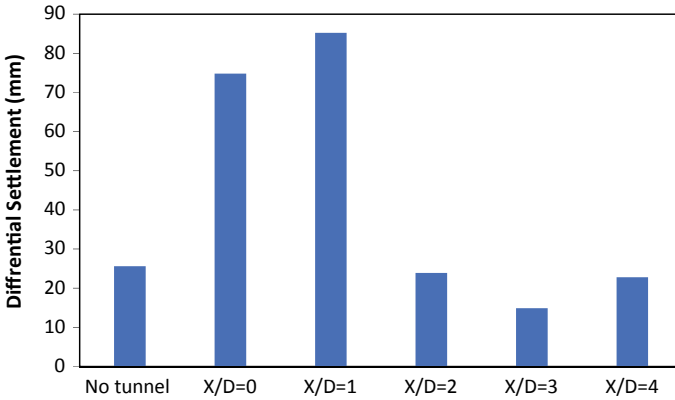


Fig. 4 Inter-storey drift of the building set on clayey soil with horizontal location of the tunnel

inter-story with and without the presence of a tunnel. The inter-story drift in design limitation is 1.5% [28]. Hence, it is concluded that the presence of tunnel at (X/D = 0 and 1) alters the performance level of building from safe to about the collapse level, which should consider designing the structures.



**Fig. 5** Differential settlement of foundation set on clay soil with the horizontal location of the tunnel

The differential settlement of the raft foundation under the dynamic load is presented in Fig. 5. The presence of a tunnel influences the dynamic differential settlement of the foundation. It can be detected that when the tunnel located at the center axis of the building resulted in an increase in the differential settlement compared to without tunnel by about 3 times from 25 to 75 mm and reach to it is the maximum value of 85 mm at a distance of ( $X/D = 1$ ). Thereafter, the effect of the tunnel decreased as the tunnel moves away from the building. It is noted that at a distance ( $X/D = 3$ ), the differential settlement decreased to 15 mm, which is more support to the building. It can be concluded that the maximum increase in differential settlement due to the existence of the tunnel is 240%. This means that the presence of the tunnel amplifies the seismic wave, and the maximum magnification occurs when the tunnel is located at a distance ( $X/D = 1$ ), i.e., away 10 m from the axis of the building.

**Variation of Tunnels' Location Vertically.** The variation in the horizontal displacement with the floor number of the building is shown in Fig. 6. The depth of the tunnel varies from a shallow tunnel to a deep tunnel. Generally, the displacement decreases with an increase in the tunnel depth, and the tunnel effect vanished at a depth more than 4D ( $H/D = 4$ ). When the shallow tunnel at ( $X/D = 0$ ), the horizontal displacement of the building increased from 490 to 550 mm. However, unexpected behavior was recorded at a depth ( $H/D = 3$ ) where the horizontal displacement was 440 mm, which is lower than the horizontal displacement recorded for the case without a tunnel.

Moreover, in the tunnel at a shallow depth at ( $X/D = 0$ ), the inter-story drift increased to 1.75% compared to the case without a tunnel, which recorded 1.5% as shown in Fig. 7. Then, the inter-story drift decreased to 1.55% at ( $H/D = 2$ ). It drops to less than 1.3% at a tunnel depth ratio ( $H/D = 3$ ) due to the de-amplification phenomenon, which means more support for the system. The effect of the existence of the tunnel vanished at deeper depth ( $H/D > 3$ ).

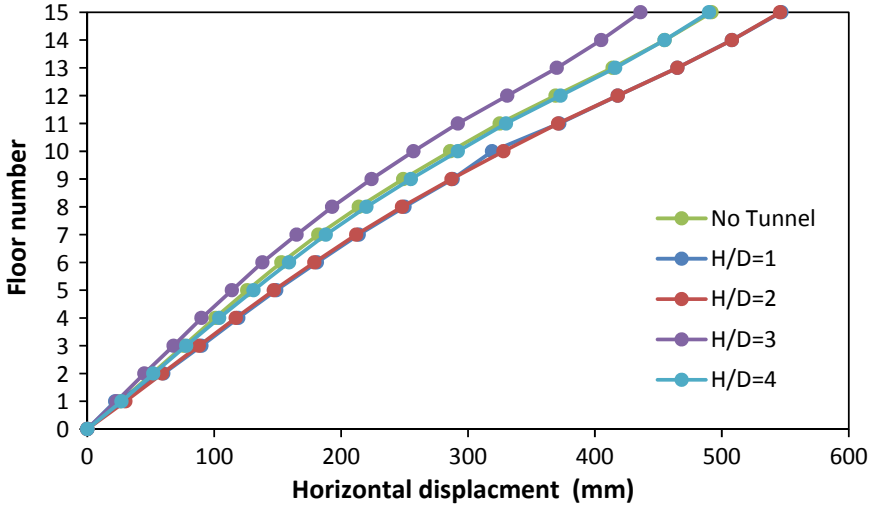


Fig. 6 Horizontal displacement of the building set on clayey soil with vertical location of the tunnel

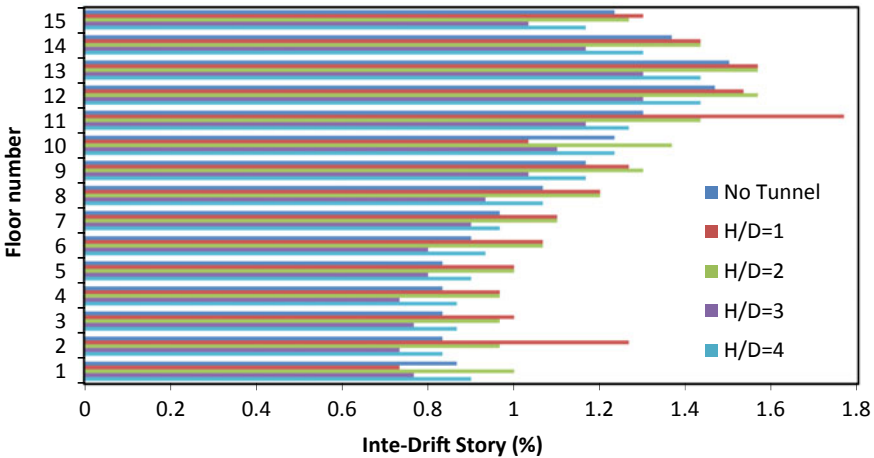
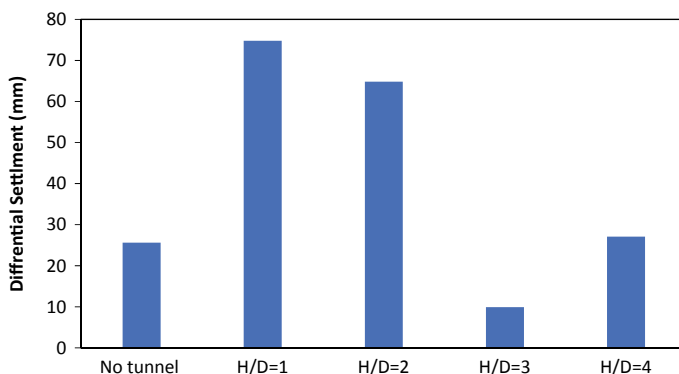


Fig. 7 Inter-storey drift of the building set on clayey soil with the vertical location of the tunnel

Figure 8 shows the variation of the differential settlement of the raft foundation with the depth of the tunnel under the dynamic load. As mentioned previously at ( $X/D = 0$ ), the differential settlement of the foundation increased from 25 to 75 mm when the tunnel was located at a depth ( $H/D = 1$ ). It was found that the differential settlement tends to decreased gradually with an increase in the depth of tunnel to reached 15 mm at ( $H/D = 3$ ), which is lower than those recorded without tunnels. Depth deeper than  $3D$ , the differential settlement increased to get a recorded value without the tunnel, i.e., the effect of tunnel vanished at ( $H/D \geq 4$ ). It can be concluded





**Fig. 8** Differential settlement of foundation set on clayey soil with the vertical location of the tunnel

that the existence of the tunnel amplified the motion that reaches the foundation at shallow depth while de-amplification occurs at the deeper tunnel.

## 4 Conclusion

The following conclusions can be stated from the results of the present study:

- The presence of tunnel under surface structures directly impacts the soil-structure interaction and, therefore, affects the structure's response.
- Increase the horizontal displacement of the building under seismic load when the tunnel present under the axis of the building ( $X/D = 0$ ) and reach the peak value when the tunnel at ( $X/D = 1$ ), then the effect decreased and vanished with ( $X/D$ ) increased.
- The inter-story drift of the building increased to more than 1.5% with the presence of tunnel at ( $X/D$ ) equal to 0 and 1, which is meant the building starts to collapse under seismic load, then the effect vanishes with increased ( $X/D$ ).
- The horizontal displacement and inter-story drift of the building increased with the presence of tunnel at depths ( $H/D = 1$  and 2), then decreased when the tunnel at depth ( $H/D = 3$ ), and it is effect vanished with a deeper tunnel ( $H/D > 4$ ).
- The differential settlement increased significantly with the presence of tunnel at ( $X/D = 1$ ), and the rate of increase is 240% over that without a tunnel, which is probably of collapse.
- The differential settlement of the foundation increased by 200% when the tunnel at ( $H/D = 1$ ), then decreased gradually to values less than without tunnel at ( $H/D = 3$ ). The effect of the tunnel vanished with increasing the tunnel's depth to more than 4D.

## References

1. Ritter, S. (2018). Experiments in tunnel-soil-structure interaction (Doctoral dissertation, University of Cambridge).
2. Hashash, Y. M. A., Hook, J. J., Schmidt, B., & I-Chiang Yao, J., (2001). Seismic design and analysis of underground structures. *Tunnelling and Underground Space Technology*, 16(4), 247–293.
3. Youd, T. L. & Beckman, C. J. (1996). Highway culvert performance during past earthquakes (No. NCEER-96-0015).
4. Yoshida, N., & Nakamura, S. (1996, June). Damage to Daikai subway station during the 1995 Hyogoken-Nunbu earthquake and its investigation. In *Proceedings of eleventh world conference on earthquake engineering* (Vol. 2151, pp. 283–300).
5. Sivakumaran, K. S., & Balendra, T. (1994). Seismic analysis of asymmetric multistorey buildings including foundation interaction and P- $\Delta$  effects. *Engineering Structures*, 16(8), 609–624.
6. Alavi, B., & Krawinkler, H. (2004). Behavior of moment-resisting frame structures subjected to near-fault ground motions. *Earthquake engineering & structural dynamics*, 33(6), 687–706.
7. Galal, K., & Naimi, M. (2008). Effect of soil conditions on the response of reinforced concrete tall structures to near-fault earthquakes. *The Structural Design of Tall and Special Buildings*, 17(3), 541–562.
8. Massumi, H., & Tabatabaiefar, A. (2008). A criterion for considering soil-structure interaction effect in seismic design of ductile RC-MRFs according to Iranian codes. In *14th World conferences earthquake engineering*, Beijing, China.
9. Tavakoli, H. R., Naeef, M., & Salari, A. (2011). Response of RC structures subjected to near-fault and far-fault earthquake motions considering soil-structure interaction. *International Journal of Civil and Structural Engineering*, 1(4), 881.
10. Hatzigeorgiou, G. D., & Beskos, D. E. (2010). Soil–structure interaction effects on seismic inelastic analysis of 3-D tunnels. *Soil Dynamics and Earthquake Engineering*, 30(9), 851–861.
11. Tabatabaiefar, H. R., & Fatahi, B. (2014). Idealisation of soil–structure system to determine inelastic seismic response of mid-rise building frames. *Soil Dynamics and Earthquake Engineering*, 66, 339–351.
12. Malidarreh, N. R., Shooshpasha, I., Mirhosseini, S. M., & Dehestani, M. (2018). Effects of reinforcement on mechanical behaviour of cement treated sand using direct shear and triaxial tests. *International Journal of Geotechnical Engineering*, 12(5), 491–499.
13. Ptilakis, K., Tsinidis, G., Leanza, A., & Maugeri, M. (2014). Seismic behaviour of circular tunnels accounting for above ground structures interaction effects. *Soil Dynamics and Earthquake Engineering*, 67, 1–15.
14. Smerzini, C., Aviles, J., Paolucci, R., & Sánchez-Sesma, F. J. (2009). Effect of underground cavities on surface earthquake ground motion under SH wave propagation. *Earthquake Engineering & Structural Dynamics*, 38(12), 1441–1460.
15. Yiouta-Mitra, P., Kouretzis, G., Bouckovalas, G., & Sofianos, A. (2007). Effect of underground structures in earthquake resistant design of surface structures. In *Dynamic response and soil properties* (pp. 1–10).
16. Abate, G., & Massimino, M. R. (2017). Parametric analysis of the seismic response of coupled tunnel–soil–aboveground building systems by numerical modelling. *Bulletin of Earthquake Engineering*, 15(1), 443–467.
17. Wang, H. F., Lou, M. L., & Zhang, R. L. (2017). Influence of presence of adjacent surface structure on seismic response of underground structure. *Soil Dynamics and Earthquake Engineering*, 100, 131–143.
18. Sica, S., Russo, A. D., Rotili, F., & Simonelli, A. L. (2014). Ground motion amplification due to shallow cavities in nonlinear soils. *Natural Hazards*, 71(3), 1913–1935.

19. Rostami, A., Ziarati, M. A., Shahi, B., & Jahani, S. (2016). Evaluation of seismic behavior and earth's surface acceleration, by interaction of tunnels with different shapes and different types of soils. *Open journal of civil engineering*, 6(2), 242–253.
20. Baziar, M. H., Moghadam, M. R., Kim, D. S., & Choo, Y. W. (2014). Effect of underground tunnel on the ground surface acceleration. *Tunnelling and Underground Space Technology*, 44, 10–22.
21. Sun, C., & Wang, Q., (2012). Effects of underground structure on acceleration response of site. In *Advanced Materials Research* (Vol. 368, pp. 2791–2794). Trans Tech Publications Ltd.
22. Fakhriyeh, H., Vahdani, R., & Gerami, M. (2019). Seismic acceleration spectrum of ground surface under Urban Subway Tunnels with circular cross sections in soil deposits based on SSI. *Shock and Vibration*.
23. Rostami, A. (2019). Effects of tunnel-soil-structure interaction and tunnel location on the seismic response of steel structures.
24. Kramer, S. L. (1996). *Geotechnical earthquake engineering*. Pearson Education India.
25. Rayhani, M. H., & El Naggar, M. H. (2008). Numerical modeling of seismic response of rigid foundation on soft soil. *International Journal of Geomechanics*, 8(6), 336–346.
26. Joyner, W. B., & Chen, A. T. (1975). Calculation of nonlinear ground response in earthquakes. *Bulletin of the Seismological Society of America*, 65(5), 1315–1336.
27. Kuhlemeyer, R. L., & Lysmer, J. (1973). Finite element method accuracy for wave propagation problems. *Journal of the Soil Mechanics and Foundations Division*, 99(5), 421–427.
28. Australian standard for concrete structure AS 3600. (2018).

# Effect of Microbial Induced Calcite Precipitation on Shear Strength of Gypseous Soil in Dry and Soaking Conditions



Alaa D. Salman, Mahdi O. Karkush, and Hussein H. Karim

**Abstract** The gypseous soils have complex and irregular behavior and are found predominantly in dry and semi-dry areas of the world; when gypseous soils are wet, they collapse suddenly. This study presents an experimental investigation for using the bacterial calcium carbonate precipitation in improving the shear strength of gypseous soils. Tests were carried out on two gypseous soils collected from two different sites in Iraq, Al-Najaf city (42% gypsum content) and Al-Samawa city (54% gypsum content). Also, two ratios of bacterial solution (4 and 8%) are used to improve the cohesion and internal friction angle of the studied soils. These percentages were measured according to the dry weight of soil samples. Also, the shear strength parameters were carried out upon dry and soaking conditions. For injecting a bacterial solution into gypseous soil samples, a special injection device was developed by gravity fed to the samples and treated for four days. The precipitation of calcite causes a significant increase in the angle of internal friction and cohesion of gypseous soils by increasing the ratio of injected bacterial solution in both dry and soaking conditions.

**Keywords** Gypseous soil · Calcite precipitation · MICP · Soaking · *S. Porosarcina Pasteurii*

## 1 Introduction

Any soil that suffers volume changes upon wetting due to the radical rearrangement of soil particles without a change in loading is known as collapsible soil [1, 2]. Gypsum, also known as hydrated calcium sulfate, is a mineral salt with the chemical formula gypsum ( $\text{CaSO}_4 \cdot 2\text{H}_2\text{O}$ ). In dry conditions, the gypseous soil is solid, but when soaked

---

A. D. Salman (✉) · M. O. Karkush  
Department of Civil Engineering, University of Baghdad, Baghdad, Iraq

M. O. Karkush  
e-mail: [mahdi\\_karkush@coeng.uobaghdad.edu.iq](mailto:mahdi_karkush@coeng.uobaghdad.edu.iq)

H. H. Karim  
Department of Civil Engineering, University of Technology, Baghdad, Iraq

or saturated by water, it loses its strength, causing collapse and compressibility of the soil structure. Wetting or soaking gypseous soils allows the calcite silicate cementing the soil particles to dissolve, reducing the soil particles' bonds [3]. Microbial induced calcite precipitation (MICP) has gained popularity as a field improvement technique in past years. It is presented as a modern and environmentally friendly treatment [4, 5]. MICP has a benefit over conventional chemical treatments, which can be toxic and harmful to the environment and have a short injection distance [6].

In contrast to chemical treatments, the MICP approach is also cost-effective [7]. The microbial-induced calcite precipitation technique has been shown to be very effective in increasing the shear intensity and decreasing sandy and gravelly soil permeability in various studies [8–10]. In sandy soil, scaled-up experiments were also carried out with high specificity [8]. The main role of bacteria in the calcite precipitation process has been to create an alkaline environment through various physiological activities [11, 12]. *Bacillus pasteurii* bacteria with a high urease activity is essential in the precipitation of calcite ( $\text{CaCO}_3$ ) [13].

The most common nutrient solutions used to provide the bacteria with the required nutrients as well as the chemical compounds needed for soil cementation are  $\text{NaHCO}_3$ ,  $\text{NH}_4\text{Cl}$ ,  $\text{CaCl}_2$ , urea, and nutrient broth (mixture of peptone, yeast extract, beef extract, and  $\text{NaCl}$ ). Under optimal environmental conditions, *B. pasteurii* uses urea as a source of energy, which contains ammonia ( $\text{NH}_3$ ) and carbon dioxide ( $\text{CO}_2$ ), and lead to a rise in the pH in the proximal setting. Calcite bonds form at particle-to-particle contacts in the soil matrix, resulting in a cementing effect between soil particles, as shown in Eq. 1.



Microbially induced calcite precipitation or cementation has been used in various civil engineering applications, including crack repair in rock and concrete, enhanced bearing capacity, decreased permeability, increased dilative tendencies, and increased strain stiffness in the sand. Several previous studies conducted a laboratory analysis to see how the geomechanical properties of microbial cemented sand are influenced by rising, dying, and resting cells [7, 14–16]. They used direct shear and California Bearing Ratio (CBR) tests for sand specimens and observed that the bacterial cells significantly increased their geomechanical properties. According to an analysis of sand from CBR specimens treated with growing cells, microbial processes caused the porous medium to clog. In the present study, the effect of two ratios of bacterial solution on the shear strength of gypseous soil has been investigated on two types of soil and in dry and soaking conditions using several standard direct shear tests.

## 2 Material and Methods

**Materials.** The soil samples used in this research brought from Al-Najaf sea, located 10 km to the west of Al-Najaf city and Sawa lake, located 23 km from Al-Samawa

city. After two days of air drying, the soil samples were carefully grinded to break down the bulk masses into grains. Tables 1 and 2 show the chemical and physical properties of natural gypseous soil samples. The particle-size distribution curves determined using sieve analysis and hydrometer analysis are shown in Fig. 1. The gypsum contents are established as stated by Al-Muftly and Nashat [17]. According to such technique, the soils get oven-dried at (45 °C) to make the specimen weight constant. Then the verification for the specimen weight at (45 °C) gets done. At that time, the drying for the sample is made by (110 °C) to make the weight constant along with recording it. The calculation for gypsum contents can be done consistent with the coming equation:

$$\chi = \left[ \frac{W_{45^{\circ}\text{C}} - W_{110^{\circ}\text{C}}}{W_{45^{\circ}\text{C}}} \right] \times 4.778 \times 100 \quad (2)$$

where  $\chi$  = gypsum contents (%),  $W_{45^{\circ}\text{C}}$  = the specimen weight by (45°C),  $W_{110^{\circ}\text{C}}$  = the specimen weight by (110°C), and 4.778 = inverting rate of molecular weight of hydrating water to the molecular weight of gypsums.

**Bacterial treatment solution preparation.** In this research, all *Bacillus* spp. were developed in urea nutrient agar. In the presence of water, this enzyme can hydrolyze

**Table 1** Chemical properties of the gypseous soils

Property	Al-Najaf soil	Al-Samawa soil	Specification
Total soluble salts (TSS) (%)	34.1	63	Earth manual E8
SO <sub>3</sub> (%)	20	24.5	BS 1377: Part 3: 1990
pH value	6.8	6.5	
Organic matter content (OMC) (%)	2.15	0.45	
CaCO <sub>3</sub> (%)	4.6	6.0	
Cl <sup>-</sup> (mg/L)	0.04	0.09	
Gypsum content (%)	42	54	–
Electrical conductivity (EC) (μS/cm)	2.43	2.23	ASTM D1125 (2014)
Exchange sodium percentage (ESP) (%)	13	15	–
Cation exchange capacity (CEC), meq/100 g	6.54	5.33	ASTM D7503 (2010)
XRD	Quartz, Gypsum, and Dolomite	Gypsum, Quartz Feldspar, and Dolomite	–

**Table 2** Physical properties of the gypseous soils

Property	Al-Najaf soil	Al-Samawa soil
Specific gravity (Gs)	2.54	2.48
Maximum dry unit weight ( $\gamma_{d,max}$ )	14 kN/m <sup>3</sup>	13.4 kN/m <sup>3</sup>
Optimum moisture content ( $\omega_{opt}$ )	18%	18%
D <sub>10</sub> , D <sub>30</sub> , and D <sub>60</sub>	0.018, 0.175, and 0.5 mm	0.075, 0.11, and 0.3 mm
Sand (S)	80.0%	90.5%
Silt (M)	17.0%	9.5%
Clay (C)	3.0%	
Soil type (USCS)	SM	SP-SM

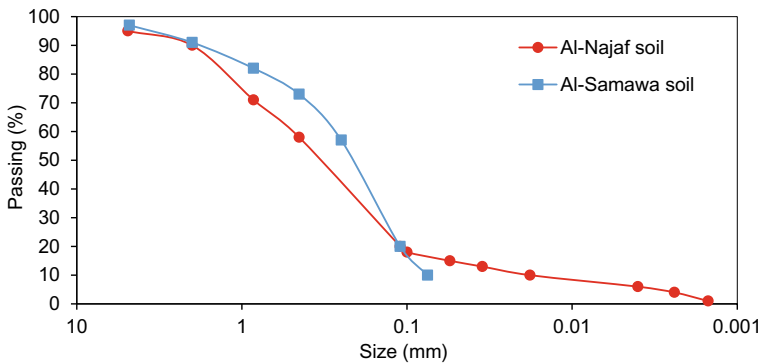


**Fig. 1** Particle size distribution curves of soil samples

urea. Table 3 shows detail about the media’s solid and liquid contents. Urea medium was first developed to create the bacteria solution treatment. As shown in Table 3, the urea medium solution was constructed by mixing nutrient broth (4 g), urea (25 g),

**Table 3** Details of solid and liquid contents of the media and treatment solution

Composition	Quantity	Agar components	Constituents	Amount (g)
Agar	15 g	Urea medium	Nutrient broth powder	4
Peptone	5 g		Urea (NH <sub>2</sub> (CO)NH <sub>2</sub> )	25
NaCl	5 g		NH <sub>4</sub> Cl	15
Yeast extract	2 g		NaHCO <sub>3</sub>	3
Beef extract	1 g		Distilled water	1 L
Urea solution	50 mL		Calcium chloride solution	CaCl <sub>2</sub> .2H <sub>2</sub> O

$\text{NH}_4\text{Cl}$  (15 g),  $\text{NaHCO}_3$  (3 g), and 500 ml distilled water. The resulting urea medium solution's pH was balanced to 6.0 with 5 N HCL before autoclaving, and any solid ingredient was thoroughly mixed in 500 mL distilled water until fully dissolved. Then, to reach the final volume needed, purified water was added (1L).

After autoclaving, the pH of the urea medium was determined and found to be 7.0. Aeration was used to boost the pH of the corresponding 1L of solution from 7.0 to 8.0. As a result, the solution lent itself to bacterial biological activity ultimately. The 800 ml aerated urea medium was sprayed over the spun *B. pasteurii* cells, and the flask was softly agitated to re-suspend the cells. The aerated urea (200 mL) was then mixed with a 20 mL calcium chloride solution (18.5 g  $\text{CaCl}_2/100$  mL filtered water), reducing the pH of the solutions substantially. The previously suspended bacterial solution was then applied to the urea–calcium chloride solution. Owing to the combined injection of bacteria and calcium, calcium carbonate precipitates in the pore fluid, at a flow rate of approximately 20 ml/min and a hydraulic head of 1 m, 500 ml of a combined solution containing urea, calcium chloride, and *B. pasteurii* cells was injected rapidly into the specimens by gravity. After the initial “biological therapy,” the microbes were allowed to attach to the soil samples particles for a duration of 12 h. After 6 h, the specimens were injected with 500 ml urea and  $\text{CaCl}_2$  nutrient treatments at the same flow rate. The nutrient treatment process was then repeated every 6 h for four days.

### 3 Result and Discussion

**Direct Shear Test Results without Treatment.** A series of direct shear tests are used to evaluate the shear strength parameters for natural gypseous soil samples. The tests were carried out by ASTM D3080 (2003); the soil sample tested in this study has dimensions of  $60 \times 60 \times 20$ . To predict shear strength parameters ( $c$ ,  $\phi$ ), two types of experiments (dry and soaked) were conducted on two types of gypseous soil samples (Al-Najaf and Al-Samawa). The soil samples were tested before and after treatment with two injected bacterial solution ratios (4 and 8%). In soaked conditions, the soil samples were tested after soaking in water for two hours. Three different confining pressures were used to assess the stress–strain relationship for the measured soil samples (75, 150, and 225 kPa). Brittle failure (the initiation, formation, and aggregation of micro-cracks) was observed as a shear failure mode in all samples stabilized with bacterial calcium carbonate precipitation. Figures 2, 3, 4 and 5 show the results of direct shear tests on gypseous soils in both dry and soaked conditions. It can be shown and cohesion is much greater in the dry state than in the saturated state. The angle of internal friction decreases marginally after soaking. The dissolution of cementation salts after soaking in water, which breaks down the bonds between soil particles, could explain this behavior. Soaking has a significant impact on the apparent cohesion but only a minor effect on internal friction angle because the soil is classified as coarse-grained textured soil with friction properties.



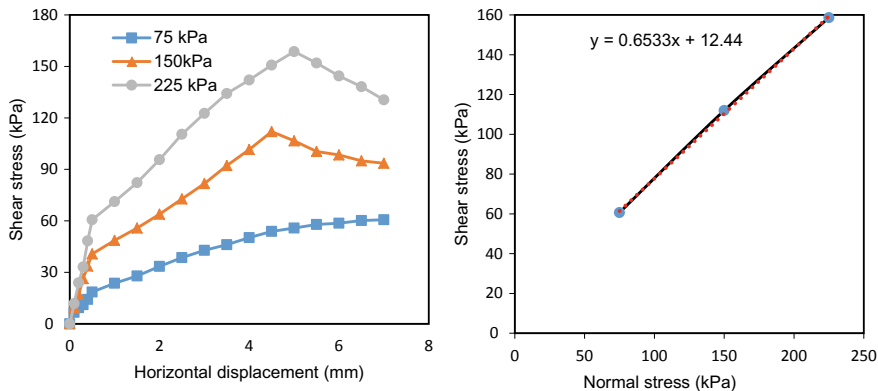


Fig. 2 Results of direct shear test for untreated dried gypseous soil (Al-Najaf soil)

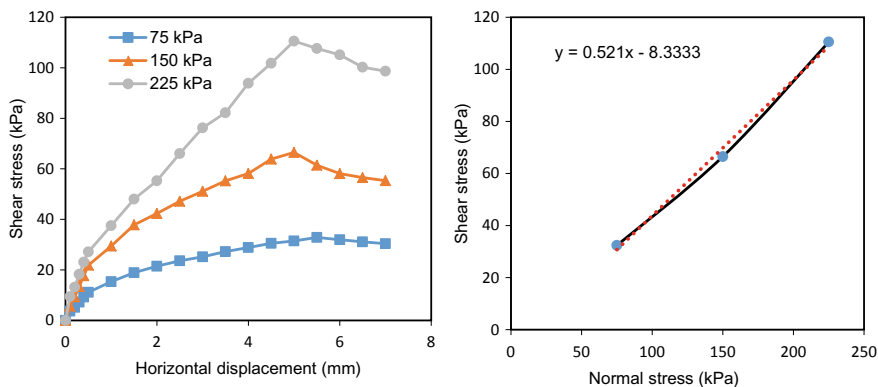


Fig. 3 Results of direct shear test on untreated soaked gypseous soil (Al-Najaf soil)

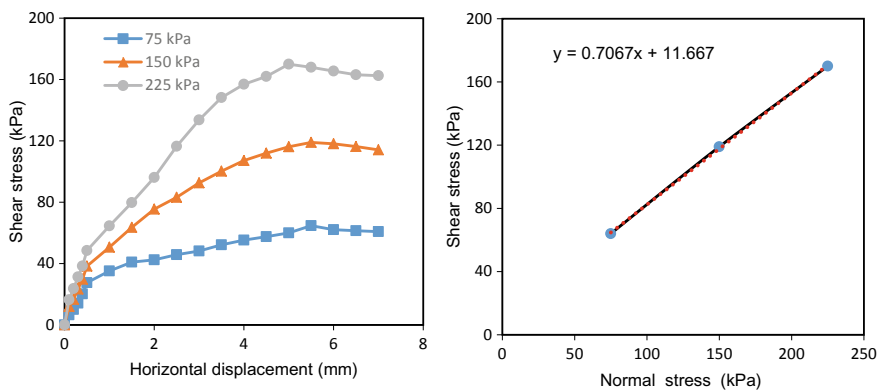
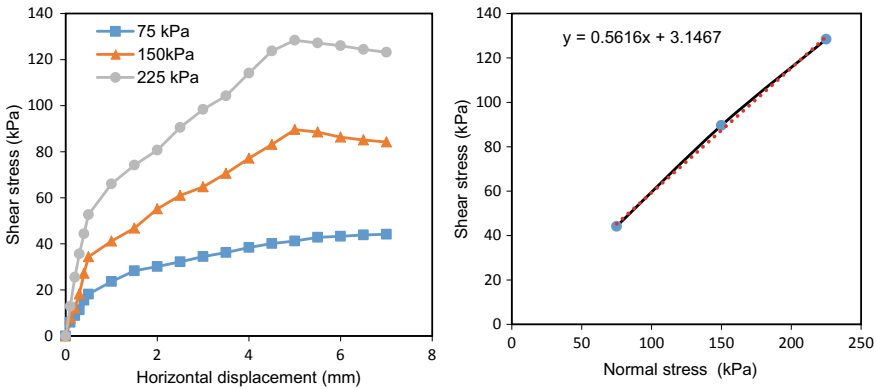
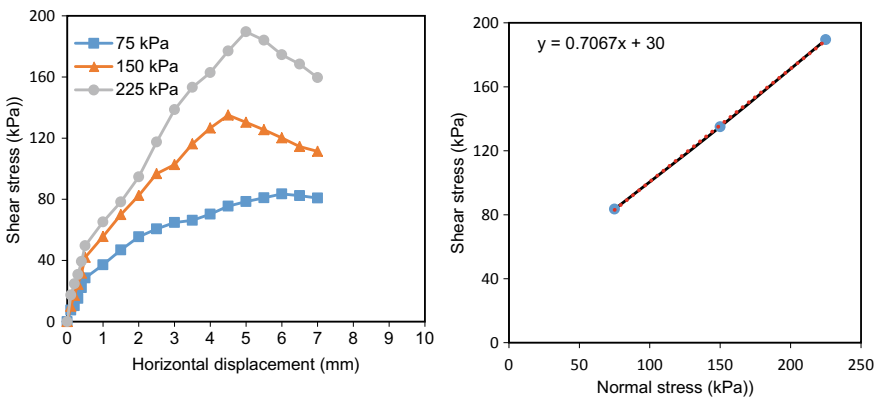


Fig. 4 Results of direct shear test for untreated dried gypseous soil (Al-Samawa soil)



**Fig. 5** Results of direct shear test for untreated soaking gypseous soil (Al-Samawa soil)

**Direct Shear Test Results with MICP Treatment.** The two types of gypseous soil samples are treated with ratios of injection of a bacterial solution (4 and 8%) and tested in both dry and soaking conditions. Figures 6, 7, 8, 9, 10, 11, 12 and 13 show the variation of shear stress versus horizontal displacement and normal stress versus shear stress under different intensities of normal stress. The shear stress values of the treated samples are higher than those of the untreated soil samples, as seen in Figs. 6, 7, 8, 9, 10, 11, 12 and 13. This action may be attributed to the cementation resulting from MICP between the soil particles. Calcite bonds between soil particles have been disrupted under regular stress, resulting in peak shear stress [18]. Increasing the concentration of bacterial solution resulted in increasing the shear strength parameters of gypseous soil; also, the soaking causes a reduction in the shear strength parameters of soil but still higher than untreated gypseous soil samples (Table 4).



**Fig. 6** Results of direct shear test for treated dried gypseous soil (4% BS Al-Najaf soil)

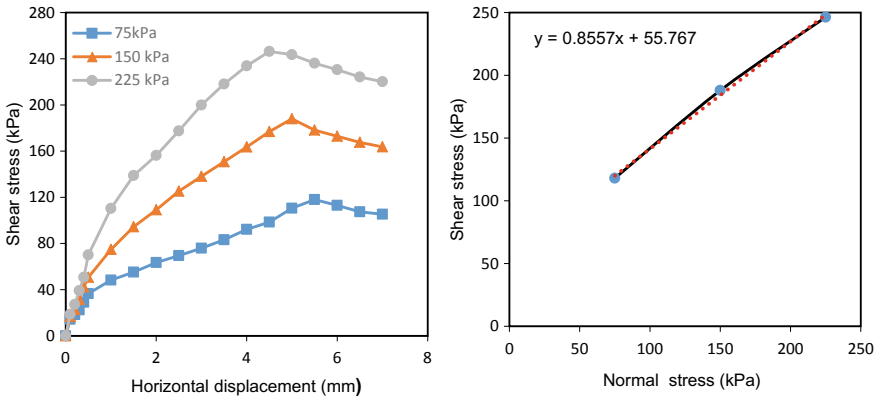


Fig. 7 Results of direct shear test on treated dried gypseous soil (8% BS Al-Najaf soil)

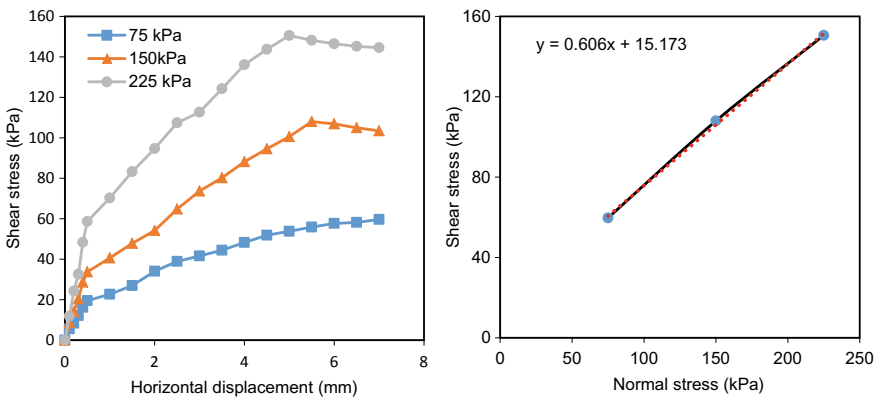


Fig. 8 Results of direct shear test on treated soaked gypseous soil (4% BS Al-Najaf soil)

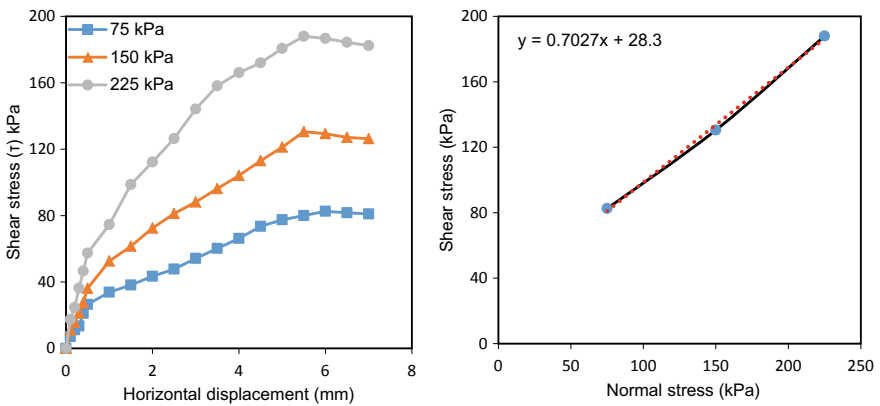
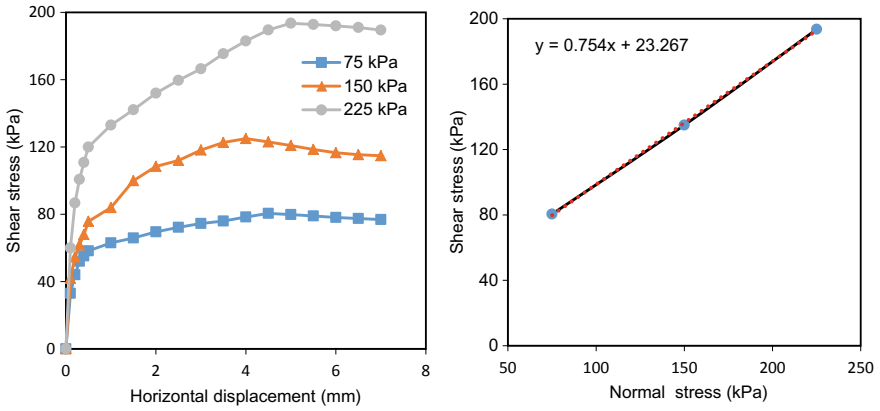
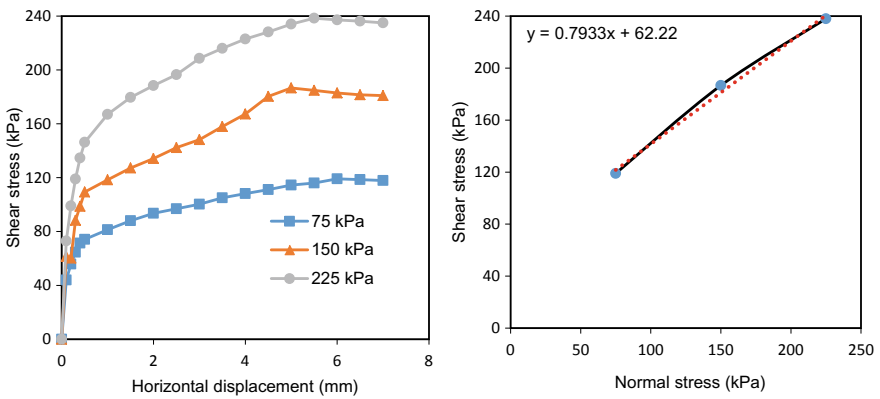


Fig. 9 Results of direct shear test on treated soaked gypseous soil (8% BS Al-Najaf soil)



**Fig. 10** Results of direct shear test for treated dried gypseous soil (4% BS Al-Samawa soil)



**Fig. 11** Results of direct shear test for treated dried gypseous soil (8% BS Al-Samawa soil)

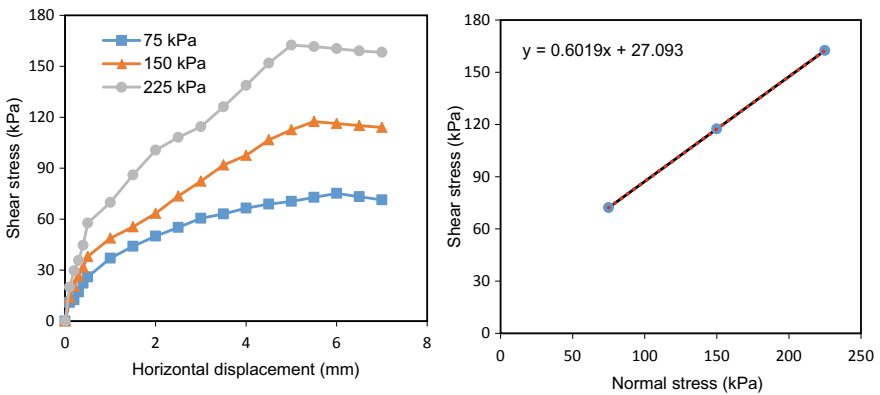


**Fig. 12** Results of direct shear test for treated soaked gypseous soil (4% BS Al-Samawa soil)

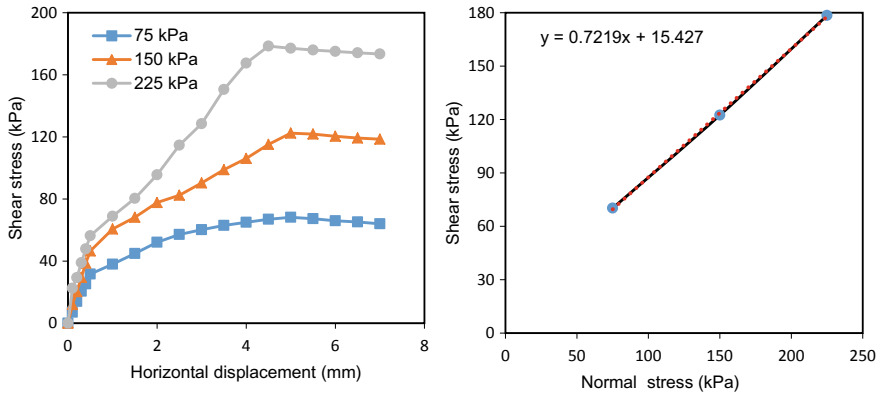


**Fig. 13** Results of direct shear test for treated soaked gypseous soil (8% BS Al- Samawa soil)

**Table 4** Variation of shear strength parameters for tested soil sample treated by MICP

Al-Najaf soil						
Property	Untreated		Treated			
	Dry	Soaked	4% BS dry	8% BS dry	4% BS soaked	8% BS soaked
c (kPa)	15	0	40.44	60.66	23	34
$\varphi$ (°)	32	28.5	33.75	40	30	34.5
Al-Samawa soil						
Property	Untreated		Treated			
	Dry	Soaked	4% BS dry	8% BS dry	4% BS soaked	8% BS soaked
c (kPa)	12	0	36	55	26.25	32
$\varphi$ (°)	33	29.45	35	39	31.6	33

## 4 Conclusions

The following conclusions can be drawn out from the results of this study:

- Soaking of untreated gypseous soils reduced the cohesion of soil by approximately ten times that of dry soil, while the angle of internal friction exhibited marginal reduction.
- In dry condition, the injection of microbial calcium carbonate precipitation in gypseous soils causes increasing the shear strength properties, where the angle of internal friction increased 5° for soil treated with 4% BS and increased by 10° for soil treated with 8% BS. The cohesion of gypseous soil also increased by 200% for soil treated with 4% BS and increased by 350% for soil treated with 8% BS. Accordingly, the injection of bacterial calcium carbonate precipitation can modify the geotechnical properties of gypseous soil.

- In soaking condition, the injection of bacterial solution causes increasing the shear strength properties of gypseous soil, where the angle of internal friction increased  $2^\circ$  for soil treated with 4% of BS and increased  $5^\circ$  for soil treated with 8% of BS, while the cohesion of gypseous soil is also increased by 220% for soil treated with 4% of BS and increased by 300% for soil treated with 8% of BS. The soaking affected the friction angle significantly and slightly on cohesion because the soil has friction properties rather than cohesion.

## References

1. Awn, S. H. A. (2010). A modified collapse test for gypseous soils. *Diyala Journal of Engineering Sciences*, 10, 299–309.
2. Mansour, Z. M., Chik, Z., & Taha, M. R. (2008). On the procedures of soil collapse potential evaluation. *Journal of Applied Sciences*, 8(23), 4434–4439.
3. Al-Murshedi, A. D. S. (2001). *The use of cut back MC-30 for controlling the collapsibility of gypseous soils*. M.Sc. Thesis, University of Technology, Baghdad.
4. Ali, N. A., Karkush, M. O., Al Haideri, H. H. (2020). Isolation and identification of local bacteria produced from soil-borne urease. In *IOP Conference Series: Materials Science and Engineering* (Vol. 901, No. 1, p. 012035). IOP Publishing.
5. DeJong, J. T., Fritzes, M. B., & Nüsslein, K. (2006). Microbially induced cementation to control sand response to undrained shear. *Journal of Geotechnical and Geoenvironmental Engineering*, 132(11), 1381–1392.
6. Karol, R. H. (2003). *Chemical grouting and soil stabilization, revised and expanded* (Vol. 12). Crc Press.
7. Ivanov, V., & Chu, J. (2008). Applications of microorganisms to geotechnical engineering for bioclogging and biocementation of soil in situ. *Reviews in Environmental Science and BioTechnology*, 7(2), 139–153.
8. van Paassen, L. A., Ghose, R., van der Linden, T. J., van der Star, W. R., & van Loosdrecht, M. C. (2010). Quantifying biomediated ground improvement by ureolysis: Large-scale biogrout experiment. *Journal of Geotechnical and Geoenvironmental Engineering*, 136(12), 1721–1728.
9. Van Wijngaarden, W. K., Vermolen, F. J., Van Meurs, G. A. M., & Vuijk, C. (2011). Modelling biogrout: A new ground improvement method based on microbial-induced carbonate precipitation. *Transport in Porous Media*, 87(2), 397–420.
10. Martinez, B. C., DeJong, J. T., Ginn, T. R., Montoya, B. M., Barkouki, T. H., Hunt, C., Tanyu, B., & Major, D. (2013). Experimental optimization of microbial-induced carbonate precipitation for soil improvement. *Journal of Geotechnical and Geoenvironmental Engineering*, 139(4), 587–598.
11. Ali, N. A., & Karkush, M. O. (2021). Improvement of unconfined compressive strength of soft clay using microbial calcite precipitates. *Journal of Engineering*, 27(3), 67–75.
12. Weaver, T. J., Burbank, M., Lewis, A., Lewis, R., Crawford, R., & Williams, B. (2011). Bio-induced calcite, iron, and manganese precipitation for geotechnical engineering applications. In *Geo-Frontiers 2011: Advances in Geotechnical Engineering* (pp. 3975–3983).
13. De Jong, J. T., Soga, K., Kavazanjian, E., Burns, S., Van Paassen, L. A., Al Qabany, A., Aydilek, A., Bang, S. S., Burbank, M., Caslake, L. F., Chen, C.Y. (2014). Biogeochemical processes and geotechnical applications: progress, opportunities and challenges. In *Bio-and Chemo-Mechanical Processes in Geotechnical Engineering: Géotechnique Symposium in Print 2013* (pp. 143–157). Ice Publishing.
14. Al Qabany, A. (2011). *Microbial carbonate precipitation in soils*. Ph.D. Thesis, University of Cambridge, UK.

15. Qabany, A.A., Soga, K. (2014). Effect of chemical treatment used in MICP on engineering properties of cemented soils. In *Bio-and Chemo-Mechanical Processes in Geotechnical Engineering: Géotechnique Symposium in Print 2013* (pp. 107–115).
16. Chou, C. W., Seagren, E. A., Aydilek, A. H., & Lai, M. (2011). Biocalcification of sand through ureolysis. *Journal of Geotechnical and Geoenvironmental Engineering*, 137(12), 1179–1189.
17. Al-Mufty, A. A., & Nashat, I. H. (2000). Gypsum content determination in gypseous soils and rocks. In *Third International Jordanian Conference on Mining* (Vol. 2, pp. 485–492). Amman, Jordan.
18. Verma, D. K., & Maheshwari, U. K. (2017). Effect of nano silica on geotechnical properties of clayey soil. *International Journal of Science and Research (IJSR)*, 6(12), 974–976.

# Suction—Resistivity Relationship in Unsaturated Gypseous Soil



Qasim A. Al-Obaidi and Ali A. Al-Shamoosi

**Abstract** Suction pressure and water potential significantly affect the geotechnical and geophysics behavior of the gypseous collapsible soil, especially under unsaturated conditions. Direct measurement for the soil suction still a big challenge due to the limitation of the test equipment, high cost, and time-consuming of the tests. In this study an attempt is made in order to find indirect method for estimating the soil suction in gypseous soil by using geophysics techniques. Soil-Model apparatus provided with highly sensitive Tensiometer, Time Domain Reflectometry, and resistivity sensors is used to investigate the relationship between the matric suction, water content, volume change, and soil resistivity. The unsaturated gypseous soil sample is brought up from Al-Ramadi city, west of Iraq, with a gypsum content of 70%. The test procedure includes different initial conditions such as applied stress and sensors level. The tests results show the soil resistivity sharply decreased with the decrease in matric suction, especially at medium range of soil suction (i.e., 1000–100 kPa), then the relationship will be relatively constant for all measurements levels. Also, the void ratio sharply decreased with the soil suction's degreasing and became relatively constant at the low range of soil suction (i.e., <100 kPa) at vertical stress of 25 kPa.

**Keywords** Suction · Gypseous soil · Unsaturated · Geophysics · Collapse · Soil resistivity

## 1 Introduction

Gypseous soil has a significant geotechnical problem during and after the construction of engineering structures [1, 2]. The progressive collapse deformation commonly occurs upon reducing soil suction and wetting processes, leading to destroying the

---

Q. A. Al-Obaidi (✉)

Civil Engineering Department, University of Technology, Baghdad, Iraq

e-mail: [Qasim.A.Jassim@uotechnology.edu.iq](mailto:Qasim.A.Jassim@uotechnology.edu.iq)

A. A. Al-Shamoosi

Al-Shams Laboratory for Structural Tests, Baghdad, Iraq

e-mail: [alialshamoosi@alshamslaboratory.com](mailto:alialshamoosi@alshamslaboratory.com)



gypsum cementing bonds between soil particles [3, 4]. Unsaturated soil can be defined as solid, water, air, and the fourth phase are the air–water interface or the contractile skin [5]. Moreover, this soil’s geological formation can be a residual soil, a lacustrine deposit, a bedrock formation, or any other soil or rock type. The unsaturated soil stratum between the natural ground level and above the water table is known as the capillary zone and having negative pore-water pressure (i.e., suction) [6]. Furthermore, total suction in unsaturated soil can be defined as the free energy state of soil water and has two components, namely matric suction, and osmotic suction as follow:

$$\psi = (u_a - u_w) + \varphi_s \quad (1)$$

where:  $\psi$  = total suction,  $(u_a - u_w)$  = matric suction and  $\varphi_s$  = osmotic suction. The osmotic suction can be ignored in engineering applications. Matric suction is defined as the difference between pore air pressure ( $u_a$ ) and pore water pressure ( $u_w$ ) [6]. Resistivity can be defined as the electrical resistance between opposite faces of a unit cube of material; the reciprocal of conductivity. Resistivity is used in preference to conductivity as an expression of the soils’ electrical character (and waters) since it is expressed in whole numbers [7]. The soil resistivity is the function of the degree of compaction, moisture content, constituent solubility, and temperature. These factors will be eliminated when the soil is at a saturated state and the soil resistivity will be a minimum value especially when the soil contains soluble salts. Some soils absorb moisture slowly and contain constituents that dissolve slowly, and the resistivity may not stabilize for as much as 24 h after saturation. Surplus water should not be poured off out of the soil as this will remove soluble constituents [7].

Direct methods to calculate the soil suction is commonly very expensive and time-consuming especially in field conditions. Therefore this study aims to find a relationship between soil suction, volume change and soil resistivity using lab resistivity tests and direct measurements for the soil suction and volumetric water content. Soil-Model apparatus provided with high sensitive Tensiometer, Time Domain Reflectometry, Resistivity sensors, and Datalogger is used for this purpose as illustrated in the following sections.

## 2 Experimental Work

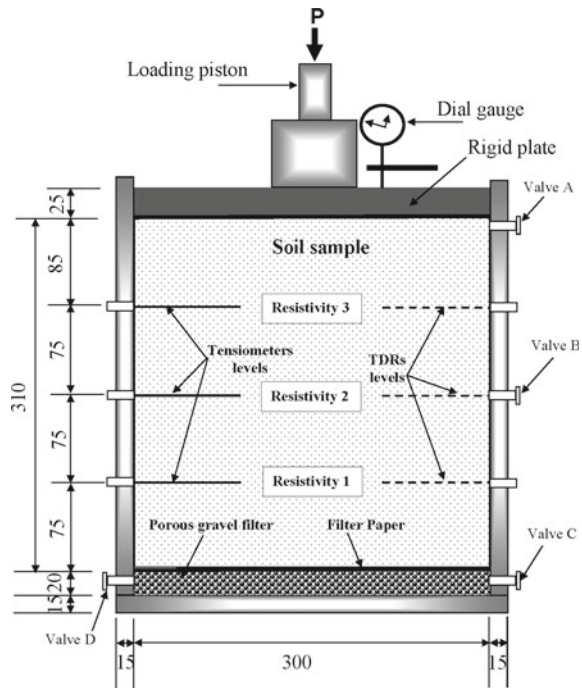
**Soil Sample.** The unsaturated soil sample from the site near Al-Anbar University, Al-Ramadi city of about 120 km west of Baghdad, Iraq is used in this study. The main physical and chemical properties of the investigated soil are shown in Table 1.

**Soil-Model Apparatus.** Soil-Model apparatus was designed and manufactured with multi-functions of laboratory soil testing by Al-Obaidi et al. [3] as shown in Figs. 1 and 2. In this study, Soil-Model Apparatus is used to investigate the volume change, matric suction, water content, and soil resistivity relationships of gypseous soil. The Soil-Model has the following technical details: rigid steel material of 1.5 cm

**Table 1** Summary of physical and chemical soil properties [3, 4]

Property	Value	Property	Value
Atterberg’s limits (%)	No plasticity	Relative density (%)	82
Specific gravity	2.35	Field dry density (g/cm <sup>3</sup> )	1.3
Initial void ratio	0.81	Maximum dry density (g/cm <sup>3</sup> )	1.57
Cu	4.5	Optimum moisture content (%)	15.5
Cc	1.4	Passing sieve 200 (0.075 mm) (%)	3.3
SO <sub>3</sub> (%)	34.5	Gypsum content (%) [8]	70
TSS (%)	11.5	Soil classification	SP

**Fig. 1** Sketch of soil-model apparatus. (All dimensions in mm)



(thickness), inner dimensions are 30.2 cm (length), 30.2 cm (width), 31.0 cm (sample height), and 2.5 cm (thickness of rigid plate cover). The Soil-Model provided with graded gravel filter bed layer of 0.5–1.0 cm (particle diameter range) and 2.0 cm (filter thickness). The gravel filter bed’s purpose is to ensure the uniform distribution of the moisture through the soil mass and flash the air bubbles under the soil sample. The filter layer level includes two opposite valves used as a water inlet and flashing of air bubbles. In addition, many valves have been provided in the horizontal and vertical directions of the model in order to mobilize the sensors to the desired level of soil. The first sensor is a susceptible Tensiometer sensor (TS) type (EQ3 equitensiometer) to

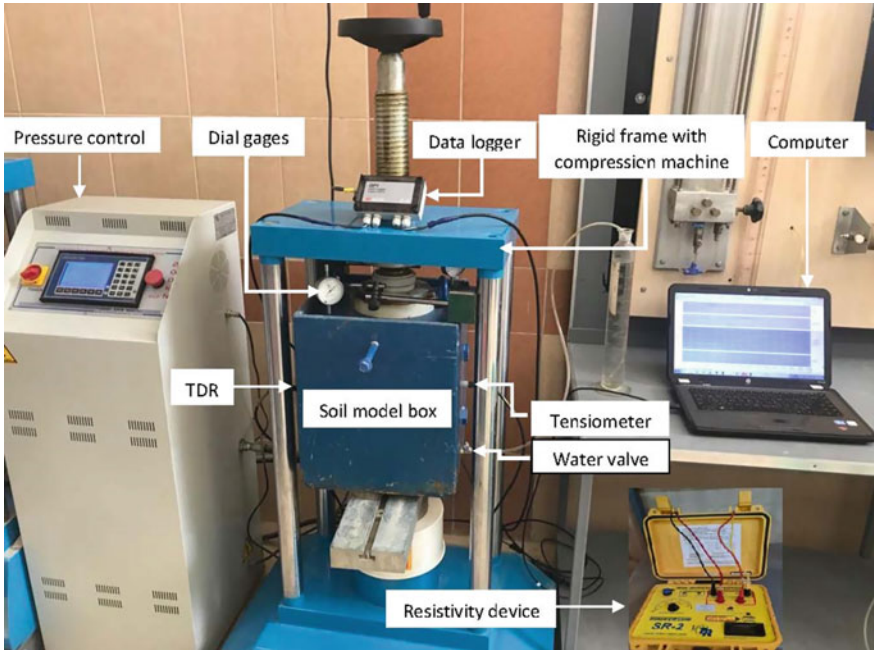


Fig. 2 View on soil-model device

measure the soil's matric suction as shown in Fig. 3a. When the EQ3 probe is inserted into the soil, the matric potential within the equilibrium body equilibrates to that of the surrounding soils. The water content of the matric material is measured directly

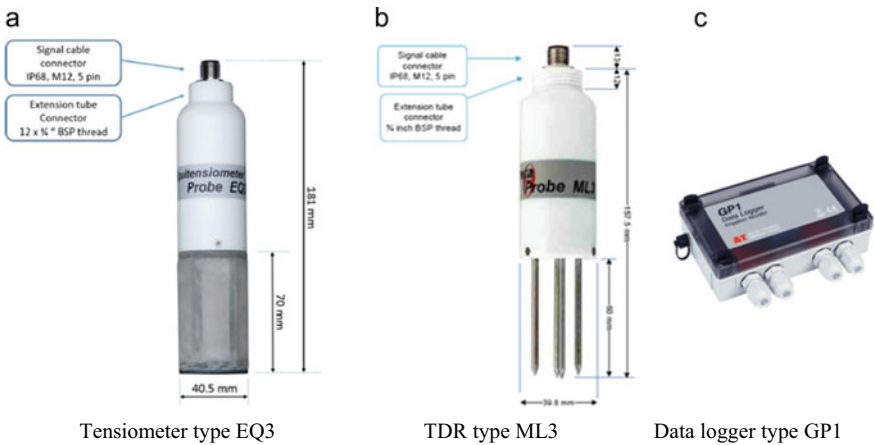


Fig. 3 Tensiometers, Time domain reflectometry, and data logger used with soil-model apparatus manufactured by Delta-T Devices Ltd company, UK

by the ML3 ThetaProbe, and this can be converted into the matric potential of the surrounding soil using the calibration curve supplied with each Equitensiometer.

The second sensor is Time Domain Reflectometry sensor (TDR) type (ML3 Theta Probe) to measure the soil's volumetric water content as shown in Fig. 3b. These two sensors are connected to the data logger type (GP1 Data Logger) and then to the special computer software as shown in Fig. 2 and Fig. 3c. The applied axial loading was controlled using an automatically rigid loading frame with a loading capacity of 200 kN. The soil settlement was monitored by using two sensitive dial gauges with a precision of 0.002 mm [3, 4]. The soil resistivity meter device type “Tinker & Rasor” model SR-2, serial 1177, 4-Pin Method was used for soil resistivity measurements as shown in Fig. 2. The Tensiometers (TS), Time Domain Reflectometry (TDR), and Wenner Four-Electrodes sensors were installed three levels within the Soil-Model Apparatus for three models tests. The first model test at the bottom level ( $H/4 = 7.5$  cm), the second model test at the middle level ( $H/2 = 15.0$  cm), and the third model test at the top level ( $3H/4 = 22.5$  cm) as shown in Fig. 1.

### 3 Testing Procedure

The test procedure can be summarized into the following steps:

1. Preparation of the soil samples inside the dried Soil-Model apparatus by static compaction of the soil in three layers according to the following initial boundary conditions: void ratio ( $e_o$ ): 0.81; dry density: 1.3 g/cm<sup>3</sup>; water content: 0%; degree of saturation: 0% and initial total suction: 139,000 kPa. The value of the initial total suction of 139,000 kPa is considered based on the soil–water characteristics curve (SWCC) measured by Al-Obaidi [9] using the chilled-mirror hygrometer technique for the identical soil sample. The applied constant vertical stress was 25 kPa for all model tests, and the deformation settlement was recorded using two dial gauges of accuracy equal to 0.002 mm
2. Before starting the tests, and to ensure the measured data's reliability and accuracy, calibrations of all sensors according to the specification manuals and standards are made on several proposed soil-model samples under different initial soil conditions.
3. The Time Domain Reflectometry (TDR) and Tensiometer (TS) sensors were previously fixed at the Soil-Model apparatus's desired level. However, care must be taken to ensure that the sensors are safe during the compaction process and have good contact with the soil particles. The installation of the TDR and TS sensors was according to their installation instructions manual.
4. The soil resistivity measurements using the Wenner Four-Electrodes methods were carried out according to the ASTM G57-2012 Standard [7]. The 4-pin sensors were installed in the soil sample at the desired model test level according to the requirement of the ASTM G57-2012 Standard [7] and “Tinker & Rasor”

model SR-2 device specification manual after finished the compacted of the soil layer. The soil resistivity is calculated according to the following equation:

$$\rho = R A/a \tag{2}$$

where:

$\rho$  = Resistivity ( $\Omega$ .cm),

$R$  = Resistance ( $\Omega$ ).

$A$  = Cross-sectional area of the container perpendicular to the current flow (=142.5 cm<sup>2</sup>), and.

$a$  = Inner electrode spacing (= 12.8 cm).

5. After the preparation of the soil sample, the model test was started under the constant vertical stress of 25 kPa. Then start the multi-step wetting stage (i.e. transformation from unsaturated state towards saturated state) by reducing matric suction simultaneously with stepwise increases of the water content in the soil mass. A multi-step wetting process was conducted after flashing the bottom reservoir to remove the air bubbles by using the graduate water cylinder through to the gravel filter through soil-model valves without applying the hydraulic gradient (see Fig. 2). The moisture content was raised in the soil skeleton based on capillary forces and suction pressure.
6. The matric suction and the volumetric water content were recorded during the test by using high accurate Datalogger (GP1) in conjunction with resistivity and volume change measurements from high suction range at unsaturated condition till very low suction range (i.e.,  $\cong$  zero) at saturated condition.

## 4 Results and Discussion

In this section, the Soil-Model tests results at measurement levels (H/4, H/2 and 3H/4) will be presented. Figures 4, 5, and 6 illustrated the relationships between the soil resistivity and suction, gravimetric water content, and degree of saturation, respectively. From Fig. 4 it can be seen that the soil resistivity sharply decreases

**Fig. 4** Relationship between suction and resistivity

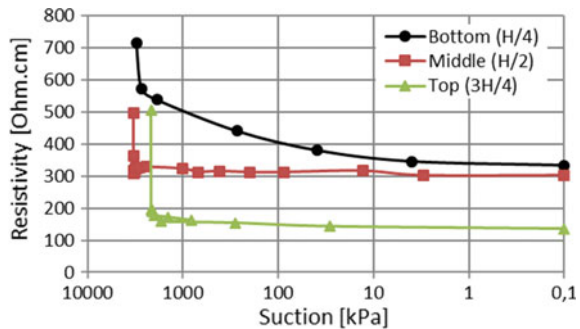


**Fig. 5** Relationship between gravimetric water content and resistivity

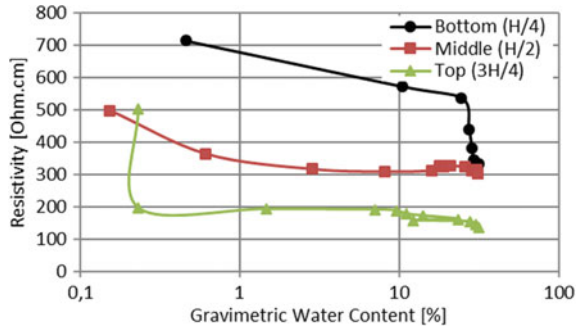
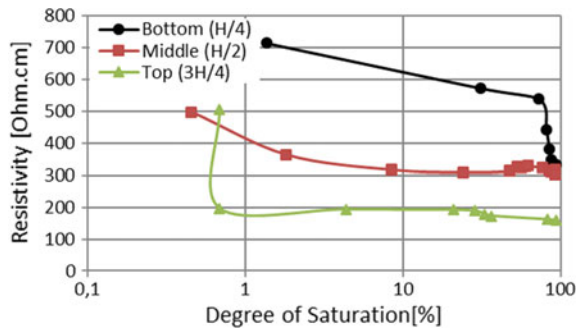


**Fig. 6** Relationship between degree of saturation and resistivity



with the decrease in matric suction, especially at a medium range of soil suction (i.e., 1000–100 kPa), then the relationship will be relatively constant for all measurements levels. This behavior can be attributed to the effect of a high percentage of the gypsum content in soil sample that present high resistance to current flow between soil particles. It’s worth mentioning that, transitional gypsum rocks, which contain gypsum content of about (55–75%) have an electrical resistivity value of (100–700 Ω cm) [10]. However, when soil suction is reduced by multi-step wetting processes (i.e., increase of the water content), the cementing bonds between soil particles will be destroyed due to the softening and dissolution of gypsum by water. In this case the positive pore water pressure will relatively increase, causing an increase in soil conductivity and reduction in soil resistivity as shown in Figs. 5 and 6.

Moreover, when the moisture content gradually increased and when soil approached the saturation state (i.e.,  $S_r > 90\%$ ), the value of soil resistance will fluctuate due to the hydration and chemical reaction gypsum with water molecules as shown in Figs. 5 and 6. The hydrated gypsum particles and water molecules cause a significant reduction in soil resistivity. This attribute is confirming with the measurement’s conception mentioned in ASTM G57-2012 [7] and [10]. It is worth mentioning that the soil at completely dry condition will be under high initial total suction as in the studied soil were the initial total suction  $\cong 139,000$  kPa [9]. At such an extremely high initial suction value, the soil resistivity will be relatively at high range also; therefore, the resistivity suction measurements were limited with

the sensor’s capacity. According to the previous argument, the resistivity- suction measurements start from medium range toward a low range of soil suction. As a summary, it can clearly observe that the soil resistivity is a function of moisture content and directly affected by the high percentage of gypsum content. This finding confirms the discussions mentioned in ASTM G57 [7 and 10].

Figures 7, 8 and 9 show the relationships between the soil suction and gravimetric water content, degree of saturation, and void ratio. Figures 7 and 8 show that the soil suction is a function of water potential, and it is highly sensitive to the variation of moisture content in the soil mass. The reduction in matric suction (i.e., negative pore water pressure) is a result of replacing the air volume with water volume in micro-structure level of soil particles, especially after the air entry value on the soil–water characteristics curve of the studied gypseous soil. These findings confirm with finding reported by [3, 4 and 9].

The relationship between suction and the void ratio can be shown in Fig. 9. The void ratio was sharply decreased with the decreasing of the soil suction due to collapse deformation of the gypsum bonds between soil particles due to softening and gypsum dissolution. However, at a low range of soil suction (i.e. <100 kPa), the variation in the void ratio becomes relatively constant due to the soil structure’s stability under the vertical stress of 25 kPa. Finally, the measurement level (i.e., sensors position) in

**Fig. 7** Relationship between suction and gravimetric water content

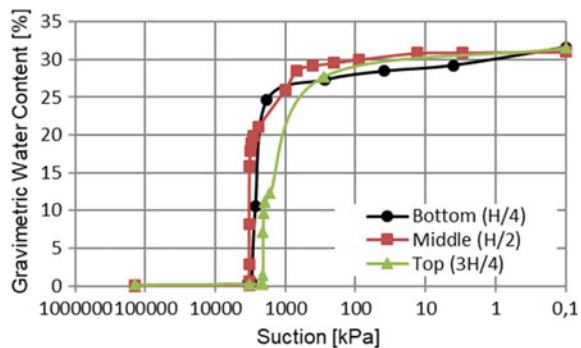


**Fig. 8** Relationship between suction and degree of saturation

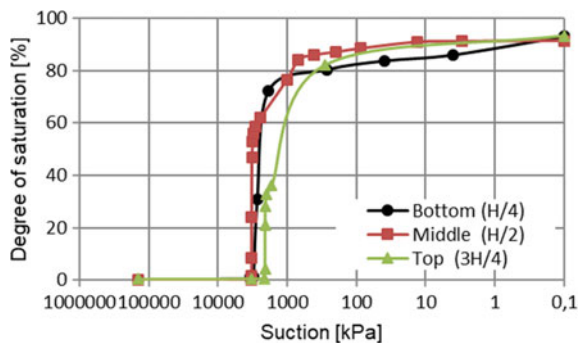
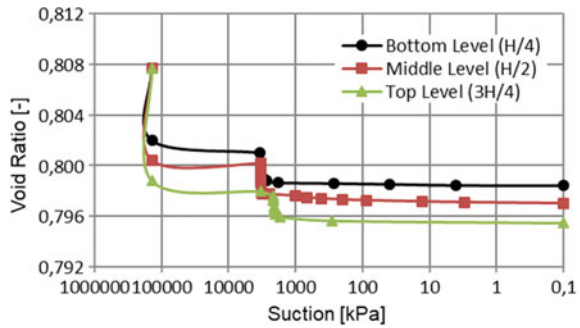


**Fig. 9** Relationship between suction and void ratio



soil-model apparatus has a considerable effect on the measured resistivity value, as shown in Figs. 4, 5, and 6. From Fig. 5 it's clear that for the same gravimetric water content of 10%, the soil resistivity was 200, 300, and 600  $\Omega$  cm for the sensors level of (H/4, H/2, and 3H/4) respectively. This behavior can be attributed to the large hydration amount of gypsum and variation of suction within the soil mass at the top level of sensors measurements.

## 5 Conclusions

- (1) The soil resistivity sharply decreases with the decrease in matric suction, especially at the medium range of soil suction (i.e., 1000–100 kPa), then the relationship will be relatively constant for all measurement levels.
- (2) When soil suction is reduced by multi-step wetting processes (i.e., increase of the water content), the cementing bonds between soil particles will be destroyed due to the softening and dissolution of gypsum by water. In this case, the positive pore water pressure will increase, causing an increase in soil conductivity and a reduction in soil resistivity.
- (3) When the moisture content gradually increases and the soil approaches the saturation state, the value of soil resistance will fluctuate due to the hydration and chemical reaction for the gypsum with water.
- (4) The reduction in matric suction (i.e., negative pore water pressure) results from replacing the air volume with water volume in the micro-structure level of soil particles, especially after the air entry value on the soil–water characteristics curve of the studied gypseous soil.
- (5) The void ratio sharply decreased with the decreasing of the soil suction and relatively becomes constant at a low range of soil suction (i.e., < 100 kPa) at vertical stress of 25 kPa.



## References

1. Nashat, I. H. (1990). *Engineering characteristics of some gypseous soils in Iraq*. Unpub. Ph. D. Thesis. University of Baghdad.
2. Al-Obaidi, Q. A., Ibrahim, S. F., & Schanz, T. (2013). Evaluation of collapse potential investigated from different collapsible soils. In *Multiphysical testing of soils and shales* (pp. 117–122). Springer.
3. Al-Obaidi, Q. A., Karim, H. H., & Al-Shamoosi, A. A. (2020, February). Collapsibility of gypseous soil under suction control. In *IOP conference series: materials science and engineering* (Vol. 737, No. 1, p. 012103). IOP Publishing.
4. Karim, H. H., Al-Obaidi, Q. A., & Alshamoosi, A. A. (2020). Variation of matric suction as a function of Gypseous soil dry density. *Engineering and Technology Journal*, 38(6A), 861–868.
5. Fredlund, D. G., & Morgenstern, N. R. (1977). Stress state variables for unsaturated soils. *Journal of the geotechnical engineering division*, 103(5), 447–466.
6. Fredlund, D. G., & Rahardjo, H. (1993). *Soil mechanics for unsaturated soils*. John Wiley & Sons.
7. ASTM International, 2012. Standard test method for field measurement of soil resistivity using the Wenner four-electrode method. ASTM International.
8. Al-Mufty, A. A. & Nashat, I. H. (2000). Gypsum content determination in gypseous soils and rocks. In *Proceedings of the 3rd Jordanian international mining conference, Amman*, (Vol. 2, pp. 485–492).
9. Al-Obaidi, Qasim A.J. (2014), “Hydro-Mechanical Behaviour of Collapsible Soils”, ISSN: 2190-3255, Ph.D. Thesis, Ruhr Universität Bochum, Germany.
10. Guinea Maysounave, A. (2012). *Geoelectrical characterization of sulphate rocks*. Doctoral dissertation, Universitat de Barcelona.

# Assessment of Effect of Tidal Level and Footing Proximities on Retaining Wall-Grain Interactions Using Finite Element Method



Zuhair Kadhim Jahanger, Qais K. Jahanger, and S. Joseph Antony

**Abstract** The study presents a simulation of a cantilever sheet pile wall considering the effects of high and low tide and spacing between the foundation and the sheet pile wall. The rising of seawater during a tidal wave, which is a shallow water wave, could be observed daily near ports (i.e., Al Faw Grand Port, Basrah, Iraq). This fluctuation of water has a significant effect on shear strength and compressibility of the soil zone above the water table next to the retaining wall of the port platform. Investigations on the displacement patterns of the subsoil of the existing sheet pile wall supporting the soil by tidal waves are relatively scarce. In this study, the local displacement fields of a dense soil layer interacting with a rigid strip footing at different proximities, which the spacing between the footing edge and the wall = 1, 2, 3, and 5 of the footing width, of the retaining wall under the plane-strain condition were examined based on the finite element method (FEM) using ANSYS software. In general, the results show a good level of agreement between the hypothesis results (analytical solution) and simulations conducted here. Overall, relatively higher displacement and stress measures are observed at the retaining wall for a closer distance of footing to the wall. As the tidal level increases 4 m, the horizontal displacement and stresses decreased by less than 1%. The study contributes to a new understanding of the horizontal displacement profile of the retaining wall and its link to the bearing capacity of the strip footing under static loading environments.

**Keywords** FEM · Retaining wall · Sheet pile · Deformation · Tidal waves

---

Z. K. Jahanger (✉)

Department of Water Resources Engineering, University of Baghdad, Baghdad 10071, Iraq  
e-mail: [zk\\_jahanger@coeng.uobaghdad.edu.iq](mailto:zk_jahanger@coeng.uobaghdad.edu.iq)

Q. K. Jahanger

Department of Civil Engineering, Mustansiriayah University, Baghdad 10047, Iraq  
e-mail: [qais.jahanger@uomustansiriyah.edu.iq](mailto:qais.jahanger@uomustansiriyah.edu.iq)

S. Joseph Antony

School of Chemical and Process Engineering, University of Leeds, Leeds LS2 9JT, UK  
e-mail: [S.J.Antony@leeds.ac.uk](mailto:S.J.Antony@leeds.ac.uk)

## 1 Introduction

Iraq needs to construct a new port built in a tide-dominated and muddy environment, as illustrated in Fig. 1. Tidal waves have significant impacts on the functions of marine structures. Marine structures such as ports and buildings require the construction of retaining structures to support the soil and the structure foundations. Sheet piles necessarily retain walls that comprise steel sheets and or precast concrete designed to support and stabilize soils such as earth retaining structures and braced cuts. In addition, to support and stabilize soils inland, sheet piles are used offshore to support soil and stabilize the foundations of the marine structure, such as cofferdams and continuous walls of waterfront structures [1, 2]. However, the behavior of load and thus stresses and strains applied on the retaining walls (sheet piles) are different offshore than onshore due to the effects of tidal waves (high tide versus low tide level). The rising of seawater during the tidal wave, which is a shallow water wave, could be observed daily near ports (i.e., Al Faw Grand Port, Basrah, Iraq). This fluctuation of water has a significant effect on shear strength and compressibility of the soil zone above the water table next to the retaining wall of the port platform. Assessment of such supporting structures for Al Faw Grand Port is yet to be conducted. This is needed to address the high and low tidal level impact on the retaining wall and thus the stability and durability of the foundation of port cranes and the distance between the retaining wall and the foundation. The stability and durability are due to the interaction between the retaining wall and the adjacent soil as well as the foundation of the structure and the adjacent soil -structure as a result of different stiffness between the soil, footing, and the sheet pile structure. The available design rules for steel sheet pile walls mainly use an elastic design based on the permissible



**Fig. 1** Al Faw Grand port, Basrah, Iraq

stress method [3]. However, a better evaluation of the behavior of the sheet pile wall in the soil can be obtained using a full-scale field test [2, 3].

The full-scale field tests are accepted in engineering practice. It may lead to more costs. Therefore, it appears that the full-scale field test could be successfully simulated with a numerical model. This full-scale model shall be validated with a full-scale in-situ test, and a calibrated model has to be used as a reference for further investigations. In addition to the deformation pattern, a relative stiffness difference between the sheet pile walls and the supporting soil may also lead to mobilize soil arching, resulting in the transfer of the load to the stiffer sheet pile wall [4]. Soil arching phenomena can be mobilized in various geotechnical applications [4]. Numerous researchers have studied the sheet pile wall using a numerical approach. GuhaRay and Baidya [5] have analyzed cantilever sheet pile walls backfilled with cohesionless and cohesive soils using the finite element approach. They have observed that the soil cohesion and water table have influenced the stability of the cantilever sheet pile walls to a great extent [5]. Emarah and Seleem [6] have numerically studied the variation of maximum values of bending moments and anchor forces driven in the sheet piles using the finite element program. They have concluded that the maximum bending moment is achieved at the stiffer sheet pile wall [6]. Furthermore, in the geotechnical engineering applications, precise understandings are yet to be established on the local displacement fields of the dense soil under the static loading on continuous footing next to the retaining wall. Also, the evolution of deformation and internal stresses against the retaining wall is yet to be addressed.

The study presents a simulation of a cantilever sheet pile wall considering the effects of two extreme cases of high and low tide level and spacing distance ( $S/B$ ) between the foundation's edge and the sheet pile wall, where  $S$  equals the edge to edge spacing and  $B$  equals the width of the foundation. To achieve this objective, the FEM using ANSYS software was used to simulate the structure, soil, and hydrostatic pressures of the tidal high and low levels. Therefore, this paper aims to study and analyze the effects of high and low tide levels on sheet pile walls to identify the horizontal deformation and yield stresses (von Mises) under the allowable settlement for different footing locations the sheet pile wall. In the current study, the cantilever sheet pile wall is backfilled by cohesionless soil and is driven into a dense soil layer.

## 2 Methodology

**Study Area.** A general view for the subsoil profile at the Al Faw grand port shows that the subsoil consists mainly of medium to soft and soft to very soft clay at the top layer. This layer strengthens with depth to stiff and very stiff with brownish and grayish appearances in colors, and lean silty clay with fine-grained green sand occasionally encountered within the strata [7, 8]. This layer is overlying dense to very dense, with grayish and greenish visions in color, fine-grained (clayey) silty sand. However, the profile could be divided into sub-layers; each one varies from the other in its strength and consistency along the depth [7, 8]. According to the tide chart, Al

Faw's maximum tide level is  $\sim 3.0\text{--}4.0$  m, and a mean tidal range exceeds 4 m at the spring tide [9]. Accordingly, the tide is well defined as a periodic vertical stream of the sea surface due to attractive mutual forces of the earth, moon, and sun resulted in a very long tide generates in the Gulf basin and circulate towards the shoreline [9].

### 3 Finite Element Method Simulations

Full-scale problems are more suited to be studied using FEM simulations, but inherently the cohesionless medium is typically considered as a continuum with a given type of the constitutive relations of the sand layer [10]. The discrete element method (DEM) is a popular method to model the mechanical behaviour of granular materials [11]. However, the simulation of large-scale granules systems is expensive and time-consuming. Using ANSYS Workbench 18.2 [12], a linear elastic FEM simulation was conducted corresponding to the real conditions in this study. A two-dimensional solid geometry of the soil and the footing created using ANSYS software were modeled under plane strain conditions. The full-scale model of the soil with a dimension of  $25\text{ m} \times 60\text{ m}$  was modeled ( $25 =$  height of the sheet pile wall to the dredge line  $\times 60\text{ m} =$  the far-right boundary). The footing with a dimension of ( $B = 2\text{ m} \times$  thickness  $= 0.7\text{ m}$ ) was modeled. An eight-noded quadratic solid element was used, having two degrees of freedom at each node (i.e., translations in the nodal  $x$  and  $y$  directions) as shown in Fig. 2. The element and node numbers verified to get a good level of convergence at the end of the applied load, in the soil body and the continuous foundation are equal to 2588 and 8032. Also, the mesh bias was chosen to maintain the same aspect ratio of the footing elements and the soil at the interface area.

An adaptive FE mesh generation [13, 14] was applied at the footing-soil-wall interface where the major strains and stresses could be considered. It is worth mentioning that the Skewness mesh metric, a measure of mesh quality, of maximum  $4.857 \times$

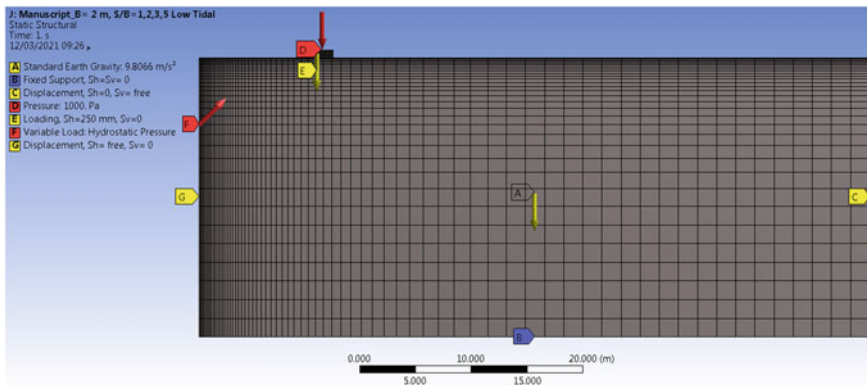


Fig. 2 Chosen domain, boundary conditions, and finite element mesh

10–6 value was accomplished, which is also considered adequate [14]. The simulations were held under identical boundary conditions for the quasi-static tests. In the simulation, bottom nodes, which are assumed as dredge lines, were fixed from the degree of freedom ( $S_h = S_v = 0$ ) (Fig. 2). The far side of the model was allowed to move in the vertical direction ( $S_v \neq 0$ ) and fixed in the horizontal direction because it is infinite ( $S_h = 0$ ) [14]. A displacement boundary was used along the left sheet pile wall ( $S_h \neq 0, S_v = 0$ ). A rough surface footing to sand contact areas was modeled where there is no sliding [12]. The free water height is used here assumed to be 2 m (water-free surface, Fig. 2) which equals the high tide level, while 6 m (water-free surface, Fig. 2) for the low tide level. The hydrostatic pressure was applied as a variable hydrostatic pressure (Fig. 2).

The Mohr–Coulomb model was used here to describe the nonlinear behavior of the dense sand. With large strain problems, it is recommended to use the Hardening Small Strain model (HSS) rather than the MC model. MC behavior is acceptable in compression rather than unloading compare to HSS that MC does not account for unloading in its formulation as far as displacements of the model (soil) are concerned. It seems likely that the constitutive plasticity models in ANSYS are applicable in both small and large deformation analyses [12]. The MC nonlinear model is often used in the geomechanical analysis to study soil failure under external loading [12]. Furthermore, dense to very dense sand physical properties were used as input to the simulations, including bulk density ( $\gamma = 20 \text{ kN/m}^3$ ), initial modulus of elasticity ( $E = 150 \text{ MPa}$  [2]), Poisson's ratio ( $\nu = 0.36$ ), peak angle of internal friction ( $\phi_{\text{peak}} = 45^\circ$ ), cohesion ( $c = 1 \text{ kPa}$ , to avoid simulation discrepancies) and dilatancy angle ( $\psi = \phi_{\text{peak}} - \phi_{\text{cr}} = 10^\circ$ ), residual angle of internal friction ( $\phi_{\text{cr}}$ ) and residual cohesion  $c_{\text{cr}} = 0.8c$  [7] as suggested by Das [2].

The maximum axial displacement loading (0.25 m) was applied here on the rigid footing geometry elements of time step in the range of 0.01–0.1 s. In the case of foundation on cohesionless soil, the settlement of the foundation controls the design of footing [15]. This time step was used to attain the convergence requirements of the simulation [12]. It is worth mentioning that such a method was earlier applied successfully to analyze the interaction behavior of strip footing-cohesionless sand interactions under the quasi-static loading [14]. The evolution of the nodal displacement characteristics in the solid geometry was traced under the allowable settlement and compared on high and low tide measures for different spacing distances ( $S/B$ ) between the footing edge and the wall. Yield failure criteria in ductile materials are theoretically measured of von Mises stress and is also popular in fatigue strength calculations.

## 4 Numerical Results and Analysis

Figures 3 and 4 illustrate the horizontal deformation profiles induced in high and low tidal levels for different spacing distances ( $S/B = 1, 2, 3, 5$ ) between the footing edge and the wall. The differences in the response under the allowable bearing capacity

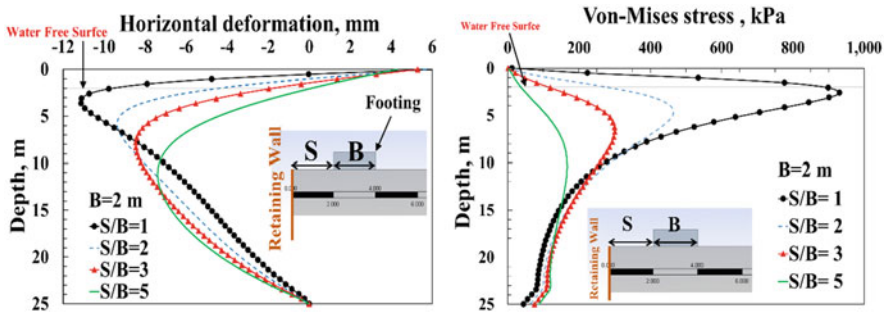


Fig. 3 High tide level on sheet pile wall with different footing spacings (S) (left) horizontal displacement along the wall (right) von Mises stress along the wall

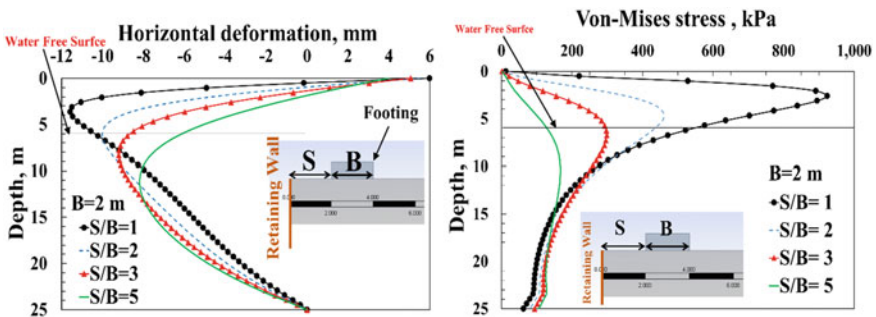
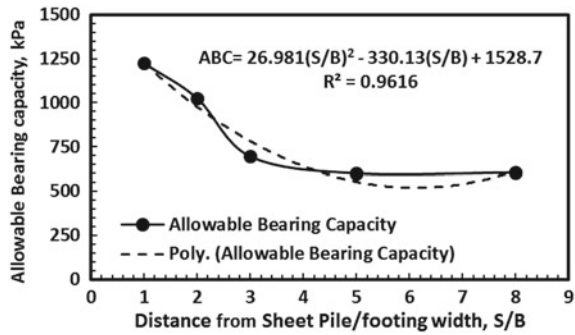


Fig. 4 Low tide level on sheet pile wall with different footing spacings (S) (left) horizontal displacement along the wall (right) von Mises stress along the wall

are further investigated by plotting the horizontal deformation, and von Mises stress profiles along the sheet pile wall. The smaller S/B, the larger the horizontal deformation and von Mises stress are. This is valid for both low and high tidal levels of sheet pile walls. This is due to the increase in the interference effect between the footing and the sheet wall for smaller spacing (S) (i.e., lateral stress close to the footing) [10]. This highlights the change in the mechanism of failure (local deformation patterns of sand beneath neighboring footing to the wall) and blocking mechanism in terms of the spacing distance (S/B) between the footings and the wall due to different spacing distances [7, 15].

The horizontal deformation and von Mises stress profiles show a nonlinear response for all cases of  $S/B = 1, 2, 3, 5,$  and  $8$  and both low and high tidal levels. Though not illustrated here, similar trends were made for  $S/B = 8$  used in this study. It seems that the horizontal deformation and von Mises stress profiles attain the peak at a depth of about the spacing (S). Therefore, failure of the sheet pile wall at a depth of about the spacing (S) is expected. Thus, a tie rod sustains the load is needed at these locations. The horizontal deformation and von Mises stress variations are

**Fig. 5** Allowable bearing capacity of the footing at low tide level with different footing spacing distances



relatively smaller in the case of the high tide level. Generally, relatively higher horizontal displacement and stress fields would be observed at the cantilever sheet pile wall for a closer distance of footing-soil structure (weaker) to the steel sheet pile wall (stiffer). However, the horizontal deformation and von Mises stress profiles show no remarkable changes between the two cases, low and high tide levels. Therefore, the horizontal deformation and von Mises stress variations are relatively smaller by less than 1% in the case of the high tide level than the low tide level.

The footing shall be designed to support the allowable bearing capacity (ultimate pressure/ safety factor) as well as to sustain the related allowable settlement under working loads [13, 16, 17]. However, the measured settlement conducted by the simulation shows that the settlement is substantial and shall exceed the 25–50 mm; a figure is recommended not to be exceeded for continuous foundations [15]. Accordingly, in the case of low tide level, which is the critical case in this study compared to the high tide level, the calculated allowable bearing capacity (ABC) shall not exceed 1225, 1025, 695, 600, and 605 kPa for S/B = 1, 2, 3, 5 and 8 respectively as illustrated in Fig. 5. It can be seen that the ABC reached a horizontal plateau for a spacing distance greater than S/B = 5, where the interference effect slightly diminishes with an increase in the spacing distance. Therefore, from the measured value of allowable bearing capacity (ABC) data used in Fig. 5, a second-order polynomial equation was obtained, as it was the best fit using the regression analysis and can be expressed as Eq. 1:

$$ABC(\text{inkPa}) = 26.981(S/B)^2 - 330.13(S/B) + 1528.7 \tag{1}$$

## 5 Summary and Conclusions

This paper presents the numerical parametric study results for sheet pile walls for port supporting cohesionless soil with footing in different space distance (S) from the wall to study the actual response of sheet wall in terms of both cases of high



and low tide levels. This study was conducted to evaluate the variation of values of horizontal deformation, and von Mises stress exerted in the sheet piles. This evaluation was affected by varying space distances of the footing, either with the high or the low tide level. The smaller S/B, the larger the horizontal deformation and von Mises stress are. This is valid for both low and high tidal levels of sheet pile walls. Also, as the tidal level increases, the horizontal displacement and stresses decreased. The horizontal deformation and von Mises stress profiles show a nonlinear response for all cases of S/B and both low and high tidal levels. The results show that the horizontal deformation and von Mises stress profiles attain the peak at a depth of about the spacing (S). The horizontal deformation and von Mises stress variations are relatively smaller by less than 1% in the case of the high tide level than the low tide level.

## References

1. Krabbenhoft, K., Damkilde, L., & Krabbenhoft, S. (2005). Ultimate limit state design of sheet pile walls by finite elements and nonlinear programming. *Computers and Structures*, 83, 383–393.
2. Das, B. M. (2018). *Principles of foundation engineering*, (8th ed.) India: Cengage Learning.
3. Kort, D. A. (2003). *Steel sheet pile walls in soft soil*. PhD Thesis. The Netherlands: Delft University Press.
4. Al-Naddaf, M. A. M. (2017). *Investigation of soil arching stability under static and cyclic surface loading using trapdoor model tests*. M.Sc thesis, University of Kansas.
5. GuhaRay, A., & Baidya, D. K. (2015). Reliability-based analysis of cantilever sheet pile walls backfilled with different soil types using the finite-element approach. *International Journal of Geomechanics* 15, 06015001.
6. Emarah, D. A., & Seleem, S. A. (2018). A numerical study of anchored sheet piles subjected to different types of sandy soils backfill. *HBRC Journal* 14, 422–430.
7. Jahanger, Z. K. (2011). Relation between standard penetration test and skin resistance of driven concrete pile in overconsolidated clay soil. *Journal of Engineering*, 17, 1355–1370.
8. Unpublished Report. (2013). Geotechnical Investigation Report, Iraq, Baghdad: Andrea Engineering Tests Laboratory.
9. Lafta, A. A., Altaei, S. A., & Al-Hashimi, N. H. N. (2019). Characteristics of the tidal wave in Khor Abdullah and Khor Al-Zubair channels. Northwest of the Arabian Gulf. *Mesopotamian Journal of Marine Science*, 34, 112–125.
10. Jahanger, Z. K. (2018). *Micromechanical investigations of foundation structures-granular soil interactions*. Doctoral Thesis, University of Leeds.
11. Sujatha, J., Jahanger, Z. K., Barbhuiya, S., & Antony, S. J. (2020). Fabrics-shear strength links of silicon-based granular assemblies. *Journal of Mechanical*, 36, 323–330.
12. ANSYS Theory Manual. (2018). ANSYS, Inc., Canonsburg, Pennsylvania.
13. Antony, S. J., & Jahanger, Z. K. (2020). Local scale displacement fields in grains–structure interactions under cyclic loading: Experiments and simulations. *Geotechnical and Geological Engineering*, 38, 1277–1294.
14. Jahanger, Z. K., Antony, S. J., Martin, E., & Richter, L. (2018). Interaction of a rigid beam resting on a strong granular layer overlying weak granular soil: Multi-methodological Investigations. *Journal of Terramechanics*, 79, 23–32.
15. Das, B. M. (2009). *Shallow foundations: Bearing capacity and settlement* (2nd ed.) London: CRC Press.

16. Jahanger, Z. K., Sujatha, J., & Antony, S. J. (2018). Local and global granular mechanical characteristics of grain–structure interactions. *Indian Geotechnical Journal*, 48, 753–767.
17. Jahanger, Z. K., Antony, S. J., & Hirani, A. (2020). Foundation relative stiffness effects in sand under static loading. *AIP Conference Proceedings*, 2213, 020002.

# Evaluation of Dam Breach Parameters Using Different Approaches for Earth-Fill Dam



Israa Dheyaa Abdulrazzaq, Qassem H. Jalut, and Jasim M. Abbas

**Abstract** The analysis of dam breach is generally used for the prediction of the flood on downstream of the dam, but it is also crucial to predict the parameters of a dam breach, the outflow hydrograph, and downstream nature of propagation. This study deals with the analysis of dam break of an earth-fill dam (Hamrin Dam). The dam checked for overtopping failure by using the two-dimensional river analysis model HEC-RAS and the different approaches that used in order to predict the parameters of dam break for use in the model. In this case, additional water levels for each method were considered. It can be seeming that the most suitable to estimate the parameters of dam breach is USBR approach.

**Keywords** Dam breach · Hamrin dam · HEC-RAS · Modelling · Flood hydrograph

## 1 Introduction

The dams provide an ability to facilitate life in numerous ways and function to control freshwater flow; they also pose an inevitable and inherent threat to public safety and the environment. Dams have been failing because of unpredictable environmental conditions, improper management, or poor engineering since creating the first dams. When the dams are failed, they do often so catastrophically due to big amount of the inherent energy involved. The dams are complex structures that are subjected to many forces because of failure, and these forces are reactive along with the dam's entire life, and the reality that the stood of a dam safely for few years is not necessarily

---

I. D. Abdulrazzaq (✉) · Q. H. Jalut · J. M. Abbas  
Civil Engineering Department, University of Diyala, Baqubah, Diyala, Iraq  
e-mail: [eng\\_grad\\_civil044@uodiyala.edu.iq](mailto:eng_grad_civil044@uodiyala.edu.iq)

Q. H. Jalut  
e-mail: [qjalut@uodiyala.edu.iq](mailto:qjalut@uodiyala.edu.iq)

J. M. Abbas  
e-mail: [jasimalshamary@uodiyala.edu.iq](mailto:jasimalshamary@uodiyala.edu.iq)

a sign that the dam will not fail. One of the forces that inducing failure is overtopping. Overtopping is a clogging of the spillways or a result of having inadequate emergency spillway capacity. The fundamental information of flood events that can be advantageous in the engineering of dam can be provided by the analysis of dam breaching, emergency action plan, and floodplain management. Various researchers and organizations have contributed their findings in an analysis of the dam break and its consequence.

The derived regression equations based on the data from historical events of dam failure, used in predicting breach geometry, are early-proposed [1]. Yi [2] characterized dam break in the aspect of model and theories. Understanding the dam break mechanics, break parameters prediction, peak outflow prediction shown as the fundamental for dam break analysis, and at last located the loss of the damage. Other relative studies about dam break using HEC-RAS are done in references [2–6] with different parameters like the elevation of reservoir and break parameters. These studies can be used to develop knowledge about this kind of issue. Therefore, this study included the simulation of a case study in Iraq using HEC-RAS with different break parameters.

## 2 Definitions of Breach Parameters

The expression of breach parameters contains (breach width, breach depth, and angles of side slopes), and these parameters explain the required time of initiation of the breach and its development. These parameters are summarized below and shown in Fig. 1 [7].

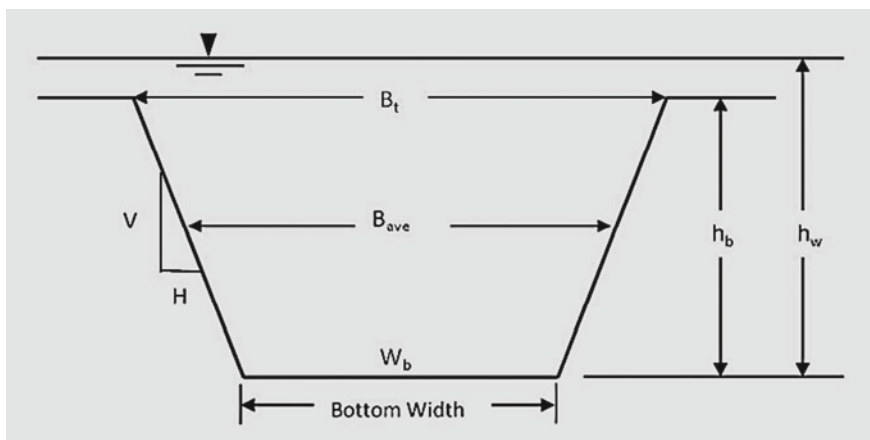


**Fig. 1** Idealized dam breach parameters

**Breach Depth.** In many publications, it is also mentioned as breach height. This is a vertical range of breaching, measured from the peak of the dam down to an invert of the breaching. Some of the publications cite that the reservoir head-on breaching, measured from the reservoir’s water surface to the invert of the breach.

**Breach Width.** The peak flow rate and the resulting immersion levels downstream from the dam can be hugely affected by the rate of the breaching width expansion and the ultimate breaching width. The case studies typically statement either breach width at top or bottom of breaching or average breach width opening.

**Breach Side Slope Factor.** The shape of the breach opening can be specified by the side slope factor, breach depth, and breach width. The exact predicting of the side slope angles are considered of secondary importance for predicting the breach depth and width.

### 3 The Governing Approaches

In this research, we used five of the most common experimental methods for predicting the breach size and the breach formation time to estimate the breach parameters for Hamrin dam. The experimental methods are Froehlich [8], Froehlich [9], MacDonald and Langridge-Monopolis, Von Thun and Gillette, and Bureau of Reclamation. For various scenarios of assumed overtopping failure mode with various ranges of initial water levels (107.5 m, 104.5 m, and 101.5 m) m.a.s.l for the reservoir, these methods were applied for estimating Hamrin dam breach. For the overtopping failure mode, the location of the breach was supposed to be at the centreline downstream of the dam. The final bottom elevation of the breach was supposed to be at the significant riverbed.

Froehlich [8]. Froehlich used sixty-three earth, zoned earth with a core wall ground dam (i.e., mud), and rockfill dam data sets to refine a group of equations to predict the average width of the breach, side slopes, and time of breaching. Table 1 shows the equations for determining the parameters of dam breach according to reference [8].

Froehlich [9]. Froehlich in 2008 modified his equations of breach based on the addition of new data. He used data sets for seventy-four earth, zoned earth, earth dam with a core wall (i.e., mud), and rockfill dam to improve a group of equations to predict the average width of the breach, side slopes, and time of breaching. Table 2 shows the equations for determining the parameters of dam breach according to reference [9].

**Table 1** Parameters required for Froehlich (1995a) formula [8]

Parameters	Values
The average breach width equation	$B_{ave} = 0.1803 K_o V_w^{0.32} h_b^{0.19}$
Time of failure equation	$t_f = 0.00254 V_w^{0.53} h_b^{0.90}$

**Table 2** Parameters required for Froehlich formula [9]

Parameters	Values
The average breach width equation	$B_{ave} = 0.27K_o V_w^{0.32} h_b^{0.04}$
Time of failure equation	$T_f = 63.2 \left( \sqrt{V_w / g h_b^2} \right)$

**Table 3** Parameters required for Macdonald and Langridge-Monopolis formula [10]

Parameters	Values
The average breach width equation	$W_b = \frac{V_{eroded} - h_b^2 (CZ_b + h_b Z_b Z_3 / 3)}{h_b (C + h_b Z_3 / 2)}$
Time of failure equation	$t_f = 0.0179 (V_{eroded})^{0.364}$

**Macdonald and Langridge-Monopolis.** MacDonald and Langridge-Monopolis used forty-two data sets (predominantly earth fill, earth fill with a clay core, and rockfill dam) to develop a relationship for the “Breach Formation Factor.” Breach Formation Factor is a product of the water volume coming out of the dam and water height above the dam. They related the breach formation factor to the importance of the material that eroded from the embankment dam. Table 3 shows the equations for determining the parameters of dam breach according to Macdonald and Langridge-Monopolis [10].

MacDonald and Langridge-Monopolis set that the side slopes of the breach were assumed to be 1H:2 V in most cases. Also presented that the time breach formation of the enveloped curve as a function of ( $V_{er}$ ).  $V_{er}$  and dam cross-section can be used for the calculation of breach width.

$$V_{er} = 0.0261 (V_{out} * h_w)^{0.796} \text{ (For earth-fill dams)} \tag{1}$$

$$V_{er} = 0.0179 (V_{er})^{0.346} \text{ (For non-earth fill dams)} \tag{2}$$

Von Thun and Gillette [11]. Von Thun and Gillette utilized fifty-seven dams from both Froehlich (1987) and MacDonald and Langridge-Monopolis (1984) to improve their methods. The method suggests utilizing breach side slopes of 1.0H:1.0 V, except for the dams with cohesive soil, where the side slopes should be on the order of 0.5H:1 V to 0.33H:1 V. Tables 4 and 5 show the equations for determining the parameters of dam breach according to Von Thun and Gillette [11].

**Bureau of Reclamation.** Bureau of Reclamation (USBR) [12], a conservative formula was presented to evaluate the dam breach’s width with respect to the depth of the water reservoir. This formulation is considered a guide for selecting the breach’s eventual width, which is used in risk rating studies. Recommended breakout formation time is 0.011 times multiplied by the width of the breach as shown in the equation:

$$B = 3h_w \text{ and } t_f = 0.011 B \tag{3}$$

**Table 4** Parameters required for Von Thun and Gillette formula [11]

Parameters	Values
The average breach width equation	$B_{ave} = 2.5 h_w + C_b$
Time of failure equation	Two various equations developed by Von Thun and Gillette are shown below: <ul style="list-style-type: none"> <li>• <math>t_f = 0.02h_w + 0.25</math> (Erosion Resistant)</li> <li>• <math>t_f = 0.015h_w</math> (Easily Erodible)</li> <li>• <math>t_f = \frac{B_{ave}}{4h_w}</math> (Erosion Resistant)</li> <li>• <math>t_f = \frac{B_{ave}}{4h_w + 61.0}</math> (Easily Erodible)</li> </ul>

**Table 5**  $C_b$  coefficient values with respect to reservoir size

Reservoir size (m <sup>3</sup> )	$C_b$ (m)
$< 1.23 \times 10^6$	6.1
$1.23 \times 10^6 - 6.17 \times 10^6$	18.3
$6.17 \times 10^6 - 1.23 \times 10^7$	42.7
$> 1.23 \times 10^7$	54.9

**Singh and Snorrason.** Singh and Snorrason gave the earlier quantitative orientation for the prediction of breaching width. They collected data from twenty registered failures of the dam. Breach width limits show in Eq. 1 as a function of the height of the dam. They found that the time of failure located between fifteen minutes and one hour [13].

$$2h_d \leq B \leq 5h_d \text{ and } 0.25 \leq t_f \leq 1.0 \tag{4}$$

## 4 The Study Area

Hamrin Dam project is one of the strategic, vital, and essential projects built on the river of Diyala in Iraq, which is located 10 km front away dam of Diyala, about 120 km northeast of Baghdad, Iraq. The evaluated life expectancy of Hamrin Dam is in the mid of 100 and 150 years. The Yugoslav firm GIK Hidrogradnja (of Sarajevo, now Bosnia-Herzegovina) were built the dam and the attached powerhouse in the years 1976–1981. The dam’s function is for irrigation, power supply, and flood control, (53) meters is the maximum height of Hamrin dam, and the length of a body of an aggregate dam is (3500) meters in the river section of the old Diyala river. The crest level height of the dam is (109.50) meters above sea level. The cross-section of an embankment of Hamrin dam shows in Fig. 5 [14]. The up-stream and down-stream sides consisted of filters and clay core, and it includes cladding as well as coarse and fine filters, and from the upstream side, blocks of pre-cast concrete are used.

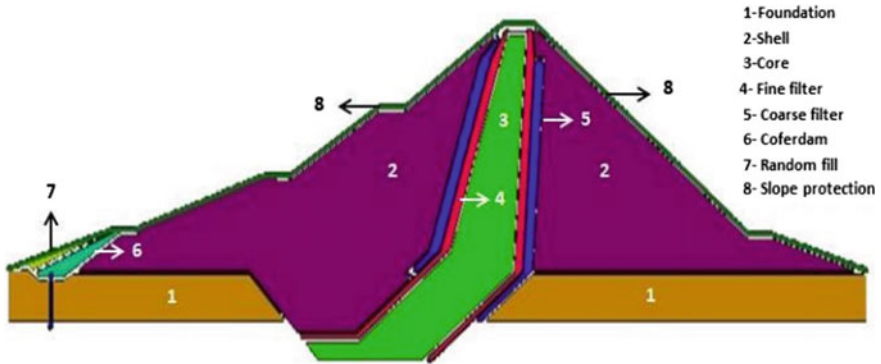


Fig. 2 Typical cross-section of Hamrin earth dam [14]

Hydrologically, the potential maximum flood of Hamrin dam is designed at (70%). The reservoir's capacity is 3.95 billion cubic meters, and the area of the reservoir is 445 km<sup>2</sup>, with the same level of flood (107.5) meters above sea level [15] (Fig. 2).

## 5 The Flood Hydrograph

In the study of a dam break, HEC-RAS (Hydrologic Engineering Centre's River Analysis System) Version 5.0.7, 2010 used for routing the inflow hydrograph throughout the reservoir and the breach outflow hydrograph throughout the river downstream. The unsteady flow model for Hamrin dam break developed within the HEC-RAS. The dam breach analysis includes routing of the outflow hydrograph from the dam that breached throughout the downstream of the river from the dam up to the boundary of the downstream. This will require the elevation data for the reservoir and the cross-section's elevation data for the river, including a flood plain. For this study, the Digital Elevation Model (DEM) 12.5\*12.5 was used as the elevation data source [16] (Figs. 3 and 4).

## 6 Results and Discussion

Different scenarios have been applied for each selected method. Table 6 shows the breach parameters estimates for reservoir elevation for Hamrin lake equal to 107.5 m.

HEC-RAS model was used to calculate the flood hydrograph resulting from Hamrin dam breach for several approaches and under various scenarios (107.5 m, 104.5 m and 101.5 m), as shown in Tables 7 and 8. The results show that Froehlich [8], Froehlich [9], and Macdonald and Langridge-Monopolis are overestimated the maximum flow discharge since the resulted breach size more significant than the



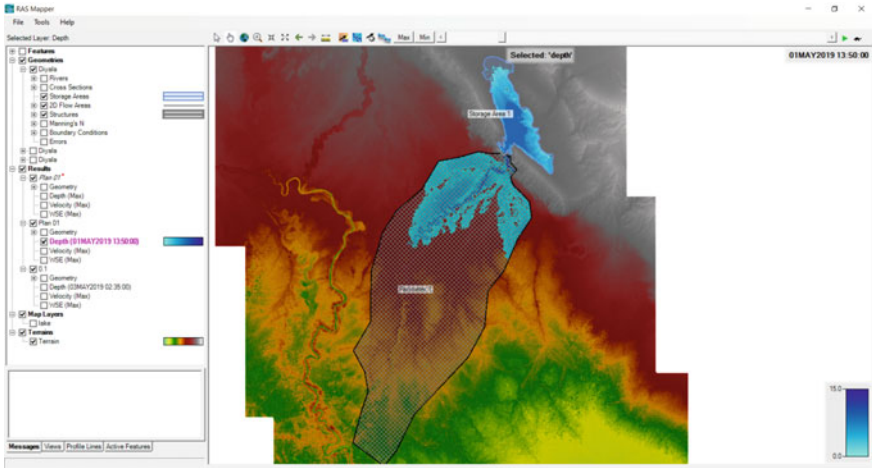


Fig. 3 RAS-Mapper

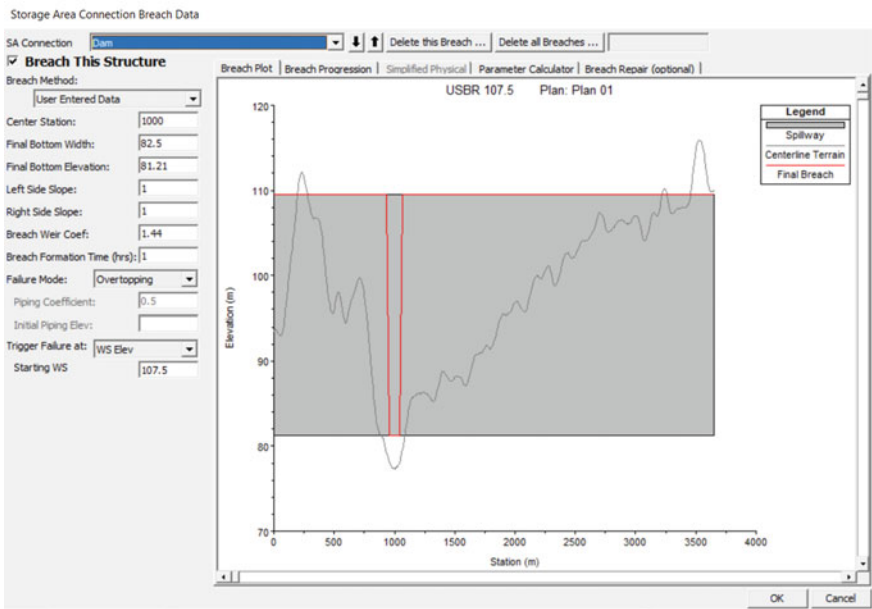
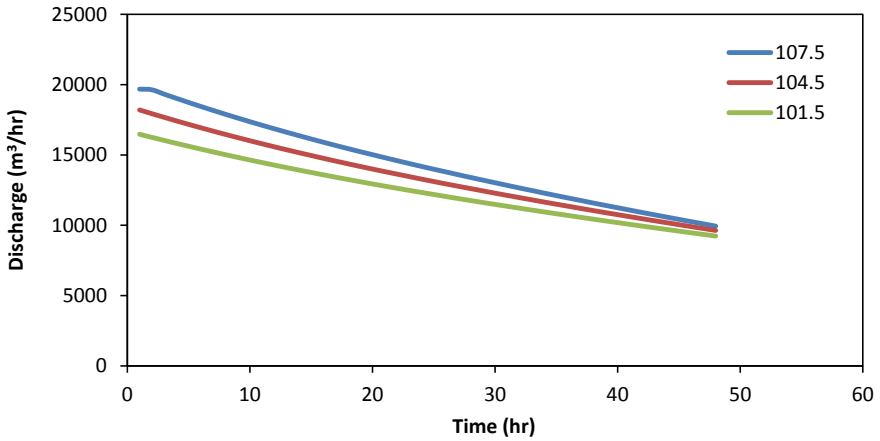


Fig. 4 Breach data for downstream of Hamrin dam

downstream of the body dam. The USBR method gives a reasonable maximum discharge depending on the final shape of the breach (Fig. 5).



**Fig. 5** Flood hydrographs for different elevations of the reservoir using USBR approach

**Table 6** Summary of the breach parameters estimates for reservoir elevation 107.5 m

Method	Bottom width of the breach (m)	Side slopes of the breach (H:1 V)	Time failure of the breach (hrs.)
Froehlich [8]	510.8	1.4	14
Froehlich [9]	432	1	11
Macdonald and Langridge-Monopolis	203.7	0.5	1.5
Von Thun & Gillete	123.65	1	1
USBR	82.5	1	1
Singh & Snorrason	185.5	0.5	1

**Table 7** The maximum discharge for all scenarios

Methods	Reservoir elevation (m)		
	107.5	104.5	101.5
	The maximum discharge in (m³/hr)		
Froehlich [8]	60,611.04	58,697.32	56,849.32
Froehlich [9]	61,909.64	58,128.45	54,472.19
Von Thun & Gillete	27,397.59	26,302.32	24,867.08
Macdonald and Langridge-Monopolis	40,070.32	44,562.13	50,028.46
USBR	19,683.54	18,202.13	16,472.23
Singh & Snorrason	36,952.66	18,315.31	16,353.33

**Table 8** Time to reach the maximum discharge for all scenarios (hrs)

Methods	Reservoir elevation (m)		
	107.5	104.5	101.5
	Time (hrs)		
Froehlich [8]	13	13	12
Froehlich [9]	11	12	11
Von Thun & Gillete	1	1	1
Macdonald and Langridge-Monopolis	2	2	2
USBR	1	1	1
Singh & Snorrason	1	2	2

## 7 Conclusion

The Flood hydrographs resulting from the dam breach are studied by applying six common approaches of the breach to Hamrin dam. To cover the overtopping failure mode, different scenarios were used. In addition, three levels of the reservoir for each approach were considered. Here are some concluding observations from the study. The following can be concluded:

- Methods of Froehlich [8], Froehlich [9] and Macdonald and Langridge-Monopolis have overestimated the maximum flow discharge since the resulted breach size more significant than the downstream of body dam.
- The USBR method gives a reasonable maximum discharge depending on the final shape of the breach.
- Froehlich [8, 9] also shows a significant value of time to reach the maximum discharge (time of failure).

## References

1. Leoul, A. (2015). *Dam breach analysis using HEC-RAS and HEC-GeoRAS the case of Kesem Kebena Dam*. M. Sc. Thesis. Addis Ababa University, Ethiopia.
2. Yi, X. (2011). A dam break analysis using HEC-RAS. *Journal of Water Resource and Protection*.
3. Gee, D. M. (2010). Dam breach modeling with HEC-RAS using embankment erosion process models. In *World environmental and water resources congress, challenges of change* (pp. 1347–1356).
4. Wahl, T. L. (1997, August). Predicting embankment dam breach parameters-A needs assessment. In *Proceedings of the Congress-International Association for Hydraulic Research* (pp. 48–53). Local Organizing Committee of the XXV Congress.
5. Xu, Y., & Zhang, L. M. (2009). Breaching parameters for earth and rockfill dams. *Journal of Geotechnical and Geoenvironmental Engineering*, 135(12), 1957–1970.
6. Zhang, L. W. M. Y., & Yuen, K. V. (2016). Empirical formulas in the prediction of breach parameters. *Japanese Geotechnical Society Special Publication*, 2(49), 1727–1731.

7. Dam Safety Office. (1998). *Prediction of embankment dam breach parameters: A literature review and need assessment*. Water Resources Laboratory, Denver, DSO-98-004.
8. Froehlich, D. C. (1995). Embankment dam breach parameters revisited. In *Proceedings of the Conference on Water Resources Engineering, San Antonio, Texas*, ASCE.
9. Froehlich, D. C. (2008). Embankment dam breach parameters and their uncertainties. *Journal of Hydraulic Engineering*, 134(12), 1708–1721.
10. MacDonald, T. C., & Langridge-Monopolis, J. (1984). Breaching characteristics of dam failures. *Journal of Hydraulic Engineering*, 110(5), 567–586.
11. Von Thun, J. L., & Gillette, D. R. (1990). *Guidance on breach parameters*. Unpublished Internal Document, U.S.
12. U.S. Bureau of Reclamation. (1988). *Downstream hazard classification guidelines*. ACER Technical Memorandum No. 11, U.S. Bureau of Reclamation, Denver, Colorado. Retrieved March 20, 2017, from [https:// www.arcc.osmre.gov](https://www.arcc.osmre.gov).
13. Singh, K. P., & Snorrason, A. (1984). Sensitivity of outflow peaks and flood stages to the selection of dam breach parameters and simulation models. *Journal of Hydrology*, 68(1–4), 295–310.
14. Jawameer, N. M. (2020). *Analysis of occurrence liquefaction in Hamrin earth dam under seismic load*. Thesis, University of Baghdad, Iraq.
15. The Ministry of Water Resources' 2016–2017 Final Report on Hamrin Earth Dam.
16. Basheer, T. A., Wayayok, A., Yusuf, B., & Kamal, M. (2017). Dam Breach parameters and their influence on flood hydrographs for Mosul Dam. *Journal of Engineering Science and Technology*, 12(11), 2896–2908.

# Manufacturing of Small-Scale Flume to Assess the Riverbank's Settlement



Asad H. Aldefae, Rusul A. Al-Khafaji, Wissam H. Humaish,  
and Evgeny K. Sinichenko

**Abstract** This paper includes designing, manufacturing, and testing a flume apparatus to simulate hydraulic and geotechnical problems occurring in natural rivers and open channels. The length of the flume is 247 cm, 80 cm wide, and 44 cm in height. The device's design was tested under physical modeling conditions by studying the failure mechanism that occurs in riverbanks as a result of the effect of water flow velocity in short-term and long-term flow duration and the type of soil used. Many laboratory tests were initially conducted to determine the properties of the soil sample. Then by applying specific limits of velocity, it was possible to determine the failure mechanism that occurs under these conditions, which has shown good compatibility with the type of failure in the prototype scale. The device consists of a steel frame, storage tank, pacification tank to restrict the flow of water that is drawn from the storage tank by the pump where a relatively large size pump has been chosen to reduce the number of revolutions per minute, conveyance pipes to transfer water, control valve to control the discharge, and the power switch. The walls and the base of the flume are made using Plexiglas plates. The main calibration results show an actual failure mechanism for the riverbank's existing Tigris River soil model and the other two models as references. The average of two side riverbank's settlement was 19.4 mm at long-term conditions (24 h of channel operation), whereas it was around 11.6 mm in the short term (4 h of channel operation). This behavior shows that most settlement occurs quickly due to the mobilization of the tension cracks along the banks.

**Keywords** Erosion rate · Flume · Stability · Riverbank's · Flow velocity

---

A. H. Aldefae (✉) · R. A. Al-Khafaji  
College of Engineering, Civil Engineering Department, Wasit University, Wasit, Iraq  
e-mail: [asadaldefae@uowasit.edu.iq](mailto:asadaldefae@uowasit.edu.iq)

W. H. Humaish · E. K. Sinichenko  
Hydraulic and Engineering Hydrology, People's Friendship University (RUDN), Moscow, Russia  
e-mail: [1042205230@pfur.ru](mailto:1042205230@pfur.ru)

E. K. Sinichenko  
e-mail: [csinichenko-ek@rudn.ru](mailto:csinichenko-ek@rudn.ru)

## 1 Introduction

The stability of the riverbanks is one of the most critical factors that must be considered by government agencies and municipal offices due to their effect on the stability of facilities near these banks [1–3]. Collapsibility of riverbank's leads to severe damages and subsequently loss of land due to problems of flood control changes in river level [4], increase in sediments, and thus the effect on the speed of drainage of these sediments along the course of the river [5, 6], as well as the effect on the water storage capacity in dams [7]. The importance of studying the stability of riverbanks and investigating the causes of failure is to avoiding similar failures and determining the cause of riverbank failure and then the necessity to choose the appropriate type of treatment that meets the hydraulic requirements at the lowest cost [8, 9]. The study of river banks' stability can be classified as major complex studies due to the interaction of many parameters with each other (i.e., geomorphological factors, hydraulic factors, and engineering factors [10, 11]). Researches in geotechnical engineering, hydraulic engineering, and water engineering have witnessed a distinguishable development in methods and measurement techniques and studying the phenomena that affect the stability of the riverbank [12]. Researchers widely use physical modeling, and it witnessed the massive development in collaborating with measurement techniques that can be utilized to assess the stability of the river bank and it has been widely captured different phenomenon in many studies on different catchments area, dams, and rivers around the world [13–15]. The physical hydraulic model represents a prototype of the state of hydraulic flow in reality, where the boundaries can be changed (i.e., the bottom and sides of the model within a certain limit) in addition to the possibility of controlling the flow conditions to suit the study condition. The purpose of constructing the hydraulic physical model is to test the design to ensure the structure's safe operation as it has an important role in the decision-making stage by helping to visualize the state of the flow field before choosing the appropriate design.

Several years ago, the research centers around the world started towards designing and manufacturing physical modeling in the laboratories by postgraduate students as it representing an alternative method to imported devices to increase students' skills, and provide a wider field for experimental activities and thus improve the quality of scientific laboratories [16–20]. Many attempts were made in various countries of the world to manufacture laboratory flumes for multiple purposes. At the University of Manitoba in Canada, a flume device was fabricated to measure erosion. The flume's length reached 243 cm, the width was 10 cm, and the height of 5 cm. The function of this device is specific, which is to measure the percentage of erosion only. Many other research facilities have manufactured flume devices and advanced technologies, but they did not consider the provision of all the influencing hydraulic and engineering factors. At the University of Tokyo in Japan, a flume device was manufactured from acrylic, with dimensions of 150 cm in length, 10 cm in width, and 15 cm in height, to study the effect of slope on sediment load, but this design did not provide the possibility of studying the impact of flow velocity or the geometry of the channel. At

National Chung Cheng University in Taiwan, a flume device was also manufactured. It was 75 cm in length, 25 cm in width, and 25 cm in height. This design aimed to study the effect of rain on the surface topography and the amount of soil erosion (Fig. 1).

From what has been mentioned above of the art and previous designs, it is clear that most of the flume devices manufactured usually serve one purpose only in other words that the possibility of studying all hydraulic, engineering, and geomorphological factors have not been combined in one device. Accordingly, the flume device was manufactured in the College of Engineering laboratories at the University of Wasit (where the design was done) that can be used in the study of many hydraulic and geotechnical phenomena that occur in natural rivers and open channels. The dimensions were chosen, and the parts of the device were connected precisely to overcome the above-mentioned obstacles and reach the closest state of the flow in natural rivers.

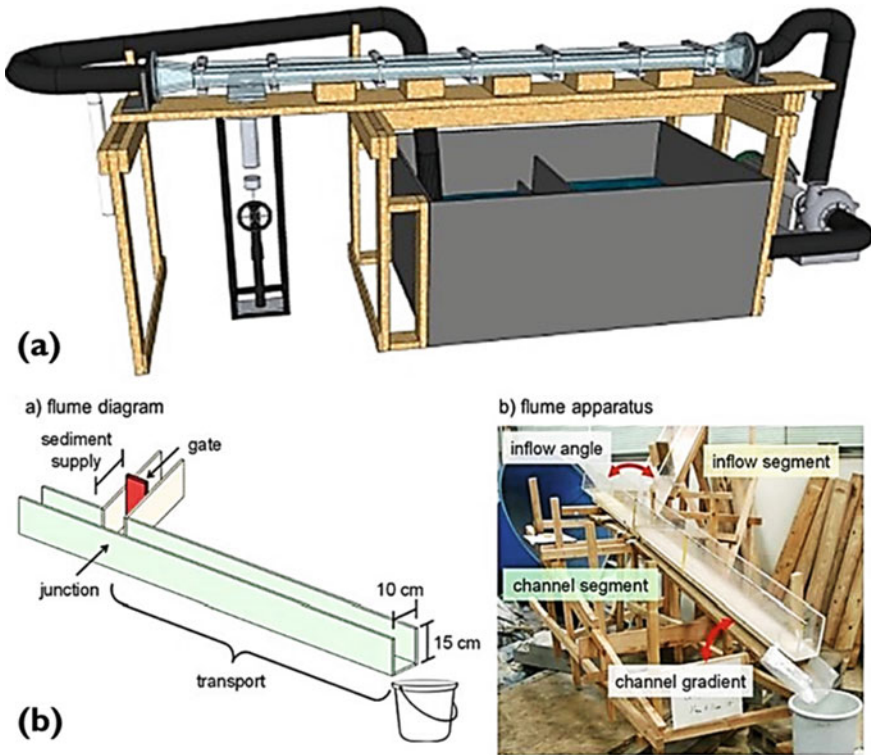


**Fig. 1** a Erosion measurement device at University of Manitoba and b An acrylic flume device at University of Tokyo

## 2 Parts of the Designed Flume

The device that was manufactured locally in the laboratories of the Department of Civil Engineering at the College of the Engineering/University of Wasit consists of a group of major and minor parts that work together to perform the required purpose of its installation, taking into consideration the physical modeling criteria in choosing the dimensions of the design. Figure 2 shows the detailed parts of the designed flume, and it will be explained in detail in the following paragraphs.

**Main Frame.** Previous researchers used different materials in manufacturing flume devices with different dimensions. In this device, the device's main body parts were manufactured and connected from an iron frame using square iron sections that hold both the storage tank and the pacification tank. The flume walls are made of transparent glass sheets (Plexiglas plates) with a thickness of 1 cm; the purpose of selecting them is to be able to observe the pattern during the examination. The dimensions of the flume were determined according to the distorted model's scale method used in modeling rivers, where a different scale is used for both the longitudinal direction and the latitudinal direction. The typical scales used were 1000: 1 for the longitudinal direction and 500: 1 for the transverse direction. These measures were determined concerning the length and width of the Tigris River, which was considered a model for the study, taking into account the neglect of a certain distance at the beginning and end of the flume because the phenomena that occur in these areas are not within the subject of the study.

**Storage Tank and Pacification Tank.** The function of the main tank is to store the water that circulates in the device, with a volume of 1 cubic meter; this tank contains inside it a cross barrier that acts as a filter to prevent fine grain soil particles

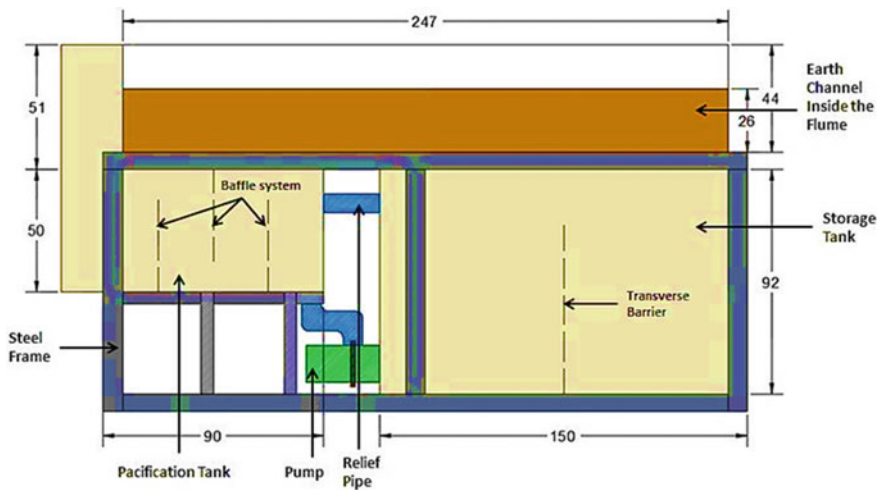
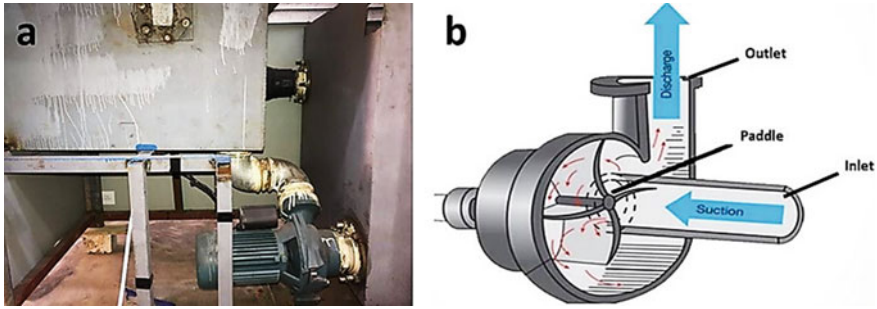


Fig. 2 Main parts of manufactured flume





**Fig. 3** Detailed parts of the manufactured flume

from crossing between different sides of the tank to avoid damage to the actuator. Water is moved from the pump’s main tank and travels through the pipelines to enter the pacification tank. The main tank has a volume of 0.225 cubic meters, containing inside it a pacification system (Baffle system), which is a cross-sectional barrier intended to increase the flow path to move away as far as possible from the source of pumping and thus restrict flow movement before the water enters the flume. The pacification tank’s front side height is designed to be the same level as the flume height to store the water so that the level remains the same level of the water inlet, and thus it comes out realistically as occurs in natural rivers. A vertical gate is welded and connected at the end of the flume through which it is possible to control the depth of the water. Another tube connecting between the storage tank and the dulling tank is called the release pipe, and it was essential to allow the drainage to be controlled by a valve, see Fig. 3a.

**The Actuator (Pump).** A mechanical actuator (pump) with a specific capacity was used to reduce the number of revolutions per minute, as shown in Fig. 3b. In this way, the flow could be controlled easily in addition to the presence of a pacification system (Baffle system) in the pacification tank to achieve the required speed, which is the average speed of the Tigris River (case study in the calibration section). The water flows by a simple mechanical action is controlled by the pump under the mechanism of the pumping system that consists of three stages, the stage of entering the water at the moment of operation through a part called the inlet where the liquid pressure is low at this stage, after that the stage of liquid containment during a process inside the named part casing. The final stage, which is the exit of the liquid through the outlet, or what is called the discharge part, where the liquid pressure is high at this stage. Inside the pump, there is also an installation called the fan (Paddle), which is responsible for the movement of liquid through the pump, the type of fan that determines the type of pump.

### 3 Test of Models

A test program was performed to assess the stability of natural riverbanks and investigate the failure surface mechanism, and the amount of the riverbank's settlement as the stability of the riverbanks is strongly influenced by the water flow velocity with different flow periods. Also, study the effect of tension cracks on failure mechanism by its influence on failure angle. Three samples were tested in the manufactured device, and all the tested models have similar preparation procedures, except that the first model was an actual model, where the soil used was 100% natural collected soil from the banks of the Tigris River. The second model is a virtual model (i.e., man-made model) in which the soil type was mixed between the Tigris river natural soil and sandy soil (i.e., 50% each). The test period for each of the models mentioned above is (5 h) short-term flow duration. The third model is also an actual soil model, as explained in the first model, but the channel's flow remains for 24 h (i.e., long-term flow duration). After the properties of the used soil sample were determined through laboratory tests, a soil density calibration was performed using a hammer specially made for this purpose to achieve the actual field density in the model (see Fig. 4).

The design of the channel dimensions and the side slope was done using the Manning equation; then, the channel was built inside the flume by performing the following steps:

- (a) The soil was placed in the flume in multilayers. Each layer is compressed and compacted in a certain ratio using a hammer specially made to achieve the desired density, as explained before, after marking the walls of the flume to determine the design dimensions of the channel (i.e., Fig. 5).
- (b) To achieve the required side slope, a wooden board (see Fig. 6) was used that extends along the flume and was fixed on both sides during the process of soil application and compaction, and then it was removed after the completion of the process.

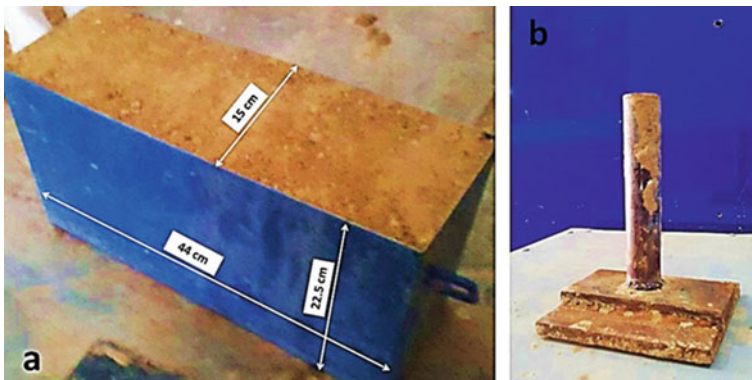


**Fig. 4** Soil density calibration using manufactured steel hammer

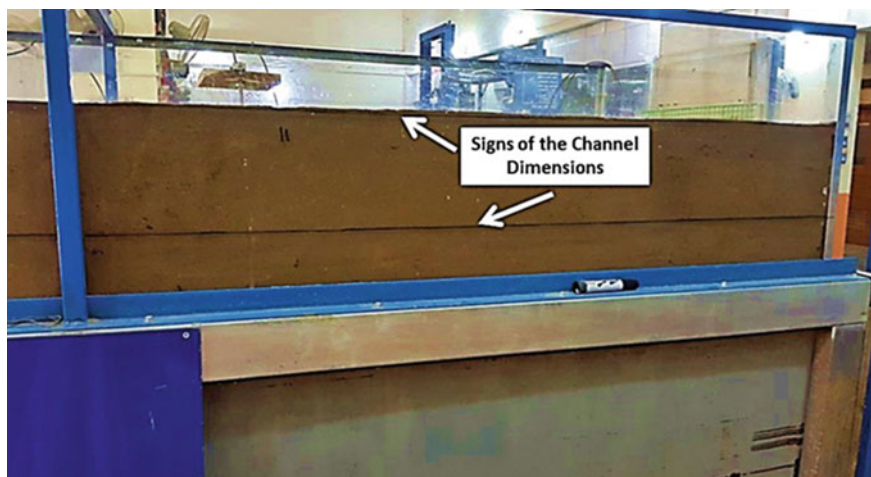


**Fig. 5** Designed dimensions of the channel with marks

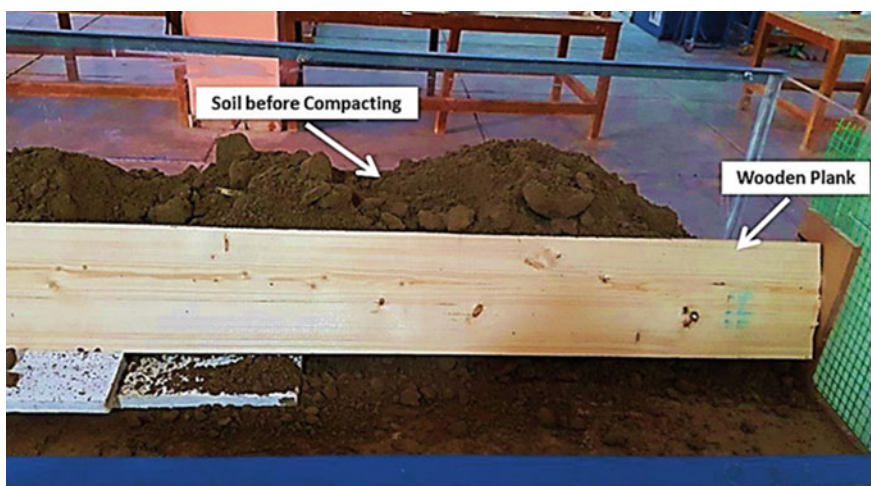


**Fig. 6** Building a side ramp using a wooden board

- (c) To control the flow turbulence occurs at the beginning of the channel, a stone cladding treatment of half a meter was used [14].

### 4 Operating, Measuring Equipment, and Control Unit

**Flow Control Valve.** It is a tool used to control the rate of fluid flow in the pipes as it has a passage with a variable flow area; the control valve plays an essential role in achieving the optimum performance of the hydraulic system (see Fig. 7).

**Flow Meter Device.** An open channel flow velocity meter is a tool for measuring the amount of fluid passing through a certain medium during a unit time. The used device provides the ability to measure the velocity of water flow with an accuracy of  $\pm 2\%$  (see Fig. 8).

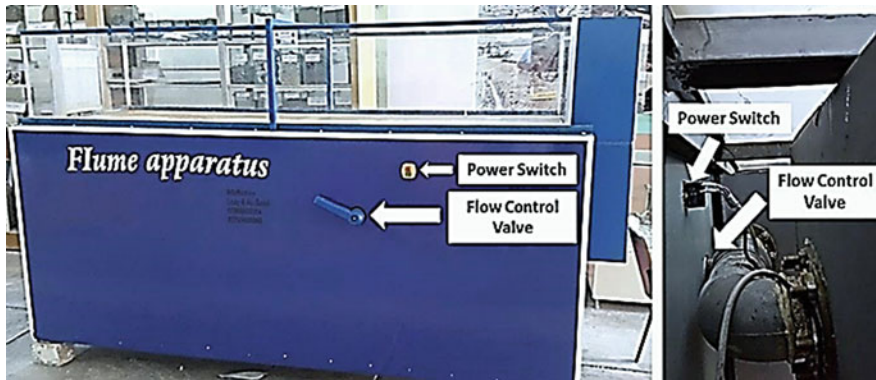


Fig. 7 The valve used to control the flow



Fig. 8 Flowmeter device; a control panel box, b small fan

## 5 Differential Linear Displacement Sensor (LVDT, Linear Variable Differential Transducer)

Linear displacement measuring tool of 10 mm, made by the English company ELE. The LVDTs were installed at two different locations on the bank's surface of the channel model to measure the soil settlement (i.e., Fig. 9).

Finally, the failure mechanism behavior was recorded by capturing short photos and videos with a high-speed camera.

**Data Logger.** It is a multifunctional device: Wi-Fi, Ethernet, USB. The device's working principle is to acquire data in large numbers while being able to control it with high accuracy. Its small size characterizes the device as its dimensions are (175, 75, 25 mm), and it can work at a temperature ranging from (-40 to + 85 °C). The device was used to capture data from the displacement sensor of the amount of settlement in the banks' soil (see Fig. 10).

**Capture and Save Data.** A sub-program was created that works as an interface to transfer data from the test sensor to the data processor during the examination, using the Labview program's basics from the National Instruments Company in the College of Engineering at Wasit University. To ensure that the sensors are not damaged, consideration has been given to the parameters that must be adopted in terms of the power supplier and the sensor voltage's maximum values (Fig. 11).

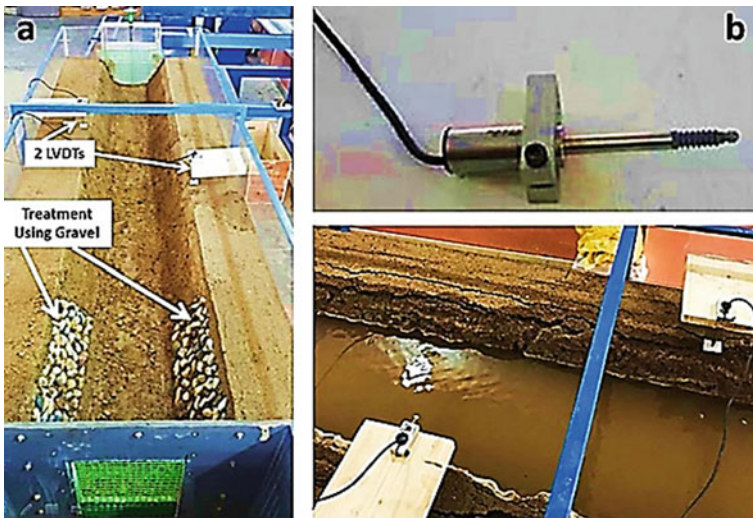


Fig. 9 Linear displacement sensor (LVDT)

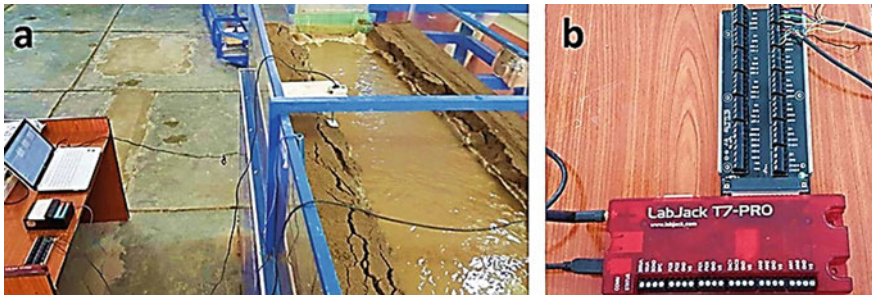


Fig. 10 The general form of connection system and data processor

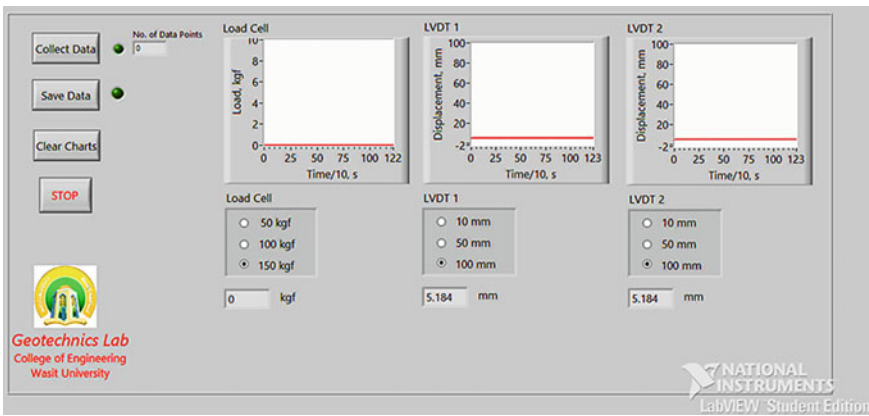


Fig. 11 LabView Interface of the program for capturing and saving data

## 6 Model Test Results

The experimental test results, soil erosion calculations were made by applying the theories and equations of previous researchers and failure angle calculations using experimental results of tension cracks. Full details of the tested models, flow condition, procedure, and the soil used in this paper can be found in detail in [9]. As for the failure mechanism results, it was determined the type of failure, and the reasons leading to its occurrence. The results of riverbank settlement were obtained directly using the displacement sensor (LVDT), which varied between the three models due to their being highly affected by the flow period and soil cohesion, where the highest value of soil settlement was recorded in the actual model (The actual model here means that the soil specimen is collected from the Tigris riverbanks in Al-Kut City (180 km south the Capital, Baghdad) with the long-term and short term flow period (see Figs. 12 and 13). In the long term flow period, the settlement was (19.5 mm), while the lowest value was in the actual model with the short-term flow period (9.4 mm), while in the non-actual model (mixing of 50% sandy soil and

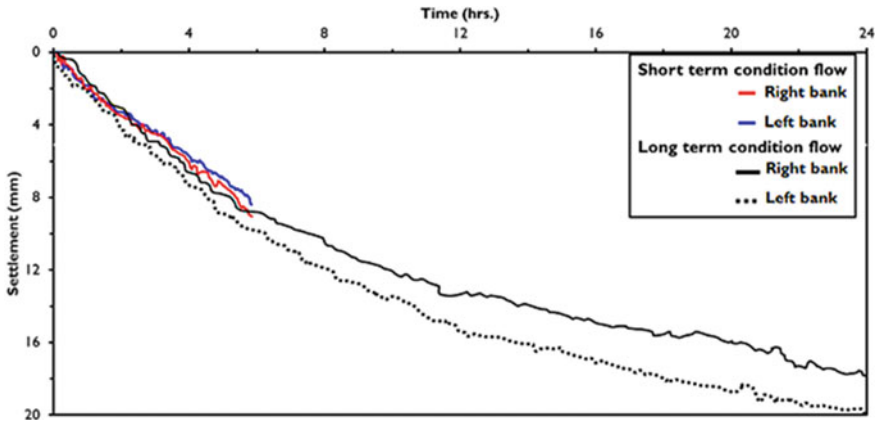


Fig. 12 Results of soil settlement for the actual models

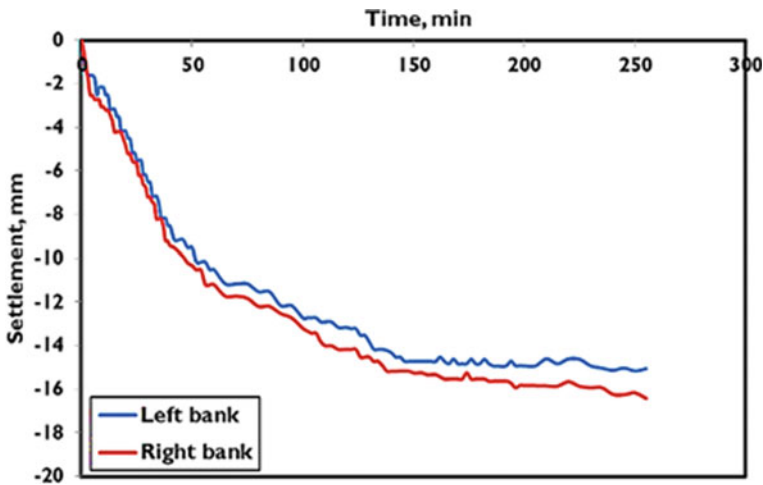


Fig. 13 Results of soil settlement for the non-actual model

50% collected from the site), the value of soil settlement was (16.4 mm) because the type of soil cohesion was tiny compared to natural soil since the non-actual model contains a proportion of sand. Results were compared with previous researchers, and the concordance was good. Depending on the experimental test results and using one of the statistical analysis programs, two empirical equations were derived: calculating the percentage of the settlement in the banks' soil and the other for calculating the angle of failure of the slope. Analytical Numerical and analytical solution was also performed using finite element and dimensional analysis [9, 11] which are not mentioned in this paper, and the compatibility was well-recognized, as the error rate ranged between (1.8–6.9%).

## 7 Conclusions

In addition to what was mentioned above of the parts that together formed the Flume apparatus, which can simulate many hydraulic and geotechnical phenomena that occur in natural rivers and open channels, this locally manufactured device is distinguished by the following (i) Several factors contribute to the destabilization of the riverbank, which includes hydraulic factors, geomorphic factors, and geometric factors; (ii) Manufacture of a physical model that simulates rivers (the Tigris River in particular) based on the principles of physical modeling in terms of hydraulic and engineering design; (iii) Using the distorted model's scale method for modeling rivers to determine the dimensions of the flume concerning the length and width of the Tigris River for the first time in Iraq and (iv) The possibility of controlling a wide range of speed limits, either very low or high speed, thanks to the delicate design of the calming tank with the use of a relatively large capacity pump.

- To understand the main reasons of the collapsibility of the riverbank's that led to severe failure, The small scale flume model is designed, and a simple river simulation is performed to determine the necessary treatment for the failed parts of the banks with the limits of the hydraulic requirements to prevent the failure occur in the future. Also, to obtain stable slopes, it is highly recommended to know any changes that happen in the bank's soil properties along the slope under different circumstances of factor changes that lead to severe failure.
- The calibration of the settlement of the riverbank's model results using the designed flume device showed good agreement with the actual comment settlement at the prototype scale. Most of the settlement occur at the short time channel operation (11.6 mm ar 5 h. Channel operation) whereas only 19.5 mm is noticed at long term operation (i.e., 24 h.)
- The experimental test results showed that the manufacturing of the small-scale flume replicated the required objective of this paper. The physical model can represent an actual phenomenon that occurs in natural rivers and the water flow in open channels to a large extent.
- The small-scale flume can be used for future studies in the field of hydraulic geotechnical and geoenvironmental engineering using many types of soil. It can be used in many applications such as the effect of changing water levels on slope stability, the effect of meandering rivers on soil erosion and sediment transport, testing different treatment methods for river banks according to different conditions to determine the best treatment type that provides the hydraulic requirements at the lowest cost, study the management of gate operation and its effect on river scour, study the effect of (Backwater) on open channels and study of wave formation in open channels.
- Riverbank collapsibility is strongly influenced by the erosion of the fine-grain bank's soil. Erosion rate is depending on the fluid shear stress in collaboration with the critical shear stress and the flow velocity.



## References

1. Duong Thi, T., & Do Minh, D. (2019). Riverbank stability assessment under river water level changes and hydraulic erosion. *Water*, *11*(12), 2598.
2. Oberhagemann, K., Haque, A. M., & Thompson, A. (2020). A century of riverbank protection and river training in Bangladesh. *Water*, *12*(11), 3018.
3. Mosselman, E. (2020). Studies on river training. *Water Journal*, *12*(11), 3100
4. Yu, L. (2002). The Huanghe (Yellow) River: A review of its development, characteristics, and future management issues. *Continental Shelf Research*, *22*(3), 389–403.
5. Kummu, M., & Varis, O. (2007). Sediment-related impacts due to upstream reservoir trapping, the lower Mekong River. *Geomorphology*, *85*(3–4), 275–293.
6. Neil, D. T., Orpin, A. R., Ridd, P. V., & Yu, B. (2002). Sediment yield and impacts from river catchments to the great Barrier Reef Lagoon: A review. *Marine and Freshwater Research*, *53*(4), 733–752.
7. Abedini, M., Said, M. A. M., & Ahmad, F. (2012). Effectiveness of check dam to control soil erosion in a tropical catchment (The Ulu Kinta Basin). *CATENA*, *97*, 63–70.
8. Nardi, L., Rinaldi, M., & Solari, L. (2012). An experimental investigation on mass failures occurring in a riverbank composed of sandy gravel. *Geomorphology*, *163*, 56–69.
9. Aldefae, A. H., & Alkhafaji, R. A. (2021). Experimental and numerical modeling to investigate the riverbank's stability. *SN Applied Sciences*, *3*(2), 1–16.
10. Tehrani, M. S., Jones, S., & Shabani, F. (2019). Identifying the essential flood conditioning factors for flood prone area mapping using machine learning techniques. *CATENA*, *175*, 174–192.
11. Aldefae, A.H., & Alkhafaji, R.A. (2021, February). Development of equations relates the factors affecting riverbank stability using dimensional analysis. In *IOP Conference Series: Materials Science and Engineering* (Vol. 1058, No. 1, pp. 012025). IOP Publishing.
12. Aldefae, A. H., Shamkhi, M. S., & Khalaf, T. (2019). Design and manufacturing of geotechnical laboratory tools used in physical modeling. *Cogent Engineering*, *6*(1), 1637622.
13. Samadi, A., Amiri-Tokaldany, E., Davoudi, M. H., & Darby, S. E. (2013). Experimental and numerical investigation of the stability of overhanging riverbanks. *Geomorphology*, *184*, 1–19.
14. Aldefae, A. H., Alkhafaji, R. A., Shamkhi, M. S., & Kumer, H. Q. (2019). Design and manufacturing of flume apparatus to investigate the failure mechanism of riverbanks. *Cogent Engineering*, *6*(1), 1655234.
15. Darby, S. E., Trieu, H. Q., Carling, P. A., Sarkkula, J., Koponen, J., Kummu, M., Conlan, I., & Leyland, J. (2010). A physically based model to predict hydraulic erosion of fine-grained riverbanks: The role of form roughness in limiting erosion. *Journal of Geophysical Research: Earth Surface*, *115*(F4).
16. Al-Aayedi, H. K., Aldefae, A. H., & Shamkhi, M. S. (2020, June). Seismic performance of bridge piers. In *IOP Conference Series: Materials Science and Engineering* (Vol. 870, No. 1, pp. 012069). IOP Publishing.
17. Aldefae, A. H., & Saleem, H. D. (2020, June). Design, manufacturing and testing of biaxial mechanical travelling pluviator. In *IOP Conference Series: Materials Science and Engineering* (Vol. 870, No. 1, pp. 012071). IOP Publishing.
18. Aldefee, A. N., & Aldefae, A. H. (2021, February). Seismic performance of gravity quay wall. In *IOP Conference Series: Materials Science and Engineering* (Vol. 1058, No. 1, pp. 012033). IOP Publishing.
19. Saleem, H. D., Aldefae, H. K., & 'd Humaish, W. H. (2021). Verification of strength resistance of sandy soil using small scale penetrometer tests. In *IOP Conference Series: Materials Science and Engineering* (In press). IOP Publishing.
20. Alayedi, H. K., Aldefae, A. H., Shamkhi, M. S., & Humaish, W. H. (2021, February). Dynamic response of different bridge piers. In *IOP Conference Series: Materials Science and Engineering* (Vol. 1058, No. 1, pp. 012045). IOP Publishing.

# Groundwater Analysis Based on the Hydrogeological Model of Taichung Basin, Taiwan



K. J. Shou and C. C. Pan

**Abstract** In this study, a hydrogeological model was established and applied for the analysis of flooding potential in Taichung Basin. The groundwater level data from 10 monitoring stations in the past 10 years were used to calibrate the hydrogeological model, before used to predict the groundwater conditions for the extreme scenarios of climate change. The results revealed that Taichung City was influenced by the groundwater recharge effects of Dajia River in the north, the border of Dadu Plateau in the west, Dali River in the south, and the no-flow boundary of Chelungpu Fault in the east. In general, the groundwater level in the Taichung basin was higher in the north and lower in the south. Most areas of the Taichung basin exhibit a seepage coefficient around 0.1 cm/s, however, the areas to the north, near the Dajia River, exhibit a lower seepage coefficient around 0.02 cm/s. The results suggest that the southern part of Taichung basin possess the potential of flooding induced outflow of groundwater. The flooding due to surface flow could be stagnated by the groundwater as well.

**Keywords** Groundwater · Hydrogeological model · Gravel formation · Flooding potential · MODFLOW

## 1 Introduction

Groundwater considerably contributes to water resources in Taiwan area. However, excessive groundwater withdrawal and impact of climate change have significantly affect the groundwater condition, and need to be analyzed in more details. This paper addresses the situation of the groundwater located in the gravel layer of Central Taiwan. The groundwater level of Central Taiwan is located between five to eight

---

K. J. Shou (✉) · C. C. Pan

Department of Civil Engineering, The National Chung Hsing University, 145, Xingda Road, Taichung 40227, Taiwan

e-mail: [kjshou@dragon.nchu.edu.tw](mailto:kjshou@dragon.nchu.edu.tw)

C. C. Pan

e-mail: [boy880246@yahoo.com.tw](mailto:boy880246@yahoo.com.tw)

meters beneath the ground level [1–3]. This gravel layer exhibits a high seepage coefficient and fast groundwater flow. However, numerous factors can be held accountable for changes in the groundwater level [4, 5].

To further evaluate the correlation between rainfall and groundwater levels, this study focused on 10 groundwater monitoring stations in Central Taiwan as research targets and conducted a numerical analysis of the groundwater level measurements and rainfall station data in this region. The researchers aimed to gain a deeper understanding of the groundwater distribution in the gravel layer of Central Taiwan, and further analysis on the flooding potential in the study area.

## 2 Numerical Analysis Software and Theory Introduction

This study used the Modular Three-Dimensional Finite-Difference Ground-Water Flow Model (MODFLOW), which was adopted by the United States Geological Survey in 1988 as a numerical simulation software program to simulate the three-dimensional flow of groundwater in porous media. This analytic numerical solution employs a finite difference method to compute groundwater flow data. MODFLOW generates grids similarly to those of finite element model software programs, in which numerical analysis are performed in grids created through meshing. MODFLOW divides the region selected for analysis into numerous meshes, which are similar to the elements used in a finite element model.

Groundwater flow data are computed using the following preexisting partial differential equation with fixed density values:

$$\frac{\partial}{\partial x} \left( K_{xx} \frac{\partial h}{\partial x} \right) + \frac{\partial}{\partial y} \left( K_{yy} \frac{\partial h}{\partial y} \right) + \frac{\partial}{\partial z} \left( K_{zz} \frac{\partial h}{\partial z} \right) + W = S_S \frac{\partial h}{\partial t} \quad (1)$$

where  $K_{xx}$ ,  $K_{yy}$ , and  $K_{zz}$  represent the seeping coefficient of coordinate axes  $x$ ,  $y$ , and  $z$ , respectively. Furthermore, the coordinate values of the three coordinate axes are assumed to be anisotropic.  $h$  represents the potentiometric head (L). Variable  $h$  is the function of  $x$ ,  $y$ ,  $z$ , and  $t$  and can be expressed as  $h(x, y, z, t)$ .  $W$  represents the volumetric flux of groundwater sources or sinks. The unit is ( $T^{-1}$ ).  $W < 0$  and  $W > 0$  indicate that groundwater is leaving and entering the system, respectively.  $S_S$  is the specific storativity of the porous medium. This value represents the amount of water that flows out of a unit volume of the aquifer when the water pressure head value is increased by one unit.

The initial conditions and boundary conditions are combined and introduced into Eq. (1), that describes the transient three-dimensional groundwater flow in non-homogenous and anisotropic media ( $x$ ,  $y$ , and  $z$  coordinate axes). Subsequently, the researchers conducted an onsite investigation to identify inactive cells, which are defined as regions that groundwater cannot flow in. The groundwater flow computed

in MODFLOW can only flow in active cells, thus comprehensively and accurately representing the actual conditions in the region [6–8].

Equation (1) displays the finite difference groundwater flow calculation and indicates that the influx and out-flux of each grid square must be equal to the storage variation of the grid square. By assuming that groundwater has a fixed density, the groundwater quantity balance equation is presented as the following continuity equation:

$$\sum Q_i = S_s \frac{\Delta h}{\Delta t} \Delta V \tag{2}$$

where  $\sum Q_i$  represents the total influx and outflux quantity of the unit grid square.  $S_s$  represents the hydrophobic parameter, namely the specific storativity coefficient.  $\Delta V$  represents the size of the grid square.  $\Delta h/\Delta t$  represents the water pressure head value variations during  $\Delta t$ .

Then, any element in the MODFLOW grid (i, j, k) can exchange water with its six other neighboring elements, namely (i - 1, j, k), (i + 1, j, k), (i, j - 1, k), (i, j + 1, k), (i, j, k - 1), and (i, j, k + 1). Each of the six neighboring elements accounts for six neighboring grid squares. By integrating the six grid squares into Darcy’s law equation, the groundwater flow from (i - 1, j, k) to (i, j, k) is as follows:

$$Q_{(i-\frac{1}{2},j,k)} = \left( KR_{(i-\frac{1}{2},j,k)} \right) (\Delta C_i) (\Delta V_k) \frac{h_{(i-1,j,k)} - h_{(i,j,k)}}{\Delta r_{(i-\frac{1}{2})}} \tag{3}$$

where  $h_{(i,j,k)}$  represents the water pressure head grid square unit (i, j, k).  $(\Delta C_i)(\Delta V_k)$  represents the size of the plane vertical to direction i.  $\Delta r_{(i-\frac{1}{2})}$  represents the distance between nodes (i, j, k) and (i - 1, j, k).  $KR_{(i-\frac{1}{2},j,k)}$  represents the seepage coefficient between grid squares. Equation (3) is the groundwater flow equation for a single direction and is applicable for all six directions (Fig. 1).

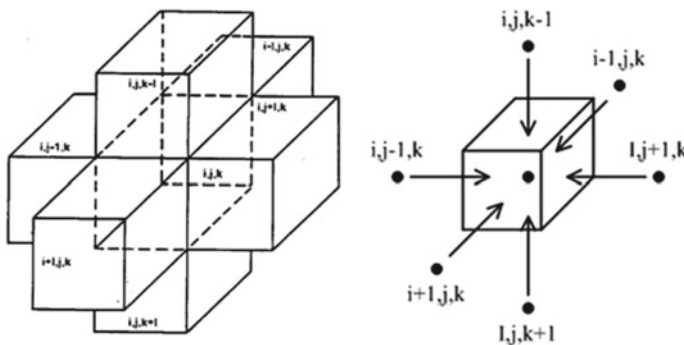


Fig. 1 Six directions of the simulation grid

### 3 Research Site and Data Collection

This study adopted Taichung City as the modeling site to provide reference data for quick and accurate analysis of the groundwater flow under the city in case of excavation required for urban construction purposes and to facilitate the dewatering process during excavation [7, 9]. Subsequently, this study aimed to unveil an optimal solution for estimating rainfall to facilitate smooth construction processes. The model area encompassed multi-layered self-recording monitoring wells in several stations, namely Tai'an, Tanzih, Sihjhangli, Dongshan, Jhongshan, Fongjhou, Jianping, Wurih, Dali, and Cicong, which are illustrated in Fig. 2. Additionally, groundwater station data from 2008 to 2018 were selected as the actual observation data for analysis and simulation within the research area because the dataset exhibited high completeness.

### 4 Historical Rainfall Distribution

To identify the rainfall distribution in the Taichung basin, this study collected rainfall data from Central Weather Bureau stations, including Dakeng, Chong-chu-lin, Dadu, Dali, Tan-zi, Wurih, Xi-tun, Nan-tun, Daya (Central Taiwan Science Park), Fengyuan, Taichung, Ton-lin, and Shengang. This study used rainfall data from the past 10 years for follow-up analysis and to serve as the source for actual observation data input under the model parameter settings. Subsequently, the Kriging method was adopted to analyze the rainfall distribution in the research area. Figures 3, 4, 5 and 6 display the comprehensive mean monthly rainfall and mean monthly rainfall data for the past 10 years collected by the monitoring stations.

Observing the mean monthly rainfall of the most representative monitoring station in the the Taichung basin, that is, Taichung station, revealed that the mean annual rainfall in Taichung City was 1,708.9 mm. The city's wet season was between April and September, thus exhibiting increased rainfall from May to August and the most important rainfall in August. During the wet season, the mean monthly rainfall exceeded 102.5 mm. By contrast, the city's dry season was between October and March of the following year, with the lowest amount of rainfall occurring in October. During the dry season, the mean monthly rainfall was below 51.6 mm.

### 5 Historical Groundwater Levels and Analysis

The oldest groundwater level data recorded by monitoring stations in the Taichung basin date back to 1975 and were recorded by the Cie-Lao Elementary School monitoring station. At the time, the Cie-Lao Elementary School monitoring station did not have modern monitoring systems such as an observation function for different

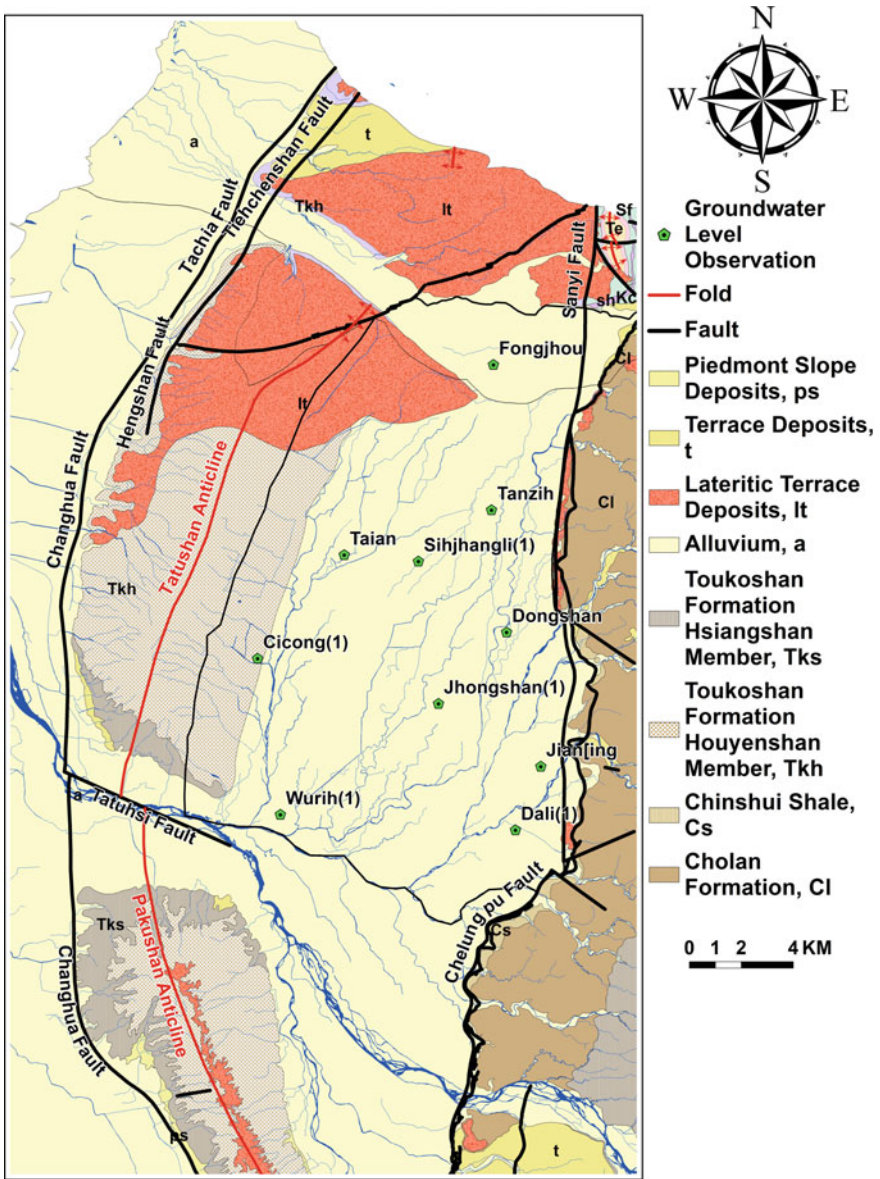


Fig. 2 Location of the monitoring wells in Taichung and the research site of this study

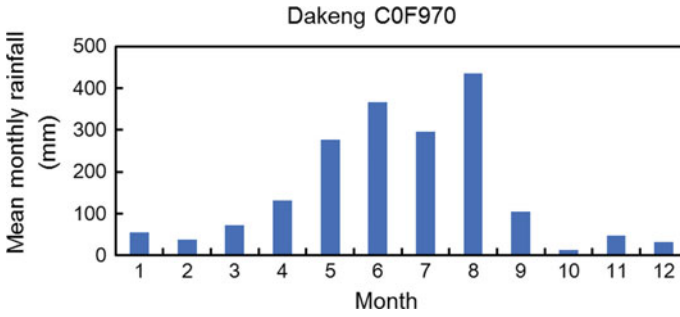


Fig. 3 Comprehensive mean monthly rainfall of the Dakeng station

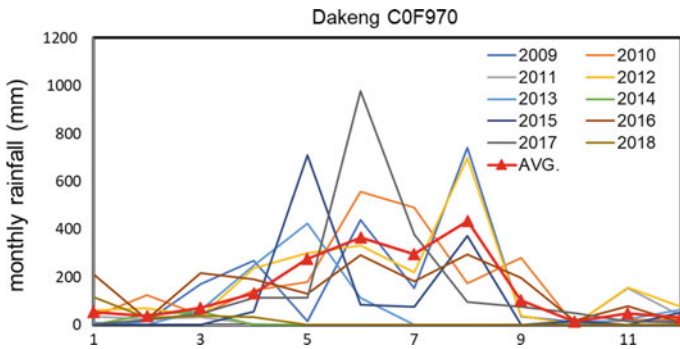


Fig. 4 Mean monthly rainfall of the Dakeng station in the past 10 years

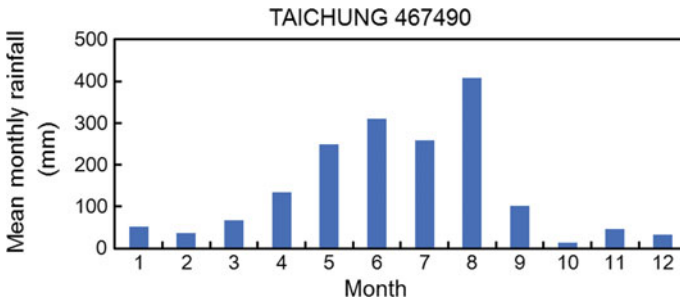
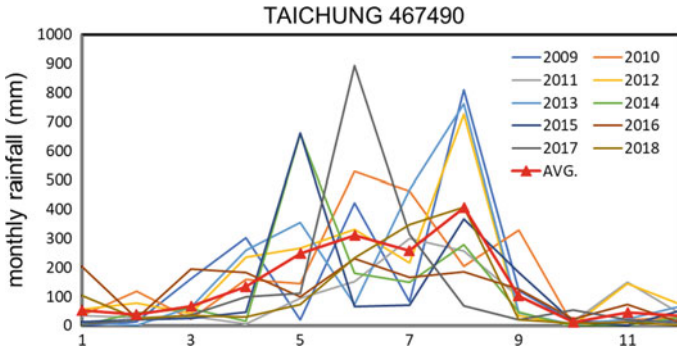


Fig. 5 Comprehensive mean monthly rainfall of the Taichung station

aquifers. Since 1991, the Ministry of Economic Affairs of the Executive Yuan has promoted a groundwater monitoring network program in Taiwan. Currently, the distribution planning and the construction of monitoring stations are ongoing. The Taichung basin possesses 21 groundwater monitoring stations. The research scope of this study encompassed the multi-layered aquifer self-recording monitoring wells established by the Water Resources Agency of the Executive Yuan, including Tai'an,



**Fig. 6** Mean monthly rainfall of the Taichung station in the past 10 years

Tanzih, Sihjhangli, Dongshan, Jhongshan, Fongjhou, Jianping, Wurih, Dali, and Cicong. Figure 7 displays the location of each station. Groundwater station data from 2008 to 2018 were used as the actual observation data for analysis and simulation within the research area given that the dataset exhibited high completeness.

The aforementioned water level elevation from the groundwater monitoring stations indicates that Taichung's groundwater level is influenced by the terrain, which descends from north to south. A comparison with the aforementioned rainfall distribution graphs reveals that Taichung City exhibits the highest water level in August (Figs. 9 and 11). In addition, different groundwater applications and distances from the recharge source may have varying influences on the spatial and temporal distribution of groundwater levels. Figure 10 indicates that the water level of Fongjhou station is greatly influenced by the recharging effect of Dajia River, which is situated north of the station. This resulted in the Fongjhou station exhibiting substantial changes in its water levels. Figure 8 depicts that the Wurih station exhibits a 1-m water level change annually, which is significantly less than that of the Fongjhou station. This is because Wurih station is situated downstream of Wurih River and near water catchment areas. Because the nearby region terrain exhibits minimal hydraulic slopes, the Wurih station thus exhibits minor water level variations. However, the figures reveal that some water level elevation trends do not comply with that of the Wurih station. This difference might be attributable to agricultural groundwater withdrawal (Figs. 12 and 13).

The actual water elevation data were used as the model boundaries to portray the landscape elevation on the model surface (Fig. 14). The northern, western, eastern, and southern boundaries were established as Dajia River, the border of the Dadu Plateau, Chelungpu Fault, and Dali River situated north of Wurih River, respectively. The numerical model boundaries included no-flow boundaries and fixed flow boundaries. Table 1 lists the locations of these boundaries and explains the reasons behind these configurations. In accordance with the rainfall data from different rainfall stations, this study used the Thiessen polygons to analyze the mean monthly rainfall quantity in the research site (Fig. 15). This study determined the monitoring range of each rainfall station to examine the groundwater level effect of rainfall.





**Fig. 7** Location of the groundwater monitoring wells established by the Water Resource Bureau in the research area

The researchers took as reference the default settings of groundwater observation wells from the network established by the Water Resources Bureau to determine the seepage coefficient. The parameter range was between  $1 \times 10^{-3}$  and  $1 \times 10^{-5}$  and was adequately adjusted when the model was calibrated. To compute the vertical recharge quantity of the groundwater level, this study only considered rainfall recharge and excluded the recharge from agricultural applications. Figure 15 displays the rainfall recharge in the moderating region of each rainfall station, which was inputted as default value in the model for computing. A complete analysis was performed by

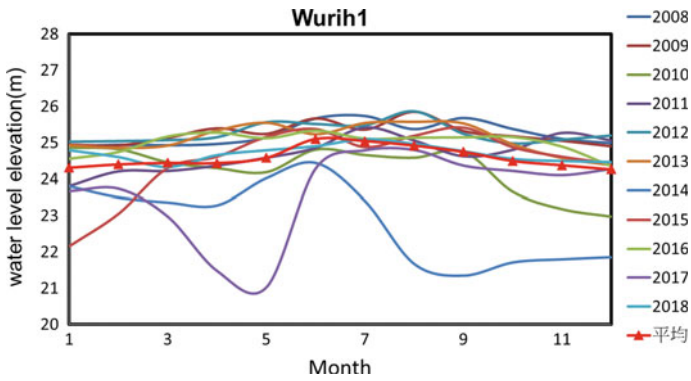


Fig. 8 Mean water level evaluation of the Wurih station for the past 10 years

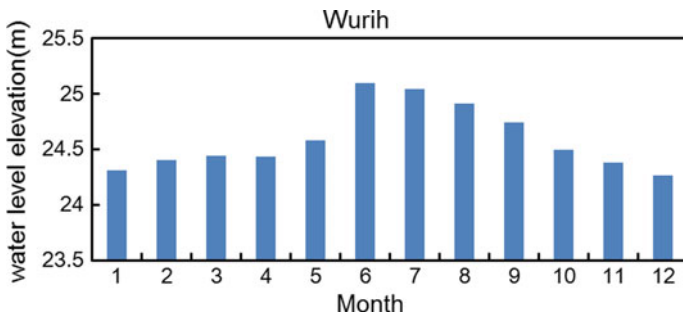


Fig. 9 Comprehensive mean monthly water level elevation of the Wurih station

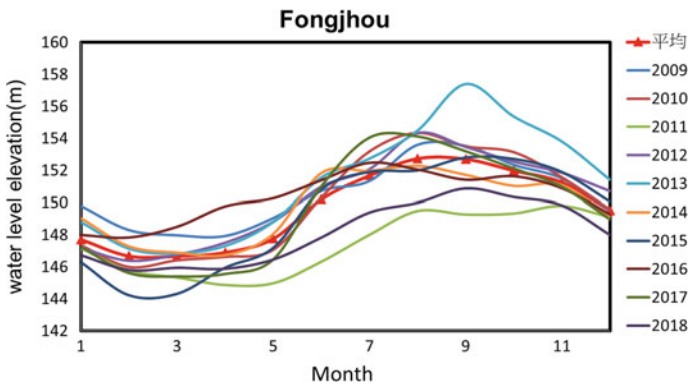


Fig. 10 Mean water level elevation of the Fongjhou station for the past 10 years

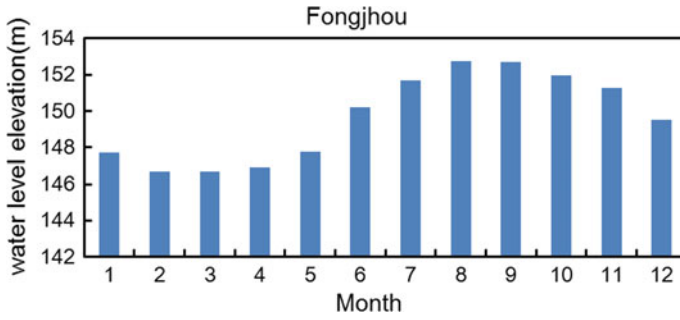


Fig. 11 Comprehensive mean monthly water level elevation of the Fongjhou station

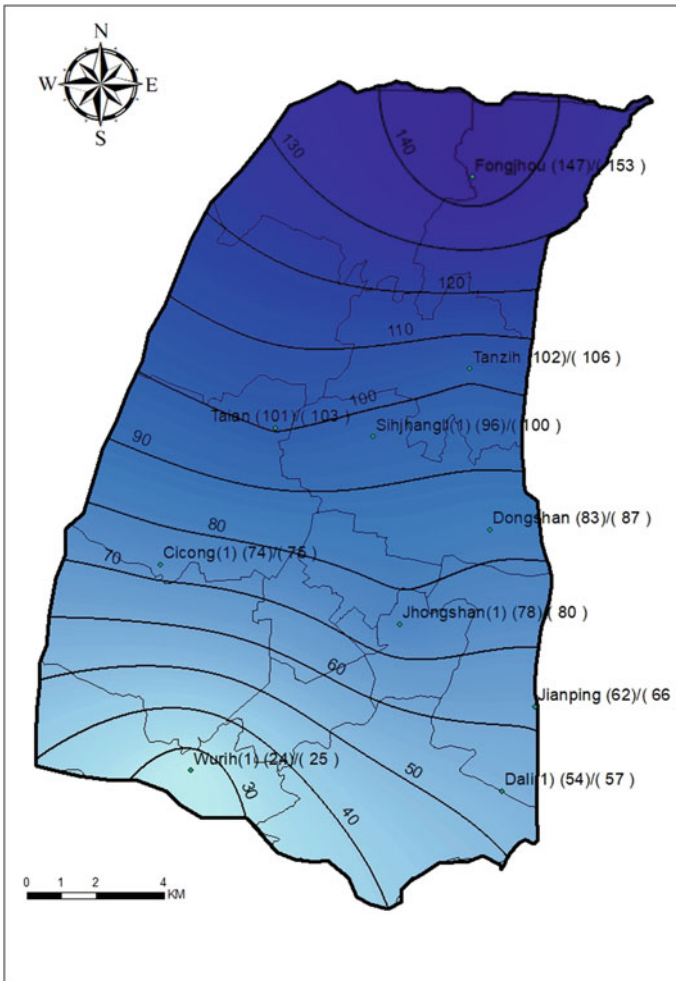
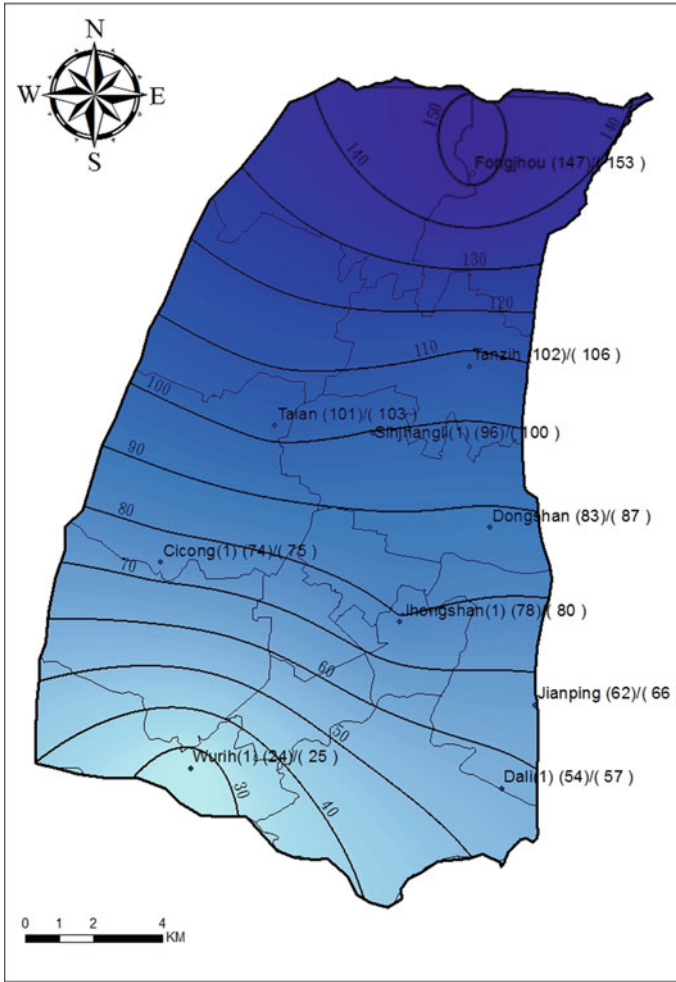


Fig. 12 Mean groundwater level distribution in March obtained using the Kriging method



**Fig. 13** Mean groundwater level distribution in August obtained using the Kriging method

inputting the mean monthly rainfall quantity between March and August into the model according to the Thiessen polygon method.

As displayed in Fig. 16, the monitored water level elevations generally complied with the model-simulated groundwater level. However, some regions differed between the monitored water level elevations and the model-simulated groundwater levels. This difference might be due to the effect of the hydrogeological parameters used in the model and those of the actual regions. To achieve a more accurate seepage coefficient, this study conducted top-down adjustments and recalibration. The adjusted seepage coefficients are displayed in Table 2.

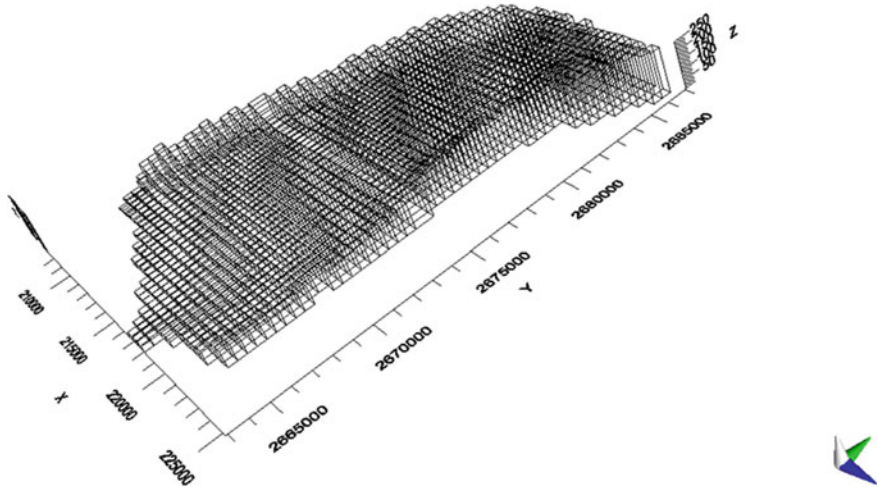


**Fig. 14** Thiessen polygons of the research site and TWD97 coordinates

**Table 1** Planning of the numerical model boundaries

Locations of boundary	Types of boundary	Description
Chelungpu fault	No-flow boundary	Fault structure
The border of Dadu Plateau	Fixed flow boundary	Groundwater outflow
Dajia River in the north and Dali River in the south	Fixed flow boundary	River recharge groundwater

Figure 17 displays the rainfall records from the various Taichung rainfall stations in the past 10 years. This study selected the highest rainfall records from the March to August; April, June, August; and April and July periods. The maximum rainfall distribution data were applied to the model using the Thiessen polygon method, this study adopted a landscape elevation distribution to simulate flooding scenarios.

## 6 Conclusions

This study referred to preexisting groundwater hydrogeological data of the Taichung basin, groundwater level data from self-recording groundwater monitoring wells constructed by the Water Resources Bureau of the Ministry of Economic Affairs, and rainfall data from weather stations in the Taichung basin to simulate groundwater levels in Taichung City. Subsequently, the researchers superpositioned the collected terrain elevation figures to predict areas in Taichung City that could easily flood in the event of heavy rainfall, thus proposing a seepage coefficient distribution for Taichung City.

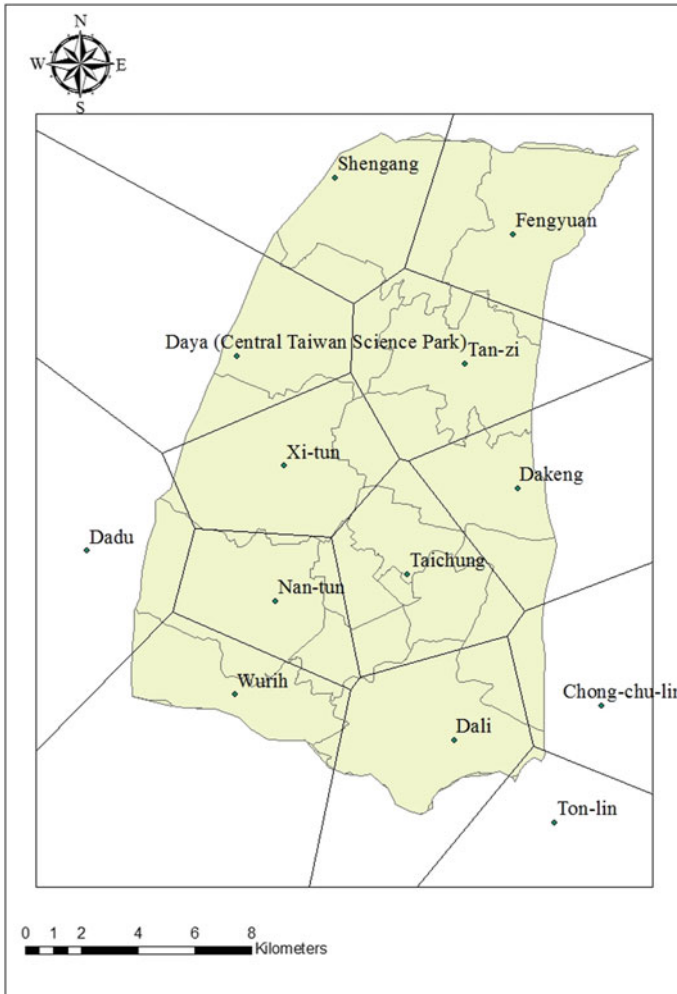


**Fig. 15** Thiessen polygons of the monitoring areas of each rainfall station in the Taichung basin

According to the March mean groundwater level in the Taichung basin, this study adopted the Kriging method to compute a groundwater level distribution of Taichung City in the same month. Similarly, the researchers computed the groundwater level distribution of Taichung City in August. By inputting the mean monthly rainfall into VISUAL MODFLOW FLEX 5.1 according to the Thiessen polygon method and adopting the boundary conditions of Dajia River, Dali River, Chelungpu Fault, and Dadu Plateau, this study simulated the seepage coefficient distribution of the Taichung basin. This study also revealed that the seepage coefficient for most regions around Taichung is 0.001 m/s. However, southern regions of the Taichung basin exhibited a lower seepage coefficient between 0.0004 and 0.0008 m/s. Overall, the

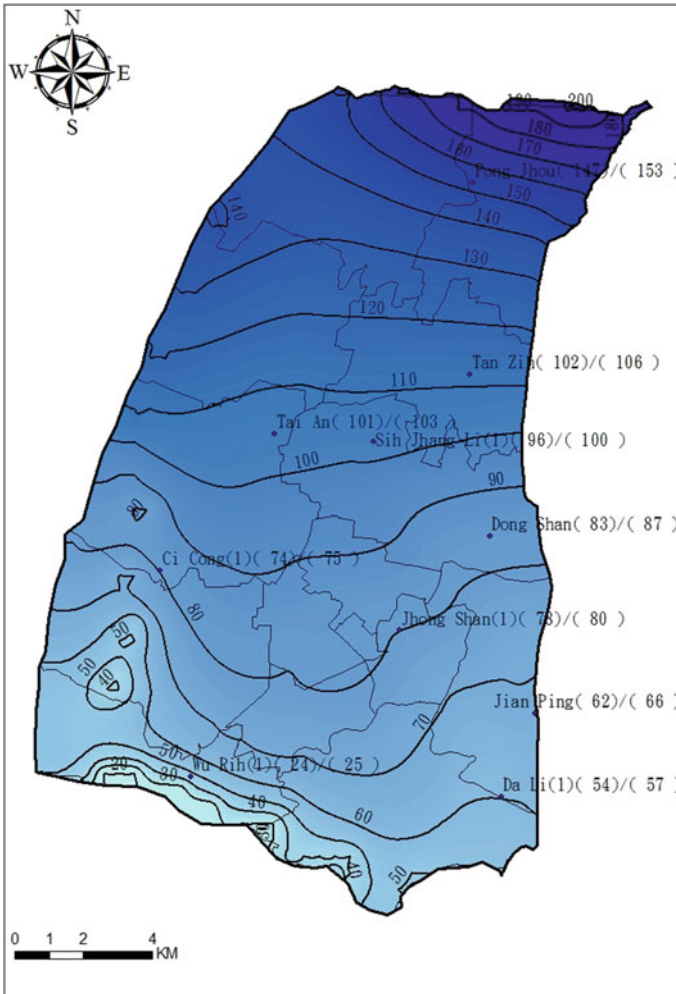


Fig. 16 Post-precipitation water level distribution (MODFLOW)

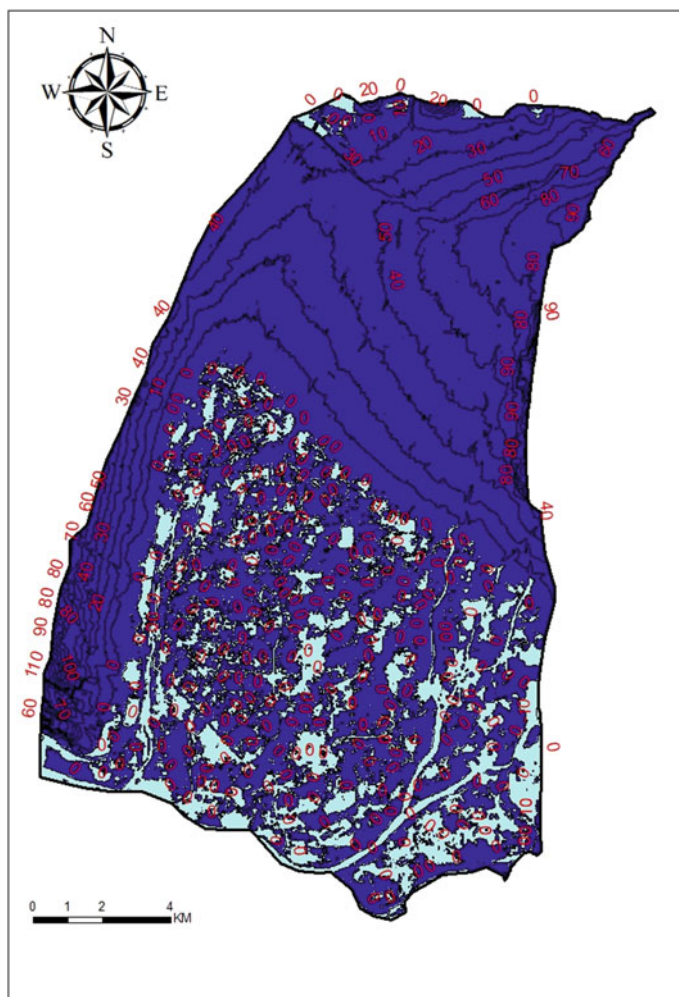
Table 2 Seepage coefficient of each monitoring station

Monitoring station	K (m/s)
Fongjhou	0.00022
Tanzih	0.001
Tai'an	0.001
Sihjhangli	0.001
Cicong	0.001
Jhongshan	0.0008

(continued)

**Table 2** (continued)

Monitoring station	K (m/s)
Dongshan	0.001
Jianping	0.004
Dali	0.004
Wurih	0.005

**Fig. 17** Flood diagram of the Taichung basin from April to August due to continuous heavy rainfall



Taichung basin demonstrated high seepage coefficient values, which are attributable to a thick gravel layer within 100 m below surface in the basin.

This study collected Taichung rainfall records of the past 10 years and selected the maximal rainfall record periods, namely from March to August; April, June, August; and April and July. After inputting the maximum rainfall distribution into the model using the Thiessen polygon method, this study simulated flood scenarios according to the terrain elevation distribution (Figs. 17, 18 and 19).

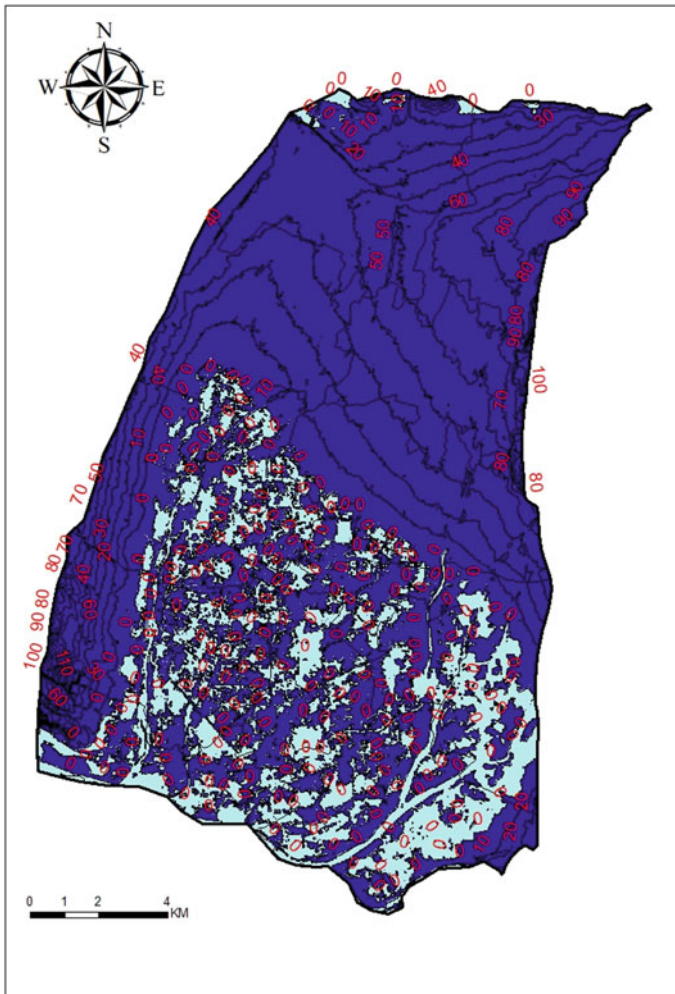


**Fig. 18** Flood diagram of the Taichung basin in April, June, and August due to continuous heavy rainfall

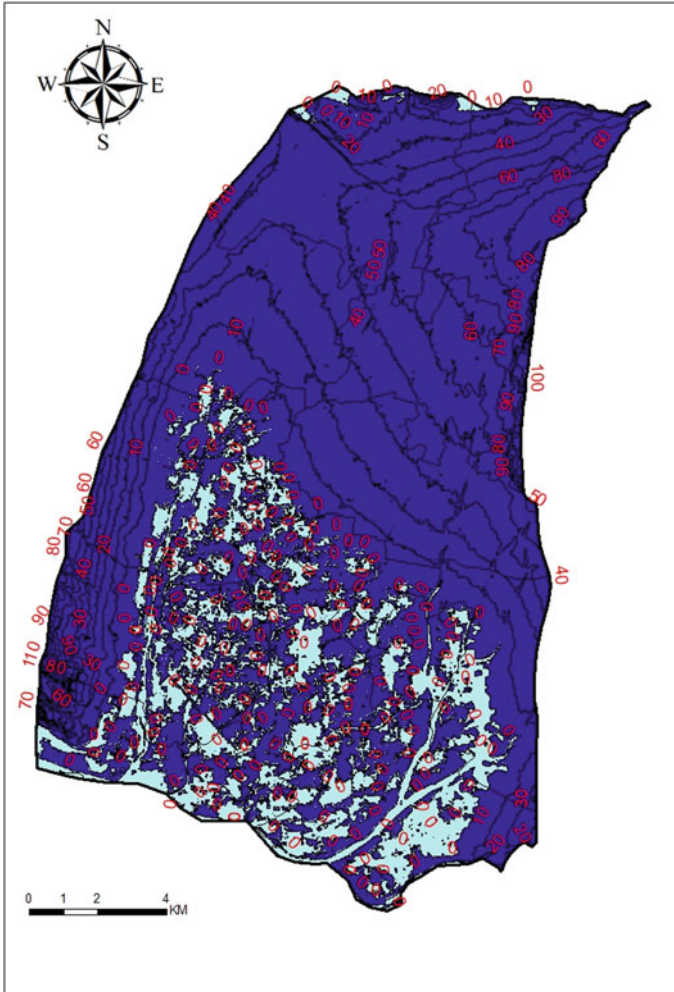


**Fig. 19** Lood diagram of the Taichung basin in April and July due to continuous heavy rainfall

## References

1. San, H.-H. (2009). *Estimation of the Hydraulic Conductivity by Using Field Test*, master's thesis. Chung Yuan Christian University.
2. Culture Affairs Bureau of Taichung City Government. (2003). The avulsion of Dajia River and the evolution of Taichung Basin. *Taichung Literature*, 6
3. Moea, R. O. C. (2007). *Water resources planning institute. A study on the possibility of Tai-Chung basin as an underground-water reservoir.*
4. Chiang, K.-S. (2017). *Using Electrical Resistivity Imaging method to Investigate Main Hydrogeology in Taichung Basin*, master's thesis. National Central University.

5. Cheng, W.-C., & Ni, J. C. (2008). Data Analysis of a Constant-Rate Pumping Test using a Partially Penetrating Well in a Confined Aquifer. *Journal of National Taipei University of Technology*, 41-1, 107-126.
6. Chen, H.-C. (2013). *Establishment of groundwater conceptual and simulation model in taichung basin*. Master's thesis, National Taiwan University, Taiwan.
7. Salih, S. H., Hassan, M. M., & Shiau, J. Z. H. (2018). Numerical simulation of staged braced excavation in sand—O6 MRT station. *International Journal of Geomate*, 14-43, 104-111.
8. Thiem, G. (1906). *Hydrologische Methoden*. Gebhardt.
9. Khoiri, M. (2014). Chang-Yu Ou, and Fu-ChenTeng, A comprehensive evaluation of strength and modulus parameters of a gravelly cobble deposit for deep excavation analysis. *Engineering Geology*, 174, 61-72.

# Design and Manufacturing of Rainfall Simulator Machine for the Soil Erosion Investigation



Shereen A. Alzamly, Asad H. Aldefae, Wissam H. Humaish,  
Evgeny K. Sinichenko, and Salah L. Zubaidi

**Abstract** The paper focuses on designing, manufacturing, operating, and calibration of rainfall simulator machines at the College of Engineering, Wasit University, to investigate the effect of rainfall intensity on channel sediments due to inter-rills formation rills, gullies, and streams because of soil erosion. Due to the difficulty of concluding the soil erosion and generating sediments in situ, the principles of physical modeling were used to design this machine with variable intensity and achieve high intensity. Steel and PVC materials from the local market formed the main parts of the machine. When the raindrops impact soil, soil particles begin to erode and transport by the runoff. The spray of raindrops causes regular removal of soil particles called sheet erosion or inter-rills erosion, the increasing and concentrating the overland flow led to the form of tiny channels called (Rills), then steep channels called (Gullies). The calibration of the machine and verification of the testing showed that the machine is applicable to use in the laboratory work to simulate the rainfall correctly and can be used to inspect other hydraulic engineering problems.

**Keywords** Rainfall · Erosion · Inter-rills · Nozzles · Raindrop

---

S. A. Alzamly · A. H. Aldefae (✉) · S. L. Zubaidi  
Civil Engineering Department, College of Engineering, Wasit University, Wasit, Iraq  
e-mail: [asadaldefae@uowasit.edu.iq](mailto:asadaldefae@uowasit.edu.iq)

S. A. Alzamly  
e-mail: [sadnan@uowasit.edu.iq](mailto:sadnan@uowasit.edu.iq)

S. L. Zubaidi  
e-mail: [salahlafta@uowasit.edu.iq](mailto:salahlafta@uowasit.edu.iq)

W. H. Humaish · E. K. Sinichenko  
Engineering Academy, Peoples' Friendship, University of Russia (RUDN University), Moscow,  
Russia  
e-mail: [1042205230@pfur.ru](mailto:1042205230@pfur.ru)

E. K. Sinichenko  
e-mail: [csinichenko-ek@rudn.ru](mailto:csinichenko-ek@rudn.ru)

## 1 Introduction

Soil erosion is one of the most significant problems of land degradation worldwide [1]. It is a separation and movement of soil particles [2]. Soil erosion forms have included four main forms: sheet, gully, rill, and stream [1]. The intensity of rainfall and slope gradient are more essential factors influencing soil erosion [3]. There are two main factors of rainfall characteristics that control the hydrologic reaction, duration, and intensity of rainfall. Higher runoff peak is generated by longer duration and/or higher intensity rainfall [4]. When the rainfall has high intensity, soil erosion can evolve quickly from sheet to rill, even gully erosion [5]. In an eroding rill, the flow concentrates and produces hydrodynamic characteristics with rising washing out power, which drives to a fluent increase in soil erosion [6]. The effectiveness of raindrops water influences as an energy source causing separation of the soil particles at the soil surface causing degradation in the soil shear strength with time [7]. The surface runoff produced by heavy rainfall leads to sediment formation and has been affected by the previous formation of subsurface water or catchments area and water pressure for soil [8–10]. Therefore, a reduced detachability by raindrops effect and shear forces of runoff can occur because of increasing cohesiveness, which is caused by a lower soil content of water and a raised negative pore water pressure. Moreover, enhancement of soil detachment by raindrop effect and dependent transport by surface flow may happen because of an increasing period of aggregate saturation and collapse due to air fleeing upon quick wetting, which is caused by lower water content because of previous events of rainstorm [2]. The concentrated runoff caused higher soil erodibility and transportability than that caused by raindrops [1].

Sediment yield is the final result of wearing away the soil by water, ice, wind, and gravity [11]. The transportation process of sediment is started on the surface of land when raindrops impact in sheet, gullies, rills, and streams then do it as a channel for sediment movement [11]. These eroded sediment particles are moved and transported to the river system, then some of them deposited as alluvial fans along river channels and across the flood plain, and the other part is eventually deposited in the reservoir, lake, and sea [12]. Many of researchers worldwide designed and fabricated a machine for simulating natural rainfall with erosion flume to find rainfall effect on soil erosion, soil infiltration, surface runoff and drifting of a large amount of sediment due to removing of layers of soil surface. In Valencia University, a rainfall simulator to perform experimental tests in remote and rugged areas is manufactured [13]. This rainfall simulator allows running experiments on a steep slope because of its portability. The rainfall simulator can apply  $0.24 \text{ m}^2$  of water-like rainfall on the plotted area; the rainfall intensity was (55 mm/hr), see Fig. 1a.

In Tucson/University of Arizona, a removable, controlled computer simulator, called the Walnut Gulch Rainfall Simulator (WGRS) was designed and produced [14]. Rainfall intensity was variable and used for the research of rainfall-runoff erosion. This rainfall simulator has a single focal swing boom and supplies water above a  $2 \times 6.1 \text{ m}$  plot area, and the rainfall simulator applies rates of rainfall ranged from 13–178 mm/hr, with an increment of 13 mm/hr see Fig. 1b. A simple rainfall

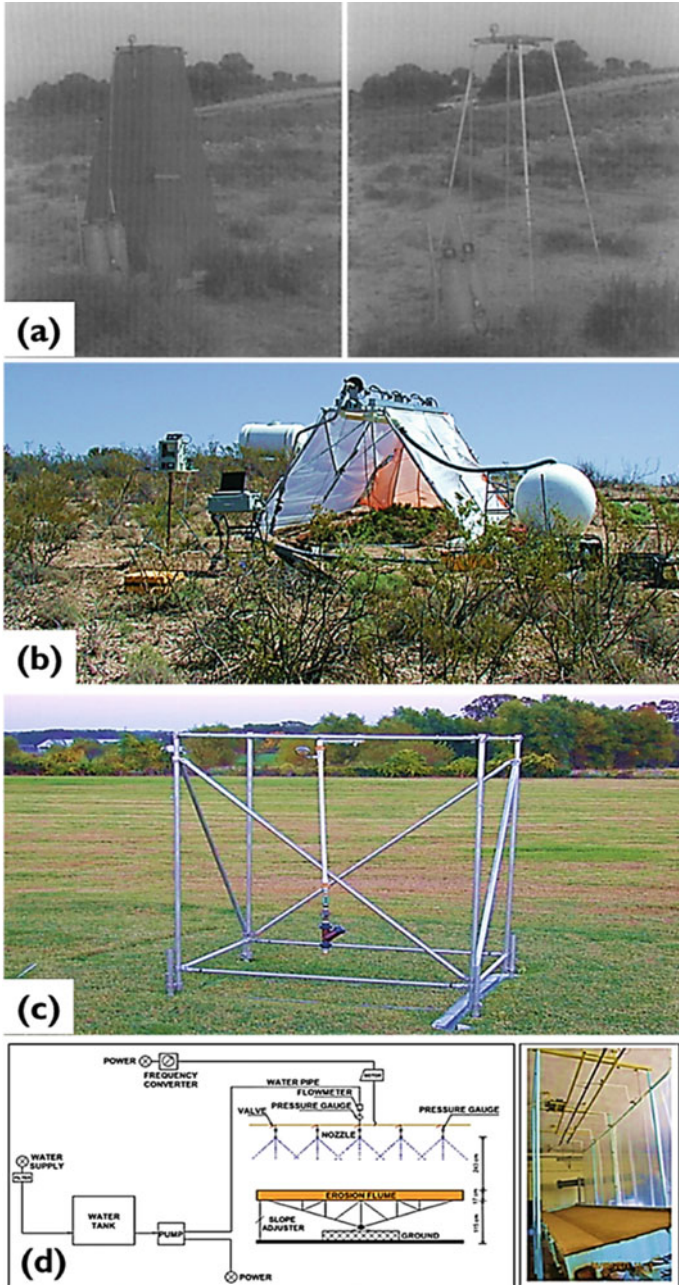


**Fig. 1** a View of the rainfall simulator at a Valincia University. b Tucson/University of Arizona. c Arkansas University. d Istanbul Technical University

simulator in Arkansas University is designed, and this tool was comparatively easy in operation and transportation from and to the field with conservation on critical intensity, characteristics of energy, and distribution of natural rainfall [15]. The frame of this rainfall simulator is made from lightweight aluminum pipes with a single spraying system's full jet (HH50W5Q) nozzle. This nozzle is centered at the upper side of the rainfall simulator frame 3 m high. The operation pressure is 28 kPa or nozzle gives an intensity of 70 mm/hr with an area of  $1.5 \times 2$  m. This rainfall simulator can be easily assembled or disassembled in 10 min approximately (See Fig. 1c).

At Istanbul Technical University, a rainfall simulator for laboratory experiments was developed and manufactured to simulate natural rainfall conditions with reasonable accuracy [16]. Rainfall intensity from 45 to 105 mm/hr, coefficient of uniformity ranged between 82 to 89%, the height of raindrops is 2.43, the slope of erosion flume that accompanies this rainfall simulator is up to 20% in the longitudinal and lateral direction (i.e., Fig. 1d). In South Korea (Kikam Institute for Geosciences) 2013, a device has been invented for simulating the rainfall (the patent number is (KR101113267B1) based on the vibration principle of a platform containing several nozzles which automatically get down the drops because of the platform vibration. This invention's problem is the intensity of the drops falling, which depends on the starting velocity, was not taken into consideration as well. The hydraulic control in the density of raindrops is not available, and the rainfall intensity cannot be changed [17]; see Fig. 2.

In China, Sichuan university [16], the numbered patent (CN204008636U) in 2014, a rainfall simulator invented to study the rainfall effect on the cultivated soils. The rainfall simulator was very simple, but there was a problem in the movement of the pierced platform to different height for the free-falling of the raindrops in addition to the same size of the holes in the platform to fall the raindrops which make the change of the rainfall intensity challenging to control on it by the pump. This is entirely inverse to the invented rainfall simulator machine, in which the opening of

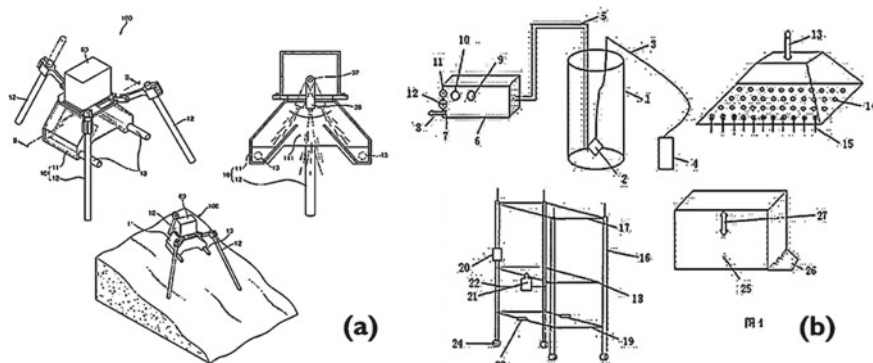


**Fig. 2** Rainfall simulator machine in **a** South Korea/ Geologic Institute (the patent number KR101113267B1) and **b** China (the patent number CN204008636U)

the nozzles can be controlled as well the flow rate controlled by the pump through the back pipe as shown in Fig. 2b. Due to the difficult circumstances which Iraq is going through, the ministry of higher education guided the universities to manufacturing the machine by their researchers instead of import it to enhance the postgraduate students' options in making the experience of scientific research [18–20]. So, the physical modeling fundamental is used to design the rainfall simulator machine to simulate the natural rainfall at the engineering laboratories at Wasit University. In this modified rainfall simulator machine, different rainfall intensity can be performed as well as the water in the tank that was fixed for being a main source of the water make recycled and goes via a small gate to the tank again after the raining simulation whereas electrical fan to simulate the rainstorm as similar to the natural rainstorm and to give a slope to the raindrops.

## 2 Design of Rainfall Simulator Machine

The rainfall simulator machine is manufactured in the laboratories of Engineering College/Wasit University. This machine consists of many main and secondary parts; they work together to design the machine with maintaining the principle of the physical modeling to study the rainfall effect on the soil.

**Main Frame.** The rainfall simulator machine's main structure contains a steel frame, storage tank, pump, fan, nozzles, two control valves to set rainfall intensity, and erosion flume with dimensions of 200 cm long, 96 cm width, and 37 cm depth. The storage tank has a volume of 1 cubic meter and contained two transverse barriers to prevent the sediment particles from arriving to the other side of the tank and causing malfunction to the pump because the water has been recycled. The water is withdrawn from the tank by the pump to the conveyance pipes and then transported to the nozzles to simulate the rainfall. The amount of water that goes to the nozzles was controlled by the main pipe's main valve. Figure 3 shows the details of the designed frame of the rainfall simulator machine.

**The Erosion Technique.** Many researchers have designed a rainfall simulator with erosion flume to study soil erosion by the rainfall effect. Figure 4 shows the designed machine. In the calibration process (discussed later), the erosion flume was sufficient to accommodate the channel's model and shoulder. The dimensions were 200 cm in length to contain the designed channel, 96 cm in width, whereas the top width of the channel is 36 cm and the width of the adjacent area is 60 cm, and 37 cm in depth to contain the depth of clay fill with 36.5 cm depth.

**Control Panel and Valves.** Control valves are tools used to set the flow rate that arrived to the nozzles. One of these valves used to set the rainfall intensity, and the other used to reduce the quantity of water that reached the first valve by converting it to the storage tank. The control panel contains a group of buttons that control on/off switch of the electric circuit of the machine. The button of emergency is added to the machine to switch off it if any problem happens. There are two accurate speed regulators to control the raindrops' velocity during raining (i.e., it can be controlled



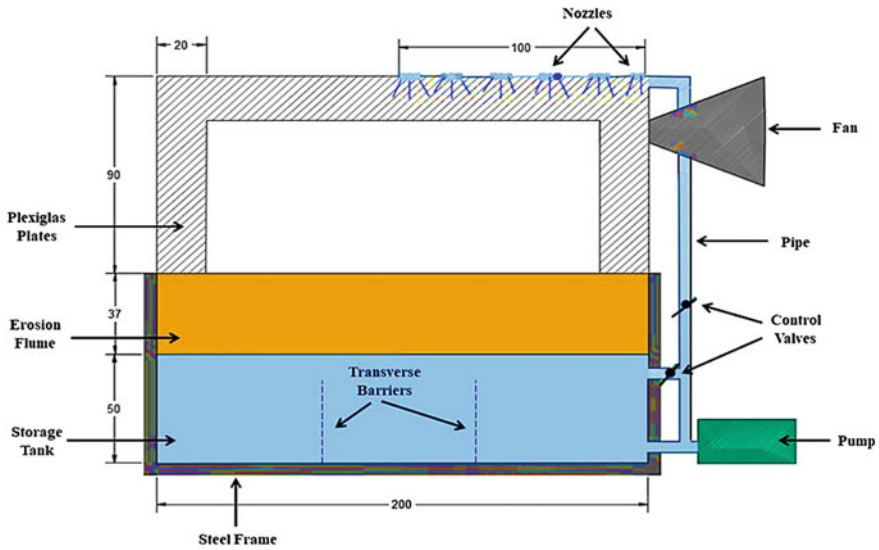
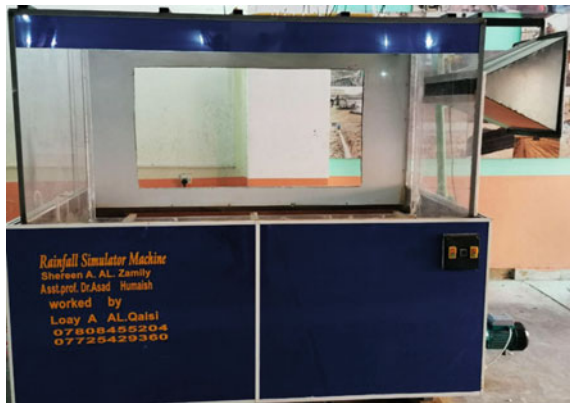


Fig. 3 Details of the designed rainfall simulator machine

Fig. 4 The designed rainfall simulator machine



manually) until it reaches the desired intensity during the test. This is done by prior calibration to get the current frequency which corresponds to the necessary speed (the linear velocity, which controls the rise of pump velocity to control rainstorm intensity). Timer added to the control panel to set the time needed to complete the process (rainfall intensity), and there is a light to clarify the machine’s operated case; if any problem appeared, the red light would switch on and off quickly (see Fig. 5).

**The Actuator Pump.** The pump was chosen in a certain capacity to achieve the required high rainfall intensity. Table 1 lists the pump specification, whereas Fig. 6 shows the photo for the pump.

**Fig. 5** The control valves**Table 1** Motor (pump) specification

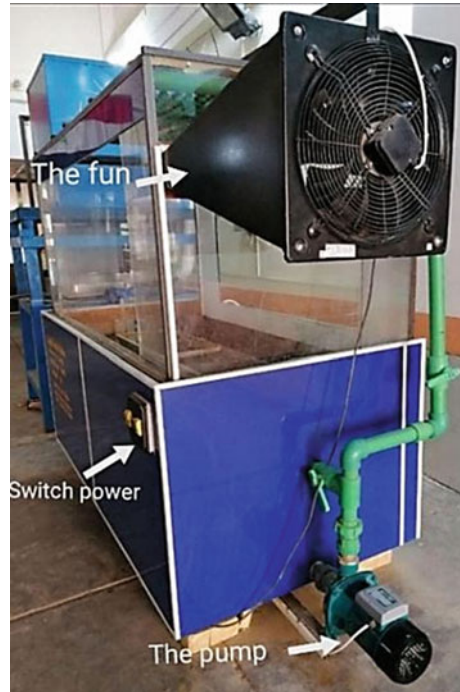
Specification	Grade	Specification	Grade
Type	TWP215002	HP	2.0
$Q_{\max}$	450 L/min	kW	1.5
$H_{\max}$	18 m	VL	450 V
C	30 $\mu$ F	V	220–240 ~
In	8.0 A	R/min	2850

**Fig. 6** The nozzles

**The Nozzles Set.** Conveyance pipes contain big pipes, transported pipes (transport the water from the pump to the small pipes), and small pipes that transport water to the nozzles (the number of nozzles is 460) in Fig. 6.

**Table 2** Fan specification

Specification	Value	Specification	Value
Type	VIK-40L4S	Capacity	4 $\mu$ F
Voltage	220 V	Frequency	50 Hz
Electric current	0.78 A	Discharge	3300 m <sup>3</sup> /hr
Velocity	1300 rpm	IP	54
Weight	7.2 kg	–	–

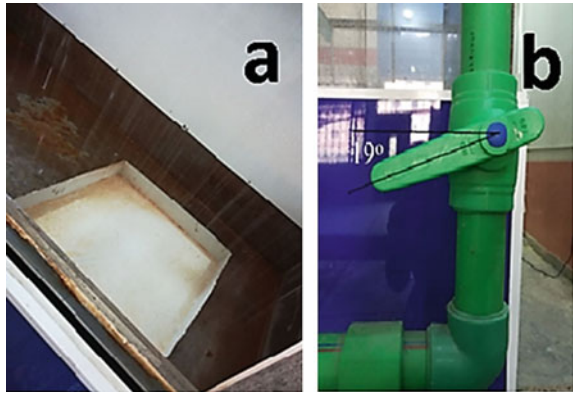
**Fig. 7** The pump and the fan of the rainfall machine

**The Convertor Fan.** The fan used to give the slope to the raindrops and make the storm as same as the natural storm. Specification of the used fan is shown in Table 2, whereas the fan photo is shown in Fig. 7.

### 3 The Rainfall Simulator Machine Performance

**The Rainfall Intensity.** Sheet steel pan was used to calibrate and measure the rainfall intensity and directly put it under the rainfall (See Fig. 8a). The machine switched on for 30 min (the time required to achieve the high rainfall intensity as described by Cerdà et al. [13]) and observed the level of water in the pan and determined by

**Fig. 8** **a** The sheet pan that used to measure the rainfall intensity. **b** The valve that controlling on rainfall intensity



measurement tape. The rainfall intensity was controlled by the valve, set at different angles until recording the required intensity. In this rainfall simulator machine, high rainfall intensity was considered during the test, and a similar procedure proposed by Liu et al. [4] is followed. The rainfall set on 16 cm/hr, and the valve set an angle 19° (see Fig. 8b). It should be noted that though the rainfall intensity used in this study was higher than the always observed values and it was in the acceptable range for laboratory experiments.

#### 4 The Rainfall Uniformity

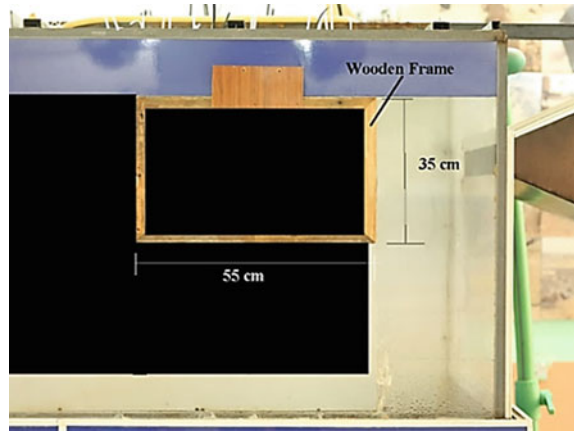
The performance of the nozzles grid can be assessed by measuring the spatial uniformity of distribution for rainfall on erosion flume. The coefficient of uniformity can be calculated by using vessels under the rainfall area and switched on the machine for (30 min) [2]. For this simulator, 6 vessels were used to find the coefficient of uniformity according to Eq. 1 [14].

$$C_u = 100 \left( 1 - \frac{\sum_i^N |x_i - \bar{x}|}{N\bar{x}} \right) \tag{1}$$

where  $C_u$  is the uniformity coefficient,  $N$  is the number of vessels;  $x_i$  is rainfall amount at location  $i$ , and  $\bar{x}$  is the average amount of rainfall. The uniformity coefficient = 87.75%. The more uniform the rainfall pattern when the  $C_u$  approaches to 100%. According to reference [14], the rainfall can be considered uniform when the  $C_u$  is higher than 80% (in some studies is higher than 70%).

**The raindrop size.** The raindrop size directly affects the other rainfall parameters like terminal velocity and kinetic energy. Also, rainfall erosivity plays a significant role in the processes of soil erosion. Therefore, many techniques were used to find

**Fig. 9** The wooden frame and black background



the raindrop size, such as the flour method, the disdrometer, the optical method, the radar technique, the momentum method, the stroboscope technique, the submersion technique, the stain method, and the photography method [21]. Due to the comparison between these techniques presented by Sadeghi et al. [21], choosing the appropriate method depends on the equipment availability. In this paper, the size of droplets can be found by using the photography technique described in detail by Eigel and Moore [22]. A digital high-resolution, high-speed camera (Canon 5D) is used to capture the raindrops. The optimum focal distance of the camera is 71 mm. Black background and wooden frame with dimensions of  $55 \times 35$  cm used to catch raindrops, as shown in Fig. 9. The picture was taken by zooming on the center of the frame.

A software processing of Image J (Version 1.46r) is used for processing and measuring simulated raindrops size. This software supports standard image processes like logical and arithmetical operations between images, contrast manipulation, Fourier analysis, convolution, smoothing, edge detection, sharpening, and median filtering. In this paper, the method of edge detection is used to separate drops from the background. This method is usually used to process images in many applications like registration, feature extraction, segmentation, and identification of objects in the scene. All drops out of the frame have been neglected and focused on the drops that appeared in the frame (see Fig. 10). The drop diameter was calculated automatically by drawing a straight horizontal line in the middle of the drop. According to the image's applied scale, every 9 pixels were equaled to 1 mm, as shown in Fig. 11.

**The Raindrops Velocity.** The velocity of the raindrop was measured in the laboratory with the intensity of 16 mm/hr. The elongation of the drop was found as the difference between the length and the diameter, where the diameter of the raindrop was represented as (a), and the length of the same drop was (b), as shown in Fig. 12. The length was calculated by drawing a vertical line in the middle of the drop. After that, the elongation of drop calculated is  $1/4000$  s (the speed of camera). The velocity of the droplets was calculated by converting the unit of the drop elongation to m/sec

**Fig. 10** **a** Raindrop original image and binary image (black and white). **b** Edge detected image of the raindrops

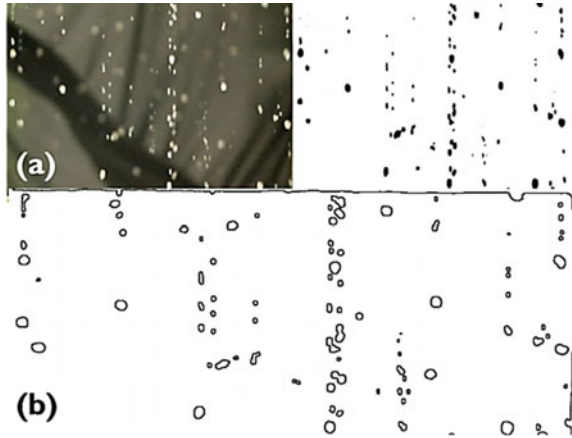


**Fig. 11** **a** Set scaling at the software. **b** The outputs

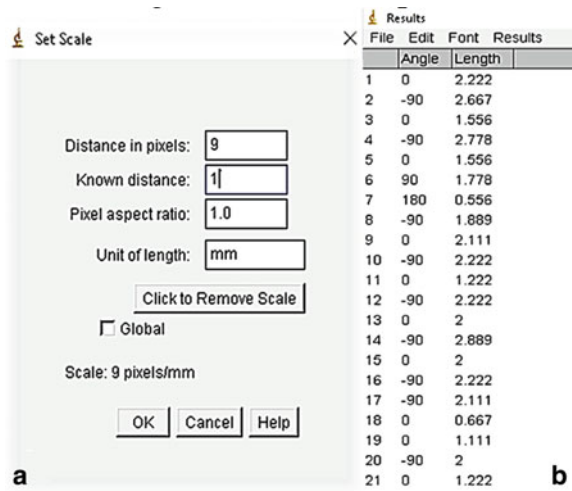


**Fig. 12** The different shapes of the droplet through its falling

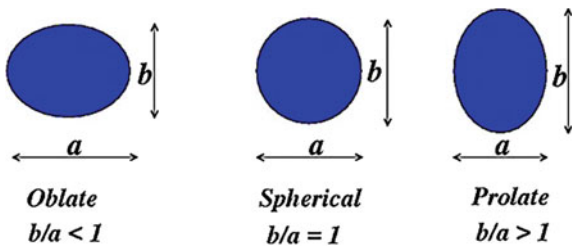
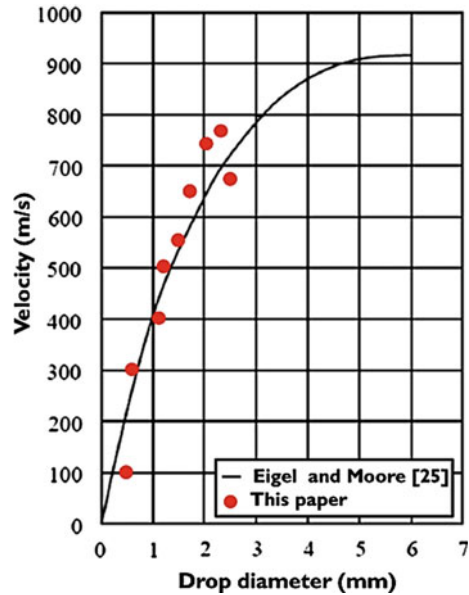


**Fig. 13** The relationship between the drop diameter and terminal velocity



for each droplet. This procedure modified by Kaviani et al. [23] is followed in this paper (i.e., raindrop elongation converted to velocity).

According to Aldefae and Alkhafaji [20], the minimum diameter of the droplets for the natural rainfall is 0.2 mm, and the maximum diameter is 5 mm (rarely reaches 5 and 6 mm). Therefore, the diameters of raindrops for the simulated rainfall are within the acceptable range. Based on the above results of the machine calibration of rainfall intensity, uniformity coefficient, raindrop sizes, and velocity, the rainfall simulator machine is applicable to the laboratory work to simulate the rainfall. The relationship between the computed rain drops size, and the terminal velocity is plotted in Fig. 13 with the natural rainfall relationship determined by Eigel and Moore [22]. It should be noticed that the rainfall simulator machine is captured the real phenomenon of rainfall.

**The Kinetic Energy.** The kinetic energy calculation is determined by utilizing the drop-size distribution (DSD), terminal or impact velocity, and the fall height [16]. In this study, the kinetic energy calculated according to Eq. 2 [20]:

$$\text{KE} = \frac{1}{2} \rho \frac{\sum_{i=1}^N d_i^3 v_i^2 n_i}{\sum_{i=1}^N d_i^3 n_i} \quad (2)$$

where KE is the kinetic energy,  $\rho$ : is the density of the raindrops ( $\text{g/cm}^3$ ) which equal ( $1 \text{ g/cm}^3$ ),  $n_i$ : is the number or fraction of raindrops in the drop diameter interval  $\Delta d_i$  and characterized by an effective diameter  $d_i$  (mm),  $v_i$ : is the velocity of the raindrop on impact (m/s), and  $N$ : is the number of drop diameter intervals. The simulated

rainfall's calculated kinetic energy using the simulator machine is ranged from 0.72 to 28.88 Jm<sup>-2</sup> mm<sup>-1</sup>. These values are within the acceptable range referred to in previous studies [12, 13].

## 5 Conclusions

The rainfall simulator machine's design to simulate the prototype rainfall storm phenomenon using the physical modeling principles is essential to understand the sediments, erosion, and other problems resulting from this phenomenon. The following conclusions can be emphasized:

- The obtained results of the raindrops utilizing the photography technique verified the real configurations of raindrops in prototype scale, mainly the kinetic energy compared with rainfall on prototype scale. Thus, the designed rainfall simulator machine achieved the primary goal.
- Uniform raining is inspected during model tests, and different intensities can be obtained using an electrical inverter actuator (pump).
- This designed and manufactured rainfall simulator machine was essential to provide an excellent chance for future studies in hydraulic and geotechnical engineering. These are many engineering problems that can be simulated using this machine like the effect of rainfall on surface runoff, sediment yield effect on the cross-section of the channel, the impact of rain and the antecedent soil moisture on soil filterability, the study of flood yield from rainfall and its effect on the channel and the adjacent area, analysis of the rainfall effect on the riverbank stability.
- The ministry of water resources in Iraq is the beneficiary to study the sediment yield due to the erosion resulting from the heavy rainfall, and the ministry of agriculture to study the spring rainfall effect on the strategic crops.

## References

1. Sun, L., Fang, H., Qi, D., Li, J., & Cai, Q. (2013). A review on rill erosion process and its influencing factors. *Chinese Geographical Science*, 23(4), 389–402.
2. Römkens, M. J., Helming, K., & Prasad, S. N. (2002). Soil erosion under different rainfall intensities, surface roughness, and soil water regimes. *CATENA*, 46(2–3), 103–123.
3. Shen, H., Zheng, F., Wen, L., Han, Y., & Hu, W. (2016). Impacts of rainfall intensity and slope gradient on rill erosion processes at loessial hillslope. *Soil and Tillage Research*, 155, 429–436.
4. Liu, Q. Q., Li, J. C., Chen, L., & Xiang, H. (2004). Dynamics of overland flow and soil erosion (II)-soil erosion. *Advances in Mechanics*, 4(25), 193–506.
5. Fang, H., Sun, L., & Tang, Z. (2015). Effects of rainfall and slope on runoff, soil erosion and rill development: An experimental study using two loess soils. *Hydrological Processes*, 29(11), 2649–2658.
6. Wang, Y. C., & Lai, C. C. (2018). Evaluating the erosion process from a single-stripe laser-scanned topography: A laboratory case study. *Water*, 10(7), 956.



7. Mahabaleshwara, H., & Nagabhushan, H. M. (2014). A study on soil erosion and its impacts on floods and sedimentation. *International Journal of Research in Engineering and Technology*, 3(03), 443–451.
8. Aldefae, A.H., Al-Khafaji, R.A., Shamkhi, M.S., & Kumar, H.Q. (2020). Erosion, sediments transport and riverbank stability: A review. In *IOP Conference Series: Materials Science and Engineering* (Vol. 901, No. 1, p. 012014). IOP Publishing.
9. Rodrigo-Comino, J., Senciales-González, J. M., Terol, E., Mora-Navarro, G., Gyasi-Agyei, Y., & Cerdà, A. (2020). Impacts of weather types on soil erosion rates in vineyards at “Celler del Roure” experimental research in eastern Spain. *Atmosphere*, 11(6), 551.
10. Adnan, S., Aldefae, A.H., Humaish, W.H. (2021). Soil erosion and the influenced factors: A review article. In *IOP Conference Series: Materials Science and Engineering* (Vol. 1058, No. 1, p. 012041). IOP Publishing.
11. Garcia, M. ed. (2008). Sedimentation engineering: Processes, measurements, modeling, and practice. *American Society of Civil Engineers*.
12. Whisman, M. (2013). *Revegetation of post-dam-removal riparian sediments in the lower Elwha River*. WA (Doctoral dissertation, Thesis. The Evergreen State College, Olympia, Washington, USA).
13. Cerdà, A., Ibáñez, S., & Calvo, A. (1997). Design and operation of a small and portable rainfall simulator for rugged terrain. *Soil Technology*, 11(2), 163–170.
14. Paige, G. B., Stone, J. J., Smith, J. R., & Kennedy, J. R. (2004). The Walnut Gulch rainfall simulator: A computer-controlled variable intensity rainfall simulator. *Applied Engineering in Agriculture*, 20(1), 25.
15. Humphry, J. B., Daniel, T. C., Edwards, D. R., & Sharpley, A. N. (2002). A portable rainfall simulator for plot-scale runoff studies. *Applied Engineering in Agriculture*, 18(2), 199.
16. Aksoy, H., Unal, N. E., Cokgor, S., Gedikli, A., Yoon, J., Koca, K., Inci, S. B., & Eris, E. (2012). A rainfall simulator for laboratory-scale assessment of rainfall-runoff-sediment transport processes over a two-dimensional flume. *CATENA*, 98, 63–72.
17. Korea Institute Geoscience and Minerals Resources (KIGAM). (2013). Potable automatic-oscillating control rainfall simulator. Report No. KR101113267B1, Classification IPC A01G15/00.
18. Aldefae, A.H., Saleem, H.D. (2020). Design, manufacturing and testing of biaxial mechanical travelling pluviator. In *IOP Conference Series: Materials Science and Engineering* (Vol. 870, No. 1, p. 012071). IOP Publishing.
19. Aldefae, A. H., Alkhafaji, R. A., Shamkhi, M. S., & Kumer, H. Q. (2019). Design and manufacturing of flume apparatus to investigate the failure mechanism of riverbanks. *Cogent Engineering*, 6(1), 1655234.
20. Aldefae, A. H., & Alkhafaji, R. A. (2021). Experimental and numerical modeling to investigate the riverbank’s stability. *SN Applied Sciences*, 3(2), 1–16.
21. Sadeghi, S. H., Abdollahi, Z., & Darvishan, A. K. (2013). Experimental comparison of some techniques for estimating natural raindrop size distribution on the south coast of the Caspian Sea Iran. *Hydrological Sciences Journal*, 58(6), 1374–1382.
22. Eigel, J. D., & Moore, I. D. (1983). A simplified technique for measuring raindrop size and distribution. *Transactions of the ASAE*, 26(4), 1079–1084.
23. Kavian, A., Mohammadi, M., Cerda, A., Fallah, M., & Abdollahi, Z. (2018). Simulated raindrop’s characteristic measurements. A new approach of image processing tested under laboratory rainfall simulation. *CATENA*, 167, 190–197.

# Numerical Analysis of Water and Crude Oil Flux from Clayey Soil by GeoStudio-SEEP/W



Amina Hamid Alwan and Aqeel Al-Adili

**Abstract** In this study, the finite element computer program Geo Studio SEEP/W was used to simulate water and crude oil leakage on the top and side surface of clayey soil. The accumulative flux increased with increasing time until a specific quantity after that increasing the time does not cause increasing the flux quantity. The accumulative water flux quantity ( $\text{m}^3/\text{sec}$ ) is less than the accumulative crude oil flux quantity by  $3.2748\text{E-}05$  Section 1,  $1.9600\text{E-}04$  on section 2,  $2.0370\text{E-}04$  on section 3,  $5.1870\text{E-}06$  on section 4 in the first five minutes. The results have shown the accumulative quantity in both cases continues to increase parallel until minute 1320 (22 h), then the soil in the model becomes saturated. For the comparison of effects of water and crude oil leakage on the model's side surface, found the accumulative water flux quantity ( $\text{m}^3/\text{sec}$ ) is less than the accumulative crude oil flux quantity, by  $5.4760\text{E-}03$  section 1,  $2.1961\text{E-}04$  on section 2,  $2.0863\text{E-}04$  on section 3,  $3.3236\text{E-}08$  on section 4 in the first five minutes. The accumulative amount continues increasing for both until 1080 min (18 h), then the soil in the model becomes saturated.

**Keywords** Seepage · Crude oil · SEEP/W · Leakage · Clayey soil

## 1 Introduction

In permeable soil layers such as sand, a fluid's flow is referring to the seepage flow. The fluid can fill the unsaturated bottom layer's pores and because of the gravity, the effect passes into deeper layers. The soil must be permeable in order not to store the water that is drained. Soil permeability is defined by the coefficient of permeability  $k$  in  $\text{m/s}$  and is dependent on the size of the grain and the useful pore space. The drainage water may be temporarily stored in less permeable soils. If an impermeable soil layer or impermeable rock meets the infiltration water, infiltration can no longer occur, and the infiltration water accumulates permanently. These underground water accumulations are known as the movement of water within the soil through the porous media and are a highly complex phenomenon due to the difference in the states and

---

A. H. Alwan (✉) · A. Al-Adili  
Civil Engineering Department, University of Technology, Baghdad, Iraq

directions in which water travels and the variation in the forces causing it to travel [1]. In most of the world's oil-producing countries, hydrocarbons' leaks and spills have become a serious concern. It is not possible to ignore or neglect the effect of these leaks and spills on the ecosystem. One of these consequences is that they cause a change in soil and groundwater engineering properties and behavior.

If the oil is purposely or accidentally released, the local and nearby area, including the soil, is polluted. Not only environmentalists but geotechnical engineers face the problem of polluted soils. Electrochemically active soil is often affected when the environment is contaminated by liquid substances [2]. Oil contamination may occur in water or on the ground due to spills. Crude oil contamination on the ground relies upon a variety of elements, such as the properties of soil adsorption, the permeability of the soil, and the coefficient of partitioning [3]. The degree of pollution relies on the composition of the contaminant's chemical compounds and the soil properties [4]. Khamchian et al. [5] studied the geotechnical properties of clayey and sandy soil specimens polluted by crude oil. The result showed that the dry density, shear strength, optimum moisture content, and Atterberg limits were significantly reduced by raising the soil's Crude oil content. The impact of four different types of pollutants on the geotechnical properties of clayey soil was studied by Karkush et al. [6]. The contaminants are kerosene, ammonium nitrate, copper, and lead, each of them in two percentages (10 and 25) mixed with soil. The study results indicate that these pollutants have various impacts on the geotechnical properties of clayey soil. Karkush and Kareem [7] investigated the influence of total petroleum hydrocarbons on the geotechnical properties of clayey soil specimens polluted in the field. The findings showed that industrial wastewater has different impacts on a sample of clay soil's geotechnical properties.

Karkush and Jihad [8] The effects of kerosene on the physical, mechanical, and chemical properties of clay soil are being studied. The soil samples are artificially polluted with six kerosene ratios (5, 10, 20, 30, 40, and 50%) based on the soil's dry weight. Test results have shown that different kerosene ratios have different effects on soil samples' engineering and chemical properties. Specific gravity, fine particle percentages, optimum water content, initial and final void ratio, consolidation coefficient, index of swelling, permeability, undrained shear strength, effective parameters of shear strength, and the rate of reduction of the initial pore water pressure are reduced by increasing the soil kerosene content. In general, kerosene concentrations less than 10% have mild effects on soil samples' studied characteristics. This study aims to study and analyze the water and crude oil leakage flow on clayey soils by Geo studio-SEEP/W program using saturated and non-saturated soil media.

## 2 Methods and Materials

The first step to generate the model is by drawing it as a 2D model by the finite Elements program Geo studio-SEEP/W. The leakage flow of hydrocarbon contaminants on clayey soil will be studied in this numerical method, where the type of

soil with specific geometry value and two types of fluids will be used: water and crude oil. With vertical/horizontal fluid flow, the model built as a case study has a cross-section length of 1000 mm and a height of 350 mm, and as presented in Fig. 1.

The work is subdivided into two sections. The first section was to simulate the water and crude oil leakage flow on the top surface of the clayey soil models, and the second is to simulate the leakage flow of the water and crude oil on the side surface of the clayey soil models, collecting the results, analyze it by using SEEP/W routine and then compare the results. The properties of the material used in this study are described in Table 1. The input parameters for the program are related to these properties: the hydraulic conductivity (permeability), the volume of water content, the coefficient of compressibility ( $m_v$ ) (typical value  $1.0E-5$ ) [9], unit weight of water, and the hydrocarbon (crude oil).

The unit weight of water =  $9.81 \text{ kN/m}^3$  and the crude oil's unit weight =  $8.5298 \text{ kN/m}^3$ . The crude oil sample collected from Majnoon oil field export line and tested at Majnoon oil field laboratory by using DMA 4500 M device, as shown in Fig. 2 and Table 2.

The finite element mesh is the part that deals with the domain's physical dimensions, an unstructured mesh with an element size of approximately 0.05 m was chosen. The model type for the material was considered as saturated/unsaturated. It was needed to set a water content function and hydraulic conductivity function estimated using the Van Genuchten approach [11]. For the first simulation, two types of boundary condition have been used, first is head/ unit flux on the centerline of the top surface of the model to simulate the water and crude oil leakage flow, and the second is assigning the pore water zero pressure, and as explained in Fig. 3.

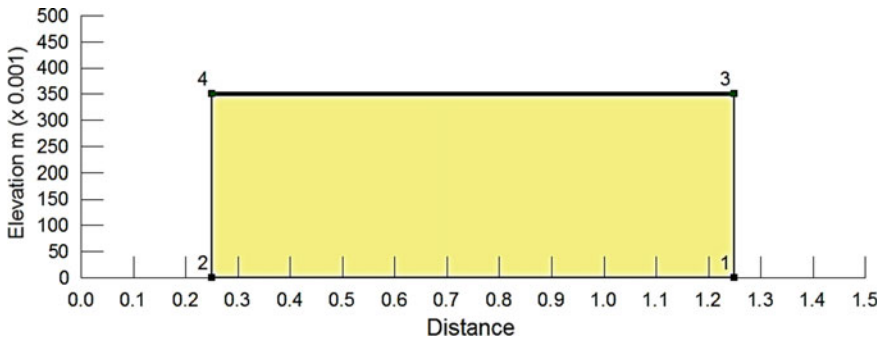


Fig. 1 Model cross-section

Table 1 Material properties

Model number	Type of soil	Permeability k (m/s)	Reference	Volume of water content ( $\text{m}^3/\text{m}^3$ )
1	Clay	$1.0E-9$	[10]	0.5

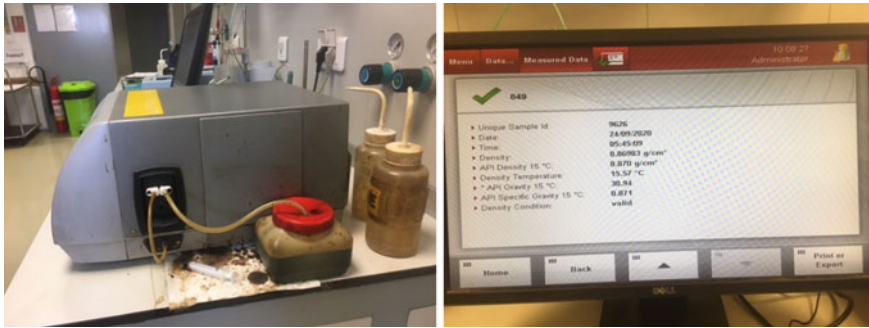


Fig. 2 Crude oil sample test

Table 2 Crude oil sample test result

Analysis parameters	Method	Result	Units
Density at 60°F	ASTM D 5002	0.8698	g/cm <sup>3</sup>

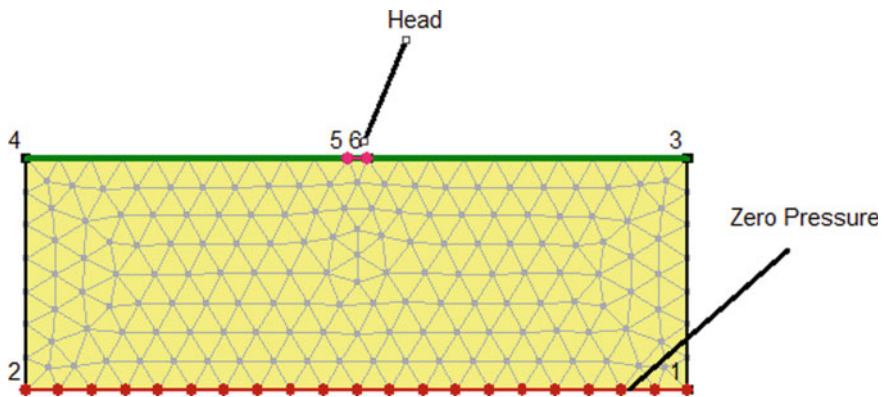


Fig. 3 Boundary conditions, 1 m head, and zero pressure

For the second simulation (horizontal flow), two types of boundary condition have been used, first is a pressure head/unit flux on the left side of the model to simulate the water and crude oil flow, and the second is assigning the pore water zero pressure, and as explained in Fig. 4.

### 3 Results and Discussions

SEEP/W is a software product (version 2007) for finite elements that can be used to model the distribution of movement and pore-water pressure within porous materials



Fig. 4 Boundary conditions, 10 m head, and zero pressure

such as soil. It is a general analytical software for seepage that models both saturated and unsaturated flow. The ability to model unsaturated flow enables SEEP/W to manage a wide variety of real problems than many other seepage software items. Two main types of analysis can be implemented by the software: steady-state and transient. The transient analysis used in this study, and, it is describing something that is constantly evolving. It is evolving because it takes a long period for the soil to react to define user boundary conditions. One of the SEEP/W and transient flow characteristics can provide the user with the quantity of fluid accumulated and the flux on the appropriate section over time [12]. In this study, unit flux ( $m^3/sec$ ) was applied to the clayey soil model once on the top surface, then on the side surface as a case study. The defined view window is the first stage to determine model geometry and geometry to create a Finite Element software SEEP/W model. In choosing the right model scale and geometry, the geometry step is essential. The scale will affect the outcome significantly. The next step is defining the properties of the material and choosing the appropriate function and the appropriate boundary for the model's geometry. After completing these essential steps, the model was ready, click the check/optimize button for checking up and for the alert about missing item, and then click the analysis button [12].

**Flow Path and Velocity Vectors.** As in the conventional flow network, the SEEP/W flux routes are not flux lines or streamlines. The flow paths are also so close to the streamlines but not similar. The flow routes are merely a lane dependent on velocity vectors in an element which is followed by a fall of water in steady-state conditions. Velocity vectors are not just a beneficial method to look at the flow, it is also to see how much flow happens in comparison to other domain areas. In its measurement of how big the vector can show, SEEP/W uses the scale of the real velocity so that the velocities are low or high can be displayed. Gauss point velocity values will be utilized to determine the average x velocity and the average y velocity by computing them, and then these values shall be combined in order to achieve a mean rate of the velocity vector of each object. In Figs. 5 and 6, the flow path and vectors are explained [12].

**Flux Sections.** For the transient flow analysis, SEEP/W can measure the immediate quantities of seepage, which flows through an end-to-end portion [13]. The

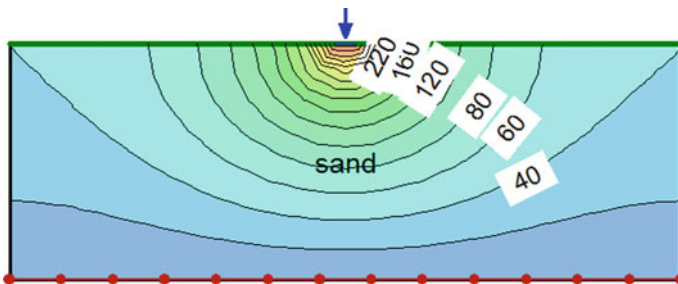


Fig. 5 Water flow path

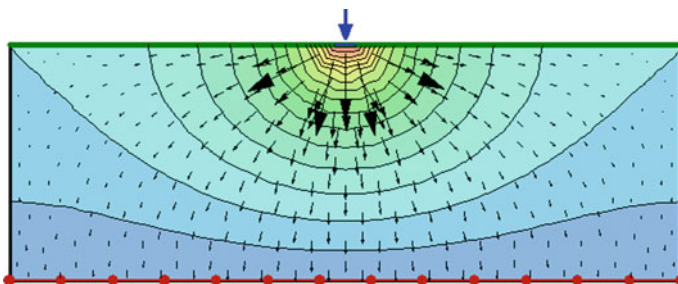


Fig. 6 Water flow velocity vectors

subsections as identified are the fictitious streamlines from one end of the segment to the other end. SEEP/W defines the section of user-defined flux as well as all the subsections, the SEEP/W does also the calculations of the subsections' total flows throughout the section of the flux by calculating the flow for each individually [11]. Flux sections can be applied in several directions, so wherever you want to know the flux can be drawn, in this thesis will study the total flow through the flux sections at four locations and for all situations, near and far to the source of leakage, as shown in Table 3 and Fig. 7.

**Case Study.** For the clayey soil, four scenarios were considered in this study, as below:

**Water unit flux on the top surface of the clayey soil model.** In this analysis, 1 m<sup>3</sup>/sec water unit flux has been applied for the clayey soil model on the centerline of the model's top surface, and for a total period of 24 h, the readings have been recorded as shown in Table 5. To investigate the flow paths, vector, and flux quantity, series of analyses were conducted for the soil. This sensitivity analysis included the

Table 3 Flux sections location

Section number	Section 1	Section 2	Section 3	Section 4
Distance from left edge of the model (m)	0.1	0.35	0.65	0.9

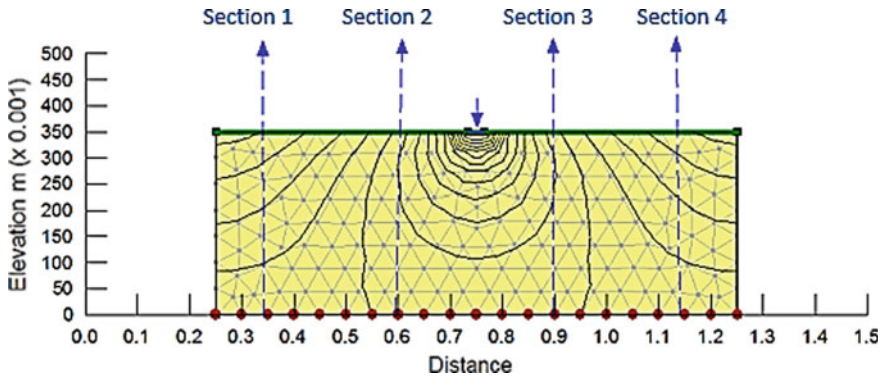


Fig. 7 Locations of measured flux sections

Table 4 Accumulative flux data-water leakage on the clayey soil top surface

Time elapsed (sec)	Flux (m <sup>3</sup> /sec)			
	Section 1	Section 2	Section 3	Section 4
300	1.0962E-05	1.0817E-03	1.0978E-03	1.5806E-05
600	4.0674E-05	2.4162E-03	2.4798E-03	5.8552E-05
1200	1.8472E-04	4.5254E-03	4.7527E-03	2.5885E-04
1800	4.0844E-04	5.7929E-03	6.2114E-03	5.6473E-04
3600	1.0287E-03	7.3039E-03	8.1982E-03	1.4366E-03
14,400	1.3056E-03	7.5684E-03	9.0918E-03	2.0966E-03
36,000	1.3626E-03	7.6420E-03	9.4504E-03	2.3272E-03
64,800	1.3585E-03	7.6325E-03	9.4594E-03	2.3346E-03
79,200	1.3583E-03	7.6323E-03	9.4596E-03	2.3347E-03
86,400	1.3583E-03	7.6322E-03	9.4596E-03	2.3348E-03

cumulative water flux in m<sup>3</sup>/sec per unit area for each section on the soil, as shown in Figs. 8, 9 and 10 and Table 4.

**Crude oil unit flux on the top surface of the clayey soil model.** In this analysis, 1 m<sup>3</sup>/sec of crude oil has been applied as a unit flux on the centerline of the clayey soil model’s surface for a total period of 24 h, and the readings have been recorded as shown in Table 6. To investigate the flow paths, vector, and flux quantity, series of analyses were conducted for the soil. This sensitivity analysis included the cumulative crude oil flux in m<sup>3</sup>/sec per unit area for each section on the soil, shown in Figs. 11, 12, 13 and Table 5.

From the comparison between the study results of the effects of crude oil and water leakage on the top of the sandy soil model (Tables 4 and 5) with a period of 24 h, observed:



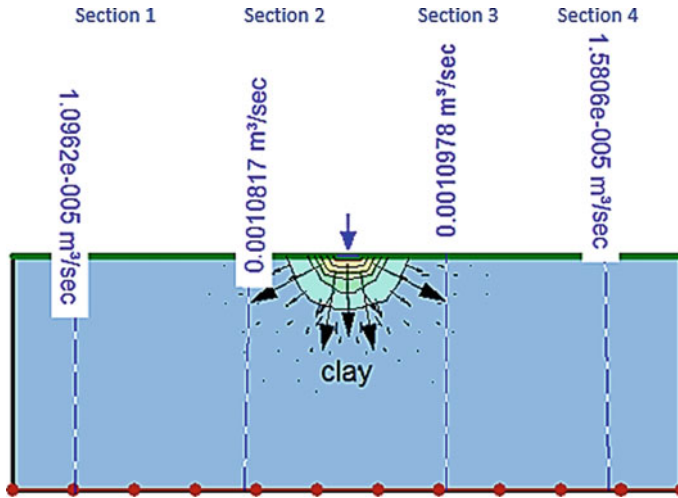


Fig. 8 Accumulative water flux-leakage on the model's top surface after 5 min

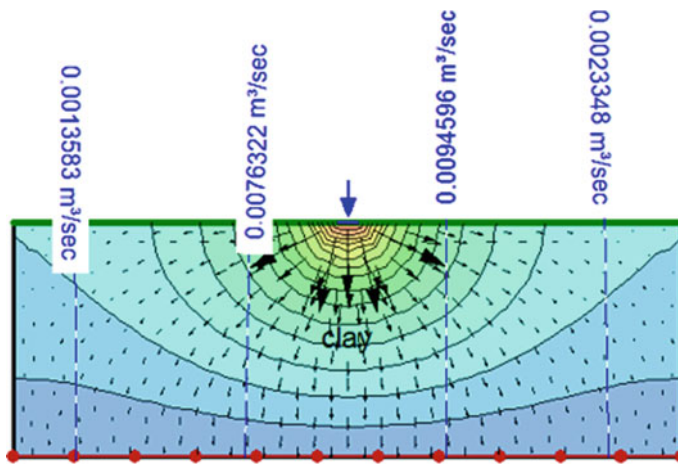


Fig. 9 Accumulative water flux-leakage on the model's top surface after 24 h

- There is an increment in the accumulative flux quantity ( $m^3/sec$ ), as shown in Table 6.
- There is a positive correlation somewhat between the accumulative flux and the duration, the accumulative flux data continue increasing until about min 1320, then, the results show there is no change in the flux quantity ( $m^3/sec$ ) for both models, which means the soil in both models became saturated after 22 h.

**Water unit flux on the side surface of the clayey soil model.** In this analysis,  $10 m^3/sec$  water unit flux has been applied for the clayey soil model on a selected

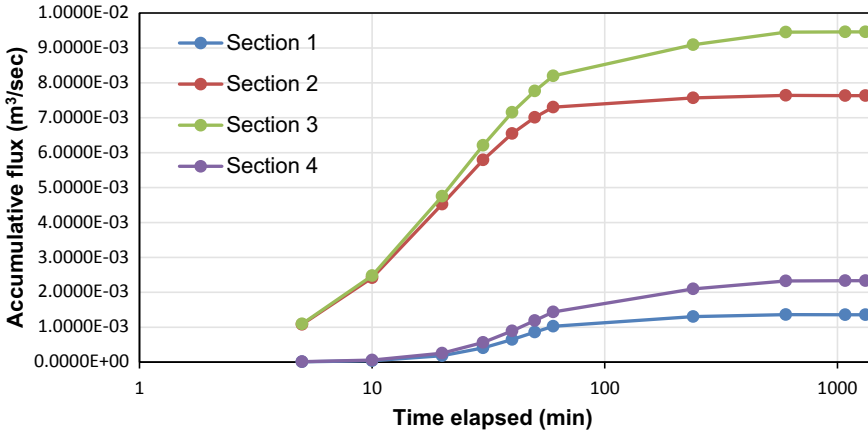


Fig. 10 Accumulative water flux-leakage on the model’s top surface

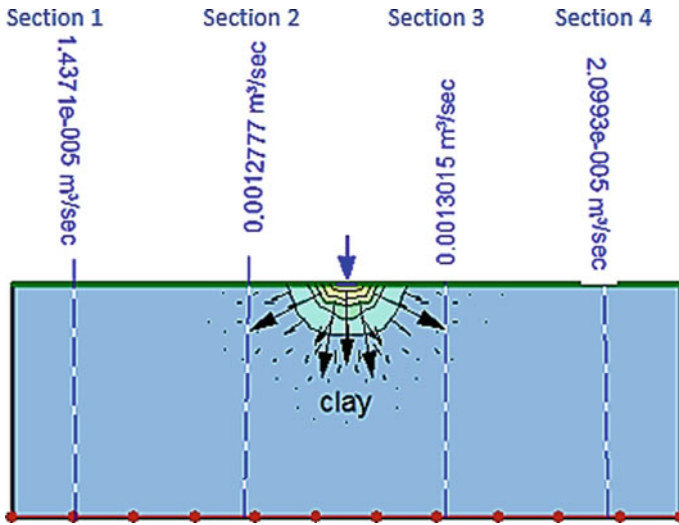


Fig. 11 Accumulative crude oil flux-leakage on the model’s top surface after 5 min

point at the left side face of the model, and for a total period of 24 h, the readings have been recorded as shown in Table 8. To investigate the flow paths, vector, and flux quantity. Series of analyses were conducted for the soil. This sensitivity analysis included the cumulative water flux in (m<sup>3</sup>/sec) per unit area for each section on the soil as shown in Figs. 14, 16 and Table 7 (Fig. 15).

**Crude oil unit flux on the side surface of the clayey soil model.** In this analysis, 10 m<sup>3</sup>/sec crude oil has been applied as a unit flux on a selected point at the side face of the clayey soil model for a total period of 24 h, and the readings have been

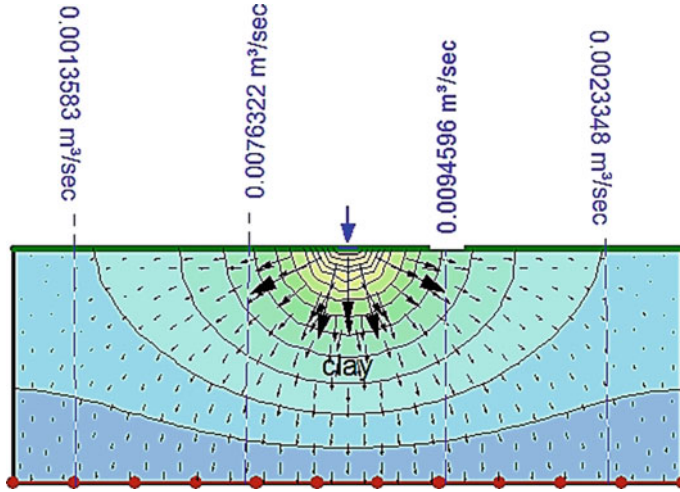


Fig. 12 Accumulative crude oil flux-leakage on the model’s top surface after 24 h

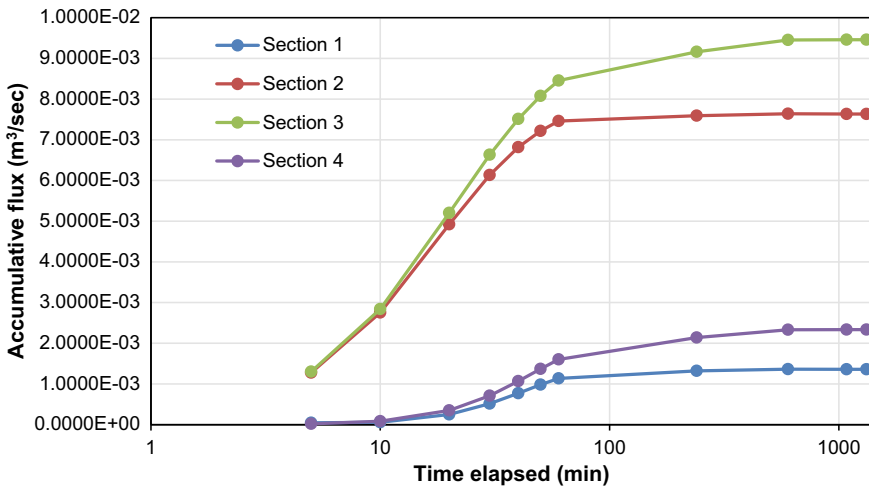


Fig. 13 Accumulative flux–crude oil on the top surface of clayey soil

recorded as shown in Table 9. To investigate the flow paths, vector, and flux quantity. Series of analyses were conducted for the soil. This sensitivity analysis included the cumulative crude oil flux in  $m^3/sec$  per unit area for each section on the soil, as shown in Figs. 17, 18, 19 and Table 8.

The comparison between the study results of the influences of water and crude oil leakage on the sandy soil model’s side surface (Tables 7 and 8) observed: There is an increment in the accumulative flux quantity ( $m^3/sec$ ) as shown in Table 9.

**Table 5** Accumulative flux data—crude oil leakage on the clayey soil top surface

Time elapsed (sec)	Flux (m <sup>3</sup> /sec)			
	Section 1	Section 2	Section 3	Section 4
300	4.3710E-05	1.2777E-03	1.3015E-03	2.0993E-05
600	5.9060E-05	2.7524E-03	2.8391E-03	8.4426E-05
1200	2.4993E-04	4.9201E-03	5.2045E-03	3.4824E-04
1800	5.1500E-04	6.1334E-03	6.6326E-03	7.1115E-04
3600	1.1348E-03	7.4592E-03	8.4559E-03	1.6025E-03
14,400	1.3198E-03	7.5902E-03	9.1622E-03	2.1402E-03
36,000	1.3612E-03	7.6387E-03	9.4537E-03	2.3299E-03
64,800	1.3584E-03	7.6324E-03	9.4595E-03	2.3347E-03
79,200	1.3583E-03	7.6322E-03	9.4596E-03	2.3348E-03
86,400	1.3583E-03	7.6322E-03	9.4596E-03	2.3348E-03

**Table 6** Comparison of accumulative flux data of crude oil and water leakage on the top surface of clayey soil

Time elapsed (sec)	Flux (m <sup>3</sup> /sec) (oil–water)			
	Section 1	Section 2	Section 3	Section 4
300	3.2748E-05	1.9600E-04	2.0370E-04	5.1870E-06
600	1.8386E-05	3.3620E-04	3.5930E-04	2.5874E-05
1200	6.5210E-05	3.9470E-04	4.5180E-04	8.9390E-05
1800	1.0656E-04	3.4050E-04	4.2120E-04	1.4642E-04
3600	1.0610E-04	1.5530E-04	2.5770E-04	1.6590E-04
14,400	1.4200E-05	2.1800E-05	7.0400E-05	4.3600E-05
36,000	-1.4000E-06	-3.3000E-06	3.3000E-06	2.7000E-06
64,800	-1.0000E-07	-1.0000E-07	1.0000E-07	1.0000E-07
79,200	0.0000E + 00	-1.0000E-07	0.0000E + 00	1.0000E-07
86,400	0.0000E + 00	0.0000E + 00	0.0000E + 00	0.0000E + 00

There is a positive correlation somewhat between the accumulative flux and the duration, the accumulative flux data continue increasing until about minute 1080, then, the results show there is no change in the flux quantity (m<sup>3</sup>/sec) for both models, which means the soil in both models became saturated after 18 h.

## 4 Conclusions

The following conclusions have been drawn from the study of the transient flow in a clayey soil model:

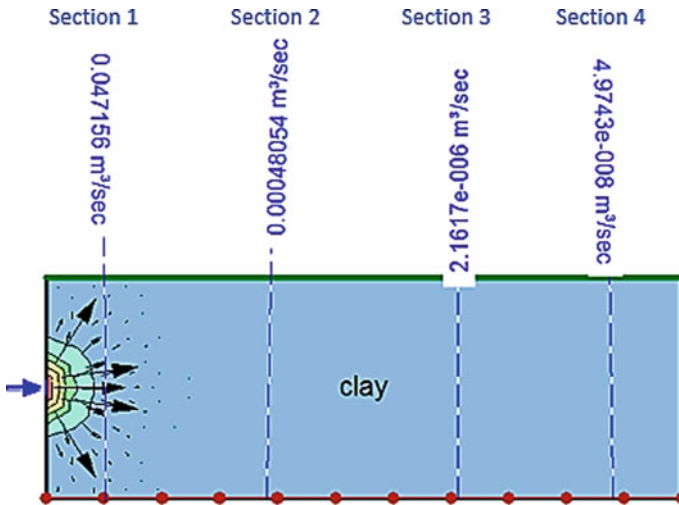


**Fig. 14** Accumulative water flux—leakage on the model’s side surface after 5 min

**Table 7** Accumulative flux data-water leakage on the clayey soil top surface

Time elapsed (sec)	Flux (m <sup>3</sup> /sec)			
	Section 1	Section 2	Section 3	Section 4
300	4.7156E-02	4.8054E-04	2.1617E-06	4.9743E-08
600	8.5635E-02	1.8200E-03	1.2788E-05	1.9455E-07
1200	1.2690E-01	6.9305E-03	1.0810E-04	2.3310E-06
1800	1.4537E-01	1.3614E-02	3.8840E-04	1.2492E-05
3600	1.6519E-01	3.0879E-02	2.5663E-03	1.9031E-04
14,400	1.7396E-01	4.6980E-02	9.9527E-03	1.9870E-03
36,000	1.7780E-01	5.2855E-02	1.3001E-02	2.9184E-03
64,800	1.7790E-01	5.3036E-02	1.3144E-02	2.9820E-03
79,200	1.7790E-01	5.3038E-02	1.3146E-02	2.9831E-03
86,400	1.7790E-01	5.3038E-02	1.3146E-02	2.9832E-03

- In the comparison of effects of water and crude oil leakage on the model’s top surface, found the accumulative water flux quantity (m<sup>3</sup>/sec) is less than the accumulative crude oil flux quantity, by 3.2748E-05 section 1, 1.9600E-04 on section 2, 2.0370E-04 on section 3, 5.1870E-06 on section 4 in the first five minutes, and the results shown the accumulative quantity in both cases continue increasing parallelly until 22 h, then, the soil in the model become saturated
- In the comparison of effects of water and crude oil leakage on the model’s side surface, found the accumulative water flux quantity (m<sup>3</sup>/sec) is less than the accumulative crude oil flux quantity, by 5.4760E-03 section 1, 2.1961E-04 on section 2,

**Table 8** Accumulative flux data—crude oil leakage on the clayey soil side surface

Time elapsed (sec)	Flux (m <sup>3</sup> /sec)			
	Section 1	Section 2	Section 3	Section 4
300	5.2632E-02	7.0015E-04	4.2480E-06	8.2979E-08
600	9.2595E-02	2.5267E-03	2.4421E-05	4.4452E-07
1200	1.3275E-01	8.9109E-03	1.8812E-04	5.2303E-06
1800	1.4983E-01	1.6567E-02	6.2376E-04	2.5605E-05
3600	1.6755E-01	3.4301E-02	3.4623E-03	3.1101E-04
14,400	1.7471E-01	4.8069E-02	1.0476E-02	2.1381E-03
36,000	1.7784E-01	5.2924E-02	1.3055E-02	2.9419E-03
64,800	1.7790E-01	5.3037E-02	1.3146E-02	2.9827E-03
79,200	1.7790E-01	5.3038E-02	1.3146E-02	2.9832E-03
86,400	1.7790E-01	5.3038E-02	1.3146E-02	2.9833E-03

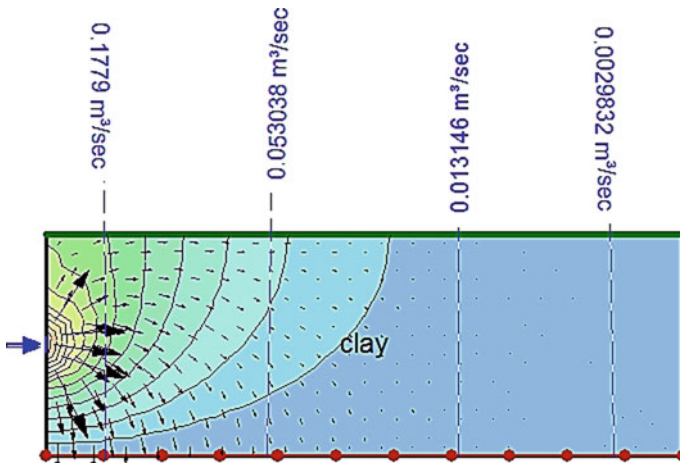


**Fig. 15** Accumulative water flux-leakage on the model’s side surface after 24 h

2.0863E-04 on section 3, 3.3236E-08 on section 4 in the first five minutes. The accumulative amount continues increasing for both cases but at a lower rate, and the results shown the accumulative quantity in both cases continues growing parallelly until 18 h. Then, the soil in the model becomes saturated.

- There is a positive correlation somewhat between the accumulative flux and the duration. The accumulative flux is increased with the time increasing until a specific quantity. After that, the increase in the time not increasing the flux quantity. This shows that whenever the soil is not saturated or partially saturated, pore water rises, allowing further fluid to access the soil. On either side, when the soil is saturated, and that occurs for a time after a flow, the pore water pressure decreases, meaning less water enters from the external circumstances.

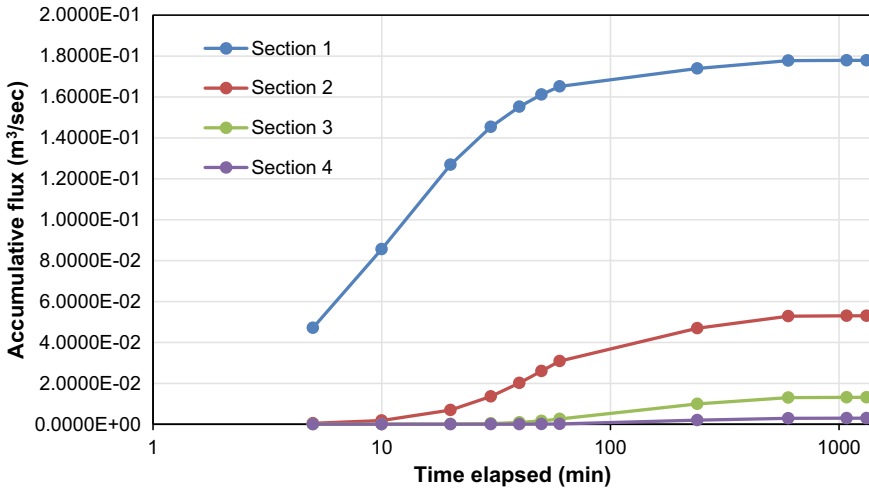


Fig. 16 Accumulative Flux—water on the clayey soil side surface

Table 9 Comparison accumulative flux data of crude oil and water leakage on the clayey soil side surface

Time elapsed (sec)	Flux (m³/sec) (oil–water)			
	Section 1	Section 2	Section 3	Section 4
300	5.4760E-03	2.1961E-04	2.0863E-06	3.3236E-08
600	6.9600E-03	7.0670E-04	1.1633E-05	2.4997E-07
1200	5.8500E-03	1.9804E-03	8.0020E-05	2.8993E-06
1800	4.4600E-03	2.9530E-03	2.3536E-04	1.3113E-05
3600	2.3600E-03	3.4220E-03	8.9600E-04	1.2070E-04
14,400	7.5000E-04	1.0890E-03	5.2330E-04	1.5110E-04
36,000	4.0000E-05	6.9000E-05	5.4000E-05	2.3500E-05
64,800	0.0000E + 00	1.0000E-06	2.0000E-06	7.0000E-07
79,200	0.0000E + 00	0.0000E + 00	0.0000E + 00	1.0000E-07
86,400	0.0000E + 00	0.0000E + 00	0.0000E + 00	1.0000E-07

- The program output shows in somewhat the result of the study are close because the unit weight of the used crude oil is 8.5298 kN/m<sup>3</sup>, which is close to the water unit weight (9.81 kN/m<sup>3</sup>), and the model size is small (1000 × 350 mm).

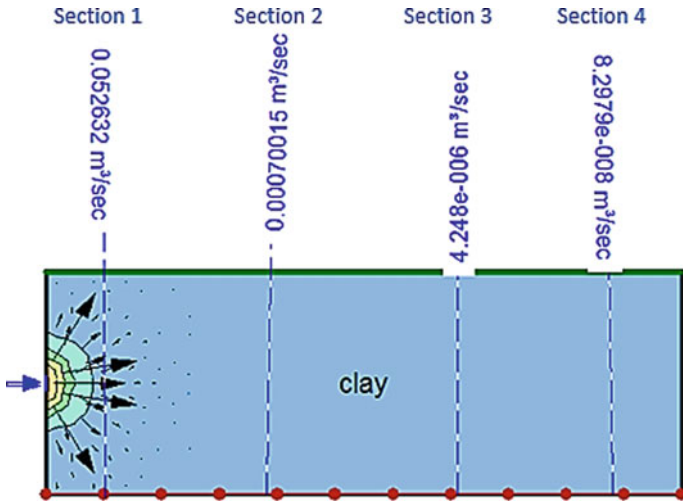


Fig. 17 Accumulative crude oil flux-leakage on the model's side surface after 50 min

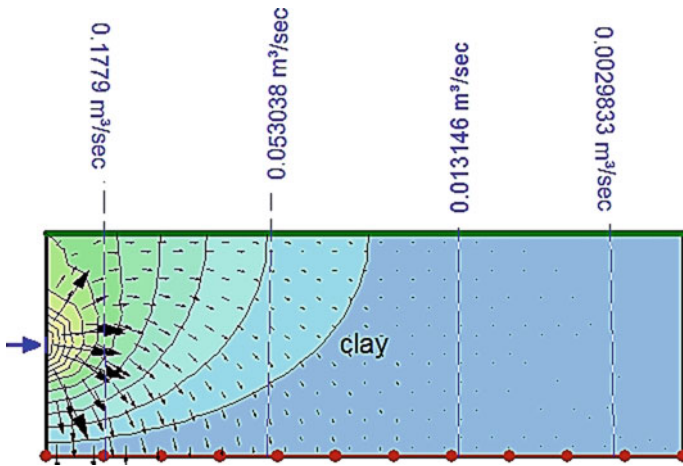


Fig. 18 Accumulative crude oil flux—leakage on the model's side surface after 24 h



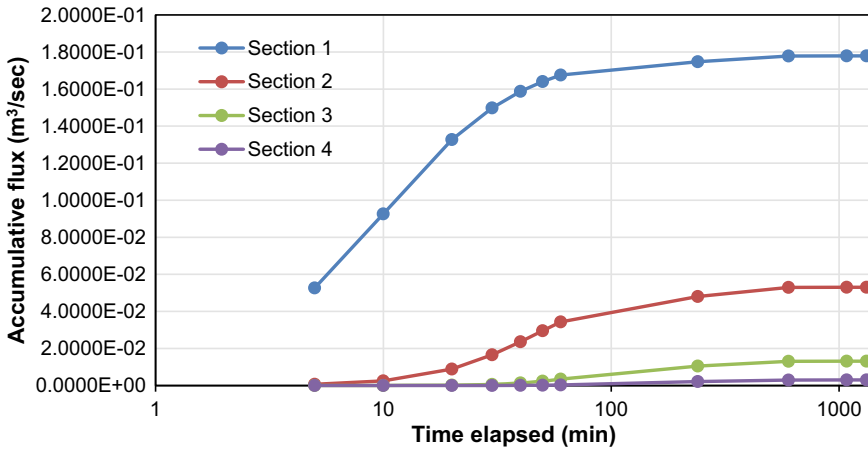


Fig. 19 Accumulative flux—crude oil on the clayey soil side surface

## References

- Namitha, M. R. (2016). Soil water—saturated and unsaturated flow. M. TECH (LWME) TNAU SAC 604,1–33.
- Ur-Rehman, H., Abduljawwad, S. N. & Akram, T. (2007). Geotechnical behavior of oil-contaminated fine-grained soils. *Electronic Journal of Geotechnical Engineering*, 12(2007).
- Al-Adili, A. S., Al-Rubaei, R. H., & Fouad, M. O. (2020). Numerical solution of rain-fall infiltration beneath flexible pavement. In *IOP Conference Series: Materials Science and Engineering* (Vol. 737, No. 1, p. 012137). IOP Publishing.
- Fine, P., Graber, E. R., & Yaron, B. (1997). Soil interactions with petroleum hydrocarbons: Abiotic processes. *Soil Technology*, 10(2), 133–153.
- Khamehchiyan, M., Charkhabi, A. H., & Tajik, M. (2007). Effects of crude oil contamination on geotechnical properties of clayey and sandy soils. *Engineering Geology*, 89(3–4), 220–229.
- Karkush, M. O., Zaboon, A. T., & Hussien, H. M. (2013). Studying the effects of contamination on the geotechnical properties of clayey soil. In *Coupled phenomena in environmental geotechnics* (pp. 599–607). Taylor & Francis Group
- Karkush, M. O., & Kareem, Z. A. (2017). Effects of fuel oil on the geotechnical properties of clay soil. *Journal of Engineering*, 23(8), 1–12.
- Karkush, M. O., & Jihad, A. G. (2020). Studying the geotechnical properties of clayey soil contaminated by Kerosene. *Key Engineering Materials*, 857, 383–393.
- Spangler, M. G., & Handy, R. L. (1982). *Soil engineering* (4th ed.). Harper & Row Publishers.
- Terzaghi, K., Peck, R. B., & Mesri, G. (1996). *Soil mechanics in engineering practice*. John Wiley & Sons.
- Al-Taei, M. H., Al-Adilli, A., & Sivakugan, N. (2017). Predicting movement of soil around Baghdad Metro Under buildings loads using three-dimensional numerical simulation. *International Journal of Civil Engineering and Technology*, 8(10), 1096–1106.
- Seepage Modeling with SEEP/W2007. (2008). *An Engineering Methodology* (3 ed). GEO-SLOPE International Ltd.
- Al-Adili, A., Abdul-Amir, R. H., & Chfat, O. (2018). Numerical analysis to assess the vertical drainage within flexible pavement. *International Journal of Engineering & Technology*, 7(420), 95–102.

# Evaluation of the Efficiency of a Selected Section of the Mosul Dam Grout Curtain



Mohammed Khalid Ibrahim and Suhail Idrees A. Khattab

**Abstract** Mosul Dam was built on a complex foundation including gypsum/anhydrite rocks that could be subjected to dissolution. So, the dam requires continuous foundation grouting, maintaining the grout curtain's efficiency, controlling the seepage velocities, and reducing the internal erosion risks. Piezometer readings are used on both sides of the grout curtain to calculate and monitor the efficiency of the curtain to treat the sections that show a deterioration in the curtain efficiency before others. In this study, the finite element method using GeoStudio-2018 R2 (SEEP/W) software was used to construct a model for a cross-section in Mosul Dam to simulate the seepage behavior through the dam and the foundations. On the other hand, studying the distribution of the pore water pressure on both sides of the grout curtain and calculating the net head dissipated (NHD) and the efficiency of the curtain, with the illustration of its change with the depth. Before and after the formation or maintenance of the grout curtain. Finally, a comparison between the calculated pressures with the piezometer's readings was conducted. The main results show that the efficiency changes along with the depth of the grout curtain, and it's influenced by the distance between the piezometers and the grout curtain. As the piezometer is located further from the curtain, the efficiency values calculated through it are higher. Finally, a conclusion was attained that the curtain efficiency of each geological layer should be evaluated independently from the rest of the geological strata.

**Keywords** Mosul dam · Grouting · Grout curtain efficiency · NHD · Piezometers · SEEP/W

---

M. K. Ibrahim (✉)  
Mosul Dam Project, Mosul, Iraq

S. I. A. Khattab  
College of Civil Engineering, University of Mosul, Mosul, Iraq  
e-mail: [suhail59@uomosul.edu.iq](mailto:suhail59@uomosul.edu.iq)

# 1 Introduction

Mosul Dam is the largest multi-purpose dam in Iraq, and it is one of the largest systems of storage dams in the Middle East. This dam is located on the Tigris River, 50 km north of Mosul city, as shown in Fig. 1. It was established in the period between (1981–1986) to prevent flooding, store water through its lake with a storage capacity of (11.11) billion cubic meters, to provide the necessary supplies of water for irrigation and other uses, and generate electricity (750 Megawatts from the main dam, 60 Megawatts from the regulatory dam, 240 Megawatts from the pumped storage project) [1]. The dam is an earthen zoned dam (central impervious core) and filter zones. The maximum height of the dam is 113 m, its width at the top is 10 m, and its total length is 3650 m. One of the main causes of the failure in the earth dams is the seepage from its bodies and foundations. Many studies were conducted concerning the problem of foundation erosion and seepage in Mosul Dam.



Fig. 1 Location of the Mosul dam with the general facilities (sentinel aerial photos edited by authors using ArcMap)

Khattab [2] studied the stability of Mosul Dam, under saturated and unsaturated soil conditions, by numerical simulations using the finite element method. Khattab and Khalil [3] created a numerical model to study pore water pressure development in the embankment of the Mosul Dam. Irzooki [4] studied the efficiency and performance of Mosul Dam with respect to the seepage. Adamo et al. [5] reviewed the foundation treatment during the construction of Mosul Dam.

The most important factor affecting the efficiency of the grout curtain is its geometry [6]. The geometry of the grout curtain means its depth, lateral expansion, and its thickness. The depth and lateral expansion of the grout curtain are related to the geological conditions and the hydrological regime of the dam site [7]. As for the thickness of the grout curtain, it depends mainly on the ability of the grout mixture to travel farther distances and penetrate the narrow cracks, fill and close it. This is known as grout penetration radius [8]. This study aims to understand and illustrate the change in the grout curtain efficiency with the depth and change of the geological layers that the curtain penetrates. Studying the effect of the location of the piezometers relative to the grout curtain (the depth and the horizontal distance from the curtain), on the efficiency that is calculated based on this piezometer's readings. By the numerical simulations using the finite element method.

## 2 The Grout Curtain in Mosul Dam Foundations

The bedrock that makes up the dam foundation consists of low-quality and soluble layers of karstic rock (marl, limestone, gypsum, and anhydrite). The layers of gypsum (gypsum breccia) and anhydrite are subject to dissolution over time, forming voids, cavities, and potentially large interconnected voids that could form large seepage paths the foundation. Water flow through the foundation rock can cause foundation and embankment materials to erode into these openings resulting in a collapse that could threaten the dam's ability to retain the reservoir water. The high dissolution rate of the gypsum/anhydrite at the Mosul dam site dictates that much more intensive monitoring and periodically grouting are needed for the dam to function as designed [9]. The original design for Mosul Dam incorporated a reinforced concrete grouting gallery at the base of the dam at the foundation/embankment contact on the dam's centerline for most of the dam's length. The grouting gallery provides direct access for grouting of the foundation under the impervious core of the dam without requiring drilling through the dam embankment. This gallery was intended to facilitate a continual maintenance grouting of the foundation for the life of the project to combat the formation of seepage pathways through the erodible foundation over time.

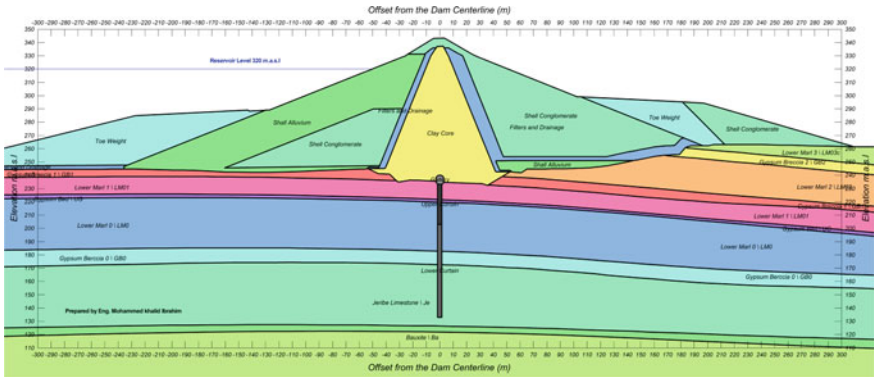


Fig. 2 The model in SEEP/W software for Mosul dam cross-section at km. 3200

### 3 Grout Curtain in Mosul Dam

The deep grout curtain in Mosul Dam was designed to extend along the centerline of the dam at the base of the core, from the grouting gallery (at the base of the embankment dam) and surface (from the service spillway to the East and on the West abutment). The gallery was specifically designed to deal with the considerable challenges posed by the karst foundation and allow repeated grouting efforts to continue over the dam’s lifetime. Deep grouting curtain consists of three rows of boreholes, downstream, upstream, and midstream. The distance between the upstream line and the downstream line is 1.2 m. The depth of the grouting curtain ranged from 80 up to 100 m, depending on the geological condition encountered. Figure 2 showing the geometry of the dam body and the grout curtain location at km 3200. Note that the top of the dam body is 340 m above sea level (m.a.s.l), and the highest operational level is 330 m above sea level (m.a.s.l).

### 4 Mosul Dam Instrumentation (Piezometers)

As part of the original design of Mosul Dam, a series of various instrument types were installed to monitor foundation dissolution/deterioration and project performance. One means of monitoring the project’s performance including the installation of piezometers to monitor the piezometric pressure, which is installed on the downstream side of the grout curtain or on both sides to monitor the behavior and performance of the curtain Figs. 4 and 5. Originally, installed instrumentation consisted of both a closed system (manually read piezometer from a manometer gauge) and an open system (manually read piezometer with a water level indicator/dip meter). Between 2015 and 2019, the Mosul Dam instrumentation program was vastly modified by the US Army Corps of Engineers (USACE) to improve the monitoring

capabilities of the project. Automated Data Acquisition System (ADAS) was newly installed to facilitate a much higher monitoring frequency. Also, the existing instruments were automated, and the installation of new automated instruments at critical monitoring locations. The number of Piezometers (sensors) is now up to 270. A customized instrumentation application was developed to aid in data management, processing, and plotting [10].

## 5 The Efficiency of the Grout Curtain

By constantly monitoring the readings of the piezometers. The performance of the grout curtain could be estimated; one method is the theoretical concept of net head dissipation (NHD), which gives an idea of the amount of seepage pressure dissipation (hydraulic gradient) between the two sides of the grout curtain. (NHD) values can be computed using the measured downstream piezometric pressure, reservoir elevation, and tailwater (River) elevation as shown in Eq. 1.

$$\text{Net Head Dissipated (NHD)\%} = (\text{R.L} - \text{DS Piez.})/(\text{R.L} - \text{T.L}) * 100 \quad (1)$$

where: -

US Piez. = Upstream Piezometers Water Total Head/T.L = Tailwater (River) Elevation.

DS Piez. = Downstream Piezometers Water Total Head/R.L = Reservoir Elevation.

When evaluating (NHD) values, decreasing downstream piezometric levels are reflected by increasing (NHD) values and vice versa. (NHD) values should remain constant through time (at the steady-state hydrostatic condition) unless boundary conditions change (e.g., installation or change in the efficiency of relief wells, upstream silting of seepage entrances, construction activity, clogging of toe drains, piping) [11]. In Mosul Dam, the Swiss construction consultant recommended that the same concept be used, but depending on the piezometer readings at the upstream side of the grout curtain instead of the reservoir level, to calculate the efficiency of the grout curtain (Ef) so the equation becomes as shown in Eq. 2.

$$\text{Grout Curtain Efficiency (Ef)\%} = (\text{US Piez.} - \text{DS Piez.})/(\text{R.L} - \text{T.L}) * 100 \quad (2)$$

This method requires the presence of two opposite sensors on both sides of the curtain (at the same depth and offset from the curtain). If only one sensor on the downstream side is located, the reservoir level relies on calculating the efficiency. This will lead to a difference in the comparison criteria from one location to another or from some geological layer to another geological layer in the same location.

## 6 Modeling the Dam in SEEP/W Software

In this study, the numerical simulation of the seepage conditions was considered for a cross-section in Mosul Dam at km 3200. The location of the cross-section is shown in Fig. 1. The model includes all the embankment material and the geological layers that form the dam’s foundation. The model was created and analyzed using the GeoStudio-2018 R2 (SEEP/W) software, which is based on the finite element method. Figure 2 shown the developed model.

To obtain the most accurate geometric representation of the cross-section under study. The construction drawings were used with geological investigations maps of the dam foundations during the construction period. With the help of other programs such as Geographic Information Systems (GIS) and (AutoCAD). Were used to obtain high accuracy in representing the details of the geometric shape for the cross-section under study [12]. As for the engineering properties, the embankment material is represented as a (Saturated/Unsaturated) material model. Where it was used (Sample functions) method to estimate the (Volumetric Water Content Functions). Van Genuchten’s method was used to estimate the (Hydraulic Conductivity Functions) [13]. The coefficient of permeability relied on the average results of in-site permeability tests of the embankment during the dam construction period. The soil–water characteristic curves predicted by (Van Genuchten) model for the embankment materials are shown in Fig. 3.

As for the geological layers of the foundations, they were represented as a saturated material model. The coefficient of permeability relied on the initial investigations of the dam site. The foundation strata are represented as an anisotropy material, ( $k_h/k_v$  Ratio) is the ratio of vertical to horizontal permeability usually, it is ( $k_h > k_v$ ) In the rock strata [14]. The model includes piezometers located at a distance of (25) meters from each side of the chosen cross-section at km 3200. (i.e., from 3175 to 3225 km). It represented as points in the model to calculate the total water head at these points. The grout curtain was represented according to the designer standards

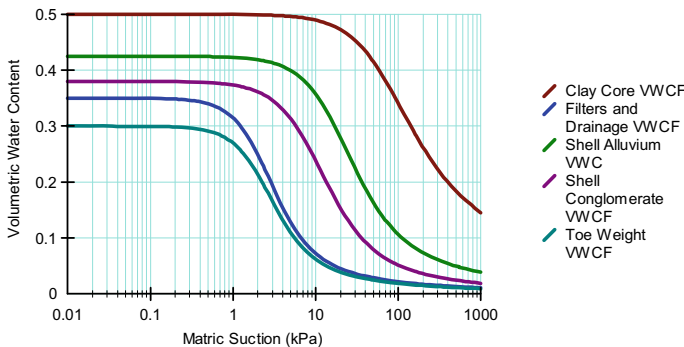


**Fig. 3** The soil–water characteristic curves for the embankment materials (generated by authors using SEEP/W)

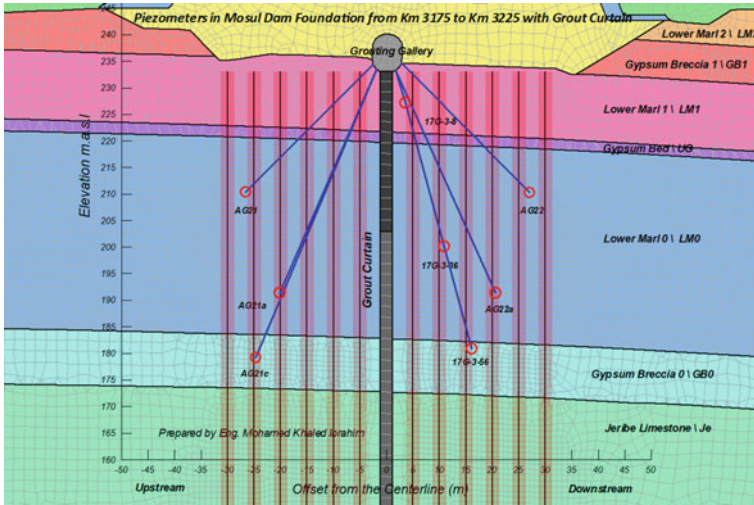


Fig. 4 Grout curtain, and piezometer's locations in Mosul Dam (km. 3200) (created by authors)

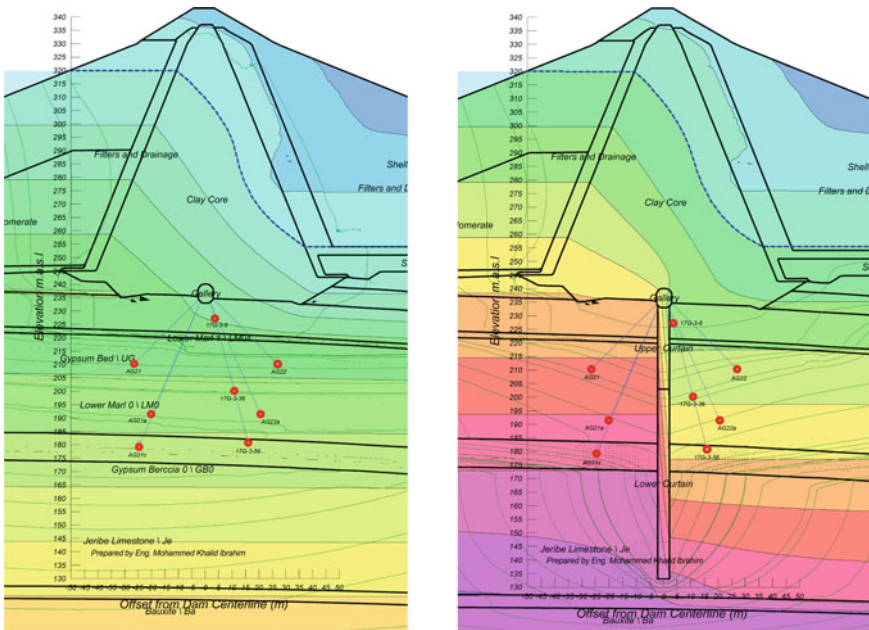


Fig. 5 The model analysis results show the Phreatic line and seepage paths and the gradient of the pore water pressure distribution, at the left side without grout curtain, at the right side with grout curtain



(Swiss Consultants). The depth is 100 m and divided into two parts (Upper Grout Curtain) and (Lower Grout Curtain). The depth and the coefficient of permeability for each part are as follows.

The Upper Grout Curtain from 0 to 30 m and its permeability  $\approx 2$  Lugeons  $\approx 2.6E-05$  (cm/s).

The Lower Grout Curtain from 30 to 100 m and its permeability  $\approx 5$  Lugeons  $\approx 6.5E-05$  (cm/s).

Where the Lugeon is defined as (one liter per minute of water injected into a one-meter length of the borehole at a pressure of ten bars) [15].

1 Lugeon = 1 LU  $\approx 1.3E-07$  (M/s)  $\approx 1.3E-05$  (cm/s) (Approx.)

The seepage analysis was done in steady-state conditions, and with fixed boundary conditions in upstream and downstream, the reservoir level is taken equal to (320 m.a.s.l  $\pm 0.5$  m), the tailwater level is taken equal to (254 m.a.s.l  $\pm 1$  m), the water head difference between upstream and downstream is 66 m in all analysis [16].

## 7 Analysis of the Model and Discussion of the Results

The model was analyzed in four cases. The first case was without the grout curtain. The rest cases were with the presence of the grout curtain with changing the thickness of the curtain (2.4, 3.2, and 4.2) meters, respectively. The thickness of the grout curtain depends on the grout penetration radius. The calculated pore water pressure at the same piezometers locations was recorded and compared with the real values that are recorded by the in-site piezometers through the Automated Data Acquisition System (ADAS). The comparison between the actual readings of the piezometers at the site and the results obtained using numerical modeling showed great convergence when the grout curtain thickness is 4.2 m, as explained in Table 1 that is evidence of the accuracy of the numerical model in representing reality.

The main goals of this research are to study the changes in the efficiency of the grout curtain in the dissipating of seepage pressure along with its depth, explain the effect of different geological strata with depth on the efficiency. Understanding the relationship between the efficiency of the curtain and the piezometers' location (the depth of the piezometer and the horizontal distance between it and the curtain). Using the numerical seepage model, the pore water pressure was calculated along with the depth of the grout curtain at every meter of the depth, and vertical lines parallel to the curtain, the distance (offset) between it and the curtain is (5, 10, 15, 20, 25, and 30) meter, respectively, and at both sides of the curtain as shown in Fig. 4. The efficiency and the net head dissipated (NHD) were calculated and plotted by using the pore water pressures from opposite points on the two sides of the grouting curtain and at different offsets from the curtain. For three Cases: The first case is without a grout curtain. The second case is with a 3.2 m thickness grout curtain. The third case is with a 4.2 m thickness grout curtain. In the first case, the model was analyzed without the

**Table 1** Comparison between the actual and SEEP/W piezometers readings around km 3200

Piezometer_Name	Locatin of piezometers			Upstream			Downstream		Piez. actual readings (m)			Seep/W readings water total head (m)		
	Section	Side	Offset X (m)      Y (m)	Reservoir Elev. $\pm$ 0.5 (m)	Tail Water Elev. $\pm$ 1 (m)	Max. Value	Min. Value	Average	Without curtain	Curtain thickness (2.4) (m)	Curtain thickness (3.2) (m)	Curtain thickness (4.2) (m)		
AG21b	89	Upstream	-25      179	320	254	315.1	314.07	314.54	289.03	301.47	315.45	315.83		
No Piez./imaginary	89	Downstream	25	320	254				288.85	274.66	259.17	258.75		
AG21a	90	Upstream	-20.16      191.43	320	254	317.32	316.13	316.63	289.33	301.6	315.58	315.97		
AG22a	90	Downstream	20.66      191.43	320	254	258.93	245.35	257.42	289.03	274.67	259	258.58		
AG21	91	Upstream	-26.57      210.31	320	254	320.35	317.93	319.31	290.42	302.97	315.98	316.34		
AG22	91	Downstream	27.01      210.26	320	254	257.87	256.79	257.08	289.4	273.96	258.69	258.27		
AG21c	91	Upstream	25      179	320	254	315.82	314.65	315.14	289.03	301.47	315.45	315.83		
17G-3-56	91	Downstream	16.03      180.85	320	254	257.97	256.83	257.2	288.88	274.67	259.17	258.75		
No Piez./imaginary	91	Upstream	-10.85      200.17	320	254				289.62	301.87	315.75	316.1		
17G-3-36	91	Downstream	10.85      200.17	320	254	252.96	251.76	252.44	289.35	274.54	258.86	258.44		
No Piez./imaginary	91	Upstream	-3.6      227.21	320	254				292.14	301.24	315.93	316.33		
17G-3-8	91	Downstream	3.6      227.21	320	254	257.01	255.3	256.1	289.8	277.15	259.18	258.6		

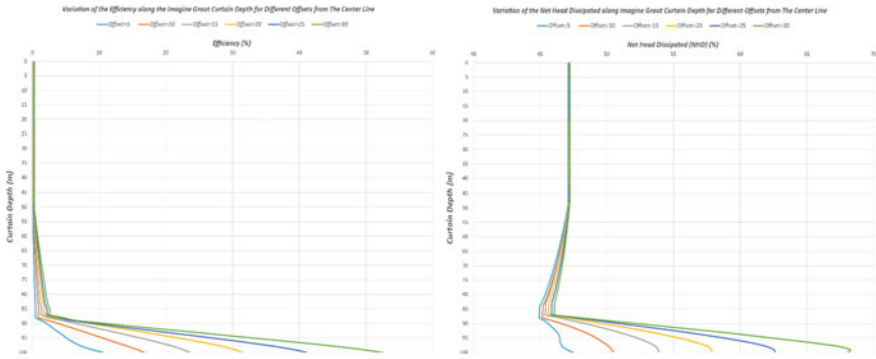


**Fig. 6** Variation of the efficiency and net head dissipated (NHD) along imagining grout curtain depth for different offsets from the centerline

presence of the grout curtain, as shown in Fig. 5 on the left side. The efficiency and the Net Head Dissipated (NHD) were calculated along the imaginary grout curtain.

The efficiency and (NHD) change were plotted along the grout depth and for a different distance (offset) from the centerline, as shown in Fig. 6. As expected, the efficiency is zero and for the different offsets. After the depth (90 m) the efficiency value will be increased according to the increased offset distance from the centerline. This unexpected increase took place due to the low permeability of the layer at this depth (Jeribe LimestoneJe), relative to the permeability of the layer above it (Gypsum Berccia\GB0), which leads to the curvature of the seepage paths, and a difference between the pore water pressures recorded on both sides of the imposed curtain. Thus, forming an imaginary efficiency. As for the behavior of the values of (NHD) with the depth of the curtain, it is noted that the initial value is around (47%). This is due to the continuous dissipation of seepage pressure along the seepage path that starts from the reservoir until it reaches its measuring location at the rear of the imaginary grout curtain. Of course, this value does not represent the effectiveness of the grout curtain alone in dissipating the seepage pressure.

In the second and third cases, the numerical model was analyzed with the grout curtain as shown in Fig. 5 on the right side and for two thicknesses of the grout curtain (3.2 m) and (4.2 m). The efficiency and (NHD) were also calculated and plotted in the same manner that was used in the first case. Noted from the variation of the efficiency values along the grout curtain depth, and for a different horizontal distance (offset) from the centerline, as shown at the left side of Figs. 7 and 8, there is a wide range of variation in the efficiency values along the grout curtain, where the efficiency values appear at a low value and increase almost linearly to the depth of (37 m). From this depth up to (62 m), the value of efficiency remains constant. After that, again, the efficiency values begin to decrease and almost linearly return to the initial values. It is also noted that the efficiency will increase with the increase of the displacement of the points used in the calculation from the grout curtain, vice versa.

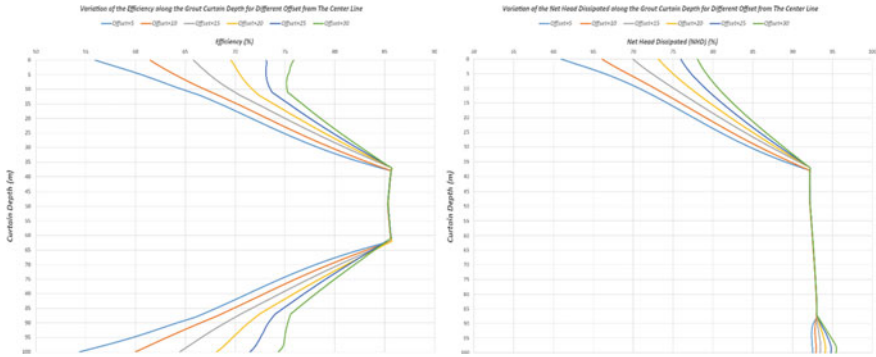


**Fig. 7** Variation of the efficiency and net head dissipated (NHD) along grout curtain depth for different offsets from the centerline (certain thickness 3.2 m)

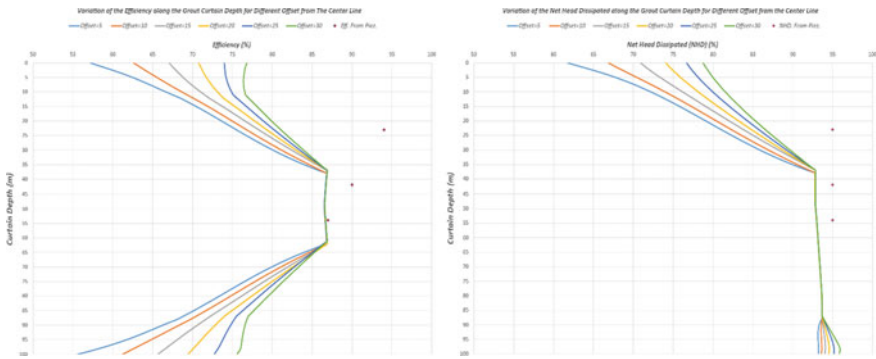


**Fig. 8** Variation of the efficiency and (NHD) along with grout curtain depth for different offsets from the centerline with the actual (Eff.) and (NHD) from the in-site piezometers readings (curtain thickness 4.2 m)

Concerning the variation of the Net Head Dissipated (NHD) values with the grout curtain depth, as shown at the right side of Figs. 7 and 8, the (NHD) values behave similarly to the efficiency values. As the values increase with the increase of the depth up to the center of (37 m) to become stable until the depth of (87 m). After, a slight difference in the values was recorded according to the offsets of the points from the curtain. This behavior was continued until the final depth. In Fig. 8, the real efficiency values calculated from the in-site piezometer readings were plotted with the piezometer depth as a small redpoint. It can be seen it gives higher efficiency values than the numerically calculated values, especially at the low depths, and the difference increases with the increase of the horizontal distance between the piezometer and the grout curtain. That because of considering an average value of the in-site piezometer readings for a long period. The model predicts the asymmetry of the seepage path on both sides of the grout curtain. This justifies the difference in the calculated efficiency and (NHD) values with the depth. This is to be expected because of the change in the

coefficient of permeability with the change of the geological strata. This leads to a change in the values of the pore water pressure on both sides of the curtain, and this difference increases with the increase of the horizontal distance (offset) between the piezometer and the grout curtain.

## 8 Conclusion

The method of numerical analysis and simulation of the grout curtain is advantageous in studying the behavior of the grout curtain where any change in its geometry could be studied separately, such as increasing the thickness, increasing the depth, or studying the effects of executing a new inclined curtain on the efficiency of the main curtain. The most important conclusion is the following.

- The Net Head Dissipated (NHD) concept does not represent just the efficiency of the grout curtain and the effect of the geological layers in the dissipation of the pressure along the seepage path. The numerical analysis model without the grout curtain gives a value for the (NHD) (45%).
- The best location to install the piezometer is near the grout curtain. Whenever the piezometer is closer to the grout curtain, it gives a more accurate idea of the curtain situation. It was observed that the difference in efficiency at some depths is about 20% when the horizontal distance between the piezometer and the grout curtain is from 5 to 30 m.
- The calculated efficiency from the piezometer readings represents the situation of the grout curtain just at the level where the piezometer is located. And it is illogical to generalize this efficiency to the entire depth of the curtain.
- The efficiency value of the grout curtain varies with the depth of the curtain between (10%) and (30%).
- To obtain an accurate assessment of the efficiency of the grout curtain. The curtain efficiency of each geological layer should be evaluated independently from the rest of the geological strata.
- The efficiency values calculated from the in-site piezometer's readings gave (7%) higher values than those calculated using the numerical model because of considering an average value of the in-site piezometer readings for an extended period.

## References

1. Adamo, N., & Al-Ansari, N. (2016). Mosul dam the full story: Engineering problems. *Journal of Earth Sciences and Geotechnical Engineering*, 6(3), 213–244.
2. Khattab, S. A., & Khalil, A. A. (2013). Numerical modeling of pore water pressure development in MOSUL dam. *Journal of Engineering and Technology*, 31(4).

3. Khattab, A. (2010). Stability analysis of Mosul dam under saturated and unsaturated soil conditions. *Al-Rafidain Engineering Journal (AREJ)*, 18(1), 13–27.
4. Irzooki, R. H. I., & Hasan, A. A. (2012). Seepage evaluation of Mosul Earth Dam. *Anbar Journal of Engineering Sciences*, Special issue, (In Arabic).
5. Adamo, N., Al-Ansari, N., Issa, I., Sissakian, V., & Knutsson, S. (2015). Mystery of Mosul dam the most dangerous dam in the world: Foundation treatment during construction. *Journal of Earth Sciences and Geotechnical Engineering*, 5(3), 59–69.
6. Owen, P. E. (2017). Engineering and design grouting technology. Washington, DC 20314-1000: US Army Corps of Engineers, Manual No. 1110-2-3506.
7. Elgadir, M. A. S. (2019). Assessment of curtain grouting used in the foundation treatment at dam complex of upper AtbaraRiver (Doctoral dissertation, Sudan University of Science and Technology).
8. Saif, A., & Ahmed Sheikh, K. (2020) Design of grout curtain for temporary embankments on rock foundation. *Geomechanics and Geoengineering*, 1–16.
9. Hlepas, G., Bateman, V., & Robison, L. (2020). 2017-2019 investigations of subsurface conditions at Mosul Dam. In *U.S. National Committee of ICOLD USSD 2020 Annual Conference*, 20–24 April 2020. USA, Denver: Denver Convention Center.
10. Hlepas, G., Paniagua, V., & Malavolta, M. (2020). Fully grouted vibrating wire piezometer installations in artesian and karst conditions at Mosul Dam. In *U.S. National Committee of ICOLD USSD 2020 Annual Conference*, 20-24 April 2020. USA, Denver: Denver Convention Center.
11. Federal Emergency Management Agency (FEMA). (2015). Evaluation and monitoring of seepage and internal erosion. In *Interagency Committee on Dam Safety, Interagency Committee on Dam Safety (ICODS)* (1st ed., Vol. 8, no. 5, pp.13–16).
12. Rosen, J. B., Bachus, R. C., Siebenmann, R., Carr, P., & Rathburn, C. (2012). Using GIS to track, visualize, analyze and report grouting data. In *Grouting and Deep Mixing 2012* (pp. 1013–1022).
13. Geo-Studio. (2015). User guide, seepage modeling with SEEP/W, An engineering methodology, June 2015 Edition, GEO-SLOPE International Ltd.
14. Walshire, L. A., & Robbins, B. A. (2017). SWCC prediction: Seep/W add-In functions. Geotechnical and Structures Laboratory (US).
15. Quiñones-Rozo, C. (2010). Lugeon test interpretation, revisited. In *Collaborative management of integrated watersheds* (pp. 405–414).
16. GEOSLOPE International Ltd. (2017). *Heat and mass transfer modeling with GeoStudio 2018* (2nd ed.). Calgary, Alberta, Canada.

# Stability of Slopes Under Unsaturated Conditions Using a Modified Upper Bound Theorem



Bestun J. Shwan

**Abstract** It has been widely accepted that the contribution of suction stress has a considerable influence on the mechanical characteristics of soils. This contribution has demonstrated suction stress's ability to impart strength to many geotechnical structures such as slopes and vertical cuts through partial saturation. This paper, therefore, reports a numerical study of the suction influence on the mechanical characterization of a slope at various saturation conditions using an upper bound theorem modified by the author. Therefore, a parametric study was carried out to examine the influence of the suction at various  $\phi'$  and  $c'$  on the stability number (N). A substantial decrease in N was obtained for unsaturated cases when compared to the full saturation. This was over and above that can be expected due to a slight rise in shear strength parameters. A decrease of  $\sim 34.1\%$  in N, equivalent to an increase of  $\sim 1.52$  fold in factor of safety at  $\phi' = 30^\circ$  and  $c' = 5$  kPa, was obtained when the water table dropped 3 m from the surface (full saturation). This was equivalent to model the fully saturated case at  $\phi' = 30^\circ$  but with  $c' \approx 9$  kPa. Failure mechanisms were also studied using a variety of cases where a considerable role of suction was obtained.

**Keywords** Unsaturated · Suction · Numerical analysis · Upper bound · Slope stability

## 1 Introduction

Many geotechnical applications such as slopes, tunnels, vertical excavations, retaining walls, and footings can be encountered in unsaturated conditions as a result of seasonal changes. The unsaturated conditions impart additional strength due to partial saturation and surface tension, and subsequently, these applications can stand up for a longer time, e.g., higher strength. However, uncertainties related to the unsaturated conditions have led to assume dry/saturation conditions above the water table. To overcome these uncertainties, significant attention to unsaturated soil mechanics

---

B. J. Shwan (✉)

Department of Geotechnical Engineering, Koya University, KOY45, Kurdistan Region, Koya, F R, Iraq

e-mail: [bestun.shwan@koyauniversity.org](mailto:bestun.shwan@koyauniversity.org)

by scholars has been received in the last four decades. For example, slope stability problems under various saturation conditions have been studied, e.g. [1–4]. Although the researchers' considerable contribution, however, applications of computational limit analysis (LA) based on a rigorous upper bound theorem to unsaturated slope problems have also been limited.

Therefore, this paper aims to examine the effects of partial saturation on slope stability numerically using an upper bound theorem, discontinuity layout optimization (DLO) modified by the author. A parametric study is carried out to investigate the effect of various saturation conditions on strength and the failure mechanism for a simulated soil.

## 2 Modified DLO Approach

Shwan [5] extended the DLO approach to consider for unsaturated conditions as follows:

$$\min \mathbf{FL}^T \mathbf{d} = -\mathbf{D}^T \mathbf{d} + \mathbf{f}^T \mathbf{p} + U_i n_i \quad (1)$$

where  $F$  is the adequacy factor,  $L^T$  and  $D^T$  are the live and dead loads, respectively,  $\mathbf{d}$  is a matrix that contains displacement vectors,  $\mathbf{f}^T$  corresponds to dissipation coefficients,  $n$  is the normal displacement, and  $U$  is the pore water pressure and subjected to, as it is proposed by [5]:

$$U = - \int_0^L s S_r \tan \varphi' dl \quad (2)$$

where  $s$  and  $S_r$  (given by Eq. 3) are suction and degree of saturation for a discontinuity of length ( $L$ ), respectively, and  $\varphi'$  is the effective internal friction angle. Equations 1 and 2 were implemented in the research version of LimitState :GEO software, and then the modified version of the software was utilized to carry out a parametric study into the effect of various suction profiles of a slope stability problem.

## 3 Modeling Unsaturated Condition

The simulated material used in this study represented a fine sand. Equation 3 [6], is used to determine the soil water retention curve (SWRC) for the simulated sand:

$$S_r = \exp^{-\xi \times (s - \kappa)} \quad (3)$$



where  $\xi$  is a fitting parameter ( $\text{kPa}^{-1}$ ) and  $\kappa$  is the air entry suction ( $\text{kPa}$ ), related to capillary rise height, ( $H_c = \kappa/\gamma_w$ ), where  $\gamma_w$  is the unit weight of water, see [5] for more detail. Figure 1 displays the (SWRC). The obtained  $\kappa$ ,  $\zeta$  and residual suction are 15, 0.05  $\text{kPa}^{-1}$  (best fit), and  $\sim 70 \text{ kPa}$ , respectively, see Fig. 1. Sands attain the residual suction at suction  $< 200 \text{ kPa}$  [7].

Figure 2a depicts the schematic diagram of the modeled slope. The analysis was carried out for a  $45^\circ$  slope at a drained condition for a range of saturation (suction) cases. In the simulation, suction was applied by lowering the water table's position ( $H_w$ ) from the surface. This corresponded to lowering  $H_w$  from 3 m (from the surface-fully saturated case) to four different  $H_w$ : 0 (origin),  $-1$ ,  $-2$ , and  $-3 \text{ m}$ , see Fig. 2a. Dry, unsaturated, and saturated unit weights were 15, 17.5, and  $20 \text{ kN/m}^3$ , respectively. A series of effective angles of shearing resistance values ( $\phi' = 30, 35$ ,

**Fig. 1** SWRC for the simulated sand

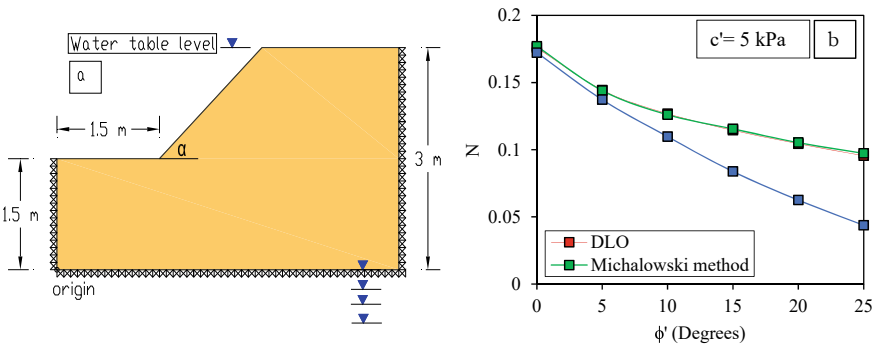
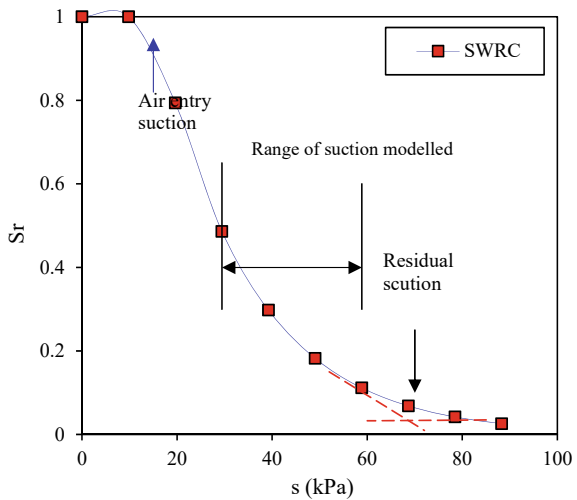


**Fig. 2** a Problem geometry for the slope case study. b Validation of DLO approach against Taylor and Michalowski's methods

40, and 45°) at different effective cohesion ( $c'$ ) values were utilized for each case. In the simulation, the soil was considered as fully saturated until  $H_c$ . Above  $H_c$ , an unsaturated condition was considered for 1 m. Above this 1 m, the soil was modeled as fully dry. The DLO approach was, then, validated against [8, 9] methods for the same geometry shown in Fig. 2a at a dry condition for a range of  $\phi'$  and  $c' = 5$  kPa. The results are shown in Fig. 2b, where  $N$  is the stability number, obtained using Eq. 4:

$$N = \frac{c'}{\text{FOS} \times \gamma \times H} \quad (4)$$

where FOS is the factor of safety and  $H$  is the slope's height (1.5 m). Michalowski's method is based on LA's kinematic approach, where a rigid rotational collapse mechanism is considered. Excellent agreement of DLO with the Michalowski's method is obtained. In addition; the validation with the Taylor method [8], an approach that is often utilized as a tool for the first assessment of a slope, shows considerable agreement at low  $\phi'$ . However, the agreement diverges at higher  $\phi'$  values. The main reason is attributed to the constraint associated with the Taylor method. The failure mechanism is pre-determined and passes through the toe. However, DLO considers various rupture circles at toe and extends beyond the toe for the modeled  $\phi'$  values.

## 4 Numerical Results

The numerical results for the modeled scenarios are shown in Fig. 3. The results were presented in terms of stability factor ( $N$ ), except for the case when  $c' = 0$  (gives  $N = 0$ ) was presented as FOS. For  $H_w = -1$  m at  $\phi' = 45^\circ$ , it was not possible to obtain a solution as DLO returns to "Locked" results which are accredited to a highly constrained geometry with a large  $\phi'$ . In other words, for a purely frictional soil, the problem is either locked or unstable. There is only one value of  $\phi'$  where it is at the point of collapse. A significant increase in FOS was obtained for unsaturated cases, Fig. 3a, compared to the saturated condition well in excess that can be predicted due to increased shear strength parameters. For example, at  $\phi' = 30^\circ$  and  $c' = 0$  kPa (see Fig. 3a), an increase of  $\sim 4.7$  fold in FOS was obtained when  $H_w = -1$  m compared to  $H_w = 3$  m (fully saturated case). This was equivalent to about a 5.7 kPa increase in  $c'$  if the case  $H_w = 3$  m was modeled at  $\phi' = 30^\circ$ . The range of increase here is almost identical to that obtained by [10] (4–6 folds) and [6] (4–10 folds) for bearing capacity problems. For all cases, the minimum stability number ( $N$ ), which corresponded to a maximum FOS, was obtained at  $H_w = -1$  m. This was attributed to the effect of suction stress ( $s_{S_r}$ ) in Eq. 2 and hence a higher FOS ( $F$ ) in Eq. 1. It can be prudent to investigate for point of interest in which  $\text{FOS} = 1$  (the case where the slope is at the ledge of failure) which provides the critical height ( $H_{\text{critical}}$ ).  $H = 1.5$  m is a critical height if  $\phi'$  is reduced by  $\sim 20.7^\circ$  (from  $30^\circ$ ) at  $c' = 0$  kPa for  $H_w = -1$  m.

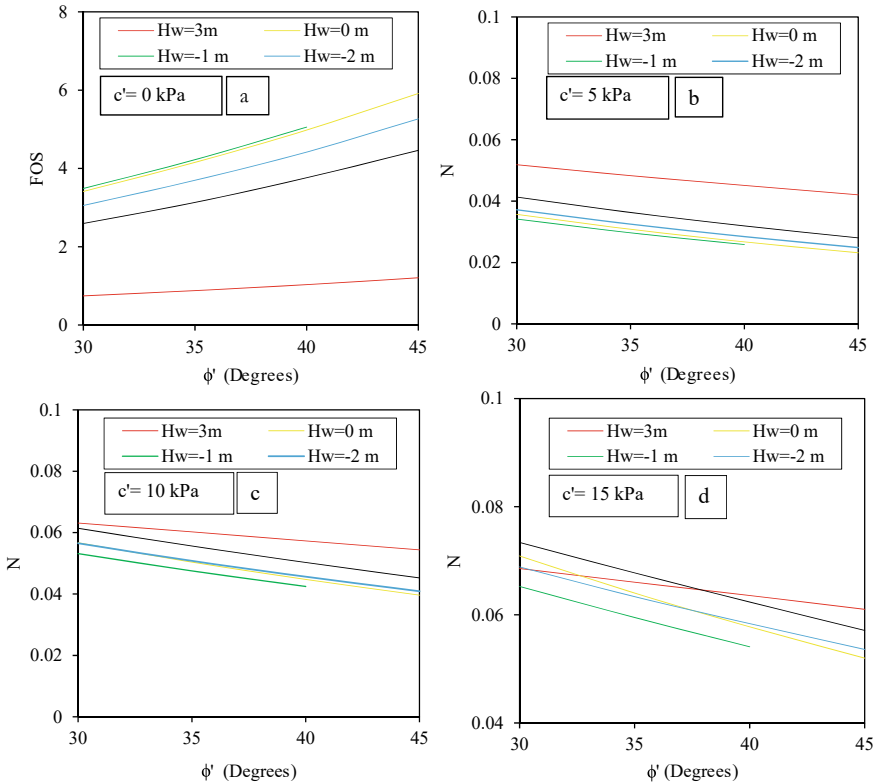


**Fig. 3** Results of various saturation scenarios at different  $c'$  values

Beyond  $H_w = -1$  m,  $N$  increased due to stability reduction induced desaturation, e.g., at the residual saturation due to low water content, the transmission of suction to the reduced aggregate particles did not complete effectively. This increase in  $N$  was also shown in Fig. 3b, c, and d and further clarified in the design chart in Fig. 4a when  $H_w = 0$  m compared to  $H_w = -3$  m where the latter provided higher  $N$  values and therefore lower FOS. For example, at  $c' = 10$  kPa, an increase in  $N$  by  $\sim 8.3\%$ , lower FOS, was obtained when  $H_w$  dropped from 0 m to  $-3$  m. This was equivalent to the rise of  $4^\circ$  in  $\phi'$  if  $H_w = -3$  m was modeled to put this into context. Finally, the role of suction on the failure mechanisms was also studied where  $H_w = 3$  m was compared to  $H_w = -1$  m and plotted in Fig. 4b–e. Different cases were considered: at various  $\phi'$  and  $c'$  values for a constant suction, and various applied suctions at constant  $\phi'$  and  $c'$ . All the failure mechanisms intersected with the toe due to the slope's steep inclination ( $\alpha = 45^\circ$ ). The influence of  $c'$  was seen to be more effective than  $\phi'$  where the former showed wider failure mechanisms. However, a considerable role of suction on failure mechanisms was seen when  $H_w = 3$  m compared to  $H_w = -1$  m, see Fig. 4d. The wider and deeper mechanisms for  $H_w = -1$  m was attributed to the larger effective stresses and implied lower  $N$  value (higher FOS).

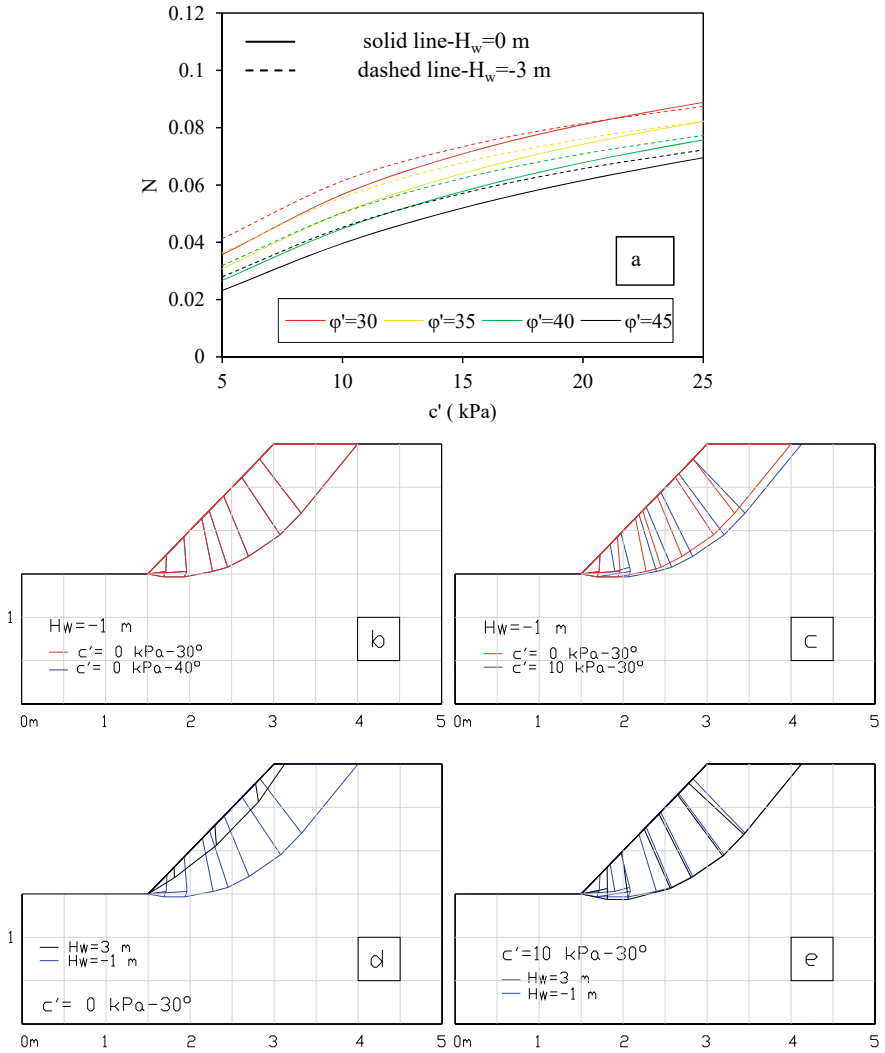


**Fig. 4** a  $N$  at different  $c'$  at two different  $H_w$ . **b-d** Different failure mechanisms for a variety of cases

## 5 Conclusions

The suction and degree of saturation's ability to impart strength to many geotechnical applications such as slopes through partial saturation are significant. This paper examined the influence of suction and degree of saturation on the mechanical characterization of a slope at various saturation conditions using a modified upper bound theorem. The influence of the suction, at various  $\phi'$  and  $c'$ , on the factor of safety (FOS) was

examined using a parametric study, and a set of design charts was produced. FOS was seen to rise for the unsaturated condition compared to the full saturation and then followed by a decrease. An increase of  $\sim 4.7$  fold in FOS, at  $\varphi' = 30^\circ$  and  $c' = 0$  kPa, was obtained when  $H_w$  dropped from fully saturated to 3 m below the surface. This increase was equivalent to about a 5.7 kPa increase in  $c'$  if the fully saturated case was modeled at  $\varphi' = 30^\circ$ . The effect of a number of modelled scenarios on the failure mechanisms was also produced using the modified DLO approach, where the role of suction was seen to be significant.

## References

1. Zhang, L. L., Fredlund, D. G., Fredlund, M. D., & Wilson, G. W. (2014). Modeling the unsaturated soil zone in slope stability analysis. *Canadian Geotechnical Journal*, 51(12), 1384–1398.
2. Qi, S., & Vanapalli, S. K. (2015). Hydro-mechanical coupling effect on surficial layer stability of unsaturated expansive soil slopes. *Computers and Geotechnics*, 70, 68–82.
3. Lin, H., & Zhong, W. (2019). Influence of rainfall intensity and its pattern on the stability of unsaturated soil slope. *Geotechnical and Geological Engineering*, 37(2), 615–623.
4. Wang, L., Chen, B., & Li, J. (2019). Three-dimensional seismic stability of unsaturated soil slopes using a semi-analytical method. *Computers and Geotechnics*, 110, 296–307.
5. Shwan, B. J. (2015). Experimental and numerical study of the shear strength of unsaturated sand. Doctoral dissertation, University of Sheffield.
6. Shwan, B. J., & Smith, C. C. (2014). Application of limit analysis in unsaturated soils: numerical and experimental study of bearing capacity. In *Unsaturated Soils: Research and Applications- Proceedings of the 6th International Conference on Unsaturated Soils, UNSAT 2014*.
7. Vanapalli, S. K., Fredlund, D. G., Pufahl, D. E., & Clifton, A. W. (1996). Model for the prediction of shear strength with respect to soil suction. *Canadian Geotechnical Journal*, 33(3), 379–392.
8. Taylor, D. W. (1937). Stability of earth slopes. *Journal of Boston Social Civil Engineers*, 24(3), 197–247.
9. Michalowski, R. L. (2002). Stability charts for uniform slopes. *Journal of Geotechnical and Geoenvironmental Engineering*, 128(4), 351–355.
10. Steensen-Bach, J. O., Foged, N., & Steenfelt, J. S. (1987). Capillary induced stresses—fact or fiction. In *European Conference on Soil Mechanics and Foundation Engineering* (vol. 9, pp. 83–89).

# Monitoring of the Western Breakwater of Al-Faw Grand Port-South of Iraq Using Differential InSAR-ISBAS Technique



Lubna Alshammari and Omar Natiq Mohammed

**Abstract** While ports are gateways to the country's transportation networks, breakwaters protect port entry channels into and out of the ports. Therefore, such structures require regular monitoring to keep the port functioning. This paper investigates the use of the Intermittent Small Baseline Subset (ISBAS) DInSAR technique to monitor the deformation and the stability for the western breakwater of Al-Faw Grand Port in the south of Iraq (the longest breakwater according to Guinness World Records). The preliminary results exposed by high and low resolution (ISBAS) analysis are presented using the Sentinel-1 SAR dataset from May 2017 to January 2019. The analysis of ISBAS results shows deformation, particularly in the northern part of the western breakwater while the rest are stable. The study shows that the low-resolution ISBAS method (suitable to monitor a natural surface) can give excellent results, highly comparable to high-resolution (convenient for the analysis of infrastructures) for monitoring large structural systems such as breakwater. This can provide crucial information on the potential of using the ISBAS technique (high and low-resolution) for long-term breakwater monitoring and give new insights into the behavior of the breakwater structure where other monitoring data are lacking.

**Keywords** Interferometric SAR · Intermittent SBAS (ISBAS) · Breakwater · Deformation · Monitoring

## 1 Introduction

The long-term monitoring of breakwaters is of considerable interest to the designers, builders, and authorities responsible for understanding the maintenance requirements

---

L. Alshammari (✉)

Faculty of Engineering, Al-Mustansiriyah University, Baghdad, Iraq

e-mail: [Lubna.alshammari@uomustansiriyah.edu.iq](mailto:Lubna.alshammari@uomustansiriyah.edu.iq)

O. N. Mohammed

Nudhum Al-Omran Company for Consultancy Services, Baghdad, Iraq

e-mail: [omar.nmohammed@naoconsultancy.com](mailto:omar.nmohammed@naoconsultancy.com)

and keeping the port functioning. Depending on the marine environment, the breakwater will deteriorate in time if not properly maintained. The deterioration of the breakwater can be related to the external events which probably lead to cause deformation (severe damage or failure) such as foreshore erosion due to waves attack, settlement of core and subsoil due to currents, sliding failure of slopes or mound (depending on the type of the breakwater) due to Tsunamis, and uplift of backfill due to earthquake. Consequently, breakwater damage or failure often is due rather than to any single factor to a combination of circumstances, and it is important to recognize the exact causes of this failure as precisely as possible. If this is not done, the risk of additional damage or failure for the same unidentified reasons will be high [1]. Therefore, detection of deterioration such as the deformation along the breakwater structure is essential [2]. Monitoring of breakwaters provides an early warning system to detect any weak parts before the breakwater stability is threatened.

Additionally, breakwater monitoring is valuable for understanding possible breakwater failure mechanisms and their role in existing sea conditions and the supports that the breakwater rests on. Several monitoring techniques have been adopted for structural health monitoring, such as contact (sensor) methods and traditional geodetic surveying techniques (leveling and DGPS) [3]. However, these techniques provide the deformation information/data only for separated points on selected locations of the structure. The Differential Interferometric Synthetic Aperture Radar (DInSAR) has proved to be a powerful tool for surface deformation monitoring, capable of monitoring large areas at low cost at spatial scales impossible to achieve using conventional ground measurements over inaccessible regions [4]. Due to these advantages and characteristics, DInSAR techniques have been successfully applied to the monitoring of landslides [5], land subsidence [6], volcanic activity [7], and anthropogenic activity like tunneling [8]. However, the density and distribution obtained by DInSAR measurements can be extremely affected by phase decorrelation or incoherence [9] which is most prevalent over vegetated areas, semi-natural lands, and wetlands. This limits the DInSAR algorithms that support the deformation monitoring, such as Persistent Scatterer Interferometry (PSI) and Small Baseline Subset (SBAS) method. Although the SBAS method has proved to produce reliable results over areas unfavorable for DInSAR analysis (e.g. [10]), the distribution and density of the measurements are still restricted [11]. Moreover, the availability of data has been an additional limitation, as it is critical to obtain adequate data acquisitions during the deformation event with a suitable revisit period for a reliable analysis.

The development of the Intermittent Small Baseline Subset ISBAS DInSAR technique [12, 13] and the launch of Sentinel-1 satellite that increases data availability have the potential to overcome the major DInSAR limitation. The ISBAS technique is a modified version of the SBAS method [14] that can provide sufficient spatial coverage at millimeter-level accuracy over unfavorable land cover types such as bare soils and vegetated areas [15]. The ISBAS technique can also provide both high-resolution of the input SAR image, which is convenient for the analysis and monitoring of infrastructures or any phenomena that requires great observation detail (e.g. [16]), and low-resolution that is suitable to monitor a natural surface such

as forest canopies [17]. ISBAS is a multi-temporal technique that aids in eliminating the atmospheric component’s contribution to the observed phase difference and subsequent ground displacement measurements [18]. The ISBAS method has previously been used to monitor ground deformation due to groundwater abstraction [13], underground coal mining [19], wetland condition [4, 17, 20], and infrastructure monitoring [16]. In this study, freely available Sentinel-1 C band SAR images with a repeat cycle of 12 days (increased to 6 days over Europe) acquired between May 2017 and January 2019 were processed using low and high-resolution ISBAS technique to monitor surface deformation over the western breakwater of Al-Faw Grant Port, South of Iraq. The results were analyzed and compared to evaluate the ability of the low-resolution ISBAS technique compared to a high-resolution approach for breakwater deformation monitoring.

## 2 Study Area

Al Faw Grand Port is located in the north end of the Arabian Gulf and a short distance west of Shatt Al-Arab outlet. The project area is about 5–10 km South of Al Faw city, approximately 80 km South- East of Al-Basrah city, facing Bubiyan Island’s Kuwaiti area of Khawr Abd Allah [21]. The port layout (Fig. 1a) shows that the port will be developed partly in the intertidal zone and partly offshore. Two breakwaters bound the port; the eastern is about 8 km north–south, and the western is approx. 16 km long from the northwest to the southeast of the port location (Fig. 1b). In 2013,

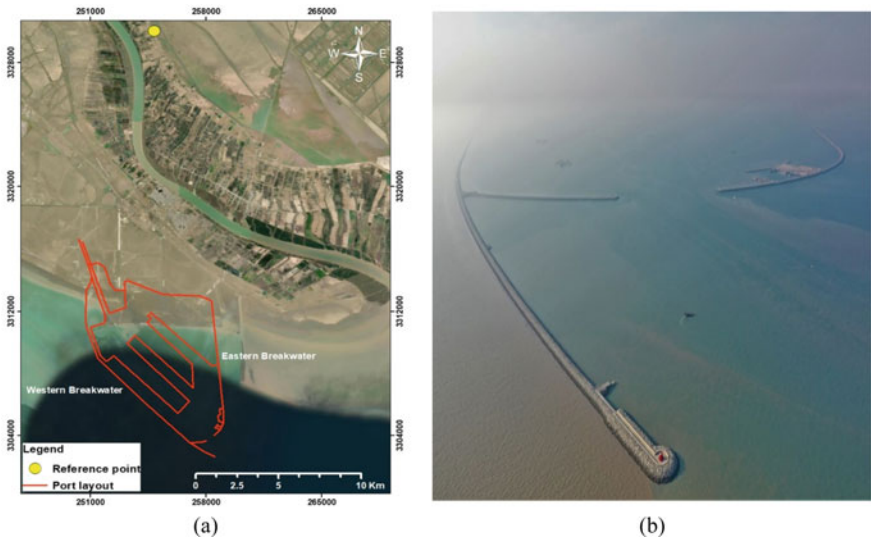


Fig. 1 a New Al Faw port breakwaters layout [21]. b The construction of the western breakwater



the construction works of the western breakwater (16 m long) were started. The period of construction is 36 months from the groundbreaking [22]. The breakwater infrastructures are placed on mudflats, which are compressible soil that may cause a considerable settlement during the breakwater construction at such a tidal flat site [23]. Consequently, long-term monitoring is required to monitor the breakwater’s stability and distinguish deformation due to significant storms or other causes from the theoretic settlements [24].

**Site Conditions.** The geological history of the port area followed the region’s history where Shatt Al-Arab river flows into the Arabian Gulf. However, this region has been influenced by the massive action of the Shatt Al-Arab river and marine sedimentation processes [25]. Although the tidal flat deposits are widely distributed across this region, the New Port structures and infrastructures will be built on. The project’s location lies closely in the northern coastal region of the Arab Gulf on the far end of the Mesopotamian Plain (Fig. 2), the geomorphic units of the Mesopotamia Plain are classified according to their geomorphic position. The Marine Origin forms the most southern part of this plain, which can be found as an accumulation type represented by tidal flat (mudflat) [26]. However, this tidal flat is the muddy coastal shore of the head of the Arabian Gulf. Besides, it lies in the intertidal zone, which is between high and low tide, ranging between (1–1.5) m [26, 27]. Therefore, in such projects, the evaluation of the main geotechnical issues (stability and settlement) should be considered during the design, construction, and operation of the port [28].



Fig. 2 Location map of the Mesopotamia plain [26]

### 3 DInSAR Data and Analysis

A stack of 50 Sentinel-1 IW SLC C-band (5.6 cm wavelength, 5.3 GHz frequency) SAR images acquired in ascending orbit (track 174) from 22 May 2017 to 12 January 2019 were used in the processing and listed in Table 1 along with the perpendicular orbital baseline relative to the reference image (master image) (22 May 2017). All images were downloaded from the open-access data hub, and only the VV polarization mode was used during processing. The dataset was processed using the low and high-resolution ISBAS DInSAR technique [13, 16] to examine the annual velocity of surface motion and its standard error detected during the respective monitoring period across Al-Faw Grand Port, South of Iraq. Using the Shuttle Radar Topography Mission (SRTM) digital elevation model (DEM), the DInSAR results were projected to a Universal Transverse Mercator (UTM). The ISBAS technique is a modified version of the widely-used SBAS algorithm [19, 29]. It was created to improve the distribution and density of the measurements in vegetated areas where traditional DInSAR algorithms (such as SBAS) typically fail because of incoherence [30].

All Sentinel-1 images were co-registered to the reference master scene obtained on 22 May 2017 with sub-pixel precision. The average LOS velocities for each ISBAS pixel from low and high-resolution ISBAS processing were calculated using

**Table 1** Sentinel-1 images dates and perpendicular baseline (B<sub>⊥</sub>) relative to the master image (22-05-2017)

Date	B <sub>⊥</sub>	Date	B <sub>⊥</sub>	Date	B <sub>⊥</sub>
2017-05-22 (Master)	0.000	2017-12-24	66.291	2018-07-16	11.145
2017-06-03	-47.668	2018-01-05	50.671	2018-07-28	56.255
2017-06-15	-9.962	2018-01-17	61.300	2018-08-09	50.275
2017-06-27	2.907	2018-01-29	74.889	2018-08-21	-20.434
2017-07-09	67.565	2018-02-10	-12.219	2018-09-02	-102.387
2017-07-21	44.466	2018-02-22	-18.171	2018-09-14	-10.641
2017-08-02	-30.835	2018-03-06	15.520	2018-09-26	32.558
2017-08-14	-85.610	2018-03-18	41.441	2018-10-08	66.876
2017-08-26	-15.750	2018-03-30	42.489	2018-10-20	-22.329
2017-09-07	87.516	2018-04-11	7.619	2018-11-01	-55.108
2017-09-19	17.876	2018-04-23	-13.440	2018-11-13	-27.703
2017-10-13	-85.023	2018-05-05	18.104	2018-11-25	67.011
2017-10-25	-65.847	2018-05-17	10.792	2018-12-07	30.250
2017-11-06	46.475	2018-05-29	31.107	2018-12-19	107.330
2017-11-18	45.399	2018-06-10	-20.515	2018-12-31	17.996
2017-11-30	61.737	2018-06-22	-11.195	2019-01-12	-23.029
2017-12-12	51.098	2018-07-04	77.001		

maximum orbital and temporal baselines of 250 m and 6-months, respectively. To minimize noise and improve coherence, the low-resolution ISBAS processing was used with multi-looking factors of 6 in azimuth and 21 in range resulting in pixels with a ground resolution of about 100 m. Using the constraints of the baselines above a set of 500 multi-looked differential interferograms were generated. These constraints minimize the decorrelation in the resulted interferograms spatially and temporally, thus improving the coherence and the quality of the resulted phase and reducing the contribution of the digital elevation modal (DEM) errors in the resulted interferograms [4].

The analysis of the standard coherent scatterer was applied on the multi-looked data so that only pixels that have an average coherence of greater than 0.25 across all interferograms were considered in the processing. This describes the SBAS technique [31]. However, the ISBAS technique specifies appropriate pixels for the processing by integrating the coherence with a minimum quality criterion [12]. Specifically, a pixel with a coherence of greater than 0.25 in a minimum interferogram is preserved for later processing allowing the analysis of intermittent coherent pixels in the data. The threshold of the minimum interferograms permits a trade-off between the density of the derived pixels and the accuracy of the deformation measurements retrieved. The results are more accurate for a larger number of interferograms, but the measurements' distribution is sparser. The best threshold value can be determined from the empirical relationship between the ISBAS velocity standard error and interferograms used [29]. For low-resolution ISBAS processing, the minimum interferograms used was 200.

The high-resolution ISBAS processing is the same as low resolution. However, to improve both the spatial resolution and the quality of the derived pixels, the multi look factors of  $2 \times 7$  (azimuth  $\times$  range) was used to generate pixels with a ground resolution of 20 m. A minimum of 380 interferograms with coherence greater than 0.45 was considered in the processing. Before using statistical models for cost functions algorithm [32] to unwrap both SBAS and ISBAS points within each differential interferogram, the simulated topographic phase was removed using the 90 m Shuttle Radar Topography Mission (SRTM), digital elevation model [33]. The mean linear velocity for each ISBAS pixel was then calculated relative to a reference point with coordinate (254,823 E, 3,330,009 N) located in a small village (high coherence area) north Al-Faw city (Fig. 1a). All ISBAS velocity results are in the line of sight (LOS) direction, moved towards or away from the radar sensor. Positive LOS velocities indicate surface uplift (or heave) whilst negative velocities represent surface subsidence.

## 4 Results and Discussion

Mean linear (LOS) velocity ground measurements were derived using the high and low-resolution ISBAS technique. From both cases, the ISBAS results show ground surface displacements spread along the northern part of the western breakwater for the

period May 2017–January 2019 (Figs. 3a and 4b); this deformation is not completely detected using a small baseline subset SBAS approach (Fig. 3b), which covers 62% of the processed area compared with 91% using ISBAS technique. The processed data using the high-resolution ISBAS method reveals surface deformation in the northern part of the western breakwater with deformation rates of up to  $-0.025$  m/year (Fig. 4a and 4b). The rest parts of the breakwater are stable.

This irregular velocity in the northern part of the breakwater may probably due to some geotechnical issues or intermittent storm damage during the monitoring period. Although the resulting pixel densities using high-resolution ISBAS cannot be compared numerically with the low-resolution (Figs. 4a and 3a) [29] (due to the nature of the low-resolution ISBAS results, which are in the form of points located at the center of  $\sim 100$  m by 100 m), a similar pattern of the displacements is observed using low-resolution ISBAS technique. The difference in the magnitudes of LOS velocities along the breakwater between the high and low-resolution ISBAS results can be primarily attributed to the corresponding ground range dimension of the produced pixel. However, a higher degree of similarity between the deformation trends confirming the deformed parts of the breakwater (Fig. 5).

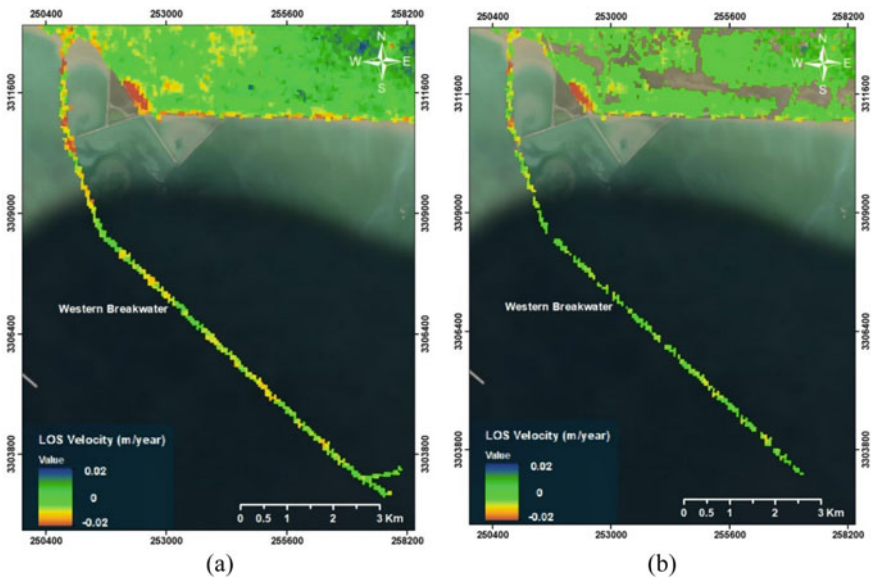


**Fig. 3** Western breakwater deformation maps showing mean linear velocities computed from Sentinel-1 data for the period (May 2017–January 2019) using **a** low-resolution ISBAS **b** SBAS technique. Positive velocities imply uplift and negative velocities indicate subsidence

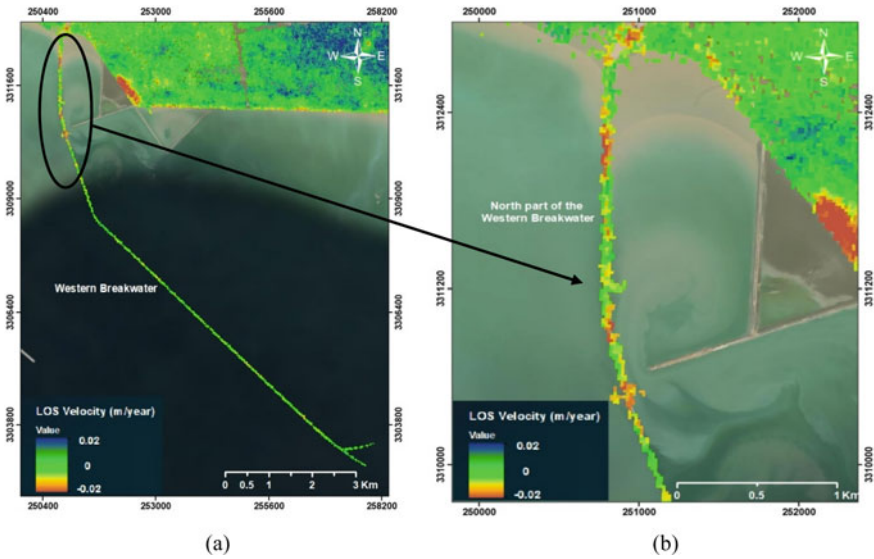


**Fig. 4** Western breakwater deformation maps showing mean linear velocities computed from Sentinel-1 data for the period (May 2017–January 2019) using high-resolution ISBAS **a** entire western breakwater **b** north part of the western breakwater. Positive and negative velocities indicate uplift and subsidence respectively

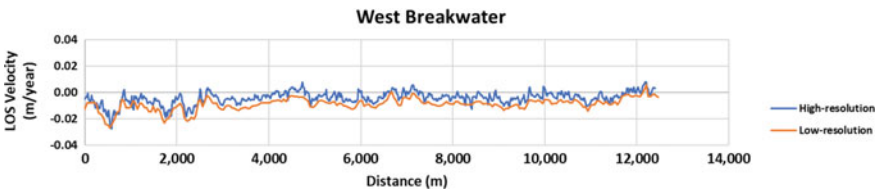


**Fig. 5** Longitudinal profile showing the ground motion along the western breakwater using high and low-resolution ISBAS technique for the monitoring period May 2017–January 2019

## 5 Conclusion

This study evaluates the recently developed ISBAS DInSAR approach for monitoring the deformation and stability of the western breakwater of Al-Faw Grand Port, South of Iraq. The trail with ISBAS successfully allows the retrieval of comprehensive information of the deformation along the breakwater, which is not completely detected using a conventional DInSAR method (i.e., SBAS). Analysis of Sentinel-1 data from May 2017 to January 2019 reveals a higher degree of similarity between the deformation trends derived from high and low resolution (ISBAS) methods, confirming the deformed parts of the breakwater. The study highlights that the low-resolution

ISBAS method can give excellent results, which are highly comparable with high-resolution for monitoring the health of large structural systems such as breakwater. The use of ISBAS DInSAR with Sentinel-1 data assisted in the identification of the deformation, and with continued monitoring, this can provide the most cost- and time-effective technique for long-term structural health monitoring than traditional ground-based monitoring methods.

**Acknowledgements** The authors would like to acknowledge AL-Mustansiriyah University/Faculty of Engineering, Baghdad-Iraq, for its support in the present work, ESA, to provide Sentinel-1 SAR data. The data were processed using the Punnet software. Andrew Sowter (Terra Motion Limited) developed the ISBAS technique and the Punnet software.

## References

1. Groeneveld, R. L., Mol, A. & Nieuwenhuys, E. H. (1985). Rehabilitation methods for damaged breakwaters. In *Coastal Engineering 1984* (pp. 2467–2486).
2. Tulsi, K. & Phelp, D. (2009). Monitoring and maintenance of breakwaters which protect port entrances.
3. Sousa, J. J., Hlaváčová, I., Bakoň, I., Lazecký, M., Patrício, G., Guimarães, P., Ruiz, A. M., Bastosi, L. & Sousa, A. (2014). Potential of multi-temporal InSAR for bridges and dams monitoring.
4. Alshammari, L., Large, D. J., Boyd, D. S., Sowter, A., Anderson, R., Andersen, R., & Marsh, S. (2018). Long-term peatland condition assessment via surface motion monitoring using the ISBAS DInSAR technique over the Flow Country. *Scotland. Remote Sensing*, 10(7), 1103.
5. Hilley, G. E., Bürgmann, R., Ferretti, A., Novali, F., & Rocca, F. (2004). Dynamics of slow-moving landslides from permanent scatterer analysis. *Science*, 304(5679), 1952–1955.
6. Canuti, P., Casagli, N., Farina, P., Marks, F., Ferretti, A. & Menduni, G. (2005, October). Land subsidence in the Arno river basin studied through SAR Interferometry. In *Proceedings of the 7th International Symposium on Land Subsidence* (Vol. 1, pp. 407–416). Shanghai: Shanghai Institute of Geological Survey.
7. Tizzani, P., Berardino, P., Casu, F., Euillades, P., Manzo, M., Ricciardi, G. P., Zeni, G., & Lanari, R. (2007). Surface deformation of Long Valley caldera and Mono Basin, California, investigated with the SBAS-InSAR approach. *Remote Sensing of Environment*, 108(3), 277–289.
8. Roccheggiani, M., Piacentini, D., Tirincanti, E., Perissin, D., & Menichetti, M. (2019). Detección y monitoreo de movimientos de tierra inducidos en túneles usando la interferometría SAR Sentinel-1. *Sens Remote*, 11, 639.
9. Crosetto, M., Monserrat, O., Cuevas-González, M., Devanthery, N., & Crippa, B. (2016). Persistent scatterer interferometry: A review. *ISPRS Journal of Photogrammetry and Remote Sensing*, 115, 78–89.
10. Lu, Z., & Kwoun, O. I. (2008). Radarsat-1 and ERS InSAR analysis over southeastern Louisiana: Implications for mapping water-level changes beneath swamp forests. *IEEE Transactions on Geoscience and Remote Sensing*, 46(8), 2167–2184.
11. Osmanoglu, B., Sunar, F., Wdowinski, S., & Cabral-Cano, E. (2016). Time series analysis of InSAR data: Methods and trends. *ISPRS Journal of Photogrammetry and Remote Sensing*, 115, 90–102.
12. Sowter, A., Bateson, L., Strange, P., Ambrose, K., & Syafiudin, M. F. (2013). DInSAR estimation of land motion using intermittent coherence with application to the South Derbyshire and Leicestershire coalfields. *Remote Sensing Letters*, 4(10), 979–987.

13. Sowter, A., Amat, M. B. C., Cigna, F., Marsh, S., Athab, A., & Alshammari, L. (2016). Mexico City land subsidence in 2014–2015 with Sentinel-1 IW TOPS: Results using the Intermittent SBAS (ISBAS) technique. *International journal of applied earth observation and geoinformation*, 52, 230–242.
14. Berardino, P., Fornaro, G., Lanari, R., & Sansosti, E. (2002). A new algorithm for surface deformation monitoring based on small baseline differential SAR interferograms. *IEEE Transactions on geoscience and remote sensing*, 40(11), 2375–2383.
15. Grebby, S., Orynbassarova, E., Sowter, A., Gee, D., & Athab, A. (2019). Delineating ground deformation over the Tengiz oil field, Kazakhstan, using the Intermittent SBAS (ISBAS) DInSAR algorithm. *International Journal of Applied Earth Observation and Geoinformation*, 81, 37–46.
16. Grebby, S., Sowter, A., Gluyas, J., Toll, D., Gee, D., Athab, A., & Girindran, R. (2021). Advanced analysis of satellite data reveals ground deformation precursors to the Brumadinho Tailings Dam collapse. *Communications Earth & Environment*, 2(1), 1–9.
17. Alshammari, L., Boyd, D. S., Sowter, A., Marshall, C., Andersen, R., Gilbert, P., Marsh, S. & Large, D. J., 2020. Use of surface motion characteristics determined by InSAR to assess peatland condition. *Journal of Geophysical Research: Biogeosciences*, 125(1), p.e2018JG004953.
18. Zebker, H. A., Rosen, P. A., & Hensley, S. (1997). Atmospheric effects in interferometric synthetic aperture radar surface deformation and topographic maps. *Journal of geophysical research: Solid earth*, 102(B4), 7547–7563.
19. Bateson, L., Cigna, F., Boon, D., & Sowter, A. (2015). The application of the Intermittent SBAS (ISBAS) InSAR method to the South Wales Coalfield, UK. *International Journal of Applied Earth Observation and Geoinformation*, 34, 249–257.
20. Marshall, C., Large, D. J., Athab, A., Evers, S. L., Sowter, A., Marsh, S., & Sjögersten, S. (2018). Monitoring tropical peat related settlement using isbas insar, kualalumpur international airport (klia). *Engineering Geology*, 244, 57–65.
21. JICA. (2015). Master plan study for port sector in the Republic of Iraq -Final Report. General Company for Ports of Iraq (GCPI). [open\\_jicareport.jica.go.jp/pdf/12248399\\_01.pdf](http://open_jicareport.jica.go.jp/pdf/12248399_01.pdf)
22. Business-Korea, Daewoo E&C Wins Iraq Port Construction Order Worth US\$700M. 2013. <http://www.businesskorea.co.kr/news/articleView.html?idxno=2290>.
23. Bayesteh, H., & Mansouriboroujeni, R. (2020). Mechanisms of settlement of a rubble mound breakwater on a soft soil in tidal flats. *Marine Georesources & Geotechnology*, 38(10), 1163–1176.
24. Pros, F., Gonzalez-Lopez, S., Martínez-Benjamin, J. J., Palau, V. & Duro, J. (2014, July). Breakwater settlement monitoring with InSAR data. In *2014 IEEE Geoscience and Remote Sensing Symposium* (pp. 414–417). IEEE.
25. Mustafa, M. M. (2011). Mineral resources and industrial deposits in the Mesopotamia plain. *Iraqi Bulletin of Geology and Mining*, 4, 105–118.
26. Yacoub, S. Y. (2011). Stratigraphy of the Mesopotamia plain. *Iraqi Bulletin of Geology and Mining*, 4, 47–82.
27. GEOSURV. (1992). The geology of Al-Basrah, Abadan and Bubyian Quadrangle. *State Company of Geological Survey and Mining*. Ministry of Industry and Minerals, Baghdad, Iraq.
28. Del Grosso, A. E., Inaudi, D. & Cottone, I. (2011, November). Measuring deformations of large structural systems. In *Joint International Symposium on Deformation Monitoring* (pp. 2–4).
29. Cigna, F., & Sowter, A. (2017). The relationship between intermittent coherence and precision of ISBAS InSAR ground motion velocities: ERS-1/2 case studies in the UK. *Remote sensing of environment*, 202, 177–198.
30. Gong, W., Thiele, A., Hinz, S., Meyer, F. J., Hooper, A., & Agram, P. S. (2016). Comparison of small baseline interferometric SAR processors for estimating ground deformation. *Remote Sensing*, 8(4), 330.
31. Lanari, R., Casu, F., Manzo, M., Zeni, G., Berardino, P., Manunta, M. & Pepe, A. (2007). An overview of the small baseline subset algorithm: A DInSAR technique for surface deformation

- analysis. *Deformation and Gravity Change: Indicators of Isostasy, Tectonics, Volcanism, and Climate Change*, 637–661.
32. Chen, C. W., & Zebker, H. A. (2001). Two-dimensional phase unwrapping with use of statistical models for cost functions in nonlinear optimization. *JOSA A*, *18*(2), 338–351.
  33. Casu, F., Manzo, M., & Lanari, R. (2006). A quantitative assessment of the SBAS algorithm performance for surface deformation retrieval from DInSAR data. *Remote Sensing of Environment*, *102*(3–4), 195–210.



# Numerical Modelling of Surface Runoff in Watershed Areas Related to Bahr AL-Najaf



Ataa A. Farhan and Basim Sh. Abed

**Abstract** The estimation of surface runoff results from precipitation on water basins is of great importance in the field of water resources management. Hydrological modeling is usually used to describe processes of control and conserve precipitation in a watershed to runoff. The study area (Bahr Al-Najaf) is located in the south-western part of Najaf City, with a total area of 2729.4 km<sup>2</sup>. Three main valleys with variant areas are delivered water to (Bahr Al-Najaf). This study aims to conduct a predictive hydrological study for the Bahr Al-Najaf by developing a numerical model to simulate the Surface runoff and checkup the possibility of floods occurring due to high water levels. Soil and Water Assessment Tool (SWAT) related to Geographic Information System (ArcGIS) was used for the simulation. The validation results of three valleys based on the coefficient of determination ( $R^2$ ) showed that SWAT Software was successfully simulated the runoff. And it was concluded that if the precipitation depth is 90 mm, Bahr Al-Najaf will be filled with at a water level of 16 m and a filled area of 49 km<sup>2</sup>. While in an imposed case, if the rain depth is 100 mm, the water level will be at 22 m with a flooded area for some parts of the city.

**Keywords** Runoff · Bahr AL-Najaf watershed · Water balance · SWAT model

## 1 Introduction

Different hydrological models are developed in the valleys to check the climate change impact and soil characteristics on the hydrological cycle. The relation between runoff and rainfall plays an essential role in managing the available water resources through hydraulically design and flood control structures. An analysis of a hydrological study directed that the spatial distribution of average runoff depth from sub-basins

---

A. A. Farhan · B. Sh. Abed (✉)

Water Resources Engineering Department, University of Baghdad, Baghdad, Iraq  
e-mail: [bassim.shabaa@coeng.uobaghdad.edu.iq](mailto:bassim.shabaa@coeng.uobaghdad.edu.iq)

A. A. Farhan

e-mail: [a.farhan1310@coeng.uobaghdad.edu.iq](mailto:a.farhan1310@coeng.uobaghdad.edu.iq)

indicated that the intermediate sub-basins are the highest in contributing to the watershed runoff [1]. As well, the curve number (CN) method was used for the United States Soil Conservation Services (USSCS) is one of the most popular methods for estimating runoff components and peak flow rate [2]. Many studies simulated water balance issues and the rainfall-runoff process by using the SWAT Software [3, 4]. Other Studies involved the variation in surface parameters (e.g., Topography, soil, and land cover) that affected the linkage between rainfall and surface water in watersheds [5]. Another study evaluated performance for modeling the precipitations and rainfall in the Watershed of Laou, they showed the feasibility of implementing the SWAT model was enabled to simplify the representation of the flows on the watershed [6].

The importance of development and suitable strategies of runoff modeling for the designers for the purpose of watershed management, i.e., Ketar watershed was studied which consists of agricultural lands and causes soil erosion [7]. SWAT model was used in the Upper Zab river basin to forecast and simulate the flow in the Upper Zab river watershed efficiently and the obtained results helped for study and expect the future amounts of resource discharges incomes on Tigris river and its effects. Also, results show a reduction on the precipitation and flow on the river basin in the future which will cause an impact on the Tigris river resources and a major impact on hydrological regimes [8]. A related study was conducted on Bouregreg Basin of water resources to evaluate and simulate the watershed's hydrology using SWAT and analyze and define the watershed's hydrological processes with different conditions [9]. A field study was conducted in the study area Bahr Al- Najaf showed a correlation between the hydraulic and geoelectrical parameters and dictated that most of the selected wells and boreholes located in the studied area have depths of more than (100) m and that they were classified into two types of self-flowing of artesian wells [10], while the other field study has considered two sites were chosen to determine the rate of water leakage in the depth of pits filled with water in two sites in the study area with an area (2 m × 1.5 m and 0.5 m). One of the sites used to investigate infiltration characteristics and the second is to verify the results, and they classified the type of infiltration rates as moderate to high [11]. Third field research in Bahr Al-Najaf area was performed to find out the capacity of bearing for the bored pile model established in gypseous soil [12]. This study aims to develop a numerical model to simulate the Surface Runoff using SWAT software in the study area (Bahr Al-Najaf). As well as to check up the possibility of floods occurs due to high water levels.

## 2 Materials and Methods

**Soil & Water Assessment Tool (SWAT).** Soil and Water Assessment Tool (SWAT) is applied to model the Bahr AL-Najaf watershed hydrology in Iraq. In this study, the data set used in the simulation is considered a description of the study area and the hydrological model. SWAT is a physically-based model that requires specific input

details about the weather, soil properties, topography, vegetation, and land cover changes in the watersheds. In the model processes, a watershed can be partitioned into several sub-basins, which are divided into Hydrologic Response Units (HRUs). The land phase of the hydrologic cycle is based on the water balance equation [13]:

$$SW_t = SW_0 + \sum_{i=1}^t (R_{day} - Q_{surf} - E_a - W_{seep} - Q_{gw}) \tag{1}$$

where  $t$  is time measured by days,  $SW_t$  and  $SW_0$  are the water content of the soil at the final and initial time measured by mm,  $R_{day}$  is the daily precipitation depth mm,  $Q_{surf}$  is the daily surface runoff mm,  $E_a$  is the evapotranspiration in mm,  $W_{seep}$  is the percolated water in mm, and  $Q_{gw}$  is the return flow in mm, all the parameter is for the day  $i$ .

**Study Area Description.** The study area (Bahr Al-Najaf) is one of the ancient low wetlands in Iraq. It was considered a natural lake, is located in the southwestern part of Najaf City Centre. The location of the area can be specified by  $44^\circ 11' 34''$  to  $44^\circ 22' 37''$ , and  $31^\circ 47' 11''$  to  $32^\circ 04' 08''$  longitudes and latitudes respectively, with a total surface area of  $251 \text{ km}^2$ . It involves a lake with an approximate area of  $49 \text{ km}^2$  [1]. That area was increases and decrease due to inflow and precipitation as well as weather conditions summer period. The study area represents an extension of the alluvial natural plain in the western plateau that forms a tongue shape that extends across from the south towards the north side of Al-Manathira City [1]. The study area’s slope is decreasing gradually from the west and from the southwest to the north and northeast. Many valleys deliver water to the study area (Bahr Al-Najaf). Three main valleys have a large area: Kharr, Shoaib Al-Rahimawi, and Maleh, these valleys contribute to the recharge of groundwater in the study area Fig. 1.

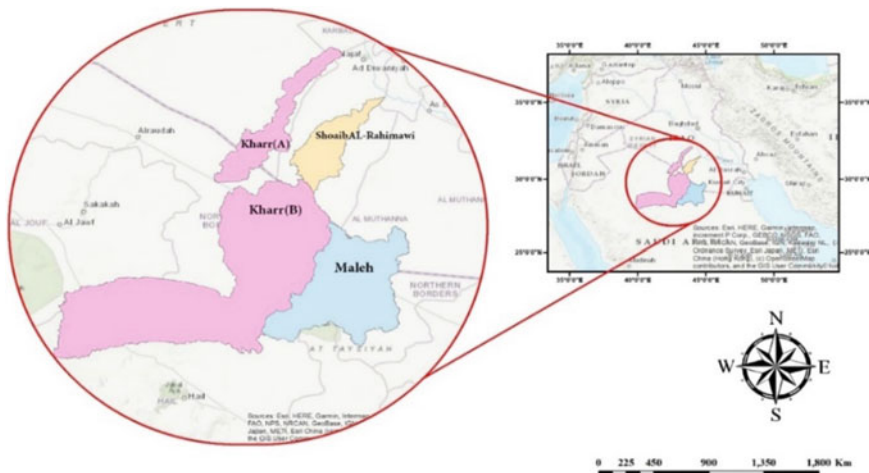


**Fig. 1** The location of the study area, Bahr al-Najaf, and the three feeding watersheds (valleys)

**Input Data.** In this research, Digital Elevation Model (DEM), the land use, the soil map, and the weather information were used to provide the inputs for the SWAT model for conducting the calibration and verification process using water level observations in the Bahr AL-Najaf watershed.

**Digital Elevation Model (DEM).** The ground topography is considered an essential input of the SWAT model. It is a helpful tool in analyzing the watershed and analysis of the characteristics of the land surface and the patterns of the drainage. Moreover, it usually affects the rate and the direction of the flow over the ground surface [14]. The digital elevation models (DEM), with 30 m resolution, were adopted for elevation ranges and spatial data of the study area provided by the global Shuttle Radar Terrain Mission (SRTM) from USGS. These DEMs were merged and reprojected to the UTM zone to be ready for the Arc SWAT processes to delineate the watersheds and flow directions. Figure 2 shows the DEM of each basin.

**Land use Map.** The global land cover map was used from the European Space Agency GlobCover Portal with a resolution of 300 m for the period December

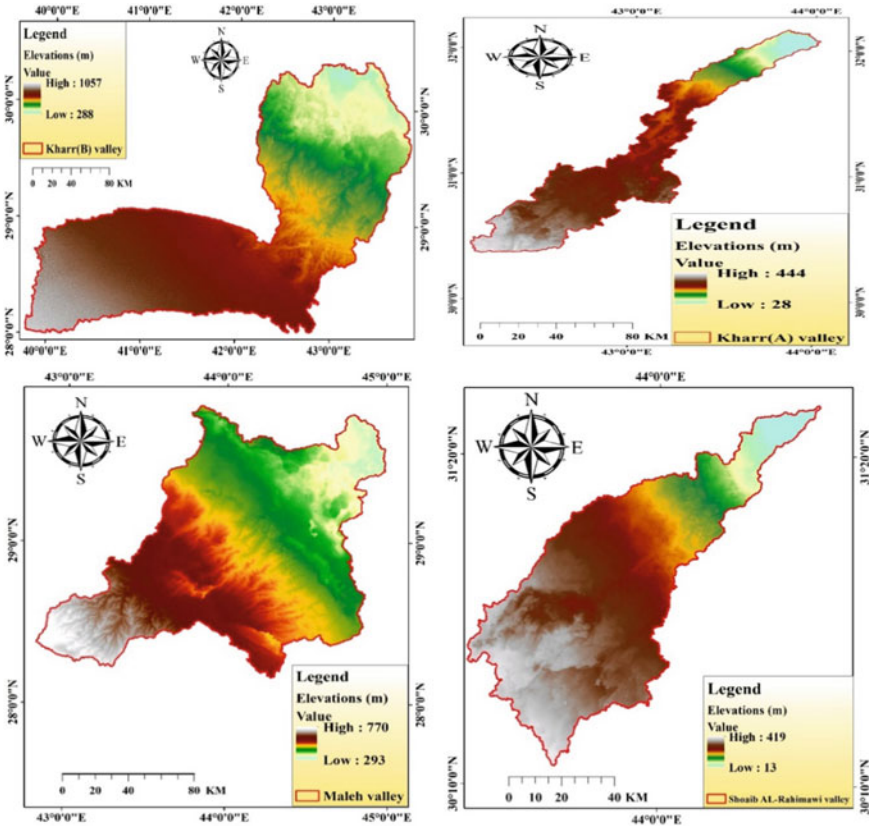
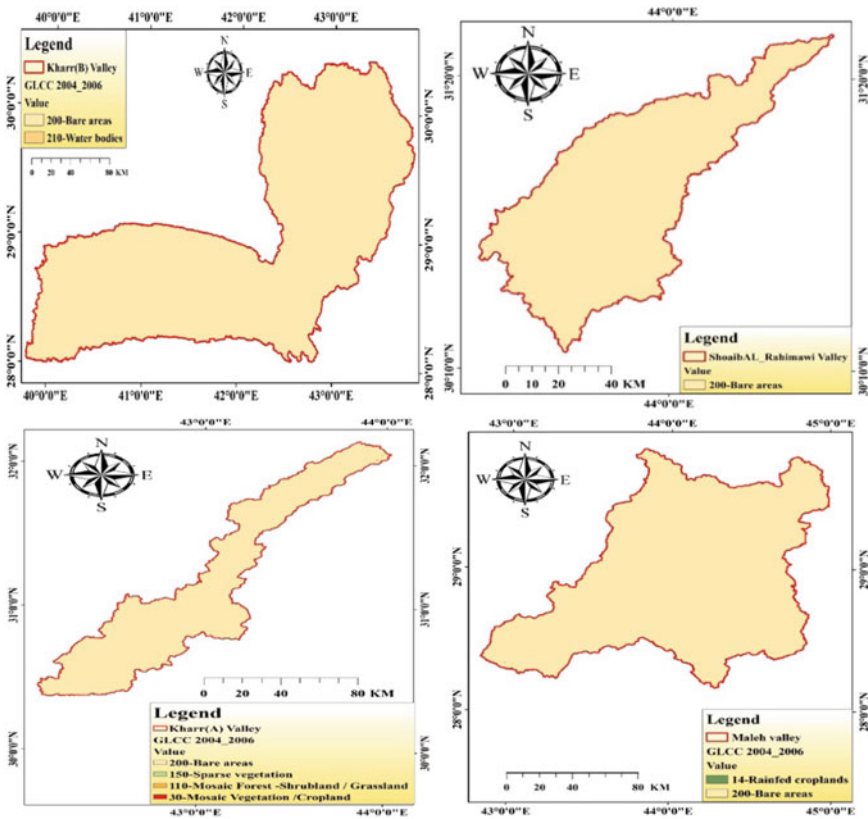


Fig. 2 Kharr(A)Valley, Kharr(B)Valley, Shoab AL\_Rahimawi Valley, and Maleh valley

2004–June 2006. The study area contains two land-use classes, including Bare areas, Rainfed croplands Fig. 3.

**Soil Map.** The study’s soil map was from the Food and Agriculture Organization at a scale of 1: 5,000,000. The map is divided into many polygons. Each polygon contains different properties of study area soils such as hydrological soil group, hydraulic conductivity, soil texture, and other physical and chemical properties matched with the FAO soil database. These polygons were clipped to identify with the watershed area then reclassified to define Hydrological Response Units (HRUs). Soil data are merged using ArcGIS processes with DEM, Land-use, and slope classes into SWAT to determine the HRU level Fig. 4.

**Weather Data.** Arc SWAT Software requires information on weather like precipitation, solar radiation, temperature, relative humidity, and wind speed. Previous daily rainfall was obtained from the Iraqi Metrological Organization and Seismology (IMOS) for the period (2009–2019). It is stated that these data are invalid for use in



**Fig. 3** Kharr(A)Valley, Kharr (B)Valley, Shoaib AL\_Rahimawi Valley, and Maleh valley for Land use map

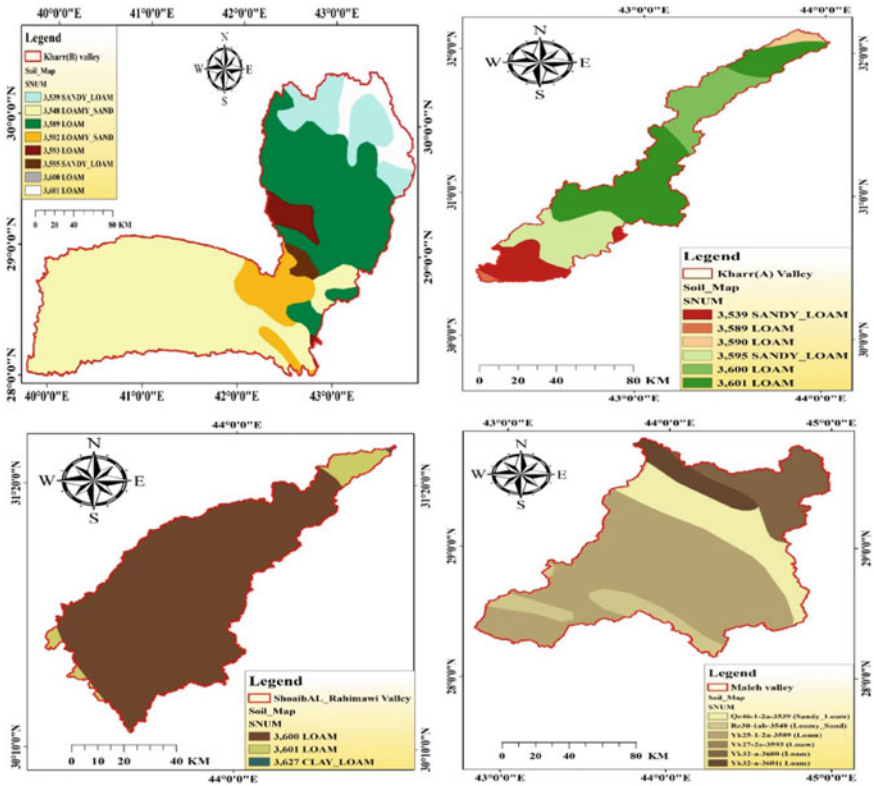


**Fig. 4** Kharr(A)Valley, Kharr (B)Valley, ShoaibAL\_Rahimawi Valley, and Maleh valley for Soil map

the SWAT simulations. Weather data that needed to run SWAT should be a continuous daily time-step. However, the weather data from IMOS is losing years and some months of weather data. Therefore, another source of weather data was used in the Climate Forecast System Reanalysis (CFSR) study. Weather data for regions that CFSR can provide missing weather stations. CFSR climate data are available for the period (1979–2014). A survey by Fuka [15]s showed that the weather data produced by the CFSR to use for watershed simulations are good or better than weather data used in simulations produced by traditional weather stations. These data were compared and calibrated with data from The Iraqi Meteorological Organization and Seismology (IMOS) for station Al-Najaf for the period (2009–2014). The  $R^2$ , NSE, and RMSE were 0.85, 0.77, and 6.88 for the calibration, respectively Fig. 5.

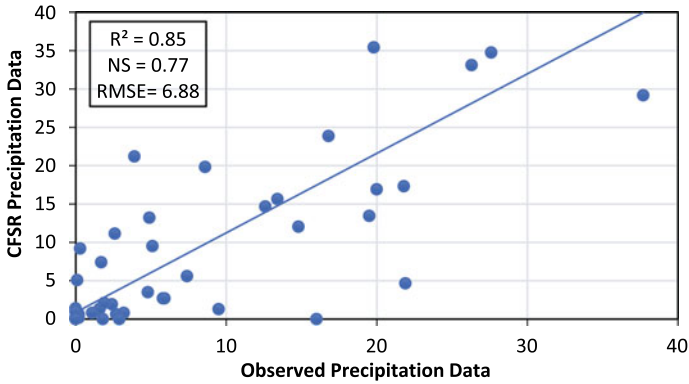


**Fig. 5** Result of correlation between the climate forecast system reanalysis weather data With AL-Najaf gauge station weather data

### 3 Results of Calibration and Validation

Calibration and verification were performed for the three main Valleys, Kharr Shoab AL\_Rahimawi and Maleh, from (2012/10/1) to (2014/6/1). These periods were chosen due to the availability of measured water level data for these periods only to compare the measured and simulated water levels. The investigation of the calibration and validation results revealed that the coefficient of determination ( $R^2$ ) showed that SWAT was successfully simulated runoff in the study area with acceptable values of  $R^2$  equals 0.86 and 0.89 for the two processes, respectively. Figure 6 shows the calibration and validation periods involved in the present study. The surface runoff curve number coefficient was an important parameter in the Arc SWAT model simulation for the three valleys. The curve number extracted from the Swat Software simulation was relied upon in Fig. 7. The CN values for each sub-basin in the three valleys.

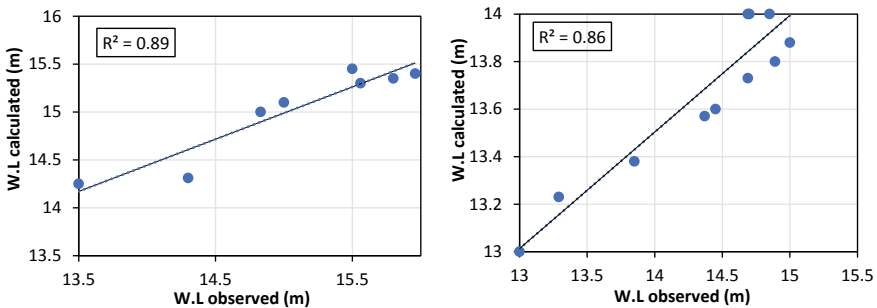


**Fig. 6** Comparison between the simulated and observed Water levels for both the calibration and validation periods

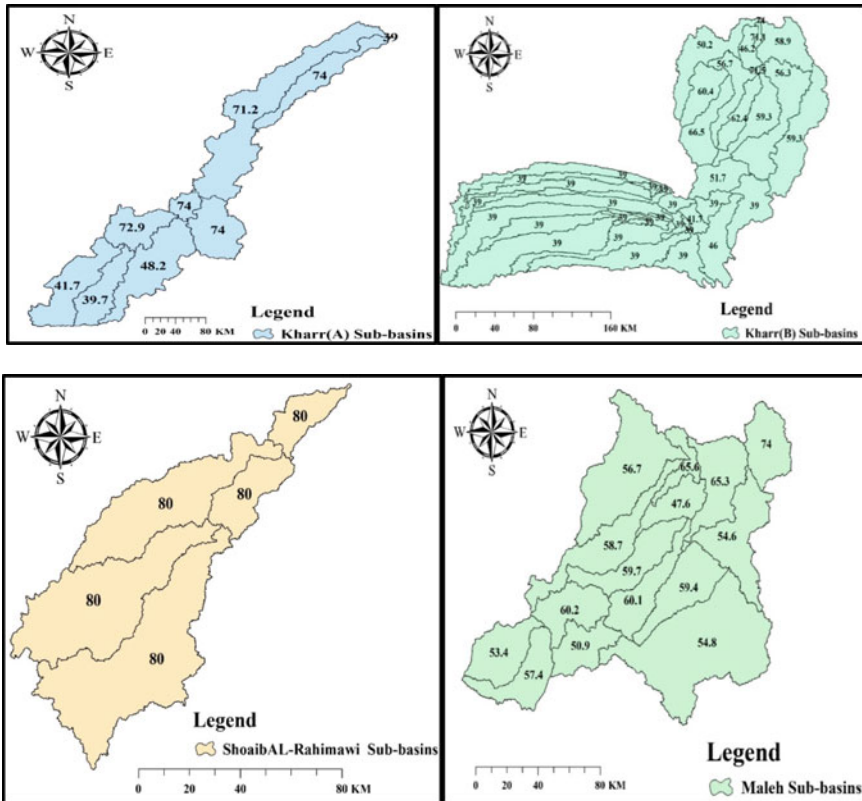


**Fig. 7** Curve Number Value for each sub-basin for Kharr(A)Valley, Kharr(B)Valley, Shoaib AL\_Rahimawi Valley and Maleh valley

Figure 8 shows the sub-basins for each of the three valleys in the Bahr Al-Najaf region, after the process of entering the digital elevation map (Dem) for the SWAT Software and the process of determining watersheds runoff paths, and areas where the valley’s water collects. Finally, it was concluded that the proposed scenarios in the studied area are if the precipitation depth is 90 mm, the Najaf lake will be filled with water to a water level of 16 m and an area of 49 km<sup>2</sup>. The other proposed scenario if the rain depth is 95 mm for the water level of 18 m, the lake with an area of 251 km<sup>2</sup> will be full, and the last proposed scenario is the probability of flooding in the city if the rain depth is 100 mm for a water level of 22 m for the area of the city is 2729 km<sup>2</sup> Fig. 9.



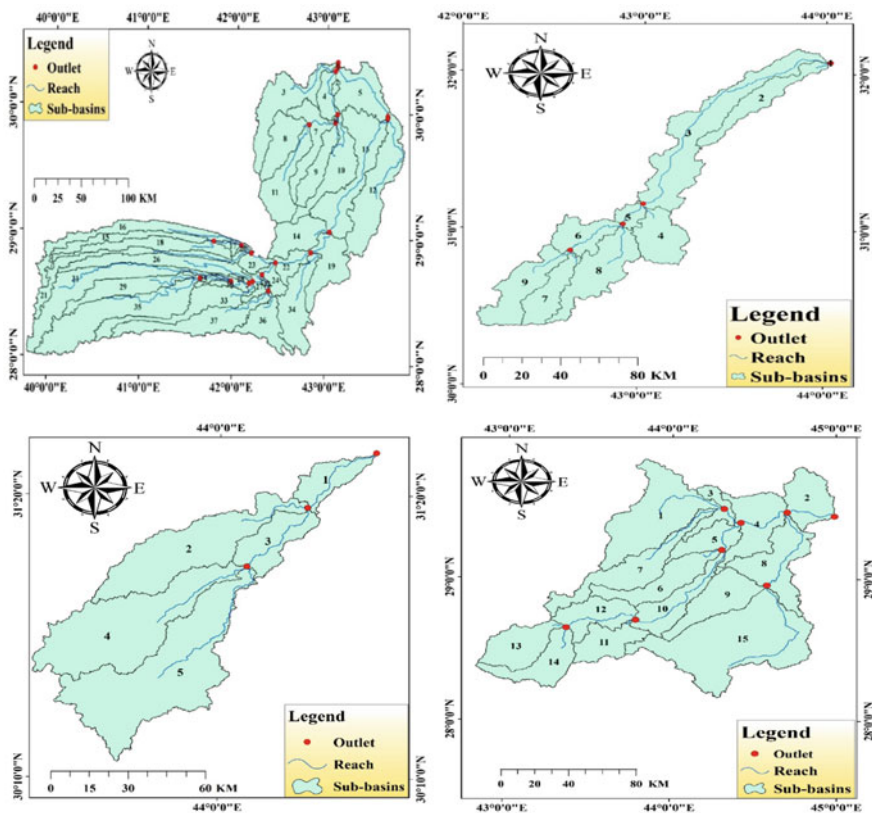


Fig. 8 Map showing watershed characteristics for Kharr(A)Valley, Kharr(B)Valley, Shoab AL\_Rahimawi Valley and Maleh valley

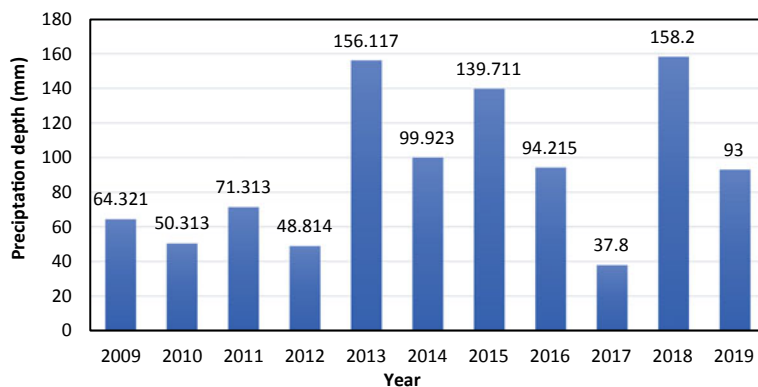


Fig. 9 Shows Precipitation depth (mm) for ten years

## 4 Conclusions

In the current study, Arc SWAT Software was used to conduct a hydrological simulation of the three main valleys in the Bahr Al-Najaf region. The simulation was done using a digital elevation map to draw water flow paths in the three valleys and identify points where water flows into each valley, after which the required weather data was obtained for simulation from analysis of the climate Prediction System (CFSR).

- One of the most important results that were reached was the runoff curve number (CN). It was one of the basic parameters in the simulation's SWAT software, as its value that was reached through simulations for all three valleys was relied upon.
- Throughout the calibration and verification period, a comparison was made for the two mentioned periods between the observed water levels in the study area with the simulated water levels. The statistical indicators were good and satisfactory, and the model efficiency was good. The results indicate that the coefficient of determination ( $R^2$ ) of the simulation was 0.86 for calibration and 0.89 for validation.
- The weather data of the Climate Forecast System Reanalysis (CFSR) was compared and calibrated with data from The Iraqi Meteorological Organization and Seismology (IMOS) for station Al-Najaf for the period (2009–2014). The  $R^2$ , NSE, and RMSE were 0.85, 0.77, and 6.88, respectively.
- Finally, it was concluded that the proposed scenarios in the studied area are if the precipitation depth is 90 mm, the Najaf lake will be filled with water to a water level of 16 m and an area of 49 km<sup>2</sup>. The other proposed scenario if the rain depth is 95 mm for the water level of 18 m, the lake with an area of 251 km<sup>2</sup> will be full, and the last proposed scenario is the probability of flooding in the city if the rain depth is 100 mm for a water level of 22 m for the area of the city is 2729 km<sup>2</sup>.

## References

1. Omran, H. A., Mahmood, M. S., & Abbas, A. (2014). *Quantity and distribution of the current surface and groundwater resources in Bahr An-Najaf in Iraq*.
2. Suliman, N. M., & Al-Zubaidi, N. S. (2020). Improve rheological properties of Palygorskite water-based drilling fluid by caustic soda and soda ash. *Journal of Engineering*, 26(6), 1–17.
3. Raihan, F., Beaumont, L. J., Maina, J., Saiful Islam, A., & Harrison, S. P. (2020). Simulating streamflow in the Upper Halda Basin of southeastern Bangladesh using SWAT model. *Hydrological Sciences Journal*, 65(1), 138–151.
4. Farhan, A. M., & Al-Thamiry, H. A. (2020). Estimation of the surface runoff volume of Al-Mohammedy valley for long-term period using SWAT model. *Iraqi Journal of Civil Engineering*, 14(1).
5. Shivhare, V., Goel, M. K., & Singh, C. K. (2014). Simulation of surface runoff for upper Tapi subcatchment Area (Burhanpur Watershed) using swat. *The International Archives of Photogrammetry, Remote Sensing and Spatial Information Sciences*, 40(8), 391.
6. Aqnouy, M., El Messari, J. E. S., Ismail, H., Bouadila, A., Moreno Navarro, J. G., Loubna, B., & Mansour, M. R. A. (2019). Assessment of the SWAT model and the parameters affecting

- the flow simulation in the watershed of Oued Laou (Northern Morocco). *Journal of Ecological Engineering*, 20(4).
7. Sime, C. H., Demissie, T. A., & Tufa, F. G. (2020). Surface runoff modeling in Ketar watershed, Ethiopia. *Journal of Sedimentary Environments*, 1–12.
  8. Tamween Ajeel AL-Heetimi, O., Abidalla, W. A., & Abbas Jaber, J. (2015). Flood forecasting in upper Zab River using SWAT hydrological model. *Journal of Kerbala University*, 11(4), 133–144.
  9. Fadi, A., Rhinane, H., Kaoukaya, A., Kharchaf, Y., & Bachir, O. A. (2011). Hydrologic modeling of the Bouregreg watershed (Morocco) using GIS and SWAT model. *Journal of Geographic Information System*, 3(04), 279.
  10. Thabit, J. M., Al-Yasi, A. I., & Ala'a, N. (2014). Estimation of hydraulic parameters and porosity from geoelectrical properties for fractured rock aquifer in middle Dammam formation at Bahr Al-Najaf Basin, Iraq. *Iraqi Bulletin of Geology and Mining*, 10(2), 41–57.
  11. Mahmood, M. S., & Al-Saoudi, N. K. (2014). *Infiltration characteristics in agriculture area of Bahr al Najaf*.
  12. Al-Busoda, B. S., & Al-Rubaye, A. H. (2015). Bearing capacity of bored pile model constructed in gypseous soil. *Journal of Engineering*, 21(3), 109–128.
  13. Neitsch, S. L., Arnold, J. G., Kiniry, J. R., & Williams, J. R. (2011). *Soil and water assessment tool theoretical documentation version 2009*. Texas Water Resources Institute.
  14. Al-Khafaji, M. S., & Saeed, F. H. (2018). Effect of DEM and land cover resolutions on simulated runoff of Adhaim Watershed by SWAT model. *Engineering and Technology Journal*, 36(4 Part A), 439.
  15. Fuka, D. R., Walter, M. T., MacAlister, C., Degaetano, A. T., Steenhuis, T. S., & Easton, Z. M. (2014). Using the climate forecast system reanalysis as weather input data for watershed models. *Hydrological Processes* 28(22), 5613–5623.

# **Challenges in Foundation Engineering**

# Bearing Capacity of Model Strip Footing on Unsaturated Very Loose Sand



Khashayar Nikoonejad and Reza Imam

**Abstract** Shallow footings are generally constructed above groundwater level. Because of a capillary zone in the underlying soil layers, the behavior of the unsaturated soils supporting the footings needs to be known. Evaluation of shallow footings' bearing capacity on unsaturated soils is therefore important from a practical point of view. The current research focuses on understanding the effects of matric suction on the bearing capacity of shallow strip footings placed on very loose uniform sands, using experimental and numerical methods. The experimental program is implemented using a test tank equipped with a loading frame and a specially designed telescopic pipe system to control the soil's water level inside the tank. Results are then modeled numerically using commercial software with capabilities to model the behavior of unsaturated soils. The experimental results indicate that the increase in the matric suction in the unsaturated very loose sand can lead to up to a sixfold increase in strip footing bearing capacity compared to the fully saturated condition. In addition, numerical analysis results indicate that the soil's failure mechanism underlying the footing seems to move from punching shear in the saturated soil to the local or general shear failure in the soils with greater shear strength caused by matric suction. It was also concluded that taking into account the unsaturated soil mechanics in numerical modeling leads to a generally satisfactory prediction of the load-settlement behavior obtained from the experimental results.

**Keywords** Unsaturated soil · Very loose sand · Bearing capacity · Physical modeling · Finite element analysis

## 1 Introduction

Application of conventional soil mechanics theoretically relevant to the behavior of dry or saturated soils to the determination of bearing capacity of shallow footings

---

K. Nikoonejad · R. Imam (✉)

Department of Civil and Environmental Engineering, Amirkabir University of Technology, Tehran, Iran

e-mail: [rimam@aut.ac.ir](mailto:rimam@aut.ac.ir)

placed on unsaturated soils leads to conservative results. This is because the contribution of matric suction in increasing the shear strength of the soil is neglected. Studies of the bearing capacity of shallow footings placed on unsaturated soils should therefore be carried out independently. The shear strength of an unsaturated soil ( $\tau_{unsat}$ ) may be determined by the following relationship proposed by Vanapalli et al. [1]:

$$\tau_{unsat} = c' + (\sigma - u_a)tg\phi' + (u_a - u_w)(\Theta^\kappa)tg\phi' \tag{1}$$

where  $c'$  and  $\phi'$  are the effective cohesion and friction angle of the soil in the saturated state,  $(\sigma - u_a)$  is the net normal stress,  $(u_a - u_w)$  is the matric suction,  $u_a$  and  $u_w$  are the air and water pressures, respectively,  $\Theta$  is the normalized volumetric water content, and  $\kappa$  is a fitting parameter that depends on the soil plasticity and is equal to 1.0 for sandy soils. Since the osmotic suction is negligible in cohesionless soils, the total suction is usually equal to the matric suction. Consideration of the matric suction effect by adding an apparent cohesion to the soil leads to an increase in its shear strength. The magnitude of the added apparent cohesion can be calculated using the third term in Eq. 1. Soil suction is related to the soil water content by a curve known as the soil–water retention curve (SWRC) or the soil–water characteristic curve (SWCC). A typical SWRC is schematically depicted in Fig. 1, in which the horizontal axis shows the soil matric suction, and the vertical axis is the volumetric water content,  $\theta_w$ , which is the ratio of water volume to the total soil volume.

Variation in soil suction versus the water content exhibits a hysteresis type behavior and depends on the hydraulic path (drying or wetting) that the soil can

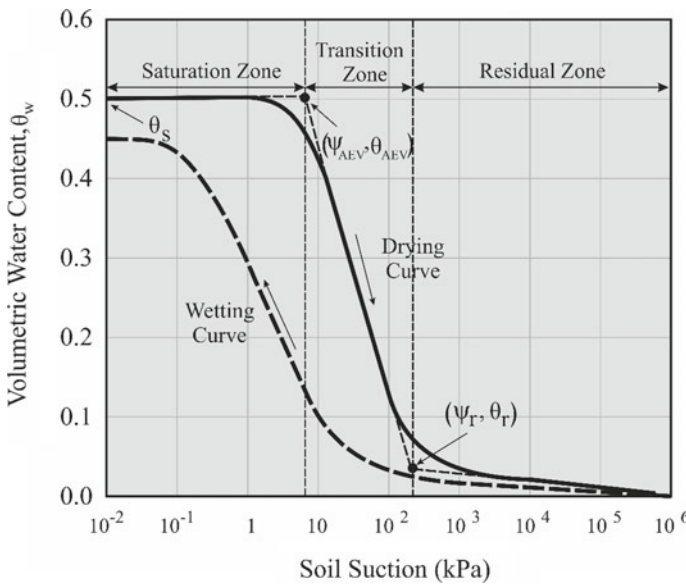


Fig. 1 Typical soil–water retention curve (SWRC)

experience when its matric suction changes. Soil suction decreases during the wetting processes, which may occur, for instance, due to precipitation or an increase in the groundwater level. On the other hand, in a drying process, such as evaporation or a decrease in the groundwater level, soil suction increases, and the soil follows a drying curve as shown in Fig. 1. The suction at which the first air bubbles start to enter the voids is called the air entry value (AEV),  $\psi_{AEV}$ , and that after which there is no continuous water path inside voids is the residual suction,  $\psi_r$ . Accordingly, the SWRC can be divided into the three zones shown in Fig. 1, representing states of saturation, transition, and residual moisture conditions.

Findings from the study of Steensen-Bach et al. [2] on coarse sand indicate that as the water level below the footing is lowered, bearing capacity first increases, but it follows a decreasing trend by further lowering the water level. However, for finer sand, the bearing capacity continuously increases by lowering the water level, and in its ultimate stage, reaches a value eleven times higher than the saturated condition. Vahedifard and Robinson [3] observed that the ultimate bearing capacity under various flux boundary and saturation conditions could increase up to 5–7 times that in the saturated situation. Furthermore, effect of flow rate on the ultimate bearing capacity is more pronounced in clay than the similar conditions in the sand. From the studies of Schanz et al. [4] on dense sand, a 2.5 to 4 times increase in the bearing capacity is observed to occur just by increasing the matric suction. Maghvan et al. [5] showed that the bearing capacity of footings placed on unsaturated soils could be predicted satisfactorily using bearing capacity equations modified for the effects of the soil's unsaturated state. For a circular footing placed on fine-silty sand, they obtained the greatest bearing capacity for a degree of saturation of about 16%. Moreover, Maghvan et al. [6] showed that relative density also affects bearing capacity and mode of failure significantly in unsaturated granular soil. In loose soils, a transition of failure mechanism from punching and local shear to general shear failure may occur at the degree of saturation for which the most significant bearing capacity is reached. However, in dense sand, the general shear mechanism governs the soil failure for all degrees of saturation.

In the current study, matric suction effects in a uniform unsaturated very loose sand on the bearing capacity of a shallow strip footing are first experimentally evaluated using physical modeling tests. The tests are then numerically modeled using commercial software to assign the unsaturated parameters to the soil model. The experimental results are also compared with the bearing capacity values obtained from the equation proposed by Vanapalli et al. [7] to evaluate the accuracy of the existing relationship in predicting the bearing capacity of footings in very loose uniform sands.

## 2 Model Testing Procedure

Model tests were conducted using model strip footings atop sand placed in a test tank. The sand specimen placed in the tank was 750 mm in length, 650 mm in height, and

300 mm in width. The strip model footing was made of aluminum and was 298 mm long, 50 mm wide, and 25 mm high. As illustrated in Fig. 2, a water tank with the ability to maintain a constant water head was attached behind the test tank. A 100 mm high opening towards the test tank and near the bottom of the water tank allowed entry of water into the test tank and maintaining a constant water level in the sand for each test. The water tank's constant head was kept using a telescopic vertical pipe inside the water tank through which extra water above the required water level could drain outside the water tank. The dry sand condition was obtained by keeping the water level inside the water tank below the soil specimen's bottom level. Various water depths below the soil surface were achieved by adjusting the water tank's water level at the required elevation. For each test, the water level was kept at the elevation needed for more than 24 h such that a variable moisture profile starting from full saturation at water level to a lower degree of saturation at the soil surface (depending on the water level) could develop.

Steps and procedures used for placing the soil inside the tank are described as follows: (1) A 100 mm thick layer of gravel was placed at the bottom of the test tank such that it provided a path needed for entering and rising water level uniformly from the tank base, as shown in Fig. 2b. (2) A geosynthetic layer was then placed on the gravel layer, which acted as a filter, allowing the free flow of water from the gravel into the sand, but preventing the sand from entering and clogging the gravel layer. (3)

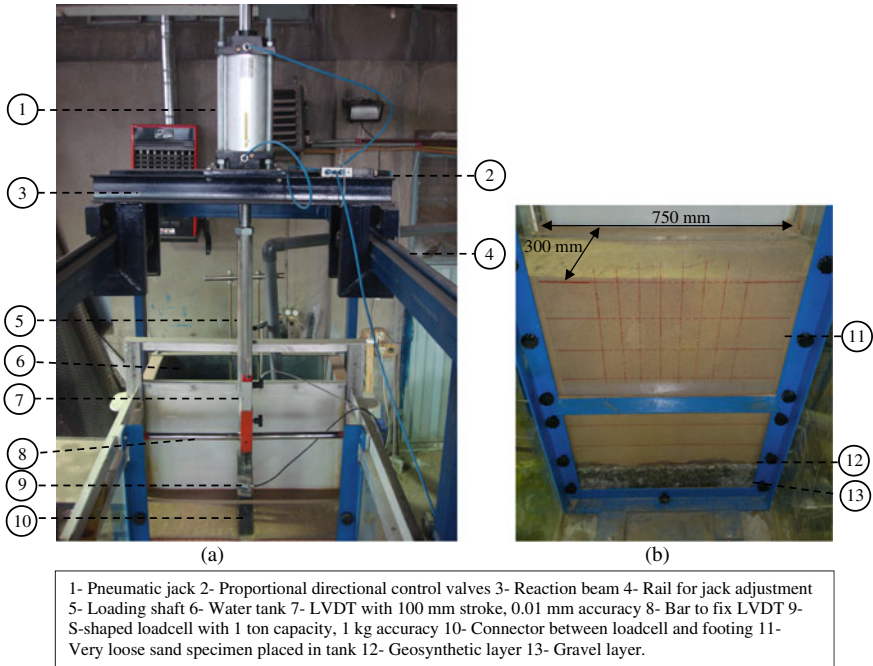


**Fig. 2** Model testing Equipment: **a** Test tank and loading frame, **b** Soil specimen after placement in the test tank



The sand with initial moisture of 2.5% (except for the case of dry sand test for which no moisture was added) was then placed in the tank using the moist tamping method [8] in 6 layers until a total thickness of 650 mm was reached for the sand placed on the geosynthetic layer. (4) The specimen was then saturated by raising the water level up to the specimens' surface. The water was allowed to enter the soil at a low flow rate to prevent liquefaction from occurring during saturation (5) After soil saturation, the water level was lowered to the desired depth and kept at that depth during loading. (6) Loading was then applied to the footing, and the load–displacement behavior of the footing was recorded and plotted by a computer program. (7) water content profile of the soil under the footing was measured by sampling the soil up to 200 mm depth below the footing base immediately after each test. After placing the soil specimens in the tank, the shallow strip footing was loaded at a rate of 1.2 mm/min to evaluate its bearing capacity and settlement behavior for various degrees of saturation. The footing settlement was controlled by a LVDT placed atop the footing, and variation of the load was measured by an S-shaped load cell during the loading by a pneumatic jack.

It is noted that since the soils tested in the current study were first saturated, and the water level was then lowered to a certain depth before application of the load to the footing commenced, only the drying curve was considered in the determination of the unsaturated soil parameters.

### 3 Properties of the Tested Soil

The soil tested in the current study is the Firuzkuh No. 161 sand, which, according to the USCS classification system, is considered a uniformly-graded fine sand (SP). The SWRC of the soil was predicted for the tested soil using the method proposed by Aubertin et al. [9]. The soil physical parameters needed for predicting the SWRC for a cohesionless soil using this method are the grain size properties ( $D_{10}$  and  $D_{60}$ ) and the porosity. The grain size distribution curve and the SWRC for the tested soil are shown in Fig. 3. Soil physical properties, strength, and the SWRC parameters

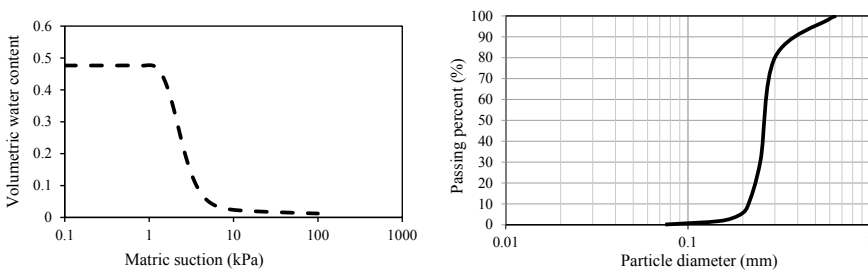


Fig. 3 Grain size distribution curve and soil–water retention curve (SWRC) for the tested soil

**Table 1** Properties of the tested soil

$\psi_r$ (kPa)	AEV (kPa)	$D_{50}$ (mm)	$C_u$	$C_c$	$e_{max}$	$e_{min}$	$G_s$	$C'$ (kPa)	$\phi'$
4.2	1.43	0.268	1.3	1.03	0.91	0.6	2.65	0	32

$D_{50}$ : grain size corresponding to 50% finer;  $C_u$ : coefficient of uniformity;  $C_c$ : coefficient of curvature;  $e_{max}$ : maximum void ratio;  $e_{min}$ : minimum void ratio;  $G_s$ : specific gravity;  $\phi'$ : effective internal friction angle;  $C'$ : effective cohesion; AEV: Air Entry Value;  $\psi_r$ : residual suction

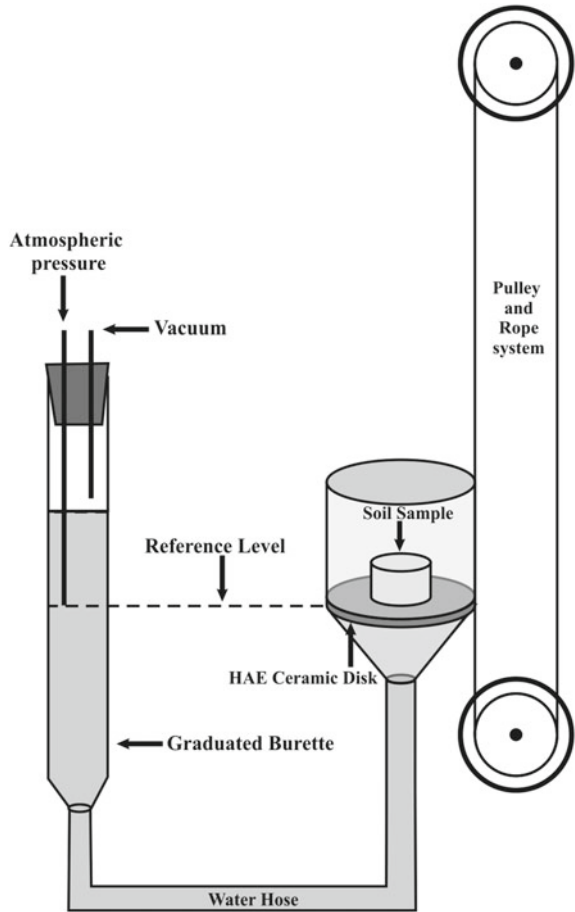
for the very loose condition in which the specimens were prepared ( $D_r = 0\%$ ) are summarized in Table 1, the strength parameters are measured from direct shear tests.

Moreover, experimental data obtained from using the hanging water column technique [10] were also used to verify the SWRC employed in the numerical analysis. The hanging water column technique is based on the idea that a column of water hanging under a high-air-entry (HAE) ceramic disk forming the bottom of a closed container applies suction to the disk, and this suction will, in turn, be applied to a soil sample placed inside the container. By moving up the container using a pulley and rope system, suction of up to 20 kPa (equivalent to 2 m of water head) may be applied in steps of 0.1 kPa (equal to 1 cm head applied by moving up the container 1 cm). After each step of application of suction to the soil specimen, its water content can be determined by measuring the volume of water extracted from the sample and collected in a burette. The schematic view of the apparatus is shown in Fig. 4. As noted in Fig. 5, there is a good agreement between the SWRC obtained from the hanging water column data and the curve estimated from the Aubertin et al. [3] method used in this study.

## 4 Results of the Model Tests

Details of the test tank and testing procedure are provided elsewhere [11]. Model test results showing variations of vertical pressure applied by the strip footing versus the vertical displacement of the footing for various depths of water level below soil surface are provided in Fig. 6. As shown in this figure, bearing capacity initially increases with an increase in the depth of water level ( $d$ ) up to 31 cm below soil surface. This can be attributed to the decrease in moisture and increase in soil suction as the water level below footing is lowered. This is a result of an increase in soil suction and, consequently, soil shear strength, with a decrease in moisture as indicated by the SWRC. However, further increase in water depth leads to the decrease in bearing capacity, and this decrease continues until soil moisture is completely removed and the underlying soil becomes completely dry. As shown in Eq. 1, shear strength caused by soil suction is directly related to the product of the degree of saturation and soil suction. Soils having very low degrees of saturation, or dry soils, have low strength components resulting from suction since, despite the higher value of suction as shown

**Fig. 4** Schematic view of the hanging water column apparatus



by the SWRC, the very small degree of saturation multiplied by the suction results in a lower added strength caused by the suction term.

## 5 Numerical Modeling

Numerical modeling of unsaturated soils' stress-settlement behavior was carried out using the linear elastic model combined with the Mohr–Coulomb failure criterion. For each test, the water table was first assigned to the model at the depth relevant to that test. A linear variation of negative pore water pressure above water level with a slope equal to the positive hydrostatic pressure slope was assumed. If the maximum negative pressure head ( $H_{max}$ ) is smaller than the height of the unsaturated soil layer ( $H_{unsat}$ ), the negative porewater pressure remains constant and equal to the maximum

**Fig. 5** Comparison between the SWRC estimated by Aubertin et al. [9] and hanging water column results

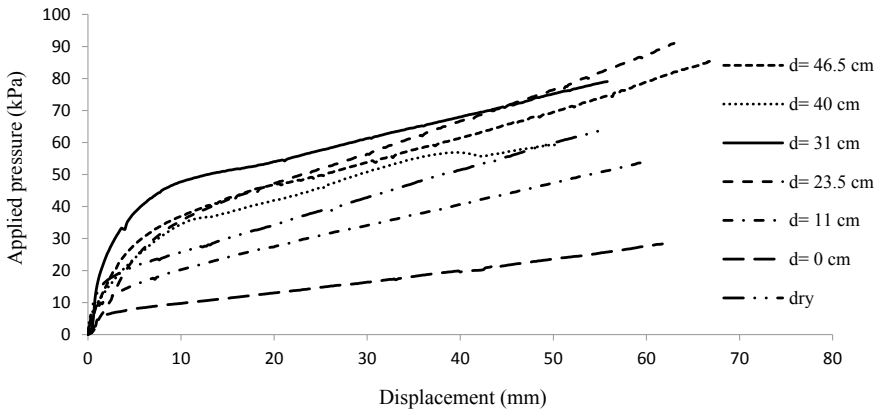
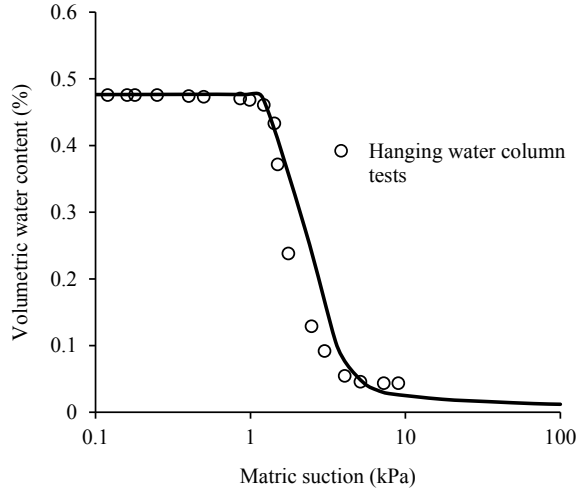


**Fig. 6** Results of model tests on the stress-displacement behavior of unsaturated soils

negative pore pressure after reaching this maximum. However, if  $H_{max} > H_{unsat}$ , the negative porewater pressure continues to increase up to the soil surface. The added soil strength resulting from the soil's unsaturated state was taken into account by adding an apparent cohesion according to Eq. 2 as suggested by Vanapalli et al. [1].

$$C = (u_a - u_w) \text{tg} \phi' \frac{(\theta - \theta_r)}{(\theta_s - \theta_r)} \tag{2}$$

in which  $\theta_s$  and  $\theta_r$  are the saturated and residual volumetric water content of the soil. The effective friction angle is assumed to remain the same for saturated and

unsaturated soils. Figure 7 shows comparisons of experimental and numerical analysis results of the footing’s pressure-settlement behavior for various depths of water level. Satisfactory agreement is observed between the experimental and numerical analysis results, indicating that the relatively simplified physical aspects of behavior of unsaturated soils considered in the numerical modeling is sufficient for obtaining satisfactory analysis results. The effective cohesions obtained from Eq. 2 were averaged over a depth equal to the footing width, and their values as obtained from test results and numerical analysis are shown in Table 2 for the various cases of water depth. Satisfactory agreement between the predicted and measured values is observed.

An important aspect of the behavior of footings is their failure mechanism under applied loads. Figure 8 shows the yield zones developed in the underlying soils for various depths of water level. The plain strain and symmetrical conditions allow half

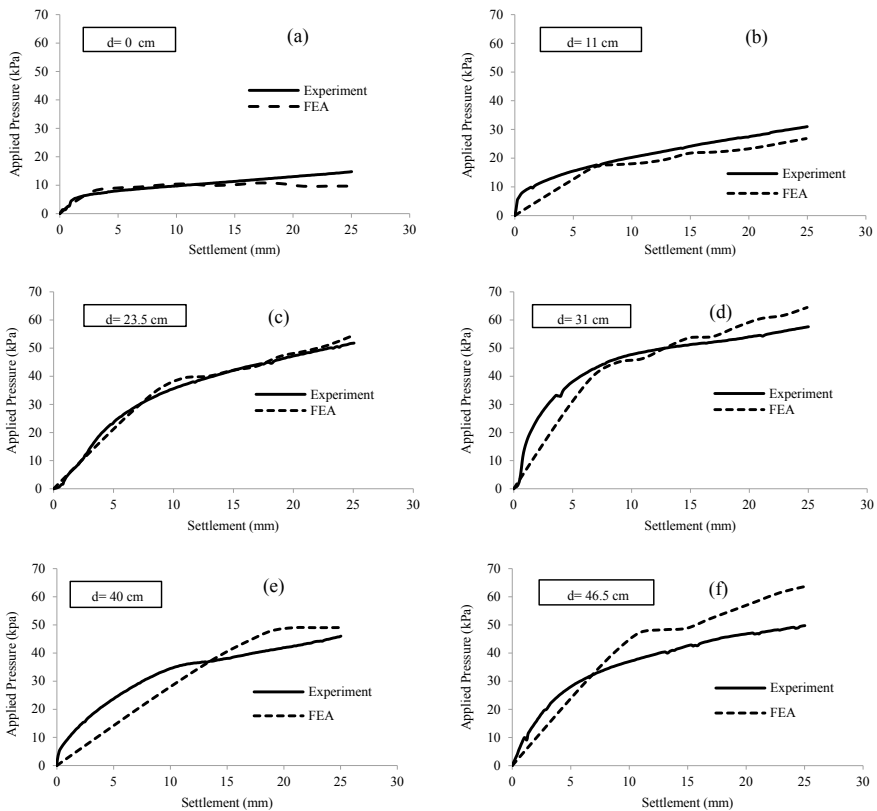


**Fig. 7** Comparison of experimental and modeled unsaturated soil pressure-settlement behavior for various depths of water level below soil surface, *d*, **a** *d* = 0 cm, **b** *d* = 11 cm, **c** *d* = 23.5 cm, **d** *d* = 31 cm, **e** *d* = 40 cm, **f** *d* = 46.5 cm

**Table 2** Effective cohesions used in the determination of bearing capacities

d (cm)	S(%)	$(u_a - u_w)_{AVR}$ (kPa) Test	$(u_a - u_w)_{AVR}$ (kPa) FEA	C (kPa) Test	C (kPa) FEA
46.5	8.4	5.65	4.15	0.29	0.22
40	12.97	4.44	3.5	0.36	0.28
31	14.81	4.17	2.6	0.38	0.24
23.5	39.44	2.73	1.85	0.67	0.45
11	75.91	1.79	6	0.85	0.28
0	100	0	0	0	0

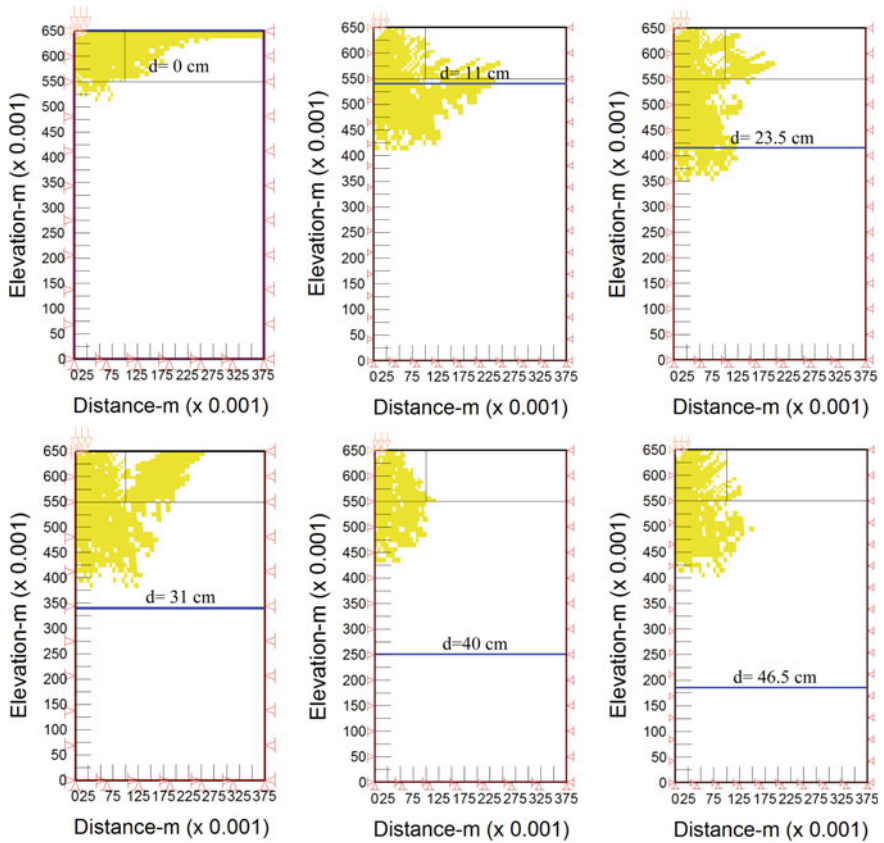


**Fig. 8** Yield zones developed in the soil for various depths of water level below soil surface

of the problem geometry to be modeled in the horizontal direction. Therefore, the no-horizontal displacement boundary conditions were assigned to the left boundary of the model in addition to the right boundary. A comparison of the pressure-settlement curves shown in Fig. 7 with the sizes and shapes of the yield zones shown in Fig. 8

indicate that as the load retained by the footing increases, the size of the yield zone increases and its shape represents failures modes moving from punching shear (yield zones extending mostly vertically into greater depths) to local and possibly general (for  $d = 31$  cm) shear failure (yield zones spreading somewhat laterally around the footing). An exception is a case for  $d = 0$  in which the soil is almost fully saturated, and its behavior may not be fully drained as in other cases.

## 6 Prediction of Bearing Capacity

Bearing capacity of footings placed on unsaturated soils may be estimated using conventional bearing capacity equations modified for considering the effects of unsaturated soils. Bearing capacities of the model footings loaded in the current study were determined using the curves shown in Fig. 6. For each case, two tangent lines were drawn to the two portions of the curve with different slopes, and the pressure corresponding to their point of intersection was taken as the bearing capacity [12]. Table 3 shows the bearing capacities obtained for each case and the ratios of these capacities to the saturated soil’s capacity. Settlements at ultimate capacities are also provided in the table.

Figure 9 compares bearing capacities obtained from test results with those estimated using the Vanapalli and Mohammad [7] bearing capacity equation for unsaturated soils. Due to the very loose state of the soil and the mostly punching shear failure modes shown by the numerical analysis results, the friction angle used in the determination of bearing capacity was reduced according to the suggestion of Terzaghi [13] such that  $\phi_m = \tan^{-1}(\frac{2}{3} \tan \phi)$ . Moreover, for the strip footing tested, a plane strain failure condition is expected and a correction for friction angle according to the suggestion of Stroud [14] was used such that:  $\tan \phi_{ps} / \tan \phi_{ds} = 1.2$ , in which  $\phi_{ps}$  is the plain strain and  $\phi_{ds}$  is the direct shear angles of friction. Comparison of measured and predicted bearing capacities are shown in Fig. 9. It may be noted from this figure that measured bearing capacity is highest at a matric suction of 4.2 kPa at

**Table 3** Bearing capacities and settlements at ultimate capacity for various water depths below the soil surface, d

d (mm)	Ultimate bearing capacity $q_{ult}$ (kPa)	$q_{ult}/q_{ult,sat}$	Settlement at ultimate bearing capacity (mm)
0 (saturated)	7.7	1	4.1
11	18	2.3	5.3
23.5	41	5.3	13.5
31	46.3	6	8.81
40	37	4.8	13.6
46.5	41.4	5	13.9
Dry	21.5	2.8	5.0

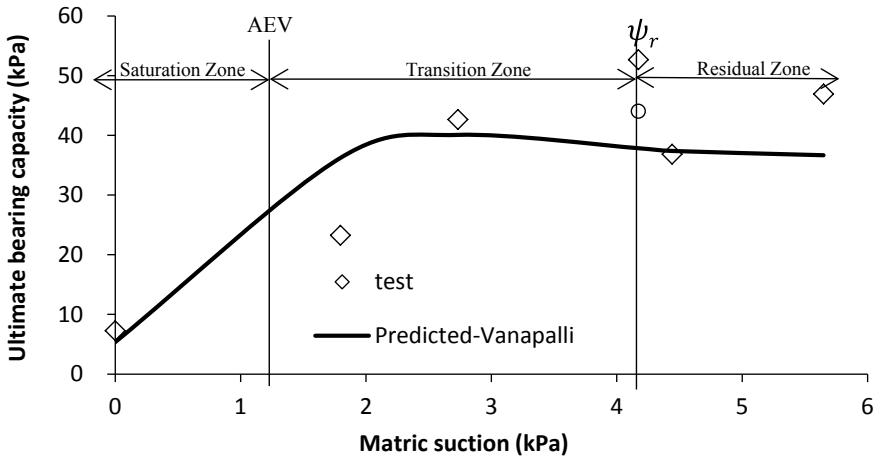


**Fig. 9** Measured and predicted bearing capacities of strip footing for various depths of the water below soil surface

the end of the transition zone, and then decreases slightly as matric suction increases (and therefore, degree of saturation decreases). On the other hand, the Vanapalli and Mohammad [7] equation, while providing satisfactory predictions of bearing capacity for most values of matric suctions, predicts the highest bearing capacity at a matric suction of about 2 kPa. Similar results were also reported by Alabdullah et al. [15]. The greatest difference between the predicted and measured bearing capacities was observed for the case with  $d = 31$  cm for which the bearing capacity was the highest. The numerical analysis results indicated that the failure mode, in this case, seems to be closer to a general shear mode, for which a reduction in the friction angle is not applicable. Figure 9 shows that if the bearing capacity equation's friction angle is not modified, the predicted bearing capacity will be closer the measured value. Therefore, it is important to take into account the mode of failure when using bearing capacity equations to predict ultimate footing loads. Moreover, the unsaturated state of the soil may alter the mode of bearing capacity failure of a footing such that a footing placed on very loose sand may not fail due to punching shear, but rather due to local or general shear failure as a result of the added soil strength caused by the unsaturated state of the underlying soil.

## 7 Summary and Conclusions

Effects of matric suction in an unsaturated, very loose fine sand on a strip footing behavior were first evaluated using physical modeling tests. The tests were then numerically modeled using commercial software with the ability to consider the unsaturated soil state. Test results were also compared with the bearing capacities



obtained from a published equation to evaluate its predictive capability for very loose sand. The main results of the study are summarized below:

- The experimental results indicated that an increase in the matric suction in the very loose sand could lead to up to a sixfold increase in the bearing capacity of model strip footings compared to the condition of fully saturated soil.
- The numerical analysis results indicated that the soil's failure mechanism underlying the footing seems to move from punching shear in the relatively weak, nearly dry or saturated soil to local or possibly general shear failure for soils with greater shear strength caused by the soil matric suction. This indicates that even in very loose sand, the additional strength due to matric suction in unsaturated soils may result in changes in the failure mechanism. This should be considered when applying reduction factors to soil strength parameters for use in bearing capacity equations.
- For the model strip footing placed on very loose fine sand, the greatest bearing capacity of 46.3 kPa was obtained at a degree of saturation of approximately 15%. The lowest measured capacity was 7.7 kPa, obtained for fully saturated sand, and a 21.5 kPa capacity was obtained for the case of dry sand.

## References

1. Vanapalli, S. K., Fredlund, D. G., Pufahl, D. E., & Clifton, A. W. (1996). Model for the prediction of shear strength with respect to soil suction. *Canadian Geotechnical Journal*, 33(3), 379–392.
2. Steensen-Bach, J. O., Foged, N., & Steenfelt, J. S. (1987). Capillary induced stresses-fact or fiction? In *Proceedings of the 9th European Conference on Soil Mechanics and Foundation Engineering* (pp. 83–89). Ireland: Dublin.
3. Vahedifard, F., & Robinson, J. D. (2016). Unified method for estimating the ultimate bearing capacity of shallow foundations in variably saturated soils under steady flow. *Journal of Geotechnical and Geoenvironmental Engineering*, 142(4), 04015095.
4. Schanz, T., Lins, Y., & Vanapalli, S. K. (2010). Bearing capacity of a strip footing on an unsaturated sand. In *Proceedings of the 5th International Conference on Unsaturated Soils* (pp 1195–1220). Spain: Barcelona.
5. Maghvan, S. V., Imam, R., & McCartney, J. S. (2019). Physical modeling of stone columns in unsaturated soil deposits. *Geotechnical Testing Journal*, 43(1), 253–274.
6. Maghvan, S. V., Imam, R., & McCartney, J. S. (2019). Relative density effects on the bearing capacity of unsaturated sand. *Soils and Foundations*, 59(5), 1280–1291.
7. Vanapalli, S. K., & Mohamed, F. M. O. (2007) Bearing capacity of model footings in unsaturated soils. In: *Experimental Unsaturated Soil Mechanics, Springer Proceedings in Physics* (Vol. 112. pp. 483–493) Berlin, Heidelberg: Springer-Verlag.
8. Ladd, R. S. (1974). Specimen preparation and liquefaction of sands. *Journal of Geotechnical and Geoenvironmental Engineering*, 100(10), 1180–1184.
9. Aubertin, M., Mbonimpa, M., Bussiere, B., & Chapuis, R. P. (2003). A model to predict the water retention curve from basic geotechnical properties. *Canadian Geotechnical Journal*, 40(6), 1104–1122.
10. McCartney, J. S., Villar, L. F. S., & Zornberg, J. G. (2008). Nonwoven geotextiles as hydraulic barriers to capillary rise. *Proceedings of GeoAmericas*, 252–261.

11. Nikoonejad, K. H., & Imam, R. (2013). Bearing capacity and settlement of shallow foundations on unsaturated soil. In *7th National Congress on Civil Engineering, Iran (Islamic Republic of)*.
12. Vesic, A. S. (1963). *Bearing capacity of deep foundations in sand*, *National Academy of Sciences* (pp. 112–153). Highway Research Record, No. 39, Washington, D.C.: National Research Council.
13. Terzaghi, K. (1943). *Theoretical Soil Mechanics*. John Wiley.
14. Stroud, M. A. (1971). *The Behaviour of Sand at Low Stress Levels in the Simple-Shear Apparatus*. Doctoral dissertation, University of Cambridge.
15. Alabdullah, J. (2010). *Testing Unsaturated Soil for Plane Strain Conditions: A New Double-Wall biaxial Device*, Ph.D. thesis, Univ. of Bauhaus-Weimar.

# Overall Static and Seismic Stability of Oil Tank Resting on Shallow Foundation: A Case Study



Chaidul Haque Chaudhuri, Rana Acharyya, Milind Patil,  
and Deepankar Choudhury

**Abstract** The design of the shallow foundation of oil tanks is the prime concern for civil engineers as these are important structures for the industries. In this paper, a field case study has been taken into account where the stability of an oil tank required to be installed at Sidhpur in Gujarat, India. The behavior of oil tank foundation has been investigated using finite element tool PLAXIS-3D. It has been comprehended from the soil investigation results and numerical analysis that the oil tank could not be filled completely with oil at the present site condition due to large differential settlement. The maximum vertical settlement of 96.80 and 136.2 mm has been found from the numerical analysis for the case of present site condition and considering water level at the ground surface. Moreover, a soil improvement technique has been proposed to reduce the settlement and enhance the stability of oil tank. Finally, a maximum vertical settlement of 54.88 mm has been observed for improved soil considering water level at the ground surface, and the influence of earthquake loading on the stability of the tank is found negligible.

**Keywords** Shallow foundation · Oil tank · Settlement · Stability · Seismic loading

---

C. H. Chaudhuri · D. Choudhury  
Department of Civil Engineering, Indian Institute of Technology Bombay, Powai, Mumbai, India  
e-mail: [chaudhuri.ch@iitb.ac.in](mailto:chaudhuri.ch@iitb.ac.in)

D. Choudhury  
e-mail: [dc@civil.iitb.ac.in](mailto:dc@civil.iitb.ac.in)

R. Acharyya (✉)  
Department of Civil Engineering, DIT University, Dehradun, India  
e-mail: [rana.acharyya@dituniversity.edu.in](mailto:rana.acharyya@dituniversity.edu.in)

M. Patil  
AFRY India Pvt Ltd, Noida, India  
e-mail: [milind.patil@afry.com](mailto:milind.patil@afry.com)

## 1 Introduction

Oil tanks are essential structures for the industries and are commonly constructed near airports, oil refineries, power plants, railway yards, and other national prominence places. The stability of tanks depends on the foundation and the subsoil condition. If the subsoil condition is not suitable to bear the tank's load, then either the strength and stiffness of the soil to be improved or a special type of foundation to be provided. Various ground improvement techniques are available, such as vibro compaction, soil replacement, cement grouting, etc. The ultimate bearing capacity (UBC) and settlement criteria are the prime concern for the safe design of shallow foundations for geotechnical engineers. The UBC, bearing capacity factors ( $N_c$ ,  $N_q$ ,  $N_\gamma$ ) and failure mechanism of shallow foundation have been investigated by several researchers [1–6]. The settlement of shallow foundation resting over-saturated clayey soil or cohesionless soil has been experimented by scholars [7–9]. The researchers carried out field plate load tests [10, 11] to observe the effect of plate size in estimating the settlement and bearing capacity for cemented and non-cemented soil. In the field experiment, circular plates of sizes ranging from 0.3 to 0.6 m and square footings of width ranging from 0.4 to 1 m had been considered. The vertical load had been applied over the plate, and corresponding settlement had been recorded. It had been perceived that the pressure-settlement pattern obtained from plates and footings was not unique because of considering diameter and width for circular and square footing. Furthermore, it had been concluded that the pressure-settlement pattern became unique after making the test results normalized. Specialists [12–14] had investigated experimentally and numerically the scale effect on UBC and shape factor  $s_\gamma$  of circular footing resting over dry, dense sand. It has been concluded that the UBC has been exponentially increased with increasing the dimension of the footing.

However, the bearing capacity factor (BCF)  $N_\gamma$  has been decreased by increasing the circular footing dimension. Moreover, the shape factor  $s_\gamma$  has been enhanced by increasing the footing dimension. Researchers [15–20] had numerically investigated the UBC for circular footing by considering smooth and rough base with the aid of FLAC software. In the numerical analysis, the non-associativity of soil has been considered. It has been revealed from the investigation that the magnitude of BCFs has been reduced significantly with increasing the non-associativity. Researchers [21–24] had performed laboratory and numerical investigations to determine UBC and settlement of circular footing resting on geocell-reinforced soft clay. It has been concluded from the research that the load-carrying capacity of circular footing resting over reinforced clay has been increased by 4.8 times than footing on unreinforced clay. Moreover, it has resulted that the heaving has been significantly reduced by providing the geocell-reinforcement of optimum height and width. Kumar et al. [25] had provided the design of pile foundation arrangement for static as well as the seismic case for oil tank resting over soft soil through numerical simulation with the aid of PLAXIS-3D. The pile group was consisted of 89 piles. It had been concluded that maximum differential settlement of 4 mm had been found for the pile group for static as well as seismic instance. Choudhury et al. [26, 27] had effectively used the

deep foundation units such as pile, piled raft, barrettes and ring foundation for various mega industrial projects across the globe like nuclear power plant (NPP), fertilizer plant, petroleum-oil-lubricant (POL) terminal, tall towers. Chatterjee et al. [28, 29] performed high strain dynamic testing of piles at three commercial sites of Kolkata city, India, and performed numerical analysis using finite difference-based software FLAC3D simulating the field conditions by considering similar soil-pile models for each case. A comparative study between the pile and piled raft foundation is also assessed in liquefaction conditions using FLAC3D [30].

Lee et al. [31] had investigated the benefits of piled foundation to support the oil tank in soft soil through centrifuge tests. In most of the case, ground improvement is preferable over the deep foundation from the economic point of view.

Hence, the present study is focused on shallow foundations. Static and dynamic soil-structure interaction response of pile group of an oil tank foundation had been numerically investigated considering FLAC3D by the researchers [32]. It had been revealed that the factored ultimate load-carrying capacity of a single pile was 2052 kN. The maximum rotational displacement had been found as  $5.81 \times 10^{-4}$  for the pile group, which is safe for the oil tank. Hamidi and Varaksin [33] had highlighted some case histories for ground improvement methods with the aid of dynamic compaction to reduce the settlement of tank foundation as to distribute the super-structural load to the soil. In the present investigation, the settlement analysis has been conducted for an oil tank with full oil height, which is going to be installed at the site. Various laboratory experiments have been conducted to determine the geotechnical parameters of the site soil. Moreover, geotechnical and geometrical parameters have been used in the numerical analysis. It has been observed from the settlement analysis that the oil tank cannot be kept with full oil height inside the tank. Moreover, the effect of water table depth on the settlement has also been analyzed. Finally, modified, improved soil layers are proposed so that the oil tank can be installed with full oil height without excessive settlement, considering both static as well as dynamic loading.

## 2 Site Characterization

The site, oil refinery terminal is situated at Sidhpur, Gujarat in India as shown in Fig. 1. An oil tank of 28 m diameter and 20 m height has been required to be installed at the refinery terminal. Bore log data (Fig. 2) have been obtained from field investigation through boring method. The diameter and the depth of the borehole have been considered as 0.15 m and 10 m, respectively. The borehole depth has been evaluated from the ground surface. In the field, the boring has been performed by the auger drilling method without any casing. The water table has not been encountered during boring within the depth of 10 m. Furthermore, for collecting undisturbed samples, thin-walled Shelby tubes and piston type sampler have been considered standard practices [34]. Standard Penetration Tests (SPT) have been carried out in borehole at predetermined depths as per IS 2131 [35]. It has been perceived from the bore log (Fig. 2) that the soil stratification at the site is primarily comprised of brownish

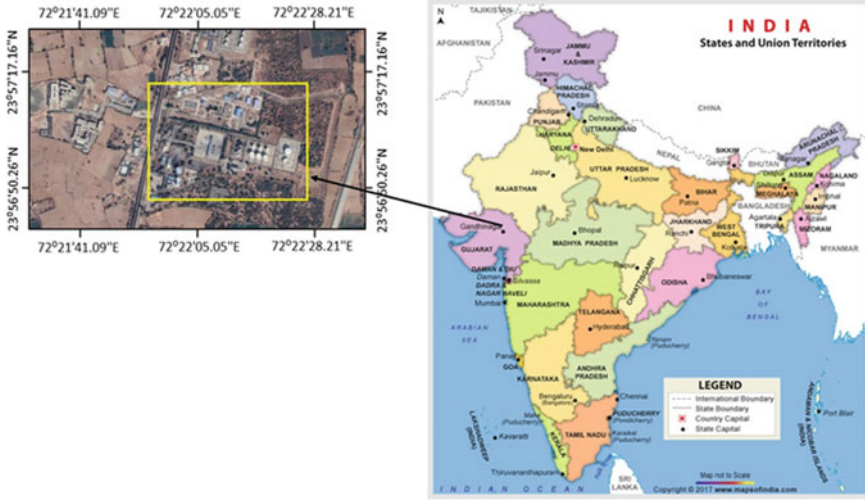


**Fig. 1** Location of oil storage tank at Sidhpur in India

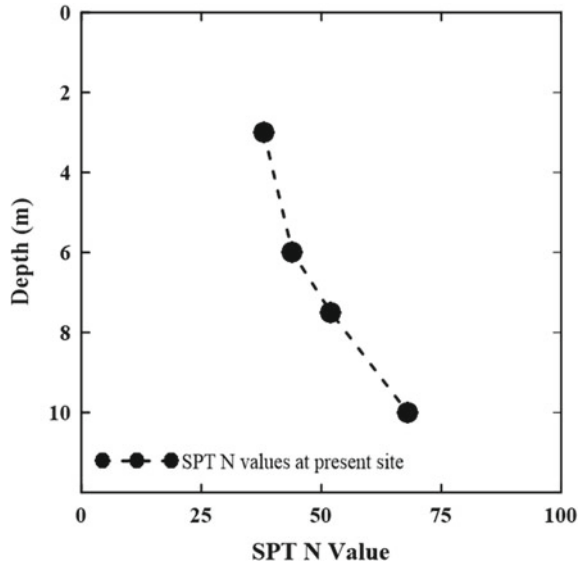
**Fig. 2** Soil stratification and in situ description in field

Description of Sample	Legend	Thickness of Strata (m)
Filled up soil	FS	0.30
Brownish non plastic silty sand	SM	1.70
Yellowish hard to very hard silty clay having high to low plasticity	CH/CL	8.00

non-plastic silty sand to low plasticity silty clay with SPT-N values ranging from 38 to 68. The variation of SPT value with depth is depicted in Fig. 3. The disturbed soil samples have been collected from the boring operation and split spoon sampler, have been considered for detailed laboratory tests for the determination of various geotechnical parameters. The soil parameters obtained from various laboratory tests have been mentioned in Table 1.

The cross-sectional details of the tank foundation and corresponding footing parameters are shown in Fig. 4 and tabulated in Table 2. It has been perceived from Fig. 4 that the top 300 mm a coarse sand blanket has replaced filled-up soil, and above the sand blanket well-compacted tank pad (Moorum) of 600 mm thick has been provided. Furthermore, on the top of the tank pad, an anticorrosive layer of

**Fig. 3** SPT N-value observed during field test



75 mm thick has been considered to avoid any oil or other liquid injection below the tank foundation [36]. The fixed roof High-Speed Diesel (HSD) storage tank has a 28 m and a height of 20 m. The oil tank is resting on a trapezoidal crushed stone ring of size 900 mm × 300 mm × 300 mm as shown in Fig. 4. The density of the inside stored material is 840 kg/m<sup>3</sup>.

### 3 Numerical Modelling

In the numerical study, three-dimensional finite element package PLAXIS-3D version 2017.01 has been utilized for modelling various geotechnical aspects such as flow analysis, stability analysis, and deformation assessment. In the numerical investigation, the model dimension has been considered in such a way that the generated mechanism should not be affected by the boundaries of the domain, as shown in Fig. 5. The model has been discretized (termed as meshing), using 10-noded tetrahedral elements for soil and footing, and 6-noded triangular elements have been considered for plate element which has been used for tank modeling as shown in Fig. 5.

In the modeling, standard fixity has been considered. Horizontal fixities have been used for vertical boundaries. In case of the bottom boundary, horizontal and vertical fixities have been provided, considering it non-yielding. In the numerical investigation, the soil has been modeled with Mohr–Coulomb (M-C) model. Although more advanced constitutive soil models are available, such advanced models require more input parameters, leading to more complexity in the model than the M-C model.

**Table 1** Soil parameters

Identification	Depth (m)	Dry unit weight (kN/m <sup>3</sup> )	Wet unit weight (kN/m <sup>3</sup> )	Soil model adopted	SPT-N value	Young's modulus (E) (kPa)	Poisson's ratio ( $\mu$ )	Cohesion (c) (kPa)	Friction angle ( $\phi$ )
Top Filled up soil (FS) replaced by Sand blanket	0-0.3	18	20	MC	-	17,500	0.25	1	30
Sand blanket	0-0.3	18	20	MC		30,000	0.25	0.1	35
Brownish Non Plastic Silty Sand (SM)	0.3-2	18.2	19.3	MC	-	14,500	0.25	0	22
Yellowish hard to very hard silty clay having high to low plasticity (CH/CL)	2-3.5	18.4	20.5	MC	38	16,960	0.30	20	28
	3.5-6.5	18.4	20.5	MC	44	18,880	0.30	20	28
	6.5-8	18.4	20.5	MC	52	21,440	0.30	20	28
	8-10	18.4	20.5	MC	68	26,560	0.30	20	28



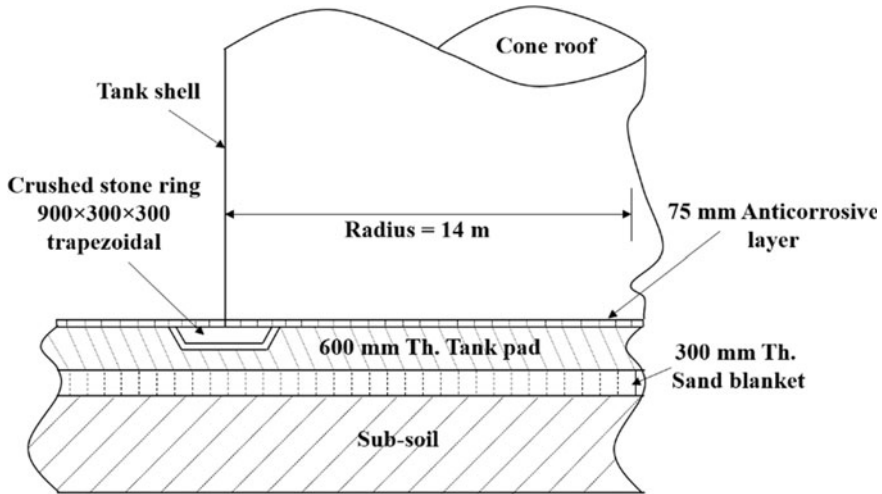


Fig. 4 Schematic representation of a tank foundation system

Table 2 Footing parameters

Identification	Dry unit weight ( $\gamma_{dry}$ ) (kN/m <sup>3</sup> )	Soil model adopted	Young's modulus (E) (kPa)	Poisson's ratio ( $\mu$ )	Cohesion (c) (kPa)	Friction angle ( $\phi$ )
Tank pad (Moorum)	18	MC	50,000	0.30	35	–
Crushed stone	22.64	LE	$3 \times 05$	0.35	–	–
Anticorrosive layer (Bitumen)	15	MC	5000	0.40	20	10
Tank	77	LE	$2 \times 108$	0.15	–	–

So, in order to avoid time-consuming and complex, the present model adapted M-C model. However, earlier studies also successfully used M-C model in the various static and dynamic analyses [37–41]. M-C model has consisted of strength parameters and deformation parameters. Strength parameters are comprised of cohesion (c), angle of internal friction ( $\phi$ ), and dilatancy angle ( $\psi$ ). Deformation parameters are included modulus of elasticity (E) and Poisson's ratio ( $\mu$ ). The steel oil tank of a thickness of 12 mm has been modeled with the aid of a linear elastic (LE) model. In the simulation,  $K_0$  procedure has been adopted for generating the initial stress condition in the model.

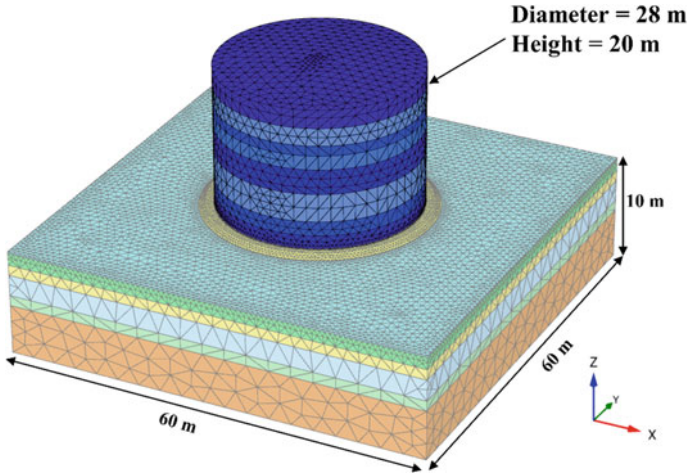


Fig. 5 Three-dimensional model of oil tank foundation system in PLAXIS-3D

#### 4 Validation of the Present Numerical Analysis

The validation work has been considered in the present investigation to realize the intricacies involved in the 3D finite element (FE) modeling and confidence over the FE modeling. In the present numerical investigation, the field plate load test conducted by researchers [10] has been taken into account to validate the present numerical models. In the field experiment, the researchers [10] have considered a circular plate with a diameter of 300 mm and thickness of 25.4 mm. The loading arrangement has been taken into account consisted of load platform, hydraulic jack, and reaction beam to provide load over the plate. The calibrated load cell has been used in the experiment for measuring the applied load. Four dial gauges have been considered in the test to measure the plate settlement. According to particle size data, the field soil was comprised of 24% clay, 38% fine sand, 6% medium sand, and 32% silt. The cohesion ( $c$ ), angle of internal friction ( $\phi$ ), and bulk unit weight ( $\gamma_b$ ) of soil were  $17 \text{ kN/m}^2$ ,  $26^\circ$  and  $18.2 \text{ kN/m}^3$ , respectively. In the numerical simulation, the same field soil properties have been considered in the validation investigation. The model dimension has been considered in such a way that the overall mechanism of the foundation should not be affected by the boundaries of the domain as shown in Fig. 6. In the investigation, mesh convergence study has been conducted to get an optimal mesh size for precise results [42]. In the convergence study, load-settlements curves are plotted for various meshing schemes, as shown in Fig. 7, and it has been perceived that results are almost identical for both fine and very fine meshing. Moreover, a fine meshing scheme has been taken into account for validation as well as further numerical investigation to maintain a balance between time and accuracy. It has been comprehended from Fig. 8 that there is a good agreement in results between the field test and numerical outcomes.

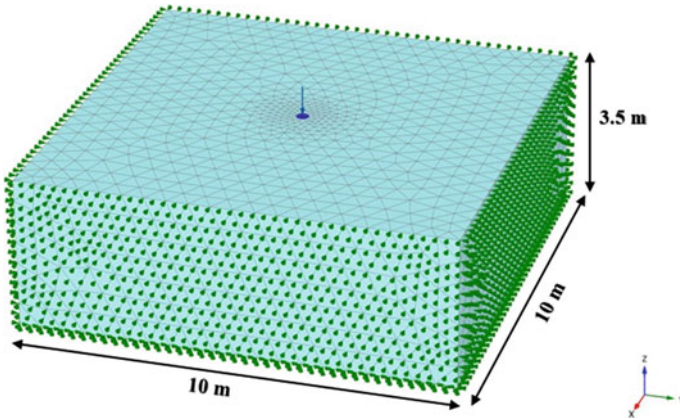


Fig. 6 Plate load test [10] modeled in PLAXIS-3D

Fig. 7 Mesh convergence study

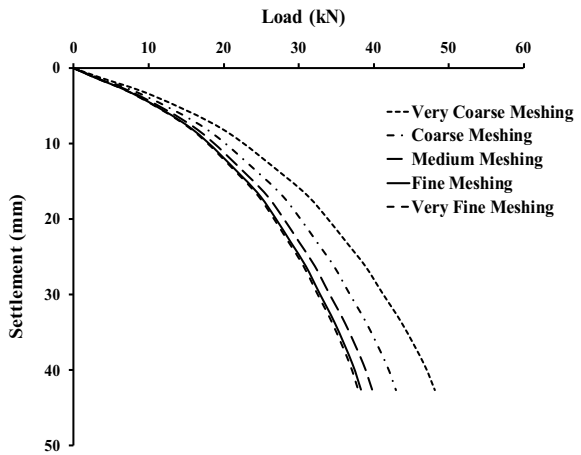
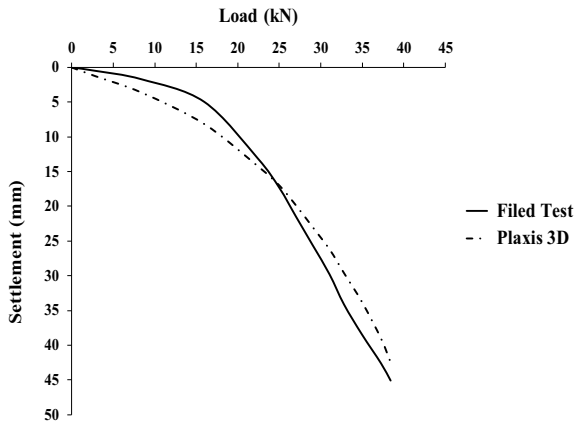


Fig. 8 Comparison of load-settlement plots between field plate load test and PLAXIS-3D



## 5 Results and Discussion

In the current investigation, an oil tank settlement has been assessed by considering the soil properties and water table conditions present at the site. It has been perceived from the bore log data that the water table has not been found up to the depth of 10 m. Firstly, the analysis has been performed by considering the oil tank resting over the dry soil. Afterward, the investigation has been carried out by considering the water table effect on the oil tank settlement. In the simulation, different water table positions below the ground surface have been taken into account. Finally, the analysis has been conducted by considering the improved soil properties to install the oil tank with full oil height.

## 6 Oil Tank Resting Over Untreated Soil

**Analysis Without Water Table.** In the present research, the oil tank settlement has been assessed by considering various normalized oil heights ( $h_o/H_{full}$ ,  $h_o$  = oil height inside the tank,  $H_{full}$  = full oil height) inside the tank, as mentioned in Table 3. The differential settlement is the difference between maximum settlement ( $s_{max}$ ) and minimum settlement ( $s_{min}$ ) generated beneath the oil tank. The safe oil filling height inside the tank for the corresponding safe differential settlement has been evaluated from the research materials [43, 44]. The safe differential settlement criteria have been calculated from the following expressions (Eqs. 1 and 2)

$$s_{max} - s_{min} < \frac{1}{300}(\text{Distance between points of } s_{max} \text{ and } s_{min}) \text{ [Safe]} \quad (1)$$

$$s_{max} - s_{min} > \frac{1}{300}(\text{Distance between points of } s_{max} \text{ and } s_{min}) \text{ [Unsafe]} \quad (2)$$

**Table 3** Differential settlement for different oil filling height

Loading case (Normalized filling height $h_o/H_{full}$ )	Max. differential settlement below tank (mm)	Safe criteria as per Bowles [44]
1	20	Not Safe
0.75	17	Not safe
0.625	14	Safe
0.5	10	Safe
0.35	9	Safe
0.3	7.3	Safe
0.25	5	Safe

It has been perceived from Table 3 that the oil tank can be safely installed with a maximum normalized oil height of 0.625 inside the tank at the present site condition. Further increase of normalized oil height inside the tank shall be unsafe for installing the oil tank. Figures 9 and 10 depict the typical color contours of the vertical settlement of the oil tank’s footing with full normalized oil height ( $h_o/H_{full} = 1$ ) inside the tank. Figure 9 is the top view of the footing’s vertical settlement, and Fig. 10 is the vertical cross-section of the top view (Fig. 9). It has been perceived that the maximum vertical settlement of 96.80 mm has been generated for full storing of oil inside the tank.

**Analysis With Water Table.** In the field investigation, the water table has not been found at the site within the boring depth of 10 m. However, the effect of different water table depths on safe oil storing height has been investigated in the present analysis for considering the seasonal variation of water table depth. In the investigation, various normalized depths ( $H_w/D$ ,  $H_w =$  water table depth below ground surface, and  $D =$  diameter of the oil tank) of the water table have been considered. It has been revealed from Fig. 11 that the water table has a significant effect on normalized safe oil storage height ( $H_{safe}/H_{full}$ ,  $H_{safe} =$  safe oil storage height, and  $H_{full} =$  full oil storage height). It has been perceived that the normalized safe oil storage height

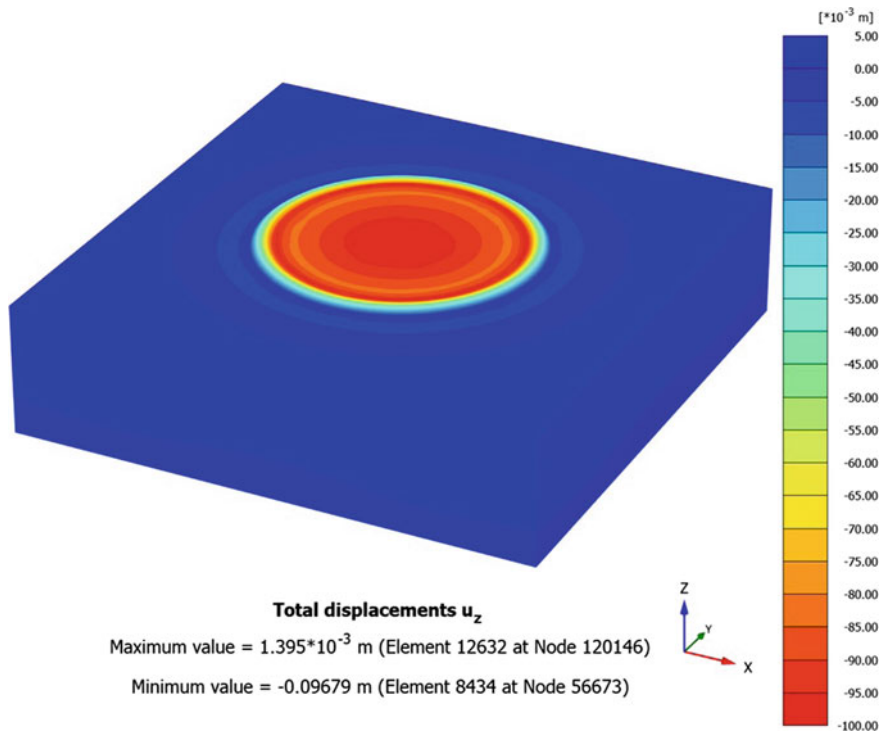


**Fig. 9** A typical view of vertical settlement at the foundation level of the tank when completely filled with oil ( $h_o/H_{full} = 1$ )

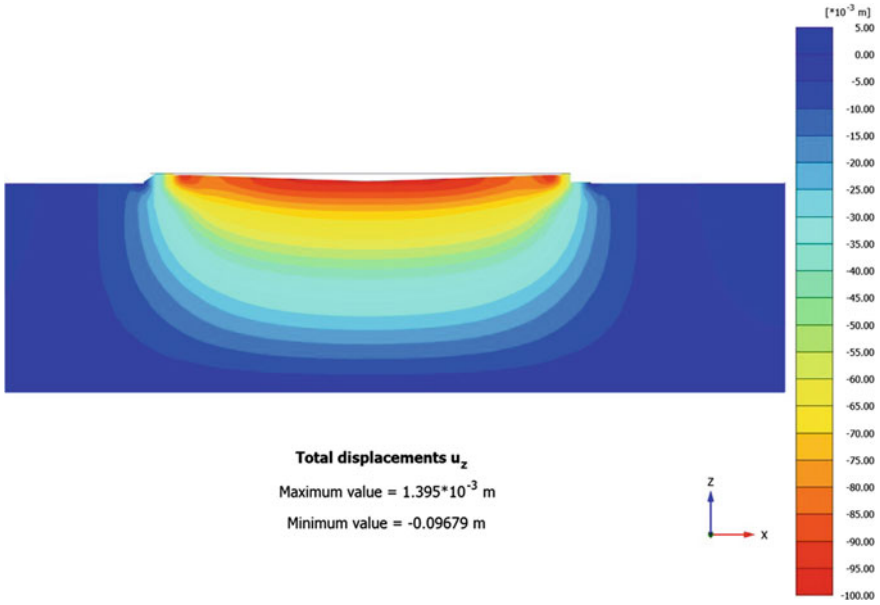
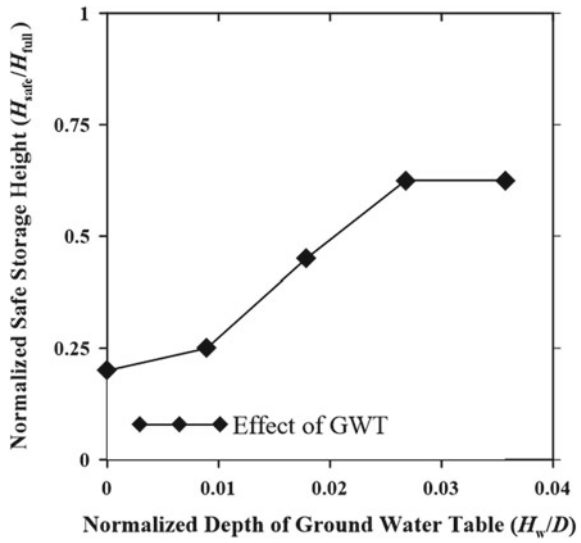


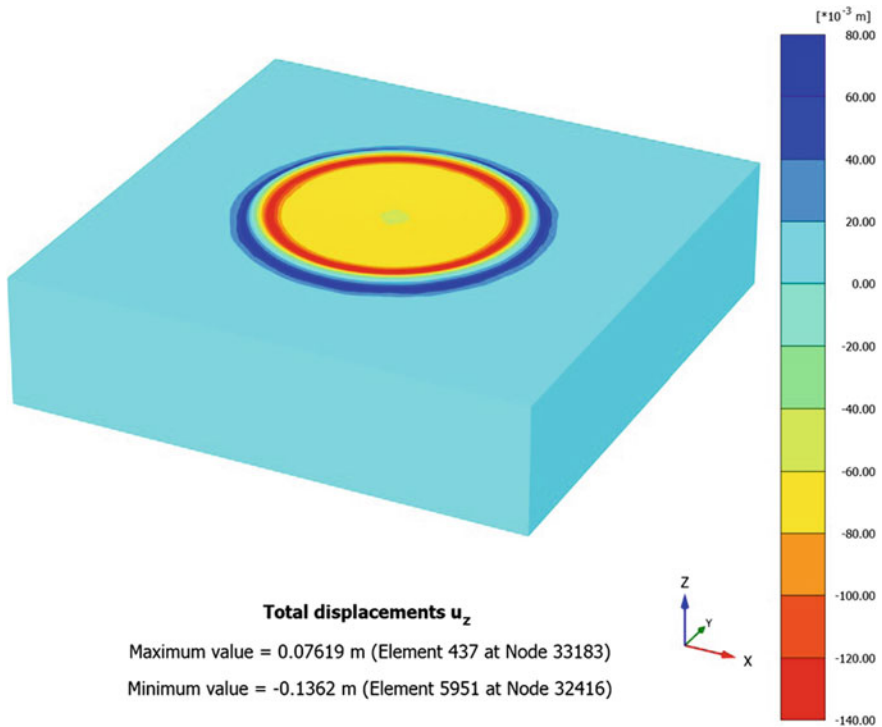
Fig. 10 Settlement contours in vertical direction of footing during full tank condition ( $h_0/H_{full} = 1$ )

Fig. 11 Effect of depth of water table on safe storage height of the oil



increases with increasing the normalized water table depth. The minimum normalized safe oil storage height of 0.2 has been found for zero normalized water table depth (water table at the ground surface).

It has been observed that beyond critical normalized water table depth  $[(H_w/D)_{critical}]$  of 0.027 beneath the ground surface, the water table depth does not affect safe oil storage height. The normalized safe oil storage height for the corresponding  $(H_w/D)_{critical}$  of 0.027 is 0.625, which has been found as normalized safe oil storing height for no water table condition. Figure 12 depicts the typical color contours of vertical settlement of the oil tank's footing with full oil storage for a water table at ground surface. It has been revealed that the maximum vertical settlement of 136.20 mm has been generated for full oil storage inside the tank. The settlement has been increased by 40.70% for the water table at the ground surface compared to dry soil.



**Fig. 12** Typical top view of vertical settlement of footing for water table at ground surface and  $h_0/H_{full} = 1$

### 7 Oil Tank Resting Over Improved Soil

The present research’s prime goal is to install the oil tank with full oil height inside the tank at the site. It has been revealed from the above discussion that the oil tank cannot be installed with full oil height at the present site condition. Moreover, the scenario shall be more critical for the water table at the ground surface. It has been perceived that soil improvement is required to install the oil tank with full oil height at the site. In the analysis, various modified SPT-N values have been taken into account for the soil layers and safe oil storage height has been evaluated. Finally, optimum SPT-N values, as shown in Fig. 13, have been considered to modify the soil layers accordingly to sustain the oil tank’s footing load with full oil storage height without any excessive settlement. The SPT-N values shown in Fig. 13 are the minimum required ‘N’ values at the site to utilize the tank’s full height. According to modified SPT-N values, the improved soil properties have been taken into account for the soil layers according to modified SPT-N values [44]. The modified soil properties have been provided in Table 4. Moreover, the modified SPT-N values are considered in such a way that the oil tank can be installed with full oil height for the water table at the ground surface. Figure 14 portrays the color contours of vertical settlement of the oil tank’s footing with full oil storage for the ground surface’s water table. It has been revealed that the maximum vertical settlement observed was 54.88 mm. The total vertical settlement has been reduced by 59.71% by considering modified soil layers. Furthermore, various soil improvement techniques are available, specifically vibro-compaction, soil replacement, and cement grouting [45, 46], to achieve the target optimum SPT-N values.

**Fig. 13** Modified SPT value for the site

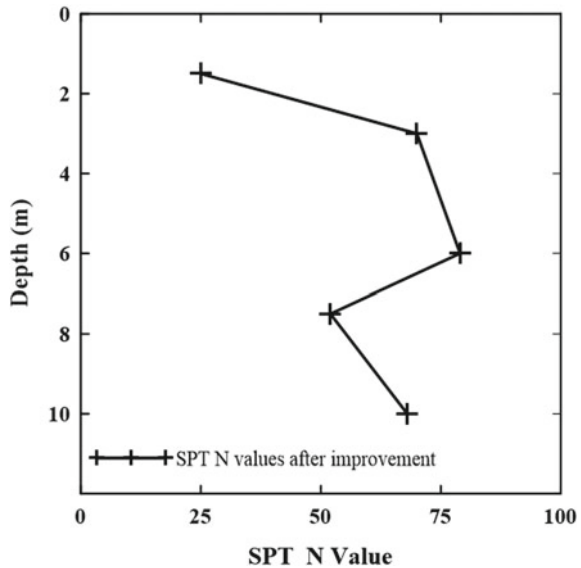




**Table 4** Improved soil properties after ground improvement

Identification	Depth (m)	Dry unit weight (kN/m <sup>3</sup> )	Wet unit weight (kN/m <sup>3</sup> )	Soil model adopted	SPT-N value	Young's modulus (E) (kPa)	Poisson's ratio ( $\mu$ )	Cohesion (c) (kPa)	Friction angle ( $\phi$ )
Brownish Non-Plastic Silty Sand (SM)	0.3-2	19	20	MC	25	20,000	0.25	0	35
Yellowish hard to very hard silty clay having high to low plasticity (CH/CL)	2-3.5	19	21	MC	70	23,000	0.30	20	35
	3.5-6.5	19	21	MC	79	25,500	0.30	20	35

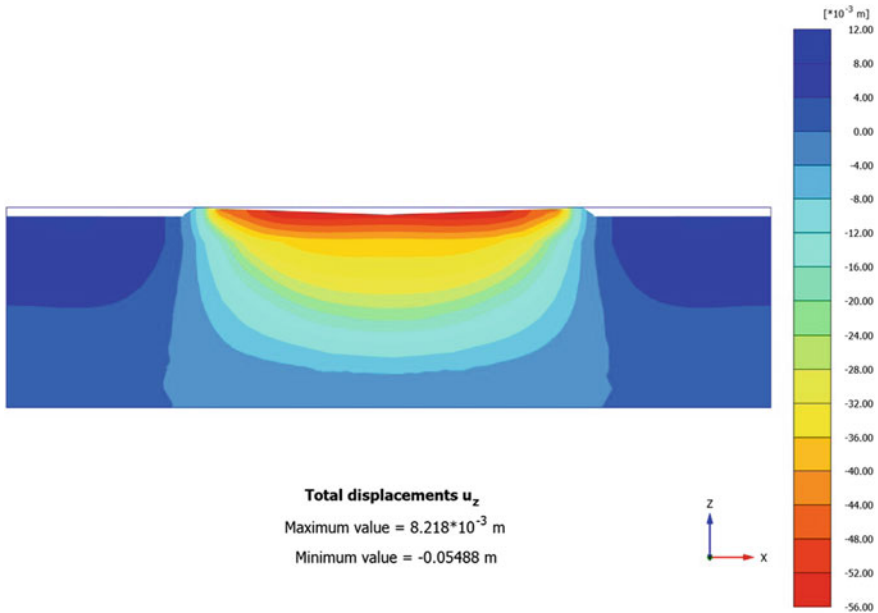


**Fig. 14** Typical cross-sectional view of vertical settlement contours of footing of oil tank with full oil height for improved soil layers and water table at the ground surface

## 8 Dynamic Analysis

In this section, the oil tank's stability with full oil height resting on improved soil has been assessed considering earthquake loading. The water table is considered at ground surface level to simulate the worst situation. Since the study area is located at Sidhpur in Gujarat, India. Bhuj 2001 earthquake with PGA value of 0.106 g is used as input ground motion in the present analysis. The acceleration time history of the input ground motion is shown in Fig. 15. Material damping of 5% [47] is used under dynamic analysis using Rayleigh damping coefficients in PLAXIS 3D. The values of Rayleigh damping coefficients are calculated following the published paper elsewhere [39]. Side boundary conditions are simulated using viscous boundary conditions to avoid any reflection of waves. The input seismic motion is provided at the base of the model. Figures 16, 17 and 18 illustrate the resulting deformation of the oil tank foundation system in x, y, and z direction respectively subjected to input ground motion. The maximum displacement of 8.762 mm is observed in x-direction as shown in Fig. 16. From Figs. 16, 17 and 18, it has been observed that the influence of input seismic motion on the foundation displacement is negligible. Hence, it can be concluded that the oil tank with full oil height is stable under the proposed improved soil.

**Fig. 15** Input ground motion of Bhuj (2001) earthquake having PGA of 0.106 g

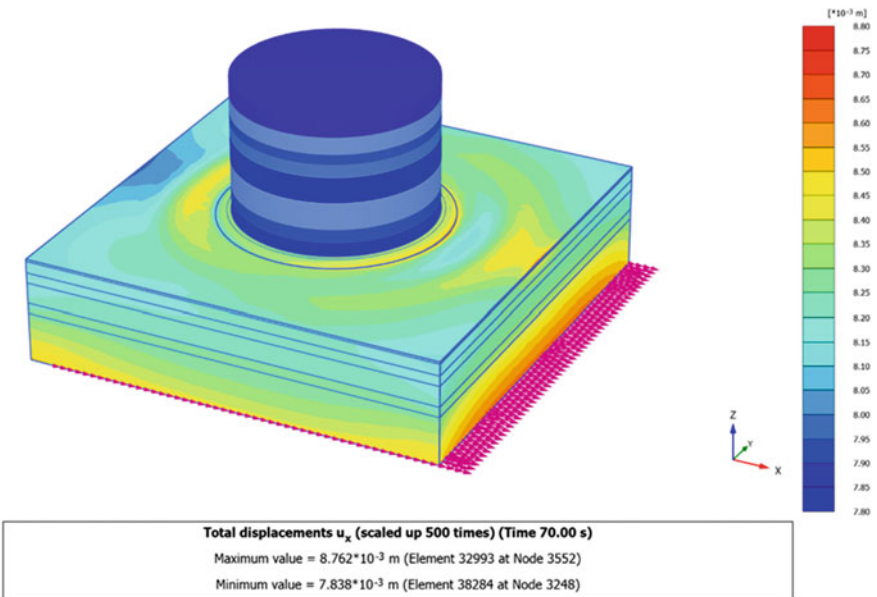
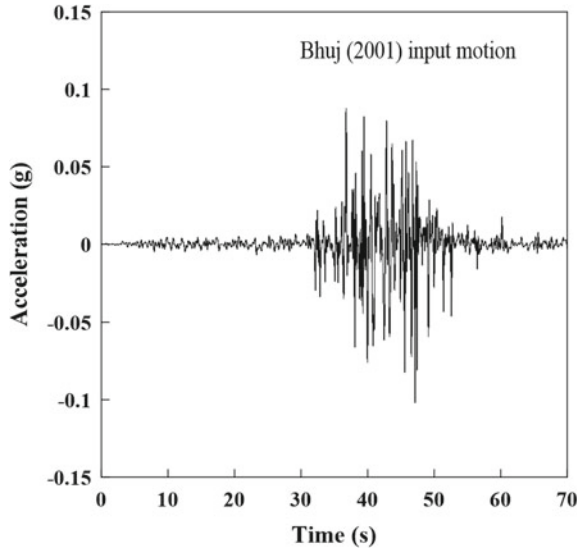


**Fig. 16** Displacement in x-direction due to seismic loading with full oil height for improved soil layers and water table at the ground surface

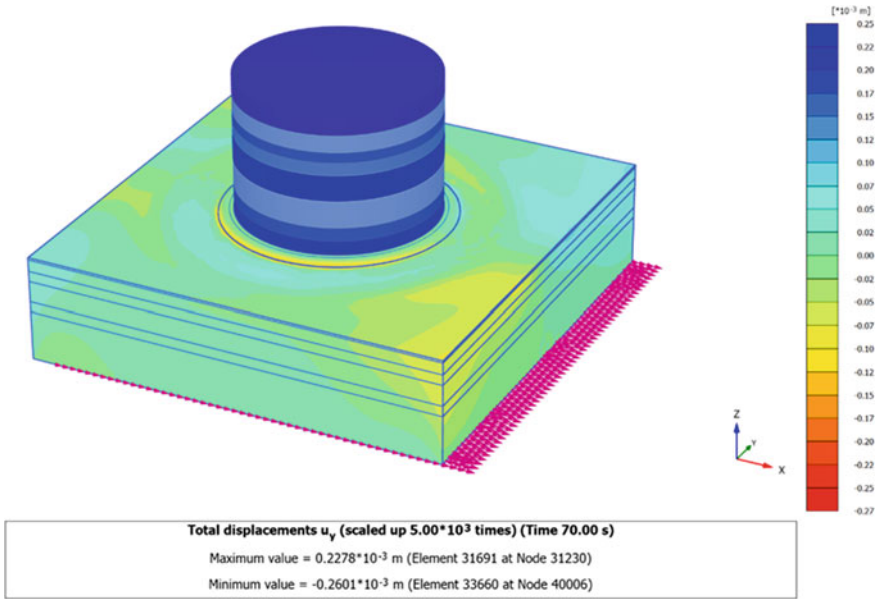


**Fig. 17** Displacement in y-direction due to seismic loading with full oil height for improved soil layers and water table at the ground surface

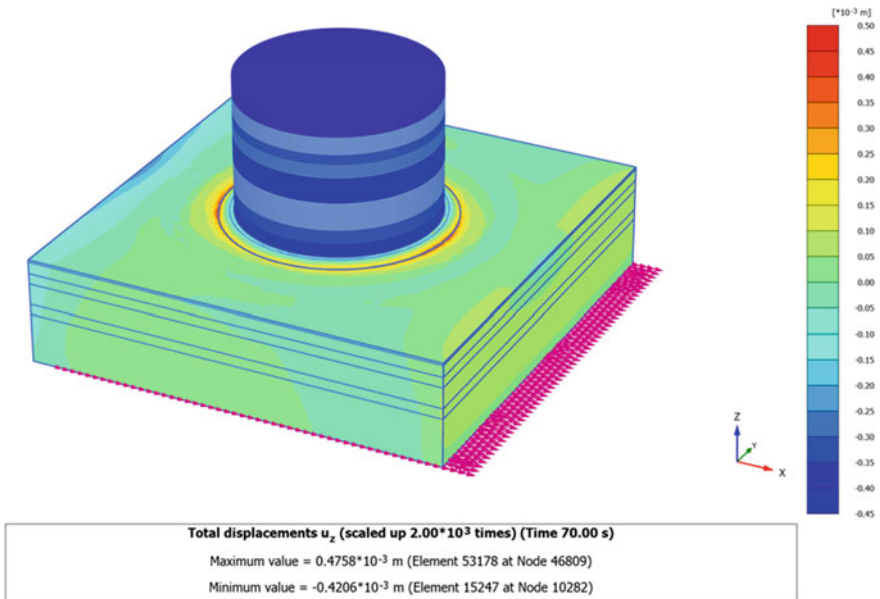


**Fig. 18** Displacement in z-direction due to seismic loading with full oil height for improved soil layers and water table at the ground surface

## 9 Summary and Conclusions

In the present research, the stability of an oil tank of 28 m diameter and 20 m height has been assessed in terms of settlement with the aid of numerical tool PLAXIS 3D. The main goal was to install the oil tank with full oil storage safely at the site within the permissible limit of settlement. In this regard, the analysis has been carried out for evaluating the settlement and safe oil storage height for tank resting over soil at present site condition. Then, the water table's effect on the settlement and safe oil storage height has been calculated. Finally, ground improvement recommendations have been given for installing the oil tank with full oil capacity safely considering the effect of earthquake loading as well. From the above numerical investigations, the following conclusions are drawn:

- The oil tank with full oil storage height cannot be installed for the present ground condition. Moreover, the oil tank can safely be installed with a normalized oil storage height of 0.625.
- The settlement of footing of the oil tank increases with increasing the water table at the site. The normalized safe oil storage height of 0.2 has been found for the water table at the ground surface. The water table depth has no effect on settlement and safe oil storage height beyond a critical normalized water table depth  $[(H_w/D)_{critical}]$  of 0.027. Moreover, the oil tank settlement has been increased by 40.70% for the water table at the ground level and for full oil storage height compared to dry soil.
- An optimum set of SPT-N values have been suggested for improving the soil properties of layers at the site for the successful installation of the oil tank with full oil height. Furthermore, the oil tank settlement has been reduced by 59.71% for a water table at ground level and full oil height inside the tank through soil improvement at the site compared to the present soil condition with the water table at the ground level.
- It is found that an oil tank with full oil height resting on the improved soil is also stable under earthquake loading conditions.

**Acknowledgements** Authors want to acknowledge the fund received from Indian Oil Corporation Limited (IOCL), Gujarat State Office, Indian Oil Bhavan, Ahmedabad, India, with project code RD/0219-CEIOCLG-167 (DRD/CE/DC-2/19-20), to carry out the industrial research work mentioned in this paper.

## References

1. Terzaghi, K. (1943). *Theoretical soil mechanics*. Wiley.
2. Skempton, A. W. (1951). *The bearing capacity of clay*. Building Research Congress.
3. Meyerhof, G. G. (1951). The ultimate bearing capacity of foundations. *Geotechnique*, 2, 301–332.

4. Hansen, B. J. (1970). *A revised and extended formula for bearing capacity*. Danish Geotechnical Institute.
5. Vesic, A. S. (1973). Analysis of ultimate loads of shallow foundation. *Journal of the Soil Mechanics and Foundations Division ASCE*, 99, 45–73.
6. Bureau of Indian Standards BIS 1981, Code of practice for determination of bearing capacity of shallow foundations, (IS 6403:1981). Bureau of Indian Standards.
7. Schleicher, F. (1926). Zur theorie des baugrundes. *Bauingenieur*, 48, 931–935.
8. DeBeer, E. E., & Martens, A. (1957). Method of computation of an upper limit for the influence of heterogeneity of sand layers in the settlement of bridges. In *Proceedings, 4th International Conference on Soil Mechanics and Foundation Engineering, London* (Vol. 1, pp. 275–281).
9. Schmertmann, J. H., Hartman, J. P., & Brown, P. R. (1978). Improved strain influence factor diagrams. *Journal of the Geotechnical Engineering Division*, 104(8), 1131–1135.
10. Consoli, N. C., Schnaid, F., & Milititsky, J. (1998). Interpretation of plate load tests on residual soil site. *Journal of Geotechnical and Geoenvironmental Engineering*, 124(9), 857–867.
11. Consoli, N. C., Vendruscolo, M. A., & Prietto, P. D. M. (2003). Behavior of plate load tests on soil layers improved with cement and fiber. *Journal of Geotechnical and Geoenvironmental Engineering*, 129(1), 96–101.
12. Zhu, F., Clark, J. I., & Phillips, R. (2001). Scale effect of strip and circular footings resting on dense sand. *Journal of Geotechnical and Geoenvironmental Engineering*, 127(7), 613–621.
13. Chakraborty, D., & Kumar, J. (2013). Dependency of  $N_{\gamma}$  on footing diameter for circular footings. *Soils and Foundations*, 53(1), 173–180.
14. Shafiqul Islam, M., Rokonuzzaman, M., & Sakai, T. (2017). Shape effect of square and circular footing under vertical loading: experimental and numerical studies. *International Journal of Geomechanics*, 17(9), 06017014.
15. Erickson, H. L., & Drescher, A. (2002). Bearing capacity of circular footings. *Journal of Geotechnical and Geoenvironmental Engineering*, 128(1), 38–43.
16. Cassidy, M. J., Airey, D. W., & Carter, J. P. (2005). Numerical modeling of circular footings subjected to monotonic inclined loading on uncemented and cemented calcareous sands. *Journal of Geotechnical and Geoenvironmental Engineering*, 131(1), 52–63.
17. El Sawwaf, M., & Nazer, A. (2005). Behavior of circular footings resting on confined granular soil. *Journal of Geotechnical and Geoenvironmental Engineering*, 131(3), 359–366.
18. Lee, J., & Salgado, R. (2005). Estimation of bearing capacity of circular footings on sands based on cone penetration test. *Journal of Geotechnical and Geoenvironmental Engineering*, 131(4), 442–452.
19. McMahon, B. T., Haigh, S. K., & Bolton, M. D. (2014). Bearing capacity and settlement of circular shallow foundations using a nonlinear constitutive relationship. *Canadian Geotechnical Journal*, 51(9), 995–1003.
20. Benmebarek, S., Saifi, I., & Benmebarek, N. (2017). Depth factors for undrained bearing capacity of circular footing by numerical approach. *Journal of Rock Mechanics and Geotechnical Engineering*, 9(4), 761–766.
21. Sitharam, T. G., Sireesh, S., & Dash, S. K. (2005). Model studies of a circular footing supported on geocell-reinforced clay. *Canadian Geotechnical Journal*, 42(2), 693–703.
22. Naderi, E., & Hataf, N. (2014). Model testing and numerical investigation of interference effect of closely spaced ring and circular footings on reinforced sand. *Geotextiles and Geomembranes*, 42(3), 191–200.
23. Badakhshan, E., & Noorzad, A. (2015). Load eccentricity effects on behavior of circular footings reinforced with geogrid sheets. *Journal of Rock Mechanics and Geotechnical Engineering*, 7(6), 691–699.
24. Tafreshi, S. M., Sharifi, P., & Dawson, A. R. (2016). Performance of circular footings on sand by use of multiple-geocell or-planar geotextile reinforcing layers. *Soils and Foundations*, 56(6), 984–997.
25. Ashutosh, K., Deepankar, C., Jaykumar, S., et al. (2015). Seismic design of pile foundation for oil tank by using PLAXIS3D. *Disaster Adv*, 8(6), 33–42.

26. Choudhury, D., Kumar, A., Patil, M., Rao, V. D., Bhaduri, A., Singbal, P., & Shukla, J. (2019). Sustainable foundation solutions for industrial structures under earthquake conditions-theory to practice. In *Proc., 16th Asian Regional Conf. on Soil Mechanics and Geotechnical Engineering* (pp. 1–11).
27. Choudhury, D., Biswas, S., Patil, M., & Manoj, S. (2021). Solutions for foundation systems subjected to earthquake conditions. *Indian Geotechnical Journal*, 51(1), 165–181.
28. Chatterjee, K., Choudhury, D., Rao, V. D., & Mukherjee, S. P. (2015). Dynamic analyses and field observations on piles in Kolkata city. *Geomechanics and Engineering: An International Journal*, Techno-Press, Korea, 8(3), 415–440.
29. Chatterjee, K., Choudhury, D., Rao, V. D., & Poulos, H. G. (2019). Seismic response of single piles in liquefiable soil considering P-delta effect. *Bulletin of Earthquake Engineering*, 17(6), 2935–2961.
30. Bhaduri, A., Rao, V. D., & Choudhury, D. (2020). The behaviour of pile group and combined piled-raft foundation in liquefiable soil under seismic conditions. *Geotechnical Engineering, Journal of the Southeast Asian Geotechnical Society (SEAGS) and Association of Geotechnical Societies in Southeast Asia (AGSSEA)*, 51(2), 130–138.
31. Lee, S. C., Leung, C. F., & Chow, Y. K. (2005). Performance of oil tank foundation. In *Advances in deep foundations* (pp. 1–10).
32. Kumar, A., & Choudhury, D. (2016). DSSI analysis of pile foundations for an oil tank in Iraq. *Proceedings of the Institution of Civil Engineers-Geotechnical Engineering*, 169(2), 129–138.
33. Hamidi, B., & Varaksin, S. (2017, July). Ground improvement of tank foundations in the middle east. In *International Congress and Exhibition “Sustainable Civil Infrastructures: Innovative Infrastructure Geotechnology”* (pp. 194–209). Springer
34. Bureau of Indian Standards BIS 1986, Thin-walled tube sampling of soils- code of practice, (IS 2132:1986). Bureau of Indian Standards.
35. Bureau of Indian Standards BIS 1981, Method for standard penetration test for soils-code of practice, (IS 2131:1981). Bureau of Indian Standards.
36. Bureau of Indian Standards BIS 1976, design, fabrication and erection of vertical mild steel cylindrical welded oil storage tanks-code of practice, (IS 803:1976). Bureau of Indian Standards.
37. Rayhani, M. H., & El Naggar, M. H. (2008). Numerical modeling of seismic response of rigid foundation on soft soil. *International Journal of Geomechanics*, 8(6), 336–346.
38. Kumar, A., Choudhury, D., & Katzenbach, R. (2016). Effect of earthquake on combined pile-raft foundation. *International Journal of Geomechanics*, 16(5), 04016013.
39. Patil, M., Choudhury, D., Ranjith, P. G., & Zhao, J. (2018). Behavior of shallow tunnel in soft soil under seismic conditions. *Tunnelling and Underground Space Technology*, 82, 30–38.
40. Acharyya, R., Dey, A., Kumar, B. (2018). Finite element and ANN-based prediction of bearing capacity of square footing resting on the crest of  $c-\phi$  soil slope. *International Journal of Geotechnical Engineering*.
41. Chaudhuri, C. H., Choudhury, D. (2020). Buried pipeline subjected to seismic landslide: A simplified analytical solution. *Soil Dynamics and Earthquake Engineering*, 134, 106155.
42. Acharyya, R., & Dey, A. (2017). Finite element investigation of the bearing capacity of square footings resting on sloping ground. *INAE Letters*, 2(3), 97–105.
43. Bureau of Indian Standards BIS 1986, Design and construction of foundations-code of practice, (IS 1904:1986). Bureau of Indian Standards.
44. Bowles, L. E. (1996). *Foundation analysis and design*. McGraw-hill Inc.
45. Raj, P. P. (1999). *Ground improvement techniques*. Laxmi Publications.
46. Han, J. (2015). *Principles and practice of ground improvement*. Wiley.
47. Roy, R., & Dutta, S. C. (2010). Inelastic seismic demand of low-rise buildings with soil-flexibility. *International Journal of Non-Linear Mechanics*, 45(4), 419–432.

# Numerical Modeling of Screw Piles Performance Under Static and Seismic Loads in Soft Soils



Ahmed D. Alkaby and Mahdi O. Karkush

**Abstract** The steel helical (screw) piles are a type of deep foundation that consists of a square or circular shaft and one or more from helical bearing plates. This study is devoted to simulating the behavior of helical piles under static and seismic loadings numerically. Moreover, the lateral performance of helical piles under seismic loading was investigated. Two types of helical piles, HPC1 and HPC2, were analyzed numerically using PLAXIS 3D software, and results were compared with those obtained from a field study conducted by other researchers. The axial static load was applied to both types of screw piles, while the seismic loading was applied only to (HPC1) with two intensities of spectral acceleration (0.28 and 0.47 g). The static failure load obtained from numerical analysis corresponding to displacement about 5% of helix diameter well agreed with those measured experimentally. The failure pattern for a helical pile of spacing to diameter ratio ( $S/D = 3$ ) was individual plate bearing, while for the helical pile with ( $S/D = 2$ ), the failure pattern was a cylindrical shear failure. Also, the application of lateral dynamic loading at the top of the helical pile reduces the axial failure capacity of such piles under seismic loading. The zone of maximum displacement of helical piles under seismic loading extended from the top of the pile to a distance of 20% from pile length.

**Keywords** Helical piles · Seismic load · Numerical modeling · PLAXIS 3D · Screw piles · Soft clay

## 1 Introduction

The steel helical (screw) piles are a type of deep foundation that consists of a square or circular or circular shaft and one or more from helical bearing plates [1]. The screw piles are used in many applications to support buildings and foundations that fail [2].

---

A. D. Alkaby (✉) · M. O. Karkush  
Department of Civil Engineering, University of Baghdad, Baghdad, Iraq  
e-mail: [a.alkaby1901m@coeng.uobaghdad.edu.iq](mailto:a.alkaby1901m@coeng.uobaghdad.edu.iq)

M. O. Karkush  
e-mail: [mahdi\\_karkush@coeng.uobaghdad.edu.iq](mailto:mahdi_karkush@coeng.uobaghdad.edu.iq)



Recently, the screw piles have tremendous applications due to many advantages they have such as low cost, simple construction, can be used in restricted areas, and can support different types of loading at the same time. The helical piles are often used to support medium and light loads such as buildings, transmission towers, transportable buildings, solar panels, and oil pipelines [3, 4]. Conventional piles used in structures with high loads are of large diameter and descend to great depths to transfer the load from weak soil layers to strong soil layers. These piles affected by seismic loading due to their large diameter so the screw piles are used to resist earthquake forces due to the small diameter of the shaft and the large diameter of the helices [5]. Screw piles were used all over England in the mid-nineteenth century, and then in Britain, it expanded further in the globalization of the helical piles. Alexander Michel visited the United States in the mid-1800s century to consult on screw foundations for the first time in the states. Nearly 100 lighthouses were builds over forty years on helical foundations on the east coast of North America. From 1900 to 1950, their use declined dramatically due to the proliferation of mechanical piles and drilling piles [6].

Abdrabbo and El-Wakil [7] studied the helical piles' behavior inserted in sandy soil and loaded laterally. The behavior of helical piles of different diameters was compared with piles without helices. The results showed that the percentage of improvement resulting from the presence of helices reached 2.83 of failure load corresponding to a displacement equivalent to 2.5% of the diameter of the helix. Orang et al. [8] reported in their study the behavior of a helical pile below a shallow foundation in a shaking table for liquefied soil at the University of California. The results highlight the significant improvement in the shallow foundations behavior supported by helical piles and reduced settlement due to liquefaction. Costa [9] conducted seven load tests on a helical pile to check pullout capacity with cyclic loading in pure sand deposit and three tests on cyclic static loading. In addition, two tests on a semi-static cyclic loading were conducted. The results show that cyclic static loading increases the stiffness of the soil-pile system. In contrast, the results that appeared for the second test reduces pile stability and the stiffness of the soil pile system. This study aims to numerical modeling of helical piles of different configurations installed in soft soil and determine the spacing ratio between the helical bearing plates and the helix plate diameter ( $S/D$ ). In addition, the lateral performance of helical piles under seismic loading was investigated using PLAXIS 3D (V20) software.

## 2 Numerical Modeling

Numerical modeling is widely used to simulate the foundations behavior and computational simulation of scenarios in different geotechnical projects. One of the advantages of PLAXIS is using various soil models in the calculation, which allows modeling (evaluate) their behavior under loading and unloading [10]. The pile response under arbitrary static axial loading and seismic loading was computed

**Table 1** Materials proprieties of the soft soil layers [11]

Depth (m)	Description	$c_u$ (kPa)	$\gamma$ (kN/m <sup>3</sup> )	Ks	$\nu$	E (MPa)
0–3.0	Sandy silt	36	17	1	0.49	24
3.0–10.25	Silty clay (very soft)	9	17	1	0.49	7

**Table 2** The pile dimensions used in the analysis [11]

Piles	Shaft diameter (mm)	Wall thick. (mm)	Depth (m)	Helix diameter (mm)	Spacing between helices (m)	$\nu$	E (GPa)
HPC1	178	10	7.2	610	1.83	0.3	200
HPC2	114	10	3.2	406	0.81	0.3	200

using FEM code PLAXIS 3D within this study. PLAXIS 3D is a worldwide used code for the stress–strain, stability, and groundwater flow analysis in geotechnical engineering, which supports an easy graphical input of the models with complex geometry and the symbolic presentation of the results.

**Piles and Soils.** Two models of helical piles tested in the field are analyzed using PLAXIS 3D V20 [11]. The screw piles were inserted in soil mass consists of sandy silt layer extended from the soil surface to a depth of 3 m underline by a very soft silty clay layer of thickness 7.25 m as shown in Table 1. The water level was at 1 m below the ground surface. The first pile (HPC1) was a hollow shaft pipe pile with three bearing helix-plates with a diameter of 610 mm and 7.2 m. The second pile (HPC2) is a hollow shaft pipe pile that has two bearing helix-plates with a diameter of 406 mm and a length of 3.2 m. The dimensions of the two piles are given in Table 2 and Fig. 1.

**Pile–Soil Interface.** The connection between the pile and the surrounding soil is not rigid, it is considered a weak region, so there is a relative displacement between the pile and the surrounding soil. The surrounding soil can be affected and disturbed by the installation of the helical pile due to a rotation inside the soil by the action of helices. The disturbance of soil depends on the soil interfaces strength and the type of pile used (steel, concrete, wood). The elastic-perfectly plastic Mohr–Coulomb (MC) model with a non-associated flow rule and zero tension cut-off criterion defines the pile-soil interfaces constitutive behavior (when tension develops a gap between the pile and the surrounding soil generated). The strength reduction factor ( $R_{inter}$ ) depends on the parameters of shear strength of the pile-soil interface ( $c_{inter}$ ,  $\phi_{inter}$ ), where the reduction in the shear strength parameters ( $c'$  and  $\phi'$ ) of the MC model can be calculated according to the following Equations [12]:

$$c_{inter} = R_{inter} \cdot c' \tag{1}$$

$$\tan\phi_{inter} = R_{inter} \cdot \phi' \tag{2}$$

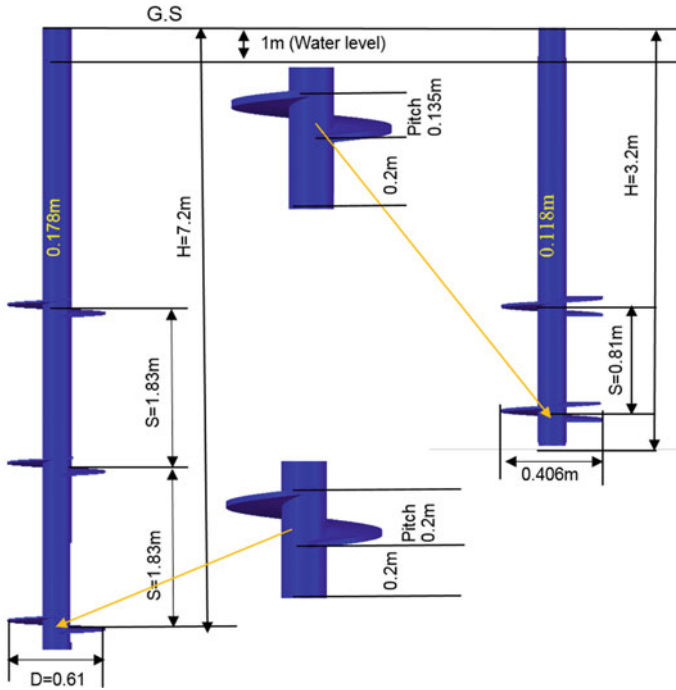


Fig. 1 Dimensions of two helical piles used in this study

where.

$R_{inter}$ : Interface factor.

$c_{inter}$ : Cohesion of the interface ( $kN/m^2$ ).

$c'$ : Cohesion of soil ( $kN/m^2$ ).

$\varphi_{inter}$ : Friction angle of the interface ( $^\circ$ ).

$\varphi'$ : Friction angle of the soil ( $^\circ$ ).

The pile-soil interface values in PLAXIS can be set directly using a strength/stiffness reduction factor ( $R_{inter} \geq 1.0$ ). The default value is  $R_{inter} = 0.7$  represents a fully bonded pile-soil interface. In the finite element analysis, the boundary conditions necessary to properly be taken into account for reliable pile behavior prediction. In static substrate analysis, it is placed in a fixed boundary that is sufficient not to affect the results extracted within the region of interest. On the other hand, in dynamic analysis in general, the boundary conditions have large and affective states of great importance, and their treatment is more complex than in static analysis as it depends on the dynamic frequency range and the type of loading. For geotechnical engineering, dynamic forces are either in the form of cycles or vibrations that result from within the model or earthquakes. Abbas et al. [13] presented a finite element modeling of the pile boundary conditions to the outer boundaries that could not affect the results. The soil surface distances are of a cube shape of 10D

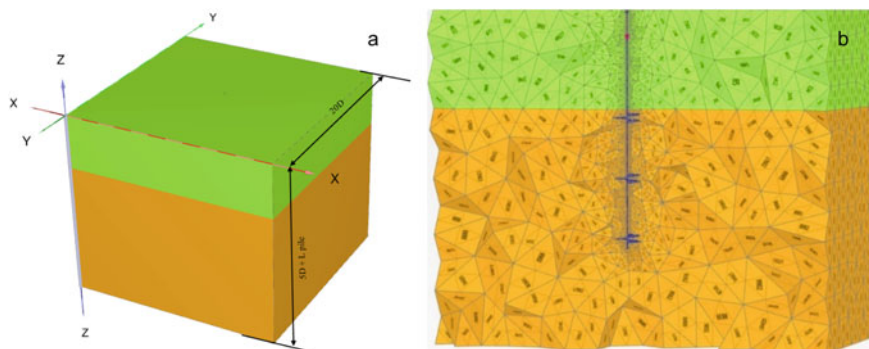


**Fig. 2** Dimensions and cross-section of a typical mesh and an embedded helical pile of the numerical model

on each side of the center of the pile diameter and  $5D$  below the base of the pile, as shown in Fig. 2a.

**Mesh Properties.** The soil is modeled in a rectangular with external dimensions equivalent to  $(20D)$  for the surface dimensions ( $x, z$ ) and  $(5D + L_{pile})$  for the depth dimensions ( $y$ ). A mesh containing  $(10)$  noded elements are sufficient to give accurate results, and this number of elements is the largest number used by the program PLAXIS 3D (V20). The study focuses on the horizontal and vertical displacement and soil reaction. The head of the pile is at the level of the soil surface. The piles weight is the same as the soils weight to avoid the helical piles vertical settlement. The coarseness of the grid was select as a medium. The result of soil mesh generated by PLAXI 20,591 elements and 33,193 nodes that form medium-mesh as shown in Fig. 2b.

**Seismic Loading.** The vibrating of soil imposes large curvatures on the piles, which will generate forces, especially bending moments, because even if the superstructure was not present, such moments generated. These are called "kinematic moments" to distinguish them from those moments resulting from the structures above the head of the pile "moment of inertia". In addition to those mentioned above, it is necessary to focus on the moments "kinematics and inertia" to predict piles response under seismic loading and meet the design requirements [14]. Iraq is geographically located on the Arabian Plates northeastern boundaries and technically in areas with relatively active earthquakes. The seismic history of Iraq shows the presence of annual seismic activity of varying strength. The southern and southwestern regions have less seismic activity than the northern and northeastern regions. The statistical results of earthquakes with magnitudes 4–5.4 Richter scale constitute 90.95%, while units with magnitudes 5.5–7.4 Richter scale constitute 6.03% of the total events. These results for the regions of Iraq with the classifications were agreed upon [15].

Gazetas and Dobry [16] presented a simplified linear method that predicted the response of piles to radiation damping and material using the available static stiffness (taken from a finite element or through another acceptable method) as this method was

considered useless for seismic analysis due to the linearity assumptions. The seismic range for typical frequencies is 0–10 Hz, while 0–1 is for marine environmental loading, and 5–200 is for machine foundations [17]. A study by Farman and Said [18] presented the spectral acceleration for the governorates (Baghdad, Erbil, and Basra), where the spectral acceleration amount was ranged from 0.17 to 0.47 g for type (PGA). The values (0.28 and 0.47 g) were used in this study according to the 2016 Iraq code for the values of PGA, as shown in Fig. 3. The Baghdad governorate spectral acceleration was applied in this study for values of and the failure load under seismic loading assumed corresponding to a displacement (amplitude) of 5% of D (where D is the diameter of the helix) was applied. Equation 3 was used to extract the frequency value, where the value of the frequency for (0.28 g) was (4 Hz), and for (0.47 g) equivalent to (5 Hz), through (0.5 s) [19].

$$F = \sqrt{\frac{GA}{2\pi^2D}} \tag{3}$$

where D is displacement (mm), A is the acceleration (g), F is the frequency (Hz), and G is a constant (9.80665 m/s<sup>2</sup>).

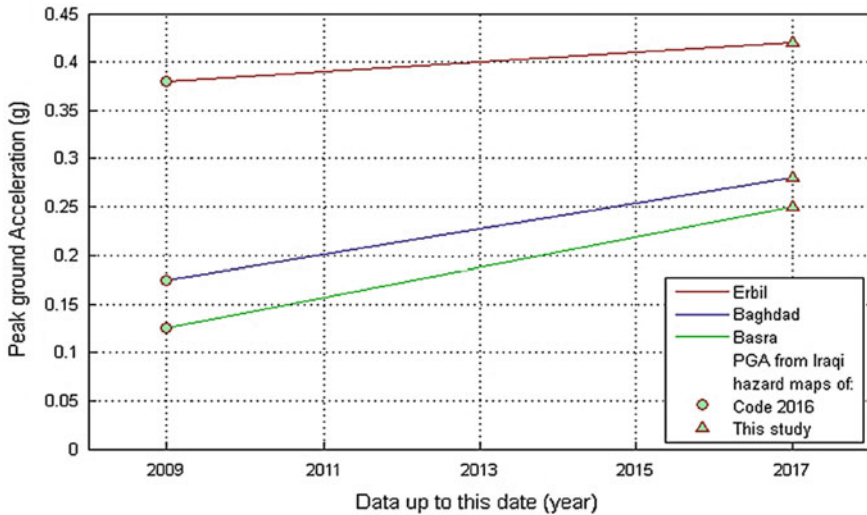


Fig. 3 PGA values from the seismic design code of Iraq (2016) [18]

### 3 Results and Discussion

A numerical analysis conducted in this study using PLAXIS 3D software is implemented on a model of dimensions  $12 \times 12 \times 10.25$  m. A theoretical model is developed to predict the axial compression of the helical piles in soft soils. The applied load of 143 kN for (HPC1) and an applied load of 106 kN for (HPC2) are applied on the head of helical piles. Figure 4 shows a comparison between the results of the load-settlement obtained from the current study with Elsherbiny and El Naggar [11] field study results. The failure load can be determined from the standard of 5% of the helix diameter of the helical pile (displacement of 30 mm), where the failure rate for the helical pile (HPC1) was (136 kN) for the field study [20], in contrast, the failure rate for the numerical analysis was (139 kN). The failure rate for the helical pile (HPC2) was (92 kN) for the field study. In contrast, the failure rate for the numerical analysis was (89 kN).

The helical pile (HPC1) has a spacing ratio between the helical bearing plates to its diameter (S/D) of 3, and the helical pile (HPC2) has S/D equals 2. The numerical analysis results showed the distribution of plastic points for HPC1 reflected a failure pattern of individual plate bearing, and for HPC2, the failure is cylindrical surface, as shown in Fig. 5. Therefore, comparing the failure load of two helical piles (HPC1) with (HPC2) depends on the length, the number of helices, and the diameters of the shaft and the helix. However, the cylindrical resistance of helical piles is more than the individual load-bearing of helical piles.

**Seismic Loading.** This part includes implementing a numerical study on screw pile HPC1 under the effect of seismic loading of spectral acceleration of 0.47 g and subjected to dynamic lateral load at the top of the helical pile, as shown in Fig. 6. Lateral seismic loading affects the resistance of the soil to the axial loads imposed on the helical pile as the vibrations resulting from earthquakes distort the soil adjacent

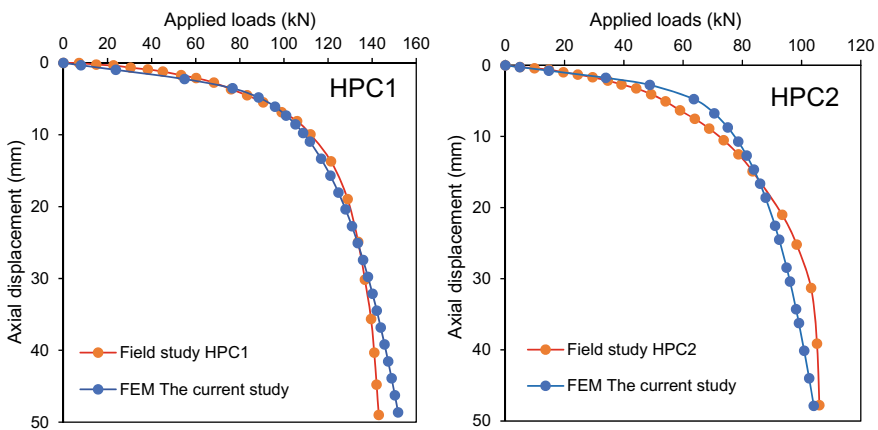


**Fig. 4** Verified between the numerical models in this study and field study

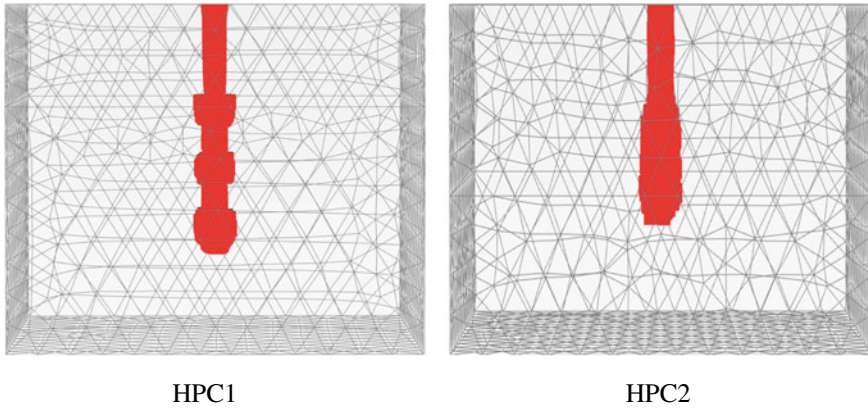


**Fig. 5** The plastic points (individual bearing) for HPC1 and cylindrical shear resistance for HPC2

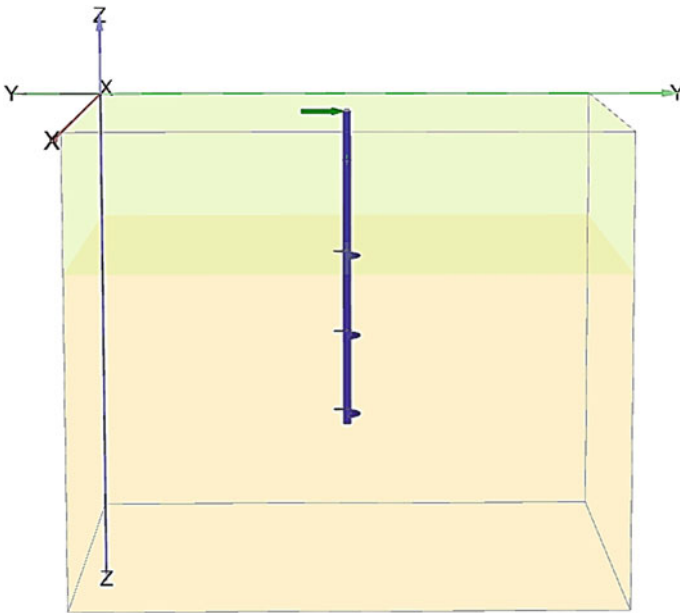


**Fig. 6** The helical pile under seismic loading

to the helical pile, which leads to settlement in the soil. Figure 7 shows the axial settlement of helical piles subjected to seismic loading, the first phase represents the seismic loading (0.47 g) without dynamic loading, while the other phase with dynamic loading (10 kN). The helical pile is subject to a high lateral displacement resulting from seismic loading (0.47 g) in addition to lateral dynamic loading on the surface of HPC1. Figure 8 shows the lateral displacement result from the seismic

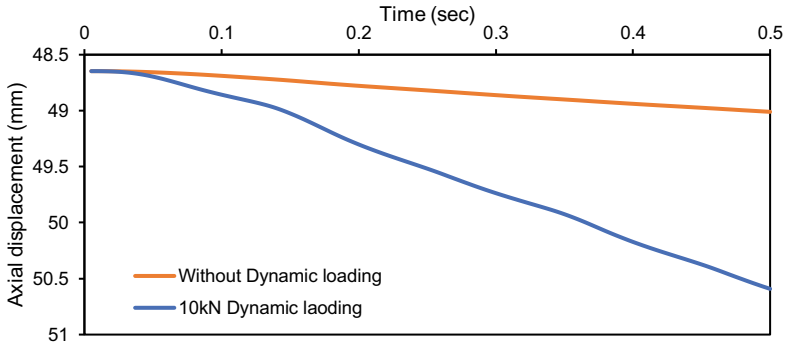


Fig. 7 Axial displacement under seismic loading applied on surface of HPC1 with static load (143 kN)

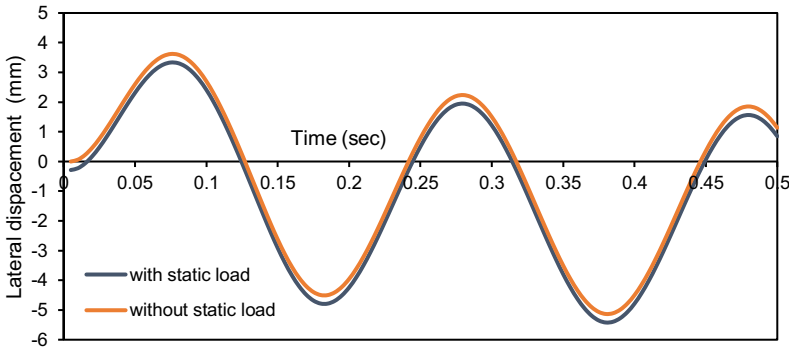
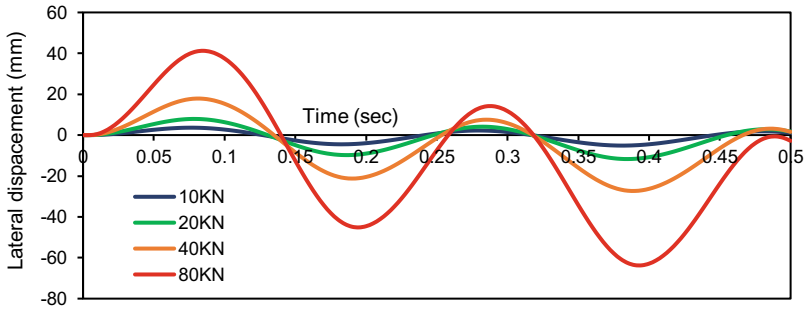


Fig. 8 Effect the lateral displacement through seismic loading with dynamic loading (10 kN)

loading for the same PGA above that is under static axial loading of HPC1. It is possible to compare the lateral displacement resulting from lateral seismic loading with and without static axial loading. Figure 8 shows a slight reduction in the lateral displacement under seismic loading when the screw piles support an axial static loading. While the axial load application causes a significant decrease in the lateral displacement of piles subjected to passive earth pressure [21–23].

To investigate the effect of lateral loads on helical pile response, several intensities of lateral dynamic loading were applied at the top of the helical pile (HPC1) and subjected to seismic loading of intensity (0.47 g). The variation of lateral displacement of the helical pile subjected to lateral loading of several intensities (10, 20, 40, and 80 kN) are shown shown in Fig. 9. The variation of lateral displacement with time at several depths of helical pile HPC1 subjected to a seismic loading of intensity 0.47 g and lateral dynamic loading of intensity 10 kN is shown in Fig. 10. The results showed decreasing the lateral displacement of the helical pile with depth





**Fig. 9** Effect the lateral dynamic loading on the lateral displacement of helical pile HPC1 subjected to seismic load of intensity (0.47 g)

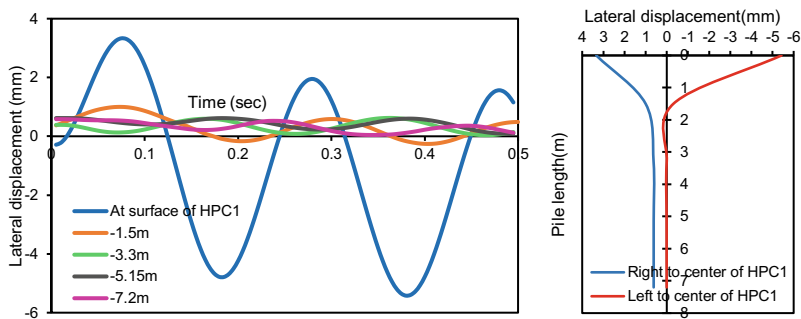


**Fig. 10** Variation of the lateral displacement of helical pile HPC1 with time at several depths from the soil surface (seismic loading intensity (0.47 g) and lateral dynamic loading (10 kN))

and the maximum value registered at the soil surface. Mostly, the lateral displacement of the helical pile under both seismic loading and lateral loading at soil surface vanish at depth equals 20% of pile length as shown in Fig. 10. The variation of lateral displacement with lateral dynamic loading is shown in Fig. 11. According to the failure criterion of failure load corresponding to the displacement of % from helix diameter, the failure later load is 48 kN.

Figure 12 shows the effect of lateral displacement resulting from seismic loading for two intensities of spectral acceleration (0.28 and 0.47 g) without axial static load and subjected to a lateral dynamic load of the intensity of 10 kN. The results showed that the PGA 0.28 g causes a more significant lateral displacement than the lateral displacement resulting from the PGA 0.47 g. This difference can prove from Eq. 3, in which an inverse relationship between the acceleration and displacement. Figure 13 shows the axial displacement resulting from applying the two spectral accelerations, where no difference was noted between the two intensities of acceleration on the vertical displacement of the pile.

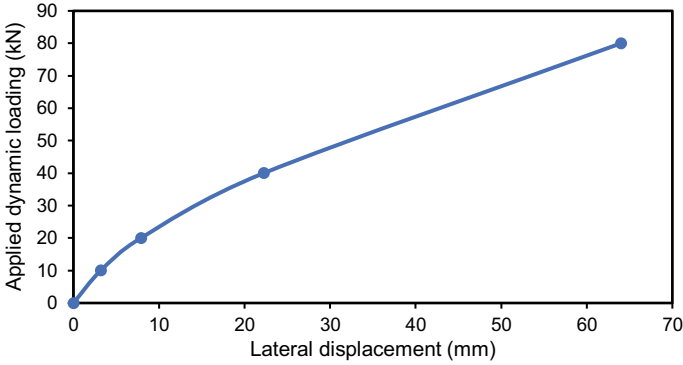


Fig. 11 Applied lateral dynamic loading on the surface of helical pile with seismic load (0.47 g)

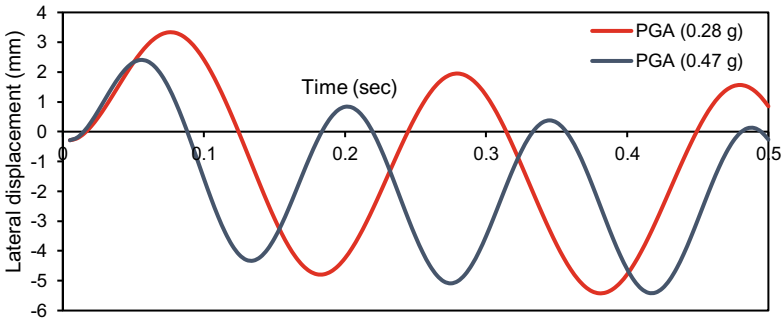


Fig. 12 Comparison of results between the spectral acceleration (0.28 and 0.47 g) with lateral dynamic loading (10 kN) applied on top of (HPC1) for lateral displacement

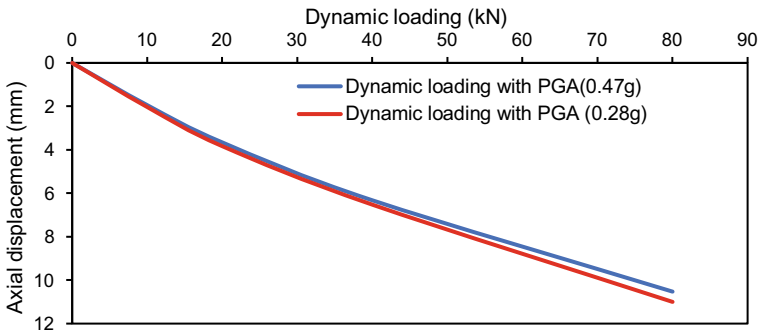


Fig. 13 Variation of axial displacement with lateral dynamic loading of pile HPC1 under spectral accelerations (0.28 and 0.47 g)

## 4 Conclusions

3D numerical simulations of the large-scale model using PLAXIS software were performed on two types of helical piles under the effects of static and seismic loading. The two types of helical piles were subjected to axial static loading, and then one of them was subjected to seismic loading of acceleration intensity of 0.28 and 0.47 g. Based on the results of this study, the following points can be drawn out:

- The failure load obtained from numerical analysis, corresponding to a displacement of 5% of helix diameter, is well agreed with those measured experimentally from field tests conducted on helical piles (HPC1 and HPC2).
- Increasing the number of helices causes increasing the ultimate carrying capacity of screw piles under static loading.
- Increasing the spacing ratio between the helices and the diameter of the helix (S/D) from 2 to 3 changes the failure mechanism from cylindrical shear failure to individual bearing failure.
- The lateral displacement of screw pile resulting from the seismic loading of acceleration of 0.28 g is 1.5, resulting from the seismic loading of acceleration of 0.47 g. Increasing the intensity of acceleration causes decreasing the resulted lateral displacement.
- The application of lateral load on the top of the helical pile causes reduction of failure axial capacity of the pile under the effect of seismic loading of intensity 0.47 g.
- The maximum lateral displacement of the helical pile under seismic loading occurred in the zone extending from the top of the helical pile to a depth of 20% from pile length.

## References

1. Hosseini, M. (2015). *Evolution of pile shaft capacity over time in soft clays (Case study: Leda clay)*. Thesis, Carleton University, Ottawa, Ontario.
2. Chiluwal, S., & Guner, S. (2019). Design recommendations for helical pile anchorages subjected to cyclic load reversals. M.Sc. Thesis, Department of Civil & Environmental Engineering, The University of Toledo.
3. El Sharnouby, M. M., & El Naggar, M. H. (2018). Field investigation of lateral monotonic and cyclic performance of reinforced helical pulldown micropiles. *Canadian Geotechnical Journal*, 55(10), 1405–1420.
4. Sirsikar, R. A. (2018). *Study of helical pile behaviour in cohesionless soil*. B.Sc. Dissertation, National Institute of Technology Durgapur, India.
5. Cerato, A. B., Vargas, T. M., & Allred, S. M. (2017). A critical review: State of knowledge in seismic behaviour of helical piles. *DFI Journal-The Journal of the Deep Foundations Institute*, 11(1), 39–87.
6. Perko, H. A. (2009). *Helical piles: A practical guide to design and installation*. John Wiley & Sons.

7. Abdrabbo, F. M., & El Wakil, A. Z. (2016). Laterally loaded helical piles in sand. *Alexandria Engineering Journal*, 55(4), 3239–3245.
8. Orang, M. J., Boushehri, R., Motamed, R., Prabhakaran, A., & Elgamal, A. (2020). *Large-scale shake table experiment on the performance of helical piles in liquefiable soils*. 45th DFI Annual Conference On Deep Foundations
9. Costa, J. D. S. (2017). Uplift behaviour of helical piles in sand subjected to cyclic loading (Doctoral dissertation, Master's Thesis—Department of Civil Engineering, Centre of Technology, Federal University of Rio Grande do Norte).
10. Polishchuk, A. I., & Maksimov, F. A. (2017). Numerical analysis of helical pile–soil interaction under compressive loads. *IOP Conference Series: Materials Science and Engineering*, 262(1), 012099.
11. Elsherbiny, Z. H., & El Naggar, M. H. (2013). Axial compressive capacity of helical piles from field tests and numerical study. *Canadian Geotechnical Journal*, 50(12), 1191–1203.
12. Marjanović, M., Vukićević, M., & König, D. (2020). Flexible pile group interaction factors under arbitrary lateral loading in sand. *Journal of Marine Science and Engineering*, 8(10), 800.
13. Abbas, J. M., Chik, Z., & Taha, M. R. (2018). Modelling and assessment of a single pile subjected to lateral load. *Studia Geotechnica et Mechanica*, 40(1), 65–78.
14. Basile, F., (2012). Pile-group response under seismic loading. In Proceedings of the 2nd International Conference on Performance-Based Design in Earthquake Geotechnical Engineering, Taormina, Italy (pp. 28–30).
15. Said, A. I. (2010). Development of design response spectra for Baghdad area. In *Urban Habitat Constructions Under Catastrophic Events: Proceedings of the COST C26 Action Final Conference* (p. 71). CRC Press.
16. Gazetas, G., & Dobry, R. (1984). Horizontal response of piles in layered soils. *Journal of Geotechnical Engineering*, 110(1), 20–40.
17. El Naggar, M. H., & Bentley, K. J. (2000). Dynamic analysis for laterally loaded piles and dynamic py curves. *Canadian Geotechnical Journal*, 37(6), 1166–1183.
18. Farman, M. S., & Said, A. I. (2018). Updated probabilistic seismic hazard assessment for Iraq/2018. *Civil Engineering Journal*, 4(7), 1610–1628.
19. Brinkgreve, R. B. J., Kumarswamy, S., Swolfs, W. M., Waterman, D., Chesaru, A., & Bonnier, P. G. (2016). *PLAXIS 2016*. PLAXIS bv.
20. Sakr, M. (2018). Performance of laterally loaded helical piles in clayey soils established from field experience. *DFI Journal-The Journal of the Deep Foundations Institute*, 12(1), 28–41.
21. Karkush, M. O., & Kareem, Z. A. (2019). Behavior of Passive Pile Foundation in Clayey Soil contaminated with Fuel Oil. *KSCCE Journal of Civil Engineering*, 23(1), 110–119.
22. Karkush, M. O., Jaffar, G. S., & Al-Kubaisi, O. K. (2021). Evaluating the performance of flexible passive pile group in cohesionless soil under the effect of a nearby embankment. *Lecture Notes in Civil Engineering*, 112, 1–12.
23. Karkush, M. O. (2020). Simulation the behavior of passive rigid pile in sandy soil. *Journal of Engineering & Technological Sciences*, 52(4).

# Numerical Simulation of Driven Piles Under Static Axial Compressive Load Testing Using Finite Element Model



Hazim AlKhafaji and Meysam Imani

**Abstract** The pile load capacity is driven in soil using the numerical simulation depending on the finite element method employed PLAXIS 3D program was investigated. A full 3D model of a driven pile under static compressive load was created. The model was validated with three experiential static load tests located in Baghdad-Iraq, employed ASTM 1143–07. The results show good agreement and validity between test results in different methods. The numerical analysis indicates a settlement (7–8%) more than the experiential settlement, the low difference in the results due to increased soil stiffness below the driven pile in the site through the installation process. The predicted results extended to be more comprehensive by using sensitivity analysis with different soil parameters, indicate that the numerical simulation appears an appropriate analysis for the driven pile installation process. The study provided a numerical simulation method because of charts and figures to be useful for geotechnical engineers.

**Keywords** Settlement · Numerical method · PLAXIS 3D · Driven pile

## 1 Introduction

Driven piles or displacement piles are prefabricated components (concrete, steel, or wood), pushed into the ground by hammering, pressing, or vibration. During the installation process of the driven pile, the soil neighboring the pile will be changed in its structure with a degree of remolding. This behavior will increase the soil stiffness and compacted beneath and surrounding the pile [1]. The simulate of the installation process of the driven pile model in FEM is intricate compared with modeling

---

H. AlKhafaji (✉)

Al-Mustafa University College, Palestine Street, Baghdad, Iraq

e-mail: [hazim.alkhafaji@aut.ac.ir](mailto:hazim.alkhafaji@aut.ac.ir)

Al Hazim Bureau for Engineering Services, Baghdad, Iraq

M. Imani

Amirkabir University of Technology, Garmsar Campus, Garmsar, Iran

e-mail: [imani@aut.ac.ir](mailto:imani@aut.ac.ir)

the bored piles since the soil is compacted and displaced, not removed, and significant change in the soil fabric with an increase in the stiffness and strength. Unclear understanding of the complicated installation process of the driven piles model in the FEM led to few published papers in this field [2]. Numerical simulation was investigated, and the hardening model was considered for soil surrounding the pile [3]. For complicated geometries in foundation problems, it is highly recommended to use PLAXIS 3D [4]. The PLAXIS has the ability of capable of considerable deformation and employed the program under concept FEM to model the pile installation in complex soil behavior adjacent to the pile [5]. The simulation of pile foundations testing using the computer program PLAXIS 3D Foundation reduces the time for calculation of pile settlement and money spent on arranging pile groups and testing [6]. Since the analysis of the problem is sophisticated, PLAXIS 3D program was used to model the complexity arising from geometrical [7].

The remodeling of soil structure due to pile installation process changed the base capacity, and the numerical simulation was considered to tests two piles in the sand [8]. The random finite-element method to analyze piled raft foundation was investigated, the spatial variability of soil parameters was considered [9]. Later, [10] studied an analytical approach for predicting single pile behavior in clay and the changes in both the strength and stiffness of the surrounding soil of installed single pile to predict the permanent change in mean effective stress.

In this paper, the finite element method was applied for modeling driven piles (precast concrete pile) under a static axial compressive load test. Sensitivity analyses were performed, considering different soil properties. Emphasis was performed on the load capacity and the settlement at design loads for the driven pile. The validity of the obtained results was made with three experiential static load tests using kentledge systems performed et al.-Rashdiah district, Baghdad city, Iraq, in May 2013, five weeks after piles installation.

## 2 Site Characterization

The test site is located in Iraq-Baghdad governorate, et al.-Rashdiah district, Fig. 1-a. The site, in general, is a flat area composing of a cohesive soil layer, which consists of soft to very stiff brown lean or fat clay to silt (CL, CH, ML), sometimes with sand. This layer extends from the natural ground surface (N.G.S.) down to the depth range between (8.75–15.0) m, as shown in Fig. 1b. Figure 1c presented the Standard Penetration Test (S.P.T) profile. The water level depth was between (1.25 and 1.5) m under the ground level (N.G.S). Table 1 presented the soil properties.

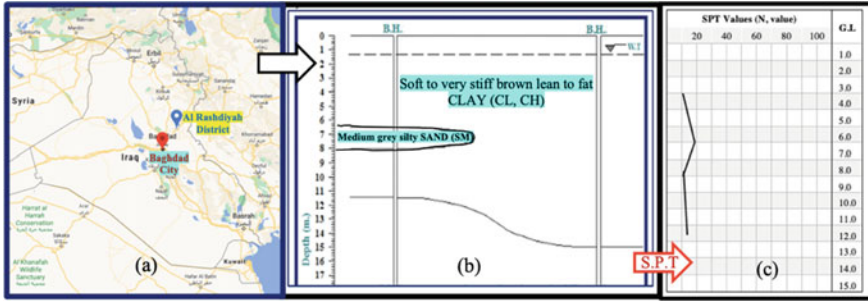


**Fig. 1** a Site location (33° 31' N, 44° 12' E), b soil profile through boreholes, c (S.P.T) standard penetration test profile

**Table 1** Properties of the soil foundation

Soil type	Saturated density $\gamma_{sat}$ (kN/m <sup>3</sup> )	Dry density, $\gamma_d$ (kN/m <sup>3</sup> )	Elasticity, $E$ (kN/m <sup>2</sup> )	Friction angle, $\phi$	Poisson's ratio, $\nu$	Cohesion, $c$ (kN/m <sup>2</sup> )
Silty clay	20	17	15,000	39°	0.32	0

### 3 Experiential Static Axial Compressive Load Test

The static axial compressive load test was performed according to the American Standard Test Method, ASTM D1143/ D1143-07 [11], in which the dead load weight (Kentledge) system was applied using a hydraulic jack acting against a reaction beam. A schematic of the test is shown in Fig. 2a. The maintained vertical compression load test is commonly executed to predict the settlement and ensure the structural and geotechnical soundness of the piles. The test steps are to increase the load

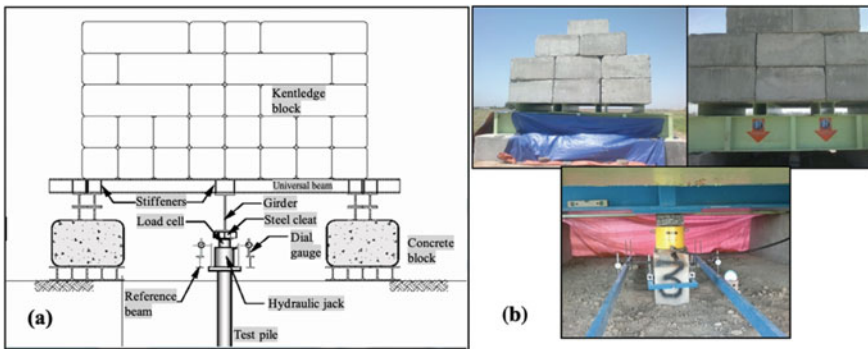


**Fig. 2** a Scheme of compression load test installation using dead load weight (Kentledge), b photograph of the three performed tests

**Table 2** Load and settlement values for single piles in compression tests

Test No	Load (kN)	147	294	441	588	735	883
Test No.1	Settlement (mm)	0.25	0.68	1.29	2.15	3.02	4.68
Test No.2		0.32	0.71	1.35	2.11	3.09	4.83
Test No.3		0.35	0.78	1.38	2.19	3.23	5.4

incrementally to reach the working load at the specific safety factor. If the failure occurs during loading, the applied load is kept fixed until the total axial movement equals 15% of the pile diameter or width is reached.

As shown in Fig. 2b, three compression tests were performed on single piles with square cross-Sect. (285 mm × 285 mm) and 11.5 m penetration length. 294 kN (30 tons) design load considered, the load increment was increased to three times of design load as maximum to predict the maximum settlement. The test was applied for increased load incrementally and cumulatively with six values started 147 kN (15 tons) for the pile. Each increment value was preserved for a time interval of about 15 min until pile displaced occurred at a small or no load applied. The dial gauge readings were recorded for each increment. However, the test was stopped when the maximum load increment reached or the total axial movement equals to 15% the pile diameter or width occurred. The results for the three test piles are presented in Table 2, which shows little scatter.

## 4 Numerical Modeling

**Modeling Characteristics.** Using Finite element analysis is widespread for many practical engineering projects. In this study, the PLAXIS 3D-2013 program was employed to simulate a single driven pile. The obtained results were verified using the experiential pile load tests discussed in the previous section. Also, Sensitivity analyses were performed.

**Boundary Condition.** Figure 3 shows a general view of the constructed model with dimensions equal to 50 × 50 × 20 m. The pile penetration length and cross-section are equal to 11.5 m and 285 mm × 285 mm, respectively. The distance between the pile body and the model boundaries was considered equal to more than four times the pile length [8, 12]. The bottom boundary of the model was fixed in all directions, while the side boundaries were free to displace in the vertical direction. According to the site investigation, the groundwater level was considered at a depth equal to 1.3 m.

**Materials Model.** The Hardening soil model (HS) was considered for the soil material. In contrast with the Mohr–Coulomb model (MC), (HS) can take into account the difference in soil stiffness between Virgin-Loading and unloading- reloading. This capability results in higher accuracy of the findings. For activating such a capability,



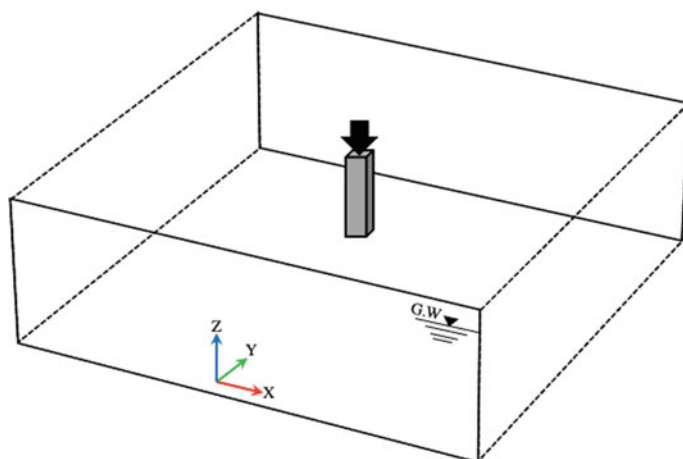


**Fig. 3** A general view of the 3D model for a single driven pile

the unloading—reloading elasticity modulus  $E_{ur}$  of soil should be introduced for the model. Referring to [13], it can be assumed that unloading—reloading modulus  $E_{ur} = 3E_{50}$ , in which  $E_{50}$  is equal to the tangent stiffness modulus  $E_{ord}$  of the soil,  $E_{ord} = E_{50}$ ,  $E_{50}$  is equal to the soil elasticity modulus  $E$ . In addition, the pile concrete was assumed to behave as a linear elastic- Non-porous material with the elasticity modulus equal to  $3 \times 10^7$  kN/m<sup>2</sup> and the unit weight equal to 24 kN/m<sup>3</sup>.

**Numerical Analysis.** An interface reduction factor between pile and soil was considered to get reliable data and decrease in calculation time [14]. For the interface for the soil—pile contact surface, a strength reduction factor equal to 0.67 was multiplied by the shear strength properties of the soil [15]. The coefficient of lateral earth pressure,  $K_0 = 0.48$  (corresponding to  $\nu = 0.32$ ) was considered, after [16] formula  $K_0 = \nu / (1 - \nu)$  ( $\nu$  being Poisson's ratio). The soil and pile clusters were modeled using a fine mesh with 8-noded in the tridimensional model to obtain a better gradient along the pile penetration length, as shown in Fig. 4. The numerical analysis was performed in three phases: generating the initial stresses, activating the pile elements, and applying the incremental load to the pile head according to the loading steps in the real experiment of the considered project.

## 5 Results and Discussion

**Verification.** Figure 5 shows a comparison between the load-settlement curve obtained from the numerical analysis and those obtained from the driven pile tests (according to Table 2). Good agreement can be seen among the results. The maximum difference between the results of the numerical method and in-situ tests is about 7%.

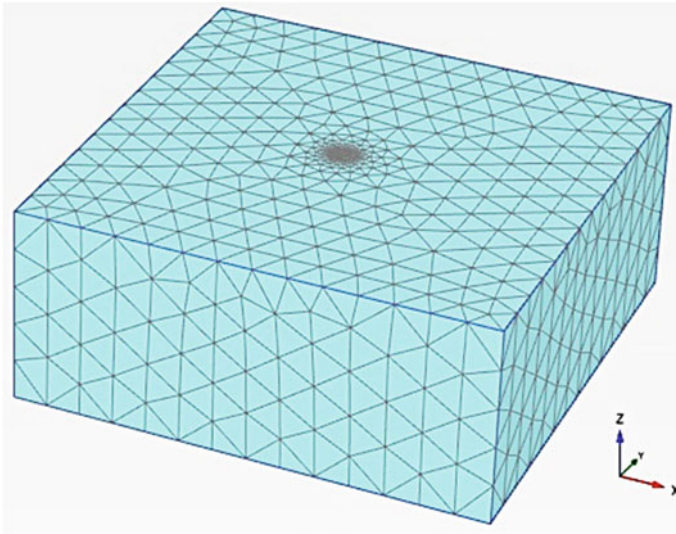


Fig. 4 3D Numerical model of the problem

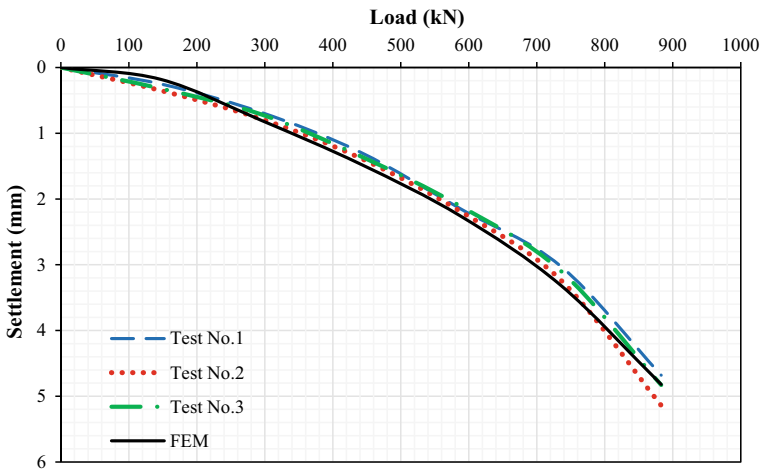


Fig. 5 Comparison between the finite element method (FEM) and in situ test results

**Sensitivity Analyses.** The critical issue in applications such as pile is probably the magnitude of vertical displacements during operation conditions, not estimating the axial capacity of pile foundation [17]. For checking the effect of different parameters on the load–settlement curve of the pile, sensitivity analyses were performed. Three cases were considered in the analyses, using the properties pointed out in Table 3. One

**Table 3** Properties of the materials models

Material type	Model type	Saturated density (kN/m <sup>3</sup> )	Dry density (kN/m <sup>3</sup> )	Elasticity (MPa)	Friction angle,	Dilatancy angle,	Poisson's ratio	Cohesion kN/m <sup>2</sup>
Case (1)	(HS) Drained	20	17	15	25°, 30°, 35°	0, 0, 5°	0.32	0
Case (2)		20	17	15	0	0	0.32	20, 50, 100
Case (3)		20	17	15, 30, 60	39°	9°	0.32	0

of the surrounding soil properties was changed in each case, while other parameters were kept fixed.

Figure 6 shows the load–settlement curve for case 1. It is clear that by increasing the soil friction angle from 25° to 39°, the asymptotic line to the curve occurs in higher magnitudes of applied load, which means a higher bearing capacity using the tangent intersect method. As practically, the dilatancy angle assumed about 30° less than the friction angle [8]. The ultimate load-bearing capacity for the cases of  $\phi = 25, 30, 35,$  and  $39^\circ$  are equal to 860, 910, 960, and 1000 kN, respectively.

Figure 7 shows the load–settlement curve for case 2. Three different soil cohesion were considered, and the friction angle equal to zero was used. The incremental load was increased until the asymptotic line to the curve occurs. The load-settlement curve's behavior showed by increasing the soil cohesion for selected values, the ultimate load-bearing capacity increase for the cases of  $c = 20, 50,$  and  $100$  kN/m<sup>2</sup> is equal to 980, 1180, and 1200 kN, respectively.

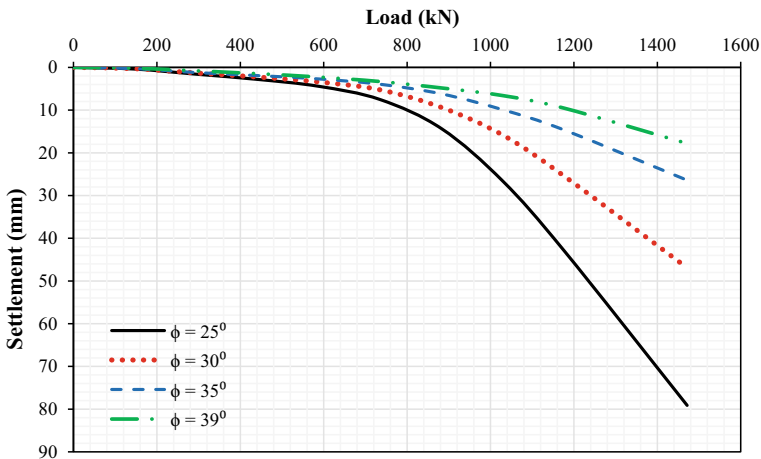


**Fig. 6** Effect of the soil friction angle on the load—settlement curve

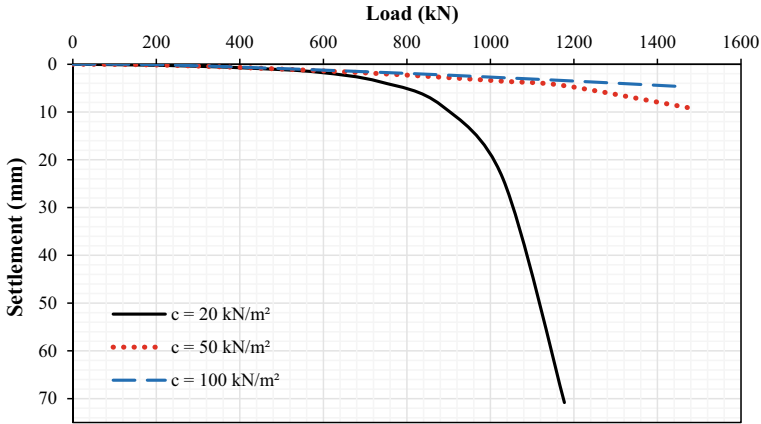


Fig. 7 Effect of the soil cohesion on the load—settlement curve

Figure 8 shows the load—settlement curve for case 3. Three different soil elasticity modulus were considered, the incremental load was increased until the asymptotic line to the curve occurs, the behave of the load—settlement curve showed by increasing the soil elasticity modulus for selected values, the ultimate load-bearing capacity increase, for the cases of  $E = 15,000, 30,000$  and  $60,000 \text{ kN/m}^2$  are equal to 980, 1180 and 1200 kN, respectively.

**Effect of Penetration Pile Length ( $L_p$ ).** The apparent increase in pile shaft friction by increasing penetration pile depth ( $L_p$ ) could significantly increase capacity, as shown in Fig. 9. Using the soil properties in Table 1, three different penetration pile depths ( $L_p$ ) were considered. The ultimate load-bearing capacity for the cases of  $L_p$

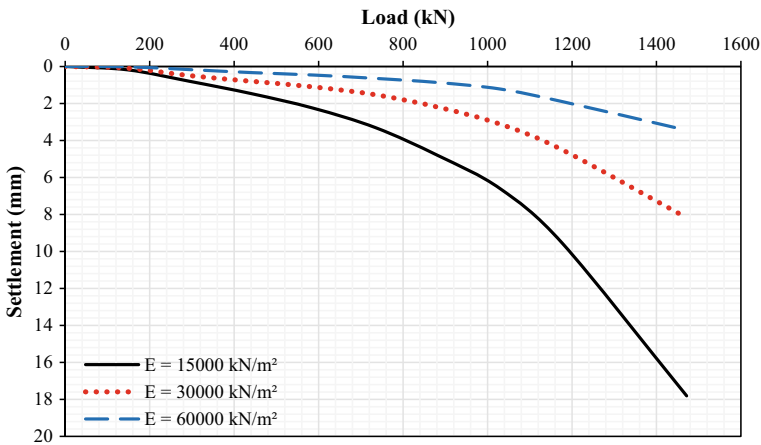


Fig. 8 Effect of the soil elasticity modulus on the load—settlement curve

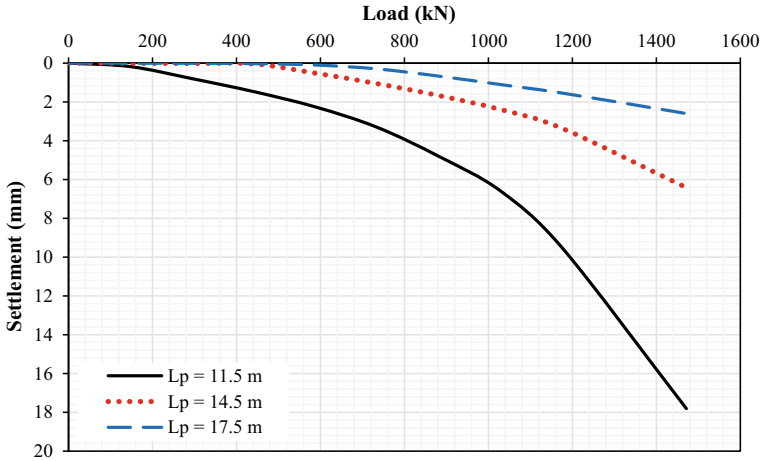


Fig. 9 Effect of the penetration pile length ( $L_p$ ) on the load–settlement curve

= 11.5 m, 14.4 m, and 17.5 are equal to 975, 1080, and 1170 kN, respectively. This figure will be helpful for the designer to select the suitable pile penetration length with appropriate load capacity and minimum settlement.

## 6 Conclusions

The present study investigated the numerical simulation employed PLAXIS 3D and experiential method using ASTM 1143–07 to test-driven pile under static axial load. The results show a good agreement between the two methods is about 7%. In addition, the numerical simulation analysis proved that the interface reduction factor between pile and soil was influential. The predicted results extended using the Sensitivity analyses for different soil parameters show acceptable values to introduced load–ettlement curve, penetration pile depth ( $L_p$ ) was investigated, and increased capacity with increasing penetration pile depth. The obtained result is presented because of figures to be easy to use by the geotechnical designer.

## References

1. Bond, A. J., & Jardine, R. J. (1991). Effects of installing displacement piles in a high OCR clay. *Geotechnique*, 41(3), 341–363.
2. Broere, W., & van Tol, A. F. (2006). Modelling the bearing capacity of displacement piles in sand. *Proceedings of the Institution of Civil Engineers-Geotechnical Engineering*, 159(3), 195–206.

3. Aghayarzadeh, M., & Khabbaz, H. (2019). Numerical simulation of concrete pile groups' response bored in cemented sand deposit under axial static load testing. In *E3S Web of Conferences* (Vol. 92, p. 16011). EDP Sciences.
4. Alkhafaji, H., Imani, M., & Fahimifar, A. (2021). Determining the stress-settlement distribution of a gravity dam foundation considering different water levels using finite element method. In *Modern applications of geotechnical engineering and construction* (pp. 217–227). Springer.
5. Dijkstra, J., Broere, W., & Heeres, O. M. (2011). Numerical simulation of pile installation. *Computers and Geotechnics*, 38(5), 612–622.
6. Lozovyi, S., & Zahoruiko, E. (2014). Plaxis simulation of static pile tests and determination of reaction piles influence. arXiv preprint [arXiv:1411.0929](https://arxiv.org/abs/1411.0929).
7. Zhang, C., Nguyen, G. D., & Einav, I. (2013). The end-bearing capacity of piles penetrating into crushable soils. *Géotechnique*, 63(5), 341–354.
8. De Gennaro, V., Frank, R., & Said, I. (2008). Finite element analysis of model piles axially loaded in sands. *Rivista Italiana di Geotecnica*, 2, 44–62.
9. Johari, A., & Talebi, A. (2021). Stochastic analysis of piled-raft foundations using the random finite-element method. *International Journal of Geomechanics*, 21(4), 04021020.
10. Sheil, B. B., & McCabe, B. A. (2016). An analytical approach for the prediction of single pile and pile group behaviour in clay. *Computers and Geotechnics*, 75, 145–158.
11. ASTM, A. (2007). Standard test methods for deep foundations under static axial compressive load. D1143M-07.
12. Dewi, S., & Liong, G. T. (2011). Analysis on laterally loaded group piles by PLAXIS 3D foundation. *Jurnal ComTech*, 2(02), 1023–1030.
13. Schanz, T., & Vermeer, P. A. (1996). Angles of friction and dilatancy of sand. *Géotechnique*, 46(1), 145–151.
14. Wehnert, M., & Vermeer, P.A. (2004). Numerical analyses of load tests on bored piles. Numerical methods in geomechanics–NUMOG IX, pp. 505–511.
15. PLAXIS b.v. PLAXIS 3D, Reference manual. (2013).
16. Yang, Z. X., Jardine, R. J., Zhu, B. T., Foray, P., & Tsuha, C. D. H. C. (2010). Sand grain crushing and interface shearing during displacement pile installation in sand. *Géotechnique*, 60(6), 469–482.
17. Randolph, M. F. (2003). Science and empiricism in pile foundation design. *Géotechnique*, 53(10), 847–875.

# Experimental Investigation of Pullout Capacity of Screw Piles in Soft Clayey Soil



Asaad A. Hussein and Mahdi O. Karkush

**Abstract** Screw piles are considered one of the distinctive and unique engineering solutions because of the characteristics and advantages that it possesses such as its appropriate cost, the speed and ease of implementation and the suitability of its use with places with restricted access, with the flexibility of design and manufacture according to the conditions of the ground and the amount of forces required to resist. In this study, a series of experiments conducted on a single screw pile with a variable aspect ratio ( $L/D = 10, 13.33, \text{ and } 20$ ) under the influence of static pullout loads. The screw piles were inserted in soft soil of unit weight ( $18.72 \text{ kN/m}^3$ ) and moisture content ( $30.19\%$ ) and with a liquid limit =  $55\%$ , and plasticity index =  $32$ . A physical model with a laboratory scale was designed for this purpose and instrumented with the necessary equipment. The load-settlement curves and from these curves were used to calculate the ultimate pullout capacity of screw piles by adopting the failure criterion of settlement equals to  $20\%$  of helix diameter. The results of experimental tests showed a significant increase in the pullout capacity of screw piles in comparison with an ordinary pile ( $426.6, 766.67, 1186.67$ ) %. Also, the results showed increasing the pullout capacity of piles with increasing the aspect ratio and well agreed with those obtained theoretically.

**Keywords** Screw pile · Soft soil · Pullout loads · Upward movement

## 1 Introduction

Helical or screw piles are an improved type of steel tube piles by adding loading plates around the shaft of the regular steel pile. These plates are fixed to the iron shaft of the pile by welding or riveting consisting of one or more bearing plates and sometimes these plates are multiple and connected to form a continuous screw thread along the iron shaft. In general, the helical plates increase the interaction between soil and pile which resulted in increasing the bearing capacity of screw

---

A. A. Hussein · M. O. Karkush (✉)  
Civil Engineering Department, University of Baghdad, Baghdad, Iraq  
e-mail: [mahdi\\_karkush@coeng.uobaghdad.edu.iq](mailto:mahdi_karkush@coeng.uobaghdad.edu.iq)

piles for tension, compression, and lateral loading conditions. The screw piles used effectively in many applications on land and in the sea, they are used in construction sites that suffer from high levels of groundwater and in the foundations of power transmission and communication towers as well as to provide support to the sides of the excavation. Also, the construction of screw piles is very easy which not required specific equipment and speed of implementation that does not require filling or grouting and is used in the sea to install pipelines to the seabed and platforms at the coast [1]. The construction in problematic soils such as soft soils is considered one of the widespread problems facing the geotechnical engineers, so using screw piles is considered one of the solutions to avoid such obstacles. The factor that will govern the design process is the amount of settlement and not the bearing capacity alone, as what distinguishes soft soils is high compressibility and weak bearing capacity compressibility ( $C_c$  ranges from 0.19 to 0.44) and the low undrained shear strength ( $c_u$  is less than 40 kPa) [2].

The ultimate pullout capacity of screw piles inserted in clayey soil compared with the estimated ultimate pullout capacity of screw piles using two approaches of failure: individual plate bearing or cylindrical soil shearing along the surface between the plates. The results of tests showed a significant influence for the spacing between helices on the ultimate pullout capacity of multi-helix [3]. The performance of helical piles under pullout loading in organic soils was investigated. Several parameters had been studied such as the density of soil, the number of piles, and spacing between helices ranged from 0.1 to 0.5. The results of the tests proved that the ultimate pullout capacity of screw piles depends mainly on the spacing to the diameter ratio [4]. A comprehensive numerical and physical modeling into the mechanics of screw piles and the effect of installation was investigated. Also, a closed-form solution was proposed to calculate the ultimate bearing capacity of screw piles inserted in saturated clay using finite element software ABAQUS to account for installation effects with various configurations and loading conditions. The results obtained from experimental work well agreed with those estimated by the proposed numerical model taking into consideration the factors affecting the installation of screw piles [5].

The behavior of a single screw pile embedded in soft clay soil overlying sandy soil loaded in compression was investigated by conducting a series of experiments in the laboratory. Several parameters were investigated such as embedded depth, number of helices, diameter of helix, and spacing between helices. The experiment results showed that the ultimate bearing capacity of screw piles (9–16) times more than ordinary piles [6, 7]. Mukhleif et al. [8] investigated the behavior of screw piles having several aspect ratios ( $L/D$ ) inserted in gypseous soils and subjected to axial loading. The tests were conducted in dry and soaking conditions to evaluate the effect of gypsum dissolution on the bearing capacity of screw piles. The results of tests showed increasing the bearing capacity of screw piles with decreasing the aspect ratio. Also, the soaking of soil causes a significant decrease in the bearing capacity of screw piles in gypseous soil. The pullout capacity of screw piles with continuous helices over the embedded depth ( $L$ ) in soft clay has been investigated in this study. The aspect ratio of screw piles ( $L/D$ ) has a significant influence on the behavior of screw piles which can be divided into two groups: flexible piles with  $L/D > 20$  and



rigid piles with  $L/D < 20$ . The experimental results of ultimate pullout capacity were compared with those calculated theoretically to evaluate the validity and applicability of existing theoretical equations for estimation the ultimate pullout capacity of screw piles in soft soils.

## 2 Geotechnical Properties of Soft Clay

The soil samples were obtained from the quarry of the Kufa cement plant located southwest of the Qadisiyah Governorate. The groundwater table was encountered at depth of 4 m from natural ground level and the soil samples were obtained from a depth of (4.25 to 4.5) m below the level of the natural ground. The visual classification of soil indicated that the soil samples are cohesive pure clay loamy soil. In order to determine the geotechnical properties of the soil used in this study, these samples were subject to a program of tests that included determining the field density and moisture content, which are the main factors in the preparation of bedding soil in the physical model. The chemical, physical, and mechanical properties of used soil are summarized in Table 1.

## 3 Physical Model and Piles

**Model Piles.** Three models of screw piles have an aspect ratio ( $L/D$ ) of 20, 13.33, and 10, and one ordinary pile of regular circular cross-sectional area of an aspect ratio of 30.77. The ratio of (1:10) was adopted to correlate between the laboratory models and field models. The screw piles were used with a constant embedded length ( $L$ ) of 400 mm and variable configurations of diameters and spacing between helices. A constant ratio between the diameter of helices ( $D$ ) to the diameter of shaft ( $d$ ) was equal to 2.5. Details and dimensions of used piles in tests are given in Table 2 and shown in Fig. 1.

**Physical model.** The model consists of two main parts: the first part is a steel container that contains the soil and consists of separate and removable parts. It was made of iron plates with a thickness of 8 mm and dimensions of 70 cm length, 70 cm width, and 70 cm height and is seated on a base of iron plate. At the center of the base, the container has an opening of 1.25 cm in diameter which is connected to a valve. This valve is connected to a tank to conduct soil saturation from the bottom to the top of the soil. The water level in the reservoir is usually 20 cm more than the soil surface to ensure soil saturation, ensure soil saturation and equalize pore pressure with a pore water pressure transducer (Model 4500DP). The transducer is made of high-quality stainless steel and designed to handle pressure from  $-50$  to  $4000$  kPa, as it can measure negative water pressures up to  $-50$  kPa. This container is coated with anti-rust paint and two layers of oil paint to avoid corrosion during the inspection

**Table 1** Chemical and geotechnical properties of soft clay

Test name	Specification	Soil property		Unit	Value
Specific gravity	ASTM D854	Specific gravity, G <sub>s</sub>		–	2.75
Atterberg's limits	ASTM D4318	Liquid limit, LL		%	55
		Plastic limit, PL		%	23
	–	Plasticity index, PI		%	32
Grain size analysis	ASTM D422	CH	Clay	%	36.3
			Silt	%	62.7
		Maximum dry unit weight		kN/m <sup>3</sup>	15.4
Standard Compaction	ASTM D698	Optimum moisture content		%	22
		Field unit weight		kN/m <sup>3</sup>	18.72
Field unit weight	–	Field unit weight		kN/m <sup>3</sup>	18.72
Moisture content	ASTM D2216	Moisture content		%	30.19
Falling head	ASTM D5084	Permeability, k		m/s	$2.84 \times 10^{-8}$
Chemical properties	BS 1377 (1990) Part 3	Sulfur content, SO <sub>3</sub>		%	0.28
		Chloride content, Cl <sup>-1</sup>		%	0.03
		Total Dissolved Solids, TDS		mg/l	110
		Gypsum content		%	2.00
		CaO content		%	17.61
		pH value		–	9.50
		Organic matter content, OMC		%	2.8
1-D Consolidation	ASTM D2435	Compression index, C <sub>c</sub>		–	0.183
		Swelling index, C <sub>s</sub>		–	0.043
Unconsolidated undrained triaxial	ASTM D2850	Undrained shear strength, c <sub>u</sub>		kPa	20.35
Unconfined compressive strength	ASTM D2166	Unconfined shear strength, S <sub>u</sub>		kPa	21.5

**Table 2** The details of the dimensions of the piles

Pile	Shaft Dia. (mm)	Embedded depth, L (mm)	No. of helices	Spacing between helices, S (mm)	Diameter of helix, D (mm)	L/D ratio	S/D ratio
PD13	13	400	–	–	–	30.8	0
PD20	8	400	21	15	20	20.0	0.75
PD30	12	400	15	25	30	13.3	0.83
PD40	16	400	13	30	40	10.0	0.75

**Fig. 1** Model piles used in tests



period of tests, the schematic diagram of the physical model is shown in Fig. 2. The second part consists of a hydraulic piston used to apply load on the pile head. The magnitude of applied load was measured by a load cell that is fixed to the head of the hydraulic piston and the vertical displacement of the pile was measured by using a linear variable differential transformer (LVDT). The signal generated in each LVDT and load cell, are received and converted into the values of the settlement and the applied load by using the Arduino software as well as the LabVIEW program, where the outputs of each examination are controlled through these two programs.

**Soil bedding.** The soil bed was prepared according to the field unit weight of  $18.72 \text{ kN/m}^3$  and corresponding moisture content of 30.19%. The soil bed in the iron box was divided into six layers, so that the thickness of one layer after compaction does not exceed 9 cm, where the final height of soil in the container will be 60 cm. A layer of sand of 3 cm thickness was placed at the bottom of the container and used to protect the bottom of soil from disturbance during the saturation process which continued for 48 h and to ensure that the saturation process occurs in a smooth and complete manner. Also, a torque is applied on the head of screw piles gradually to insert the pile in the center of the soft soil bed and torque stopped after reaching

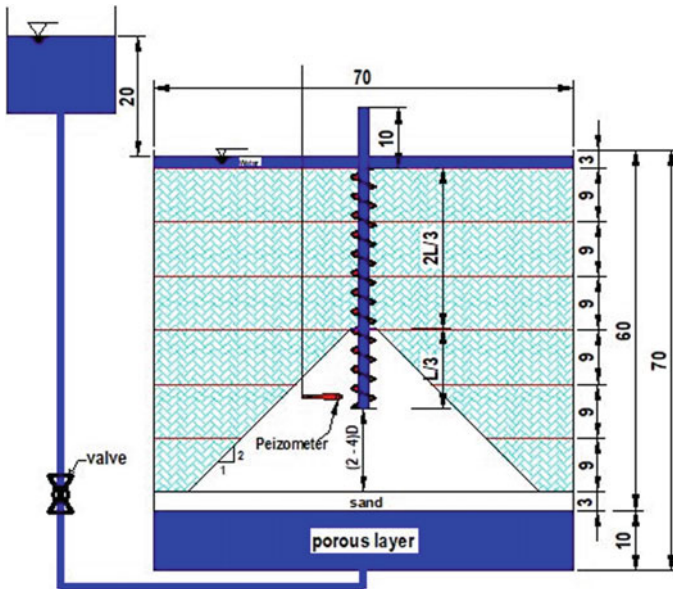


Fig. 2 Section in the physical model (Dimensions in cm)

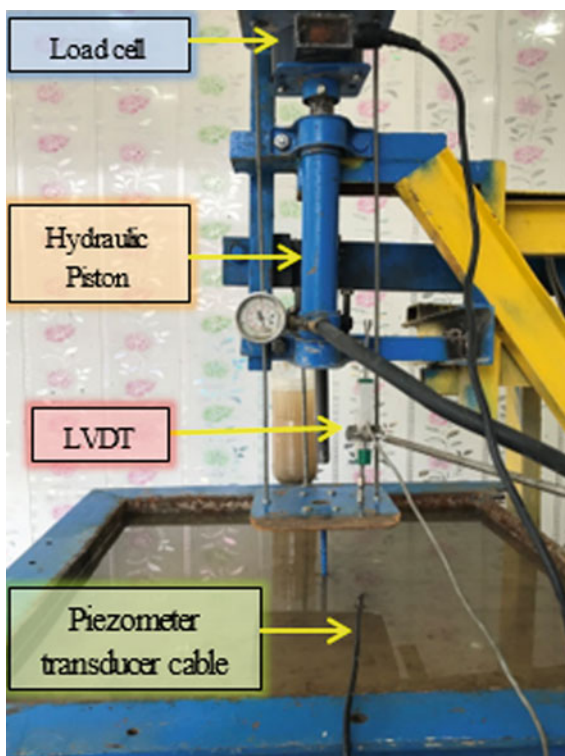
the required depth of 40 cm. Enough care and control should be taken to keep the vertical line of the screw pile.

## 4 Testing Procedure

The axial pullout load tests on screw piles are typically conducted in accordance with ASTM D1143-07 [9], where a pullout test is performed on a single pile embedded into the prepared soft soil, then the loading and measurement system tools are tightened to the pile cap, and after ensuring that the soil is saturated, it was found that a time interval of 24–48 h was required to balance 95% of Pore pressure. The pullout load test is performed as described in the following steps:

- (1) The pullout load test system is prepared by equipping a hydraulic piston, supported from the bottom and fixed to the loading frame and connected from the top with the load cell. The load cell is mechanically connected to the head of the screw pile by special tools as shown in Fig. 3. The load cell is connected to an Arduino programmer that works with the LabVIEW program to record the increments of the applied load.
- (2) The pullout load is applied and controlled by equipping a hydraulic piston and load cell. This piston has the ability to move upward and apply pullout load on

**Fig. 3** The pullout test system



the load cell, which is fixed on the pile cap and connected with an indicator to the LabVIEW program to display the values of the pullout load.

- (3) The pullout load is applied gradually and incrementally, the average upward movement of the screw pile under each increment is measured by using the LVDT, which is connected to the screw pile cap and LabVIEW program to display the values of upward movement.
- (4) The test will continue until reaching the failure of the pile, the adopted failure criterion in this study defined the ultimate pullout capacity of the pile as the load corresponding to a displacement equals 20% of the helix diameter, where this criterion is considered moderate among other standards, as it was adopted in most of the previous studies as Heerma (1979), Smith (1987), Fellenius (2006), (Lutenegger, 2009) and Warna (2015).

## 5 Load Transmission Mechanism

The screw piles used for tension purposes and inserted in clayey soil are not different from that are used in axial compression in terms of design, except to reduce the sectional area to avoid disturbance that may occur during installation. The total

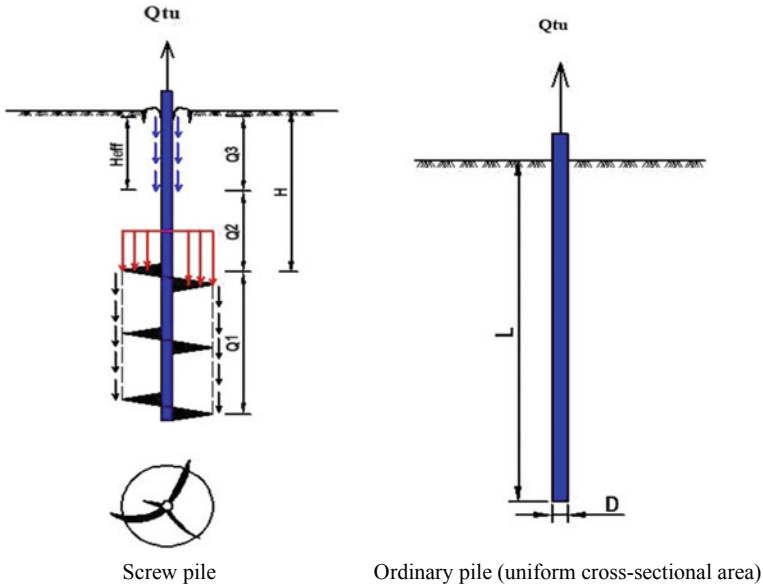


Fig. 4 Pullout resistance components of piles

capacity of screw piles consists of three basic components as shown in Fig. 4 and can be calculated according to the following equation [10–13]:

$$Q_{tu} = Q_1 + Q_2 + Q_3 + W_a + \text{suction force} \tag{1}$$

where

- $Q_{tu}$  = Ultimate pullout capacity of the pile;
- $Q_1$  = Cylindrical shear resistance =  $S_F (\pi D L_C) c_u$ ;
- $Q_2$  = Bearing resistance on the top helical plate =  $A (c_u N_{tu} + \gamma H)$ ;
- $Q_3$  = Skin friction resistance =  $\pi d H_{eff} \alpha c_u$ ;
- $W_a$  = Self-weight of the pile;
- $S_F$  = Spacing ratio factor.
- $S_R(S/D)$  = Spacing ratio: the spacing between any two adjacent helical plates/their average diameter;
- $S$  = Spacing between helices.

$$S_F = 1.0 \text{ for } S_R \leq 1.5$$

$$S_F = 0.863 + 0.069(3.5 - S_R) \text{ for } 1.5 < S_R < 3.5$$

$$S_F = 0.700 + 0.148(4.6 - S_R) \text{ for } 3.5 < S_R < 4.6$$

$D$  = Diameter of helix;

- $L_C$  = The distance between top and bottom helical plates;
- $c_u$  = Undrained shear strength (kPa);
- $A$  = Area of the helix =  $\pi(D^2 - d^2)/4$ ;
- $N_{tu}$  = The break out factor;
- $\gamma$  = The unit weight of soil;
- $H$  = Depth of embedment of the top helical plate;
- $H_{eff}$  = The effective length of the shaft;
- $d$  = Diameter of the pile shaft;
- $\alpha$  = Adhesion factor.

The suction force is neglected due to the difficulty in estimating it and its temporary effect, and the safety factor is taken unity because the spacing between the plates is less than the diameter of the helices [11]. The ultimate pullout capacity of the ordinary pile can be estimated according to the following equation:

$$Q_{tu} = W_a + \pi DL\alpha c_u \tag{2}$$

It is clear that, the main factor is the adhesion factor ( $\alpha$ ), which depends on the type of the pile material and the soil. Based on previous studies conducted on this topic and concluded that the parameters of the adhesion factor for the pipe piles were determined approximately using the following relationships [12]:

$$\alpha = 0.715 - 0.0191c_u \text{ (for } c_u \leq 27 \text{ kPa)} \tag{3}$$

$$\alpha = 0.2 \text{ (for } c_u > 27 \text{ kPa)} \tag{4}$$

## 6 Results and Discussion

In order to observe the change in the capacity of the screw piles and the gain obtained as a result of adding the helical bearing plates, an ordinary pile with three screw piles was used, moreover, a different shape ratio for all the piles used was adopted to study the effect of the embedded length on its capacities. The results of the experimental tests of the piles and the ordinary pile represented by the curves of the pullout load with the upward movement are given in Fig. 5. It is clear that there is a significant and remarkable development in the capacity of the piles compared to the capacity of the ordinary pile despite the convergence of the average diameter of the shaft of the piles with the ordinary pile. Increasing the pullout capacity of screw piles is resulted from adding helical plates which increases the interaction between the pile and the surrounding soil. Also, there was a proportional and steady increase in the pullout capacity of screw piles with increasing the diameter of the helical plate. Despite constant the embedded depth of the pile in the soft clayey soil as summarized in

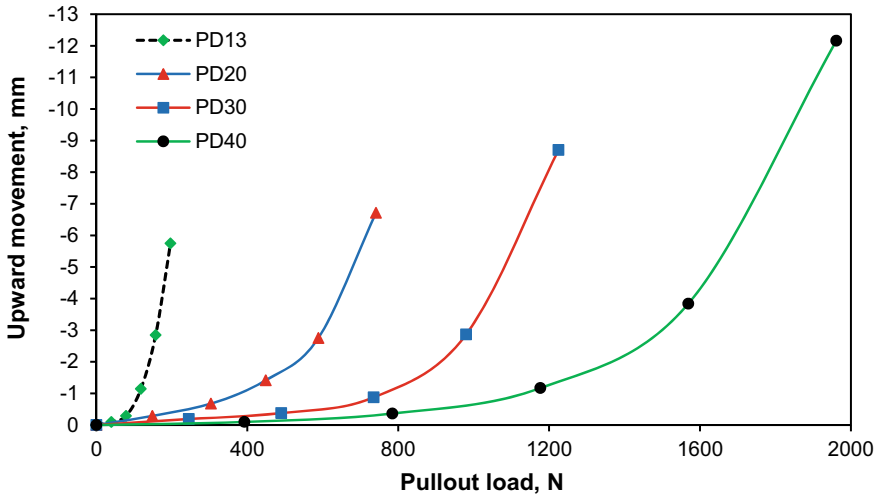


Fig. 5 Variation of upward movement with axial pullout load applied on tested piles

Table 3, it is noticed that the pullout capacity of the piles is inversely proportional to the aspect ratio of the pile. In general, the failure surface of screw piles is cylindrical (SR < 1.5) [11].

There are several approaches and criteria that can be used for conceptual design that must be compared with the ultimate capacities of the screw pile obtained from the experimental load-settlement tests. The load value corresponding to a displacement of 20% from the diameter of the helix was used as a criterion to determine the ultimate pullout capacity of screw piles. The results of the ultimate pullout capacity of screw piles calculated from experimental tests are compared with the corresponding values calculated from theoretical equations are given in Table 4. It is noticed that there is a discrepancy between the experimental results and the estimated results calculated from Eqs. 1 and 2, and this discrepancy increases as the (L/D) ratio decreases. Figure 6 shows the variation of upward displacement of the piles during the tests period, it is noticed that the behavior of screw piles is similar, where all screw piles reach a displacement of 20% at approximately the same time (1050–1080 s) and this behavior is somewhat different from the behavior of ordinary pile (D13) which reaches this

Table 3 Experimental and estimated results of the pullout capacity of tested piles

Pile	L/D ratio	Ultimate pullout capacity, $Q_{tu}$ (N)		Deviation (%)
		Experimental	Theoretical	
PD13	30.8	150	139.33	7.11
PD20	20.0	640	542.01	15.31
PD30	13.3	1150	798.39	30.58
PD40	10.0	1780	1058.86	40.51



**Table 4** The increases in capacity of screw pile versus ordinary pile capacity

Pile	L/D ratio	Ultimate pullout capacity, $Q_{tu}$ (N)	Increases (%)
PD20	20.0	640	426.6
PD30	13.3	1150	766.67
PD40	10.0	1780	1186.67

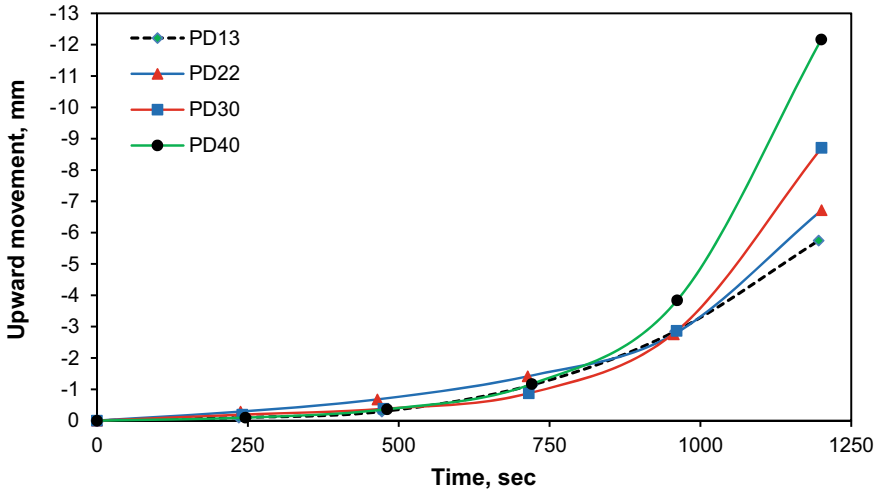


**Fig. 6** Variation of upward movement with the time of tested piles

amount of displacement in less time (900 s). The growth of upward displacement was very slow during the first 500 s, but starts to increase rapidly thereafter with respect to pile D13. The same behavior was noted for screw piles but after 900 s, which means screw piles take a longer time to fail.

The pile is classified according to the aspect ratio of the pile (L/D) into two major categories: rigid piles (aspect ratio less than 20) and flexible piles (aspect ratio more than 20) [13, 14]. By comparing the results obtained from the experimental work with the estimated using Eqs. 1 and 2, observe that the results for the flexible (long) piles are compatible to some extent, but they become disparate to a large extent when the piles are rigid (short) screw piles where the estimated capacity becomes much less compared to the experimental value. Therefore, Eqs. 1 and 2 can be used with confidential results to estimate the ultimate pullout capacity of flexible screw piles.

## 7 Conclusions

This study was devoted to investigate the behavior of flexible and rigid screw piles in soft clay under axial pullout loading. Based on the results of experimental tests, the following conclusions can be drawn out:

- The results of the research showed that screw piles are very useful in resisting axial pullout loads in soft cohesive soils.
- The failure pattern associated with these screw piles of cylindrical shape due to the close distance between the helices which is less than the helices diameter.
- The results of tests showed increasing the ultimate pullout capacity of the screw pile as a result of adding the helical plates in comparison with the ordinary pile, where the ultimate pullout capacity of screw piles increases with decreasing the aspect ratio of the pile (L/D).
- There was a convergent between the estimated ultimate pullout capacity and the experimental ultimate pullout capacity of flexible screw piles and there was a large disparity when the screw piles are rigid.

## References

1. Hoyt, R. M., & Clemence, S. P. (1989). Uplift capacity of helical piles in soil. In *Proceedings of 12th International Conference on Soil Mechanics and Foundation Engineering* (Vol. 2, pp. 1019–1022), Rio de Janeiro, Brazil.
2. Kempfert, H. G., & Gebreselassie, B. (2006). *Excavations and foundations in soft soils*. Springer Science & Business Media.
3. Lutenegeger, A. J. (2009). Cylindrical shear or plate bearing?—Uplift behavior of multi-helix screw piles in clay. In *Contemporary Topics in Deep Foundations International Foundation Congress and Equipment Expo 2009* (pp. 456–463).
4. Hamed, M., Canakci, H., & Khaleel, O. (2019). Performance of multi-helix pile embedded in organic soil under pull-out load. *Transportation Infrastructure Geotechnology*, 6(1), 56–66.
5. Todeshkejoei, K. (2019). Mechanics of screw piles in clay. Doctoral dissertation, University of Newcastle.
6. Ali, O. K., & Abbas, H. O. (2019). Performance assessment of screw piles embedded in soft clay. *Civil Engineering Journal*, 5(8), 1788–1798.
7. Abbas, H. O., & Ali, O. K. (2020). Parameters affecting screw pile capacity embedded in soft clay overlaying dense sandy soil. *IOP Conference Series: Materials Science and Engineering*, 745(1), 012117.
8. Mukhleif, O. J., Karkush, M. O., & Zhussupbekov, A. (2020). Strength and compressibility of screw piles constructed in gypseous soil. *IOP Conference Series: Materials Science and Engineering*, 901(1), 012006.
9. ASTM D1143, A. (2013). *Standard test methods for deep foundations under static axial compressive load*. ASTM International.
10. Lutenegeger, A. J. (2015). *Quick design guide for screw-piles and helical piles in soils*. International Society for Helical Foundations.
11. Rao, S. N., Prasad, Y. V. S. N., & Veeresh, C. (1993). Behaviour of embedded model screw piles in soft clays. *Geotechnique*, 43(4), 605–614.

12. Ullah, S. N., & Hu, Y. (2020). Discussion: A review on the behaviour of helical piles as a potential offshore foundation system. *Marine Georesources and Geotechnology*, 38(9), 1121–1127.
13. Sharma, A. K., Tallapragada, K. R., & Pachpor, P. D. (2020). Pullout behaviour of screw and suction piles in clayey soil. *Helix*, 10(01), 84–88.
14. Das, B. M., & Seeley, G. R. (1982). Uplift capacity of pipe piles in saturated clay.
15. Darvishi Alamouti, S., Bahaari, M. R., & Moradi, M. (2017). Effect of pile bending stiffness on static lateral behavior of a short monopile in dry sand. *International Journal of Coastal and Offshore Engineering*, 5, 17–24.
16. Yang, M., Ge, B., Li, W., & Zhu, B. (2016). Dimension effect on Py model used for design of laterally loaded piles. *Procedia Engineering*, 143, 598–606.

# Effect of Embankment on the Behavior of Rigid Passive Pile Group in Sandy Soil



Mahdi O. Karkush, Majeed R. Sabaa, Ghofran S. Jaffar,  
and Omar K. Al-Kubaisi

**Abstract** Piles can be damaged due to the lateral soil movement induced by constructing a nearby embankment. These movements introduce lateral loads “passive loads” on the piles which in turn increase the lateral forces and bending moments within the piles. In some cases, these induced forces and moments may exceed the pile capacity and cause failure. This research investigates experimentally the effects of soil movement on the behavior of nearby axially loaded and unloaded rigid pile groups driven in sandy soil having a dry unit weight of  $13.5 \text{ kN/m}^3$ . The model piles are made of aluminum and have an embedded length ( $L_e$ ) of 360 mm, free head of 140 mm, and diameter ( $D$ ) of 10 mm. The embankment loads are applied at distances of  $2.5 D$ ,  $5 D$ , and  $10 D$  from the edge of the pile group. The obtained results showed that the presence of axial loads decreases the displacement at the soil surface. It was found that the axially unloaded pile group (UG) had displaced more than the axially loaded pile group (LG) by 16, 25, and 35% at  $2.5D$ ,  $5D$ , and  $10D$  respectively. Moreover, increasing the distance between the embankment and the edge of the pile group had significantly decreased the maximum soil reaction due to the reduction of soil movement pressure.

**Keywords** Passive pile · Rigid pile group · Embankment effect · Sandy soil · Model test

---

M. O. Karkush (✉) · G. S. Jaffar  
Department of Civil Engineering, University of Baghdad, Baghdad, Iraq  
e-mail: [mahdi\\_karkush@coeng.uobaghdad.edu.iq](mailto:mahdi_karkush@coeng.uobaghdad.edu.iq)

M. R. Sabaa  
Al-Furat Al-Awsat Technical University, Al-Najaf, Iraq  
e-mail: [omar.ismael@sydney.edu.au](mailto:omar.ismael@sydney.edu.au)

O. K. Al-Kubaisi  
The School of Civil Engineering, The Faculty of Engineering, The University of Sydney,  
Darlington, NSW 2006, Australia  
e-mail: [omar.ismael@sydney.edu.au](mailto:omar.ismael@sydney.edu.au)

## 1 Introduction

The construction of an embankment can impose excessive vertical loads on the soil underneath. These loads force the soil to move away from the loading source. This soil movement will apply lateral pressure on the front side of the pile which, in some cases, can exceed the pile capacity and cause failure. These lateral loads try to push the pile horizontally in the direction of loading which induces bending moment, rotation, and movement of the pile [1, 2]. Based on the direction of load transfer between the pile and the surrounding soil, the laterally loaded pile can be classified into active piles or passive piles [3–5]. An active pile is mainly loaded at its top, with the lateral load being transferred to the soil such as the piles underneath the foundation of transmission towers and offshore structures. While a passive pile usually experiences lateral thrusts along its shaft arising from the horizontal movement of the surrounding soil such as piles used for slope stabilization and embankments [6]. Correct prediction of the displacements, moments, and shear forces caused by the moving soil can be considered as a key element in the design, construction, and serviceability of the type of piles [7]. Different factors have been found to affect the behavior of passive piles such as the material and geometric properties of piles, the profile of the moving soil, the axial loads, and the distance at which the pile is located from the boundaries of the moving soil.

The influence of a three-dimensional soil deformation on the response of a laterally loaded pile group in the sand has been investigated by conducting a series of model tests. The three-dimensional soil surface deformations around the piles had been obtained using a newly developed technique named Stereo-PIV [8]. Both Zhao et al. [9] and Zhang et al. [10] have presented a simplified analytical method to simulate the effects of soil movement due to soil excavation on the behavior of pile groups. They found that the lateral response of the passive pile groups obtained from the proposed method well agreed with those obtained from the centrifuge model tests. Furthermore, Ersoy and Yildirim [11] have investigated the behavior of piles subjected to lateral soil movement imposed by slopes by conducting large-scale shear box experiments and the results have been compared with those found in the literature to enhance the understanding of the passive pile behavior.

In addition to that, Ibrahim and Hatem [12] have investigated the behavior of piles subjected to lateral soil movement in the sand. Different parameters have been utilized such as pile spacing, number of piles within a group, and pile head condition. The results showed that the maximum bending moment of pile groups has decreased as the pile spacing decreased and the pile has behaved as a single pile when the pile spacing has exceeded 7 times the diameter of the pile. Moreover, the influence of construction nearby embankment on the performance of existing single rigid and flexible piles inserted in sandy soil has been investigated [13–15]. The embankment load has been located at three different distances of 2.5, 5, and 10 D from the edge of existing piles where D is the diameter of the pile. The results showed that the rigid pile with a shorter embedded length,  $L_e = 360$  mm, has provided more resistance to soil movement pressure. While Ren et al. [16] have conducted large geotechnical

centrifuge model tests of two design schemes to simulate sheet-pile wharves with the load-relief platform in a homogeneous fine sand to evaluate the distribution of lateral pile-soil pressure and to distinguish between the pile’s passive part and active part. On the other hand, Karkush and Kareem [17, 18] have studied the behavior of passive piles in fine-grained textured soil contaminated with two ratios of petroleum products (MFO) under the effects of lateral soil movement. The results showed that as the percentage of soil contamination increased the impact of the embankment on the response of the passive piles has increased. In the present study, the response of the existing rigid pile group of (2 × 1) to the lateral soil movement induced by the construction of a nearby embankment has been investigated experimentally.

## 2 Material Properties

River sand can be classified as (SP-SM) according to the Unified Soil Classification System (USCS) has been used in this study. The mechanical properties of the soil have been evaluated based on ASTM and BS specifications [19, 20]. The physical and mechanical properties of the soil have been listed in Table 1. A closed-end aluminum pipe of 500 mm long has been used in this study to model the pile. The mechanical properties of the aluminum model pile have been presented in Table 1. A slenderness ratio (L/D) of 50 and an embedded depth of 360 mm have been used in this study to ensure that the model pile behaves as a rigid pile according to the flexibility factor ( $K_R$ ) shown in (Eq. 1) in which  $E_p$  is the elasticity modulus of the pile;  $I_p$  is the moment of inertia of the pile;  $E_s$  is the secant modulus of the soil elasticity and  $L_e$  is the embedded length of the pile [21].

$$K_R = \frac{E_p I_p}{E_s L_e^4} < 10^{-5} \tag{1}$$

**Table 1** Properties of the soil and the model pile

Property of soil	Value	Property of soil	Value	Property of Pile	Value
Gs	2.67	$\gamma_{d \min}$ (kN/m <sup>3</sup> )	11.87	Outer diameter of pile (D)	10 mm
Cu	2.934	$\gamma_{d \max}$ (kN/m <sup>3</sup> )	15.14	Wall thickness of pile	1 mm
Cc	1.188	$\gamma_d$ (kN/m <sup>3</sup> ) at Dr = 56%	13.5	Length of pile (L)	500 mm
Fines (%)	9.8	$\varphi$ (°) at Dr = 56%	35°	Weight of pile	42 gm
Sand (%)	90.2	c (kPa)	9	Density of pile material	2.97 gm/cm <sup>3</sup>
Dr (%)	56	Confined Modulus of Elasticity $E_{oed}$ (kPa)	65,770	Modulus of elasticity ( $E_p$ )	69.871 GPa

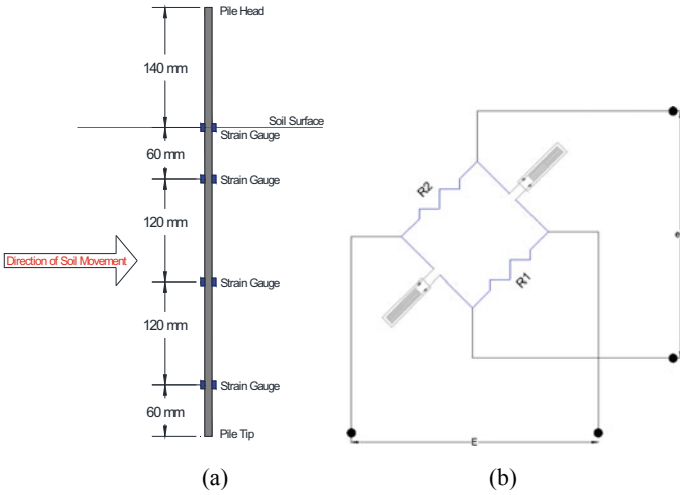


**Fig. 1** Model pile details **a** strain gauges distribution, **b** strain gauges configuration (half-bridge)

The model piles were instrumented with eight strain gauges, four of which have been located on the near side and the rest have been located on the far side of the model pile with respect to the embankment location, to measure the strain along the pile. The first pair of strain gauges have been located at the soil surface. A 60 mm spacing has been used between the first and the second pairs of strain gauges while 120 mm spacing has been used to distribute the rest as shown in Fig. 1a. The strain gauges have been numbered from SG1 to SG4 and each pair has been connected in a half Wheatstone bridge configuration as shown in Fig. 1b. The output voltage of the half-bridge configuration without including the temperature compensation can be expressed by (Eq. 2).

$$e_o = \frac{E}{2} K_s \varepsilon_o \tag{2}$$

where  $e_o$  is the output voltage;  $E$  is the bridge voltage;  $K_s$  is the gauge factor which is  $2.12 \pm 1\%$  in this study; and  $\varepsilon_o$  is the strain.

### 3 Experimental Settings and Testing Procedure

The experiments have been conducted in a steel container with dimensions of (800 mm × 800 mm × 800 mm). The raining technique has been used to pour the soil into the container from a specific height to achieve the required dry unit weight of 13.5 kN/m<sup>3</sup>. To find the required height to achieve the required soil density, four pouring heights of 100, 200, 300, and 400 mm have been used to capture the effect of

the pouring height on the soil density as shown in Fig. 2. Based on Fig. 3, a dropping height of 240 mm has been used in this study to achieve a soil density of  $13.5 \text{ kN/m}^3$ . The dropping height has been maintained by lifting the dropping cone a distance equals to the thickness of the poured soil layer. After filling the container with soil to the required height, the soil surface has been leveled and excessive soil has been removed.

A hydraulic jack with a maximum loading capacity of 10 tons has been mounted on the loading frame as shown in Fig. 3. This jack has been used for installing the pile groups into the soil to the required embedded depth as well as applying the embankment loads which have been monitored using a load cell mounted on the

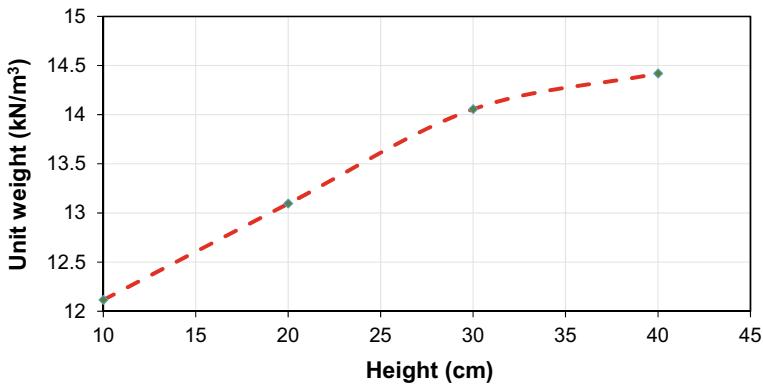


Fig. 2 Effect of soil pouring height on its dry unit weight

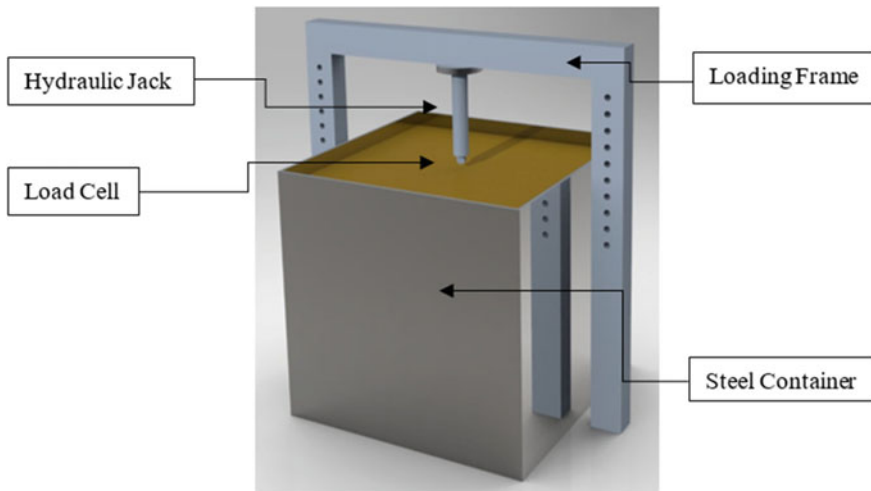


Fig. 3 Schematic view of the experimental settings



cylindrical steel shaft. Two pile groups of  $(2 \times 1)$  have been installed. The first pile group, denoted by (LG) for axially loaded pile group, has been driven into the soil at a distance greater than 10 times the pile diameter from the walls of the steel container to eliminate the effect of the tip resistance [22]. While the second pile group, denoted by (UG) for axially unloaded pile group, has been driven into the soil at distance greater than 15 times the pile diameter from the first group to eliminate any rigid boundary effects [23]. Two dial gauges have been installed horizontally for each pile group at two different locations above the soil surface to measure the horizontal displacement of the pile group.

To start the experiments, the pile group (LG) has been loaded gradually up to its working axial load capacity which had been evaluated by dividing the ultimate axial load capacity by a safety factor of 2. The incremental loads have been applied by placing weights over the cap of the pile group. As a result, there has been no restriction on the head of piles and the piles have been treated as free headed piles. Then, an embankment load ranged from 10 up to 60 kPa with an increment of 10 kPa has been applied at distances of 2.5, 5, and 10 D from the pile group to simulate the effect of nearby embankments. Each embankment increment has been applied for 2 min based on the literature [24, 25]. Both the dial gauge readings and the strain gauge readings have been recorded with time for each embankment load increment.

## 4 Data Analysis

The strain along the piles ( $\epsilon$ ) has been measured using the strain gauges. Using Hook's law, the flexural stress ( $\sigma$ ) has been calculated at the strain gauge locations. Finally, the discrete bending moment ( $M$ ) has been calculated using the flexural stress (see Eq. 3).

$$M = \frac{\sigma I_p}{D/2} = \frac{2E_p I_p}{D} \epsilon \quad (3)$$

where  $D$  is the outer diameter of the pile. To obtain a continuous response of the pile, two approaches have been reported by the literature. The first approach had been developed based on the use of a best-fit polynomial curve ranging from the 4th to the 7th order to obtain a continuous bending moment profile along the pile [26–28]. However, the drawback of this approach showed the inconsistency of the approach where multiple curves with different shapes could be used to reasonably fit the same data and, in some cases, a sudden jump in the soil reaction magnitude in the vicinity of the pile tip has been noted as reported in the literature [26–28]. The second approach had been developed based on the beam theory in which the pile responses such as the pile displacement, the pile rotation and the pile shear force profiles as well as the soil reaction profile could be derived by either differentiating or integrating the bending moment as expressed in Eqs. 4–7 [24, 28].

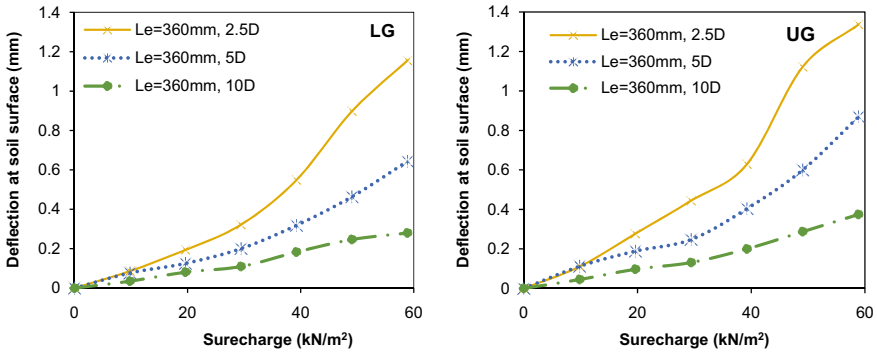


Fig. 4 Displacement at soil surface of rigid piles group

$$y(z) = \int \left( \int \frac{M(z)}{E_p I_p} dz \right) dz \tag{4}$$

$$S(z) = \int \frac{M(z)}{E_p I_p} dz \tag{5}$$

$$T(z) = \frac{dM(z)}{dz} \tag{6}$$

$$P(z) = \frac{d^2 M(z)}{dz^2} \tag{7}$$

where  $z$  is the depth measured from the soil surface downward;  $M(z)$  is the bending moment along the pile;  $y(z)$  is the pile lateral displacement;  $S(z)$  is the rotation of the axis of the pile;  $T(z)$  is the shear force along the pile and  $P(z)$  is the soil reaction along pile per unit length. In this study, a numerical integration using the trapezoidal rule has been adopted to integrate the bending moment profile. Then, the finite difference method has been used to calculate both the pile rotation and the pile deflection profiles (See Eqs. 8 and 9).

$$S_i = \sum_{i=0}^n \frac{M_i + M_{i+1}}{2} \Delta z - S_0 \tag{8}$$

$$y_i = \sum_{i=0}^n \frac{S_i + S_{i+1}}{2} \Delta z - \Delta z - n \Delta z S_0 + y_0 \tag{9}$$

where  $S_0$  and  $y_0$  are the integration constants of the pile rotation and the pile displacement respectively at the soil surface which has been measured directly using the dial gauges mounted at the pile head and  $\Delta z$  is the distance between the strain gauges. Consequently, both the shear force ( $T_i$ ) and the soil reaction profiles could be obtained

by using Eqs. 10 and 11 respectively [25]. However, to calculate the soil reaction at any point along the pile ( $P_i$ ), five bending moments should be obtained. As a result, to calculate the soil reaction ( $P_4$ ), two imaginary bending moments, denoted as  $M_5$  and  $M_6$ , have been determined to be equal to  $M_4$  and  $M_3$  respectively depending on the pile tip boundary conditions and the method described by Scott [29].

$$T_i = \frac{1}{2} \frac{M_{i-1} - M_{i+1}}{\Delta z} \tag{10}$$

$$P_i = \frac{1}{7} \frac{2M_{i-2} - M_{i-1} - 2M_i - M_{i+1} + 2M_{i+2}}{\Delta z^2} \tag{11}$$

### 5 Results and Discussion

The obtained results showed that the displacements at the soil surface for UG have been greater than those for LG for all cases due to the stiffening effect of the applied axial load on the latter as shown in Fig. 4. This behavior has been also observed and reported by the literature [30–32]. The increase percentages are 16, 35, and 34% for an embankment load at distances 2.5 D, 5 D, and 10 D from the pile edge respectively. While the pile rotation at the soil surface has decreased by (61–41) and (23–70) % for LG and UG respectively as the distance from the embankment to the pile edge increased from 2.5 to 10 D due to the rigid behavior of the pile groups as shown in Fig. 5.

For the bending moment along the pile, the results showed that as the distance between the pile group and the embankment increased, the effect of the axial loads on the pile group decreased as shown in Fig. 6. For an embankment distance of 5 D, the maximum bending moment has been found to be the same for both LG and UG. While for 10 D distance of embankment, the maximum bending moment for LG has

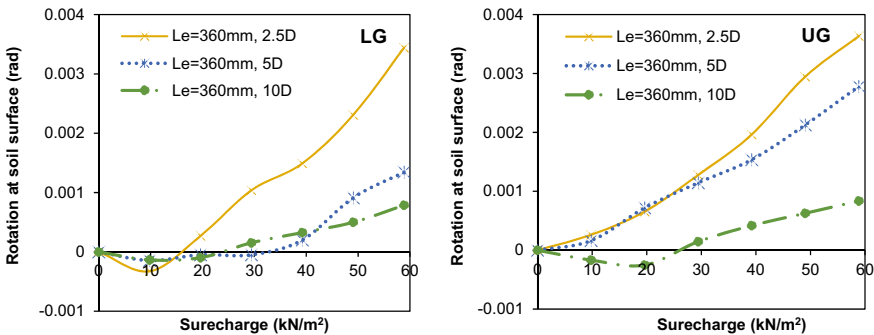


Fig. 5 Rotation at soil surface of rigid piles group

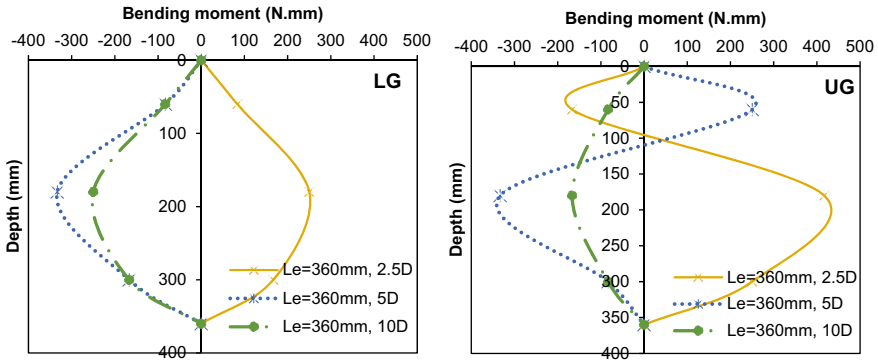


Fig. 6 Bending moment profiles of rigid piles group

been found to be greater than the one for UG by 33%. However, for the case where a 2.5 D embankment distance has been used, the maximum bending moment for LG has found to be less than the one for UG by 67% due to the stiffening effect induced by the applied axial loads on LG.

Based on the pile displacement profiles, the results showed that the maximum pile displacement decreased as the distance between the embankment and the pile edge increased as shown in Fig. 7. Moreover, the application of the axial load on LG has reduced its maximum displacement when compared to UG. The results showed that UG pile head has deflected greater than that for LG by 205, 51, and 26% as the distance between the embankment and the pile edge increased from 2.5 up to 10 D respectively.

The results of pile rotation profiles showed that the maximum pile rotation decreased as the distance between the embankment and the pile edge increased as shown in Fig. 8. These reductions are (129 and 4) % for LG and (51 and 129) % for UG as the embankment distance increased from 2.5 D to 10 D respectively. In

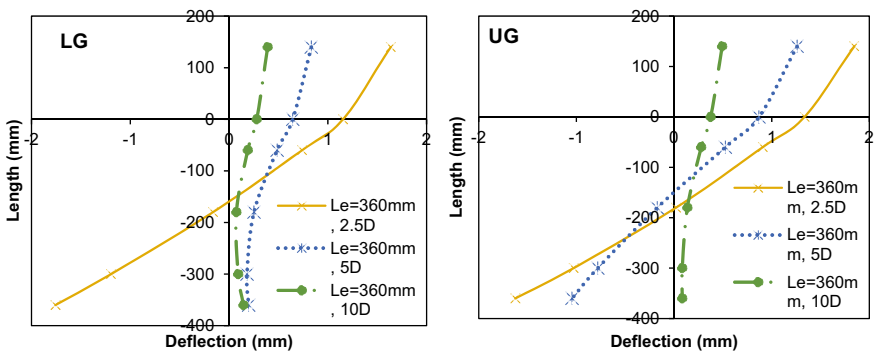
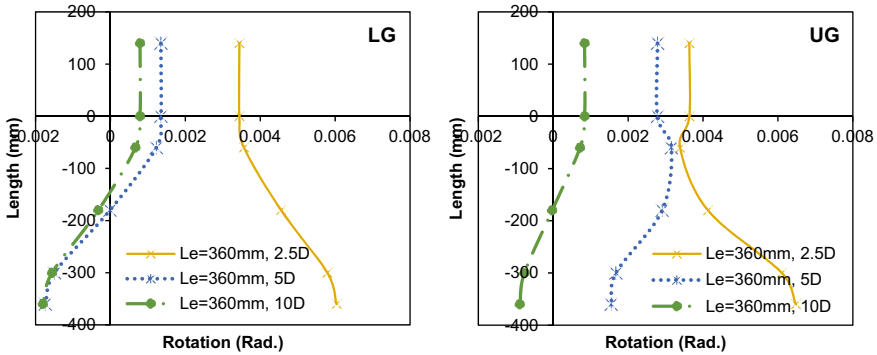


Fig. 7 Deflection profiles of rigid piles group



**Fig. 8** Rotation profiles of rigid piles group

addition, the application of axial load on LG has reduced its maximum rotation when compared to UG. The results showed that the maximum pile rotation for UG has been greater than that for LG by 7, 281, and 51% as the distance between the embankment and the pile edge increased from 2.5 D up to 10 D respectively. For the shear forces along the pile, the results showed that the maximum shear forces for LG decreased as the distance between the pile group and the embankment increased, while the maximum shear force for UG has increased by 20% then decreased by 150% as the embankment distance increased from 2.5 D to 10 D respectively as shown in Fig. 9. For LG, these reductions have been found to be (225 and 25) % as the embankment distance increased from 2.5 D up to 10 D respectively. Furthermore, the maximum shear force for UG has found to be greater than that for LG by (25 and 220) % as the embankment distance increased from 2.5–5 D due to the stiffening effect of the applied axial loads in LG. However, the maximum shear force for LG has found to be larger than that for UG by 25% when the embankment distance was 10 D.

Finally, the results of soil reaction profiles showed that the maximum soil reaction has increased at the beginning by (200 and 20) % for both LG and UG respectively

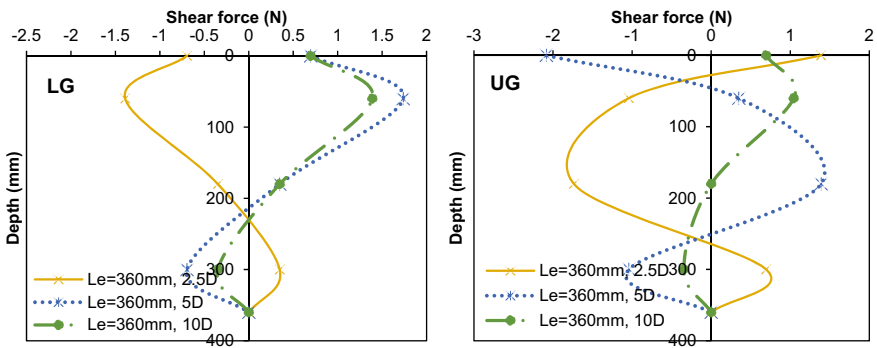


**Fig. 9** Shear force profiles of rigid piles group

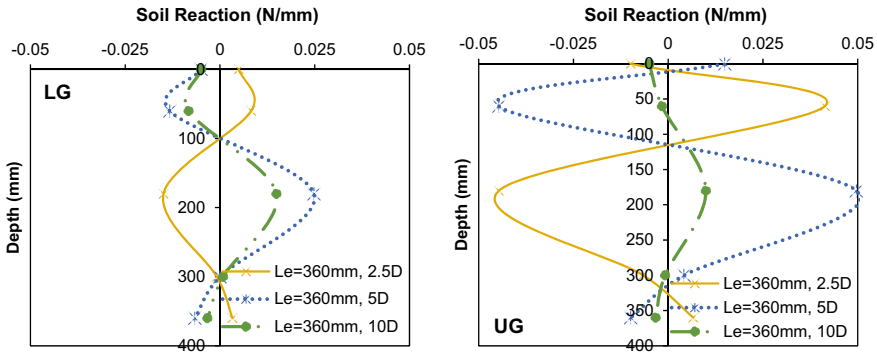


Fig. 10 Soil reaction profiles of rigid piles group

as the distance between the embankment and the pile edge increased from 2.5 to 5 D. Then, the maximum shear force has decreased by (40 and 80) % for both LG and UG respectively as the embankment distance increased from 5 to 10 D as shown in Fig. 10. It was found that the negative sign for the soil reaction has indicated the soil movement. While the positive sign has indicated the soil resistance to any movement.

## 6 Conclusions

Based on the obtained results, the following conclusions can be made:

- The displacements at the soil surface for UG have been greater than those for LG for all cases due to the stiffening effect of the applied axial load on the latter.
- The results showed that as the distance between the pile group and the embankment increased, the effect of the axial loads on the pile group decreased on the bending moment along the pile.
- The maximum displacement and maximum pile rotation are decreased as the distance between the embankment and the pile edge increased.
- The maximum shear force has increased for both pile groups as the distance between the pile edge and the embankment increased from 2.5 to 5 D. However, as the embankment distance has continued to be increased up to 10 D, the maximum shear force has decreased for both pile groups.
- The maximum soil reaction has increased for both pile groups as the distance between the pile edge and the embankment increased from 2.5 to 5 D. However, as the embankment distance has continued to be increased up to 10 D, the maximum soil reaction has decreased for both pile groups due to the reduction in the soil pressure imposed by the embankment.
- The shear forces along the pile have been found to be directly related to the soil reaction along the pile.

## References

1. Salgado, R., Basu, D., & Prezzi, M. (2008). Analysis of laterally loaded piles in multilayered soil deposits. Joint Transportation Research Program. Paper 330.
2. Fleming, W. G. K. (1992). A new method for single pile settlement for prediction and analysis. *Geotechnique*, 42(3), 411–425.
3. Ercan, A. (2010). Behaviour of pile groups under lateral loads, M.Sc. Thesis, Civil Engineering Department, Middle East Technical University.
4. Fleming, W. G. K., Weltman, A. J., Randolph, M. F., & Elson, W. K. (2008). *Piling engineering*. Taylor and Francis.
5. Beer, D. (1977). Piles subjected to static lateral loads. Doctoral dissertation, Gent Royal Institute for Soil Mechanics.
6. Qin, H. (2010). Response of pile foundations due to lateral force and soil movements. Ph.D. Thesis, Griffith University, School of Engineering.
7. Kelesoglu, M. K., & Cincioğlu, S. F. (2009). Free-field measurements to disclose lateral reaction mechanism of piles subjected to soil movements. *Journal Geotechnical and Geoenvironmental Engineering*, 136(2), 331–343.
8. Yuan, B., Chen, R., Teng, J., Peng, T., & Feng, Z. (2014). Effect of passive pile on 3D ground deformation and on active pile response. *The Scientific World Journal*.
9. Zhao, M., Liu, D., Zhang, L., & Jiang, C. (2008). 3D finite element analysis on pile-soil interaction of passive pile group. *Journal of Central South University of Technology*, 15, 75–80.
10. Zhang, C. R., Huang, M. S., & Liang, F. Y. (2009). Lateral responses of piles due to excavation-induced soil movements. In Huang & Liu (Eds.), *Geotechnical aspects of underground construction in soft ground—Ng*. Taylor & Francis Group.
11. Ersoy, C. O., & Yildirim, S. (2014). Experimental investigation of piles behavior subjected to lateral soil movement. *Teknik Dergi*, 25(4), 6867–6888.
12. Ibrahim, S. F., & Hatem, M. K. (2018). Behavior of model group piles subjected to lateral soil movement in sand. *International Journal of GEOMATE*, 14(44), 33–38.
13. Karkush, M. O., Aljorany, A. N., & Jaffar, G. S. (2020). Behavior of passive single pile in sandy soil. *IOP Conference Series: Materials Science and Engineering*, 737(1), 012106.
14. Karkush, M. O., & Jaffar, G. S. (2020). Simulation the behavior of passive rigid pile in sandy soil. *Journal of Engineering Science*, 52(4), 449–467.
15. Karkush, M. O., Jaffar, G. S., & Al-Kubaisi, O. K. (2020). Evaluating the performance of flexible passive pile group in cohesionless soil under the effect of a nearby embankment. *Lecture Notes in Civil Engineering*, 112, 1–12.
16. Ren, G. F., Xu, G. M., Gu, X. W., Cai, Z. Y., Shi, B. X., & Chen, A. Z. (2018). Centrifuge modelling for lateral pile-soil pressure on passive part of pile group with platform. *Physical Modelling in Geotechnics*, 1, 583–587.
17. Karkush, M. O., & Kareem, Z. A. (2018). Investigation the impacts of fuel oil contamination on the behaviour of passive piles group in clayey soils. *European Journal of Environmental and Civil Engineering* 1–17.
18. Karkush, M. O., & Kareem, Z. A. (2019). Behavior of passive pile foundation in clayey soil contaminated with fuel oil. *KSCE Journal of Civil Engineering*, 23(1), 110–119.
19. American Society for Testing and materials. (2003). *Annual book of ASTM standards: Soil and rock*. ASTM.
20. British Standards BS 1377. (1976). *Methods of testing for civil engineering purpose*. British Standards Institution.
21. Poulos, H. G., & Davies, E. H. (1980). *Pile foundation analysis and design*. Wiley.
22. Bolton, M. D., Gui, M. W., Garnerier, J., Corte, J. F., Bagge, G., Laue, J., & Renzi, R. (1999). Centrifuge cone penetration tests in sand. *ASCE*, 49(4), 543–552.
23. Kishida, H. (1967). The ultimate bearing capacity of pipe piles in sand. In *Proceedings of the 3rd Asian Regional Conference of Soil Mechanics and Foundation Engineering* (Vol. 1, pp. 196–199).

24. Ismael, O. K. (2014). Evaluating the behavior of laterally loaded piles under a scoured condition by model tests. Master Thesis, University of Kansas.
25. Levachev, S. N., Fedorovsky, V. G., Kurillo, S. V., & Kolesnikov, Y. M. (2002). *Piles in hydrotechnical engineering*. Taylor and Francis.
26. Springman, S. M. (1989). Lateral loading on piles due to simulated embankment construction. Unpublished doctoral dissertation, Cambridge University, England.
27. Bransby, M. F., & Springman, S. M. (1997). Centrifuge modeling of pile groups adjacent to embankment loads. *Soils and Foundations, Japanese Geotechnical Society*, 37(2), 39–49.
28. Stewart, D. P. (1992). Lateral loading of piled bridge abutments due to embankment construction. Unpublished doctoral dissertation, University of Western Australia, Australia.
29. Scott, R. F. (1981). *Foundation analysis*. Prentice-Hall.
30. Ghee, E. H. (2010). The response of axially loaded piles subjected to lateral soil movements. Doctoral dissertation, Griffith University, Gold Coast, Australia.
31. Guo, W. D., & Qin, H. Y. (2010). Thrust and bending moment of rigid piles subjected to moving soil. *Canadian Geotechnical Journal*, 47(2), 180–196.
32. Samanta, M., Bhowmik, R., & Mohanty, P. (2013). Analysis of pile group subjected to embankment induced soil movement. In *Proceedings of Indian Geotechnical Conference*, Roorkee.



# Effect of River Water Level on the Shallow Foundation Behavior with Two Slopes of Riverbank



Noor Salim Atia, Qassun S. Mohammed Shafiqu,  
and Asma Thamir Ibraheem

**Abstract** The erosion of banks is a usual geomorphic method or disturbance that takes place through or rapidly beyond the floods. The riverbanks are transitional boundaries from aquatic to terrestrial ecosystems, and its ecology shifts naturally under dynamic hydrologic conditions. In the present work, the interpretation of the results anticipated from experiments conducted in the laboratory on a riverbank model of comparatively fine (silty sand) to investigate the possible factors contributing to instability and compare the settlement and bearing capacity at varying water levels in rivers under the shallow footing near the riverbank (15 × 15 cm). The dimensions of the container are (2 × 1 × 0.9) m. The effect of strengthening the soil with geogrids is also being studied. More than 60 tests were conducted on a steel tank having a glass front side, and the banks were designed to have angles of 60° and 70° and heights of 30 cm, 50 cm, and 70 cm, also the soil type is SP-SM (ASTM 2009) (D2487-98). The shallow base on the bank was subjected to incremental loading during the experiments, and the settlement was measured. The bank's instability was known to be aligned with an interaction of primary (geometric) variables. It was noted that, in regard to failure mechanisms as well as stability, a geogrid could interpret a different noteworthy reaction. The increase in the river water level (in the flood season) is envisioned for increasing the settlement. And, the bearing capacity increase (strengthened via geogrid on the riverbank) decreases the settlement. The bearing capacity in riverbank with a slope of 60° increased by 1.8 and 1.9 times that with no geogrids for Tensar (SS2) and Netlon (CE121), respectively. Also, the bearing capacity in riverbank with a slope of 70° increased by 2 and 2.2 times that with no geogrids for Tensar (SS2) and (Netlon CE121), correspondingly.

**Keywords** Shallow foundation · Water level · Silty sand · Riverbank · Geogrid

---

N. S. Atia (✉) · Q. S. M. Shafiqu · A. T. Ibraheem  
Department of Civil Engineering, AL-Esraa University College, Baghdad, Iraq  
e-mail: [noor1988@esraa.edu.iq](mailto:noor1988@esraa.edu.iq)

Q. S. M. Shafiqu  
e-mail: [qassun.almohammed@eng.nahrainuniv.edu.iq](mailto:qassun.almohammed@eng.nahrainuniv.edu.iq)

A. T. Ibraheem  
e-mail: [drasma2005@eng.nahrainuniv.edu.iq](mailto:drasma2005@eng.nahrainuniv.edu.iq)

## 1 Introduction

The erosion of bank is a key procedure in the fluvial dynamics, influencing an extensive range of the physical, environmental, and socio-economic topics in the fluvial environment [1]. The fine-grained (clay, silt, and sand) and the cohesive banks are the most significant research subject on bank failure modeling. In addition, these banks also withdraw along tidal channels and sandy rivers, and they have been correlated with the mass of waste and the unsteadiness procedures [2]. In the research field in geotechnical engineering, the foundations bearing strength are very significant. The design of foundation upon a level surface ground being founded upon the soil mechanical properties, like shear strength, weight of unit, and so on. It was also focused upon the foundation physical properties, such as form, depth, and width. In determining the permissible-bearing pressures for various shallow foundations, just two points should be considered; the settlements shouldn't exceed the tolerable limits under the permissible-bearing pressures, and the factor of safety is contrary to the maximum shear failure should be sufficient. Some procedures can extremely predict the foundations with capability placed on or on level grounds [3–7]. These procedures are depended on results from in-situ or laboratory tests. For example, buildings built along rivers, foundations set up upon towers for electrical conveyance, and bridge piers were reinforced upon embankments. The bearing capacity (BC) and the steadiness of a foundation constructed near the edge of sloping are important parameters that affect the performance of a structure built close to the slope.

When a foundation was constructed close to a sloping land and river, one of the foundation sides may be expected to be subjected to the slanting surface and the base effect by the river's water level. Therefore, the plastic failure area is too precise, as the soil of the foundation reaches the limit condition, and it has a significant effect on the base BC and the mechanical steadiness of slope [8]. Therefore, on flat land, the foundation bearing potential is higher than sitting upon the riverbank and close to a sloped fill. The shallow foundation's conventional styles are inadequate in numerous instances, although they are highly simpler for building and economics. Based upon that, several researchers have paid extra attention in recent years to study the conduct of settlement as well as the BC of foundations close to slopes and rivers. The key approaches employed for assessing the footings BC upon flat grounds being considered to be well known. It is still essential to examine the footings BC on or close the slopes riverbanks. The theoretical procedures utilized for predicting the BC of footing upon a slope being typically evolved depending upon the footing BC equation proposed via Terzaghi [4, 6, 7, 9, 10] and being adequate for a particular limit of footing site. Meyerhof [4] proposed a theoretical approach for assessing the maximum BC of the shallow base situated on the face of a slope.

The present study's main objective is to investigate the maximum BC of square footings placed upon the top of a riverbank with lab testing. In this investigation, the relationship between the footing and the parameters includes the distance between the crest slope and the riverbank's footing, the riverbank slope, and the riverbank height.

Two forms of Netlon (CE121) and (Tensar SS2) geogrids are used to study the river water levels influence upon the BC of footing and improve the crucial conditions.

## 2 Material and Instruments Used

**Model Container.** The investigational steel soil box was built having ( $2 \times 1$  m) dimensions and a (0.9 m) height. The lateral wall is made of glass for the direct remark of the failure mechanism specifics. This box is displayed in Fig. 1. For supplying the water to the soil box, a pipe was used, and a drainpipe with a filter was located at the bottom to avoid the fine particles flow. Plates of cork are designed with a shrill edge for withstanding the waves resulting from the bank's failure. A steel frame was utilized for carrying the static load upon the foundation. Inside the tank of soil, a model of the river bank was built. For derivative geometry, the bank model was constructed. The geogrid reinforcement cross-section employed in testing the model is depicted in Fig. 2.

**The soil used.** The particle size distribution curve of the soil backfill is manifested in Fig. 3. Depending upon the unified soil classification (USCS) method, the soil is graded as SP-SM. Tests for soil physical and chemical properties were carried out according to the standard ASTM and BS requirements, respectively. The chemical and physical characteristics of the used soil are listed in Table 1.

**Test Preparation.** The model of silty sand having angles of slope ( $\beta$ ) of ( $60^\circ$ ) and ( $70^\circ$ ) was established utilizing (100 mm) thick layers that being actively compressed. To simplify the process of placing the bed of soil into layers, the test box internal surfaces were marked at (100 mm) intervals. Through the bank building and compressing, a panel made of wood being located for assigning a certain angle of bank slope. This panel was then taken out straightway before the beginning of every test. By the compression of thin sub-layers having a (10 cm) thickness made via the uniform compressed soil, following the pouring steps, the first half of the container was filled with soil, while the other half of the container was filled with water. The



Fig. 1 The box of soil: container and frame of loading

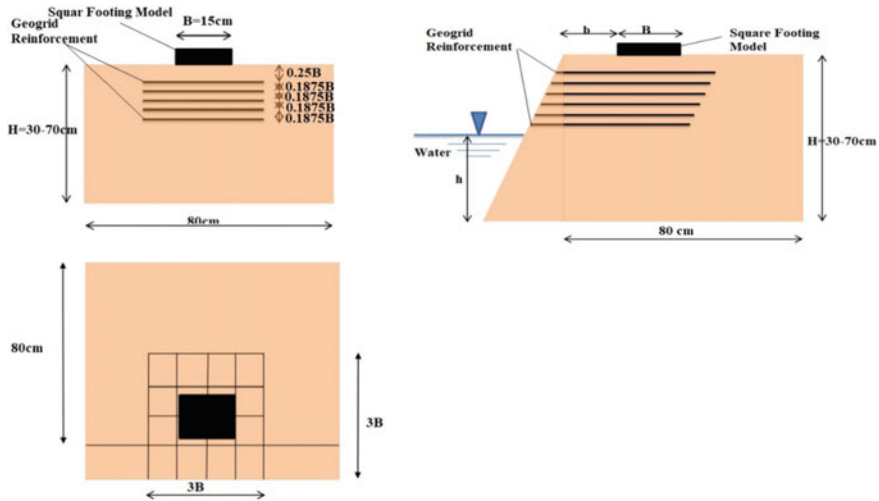


Fig. 2 The geomtry and the top lane of geogrid strengthening and the square model of footing

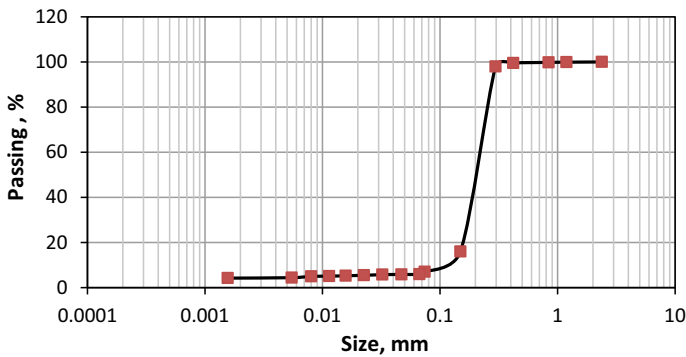


Fig. 3 The distribution of particle size

method involves placing each layer into the steel box before the target height of the slope has been reached. A bank height of 30, 50, and 70 cm was chosen, while the angles of the slope are  $60^\circ$  and  $70^\circ$ .

**The Geogrid Reinforcement.** Two geogrid forms (Netlon CE121 and Tensar SS2 geogrids) were used. The physical properties of the utilized geogrid in the present investigation are described in Fakhraldin’s Table 2 [11]. The geogrid forms are shown in Fig. 4. Within the silty sand soil layer with 45 cm to 45 cm measurements, the geogrid layers used were 5.

**Procedure of Testing.** The experimental work involves conducting a series of 60 square-footing model bearing load tests situated at different positions comparative to the slope of the riverbank, two riverbank slope angles, and various heights of the

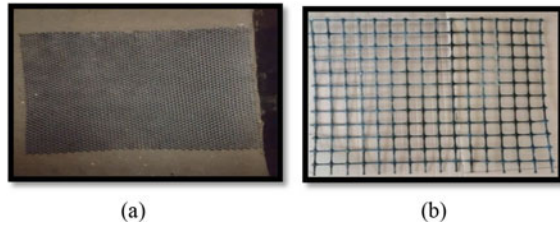
**Table 1** The chemical and physical properties of the soil

Parameters	Units	Values	Standard
Friction angle of ( $\varphi$ )	°	34.50	ASTM-D4767
Max. dry unit weight	kN/m <sup>3</sup>	15.0	ASTM-D4253
Min. dry unit weight	kN/m <sup>3</sup>	13.9	ASTM-D4254
Max. void ratio ( $e_{max.}$ )	–	0.900	–
Min. void ratio ( $e_{min.}$ )	–	0.760	–
Max. saturated unit weight	kN/m <sup>3</sup>	18.33	–
Min. saturated unit weight	kN/m <sup>3</sup>	17.34	–
Mean size, (D60)	mm	0.20	ASTM-D422
Mean size, (D30)	mm	0.170	ASTM-D422
Effective size, (D10)	mm	0.120	ASTM-D422
Coefficient of uniformity, (Cu)	–	1.667	–
Coefficient of curvature, (Cc)	–	1.204	–
Specific gravity (Gs)	–	2.66	ASTM-D854
SO <sub>3</sub>	%	0.052	-
Gypsum	%	0.112	BS-1377
Classification (USCS)	–	SP-SM	–

**Table 2** The physical characteristics of the used Geogrids; Netlon (CE121) and Tensar (SS2) [11]

Description	Properties	
	netlon (CE121)	(Tensar SS2)
Type of mesh	Diamond	Square
Polymer type	PP	PP
Type of color	Black	Black
Modules of elasticity	0.39 GPa	0.57/0.99 GPa
Tensile strength	9 MPa	24/30.7 MPa
Tensile peak resistance	6.4 kN/m	14.4/28.2 kN/m
Yield strength (upper)	5 MPa	1/3 MPa
Yield strength (lower)	5 MPa	1/3 MPa

**Fig. 4** Kinds of the utilized geogrids; **a** Netlon (CE121) and **b** Tensar (SS2)



riverbank. Five variables are considered, the height of the riverbank, footing distance from the slope of a crest (dimensions report (b/B)), where b is the distance from footing to the river edge, river water level, two riverbank slopes, and strengthening (geogrid) type. The test model's preparation method comprised compressing the silty soil sand into layers; each one ranged from a thickness of (100 mm) to a height of (300, 500, and 700 mm). Via utilizing a rammer having (150 mm) length, (150 mm) width, and (5 mm) thickness, at a comparative density, equals to (75%), the sand compaction was carried out manually. Table (3) shows the specifics of the research process. Also, by utilizing a sharpened straight plate made of steel, the shaped sand top surface was leveled, and the model of footing was then adapted upon the already compacted surface of the sand. With dial gauges on the foundation, the footing model was fixed on top of the soil's surface. A low rate of zero value increased the added load. Finally, at the end of each increment, foundation settlement values were registered utilizing dial gauges until failure occurred.

### 3 Results and Discussion

A series of 60 tests were executed upon a square footing model upon the slope of dense silty sand to examine the river water level influence, footing position to the slope of the crest, and riverbank height. The maximum BC was computed by dividing the load upon the area of the footing. For riverbanks with slopes of 60 and 70, the heights are [2B], [3B], and [5B], respectively, and the water levels of the river are [0] and [1/2 H], where [H] determines the height of the riverbank. The changes using two geogrids forms are elucidated in Figs. 5, 6, 7, showing the changes of bearing pressure (BP) with the settlement. Table 3 shows the experimental testing program design.

In Fig. 8a, for the riverbanks with slope 60°, the BP with the existing geogrids raised by (1.9) and (1.8) times the value for without Netlon (CE121) and Tensar (SS2) geogrids, correspondingly, when the (H/B) riverbank height = 2. Relative to that, without geogrids for the riverbank height (H/B = 3), the rise was (1.5) and (1.4) times. Whereas the BP raised via (1.3) and (1.2) times the value for without Netlon (CE121) and Tensar (SS2) geogrids for the riverbank height (H/B = 5), respectively. In Fig. 8b, for the riverbanks with slope 70°, the BP with the existing geogrid raised

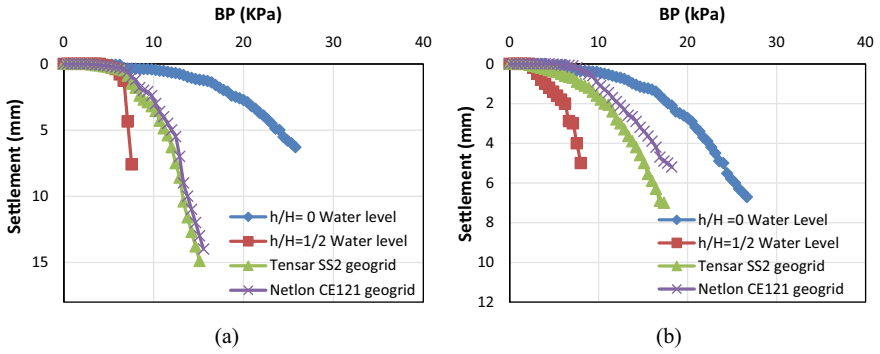


Fig. 5 BP changes with the settlement for a (2B) riverbank height: a slope 60° and b slope 70°

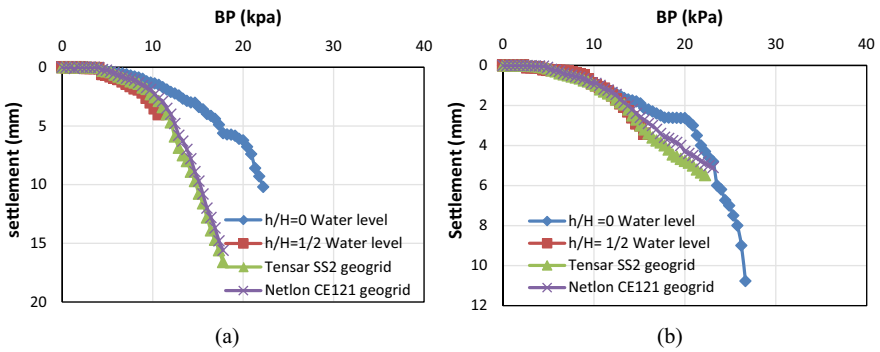


Fig. 6 BP changes with the settlement for a (3B) riverbank height: a slope 60° and b slope 70°

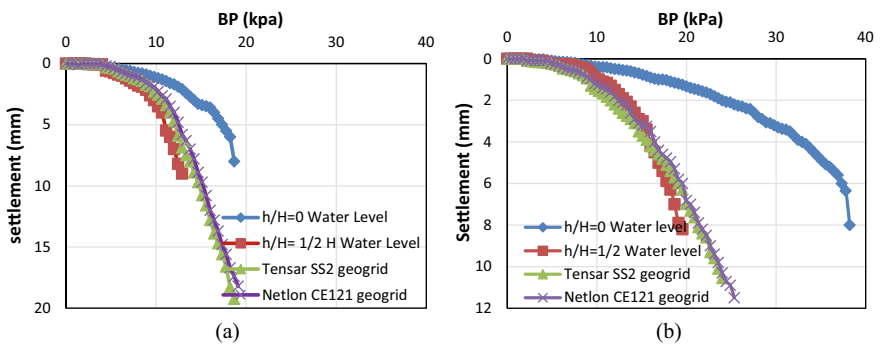
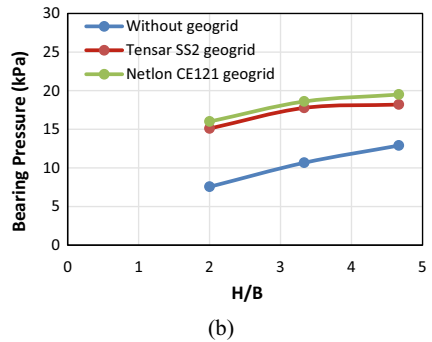
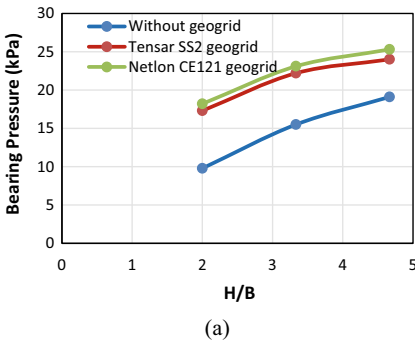


Fig. 7 BP changes with the settlement for a (5B) riverbank height: a slope 60° and b slope 70°

**Table 3** The designed experimental testing program

Footing, mm	Angle	Riverbank height (H), mm	Dimensions report (b/B)	Water level of river	Reinforcement geogrid	
150 × 150	60°	300	0	0	–	
				1/2 H	Netlon, Tensar	
			1	0, 1/2 H	–	
				2	0, 1/2 H	–
			500	0	0	–
					1/2 H	Netlon, Tensar
		1		0, 1/2 H	–	
				2	0, 1/2 H	–
		700		0	0	–
					1/2 H	Netlon, Tensar
			1	0, 1/2 H	–	
				2	0, 1/2 H	–
	70°		300	0	0	–
					1/2 H	Netlon, Tensar
		1		0, 1/2 H	–	
				2	0, 1/2 H	–
		500		0	0	–
					1/2 H	Netlon, Tensar
			1	0, 1/2 H	–	
				2	0, 1/2 H	–
			700	0	0	–
					1/2 H	Netlon, Tensar
		1		0, 1/2 H	–	
				2	0, 1/2 H	–



**Fig. 8** Comparing the riverbank bearing pressure height with two types of geogrid and without geogrid: **a** slope 60° and **b** slope 70°



via (2.2) and (2) times the value for without Netlon (CE121) and Tensar (SS2) geogrids, respectively, when the riverbank height ( $H/B$ ) = 2. Compared to that value for without Netlon (CE121) and Tensar (SS2) geogrids for the height of riverbank ( $H/B$  = 3), the rise is (1.7) and (1.6) times). While, the BP increased by (1.5) and (1.4) times the value for without Netlon (CE121) and Tensar (SS2) geogrids for the height of the riverbank ( $H/B$  = 5), respectively.

Figures 9 and 10 show the influence of the soil BP on the distance between crest and footing ( $b/B$ ). Figure 9 illustrates that increasing the distance to ( $b/B$  = 1) raises the BP via approximately 1.85, 1.8, and 1.7 times for ( $H/B$  = 2, 3, and 5) for the riverbanks with a slope of  $60^\circ$ . Raising the gap to the twice width of footing results in a higher BP of approximately 2.8, 2.7, and 2.3 times that for ( $H/B$  = 2, 3, and 5) for the slope of the riverbank of  $60^\circ$ . Figure 9b exhibits that widening the distances to ( $b/B$  = 1) raises the BP via approximately 2.1, 1.9, and 1.81 times that for ( $H/B$  = 2, 3, and 5), correspondingly for the riverbanks with a slope of  $70^\circ$ . Raising the distance to the twice width of footing results in a higher BP via around 3.5, 3.1, and 2.9 times for ( $H/B$  = 2, 3, and 5), correspondingly for riverbank with a slope of  $70^\circ$ .

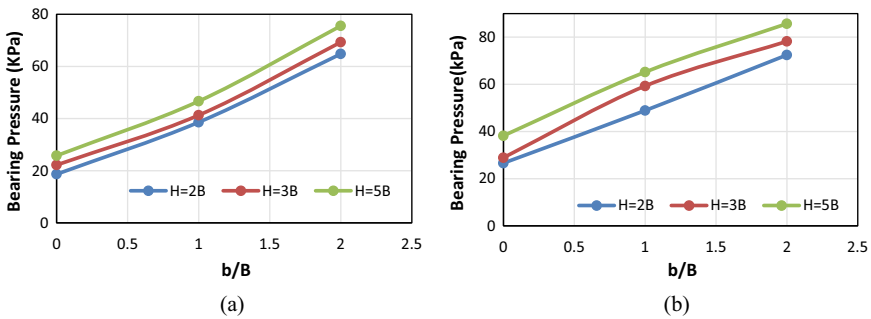


Fig. 9 Bearing Pressure–Distance changes from the crest ( $b/B$ ) at a river water level = 0 for various riverbank heights: a slope  $60^\circ$  and b slope  $70^\circ$

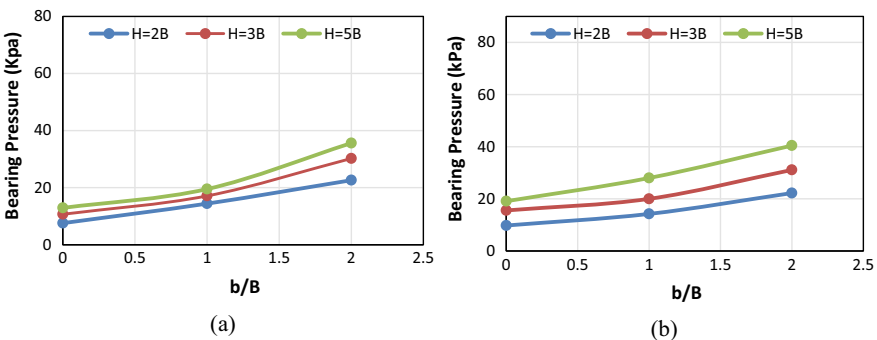


Fig. 10 BP–Distance changes from the crest ( $b/B$ ) at a river water level =  $1/2 H$  for various riverbank heights: a slope  $60^\circ$  and b slope  $70^\circ$

Figure 10 manifests the results for the water level ( $h = 1/2 H$ ), and Fig. 10a demonstrates that the BP is 1.5, 1.4, and 1.3 times that for ( $H/B = 2, 3, \text{ and } 5$ ), correspondingly when increasing the distances for the riverbank with slope  $60^\circ$ . Raising the gap to the twice width of footing results in a higher BP of approximately 2.3, 2.1, and 2 times that for ( $H/B = 2, 3, \text{ and } 5$ ) for the  $60^\circ$  slope riverbank, correspondingly. Figure 10b indicates that the BP is 1.9, 1.65, and 1.5 times that when increasing the distances for ( $H/B = 2, 3, \text{ and } 5$ ), correspondingly for the riverbanks with a slope of  $70^\circ$ . Raising the distance to the twice width of footing results in a higher BP of approximately 3, 2.83, and 2.76 times that for ( $H/B = 2, 3, \text{ and } 5$ ) for the riverbanks with a slope of  $70^\circ$ .

From Figs. 9 and 10, it can be observed that the BP decreased by 71, 62.4, and 58.4% for ( $H/B = 2, 3, \text{ and } 5$ ), correspondingly when the water level increased to ( $1/2 h$ ), and the distance of footing to crest rose to ( $b/B = 1$ ). However, the BP reduced by 70.2, 58.2, and 55.4% for ( $H/B = 2, 3, \text{ and } 5$ ), correspondingly for the riverbanks with a slope of  $60^\circ$ , by raising the gap to the twice width of footing. For ( $H/B = 2, 3, \text{ and } 5$ ), correspondingly, the BP reduced via 62.7, 58.2, and 57.4%. By raising the gap to twice the footing width, however, the BP decreased by 65, 56.4, and 53% for ( $H/B = 2, 3, \text{ and } 5$ ) correspondingly, for the riverbanks with a slope of  $70^\circ$ .

## 4 Conclusions

The conclusions that can be taken from the results of this study are:

- For the riverbank height  $H/B = 2$  and the riverbank slope =  $60^\circ$ , the BP with the existence of geogrid raised by 1.8 and 1.9 times that for without Netlon (CE121) and Tensar (SS2) geogrids, correspondingly. For slope =  $70^\circ$  riverbanks, the BP with the existence of geogrid raised by 2 and 2.2 times that for without Netlon (CE121) and Tensar (SS2) geogrids, correspondingly.
- With no level of water and riverbank slope =  $60^\circ$ , widening the footing gap from the crest to the footing width raises the BP in comparison with that for footing at the crest by 1.85, 1.8, and 1.7 times that for ( $H/B = 2, 3, \text{ and } 5$ ), correspondingly. For ( $H/B = 2, 3, \text{ and } 5$ ), correspondingly raising the distance to the twice width of footing results in a higher BP of around 2.8, 2.7, and 2.3.
- With no level of water and riverbank slope =  $70^\circ$ , widening the footing gap from the crest to the footing width raises the BP in comparison with that for the footing at crest by 2.1, 1.9, and 1.81 times that for ( $H/B = 2, 3, \text{ and } 5$ ), correspondingly. Raising the distance to the twice width of base results in a higher BP of approximately 3.5, 3.1, and 2.9, correspondingly for ( $H/B = 2, 3, \text{ and } 5$ ).
- As the water level rose to ( $1/2 H$ ), the slope of the riverbank =  $60^\circ$ , and the footing distance to crest rose to ( $b/B = 1$ ), the BP reduced via 71, 62.4 and 58.4% for ( $H/B = 2, 3, \text{ and } 5$ ), correspondingly, compared to that when there is no water

level. However, the BP decreased by 70.2, 58.2, and 55.4% for ( $H/B = 2, 3,$  and  $5$ ), correspondingly, by raising the gap to the base's twice the width.

- As the water level rose to ( $1/2 H$ ), the slope of the riverbank =  $70^\circ$ , and the footing distance to crest rose to ( $b/B = 1$ ), the BP reduced via 62.7, 58.2 and 57.4% for ( $H/B = 2, 3,$  and  $5$ ), correspondingly, compared to that when there is no water level. However, the BP decreased by 65, 56.4, and 53% for ( $H/B = 2, 3,$  and  $5$ ), correspondingly, via raising the gap to the base's twice the width.

## References

1. Rinaldi, M., & Darby, S. E. (2007). 9 Modelling river-bank-erosion processes and mass failure mechanisms: Progress towards fully coupled simulations. *Developments in Earth Surface Processes, 11*, 213–239.
2. Nardi, L., Rinaldi, M., & Solari, L. (2012). An experimental investigation on mass failures occurring in a riverbank composed of sandy gravel. *Geomorphology, 163*, 56–69.
3. Abdi, A., Abbeche, K., Athmania, D., & Bouassida, M. (2019). Effective width rule in the analysis of footing on reinforced sand slope. *Studia Geotechnica et Mechanica, 41*(1).
4. Meyerhof, G. G. (1957, August). The ultimate bearing capacity of foundations on slopes. In *Proceedings 4th International Conference on Soil Mechanics and Foundation Engineering* (Vol. 1, pp. 384–386).
5. Meyerhof, G. G. (1963). Some recent research on the bearing capacity of foundations. *Canadian Geotechnical Journal, 1*(1), 16–26.
6. Hansen, J. B. (1970). A revised and extended formula for bearing capacity.
7. Vesić, A. S. (1973). Analysis of ultimate loads of shallow foundations. *Journal of the Soil Mechanics and Foundations Division, 99*(1), 45–73.
8. Keskin, M. S., & Laman, M. (2013). Model studies of bearing capacity of strip footing on sand slope. *KSCE Journal of Civil Engineering, 17*(4), 699–711.
9. Saran, S., Sud, V. K., & Handa, S. C. (1989). Bearing capacity of footings adjacent to slopes. *Journal of geotechnical engineering, 115*(4), 553–573.
10. Terzaghi, K. (1943). In *Theoretical soil mechanics*. Wiley & Sons. (pp.11–15).
11. Fakhraldin, M. K. (2013). Properties measurements and applications of some geogrids in sand. Ph.D. Thesis, Alnahrain University, Iraq.

# Numerical Modeling of Sheet Pile Quay Wall Performance Subjected to Earthquake



Mahdi O. Karkush, Shahad D. Ali, Naghm M. Saidik, and Alaa N. Al-Delfee

**Abstract** In this study, the sheet pile quay wall's performance under seismic load was investigated using numerical modeling (Plane-strain model). This research aims to examine the stability of anchored sheet pile quay walls and evaluate the performance and efficiency of using an additional part of sheet pile quay walls under seismic loads. Dimensions of the geometry model were used based on previous studies. Also, the cohesionless soil (sandy soil) in the foundation and backfill layers was using. The output results for the numerical modeling were displacement and acceleration curves. Successfully, dynamic analysis is conducted using the PLAXIS-2D program. The results demonstrated that a dynamic load significantly influences the sheet pile quay wall, and using additional parts of the quay wall is very useful to decrease displacements. The decrease in displacement is 49.5% and 46.5% for horizontal and vertical displacement, respectively. The result showed the additional part led to decreased the values of acceleration about 19% for a point located at the top of the sheet pile and about 29.6% for a point located at the end of the sheet pile.

**Keywords** Sheet pile · Quay wall · Seismic load · Plaxis-2D · Displacement and acceleration

---

M. O. Karkush · S. D. Ali (✉)

Department of Civil Engineering, University of Baghdad, Baghdad, Iraq  
e-mail: [shahad.ali2001d@coeng.uobaghdad.edu.iq](mailto:shahad.ali2001d@coeng.uobaghdad.edu.iq)

M. O. Karkush

e-mail: [mahdi\\_karkush@coeng.uobaghdad.edu.iq](mailto:mahdi_karkush@coeng.uobaghdad.edu.iq)

N. M. Saidik

Department of Water Resources Engineering, University of Kufa, Najaf, Iraq  
e-mail: [naghem.saidik2001d@coeng.uobaghdad.edu.iq](mailto:naghem.saidik2001d@coeng.uobaghdad.edu.iq)

A. N. Al-Delfee

Wasit Municipalities Directorate, Ministry of Construction, Housing, Wasit, Iraq  
e-mail: [ANaem@uowasit.edu.iq](mailto:ANaem@uowasit.edu.iq)

## 1 Introduction

A quay wall is earth retaining structure that is used to dock floating vessels and transfer goods. There are various types of quay walls such as gravity, sheet pile, structures with a relieving platform, and open berth types are used for mooring and berthing floating vessels such are barges, container vessels, ships, and boats. The selection of any type depends on the local soil conditions and shipping requirements [1]. During earthquakes, the failure of quay walls caused by either high displacements of ground exceeding the limits or a local failure in the structure; therefore, it's necessary to investigate the quay wall's deformation and stress during earthquakes. In recent decades, many earthquakes caused significant damage to the quay walls. For example, during the Kobe Hyogo-ken earthquake in Japan, the sheet pile quay walls were roughly damaged, and the steel plates were broken. In 1983 Nihonkai-Chubu earthquake hit the Akita port, and its quay walls were severely damaged due to liquefaction of backfill, and in 1964, Niigata earthquake caused serious damage to the quay walls [2].

Several numerical simulations were done to study the seismic behavior of quay walls, and these studies centered on the mitigation of damage of quay walls. For example, Dakoulas and Gazetas [3] used numerical modeling to investigate soil effects on quay walls' deformations. Examined four cases, one as a reference model and the other 3 cases are more or less similar. They demonstrated that improving the foundation soil is successful in reducing deformations. Cilingir et al. [4] studied both centrifugal testing and finite element (FE) analysis to investigate anchored sheet pile walls under seismic loading in dry sand.

The model wall is connected to the backfill with two tie rods attached to the anchor beam. The sheet pile acceleration, the anchor beam, and the soil around the wall were measured using a miniature piezoelectric accelerometer. The results dementated a complex combination of soil-structure between the sheet pile wall, the anchor beam, and the soil in which it resides. Time-histories of acceleration reported on the sheet pile wall, the anchor beam, and surrounding soil showed significant agreement with the FE analysis results. Several useful numerical analyses were conducted to simulate seismic centrifuge experiments of a multi-block gravity quay wall. The test results demonstrate that the numerical analysis expected a more significant outward quay wall displacement, followed by a larger backfill settlement, than the centrifugal experiments [5, 6]. Sheet pile quay walls have several benefits: low cost, a few material consumptions, and simple construction, so it is commonly used in inland and coastal areas. During the sheet piles' design, the pile must consider the sheet pile's bearing for seismic action [7]. The present study discusses the effect of seismic load on sheet pile quay walls, with and without anchor beam.

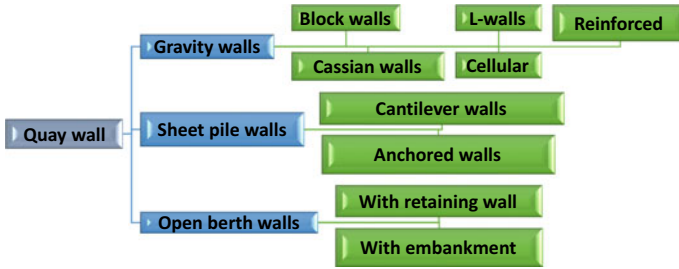


Fig. 1 General types of quay walls

## 2 Quay Walls

The major types of quay walls are gravity walls, sheet pile walls, and open berth quays. They specify any one of the quay wall types can be used depends on local soil condition and shipping requirements. Gravity quay wall is commonly used by engineers when the soil has an adequate bearing capacity because it is an economical option and necessity the depth of free water about (10–18 m) is necessary for ships [8]. Sheet pile quay walls are used where the subsoil condition is weak, and it can be easy to penetrate it into the ground up to the required depth. However, the quay wall may not be functional in the soft subsoil conditions because of the consolidation settlement. To decrease the consolidation settlement, the sand filler was used as an alternative to soft soil.

On the other hand, liquefaction of the filling sandy layer becomes another threat to the quay wall systems, so the sheet pile quay wall is not suitable as it is subjected to a tremendous amount of lateral pressure of soil as from the dynamic load. In addition to that, a considerable height of the wall and liquefiable backfill soil behind it, sheet pile quay wall might be a costly solution, especially in case of the earthquake [1, 9]. Figure 1 shows the major types and shapes of quay walls.

## 3 Seismic Loading

Seismic loading is one of the principal concepts of earthquake engineering that means implementing an earthquake-produced agitation to a structure. Mainly, seismic loading depends on the earthquakes' expected parameters at the site (seismic hazard), the site geotechnical parameters, and the structure's parameters [10]. Before the earthquake occurs, the forces that affected the quay wall are limited only to the earth and water forces, but during an earthquake, several forces are produced in the quay wall, such as the wall's inertia force, dynamic earth's force, and dynamic water's force [11]. Series of earthquakes occurred in In Japan, Hokkaido that led to destroying quay walls in Hokkaido Island. These earthquakes demonstrated that the degree of damage is strongly related to the occurrence of liquefaction in the backfill [12, 13]. When

the earthquake occurred, many seismic waves are released in space surrounding the hypocenter, and they all move in different ways. Commonly, there are two major types of waves, Body waves (compressional waves and shear waves) and surface waves (Love and Rayleigh) [14].

An earthquake's magnitude is a quantitative measure of earthquake size and fault dimensions, basically depending on the maximum amplitudes of body or surface seismic waves. The Richter scale is the most common magnitude scale that measures the maximum amplitude of the seismic wave (in microns) [15]. Intensity represents a non-instrumental perceptibility measure of damage to the earth's surface structures such as cracks and landslides, fractures, and human reactions to earthquake shaking. Intensity scales are the European Macroseismic Scale (EMS), Mercalli–Cancani–Seiberg (MCS), Medvedev–Sponheuer–Karnik (MSK), Japanese Meteorological Agency (JMA), and Modified Mercalli (MM). Intensity scales could include a description of construction quality for structures in the exposed area [15]. At the northeastern boundaries of the Arabian Plate, Iraq is situated in a relatively active seismic zone. According to Zagros-Tauros Belts, the Arabian plate subduction into the Iranian and Anatolian Plates [16]. In the upper 40 km of the earth's crust, several earthquakes have the most considerable energy. Based on the Middle East's seismic risk zonation map, the Iraq eastern border can be assessed the peak ground acceleration levels. It varies from 0.16 to 0.48 g, so a Maximum Design Earthquake (MDE) for this zone has a PGA of about 0.48 g [17, 18].

## 4 Methodology of Numerical Modeling

The two-dimensional stress analyses (PLAXIS-2D) were carried out to study and evaluate the anchored sheet pile quay wall's seismic performance before the actual application. An appropriate soil model and suitable design properties of the material should be defined as input parameters. Two models were used in the present study to study the performance of sheet pile quay wall under seismic loading. The first model was used in the sheet pile quay wall (sheet pile, pile, and tie rod), while the second model used an additional pile and tied rod as a reinforcement system. The model geometry is shown in Fig. 2, and the type of soil model and properties of materials used in this present study are given in Table 1.

## 5 Results and Discussions

The dimension and properties of soil, sheet pile, and deck pile are given in Table 1, and Fig. 3 were done in PLAXIS 2D analysis. The hardening soil model is used because it is preferred in dynamic analysis [19]. The standard seismic loading in the PLAXIS 2D model was used as a reference to dynamic load. Acceleration and displacement (horizontal and vertical) are calculated in specified points C, E, and D,

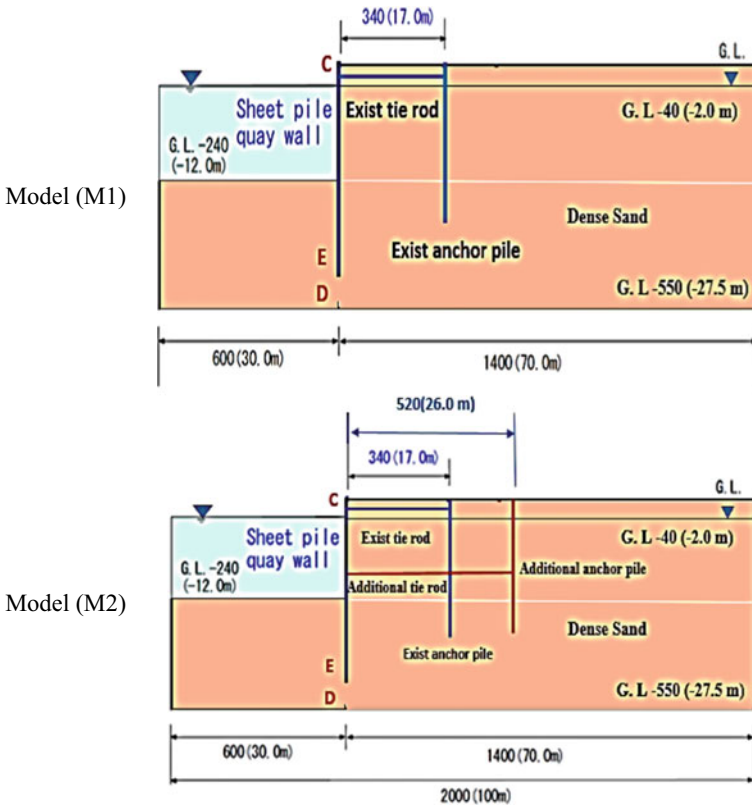


Fig. 2 Schematic diagram of the PLAXIS finite element models M1 and M2

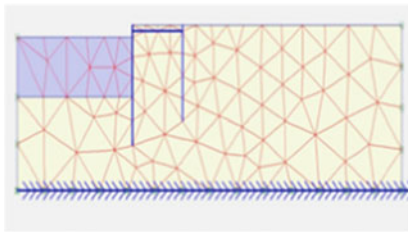
as shown in Fig. 2. Point C is located at the top of the sheet pile, and it is the more affected point, while point E is the tip of the sheet pile. Mesh and deformation that occur in two geometry models after the test are given in Fig. 3. Also, all the results of the analysis for the two models are shown in Table 2.

Displacement represents the quay wall model’s movement to the backfill and waterside’s direction (due to the water’s kinetic energy at waterside and backfill soil in the backward of the model). Both seismic positive and negative displacements (horizontal and vertical displacements, respectively) of the sheet pile quay wall at point C were computed by PLAXIS 2D. The relationship between displacements and time is given in Figs. 4 and 5. These relations show the horizontal displacements gradually increased until they reached the value of 28.3 mm in model M1 (C1) and 14.3 mm in model M2 (C2). Also, vertical displacement increased with time and reached the maximum value of 40.79 mm in C1 and 21.8 mm in C2. These displacements may be attributed to the dynamic water pressure and liquefaction of the foundation sand [19, 20]. The displacement results demonstrate that additional

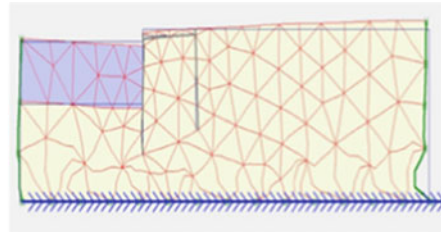


**Table 1** Material properties

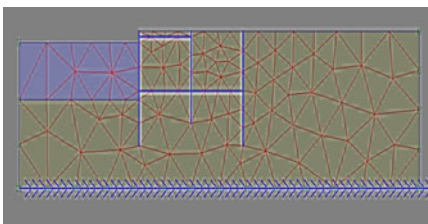
Properties	Material type		
	Sandy soil	Sheet pile	Deck pile
Type of model	Hardening soil model	–	–
$c$ (kPa)	1	–	–
$\varphi$ (°)	32	–	–
$\Psi$ (deg.)	2	–	–
$\gamma_{unsat}$ (kN/m <sup>3</sup> )	17	–	–
$\gamma_{sat}$ (kN/m <sup>3</sup> )	20	–	–
$E_{50}^{ref}$ (kN/m <sup>2</sup> )	$1.5 \times 10^4$	–	–
$E_{oed}^{ref}$ (kN/m <sup>2</sup> )	$1.102 \times 10^4$	–	–
$E_{ur}^{ref}$ (kN/m <sup>2</sup> )	$4.688 \times 10^4$	–	–
$\nu_{ur}$	0.25	0.2	0.2
EA (kN/m)	–	$1.628 \times 10^6$	$1.785 \times 10^7$
EI (kNm <sup>2</sup> /m)	–	$7.049 \times 10^4$	$9.672 \times 10^4$
D (m)	–	0.721	0.255
W (kN)	–	0.633	6.944



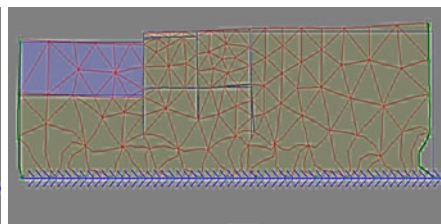
Finite element mesh of model M1



Deformation shape of model M1



Finite element mesh of model M2



Deformation shape of model M2

**Fig. 3** Mesh and shape of deformation of analyzed models

**Table 2** Results of analysis of two models M1 and M2 by PLAXIS 2D

Parameters	Model	Point C	Point E	Point D
Max. vertical displacement (mm)	M1	40.79	–	–
	M2	21.8	–	–
Max. horizontal displacement (mm)	M1	28.3	–	–
	M2	14.3	–	–
Max. Acc. (m/s <sup>2</sup> )	M1	5.799	2.705	3.01
	M2	4.697	1.894	2.856
Min. Acc. (m/s <sup>2</sup> )	M1	–5.5453	–2.1591	–2.399
	M2	–4.492	–1.511	–2.279

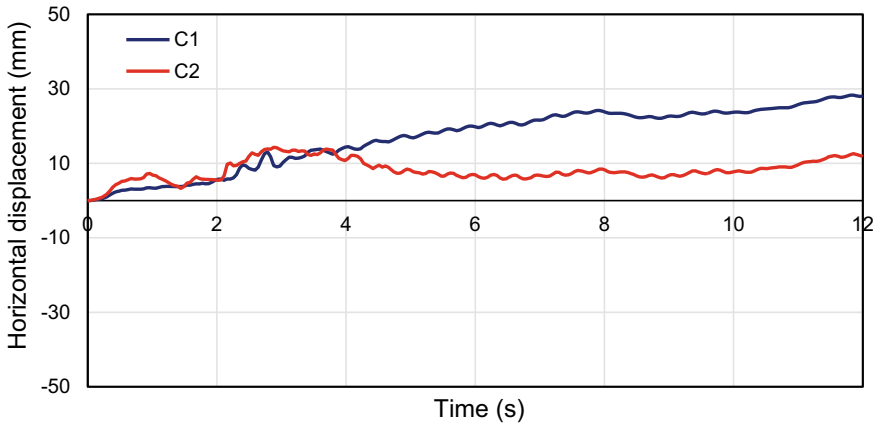


**Fig. 4** Variation of horizontal displacement with time at point C of model M1

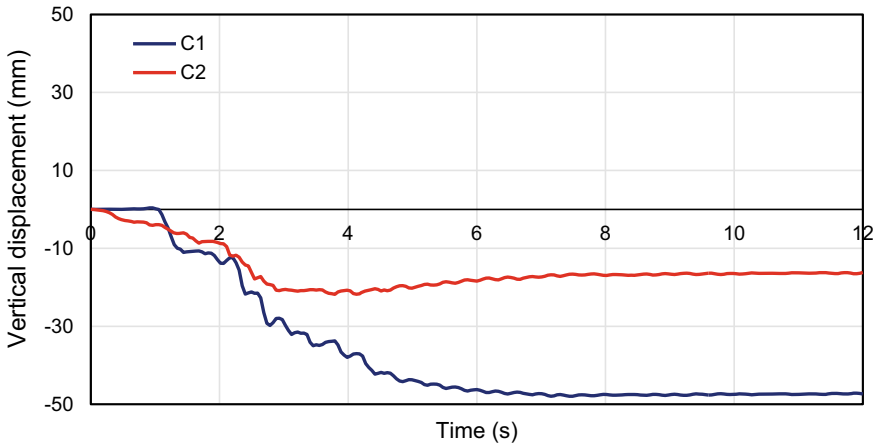


**Fig. 5** Variation of vertical displacement with time at point C of model M1

quay wall parts are very efficient to improve the system and decrease displacement by about 49.5% and 46.5% for horizontal and vertical displacement, respectively.

The accelerations are calculated in points C and E as a function of time. The value of acceleration varies from positive to negative values at the time ranged from 0 to 7 s; after that, this difference begins to decrease until reaching the end of the test, as shown in Figs. 6, 7, 8, 9, 10 and 11. As compared in acceleration between point C and E, the maximum value of acceleration is 5.8 m/s<sup>2</sup> and 4.7 m/s<sup>2</sup> in C1

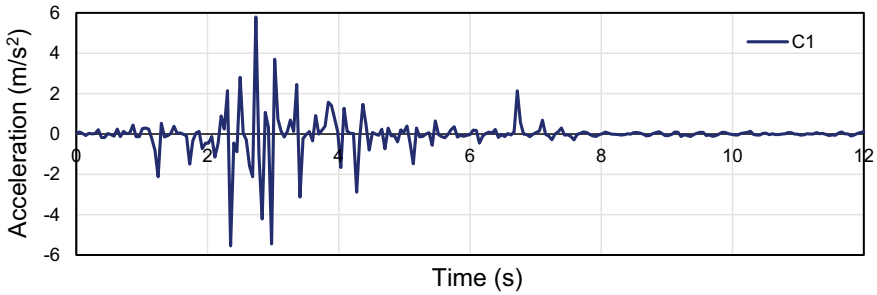


Fig. 6 Variation of acceleration with time at point C of model M1

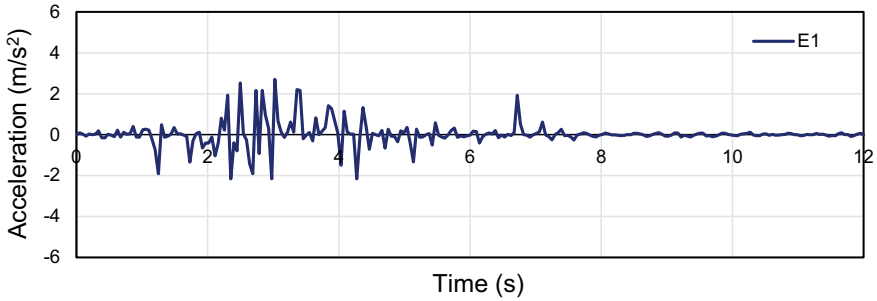


Fig. 7 Variation of acceleration with time at point E of model M1

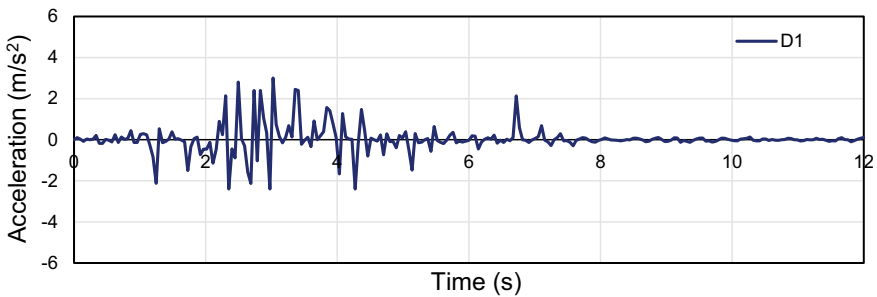


Fig. 8 Variation of acceleration with time at point D of model M1

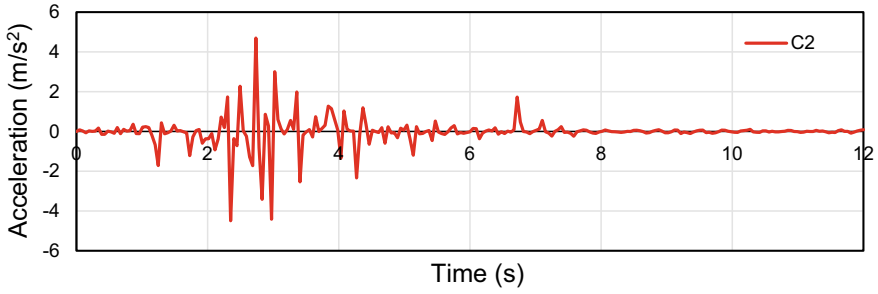


Fig. 9 Variation of acceleration with time at point C of model M2

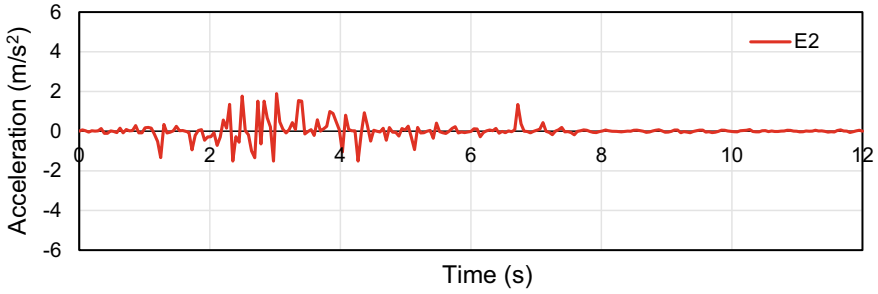


Fig. 10 Variation of acceleration with time at point E of model M2

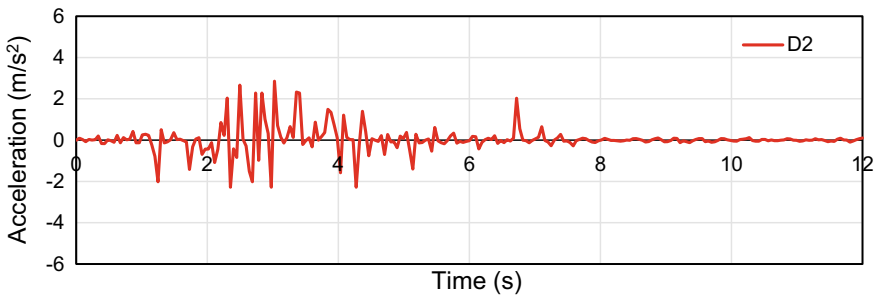


Fig. 11 Variation of acceleration with time at point D of model M2

and C2, respectively, while the maximum value is  $2.7 \text{ m/s}^2$  and  $1.9 \text{ m/s}^2$  in E1 and E2, respectively. These differences in acceleration between point C and E can be attributed to the location of point C at the top of the quay wall model and subjected to the effect of cyclic wave pressure of water at the face of the sheet pile quay wall in the waterside. In contrast, point E is located at the end of the sheet pile in sandy soil, where the pore water pressure in the foundation layer increases and thus the occurrence of the liquefaction [1, 4, 19]. The results showed the additional part of

the quay wall led to a decrease in acceleration value, about 19% and 29.6% for point Cand E, respectively.

## 6 Conclusions and Recommendations

From the results of this study, the following points can be concluded:

- The results showed that the seismic wave amplification is increased significantly from the bottom end of the sheet pile quay wall to the top end.
- Point C at the top of the sheet pile quay wall is highly influenced by seismic loading.
- The results showed that using a tie rod (anchor and pile) reduces the seismic effects on sheet pile quay walls.
- Using a tie rod (anchor) with sheet pile causes reducing the displacements resulted from seismic loading by 49.5% and 46.5% for horizontal and vertical displacement, respectively.
- The acceleration in various points at sheet pile quay wall (model M2) is less than (model M1). The additional tie rod led to decreased acceleration values, about 19% at point C located at the top of the sheet pile and about 29.6% at point E located at the tip of the sheet pile.

Three important recommendations can be constructed:

- It is recommended to conduct more study on the strain-dependent critical acceleration in dynamic analysis.
- It is suggested that further seismic test states of anchored sheet pile walls with deafferenting setups are formed.
- Increasing the value of seismic research of anchored sheet pile walls., it is believed that field measurement data requires to become obtainable. Using this data, a real investigation of this research can be achieved.

## References

1. de Gijt, J. G., & Broeken, M. L. (Eds.). (2013). *Quay walls*. CRC Press.
2. Zhang, J., & Gong, J. X. (2010). Comparative analysis on seismic design approach of sheet pile wharf in China, the US and Japan [J]. *Port and Waterway Engineering*, 9, 136–154.
3. Dakoulas, P., & Gazetas, G. (2004). Effective-stress analysis of gravity quay walls. In *Proceedings of the 11th international conference on soil dynamics and earthquake engineering and the 3rd international conference on earthquake geotechnical engineering, University of California, Berkley* (vol. 1, pp. 326–333).
4. Cilingir, U., Haigh, S. K., Madabhushi, S. P. G., & Zeng, X. (2011). Seismic behaviour of anchored quay walls with dry backfill. *Geomechanics and Geoengeering*, 6(3), 227–235.

5. Gerolymos, N., Tasiopoulou, P., & Gazetas, G. (2015). Seismic performance of block-type gravity quay-wall: Numerical modeling versus centrifuge experiment. In *SECED 2015 conference: Earthquake risk and engineering towards a resilient world*.
6. Tasiopoulou, P., & Gerolymos, N. (2016). Performance of multi-block gravity quay-wall subjected to strong earthquake motions: Numerical simulation of centrifuge test. In *Proceedings of conference 1st international conference on natural hazards and infrastructure*.
7. Zeng, X., & Steedman, R. S. (1993). On the behaviour of quay walls in earthquakes. *Geotechnique*, 43(3), 417–431.
8. Nguyen, A. D., Kim, Y. S., Kang, G. O., & Kim, H. J. (2020). 2D finite element method analysis for deepening of existing gravity quay walls. In *The 30th international ocean and polar engineering conference*. International Society of Offshore and Polar Engineers.
9. Anh-Dan, N., Young-Sang, K., Gyeong-O. K., & Hui-Jin, K. (2021). Numerical analysis of static behavior of caisson-type quay wall deepened by grouting rubble-mound. *International Journal of Geo-Engineering*, 12(1).
10. Hudson, D. E. (1979). *Reading and interpreting strong motion accelerograms* (vol. 1). Earthquake Engineering Research Institute.
11. Kim, S. R., Kwon, O. S., & Kim, M. M. (2004). Evaluation of force components acting on gravity type quay walls during earthquakes. *Soil Dynamics and Earthquake Engineering*, 24(11), 853–866.
12. Japanese Geotechnical Society, JGS. (1994). Report of the damages during 1993 Kushiro-oki and Notohanto-oki earthquakes. 175–182 (In Japanese).
13. Hokkaido Development Bureau. (1996). Report on the improvement of seismic resistance of port facilities. Cold Region Port and Harbour Research Center, In Japanese.
14. Elnashai, A. S., & Di Sarno, L. (2008). *Fundamentals of earthquake engineering* (p. 34). Wiley.
15. Wilson, R. C., & Keefer, D. K. (1983). Dynamic analysis of a slope failure from the 6 August 1979 Coyote Lake, California, earthquake. *Bulletin of the Seismological Society of America*, 73(3), 863–877.
16. Alsinawi, S. (1972). The prospects of seismological research in Iraq. In *Proceedings of the First Scientific Conf. of National Research Foundation of Iraq*.
17. Abd Alridha, N., & Jasem, N. A. (2013). Seismicity evaluation of central and southern Iraq. *Iraqi Journal of Science*, 54(4), 911–918.
18. Fouad, S. F. (2015). Tectonic map of Iraq, scale 1: 1000 000, 2012. *Iraqi Bulletin of Geology and Mining*, 11(1), 1–7.
19. Habets, C. J. W., Peters, D. J., de Gijt, J. G., Metrikine, A. V., & Jonkman, S. N. (2015). *Performance-based seismic analysis of an anchored sheet pile quay wall*. M.Sc. Thesis, TU Delft.
20. Higuchi, S., Miki, K., Nakamura, Y., Morikawa, Y., Sugano, T., Kikuchi, Y., Hoshino, M., & Higashiyama, K., (2012). Evaluation of the seismic performance of dual anchored sheet pile wall. In *15th World Conference on Earthquake Engineering, Lisboa*.

# Effect of Wing Ratio of Single Helix Screw Pile on Ultimate Compression Capacity Embedded in Cohesionless Soil



Hiba D. Saleem, Asad H. Aldefae, and Saleem M. Mearek

**Abstract** The screw piles are a well-known long foundation system that is widely used in onshore and offshore big projects. These piles are made of open/closed-ended steel shaft, and flanges/helices are welded along the shaft at different spacing. This paper focuses on investigating the effect of flange diameter for single flange screw pile models on the ultimate compression capacity. In this paper, the flange diameter ( $D_f$ ) is presented as a ratio of the shaft/core diameter (i.e.,  $D_f/D_c$ ), and the three wing ratios are used (i.e., 1.5, 2, and 2.5) correspond to (15, 20 and 25 cm of flange diameter). The total length of the screw pile model is 50 cm, and 45 cm is embedded with the sandy soil at a medium dense state. A commonly used failure criterion is performed to determine the ultimate compression capacity at the end of the loading tests from settlement-load curves (i.e., 10% of flange diameter,  $D_f$ ). The results of the ultimate capacity showed a good representation of the single flange screw pile models in cohesionless soil.

**Keywords** Wing ratio · Flange · Sand · Screw pile · Compression load

## 1 Introduction

A long foundation system is widely recommended and performed in-situ around the world when the soil strata are weak at shallow depths. In this case, carrying compression loads of the structure are transferred to the strong layers, which exist many meters under the ground surface. Such foundation system have existed in different types (i.e., pipe piles, bored piles, driven piles, and helical or screw piles). Screw piles are used to resist the compression, tension, and lateral loads. Last decades,

---

H. D. Saleem · A. H. Aldefae (✉) · S. M. Mearek  
College of Engineering, Civil Engineering Department, Wasit University, Wasit, Iraq  
e-mail: [asadaldefae@uowasit.edu.iq](mailto:asadaldefae@uowasit.edu.iq)

H. D. Saleem  
e-mail: [hdawood@uowasit.edu.iq](mailto:hdawood@uowasit.edu.iq)

S. M. Mearek  
e-mail: [smahmood@uowasit.edu.iq](mailto:smahmood@uowasit.edu.iq)

the screw piles were widely used to maintain old engineering projects such as railways that were suffering from sudden failure in the embankment and the underlying soil due to rail loading [1] or to resist sudden differential settlement of structure [2]. It may also be used as an alternative to the conventional (ordinary) piles in offshore structures such as wind energy turbine projects [3] and onshore structures [4]. One of the main advantages of the screw piles is the easiness of installation and no waste soil during the installation process compared to the conventional piles foundation. Screw piles consist of steel shaft (circular or square) section with single, double or even triple flanges. The flanges (helices) are welded along the steel shaft equally spaced. Conventionally, the first helix is fixed at the bottom of the shaft (to facilitate the penetration during installation at the first stage), whereas the others can be distributed along the shaft. The compression and tension capacity of the screw piles develop from the helix, particularly from the bottom of the flange, due to the considerable bearing resistance [5, 6]. The compression and pullout resistance may be reached three times that of conventional piles (i.e., pipe piles).

The diameter of the flange plays a significant role in the governing of the compression capacity. Experimentally, this parameter is well-known as a non-dimensional parameter rather than the diameter of the helix ( $D_f$ ). This term is called wing ratio (i.e.,  $D_f/D_c$ ), which is the ratio of the flange diameter to the core (shaft) diameter. Experimentally, many studies focused on the effect of wing ratio on the compression and tension capacity of screw piles [7–11]. Numerical modeling is also performed to investigate how the compression and tension capacity of screw piles is strongly affected by the wing ratio for single and multi-helix screw models [12–14]. This paper investigates the effect of wings ratio (i.e.,  $D_f/D_c$ ) of small-scale screw pile model installed in sandy soil on the compression capacity. The experimental tests are performed in the University of Wasit, engineering faculty, geotechnical laboratories utilizing a special pile loading machine.

## 2 Experimental Tests and Physical Modeling

The experimental tests are performed using an appropriate previously designed and fabricated loading machine. Small-scale circular hollow steel screw pile models are manufactured as well. Special data physics (data logger) to collect the data during the tests are used, and sandy soil that was pluviated in the container at medium dense state using the sand raining technique. Full details of each section and full description are shown in the next sections.

**Steel Container (Box).** The container has dimensions (750 mm in length, 600 mm in width, and 800 mm in height). These dimensions have been chosen to achieve the minimum width and height in order to prevent any boundary effect during the installation of the screw piles (see Fig. 1). It can also be seen that the interior container walls were provided by frictionless rubber layers to decrease any interaction between the walls and the adjacent soil.





**Fig. 1** The steel container

**Small Scale Screw Pile Models.** Single flange screw pile models are fabricated from mild steel (circular hollow section) at the University of Wasit/ Engineering faculty workshop. The total length of the model was 50 cm, and one flange or helix was welded close to the bottom tip of the pile model. The main hollow steel core (shaft) diameter of the screw pile element is 10 mm with a 45° conical tip (apex angle) so that the screw pile can be inserted within the sandy soil easily during installation. The three-screw pile models were made of one core diameter while the flange diameter was (15, 20, and 25 mm) respectively. The pitch of the screw pile elements has been selected so that the downward distance during installation for one pitch is equivalent to one rotation as described by [15, 16]. The bigger pitch for the flange was not necessary because the increasing of the inclined flange surface during installation leads to loose in the installation energy and subsequently decreasing the screw pile resistance [17]. These diameters represented flange to shaft ratio 1.5, 2, and 2.5, respectively. Thus, according to the wing ratio above, three main compression tests were performed for screw piles embedded in cohesionless (sandy) soil after the installation using the installation-loading machine. The total embedded depth of the screw pile models in the sandy soil was 45 cm. Moreover, the hollow steel shaft pipe model with a length similar to the length of the screw pile model is also tested under the compression load for comparison. Figure 2 shows details of the screw pile models used in this paper.

### 3 Installation and Loading Machine

A special pile loading machine is used in this paper to install the screw pile models. The loading machine is able to install pile elements up to 60 cm with maximum carrying capacity 5 kN using S- shape load cell. The electro-mechanical system of the machine is provided with two actuators. The first one is used to apply torque with a rotational speed of 0.8 mm/min. This very low rotary speed is equivalent to what has been presented by Al-Baghdadi et al. [18] when designing a controlled inflight

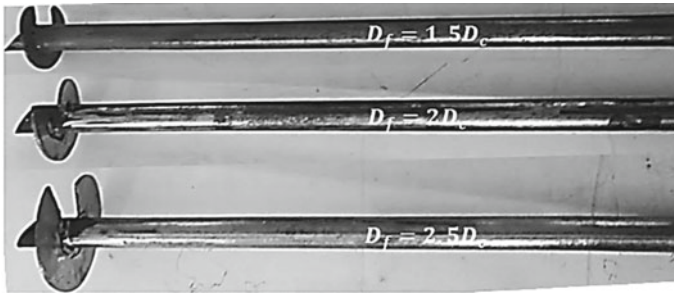


**Fig. 2** Set of screw pile models used in the tests

loading rig system for geotechnical centrifuge at the University of Dundee. The second actuator is connected through a ball screw system to apply the load during screw pile loading. The remarkable part of this machine is the slip ring that was connected to the actuator and the load cell. This slip ring is fabricated from brushes and rings and PVC materials in which the electrical poles are fixed to transmit the electrical signal from the load cell to the data logger. This technique allows the wire of the load cell to be connected to the data logger without rotation during the installation process. After the installation, the actuator is switched off. The loading process can be done using another actuator that allows via four legs of ball screw system transferring the rotary actuator motion into axial motion. In this case, the bench connected to the first motor (switched off) can be applied to an axial load on the head of the crew pile model (the load cell is connected between them). Full details of the designed loading machine can be found in [19] (Fig. 3).

**Sand Used in This Study.** Silica sand is used in this study was at a medium dense state. The sand was dried and sieved via #10 sieve in order to remove any large size particles, and this procedure was followed by many previous studies [20–25]. On the other hand, the sand was sieved to achieve the mean particle size (i.e.,  $D_{50}$ ) and the properties being close to HST95 silica sand properties that were widely used by researchers around the world in physical model preparation [26, 27]. To determine the shear strength parameters, the direct shear test was conducted on the sand specimens to find the peak angle of internal friction ( $\varphi_{pk}$ ) and critical (residual) angle of internal friction ( $\varphi_{cr}$ ). The shear cell is filled with sandy soil, and the similar technique of the physical model preparation (discussed next section) proposed by Al-Defae and Knappett [28] was followed. Theoretically, it is essential to know both values of friction angle (one at peak state and the other at residual state). That was because the soil during installation would go through the two cases. At the beginning of the screw pile insertion, the soil at the peak state and once the flanges start penetrates the soil due to the rotation during installation; the deformation of the soil in the penetrated zone would be at the residual state. As long as the screw pile penetrates the soil, the soil status around the screw pile remains at the critical condition.

These two values are important in the analytical solution using the well-known imperial equations of determining the compression resistance of the screw piles.

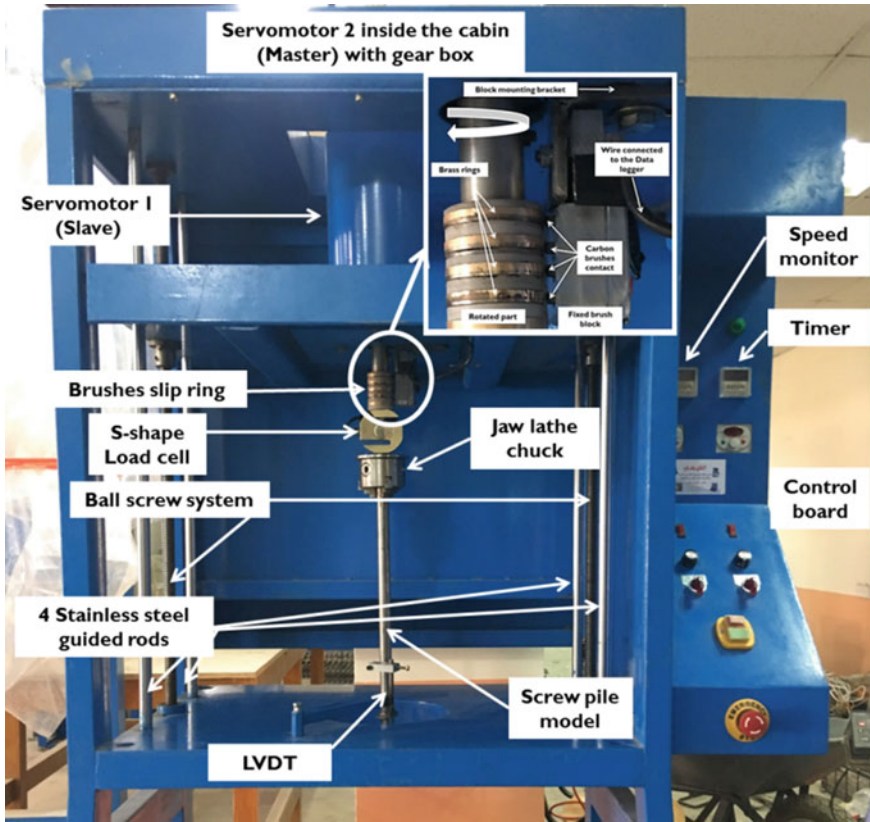


Fig. 3 Details of compression loading system [19]

The compression capacity of screw piles is not much different from determining the conventional pile resistance, except the bearing resistance develops at the lower flange of the screw piles.

From Fig. 4a, it is concluded that peak shear strength is remarkable at low strain level during the direct shear test (i.e., below 2 mm), which provided an angle of internal friction about  $39^\circ$  (Peak state). At the remaining part of the curve, specifically more significant than 3 mm of horizontal displacement, the residual strength is well-indicated as the shear stress remains constant. This point represents the threshold when the soil starts the critical state. The angle of internal friction  $32^\circ$  at this case is critical. During the installation of the screw pile model, the sheared zone makes the interaction between the disturbed soil and the soil adjacent behaves similar to the shear strength investigated from the direct shear test. Figure 5 shows the particle size distribution (PSD) of the sand used in this study and the HST95 silica sand size distribution.

**Physical Modeling Preparation.** The sand raining technique is used to prepare the model and filled the container with sand at medium dense sand (approximately

**Fig. 4** Direct shear test results; **a** Shear stress-horizontal displacement and **b** Shear vertical displacement-horizontal displacement

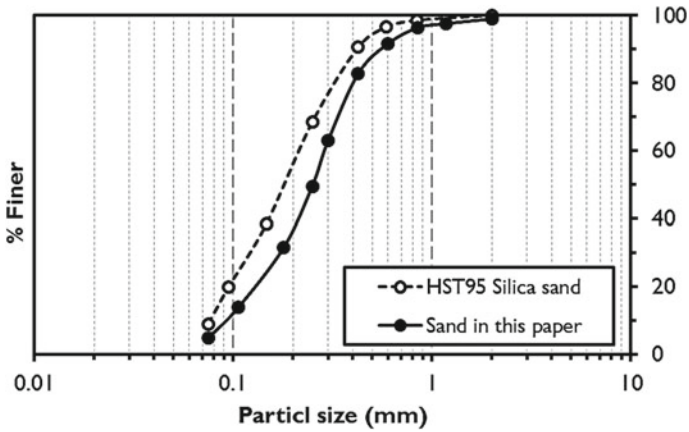
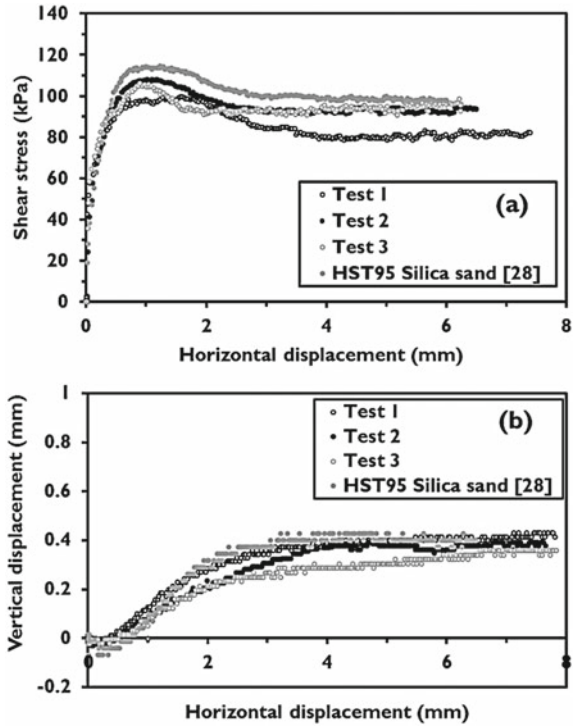


**Fig. 5** Particle size distribution (PSD) of the used sand

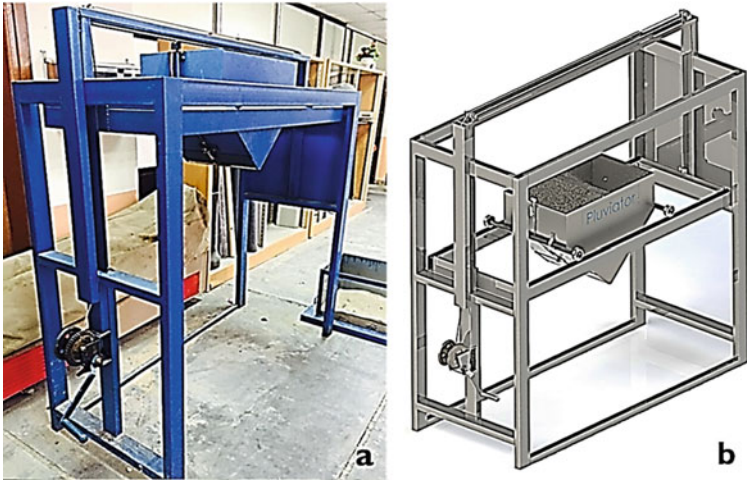


**Fig. 6** Mechanical pluviator used in the model preparation [22]

55%). The mechanical pluviator that was designed and fabricated by Aldefae and Saleem [22] is used in the pluviation process. This machine can make the sand particles fall down (from the desired depth) to the container in a way similar to the raining. The height and the slit size of the pluviator container directly affect the obtained density. Full details of this machine and how the model is prepared are found in [22] (Fig. 6).

Once the model is prepared, the container is transmitted to the compression loading machine to be ready for screw pile installation. The screw pile model is fixed tightly with an appropriate jaw set which is connected with the load cell. This set is linked with the data logger and the signals, whereas the data are collected from the computer via a controlled subroutine. The slow rotational speed makes the model of the screw pile element embedded within the soil in a way close to that in prototype scale. According to this procedure, the installation takes a long time to reach the final desired depth (i.e., approximately 45 cm of the crew pile model inserts in the sandy soil). Then, the actuator is switched off, and the other actuator is switched on for the loading process. This machine is able to conduct the pullout capacity of the screw pile element as well (which is not mentioned in this paper).

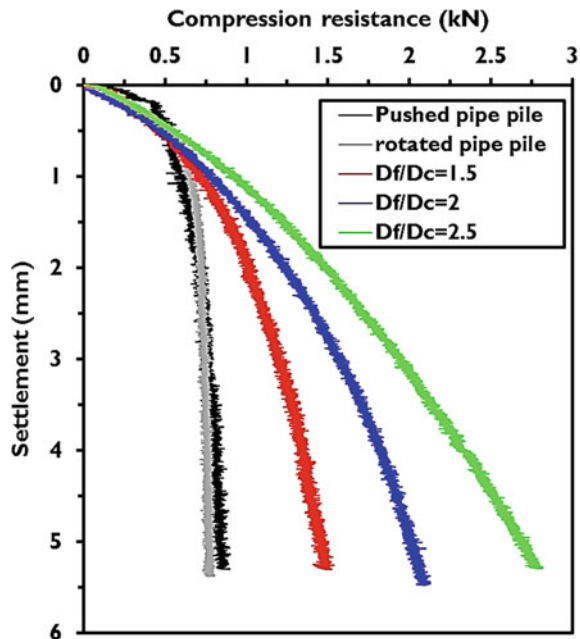
## 4 The Compression Capacity Results

As described earlier in this paper, five tests are performed. Three for screw pile models at different wing ratios (i.e.,  $D_f/D_c$ ), and the other two are for two conventional pile models (i.e., open-ended pipe pile) in two installation methods (i.e., pushed and rotational installation). The main aim of these tests is to figure out whether the flange

diameter is a good choice to increase the screw pile compression resistance. All tests have been performed according to the  $0.1D_f$  failure criterion as explained previously. Many procedures and methods have been followed and proposed to determine the ultimate capacity of piles [29–31]. The failure criteria, as proposed by Fateh et al. [32] and many others, is 5%-10% of the pile diameter. In large flanges of screw piles or in prototype scale, 10% of the flange diameter is large relatively, whereas, for small-scale screw pile models, this percentage seems to be more reasonable to estimate the ultimate compression capacity. However, the total loading tests have exceeded this limit to cover the full behavior of the loading stage. By using the 10% criterion, the ultimate compression capacities are determined (in kN) for all screw piles and the pipe pile. Figure 7 shows the compression load-settlement curve for the tested screw pile models as well as the pipe pile model in two installation methods as explained before (i.e., pushed vertically and rotationally, Black and Gray lines). The main finding here is that the screw piles model exhibited a similar trend as the load increased with the increase of the settlement. In contrast, the un-flanged pile model (in both installation methods) has a typical failure mechanism as the load increases until 1.5 mm settlement and then remains constant along the rest of the depth.

It can also be seen that the increase of the flange diameter significantly influences the measured compression load at failure ( $0.1D_f$  of settlement). The measured values of the load are (0.95, 1.25, and 1.72 kN) corresponding to the settlement (1.5, 2, and 2.5 mm) for wings ratio,  $D_f/D_c$  (1.5, 2, and 2.5), respectively. Low compression loads are measured for un-flanged (open-ended pipe pile model) in both methods (pushed and rotated installation methods), and they were 0.67 kN at pushed vertically model

**Fig. 7** Compression capacity-settlement relationship



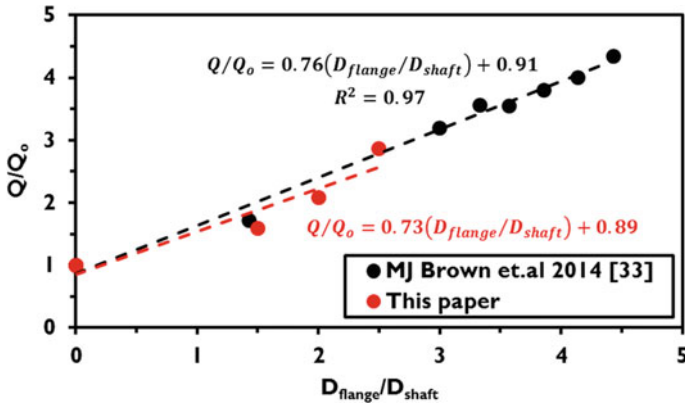


**Fig. 8** Compression capacity for flanged models (as a function of  $D_f/D_c$ ) compared with un-flanged (pipe model)

within the sandy soil. The compression resistance is slightly different from that measured at a similar screw pile installation method (0.61 kN). This behavior can be attributed to the increasing of the flange surface area strongly affected by the screw pile tip bearing resistance developed during loading. The total acquired resistance of a single flange screw pile is the summation of the sleeve (frictional resistance) along with the core (shaft) of the pipe above the flange to the soil surface, and the bearing resistance developed below the single flange (or the lower flange for multi-flange screw pile). The normalized measured compression loads of all tests were plotted against the wings ratio as shown in Fig. 8. The normalized load is the ratio of the measured compression load of screw pile models (of all three  $D_f/D_c$  ratios tests) to the measured loads of non-flanged or pipe pile (installed by screwing within the soil).

It can also be noted that the  $Q/Q_o$  does not change linearly with increasing flange diameter as compared with [33]. This is because the results of [33] are for multi screw piles, and the failure mechanism was closed to the cylindrical shear failure in which reflects the increase of the defined perimeter by the flange. The most capacity is developed due to sleeve friction along with the soil-formed cylinder. While in this paper, the screw elements have one flange. Thus, the measured load resistance is fully developed from the bearing resistance of the last/bottom flange (one flange here). However, good agreement and identical results of the screw pile under compression load are obtained (as shown in Fig. 8, the red points) and different degrees of fit as seen in the equation in Fig. 8.

## 5 Conclusions

A small-scale screw pile compression loading test was conducted using single-flange screw pile models with different wings ratios (i.e., flange/helix diameter to core/shaft

diameter ratios ( $D_f/D_c$ ). The pile models were installed in medium dense sandy soil to understand the ultimate compression load, which affected the wings ratio. The main findings of this paper can be presented in the following conclusions:

- The single-flange screw pile improved the ultimate compressive resistance (160, 208, and 289%) at the helix or flange to core or shaft diameter (i.e.,  $D_f/D_c$ ) 1.5, 2, and 2.5, respectively. This is not surprising as the bearing resistance of the flange during compression is affected by the surface area of the flange.
- The screw pile settlement- compression load curves of the screw pile models showed typical behavior, particularly the elastic zone at low displacement increments. A very well-trend is inspected for the open-ended shaft pile model.
- The pile model geometry (flange diameter here) plays a significant role in the bearing resistance and subsequently, the ultimate capacity of the screw pile models.
- The individual bearing failure mechanism is more reasonable for single-flange screw piles than the cylindrical shear failure, which typically appears in the double or multi-flange screw pile models.
- The ultimate capacity of open-ended pile models is slightly affected whether they installed using pushed axially or rotated as screw pile in sandy soil.
- Experimental tests should be performed using different relative densities of sandy soil and maybe clayey soil to confirm the main findings from this study. Large flange diameter is recommended to be tested with other shafts (core) to see whether the sleeve resistance of the shaft is more effective than the wing ratio.

**Acknowledgements** The authors would like to offers the praise and appreciation the assistant academic staff of engineers in the geotechnical laboratory in the engineering college, University of Wasit to their assistant for performing the tests. The second author would like also the gratitude to the workshop staff for manufacturing the screw pile models.

## References

1. Wheeler, L. N., Hendry, M. T., Take, W. A., & Hoult, N. A. (2018). Field performance of a peat railway subgrade reinforced with helical screw piles. *Canadian Geotechnical Journal*, 55(12), 1888–1899.
2. Abdelghany, Y., Eng, P., & El Naggar, H. (2016). Helical screw piles performance—A versatile efficient foundation system alternative for rehabilitation, new sustainable structures construction and infrastructure delivery.
3. Byrne, B. W., & Houlsby, G. T. (2015). Helical piles: An innovative foundation design option for offshore wind turbines. *Philosophical Transactions of the Royal Society A: Mathematical, Physical and Engineering Sciences*, 373(2035), 20140081.
4. Perko, H. A. (2009). *Helical piles: A practical guide to design and installation*. John Wiley & Sons.
5. Nagata, M., & Hirata, H. (2005). Study on uplift resistance of screwed steel pile. *Lateral (kPa)*, 150(150), 150.



6. Spagnoli, G., Gavin, K., Brangan, C., & Bauer, S. (2015). In situ and laboratory tests in dense sand investigating the helix-to-shaft ratio of helical piles as a novel offshore foundation system. *Front Offshore Geotech*, 3, 643–648.
7. Nagai, H., Tsuchiya, T., & Shimada, M. (2018). Influence of installation method on performance of screwed pile and evaluation of pulling resistance. *Soils and Foundations*, 58(2), 355–369.
8. Urabe, K., Tokimatsu, K., Suzuki, H., & Asaka, Y. (2015, November). Bearing capacity and pullout resistance of wing piles during cyclic vertical loading. In *Proceedings of the 6th International Conference on Earthquake Geotechnical Engineering*. Christchurch, New Zealand.
9. Mohajerani, A., Bosnjak, D., & Bromwich, D. (2016). Analysis and design methods of screw piles: A review. *Soils and Foundations*, 56(1), 115–128.
10. Al-Baghdadi, T. A., Brown, M. J., Knappett, J. A., & Al-Defae, A. H. (2017). Effects of vertical loading on lateral screw pile performance. *Proceedings of the Institution of Civil Engineers-Geotechnical Engineering*, 170(3), 259–272.
11. Davidson, C., Brown, M. J., Cerfontaine, B., Al-Baghdadi, T., Knappett, J., Brennan, A., Augarde, C., Coombs, W., Wang, L., Blake, A., & Richards, D. (2020). Physical modelling to demonstrate the feasibility of screw piles for offshore jacket-supported wind energy structures. *Géotechnique*, 1–19.
12. Sakr, M. A., Nazir, A. K., Azzam, W. R., & Sallam, A. F. (2019). Uplift capacity of single pile with wing in sand-numerical study. In *International Conference on Advances in Structural and Geotechnical Engineering*, Hurghada, Egypt.
13. Karthigeyan, S., Ramakrishna, V. V. G. S. T., & Rajagopal, K. (2007). Numerical investigation of the effect of vertical load on the lateral response of piles. *Journal of Geotechnical and Geoenvironmental Engineering*, 133(5), 512–521.
14. Livneh, B., & El Nagggar, M. H. (2008). Axial testing and numerical modeling of square shaft helical piles under compressive and tensile loading. *Canadian Geotechnical Journal*, 45(8), 1142–1155.
15. Tsuha, C. D. H. C., Aoki, N., Rault, G., Thorel, L., & Garnier, J. (2012). Evaluation of the efficiencies of helical anchor plates in sand by centrifuge model tests. *Canadian Geotechnical Journal*, 49(9), 1102–1114.
16. Lutenegeger, A. J. (2019). Screw piles and helical anchors—what we know and what we don't know: An academic perspective—2019. *ISSPEA, 2019*, 15.
17. Deeks, A. D. (2008). An investigation into the strength and stiffness of jacked piles in sand (Doctoral dissertation, University of Cambridge).
18. Al-Baghdadi, T. A., Brown, M. J., & Knappett, J. A. (2016). Development of an inflight centrifuge screw pile installation and loading system. In *3rd European Conference on Physical Modelling in Geotechnics* (pp. 239–244). IFSTTAR.
19. Aldefae, A. H., Shamkhi, M. S., & Khalaf, T. (2019). Design and manufacturing of geotechnical laboratory tools used in physical modeling. *Cogent Engineering*, 6(1), 1637622.
20. Al-Aayedi, H. K., Aldefae, A. H., & Shamkhi, M. S. (2020, June). Seismic performance of bridge piers. In *IOP Conference Series: Materials Science and Engineering* (Vol. 870, No. 1, pp. 012069).
21. Aldefae, A. H., Alkhafaji, R. A., Shamkhi, M. S., & Kumer, H. Q. (2019). Design and manufacturing of flume apparatus to investigate the failure mechanism of riverbanks. *Cogent Engineering*, 6(1), 1655234.
22. Aldefae, A. H., & Saleem, H. D. (2020, June). Design, Manufacturing and testing of biaxial mechanical travelling pluviator. In *IOP Conference Series: Materials Science and Engineering* (Vol. 870, No. 1, p. 012071). IOP Publishing.
23. Aldelfee, A. N., & Aldefae, A. H. (2021, February). Seismic performance of gravity quay wall. In *IOP Conference Series: Materials Science and Engineering* (Vol. 1058, No. 1, pp. 012033). IOP Publishing.
24. Alayedi, H. K., Aldefae, A. H., Shamkhi, M. S., & Humaish, W. H. (2021). Dynamic response of different bridge piers. In *IOP Conference Series: Materials Science and Engineering* (Vol. 1058, No. 1, pp. 012045).

25. Aldefae, A. H., & Alkhafaji, R. A. (2021). Experimental and numerical modeling to investigate the riverbank's stability. *SN Applied Sciences*, 3(2), 1–16.
26. Al-Defae, A. H., & Knappett, J. A. (2014). Centrifuge modeling of the seismic performance of pile-reinforced slopes. *Journal of Geotechnical and Geoenvironmental Engineering*, 140(6), 04014014.
27. Al-Defae, A. H., Caucis, K., & Knappett, J. A. (2013). Aftershocks and the whole-life seismic performance of granular slopes. *Géotechnique*, 63(14), 1230–1244.
28. Al-Defae, A. H., & Knappett, J. A. (2015). Newmark sliding block model for pile-reinforced slopes under earthquake loading. *Soil Dynamics and Earthquake Engineering*, 75, 265–278.
29. Davisson, M. T. (1972). High capacity piles. In *Proceedings Innovations in Foundations Construction* (Vol. 52).
30. Fellenius, B. H. (1980). The analysis of results from routine pile load tests. *Ground Engineering*, 13(6), 19–31.
31. Van der Veen, C. (1953). The bearing capacity of pile. In *Proceedings 3rd ICSMFE* (Vol. 2, pp. 84–90).
32. Fateh, A. M. A., Eslami, A., & Fahimifar, A. (2017). Direct CPT and CPTu methods for determining bearing capacity of helical piles. *Marine Georesources and Geotechnology*, 35(2), 193–207.
33. Brown, M. J., Brennan, A. J., & Hamilton, L. (2014). Optimising the compressive behavior of screw piles in sand for marine renewable energy applications.

# Numerical Analysis of Piles Group Surrounded by Grouting Under Seismic Load



Mahdi O. Karkush, Abeer H. Mohsin, Husam M. Saleh, and Bilal J. Noman

**Abstract** The present paper aims to study the behavior of piles group surrounded by grout material under the effect of seismic loads. In this study, El Centro earthquake data were used as input time acceleration history with maximum peak ground acceleration (PGA) of 0.31g. Several cases were analyzed numerically to evaluate the piles group behavior under the effect of an earthquake. The first case included the impact of seismic loads on the piles group behavior without grouting; the results showed that the maximum seismic settlement was about 45 mm. The second case included improving the soil surrounding the piles with grout material at different depths and diameters. The results showed a decrease in the maximum seismic settlement value when the piles surrounded by grouting of the radius (0.5, 1, and 1.5 m) and extended to a depth of 2 and 4 m. The maximum value of settlement of the pile group was 28, 24, and 20 mm when surrounded with grouting of radius 0.5, 1, and 1.5 m, respectively, and extended to a depth of 2 m. The maximum amount of seismic settlement decreased to 25, 21, and 19 mm for grouting radius of 0.5, 1, and 1.5 m, respectively, when the grouting depth increased to 4 m.

**Keywords** Grout · Piles group · Seismic load · Plaxis 3D · Dynamic analysis · Numerical analysis

---

M. O. Karkush · A. H. Mohsin (✉) · H. M. Saleh · B. J. Noman  
Department of Civil Engineering, University of Baghdad, Baghdad, Iraq  
e-mail: [abeer.mohsin2001d@coeng.uobaghdad.edu.iq](mailto:abeer.mohsin2001d@coeng.uobaghdad.edu.iq)

M. O. Karkush  
e-mail: [mahdi\\_karkush@coeng.uobaghdad.edu.iq](mailto:mahdi_karkush@coeng.uobaghdad.edu.iq)

B. J. Noman  
e-mail: [bilal.noman2001d@coeng.uobaghdad.edu.iq](mailto:bilal.noman2001d@coeng.uobaghdad.edu.iq)

## 1 Introduction

The behavior of pile foundations under earthquake loading is a critical factor that influences efficiency and stability of structure. Observations from previous earthquakes have shown that piles in stiff soils perform well, while piles in soft soils exhibited serious problems. The construction in or on soft soils is considered a big challenge for geotechnical engineers due to low strength and high compressibility of such soils. Many geotechnical problems for construction in soft soils can be addressed such as slope instability, shear strength failure, and excessive settlement could occur either during or after the construction period [1]. Therefore, many studies have addressed the various methods of soil improvement under different loading conditions. These studies show that improving the soil with cement is a viable method for significantly raising the pile resistance in soft soil. However, minimal experimental research has been carried out to isolate soil improvement effects around a single pile and demonstrated the influence of soil improvement on the behavior pile in soft clayey soils under seismic loads.

Rollins and Brown [2] enhanced the static and dynamic performance of full-scale piles group using a range of soil improvement techniques, including jet grouting, soil mixing, flowable fill, soil replacement, and compacted aggregate piers in treatment of soft clay in the vicinity of the pile and/or the pile cap. In general, soil improvement methods that use cement as a stabilizing agent (e.g., jet grouting, soil mixing, and flowable fill) resulted in the greatest improvements in lateral resistance compared to other soil treatment methods. The region of soil surrounded piles can be grouted in the form of block type below the pile cap and extended to the desired depth. In contrast to the non-improved piles group, the piles group's lateral resistance increased by 220 percent while the pile cap's passive resistance against the soil was ignored. Also, the initial stiffness of the improved soil increased by 14 times the results of small displacement tests (<30 mm).

Yamashita et al. [3] studied piled raft performance with ground improvement (deep cement mixing walls) subjected to seismic loading. The authors investigated a 12-storey building rest on loose silty sand underlain by soft cohesive soil and simulated this building under seismic loading using Finite Element Analysis. It is estimated that the frictional resistances around the piles enclosed by the grid-form walls were small, and also the grid-form walls reduced the bending moments at pile head, whereas those at the lower end of the grid-form walls behaved similarly to those at the pile head.

Liu et al. [4] used two centrifuge tests on a single pile installed in natural and improved soft clay (using deep cement-soil mixing), with the relative pile-soil stiffness values varying nearly two orders of magnitude and subjected to cyclic lateral loading and seismic loading. The cyclic loading results showed that improving the soil around a pile foundation using cement deep soil mixing is an effective way to enhance that foundation's lateral load behavior. Depending on the extent of soil improvement, elastic lateral stiffness and ultimate resistance of a pile foundation in improved soil increased by 2–8 times and 4–5 times, respectively, from those of a

pile in the natural soil. The present study is devoted to modeling the piles group's soft ground behavior improved by grouting and subjected to seismic loading. The study considers using cement shallow soil mixing (CSSM) instead of deep mixing, and the extent dimensions do not exceed 5D of the pile. This technique may be less costly and a simple injection process.

## 2 Soil Improvement by Grouting

One of the ground improvement techniques appropriate for soft soils is grouting. This approach is typically used to fill voids in the ground (fissures and porous structures) in order to improve resistance to deformation, supply cohesion, shear strength, compressive strength, and finally minimize hydraulic conductivity or interconnected porosity in an aquifer [5]. Many types of grouting techniques are available, the selection of suitable technique depends on the intention and the condition of the site. These techniques can be classified into compaction grouting, permeation grouting, jet grouting, hydro fracture grouting, rock grouting, and compensation grouting. Selecting the appropriate improvement technique depends on several factors such as type and layers of soil, type and magnitude of loading, and type of project [6]. In 1992, the technology of post-grouting of slurry at the bottom of the bored pile was developed successfully, and then the technology of post-grouting along pile shaft followed.

In comparison with overseas ones, the facilities for both technologies are technically simple, easy to operate, cost-effective, reliable, and applicable in terms of structure, process, and effectiveness [7]. Post grouting at pile bottom can increase tip resistance and increase side resistance at the middle and lower part of piles because cement slurry spreads upwards along the pile. The bearing capacity of both bottom and side grouting piles increases significantly from that of only bottom piles grouting.

## 3 Seismic Loading

Earthquake is the sudden, rapid and shaking of the earth caused by the breaking and shifting of subterranean rock as it releases strain that has accumulated over a long time. A series of the wave is generated by an earthquake and can be divided into: -

- (1) Body wave including: -
  - (a) P-wave
  - (b) S-wave.
- (2) Surface wave including: -
  - (a) Rayleigh wave

(b) Love wave

Each wave has a specific magnitude and direction of propagation; however, it is essential to recognize that the peak ground acceleration will be most influence by S-wave and, in some cases, by a surface wave. Note that the surface wave can be considered as especially damage to the structure. Pile often is used to transfer the load from the structure to the underlying soil (weak soil). Dynamic load for pile under building may cases large deformation and soil non-linearly. Interaction between pile and soil plays the primary role in the structure's response to the earthquake; many researchers study the behavior of piles subjected to dynamic load. Iraq is located in the seismic zone earthquakes are between (2.7–7.2 ML).

Abd Alridha and Jasem [8] carried out an earthquake assessment study in central and south of Iraq; it can be noted that the seismic zone east of Iraq is more significant than west of Iraq. The cement injection method was carried out with pressure grouting to introduce an initial force between the soil and pile base and sides to increase the pile's load-bearing capacity and reduce the pile's settlement.

## 4 Numerical Modeling

The finite element method is a numerical technique to find approximate solutions for boundary value problems. It is an effective technique to divide the enormous problems into small parts to simplify the solution. It is commonly used to solve complex engineering problems, including the problems in this study's domain [9]. This study adopted PLAXIS 3D to model the domain problem under finite element analysis technique based on specified conditions as this package is a useful tool in this domain. The capability of this program covers the behavior of structural elements and soil. In this study, the dynamic analysis was adopted using time-history acceleration as input data; the earthquake was simulated as a prescribed acceleration applied at the bottom of the finite element model (which is the base layer's location). This approach is common in simulating the earthquake's effect in the finite element analysis [10]. Figure 1 shows the El Centro earthquake's time history, which is applied to the soil's base model. This study includes numerical analysis of pile groups inserted in the soft ground; soft clay properties were adopted from reference [11]. The properties of soil are given in Table 1.

The piles group's studied model consists of  $2 \times 2$  piles with spacing between piles equals  $6d = 3.6$  m, where  $d$  is the pile's diameter. The pile cap dimensions are  $(12 \times 12 \times 0.5)$  m, and the pile's dimensions are 0.6 m in diameter and 12 m in length. The piles are modeled as volume elements with a modulus of elasticity as  $3 \times 10^7$  kPa, and the unit weight  $24 \text{ kN/m}^3$ . The boundary conditions are simulated according to the fundamental requirements as viscous with the direction of seismic movement and fixed boundary in other situations. To study the grout material's effect on the piles group behavior, the cement material used as jet grouting according to

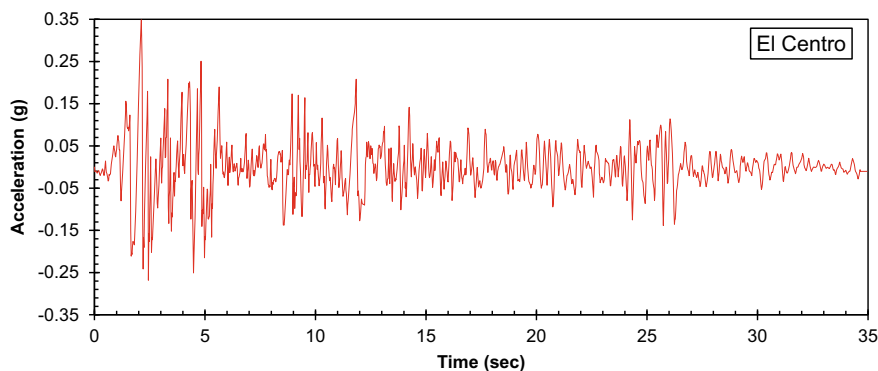


**Fig. 1** Time-history of acceleration of El Centro earthquake [10]

**Table 1** Soft soil properties [11]

$\gamma_{\text{unsat}}$ (kN/m <sup>3</sup> )	$\gamma_{\text{sat}}$ (kN/m <sup>3</sup> )	$E_{50}^{\text{ref}}$ (kPa)	$E_{\text{oed}}^{\text{ref}}$ (kPa)	$E_{\text{ur}}$ (kPa)	Power (m)	Cohesion (kPa)	Material model
13.24	18.85	600	1425	1800	1	10	Hardening soil model

**Table 2** Properties of grout material [12]

E (MPa)	N	$\varphi'$ (°)	$c'$ (kPa)	$\gamma_{\text{sat}}$ (kN/m <sup>3</sup> )
150,000	0.25	35	900	19

reference [12, 13]. The grouting material is modeled as elastic-perfect plastic using the Moher-Coulomb model with properties as shown in Table 2.

The grout material was modeled around the piles with different radii, where the piles were surrounded by the grout material, as shown in Fig. 2. Three radii (0.5, 1, and 1.5 m) of the cement grouting were used in the study and extended to depths of 2 and 4 m.

## 5 Results and Discussion

**Verification Modeling.** This verification was achieved by comparing the results obtained from the PLAXIS software with other packages of programs to ensure the realization of the program's ability to analyze seismic load. So, a case study was analyzed using PLAXIS software to achieve the mentioned goal. The case study included comparing the results obtained from a survey conducted by Eslami et al. [14] and using PLAXIS 3D under the same geometry, loading, and boundary conditions.

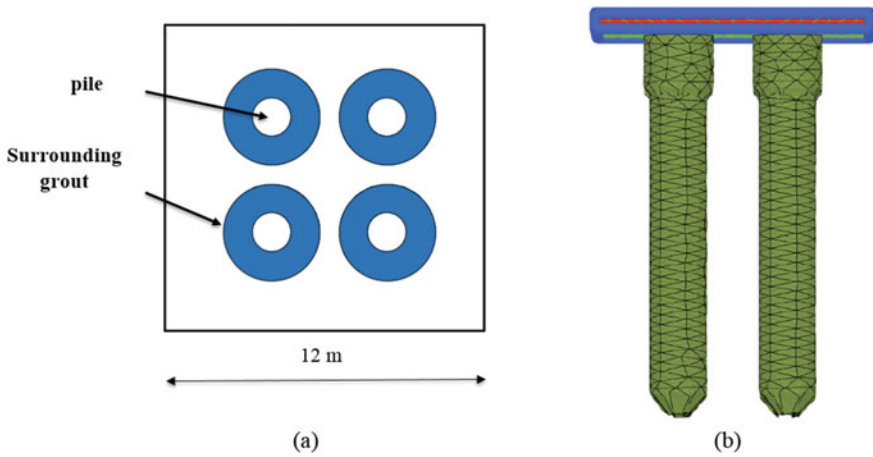


**Fig. 2** a Schematic diagram of piles group surrounded by grout b numerical modeling of the grouted pile

The study included seismic analysis of a pile group under the effect of seismic loads using the El Centro earthquake, the model was modeled using ABAQUS software, and the results were verified based on experimental work. The study adopted a pile group analysis of the rectangular pile dimensions  $0.5 \times 0.5$  m of piles with a length of 9 m. the domain model is  $28 \times 28 \times 16$  m. The soil properties are: Young’s modulus is  $40000 \text{ kN/m}^2$ , soil unit weight is  $16.3 \text{ kN/m}^3$ , Poisson’s ratio is 0.3, Friction angle is  $31^\circ$ , and soil cohesion is 10 kPa. The obtained results are shown in Table 3, where the results obtained from PLAXIS software are close to the results obtained by Eslami et al. [14].

**Piles Group Without Grout.** Figure 3 shows the relationship between time and maximum seismic settlement of piles group in natural soil under seismic load. It can be observed growing the amount of settlement reaches 45 mm at failure. The seismic settlement’s high value resulted from the softening of soil under the piles group subjected to seismic load, where the maximum PGA of El Centro earthquake

**Table 3** Comparison of the result of ABAQUS software with the results of PLAXIS 3D

Results of pile group	Results of ABAQUS [14]	Results of current study PLAXIS 3D, 2020
Maximum horizontal displacements	44.25 cm	46.203 cm
Maximum settlement displacements	10.3 cm	12.601 cm



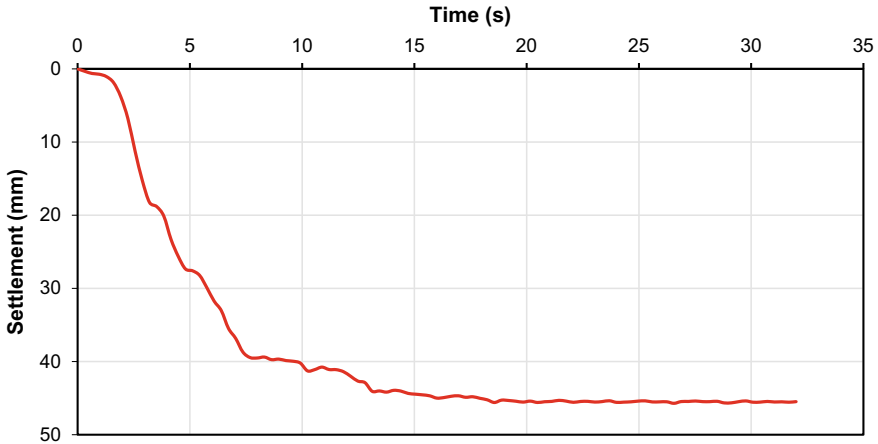


Fig. 3 Time settlement of group pile without grout

is about 0.31g. The seismic load leads to a degradation of the soil stiffness, which causes a decrease in bearing capacity and an increase in soil settlement.

**Piles Group with Grout.** This section deals with grout material’s effect on the piles group’s performance under the impact of seismic loads. Several patterns of grouting around the piles groups were investigated to study the effect of grouting on piles group performance under seismic loading, different diameters, and depths of grouting.

**Effect of Radius of Grouting.** This part includes improving the soft soil surrounding the piles group with cement grout. The grout material was injected around the piles with different radii,  $R = 0.5, 1, \text{ and } 1.5 \text{ m}$ . The results showed that the grout material reduces the piles group’s settlement under effect of seismic loads. Figure 4 shows a relationship between time history and seismic settlement of piles group for different radii of cement grouting extended to a depth of 2 m, where it can be observed a decrease of maximum settlement from 45 to 29 mm in the case that the grout material with  $R = 0.5$  surrounds the piles. Also, the maximum settlement of pile group reduced to 20 mm and 24 mm for the piles group cases surrounded by a grout with radius,  $R = 1$  and 1.5 m, respectively, as shown in Fig. 5.

**Effect of Grouting Depth.** Figure 6 shows a relationship between time history and dynamic settlement of piles group surrounded with cement grouting of radii (0.5, 1, and 1.5 m) and extended to a depth of 4 m. A decrease of maximum settlement from 45 to 25 mm can be observed in the case that the piles are surrounded by the grout material with a radius of 0.5 m. Also, a decrease in maximum settlement of piles group is 22 and 19 mm for the cases when the piles are surrounded by cement grout of radius (1 and 1.5 m), respectively. From the above results, it is clear that the optimal radius (R) of cement grouting for improving the piles group under seismic loads is 0.5 m. This radius of grouting reduces the settlement of piles group’s under seismic loads effectively, and injection a small radius of cement grouting is considered an

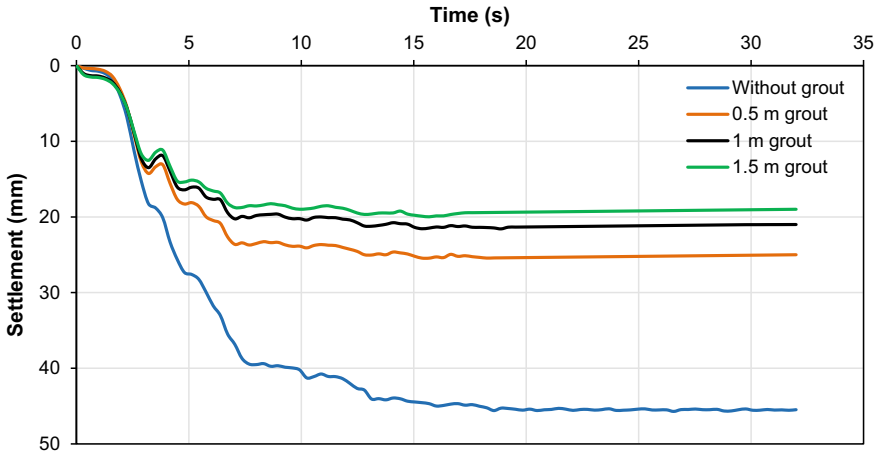


Fig. 4 Time-settlement of group pile surrounded by grouting of different radii and depth = 2 m

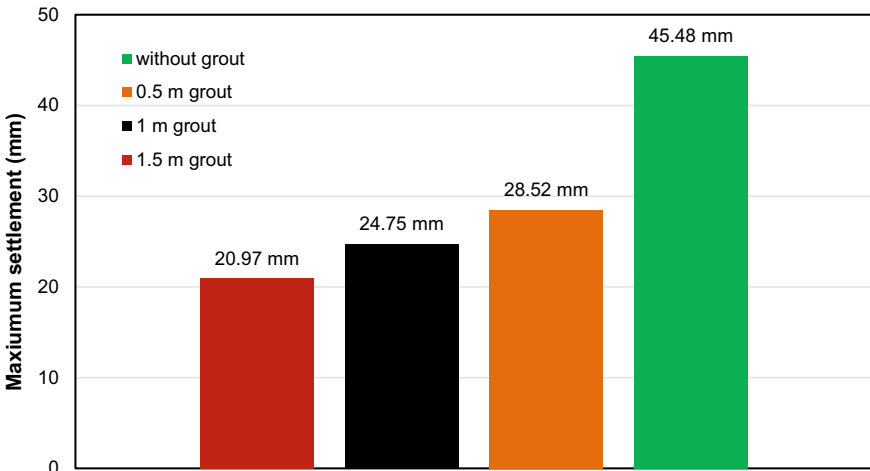


Fig. 5 Maximum settlement of pile group with different grout radii and depth = 2 m

economical solution and cheaper than grout with radii 1 and 1.5 m. When plotting the variation of maximum settlement versus depth of grouting, at a depth of 4 m and radius of 0.5 m, there is a reduction in the maximum settlement from 45 to 25 mm. While at depth 2 m, the maximum settlement reduction from 45 to 29 mm is shown in Fig. 7.

To calculate the dynamic reduction percentage in settlement ( $R_s$ ), the following Eq. 1 can be applied.

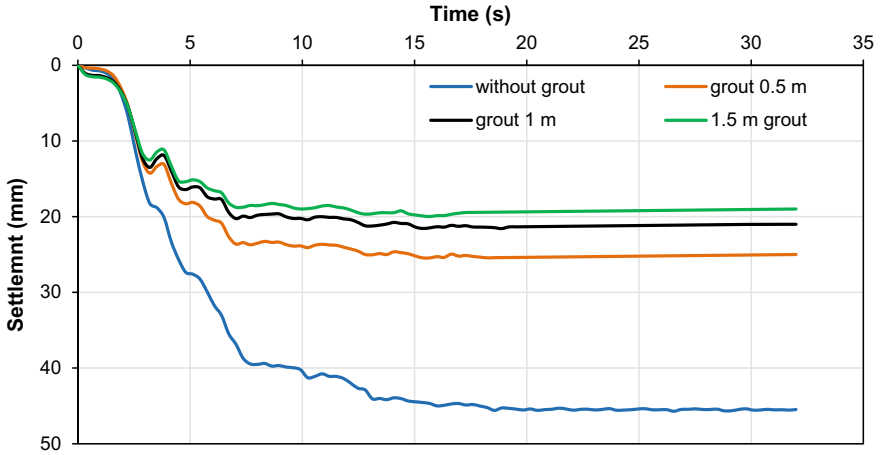


Fig. 6 Time-settlement relation of pile group with 4 m depth of grout

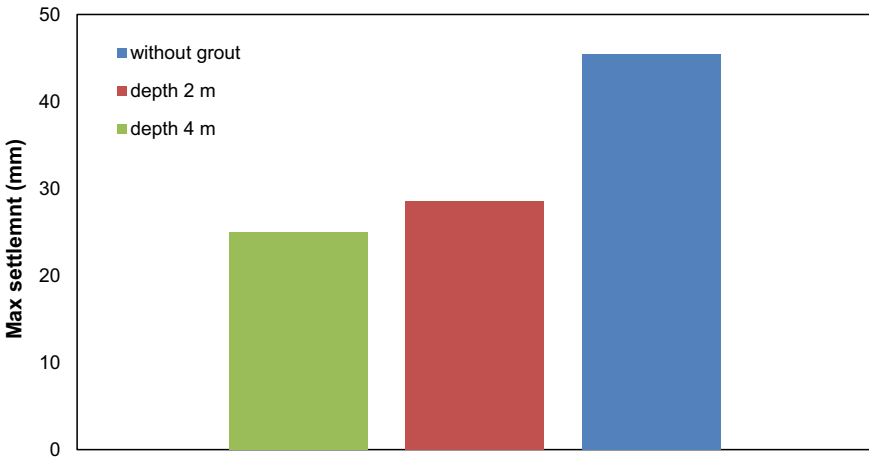


Fig. 7 Maximum settlement of pile group surrounded with grout at depths 2 and 4 m

$$R_s = \frac{S_i - S_{gr}}{S_i} \times 100 \tag{1}$$

$S_i$  is the piles group’s initial dynamic settlement without grout, and  $S_{gr}$  is the dynamic settlement with grout material. The percentage reduction of the pile group’s settlement surrounded with grout with different depths is shown in Fig. 8. It can be observed at depth 2 m; the percentage reduction ranges between 37, 46, and 55% when the grout radius is 0.5, 1, and 1.5 m, respectively. The reduction percentage increased when the grout depth was increased to 4 m. It can be noticed the percentage of reduction ranges between 46, 53, and 60% for grout of radius 0.5, 1, and 1.5 m,

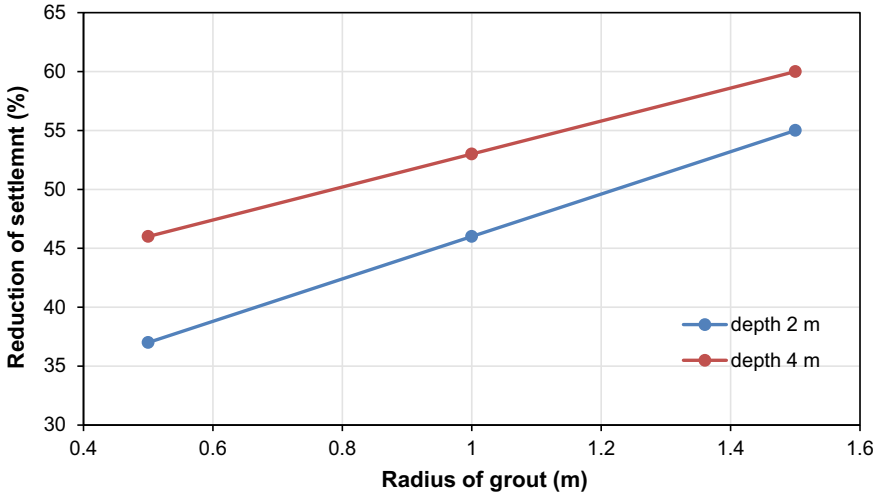


Fig. 8 Percentage reduction of settlement

respectively. It can be concluded that the grout material plays an essential role in restricting the movement of the piles under the effect of seismic load, as the grout material resists the lateral loads and thus increases the lateral resistance of soil and decreases the amount of settlement.

## 6 Conclusion

Based on the result analysis, the following conclusion could be drawn: -

- For the group pile, grouting with 0.5 m radius and depth at 2 m, the settlement decreased by 39%, while at depth 4 m decreased by 47%.
- For the group pile, grouting with a 1 m radius and depth at 2 m settlement decreased by 48%, while at depth 4 m decreased by 53%.
- For the group pile, grouting with a 1.5 m radius and depth at 2 m settlement decreased by 54%, while at depth 4 m decreased by 60%.
- When comparing the results of improvement in settlement for each grouting depth of pile group, there is a noticeable percentage of improvement at the radius of 0.5 m, and when increasing the radius of grouting to 1 and 1.5 m, the percentage of settlement improvement is small when compared with the gain with a diameter of 0.5 m.

## References

1. Mohamad, N. O., Razali, C. E., Hadi, A. A. A., Som, P. P., Eng, B. C., Rusli, M. B., & Mohamad, F. R. (2016, July). Challenges in construction over soft soil-case studies in Malaysia. In *IOP Conference Series: Materials Science and Engineering* (Vol. 136, No. 1, pp. 012002). IOP Publishing.
2. Rollins, K. M., & Brown, D. A. (2011). Design guidelines for increasing the lateral resistance of highway-bridge pile foundations by improving weak soils. *Transportation Research Board*, 697.
3. Yamashita, K., Wakai, S., & Hamada, J. (2013). Large-scale piled raft with grid-form deep mixing walls on soft ground. In *Proceedings of the 18th ICSMGE*, (pp. 2637–2640).
4. Liu, C., Soltani, H., Muraleetharan, K. K., Cerato, A. B., Miller, G. A., & Sritharan, S. (2016). Cyclic and seismic response of single piles in improved and unimproved soft clays. *Acta Geotechnica*, 11(6), 1431–1444.
5. Moseley, M. P., & Kirsch, K. (eds.). (2004). In *Ground improvement*. CRC Press.
6. Mitchell, J. M., & Jardine, F. M. (2002). *A guide to ground treatment*. CIRIA.
7. Jin-Li, L., Zhong-Cheng, Z., & Yan, Z. (1999). The technology and application of post-grouting for slurry bored piles. In *International Conference on Soil Mechanics and Foundation Engineering* (pp. 831–834).
8. Abd Alridha, N., & Jasem, N. A. (2013). Seismicity evaluation of central and southern Iraq. *Iraqi Journal of Science*, 54(4), 911–918.
9. Kirchgäßner, B. (2016). Finite elements in rotordynamics. *Procedia Engineering*, 144, 736–750.
10. Bhatnagar, S., Kranthikumar, A., & Sawant, V. A. (2016). Seismic analysis of dam under different upstream water levels. *Advances in Computational Design*, 1(3), 265–274.
11. Hassan, H. A. (2013). An experimental and theoretical study on ordinary and encased stone columns underneath embankment. Ph.D. thesis, College of Engineering, University of Baghdad, Iraq.
12. López-Acosta, N. P., Martínez-Hernández, E., & Espinosa-Santiago, A. L. (eds). (2019). Geotechnical engineering in the XXI Century: Lessons learned and future challenges: In *Proceedings of the XVI Pan-American Conference on Soil Mechanics and Geotechnical Engineering (XVI PCSMGE)*, 17–20 November 2019, Cancun, Mexico. IOS Press.
13. Jebur, M. M., Ahmed, M. D., & Karkush, M. O. (2020). Numerical analysis of under-reamed pile subjected to dynamic loading in sandy soil. In *IOP Conference Series: Materials Science and Engineering* (Vol. 671, No. 1, p. 012084). IOP Publishing.
14. Eslami, M. M., Aminikhah, A., & Ahmadi, M. M. (2011). A comparative study on pile group and piled raft foundations (PRF) behavior under seismic loading. *Computational Methods in Civil Engineering*, 2(2), 185–199.

# Effect of Spacing Ratio on the Pull-Out Capacity of Double Helix Pile in Organic Soil



Majid Hamed, Waleed Mohammed, Hanifi Canakci,  
and Abdalkhaliq Mijwel

**Abstract** Problematic soil has been critical construction problems for many decades. Field and laboratory investigations have been not often available to provide safe design and required data for analysis to deals with such soil problems. This study presents an experimental investigations on the behavior of helical pile in organic soil. During the investigations, detailed soil characteristics, scale effect as well as vertical pull-out static load were completed. Organic soil with different densities were prepared and compacted with fully saturation conditions. Helix pile with double helix plates have been installed, the effect of vertical spacing between the helix plates under vertical pull-out load were examined. Results have been showing that the load capacity with s spacing ratios of 1 and 2 is ranged from 1.25 to 1.77 times the capacity of double-helix pile with spacing ratios of 3 and 4 in both stiff and soft soils, respectively.

**Keywords** Organic soil · Helical pile · Pull-out capacity · Helix plate · Spacing ratio

## 1 Introduction

Many constructions need to be supported by pile foundations due to different loading cases, such as compression and tension axial loads along with the lateral loads. Pull-out load is an axial tension load carried out by different constructions like tall

---

M. Hamed (✉) · W. Mohammed  
Department of Civil Engineering, University of Kirkuk, Kirkuk, Iraq  
e-mail: [majid79@uokirkuk.edu.iq](mailto:majid79@uokirkuk.edu.iq)

W. Mohammed  
e-mail: [waleedkhalid@uokirkuk.edu.iq](mailto:waleedkhalid@uokirkuk.edu.iq)

H. Canakci  
Department of Civil Engineering, Hasan Kalyoncu University, Gaziantep, Turkey  
e-mail: [hanifi.canakci@hku.edu.tr](mailto:hanifi.canakci@hku.edu.tr)

A. Mijwel  
Department of Civil Engineering, Gaziantep University, Gaziantep, Turkey

chimneys, electric towers, pipe lines under water and tunnels. Although, different types and shapes of piles are used to support the construction projects, the need to develop new practical and effective type of foundation is very important. Helical pile represents a great concept to tackle many challenges in construction projects. The challenges may be the driven or drilled pile that could not be applied, no noise control, cost saving solution and innovative configuration of common piles. Ashni and Janani [1] carried out an experimental study on the use of helical pile under pull-out load in clayey soil with many numbers of helices. The study showed that the pull-out load capacity has increased when the number of helix was increased as well. Rao [2] investigated the performance of helical pile in soft marine clay that needs to support oil pipe in deep water. Rao [2] showed that the repetitive loading of the structure due to the water wave generates a significant static pull that could lead to fail the helix pile. An experimental series of tests has been conducted by Niroumand and Kassim [3] on two sizes of irregular-shaped anchors installed in sandy soil under pull-out load. Niroumand and Kassim [3] showed that an increase in the pile capacity when the soil density and the embedment ratio has increased. On the other hand, helical pile under uplift load in clayey soil has also numerically investigated for better understanding the performance of multi-helix pile instead of existing semi-empirical methods [4]. Framework as reported by the author can be confidently adopted by the design engineer to calculate the tension load capacity of helix pile installed in clay soil. Furthermore, Rao and Prasad [5] calculated the influence of spacing ratio on the tension capacity of helical pile in clay soil. The study revealed that the tension load of helical pile were controlled by the spacing ratio. An inclined pull-out load capacity of screw pile has been predicted experimentally and theoretically by Ghaly and Clemence [6]. The study showed that there is a rational arrangement between the laboratories and theoretical results, and also revealed that the rupture surface is complex and unsymmetrical. Hamed et al. [7] studied the behavior of helical pile under tension load in organic soil, the study revealed that the pull-out capacity based on the number of plates and spacing ratio. Helical micro piles subjected to horizontal and axial loading has also been analyzed by Papadopoulou et al. [8]. The analysis was made using the method of finite element to predict its tests in the fields. The results showed that the calculations used for axial and transverse loadings were reliable mostly for cohesive soils. However, in cohesionless soils, one should be careful when covering the theoretical estimations and should also take into account the scale effect of each micropile that has been loaded. The effect of vertical loading on the performance of lateral capacity of helix pile under combined horizontal and vertical loading has been numerically investigated using different pile lengths and plate diameters [9]. The research showed that the vertical compression capacity load has increased the lateral capacity of the pile whereas the pull-out load has reduced the lateral capacity. Since very little to no study, to the authors' knowledge, has been found that could the behavior of helix pile in organic soil, this study was prepared to examine the behavior of double helix pile under the effect of spacing ratio installed in organic soil.

## 2 Materials

**Soil.** In this study, the adopted soil is an organic soil which was collected from Sakarya region, Turkey. The geotechnical properties tests were conducted following ASTM standards. For ASTM D854 [10] and ASTM D422 [11] were used to determine the specific gravity and sieve analysis properties of the soil. The soil can be classified with different ASTM classification system as presented in Table 1. Under 440° C and 4 h curing, the tested soil has been ignited using a muffled furnace in order to obtain the organic content (ASTM D2974) [12]. Table 2 and Fig. 1 summarized the properties and sieve analysis of the soil, respectively.

**Table 1** ASTM soil classifications

ASTM standard	Criteria	Designation	Presented properties
Ash content (D2974)[11]	Low ash	< 5% ash	77% High ash
	Medium ash	5–15% ash	
	High ash	15% < ash	
Acidity (D2976)[12]	High acidic	pH < 4.5	6.7 Slightly acidic
	Moderately acidic	4.5 < pH < 5.5	
	Slightly acidic	5.5 < pH < 7	
	Basic	pH > 7	
Fiber content (D1997)[13]	Fibric (H1–H3)	> 67% fibers	Sapric (H7–H10)
	Hemic (H4–H10)	33–67% fibers	
	Sapric (H7–H10)	< 33% fibers	

**Table 2** Properties of organic soil presented in this research

Item	Value	Unit
Maximum dry density	10.3	kN/m <sup>3</sup>
Optimum water content	39%	
pH	6.7	
Organic content	23%	
Liquid limit	75%	
Plastic limit	45%	
Natural water content	97%	
Fine sand	23.4%	
Clay and silt	76.6%	
Specific gravity	2.24	
Angel of internal friction	360	
Cohesion	3	kN/m <sup>2</sup>



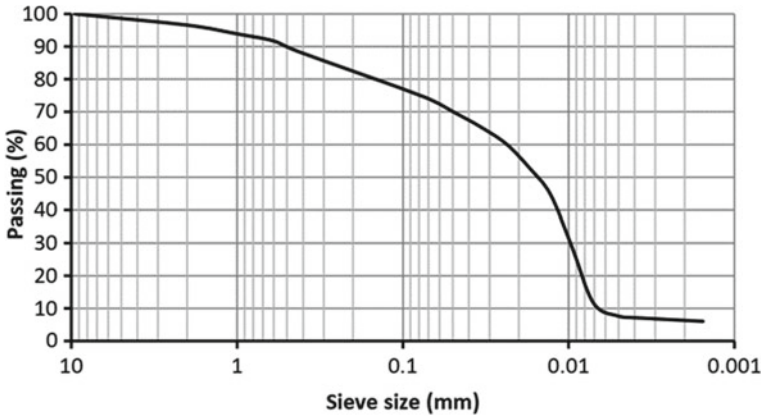
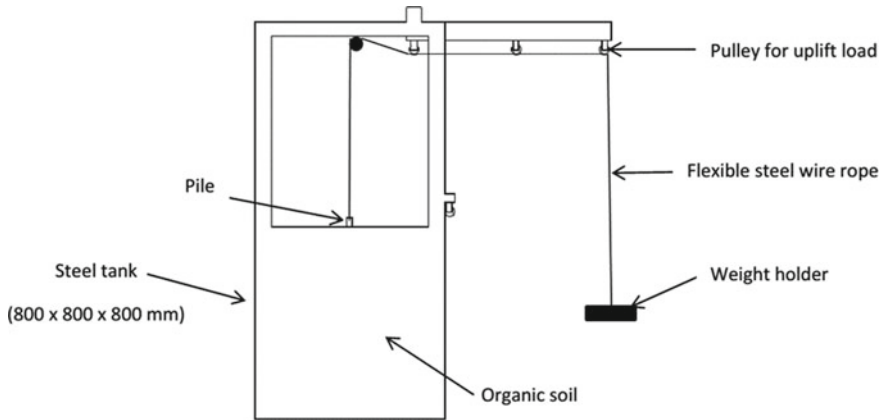


Fig.1 Particle size distribution of the tested soil

**Helical Piles.** Four different designations piles which were made from steel were used in this study; (i), a shaft pile with 16 mm diameter and 650 mm total length; (ii) a steel plate with a diameter of 50 mm welded on the steel shaft; (iii) a pitch with 50 mm has made to form helical pile Fig. 2. Each pile has two helical plates, four pile models



Fig. 2 Double-helix pile designation used in the study



**Fig. 3** Tested tank used in the study

were made namely P1, P2, P3 and P4. Different spacing ratios were designated. The spacing ratio can be well-defined as the relation of the spacing between plates to the plate diameter. Therefore, the plates of pile have a distance designated as 50, 100, 150 and 200 mm for the model P1, P2, P3 and P4, respectively.

**Testing Tank.** To examine the behavior of the pile in small scale tank using laboratory tests the size of container was given very close attention. To avoid misleading results that can be associated to the change in the container size the selected dimensions of the tank were fixed to (800 × 800 × 800) mm. Pull-out test has been carried out using the tank shown in Fig. 3. A minimum diameter of the soil tank was three times the diameter of the helix plate to prevent the scale effect [14]. Therefore, the selected dimensions achieved the scale effect requirements for the present study using a screw pile with a plate diameter 50 mm.

### 3 Test Method

Two soil densities have been used in this study (5 and 8.5 kN/m<sup>3</sup>) for soft and stiff soil cases respectively. The soil tank was divided in to multi layers and each layer of 50 mm thick. The multi-layers technique is very important to control soil density. A pre-determined soil weight has filled in each layer and compacted manually using square steel plate hammer. It is worth to note that this procedure is not a precise procedure hence, careful attention was paid to ensure obtaining uniform density. Generally, organic soil retains high water content hence the soil in the tank was soaked with water to attain the case of soil in full saturation. The model piles were installed after a fully compaction of all the soil layers has been compacted. In order to confirm the work repeatability the prepared soil bed and pile installation was similar for all the tests. The helical piles were installed through soil layers with a

suitable torque and download force until certain depth (600 mm) was reached. Four tests has been executed for each density. All experiments were repetitive to increase dependability of the obtained test results. The obtained data were very close using the model piles P1, P2, P3 and P4. Vertical uplift pile load was carried out by using flexible steel wire to the pile head that was attached to the head of the pile (see Fig. 3). The next end of the rope was bonded to the loading pan. The tests were carried out under stress control procedure. The increment loads were step by step increased beginning from the lowest load with small increases in magnitude, and the vertical displacement was recorded for each load increment. It is important to note that each load increment remains has been fixed till unimportant change in the vertical displacement has happened.

## 4 Results and Discussions

In this section, load capacity of the helical piles were measured. The curves of the respond of pile to the tension load are shown in Figs. 4 and 5 for all tested helix pile designation (H1, H2, H3, and H4) installed in both stiff and soft organic soils. Numerous study methods have been conducted in order to obtain maximum design load that has must be achieved by the screw piles. The final pull-out load of helical pile is determined at the maximum point of curvature on the curve. Similar method was conducted by Mittal and Mukherjee [15] and Mittal et al. [14]. From Figs. 4 and 5, one can conclude that an increase in the number of helix can obviously adjust the load–displacement behavior of helical pile and increases the ultimate tension load capability with the increase of the density of organic soil. The ultimate tension loads for the helical piles H1, H2, H3, and H4 are 62, 50, 40, and 35 N in the soft soil ( $5 \text{ kN/m}^3$ ), and 92, 80, 63 and 52 N in the stiff soil ( $8 \text{ kN/m}^3$ ), respectively. To deals

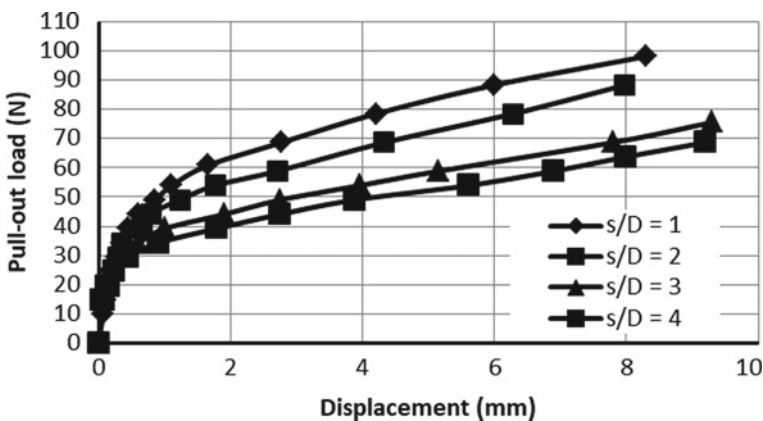


Fig. 4 Load–displacement curves of the piles for soft soil

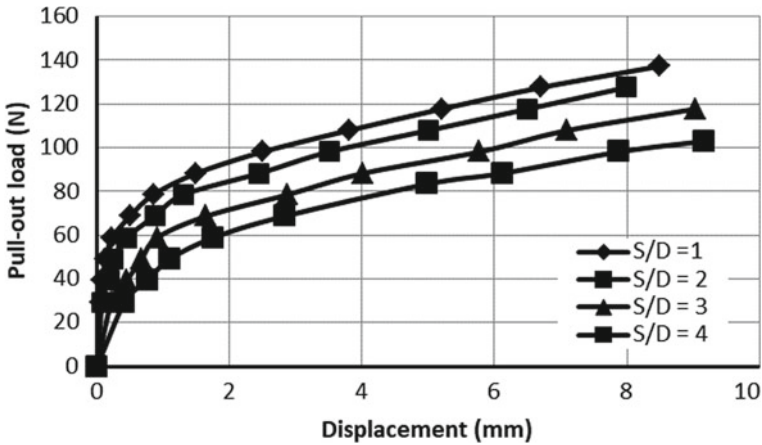


Fig. 5 Load–displacement curves of the piles for stiff soil

with the influence of vertical spacing of pile plates on the performance of helical piles the ratio of helix diameter ( $D/d$  here,  $D$  is the diameter of helix plate; and  $d$  is the diameter of the pile shaft) was maintained constant at 3.1 for all helical piles, while the defined spacing ( $S/D$ ) was rehabilitated to be 1, 2, 3, and 4. The pull-out response of the helical pile with double helices at various spacing's is shown in Fig. 6. By using the method of the maximum point of curvature that was mentioned earlier, the Figure shows that the interaction between helices decreases when the spacing ratios increased, and the helices be likely to perform individual. The obtained data for the selected screw piles are meet with the results by Rao and Prasad [5] and Abdrabbo and El Wakil [16]. It is found that an increase in the tension load of helical piles when the density of soil has increased and decreasing in spacing ratio. The obtained

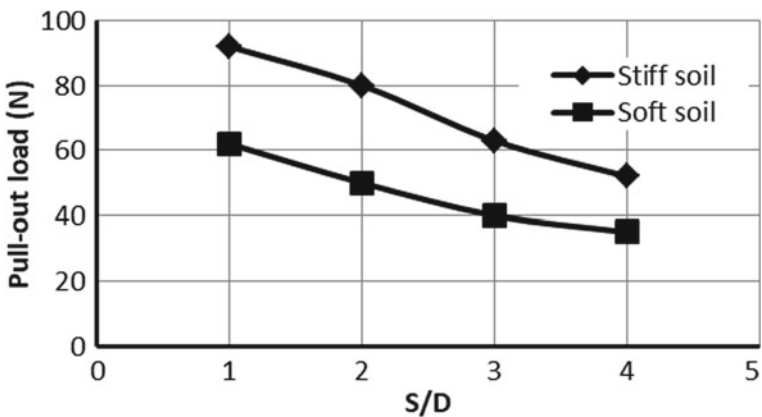


Fig. 6 Effect of the spacing ratio on the pull-out capacity

results are inconsistent with the discoveries of previous studies by Rao and Prasad [5] and Khazaie and Eslami [17]. From the results of these tests, it can be found that the selected vertical spacing relation ( $S/D$ ) were ranging from 1 to 4 which mean that both methods of cylindrical shear failure and individual bearing will be effective. Since the cylindrical failure assumption can be valid up to 2 spacing ratios [18], the cylindrical assumption may be incomplete with the increase in pile spacing. Therefore, individual bearing will be valid after 2 spacing ratios [5]. In cylindrical method, the top helix creates a shear surface like a cylindrical shape that controls its performance. The soil that was entrapped between the two plates becomes a rigid cylinder if the plates are adequately close to each other. The shear resistance along the interface is said to be governed by the angle of friction and stress state in the disturbed soil cylinder above the helix plate [19]. In the case of individual bearing, and since the helices are widely spaced, it is assumed that each helix behave independently from each other. Consequently, the tension load of the screw anchor is the summation of the bearing resistance of all helical plates and the shaft resistance [20]. Therefore, these methods clarify the cause of increasing in the load capacities of helical pile when the vertical spacing ratio ( $S/D$ ) was decreased as presented in Fig. 6.

## 5 Conclusions

The behavior of double helix pile under tension static loadings was investigated using experimental load tests. Double-helix piles were installed and were loaded axially in two soil densities: soft and stiff organic soil. Uplift performance was predicted using the axial load versus displacement readings. The points below are achieved from this study:

1. The ultimate uplift load capacities of double helix pile are controlled by the spacing helical plates.
2. Using more closely spaced of double-helix plates leads to a stiffer load response and less immediate displacement in organic soils.
3. An increase in spacing ratios causes a decrease in ultimate uplift load. Further, the increase of soil density leads to the increase in ultimate uplift load capacity of the soil.
4. The capacity of double-helix pile is greater when the spacing ratios are within the range of 1 and 2. In general, the capacity of piles with a spacing ratios of 1 and 2 is ranged from 1.25 to 1.77 times the capacity of piles with a spacing ratios of 3 and 4 in both stiff and soft soils, respectively.

## References

1. Ashni, M., & Janani, V. (2017). Experimental stud capacity of helica. *International Journal of Civil Engineering*, 8(4).
2. Singh, S. P., & Ramaswamy, S. V. (2008). Effect of shape on holding capacity of plate anchors buried in soft soil. *Geomechanics and Geoengineering: An International Journal*, 3(2), 145–154.
3. Niroumand, H., & Kassim, K. A. (2014). Uplift response of irregular-shaped anchor in cohesionless soil. *Arabian Journal for Science and Engineering*, 39(5), 3511–3524.
4. Merifield, R. S. (2011). Ultimate uplift capacity of multiplate helical type anchors in clay. *Journal of Geotechnical and Geoenvironmental Engineering*, 137(7), 704–716.
5. Rao, S. N., & Prasad, Y. V. S. N. (1993). Estimation of uplift capacity of helical anchors in clays. *Journal of Geotechnical Engineering*, 119(2), 352–357.
6. Ghaly, A. M., & Clemence, S. P. (1998). Pullout performance of inclined helical screw anchors in sand. *Journal of Geotechnical and Geoenvironmental Engineering*, 124(7), 617–627.
7. Hamed, M., Canakci, H., & Khaleel, O. (2019). Performance of multi-helix pile embedded in organic soil under pull-out load. *Transportation Infrastructure Geotechnology*, 6(1), 56–66.
8. Papadopoulou, K., Saroglou, H., & Papadopoulos, V. (2014). Finite element analyses and experimental investigation of helical micropiles. *Geotechnical and Geological Engineering*, 32(4), 949–963.
9. Al-Baghdadi, T. A., Brown, M. J., Knappett, J. A., & Al-Defae, A. H. (2017). Effects of vertical loading on lateral screw pile performance. *Proceedings of the Institution of Civil Engineers-Geotechnical Engineering*, 170(3), 259–272.
10. ASTM Committee D-18 on Soil and Rock. (2010). Standard test methods for specific gravity of soil solids by water pycnometer. ASTM International.
11. Sreedeeep, S., & Singh, D. N. (2006). Methodology for determination of osmotic suction of soils. *Geotechnical and Geological Engineering*, 24(5), 1469–1479.
12. ASTM, D. (2007). Standard test methods for moisture, ash, and organic matter of peat and other organic soils. D2974–07.
13. Nath, B. D., Molla, M., Ali, K., & Sarkar, G. (2017). Study on strength behavior of organic soil stabilized with fly ash. *International Scholarly Research Notices*.
14. Mittal, S., Ganjoo, B., & Shekhar, S. (2010). Static equilibrium of screw anchor pile under lateral load in sands. *Geotechnical and Geological Engineering*, 28(5), 717–725.
15. Mittal, S., & Mukherjee, S. (2015). Behaviour of group of helical screw anchors under compressive loads. *Geotechnical and Geological Engineering*, 33(3), 575–592.
16. Abdrabbo, F. M., & El-wakil, A. Z. (2015). Behavior of pile group incorporating dissimilar pile embedded into sand. *Alexandria Engineering Journal*, 54(2), 175–182.
17. Khazaie, J., & Eslami, A. (2016). Behavior of helical piles-as a geoenvironmental choice-by frustum confining vessel (FCV). *Advances in Science and Technology. Research Journal*, 10(31).
18. Zhang, D. J. Y. (1999). Predicting capacity of helical screw piles in Alberta soils.
19. Kulhawy, F. (1985). Drained uplift capacity of drilled shafts. In *International Conference on Soil Mechanics and Foundation Engineering*. (Vol. 11, pp. 1549–1552).
20. Clemence, S. P., Ghaly, A. (2013, August). A review of model-scale laboratory investigations of helical anchors and screw piles. In *1st International Geotechnical Symposium on Helical Foundations*, (pp. 25–45).

# Comparative Analysis of Static and Dynamic Pile Tests at the Site of the Astana Medical University Hospital in Nur-Sultan, Kazakhstan



A. Zh. Zhussupbekov, A. U. Yessentayev, B. G. Abdrakhmanova, and V. N. Kaliakin

**Abstract** A comparative study of the results of field tests to determine the bearing capacity of a pile at the facility “United University Hospital for 800 beds at the NJSC” Astana Medical University “is presented. The study aimed to carry out a comparative analysis of the results of dynamic and static tests within the same construction site to identify the difference in performance. This article provides programs and tests with static indentation load and dynamic load on a pile in different parts of the construction site under different soil conditions. Dynamic tests were carried out from 21 to 29 September 2020. Driving and finishing using the Junttan PM-25HD pile driver. Static tests during the period from December 02, 2020 to January 04, 2021. During static tests, the load on the pile was created using a 100-ton hydraulic jack “Enerpred DU100P150” with a pumping station “Enerpac P462”, resting against a test and loading stand, weighing 120.0 tons. The results of the comparative analysis are the following: Dynamic tests are needed for a preliminary assessment of the dynamic bearing capacity and the possibility of driving piles in different parts of the construction site under different soil conditions. To adjust the pile length, adhere to the static indentation test results. The bearing capacity of the pile, determined by dynamic tests, is slightly lower than during static tests, the difference between the results is 11%.

**Keywords** Static test · Dynamic tests · Pile · Comparative analysis · Bearing capacity

## 1 Introduction

The 800-bed Astana Medical University Hospital is being constructed on the right bank of the Esil River in the city of Nur-Sultan, Kazakhstan. The total area of the

---

A. Zh. Zhussupbekov · A. U. Yessentayev (✉) · B. G. Abdrakhmanova  
L.N. Gumilyov, Eurasian National University, Nur-Sultan, Kazakhstan

V. N. Kaliakin  
University of Delaware, NY, USA  
e-mail: [kaliakin@udel.edu](mailto:kaliakin@udel.edu)



**Fig. 1** Sketch design of the hospital building

hospital will be 140 thousand square meters. It will house a consultative and diagnostic center, round-the-clock and day facilities with 800 and 110 beds, respectively. The architectural rendering of the hospital complex is shown in Fig. 1.

Based on samples taken at the site, the relatively low bearing capacity of the soil necessitated the use of a piled foundation. To better determine the bearing capacity of this foundation, both static and dynamic pile field tests were performed.

## 2 Dynamic Pile Tests

Field tests of piles in group's C9-30 and C12-30, with dynamic applied loading, were performed from the 21st to the 29th of September, 2020 at the hospital construction. The piles in these groups numbered 1, 2, 3, 4, 5, 6, 7, 8, 9, 10, 11, 12, 13, 14, 15, 16, 17 were subjected to dynamic tests. Numbers 18 and 19 were immersed in the ground to a depth of 8.5 m from the absolute elevation of the bottom of the pit (i.e., 339.82 to 340.22 m). Additional information related to the piles is available in the report on dynamic testing prepared by KGS Astana LLP. Driving and finishing test piles were carried out using a Junttan PM-25HD piling rig (Fig. 2a) with an NNK-8A hydraulic hammer with a shocking mass of 8000 kg and a headband weighing 990 kg. When driving the piles (Fig. 2b), wooden spacers were used inside the metal head to prevent the destruction of the pile head. The drop height of the striking part of the hammer ranged between 0.3 and 0.4 m.

The finishing of the piles, which was carried 6 to 8 days after the end of the pile driving, consisted of two successive applications of three and five blows. Before finishing, to accurately quantify the movement, a measuring tape with a scale of 1 mm was glued to the pile. Observation of the sinking of the piles was then carried





**Fig. 2** a Junttan PM-25HD piling rig. b Typical test pile

out using a level. Failures of piles during the finishing period ranged from 0.26 to 0.42 cm, with hammer energy of 2.4 t-m. The largest average failure load of three and five blows was taken to determine the bearing capacity, obtained when finishing the pile after the aforementioned “rest” period of 6 to 8 days after the end of driving [1, 2]. Table 1 summarizes the information related to the piles involved in the dynamic tests.

The dynamic pile test results are summarized as follows:

- (1) The average load-bearing capacity of test piles in group’s C9-30 and C12-30, driven to a depth of 8.50 m at the above construction site, is 813 kN.
- (2) The permissible load on the pile considers the safety factor  $\gamma_k = 1.4$  following paragraph 3.10. of SNiP RK 5.01.-03-2002 “Pile foundations” [3] should thus be taken equal to 580 kN.

### 3 Static Pile Tests

Field tests of S10-30 driven piles with static, vertical-indentation loads were carried out from December 02, 2020 to January 08, 2021 at the site of the main hospital building and the parking structure Fig. 3. Additional information related to the piles is available in the report on static testing by KGS Astana LLP. The tests were carried out on four driven test piles C10-30 numbered 29, 40 (main building) and 62, 66 (parking structure), immersed in the ground to a depth of 9.5 m Fig. 3. Field tests were carried out after a pile “rest” period equal to 30–60 days after driving.

In the static tests, the load was applied to the pile using a 100-ton hydraulic jack “Enerpred DU100P150”, used in conjunction with a “Enerpac P462” pumping station. The jack abutted against a test and loading stand weighing 120.0 tons (Fig. 4).

Table 1 Dynamic pile test results

No.	Pile mark 30 × 30 cm	Depth of driving piles into the ground (m)	Abs. marks of the bottom (tip) of the pile (m)	Drop height of the striking part during driving (m)	Failure of piles during driving (cm)	Date of finishing control piles	The height of the fall of the striking part during finishing, (m)	Failure of piles during finishing (cm)	Partial value of ultimate resistance of piles (kN)	Bearing capacity of piles (kN)
1	3	5	6	8	9	10	11	12	13	14
1	C10-30	9.50	330.46	0.40	2.00	13.1.2021	0.30	0.34	813	813
2	C10-30	9.50	330.93	0.40	1.25		0.30	0.30	869	
3	C10-30	9.50	330.61	0.40	2.00		0.30	0.27	919	
4	C10-30	9.50	330.68	0.40	1.25		0.30	0.22	1025	
5	C10-30	9.50	330.34	0.40	1.66		0.30	0.30	869	
6	C10-30	9.50	330.84	0.30	1.25		0.30	0.20	1078	
7	C12-30	9.50	330.44	0.40	1.11		0.30	0.60	590	
8	C12-30	9.50	330.53	0.40	1.42		0.30	0.86	783	
9	C12-30	9.50	330.59	0.40	1.42		0.30	0.46	682	
10	C12-30	9.50	330.69	0.40	1.00		0.30	0.70	542	
11	C12-30	9.50	330.47	0.40	1.00		0.30	0.53	631	
12	C12-30	9.50	330.78	0.40	1.42		0.30	0.84	789	
13	C10-30	9.50	330.28	0.40	2.50		0.30	0.40	744	
14	C10-30	9.50	330.56	0.30	2.50		0.30	0.30	869	
15	C10-30	9.50	330.70	0.40	3.33		0.30	0.56	620	
16	C10-30	9.50	330.83	0.40	2.50		0.30	0.30	869	
17	C10-30	9.50	330.84	0.30	1.66		0.30	0.30	869	

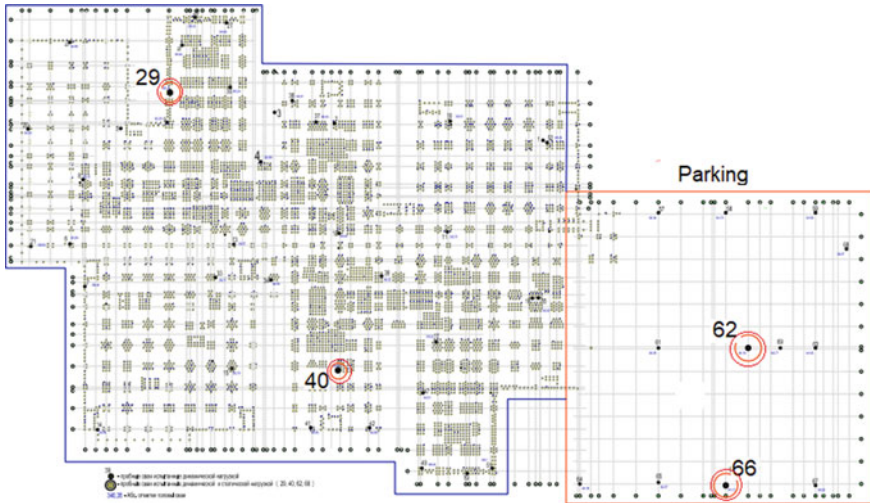


Fig. 3 Test pile layout plan

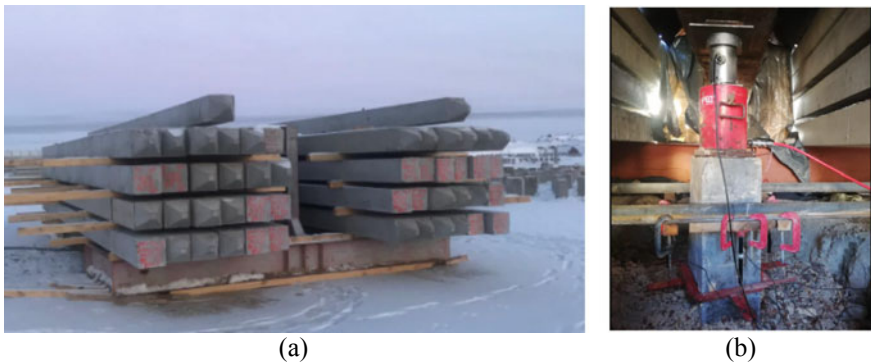


Fig. 4 a Loading stand. b Jack with the reference system

The load was recorded with a pressure gauge of MA100VU100 type with a graduation rate of 20 atm ( $\text{kgf/cm}^2$ ) and a digital dynamometer of the “Load Cell” type connected to the SLT2 monitoring system, capable of reading a maximum value 1000 atm ( $\text{kgf/cm}^2$ ). The process is described in detail in previously published articles [4–6].

The movement of each pile was measured by two 6PAO deflection meters with a scale division of 0.01 mm, and by four digital electronic displacement transducers of type 027DG1, 027DG2, 027DG3, 027DG4 working in conjunction with the aforementioned SLT2 monitoring system. The devices that are part of the SLT2 system are specially designed to monitor static load testing of piles following Eurocode 7. This system provides the ability to monitor static load testing of piles at a distance of up to 25 m and allows personnel (testers) to remotely monitor behind the settlement of the

piles and the actual load on the pile without approaching the potentially dangerous zone of the test site structure, where the system is under high pressure and load.

The piles were tested with static, stepwise increasing loads. This consisted of five load steps of 120 kN (80 atm), followed by a load of 60 kN (40 atm). The maximum load for pile No. 62 was 840 kN; for piles Nos. 29, 40, and 66, the maximum load was 960 kN. The associated displacements of the piles were 48.01, 40.14, 40.12, 40.91 mm, respectively. Each pile was unloaded in steps, with each unloading step being observed for at least 15 min. After complete unloading (to zero), observation of the elastic displacements of the pile was carried out for 60 min, with the movement of the piles being recorded every 15 min. Table 2 and Fig. 5 summarize the information related to the four piles involved in the static tests [7].

The static pile test results are summarized as follows:

- (1) The bearing capacity of the piles test at the locations of the main hospital building and the parking structure were 990 and 780 kN, respectively.
- (2) The permissible pile load, taking into account the safety factor  $\gamma_k = 1.2$  following clause 4.4.1.11. SP RK 5.01–103-2013 “Pile foundations” [3] should be taken equal to 750 and 650 kN for the main hospital building and parking structure locations, respectively.

## 4 Conclusions

- (1) Based on the results of dynamic and static tests, it is possible to determine the permissible load for piles [8] successfully.
- (2) Dynamic tests are needed for a preliminary assessment of the dynamic bearing capacity and the possibility of driving piles in different parts of a construction site under different soil conditions.
- (3) Static indentation test results must be considered when determining the correct pile length.
- (4) The bearing capacity of the pile, determined by a dynamic test, is approximately 11% lower than during static tests.

**Table 2** Static pile test

Pile No.	Pile number Mark and pile cross-section	Depth of immersion of piles in the ground (m)	Pile sinking date	Test start date	Maximum applied load (kN)	Displacement at the highest applied load (mm)	Partial value of ultimate resistance (kN)	Bearing capacity of piles (kN)
No. 62	C10-30, 30 × 30	9.5	05.11.20 y	07.12.20 y	840	48.01	780	780
No. 66		9.5	05.11.20 y	14.12.20 y	960	40.14	900	
No. 29		9.5	04.11.20 y	22.12.20 y	960	40.12	900	900
No. 40		9.5	04.11.20 y	04.01.21 y	960	40.91	900	

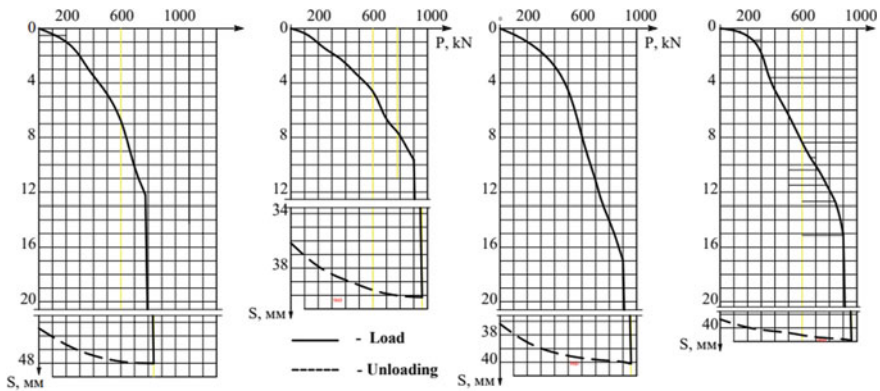


Fig. 5 Pile static test results

## References

1. GOST 5686-2012. (2012). Methods for field testing by piles. In *Research institute of bases and underground structures*.
2. MSP 5/01-101-2003. (2003). In *Design and installation of pile foundation* (pp. 4–8).
3. SP RK 5.01-103-2013. (2013). In *Pile foundations*. Almaty, Kazakhstan, (In Russian): KAZGOR.
4. Tulebekova, A. S., Zhussupbekov, A. Z., Shakhmov, Z. A., & Yenkebayev, S. B. (2012). Experience of testing according to international standard ASTM on problematical soil ground of Astana. *Bulletin LN Gumilyov Eurasian National University*, 2, 126–131.
5. Zhussupbekov, A. Z., RE, L., Omarov, A. R. (2016). The applications of dynamic and static piling tests of Astana. *Japanese Geotechnical Society Special Publication*, 2(79), 2726–2729.
6. Zhussupbekov, A., Omarov, A., Zhukenova, G., & Tanyrbergenova, G. (2017). Pile foundations of mega projects: New railway station and LRT in problematical soil ground of Astana. *Procedia Engineering*, 189, 511–518.
7. Yenkebayev, S. B. (2012). Comparison results of static and dynamic load test at the construction site of Astana. In *Proceeding of Korea-Kazakhstan Joint Geotechnical Seminar* (pp. 115–121). Incheon, Korea.
8. Tulebekova, A. S., & Zhussupbekov, A. Zh. (2020) Geotechnical specificity of international requirements and traditional standards in pile testing: Monograph. L.N. Gumilyov Eurasian National University (pp. 111). Moscow University Press.

# Vertical Displacement Analysis of Embedded Square Foundation Under Vertical Dynamic Load



Abdulrahman Ahmed Najm, Bayar J. AL-Sulayvani,  
and Mohammed N. Jaro

**Abstract** The aim of this research is to study the effect of embedment depth of square foundation subjected to dynamic machine loading on the resonance displacement of foundation. In order to validate the current theoretical method, a comparison with the experimental investigation was conducted regarding the vertical displacement. The foundation embedment depth ratio, which is defined as a ratio of embedment depth to the total depth of foundation, was taken as (0, 25, 50, 75, 100) %. The foundation embedment depth ratio affected the resonance displacement of the foundation due to changing both dynamic coefficients of damping and stiffness while applying dynamic machine loads. In addition to the embedment depth ratio of the foundation, the effect of both of dimension of square foundation ( $2B$ ) and dimensionless frequency ( $a_0$ ) on the resonance frequency was investigated. Results showed a high level of convergence between the current theoretical method with the experimental investigation regarding vertical displacement. The difference of vertical displacement results between the two methods ranged between ( $7 \times 10^{-4}$  to  $5 \times 10^{-3}$ ) mm. It was also concluded that the resonance frequency decreases with the percentage increment of foundation embedment and dimension of square foundation and with a decrement of the dimensionless frequency ( $a_0$ ).

**Keywords** Embedment depth · Square foundation · Resonance displacement · Machine load · Dynamic coefficient

---

A. A. Najm (✉) · B. J. AL-Sulayvani · M. N. Jaro  
Civil Engineering Department, University of Mosul, Mosul, Iraq

B. J. AL-Sulayvani  
e-mail: [dr.bayar.alsulayvani@uomosul.edu.iq](mailto:dr.bayar.alsulayvani@uomosul.edu.iq)

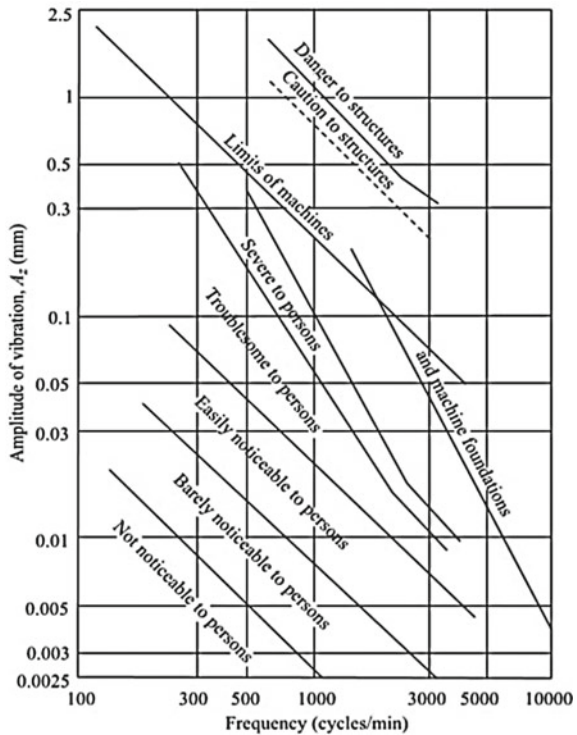
M. N. Jaro  
e-mail: [m.jaro@uomosul.edu.iq](mailto:m.jaro@uomosul.edu.iq)

# 1 Introduction

Studying the effect of embedment of foundation on displacement under dynamic load is important from a practical point of view. It was found that there is some deficiency in this direction of researches due to a little interest comparing with another field of soil dynamics. It is clear that the soil response under machine dynamic loads differs from that under static loads. However, the elastic half-space theory, which is usually used during dynamic analysis of foundation vibration, assumed that only low strain is permissible, i.e., foundation undergo low vibration amplitude [1]. Figure 1 shows the allowable vertical amplitude for a wide range of frequencies. The foundation embedment depth ratio affected the foundation displacement due to changing both dynamic coefficients of damping and stiffness while applying dynamic machine loads. Mohammed et al. [2] studied the effect of dynamic damping ( $C_{dyn.}$ ) and dynamic stiffness ( $K_{dyn.}$ ) on the maximum vertical displacement of surface circular rigid foundation. They concluded that the maximum displacement affected by dynamic stiffness for low values of dimensionless frequency ( $a_0$ ) is affected more by dynamic damping.

Mbawala et al. [4] conducted a series of experimental field investigations to study the effect of embedment on square foundation subjected to vertical vibration. It was

**Fig. 1** Allowable vertical vibration amplitudes [3]





found that increasing the embedment depth decreases the displacement and amplitude at resonance. Khalid et al. [5] performed an experimental model to study the effect of the depth of embedment on the amplitude of circular foundation resting on dry sandy soil. It was found from this study that the amplitude of displacement decreases with changing the depth of embedment from zero to 0.5B and then to B (B: footing width). The percentage of reduction ranged between 4 to 39% at depth 0.5B and about 37 to 77% at depth B.

## 2 Vertical Displacement of Square Surface Foundation

The first step toward analysis of embedded foundation includes the estimation of vertical displacement of surface foundation, which consequently includes estimation the vertical dynamic damping and stiffness [6].

$$K_{dyn} = \eta \cdot k_z \tag{1}$$

$$k_z = [2GB/(1 - \nu)](0.73 + 1.54x^{0.75}) \tag{2}$$

where

- $K_{(dyn)}$ : vertical dynamic surface stiffness.
- $\eta$ : dynamic stiffness coefficient.
- $k_z$ : static vertical stiffness for surface square foundation.
- G: shear modulus of soil.
- $\nu$ : poisson’s ratio of soil.
- B: half side length of square foundation.
- $x = \frac{A_b}{4B^2}$  for square foundation,  $x = 1$ .
- $A_b$ : foundation base area

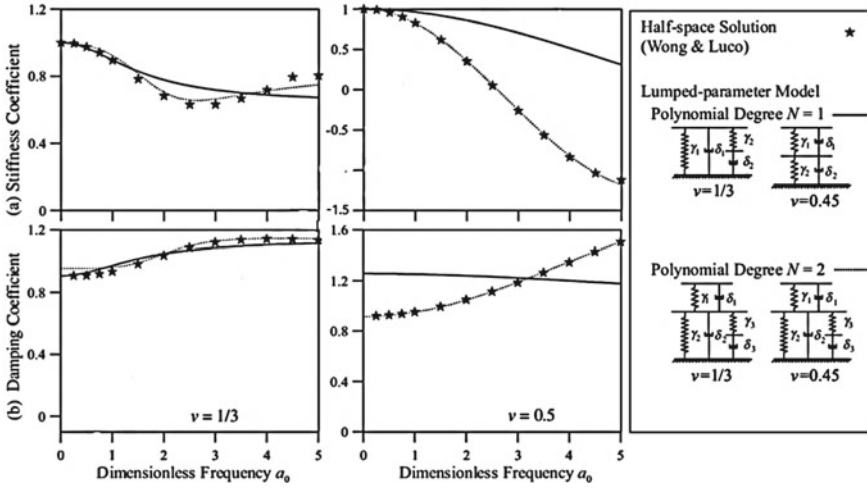
$$C_{dyn} = \lambda \cdot c_z \tag{3}$$

$$c_z = \frac{3.4r_o^2}{1 - \nu} \sqrt{\rho G} \tag{4}$$

where

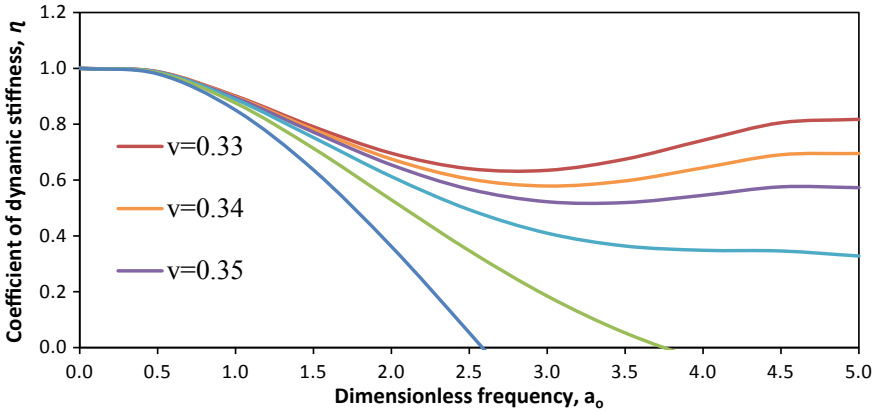
- $C_{dyn}$ : vertical dynamic surface damping.
- $c_z$ : Static vertical damping for surface foundation.
- $r_o$ : equivalent radius for square foundation,  $r_o = \frac{2B}{\sqrt{\pi}}$ .
- $\rho$ : density of the elastic material (soil).

Figure 2 shows the variation of both dynamic stiffness and damping coefficients ( $\eta$  and  $\lambda$ ) respectively with dimensionless frequency ( $a_o$ ) for Poisson’s ratio  $\nu = 0.33$  and  $\nu = 0.5$ . These relationships were suggested by Wu et al. [7]. AL-Obadee [8] developed the above relationships between the dimensionless frequency ( $a_o$ ) and



**Fig. 2** Correlation between stiffness coefficient (a), damping coefficient (b) and dimensionless frequency ( $a_0$ ) [7]

dynamic stiffness and damping coefficients to include additional values of Poisson’s ratio (i.e.,  $\nu = 0.34, 0.35, 0.37, 0.42$ ) as shown in Figs. 3 and 4.



**Fig. 3** Correlation between dynamic stiffness coefficient and dimensionless frequency [8]

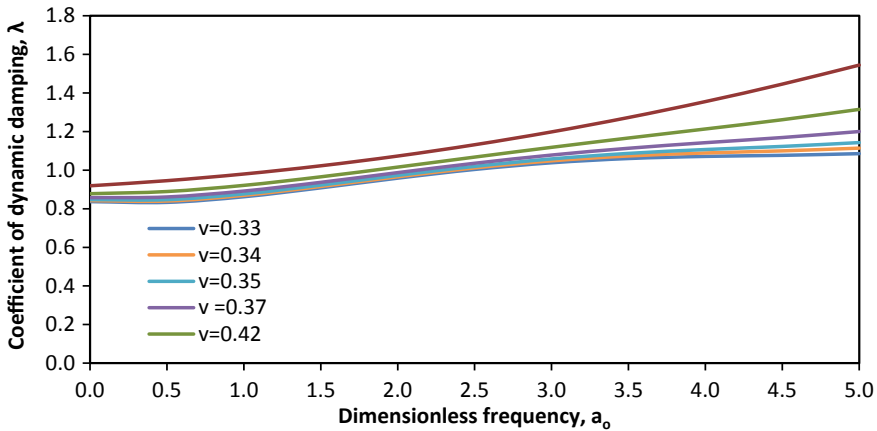


Fig. 4 Correlation between dynamic damping coefficient and dimensionless frequency [8]

### 3 Effect of Square Foundation Embedment on the Vertical Displacement

The aim of the current study is to find the convergence of the result of vertical displacement calculated from the theoretical method with those obtained from the experimental study conducted by Mbawala et al. [4], as mentioned before. After verification the results with the experimental study, the current research extended to find the effect of some parameters on the vertical displacement at the resonance of the square embedded foundation. These parameters are dimensions of square foundation ( $2B = 3, 4, 5, 6$ ) m and dimensionless frequency ( $a_0 = 0, 0.25, 0.5, 0.75, 1.0$ ). In an experimental study conducted by Mbawala et al. [4], a concrete footing with dimensions of  $1200 \times 1200$  and  $1240$  mm depth was cast in place. The space between the soil and sides of the foundation was backfilled and compacted in layers of (150 mm) each. A series of vibration tests were conducted at different levels of embedment (i.e., 310, 620, 930, 1240 mm). A harmonic vertical force was applied to the foundation at frequencies ranged from 10 to 100 Hz. The force amplitude was constant at each frequency as shown in Fig. 5. Figure 6 shows the soil-foundation model used to define vertical displacement of the foundation.

Because that the minimum value of Poisson’s ratio estimated by AL-Obadee [2] was 0.33, while the experimental analysis for Mbawala et al. [4] conducted for  $\nu = 0.25$ , the following formulas were used to calculate both of dynamic stiffness and damping coefficients of soil as:

$$\eta = 1 - b_1 \frac{(b_2 a_0)^2}{1 + ((b_2 a_0)^2)} - b_3 a_0^2 \tag{5}$$

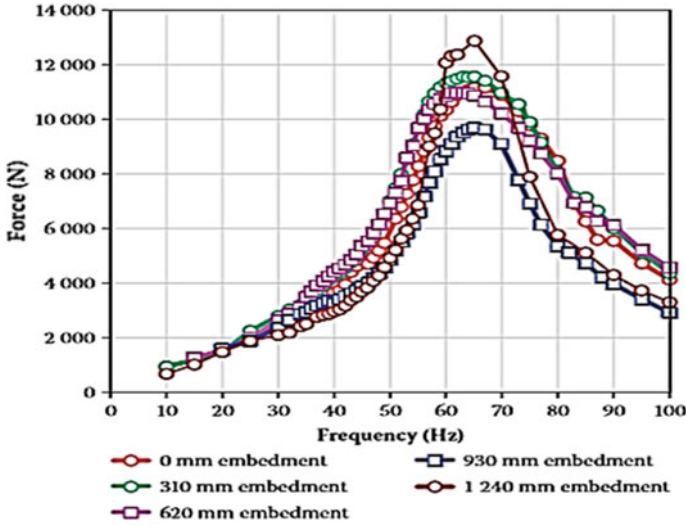


Fig. 5 Correlation between frequency and force for different values of embedment depth [4]

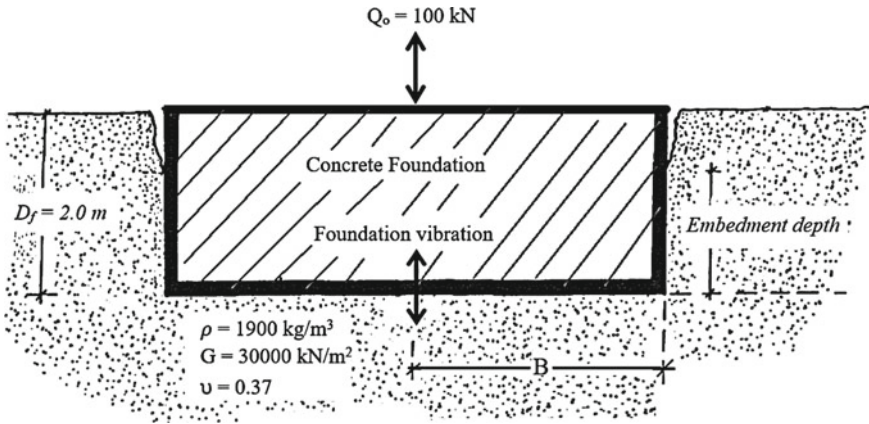


Fig. 6 Soil—foundation model

$$\lambda = b_4 + b_1 b_2 \frac{(b_2 a_0)^2}{1 + ((b_2 a_0)^2)} \tag{6}$$

where

$b_1, b_2, b_3, b_4$ : numerical coefficients, which depend on the Poisson's ratio presented in Table 1.

$a_0$ : dimensionless frequency,  $a_0 = \omega r_0 \sqrt{\frac{\rho}{G}}$ .

$\omega$ : operating frequency (rad/sec).

**Table 1** Numerical coefficients for vertical stiffness and damping [8]

Coefficient	Poisson's ratio		
	0	0.33	0.5
b <sub>1</sub>	0.25	0.35	0
b <sub>2</sub>	1	0.8	0
b <sub>3</sub>	0	0	0.17
b <sub>4</sub>	0.85	0.75	0.85

The numerical coefficients b<sub>1</sub>, b<sub>2</sub>, b<sub>3</sub>, b<sub>4</sub> for ν = 0.25 are easily obtained from Table 1 by linear interpolation. After calculating the surface dynamic stiffness in Eq. 1 and dynamic surface damping in Eq. 3, the effect of embedment of foundation can be estimated by finding both dynamic embedded coefficients for stiffness (K<sub>dyn. emb.</sub>) and damping (C<sub>dyn. emb.</sub>) as:

$$K_{dyn.emb.} = \eta \cdot k_{z.emb.} \cdot k_{emb.(\omega)} \tag{7}$$

$$k_{z.emb.} = k_{z.sur.} \cdot [1 + (1/21)(D_f/B)(1 + 1.3x)] [1 + 0.2(A_w/A_b)^{2/3}] \tag{8}$$

The dynamic stiffness Coeff. k<sub>emb. (ω)</sub> expressed as

$$k_{emb.(\omega)} = 1 - 0.09(D_f/B)^{3/4} a_0^2 \quad (\text{For fully embedded}) \tag{9}$$

$$k_{emb.(\omega)} = 1 + 0.09(D_f/B)^{3/4} a_0^2 \quad (\text{In a trench}) \tag{10}$$

where

D<sub>f</sub>: total depth of foundation.

The dynamic stiffness coefficient for partial embedment can be estimated by taking into account the two cases, i.e., fully embedment and trench embedment, based on each value of embedment (linear interpolation) [6]. The embedded damping estimated as:

$$C_{dyn.emb.} = C_{z dyn.} + \rho V_s A_w \tag{11}$$

where

C<sub>dyn. emb.</sub>: embedded dynamic damping.

C<sub>z dyn.</sub>: surface dynamic damping.

V<sub>s</sub>: shear wave velocity,  $V_s = \sqrt{\frac{G}{\rho}}$ .

A<sub>w</sub>: sidewall area (contact area).

For comparison the results with experimental study, maximum displacement at any operating force and frequency calculated by [1]:

$$Az = \frac{Q_o}{K_{(dyn.emb.)} \sqrt{\left[1 - \left(\frac{\omega^2}{\omega_n^2}\right)\right]^2 + 4D^2 \times \left(\frac{\omega^2}{\omega_n^2}\right)}} \tag{12}$$

where

$\omega$ : operating frequency.

$\omega_n$ : natural frequency.

D: damping ratio.

In addition to the above comparison between experimental and theoretical studies, the current study investigates the effect of some parameters on the vertical displacement at the resonance of the square embedded foundation. These parameters are embedment depth, dimensions of square foundation, and dimensionless frequency ( $a_o$ ). The resonance displacement ( $A_{z\ resonance}$ ) calculated by [1]:

$$Az_{resonance} = \frac{Q_o}{K_{(dyn.emb.)} 2D \sqrt{1 - D^2}} \tag{13}$$

### 4 Results and Discussion

Figure 7. shows a comparison of displacements calculated from a current theoretical study with those obtained from the experimental investigation. The difference of displacement results between theoretical and experimental studies ranged between  $((7 \times 10^{-4}$  to  $5 \times 10^{-3})$  mm. This convergence between the two studies gives big reliability for using the theoretical method to analyze displacement of embedded

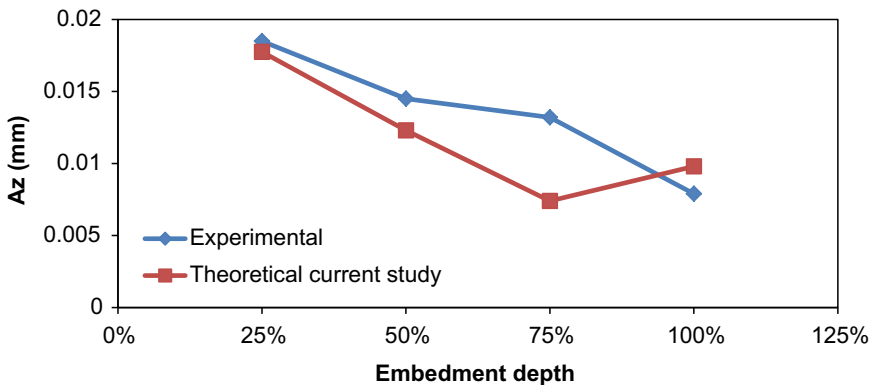
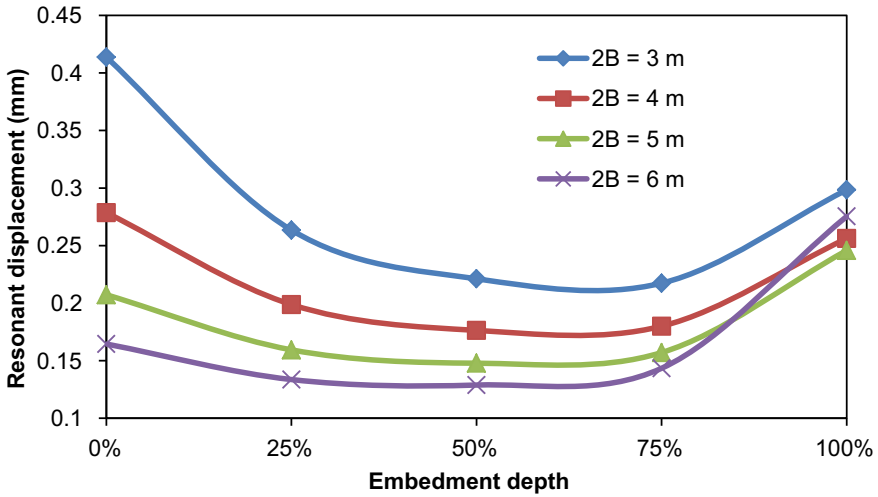
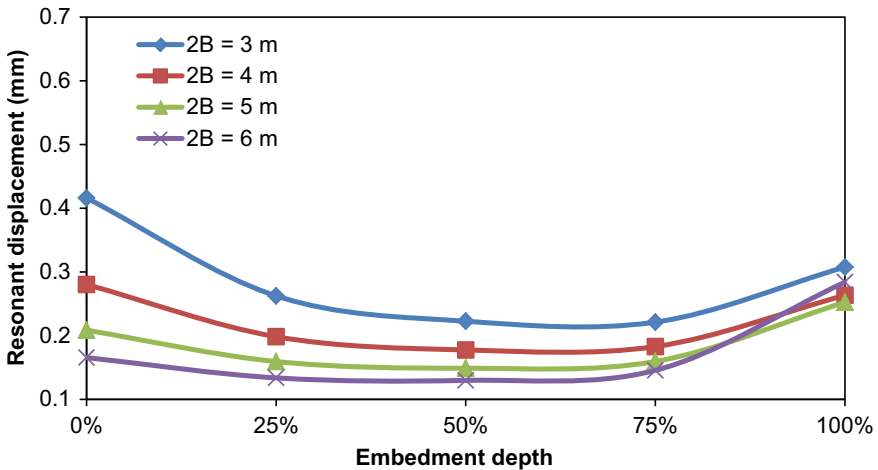


Fig. 7 Comparison of displacements between theoretical study and experimental investigation



**Fig. 8** Maximum resonance displacement of square foundation versus percentage of embedment (for  $a_0 = 0.25$ )



**Fig. 9** Maximum resonance displacement of square foundation versus percentage of embedment (for  $a_0 = 0.5$ )

square foundation. During studying the effect of each of embedment depth, dimensions of foundation, and dimensionless frequency ( $a_0$ ) on the resonance displacement, it assumed that the soil has a density of ( $1900 \text{ kg/m}^3$ ), shear modulus  $G$  of ( $30,000 \text{ kPa}$ ), Poisson's ratio  $\nu$  of ( $0.37$ ), the amplitude of the exciting force  $Q_0$  equal to ( $100 \text{ kN}$ ) and foundation depth equal to ( $2 \text{ m}$ ).

Figures 8, 9, 10 and 11 show the correlation between the maximum resonant displacement of square foundation and percentage of embedment for dimensionless frequency ( $a_0 = 0.25-1.0$ ), respectively. It can be seen that the maximum resonance displacement decreases with increasing the percentage of embedment and then increases. In general, the lower values of resonant displacement occur percentage of embedment ranged between (25–75) % for all values of dimensionless frequency ( $a_0$ ) and for all values of dimensions of foundation. It can also be seen from these

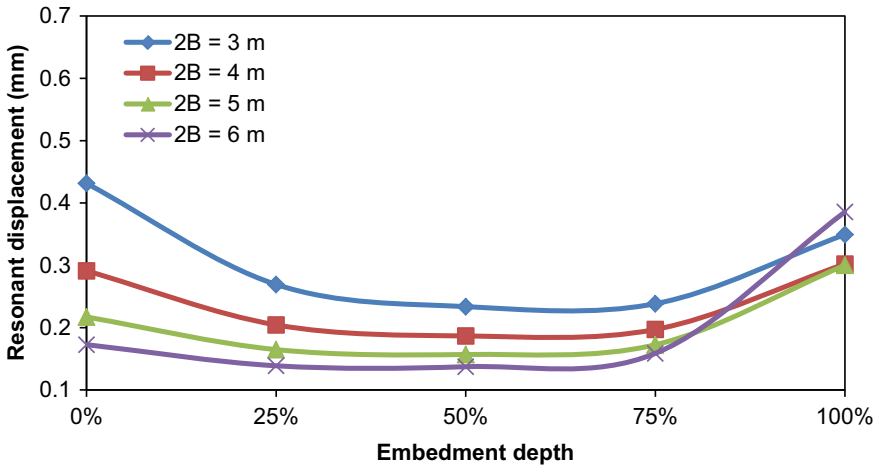


Fig. 10 Maximum resonance displacement of square foundation versus percentage of embedment (for  $a_0 = 0.75$ )

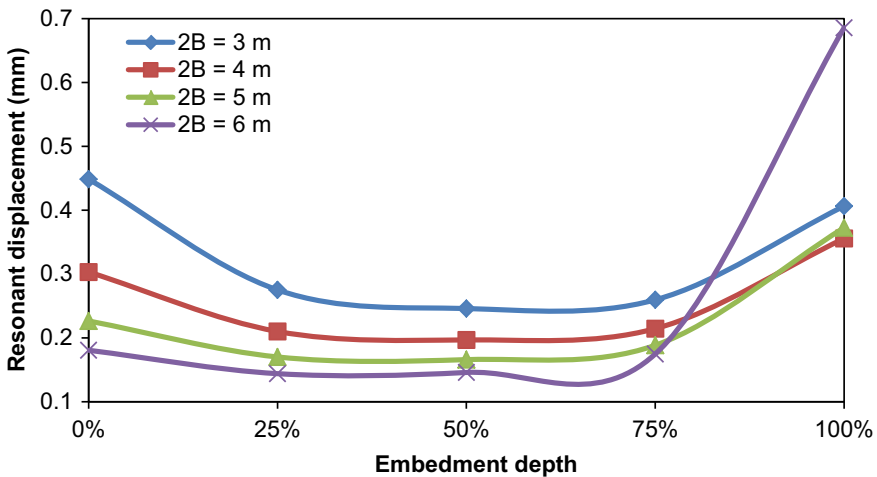
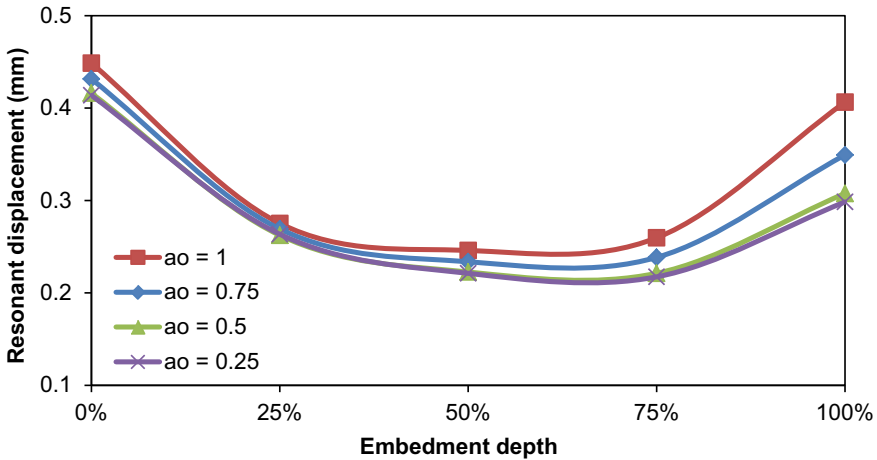


Fig. 11 Maximum resonance displacement of square foundation versus percentage of embedment (for  $a_0 = 1$ )





**Fig. 12** Maximum resonance displacement of square foundation versus percentage of embedment (for  $2B = 3$  m)

Figures that the resonant displacement decreases with increasing the dimensions of the square foundation. There is some inconsistent behavior that can be noted in resonance displacement, especially for the large dimension of foundation ( $2B = 6$  m), the high value of dimensionless frequency ( $a_0$ ), and for a percentage of embedment depth more than (80%). This behavior is due to the reduction in dynamic soil stiffness ( $K_{dyn}$ ). Referring to Eqs. 9 and 10, it can be clearly noted that the dynamic stiffness coefficient ( $k_{emb}$ ) decreases with increasing embedment depth and dimensionless frequency ( $a_0$ ) (for fully embedment, Eq. 9. In other words, with increasing embedment depth and dimensionless frequency, the effect of full embedment Eq. 9 becomes more than the effect of in trench (Eq. 10). As a result, dynamic soil stiffness decreases. The effect of dimensionless frequency ( $a_0$ ) on the resonant displacement is illustrated in Figs. 12, 13, 14 and 15, for ( $2B = 3-6$  m) respectively. The resonant displacement decreases with decreasing of dimensionless frequency ( $a_0$ ), and this decrement was a low percentage of embedment, less than 25%. The inconsistent behavior, which has been mentioned above, can also be seen in Fig. 15 for ( $2B = 6$  m,  $a_0 = 1.0$ ) with an embedment ratio of more than 80%.

## 5 Conclusions

- The comparison of displacement results between experimental investigation conducted by Mbawala [4] and the current theoretical method showed a big convergence. Based on this convergence, the theoretical method can be used to analyze the displacement of the embedded square foundation.

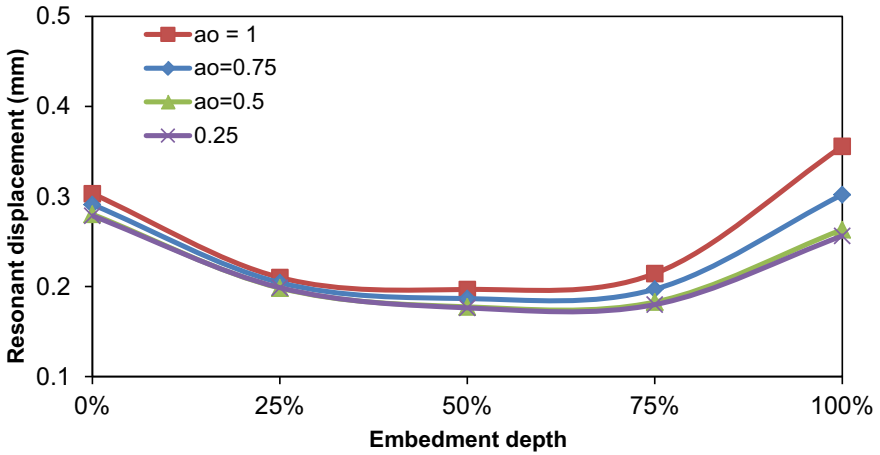


Fig. 13 Maximum resonance displacement of square foundation versus percentage of embedment (for  $2B = 4$  m)

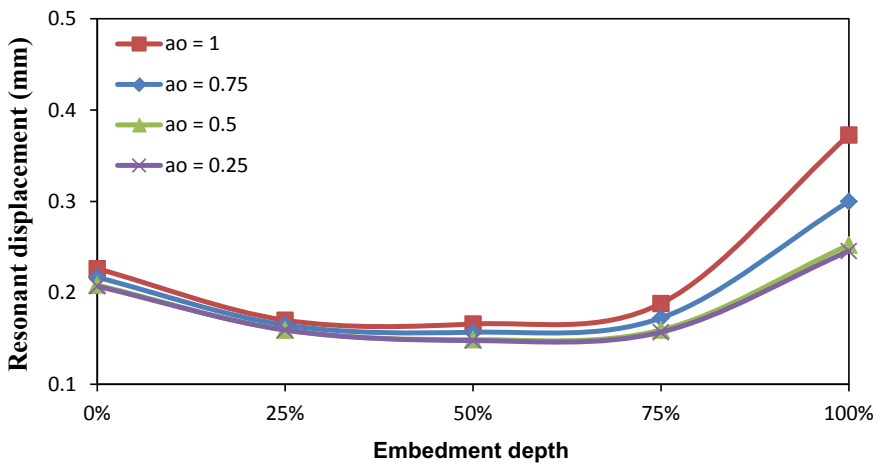
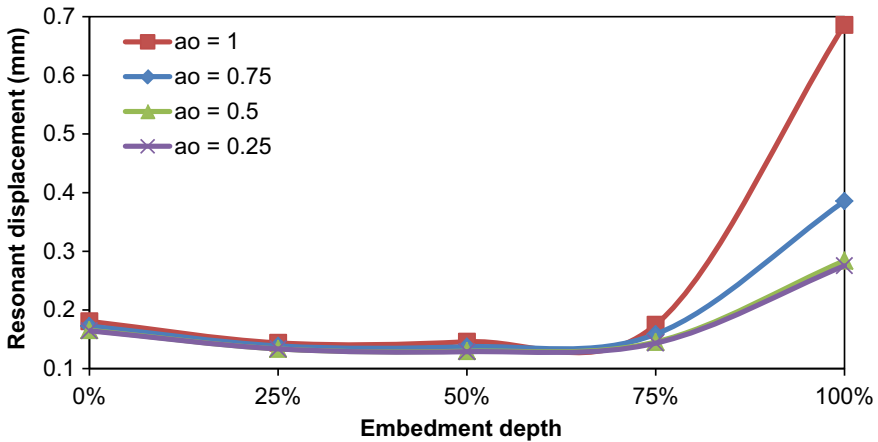


Fig. 14 Maximum resonance displacement of square foundation versus percentage of embedment (for  $2B = 5$  m)

- The resonance displacement decreases with increasing both of percentage of embedment and dimension of square foundation.
- In general, the resonance displacement decreases with decreasing of the dimensionless frequency ( $a_0$ ). The decrement was little for embedment ratio up to 25%.



**Fig. 15** Maximum resonance displacement of square foundation versus percentage of embedment (for  $2B = 6$  m)

## References

1. Das, B. M., & Ramana, G. V. (2011). *Principles of soil dynamics* (2<sup>nd</sup> ed.). Engineering publisher.
2. Mohammed A. I., Al-Sulayvani, B. J., & Jaro, M. N. (2021). Mathematical analysis of vertical vibration for circular rigid foundation resting on soil surface. In: *Lecture notes in civil engineering* (Vol 112). Springer.
3. Richart, F. E. Jr. (1962) Foundation vibrations. *Transaction ASCE*, 127(I), 863–898.
4. Mbawala, S. J., Heymann, G., Roth, C. P., & Heyns, P. S. (2017). The effect of embedment on a foundation subjected to vertical vibration – a field study. *Journal of the South African Institution of Civil Engineering*, 59(4), 26–33, Paper 1377. ISSN 1021-2019.
5. Abdul Kareem, K. W., Fattah, M. Y., Khaled, Z. M. (2020). Effect of embedment depth for circular footing on the amplitude of displacement under dynamic load. *Materials Science and Engineering*, 671, 012024.
6. Gazetas., (1991). Formulas and charts for impedances of surface and embedded foundation. *Journal of Geotechnical engineering, ASCE*, 117(9), 1363–1381.
7. Wu, W. H., & Lee, W. H. (2002). Systematic lumped-parameter models for foundations based on polynomial-fraction approximation. *Earthquake Engineering & Structural Dynamics*, 31, 1383–1412.
8. Veletsos, A. S., & Verbic, B. (1973). Vibration of viscoelastic foundation. *Earthquake Engineering and Structural Dynamics*, 2(1973), 87–102.

# Investigation of Laterally Loaded Pile Response and Cohesionless Soil Deformation Pattern Using PIV Technique



Mohammed A. Al-Neami, Mohammed H. Al-Dahlaki, and Aya H. Al-Majidy

**Abstract** Several high-rise buildings, transmission towers, retaining structures, bridges are braced by piles foundation. These buildings tolerate axial load and succumb to large lateral loads, source from quakes, slope failure, and vehement winds. So, the lateral bearing capacity of the pile is essential for the structure of deep basins. This study gives the outcomes from three models for a single pile embedded in medium dense, dry sand to determine the effect of slenderness ratio ( $L/D$ ) on the response of the lateral load pile and on the adjacent soil deformation, joined with parallel and perpendicular displacement fields measured using a particle image velocimetry (PIV) technology. The results for this study illustrate that the embedment ratio ( $L/D$ ) is an essential parameter that has an effect on the ultimate lateral load. It shows that when the embedment ratio ( $L/D$ ) increased, the ultimate lateral load is also increased. It is found that the ultimate lateral load increased by 16.7% and 28.6% when  $L/D$  increased to 25 and 30, respectively, compared to  $L/D = 20$ . The pile deformation due to the lateral load is influenced by pile slenderness ratio ( $L/D$ ) and magnitude of the applied lateral load and depending on these two parameters, the deflection values altered to positive and passed over zero. The digital image analysis (PIV) shows that the profile effect region and the displacement fields are increased as a lateral load increased. It is observed that the sand close to the ground surface behind the pile travels downward while it moves upward in front of the pile. In this research, a numerical study is done by the PLAXIS 3D analyses and compares the numerical study and experimental work on the load–deflection curve of a single pile. The result of the numerical analyses is in good alignment with those found from the laboratory work for all the ( $L/D$ ) ratios.

---

M. A. Al-Neami (✉) · A. H. Al-Majidy  
Civil Engineering Department, University of Technology-Iraq, Baghdad, Iraq  
e-mail: [40008@uotechnology.edu.iq](mailto:40008@uotechnology.edu.iq)

A. H. Al-Majidy  
e-mail: [41116@student.uotechnology.edu.iq](mailto:41116@student.uotechnology.edu.iq)

M. H. Al-Dahlaki  
Civil Engineering Department, University of Al-Mustansiriyah, Baghdad, Iraq  
e-mail: [mohammedhussein@uomustansiriyah.edu.iq](mailto:mohammedhussein@uomustansiriyah.edu.iq)

**Keywords** PIV technique · Laterally loaded pile · Deflection · Slenderness ratio

## 1 Introduction

Most of the studies around the lateral load piles were done by fastening strain gages on the pile to measure the deflection of pile, the lateral bearing capacity, and soil resistance generated by the pile [1]. It is noteworthy that the activity of the laterally loaded pile depends on the reaction of the soil and vice versa. To examine the movement of the soil around the pile, a few model tests were used. Of these, X-ray computed tomography (CT) was used by Otani et al. [2] to examine three-dimensional sand deformation around a laterally loaded pile. This technique has limited use in geotechnical engineering because of the high cost of CT scanners, but with the advent of digital image processing, geotechnical engineering has used an inexpensive, precise, and complete field image correlation technique, called “particle image velocimetry” (PIV). This research introduces the results for three scale-model tests of pile with different ( $L/D$ ) ratios embedded in medium-dense dry sand to locate the effects of embedment ratio ( $L/D$ ) ratio on the behavior of single piles subjected to lateral loading which include the variation of the load increment and lateral displacement of test at pile caps, lateral displacement along the pile shaft, both vertical and horizontal displacements area around piles due to lateral load movements using the particle image velocimetry (PIV) technique. In addition, a numerical analysis using PLAXIS 3D program is performed for single piles at different ( $L/D$ ) ratios and the obtained results from numerical analysis are compared with laboratory work. The analyses are carried out in order to produce more understanding of piles behavior embedded in medium-dense sand at progressively moving load at the pile head.

## 2 Particle Image Velocimetry Technique

In an optical method to measure instantaneous flow displacement vectors by tracking seeded particle movement. It was initially applied in the field of dynamics of experimental fluids. In other areas, the PIV technique was known by different names, such as digital image correlation (DIC), surface displacement calculation, and computer vision. The PIV approach was used to obtain two-dimensional (2D) displacement fields by correlating two consecutive images. Because of its simple implementation, PIV had been used in several fields since its first application published in 1980s. PIV is currently used in numerous disciplines, including biology, geotechnical engineering, and aerospace engineering. Nowadays, image processing and analysis of soil deformation measurements have become powerful tools with the progress of technology. The deformation measurement system is based on particle image velocimetry (PIV) and has been developed for use in geotechnical testing and observation of soil behavior in the physical modeling of geotechnical constructions [3].

**Equipment Used in PIV Technique.** The seeding particles are part of the PIV mechanism that is fundamentally critical, so it is one of the essential things in the (PIV) technique the presence of colorful targets that move with the soil matrix movement to be tracked by taking sequential pictures and to get 20% of the original soil quantity used in the models was tinted using the black ink and then mixed well with whole soil required to fill the box using mechanical mixing. To perform PIV analysis, a high-resolution camera system is needed to capture multiple frames at pre-chosen speeds and then transfer them to the computer for further analysis. The camera used in this research is Nikon camera (D5200) which is a digital SLR camera with a high resolution  $6000 \times 4000$  (effective megapixels 24.1).

### 3 Experimental Work

**Index Properties of Soil.** A material utilized as a foundation soil for this study is poorly graded sand (SP). Several tests are done as stated by the standard specification to explain and classify both mechanical and physical characteristics of the dry sand utilized in this research. The relative density of sand used is the medium dense density which represents 60%. Table 1 lists the information about the soil.

**The Experimental Box and Pile Model.** An experimental system consists of a rectangular test box that has a width of 750 mm, a height of 740 mm, and a depth

**Table 1** Properties of the sand used in the experimental models

Test	Result value	Specifications
Active sizes: $D_{10}$ , $D_{30}$ , $D_{50}$ , $D_{60}$ (mm)	0.18, 0.3, 0.4, 0.46	ASTM D 422 and ASTM D 2487 [4, 5]
Coefficient of uniformity, $C_u$	2.5	ASTM D 422 and ASTM D 2487 [4, 5]
Coefficient of curvature, $C_c$	1.087	ASTM D 422 and ASTM D 2487 [4, 5]
Specific gravity, $G_s$	2.67	ASTM D 854 [6]
Maximum dry unit weight, ( $kN/m^3$ )	17.54	ASTM D 4254 [7]
Minimum dry unit weight, ( $kN/m^3$ )	15.2	ASTM D 4253 [8]
Maximum void ratio	0.49	...
Minimum void ratio	0.72	...
Relative density, RD	60	...
Friction angle ( $^\circ$ )	38	ASTM D3080 [9]

of 250 mm. The base and two sides of the box were constructed of 6 mm thick steel plate, and one side is made from wood. In contrast, the front side of the box is a Perspex sheet with 18 mm thickness that acted as a viewing window for displacements measurement, as shown in Fig. 1. The pile model employed in this research is a square hollow aluminum pile with closed ends, with 20 mm diameter. The Pile models are manufactured with three different ratios of length to diameter ( $L/D$ ) (20, 25, and 30).

**Horizontal Drive System.** The lateral loading structure consists of the electrically controlled straight hydraulic jack and bolt steel shaft joined together to exert a horizontal load added from one side to the load cell, which linked to a weighing indicator for the object of reading the load that applied from the hydraulic jack. In contrast, the other adjacent of the weight cell is attached to a steel rod that acts as the same as a permeation cone to impose point load on the cap of the pile. The horizontal jack apparatus be composed of a cylinder, control device, and electric jack. The control device is utilized to alter the frequency value (0.5 Hz), which equals the speed of 2.5 mm/min. This apparatus is collected and manufactured by Elway [10]. After the piles were installed and the sand bed had been prepared, and the dial gauges were attached to the pile cap to read the lateral displacement. The camera was prepared in a suitable place to take the photo then the lateral system is being worked. The AC motor is switched on to move the hydraulic jack according to appropriate work. When the lateral dial gauge reading reaches 20 mm displacement reading, the loading is stopped, and the test is ended. The lateral loading system is shown in Fig. 2.

**Fig. 1** Front view of the experimental box





Fig. 2 The lateral loading system

### 4 Model Test Results

#### Effect of the Embedded Ratio (L/D) on the Load-Deflection Curve of Single Pile.

In order to clarify the effect of embedded ratio (L/D) on the horizontal displacement that occurred at the pile head, three ratios are tested (20, 25, and 30). Figure 3 shows the relation of the capacity of lateral load and horizontal movement produced at the single pile. These values present a measurement at the pile head. It can be seen that in single piles, when (L/D) ratio increased, the values of lateral load increased, and this may be attributed to the increase in soil resistance thrust due to an increase in the skin friction area resulted during the soil movement between the pile shafts and surrounding soil to resist the applied lateral load.

The methods used in this research to interpret the test data from lateral load tests and to determine the failure load are differing liable on the acceptable movement of the structure supported by the piles. In general, the acceptance criteria to evaluate the ultimate lateral load is the lower of the following two methods:

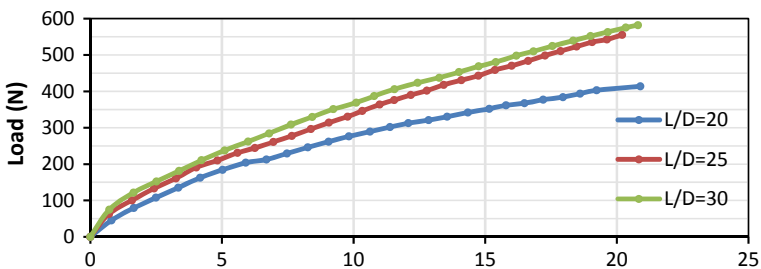


Fig. 3 Relationship between lateral load–displacement for a single pile



**Table 2** Summary of the observed and interpreted ultimate lateral load for a single pile

Embedded length of pile (mm)	Slenderness ratio [L/D]	Observed pile lateral load at test end ( $P_f$ ), (N)	Interpreted ultimate pile lateral load $H_u$ (N)		Adopted ultimate lateral load (N)	% of increasing lateral load compared with L/D = 20
			Intersection method	Load at 6.25 displacement		
400	20	414	228	210	210	–
500	25	555	250	245	245	16.67
600	30	582	272	270	270	28.57

- A failure load at the point of intersection of tangents on the load-movement curve, and
- A failure load is taken at (6.25 mm) lateral displacement or deformation (Table 2).

**Lateral Displacement along with Pile Shaft of Single Piles.** The horizontal displacement along the pile shaft for various lateral load levels is determined by analyzing the images taken for each test. It is worth mentioning that each image is analyzed corresponding to the closest value of the predicted ultimate lateral load and two images before and after it and for the image at the test end (i.e., at 20 mm lateral pile head displacement). However, the time between the selected images is 40 s in general. Figure 4 shows the displacement and the pile for (L/D) ratio (20, 25, and 30), respectively. It is clear that the lateral deflection along the pile shaft is permanently in the direction of lateral load. Based on the slenderness ratio and magnitude of the applied lateral load, the deflection value is altered to the positive and passed by zero. However, at any load level and for all slenderness ratios, the maximum lateral deflections occurred at piles top and then decreased gradually to zero. Figure 4a, b, which represents the results for the short pile, shows that as lateral load increased, the body of the pile is inclined to turn about the inflection point and produces a minor negative deflection (i.e., deflection in the opposite direction of lateral load) nearby to the pile base. The maximum negative deflection occurred precisely in the base of the pile.

However, in Fig. 4c, which represents the long pile results, there is no pile rotation, and the base deflection is always zero. Furthermore, it is noticed that for the prescribed displacement, which equals pile diameter at pile head (i.e., 20 mm), the deflection point (measured from the pile base) for piles with (L/D) = 20 and 25 are found to be about 2.5 D and 6 D respectively. However, a pile with (L/D) = 30 has a fixation point, where all lateral displacement along the pile shaft are positive values decreased to zero at about 11 D from the pile base. It is found that the location of inflection points concerning pile base (for short piles) and point of fixity (for long piles) depends not only on slenderness ratio but also on lateral load level, where it increases as slenderness ratio and lateral load level increases and vice versa. This behavior may be attributed to the increase in confining pressure around the pile shaft,

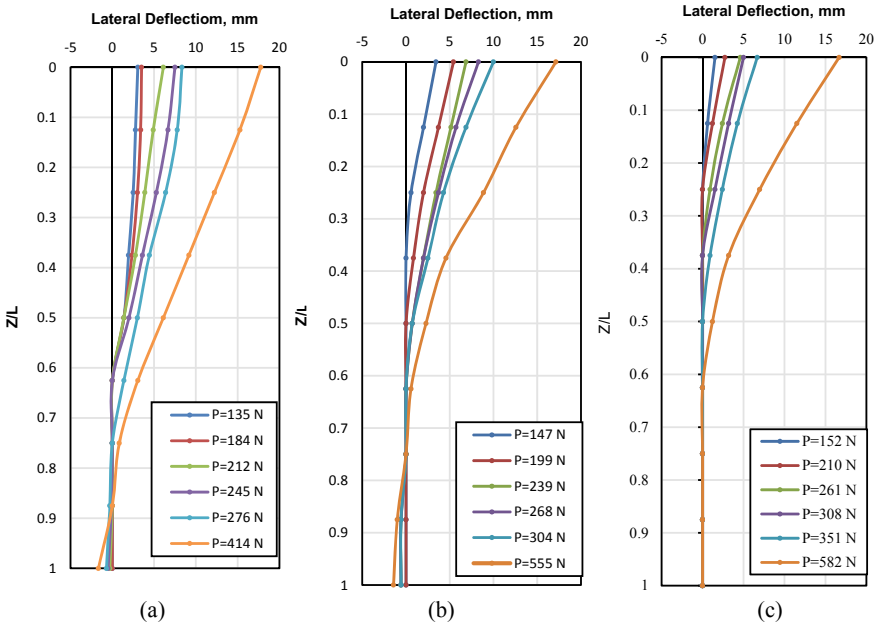


**Fig. 4** Lateral displacement along pile with (L/D) = 20, 25, 30 respectively

which restricts the lateral deflection of the pile shaft near the base. Soil confining pressure increased as the embedment depth of the pile for the same pile diameter increased. Accordingly, for low lateral load level, the confining pressure consumes a large portion of applied lateral load resulting in zero lateral displacements at the pile base.

**Investigation of Lateral Load Single Pile Response and Soil Deformation Patterns Via Particle Image Velocity Method (PIV).** To investigate the deformation of soil around the pile when subjected to lateral load particle image velocity technique (PIV), it had been used for this purpose. (PIV) the system is used to calculate the sand displacement field around a pile subjected to the lateral load, soil displacement field’s visualizations offer a better understanding of the lateral load soil-pile interaction. Fan and Long [11] stated that most of the researches concentrates on the capacities and deflection of piles subjected to lateral load. In contrast, limited data is available on soil displacements about the piles due to the nonlinear, complicated soil-pile interaction. To clarify the effect of embedded ratio (L/D) on the lateral vectorial displacement of both vertical and horizontal displacement fields, three ratios are tested (20, 21, and 30). Figures 5, 6 and 7 show the analysis of the digital image series that corresponds to ultimate lateral load (Hu) for (L/D) = 20, 25, and 30, respectively. These figures display the displacement vectors at the profile and horizontal, vertical, and resultant contour surface fields around the pile. In general, the effect region and the displacement fields are increased as lateral load increased.

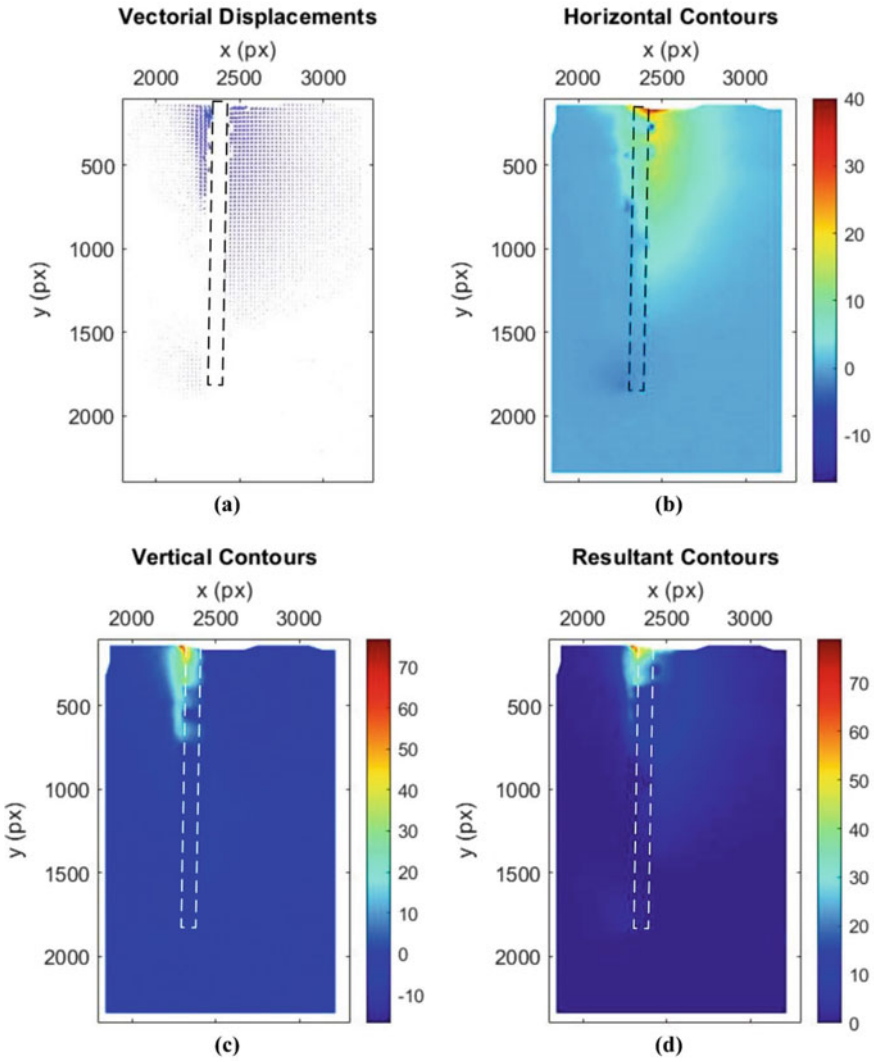


**Fig. 5** Vertical contours of displacement fields with  $(L/D)$  ratio = 20,  $H_u = 210$  N and  $CF = 15.8\%$

In addition, it is observed that the sand neighboring the ground level behind the pile moves downward while it moves upward in front of the pile. The same observation is obtained by Hajjalilue-Bonab et al. [12].

**Comparison on the Load-Deflection Curve of Single Pile.** To equate the findings obtained from the experimental test with 3D-FEM analyses, the PLAXIS 3D analysis was conducted. Figure 8a–c show the comparison of the load–deflection curves of a single pile with  $L/D$  ratio equal to 20, 25, and 30, respectively, obtained from the

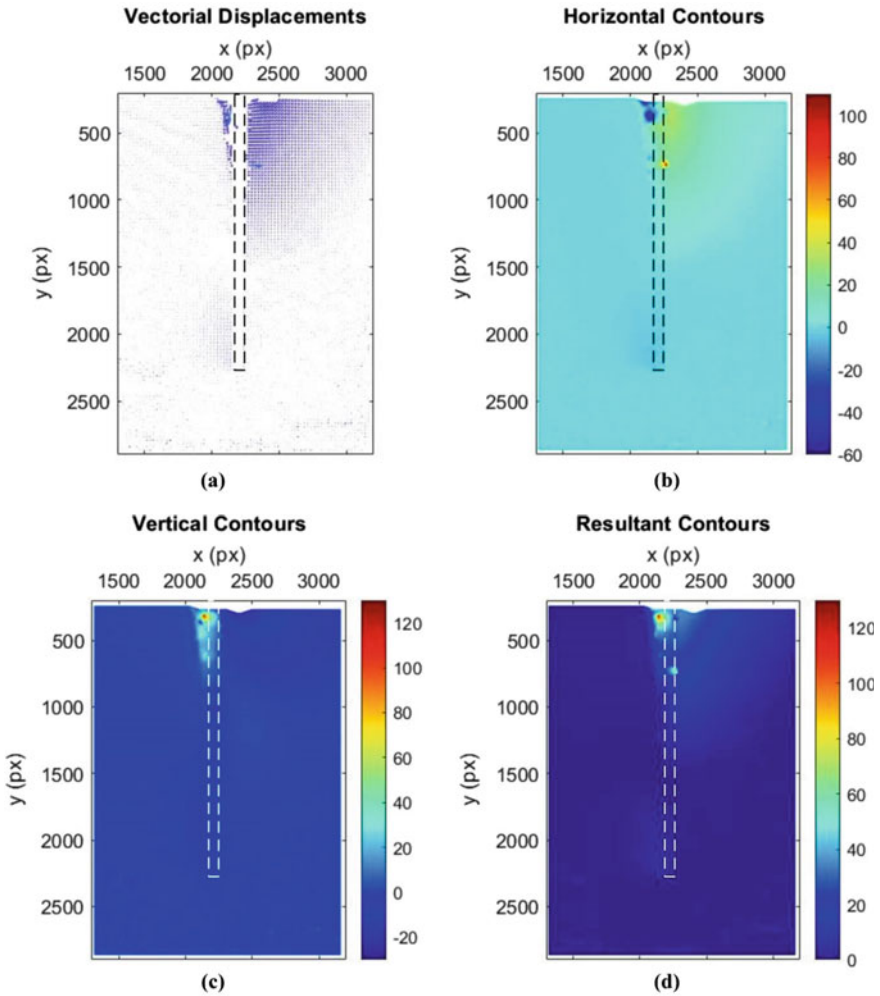


**Fig. 6** Vertical contours of displacement fields with  $(L/D)$  ratio = 25,  $H_u = 245$  N and  $CF = 22.5\%$

experimental work 3D-FEM analyses. It can be seen from Fig. 8a–c that the result of the PLAXIS 3D numerical analyses was in good alignment with those from the experimental work.

## 5 Conclusions

- (1) The relation between the horizontal load and generated displacement is nonlinear behavior for all tested models.

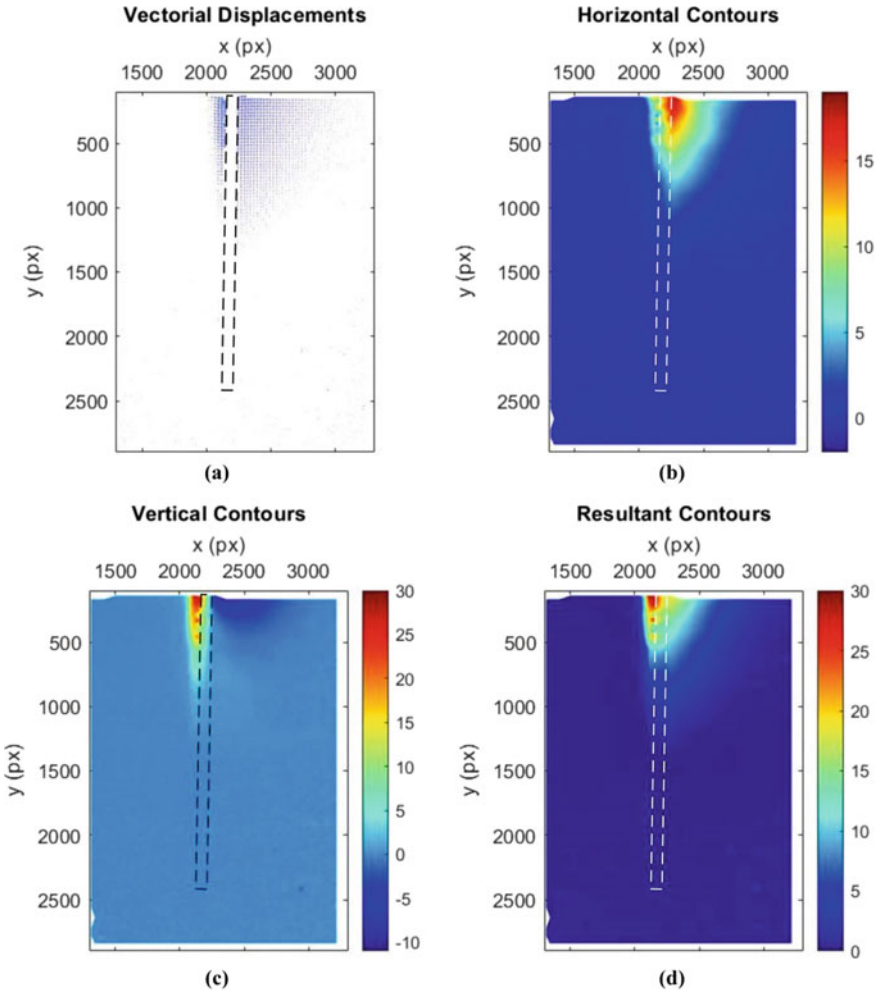
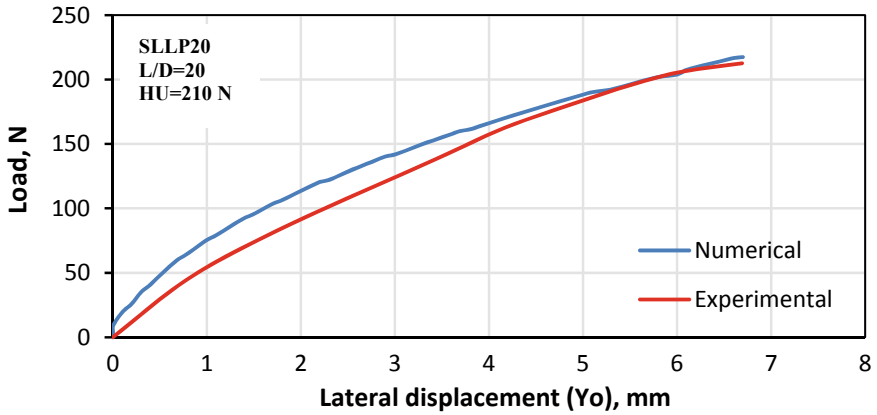
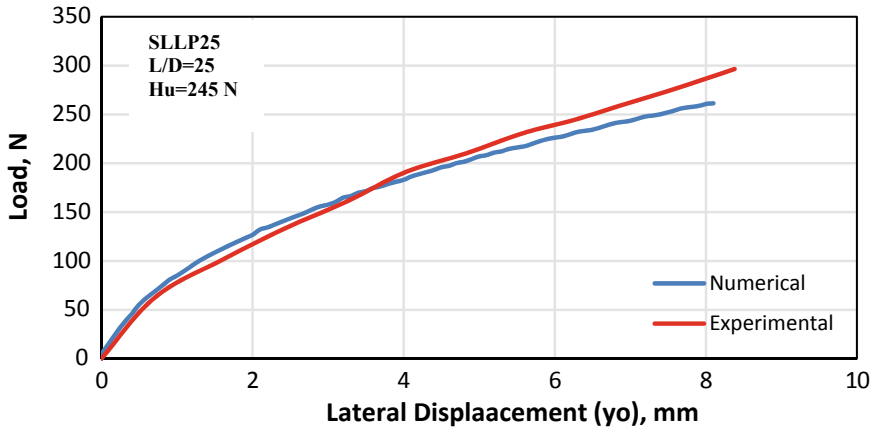


**Fig. 7** Vertical and contours of displacement fields with  $(L/D) = 30$ ,  $H_u = 270$  N and  $CF = 26.8\%$ . **a** Vertical displacement, **b** horizontal displacement, **c** vertical displacement, **d** resultant displacement

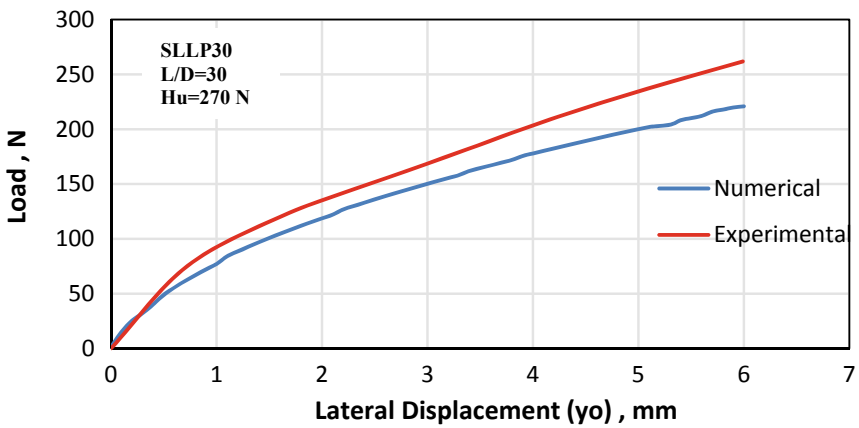
- (2) Increasing the embedment ratio  $(L/D)$  for a single pile causes an increase in the ultimate lateral load. The ultimate lateral load increases by 16.7 and 28.6% when  $L/D$  increased to 25 and 30, respectively, compared to  $L/D = 20$ .
- (3) Deflection values for single piles were altered to positive and permit over zero depending on the slenderness relation and magnitude of the applied lateral load. However, at any load level and for all slenderness ratios, the maximum lateral deflections occurred at piles top and then decreased gradually to zero. In short pile (slenderness ratio  $(L/D) = 20$ , and 25), the lateral load increased, and the body of the pile be inclined to turn about the inflection point and produces



(a)



(b)



(c)

**Fig. 8** Comparison of the experimental work and 3D-FEM analyses of the load-displacement curve of single pile with ratio  $L/D = 20, 25,$  and  $30$  respectively

a minor negative deflection (i.e., deflection in the opposite direction of lateral load) close to the pile base. The maximum negative deflection exactly occurs at the base of a pile. However, for the long pile (slenderness ratio  $(L/D) = 30$ ), pile rotation is not happened and the base deflection is always zero. The deflection point (measured from the pile base) for piles with  $(L/D) = 20$  and  $25$  are found to be about  $2.5 D$  and  $6 D$ , respectively. However, a pile with  $(L/D) = 30$  has a fixation point, where all lateral displacement along the pile shaft are positive values decreased to zero at about  $11 D$  from the pile base.

- (4) The digital image analysis for laterally loaded single pile using particle image velocimetry (PIV) technique and corresponding to ultimate lateral load ( $H_u$ ) shows that the profile influenced zone and the displacement fields are increased as lateral loads increased. Also, the sand neighboring the ground level behind the pile moves downward while it moves upward in front of the pile.
- (5) The PLAXIS 3D analyses computed the load–deflection curve of a single pile show that a good agreement of results can be achieved between the numerical studies by PLAXIS 3D and those obtained from the experimental work for all the  $(L/D)$  ratio.

## References

1. Chiou, J. S., Tai, W. L., Chen, C. H., & Chen, C. H. (2014). Lateral hysteretic behavior of an aluminum model pile in saturated loose sand. *Journal of the Chinese Institute of Engineers*, 37(3), 313–324.
2. Otani, J., Pham, K. D., & Sano, J. (2006). Investigation of failure patterns in sand due to laterally loaded pile using X-ray CT. *Soils and Foundations*, 46(4), 529–535.
3. Liu, J., Yuan, B., & Dimaano, R. (2011). Optical measurement of sand deformation around a laterally loaded pile. *Journal of Testing and Evaluation*, 39(5), 754–759.
4. ASTM D422-63. (2007). *Standard test method for particle-size analysis of soils*. ASTM International.
5. ASTM D2487-06. (2006). *Standard test method for classification of soils for engineering purposes*. West Conshohocken.
6. ASTM Committee D-18 on Soil and Rock. (2010). *Standard test methods for specific gravity of soil solids by water pycnometer*. ASTM international.
7. ASTM D4253. (2006). Test methods for maximum index density and unit weight of soils using a vibratory table. ASTM Standard 16.
8. ASTM D4254–00, 2006. Standard test methods for minimum index density and unit weight of soils and calculation of relative density.
9. ASTM D3080/D3080M. (2011). Standard test method for direct shear test of soils under consolidated drained conditions.
10. Elewi, A. S. (2017). Response of single pile and pile groups to lateral sandy soil movement, PhD. Thesis, Building and Construction Engineering Department, University of Technology, Iraq.
11. Fan, C. C., & Long, J. H. (2005). Assessment of existing methods for predicting soil response of laterally loaded piles in sand. *Computers and Geotechnics*, 32(4), 274–289.
12. Hajjalilue-Bonab, M., Azarnya-Shahgoli, H., & Sojoudi, Y. (2011). Soil deformation pattern around laterally loaded piles. *International Journal of Physical Modelling in Geotechnics*, 11(3), 116–125.

# An Experimental Investigation the Response of Pile Groups to Inclined Cyclic Loading in Sandy Soil



Reyah D. Khurshed and Jasim M. Abbas

**Abstract** In general, inclined cyclic loads applied on the pile foundation are not covered enough in previous studies. Therefore, this paper included a laboratory model on pile groups in sandy soil subjected to inclined cyclic loading in two directions. The angle of inclination that selected in this work is 45 degree. The tests are conducted on  $2 \times 2$ ,  $2 \times 3$ , and  $3 \times 2$  pile groups with aluminum hollow piles. Besides, the raining technique is used to organize the layer of sandy soil. It can be concluded that the group  $2 \times 2$  is more sensitive than another group in the case of an inclined cyclic load. In this case, the lateral resistance of group  $2 \times 2$  decreases from 32 to 55% from another group when used to  $s/d = 3$ , and the results showed that the reduction in bearing capacity of soil in group  $2 \times 3$  about 27.3, 37, and 39.4% from group  $3 \times 2$  for  $s/d = 3, 5$ , and 7, respectively.

**Keywords** Inclined loading · Pile group · Lateral deflection

## 1 Introduction

Deep foundations (i.e., piles and pile groups) are widely benefited to support many structures constructed on weak or soft soils. In general, most piles are exposed to both lateral and vertical loads as well as dynamic loading, which sometimes occurs together [1]. The source of the loadings may be caused by traffic, seasons, tide, currents, waves, wind, earthquakes, ice sheets, blasting operations, plant operations, or rotatory machinery [2]. The vertical and horizontal reactions of piles are commonly estimated alone, not including taking into consideration their potential connections [3]. The horizontal load ability of the pile groups is reliant on the source of loading, the space between the piles, in addition, the nature of the soil, and other factors [4]. Several previous studies using FEM and laboratory models have been taken into explanation the effect of cyclic loading on the lateral pile foundation performance.

---

R. D. Khurshed (✉) · J. M. Abbas  
Civil Engineering Department, University of Diyala, Baqubah, Diyala, Iraq  
e-mail: [eng\\_grad\\_civil032@uodiyala.edu.iq](mailto:eng_grad_civil032@uodiyala.edu.iq)



Some researchers use a three-dimensional (3D) finite-element technique to examine the developed for the dynamic investigation of pile media and pile groups [5]. Additional researches use a (3D) finite element method is worked to analyze the reaction of (R.C) flexible piles to inclined loads. This study concluded that the load inclination is influenced significantly by together the stiffness with the bearing capacity of the soil-pile system [6].

Furthermore, investigational research on  $2 \times 2$  typical pile groups fixed in various kinds of clay soil, the relative density of 90 and 10%, exposed to one-way lateral cyclic loading. It is discovered that the amount of the head level deflections and the maximum bending moment bigger with an increase in the number of loading cycles [7]. Other research included the performance of a single pile exposed to varying static inclined load until failure; from this work, it can be concluded that the inclined load is a large effect on pile group performance [8]. Also, some experimental studies under combined loads (i.e., instantaneous lateral and vertical load). In this case, the influence of the growth in the number of cycles on the horizontal displacement of piles under simultaneous loads is a lesser amount than after piles are exposed to only cyclic horizontal load [9]. And others investigated the lateral behavior of micropile under inclined compressive load in sandy soil. It is found that the lateral capacity of the micropile group appears to increase with the increase of the L/D ratio [10].

Lateral displacement decreases when pile spacing increases in the case of deflection, the difference attributable to pile spacing can be seen in all piles and rows, which is due to the effect of overlap between the soil and the piles in the group [11]. At the first cycles cause the lateral resistance of the pile group will decrease, and when an increasing number of cycles the deflection of the group became constant almost due to the densification of the soil [12].

Therefore, as there are limited experimental studies available on the behavior of pile groups in sandy soil exposed to inclined cyclic lateral loading. In this paper, an effort has been required to study the experimental behavior of pile groups model pile exposed to inclined load at the angle of 45% in the same magnitude in a two-way direction and studying the effects of soil on the pile. Three model pile groups  $2 \times 2$ ,  $2 \times 3$ , and  $3 \times 2$  were embedded in sandy soils and examined under two-way inclined cyclic lateral load to learn the influences of a number of cycles on load-deflection, the effect of cyclic load ratio (CLR), and the effect of spacing between piles.

## 2 Materials Used and Experimental Testing Program

**Soil.** The sandy soil used is collected from Karbala Governorate in the middle of Iraq. The sand properties represented as shown in Table 1.

**Pile and Pile Cap.** Aluminum hollow piles as a circular cross-section at 16 mm diameter in groups  $2 \times 2$ ,  $2 \times 3$ , and  $3 \times 2$  models as shown in Fig. 1. The L/D is equal to 40 in a group where's the space in the direction of loading is different (i.e.,

**Table1** Physical properties of sandy soil

Property	Value
Specific gravity, $G_s$	2.67
Angle of internal friction, $\varphi$ ( $^\circ$ )	35.5
Cohesion, $c$ (kPa)	0
Maximum dry unit weight, $\gamma_{dmax}$ ( $kN/m^3$ )	17
Minimum dry unit weight, $\gamma_{dmin}$ ( $kN/m^3$ )	15.3
Dry unit weight, $\gamma_d$ ( $kN/m^3$ )	16.5
Relative density, $D_r$ (%)	70

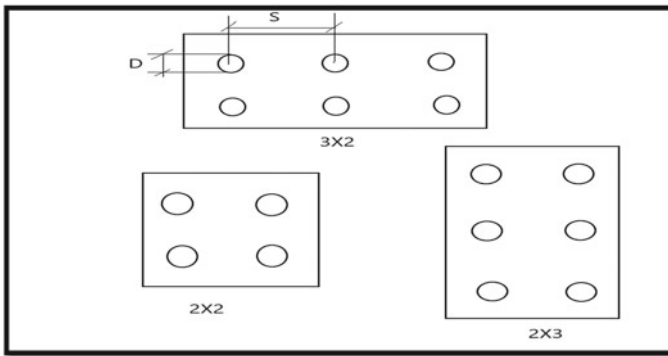


**Fig. 1** Pile group configuration

$s/d = 3, 5, \text{ and } 7$ ). The pile cap is in at the top of piles, leaving 50 mm above the ground surface as a freestanding length for the group.

**Test Setup.** The laboratory tests system is used for applying inclined cyclic lateral loading at angle 45 degrees on pile groups is shown in Fig. 2. In this case, the inclined lateral cyclic loading experiments on model piles group fixed in dry sand inside steel testing container of dimensions  $(1 \times 1 \times 1)$  m.

Lateral inclined cyclic loading is applied to the cap of pile groups. Piles head deflection in-group is measured by using a type of inductively Linear Variable Displacement Transducers (LVDTs). An automatic timer is using to controller the period of loading. A raining technique machine is designed to achieve a uniform soil layer and the required relative density  $D_r$  of 70%. The capacity of the static lateral load is taking as the load equivalent to the deflection of 3.2 mm (20% diameter of the pile) as recommended by Broom’s theory [13]. Which in turn, is necessary to determine the amount of two-way symmetric cyclic lateral loading, which is exposed on pile groups under different cyclic load ratios, CLR of 0.4, 0.6, and 0.8, the frequency used is 0.2 Hz. The period of the cyclic load is constant to 5 s. At the same time, the cyclic load is continued while waiting for 100 cycles in all the tests.

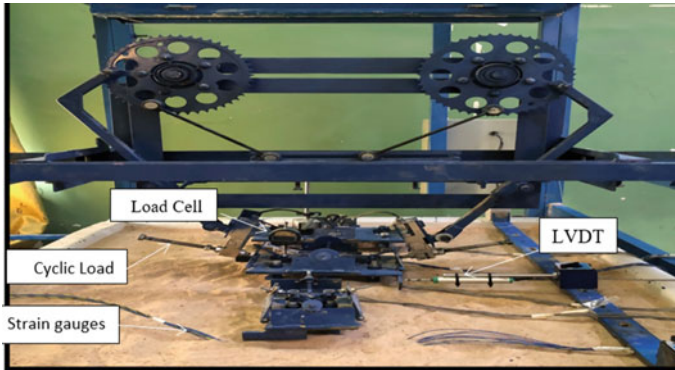


Fig. 2 Laboratory model system of the inclined cyclic loading device

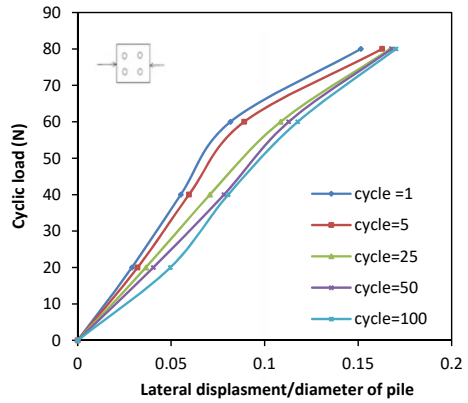
### 3 Results and Discussion

**Influence of Cycles Number of Loading on Lateral Resistance.** Figures 3, 4 and 5 represent a group of piles  $2 \times 2$ ,  $3 \times 2$  and  $2 \times 3$  respectively under inclined cyclic load at three values of  $s/d$  (i.e., 3, 5, and 7); the cycles number used in this study are 1, 5, 25, 50, and 100 to represent the different cases of cyclic loading in natural phenomena. These figures show that lateral deflection increases extensively together with the increase in cycle number of loading, and this reaches 50% from the lower to the upper limit of a number of cycles. This means the lower number is not risky compare with a high number, and this should take into account in the analysis and design for such kind of foundation. Additionally, for  $s/d = 3$ , the lateral deflection usually is greater than in wide spacing; this is due to the short distance between the piles that causes overlap stresses. This is attributing to the growth of the gap at the soil–pile line wherever the stress attention happens. For another comparison, it can seem that the pile group  $3 \times 2$  is safer against inclined loading compared with group  $2 \times 3$ , the decrease in lateral resisting of group  $2 \times 3$  about 27.3, 37, and 39.4% from group  $3 \times 2$  for  $s/d = 3, 5, \text{ and } 7$  respectively.

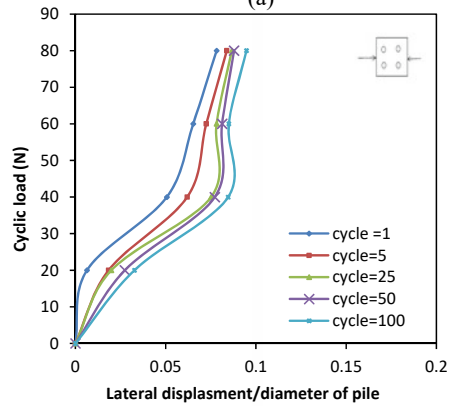
**Influence of Cycles Load Ratio CLR on Deflection of pile groups.** Figures 7, 8 and 9 showing that the lateral deflection of all pile groups with CLR = 0.2, 0.4, 0.6, and 0.8 at frequency 0.2 Hz. The result indicates the group  $(2 \times 2)$  decreases in lateral resistance from 35 to 55% compared with other groups for all spacing. In addition, the lateral resistance of group  $2 \times 3$  is less than in group  $3 \times 2$  with 15.7, 21, and 19.5% for all spacing. The deflection of pile groups generally increases progressively with the increased number of cycles, the deflection rising quickly in the first cycles; this is attributable to the decrease of passive resistance and the degradation in the pile-soil interactive performance and the number of cycles when reaching about [14].

**Influence of Spacing on Lateral Resistance.** It has been observed from Fig. 10 that piles at close spacing (i.e.,  $s/d = 3$ ) deflect extra than the other spacing. This behavior

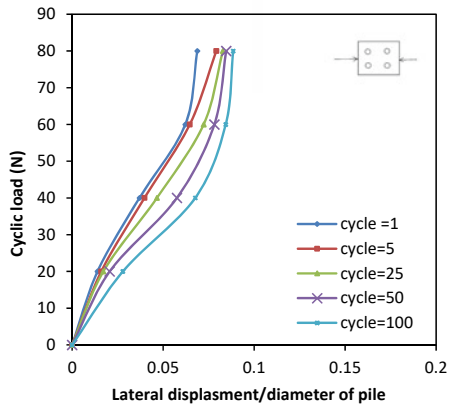
**Fig. 3** Influence of number of cycles on the load–deflection curve of piled groups model under inclined cyclic load  $2 \times 2$  group: **a**  $s/d = 3$ , **b**  $s/d = 5$  and **c**  $s/d = 7$



(a)

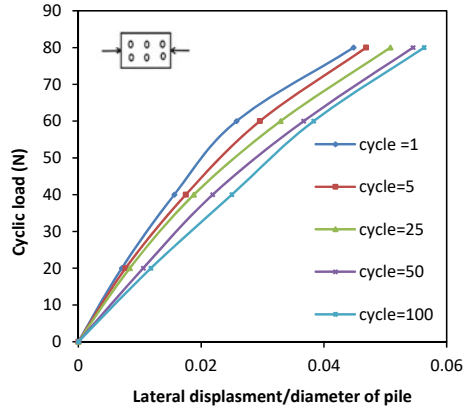


(b)

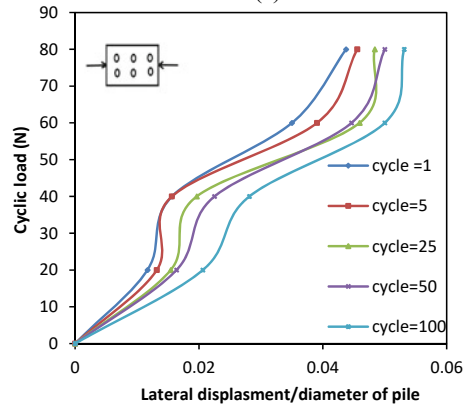


(c)

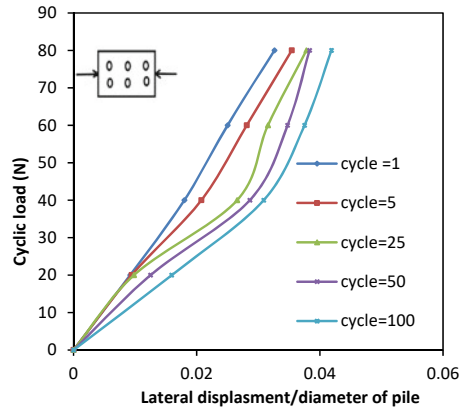
**Fig. 4** Influence of number of cycles on the load–deflection curve of piled groups model under inclined cyclic load  $3 \times 2$  group: **a**  $s/d = 3$ , **b**  $s/d = 5$  and **c**  $s/d = 7$



(a)



(b)



(c)

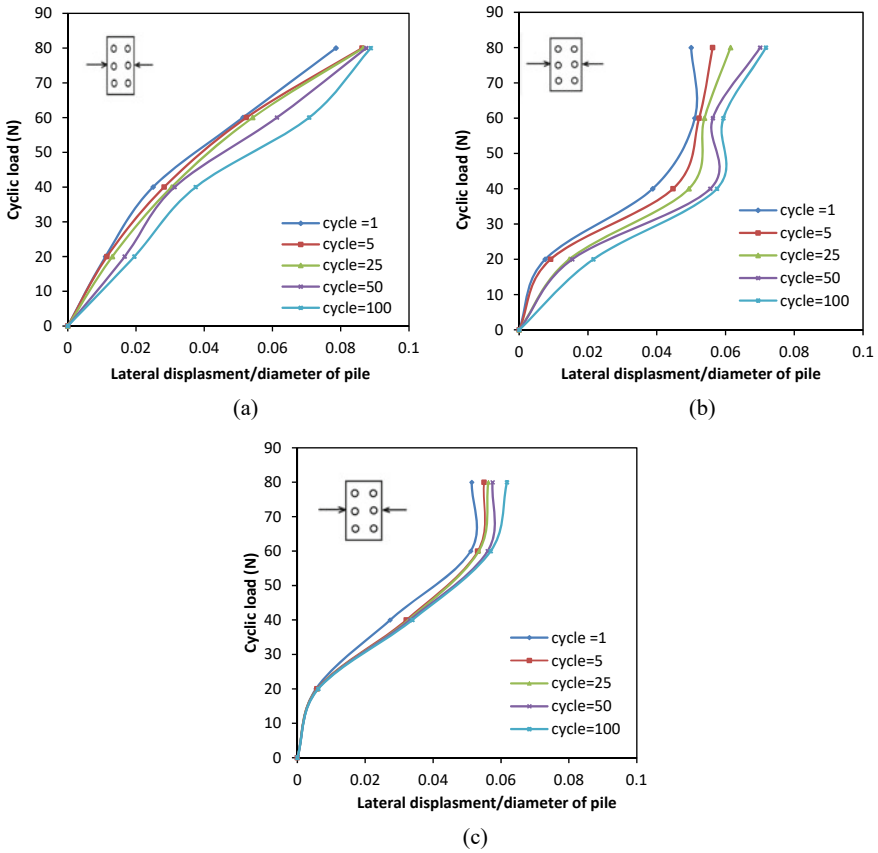


**Fig. 5** Influence of number of cycles on the load–deflection curve of piled groups model under inclined cyclic load  $2 \times 3$  group: **a**  $s/d = 3$ , **b**  $s/d = 5$  and **c**  $s/d = 7$

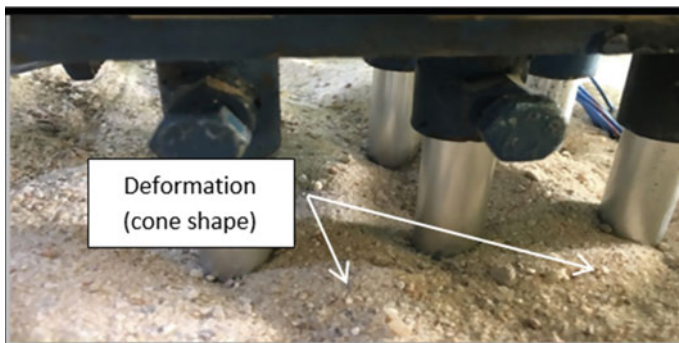
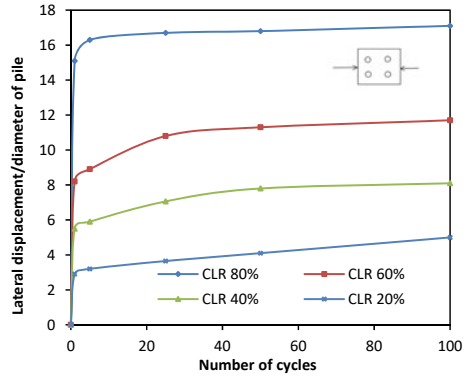
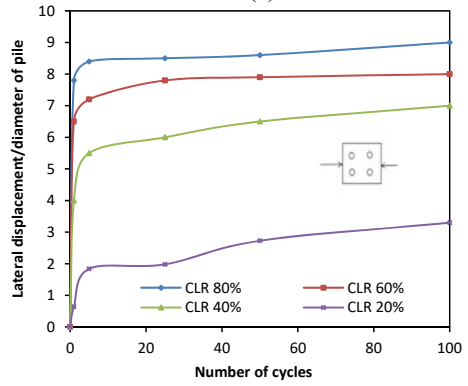


**Fig. 6** Deformation around piles due to closed spacing ( $s/d = 3$ )

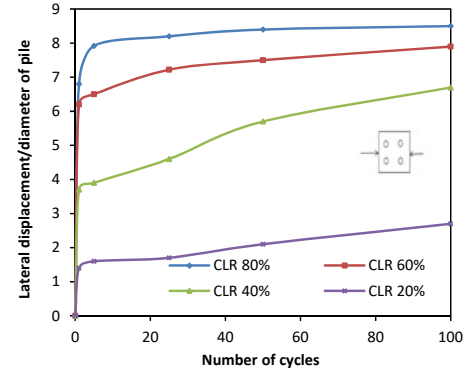
**Fig. 7** Influence of cyclic load ratio (CLR) on the lateral deflection of pile group  $2 \times 2$  under inclined cyclic load: **a**  $s/d = 3$ , **b**  $s/d = 5$  and **c**  $s/d = 7$



(a)

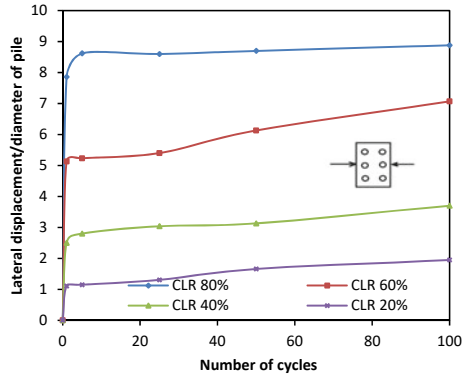


(b)

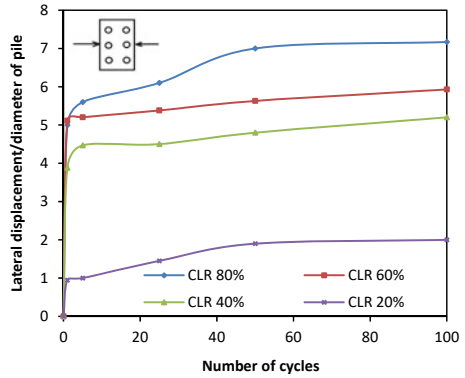


(c)

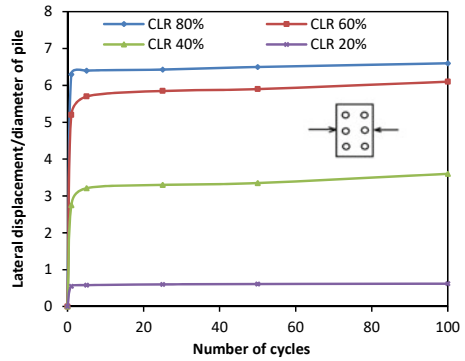
**Fig. 8** Influence of cyclic load ratio (CLR) on the lateral deflection of pile group  $3 \times 2$  under inclined cyclic load: **a**  $s/d = 3$ , **b**  $s/d = 5$  and **c**  $s/d = 7$



(a)



(b)



(c)



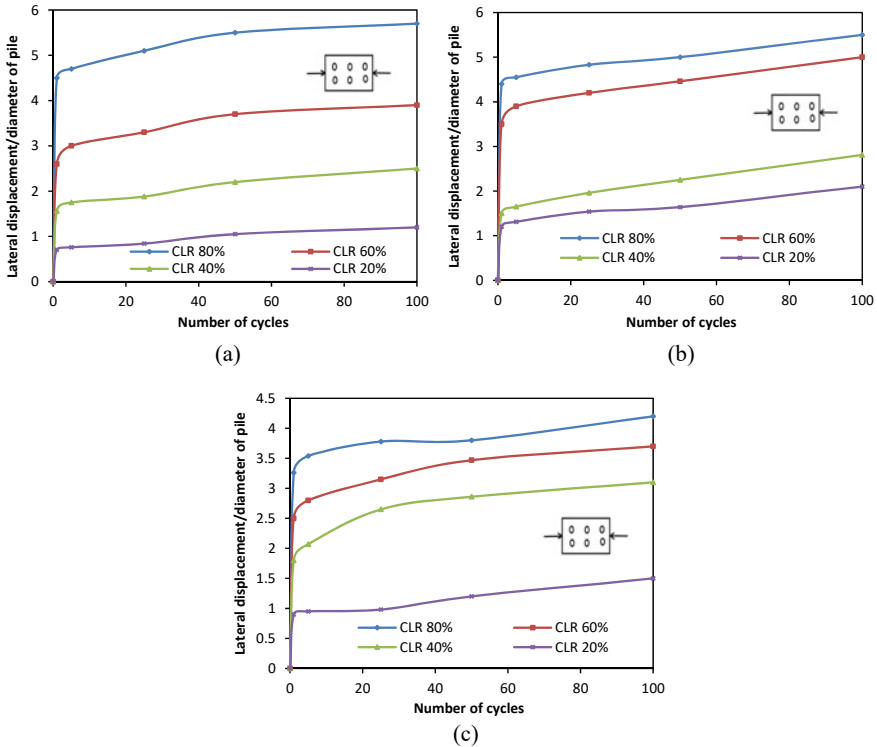


**Fig. 9** Influence of cyclic load ratio (CLR) on the lateral deflection of pile group 2 × 3 under inclined cyclic load: **a** s/d = 3, **b** s/d = 5 and **c** s/d = 7

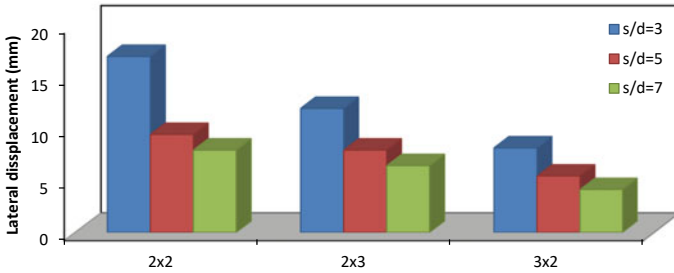


**Fig. 10** Lateral displacement for three groups at different spacing

is attributed to overlapping stresses zone of passive and active wedges. The result also shows the middle row exhibit less lateral resistance and leads to weakening the group. Group interaction consequences become less substantial as the spacing between 5 and 7. The difference becomes less important with the increase in pile spacing due to the decrease of the shadowing. Besides, the movement of the piles

placed in the first row (leading) in the direction of the applied force is resisted by the soil in front of it. In contrast, the piles in the rows behind the first row (the piles in the trailing rows) pushed on the soil, which in turn pushed on the piles in the rows in front of them [15].

## 4 Conclusions

Comparison of the test effects and theoretical estimations shows largely good accord. When the applied load on pile groups as an inclined cyclic load, this would lead the load applying divided into two components, axial and horizontal. The axial component is working as the vertical load on the pile groups, and causing the increase of the stiffness of the pile and decreasing the lateral deflection in the soil in front of the pile and no uplifting in pile groups observed due to cyclic loading. This is attributed to the axial component effect. In the case of the influence of the number of cyclic, group  $2 \times 2$  is more affected lateral deflection more than another group with about 50%. For rectangular configuration, the lateral resistance of group  $2 \times 3$  less than from group  $3 \times 2$  with about 27.3, 37, and 39.4% for  $s/d = 3, 5,$  and  $7,$  respectively.

- Furthermore, the cyclic load ratio CLR is more influence on the  $2 \times 2$  group and then decreases in lateral resistance from 35 to 55% compering with another group. Also, lateral resistance of group  $2 \times 3$  is less than in group  $3 \times 2$  with 15.7, 21, and 19.5% for  $s/d = 3, 5,$  and  $7.$
- Additionally,  $s/d = 3$  deflect extra than the other spacing; this is due to over lab stress between the piles, and the group interaction effect becomes less significant as the spacing between 5 and 7. These results well agreed with the study presented in references [8, 11, 12].

## References

1. Azeez, O., Hummadi, R., & Hasan, A. (2019). Effect of embedded length on laterally loaded capacity of pile foundation. *American Scientific Research Journal for Engineering, Technology, and Sciences (ASRJETS)*, 56(1), 182–192.
2. Puech, A. (2013). Design for cyclic loading Piles and other foundation. In *Proceedings of TC 209 workshop 18th ICSMGE, Paris.*
3. Hazzar, L., Hussien, M. N., & Karray, M. (2017). On the behaviour of pile groups under combined lateral and vertical loading. *Ocean Engineering*, 131, 174–185.
4. Karthigeyan, S., & Rajagopal, K. (2009). Lateral response of  $2 \times 2$  pile group under combined axial and lateral loading. In *Proceedings of Indian geotechnical conference* (pp. 666–668).
5. Ladhane, K. B., & Sawant, V. A. (2016). Effect of pile group configurations on nonlinear dynamic response. *International Journal of Geomechanics*, 16(1), 1–14.
6. Conte, E., Troncone, A., & Vena, M. (2015). Behaviour of flexible piles subjected to inclined loads. *Computers and Geotechnics*, 69, 199–209.
7. Raongjant, W., & Jing, M. (2017). Cyclic lateral response of model pile groups for wind turbines in clay soil. *International Journal of GEOMATE*, 12(32), 76–81.

8. Goswami, A., & Roy, S. (2017). Ultimate capacity of vertical short pile under inclined compressive load. *Indian Geotechnical Conference GeoN Est, 14–16*, 1–4.
9. Kahribt, M. A., & Abbas, J. M. (2018). Lateral response of a single pile under combined axial and lateral cyclic loading in sandy soil. *Civil Engineering Journal, 4(9)*, 1996–2010.
10. Jose, S., Prakash, V. M., & Paul, H. (2018). a model study on lateral behaviour of micropile under inclined compressive loads in sand. *International Research Journal of Engineering and Technology (IRJET), 5(4)*, 2947–2950.
11. Saleh, W. A., & Abbas, J. M. (2020). Effect of spacing and cross-sectional shape on piled raft system subjected to lateral cyclic loading. *Diyala Journal of Engineering Sciences, 13(3)*, 114–122.
12. Saleh, W. A. (2020). Effect of spacing and cross-sectional shape on piled raft system subjected to lateral cyclic loading. *Diyala Journal of Engineering Sciences, 13(3)*, 114–122.
13. Broms, B. B. (1964). Lateral resistance of piles in cohesionless soils. *Journal of the Soil Mechanics and Foundations Division, 90(3)*, 123–156.
14. Basack, S., & Nimbalkar, S. (2018). Measured and predicted response of pile groups in soft clay subjected to cyclic lateral loading. *International Journal of Geomechanics, 18(7)*, 1–20.
15. Abbas, J. M., Chik, Z., & Taha, M. R. (2010). Influence of group configuration on the lateral pile group response subjected to lateral load. *Electronic Journal of Geotechnical Engineering, 15*, 761–772.

# Numerical Modeling of Under Reamed Piles Behavior Under Dynamic Loading in Sandy Soil



Ahmed M. Najemalden, Mustafa M. Jasim, and Ansam A. Al-Karawi

**Abstract** Under-reamed piles defined by having one or more bulbs have the potential for sizeable major sides over conventional straight-sided piles, most of the studies on under-reamed piles have been conducted on the experimental side, while theoretical studies, such as the finite element method, have been mainly confined to conventional straight-sided piles. On the other hand, although several laboratory and experimental studies have been conducted to study the behavior of under-reamed piles, few numerical studies have been carried out to simulate the piles' performance. In addition, there is no research to compare and evaluate the behavior of these piles under dynamic loading. Therefore, this study aimed to numerically investigate bearing capacity and settlement of under-reamed piles compared with uniform pile sections by sinusoidal excitation machines foundation. Different geometrical under-reamed piles single and double bulbs compared with uniform pile using finite element method, PLAXIS 3D software. The result showed that uniform pile fizzles out to support the total load and the final settlement was 4.97 cm. Single under-reamed pile S.U.P and double under-reamed pile D.U.P can be reduced final settlement 76% and 81% respectively.

**Keywords** Finite element · PLAXIS · Under-reamed pile · Dynamic load · Sandy soil

---

A. M. Najemalden (✉)  
Duhok Polytechnic University, Duhok, Iraq  
e-mail: [ahmed.najm@dpu.edu.krd](mailto:ahmed.najm@dpu.edu.krd)

M. M. Jasim  
Civil Engineering Department, University of Baghdad, Baghdad, Iraq  
e-mail: [mustafa.m.j@coeng.uobaghdad.edu.iq](mailto:mustafa.m.j@coeng.uobaghdad.edu.iq)

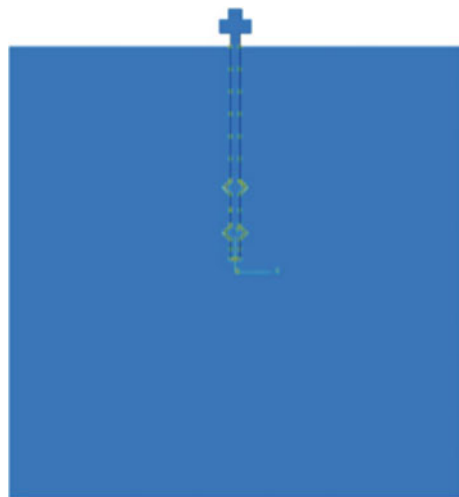
A. A. Al-Karawi  
Civil Engineering Department, University of Diyala, Diyala, Iraq  
e-mail: [ansamahmed\\_enge@uodiyala.edu.iq](mailto:ansamahmed_enge@uodiyala.edu.iq)

## 1 Introduction

Under-reamed piles are bored cast in situ concrete piles with one or more enlargements (ream, bulb) near base and pile stems. These reams are increasing both friction and bearing surface and capacity of the pile in compressive loading [1, 2]. So, these types of piles are effectively used in tower foundations, electrical transmission, bridges, and machine foundations. Several researchers have used numerical analysis to study different aspects of under-reamed piles with or without experimental verifications depending on their research targets. Researchers have employed three sophisticated and powerful programs in their analysis as Abaqus, PLAXIS, and ANSYS; two types of analysis (2D and 3D) are also dependent. However, many different parameters are considered in their studies, such as type of soil, layered soil, horizontal displacement, and bearing capacity of piles. Singh [3] study the behavior of a free vertical cast in situ reinforced concrete under-reamed pile which is exposed to horizontal dynamic; it was concluded that both shear strain and the extreme horizontal displacement increase with increasing the excitation force level at the ground position. In addition, another experimental field study associated with numerical analysis has been executed on under-reamed piles made of concrete in a silty sand deposit [4].

The experimental program has included fixing an oscillator motor on the pile cap to produce horizontal dynamic forces of purely sinusoidal type. The numerical program contained using Abaqus software to simulate the field tests of the horizontal dynamic load on the pile, as shown in Fig. 1. It was mainly concluded that the measured strain at the ground, middle and bottom level has increased with increasing the eccentricity, and the numerical results, agreed well with the field experimental results. Farokhi et al. [5] evaluated the performance of half and full bulbs under-reamed piles numerically. Then, the results have been compared with the conventional piles for the

**Fig. 1** Loading and boundary condition [4]



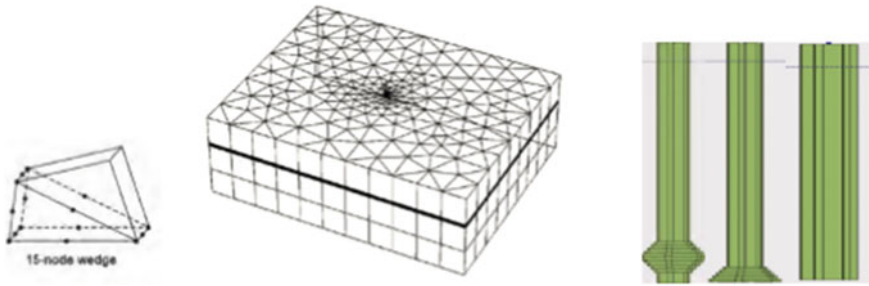


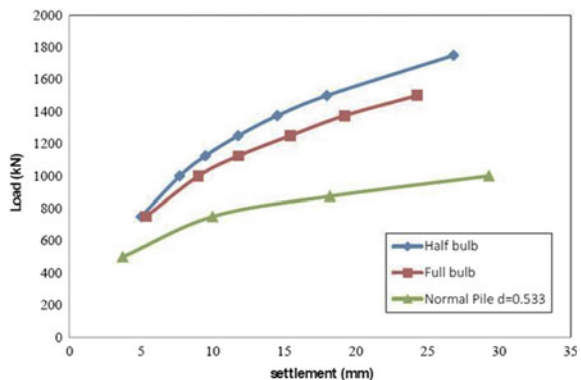
**Fig. 2** Elements types used and 3D meshing in Plaxis 3D foundation software together with modeled piles [5]

same volume and length in clayey soils, as shown in Fig. 2. To maintain the goal of the study, PLAXIS 3D has been used where the diagrams of the bearing capacity have been evaluated and compared. It was shown that the half-bulb under-reamed piles had greater ultimate compressive and tensile bearing capacity with lower displacements, Fig. 3. In addition, it was determined that the under-reamed piles had lower uplift and higher tensile bearing capacity in contrast with the conventional piles, which have the same length and volume.

A combined research program consisted of both experimental and numerical studies has been implemented in under-reamed piles, different geometries, and embedment tested under the effect of various horizontal and vertical excitations was considered [6]. The soil condition involved three soil layers with different depths, the top soil layer was silty sand up to 4.0 m, the middle soil layer was clayey soil with a thickness of 2.0 m, and the bottom soil layer was silty-sand with a thickness of 3.0 m. However, the numerical inspection included using a three-dimensional finite element program through ANSYS software; the pile-soil model is shown in Fig. 4, where the program inputs have been obtained from the experimental results.

The study has shown a good agreement between experimental and numerical results in terms of natural frequency and displacement amplitude of the pile-soil

**Fig. 3** Compressive load-settlement diagram of half-bulb and full-bulb under-reamed piles and uniform cross-section pile of the same volume ( $L/d = 12$ ) [5]



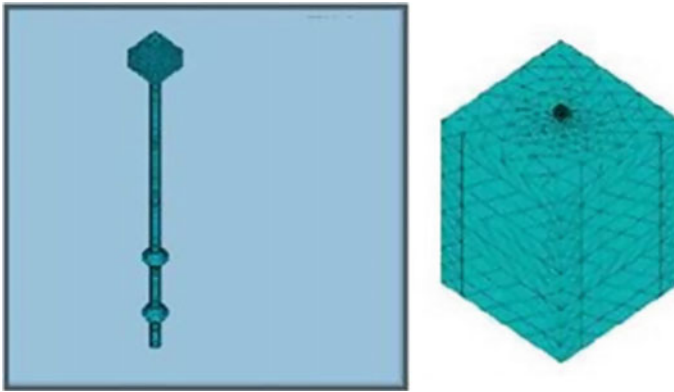


**Fig. 4** 3-D Pile-Soil Model with 5 m-2 bulb pile [6]

system. In addition, a numerical study was conducted on both bored and under-reamed piles in clayey soil to analyze the failure configuration under the effect of axial load using Plaxis three-dimensional software, where the Mohr–Coulomb model has been adopted [7]. It was concluded that the load capacity had increased by 119% and 102% for tensile and compressive loadings, respectively, when single under-reamed piles were used in comparison with bored piles whereas these values have increased to 204% and 180%, respectively for double under-reamed piles. The study has also recommended that the under-reamed piles are more effective in cohesive soil when the ground has sufficient stability to support itself throughout the cavity development. Furthermore, a numerical effort has been made to study the impact of under-reamed friction pile on the displacement conduct of four-story building under the effect of earthquake loading using ANSYS program Figs. 5 and 6 [8]. It was concluded that the total displacement was decreased as the footing was used with the under-reamed piles, and the dynamic response of the structure can be changed when the footing was used with the under-reamed piles.

**Fig. 5** Geometry of frame and foundations [8]

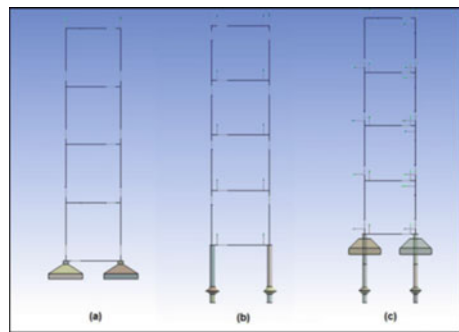
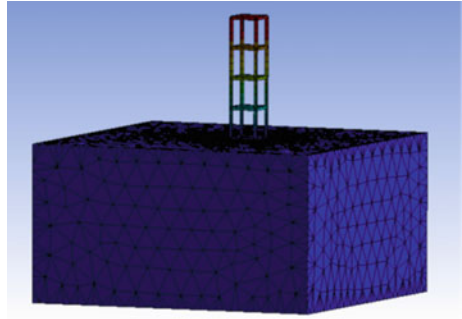


**Fig. 6** Geometry of soil and frame [8]



## 2 Numerical Model

This research’s main objective is to use a 3-Dimensional model, which has been created in PLAXIS 3D software in the analysis of machine foundation with sinusoidal excitation load. Three cases were studied, uniform pile, single under-reamed pile (S.U.P) and double under-reamed pile (D.U.P), and the diameter of reamed ( $D_r$ ) equal to double of pile stem. The analytical has been supported by 10-noded tetrahedral elements to idealize both the under-reamed pile and soil. Moreover, a plate element (used for modeling 2D structures) with a 6-node triangular element is used for modeling pile cap. The interface elements between pile and soil are composed of 12-node for the interface. The linear elastic model is considered for under-reamed pile, while the Elastic–Plastic model is invoked for soil nonlinearity. The absorbent boundary should be used to ensure that the waves do not be rebound. Similarly, ground surfaces were free to move in all directions Fig. 7, and the finite element mesh of the under-reamed pile interfaces in the present study is shown in Fig. 8.

**Fig. 7** Finite element model using PLAXIS 3D (2013)

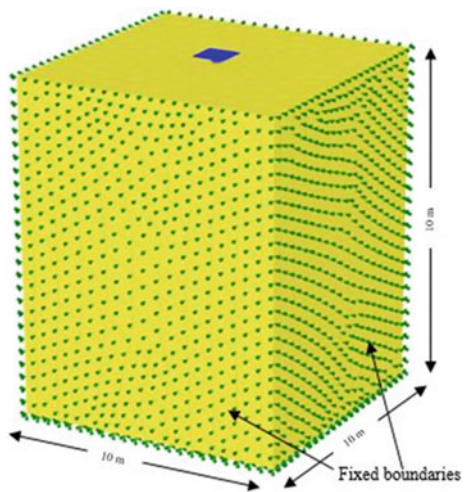




**Fig. 8** Finite element mesh of pile



The system subjected to both machine gravity load and vertical dynamic load as a part of the gravity load. However, the machine assembly was fixed on the pile cap then to free standing pile. The reference project chosen for this study was the diesel power plant in Baghdad, shown in Fig. 9, and Table 1 lists the properties of the programming input. Three cases were studied: uniform pile (S.U.P), and (D.U.P) to study the ream effect on the time-settlement under dynamic loading.



**Fig. 9** Diesel generator engine

**Table 1** The input properties of the soil, pile and cap

Material	Dimensions m	E kPa	$\gamma$ kN/m <sup>3</sup>	$\nu$	c kPa	$\phi$ Degree	$\psi$ Degree	R interface
Pile	L = 10, D = 0.4	25 × 10 <sup>3</sup> ASTM D2435	25	0.15 [9]	-	-	-	-
Under-reamed pile	L = 10, Dr = 0.8							
Pile cap	2 × 2.75							
Soil	15 × 15 × 15	5 × 10 <sup>3</sup>	16	0.30	8	38	10	1
Engine detail	Static load	Dynamic load		Frequency		-	-	-
	500 kN	20 kN		20 Hz				

### 3 Results and Discussion

In this investigation, the result was the time-settlement curve at the node resting on the pile cap center. Figures 10 and 11 show a view of the displacement distribution for uniform piles under dynamic load. In the same way, Fig. 12 provide the time-settlement curve of finite element model analysis, it can be noted that the pile with a uniform section can not be able to carry the applied load and the settlement (4.97 cm)

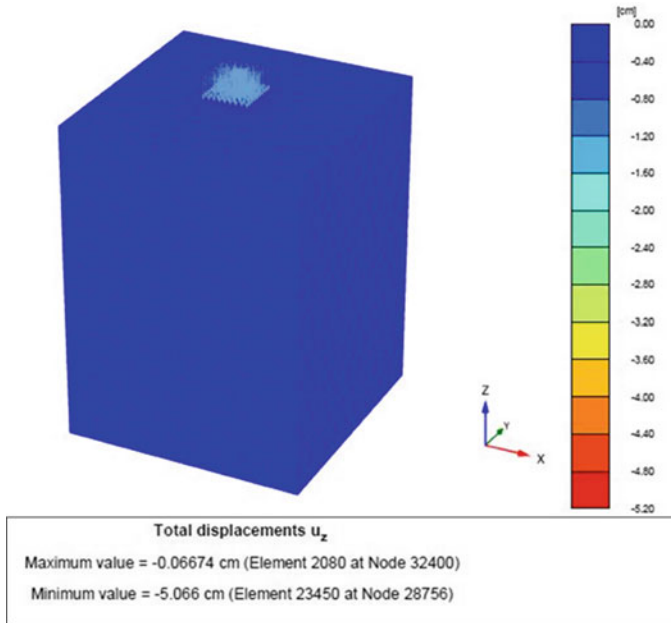


**Fig. 10** Displacements distribution for uniform pile support machine

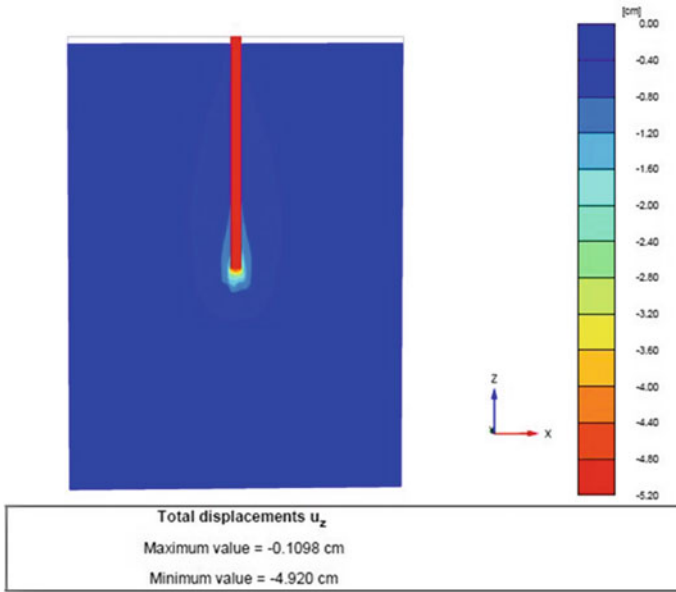


Fig. 11 Section of displacements distribution for uniform pile support machine

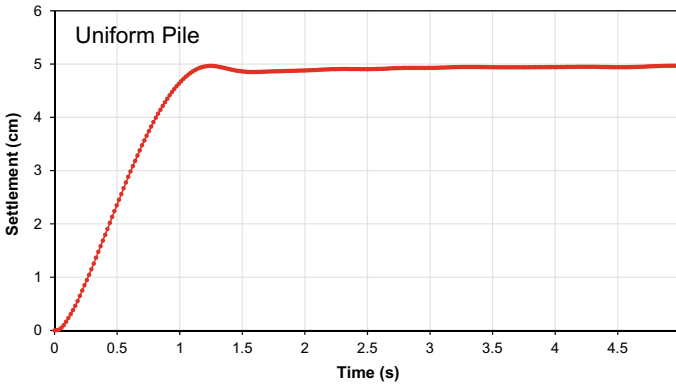


Fig. 12 Time-settlement for uniform pile support machine

more than the value of 10% of the pile diameter. So, it is intended to use a pile with a bulb to reduce the huge settlement and increasing load capacity. For a single under-reamed pile, Fig. 13 shows the deformed mesh and total displacement. So, it can be seen that increasing the surrounding soil resistance around the bulb at pile toe compared with a uniform pile. Therefore, S.U.P can reduce the settlement by 77.5% compared with the uniform pile Fig. 14. Finally, it can be seen from Fig. 15 that increasing soil mass around D.U.P to resist the dynamic load, which leads to

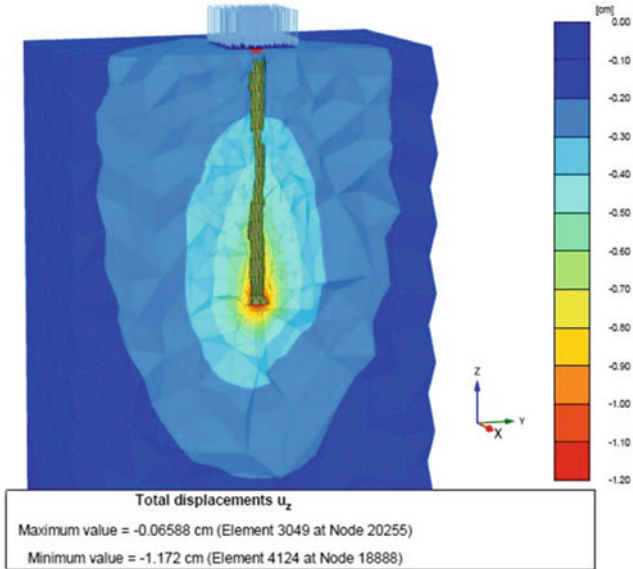


Fig. 13 Deformed mesh and total displacement for S.U.P support machine

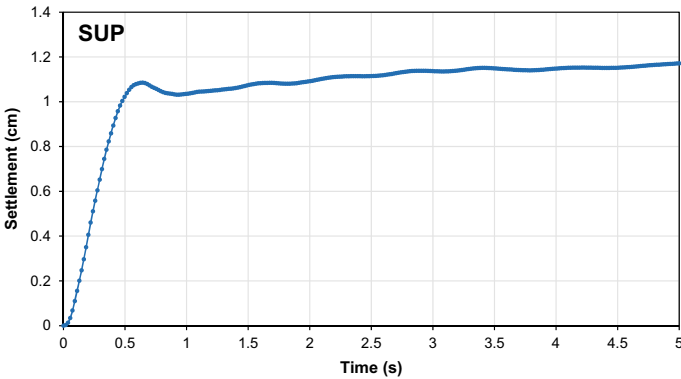


Fig. 14 Time-settlement of S.U.P support machine

more reduction in the settlement 81% compared with uniform pile Fig. 16. Also, a comparison between the three types of studied piles supporting the machine is shown in Fig. 17. The results showed significant impact for using single or double reamed, in the last quarter of pile, in reducing the vibration settlement of machine.

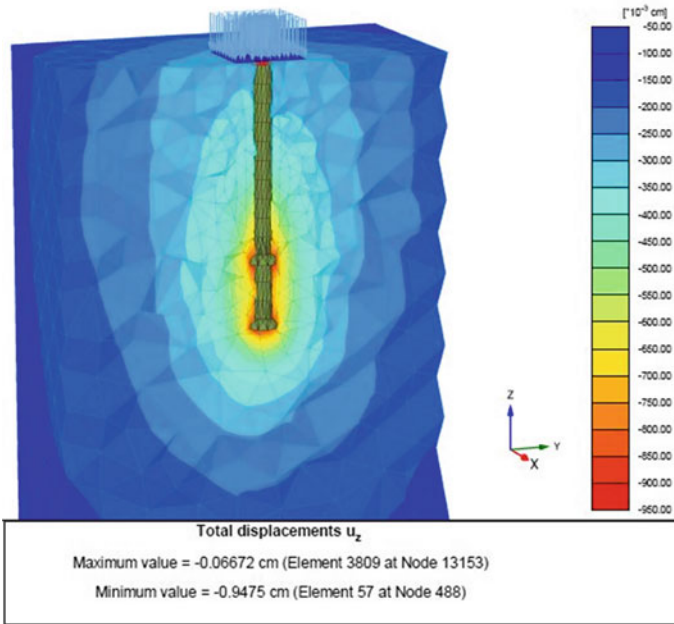


Fig. 15 Deformed mesh total displacement for D.U.P support machine

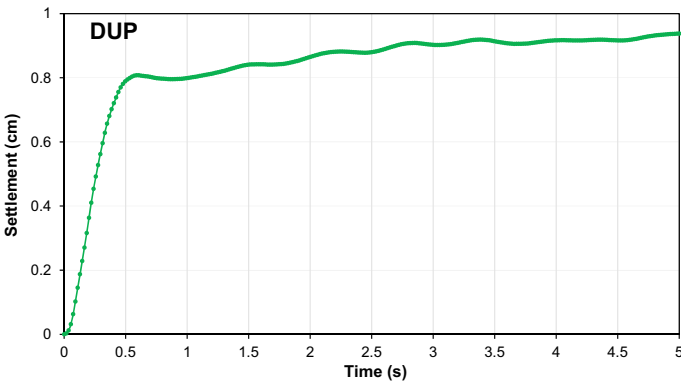
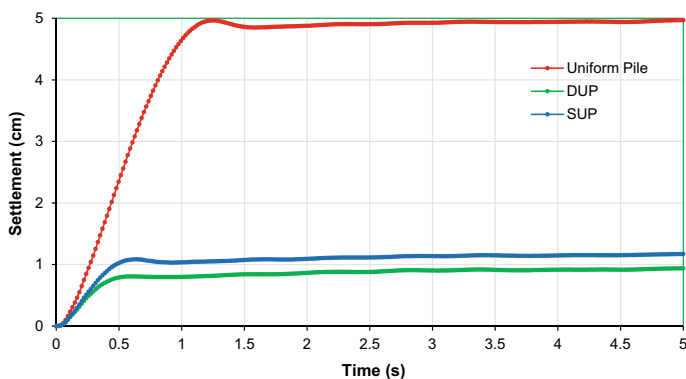


Fig. 16 Time-settlement of D.U.P support machine

## 4 Conclusions

This study clearly shows that numerical analysis can be used to modeling large-scale foundations.



**Fig. 17** Comparison of time-settlement relation for three types of piles support machine

- It was observed that the under-reamed pile could reduce the settlement from (4.97 cm) in a uniform pile to (1.172 cm) in S.U.P and to (0.9475 cm) in D.U.P.
- Increasing the number of bulbs reducing the collapsible soil settlement percent (26–94%).
- Finally, a pile with single and double bulb has more safety factor against bearing failure than the uniform pile.

## References

1. Jebur, M. M., Ahmed, M. D. & Karkush, M. O. (2020). Numerical analysis of under-reamed pile subjected to dynamic loading in Sandy soil. In *IOP conference series: materials science and engineering* (Vol. 671, No. 1, p. 012084). IOP Publishing.
2. Jebur, M. M. & Ahmed, M. D. (2020, August). Experimental investigation of under reamed pile subjected to dynamic loading in Sandy soil. In *IOP conference series: materials science and engineering* (Vol. 901, No. 1, p. 012003). IOP Publishing.
3. Singh, S. (2014). *Response of free standing under-reamed pile subjected to horizontal dynamic loads*. M. Tech Thesis, Department of Earthquake Engineering, IIT Roorkee.
4. Bharathi, M., Dubey, R. N., & Mukerjee, S. (2014). Numerical simulation of horizontal dynamic pile load tests on under-reamed piles. In *5th Asia Conference on Earthquake Engineering, Taipei, Taiwan*.
5. Farokhi, A. S., Alielahi, H., & Mardani, Z. (2014). Optimizing the performance of under-reamed piles in clay using numerical method. *Electronic Journal of Geotechnical Engineering*, 19, 1507–1520.
6. Mandal, A., Pandey, A. D. & Mukerjee, S. Numerical simulation of under reamed pile subjected to vertical and horizontal sinusoidal loading. In *50th Indian Geotechnical Conference, Pune, Maharashtra, India*.
7. George, B. E. & Hari, G. (2016). Numerical investigations of under-reamed piles. In *Proceedings of Indian Geotechnical Conference, IGC*.
8. Chourasia, J., Pendharkar, U., & Singh, R. (2018). Dynamic analysis of pile foundation with footing in different foundation soils. *International Research Journal of Engineering and Technology (IRJET)*, 5(1), 2395–0072.

9. Murthy, V. N. S. (2002). *Geotechnical engineering: Principles and practices of soil mechanics and foundation engineering*. CRC Press.

# **Merges in Structural Engineering and Construction Materials**



# Exploring Biochar as Stable Carbon Material for Suppressing Erosion in Green Infrastructure



Yuan-Xu Huang, Xia Bao, He Huang, Ankit Garg, Wei-Ling Cai,  
and Askar Zhussupbekov

**Abstract** Many biomaterials (fibers) have been proposed for minimizing soil erosion. However, those biomaterials are prone to degradation under microbial activity. In contrast, biochar, a relatively stable carbon material (half-life period >100 years) has been explored recently for minimizing soil erosion. Life period of such material is well beyond the design period of any geo-environmental infrastructure. This study evaluates individual and coupling effects as well as the relative importance of four important factors, biochar content, slope gradient, slope length, and rainfall intensity using flume tests. Bare soil (BS) and soil-biochar composites (SBCs) were subjected to flume testing under factorial experiment design. The experimental results indicate that biochar addition significantly increased water retention capacity and decreased soil loss. It lowered the sensitivity of green infrastructure to rainfall events and enhanced the resistance of green infrastructure to water-related hazards. Biochar content is the most significant effect in reducing total erosion sediment, while slope length and slope gradient are the least important factors. Based on the performance of SBCs, biochar is suggested as a promising stable carbon material for the green infrastructure.

**Keywords** Biochar · Erosion · Infiltration · Runoff · Flume experiment

---

Y.-X. Huang · X. Bao · H. Huang · A. Garg (✉) · W.-L. Cai  
Guangdong Engineering Center for Structure Safety and Health Monitoring, Shantou University,  
Shantou, China  
e-mail: [ankit@stu.edu.cn](mailto:ankit@stu.edu.cn)

Y.-X. Huang  
e-mail: [19yxhuang@stu.edu.cn](mailto:19yxhuang@stu.edu.cn)

X. Bao  
e-mail: [20xbao1@stu.edu.cn](mailto:20xbao1@stu.edu.cn)

H. Huang  
e-mail: [18hhuang2@stu.edu.cn](mailto:18hhuang2@stu.edu.cn)

A. Garg · A. Zhussupbekov  
Department of Design of Building and Construction, Eurasian National University, Nur-Sultan,  
Kazakhstan

## 1 Introduction

Soil erosion has caused irreparable losses to people's production and life. Soil erosion can be divided into surface erosion and internal erosion [1]. The surficial erosion appears on the surface of soil when runoff flow splashes, slips across the ground, and erodes soils [2]. Internal erosion occurs inside soil due to the washout effect of infiltration or seepage [3, 4]. Hence, the key to reducing soil erosion is to control the runoff and infiltration on the surficial soil layer [5, 6]. Green infrastructure, therefore, plays a critical role in soil–water conservation by improving soil water storage capacity, reducing runoff and infiltration, and decreasing soil loss [6].

As one kind of environmentally friendly material, biochar is produced from pyrolyzed biomass waste by negative carbon emission technology [7]. As compared to other biomass materials, which are prone to degradation, biochar has relatively higher stability with an average half-life period expected to go beyond 100 years. This period is well beyond any design period of green infrastructure. In previous studies, biochar was used to improve soil water retention capacity [8], minimize erosion [9], inhibit soil surface cracking [10], and increase soil fertility [11]. Besides, some studies verified the impact of other factors. For example, Cuomo et al. investigated the effect of slope geometry characteristics and rainfall rate on erosion [12]. Chen et al. studied the effect of soil properties and rainfall rates on erosion using flume tests [13]. Ekwue and Harrila [14] also observed that geometry characteristics, soil properties, and rainfall rate were the important individual impact factors on erosion. However, few studies have quantified the relative influence of slope geometry and biochar characteristics on soil loss and water retention.

This study is to evaluate the individual and relative importance of slope geometry characteristics, biochar content, and rainfall rate on infiltration flow, runoff flow, and concomitant erosions using flume tests. Factorial experiments of bare soil (BS) and soil-biochar composites (SBCs) were carried out using flume setup designed with a function of flow diversion. Through flume experiments, the hydrological response of biochar amended soil layer in green infrastructure was systematically studied.

## 2 Methodology

**Material Preparation.** Soil material was collected from the mountains of Shantou University, China. The soil concluded 82.23% medium sand, 15.93% fine sand, and 1.84% fines (silt + clay). For its particle size distribution characteristics,  $D_{50}$  was 1.58 mm,  $C_u$  was 5.69, and  $C_c$  was 1.10. It was identified as poorly graded sand (ASTM-CS), which had been exposed long term to weathering. Under the compaction degree of 90%, the void ratio can be estimated as 0.58. In-house produced biochar was derived from an invasive plant (i.e., water hyacinth) found in abundance in the coastal region of Shantou, China. Biochar was produced using pyrolysis [15].

Pyrolysis involves heating of biomass (up to 600 °C) under limited oxygen conditions. Heating of biomass at maximum temperature (600 °C) continued for 15 min [16]. Slow pyrolysis (0/min) could let the biochar with a large surface area, more functional groups and pores. During this process, CO<sub>2</sub> was supplied and sequestered in water hyacinth biomass. The zeta potential, electrical conductivity, Debye length, and surface charge of the biochar were 16.9 mV (unstable colloid), 2.1 S/m, 0.8 nm, and  $1.5 \times 10^{-6} \text{ C/cm}^2$ , respectively. Functional groups of biochar were obtained using FTIR (Fourier transform infrared) spectroscopy analysis. These groups include -COOH, -OH, C = C and C-O.

**Experimental Design.** Two-level experiments were designed to investigate the effects of slope geometry, rainfall characteristics, and biochar content on erosion, runoff, and infiltration in flume tests. As shown in Fig. 1, high and low levels were selected for varying rainfall intensity, slope gradient, and slope length, respectively. For the rainfall rate designed for this research, 60 mm/h and 90 mm/h were regarded as light and heavy rainfall in the local place [9]. Slope gradients of 7° and 20° [17] were adopted. For slope length, 1 and 2 m were considered [12]. In total, 48 experiments, including replicates involving the internal and external factors of the green slope were conducted.

**Flume Experiments.** Figure 2 presented a schematic diagram of the in-house manufactured flume set up. The flume was separated into three sections for performing rainfall simulation experiments on soil samples of BS, SBC5%, and SBC10% simultaneously. This arrangement makes it easier to compare responses under three different soil slopes (i.e., BS, SBC5%, and SBC10%). Standard compaction tests as per guidelines prescribed in ASTM D1140 were adopted for compacting soil-biochar composite. A degree of compaction of 90% was adopted in this study [15]. A model was adopted to analyse runoff flow, infiltration flow, and erosion flow [18].

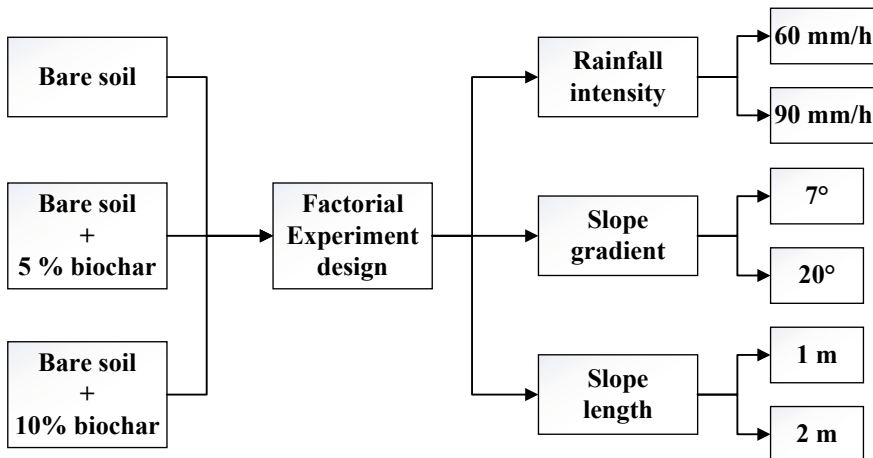


Fig. 1 Factorial experiment design for flume tests

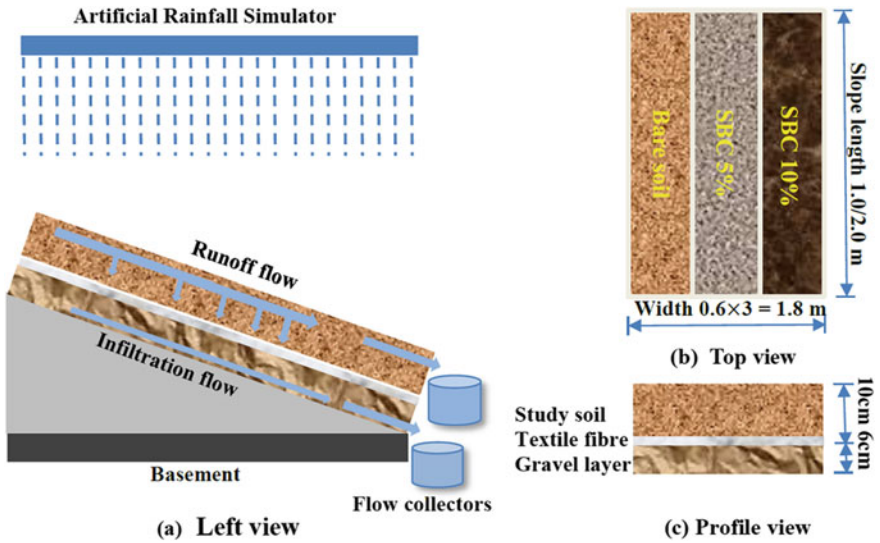


Fig. 2 Schematic diagram of flume experiments

### 3 Results and Discussion

The influence of biochar on soil erosion is shown in Fig. 3. As compared to BS, total rainwater flow in SBC5% and SBC10% is reduced by an average of 33% and 19%, respectively. The water retention properties of biochar (see Fig. 3a) cause a reduction of total rainwater flow, which is consistent with Abrol et al. [19]. Figure 3b also shows that biochar addition improves erosion control, which was also observed in Li. et al. [9]. Table 1 summarizes the reduction potential of internal and surface for SBC5% and SBC10% concerning BS. The efficiency of erosion control of SBC5% was around double that of SBC10%.

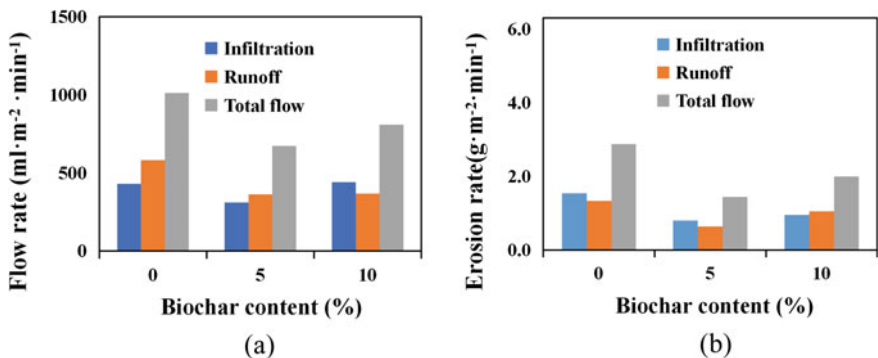


Fig. 3 Influence of biochar on a water retention and b erosion

**Table 1** Effect (i.e., reduction) of SBC5% and SBC10% as compared to BS

	Surface erosion (%)	Internal erosion (%)	Total erosion (%)
SBC5%	60	58	51
SBC10%	21	29	32

During testing, flow increases with time and reaches a peak value, where it remains more or less stable. Therefore, data analyses considered average peak erosion flows and discussed the effects of factors on peak erosion flow. Data collected was processed with a multi-factor ANOVA (analysis of variance) tool. Tables 2 and 3 summarize the results of  $2^k$  factorial analyses. The main effect of factors and their interaction is shown in Fig. 4. The sensitivity analysis in determining water retention was estimated as biochar content > rainfall rate > slope gradient > slope length (see Fig. 4a). This is because biochar formed soil-biochar aggregates, which were water-stable [20]. The elongated shape and irregularity of biochar particles changed soil composition, lengthened its pore space, and improved its water retention [17]. The relative significant parameter order is biochar > slope length > rainfall rate > slope gradient (see Fig. 4b) for erosion sediment. It showed water retention properties were also likely to be improved by the hydrophilic groups on the surface [10].

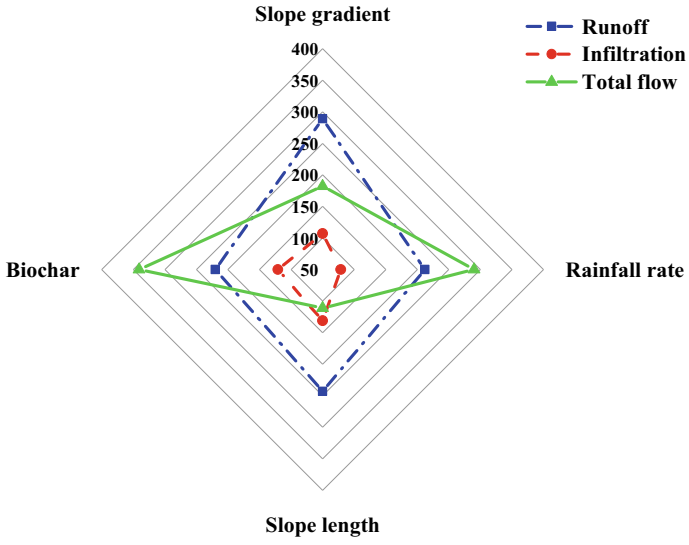
Results showed the effects of biochar on hydrologic responses to rainfall events in the short term. Biochar has immense potential for the contribution to green infrastructure based on the reported performance of water retention [20], wastewater treatment [21], erosion control [12]. Biochar can be a promising material for the application of green infrastructure in experiments [22]. After all, an optimized strategy of adopting biochar type and biochar dosage for targeted soil in green infrastructure needs to be developed.

**Table 2**  $2^k$  factorial analyses showing the main effect on erosion flow

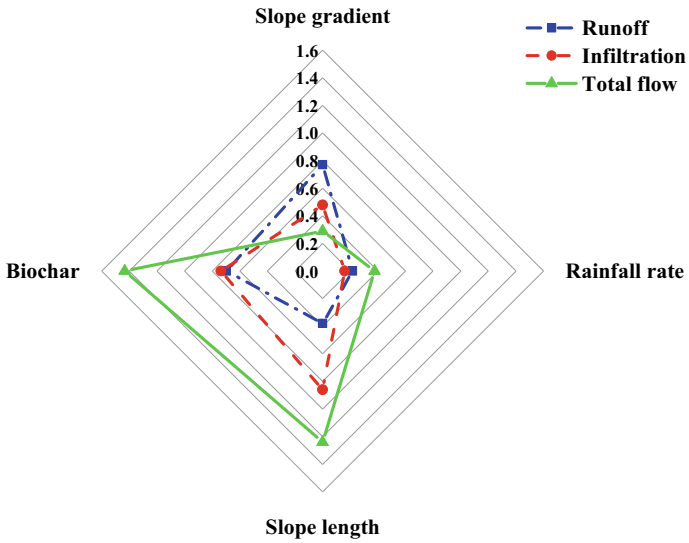
	Total flow	Infiltration	Runoff
Biochar	289	107	182
Slope gradient	212	79	290
Rainfall rate	243	131	111
Slope length	220	121	341

**Table 3**  $2^k$  factorial analyses showing the main effect on erosion sediment

	Total flow	Infiltration	Runoff
Biochar	0.769	0.479	0.289
Slope gradient	0.216	0.160	0.377
Rainfall rate	0.380	0.859	1.239
Slope length	0.697	0.737	1.434



(a) Effect of various factors affecting erosion flow



(b) Effect of various factors affecting erosion sediment

**Fig. 4** The contribution of various factors in erosion control

## 4 Conclusions and Future Work

Biochar addition decreased runoff and increased water retention capacity significantly. The erosion resistance of SBCs was improved effectively. This was attributed to porosity, roughness as well as the presence of functional groups in biochar. Besides, biochar content was a sensitive factor in erosion experiments. The most influential factors determining erosion sediment induced by runoff and infiltration erosion are slope gradient and slope length. Soil with a biochar content of 5% has better performance than bare soil and 10% biochar content. Due to the great potential of biochar in water conservation and wastewater treatment, future research needs to be conducted to consider biochar's effect on soil erosion in the long term.

## References

1. Indraratna, B., Muttuvel, T., Khabbaz, H., & Armstrong, R. (2008). Predicting the erosion rate of chemically treated soil using a process simulation apparatus for internal crack erosion. *Journal of Geotechnical and Geoenvironmental Engineering*, 134(6), 837–844.
2. Fu, B., Newham, L. T., & Ramos-Scharon, C. E. (2010). A review of surface erosion and sediment delivery models for unsealed roads. *Environmental Modelling & Software*, 25(1), 1–14.
3. Moffat, R., Fannin, R. J., & Garner, S. J. (2011). Spatial and temporal progression of internal erosion in cohesionless soil. *Canadian Geotechnical Journal*, 48(3), 399–412.
4. Bradford, J. M., Ferris, J. E., & Remley, P. A. (1987). Interrill soil erosion processes: I. Effect of surface sealing on infiltration, runoff, and soil splash detachment. *Soil Science Society of America Journal*, 51(6), 1566–1571.
5. Nguyen, T. T., Ngo, H. H., Guo, W., Wang, X. C., Ren, N., Li, G., Ding, J., & Liang, H. (2019). Implementation of a specific urban water management-Sponge City. *Science of the Total Environment*, 652, 147–162.
6. Wang, H., Mei, C., Liu, J., & Shao, W. (2018). A new strategy for integrated urban water management in China: Sponge city. *Science China Technological Sciences*, 61(3), 317–329.
7. Singh, R., Babu, J. N., Kumar, R., Srivastava, P., Singh, P., & Raghubanshi, A. S. (2015). Multi-faceted application of crop residue biochar as a tool for sustainable agriculture: An ecological perspective. *Ecological Engineering*, 77, 324–347.
8. Garg, A., Bordoloi, S., Ni, J., Cai, W., Maddibiona, P. G., Mei, G., Poulsen, T. G., & Lin, P. (2019). Influence of biochar addition on gas permeability in unsaturated soil. *Géotechnique Letters*, 9(1), 66–71.
9. Li, Y., Zhang, F., Yang, M., & Zhang, J. (2019). Effects of adding biochar of different particle sizes on hydro-erosional processes in small scale laboratory rainfall experiments on cultivated loessial soil. *CATENA*, 173, 226–233.
10. Bordoloi, S., Garg, A., Sreedeeep, S., Lin, P., & Mei, G. (2018). Investigation of cracking and water availability of soil-biochar composite synthesized from invasive weed water hyacinth. *Bioresource Technology*, 263, 665–677.
11. Gao, S., & DeLuca, T. H. (2018). Wood biochar impacts soil phosphorus dynamics and microbial communities in organically-managed croplands. *Soil Biology and Biochemistry*, 126, 144–150.
12. Cuomo, S., Della Sala, M., & Pierri, M. (2016). Experimental evidences and numerical modelling of runoff and soil erosion in flume tests. *CATENA*, 147, 61–70.

13. Chen, S. C., Lin, T. W., & Chen, C. Y. (2015). Modeling of natural dam failure modes and downstream riverbed morphological changes with different dam materials in a flume test. *Engineering Geology*, *188*, 148–158.
14. Ekwue, E. I., & Harrilal, A. (2010). Effect of soil type, peat, slope, compaction effort and their interactions on infiltration, runoff and raindrop erosion of some Trinidadian soils. *Biosystems Engineering*, *105*(1), 112–118.
15. Bordoloi, S., Gopal, P., Boddu, R., Wang, Q., Cheng, Y. F., Garg, A., & Sreedeeep, S. (2019). Soil-biochar-water interactions: Role of biochar from *Eichhornia crassipes* in influencing crack propagation and suction in unsaturated soils. *Journal of Cleaner Production*, *210*, 847–859.
16. Suliman, W., Harsh, J. B., Abu-Lail, N. I., Fortuna, A. M., Dallmeyer, I., & Garcia-Perez, M. (2016). Influence of feedstock source and pyrolysis temperature on biochar bulk and surface properties. *Biomass and Bioenergy*, *84*, 37–48.
17. Zhao, Q., Li, D., Zhuo, M., Guo, T., Liao, Y., & Xie, Z. (2015). Effects of rainfall intensity and slope gradient on erosion characteristics of the red soil slope. *Stochastic Environmental Research and Risk Assessment*, *29*(2), 609–621.
18. Morbidelli, R., Corradini, C., Saltalippi, C., Flammini, A., Dari, J., & Govindaraju, R. S. (2019). A new conceptual model for slope-infiltration. *Water*, *11*(4), 678.
19. Abrol, V., Ben-Hur, M., Verheijen, F. G., Keizer, J. J., Martins, M. A., Tenaw, H., Tchehansky, L., & Graber, E. R. (2016). Biochar effects on soil water infiltration and erosion under seal formation conditions: Rainfall simulation experiment. *Journal of Soils and Sediments*, *16*(12), 2709–2719.
20. Wang, D., Li, C., Parikh, S. J., & Scow, K. M. (2019). Impact of biochar on water retention of two agricultural soils—A multi-scale analysis. *Geoderma*, *340*, 185–191.
21. Ahmad, M., Rajapaksha, A. U., Lim, J. E., Zhang, M., Bolan, N., Mohan, D., Vithanage, M., Lee, S. S., & Ok, Y. S. (2014). Biochar as a sorbent for contaminant management in soil and water: A review. *Chemosphere*, *99*, 19–33.
22. Schulz, H., Dunst, G., & Glaser, B. (2013). Positive effects of composted biochar on plant growth and soil fertility. *Agronomy for Sustainable Development*, *33*(4), 817–827.



# Dynamic Response of Slender Reinforced Concrete Columns Strengthened by Using CFRP and Circularization Subjected to Seismic Excitation



Zena H. Abdulghafoor and Hayder A. Al-Baghdadi

**Abstract** This paper presents a numerical study comparing the drift of slender columns with different strengthening techniques subjected to different amplitude seismic with a pure axial compressive load. A total of three 1:3 scale square concrete column models were used throughout the study. The first column consisted of a square column without CFRP (carbon fiber reinforced polymer) strip confinement and shape modification; it was considered as a reference member. The second one consisted of a square column confined with CFRP strips using Near-Surface-Mounted (NSM) technique and then strengthened with CFRP wraps. The third column and last one consisted of a square column confined with CFRP strips, then circularized and confined with CFRP wrappings. All columns are tested using a time-compressed El Centro 1940 earthquake at different amplitudes (0.05 g, 0.15 g, 0.32 g). Numerical results showed that the displacement of columns, which strengthened with CFRP strips, the circularized and confined with CFRP wrappings technique, was decreased of about 89.14%, 88.33%, 88.71% at 0.05 g, at 0.15 g, and at 0.32 g, respectively, compared with the reference column.

**Keywords** Circularization · Slender Columns · Confinement · Drift · CFRP · NSM · Seismic

## 1 Introduction

Damage of (RC) (reinforced concrete) columns under seismic and in impact due to fire and explosion can prompt the whole RC structure's catastrophic failure. Columns are the primary member bearing loads in the structure and cannot go through extreme severe damages to stay in their function [1]. Through the earlier 90s, the major technique that was used to strengthen columns included expanding the segment

---

Z. H. Abdulghafoor (✉) · H. A. Al-Baghdadi  
Department of Civil Engineering, College of Engineering, University of Baghdad, Baghdad, Iraq  
e-mail: [z.abdulghafar1901m@coeng.uobaghdad.edu.iq](mailto:z.abdulghafar1901m@coeng.uobaghdad.edu.iq)

H. A. Al-Baghdadi  
e-mail: [baghdadi.hayder@coeng.uobaghdad.edu.iq](mailto:baghdadi.hayder@coeng.uobaghdad.edu.iq)

by adding concrete cages or by injecting grout in steel jackets. The two methods are workers intensive and present challenges at the site [2]. “Fiber-reinforced polymer” (FRP) has been used effectually in current years as an alternate material for rehabilitate, strengthened damaged reinforced concrete structures according to its preferred tensile strength, corrosion resistance, durability, and lightweight property with comparison to steel jacketing. Many research types have proven that FRP wrapping of reinforced concrete columns is an effective method of increasing the column’s strength and ductility as it presents confinement to the concrete core [3]. External wrappings of RC columns is a high spread strengthening method that is accepted to cause gain in axial load and bending moment capacity and causing ductility improvement. The composition of CFRP sheets and longitudinal CFRP plates for slender columns is a system that can take the benefit of longitudinal stiffening members and transverse members with confinement and buckling support functions [4]. Many buildings in Iraq were designed only for gravity loading. These make structures attend a great difficulty for the persons caring with decreasing earthquake risk. However, the most building was established earlier to any particular specifications to design against earthquakes. Therefore, retrofit of these buildings was important. Results have displayed that columns wrapped by CFRP sheets enhance their strength, ductility, and energy dissipation capacity without adding stiffness to the members. The ease of installation makes the use of the CFRP sheet an effective alternative in the earthquake retrofit of existing structures [5].

Since Iraq is situated in the middle east, this is making it affected by earthquakes, and the building must be designed and constructed against seismic [6]. Most of the buildings are defective to withstand for future extensive earthquakes. Most of these buildings have common deficiencies such as insufficient reinforcing details, poor construction quality and part ratios of members was caused strong beams, weak columns, short columns, and soft stories. The concrete strength in existing structures is far less than the chosen strength values due to poor labor. The transverse confinement in members, especially near the potential plastic hinging regions is not enough. Studies on lapped bars subjected to the earthquake have shown that many of the bond mechanisms accessible through static loading of splices degrade with the number of cycles and deformations amplitude. Throughout the seismic load, confinement plays a significant part in the lapped splice strength. The reason is confinement controls the loss of mechanical connections after the enlargement of concrete [7]. One of the most effective ways to make efficient use of FRP in square columns is to modify the shape of the square sections before applying the FRP jacketing. The circularizing of a square column to change its shape is known as section circularization, and the resulting shape-modified column is known as a circularized square column [8].

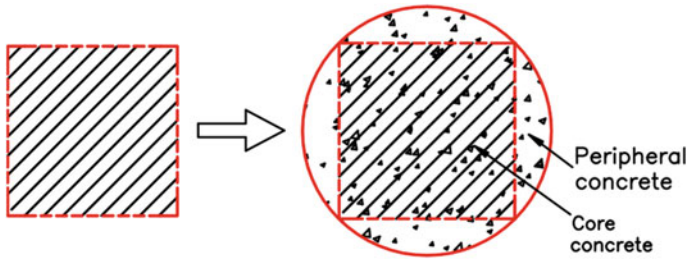


**Fig. 1** Circularization for the square column

## 2 Circularization

Circularization is transforming non-circular concrete members into circular ones by changing their cross-sectional structure from non-circular to circular. This may be a rectangle, square, or another shape, as cited by [9]. Shape-modifications, or changing a rectangular or square column section into an elliptical, oval, or circular section, is one way to increase the usefulness of FRP-confined rectangular columns [10] (Fig. 1).

## 3 Methodology of Study

In this study, three reinforced concrete columns were analyzed numerically using the finite element software Abaqus (as a qualitative study to investigate the behavior of columns with different strengthening methods subjected to different amplitude 0.5 g, 0.15 g, 0.32 g El Centro 1940 earthquake before starting with the experimental study), include:

- Reference column (R): (unstrengthen square column  $130 \times 130 \times 1500$  mm) was analyzed under 0.5 g, 0.15 g, 0.32 g El Centro 1940 earthquake.
- Strengthened column (N-C): square column  $130 \times 130 \times 1500$  m was strengthened by four CFRP strips using (NSM) technique in the direction of seismic (x direction) then confined with CFRP wrapping was analyzed under El Centro 1940 earthquake with amplitudes of 0.5 g, 0.15 g, and 0.32 g.
- Strengthened column (N-CI-C): square column  $130 \times 130 \times 1500$  m was strengthened by four CFRP strips using (NSM) technique in the direction of seismic (x-direction) then circularized and confined with CFRP wrapping was analyzed under El Centro 1940 earthquake with amplitudes of 0.5 g, 0.15 g, and 0.32 g.
- The columns were designed using concrete strength of  $f_c' = 30$  MPa.
- The CFRP plate dimension is  $(1.2 \times 6)$  mm with 1800 mm length, embedded in the base about 300 mm according to ACI 440.2R-17.

- The CFRP sheet thickness is 0.381 mm.

### 4 Material Properties

The geometry and materials properties used in the numerical modeling are given in Fig. 2 and Tables 1, 2 and 3.

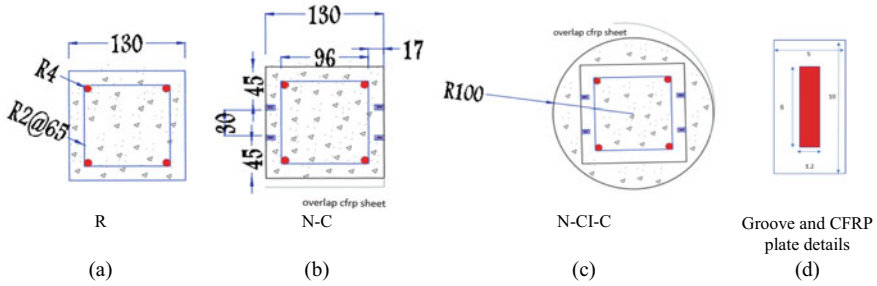


**Fig. 2** Cross-section of column models (dimensions in mm)

**Table 1** Sikadur 30 epoxy resin properties used with CFRP plates

Property	Value
Resin tensile strength	29 N/mm <sup>2</sup> (7 days at +35 °C)
Resin tensile modulus of elasticity	11,200 N/mm <sup>2</sup> (+23 °C)
Resin tensile adhesion strength	(>4 N/mm <sup>2</sup> )
Resin density	1.65 ± 0.1 kg/l (component A + B mixed) (at +23 °C)

**Table 2** Sikadur 330 epoxy resin properties used with CFRP sheets

Property	Value
Resin tensile strength	30 N/mm <sup>2</sup> (7 days at +23 °C)
Resin tensile modulus of elasticity	4500 N/mm <sup>2</sup> (23 °C)
Resin elongation at break	0.9% (7 days at +23 °C)
Resin tensile adhesion strength	(>4 N/mm <sup>2</sup> )
Resin density	1.3 ± 0.1 kg/l (component A + B mixed) (at +23 °C)

**Table 3** Properties of CFRP plates and sheets

Property	Value	
	Plates	Sheets
Dry fiber tensile strength	3100 N/mm <sup>2</sup>	3450 N/mm <sup>2</sup>
Dry fiber tensile modulus of elasticity	165,000 N/mm <sup>2</sup>	230 000 N/mm <sup>2</sup>
Dry fiber strain at break	1.7%	1.5%
Dry fiber density	1.6 g/cm <sup>3</sup>	1.8 g/cm <sup>3</sup>

## 5 Numerical Modeling

- In this study, the mass, column, and the base of the column, circularized column, CFRP strips, epoxy resin was modeled of C3D8R: (An 8-node linear brick, reduced integration), steel reinforcement was modeled of T3D2: (A 2-node linear 3-D truss), CFRP wrap was modeled of S4R: (A 4-node doubly curved thin or thick shell, reduced integration).
- (CDPM) concrete damage plasticity model, the dynamic, implicit method was used for analyzing the models.
- Steel mass with a dimension of 0.3 × 0.3 × 0.4 m was applied on the top of the column.
- The seismic amplitudes were applied in x-direction, and the bottom block reinforced concrete (base with a dimension of 0.5 × 0.5 × 0.4 m) was assumed to be fixed and given no degree of freedom.
- For interactions between epoxy resin and concrete, between the epoxy resin and CFRP strips, and between concrete and CFRP wrapping, tie constraint was modeled. With this constraint, the members attached together and stay tied during the analysis. The constraints of concrete with steel reinforcement were modeled using the embedded region constraint. To ensure that both have the same degrees of freedom (Fig. 3).

## 6 Test Results and Discussion

Each model was analyzed three times using (0.05 g, 0.15 g, 0.32 g) El Centro 1940 earthquake. The max displacements were measured for each model, and for three earthquake amplitude, the numerical test results are summarized in Table 4. Figure 4 represents the displacement of the models under seismic excitation.

Figures 5, 6, 7, 8, 9 and 10 represent the displacement -time response for the models. The columns strengthened with CFRP strips, then circularized, and finally wrapped with CFRP have small displacement compared with reference column and column that strengthen with CFRP strips. Figures 11, 12 and 13 represent the displacement -time response for the same strengthening technique with the El Centro 1940 earthquake’s different amplitude. It is observed that the (R) model under the

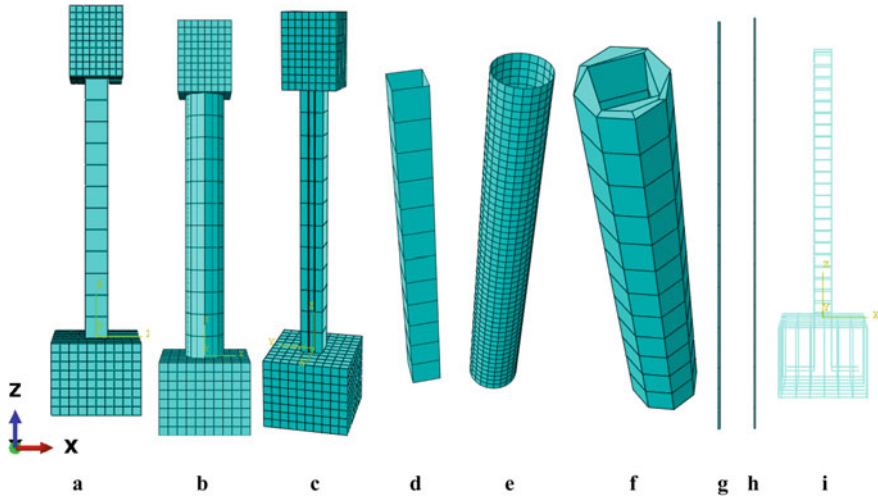


**Fig. 3** Components of the numerical model: **a** R model, **b** N-CI-C model, **c** N-C model, **d, e** CFRP jacket, **f** circularized shape, **g** epoxy resin, **h** CFRP strip, **i** steel reinforcement

**Table 4** Summary of the numerical test result

Column Type	Strengthening technique	Earthquake Amplitude (g)	Absolute Displacement (mm)		Relative Displacement (mm)	
			Max	Min	Max	Min
R	–	0.05	6.55034	–6.62044	6.329961	–6.3314
	–	0.15	19.9159	–19.7218	19.16798	–18.9763
	–	0.32	42.5623	–41.8167	37.87404	–39.7361
N-C	NSM strips with CFRP wrapping	0.05	3.38543	–2.34045	2.360752	–2.45694
		0.15	13.2692	–10.8587	5.06181	–4.85824
		0.32	24.9488	–19.8048	8.967478	–9.7981
N-CI-C	NSM strips with circularization then CFRP wrapping	0.05	3.20055	–2.86299	0.686956	–0.63808
		0.15	10.1474	–8.70042	2.236297	–2.27933
		0.32	21.7935	–17.0673	4.27452	–2.92976

different amplitude has the same behavior with different magnitudes. For the (N-C) and (N-CI-C) models under 0.15 g, 0.32 g amplitudes, also it has the same behavior with different magnitudes, but in 0.05 g the behavior is different.

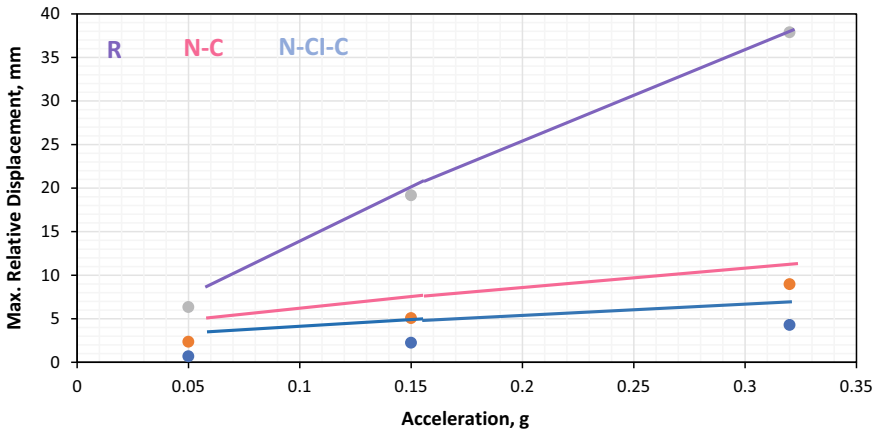


Fig. 4 Max. Relative displacement with different amplitudes earthquake to the three models

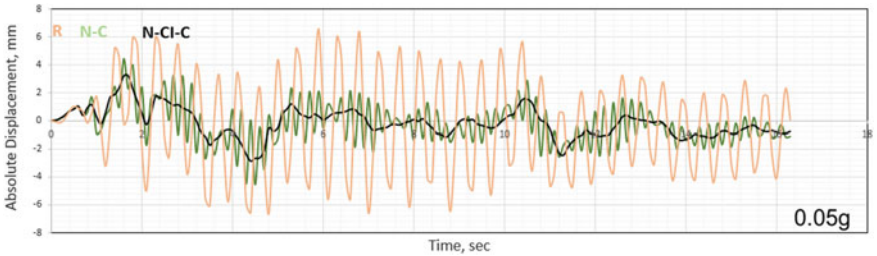


Fig. 5 Absolute displacement–time response for inelastic behavior in the x-direction for acceleration amplitude 0.05 g

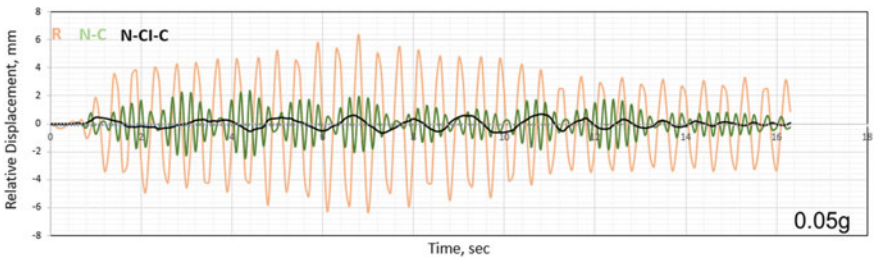
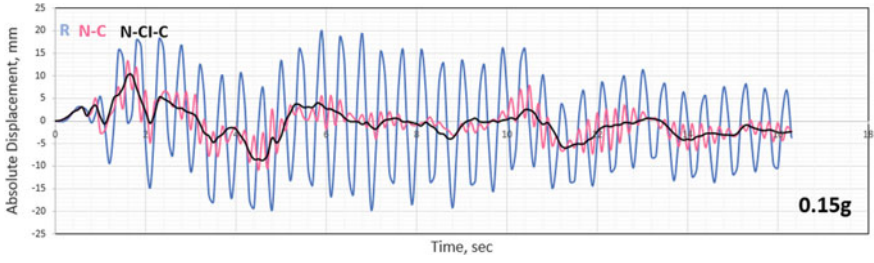
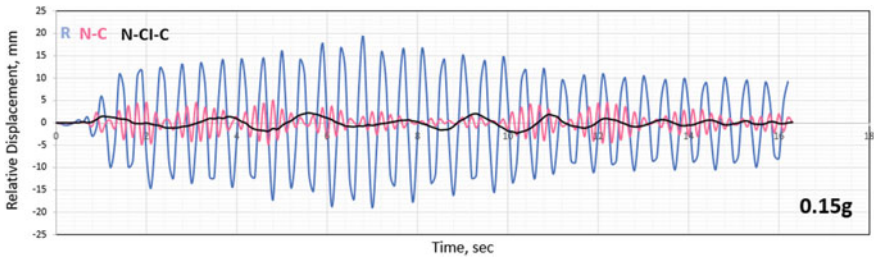


Fig. 6 Relative displacement–time response for inelastic behavior in the x-direction for acceleration amplitude 0.05 g



**Fig. 7** Absolute displacement–time response for inelastic behavior in the x-direction for acceleration amplitude 0.15 g



**Fig. 8** Relative displacement–time response for inelastic behavior in the x-direction for acceleration amplitude 0.15 g

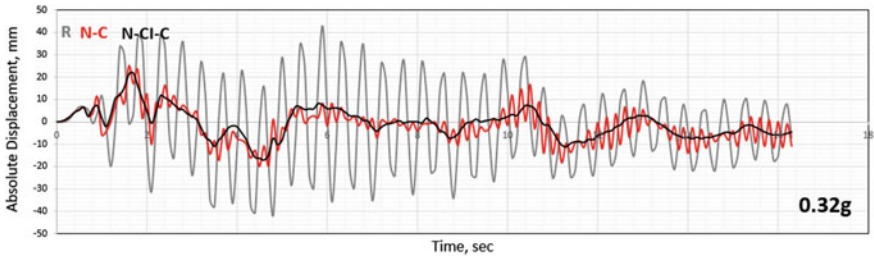


**Fig. 9** Absolute displacement–time response for inelastic behavior in the x-direction for acceleration amplitude 0.32 g

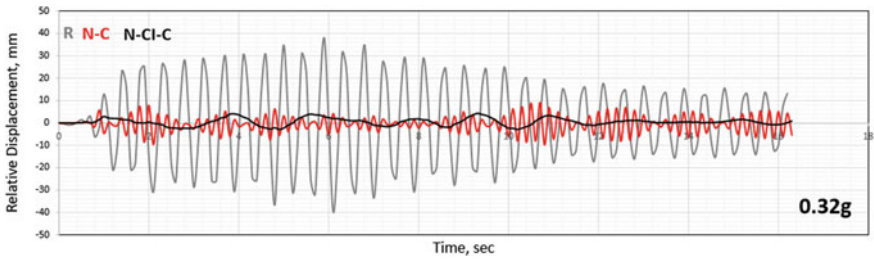


**Fig. 10** Relative displacement–time response for inelastic behavior in the x-direction for acceleration amplitude 0.32 g



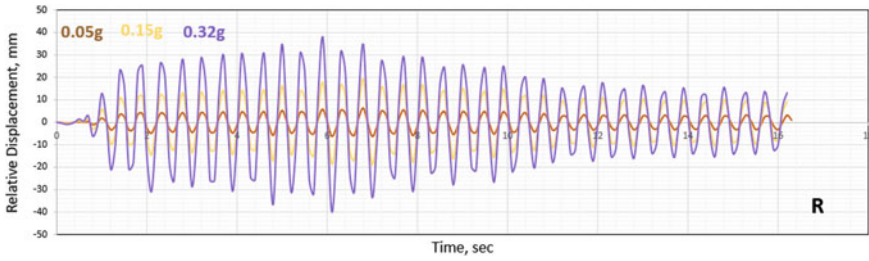


Fig. 11 Relative displacement–time response for inelastic behavior in the x-direction for R model

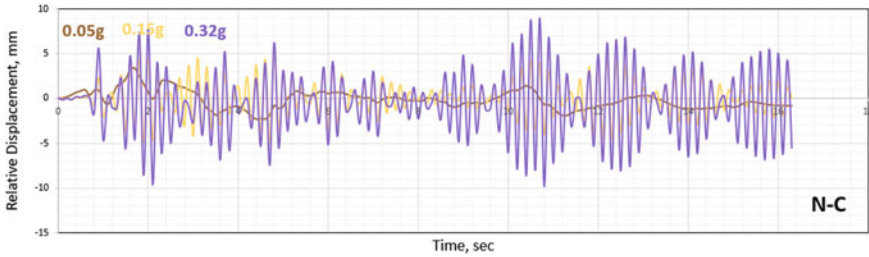


Fig. 12 Relative displacement–time response for inelastic behavior in the x-direction for N-C model

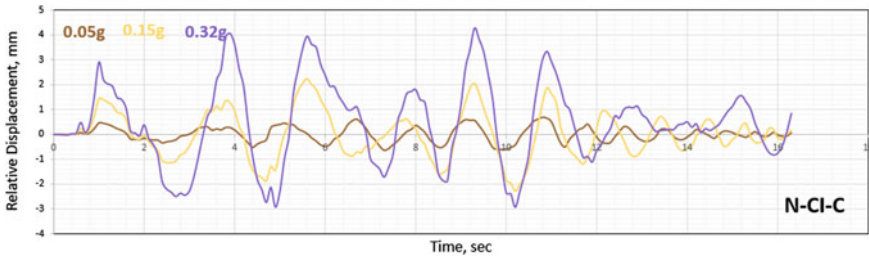


Fig. 13 Relative displacement–time response for inelastic behavior in the x-direction for N-CI-C model

## 7 Conclusions

A numerical study was conducted to investigate the reinforced concrete column’s behavior strengthened with different techniques under different amplitude El Centro 1940 earthquake. The following conclusions were drawn.

- The circularization process essentially reduced tension accumulation areas that would otherwise exist when a non-circular column was covered in CFRP.

- Confinement with CFRP wrapping and circularization proved efficient in improving the structural performance of reinforced columns subjected to seismic excitation.
- The method of strengthening square columns using CFRP-NSM with the CFRP wrapping strengthening technique produced remarkably good results compared with the reference model. It was noticed that decreases the displacement of a column of about 62.7% of the reference model under (0.05 g), 73.59% under (0.15 g), and 76.32% under (0.32 g) and this means that the efficiency of this technique increased with increasing the earthquake amplitude.
- The method of strengthening square columns using the circularization technique and applying external confinement offered by CFRP wraps produced excellent results to reduce the displacement. For the NSM CFRP with circularization and CFRP wrapping, it is noticed that the displacement of the column is reduced about 89.14% of the reference model under (0.05 g), 88.33% under (0.15 g), and 88.71% under (0.32 g).
- The max. displacement in N–CI–C model is significantly less than the R and N–C models.
- In summary, it is possible to use these methods in Iraq for the efficiency and ease of work to strengthen the columns of buildings not designed according to the seismic load instead of “thinking about demolishing them”.

**Acknowledgements** The authors would like to express special thanks of gratitude to the staff at the Department of Civil Engineering, College of Engineering, University of Baghdad for their support and help for making this project.

## References

1. Chellapandian, M., & Prakash, S. S. (2018). Rapid repair of severely damaged reinforced concrete columns under combined axial compression and flexure: An experimental study. *Construction and Building Materials*, 173, 368–380.
2. Elsanadedy, H. M., Al-Salloum, Y. A., Alsayed, S. H., & Iqbal, R. A. (2012). Experimental and numerical investigation of size effects in FRP-wrapped concrete columns. *Construction and Building Materials*, 29, 56–72.
3. Abdurra'uf, M. G., Jaganathan, J., Anwar, M. P., & Leung, H. Y. (2019). Experimental studies and theoretical models for concrete columns confined with FRP composites: a review. *World Journal of Engineering*.
4. Khorramian, K., & Sadeghian, P. (2018, June). Strengthening slender circular concrete columns with a novel hybrid FRP system. In *CSCE Annual Conference 2018, Fredericton, NB, Canada*. Canadian Society for Civil Engineering.
5. Alubaidi, I. H. K. (2011). Seismic evaluated and retrofit of existing buildings. *Journal of Engineering and Sustainable Development*, 15(2)
6. Al-Asadi, A. K. (2019). Modelling of earthquake repellent fibre reinforced concrete. *Periodicals of Engineering and Natural Sciences (PEN)*, 7(4), 1996–2011.
7. Breña, S. F., & Schlick, B. M. (2007). Hysteretic behavior of bridge columns with FRP-jacketed lap splices designed for moderate ductility enhancement. *Journal of Composites for Construction*, 11(6), 565–574.

8. Guo, Y. C., & Zeng, J. J. (2018, June). Behavior of partially and fully FRP-confined Circularized Square Columns (CSCs) under axial compression. In *International Conference on Theoretical, Applied and Experimental Mechanics* (pp. 44–49). Springer.
9. Zakaria, A. W., & Al-Baghdadi, H. (2020). Experimental and numerical study on CFRP-confined square concrete compression members subjected to compressive loading. *Journal of Engineering*, 26(4), 141–160.
10. Pantelides, C. P., Yan, Z., & Reaveley, L. D. (2004). *Shape modification of rectangular columns confined with FRP composites* (No. UT-05.03).

# Experimental and Numerical Study of the Influence of Various Parameters on the Development of Deformations in Reinforced Base



V. M. Antonov and I. A. Al-Naqdi

**Abstract** Experimental study results are presented to understand the parameters that affect reinforcing soil under static as well as cyclic loading. The results of plate tests held in the laboratory in a tray with rigid-sided walls are presented. Reinforced and unreinforced sand was implemented. Variable parameters were studied: the cycles number, the size of the reinforcing element, the eccentricity of the load applied, and the displacement of the reinforcing element. Numerical analysis was performed using the finite element method by programs Plaxis 3D v20 and Midas GTS NX. It was observed that cycling at one of the loading stages led to compaction of the soil and that the values of the total settlement and the increment of settlement during the application of the cyclic loading increased till a certain number of cycles. The total settlement value due to reinforcement decreased under static and cyclic loading compared to unreinforced soil. The maximum value of the ultimate load was observed at the grid with dimensions  $2D \times 2D$  and the maximum value of the ultimate load was when the axis of the reinforcement grid coincided with the axis of the load action.

**Keywords** Stepwise increasing load · Cyclic load · Settlement · Modulus of deformation · Plate · Soil reinforcement

## 1 Introduction

Numerous methods have been used in the past and recent times to enhance the bearing capacity of the soils; Antonov [1] provided laboratory studies of the load-bearing capacity of reinforced sand. The dependences of the settlement and the ultimate load on various reinforcement parameters were presented. Chakraborty et al. [2] studied the ultimate bearing capacity of a circular footing, placed over a soil mass that was reinforced with horizontal layers of circular reinforcement sheets. The analysis clearly reveals that the inclusion of the reinforcement causes a significant increase in the bearing capacity. A new unified bearing capacity formula was formulated by Chen et al. [3]. Azzam and Nasr [4] carried out a series of loading tests on model

---

V. M. Antonov · I. A. Al-Naqdi (✉)  
Tambov State Technical University, Tambov, Russia

shell footing. The existence of a reinforced layer below the shell was found to modify the bearing capacity failure. The wedge of rupture surface for the shell footing with reinforcement layer is deeper than those of flat and shell footing without reinforcement. Cicek et al. [5] observed that reinforcement length affects the load-settlement curve's behavior. Fattah et al. [6] showed that using the granular trench in soils will increase foundations' bearing capacity and reduce the settlement. Moreover, polymers as a reinforcement material have a significant effect on both bearing capacity and settlement; the reduction of settlement exceeded 60%.

At the construction stage, the bases and foundations first experience a gradually increasing load, and then, if the technological process uses equipment that repeatedly experiences variable loads, then this means that cyclic loads are applied. The characteristics of cyclic loading—the number of cycles, the maximum and minimum values of loads, and the coefficient of cycle asymmetry, significantly affect the foundation bases' strength and deformability. Fahmi et al. [7] used the stone column as a technique for enhancing the soft ground. The key goal of utilizing stone columns is to decrease settlement and increase the soil bearing ability and decrease the consolidation period under cyclic loading. Najim et al. [8] carried out experimental investigations to investigate the footing shape's impact when rested on clayey soil under cyclic loading conditions. A total of sixty-three models have been tested to study shallow footings' behavior under cyclic load of different rates by Fattah et al. [9]. The loss of the bearing capacity and strength of the soil base under the influence of cyclic loading occurs due to the accumulation of shifts of individual volumes of soil under normal and tangential stresses. In order to redistribute the stresses on the additional volume of the soil, increase the rigidity of the base, and in some cases, change the natural frequency of vibrations, all this is possible by using soil reinforcement. Khryanina [10] showed that geogrids perceive the shear forces developing in the ground and restrain plastic deformations' growth in the marginal zones under the foundation. The behavior of geosynthetic-reinforced sandy soil foundations was investigated by Abu-Farsakh et al. [11], and the effect of different parameters contributing to their performance using laboratory model tests were performed. The parameters included top layer spacing, number of reinforcement layers, the vertical spacing between layers, tensile modulus and type of geosynthetic reinforcement, embedment depth, and footing shape.

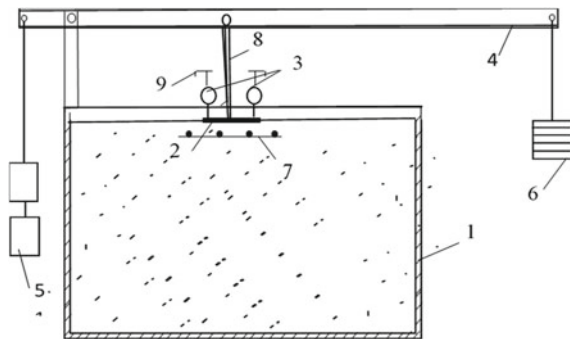
The potential benefits of geogrid-reinforced sand over collapsible soil were studied by Alawaji [12] to control wetting-induced collapse settlement. In his work [13], Safin investigated the deformability of the soil in the form of clay reinforced with vertical elements. It was found that settlement of the soil mass without reinforcement is 70% greater than the settlement of the reinforced soil mass, and the difference in the settlement at a pressure of up to 50 kPa is practically the same. This article presents the results of comparing numerical simulations and experimental results on a reinforced and unreinforced base with variations in the following parameters: the number of loading cycles, the load stage from which cycling began, the size of the reinforcing element, the load eccentricity, and the displacement of the reinforcement relative to the center of the model.

## 2 Materials and Methods

An experimental study was carried out to analyze the reinforced ground base behavior under static and cyclic loads to determine optimal parameters based on static and cyclic tests. The study was carried out in a metal tray with rigid-sided walls measuring  $70 \times 55 \times 55$  cm. The base sand is fine, homogeneous, in an air-dry state. The base was formed by layer-by-layer compaction using a metal rammer up to density,  $\rho = 1.53 \text{ g/cm}^3$ . The thickness of each compacted layer was 5 cm, and the reinforcement element was laid to the desired depth in case of a reinforced base. During the tests, deformations were determined over the entire load range using the ICH-10 clock-type indicators mounted on a support frame. A rigid metal plate with a diameter of 120 mm was used as the foundation model. The load on the plate was transmitted using a lever system with a gear ratio of 1:5. The loading stages were assumed to be equal to 0.1 of the previously found ultimate load. Each stage was maintained until the settlement was conditionally stabilized (20 min). Loading was carried out either till failure, in which the settlement grew without increasing the load or until the conditional maximum foundation settlement  $S_u$  was obtained. In Fig. 1 is shown a diagram of the setup used during experimental work.

The experiments' numerical simulations were carried out using the finite element software programs "MIDAS GTS NX" and "Plaxis 3D". The development of displacements was limited in the directions  $x$  and  $y$ , i.e., displacements could only develop in the vertical direction  $z$  ( $x = 0$  and  $y = 0$ ). A special feature of the Plaxis 3D complex is the ability to provide static as well as cyclic loading. A reasonable prediction is given on the basis of the plain strain Mohr–Coulomb model (an ideal elastic–plastic model), where the used modulus of deformation for sand is calculated at the stage of ultimate load using the Schleicher formula, Full 10-noded model is used for modeling reinforced sand. The plate was created using the plate option in the program, and steel reinforcement was modeled using the 3D ability of the Plaxis 3D, the steel properties that were assigned to the reinforcement. Fine meshing is selected for meshing for more accuracy, cyclic loading was applied with the help of phase

**Fig. 1** Diagram of the setup:  
 1-metal tray; 2-plate;  
 3-indicators; 4-lever;  
 5-counterweight; 6-weights;  
 7-reinforcing element;  
 8-knife, and 9-reference  
 frame



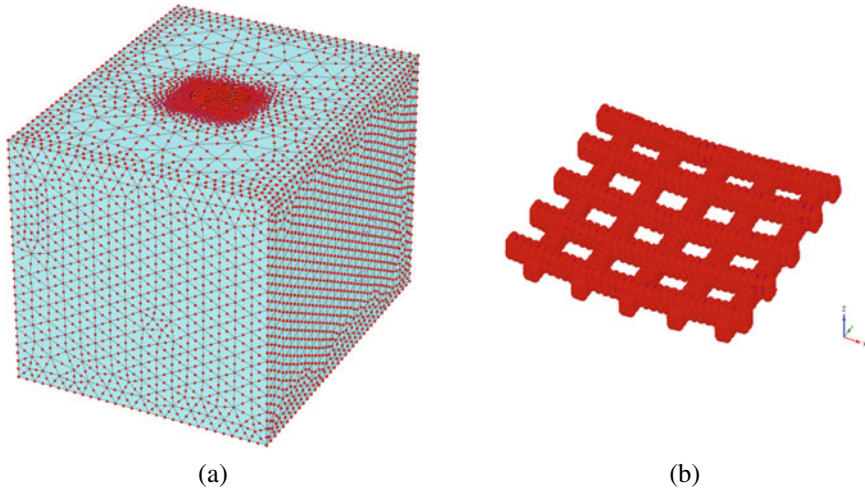


**Fig. 2** Finite element discretization of **a** reinforced sand foundation model, and **b** grid modeling, by Plaxis 3D

option in staged construction feature of Plaxis 3D v20. Very close results to experimental ones are obtained for the reinforced base at static and cyclic loading. Finite element discretization of the reinforced sand-foundation model, and grid modeling used in Plaxis 3D is shown as in Fig. 2.

The modulus of sand deformation used in numerical analysis was calculated using the Schleicher formula based on experimental data at ultimate load, the density was calculated under laboratory conditions, and the remaining values were assumed using tables [14] and program Plaxis 3D. These parameters are shown in Table 1.

### 3 Results and Discussion

**Influence of the number of loading cycles on the load-bearing capacity of the reinforced and unreinforced base.** In the first series of tests, the load stage from which cycling began ( $F$ ) was 0.2 of the ultimate load ( $F_u$ ). The number of cycles varied from 4 to 36, with a step of 4 cycles (4/8/12/16/20/24/28/32/36). Table 2 shows the experiments' results on an unreinforced base, and Table 3 on a reinforced base. The comparison was carried out to the pressure at the plate foundation, at which there was a loss of the bearing capacity of the base  $P_u$ , corresponding to the settlement  $s_u$ , and the increment of the settlement during cycling  $\Delta s$ . The limiting pressure during the transfer of the cyclic load to the unreinforced base was  $P_u = 0.09$  MPa.

In experiments when a reinforced base, with a steel grid of  $145 \times 125$  mm, the grid was placed under the plate foundation at a relative depth of  $h_s = 0.2 D$ . The diameter of the grid rebars, 4 mm, and 35 mm is the rebars' pitch.

**Table 1** Materials and interface properties of sand and plate

Materials	Models	Density (g/cm <sup>3</sup> )	Strength characteristics	Modulus of deformation (MPa)	Poisson's ratio	Shear modulus (MPa)	Oedometer modulus $E_{oed}$ (MPa)
Sand	Mor-coulomb	1.53	$c = 8 \text{ kPa}$ $\varphi = 34^\circ$	0.493500	0.3	0.189	0.662
Plate	Linear elastic	7.8	–	$2.06 \times 10^5$	0.3	$79.2 \times 10^3$	–
Reinforcement	Linear elastic	7.8	–	$2.06 \times 10^5$	0.3	$79.2 \times 10^3$	$277 \times 10^3$
Sand-rebar and plate interface	Coulomb model of friction	–	$\mu = 0.6$	–	–	–	–



**Table 2** The results of experiments on unreinforced base at  $F = 0.2 F_u$

Number of cycles (n)	4	8	12	16	20	24	28	32	36
$P_u$ (Mpa)	0.09	0.09	0.085	0.09	0.09	0.09	0.09	0.09	0.09
$s_u$ (mm)	17.06	17.1	21.76	20.6	23.4	23.6	19.7	19.9	19.8
$\Delta s$ (mm)	0.67	1.29	0.62	0.97	1.58	1.45	2.2	1.3	1.9

**Table 3** Results of experiments on a reinforced base at  $F = 0.2 F_u$

Number of cycles (n)	4	8	12	16	20	24	28	32	36
$P_u$ (Mpa)	0.16	0.16	0.16	0.16	0.16	0.192	0.176	0.197	0.16
$s_u$ (mm)	18.8	20.5	20.8	20.6	22.6	23.07	23.04	25.6	18.3
$\Delta s$ (mm)	0.39	0.515	0.63	0.566	0.83	0.76	0.65	0.915	0.93

Figures 3 and 4 show a comparison of experimental results on a reinforced and unreinforced sand with different load cycles. The comparison was carried out by the values of settlement at specific loading stages.

In the second series of tests, the load stage from which cycling began was changed to  $F = 0.64(F_u)$ , while the other parameters remained the same as in the previous series. Table 4 shows this series of experiments for unreinforced sand and Table 5 for reinforced one. Figure 5 shows the results of the series for experiments at a pressure of 0.06 MPa. In Table 6 listed a comparison of experimental and numerical values of settlement at  $F = 0.2 F_u$  for reinforced, and unreinforced bases.

**Influence of the size of reinforcing elements on the strength and deformability of the base.** This series presents the results of laboratory experiments to assess the effect of the size of reinforcing elements on the rate and amount of development of deformations and the base’s bearing capacity under cyclic loading. The load stage

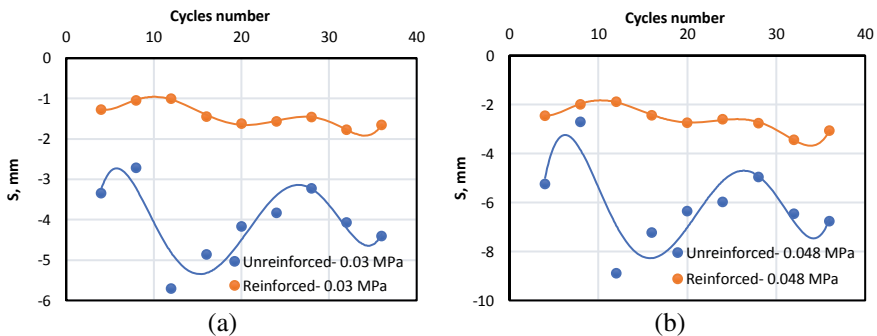


**Fig. 3** Dependence of settlement on the number of load cycles for reinforced and unreinforced sand at foundation, and at certain pressure values,  $F = 0.2 F_u$

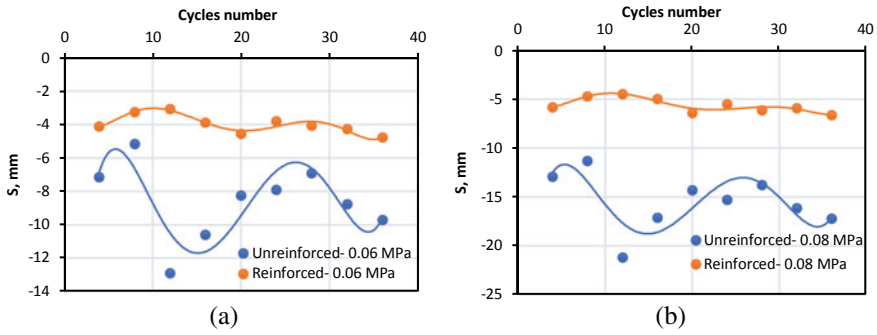


**Fig. 4** Dependence of settlement on the number of load cycles for reinforced and unreinforced sand at the foundation and at specific pressure values,  $F = 0.2 F_u$

**Table 4** Results of experiments on unreinforced base at  $F = 0.64 F_u$

Number of cycles (n)	4	8	12	16	20	24	28	32	36
$P_u$ (Mpa)	0.069	0.069	0.08	0.069	0.085	0.069	0.069	0.069	0.069
$s_u$ (mm)	16.1	16.4	18.69	18.69	20.84	18.27	17.89	16.12	16.12
$\Delta s$ (mm)	2.2	5.4	2.8	3.75	2.66	3.6	4.09	2.65	3.3

**Table 5** Results of experiments on reinforced base at  $F = 0.64 F_u$

Number of cycles (n)	4	8	12	16	20	24	28	32	36
$P_u$ (Mpa)	0.176	0.17	0.197	0.181	0.224	0.149	0.149	0.149	0.149
$s_u$ (mm)	16.47	15.34	15.5	16.8	16.9	20.8	19.45	17.19	16.5
$\Delta s$ (mm)	0.775	0.87	1.09	1.6	1.09	1.9	1.7	1.84	1.88

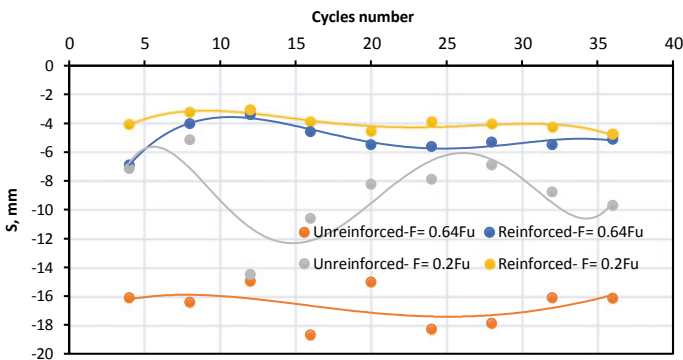


**Fig. 5** The influence of reinforcement on the development of settlements in the foundation at a pressure of 0.06 MPa

**Table 6** Comparison of experimental and numerical values of settlement at  $F = 0.2 F_u$  for reinforced and unreinforced bases

Number of cycles (n)	For unreinforced base			For reinforced base		
	$P_u$ (Mpa)	$s_u$ (mm) (Experimental)	$s_u$ (mm) Plaxis	$P_u$ (MPa)	$s_u$ (mm) (Experimental)	$s_u$ (mm) Plaxis
4	0.09	17.06	15.7	0.16	18.8	17.1
8	0.09	17.1	15.7	0.16	20.5	18.7
12	0.085	21.76	19.8	0.16	20.8	18.9
16	0.09	20.6	18.9	0.16	20.6	18.7
20	0.09	23.4	21.5	0.16	22.6	20.5
24	0.09	23.6	21.7	0.192	23.07	22.4
28	0.09	19.7	18.1	0.176	23.04	21.8
32	0.09	19.9	18.3	0.197	25.6	25.2
36	0.09	18.2	18.2	0.16	18.3	16.8

from which the cycling started was  $F = 0.6 F_u$ . The relative depth of the reinforcement in this series was  $h_s = 0.2D$ , where  $D = 120$  mm—is the plate diameter. The number of cycles was 20. The cycle asymmetry coefficient  $r = \frac{P_{min}}{P_{max}} = 0$ , i.e., unloading was carried out to zero initial value. Grid sizes were  $D \times D$ ;  $D \times 1.5D$ ;  $D \times 2D$ ;  $D \times 3D$ ;  $D \times 3.6D$ ;  $1.5D \times 1.5D$ ;  $2D \times 2D$ ; the rebar rods' diameter is 4 mm, and the pitch is 35 mm. Figure 6 shows a diagram of the settlement developed over the cycles period for the unreinforced and reinforced base, and Fig. 7 shows a diagram of the dependence of settlement on the pressure at  $p = 0.085$  MPa. Table 7. shows a comparison of reinforcement options by specific load-bearing capacity – which equals relation of the load-bearing capacity of the reinforced base  $F_{us}$  to the

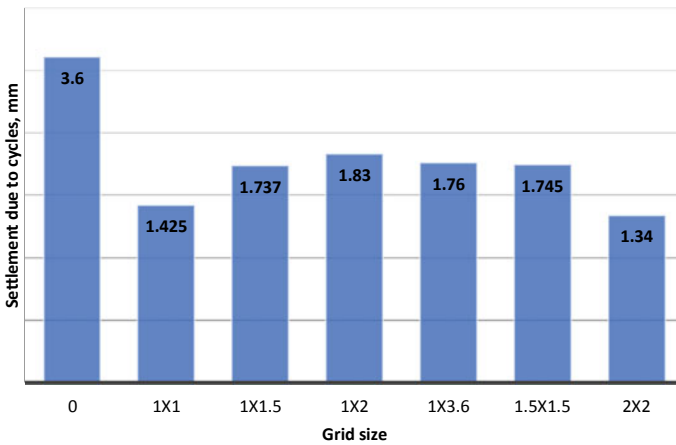


**Fig. 6** Settlement over the cycles period for the unreinforced and reinforced base

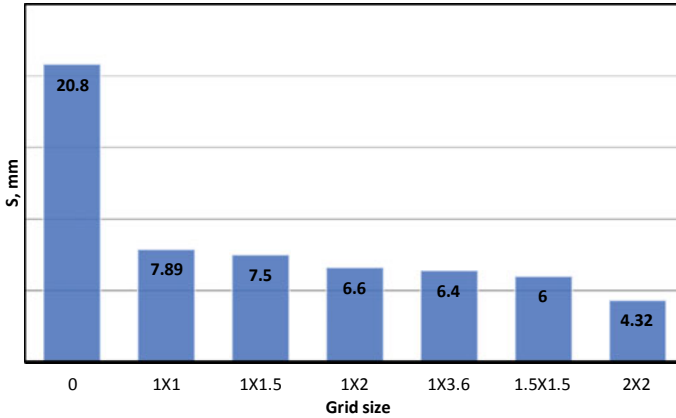


Fig. 7 Values of settlement at the plate foundation where pressure  $p = 0.085$  MPa

Table 7 Effect of the grid size on the specific load-bearing capacity of the base

Grid size	D × D	D × 1.5D	D × 2D	D × 3D	3.6D × D	1.5D × 1.5D	2D × 2D
Ultimate load, $F_{us}$ , N	2293	1627.7	1989.5	2473.94	2769.4	2170.3	4216.3
Grid volume, $mm^3$ , $V_s$	17,200	19,100	27,900	37,516	49,624	27,500	56,000
Specific bearing capacity $F_{us}/V_s$ , $N/mm^3$	0.133	0.0852	0.0713	0.065	0.055	0.0789	0.0752

volume of reinforcement  $V_s$ . Table 8 presents a comparison of experimental data and numerical simulations for the settlement values preceding the base’s loss of the bearing capacity.

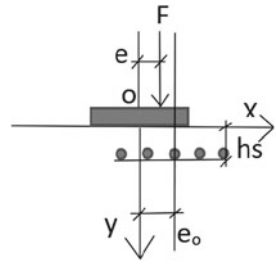
**The influence of eccentricity by applying static and cyclic vertical loading on the base’s bearing capacity when the reinforcing element is displaced.** In this series of experiments, a static central and off-center load with an eccentricity of  $e = 0.075 D$  and  $0.15 D$  was applied to the plate foundation (Fig. 8).

Table 9 shows a comparison of results of experiments and simulations for the unreinforced base. The comparison was carried out by the load at which the loss of the bearing capacity of the base  $F_u$  and the corresponding settlement  $s_u$  occurred. The base was reinforced with a grid of  $145 \times 125$  mm dimensions, the diameter of the grid rods is 4 mm, the pitch of the rods is 35 mm. The reinforcing element was located under the plate foundation at a depth of  $h_s = 0.1D$  and  $0.2D$ . A static central and off-center load was transmitted to the plate with the same eccentricity as in previous experiments. The grid offset relative to the center of the model was  $e_0 = 0.075D$  and  $0.15D$ . Table 10. shows a comparison of the results of experiments and simulations at a grid depth of  $h_s = 0.1D$ , and in Table 11 at  $h_s = 0.2D$ .

**Table 8** Comparison of experimental and numerical simulation results

Grid size	Unreinforced base	D × D	D × 1.5D	D × 2D	D × 3D	D × 3.6D	1.5D × 1.5D	2D × 2D
P <sub>u</sub> (Mpa)	0.085	0.202	0.144	0.176	0.218	0.245	0.192	0.373
s <sub>u</sub> (mm) Experimental	20.8	22.3	20.8	19.8	24.4	25.5	22.15	29.25
s <sub>u</sub> (mm) (Plaxis-3D)	18.8	29.7	16.4	19.2	29.9	19.57	21.6	31.2

**Fig. 8** Diagram of the location of reinforcing element under static and cyclic applied loading



**Table 9** Comparison of experimental and simulation results for the unreinforced base

Relative eccentricity $\bar{e} = e/D$	$F_u$ (N)	$s_u$ (mm) (Experimental)	$s_u$ (mm) (Plaxis)	$s_u$ (mm) (Midas GTS NX)
0	845	11.04	11.5	7.99
0.075	604	13.8	13	9.75
0.15	422	13.2	11	9.6

**Table 10** The results of experimental and numerical simulations on a reinforced base at  $h_s = 0.1D$

e	$e_o$	$F_u$ (N)	$s_u$ (mm) (Experimental)	$s_u$ (mm) (MIDAS GTS)
0.075D	0	1250	13.3	12.1
	0.075D	1550	18.9	14.2
	0.15D	1550	14.6	14.4
0.15D	0	800	11.8	7.5
	0.075D	1050	10.42	13.4
	0.15D	1100	16.6	9.9

**Table 11** Experimental and numerical results when reinforcement at  $h_s = 0.2D$

e	$e_o$	$F_u$ (N)	$s_u$ (mm) (Experimental)	$s_u$ (mm) (MIDAS GTS)
0.075D	0	1050	12.59	10.4
	0.075D	1200	14.4	11.9
	0.15D	1500	17.9	14.7
0.15D	0	750	13.8	14.9
	0.075D	950	14.91	18.2
	0.15D	1050	13.8	10.1

In the next series of experiments, the load was brought up at a stage of  $F = 0.6 F_u$ , 20 cycles were performed, and further static step load was applied until failure occurred. The reinforcing element was located at a distance of  $h_s = 0.1D$  (Table.12) as well as at a distance of  $h_s = 0.2D$  (Table.13) from the plate. Tables 12, 13 show the

**Table 12** Experimental and numerical results of reinforced base under cyclic loading ( $h_s = 0.1D$ )

e	$e_o$	$F_u$ (N)	$s_u$ (mm) (Experimental)	$s_u$ (mm) (Plaxis 3D)	Roll, i
0.075D	0	1300	14.7	17	0.02
	0.075D	1400	18.75	17.8	0.04
	0.15D	1500	18.9	19	0.0033
0.15D	0	900	8.9	10.75	0.027
	0.075D	1050	12.59	10.7	0.03
	0.15D	1100	15.3	13.25	0.025

**Table 13** Experimental and numerical results of reinforced base under cyclic loading ( $h_s = 0.2D$ )

e	$e_o$	$F_u$ (N)	$s_u$ (mm) (Experimental)	$s_u$ (mm) (Plaxis 3D)	Roll, i
0.075D	0	1050	13	14	0.021
	0.075D	1500	23.3	20.2	0.02
	0.15D	1500	15.7	20	0.022
0.15D	0	650	7.9	8.4	0.028
	0.075D	1050	12.36	13.25	0.054
	0.15D	1100	12.8	13.7	0.023

foundation settlement and roll values corresponding to the ultimate load according to the results obtained during laboratory work and numerical modeling.

## 4 Summary

Cycling at one of the loading stages led to compaction of the soil and, as a result, to an increase in shear resistance, consequently, the absolute values of the bearing capacity of the base increased also.

- The values of the total settlement and the increments of settlement during the application of cyclic loading increased till a certain number of cycles, at which the optimal density value was reached. In our case, this value was 20–24 cycles. Then the settlement either stabilized or decreased slightly.
- The total settlement value for reinforced sand decreased by 40–80%, and the settlement in the case of cyclic loading is 1.4–2.1 times less compared to unreinforced soil.
- The base's load-bearing capacity increased by 1.7–4.3 times, depending on the size of the reinforcing element and the depth of its placement. The highest values of the load-bearing capacity were obtained when the reinforcing element is located in the zone of maximum tangential stresses, at a depth of  $h_s = (0.1D - 0.2D)$  from the plate.

- The maximum value of the ultimate load was observed for grid with dimensions  $2D \times 2D$ , the maximum specific load-bearing capacity (per unit volume of reinforcement)—is obtained in the case of the grid with dimensions  $D \times D$ . Increasing the size of the reinforcing element is no longer effective in terms of rebar consumption.
- In loading with eccentricity, greater pressure on the base was observed when the reinforcing element shifted in the direction of the load action, and the maximum value is when the axis of the reinforcement grid coincided with the axis of the load action.

## References

1. Antonov, V. M. (2011). Experimental studies of reinforced bases (In Russ).
2. Chakraborty, M., & Jyant, K. (2014). Bearing capacity of circular foundations reinforced with geogrid sheets. *Soils and Foundations*, 54(4), 820–832.
3. Chen, Q., & Abu-Farsakh, M. (2015). Ultimate bearing capacity analysis of strip footings on reinforced soil foundation. *Soils and Foundations*, 55(1), 74–85.
4. Azzam, W. R., & Nasr, A. M. (2015). Bearing capacity of shell strip footing on reinforced sand. *Journal of advanced research*, 6(5), 727–737.
5. Cicek, E., Guler, E., & Yetimoglu, T. (2015). Effect of reinforcement length for different geosynthetic reinforcements on strip footing on sand soil. *Soils and Foundations*, 55(4), 661–677.
6. Fattah, M., Al-Baghdadi, W., Omar, M., & Shanableh, A. (2010). Analysis of strip footings resting on reinforced granular trench by the finite element method. *International Journal of Geotechnical Engineering*, 4(4), 471–482.
7. Fahmi, K. S., Fattah, M., & Shestakova, A. (2018). Behavior of foundation soil improved by stone column under cyclic load. In *MATEC Web of Conferences* (Vol. 239, p. 05015). EDP Sciences.
8. Najim, A. N., Fattah, M. Y., & Al-Recaby, M. K. (2020). Cyclic settlement of footings of different shapes resting on clayey soil. *Engineering and Technology Journal*, 38(3A), 465–477.
9. Fattah, M. Y., Karim, H. H., & Al-Qazzaz, H. H. (2017). Cyclic behavior of footings on dry sand under different rates of loading. *International Journal of Construction Engineering and Management*, 6(6), 240–253.
10. Khryanina, O. V. (2018). Experimental studies of the interaction of a rigid plate with a reinforced base. *Prospects of Science*, 8(107), 46–50. (In Russ).
11. Abu-Farsakh, M., Chen, Q., & Sharma, R. (2013). An experimental evaluation of the behavior of footings on geosynthetic-reinforced sand. *Soils and Foundations*, 53(2), 335–348.
12. Alawaji, H. A. (2001). Settlement and bearing capacity of geogrid-reinforced sand over collapsible soil. *Geotextiles and Geomembranes*, 19(2), 75–88.
13. Safin, D. R. (2014). Experimental studies of VAT of weak water-saturated clay soils reinforced with vertical elements. *Proceedings of the Kazan State University of Architecture and Civil Engineering*, 4(30). (In Russ)
14. Bowles, J. E. (1996). *Foundation Analysis and Design* (5th ed.). McGraw-Hill Book Co.



# Human-Induced Vibration on Light-Gauge Steel Lightweight Concrete Composite Floors



Tiba H. Saadi and Salah R. Al-Zaidee

**Abstract** Light-gauge steel lightweight concrete composite floors have several attractive properties and are increasingly used for construction. However, under human walking activity, these floor systems are vulnerable to excessive and complicated vibration, resulting in discomfort and complaints from people. A finite-element numerical study has been performed to investigate the vibration of light-gauge steel lightweight concrete composite floors. Two methods have been adopted in this study. The first method uses time-domain analysis to predict the peak acceleration response under the human walking excitation represented by the Fourier series loading function. The second method is a simplified frequency domain analysis that can predict the steady-state response to walking using the acceleration frequency response function with a reduction considering the incomplete resonant build-up. Various light-gauge composite floor structural models have been considered taking into account two types of concrete, lightweight and normal weight, and floor beam span ranging from 5 to 8 m. Results show that human walking activity could induce the light-gauge steel lightweight concrete composite floors to reach inappropriate levels of vibration when used in the quiet areas, and resulting in a violation of the human comfort criteria for these types of structures.

**Keywords** Vibration · Composite floor · Finite element method · Serviceability · Human walking load

## 1 Introduction

Structures are designed to be safe and functional to perform day-to-day service satisfactorily throughout their lifetime. If a system is unsafe or is secure but fails to work in use, then one or more of the limit states are reached. The key concept behind the limit state design method is to follow a probabilistic approach and to prevent the system from entering the limit states with a certain degree of confidence that is

---

T. H. Saadi (✉) · S. R. Al-Zaidee  
Department of Civil Engineering, University of Baghdad, Baghdad, Iraq  
e-mail: [t.saadi1101@coeng.uobaghdad.edu.iq](mailto:t.saadi1101@coeng.uobaghdad.edu.iq)

predetermined. Thus, systems are designed to satisfy two limit states, the ultimate limit state (ULS) and serviceability limit state (SLS) [1]. Ultimate limit states (ULS) are reached when a system fails due to some cause, such as loss of the entire structure's equilibrium, instability, rupture, or transformation into a mechanism. In contrast, the serviceability limit state (SLS) is the one that reaches due to cracking, deflection, and vibration. Thus, the floor vibration is a serviceability issue that can occur in a system that is completely valid from a strength point of view. This problem is caused largely by the increasing use of lightweight concrete and high-strength materials to produce flexible and long-span flooring systems [1].

In severe cases, floor vibration problems can make a facility entirely unusable by the occupants, based solely on personal comfort levels. Due to the human-based factor, accurate prediction is not an easy goal. Each has a different degree of tolerance, based on their definition of personal comfort [2]. The use of light-gauge steel in multi-story buildings and occupancy residences as a framework for floor structures is becoming a more and more common alternative to traditional materials and techniques. Designers and builders have acknowledged that the high strength-to-weight ratio of lightweight steel components offered by the cross-section enables longer spans and lighter structures. The lighter structures and longer spans associated with light-gauge steel floor systems can contribute to vibration serviceability problems [3]. Moreover, the problem becomes more apparent when they are used in composite floors with lightweight concrete.

The composite floors are usually designed using static methods that do not consider the true behavior under dynamic loads induced by humans. Their one-way spanning behavior, in comparison to the traditional two-way reinforced concrete floor slabs, makes them much more susceptible to vibration issues [4]. This study aims to investigate the behavior of light-gauge steel lightweight concrete floor when subjected to human-induced vibration. Firstly, the human-induced walking excitation has been concluded from the related literature in terms of the time and frequency domains. Then, a finite element model has been prepared to simulate the lightweight concrete floor and the supporting light-gauge steel beams. The supporting hot rolled girders and columns have been included in the model for a more accurate mimic of the system mass and stiffness. Finally, the response has been determined and compared to show how lightness of concrete and supporting steel beams affect the efficiency of the flooring system in vibrational aspects.

## 2 Human-Induced Dynamic Load

The floor vibration caused by the human load is considered a complex problem as the dynamic excitation generated due to activities such as walking, jumping, running, or even aerobics are directly linked to the adversities of the individual body and the particular way in which each person performs a certain rhythmic activity [5]. A lot of researchers have studied the walking force caused by a single person. Dynamic

loads induced by humans generally have three components: vertical, horizontal-lateral, and horizontal-longitudinal. Since the vertical portion of the loads has the highest magnitude, and due to the flexibility of the floors in the vertical direction, the vertical component is the only one that is usually considered [6].

Typical force–time history is presented in Fig. 1 for a single footstep. It indicates a high initial impulse load occurring as the heel hits the floor (A). The first hump (B) represents the person’s weight in addition to the inertial portion when touching the plate due to its momentum. This hump rises above the person’s static weight as the plate measures the full combined force. As the person bends his knee, swings his opposite leg, and moves the body weight to the opposite limb, the trace then dips underneath the static weight (C). The final hump (D) happens as the person lifts the toes off the plate, and eventually (E) the person ends the entire contact with the plate [7]. Galbraith and Barton in 1970 reported the results of a series of measurements of walking forces made for obtaining basic data as part of a study to help detect intruders. For three subjects, weight varies between 115 and 250 lbf on a plate placed on a 16 ft walkway; seventy-nine footstep force waveforms were reported. There were three different surface materials, ranging from very soft (sand and rubber pads) to extremely rough. The investigators indicated that weight and step frequency were the main influence of the footstep waveforms [8].

In 1988 Rainer et al. measured the vertical dynamic forces from walking and running using an instrumented platform. The results revealed that the dynamic forces are composed of wave trains of harmonics of the walking or running rate. In the initial three or four harmonics, the major low-frequency contributions are usually included. They also noticed that a resonance would occur when the frequency, or the integer of it, coincident with a natural frequency of the floor by the characterization of the force spectrum [9]. In 1998, Kerr presented the results of more than a thousand footstep forces results for walking on a flat floor plate. In his study, at first, the vertical component of the ground reaction of footsteps was recorded. As Fourier analysis can only be carried out on a repetitive time history, a modification was made to modify

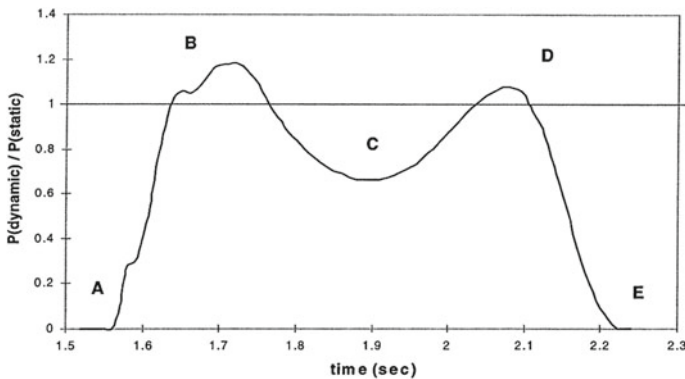


Fig. 1 Walking force [10]

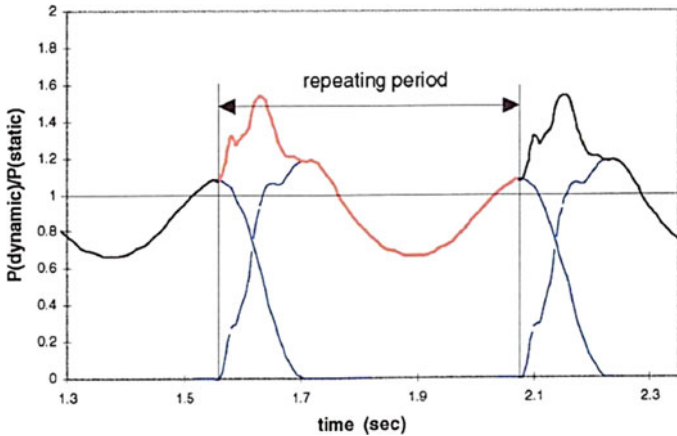


Fig. 2 Summing the individual traces to form a continuous trace [10]

the single footfall traces that represent in Fig. 1 into continuous trace that presented in Fig. 2 with the assumption that the footfall traces for the left and right foot are similar and overlapping the traces by the exact period between heel strikes.

The Fourier analysis showed that the first harmonic amplitude is substantially distributed near the average footfall rate of 2 Hz and follows a constant pattern of approximately 24% to about 46% of the walker’s static weight. At the same time, there is no obvious pattern for the second, third, and fourth harmonic. He indicated that the second amplitude of the harmonics was significantly lower than the first, and the third and fourth harmonics were also smaller. The amplitudes were approximately zero, beyond the fourth harmonic [10].

Later Willford et al. [11] noticed that the footsteps harmonic force measurements obtained by Kerr [10] have considerable dispersion in their values. Thus, it is essential to recognize that no one value is correct, but their values may instead be selected to be more or less conservative within the range. Generally speaking, the chosen values should then have the probability of exceedance assigned to them. Hence, they determined the “Mean” and “Design” (75th percentile) of the harmonics of the footstep forces as presented in Fig. 3. Therefore, the force generated by a walker comprises of distinct frequency components at integer multiples (harmonics) of the pacing frequency and can be represented as below [12].

$$F(t) = Q + \sum_{i=1}^N Q\alpha_i \sin(2\pi i f_{\text{step}} t - \Phi_i) \tag{1}$$

where:

- Q is the walker’s weight,
- $f_{\text{step}}$  is the step frequency of the walker,
- i is the harmonic multiple of the step frequency,

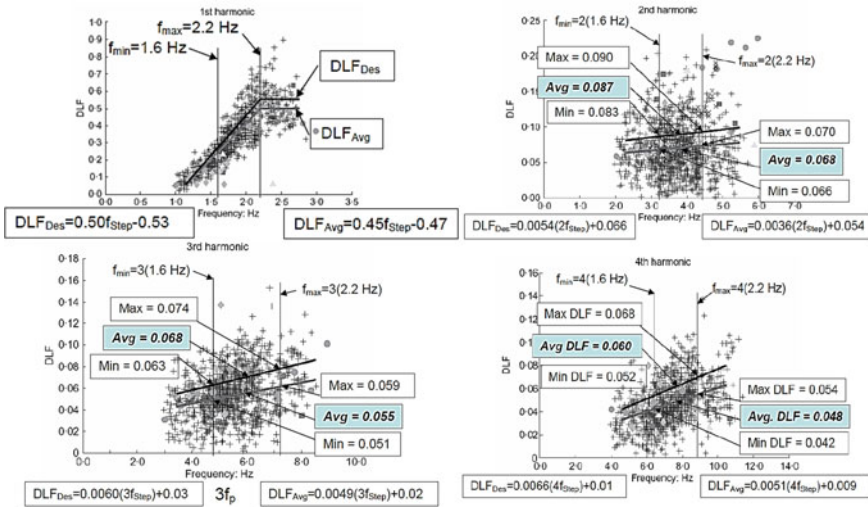


Fig. 3 Harmonic amplitude [13]

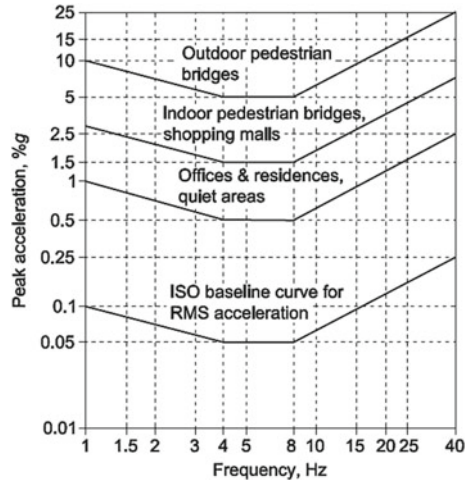
$\alpha_i$  is the dynamic load factor of the  $i$ th harmonic,  
 $\Phi_i$  is the phase lag of  $i$ th harmonic.

### 3 Assessment of Vibration Problem Due to Human Load

The design of vibration serviceability for floors under human loads of civil engineering systems is not strictly regulated by national codes of practice. Most commonly, it is based on typically considered ‘guidelines’ concept guides. Such publications are primarily advisory and give recommendations to an engineer in charge of the design of civil engineering systems [14]. The AISC Design Guide 11 uses hand calculation methods to check the vibration serviceability for typical floor framing [15]. Later they introduce finite element analysis using acceleration frequency response for irregular framing systems. As the hand calculation methods are cumbersome to apply and need complex computations, using finite element analysis to predict the vibration response to walking is the logical choice.

Vibration assessment of light-gauge steel lightweight concrete composite floor due to walking is presented in this paper. Two methods have been used. The first method uses the time domain analysis to predict the acceleration waveform using the human walking load function presented in Eq. 1. The second method is a simplified frequency domain analysis that is applied by the AISC Design Guide and uses the acceleration frequency response function that estimates the steady-state response to walking, with a reduction taking into account the incomplete resonant build-up. Finally, the peak accelerations results have been compared with the human tolerance presented in Fig. 4. The frequency response function (FRF) is a steady-state response

**Fig. 4** Recommended tolerance limits for human comfort [15]



plot due to a sinusoidal load with a unit amplitude versus frequency. This approach considers that the majority of the walking reaction is due to the harmonic force of the footstep that matching the natural frequency ( $f_n$ ) of the dominant mode, therefore using Eq. 2 to compute the peak acceleration from the FRF plot.

$$a_p = (FRF_{Max}(\alpha Q))\rho \tag{2}$$

where:

- FRF<sub>Max</sub> is maximum FRF magnitude at frequencies below 9 Hz, %g/N,
- Q is the walker's weight,
- $\alpha$  is the dynamic load factor,
- $\rho$  is the resonant build-up factor that is assumed for six footsteps build-up, see Eq. 4.

As the walking loads are somewhat simplified, without losing substantial accuracy, by finding that the harmonic loads do not differ greatly across the frequency ranges that they can be applied. Thus, the average design-level forces are recommended [13]. Therefore, AISC Design Guide approximate the fittings of Fig. 3 by Eq. 3:

$$\alpha = 0.09e^{-0.075 f_n} \tag{3}$$

$$\begin{aligned} \rho &= 50\xi + 0.25 && \text{if } \xi < 0.01 \\ \rho &= 12.5\xi + 0.625 && \text{if } 0.01 \leq \xi < 0.03 \\ \rho &= 1 && \text{if } \xi \geq 0.03 \end{aligned} \tag{4}$$

where  $\xi$  is the viscous damping ratio.

### 4 Structural Model

In this paper, the floors are presented parametrically in Fig. 5. They are one-way in nature where the uniformly distributed loads act on the slab directly to transfer to the floor beams in a one-way action. The loads are in turn transferred to the supporting girders and finally to the supporting columns. Supporting columns are included in the model to have a more accurate stiffness simulation for the vibration analysis. The parametric analysis has been achieved taking into account two types of concrete, lightweight (LC) and normal weight (NC), keeping constant girder span equal to 6 m and varying the floor beam span from 5 to 8 m. Steel sections of HEA300 and IPE300 are adopted for the columns and girders, respectively, while a hollow rectangular section of  $260 \times 180 \times 5$  is adopted for the floor beams. A concrete slab with a metal deck of 250 mm rib spacing and a thickness of 1 mm is used. Finally, an imposed dead load of 1.5 kPa and a live load of 2 kPa are assumed during the analysis.

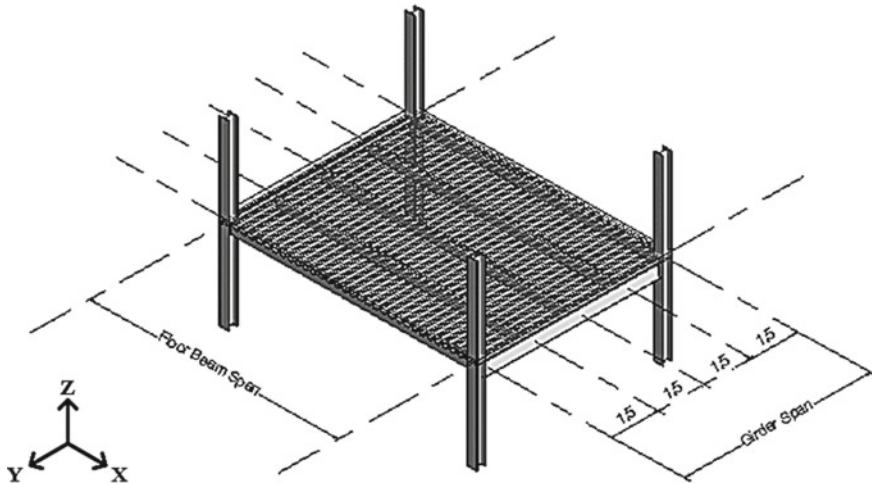


Fig. 5 Composite floor system adopted in this study

Table 1 Material properties of the floor system

Material	Modulus of elasticity in (MPa)	Material density in (kg/m <sup>3</sup> )
Light weight concrete	19,343	1700
Normal weight concrete	33,575	2400
Steel	200,000	7800

The material properties used in the analysis have been formulated in Table 1. In the case of a composite floor excited by dynamic loads, the concrete is stiffer than when it is subjected to static loads. As a result, the conventional concrete modulus of elasticity has been increased by 35%, according to AISC design guide 11 [15].

### 5 Modeling of The Structural Orthotropy

The orthotropic plate is defined as a plate with different bending stiffnesses ( $D = EI$ ) in two orthogonal directions X and Y in the plate’s plane. The difference in bending stiffness can be induced either from different moduli of elasticity  $E_x$  and  $E_y$  of the materials in two directions, as in the situation of naturally or elastically orthotropic plates, or from different moments of inertia per unit width, as for structurally orthotropic plates [16]. When the steel element in a composite action with a concrete element, the cross-sectional shape used in the structural analysis depends on the relative orientation of the concrete slab’s ribs to the span of the composite steel beam.

The composite member when the ribs of the metal deck are in the same orientation of the composite beam is presented in Fig. 6(a), where  $h_{rib}$  is the height of the rib,  $h_{solid}$  is the height of a solid part above the metal deck,  $A_{rib}$  is the area of an individual rib,  $A_{void}$  is the area of an individual void between the ribs, and  $\theta$  equals zero where  $\theta$  is the angle, in degrees, between the orientation of the span of the ribs, and that of the composite beam as shown in Fig. 7. For simplicity, the structural system be

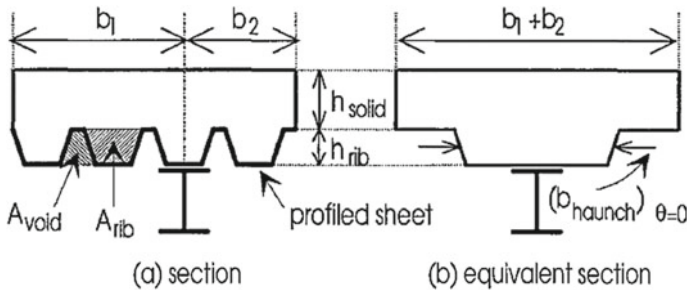
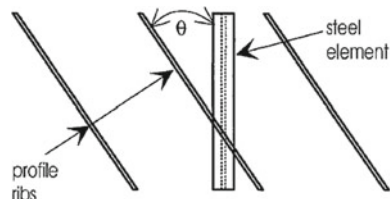


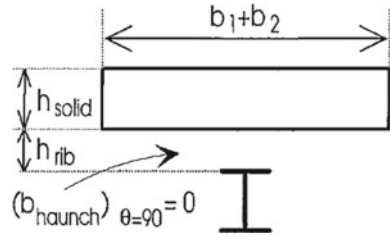
Fig. 6 Longitudinal ribs (section of a girder)

Fig. 7 Oblique ribs





**Fig. 8** Transverse ribs  
(section of a floor beam,  $\theta = 90^\circ$ )



analyzed as presented in Fig. 6b, where the haunch area is equal to the sum of the individual ribs' areas over the effective section width [17]. In contrast, when the ribs of the metal deck are transverse to the span of the composite beam, the cross-section of the composite member is presented in Fig. 8, when  $\theta$  equals  $90^\circ$ . Therefore, in the structural analysis, the weakest cross-section is used, and this takes place in a section by a gap between the ribs. Hence  $(b_{haunch})_{\theta=90}$  equals zero when  $\theta$  equals  $90^\circ$ .

Therefore, the rigidity of the slab with the metal deck can be calculated using the composite moment of inertia for the composed section of the concrete and the transformed steel deck along the ribs ( $D_x$ ), while in the other direction, only the concrete above the metal deck has been considered in calculating the rigidity ( $D_y$ ) using Eqs. 5 and 6 [18]:

$$D_x = \frac{E_c}{1 - \nu_c^2} (I_{cx} + nI_{sx}) \tag{5}$$

$$D_y = \frac{E_c I_y}{1 - \nu_c^2} \tag{6}$$

$$\gamma = \frac{D_x}{D_y} \tag{7}$$

$$E_y = E_c \tag{8}$$

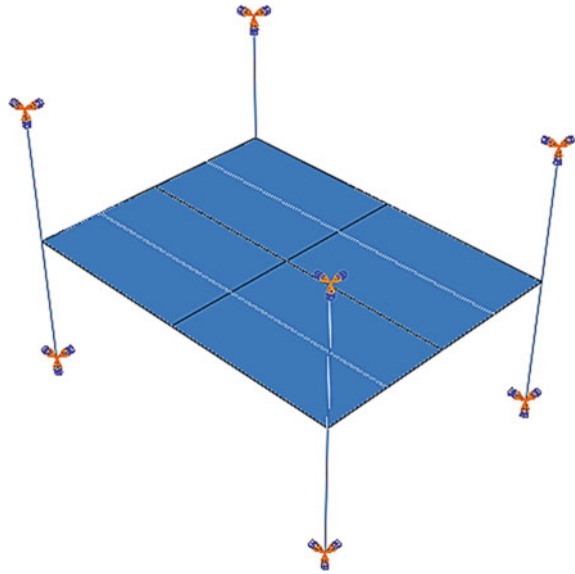
$$E_x = \gamma E_y \tag{9}$$

Using the previous method to define the orthotropic properties in the finite element model, an additional mass has been added to compensate for the volume of the concrete within the ribs.

## 6 Finite Element Model

Abaqus software has been used to develop the computational model for the modal transient and steady-state analyses of the considered floor systems. In the Abaqus

**Fig. 9** Composite floor system simulation using Abaqus



model, the slab has been simulated using (S4R) shell element with orthotropic properties as described in the previous section. Beam element (B31) has been used to represent columns and beams. As shown in Fig. 9, fixed supports have been assigned to all columns. A “Tie” constrain has been adopted to mimic the perfect bond and neglect the possible slip between the slab and beams. This assumption is true as the beams are in direct contact with the slab and act compositely. Since floor vibration caused by humans typically results in minimal mid-bay displacement, the full composite action is ensured irrespective of the existence of stud shear connectors [19].

## 7 Dynamic Analysis

Free vibration analyses have been carried out to determine the natural frequencies of the structural models and their corresponding mode shapes. Figure 10 shows the first five modes of vibration and the corresponding natural frequencies of the structural model with a floor beam span of 8 m. Time history response has been performing using modal dynamic analysis where the proposed floor has been subjected to a human walking load considering the most unfavorable situation. The walking frequency was considered to be  $3.91/2 = 1.955$  Hz. In this situation, the second harmonic of the load was the same as the fundamental frequency of the composite flooring, and it would be easy to excite the resonant response. The individual human weight has been assumed equal to 750 N [15]. The load has been applied to the central point of the slab panel to consider the worst scenario.

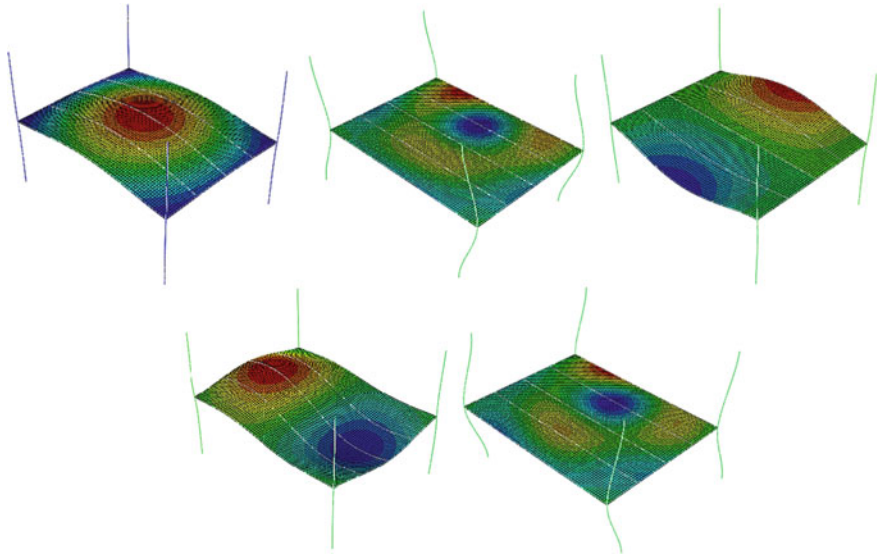


**Fig. 10** Mode shapes of the composite floor system with 8 m floor beam span **a** mode 1: 3.91 Hz; **b** mode 2: 5.52 Hz; **c** mode 3: 6.99 Hz; **d** mode 4: 8.9 Hz; **e** mode 5: 10.14 Hz

The load has been expressed by Eq. 1 for six footsteps [15], and presented in Fig. 11, the phase angle of  $0, -\pi/2, \pi,$  and  $\pi/2$  for the four harmonics, respectively, while dynamic load factors have been taken according to Willford et al. [11]. Results of the time history acceleration of the floor’s center point and its Fourier amplitude spectrum are shown in Fig. 12. To calculate the resonant build-up, factor  $\rho$ , another simulation with a sufficient loading time of ten seconds has been considered to guarantee that build-up resonance occurs. The resonant build-up factor is then calculated

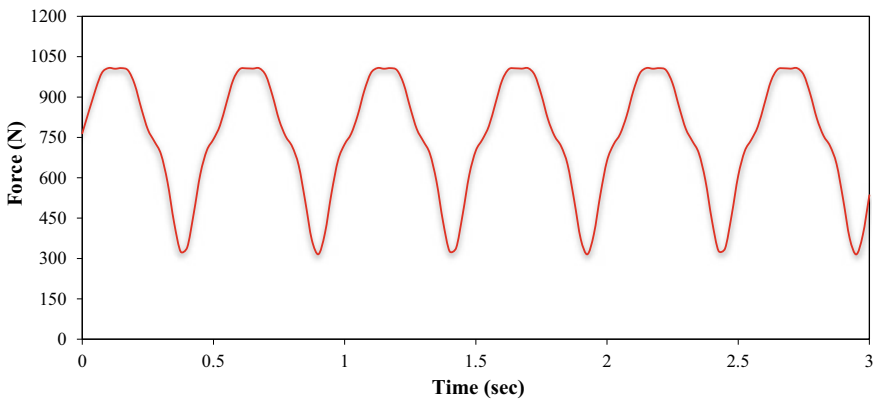


**Fig. 11** Human load due to walking

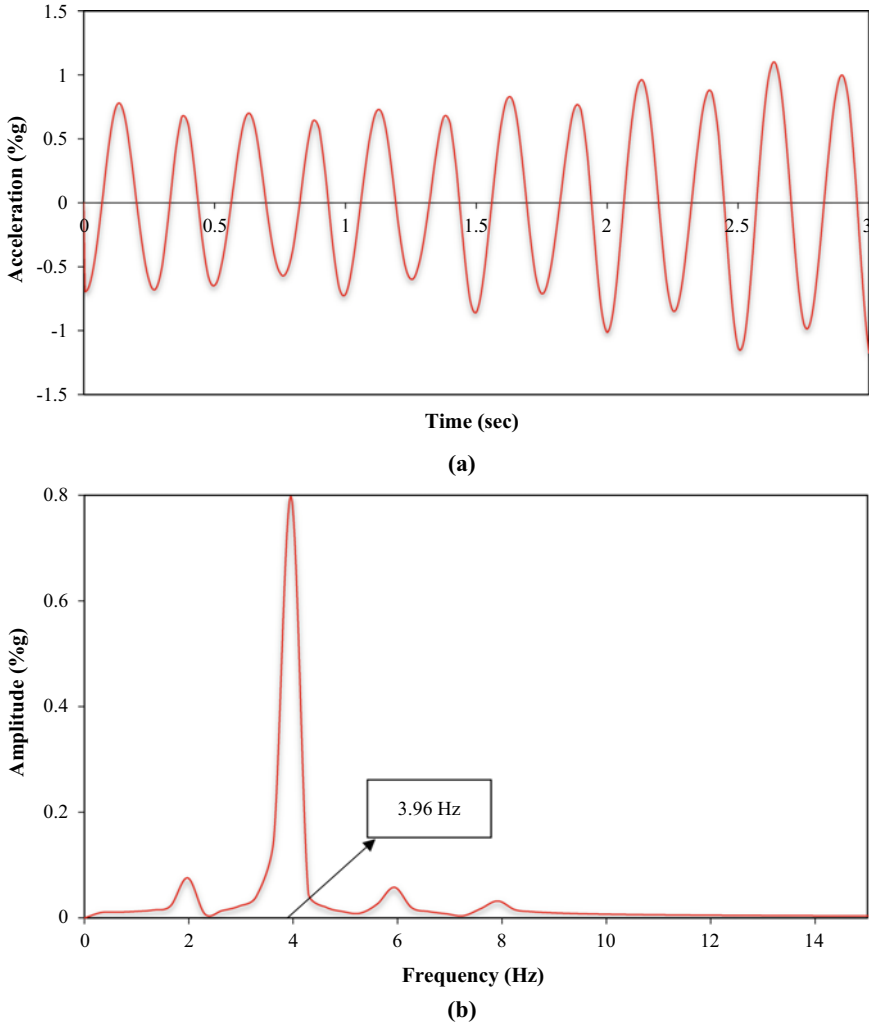


**Fig. 12** Response of the floor system with 8 m span length under human walking excitation: **a** time history acceleration, **b** acceleration amplitude spectrum

by dividing the acceleration response of six footsteps by the build-up resonant acceleration response. In the other simulation, the acceleration FRF magnitude for the unit load applied at the panel center point is computed using a steady-state modal analysis procedure. The single-mode response to one harmonic of the Fourier series representing human walking is then predicted. The FRF has been scaled to display the acceleration in the units %g/N. The peak acceleration has been calculated using Eq. 2. The result of steady-state analysis of composite floor of 8 m floor beam span

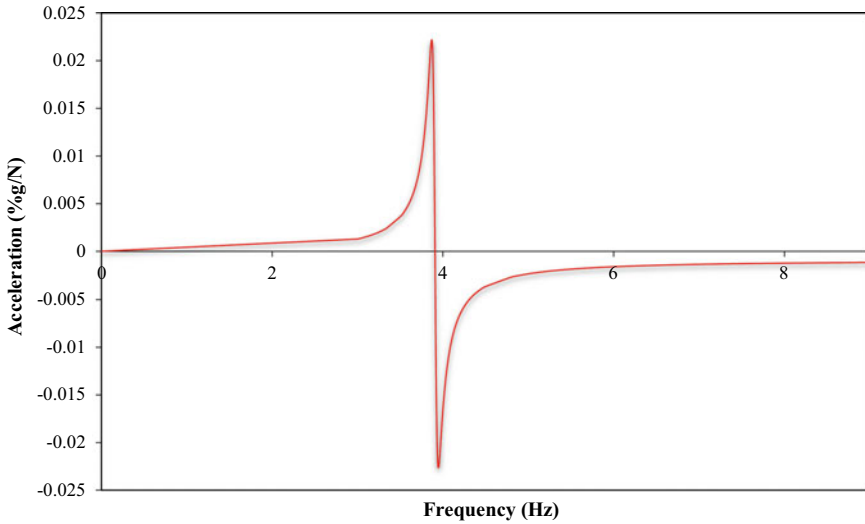


**Fig. 13** Results of steady-state modal analysis of the floor system with 8 m span length

length is presented in Fig. 13. In both simulations, a damping ratio of 1% has been assumed.

## 8 Results and Conclusions

The natural frequencies and the accelerations of the light-gauge steel–concrete composite floors under human dynamic loading have been presented in Tables 2 and 3. Results show that:

**Table 2** Time-domain analysis results

Span length	Concrete type	Dominant mode	$a_p$ (%g), for six-foot steps	$a_p$ (%g), for build-up resonance	Resonant build-up factor, $\rho$
5	NC	7.52	1.675	2.257	0.742
	LC	7.42	2.026	2.73	0.742
6	NC	5.99	1.278	2.251	0.568
	LC	6.33	1.562	2.776	0.563
7	NC	4.73	1.085	1.842	0.589
	LC	4.79	1.155	2.241	0.515
8	NC	3.88	0.953	1.826	0.522
	LC	3.91	1.150	2.194	0.524

**Table 3** Frequency domain analysis results

Span length	Concrete type	FRF	$a_p(\%g)$
5	NC	0.033	0.921
	LC	0.039	1.132
6	NC	0.027	0.872
	LC	0.032	1.047
7	NC	0.022	0.771
	LC	0.026	0.905
8	NC	0.018	0.696
	LC	0.022	0.842

- Natural frequency increases with a decrease in the floor beam span length.
- Peak accelerations of time-domain analysis are higher than the simplified frequency domain analysis. The difference comes from the essence of the other harmonics.
- Peak accelerations of normal weight concrete floors are less than lightweight concrete floors.
- In the time domain analysis, the resonant build-up factor is in the range of 50–75%.
- The floor vibration is a complicated issue that the peak acceleration doesn't decrease with the floor beam span decrease. This is due to the interaction between the human load with very particular dynamical characteristics associated with the structural system, such as mass and stiffness [5].
- The human walking activity could induce the light-gauge steel lightweight concrete composite floors to reach inappropriate vibration levels when used in the quiet areas, resulting in a violation of the human comfort criteria for these types of structures. Therefore, it is crucial to assess the floor vibration's serviceability assessment from walking activity in the design stage of these floors.

## References

1. Pavic, A., & Reynolds, P. (2002). Vibration serviceability of long-span concrete building floors. Part I: Review of background information. *The Shock and Vibration Digest*, 34(3), 191–211.
2. Alvis, S. R. (2001). *An experimental and analytical investigation of floor vibration*. Ph.D. Thesis, Virginia Polytechnic Institute and State University, Virginia.
3. Parnell, R. A. (2008). *Vibration serviceability and dynamic modeling of cold-formed steel floor systems*. MSc. Thesis, University of Waterloo, Canada.
4. De Silva, S. S. (2007). *Vibration characteristics of steel-deck composite floor systems under human excitation*. Ph.D. Thesis, University of Technology, Queensland.
5. Mello, A. V., da Silva, J. G., da Vellascoc, P. C. S., de Andrade, S. A., & de Lima, L. (2008). Dynamic analysis of composite systems made of concrete slabs and steel beams. *Journal of Construction Steel Research*, 64(10), 1142–1151.
6. Cai, Y., Gong, G., Xia, J., He, J., & Hao, J. (2019). Simulations of human-induced floor vibrations considering walking overlap. *SN Applied Sciences*, 2(1), 1–19.

7. Kerr, S. C., & Bishop, N. W. (1999). Human-induced loading on flexible staircases. *Engineering Structures*, 23(1), 37–45.
8. Galbraith, F. W., & Barton, M. V. (1970). Ground loading from footsteps. *The Journal of Acoustical Society of Engineering*, 48(5B), 1288–1292.
9. Rainer, J. H., & Pernica, G. (1988). Vertical dynamic forces from footsteps. *Canadian Acoustics*, 14(2), 12–21.
10. Kerr, S. C. (1998). *Human-induced loading on staircases*. Ph.D. Thesis, University of London.
11. Willford, M., Young, P., & Field, C. (2007). Predicting footfall-induced vibration: Part 1. *Structures & Buildings*, 160(SB2), 65–72.
12. Muhammad, Z., Reynolds, P., Avci, O., & Hussein, M. (2018). Review of pedestrian load models for vibration serviceability assessment of floor structures. *Vibration*, 2(1), 1–24.
13. Davis, D. B. (2008). *Finite element modeling for prediction of low frequency floor vibrations due to walking*. Ph.D. Thesis, Virginia Polytechnic Institute, and State University, Blacksburg, Virginia.
14. Racic, V., Pavic, A., & Brownjohn, J. M. (2009). Experimental identification and analytical modelling of human walking forces: Literature review. *Journal of Sound and Vibration*, 326(1–2), 1–49.
15. Murray, T. M., Allen, D. E., Ungar, E. E., & Davis, B. D. (2016). *Vibrations of steel-framed structured system due to human activity: AISC design guide 11* (2nd ed.). American Institute of Steel Construction.
16. Troitsky, M. S. (1976). *Stiffened plates bending, stability and vibrations*. Elsevier.
17. Oehlers, D. J., & Bradford, M. A. (1995). *Composite steel and concrete structural members fundamental behaviour* (1st ed.). Pergamon.
18. Timoshenko, S., & Woinowsky-Krieger, S. (1959). *Theory of plates and shells*. McGraw-hill.
19. Liu, D. (2015). *Vibration of steel-framed floors supporting sensitive equipment in hospitals, research facilities, and manufacturing facilities*. Ph.D. Thesis, University of Kentucky, Kentucky

# Evaluating Nonlinear Behavior of a Reinforced Concrete Building with Shear Walls and Concentric Steel Bracings



Anwar Jabar Qadesheen, Esra Mete Güneyisi, and Halmat Ahmed Awla

**Abstract** In this study, the seismic performance of buildings with shear wall and steel bracing were evaluated. To this, a nine-storey reinforced concrete (RC) building having a square plan with five bays in both directions and identical story height was considered. The building consists of typical beam-column frames. RC shear walls and concentric steel bracings were used to improve the seismic behavior of the structure. A total of five building cases were taken into account as the existing building and those upgraded with the shear wall, X-bracing, inverted-V bracing, and diagonal bracing. The nonlinear static pushover and nonlinear time history analyses were performed through ETABS Software. From these analyses, the normalized base shear versus roof drift ratio, variation of maximum displacement and inter-storey drift ratio with story level, and time history plots were obtained for each of the buildings with and without shear walls and steel bracings. It was observed that the seismic capacity of the existing RC building was noticeably enhanced with the applied wall and brace, and its performance state altered from collapse prevention to life safety.

**Keywords** Nonlinear analysis · Reinforced concrete building · Retrofitting system · Shear wall · Steel bracings

---

A. J. Qadesheen (✉)

Department of Civil Engineering, Soran University, Erbil, Iraq

e-mail: [anwar.qadersheen@cive.soran.edu.iq](mailto:anwar.qadersheen@cive.soran.edu.iq)

E. M. Güneyisi

Department of Civil Engineering, Gaziantep University, Gaziantep, Turkey

e-mail: [eguneyisi@gantep.edu.tr](mailto:eguneyisi@gantep.edu.tr)

H. A. Awla

Department of Information Technology, Choman Technical Institute, Erbil Polytechnic University, Erbil, Iraq

e-mail: [halmat.awlla@epu.edu.iq](mailto:halmat.awlla@epu.edu.iq)



## 1 Introduction

Thousands of reinforced concrete (RC) buildings are placed on hazardous seismic zones, and they have a high susceptibility to damage. The common structural destruction and various total or partial failures measured in the out-coming of the late disturbing ground shakes have witnessed the urgent need to assess the seismic susceptibility of the existing RC structures and performing strengthening strategies as suitable. The use of nonlinear analyses is essential to evaluate the behavior of structures under special seismic effects. It is commonly agreed that RC frames show highly nonlinear load-deformation response because of principally to the nonlinear stress-strain relationship of the basic materials [1]. Under strong earthquakes, the structural components undergo cracks, and materials inelasticity occur instead of responding elastically. This concept is cost-effective from the design perspective [2]. Nowadays, for lateral load resisting systems, steel bracings and reinforced concrete shear walls are commonly utilized in the structures. Reviewing the action of reinforced concrete structures as exposed to seismic loads provides that these structural systems can show sufficient strength because of the material inelasticity properties and the number of adequate deformations of the buildings. The earthquake's input energy is absorbed by these structures and dissipated by bearing significant displacements under nonlinear seismic behavior [3]. To moderate the seismic hazard of existing buildings, the retrofitting system should be performed. The main objective of retrofitting systems and evaluation processes is to prevent total collapse and identify damage of structural and nonstructural components to reduce the risk of injury and remain necessary circulation routes available during earthquakes [4].

Some retrofitting techniques were utilized as RC shear walls, strengthening of columns by using steel angles, column jacketing, and steel bracings [4]. It was found that the application of retrofitting techniques to the structural system improved the capacity of the bare frame as predicted. Esmaili et al. [3] showed that the retrofitted steel moment-resisting frames using shear walls had higher response modification and higher ductility than those retrofitted by steel braces. Ghobarah and Elfath [5] studied the effect of arranging steel bracings and distributing over the frame height for RC structures. It was found that the distribution of the steel bracings plays a significant role on the formation of plastic hinges mechanisms. Massumi and Absalan [6] conducted an investigation on RC frames using steel bracings. They demonstrated a development in the ultimate strength of the dual system because of the interaction between two systems. Maheri and Hadjipour [7] showed the strength capacity and the yield capacity of the ductile RC frame increased, and the total displacement decreased by directly applying either an X-bracing or knee-bracings which could be performed to retrofit or design for damage level earthquake.

Durucan and Dicleli [8] suggested a system for retrofitting that arranged to advance the performance of seismically susceptible RC structures. The proposed seismic retrofitting scheme was collected of a rectangular steel housing frame with V-shape braces and a yielding shear link linked between the braces and the frame. They demonstrated that an adequate performance point was obtained for the retrofitted

structures by using the proposed retrofitting system. Kadid and Yahiaoui [9] considered the seismic characteristics of RC structures braced by different categories of steel braces such as zipper, inverted V, and X steel braces. It was established that applying braces improved the global performance of the structures concerning deformation, ductility, and strength. In the literature, it was also reported that different retrofitting approaches need to be considered for different types of buildings to better understand the compatibility and efficiency of the solution applied.

For considering the inelasticity of the frame structures, two main modeling approaches are available, lumped plasticity method and distributed plasticity method. Two zero-length nonlinear rotation springs are connected by an elastic line (beam/column) element in lumped plasticity method. The springs are computing inelasticity during loading while the rest of the element remains elastic. In the second method, the element cross-sections are discretized into fibers and the length into integration points. It is so-called fiber element modeling [10, 11]. For this study, the first method was used. Plastic hinges are defined to the ends of the structural elements for representing nonlinearity.

## 2 Case Study and Numerical Modelling

In the study, an existing nine-storey reinforced concrete (RC) building was taken into consideration. First of all, the RC building was assessed to show the structural system's nonlinear behavior and performance state. Secondly, the existing building was upgraded by adding shear walls and concentric steel bracings. As a concentric bracing, X, inverted-V, and diagonal bracing systems were used. The nine-storey RC framed building has an identical height of 3.0 m at each story with 5 bays in both X and Y directions of different spacing, as shown in Figs. 1 and 2. Five cases of the building were evaluated; case 1: RC building frames that were taken as existing building (EB), case 2: RC building retrofitted by shear walls (RB-SW), case 3: building retrofitted by X-steel bracing (RB-XB), case 4: building retrofitted by inverted V-steel bracing (RB-IVB), and case 5: building retrofitted by diagonal-steel bracing (RB-DB). The existing building had a first natural vibration period of 1.17 s, while the upgraded building's first natural vibration period varied between 1.02 and 0.90 s. The sections of the frame elements such as columns and beams were formed as square and rectangular sections, respectively, and their cross-sectional properties are varied depending on the story level. For the steel braces, pipe hollow steel sections were utilized as profiles of HSS323.9 × 12.7. For the shear walls, RC walls having the same thicknesses of 250 mm were inserted to each floor level. In addition to these, the braces and shear walls were used in the same bays over the structure's height. In this study, the base of the existing and retrofitted structures was assumed as a fixed base concept. However, many researchers reported that soil-structure interaction influences the dynamic responses of structures among them [12–16]. The dimensions of the structural elements are given in Table 1.

**Fig. 1** Plan view of a nine story existing reinforced concrete building

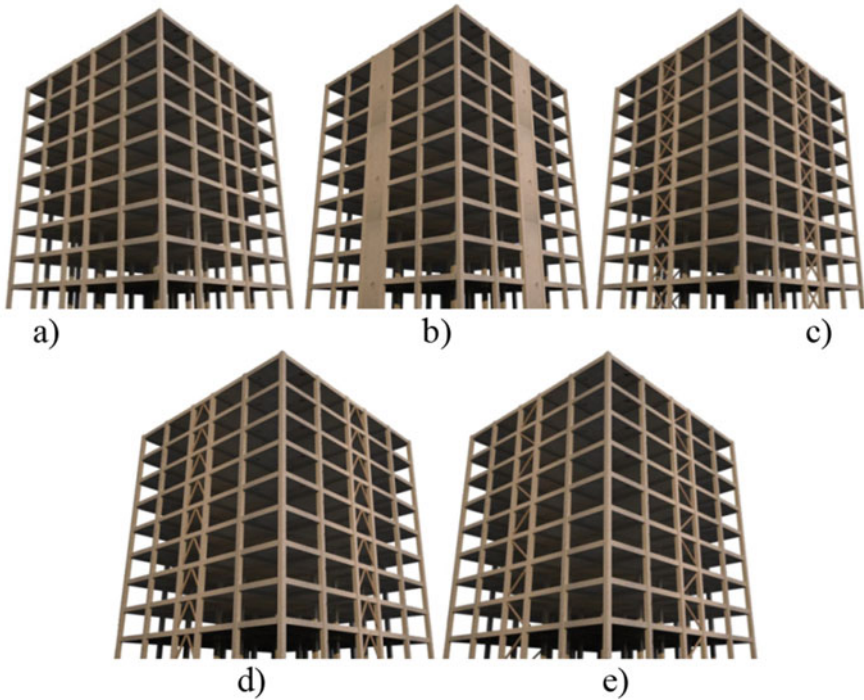
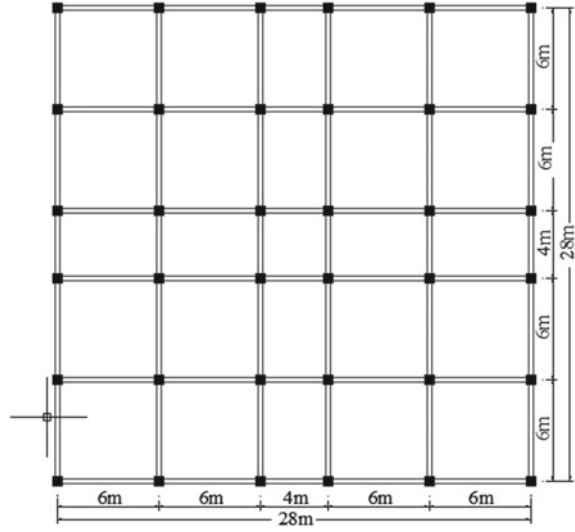


**Fig. 2** View of nine-storey RC buildings: **a** existing building (EB), retrofitted buildings **b** by shear wall (RB-SW), **c** by X-steel bracing (RB-XB), **d** by inverted V-steel bracing (RB-IVB), **e** by diagonal-steel bracing (RB-DB)

**Table 1** Section element properties of the structure

Storey No	Reinforced concrete members						Steel-section	
	Column		Beam		Slab	Shear wall	HSS323.9X12.7	
	Length (mm)	Width (mm)	Width (mm)	Height (mm)	Thickness (mm)	Thickness (mm)	Inside Dia. (mm)	Thickness (mm)
1	550	550	300	600	150	250	324	12.7
2	550	550	300	600	150	250	324	12.7
3	550	550	300	600	150	250	324	12.7
4	500	500	300	600	150	250	324	12.7
5	500	500	300	600	150	250	324	12.7
6	500	500	300	600	150	250	324	12.7
7	450	450	300	600	150	250	324	12.7
8	450	450	300	600	150	250	324	12.7
9	450	450	300	600	150	250	324	12.7

**Table 2** Reinforcement details of the structural elements

Element	Floor 1,2,3	Floor 4,5,6	Floor 7,8,9
Column	12# 25 mm	12# 20 mm	12# 16 mm
Beam	8# 16 mm (4top + 4 bottom)		

The concrete with compressive strength of 26 MPa was used for all the RC framed structures, the modulus of elasticity and yield stress of the steel reinforcement were taken as 200 GPa and 420 MPa, respectively. The yield stresses of the steel braces were considered as 350 MPa. The reinforcement details of the structural elements are given in Table 2. For the design and analysis of the buildings, ETABS 2013 Software was utilized. For assessing the performance levels of the buildings, a nonlinear static analysis was conducted. For this, to model the nonlinear behavior, the lumped plastic hinges were applied to the ends of the beams and columns using FEMA-356.

Additionally, the nonlinear time history analysis was performed. The ground motion acceleration of the 1999 Hector Mine earthquake was used, as seen in Fig. 3. The earthquake’s magnitude was 7.13 ( $M_w$ ), which was recorded at a distance of 195.9 km away from the source. The earthquake acceleration had peak ground acceleration of 0.268 g, peak ground velocity of 100.22 cm/s, peak ground displacement of 146.83 cm, and strike-slip mechanism (Pacific Earthquake Engineering Research Centre (PEER)) [17].

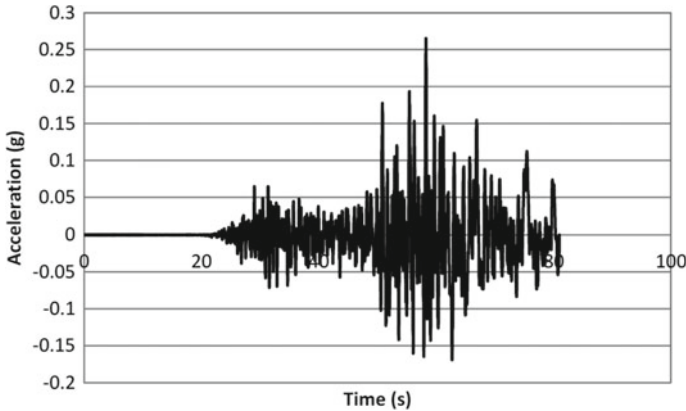


Fig. 3 Acceleration time plot of the earthquake ground motion

### 3 Results and Discussion

From the nonlinear static analysis, capacity curves were obtained for the existing building (EB) and upgraded buildings with a shear wall (RB-SW), X-bracing (RB-XB), inverted-V bracing (RB-IVB), and diagonal bracing (RB-DB). The capacity curves are given in Fig. 4. It was seen that the lateral load-carrying capacity of the building upgraded with the shear wall was about 2.32 times greater than the existing building. The lateral load-bearing capacity of the building retrofitted with X-bracing was increased by 2.23 times. Moreover, the upgraded buildings with inverted-V and diagonal bracing were measured about 1.80 and 1.61 times higher compared to the existing building, respectively. As expected, the initial stiffness of the upgraded buildings also increased due to the inclusion of the shear walls or bracings. The behavior of

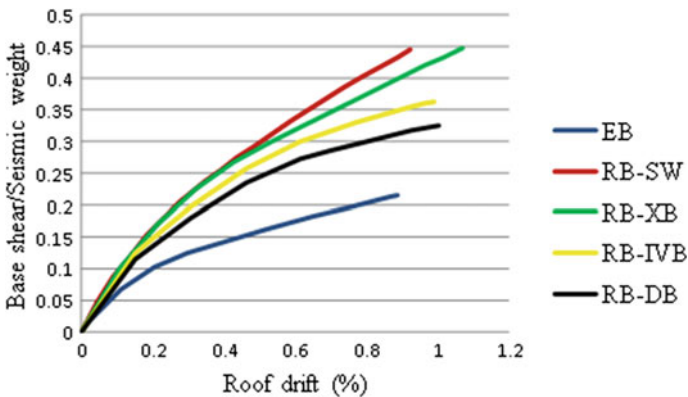


Fig. 4 Comparison of capacity curves of existing and upgraded buildings

**Table 3** Performance limit states of the buildings

Building	Performance points		Natural periods			Performance level
	Displacement (mm)	Base shear (kN)	T <sub>1</sub> (s)	T <sub>2</sub> (s)	T <sub>3</sub> (s)	
EB	287.8	9646.6936	1.17	1.05	0.41	CP
RB-SW	298.5	22,417.508	0.90	0.68	0.25	LS
RB-XB	347.1	21,520.8175	0.98	0.76	0.31	LS
RB-IVB	321.4	17,385.9578	0.99	0.77	0.33	LS
RB-DB	325.4	15,601.6474	1.02	0.80	0.34	LS

the retrofitted buildings with the shear wall, X-bracing, inverted-V bracing, and diagonal bracing was similar in the elastic region based on the capacity curves, however, in the inelastic region, it was varied. Among the concentric bracings, the X-braced framed building seemed to be capable of more lateral load carrying and energy absorption capacities than the inverted-V braced framed building. Also, inverted-V braced framed building had more lateral load carrying and energy absorption capacities than the diagonal braced framed building.

The performance points and corresponding performance levels were obtained based on FEMA-356. As seen in Table 3, the existing building had a performance level of collapse prevention (CP) while the upgraded ones improved to life safety (LS) Fig. 5.

From the nonlinear time history analysis conducted under the Hector Mine earthquake, the maximum displacement and inter-story drift variations along the height of different buildings were obtained as given in Figs. 6 and 7, respectively. It was observed that the story displacement reduced with the use of upgrading schemes. The level of the reduction was dependent on the retrofitting method. Moreover, the inter-story drift ratio distribution of the retrofitted buildings had a leaning towards being more uniform along with the building's height compared with the existing building. It was found that the maximum inter-story drift ratio of the existing building was about 0.82% while this ratio varied for the buildings with shear walls, X-bracings, inverted-V bracings, and diagonal bracing as about 0.42%, 0.44%, 0.49%, and 0.57%, respectively.

Furthermore, the roof story displacement variation with the time of the existing and retrofitted buildings is given in Fig. 8, while the base shear time history variation of the current and retrofitted buildings is shown in Fig. 9.

## 4 Conclusion

The following conclusions were drawn from this study:

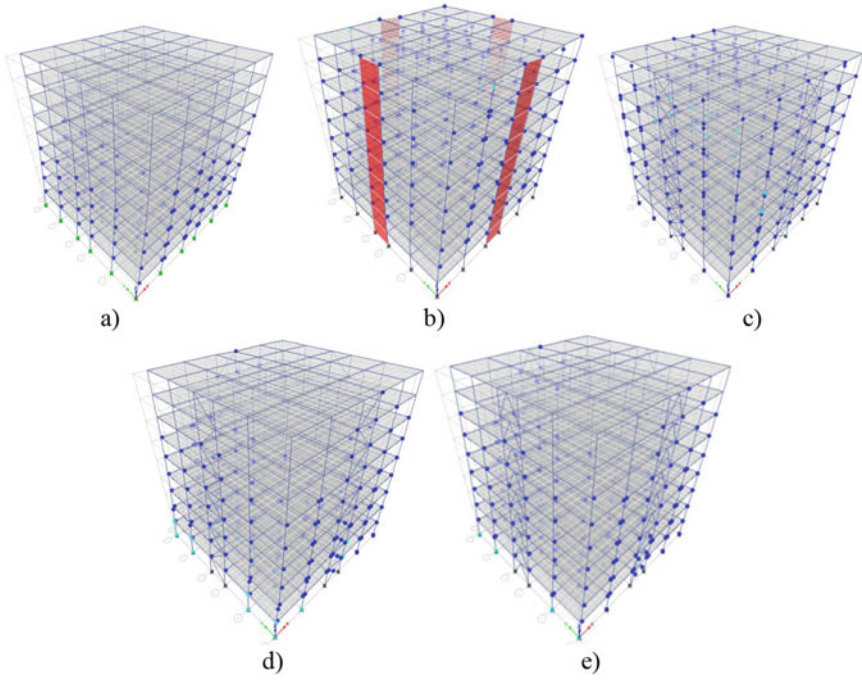


Fig. 5 View of the plastic hinge formation for; a EB, b RB-SW, c RB-X, d RB-IV, e RB-D

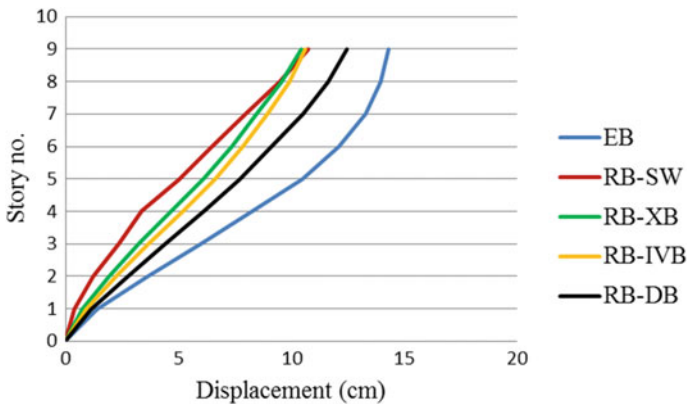
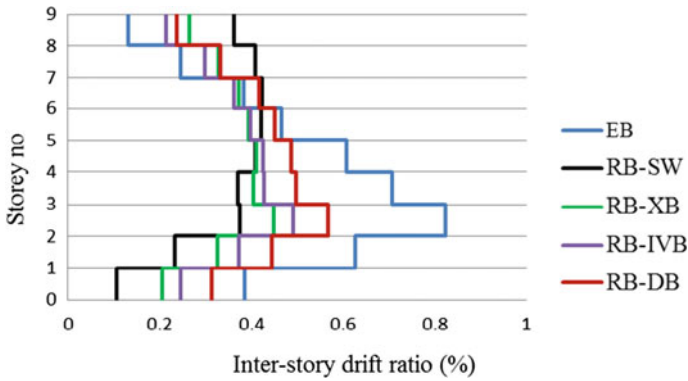


Fig. 6 Maximum story displacement for the buildings under the earthquake

- The nonlinear analysis carried out on the existing and retrofitted buildings indicated that the capacity curves had more significant values of lateral strength and stiffness for the upgraded buildings than the existing building.



**Fig. 7** Maximum inter-story drift for the buildings under the earthquake

- The retrofitted cases with shear wall and X-bracing systems had about 2.32 and 2.23 times higher load-carrying capacity than the existing building, respectively. In the case of using an inverted-V brace and diagonal brace, these values were about 1.80 and 1.61, respectively.
- X-braced framed buildings seemed to be the highest load carrying and energy absorption capacity among the upgraded buildings with concentric bracings based on the capacity curves.
- The performance level of the existing building improved from collapse prevention to life safety after retrofitting.
- From the time history analysis results, it was observed that the maximum inter-story drift ratio of the retrofitted buildings varied from 0.42 to 0.57% while that of the existing one was obtained as 0.82%.
- It was also noted that the seismic behavior of the buildings could be modified by selecting a proper retrofitting solution.



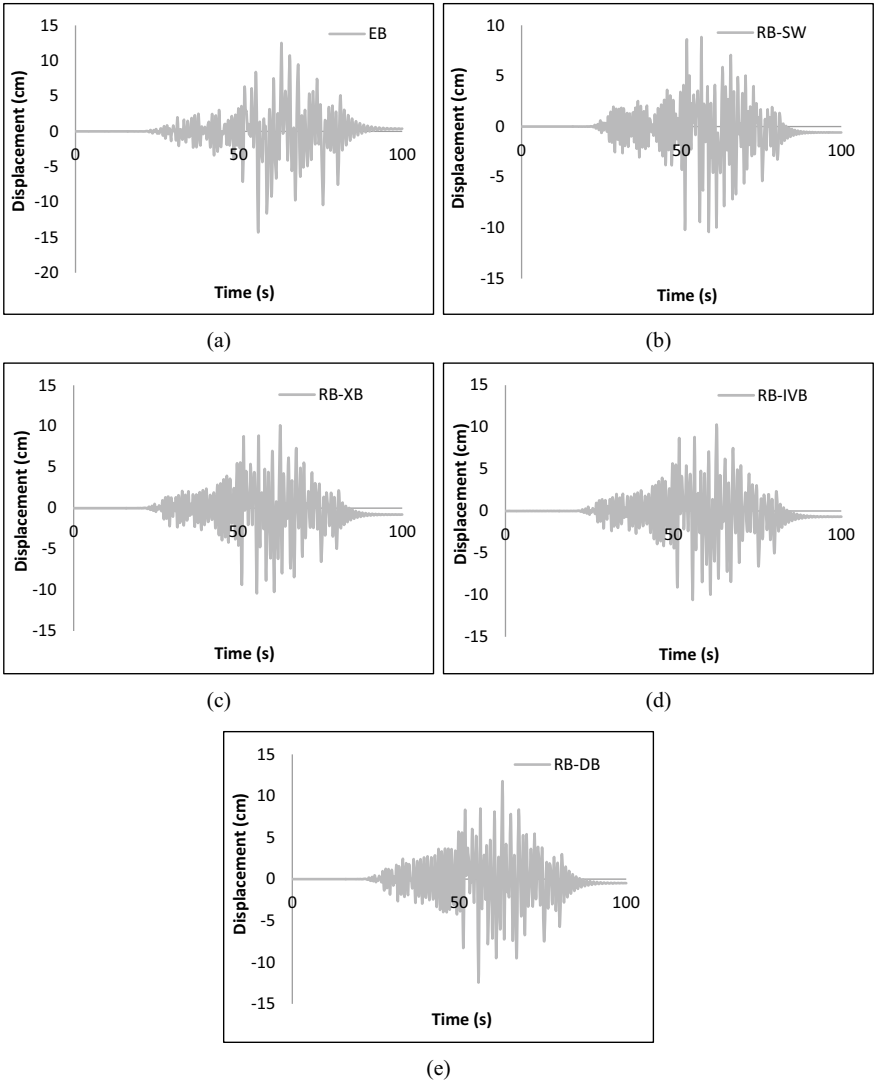


**Fig. 8** The ninth story-displacement time history variations of the existing and retrofitted buildings

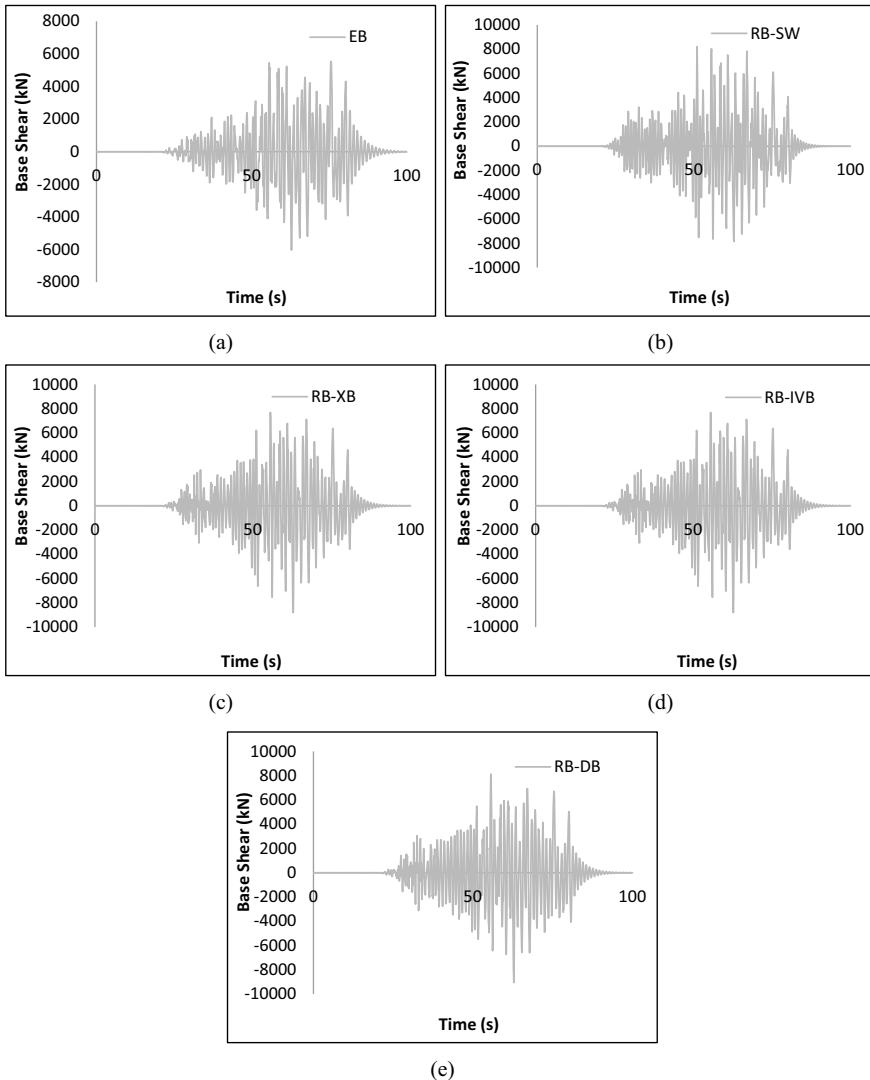


Fig. 9 Base shear time-history of the existing and retrofitted buildings

## References

1. Vecchio, F. J., & Tang, K. (1990). Membrane action in reinforced concrete slabs. *Canadian Journal of Civil Engineering*, 17(5), 686–697.
2. Abd-Elhamed, A., & Mahmoud, S. (2017). Nonlinear static analysis of reinforced concrete framed buildings—A case study on Cairo earthquake. *Journal of Engineering Research*, 4(4).
3. Esmaeili, H., Kheyroddin, A., Kafi, M. A., & Nikbakht, H. (2013). Comparison of nonlinear behavior of steel moment frames accompanied with RC shear walls or steel bracings. *The Structural Design of Tall and Special Buildings*, 22(14), 1062–1074.

4. Farghaly, A. A., & Abdallah, A. M. (2014). Evaluation of seismic retrofitting techniques used in old reinforced concrete buildings. *Evaluation*, 4(06).
5. Ghobarah, A., & Abou Elfath, H. (2001). Rehabilitation of a reinforced concrete frame using eccentric steel bracing. *Engineering Structures*, 23(7), 745–755.
6. Massumi, A., & Absalan, M. (2013). Interaction between bracing system and moment resisting frame in braced RC frames. *Archives of Civil and Mechanical Engineering*, 13, 260–268.
7. Maheri, M. R., & Hadjipour, A. (2003). Experimental investigation and design of steel brace connection to RC frame. *Engineering Structures*, 25(13), 1707–1714.
8. Durucan, C., & Dicleli, M. (2010). Analytical study on seismic retrofitting of reinforced concrete buildings using steel braces with shear link. *Engineering Structures*, 32(10), 2995–3010.
9. Kadid, A., & Yahiaoui, D. (2011). Seismic assessment of braced RC frames. *Procedia Engineering*, 14, 2899–2905.
10. Karaton, M., & Awla, H. A. (2018). Numerical investigation of the effect on ultimate loading capacity of different longitudinal reinforcement ratios of a RC portal frame. *Journal of Structural Engineering*, 1(3), 147–154.
11. AWLA, H. A. (2019). Investigation of a reverse engineering method for determination of material properties of damaged or collapsed reinforced concrete building.
12. Lin, J. W., Betti, R., Smyth, A. W., & Longman, R. W. (2001). On-line identification of nonlinear hysteretic structural systems using a variable trace approach. *Earthquake Engineering & Structural Dynamics*, 30(9), 1279–1303.
13. Bourouaiah, W., Khalfallah, S., & Boudaa, S. (2019). Influence of the soil properties on the seismic response of structures. *International Journal of Advanced Structural Engineering*, 11(3), 309–319.
14. Awlla, H. A., Taher, N. R., & Mawlood, Y. I. (2020). Effect of fixed-base and soil structure interaction on the dynamic responses of steel structures. *International Journal of Emerging Trends in Engineering Research*, 8(9).
15. Oz, I., Senel, S. M., Palanci, M., & Kalkan, A. (2020). Effect of soil-structure interaction on the seismic response of existing low and mid-rise RC buildings. *Applied Sciences*, 10(23), 8357.
16. Awlla, H. A., Taher, N. R., & Aksoy, S. H. (2021). Effect of SSI and fixed-base concept on the dynamic responses of Masonry Bridge structures, Dalal Bridge as a case study. *Academic Journal of Nawroz University (AJNU)*, 10(4).
17. Center, P. E. E. R. (2011). *Users manual for the PEER ground motion database web application*. Pacific Earthquake Engineering Research Center.

# Yield Line Model for Estimation Shear Strength UHPC Non-prismatic Beams



Nasser H. Tu'ma and Abdulmuttalib I. Said

**Abstract** The massive and rapid development of material technology, including Ultra-High-Performance Concrete (UHPC), has prompted researchers to study the behavior of the specific structural elements under the influence of various resistances, including shear resistance. Despite the large number of tests database that highlighted the study of shear resistance, the shear design of UHPC beams with variable cross section was yet not treated as a physical model based on the theory of plasticity. Eleven UHPC non-prismatic beams arranged as five groups with multiple variables of the shear span to depth ratio, the concentration of steel fibers, change of geometry slope, longitudinal rebar ratio and hollows positions were studied without shear reinforcement. Yield Line Model was derived for the UHPC non-prismatic beam and compare it with experimental results. The Yield Line Model gave a very good accuracy than its experimental data.

**Keywords** Yield line theory · Inclination angle · Shear capacity · Steel fibers · Non-prismatic beam · UHPC

## 1 Introduction

The tapered beam is widely used in mid-rise buildings, bridges, and structures as well as its aesthetic advantage. The presence of longitudinal hollows plays an important role in reducing dead weights that contributes to increasing space and raising the efficiency of the structural member. On the other hand, facilities can be passed through. No studies are available to determine the shear resistance of UHPC variable shaped structural members having longitudinal holes. Besides, no plastic method as analysis aid was carried out in estimation the shear resistance of such members. The

---

N. H. Tu'ma (✉)

Department of Civil Engineering, University of Misan, Misan, Iraq

e-mail: [naserhakeem@uomisan.edu.iq](mailto:naserhakeem@uomisan.edu.iq)

A. I. Said

Department of Civil Engineering, University of Baghdad, Baghdad, Iraq

e-mail: [Dr.AbdulMuttalib.I.Said@coeng.uobaghdad.edu.iq](mailto:Dr.AbdulMuttalib.I.Said@coeng.uobaghdad.edu.iq)

present study provides a method for the upper limited solution so-called Yield Line Model.

Generally, the shear capacity depends on five mechanisms which are shear stress in the compressive concrete zone, Aggregate interlock, dowel action of the longitudinal reinforcing bars, arch action, and residual tensile stresses transmitted directly across the cracks [1]. The shear load carrying mechanism for UHPC was proposed and it is hypothetically divided it into three components: (i) composite action of the matrix and the fiber; and (ii) the shear capacity provided by the average fiber tensile resistance (before fiber pull out) acting along the diagonal cracks; and (iii) is shear provided by stirrups and prestressing [2, 3]. The shear strength of prestressed UHPC I—beam as well as the flexural behavior were studied [4]. The theoretical shear strength was carried out by adding truss analogy with a constant crack inclination of (45°). The truss model consisted of a lower cord, top cord, vertical ties, and inclined struts. The effecting of prestressing modeled by an external force applied on pin support. Additional lateral strut(s) modeled to represent the vertical component of an inclined or curved tendon. The model for UHPC specimens without shear reinforcement was introduced as [5]:

$$V_{u,ct} = \frac{2}{3} \cdot b_w \cdot k_x \cdot d \cdot f_{ct} \cdot \left( \frac{4 \cdot d}{a} \right)^{\frac{1}{4}} \cdot \left( \frac{5 \cdot l_{ch}}{d} \right)^{\frac{1}{4}} \quad (1)$$

where  $l_{ch} = \frac{E_c G_f}{f_{ct}^2}$  is the characteristic length;  $G_f$  is the fracture energy of HUPC and has a value of 143 N/m. The shear capacity of varying depth beam was studied [6]. The analysis based on British standard and ACI-318 combined with inclined forces can be used to reduce shear forces in the web of a beam section. The effective shear force method was following force equilibrium and assumed as a parabolic distribution of shear stress on each cross-section. The behavior of 18 concrete haunch beams subjected to high shear load without shear reinforcement was investigated [7]. German Code (DIN1045-01), the Swiss Code (SN 262–2003), the ACI Code (ACI 318 – 05) and the Canadian Standards (CSA A23.3–2004) were chosen and compared with the experimental results. Many variables were included such as longitudinal rebar, inclined angle, and shear span to depth ratio. All beams were tested by single point load.

## 2 Yield Line Model

**Equation Derivation.** It is also known Crack Sliding Model (CSM) for plain concrete and was considered as an application of plasticity model for structural concrete elements [8]. In CSM, it is assumed that diagonal crack is generated as straight lines from the load point to the horizontal distance of the diagonal crack from the support ( $x$ ). Also, it assumes that the over reinforcement case of main bars. The relative displacement ( $u$ ) along the critical diagonal crack was to be vertically directed

(Fig. 1a). Using the upper bound approach of plastic theory and based on the beam failure mechanism in Fig. 1b. The work equation  $W_i = W_e$  and the upper bound solution will be:

$$V_u \times u = \frac{1}{2} \times f_c^* \times b \times (1 - \sin \alpha) \times \frac{h(x)}{\sin \beta} \times u \tag{2}$$

where  $b$  = width of the beam,  $\alpha = 90 - \beta$ ,  $\sin(90 - \beta) = \cos(\beta)$ ,  $h(x) = h_1 + 2(h_2 - h_1).x/L$  and  $f_c^*$  is the effective compressive strength Which will be discussed hereafter. The  $V_{cr}$  can be obtained by taking moment about point (A), Fig. 1b.

$$V_{cr} \times a = \frac{1}{2} \times f_t^* \times b \times [h(x)^2 + (a - x)^2] \tag{3}$$

where  $f_t^*$  is the effective tensile stress which will also be discussed hereafter. According to the plastic theory, when the two curves intersect the crack may develop into a yield line and a shear failure takes place. So, the solution may be obtained by equal Eqs. (2)–(3) as:

$$f_c^* \times \left\{ \sqrt{1 + \left[ \frac{a - x}{h(x)} \right]^2} - \frac{a - x}{h(x)} \right\} = f_t^* \times \frac{h(x)}{a} \left\{ 1 + \left[ \frac{a - x}{h(x)} \right]^2 \right\} \tag{4}$$

The solution of Eq. (4) can be carried out by trial and error for (x) value and  $0 \leq x \leq a$ .

**Effective Stresses.** For compressive concrete, the evaluation of the effective compressive strength ( $f_c^*$ ) was done by multiplying the cylinder compressive strength  $f_c'$  by the effectiveness compressive factor  $v_c$ , which accounts for the limited crack sliding resistance and ductility of the material as 0.8 [9]. Variable Engagement Model (VEM06) to represent the slip between the fibers and the concrete matrix that occurring before full bond stress and the fibers across a crack had been created [10]. The constitutive tensile law was used in terms of tensile tension and crack opening

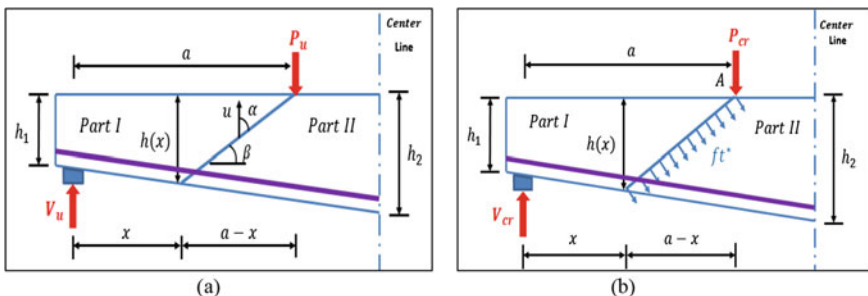


Fig. 1 Yield line model a yield line, b cracking load

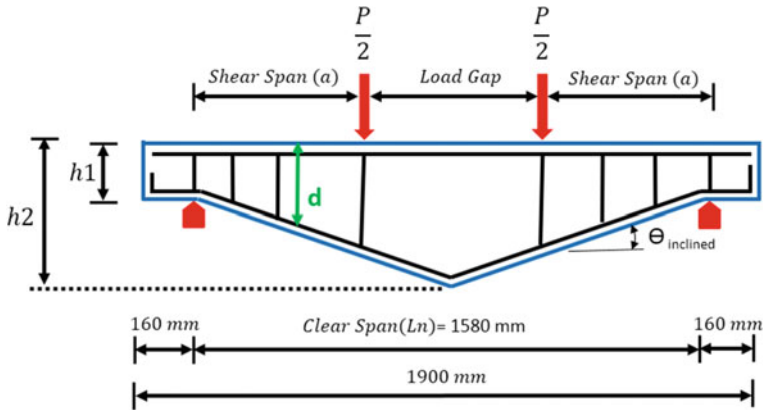


Fig. 2 Geometry and details of tested beam [12]

displacements ( $w$ ). Effective tensile stress ranged from 70 to 90% of tensile stress that corresponding to crack width 0.5–1.5 mm. Therefore, the effectiveness tensile factor was taken as ( $v_t = 0.8$ ). The average residual tensile stress carried by the fibers across a shear crack from cracking until a limiting strain value was assumed as a uniform intensity of 6.9 MPa (1.0 ksi). As well as a suggestion of a uniformly distributed residual tensile stress along with the tensile depth of approximate 8 MPa (reducing the tensile strength which that was taken as 10 MPa (1.5 ksi) by multiplying by 0.75 factor) [11].

**Collection Data.** Generally, all preparing and collected data are taken from previous study available for verification purpose of the proposed model. The details of the data, and geometry of the beams is presented in Fig. 2 [12]. The shear span to depth ratio of all beams is 2.73 except for the specimens UHPCTB 1 and UHPCTB 9 which were 2.3 and 2.94, respectively. The inclination angle of all beams kept constant and equal to  $15.9^\circ$ , while in specimens UHPCTB 2 and UHPCTB 3 were  $9.7^\circ$  and  $12.8^\circ$ , respectively. The steel fiber ratio considered is 2% for all specimens and 0%, 1% for the specimens UHPCTB 19 and UHPCTB 20; respectively. The depth of the beam at the support is 180 mm and varied at mid span to become 315, 360 and 405 mm. All beams were reinforced with main steel of 2  $\Phi$  25 mm, but in the specimen UHPCTB 8, UHPCTB 19, and UHPCTB 20 is 4  $\Phi$  16 mm (Fig. 3).

### 3 Results and Discussion

In this paper, the residual tensile stress values were obtained from equating the laboratory shear resistance with the theory and then subtracting the values of the concrete shear compounds ( $V_c$ ) and dowel action ( $V_{da}$ ) to obtain the steel fibers shear component ( $V_f$ ) and then dividing it by the equation constants to obtain the residual stress.

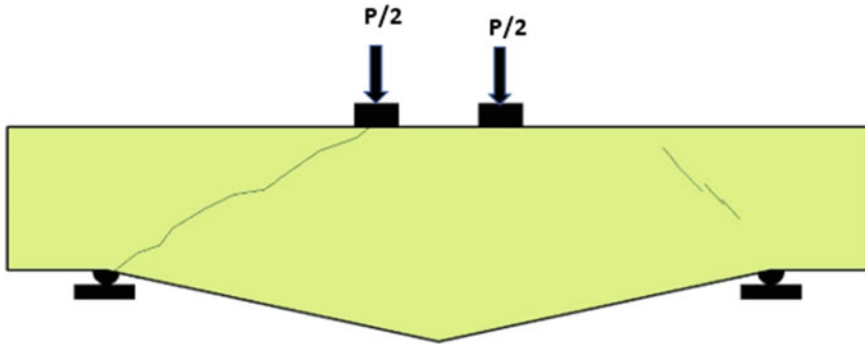


Fig. 3 Mode of failure for specimen UHPCB10 [12]

Figure 4 shows the residual tensile stress values for all samples based on the laboratory results. Also, the values of the horizontal distance of the yielding line from the support ( $x$ ) were fixed in practice and it was zero for all beams. Effective stress coefficients for both compression and tensile were adjusted to obtain the required convergence and perform a solution of Eq. 4. Comparison of laboratory shear resistances with yield model, failure angles, effective stress coefficients in the below Figs. 4 and 5 and Table 1.

The Residual Tensile Stress (RTS) depends on the volumetric fraction of steel fibers, aspect ratio and the shape of their ends. For beams with 2% of steel fiber, RTS had an average value of 7 MPa which it is close to most sources such as Japanese as well as US codes. While the beam with a ratio of 1% steel fiber, RTS was found 4.75 (two-thirds of the stress value at 2% steel fibers). For the specimen without steel fibers (0%) is not included in this model due to impossibility to generate effective tensile stress. The effective compressive stress and tensile coefficients ( $v_c$  and  $v_t$ ) were obtained from trial and error method to obtain a plastic solution of Eq. 4, Table 1.

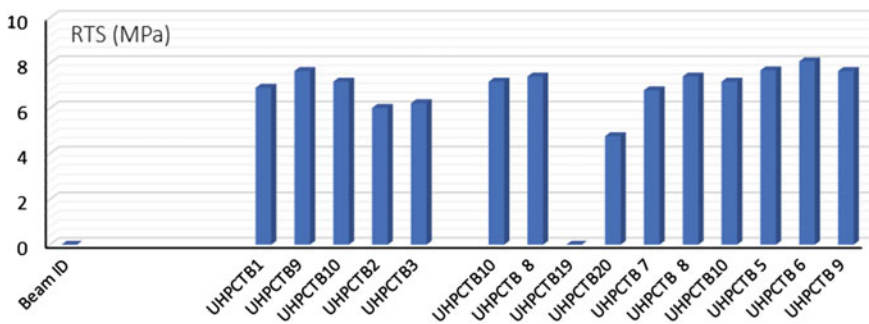


Fig. 4 Residual tensile stresses



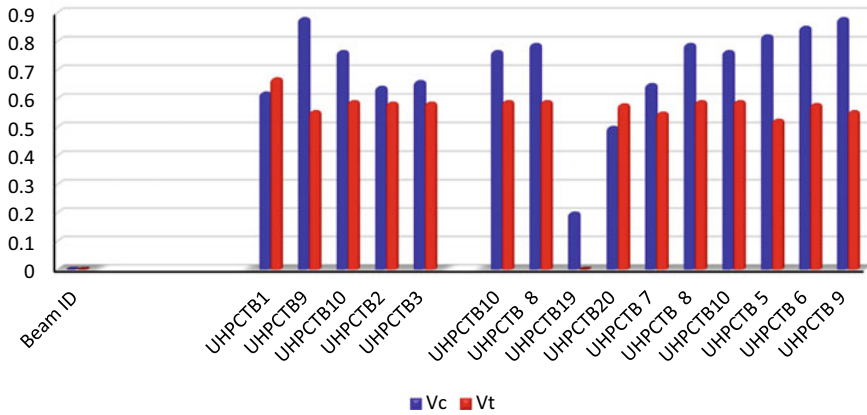


Fig. 5 Effective compression and tension coefficients

Table 1 Experimental and yield shear loads

Beam ID	Experimental		Yield line model		V <sub>Y</sub> /V <sub>exp.</sub> (%)
	V <sub>EXP</sub> (kN)	θ <sub>Exp</sub> (Degree)	V <sub>Y</sub> (kN)	θ yield (Degree)	
UHPCTB1	208.0	18.4	208.5	18.4	100.2
UHPCTB9	230.0	20.4	233.9	14.6	101.7
UHPCTB10	216.0	19.8	218.7	15.7	101.2
UHPCTB2	181.0	22.3	183.0	15.7	101.1
UHPCTB3	187.5	21.2	188.7	15.7	100.6
UHPCTB10	216.0	19.8	218.7	15.7	101.2
UHPCTB 8	223.0	16.9	225.8	15.7	101.3
UHPCTB19	55.5	19.8	57.2	NA	NA
UHPCTB20	140.5	17.2	142.9	15.7	101.7
UHPCTB 7	185.0	20.1	185.8	15.7	100.4
UHPCTB 8	223.0	16.9	225.8	17.1	101.3
UHPCTB10	216.0	19.8	218.7	15.7	101.2
UHPCTB 5	231.0	18.3	234.4	15.7	101.5
UHPCTB 6	243.0	18.1	243.0	15.7	100.0
UHPCTB 9	230.0	20.4	233.9	15.7	101.7
Average					101.1

The average effective compressive coefficient ( $v_c$ ) was 0.75, while the average effective tensile coefficient ( $v_t$ ) was 0.58. For the beam of one percentage steel fibers,  $v_c$  reached a value of 0.5 (two-thirds of 0.75) whereas  $v_t$  remained 0.58 that indicates the effective contribution of steel fibers in raising the efficiency of the section in terms of shear and its minimal impact on bending resistance. The results of shear angle

of failure were also closed except the specimen without steel fiber which consider out of comparison due to absence of steel fibers and therefore zero residual tensile stress.

## 4 Conclusion

The procedure that followed in design UHPC tapered beam gave a significant convergence between theoretical and experimental shear strength and ensuring the shear failure mode. All beams had the tip point of failure line ends experimentally at support ( $x = 0$ ). The volumetric steel fiber of two percentage gave higher results. The effective compressive ( $v_c$ ) and tensile coefficient ( $v_t$ ) can be used as mean values of 0.75 and 0.58; respectively. Both The shear plane failure (angle of failure) for YLM and experimental are closed and were less than  $25^\circ$ . The using of residual tensile stress that adopted in this paper of 7 MPa for all beams of 2% steel fiber content and two-thirds of it for 1 percentage of steel fiber. Also, Yield Line Model can cover the varying in longitudinal rebar ratios, existing longitudinal hollows and varying volumetric steel fiber ratios. Max. experimental and YLM shear strength can be obtained when increasing the geometry slop ( $h_1 = 2.25 h_2$ ).

**Acknowledgements** This project is supported by Amarah Technical Institute/Missan Governorate/Iraq through testing and supplying raw materials needed to achieve this work. The author is gratefully acknowledging the support received from them.

## References

1. Mondo, E. (2011). *Shear capacity of steel fiber reinforced concrete beams without conventional shear reinforcement*. Master Thesis, Royal Institute of Technology, Department of Civil and Architectural Engineering, Division of Structural Design and Bridges, Stockholm, Sweden.
2. AFGC. (2002). Ultra-high-performance fibre-reinforced concretes, interim recommendations.
3. JSCE. (2004). Recommendations for design and construction of ultra high strength fiber reinforced concrete structures, outlines.
4. Ali, A. (2013). *Behavior of prestressed ultra-high-performance concrete I-beams subjected to shear and flexure*. Master Thesis, Applied Science in Civil Engineering, Ottawa University, Canada.
5. Bunje, K., & Fehling, E. (2004). About shear force and punching shear resistance of structural elements of Ultra-High-Performance Concrete, Ultra-High-Performance Concrete (UHPC). In *International Symposium on Ultra-High-Performance Concrete* (pp. 401–411). Kassel University.
6. Yuanzhang, Y., John, O., Tim, I., & Antony, D. (2015). Shear strength theories for beams of variable depth. In *Proceedings of the International Society of Flexible Formwork (ISOFF) Symposium, Amsterdam, The Netherlands*.
7. Nghiep, V. H. (2011). *Shear design of straight and haunched concrete beams without stirrups*. Ph. D. thesis, Technology University Hamburg.

8. Zhang, J. P. (1997). Diagonal cracking and shear strength of reinforced concrete beams. *Magazine of Concrete Research*, 178, 55–65.
9. Colajanni, P., Recupero, A., & Spinella, N. (2008). A model for SFRC beams without shear reinforcement. In *Tailor Made Concrete Structures—Walraven & Stoelhorst (Eds.)*, Taylor & Francis Group. ISBN 978-0-415-47535-8.
10. Voo, Y. L., Poon, W. K., & Foster, S. J. (2006). Shear strength of fiber reinforced reactive powder concrete prestressed girder without stirrups. *Journal of Advanced Concrete Technology*, 4(1).
11. Graybeal, B. A. (2006). *Material property characterization of ultra-high-performance concrete, FHWA-HRT-06-103*. Federal Highway Administration, U.S. Department.
12. Jaaly, H. J. (2020). *Shear behavior of ultra high performance concrete UHPC tapered beams with longitudinal openings*. Master Thesis, University of Misan.

# Evaluation of Live Load Distribution Factors of a Highway Bridge



Abbas A. Allawi, Abdulmuttalib I. Said, Mohannad H. Al-Sherrawi, Amjad Albayati, Mohammed Al Gharawi, and Ayman El-Zohairy

**Abstract** The design of bridges depends on the transverse distribution characteristics of the live load that is carried. The study goal is to evaluate experimentally and numerically the Live Load Distribution Factors (LLDFs) proposed by the American Association of State Highway and Transportation Officials (AASHTO) specifications for a case of highway bridge with a composite steel–concrete structural system. Different trucks have been used to attain the static tests and achieve maximum values for the design live loads and deflections for the composite steel–concrete bridge girders. Furthermore, a linear finite element analysis has been executed for the composite bridge to outspread the LLDFs assessment and to study the influence of the Cross-Frame Diaphragm (CFD) on the LLDFs. The moment LLDFs quantities have been calculated according to AASHTO specifications, they have been found more conservative while shear quantities have been found critical, especially in exterior girders. Also, the contribution of CFD in the spread of the live load among the girders has been verified by the redistribution of the LLDFs between the internal and exterior girders.

**Keywords** AASHTO · Composite bridge · LLDFs · Static load test · Finite element

---

A. A. Allawi · A. I. Said · M. H. Al-Sherrawi (✉) · A. Albayati  
Department of Civil Engineering, University of Baghdad, Baghdad 10071, Iraq  
e-mail: [dr.mohannad.al-sherrawi@coeng.uobaghdad.edu.iq](mailto:dr.mohannad.al-sherrawi@coeng.uobaghdad.edu.iq)

A. A. Allawi  
e-mail: [a.allawi@coeng.uobaghdad.edu.iq](mailto:a.allawi@coeng.uobaghdad.edu.iq)

A. I. Said  
e-mail: [dr.abdulmuttalib.i.said@coeng.uobaghdad.edu.iq](mailto:dr.abdulmuttalib.i.said@coeng.uobaghdad.edu.iq)

M. Al Gharawi  
Department of Civil and Environmental Engineering, University of Missouri, Columbia, MO  
65211-2200, USA

A. El-Zohairy  
Department of Engineering and Technology, Texas A&M University-Commerce, Commerce, TX  
75429, USA  
e-mail: [ayman.elzohairy@tamuc.edu](mailto:ayman.elzohairy@tamuc.edu)

## 1 Introduction

In the bridge deck design process, the internal forces and moments in different bridge members are needed to be known. The Live Load Distribution Factors (LLDFs) are usually utilized to compute stresses in bridge members due to shear forces and bending moments. The availability of these factors can certainly make the design of such complex structural systems easy. By using finite element (FE) analysis, these factors can be determined. Other researchers made many attempts who adopted live load configurations presented by different specifications and codes. Over the past two decades, the efforts of improving LLDFs have been steadily growing.

## 2 Related Works

Zokaie [1] presented the background on the development of the formulas and compared their accuracy. Tabsh and Tabatabai [2] performed a FE analysis on different bridges to study the effect of span length on the LLDFs obtained by American Association of State Highway and Transportation Officials (AASHTO) specifications, and the main conclusion confirmed minor effects on the LLDFs. Kim et al. [3] introduced the LLDFs of various NATO wheeled military trucks on a simple-span steel I-girder bridge using three-dimensional finite element analysis. Li and Chen [4] presented a framework to calculate the LLDFs for a bridge girder. A combination of a single girder in the longitudinal direction and a cross-section frame sitting on the girder springs in the transverse direction. Seo et al. [5] presented a novel statistical framework to calculate the LLDFs for steel–concrete composite bridge girders exposed to agricultural vehicles. This framework was consisted of multiple parts, including live load field testing, FE analysis, and statistical analysis. Fatemi [6] used FE modeling to determine the LLDFs of steel concrete composite bridges subjected to loads recommended by the Australian Bridge Design Code. Based on FE analyses, Tabsh and Mitchell [7] developed a simple approach by adjusting the AASHTO's bridge girder distribution factor in a concrete slab on a steel girders bridge. The proposed factors allowed for obtaining the oversized vehicle bending moment and the shear force effect in the individual girders. Allawi et al. [8] investigated AASHTO specifications LLDFs for prestressed reinforced concrete bridges experimentally and numerically using three load cases to obtain maximum live load and deflection values for all bridge girders.

The cross-frame diaphragms (CFD) are secondary elements, placed at bridge ends and at intermediate locations with spacing not to exceed 7.5 m as in AASHTO specifications. The CFD fixed in a continuous line across the bridge [9]. Several previous researchers reported the effects of using the CFD on the LLDFs in bridges [10]. Bishara [11] utilized the FE program ADINA to investigate simple span steel bridges and improved a procedure to obtain internal forces in the CFD and stated that it could provide load-sharing capabilities. Shi [12] stated that the critical stage for the

buckling of the steel girders occurs during the concrete pouring process; therefore, using intermediate CFD can solve the problem and help negative moment regions resist wind loads girders bottom flange. Khaloo and Mirzabozorg [13] confirmed that the arrangement of CFD has a significant effect on the LLDFs associated with the skew angles. Watheej and Al-Sherrawi [14] have studied the effects of CFD shape, spacing, and connection with steel girders on the deflection of the bridge by using linear FE method. Morera [15], using FE analysis, recognized that increasing the torsional strength of the cross-section has more positive effects than increasing the CFD number in a skew steel bridge. Hassel et al. [16] evaluated, using 3D FE models, the effects of stiffness, layout, and spacing of CFD and load placement on a skew steel bridge. Fettahoglu [17] generated the complex geometry of conventional steel orthotropic bridge by FE program, and the effect of the span and the web thickness of the cross-beam on the steel bridges were evaluated.

Said and Lateef [18, 19] investigated the effect of the bridge deck curvature on the shear and moment distribution factor under the impact of AASHTO LRFD HL-93 live load. Zhang [20] analyzed the LLDFs of hollow core slab bridges before and after widening using a theoretical and FE method. At the same time, Tabsh [21] developed simple girder distribution factors for shear and flexure for short slab-on-girder bridges subjected to oversize vehicles. The contribution of the concrete deck bridge and the composite action to shear and moment strengths of a composite beam is not taken into account in current design specifications and codes [22]. Liu et al. [23] calibrated LLDFs in AASHTO Specifications by using a large amount of collected data in the USA for years between 2001 and 2013. Peker and İnce [24] demonstrated the accuracy and appropriateness of using LLDFs calculations in structural analysis according to AASHTO specifications by comparing the results obtained with the FE results that perform precise and exact analysis. While the results of Dong et al. [25] showed that the LLDFs calculated by the AASHTO standard gave more conservative results when compared with the experimental and FE analysis approaches.

This study aims to evaluate experimentally and numerically LLDFs recommended by AASHTO specifications for Al-Mustansria highway composite steel–concrete bridge. The bridge is located in Baghdad-Iraq and is made of four steel plate girders connected by the shear connectors to the 200 mm thick reinforced concrete deck. The experimental work has been done using different arrangements of trucks to get maximum moment due to values of live loads and deflections for all the bridge girders. A FE analysis was implemented for the bridge to extend the LLDFs evaluation and obtain the effect of CFD on the LLDFs.

### 3 Experimental Test

Al-Mustansria bridge is a simply supported steel–concrete composite bridge with straight axes and spanning 33.95 m with 7.5 m width. The cross-section of the composite bridge is shown in Fig. 1. The steel plate girder has three different steel cross-sections along its length, as defined in Fig. 2 and Table 1. Two rows of steel

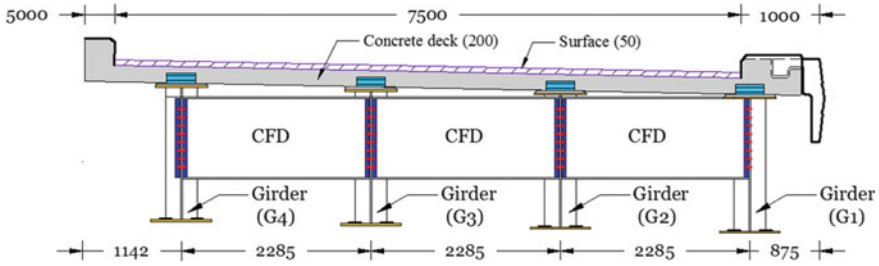


Fig. 1 Al-Mustansria highway bridge cross-section

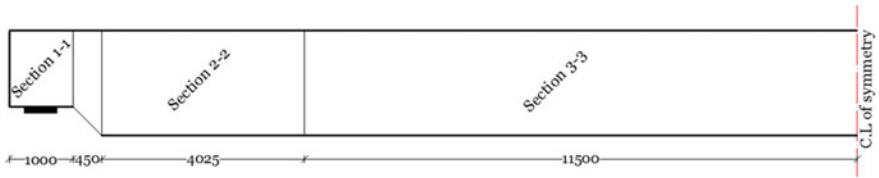


Fig. 2 The three different steel cross-section locations

Table 1 Section details of the three different steel cross-sections

Cross-section	1-1	2-2	3-3
Height, $d$ (mm)	1200	1630	1650
Bottom flange width, $b_1$ (mm)	500	500	500
Bottom flange thickness, $t_1$ (mm)	25	25	25
Top flange width, $b_2$ (mm)	450	450	450
Top flange thickness, $t_2$ (mm)	25	25	25
Web thickness, $t_w$ (mm)	14	14	14
Cover plate width, $b_c$ (mm)			450
Cover plate thickness, $t_c$ (mm)			20

channels (C 100 × 50 × 10) shear connectors have been used to connect the bridge deck to the steel plate girders. Each shear connector was welded to the top steel flange at 350 mm center to center.

Figure 3 shows the steel plate girders’ top view and the locations of the CFD, and Fig. 4 illustrates details of CFD that have been used in the bridge.

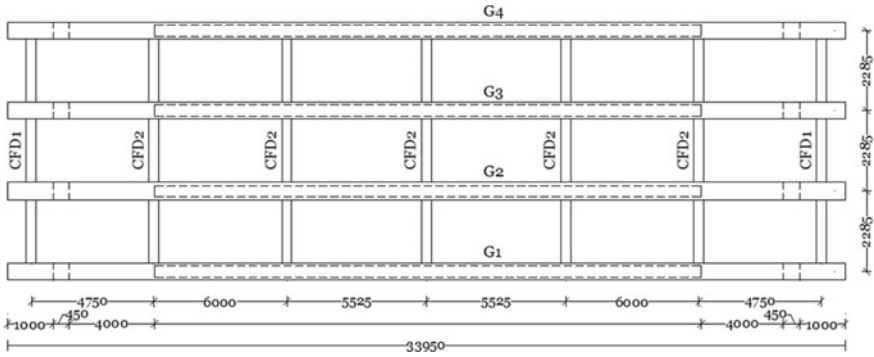
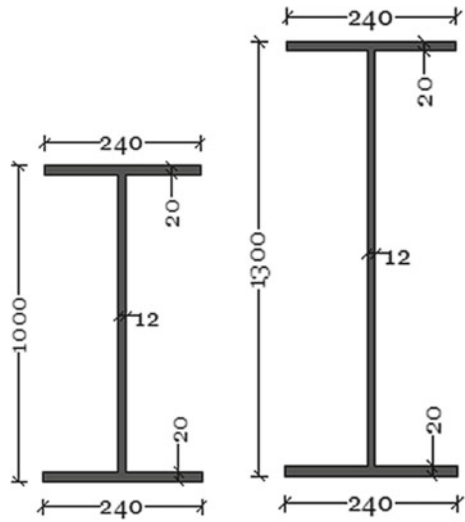


Fig. 3 Steel girders top view

Fig. 4 Details of cross-frame diaphragms



#### 4 Locations of the Trucks

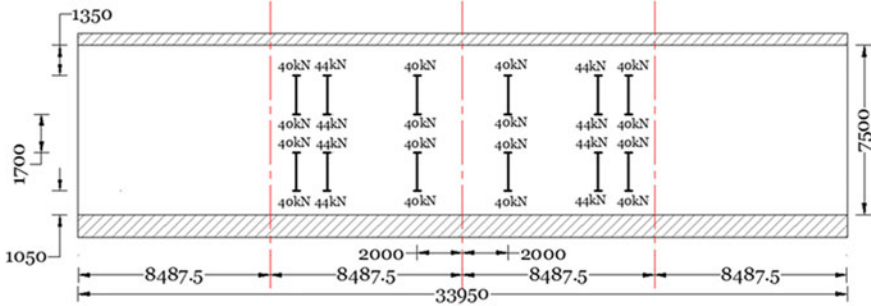
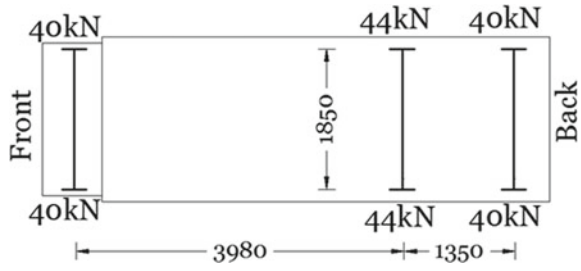
Figure 5 shows the details of the three axles, 248 kN truck, that has been used in the experimental work. The bridge load test had been done by dividing the carriageway of the bridge into two notional lanes and arranging the trucks in two cases:

**Case one:** Four trucks located at the central zone of the carriageway of the composite bridge, as shown in Fig. 6a.

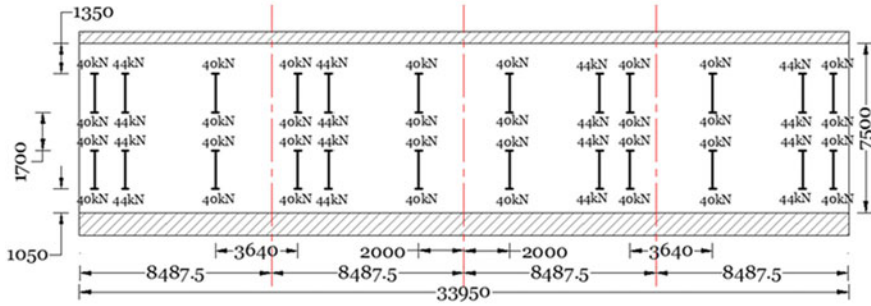
**Case two:** Eight trucks located and regularly spaced at the whole carriageway of the bridge, as shown in Fig. 6b, to get maximum moments and deflections due to living load in the bridge girders.



**Fig. 5** Details of the three-axle 248 kN truck



(a)



(b)

**Fig. 6** The arrangement of vehicles, **a** case one, **b** case two

## 5 Finite Element Analysis

In this work, ANSYS program has been employed in linear analysis of Al-Mustansria composite steel–concrete bridge. Figure 7 presents FE model for the bridge under consideration. SHELL63 element has been adopted to represent the web, flanges, and vertical stiffeners of the steel plate girders [26]. While the solid element, SOLID65, has been used to model the concrete bridge deck [27]. Two special elements, TARGE170 and CONTA175, were used to simulate the inconsistency of DOFs between the top flange of steel flange shell element and deck solid element [28].

**Fig. 7** FE model for bridge under consideration

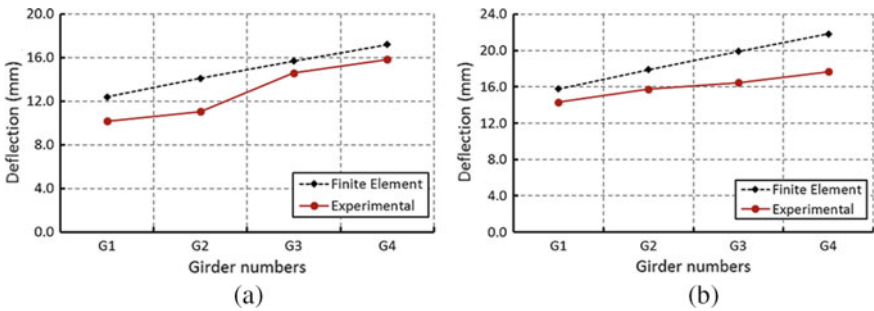
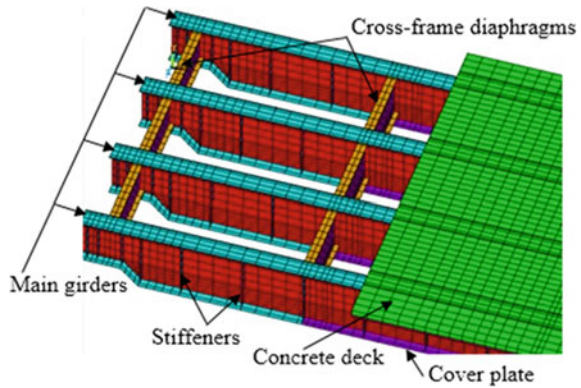


**Fig. 8** Comparison between the measured and FE deflection values for, **a** case one, **b** case two

The full connection between steel flanges and the concrete deck has been adopted [29].

For all FE models, the deflection values at the mid-girders span have been attained. Figure 8 is a plot of the field measured and the FE deflection values. According to this comparison, it can be noticed that there is a good agreement between deflection values of experimental and FE analysis. The main reason for higher values in the FE analysis is that assuming a theoretical simply supported ends in the FE model made the bridge more flexible.

## 6 Evaluation of the LLDFs

Nowadays, most bridges' designers use empirical formulas or simplified methods listed in specifications and codes to calculate the LLDFs for non-skewed bridges. AASHTO specifications present procedures for estimating moment and shear distribution factor ( $g$ ) for a composite steel–concrete girder as following [30]:

### A. LLDFs for Internal Girders.

In the case of one design lane loaded,  
For moment:

$$g_{\text{int.}} = 0.06 + \left(\frac{S}{4270}\right)^{0.4} \left(\frac{S}{L}\right)^{0.3} \left(\frac{K_g}{L t_s^3}\right)^{0.1} \quad (1)$$

For shear:

$$g_{\text{int.}} = 0.36 + \frac{S}{7620} \quad (2)$$

In the case of two or more design lanes loaded,  
For moment:

$$g_{\text{int.}} = 0.075 + \left(\frac{S}{2900}\right)^{0.6} \left(\frac{S}{L}\right)^{0.2} \left(\frac{K_g}{L t_s^3}\right)^{0.1} \quad (3)$$

For shear:

$$g_{\text{int.}} = 0.2 + \frac{S}{3657.6} - \left(\frac{S}{10668}\right)^2 \quad (4)$$

where  $L$  is the span of the girder (mm),  $S$  is the spacing between girders (mm),  $t_s$  is the depth of the concrete bridge deck (mm), and  $K_g$  is the longitudinal stiffness parameter that can be obtained from [30]:

$$K_g = n(I + Ae_g^2) \quad \text{and} \quad n = \frac{E_B}{E_D} \quad (5)$$

where  $n$  is the modular ratio,  $I$  is the moment of inertia of the bridge girder ( $\text{mm}^4$ ),  $A$  is the cross-section area of each girder ( $\text{mm}^2$ ),  $e_g$  is distance between the center of gravity of the basic beam and the deck (mm),  $E_B$  is girder material modulus of elasticity (MPa), and  $E_D$  is deck material modulus of elasticity (MPa).

#### B. LLDFs for External Girders.

In the case of one design lane loaded, Lever Rule for moment and shear.

In the case of two or more design lanes loaded,

For moment:

$$g_{\text{ext.}} = \left(0.77 + \frac{d_e}{2775}\right) g_{\text{int.}} \quad (6)$$

For shear:

$$g_{ext.} = \left(0.6 + \frac{d_e}{3048}\right) g_{int.} \tag{7}$$

where  $d_e$  is horizontal distance from interior edge of curb or traffic barrier to center-line of web of exterior girder at the bridge deck level (mm). In a slab-multi-girders bridge with CFD, the distribution factors for the moment in an exterior girder shall not be taken to be less than that which can be calculated by supposing bridge cross-section deflects and rotates as rigid body [30]:

$$R = \frac{N_L}{N_b} + \frac{X_{ext} \sum_{N_L} e}{\sum_{N_b} X^2} \tag{8}$$

where  $R$  is the reaction on an exterior girder in terms of lanes,  $N_L$  is the number of loaded lanes that under consideration,  $N_b$  is the number of the bridge girders,  $X_{ext}$  is the horizontal distance from center of gravity for configuration of girders to exterior girder (mm),  $e$  is the eccentricity of the design truck or the design lane load from center of gravity of configuration of girders (mm) and  $X$  is horizontal distance from the center of gravity of configuration of girders to each bridge girder (mm). The extreme live load force effect can be determined by considering all possible combinations of a number of the loaded lanes multiplied by the corresponding multiple presence factor to account for the probability of the simultaneous lane occupation by design live load [30]. This factor shall not be applied in conjunction with the approximate LLDFs, except where the lever rule is used or where special conditions for exterior girders in slab on multi girders bridges.

## 7 LLDFs from Experimental and FE

LLDFs for a moment in a bridge girder can be calculated by dividing the obtained experimental or FE deflections by deflection obtained from structural analysis of a single line of loaded lane affected on a single girder. Table 2 lists the obtained LLDFs for all four girders for the steel–concrete composite bridge under the two cases of loading. Moreover, Fig. 9 presents the LLDFs for the moment due to experimental

**Table 2** Comparison of LLDFs for moment in the bridge

Girders	Case one			Case two		
	Experimental	FE	AASHTO	Experimental	FE	AASHTO
G 1	0.308	0.376	0.491	0.338	0.378	0.491
G 2	0.337	0.428	0.632	0.372	0.423	0.632
G 3	0.445	0.476	0.632	0.389	0.471	0.632
G 4	0.482	0.522	0.631	0.418	0.516	0.631

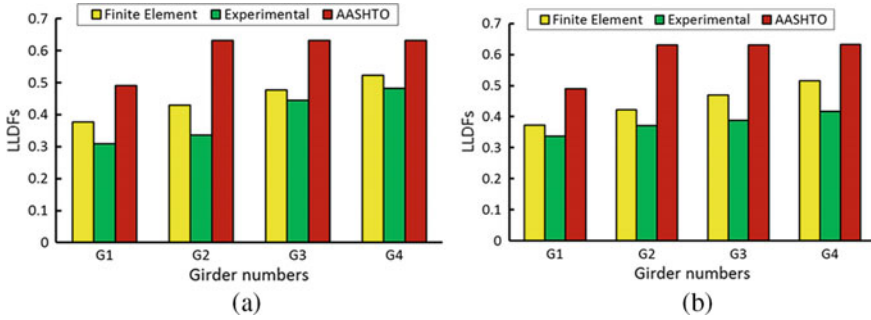


**Fig. 9** The LLDFs for moments due to experimental test, FE analysis, and AASHTO formulas, **a** case one, **b** case two

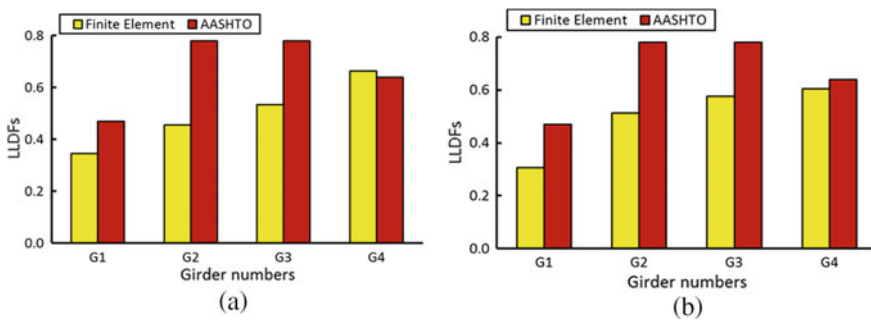


**Fig. 10** The LLDFs for shear due to FE analysis and AASHTO formulas, **a** case one, **b** case two

test, FE analysis, and AASHTO in two loading cases. Interestingly, LLDFs values calculated according to AASHTO formulas seem to be more conservative compared to experimental and FE results. This reveals a need to improve new formulas to calculate LLDFs that are closer to the actual values. At the same time, LLDFs for shear have been calculated from FE analysis results and AASHTO formulas. Figure 10 illustrates the LLDFs for shear for FE analysis and AASHTO formulas for the bridge girders due to the two loading cases. The values of the LLDFs of shear obtained from AASHTO formulas are more conservative for the interior bridge girders, but it seems more critical for the external girders.

### 8 Effect of CFD

A parametric study has been done to inspect the effects of CFD on deflection behavior and LLDFs for the moment and shear of the bridge under consideration. With and without CFD, two FE models have been modeled and analyzed to perform this parametric study. Figure 11 compares the mid-span FE deflection due to Case two loading

**Fig. 11** The mid-span FE deflections due to Case two loading for the composite bridge

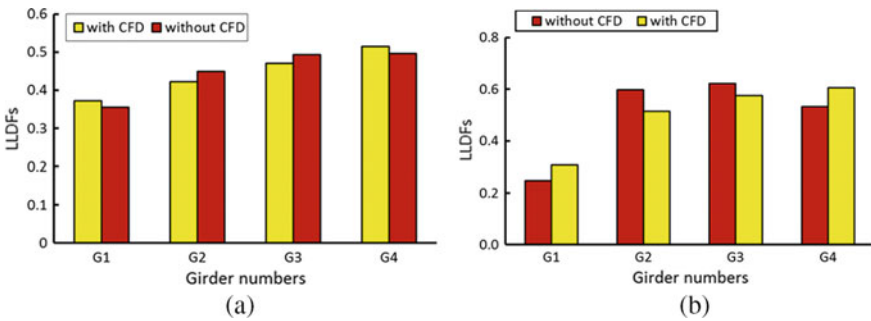
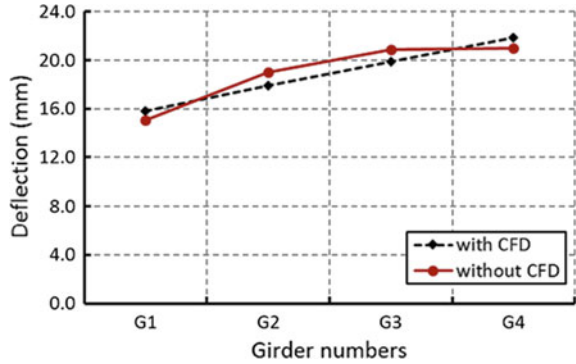


**Fig. 12** Effect of CFD on the LLDFs for composite bridge, **a** for the moment, **b** for shear

for the composite bridge with and without CFD. The results report the importance of the CFD to redistribute live load among bridge girders. Figure 12 presents the effect of CFD on the LLDFs for the moment and shear for the bridge. The CFD effects on the live loads distribution between bridge girders were set by decreasing and increasing the LLDFs for the internal and exterior girders.

## 9 Conclusions

Depending on the experimental test, FE analysis, and AASHTO formulas results obtained in this study for a composite highway bridge, the following conclusions can be drawn:

- Moment LLDFs values calculated according to AASHTO formulas are more conservative than the experimental and FE values.
- AASHTO LLDFs shear formula values seem to be critical for exterior girders.
- The presented FE method can be adopted accurately in analyzing composite steel–concrete bridges.

- The importance of the CFD to dispense live load effects on bridge girders was set by decreasing and increasing the LLDFs for the internal and the exterior girders, respectively.

**Acknowledgements** The authors would like to gratefully present their acknowledgments to the Consulting Engineering Bureau (CEB) and the Department of Civil Engineering at the University of Baghdad for the support received to achieve this work.

## References

1. Zokaie, T. (2000). AASHTO-LRFD live load distribution specifications. *Journal of Bridge Engineering*, 5(2), 131–138.
2. Tabsh, S. W., & Tabatabai, M. (2001). Live load distribution in girder bridges subject to oversized trucks. *Journal of Bridge Engineering*, 6(1), 9–16.
3. Kim, Y. J., Tanovic, R., & Wight, R. G. (2010). Load configuration and lateral distribution of NATO wheeled military trucks for steel I-girder bridges. *Journal of Bridge Engineering*, 15(6), 740–748.
4. Li, J., & Chen, G. (2011). Method to compute live-load distribution in bridge girders. *Practice Periodical on Structural Design and Construction*, 16(4), 191–198.
5. Seo, J., Phares, B. M., Dahlberg, J., Wipf, T. J., & Abu-Hawash, A. (2014). A framework for statistical distribution factor threshold determination of steel–concrete composite bridges under farm traffic. *Engineering Structures*, 69, 72–82.
6. Fatemi, S. J. (2016). *Load distribution factors of straight and curved steel concrete composite box and I girder bridges* [Ph.D. Dissertation]. University of Adelaide, Australia.
7. Tabsh, S. W., & Mitchell, M. M. (2016). Girder distribution factors for steel bridges subjected to permit truck or super load. *Structural Engineering and Mechanics: An international Journal*, 60(2), 237–249.
8. Allawi, A., Al-Sherrawi, M., Al-Gharawi, M., & El-Zohairy, A. (2019). A case study to evaluate live load distributions for pre-stressed RC bridge. In *Challenges in mechanics of time-dependent materials* (Vol. 2, pp. 73–85). Springer.
9. Bakht, B. (1988). Analysis of some skew bridges as right bridges. *Journal of Structural Engineering*, 114(10), 2307–2322.
10. Mertz, D. R. (2001). *Designer's guide to cross-frame diaphragms*. American Iron and Steel Institute.
11. Bishara, A. G. (1993). Cross frames analysis and design, FHWA/OH-93/004. Federal Highway Administration, Washington, D.C. and Ohio Department of Transportation, Columbus, OH.
12. Shi, J., 1997. *Brace stiffness requirements of skewed bridge girders* [M.Sc. Dissertation]. University of Houston, Houston, TX.
13. Khaloo, A. R., & Mirzabozorg, H. (2003). Load distribution factors in simply supported skew bridges. *Journal of Bridge Engineering*, 8(4), 241–244.
14. Watheej, Z., & Al-Sherrawi, M. H. (2009). Effect of cross frame diaphragms on the measurements and finite element modeling of the non-composite deflections of steel plate girder bridges during construction stage. In *6th Engineering Conference College of Engineering* (pp. 46–64), Baghdad, Iraq.
15. Morera, F. J. (2010). *Lateral flange bending in heavily skewed steel bridges* [Ph.D. Dissertation]. North Carolina State University, Raleigh, N.C.
16. Hassel, H. L., Bennett, C. R., Matamoros, A. B., & Rolfe, S. T. (2013). Parametric analysis of cross-frame layout on distortion-induced fatigue in skewed steel bridges. *Journal of Bridge Engineering*, 18(7), 601–611.

17. Fettahoglu, A. (2015). Effect of cross-beam on stresses revealed in orthotropic steel bridges. *Steel and Composite Structures*, 18(1), 149–163.
18. Said, A. I., & Lateef, H. K. (2017). Effect of curvature on the shear distribution factor for horizontally curved concrete box girder. *International Journal of Science and Research*, 6(12), 77–82.
19. Said, A. I. (2018). Experimental study for horizontally curved box girder bridges with special reference to the live load moment distribution factor. *Association of Arab Universities Journal of Engineering Sciences*, 25(3), 200–215.
20. Zhang, L. F., Wang, Y., Lei, Y. G., & Chang, Y. (2019). Analysis on live load distribution factors of widened hollow core slab bridges. In *Materials science forum* (Vol. 953, pp. 215–222). Trans Tech Publications Ltd.
21. Tabsh, S. W. (2019). Load distribution in short bridges subjected to oversize vehicles. In *Australian Small Bridges Conference, 9th, 2019, Surfers Paradise, Queensland, Australia*.
22. Al-Sherrawi, M. H., & Mahmoud, K. S. (2018). Shear and moment strength of a composite concrete beam. *International Research Journal of Advanced Engineering and Science (IRJAES)*, 3(4), 128–132.
23. Liu, L., Ren, Q., & Wang, X. (2020). Calibration of the live load factor for highway bridges with different requirements of loading. *Advances in Civil Engineering*, 2020.
24. Peker, F. Ü., & İnce, R. (2020). Investigation of live load distribution factors effect in structural analysis of bridges. *BEU Journal of Science*, 9(3), 1297–1305.
25. Dong, C., Bas, S., Debees, M., Alver, N., & Catbas, F. N. (2020). Bridge load testing for identifying live load distribution, load rating, serviceability and dynamic response. *Frontiers in Built Environment*, 6, 46.
26. ANSYS Manual, 10th Ed., Release 4.1, Swanson Analysis Systems, Canonsburg, PA (2008).
27. El-Shihy, A. M., Fawzy, H. M., Mustafa, S. A., & El-Zohairy, A. A. (2010). Experimental and numerical analysis of composite beams strengthened by CFRP laminates in hogging moment region. *Steel and Composite Structures*, 10(3), 281–295.
28. Al-Sherrawi, M. H., & Mohammed, S. N. (2018). Shear lag in composite steel concrete beams. In *2018 1st International Scientific Conference of Engineering Sciences-3rd Scientific Conference of Engineering Science (ISCES)* (pp. 169–174). IEEE.
29. Al-Sherrawi, M. H., & Mohammed, S. N. (2014). The effective width in composite steel concrete beams at ultimate loads. *Journal of Engineering-Univ. of Baghdad*, 20(8), 1–17.
30. American Association of State Highway and Transportation Officials. (2012). *AASHTO-LRFD, Bridge Design Specifications*. Washington D.C., USA.



# Numerical Analysis of Historical Masonry Minaret Subjected to Wind Load



Alaa Hussein Al-Zuhairi, Ammar R. Ahmed, and Salah R. Al-Zaidee

**Abstract** The present paper describes the behavior and response of an unreinforced masonry historical minaret when subjected to wind pressure as a main external loading. Three-dimensional nonlinear finite element analysis was performed to obtain lateral displacements of the minaret shaft and stresses in its components. Abaqus software with implicit solver was utilized for finite element modeling and nonlinear analysis of a historical masonry minaret subjected to wind load. Clay brick masonry units, mortar, and unit-mortar interfaces were modeled individually to permit the studying of each component separately. The shaft of the minaret was divided into brick courses (Bayors) separated by horizontal mortar joints. Two analyses were conducted on the minaret model, considering first its weight alone and in addition to wind loading second. The results showed that the unreinforced masonry minaret could resist the compressive stresses induced by the self-weight of its components. Also, lateral displacements and compressive and tensile stresses results due to the effect of wind pressure and minaret's weight simultaneously were obtained, which showed that the minaret exhibited an adequate resistance to the wind with a speed of 120 km/h.

**Keywords** Abaqus · Finite element method (FEM) · Nonlinear analysis · Unreinforced masonry minaret · Wind loading

## 1 Introduction

Minarets are tall, slender constructions; they are prominently observed in Islamic culture. It is regularly built close to or adhered to the sidewall of mosque structures. In several Islamic majority nations, minarets play the landmark role for being the identifier of mosques from a far distance. Also, it is the place at which the

---

A. H. Al-Zuhairi (✉) · A. R. Ahmed · S. R. Al-Zaidee  
Civil Engineering Department, University of Baghdad, Baghdad, Iraq  
e-mail: [alaalwn@coeng.uobaghdad.edu.iq](mailto:alaalwn@coeng.uobaghdad.edu.iq)

S. R. Al-Zaidee  
e-mail: [Salah.R.Al.Zaidee@coeng.uobaghdad.edu.iq](mailto:Salah.R.Al.Zaidee@coeng.uobaghdad.edu.iq)

muezzin announces azan. Azan calls on people to gather for the coming prayer; azan is announced five times every day through the minarets. Mosques were constructed at the beginning of the Islamic era without minarets. The prayer calls for that period of time were accomplished by standing on an elevated platform or the rooftop of the house of Prophet Muhammad; may God bless him [1]. It is not clear when the first-ever minaret was built. However, it is agreed upon by several scholars that the first minaret in its present form was built during Umayyad caliphate rule in Damascus (Syria) in the early 700 s [2, 3].

The majority of the recent minarets are constructed as reinforced concrete (RC) structures that permit structural engineers and architects to design and revolutionize tall minarets with lower fundamental vibration frequencies than masonry minarets. Even though minarets were not a familiar façade of most primitive mosques nonetheless, they are still regarded in various Islamic countries like Iraq, Turkey, Egypt, Saudi Arabia, Morocco, etc. as the most architecturally significant objects of the cultural heritage from the era of Othman empire that became adjacent with Islamic shrines. The architectural design and structural system differences found in minarets stem from differences in the cultural society, construction materials available, construction techniques, and workmen background [1]. A typical minaret in the Othman empire era is an assembly of standard components comprising of foundation or footing, pulpit or boot, transitional segment, body/shaft which has a cylindrical shape, one or more balconies, the spire crest, ornamented end, and internal helical stairs, as depicted in Fig. 1.

The minaret's foundation is built either as separate footing or in attachment to some of the bearing walls of the mosque. The base of the minaret, which is referred to as the pulpit, is the minaret's lower part that rises above the foundation. It commonly has a square or polygonal shape. The function of the transitional segment is to avoid interrupting transition from the larger-size base (pulpit) to the lesser-size minaret body that usually has cylindrical or polygonal shapes. The main component of the minaret (minaret shaft) that comprises a cylindrical or polygonal column is surrounded by a set of helical stairs arranged so that they are running counter-clockwise on the way around the shaft and up to the balcony (or balconies). The internal running spiral stairs enhance the minaret body's structural resistance against the effects of lateral loads such as wind and seismic loadings. The balconies act as structural connectors between the two successive cylindrical parts along the minaret height. Historically, minaret balconies were functioned to be the platform from azan is announced. With the invention and accessibility of loudspeakers, balconies are no longer utilized for this purpose; instead, balconies are now constructed for aesthetics and decoration purposes. The minaret crest is the segment between the last balcony and spire. Finally, the spire or minaret cap functions as a roof. It normally has a conical shape, built with materials of the same or different properties than those used for the minaret body [4].

The behavior of minarets subjected to horizontal loads is somewhat different from the trend of other structures due to their unique features like supporting, shape, and slenderness ratio [1]. Many minarets were destroyed due to lateral loads such as destructive seismic activities and strong winds, causing loss of livelihoods and

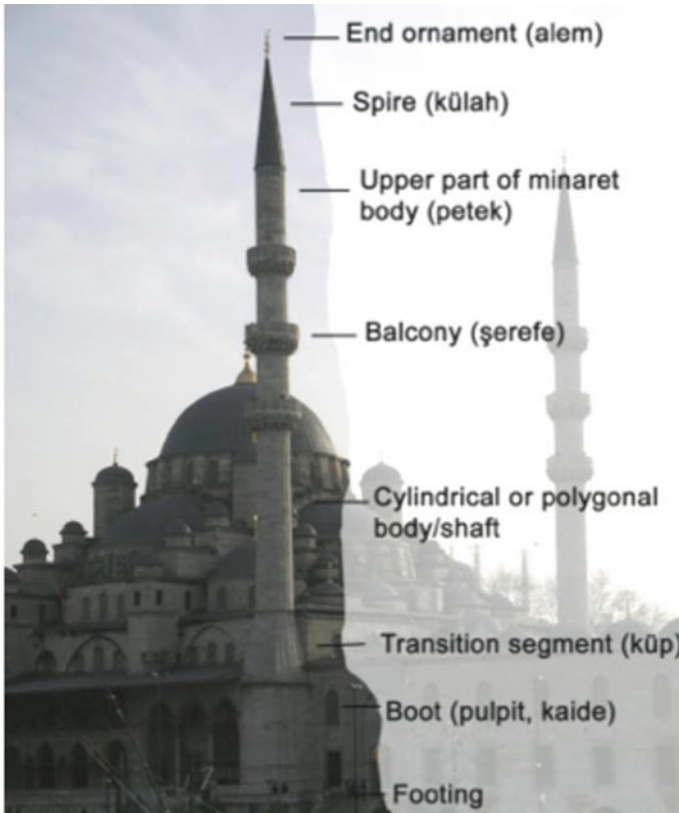


**Fig. 1** Parts of a typical Othman minaret [4]

belongings. Several studies investigated the behavior and performance of minaret constructions subjected to lateral loads, while other researchers like [4–7] studied the seismic response of cylindrical structures such as chimneys and minarets. An analytical study using a three-dimensional FE model was conducted by [8] to investigate the seismic response of a historical minaret in Istanbul. The study comprised of two FE models, one of natural stone block masonry minaret and the other of a retrofitted minaret by fiber reinforced cementitious matrix (FRCM) material. The researcher concluded the efficiency of applying FRCM confinement to eliminate the high risks for existing non-strengthened historical minaret due to the effect of probable (above 0.6 g PGA) earthquakes with a considerable chance of occurring for the following 30 years near Istanbul. However, only a few obtainable studies were concerned with the response of minaret under wind loading.

Not too long ago, the Turkish press media reported that some minarets were damaged or destroyed during a wind storm because of the effects of wind. However, detailed information regarding the number of disasters was absent from the press. However, the news dated 27 Feb 2002 stated that the historical minaret in Icel in

Mersin Province was destroyed due to a wind speed of 96 km/h. Likewise, the 15 m height minaret of Ulu mosque in Kahramanmaras city was damaged due to the wind speed of 60 km/h [1] on 24 July 2005. Even if the casualty numbers because of the fallen minaret as a consequence of the effects of wind pressure are not stated in the press and may be very small but, in many cases, causes significant economic and sentimental damages [1]. This paper aims to study the response of a virtual historical masonry minaret subjected to wind pressure. Numerical FE analysis based on the separation of masonry unit layers and bonding mortar was conducted on the body of the minaret implementing the well-known FE software program Abaqus.

## 2 Nonlinear Structural Analysis of the Minaret

A finite element simulation was constructed for the minaret and analyzed linearly and nonlinearly. ABAQUS [9] software was used for the modeling and analysis of the masonry minaret. Three-dimensional continuum tetrahedral and hexahedral elements were used. The tetrahedral elements have 10 nodes, and the hexahedral elements have 8 nodes. Both elements have three displacement degrees of freedom per node. The displacements are in the three Cartesian directions. Full restricted have been assigned to the bottom surface to simulate the fixed support condition of the minaret. A total number of 12,220 elements and 51,424 nodes were defined for the minaret numerical model. 11,572 linear hexahedral elements of type C3D8R and 648 quadratic tetrahedral elements of type C3D10. A reduced integration technique has been used for the hexahedral elements to avoid the possible shear locking phenomena. The minaret was modeled using the detailed micro-modeling method in which masonry components and joint bonding mortar are modeled separately as solid elements [10–12]. According to this simulation method, the masonry structure was considered as a composite of the units, mortar and unit-mortar interface. Nevertheless, the vertical joints (headers) were ignored in this study while the minaret shaft has been discretized into a number of monolithic masonry rings with one unit in thickness and separated by mortar bedding (horizontal) joints. The geometry of the analyzed virtual historical minaret is presented in Fig. 2.

The total height of the minaret is in the range of 19.5 m. The external and internal diameters of the pulpit were 2.2 m and 1.4 m, respectively. As for the cylindrical shaft, the external diameter was 1.5 m, and the internal diameter was 1.2 m. For the upper part of the minaret, 1.26 m was the external diameter, and 1.1 m was the internal diameter. The compressive and tensile strengths, linear and nonlinear mechanical properties of clay brick units, and cement bonding mortar was adopted from [10, 13] and listed in Table 1. Regarding the load, the following load cases have been considered during the nonlinear analysis of the minaret:

**Nonlinear Dead Load Analysis.** For this loading case, the response of the minaret was determined under its weight only. The self-weight has been selected as body force equal to the material density, defined in the material modeling process, times

**Fig. 2** Finite element model of the minaret

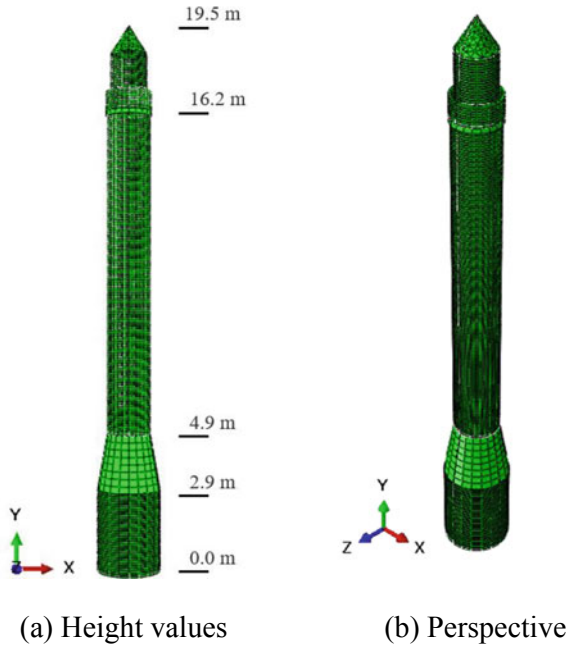


**Table 1** Adopted mechanical properties of units and mortar [10, 13]

Component	Compressive strength**, $f_c$ (MPa)	Tensile strength*, $f_t$ (MPa)	Linear properties*		Nonlinear properties*		
			Modulus of elasticity, $E_c$ (MPa)	Poisson's ratio, $\nu$	Cohesion, $c$ (MPa)	Angle of internal friction, $\phi$	Dilatation angle, $\psi$
Clay bricks (units)	10.96	1.32	16,700	0.15	1.85	0	36.87
Cement mortar	8.30	2.30	18,000	0.10	0.35	0	36.87

Note (\*) the values were adopted from [10], (\*\*) the values were adopted from [13]

element volume deduced by the software based on the spatial discretization process. The resulting deformations, strains, and stresses have been propagated from the dead load analysis to be used to define the deformed shape and initial strains and stresses for the subsequent wind analysis.

**Nonlinear Wind Load Analysis.** In this simulation, the minaret is analyzed under wind-induced loading as well as its weight. The nonlinear response is determined against the excitation of the wind-induced pressure. The deformations, strains, and stresses from the dead load analysis have been included in the stiffness and load

vector formulation to reflect the nonlinear nature of the problem. Finally, a pseudo time of 1.0 s has been adopted for each analysis to monitoring the loading steps and loading iteration process through the modified Newton–Raphson solution scheme.

**Minaret Response for the Self-Weight Loading.** The nonlinear analysis was conducted on the minaret structure under the action of its self-weight. Vertical displacement and normal stress contours are shown in Figs. 3 and 4, respectively. According to the displacement contours, the maximum displacement that occurred in the vertical direction was 0.14 mm. On the other hand, the maximum tensile and compressive stresses, which were 0.059 and 0.246 MPa, respectively, took place at the bottom of the cylindrical body of the minaret, as illustrated in Fig. 4.

**Minaret Response for Wind Load Effects.** After completing the first step of the analysis examining the minaret’s stability under its own weight, the second step was examining the minaret by subjecting wind load along its height and weight. A wind pressure of 563 N/m<sup>2</sup> has been calculated according to ASCE 7-16 [14]. The minaret was assumed to be located in Iraq. The maximum wind speed (44 m/s) shown in Fig. 5 was adopted as the basic wind speed in wind pressure calculation. This wind pressure was uniformly applied along with the entire minaret height, as shown in Fig. 6a. The minaret model was colored with a grey color, represents the undeformed mode before using the wind load, while the green-colored model represents the deformed mode of the analyzed minaret after applying the wind pressure as illustrated in Fig. 6b. The maximum lateral displacement (maximum drift) resulted from the wind load

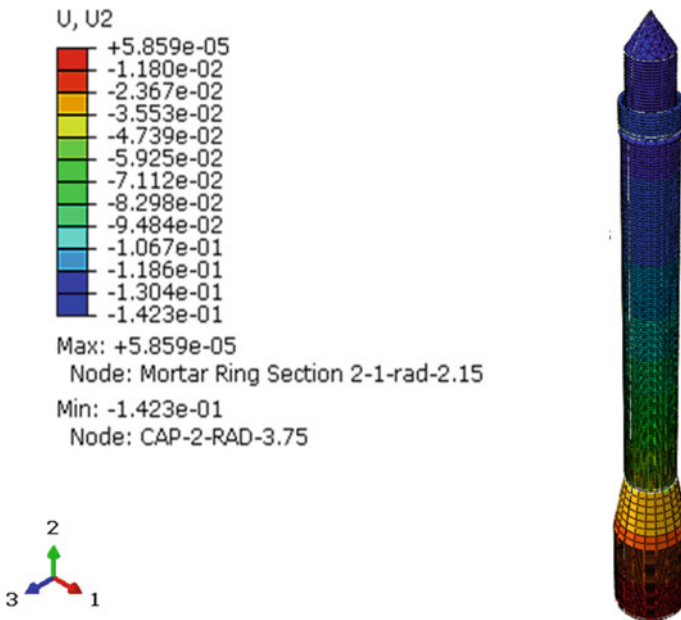
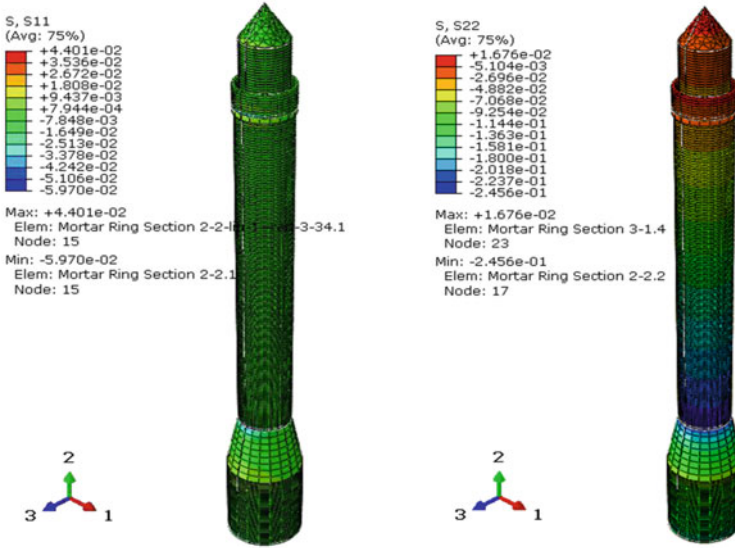


Fig. 3 Vertical displacement contours result from self-weight analysis ( $\Delta_{max} = 0.14$  mm)



(a) Horizontal tensile stress (S11) contours of self-weight analysis in MPa      (b) Vertical compressive stress (S22) contours of self-weight analysis in MPa

**Fig. 4** Results from dead load analysis

analysis was 55 mm. As it is evident in Fig. 6b, the lateral displacement increased with the height of the minaret shaft.

On the other hand, horizontal stresses and strain contours are shown in Fig. 7. It was found that the maximum horizontal tensile and compressive stresses were 0.733 and 0.738 MPa, respectively. These values seem to fall in the range of allowable tensile and compressive stresses for both masonry brick and cement mortar. The maximum tensile stress occurred in the bedding mortar on the bottom of the loading surface of the minaret’s cylindrical body. This finding came compatible with [12]. Besides, the maximum compressive stress occurred in the bedding mortar on the lee-ward surface at the bottom of the cylindrical body of the analyzed minaret.

### 3 Conclusions

A structural investigation of the behavior of a 19.5 m height unreinforced masonry minaret was conducted using modified detailed micro-modeling for the minaret components (i.e., masonry units, mortar bedding joints, and unit-mortar interface). In this method of modeling, horizontal unit courses are separated by bedding mortar joint elements. Two analysis stages were performed on the minaret body. One by considering the self-weight, and the other is based on the effect of wind

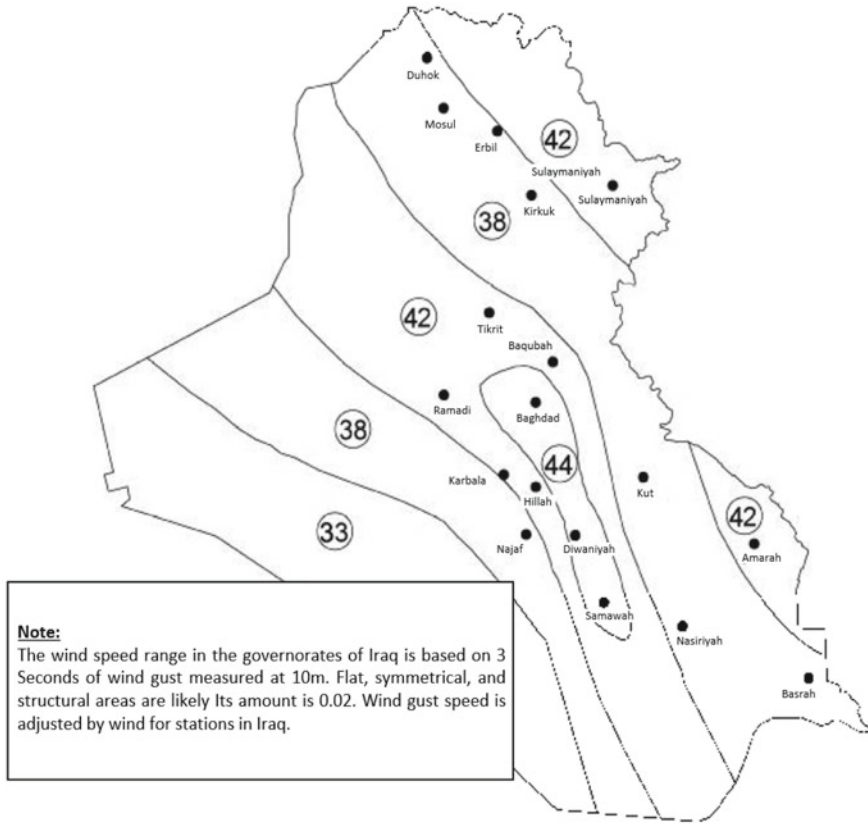
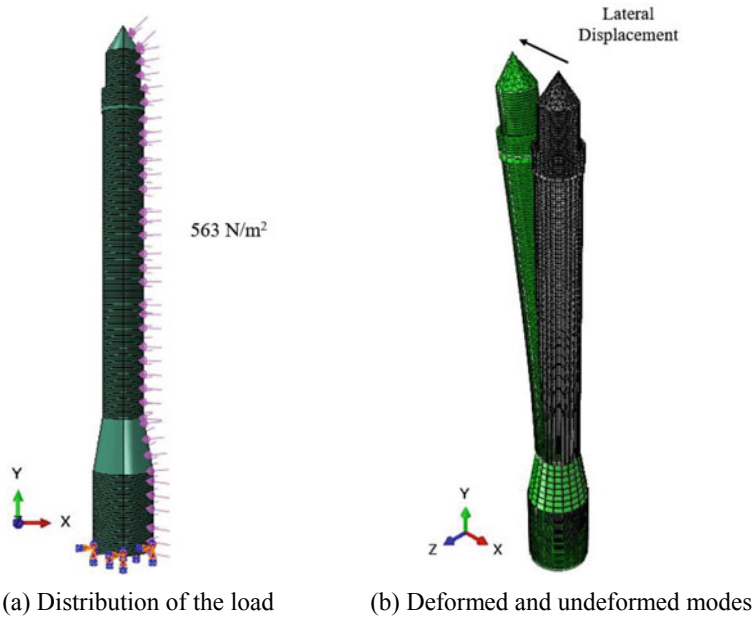


Fig. 5 The basic wind speed contour map for the governorates of Iraq [15]

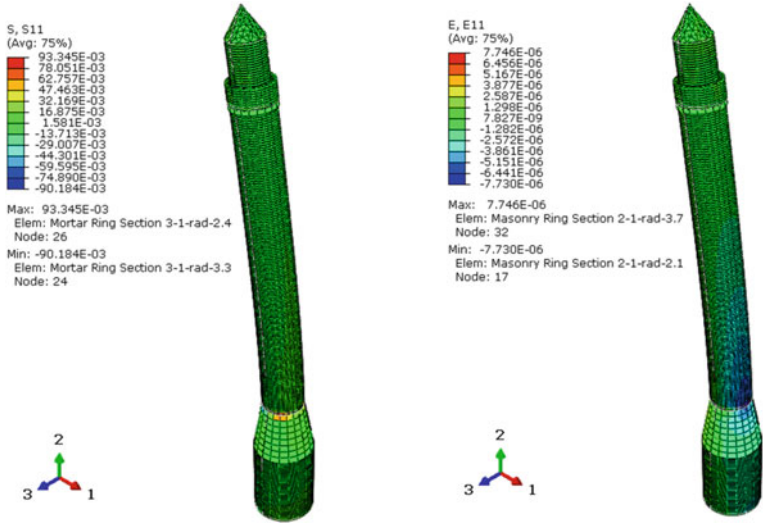
loadings in addition to own weight. These analyses were performed with implementing nonlinear material properties, hence, nonlinear material behavior. The main conclusions inferred from this study are given below:

- Since the Young modulus is relatively high for the masonry units, they behaved stiffly, and the resulting vertical displacements are relatively small.
- When subjected to self-weight and wind-induced forces, the minaret has the maximum compressive and tensile stresses at the base of its cylindrical shaft.
- The ratio of the maximum compressive stress results from wind-induced loads to that results from self-weight loads is in the range of 3, while the ratio of the maximum tensile stress due to wind forces to that results from self-weight loading is approximately 12.4. These findings indicate the importance of considering the effects of wind loading for accurate analysis and safe design of masonry minarets because of the brittleness nature of both masonry components.

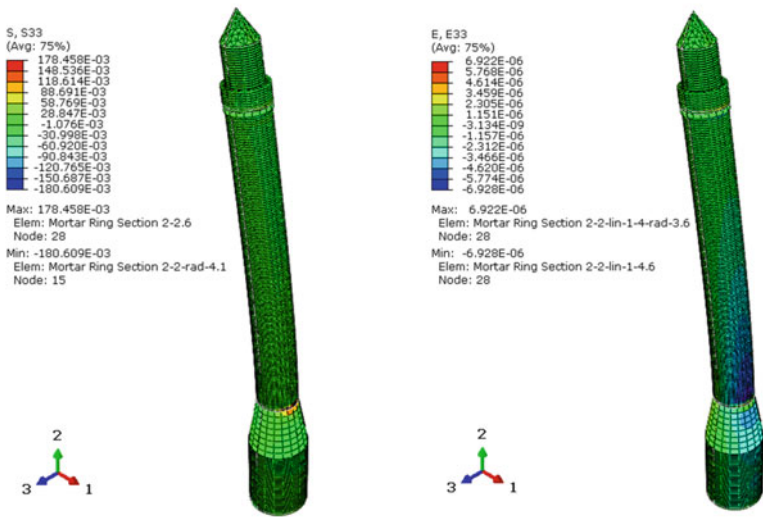




**Fig. 6** The overall behavior of the minaret under the wind



(a) Horizontal normal stress (S11) contours in MPa (b) Horizontal normal strains (E11) contours



(c) Horizontal normal stress (S33) contours in MPa. (d) Horizontal normal strains (E33) contours.

**Fig. 7** Results of the wind load analysis

### References

1. Abdullahi, S. (2014). Structural behaviour of reinforced concrete minaret under wind effect using SAP2000 V. 15. M. Sc. Thesis, Near East University, Nicosia.
2. Dogangun, A., Sezen, H., Tuluk, Ö. I., Livaoglu, R., & Acar, R. (2007). Traditional Turkish

- masonry monumental structures and their earthquake response. *International Journal of Architectural Heritage*, 1(3), 251–271.
3. Bayraktar, A., Sevim, B., Altunisik, A. C., & Turker, T. (2009). Analytical and operational modal analyses of Turkish style reinforced concrete minarets for structural identification. *Experimental Techniques*, 33(2), 65–75.
  4. Çaktı, E., Oliveira, C. S., Lemos, J. V., Saygılı, Ö., Görk, S., & Zengin, E. (2013, June). Earthquake behavior of historical minarets in Istanbul. In *4th ECCOMAS Thematic Conference on Computational Methods in Structural Dynamics and Earthquake Engineering* (pp. 12–14).
  5. Sezen, H., Acar, R., Dogangun, A., & Livaoglu, R. (2008). Dynamic analysis and seismic performance of reinforced concrete minarets. *Engineering Structures*, 30(8), 2253–2264.
  6. Dogangun, A., & Sezen, H. (2012). Seismic vulnerability and preservation of historical masonry monumental structures. *Earthquake and Structures*, 3(1), 83–95.
  7. Turk, A. M., & Coşgun, C. (2012). Seismic behavior and retrofit of historic masonry minaret. *Gradevinar*, 64(1), 39–45.
  8. Turk, A. M. (2013). Seismic response analysis of masonry minaret and possible strengthening by fiber reinforced cementitious matrix (FRCM) materials. *Advances in Materials Science and Engineering*, 14. Article ID 952497.
  9. ABAQUS CAE. (2014). Finite element analysis software products. In *Finite element system*. Dassault Systems.
  10. Laurenco, P. B., Rots, J. G., & Blaauwendraad, J. (1995). Two approaches for the analysis of masonry structures: Micro and macro-modeling. *HERON*, 40(4), 1995.
  11. Ahmed, A. R., & Al-Zuhairi, A. H. (2019). Behavior of clay masonry prism under vertical load using detailed micro modeling approach. *Association of Arab Universities Journal of Engineering Sciences*, 26(1), 67–73.
  12. Ahmed, A. R., & Al-Zuhairi, A. H. (2018). Finite element analysis for the response of URM walls supporting RC slab. *International Journal of Engineering and Technology*, 7(4.20), 259–265.
  13. Mohamad, G., Lourenço, P. B., Rizzatti, E., Roman, H. R., & Nakanishi, E. Y. (2012). Failure mode, deformability and strength of masonry walls. In *15th International Brick and Block Masonry Conference*. Florianopolis, Brazil.
  14. American Society of Civil Engineers. Minimum design loads for buildings and other structures (ASCE7-16). Structural Engineering Institute Minimum Design Loads and Associated Criteria for Buildings and Other Structures (ASCE/SEI 7-16).
  15. Ministry of Planning-Central Organization for Standardization and Quality Control. (2016). Loads and Forces Code. Iraq Building Code 301 (1st Ed.).

# Accuracy Assessment of Shell Finite Elements for Considering to Masonry Structures Under Seismic Loading



Halmat Ahmed Awla and Mohamed M. Arbili

**Abstract** For assessment or seismic-resistant design of masonry buildings, an appropriate numerical model is required. Since reproducing an actual masonry structure in a computer model is impossible and computationally expensive, the researchers have always tried to consider these structures with a rationally proper method in the best compromise between accuracy in results and simplicity in application. Solid finite elements are a very popular method for modeling masonry structures because of the accuracy of results for both elastic and inelastic analysis, but it is computationally expensive. Thus, selecting a proper method for modeling these structures is the first and most important step. The aim of this study is to examine the accuracy of shell elements when considered for modeling masonry structures. For this purpose, dynamic responses in terms of stresses, displacements, base shear, and natural periods of a two-story masonry structure modeled by shell elements were compared with its prototype examples modeled using solid finite elements. According to the obtained results, very good agreement was observed between the two models. And it can be concluded that using shell elements for modeling these types of structures is effectively adequate.

**Keywords** Masonry structures · Shell finite elements · Solid finite elements · Seismic assessment

## 1 Introduction

For modeling masonry buildings using finite element procedures, three modeling techniques are used for static and dynamic loading conditions: Micro, Simplified micro, and Macro modeling.

---

H. A. Awla (✉) · M. M. Arbili  
Department of Information Technology, Choman Technical Institute, Erbil Polytechnic University, Erbil, Iraq  
e-mail: [halmat.awlla@epu.edu.iq](mailto:halmat.awlla@epu.edu.iq)

M. M. Arbili  
e-mail: [mohamed.arbili@epu.edu.iq](mailto:mohamed.arbili@epu.edu.iq)

Figure 1 Concrete blocks, brick, stone, and mortar are homogenized as a continuum domain in the macro modeling approach. Thus, minimum finite element numbers are used; consequently, less computational time and physical memory are required. However, in micro and simplified modeling, concrete blocks, brick, stone, and mortar are independently modeled. This technique is a more complex and sophisticated method; the technique is the most accurate method for analyzing masonry structures. Crack patterns, damaged contours, and ultimate load capacity can be calculated accurately. Micro modeling approaches are computationally prohibitively expensive and require large computer memory [1, 2]. Therefore, many researchers have focused on developing simplified alternative methodologies to decrease computational time to best suit everyday engineering practice [3–5]. In Iraq and Kurdistan region, unreinforced masonry structures (URM) are popular. Still, a more significant percentage of the population are living in masonry structures. Thus the seismic assessment of these structures is a must since masonry structures are known as the most vulnerable building against earthquakes. Moreover, protecting ancient masonry buildings as they were built and transforming to the future generation is essential because they are national heritage. Because seismic hazards are the main source of damage for heritage masonry structures [6, 7], seismic assessment of these structures also an essential task.

Mainly there are three types of masonry structures in the country; concrete block and brick masonry, natural stone masonry, and mixed masonry with RC or steel structures. In the current study, a typical two-story concrete block masonry is considered a case study, bearing walls constructed using concrete blocks, the floors are built up by reinforced concrete, and steel bars are used as reinforcement material. Generally, solid finite elements are employed for modeling masonry structures because it is known as the most efficient method, which cracks, damages, and many other physical characteristics of materials can be considered in the method [8]. The main drawback of solid finite elements, it is not cost-effective in the perspective of computational efforts. Shell elements are employed for masonry modeling as an alternative

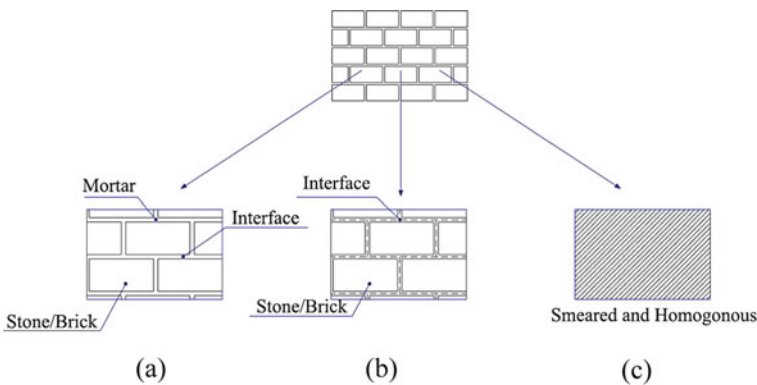


**Fig. 1** Masonry modeling techniques; **a** micro, **b** simplified micro, and **c** macro modeling [1, 2, 6]

method, and the equivalent frame method is another simplified method for considering masonry structures, and the latest one is principally utilized for nonlinear evaluation of masonry buildings. For evaluation of global behavior of structural systems, generally linear (static and dynamic) and pushover analysis are utilized [9].

Mainly the nonlinear static analysis is used for the assessment of the seismic performance of existing buildings. However, the nonlinear static analysis outweighs some drawbacks of the linear dynamic analysis, especially in assessing existing buildings. It is recommended to adopt different analysis strategies for the same problem, and their results should be discussed critically [9]. For considering inelasticity of the frame element structures, two main modeling types are available, distributed plasticity method and lumped plasticity method [10, 11]. The most accurate and sophisticated method for considering inelasticity is by using solid finite elements that can be applied to any structure anywhere. In the method, the structural members are mesh into massive numbers of solid finite elements, geometric and constitutive nonlinearity is introduced at the stress–strain level. The thermal phenomenon, interface friction, cracks, relaxation, and creep characteristics can be simulated in the method. Since this method is computationally prohibitively expensive for real scale structures for considering nonlinear dynamic analysis, it is generally limited to the critical parts of the structures like joints and the regions expected to undergo large displacements, rotations, and nonlinearity [8].

The computational time that is needed for analyzing the same finite element problems, which were modeled by a shell and solid elements, was studied by [12]. According to the outcomes of their research, it was found that the computational time for shell elements less than 10% of the time needed for solid elements. Based on the finite element models, several numerical methods can be applied for the analysis of the seismic behavior of masonry buildings. These numerical methods are usually expensive in the scene of computational efforts. To overcome this complexity, reasonable simplicities have been made [13]. The aim of this study is to assess the accuracy of shell elements for considering masonry structures. For this purpose, the dynamic responses of a two-story masonry building modeled by shell elements were compared with the results of the same problem modeled using solid elements. Both models were linearly analyzed under earthquake loading. The advantage of these simplified models is a huge number of masonry structures are analyzed in a very short time. Thus, seismic vulnerability assessments are accelerated, and optimal solutions for structural retrofitting can be suggested [14].

The seismic capacity of masonry stone structures could be low or reasonably accepted depending on structural element details, physical characteristics of materials, and architectural arrangements. Generally, local failure modes are dominant in the collapse mechanisms of masonry structures. However, the global failure modes can be achieved by enhancing the overall quality of the masonry structure. Many laboratory tests have taken place for understanding the actual seismic response of masonry stone structures because of such laboratory experiment campaigns. Many numerical methods were validated and improved for both assessment and strengthening existing buildings against earthquake loadings [15]. Because of the availability of efficient nonlinear analysis models, meaningful evaluations for existing masonry structures

can be achieved. The macro-element models provided an adequate depiction of the lateral behavior of masonry structures [16]. Moreover, laboratory cyclic pushover investigations on masonry structures contributed to the general understanding of crack patterns and force–deflection curves [17].

An assessment study for mixed masonry RC buildings was performed by Lagomarsino et al. [18], nonlinear static and linear dynamic analysis were investigated. It was concluded that the most critical parts of masonry structures are surrounding openings and sidewalls. Moreover, it was observed that the seismic resisting capacity of isolated these types of structures is lower than the same structures in compound blocks. Additionally, it was concluded that the provisions of Euro-code and Italian-code were not adequate for seismic performance-based assessment. Even though the bigger ratio of loss of life caused by earthquakes is because of the low seismic resisting capacity of masonry structures, the attempts are still smaller to improve their seismic performance compared to the efforts consuming for enhancing seismic performance of RC buildings [19, 20].

## 2 Numerical Modelling

SAP-2000 offers elastic solid brick finite elements. However, inelasticity can be incorporated into the solid brick elements utilizing nonlinear link elements. For performing this behavior, the link elements are positioned between adjacent solid objects, and nonlinear relationships of the material are assigned to these link elements. Thus the system can reflect the actual problem [21]. But this is out of the scope of this study, and this topic can be investigated in future studies. For the current work, the only elastic region was studied. Still, elastic analysis through solid finite elements can tell us many about the assessment, design, and retrofitting of masonry structures.

Shell elements are a three or four-node area object. Shell elements are used to modeling bridge decks, walls, and floors. Many other structural systems components can be modeled by shell elements such as flanges and webs of a W-section. Shell elements are utilized for representing plate bending or membrane behavior. At the same time, solid elements are eight-node objects that can be used for modeling any structural system Fig. 2. Solid elements have six quadrilateral faces with a joint at each corner. Anisotropic properties and temperature-dependent can be assigned [21].

For the current study, two models were created and named model-A and model-B; solid finite elements were used for modeling the walls of the first model, and shell finite elements were utilized for the walls of the second model, while floors are modeled by using solid elements for both model-A and Model-B. SAP-2000 software package was used for this study. It is general structural engineering finite element software that is well known as a user-friendly interface and the most structural engineering program popular in the structural engineering community worldwide. Both numerical models were analyzed under El Centro time history acceleration loading [22, 23]. The acceleration curve is shown in Fig. 3. Dynamic responses in terms

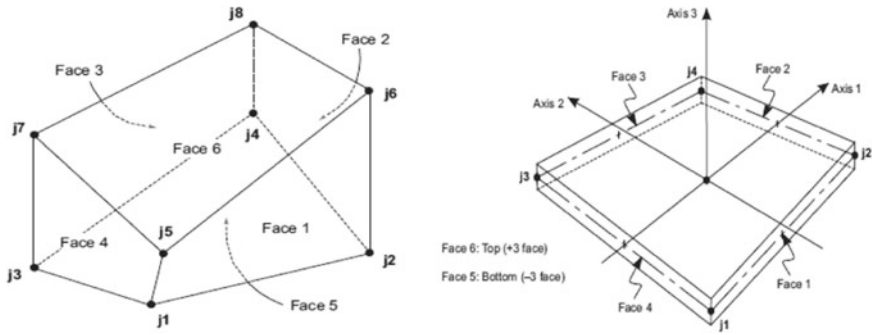


Fig. 2 Solid and shell elements [21]

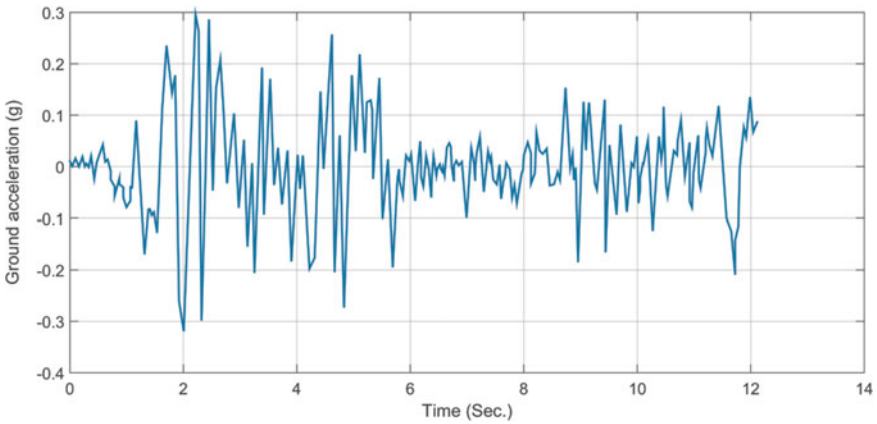


Fig. 3 El Centro ground acceleration curve

of time history top story displacements, maximum stresses, and natural periods are reported.

### 3 Description of the Structure

Plan dimensions and the general layout of the structure are shown in Fig. 4. The net height of each story is 3 m. Walls and slab thicknesses are defined as 0.2 m. Solid concrete blocks are used for the walls, and the slabs are reinforced concrete; 12 mm diameter steel bars were used in two layers in the slabs, 40 cm is center to center spacing for steel rebars for both top and bottom layers. Tie constraint is utilized to connecting different parts of the numerical models, and steel rebars were embedded in the concrete regions. This type of building is popular in Iraq and Kurdistan region.



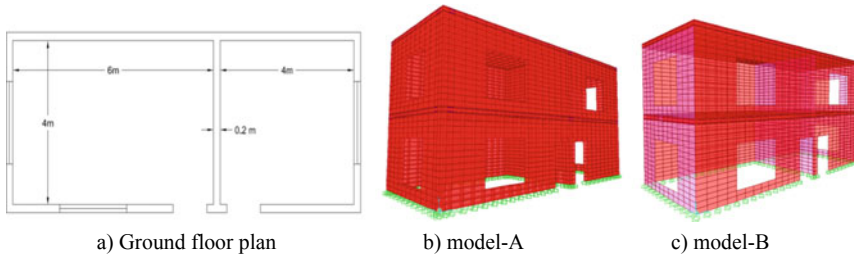


**Fig. 4** The general layout of the structure

**Table 1** Material properties used for modeling

Material	Concrete compressive and steel tensile strength (MPa)	Modulus of elasticity (MPa)	Poisson's ratio
Concrete Block	27.6	24,855.6	0.2
Steel rebar	413.7	200,000	0.3

The base of the structures is assumed to be fully restrained against rotation and translation in all three principal directions. However, many researchers have reported that soil-structure interaction has great influences on the dynamic responses of buildings [24–29]. A total ultimate load of 0.5 ton/m<sup>2</sup> was added to the self-weight of the floors. Uniaxial compressive strength of concrete is 27.6 MPa, and uniaxial tensile strength of steel rebars is 413.7 MPa, modulus of elasticity of concrete and steel rebars are 24,855.6 and 200,000 MPa, respectively. The input data are tabulated in Table 1.

## 4 Results and Discussion

Firstly, modal analysis has been done in order to capture the first mode shapes and their natural periods for both models. Secondly, the dynamic linear analysis was performed, and the dynamic responses in terms of maximum stresses, base shear, and top story displacements were recorded step by step for both numerical models Model-A and Model-B. The percentage difference of the natural period for the first mode shape of Fig. 5 is given in Table 2. A percentage difference of about 14.2% was observed between both numerical models. Since this difference hasn't much influence on the dynamic responses in terms of top story displacements and maximum stress distribution, it can be justified that this slight difference is reasonable and natural periods are compatible for both numerical models.

Maximum stress distributions in the three-dimensional view and separately for each wall facade are presented in Figs. 6, 7 and 8 for both model-A and Model-B.

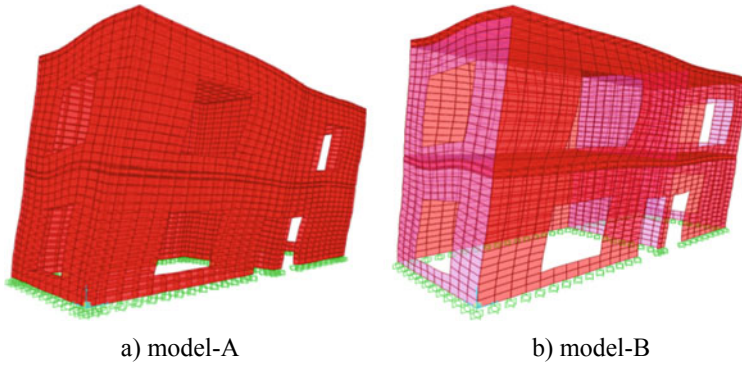


Fig. 5 First mode shape for both numerical models

Table 2 Percentage difference for the first natural period (T1) in seconds for both models

Model	T1	Difference (%)
Model-A	0.07886	14.2
Model-B	0.06766	

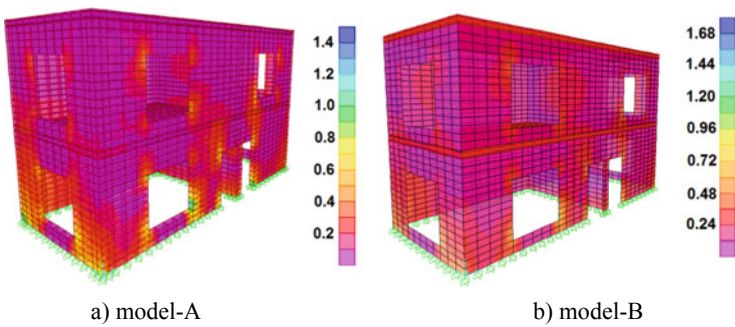


Fig. 6 Maximum stress distribution scale in MPa

According to the obtained results of the stress distribution, it can be concluded that the results are similar, and both models are very compatible with each other.

Relative and absolute (total) time history displacements for the top of both numerical models are presented in Figs. 9 and 10, respectively. On the other hand, time history base shear is shown in Fig. 11. It can be noticed from the figures that the time history displacement and base shear values are almost identical.

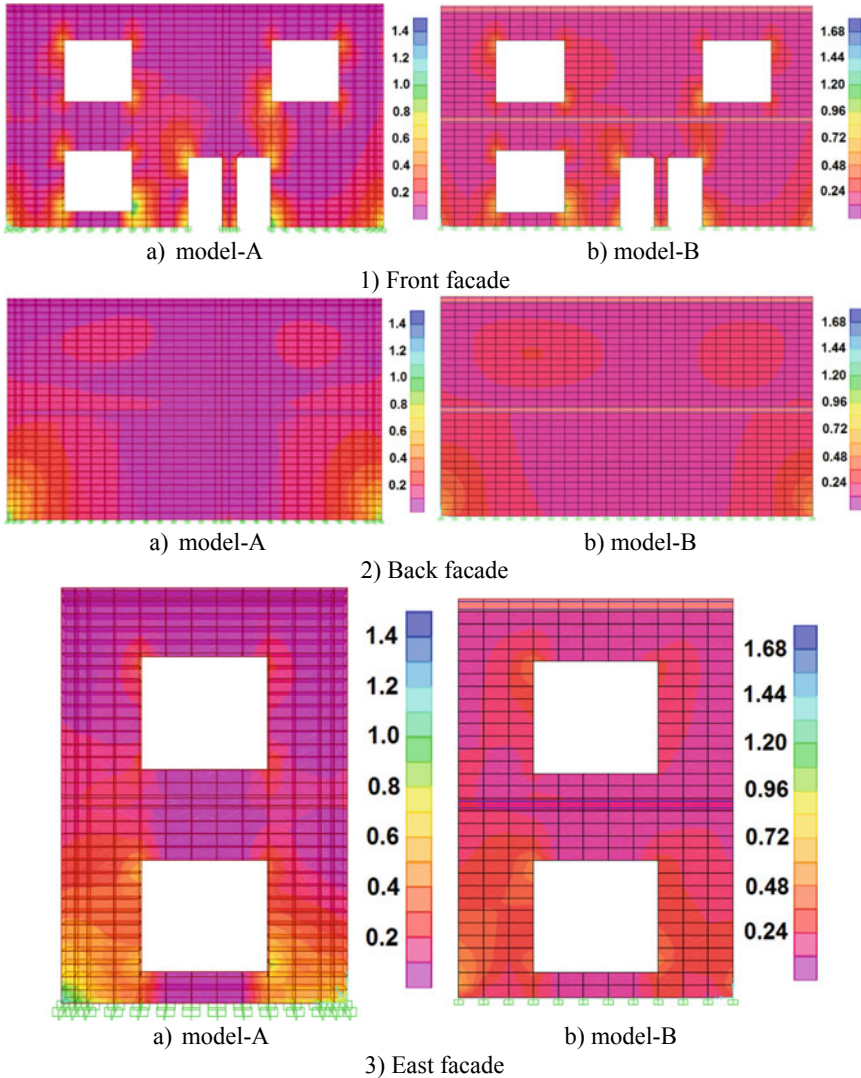
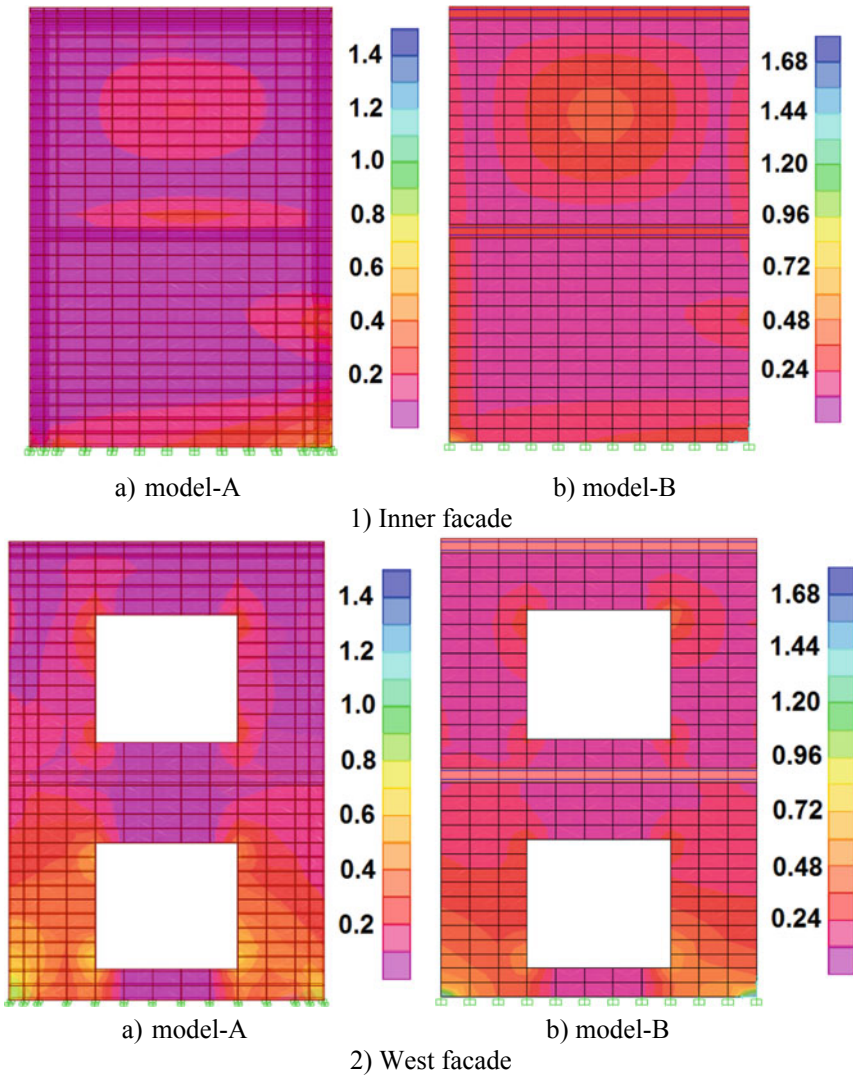


Fig. 7 Maximum stress distribution for (1) Front facade, (2) Back facade, (3) East facade in MPa. for **a** model-A and **b** Model-B, respectively

## 5 Conclusion

According to the numerical results, the following conclusions can be drawn:

- The obtained top storey time history displacements, time history base shear, and maximum stress results are very near each numerical model.



**Fig. 8** Maximum stress distribution for (1) Inner facade, (2) West facade in MPa. for **a** model-A and **b** Model-B, respectively

- On the other side natural periods for the first mode shapes were compared for both models, a slight difference was observed about 14.2%, but it is still small enough to influence the overall dynamic responses. Thus, it can be justified that this little difference is reasonable and natural periods are compatible for both numerical models.
- Overall, it can be concluded that shell elements can be employed for modeling masonry structures. Still, this simplified technique can give us more understanding

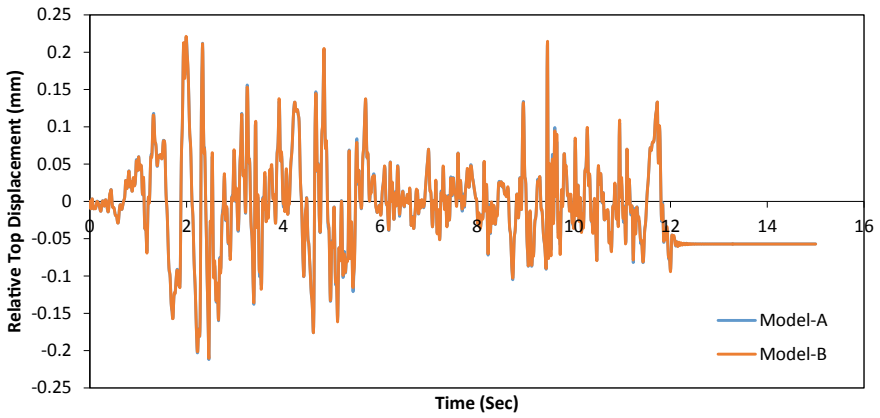


Fig. 9 Top story time history relative displacement for both model-A and model-B

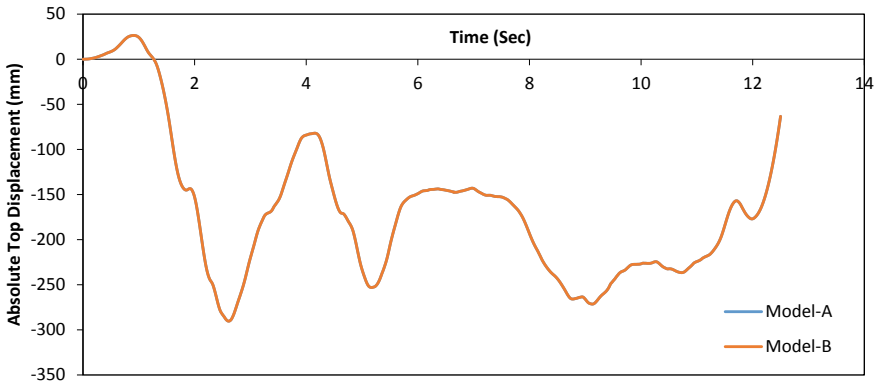


Fig. 10 Top story time history absolute displacement for both model-A and model-B

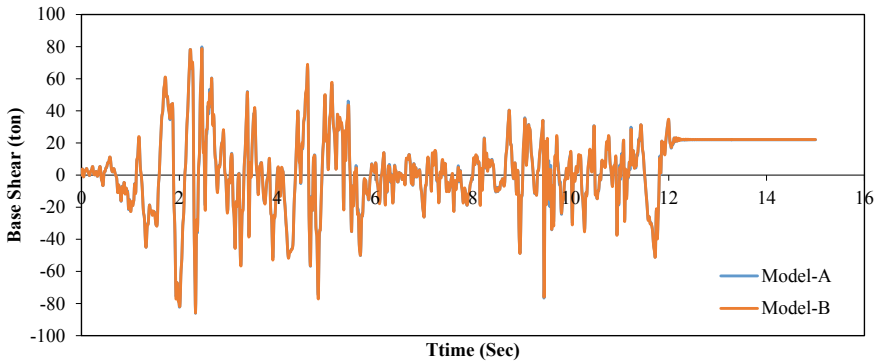


Fig. 11 Time history base shear in (tons) for both model-A and model-B

of the dynamic responses of these structures, and this method can be utilized for the design and assessment of masonry buildings.

## References

1. Karaton, M., Aksoy, H. S., Sayın, E., & Calayır, Y. (2017). Nonlinear seismic performance of a 12th century historical masonry bridge under different earthquake levels. *Engineering Failure Analysis*, 79, 408–421.
2. Karaton, M., & Çanakçı, K. (2020). Micro model analysis of JD6 and JD7 Eindhoven walls with fixed smeared crack model. *Journal of Structural Engineering*, 3(1), 18–24.
3. Giambanco, G., Rizzo, S., & Spallino, R. (2001). Numerical analysis of masonry structures via interface models. *Computer methods in applied mechanics and engineering*, 190(49–50), 6493–6511.
4. Chen, S. Y., Moon, F. L., & Yi, T. (2008). A macroelement for the nonlinear analysis of in-plane unreinforced masonry piers. *Engineering Structures*, 30(8), 2242–2252.
5. Xu, C., Xiangli, C., & Bin, L. (2012). Modeling of influence of heterogeneity on mechanical performance of unreinforced masonry shear walls. *Construction and Building Materials*, 26(1), 90–95.
6. Saeed, M. H., & Abbas, A. L. A. (2019). Simulation two storey house of masonry wall under the earthquake load. *Diyala Journal of Engineering Sciences*, 12(2), 1–12.
7. Lagomarsino, S., & Cattari, S. (2015). Seismic performance of historical masonry structures through pushover and nonlinear dynamic analyses. In *Perspectives on European earthquake engineering and seismology* (pp. 265–292). Springer.
8. Taucer, F., Spacone, E., & Filippou, F. C. (1991). *A fiber beam-column element for seismic response analysis of reinforced concrete structures* (Vol. 91). Earthquake Engineering Research Center, College of Engineering, University of California.
9. Magenes, G. (2006, September). Masonry building design in seismic areas: recent experiences and prospects from a European standpoint. In *First European conference on earthquake engineering and seismology*.
10. Karaton, M., & Awla, H. A. (2018). Numerical investigation of the effect on ultimate loading capacity of different longitudinal reinforcement ratios of a RC portal frame. *Journal of Structural Engineering*, 1(3), 147–154.
11. AWLA, H. A. (2019). Investigation of a reverse engineering method for determination of material properties of damaged or collapsed reinforced concrete building.
12. Peeters, M., Santo, G., Degroote, J., & Van Paeppegem, W. (2018). Comparison of shell and solid finite element models for the static certification tests of a 43 m wind turbine blade. *Energies*, 11(6), 1346.
13. Furtmüller, T., & Adam, C. (2011). Numerical modeling of the in-plane behavior of historical brick masonry walls. *Acta mechanica*, 221(1), 65–77.
14. Belmouden, Y., & Lestuzzi, P. (2009). An equivalent frame model for seismic analysis of masonry and reinforced concrete buildings. *Construction and building materials*, 23(1), 40–53.
15. Penna, A. (2015). Seismic assessment of existing and strengthened stone-masonry buildings: Critical issues and possible strategies. *Bulletin of Earthquake Engineering*, 13(4), 1051–1071.
16. Penna, A., Lagomarsino, S., & Galasco, A. (2014). A nonlinear macroelement model for the seismic analysis of masonry buildings. *Earthquake Engineering & Structural Dynamics*, 43(2), 159–179.
17. Lagomarsino, S., Penna, A., Galasco, A., & Cattari, S. (2013). TREMURI program: An equivalent frame model for the nonlinear seismic analysis of masonry buildings. *Engineering structures*, 56, 1787–1799.

18. Ferrito, T., Milosevic, J., & Bento, R. (2016). Seismic vulnerability assessment of a mixed masonry–RC building aggregate by linear and nonlinear analyses. *Bulletin of Earthquake Engineering*, 14(8), 2299–2327.
19. Erberik, M. A. (2008). Generation of fragility curves for Turkish masonry buildings considering in-plane failure modes. *Earthquake Engineering & Structural Dynamics*, 37(3), 387–405.
20. Tomazevic, M. (1999). *Earthquake-resistant design of masonry buildings* (Vol. 1). World Scientific.
21. SAP2000, C., CSI analysis reference manual for SAP2000. 2009, Computers and Structures, Inc.
22. Zhai, C. H., & Xie, L. L. (2007). A new approach of selecting real input ground motions for seismic design: The most unfavourable real seismic design ground motions. *Earthquake engineering & structural dynamics*, 36(8), 1009–1027.
23. Center, P.E.E.R. (2011). Users manual for the PEER ground motion database web application. *Pacific Earthquake Engineering Research Center*.
24. Ceroni, F., Sica, S., Pecce, M. R., & Garofano, A. (2014). Evaluation of the natural vibration frequencies of a historical masonry building accounting for SSI. *Soil Dynamics and Earthquake Engineering*, 64, 95–101.
25. Güllü, H., & Jaf, H. S. (2016). Full 3D nonlinear time history analysis of dynamic soil–structure interaction for a historical masonry arch bridge. *Environmental Earth Sciences*, 75(21), 1–17.
26. Awla, H. A., Taher, N. R., & Mawlood, Y. I. (2020). Effect of fixed-base and soil structure interaction on the dynamic responses of steel structures. *International Journal of Emerging Trends in Engineering Research*, 8(9).
27. Steinfeld, B., Scott, J., Vilander, G., Marx, L., Quirk, M., Lindberg, J., & Koerner, K. (2015). The role of lean process improvement in implementation of evidence-based practices in behavioral health care. *The Journal of Behavioral Health Services & Research*, 42(4), 504–518.
28. Hökelekli, E. & Al-Helwani, A. (2020). Effect of soil properties on the seismic damage assessment of historical masonry minaret–soil interaction systems. *The Structural Design of Tall and Special Buildings*, 29(2), e1694.
29. Awla, H. A., Taher, N. R., & Aksoy, S. H. (2021). Effect of SSI and fixed-base concept on the dynamic responses of Masonry Bridge structures, Dalal Bridge as a case study. *Academic Journal of Nawroz University (AJNU)*, 10(4).

# Stability and Seismic Performance of Tall Steel Structures with Hybrid Energy Absorbers Including P-Delta Effect



Rafaa M. Abbas and Ameer J. Abdulkareem

**Abstract** This paper presents a numerical study of the seismic response of seismically isolated buildings when using Hybrid Energy Absorbers at the base of high-rise buildings in terms of their ability to reduce the influence of ground excitation forces. Focus placed on the seismic response for the displacement, story drift, story shear, and acceleration to show such buildings' stability bearing into account second-order effect due to P-delta. The analysis has been performed using time-domain spectral matching to generate three different synthetic seismic time histories derived from real earthquakes compatible with the design response spectrum for different earthquake intensities. Three different types of base isolators were used; High Damping Rubber Bearing, Lead Rubber Bearing, and Friction Pendulum Bearing. The results showed that base isolation minimizes the effect of P-delta and, thus, reduces induced forces due to building sway. Also, a significant reduction in the seismic design forces such as story drift, shear, and acceleration was achieved. The study revealed that base isolation had improved such buildings' stability, especially when using high damping base isolators.

**Keywords** Stability · Base isolation · Time-domain method · Dynamic analysis · Synthetic earthquake · P-delta analysis · High-rise buildings

## 1 Introduction

The risk of earthquakes has always been a threat to high-rise buildings. Reducing damage caused by the dynamic loads effect is one of structural engineering's main concerns [1]. At present, various methods have been proven to improve the capacity of structures to withstand earthquake loads. Unlike other lateral forces, the effect of

---

R. M. Abbas (✉)

Department of Civil Engineering, University of Baghdad, Baghdad, Iraq

e-mail: [dr.rafaa@coeng.uobaghdad.edu.iq](mailto:dr.rafaa@coeng.uobaghdad.edu.iq)

A. J. Abdulkareem

Department of Civil Engineering, Al Muthanna University, Al-Samawah, Iraq

e-mail: [ameer.jabbar@mu.edu.iq](mailto:ameer.jabbar@mu.edu.iq)



an earthquake transfers from the base to the entire building, causing serious damage in most cases and can lead to the collapse of the building [2]. Many solutions and techniques have been developed to resist and minimize the impact of seismic forces. These technologies and solutions are represented by the use of different construction systems or by the addition of interstorey dampers between the floors, which reduce the displacement and dispersion of energy transmitted from the earthquake [3, 4]. Many techniques have been proposed over the years and proven to effectively reduce the impact of earthquakes and maintain the building integrity after ground shaking with minimal damage in Base isolation [5]. As a result of these lateral forces, horizontal displacement is generated for the entire building. This displacement creates additional forces called the second-order or P-delta effect, consisting of the building's weight acting through the horizontal displacement creating additional moments [6]. This displacement is evident in tall buildings and, therefore, increases with increasing height. The increasing building height and greater structural efficiency of high-rise buildings have led to smaller precautions of stiffness and, thus, stability. Checking the stability reduction has become an essential part of tall building analysis and design as recommended by ASCE/SEI 7–10 [7].

The P-Delta analysis considers the effects of many factors; building height is the most effective one [8]. It is well known that for linear and geometric nonlinear behavior of isolated buildings, it is most important to perform the dynamic analysis by using the direct integration for the time history of the excitation force, which achieves all considerations, including heights [9]. It is known that the response spectrum consists of the influence of several earthquakes or a single earthquake and different properties of the building. Moreover, the response spectrum varies respectively to soil characteristics and seismic activity [10]. This study will review the effect of P-Delta on the seismic performance of base-isolated tall buildings with different heights and study the effectiveness of base isolation on reducing the second-order effect. Moreover, special concern is devoted to study the stability of such tall buildings with hybrid energy absorbers under seismic loading, taking into account the second-order effect due to building drift and comparing the outcomes with the current international building standards specified limits on the drift and stability requirements.

## 2 Research Methodology

Five high-rise steel building structures with different heights and number of floors (10 to 30 stories) were modeled and analyzed numerically to achieve the proposed goals. The superstructure of the adopted base-isolated building models was represented by a 3-D finite element model using ETABS software. Three different hybrid energy absorber devices were employed in the building models at the foundation level to investigate base isolation effects. The dynamic analysis was performed using synthetic time history analysis. Finally, the dynamic response due to different earthquake intensities' influence was accounted for in this research by considering three

different seismic design categories with site soil class (D) as recommended by the ASCE7-10 [7].

### 3 Earthquake Excitation

Current design codes and specifications recommend time history analysis to estimate tall buildings’ dynamic response with base isolation science they can reflect the influence of the isolators in the analysis. Moreover, at the construction site, real-time history data might not be available, and applying time history records of earthquakes from other locations generally yields the response spectrum not compatible with the design spectrum. Therefore, using artificial time histories instead for the analysis is recommended [11]. In the current study, time-domain spectral matching was used to generate synthetic time series compatible with the design response spectrum at the construction site by modifying the N-S component of the 1940 El Centro earthquake. Accordingly, the adopted five-building models subjected to three seismic base excitation intensities adjusted from past real records will be analyzed. The adopted seismic design categories (SDC C, CDC D, and SDC E) simulate moderate, strong, and very strong ground excitations, respectively. Figure 1 shows the design “target” response spectrums, with the seismic coefficients compiled in Table 1. Also, the time records of the 1940 El Centro earthquake N-S component are shown in this figure. To adjust the time records shown in Fig. 1 to match the design spectrum, the initial time series frequency content is modified by using the spectral matching technique at all periods [12, 13]. The matching presented in Fig. 2 shows the generated time series characteristics, which revealed that reference time series characteristics had

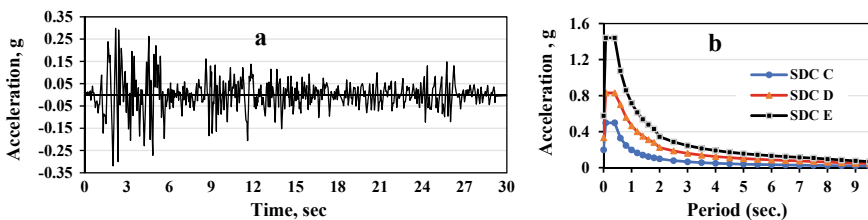


Fig. 1 a Initial time seires for the 1940 El Centro earthquake, b target response spectrums

Table 1 Seismic Coefficients for the design ‘target’ response spectrums

Site Class	SDC	F <sub>a</sub>	S <sub>S</sub>	S <sub>MS</sub>	S <sub>DS</sub>	F <sub>v</sub>	S <sub>1</sub>	S <sub>M1</sub>	S <sub>D1</sub>
D	C	1.36	0.55	0.748	0.4987	2.28	0.13	0.2964	0.1987
	D	1.004	1.24	1.2449	0.83	1.5	0.56	0.84	0.56
	E	1	2.16	2.16	1.44	1.5	0.86	1.29	0.86

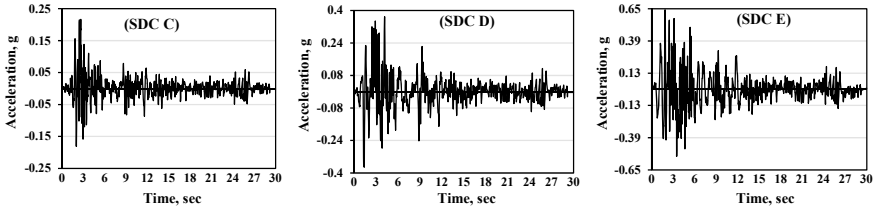


Fig. 2 Generated acceleration time histories matched to target SDCs

been kept, whereas frequency content for the initial time series adjusted for each targeted seismic design intensity.

### 4 Stability Index

According to American Society of Civil Engineers, ASCE/SEI 7–10 [7], the stability requirement of tall buildings needs to be evaluated through the stability coefficient or index ( $\theta$ ) by the following equation

$$\theta = \frac{P_x \Delta I_e}{V_x h_{sx} C_d} \tag{1}$$

where

$P_x$  = the sum of the total vertical load at that level; when computing  $P_x$ , the load factor must be taken equal 1.0.

$\Delta$  = story drift computed as the difference of the deflections at the centers of floors above and below that story.

$I_e$  = the importance factor.

$V_x$  = the seismic shear force is acting between that levels and below.

$h_{sx}$  = the story height below that level.

$C_d$  = Deflection amplification factor.

ASCE/SEI 7–10 recommends that when the stability coefficient ( $\theta$ ) is equal to or less than (0.10) the increase in the member forces and the story drifts due to P-delta effect can be neglected. Moreover, the stability coefficient ( $\theta$ ) must not exceed  $\theta_{max}$  determined as follows:

$$\theta_{max} = \frac{0.5}{\beta C_d} \leq 0.25 \tag{2}$$

where ( $\beta$ ), is the ratio of shear demand to shear capacity for that story and for the one below. Generally, ( $\beta$ ) is taken equal (1.0), as permitted by ASCE/SEI 7–10. The increments in the drift and member forces due to P-Delta effects shall be determined

by any accepted method of analysis, otherwise, it is allowed to amplify displacements and member forces values by the factor  $[1.0 / (1 - \theta)]$ . Finally, where the stability index is more significant than  $(\theta_{max})$ , the structure is considered unstable.

### 5 Building Models

Five multistory steel structures were modeled using ETABS V19.0.2 software ranging from 10 floors up to 30 floors with total heights equal 35, 52.5, 70, 87.5, and 105 m for five stories increment. The plan of the building, Fig. 3, consisted of five bays in each direction with 25 m in the x and y directions. Building models were analyzed using the fixed base for the first; after that, analyses were performed for the same models with various hybrid energy absorbers. Three types of hybrid energy absorber devices usually used for base isolation [14]; High Damping Rubber Bearing (HDRB), Lead Rubber Bearing (LRB), and Friction Pendulum Bearing (FPB) were adopted in the analyses. The building frames consisted of steel columns using HP sections; the main steel beams were all W sections, whereas W and HSS sections were used for the secondary beams and cross-bracing, respectively. Section details for the building members used are compiled in Table 2.

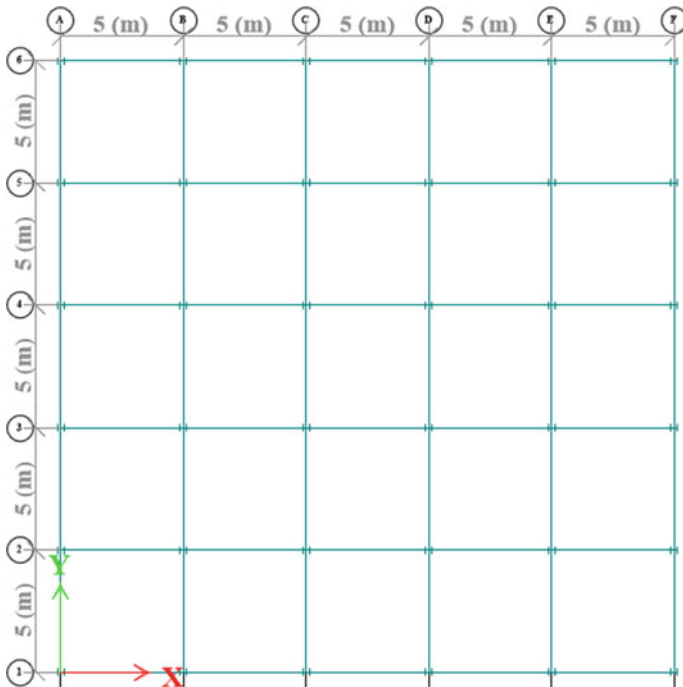


Fig. 3 Plan details for building models

**Table 2** Structural section details for building models

Building	No of floors	Height(m)	Main beams	Secondary beams	Columns	Bracing
B (10)	10	35	W14X22	W10X12	HP10X57	HSS6X6X1/2
B (15)	15	52.5	W16X26	W10X12	HP12X63	HSS6X6X1/2
B (20)	20	70	W16X26	W10X12	HP14X73	HSS6X6X1/2
B (25)	25	87.5	W16X36	W10X12	HP16X121	HSS8X8X3/8
B (30)	30	105	W18X35	W10X12	HP16X183	HSS8X8X1/2

## 6 Analyses Results

To demonstrate the seismic performance and stability, the seismic response results of the adopted tall building models with the various hybrid energy absorbers due to selected matched seismic time histories will be firstly presented and discussed for the 20-storey building (B 20), and SDC D. After that, results for all building heights starting from 10 floors up to 30 floors and for the various seismic design categories and base isolator types will be presented and discussed thoroughly. Science reducing the induced accelerations in the building floor masses as a result of an earthquake ground excitation is the major task of base isolators. Figure 4 shows the effectiveness of base isolation in reducing top story acceleration generated within the building. Acceleration results presented for the 20 story (B 20) building with HDRB isolators and SDC D. Table 3 summarizes the variations in the maximum top story acceleration due to P-Delta analysis of different building models and SDC categories. It can be noted that a maximum reduction of about 3.6% in the top story acceleration is achieved for isolated buildings when using HDRB isolators. This indicated that P-delta effect helps at reducing building’s acceleration.

Figure 5 presents comparison for the seismic response for the linear and nonlinear (P-delta) analysis considering displacement, drift ratio, and story shear values for B 20 building and for seismic design category SDC D. The result for building sway or displacement reveals that displacement values increased as building height increased. The other important criterion is the drift, where base isolation worked to reduce drift

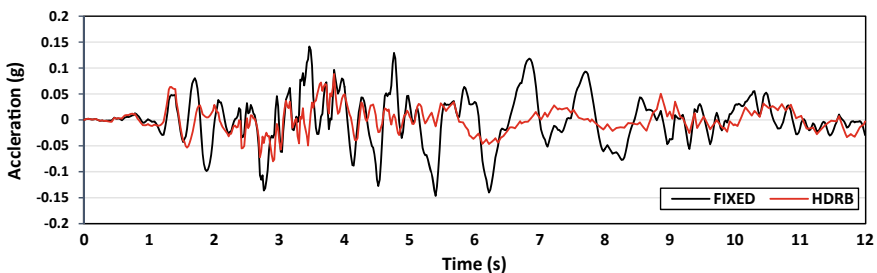


**Fig. 4** Comparison of top story acceleration for the 20-storey building with HDRB isolators

**Table 3** Variation in the maximum top story acceleration due to P-delta effect

Building	SDC C				SDC D				SDC E			
	Fixed	FPB	LRB	HDRB	Fixed	FPB	LRB	HDRB	Fixed	FPB	LRB	HDRB
B (10)	3.5	8.4	-0.8	-0.8	-1.6	6.8	-0.9	-2.7	0.7	7.0	-3.1	-2.2
B (15)	-0.8	9.5	-0.2	-0.2	-3.9	9.9	0.2	-2.1	0.9	10.2	-0.3	1.4
B (20)	-6.9	4.6	-2.0	-2.0	4.6	3.9	-2.5	-3.6	-4.2	3.1	-2.3	1.5
B (25)	-9.2	8.2	1.0	1.0	-5.2	6.8	1.2	-2.3	0.3	5.4	1.4	0.7
B (30)	-1.1	0.2	0.7	0.7	-0.8	2.3	-1.1	-0.3	1.1	1.2	1.2	-0.7

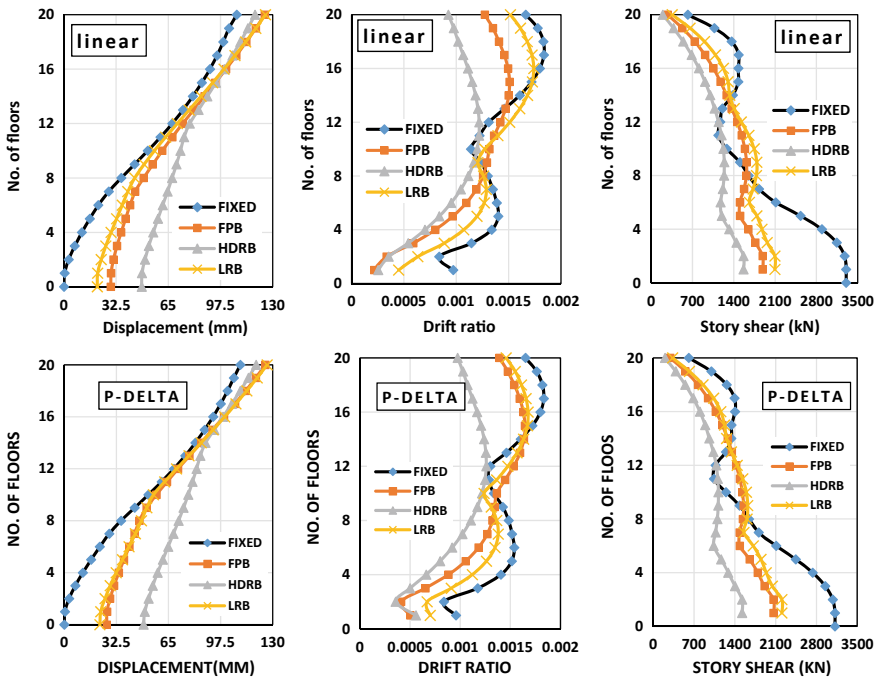


**Fig. 5** Linear and nonlinear seismic response for the 20-storey building (B 20) and SDC D

compared with fixed base. Although drift values were obtained for the fixed base is within the permissible limits according to the ASCE limitations, the base isolation reduces the drift values significantly. As for the decrease in the maximum story drift and shear values, the best performance was due to the HDRB isolator.

The displacement response of the isolated buildings directly increases with both the height of the building and the increase in the seismic intensity. Table 4 illustrates the percentage variations in the maximum displacement due to the P-delta effect. Generally, variation range was -3.48% to +4%, -2.21% to +3.73%, and -0.6% to +5.63% for FPB, LRB, and HDRB isolators, respectively and different SDCs.

**Table 4** Percentage (%) variation in the maximum displacement due to P-DELTA effects

Building	SDC C					SDC D					SDC E					
	Fixed	FPB	LRB	HDRB	Fixed	FPB	LRB	HDRB	Fixed	FPB	LRB	HDRB	Fixed	FPB	LRB	HDRB
B (10)	1.89	-3.37	1.63	1.67	0.69	-2.99	2.66	2.64	4.18	4.00	1.16	0.36	4.18	4.00	1.16	0.36
B (15)	2.48	-3.48	2.62	2.90	4.20	0.75	2.66	0.87	3.74	2.04	-0.10	-0.60	3.74	2.04	-0.10	-0.60
B (20)	3.17	1.96	3.73	3.75	2.08	0.28	0.81	0.50	4.02	-0.71	-2.21	-1.44	4.02	-0.71	-2.21	-1.44
B (25)	3.11	2.33	3.30	3.43	0.54	0.03	-0.17	0.77	-2.64	-0.74	3.07	-0.12	-2.64	-0.74	3.07	-0.12
B (30)	3.16	2.35	3.45	5.63	-0.49	-0.64	-0.08	2.83	3.17	-1.26	1.48	0.06	3.17	-1.26	1.48	0.06

The percentage variation presented in Table 4 is mainly due to the interaction of the dynamic properties for the building's structure, base isolators, and the SDCs response spectrum frequencies.

The drift ratio depends on the amount of lateral displacement in the superstructure. Results show that the drift ratios have decreased with the use of isolators at the structure base as inter-story displacements have decreased. Table 5 shows the effect of P-delta on the variations in the maximum story drift ratios. Generally, percentage variations of about  $-5.85\%$  to  $+9.08\%$ ,  $-6.78\%$  to  $+8.38\%$ , and  $-9.6\%$  to  $+7.21\%$  in the drift ratios due to the P-delta effect is noted for FPB, LRB, and HDRB isolators, respectively. As for displacements, the trend for drift ratio variation is attributed to the building's interaction, base isolators, and dynamic excitation characteristics.

The horizontal forces generated at each floor level during an earthquake are transmitted from the ground to the building. The isolators reduce the share of these forces due to increasing 'extending' of building's period. Results for percentage values compiled in Table 6 indicated that the maximum story shear values reduced due to the P-delta effect. Generally, a reduction percentage of about  $6.08\%$ ,  $3.95\%$ , and  $9.88\%$  in the maximum story shear values due to the P-delta effect is noted for FPB, LRB, and HDRB isolators, respectively. To summarize the isolators capability to improve the seismic performance of tall buildings, Fig. 6 showed the percentage variation of displacement, drift, story shear, and acceleration values when buildings analyzed for SDC D earthquake excitation. It is noted that HDRB isolators have provided the best performance regarding reducing the dynamic response. Significant reduction in the drift, story shear, and story acceleration values achieved when using hybrid energy absorbers. It is noted that isolators' ability to reduce drift, story shear, and acceleration values is inversely proportional to the increase in the building height.

The main criterion that summarizes all of the above and describes the effect P-Delta is the building stability index. The ASCE 7-10 stability index " $\theta$ ", determined that the P-delta effect could be neglected if the  $\theta$  index's value does not exceed 0.1. Figure 7 shows  $\theta$  values for each floor of the 20-storey building B (20). Emphasis is focused on the results due to HDRB base isolation as it has proved to the most efficient to enhance dynamic response. Results presented showed a significant reduction in the stability index as a result of using base isolation. This result demonstrates that tall buildings' stability is more secured when Hybrid Energy Absorbers are employed to safeguard buildings against earthquakes.

Figure 8 shows the effectiveness of each type of base isolation on the stability index. From the comparison presented in the figure it is clear that the HDRB bearing has superior properties to enhance building stability and thus reduces the amount of  $\theta$  index and assures the building greatest stability. Finally, from the case study presented, almost all isolators had worked to enhance building stability. Therefore, it can be concluded that base isolation helps to minimize the second-order effect due to P-Delta and, thus, reduces the additional forces due to building sway under seismic excitation.



**Table 5** Variation in the maximum story drifts ratios due to P-delta effects

Building	SDC C					SDC D					SDC E					
	Fixed	FPB	LRB	HDRB	Fixed	FPB	LRB	HDRB	Fixed	FPB	LRB	HDRB	Fixed	FPB	LRB	HDRB
B (10)	3.11	-5.85	-0.45	3.86	-0.05	5.88	3.88	3.69	4.40	2.78	-0.37	0.93	4.40	2.78	-0.37	0.93
B (15)	3.08	4.33	2.34	1.32	-4.10	6.96	8.32	0.10	4.85	2.49	0.30	1.79	4.85	2.49	0.30	1.79
B (20)	3.25	1.59	2.38	-9.60	-0.16	9.08	-3.62	3.36	5.64	1.52	1.98	1.50	5.64	1.52	1.98	1.50
B (25)	-5.52	6.71	-4.40	5.60	8.86	1.71	2.27	-2.21	0.62	0.65	-0.44	0.40	0.62	0.65	-0.44	0.40
B (30)	-6.61	-2.34	-6.78	0.62	-2.22	-1.52	0.80	7.21	3.22	-0.75	-0.89	-0.68	3.22	-0.75	-0.89	-0.68

**Table 6** Percentage (%) reduction in the maximum story shear due to P-DELTA effect

Building	SDC C				SDC D				SDC E			
	Fixed	FPB	LRB	HDRB	Fixed	FPB	LRB	HDRB	Fixed	FPB	LRB	HDRB
B (10)	0.40	1.48	1.68	2.47	4.19	2.52	0.32	1.85	1.15	3.28	0.52	2.64
B (15)	3.60	6.08	2.77	3.24	3.06	1.29	3.67	6.17	2.24	5.26	1.3	5.25
B (20)	3.97	2.86	2.12	5.21	6.75	5.14	2.22	2.61	1.00	4.47	0.7	5.33
B (25)	5.60	3.89	3.95	4.49	5.06	3.79	1.98	5.22	3.69	1.55	2.68	6.06
B (30)	2.19	2.52	2.75	5.07	4.27	0.47	2.40	9.88	1.19	4.79	1.1	0.45

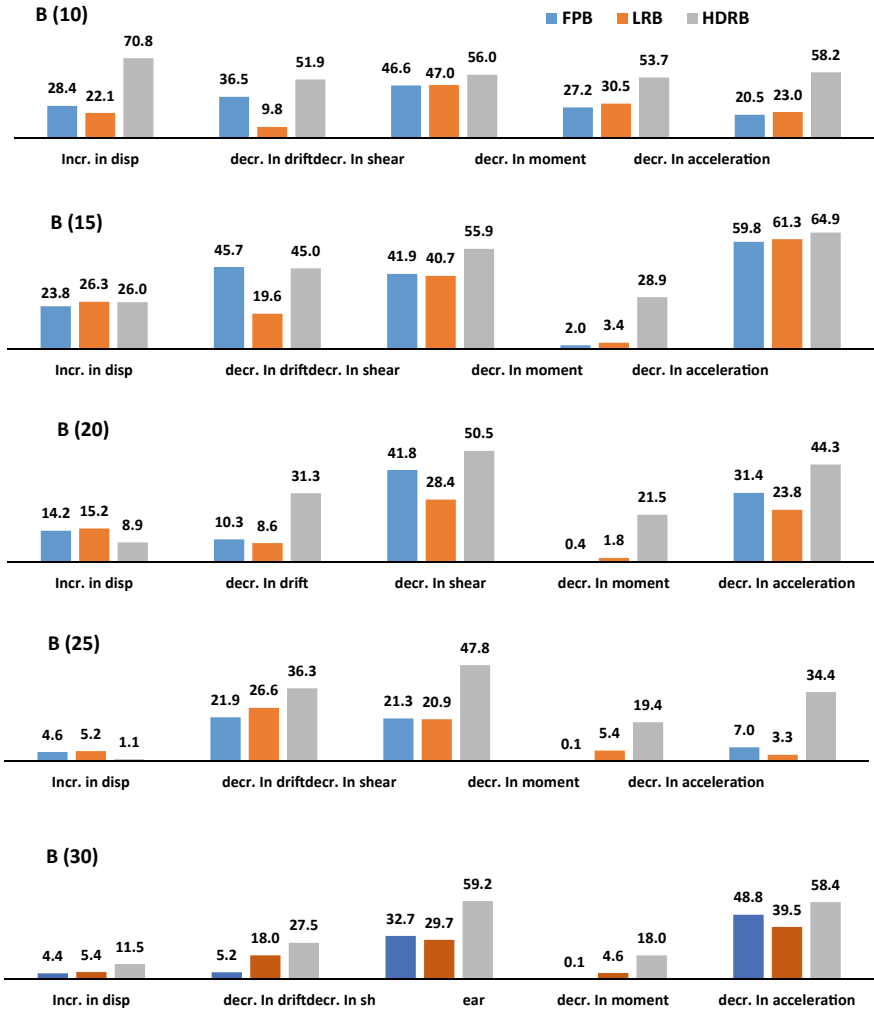


**Fig. 6** Percentage variations in seismic response due to base isolation for SDC D

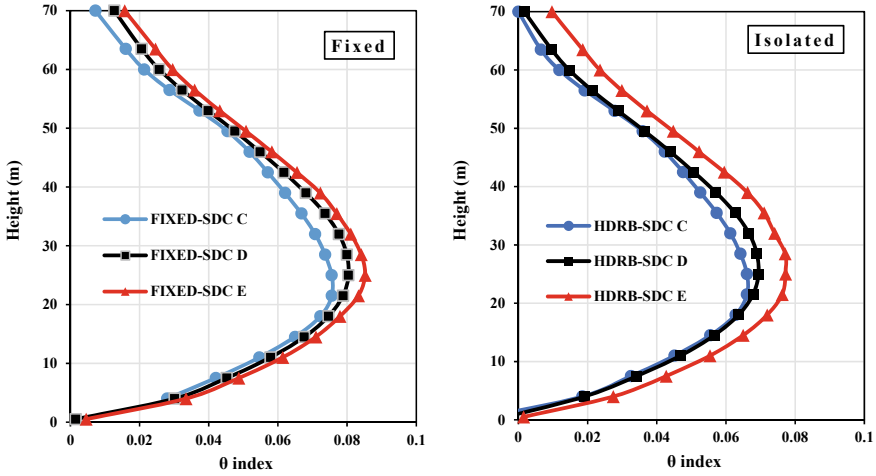


Fig. 7 Stability index ( $\theta$ ) for 20 story building (B20)

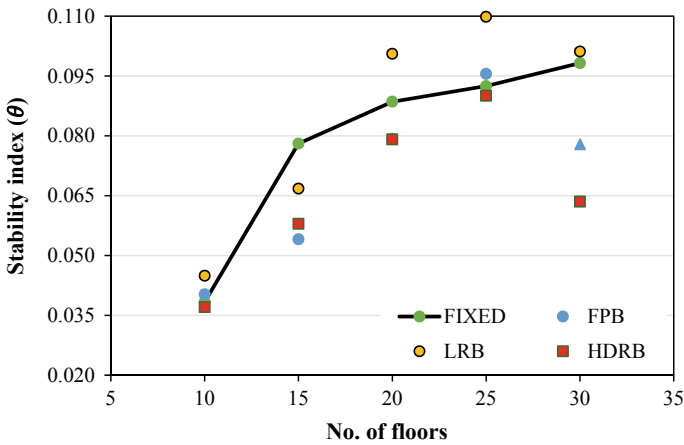


Fig. 8 Stability index ( $\theta$ ) for the fixed and base-isolated buildings

## 7 Conclusions

Based on the numerical simulation and parameters considered the following conclusions can be drawn:

- The synthetic time history method helps at reducing the efforts needed by researchers as it gives a time history with response spectrum compatible with the seismic response spectrum of the specified location.

- Significant reduction in the story drift ratios, story shear, and acceleration values achieved when using hybrid energy absorbers.
- The different performance of the base isolation according to the type of isolation device has its unique characteristics. The best performance is due HDRB isolator regarding decrease in the story drift and shear. On the other hand, the minor displacement occurred when using LRB and FPB isolators.
- Maximum reduction in the story acceleration values is about 3.6% due to HDRB isolator when accounting for P-Delta effect. This indicated that P-Delta effect helps at reducing building's acceleration.
- The study indicated the effectiveness of the different base isolation systems to improve building's stability with the best performance is due HDRB isolator to assure the building greatest stability.
- Base isolation minimize the second-order effect due to P-Delta and reduces the additional forces due to gravity loads acting on the laterally displaced building.
- The ability of isolators to reduce drift, story shear, and acceleration values is inversely proportional to the building height increase.

**Acknowledgements** The authors wish to thank the Department of Civil Engineering at the University of Baghdad for their valuable support to complete this work. The authors gratefully acknowledge the support received from the head and the staff of the Department.

## References

1. Guo, W., Zhai, Z., Cui, Y., Yu, Z., & Wu, X. (2019). Seismic performance assessment of low-rise precast wall panel structure with bolt connections. *Engineering Structures*, 181, 562–578.
2. Yuen, Y. P., & Kuang, J. S. (2015). Nonlinear seismic responses and lateral force transfer mechanisms of RC frames with different infill configurations. *Engineering Structures*, 91, 125–140.
3. Radmehr, M. & Homami, P. (2020). The seismic reliability analysis of moment resisting frames with bolted end-plate connection. *Journal of Constructional Steel Research*, 171, 106134.
4. Abdulkareem, A., & Abbas, R. (2020). Geometric nonlinear time domain spectral matching seismic analysis of base isolated high rise buildings including P-delta effect. *Journal of Engineering Science and Technology*, 15(5), 3104–3121.
5. Lin, Y. S., Chan, R. W., & Tagawa, H. (2020). Earthquake early warning-enabled smart base isolation system. *Automation in Construction*, 115, 103203.
6. Abbas, R. M., & Abdulhameed, R. A. (2018). Effects of P-delta and concrete cracking on modal analysis for the seismic response of high rise reinforced concrete buildings. *International Journal of Science and Research (IJSR)*, 7(1), 363–371.
7. ASCE. (2013). Minimum design loads for buildings and other structures. *American Society of Civil Engineers*.
8. Abbas, R. M., & Abdulhameed, R. A. (2019). Frequency domain analysis for geometric nonlinear seismic response of tall reinforced concrete buildings. *Journal of Engineering*, 25(3), 102–116.
9. Andrade, P., Santos, J., & Escórcio, P. (2020). Direct Integration Methods versus Modal Superposition Method, on Predicting Staircases Vibrations. *Procedia Structural Integrity*, 28, 279–286.

10. Abbas, R. M., & Abdulkareem, A. J. (2021). Geometric nonlinear synthetic earthquake analysis of base isolated tall steel buildings under site-specific seismic loading. In *Modern Applications of Geotechnical Engineering and Construction* (pp. 349–364). Springer, Singapore.
11. Reyes, J. C., Riaño, A. C., Kalkan, E., Quintero, O. A., & Arango, C. M. (2014). Assessment of spectrum matching procedure for nonlinear analysis of symmetric-and asymmetric-plan buildings. *Engineering Structures*, 72, 171–181.
12. Lilhanand, K., & Tseng, W. S. (1987). Generation of synthetic time histories compatible with multiple-damping design response spectra. In *Transactions of the 9th international conference on structural mechanics in reactor technology*. Vol. K1.
13. Al Atik, L., & Abrahamson, N. (2010). An improved method for nonstationary spectral matching. *Earthquake Spectra*, 26(3), 601–617.
14. DOSHIN, Rubber Engineering. (2020). High damping rubber bearing. *Technical Information*. <https://doshinrubber.com/>

# Estimations the Combined Flexural-Torsional Strength for Prestressed Concrete Beams Using Artificial Neural Networks



Hend S. Zayan and Akram S. Mahmoud

**Abstract** When considering modern concrete structures, the significant role of torsional behavior is recognized in engineers' design considerations. In this paper, the practical efficiency of dissimilar Artificial Neural Networks ANNs in predicting the combined torsional strength of prestressed concrete beams is evaluated. The experimental data database on 345 rectangular pre-tensioned prestressed concrete (PC) and reinforced concrete (RC) beams often published in research literature had been used to establish an ANN model. The input parameters affecting torsional strength selected were moment, shear, distance, height, prestressed reinforcing steel strength, eccentricity, transverse steel ratio, longitudinal steel ratio, rupture strength, yielding conventional steel tension, and compressive strength of concrete. Each specification parameter was grouped into a neural network and the combined torsional strength of the prestressed concrete beam. The ANN models are designed and validated for any production and assessed across several layers of negative feedback. This study indicates that artificial neural networks have been reasonable correlated predictions of the ultimate torsional strength of prestressed concrete beams, about 92%. The analysis concluded that an ANN model measured the combined torsional strength by considering the importance factor.

**Keywords** Generalized regression · Neural network · Prestressed · Reinforced concrete · Torsion

## 1 Introduction

In civil engineering practice, space frame members or buildings, horizontally curved beams, beams that have loadings, edge beams eccentrically, and spiral concrete staircases are typical examples of structural elements exposed to predominant torsional

---

H. S. Zayan (✉) · A. S. Mahmoud  
Civil Engineering Department, Engineering College, University of Anbar, Ramadi, Iraq  
e-mail: [hind.saad@uoanbar.edu.iq](mailto:hind.saad@uoanbar.edu.iq)

A. S. Mahmoud  
e-mail: [dr.akramsh1@uoanbar.edu.iq](mailto:dr.akramsh1@uoanbar.edu.iq)

torques. However, torsional effects cannot be neglected in the design of such PC or RC members. Torsion is formed when a member transfers an internal force that does not act through its shear flow center. Hence, special care must be taken for the structural systems governed by equilibrium torsion to prevent disastrous failures. For many years, torsion in prestressed and reinforced concrete structures was regarded as a secondary effect and was not considered explicitly in design. The torsion design has received increasingly greater importance after the 1960s. The torsion provisions in the ACI Building Code ACI 318–89 were proposed in a series of papers by ACI Committee 438 in 1968 and 1969 and included for the first time in the 1971 code edition [1].

On the other hand, the British standards had recommendations for torsion design for the first time in 1972 [2]. Design codes are usually based on two main approaches, the space truss comparison, and the skew bending principle. Recent amendments introduced with the American concrete institute building code (the International Building Code (IBC) and the International Fire Code (IFC),) substituted the construction approach employed before based on a thin-walled tube truss comparison [3–5]. Neural networks refer to a series of algorithms that simulate a human brain's operations to recognize relationships between large amounts of data. The neural network will extend to different scenarios by hand-crafting the best possible performance based on what it has experienced in the past.

Many studies use the “torsional strength” of concrete beams. A researcher Huang [6], in 2012, found the capabilities of the genetic algorithm for predicting the torsional strength of reinforced concrete beams. Other than that, Huang used a Hybrid Neural Network to estimate the pure torsion strength of conventional reinforced concrete beams. Mohammed [7] implemented a neural network to construct a model that predicts the strength of ordinary reinforced concrete beams. However, thinking the torsional diameter of reinforced concrete beams diminished by utilizing fibrous reinforced plastics (FRP) as reinforcement, Naderpour and Fakharian [8] in 2018 investigated the degree of strengthening. Mahmood, in 2015 [9] established a new ANNs model to predicted the torsional strength of prestressed concrete beams and presented a parametric study on many prestressing force configurations. This paper aims to investigate the essential factors that affect the torsional behavior of pre-tensioned PC beams subjected to combined flexural and torsional loadings. The experimental data were collected from many works of literature for 345 tested specimens. These specimens were tested under various conditions such as pure torsion, bending with torsion, and bending-shear with torsional torque for prestressed concrete beams.

## 2 Generalized Regression Neural Network (GRNN)

Generalized Regression Neural Network GRNN is a probabilistic classical model established via the researcher Specht [10]. A network's complicated network structure makes it efficient at identifying patterns. The highly nonlinear mapping, simple network architecture, high fault tolerance, and robustness make nonlinear solutions

more efficient. The network depends on a maximum likelihood approach to regress. This mechanism is similar to a neural network. Bayesian networks are classified as a Bayesian network. The Bayesian approach estimates the probability of specific target values and uses that knowledge to correct the error. Bayesian networks have been used to evaluate the optimum configuration or causal relationships of variables as a form of optimization. However, other types of neuronal networks are more vulnerable to minimal local problems and over-fit-out training outcomes, using different algorithms to map intermediate/output parameters in which target values are achieved by random optimization process of weights [11]. The following possibility from GRNN analyzed model to provide the aim magnitudes is given in Eq. 1 [12, 13].

$$P(\mathcal{H}_i/D) = \frac{p(D/\mathcal{H}_i) P(\mathcal{H}_i)}{p(D)} \tag{1}$$

where, (D): represents the dataset’s object, ( $\mathcal{H}_i$ ): the independent network model. These networks are also used for analysis because they effectively solve linear problems when the linear interpolations are not reached good results. The big benefit of this approach is that the two separate models can be contrasted, ensuring that the contrast helps to be more accurate [14]. Torsional Strength of Prestressed Concrete Beams. Characteristics of Prestressed concrete beams are essentially similar to the plain concrete beams unless additional torsional reinforcement is provided. It is well known that subjecting the concrete members to axial prestress results in a substantial increase in their torsional capacities. However, axial prestress force alone will not add any post-cracking ductility index of the member. There is a state of triaxle stresses in prestressed concrete members subjected to torsion [15, 16]. Cracking occurs when the combined stress produced by the torsional shear and prestress exceeds the concrete strength as defined by an appropriate failure criterion, where ( $T_n$ ) shall be determined the lesser value get from Eqs. 2 or 3 [4, 17].

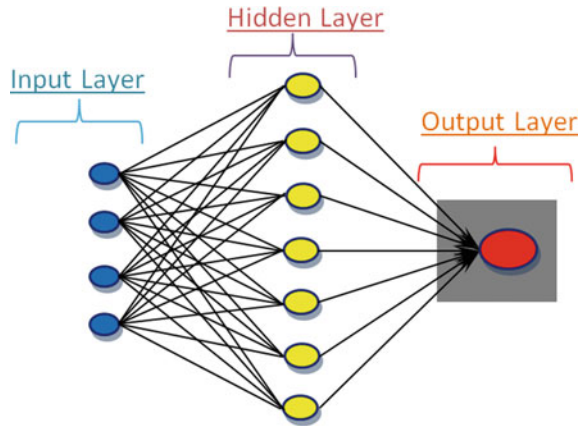
$$T_n = \frac{2A_oA_t f_{yt}}{S} \times \cot \theta \tag{2}$$

$$T_n = \frac{2A_oA_\ell f_{yt}}{P_h} \times \tan \theta \tag{3}$$

where  $A_o$  is the gross area enclosed by torsional shear flow path,  $\theta$  angle between the axis of the strut, and the tension chord of the member it shall not be taken less than 30 degrees nor greater than 60 degrees;  $A_t$  is the area of one leg of a closed stirrup resisting torsion;  $A_\ell$  is the area of longitudinal torsional reinforcement;  $s$  is the center-to-center spacing of transverse reinforcement, and  $p_h$  is the perimeter of the centreline of the outermost closed stirrup. Tests on prestressed concrete members in pure and combined torsion with bending and shear force were first carried out by many researchers [18–31], where some researchers are tested for



**Fig. 1** Structure of the Three-Layered Feed-Forward System



normal concrete specimens and others for high strength concrete prestressed rectangular beams with a concentric prestressing force. The prestressed members are observed their it has been established that the member was increased significantly when subjected to axial compression. Moreover, it has been found that the direction of the failure cracks depended on the level of prestressing. Background of Artificial Neural Network (ANN) Modelling. Multi-layers of neural network with a forwarding feeding model are always extensively applied to well-organized detail competencies [32, 33]. Figure 1 illustrates the characteristic of multi-layer neural networks with feed-forward modeling.

This neural network contains feedback input data, a structure of a hidden layer (s) or more, and a layer of output results. These layers, the so-called nodes or neurons, are exclusively connected by arrows and encompass various processing units. Input parameters called weights indicate the strength of synaptic connections. Each neuron has a visibility that is a function of the amount of influences input obtained through interconnected neurons from other neurons [34, 35]. The optimal number of layers and the number of neurons in each hidden layer. To pick an appropriate number of nodes in the hidden layer of neurons in the hidden layers, a trial and error should then be worked out [36, 37]. Backpropagation is the most efficient algorithm and is employed in this study. The production emerges from the hidden neurons and flows out to the results of findings. The network in the first hidden layer is linked to every neuron, and each network output is connected to every neuron. In this scenario, the complete relation will be called artificial neural networks ANNs. Initially, the weight values were set to random variables and the current network parameter settings. The neuron's output is calculated using Eq. 4:

$$O_i = F \left( \sum_j I_j \times W_{ij} + b_i \right) \quad (4)$$

where  $F$  represents the stimulation function of the neurons,  $W_{ij}$  represents the weight of the neuron in the simulation process,  $O_i$  represents the output of the neuron,  $I_j$  represent the neurons input networks, and  $b_i$ : represents the bias of each neuron. The function of activation is the component of the neural network where the computation is carried out absolutely. The activation function of the parameter’s maps represents input dominion to the output region (finite). Unlike most other functions in which most use phase means, most map their output to be either in the interval  $[0, 1]$  or the interval  $[-1, 1]$ . Throughout the years, there have been multiple ways of activation functions. Over the past five years, the majority of users have focused on the public activation feature as flows [38–43]: (a) linearity of activation function; (b) step of activation function; (c) activation function ramp; (d) sigmoid activation function; and (e) Gaussian activation function. The network error is then promulgated back to the input layer, where the link weights are changed from the output layer. This method is replicated till the error is reduced to the [21, 32, 33, 44–46] choice standard. The performance error may be described as a Mean Squared Error (MSE) and is measured using Eq. 5:


$$MSE = \frac{1}{nm} \sum_{i=1}^n \sum_{j=1}^m (t_{ij} - y_{ij})^2 \tag{5}$$

where  $y$  represents the prediction process’s output value, and  $t$  represents the target magnitude. ANNs Model and its results. Table 1 illustrated the parameters collected in

**Table 1** Parameter estimates for ANNs model

		Hidden layer 1	Output layer
		H(1:1)	
Input layer	(Bias)	1.792	Torsional Torque
	fypre	0.132	
	fy	-0.582	
	fr	-0.154	
	fc	-0.142	
	lstr	-0.409	
	str	-0.209	
	e	-0.007	
	pre	-1.016	
	h	-1.346	
	W	-0.727	
	sh	0.079	
M	0.513		
Hidden layer 1	(Bias)		0.054
	H(1:1)		-1.804

**Table 2** Independent variable importance

Symbol	Importance	Normalized importance (%)	Importance index	
h	0.214	100.0	High	
pre	0.17	79.7		
w	0.152	71.3		
fy	0.125	58.5		
M	0.096	45.1		
lstr	0.086	40.3		
str	0.045	21.2		
fr	0.033	15.6		
fc	0.031	14.4		
fypre	0.028	13.3		
sh	0.017	7.9		
e	0.002	0.8		Low

the ANNs model and issued the output layer of the tested specimen’s torsional torque. One hidden layer has been used because it does not need the high resolution in these parameters [42, 47]. Normalized has been chosen in variables. In partition, 20% has been chosen for testing and 80% for training. For Architecture, a hyperbolic tangent has been chosen for the hidden layer and the output layer in the activation function with adjusted normalized correction (0.05). Batch has been chosen in training and includes in the option. The most important result is the last Figure showing the model’s skeleton and Table 2 that shows the parameter weights given as input in Eq. 6:

$$y = \frac{1}{1 + e^{-\theta_2 + w_y \tanh(x)}} \tag{6}$$

where y: is the output target,  $\theta_2$ : the basis of the output layer,  $w_y$ : is the weight (H1:1) of output parameter (i.e., torsional strength), the value of (x) can be obtained from Eq. 7, it depended on the weights and their magnitudes of studied parameters:

$$x = \theta_1 + \sum_n^{i=1} w_i v_i \tag{7}$$

Also, the factors were studied in this model are M: bending moment (kN m), sh: shear force (kN), W: cross-section width (mm), h: height of cross-section (mm), pre: initial prestressed force (kN), e: eccentricity of steel strand (mm), str: steel reinforcement ratio, lstr: longitudinal steel reinforcement ratio, fr: modulus of rupture (MPa), fy: yielding congenital steel stress (MPa), fibre: yielding prestressing steel

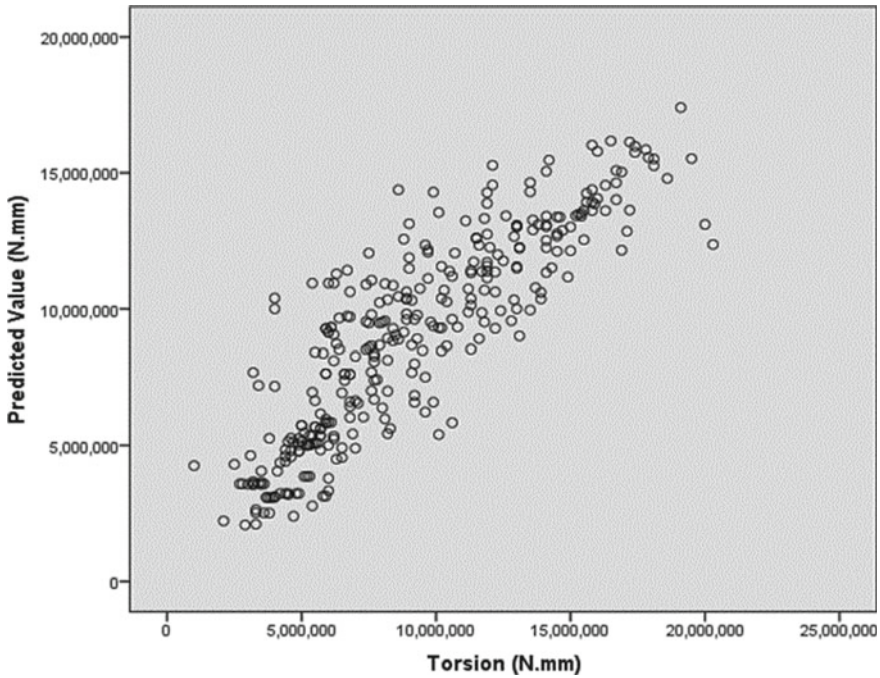


Fig. 2 Experimental data versus predicted results of max torsional capacity loads

strand stress (MPa), and  $f_c'$ : compressive concrete strength (MPa). It can be seen that in Figs. 2 and 3 they validate the predicted result compared with the experimental results. It can be estimated from these findings, the height of the prestressed concrete PC beam affects about 100%, hence the most impact on performance. It indicates the aim vector has a strong sensitivity to bending moment variations. On the other side, bending moment and shear force parameters have a proportional influence of 41.6 and 16.1%, respectively. It can be noticed that a lower effect on the ultimate torsional torque in PC combined torsion specimens. Therefore, in this study, the value of (x) can be written as Eq. 8 below:

$$\begin{aligned}
 x = & 1.792 + 0.513 * (M) + 0.079 * (sh) - 0.727 * (w) \\
 & - 1.346 * (h) - 1.016 * (pre) + 0.007 * (e) \\
 & - 0.209 * (str) - 0.409 * (lstr) - 0.142 * (f'_c) \\
 & - 0.154 * (f_r) - 0.582 * (f_y) + 0.132 * (f_{ypre}) \tag{8}
 \end{aligned}$$

All algorithms have shown strong estimation power. This study has shown that the feasibility of ANN models' potential use in combined torsional strength estimation of a beam. The skeleton of the model is illustrated in Fig. 4. The result of the ANNs design equation is expressed in Eq. 9:

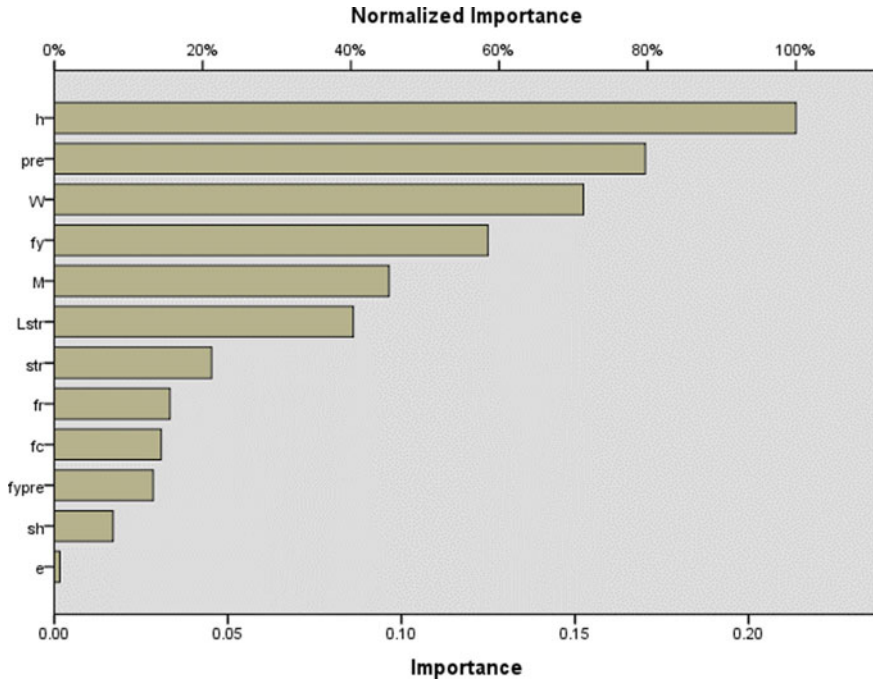


Fig. 3 Normalized importance of ANN model

$$y = \frac{1}{1 + e^{-(0.054) - (1.804 * \tanh(x))}} \tag{9}$$

where x is:

$$\begin{aligned} x = & 1.792 + 0.513 * \left( \frac{m}{10.3 * 10^6} \right) + 0.079 * \left( \frac{sh}{122300} \right) \\ & - 0.727 * \left( \frac{w - 76}{127} \right) - 1.346 * \left( \frac{h - 127}{254} \right) \\ & - 1.016 * \left( \frac{pre}{42.1} \right) + 0.007 * \left( \frac{e + 6}{118} \right) - 0.209 * \left( \frac{str}{8.9} \right) \\ & - 0.409 * \left( \frac{lstr}{2.5} \right) - 0.582 * \left( \frac{f'_c}{58.9} \right) - 0.154 * \left( \frac{fr}{4.8} \right) \\ & - 0.582 * \left( \frac{fy}{400} \right) + 0.132 * \left( \frac{f_{ypre}}{1900} \right) \end{aligned} \tag{10}$$

Each term is corrected by the equation below:

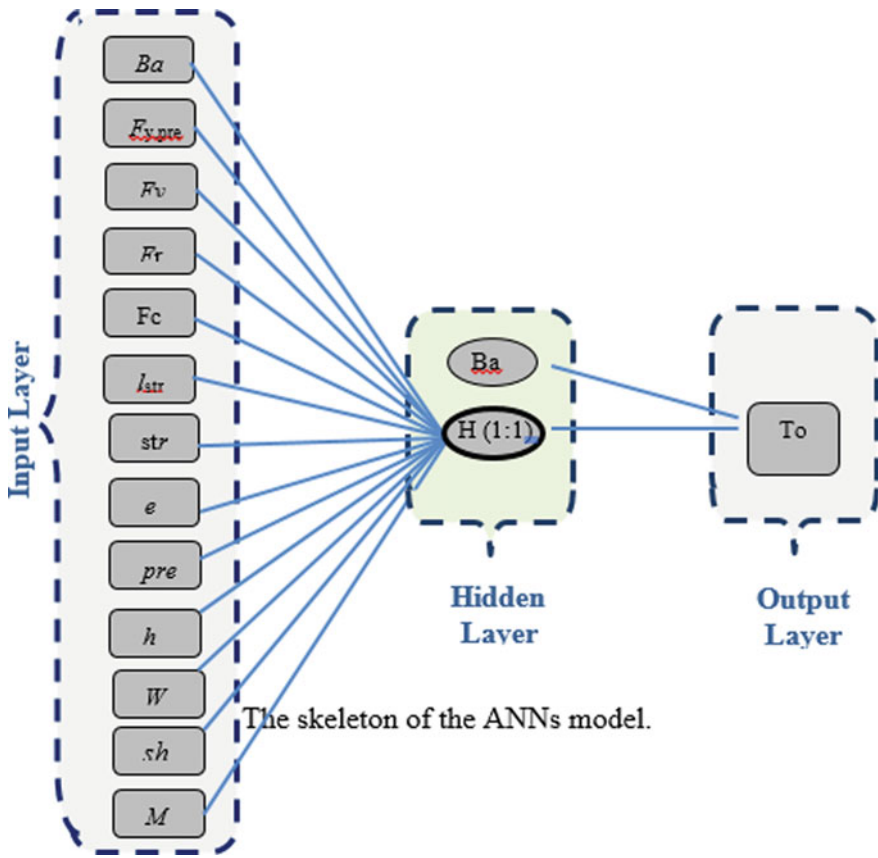


Fig. 4 The skeleton of the ANNs model

$$\beta_i = \frac{\beta - \beta_{\min}}{\beta_{\max} - \beta_{\min}} \tag{11}$$

So, the real ultimate torsion can be calculated from Eqs. 9 and 10 as follows in Eq. 12:

$$y = \frac{19.3 * 10^6}{1 + e^{-(0.054) - (1.804 * \tanh(x))}} \tag{12}$$

where y: represents the torsional strength. The mean absolute percentage error (MAPE) is:

$$MAPE = ABS\left(\frac{tor_{\text{actual}} - tor_{\text{estimate}}}{tor_{\text{actual}}}\right) \tag{13}$$

**Table 3** List of analysis coefficients

Parameter	MAPE	AA	R	R <sup>2</sup>
Percentage (%)	92.87	99.92	92.84	86.2

**Table 4** Max. and Min. values of input parameters

No	Variable	Maximum value	Minimum value	Range
1	M (kN m)	100	0	100
2	Sh (kN)	122.3	0	122.3
3	W (mm)	203	76	127
4	H (mm)	381	127	254
5	Pre (kN)	42.1	0	42.1
6	e (mm)	112	-6	118
7	str	8.9	0	8.9
8	I <sub>str</sub>	2.5	0	2.5
9	f <sub>r</sub> (MPa)	4.8	0	4.8
10	F <sub>y</sub> (MPa)	400	0	400
11	F <sub>ypre</sub> (MPa)	1900	0	1900
12	f <sub>c</sub> ' (MPa)	58.9	0	58.9
13	Tor (MPa)	20.3	1	19.3

Also, the average accuracy percentage (AA, %) is:

$$AA = 100 - MAPE \quad (14)$$

The coefficient of correlation (R) and the coefficient of determination (R<sup>2</sup>) are shown in Table 3. Also, Table 4 illustrates the values of maximum, minimum, and ranges of input parameters of this study.

This relation indicates that the ANN predicted output could be found from experimental studies with reasonably fair precision, as illustrated in Fig. 5.

### 3 Conclusions

A model proposed for estimating the combined flexure-torsion strengths of prestressed concrete beams using an artificial neural network algorithm. The findings of experimental tests on (345) pre-tensioned prestressed concrete beam's specimens under pure and combined torsion have been obtained using the existing technical evidence. The main outcomes of this study are:

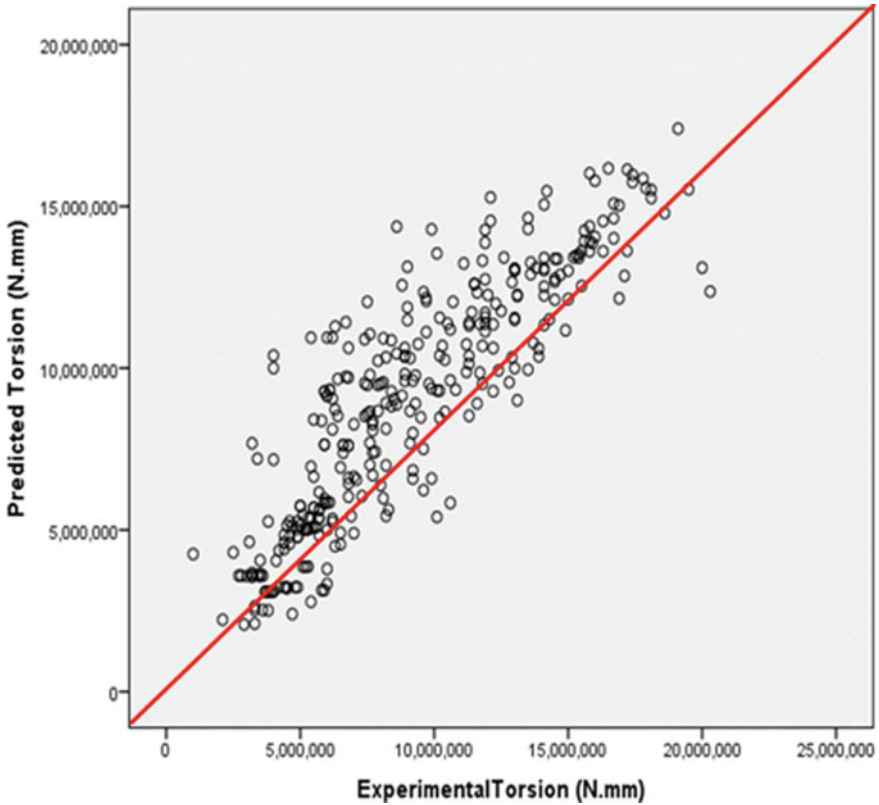


Fig. 5 Comparison between experimental data and ANN models

- After network training for network performance validation, simulation of actual data was performed, and highly accurate outputs were generated. It proved the trained neural network’s ability to estimate the torsion capacity of the prestressed concrete beams subjected to combined loadings.
- The coefficient of correlation (R) between the experimental results and the network output results was (92.84) which is a good result.
- Studying the network weights, it was resolute that in prestressed concrete beams, a discrepancy of cross-section and prestressed force parameters has the most effect on the torsion torque.
- The effect of eccentricity has the lowest importance parameter used to predict the torsional strength of the PC beam subjected to combined flexure and torsion loadings.
- Many parameters have moderate importance values that affect torsional strength, such as the value of yield stress of reinforcing steel, secondary steel reinforcement ratios, and the magnitude of bending moment in the section.



## References

1. ACI Committee 318. (1994). *Proposed Revisions to Building Code Requirements for Reinforced Concrete (ACI 318-89) (Revised 1992) and Commentary-ACI 318R-89 (Revised 1992)*. USA: Concrete International, Michigan.
2. CP 110: Part 1. (1972). *BSI code of practice for structural use of concrete*. London: British Standards Institute
3. ACI Committee and International Organization for Standardization. (2008). *Building Code Requirements for Structural Concrete (ACI 318-08) and Commentary*. Michigan, USA: American Concrete Institute
4. ACI Committee 318. (2019). *Building Code Requirements for Structural Concrete (ACI 318-19) and Commentary (ACI 318R-19)*. Michigan, USA: American Concrete Institute
5. Arslan, M. H. (2010). Predicting of torsional strength of RC beams by using different artificial neural network algorithms and building codes. *Advances in Engineering Software*, 41(7-8), 946-955.
6. Huang, H. C. (2012). Using a hybrid neural network to predict the torsional strength of reinforced concrete beams. In *Advanced materials research* (Vol. 538, pp. 2749-2753). Trans Tech Publications Ltd.
7. Yousif, S. T., & Abdul-Razzak, A. A. (2007). Analysis of elsto-plastic plates using artificial neural networks. In *The Ninth International Conference on the Application of Artificial Intelligence to Civil, Structural and Environmental Engineering* (pp. 18-21). Malta.
8. Naderpour, H., & Fakharian, P. (2018). Predicting the torsional strength of reinforced concrete beams strengthened with FRP sheets in terms of artificial neural networks. *Journal of Structural and Construction Engineering*, 5(1), 20-35.
9. Mahmoud, A. S. (2015). Predicting of torsional strength of prestressed concrete beams using artificial neural networks. *International Journal of Scientific and Engineering Research*, 6(2), 1222-1230.
10. Specht, D. F. (1991). A general regression neural network. *IEEE Transactions on Neural Networks*, 2(6), 568-576.
11. Cigizoglu, H. K., & Alp, M. (2006). Generalized regression neural network in modelling river sediment yield. *Advances in Engineering Software*, 37(2), 63-68.
12. Bishop, C. M. (1995). *Neural networks for pattern recognition*. Oxford University Press.
13. Friedman, N., Nachman, I., Pe'er, D. (2013). *Learning Bayesian network structure from massive datasets: The "sparse candidate" algorithm*. arXiv preprint [arXiv:1301.6696](https://arxiv.org/abs/1301.6696).
14. Yu, J., Smith, V. A., Wang, P. P., Hartemink, A. J., & Jarvis, E. D. (2004). Advances to Bayesian network inference for generating causal networks from observational biological data. *Bioinformatics*, 20(18), 3594-3603.
15. Broo, H., Lundgren, K., & Engström, B. (2007). Shear and torsion in prestressed hollow core units: Finite element analyses of full-scale tests. *Structural Concrete*, 8(2), 87-100.
16. Tahir, T. A. (1984). *Prestressed concrete beams with stirrups subjected to torsion, bending and shear* (Doctoral dissertation, Aston University).
17. Zia, P. (1968). *Torsion theories for concrete members* (Vol. 18, pp.103-132). Special Publication
18. Rakhshan, N., Ahmadvand, M., & Akbari, J. (2013). Evaluation of ultimate torsional strength of reinforcement concrete beams using finite element analysis and artificial neural network. *International Journal of Engineering*, 26(5), 501-508.
19. Adheim, M. A. (2006). *Study of the behavior of pretensioned concrete beams under combined bending and torsion*. Ph.D. Thesis, Civil Engineering Department, University of Baghdad, Iraq.
20. Bishara, A. (1969). Prestressed concrete beams under combined torsion, bending, and shear. In *Journal Proceedings* (Vol. 66, No. 7, pp. 522-524).
21. Gomes, H. M., & Awruch, A. M. (2004). Comparison of response surface and neural network with other methods for structural reliability analysis. *Structural Safety*, 26(1), 49-67.
22. Hsu, T. T. (1968). *Torsion of structural concrete-behavior of reinforced concrete rectangular members* (Vol. 18, pp. 261-306). Special Publication

23. Shepherd, P. (2014). Subdivision surfaces'. In S. Adriaenssens, P. Block, D. Veenendaal, C. Williams (eds) (pp. 295–300).
24. Wafa, F. F., Shihata, S. A., Ashour, S. A., & Akhtaruzzaman, A. A. (1995). Prestressed high-strength concrete beams under torsion. *Journal of Structural Engineering*, 121(9), 1280–1286.
25. Rahal, K. N., & Collins, M. P. (2006). Compatibility torsion in spandrel beams using modified compression field theory. *ACI Materials Journal*, 103(3), 328.
26. Lopes, S. M., & Bernardo, L. F. (2014). Theoretical model for the mechanical behavior of prestressed beams under torsion. *Cogent Engineering*, 1(1), 943934.
27. Mahmood, A. S. (2010). *Investigation of torsional strength of prestressed beams strengthened with CFRP*. Doctoral dissertation, University of Mosul, Iraq.
28. Kamara, M. E., & Rabbet, B. G. (2007). Torsion design of structural concrete based on ACI 318-05. Professional Development Series, Portland Cement Association. *Structural Engineer, Atlanta*, 8
29. Mohammed, A. A. (2012). Predicting of torsional strength of reinforced concrete beams using artificial neural network. *The Iraqi Journal for Mechanical and Material Engineering*, 12(4), 694–708.
30. Deifalla, A., Awad, A., Seleem, H., & Abdelrahman, A. (2020). Experimental and numerical investigation of the behavior of LWFC L-girders under combined torsion. In *Structures* (Vol. 26, pp. 362–377). Elsevier.
31. Gangarao, H. V., Zia, P. (1973). Rectangular prestressed beams in torsion and bending. *Journal of Structural Division*, 99(ST1), 183–198.
32. Razzak, A. A., Yousif, S. T. (2006). Artificial neural network model for predicting structural properties of elasto-plastic plates. In *Fourth Jordanian Civil Engineering Conference* (pp. 10–13).
33. Yousif, S. T., & Abdullah, S. M. (2009). Artificial neural network model for predicting compressive strength of concrete. *Tikrit Journal of Engineering Sciences*, 16(3), 55–66.
34. Demuth, H., Beale, M. and Hagan, M. (1994) *Neural network toolbox*. Mathworks.
35. Sanad, A., & Saka, M. P. (2001). Prediction of ultimate shear strength of reinforced-concrete deep beams using neural networks. *Journal of Structural Engineering*, 127(7), 818–828.
36. Vanluchene, R. D., & Sun, R. (1990). Neural networks in structural engineering. *Computer-Aided Civil and Infrastructure Engineering*, 5(3), 207–215.
37. Ababneh, A., Alhassan, M., & Abu-Haifa, M. (2020). Predicting the contribution of recycled aggregate concrete to the shear capacity of beams without transverse reinforcement using artificial neural networks. *Case Studies in Construction Materials*, 13, e00414.
38. George, U. A., & Elvis, M. M. (2019). Modelling of the mechanical properties of concrete with cement ratio partially replaced by aluminium waste and sawdust ash using artificial neural network. *SN Applied Sciences*, 1(11), 1–18.
39. Gupta, S. (2013). Using artificial neural network to predict the compressive strength of concrete containing nano-silica. *Civil Engineering and Architecture*, 1(3), 96–102.
40. Xi, X., Yin, Z., Yang, S., & Li, C. Q. (2021). Using artificial neural network to predict the fracture properties of the interfacial transition zone of concrete at the meso-scale. *Engineering Fracture Mechanics*, 242, 107488.
41. Sahoo, S., & Mahapatra, T. R. (2018). ANN modeling to study strength loss of fly ash concrete against long term sulphate attack. *Materials Today: Proceedings*, 5(11), 24595–24604.
42. Asteris, P. G., Mokos, V. G. (2019). Concrete compressive strength using artificial neural networks. *Neural Computing and Applications*, 1–20
43. Uchechukwu, E. A., & Austin, O. (2020). Artificial neural network application to the compressive strength of palm kernel shell concrete. *MOJ Civil Engineering*, 6(1), 1–10.
44. Oreta, A. W. C. (2004). Simulating size effect on shear strength of RC beams without stirrups using neural networks. *Engineering Structures*, 26(5), 681–691.
45. Abdul-Razzak, A. A., & Yousif, S. T. (2007). Artificial neural network model for predicting nonlinear response of uniformly loaded fixed plates. *Engineering and Technology*, 25(3), 334–348.

46. Abdul-Razzak, A. A., Yousif, S. T. (2008). Artificial neural networks model for predicting thickness of rectangular plates. In *International Conference on Innovative and Smart Structural Systems for Sustainable Habitat (INSHAB-2008)* (pp. 03–05). Coimbatore
47. Zayan, H. S., Farhan, J. A., Mahmoud, A. S. and Juma'a, A. (2017). A parametric study and design equation of reinforced concrete deep beams subjected to elevated temperature. In *Global Civil Engineering Conference* (pp. 193–214). Springer: Singapore.

# Theoretical Evaluation of Sand Subgrade Behavior Underneath the Asphalt Pavement with Rutting Deformation



Saad F. I. Al-Abdullah, Zaman T. Teama, Suha Aldahwi,  
and Maysaloon Zaidn

**Abstract** Asphalt layers in flexible pavement structure consider the most costly than other layers and play an essential role in the cost of a highway structure. This paper will investigate the influence of change in thickness of asphalt layer on rutting and strain in the flexible pavement when roads construct above sand soil subgrade. Two methods are implemented; the first is the experimental inspections by simulation of three paved highway layers, using an iron box with dimensions of 60 cm length, 50 cm width, and 40 cm depth. Sandy soil is used as a subgrade course layer to study its behavior by using it as a part of a flexible pavement structure under a traffic load at a relative density of 57%. The impact of change in the thickness of the asphalt concrete layer in the distribution pattern for rutting and strain behavior is also investigated using a three-dimensional finite element approach by the ABAQUS program ver.6.14.4. One of the models is building verify of ABAQUS simulation; after ascertaining the program, other models built to simulate the real road with dimension (5 m width and 10 m length) which represented ring road of Baghdad university, three thickness of asphalt layer 5 cm, 10 cm, 15 cm, and 20 cm are used. The thickness of the subbase layer and sand subgrade layer was stilled constant at all models, 25 cm and 250 cm. The laboratory results demonstrated that the low number of the truck passed when used sand soil at a relative density of 57% as a subgrade layer led to the failure of the flexible pavement; the verifying result shows the ABAQUS program was very good in the simulation laboratory model. The real road simulation results illustrated that when asphalt layer thickness, the number of passes increases, and the rutting and strain decrease.

---

S. F. I. Al-Abdullah (✉) · S. Aldahwi  
Faculty of Engineering, Isra University, Amman, Jordan  
e-mail: [saad.alabdullah@iu.edu.jo](mailto:saad.alabdullah@iu.edu.jo)

S. Aldahwi  
e-mail: [suha.hasssan@iu.edu.jo](mailto:suha.hasssan@iu.edu.jo)

Z. T. Teama  
Baghdad University, Baghdad, Iraq

M. Zaidn  
Faculty of Engineering, Mustansiriyah University, Baghdad, Iraq

**Keywords** Sand subgrade · Flexible pavement · ABAQUS models

## 1 Introduction

Flexible pavement layer in roads' construction considers as highest cost and more strength than other layers in the paved road [1]. The asphalt layer carries the major part of the traffic loads and reduces the stress that is progressive to subgrade to reduce the distress in the pavement body [2]. The subgrade layer is essential in keeping the pavement stable and resistant to deformation. Sand covers a large area of Iraq, reduces efficiency, and increases maintenance charges for highways [3]. So, it's necessary to make it suitable to use in road construction [4] by understanding the stress and strain behavior of it under loads.

## 2 Materials

The material which used in this paper is local and available locally.

**Subgrade.** In this research project, the experimental work was carried out using local sand, which has properties given in Table 1.

**Subbase Course.** The subbase buys from Al- Nibae quarry, north of Baghdad, this subbase is usually used as a layer in the flexible highway pavement construction [5].

**Asphalt Layer.** The asphalt cement 40–50 penetration grade coming from Doura refinery [6] is used for experimentation and aggregates confirming midpoint gradation of grade II specifications as per Iraq specification have been used [7]. Table 2 shows the properties of asphalt.

**Table 1** Properties of sand soil subgrade

Type properties	Index value
Specific gravity (Gs)	2.67
Liquid Limit (LL, %)	25
Plastic Limit (PL, %)	NP
Plasticity Index (PI, %)	NP
Maximum unit weight	18.7 kN/m <sup>3</sup>
Soil Symbols (USCS)	SP-SM

**Table 2** The properties of asphalt cement

Property	Asphalt Cement Daurah (40–50)
Penetration (25 °C, 100 gm., 5 s), (1/10 mm)	42
Softening Point (Ring and Ball), °C	51
Ductility, cm	>100
Flash Point (Cleave land open-cup)	335
Specific Gravity, 25 °C	1.048
Loss on heat (5 h, 163 °C, 1/8"), %	0.18

**Fig. 1** The steel box and laboratory model under the wheel

### 3 Laboratory Models Preparation

The model was built in the laboratory consists of a steel box with dimension 60 cm length  $\times$  50 cm width  $\times$  40 cm depth as shown in Fig. 1. The sand at a relative density of 57% installed first as a subgrade layer using the raining technique [8], the second layer put above the sand is subbase, and the final layer put is asphalt layer with 5 mm depth. The wheel of the machine put above the layer, as illustrated in Fig. 1.

### 4 Finite Element Modeling

One of the commonly important techniques employed for pavement models is the finite element approach [9] 3D model was built by using the ABAQUS program 6.14.4, to understand with more accuracy. The pattern of distribution of the rutting in the whole road layers at the different thickness of asphalt layer above the sand.

3D finite element ABAQUS program that owns the capacity to simulate real traffic loading and predict the structural response for asphalt roads are used to simulate the experimental model with the same thickness of layer as illustrated in Fig. 2. After verifying the laboratory model with ABAQUS model, real dimension of road 5 m width and 10 m length used to simulate the behavior of roads under traffic loads with different asphalt layer thickness 5 cm, 10 cm and 15 cm with a constant thickness of subbase and subgrade layer 25 cm and 250 cm respectively as illustrated in Fig. 3, the properties (elastic models and Poisson's ratio) are given in Table 3.

**ABAQUS Finite Element Types and Boundary Condition.** The 8-node continuum three-dimensional brick element (C3D8R) are used to build the model. This element owns the ability to calculate extensive deformation, also has three degrees of freedom at each node [10], Fig. 4 shows model mesh. The boundary

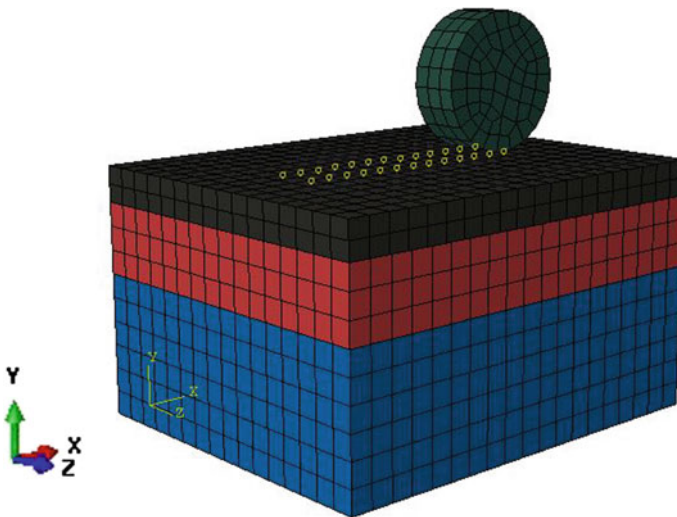
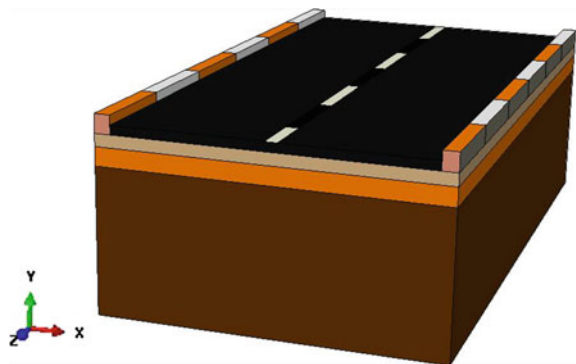


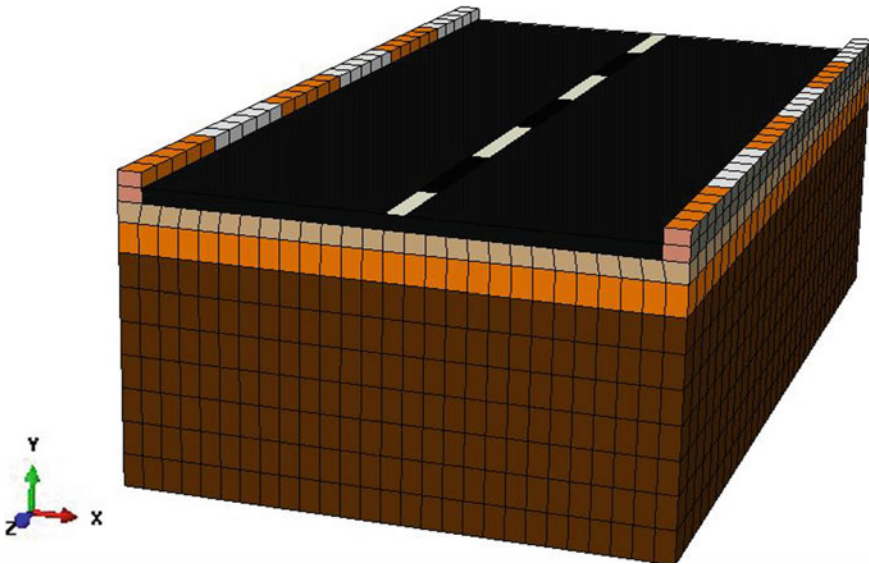
Fig. 2 Simulation of laboratory model by ABAQUS

Fig. 3 Simulation of a real road



**Table 3** The impute properties of the materials

Layers	Modulus of elasticity (MPa)	Poisson's ratio ( $\nu$ )*
Asphalt	1500	0.35
Subbase	125	0.35
Subgrade	4	0.3



**Fig. 4** Finite element mesh of studied model

conditions have a notable influence in prognosticating the response of the model, the bottom facade of the subgrade and sides of layers is considered to be fixed, and this expresses the bottom and sides of the iron box; Fig. 5 illustrated the boundary conditions for the laboratory and real models. The loading of traffic simulated by the ABAQUS model through applying a standard single axle load of 18 kips (18 kN) with dual tires and contact pressure of (0.6 MPa) is used and illustrated in Fig. 6 [11].

## 5 Results and Discussion

The moving wheel loading device was applied to estimate the rut depth. The lab. model subordinated to moving pressure of 150 MPa on the surface of asphalt pavement, the result shows the number of passes (N.) was 500 passes which consider low, the pavement with sand subgrade was weak, the Figs. 7, 8 and 9 illustrated the rutting at the asphalt layer and subbase and subgrade layer respectively. The ABAQUS model



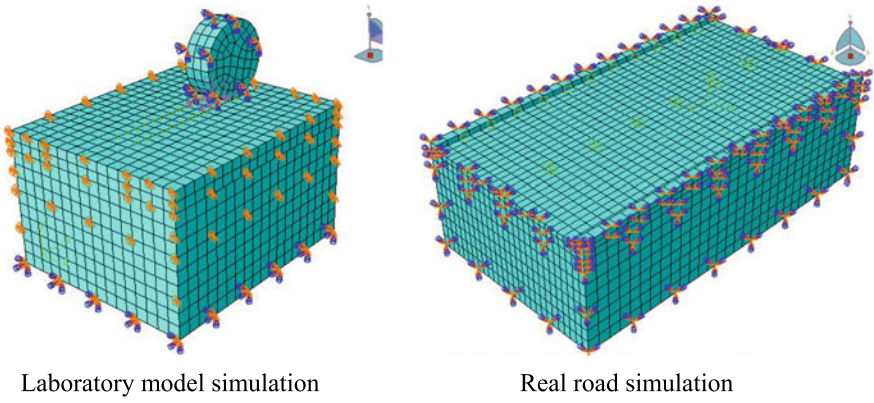


Fig. 5 Boundary condition for laboratory and real road models

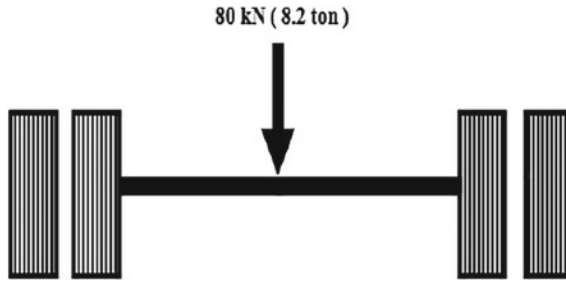


Fig. 6 Standard single axle load [10]

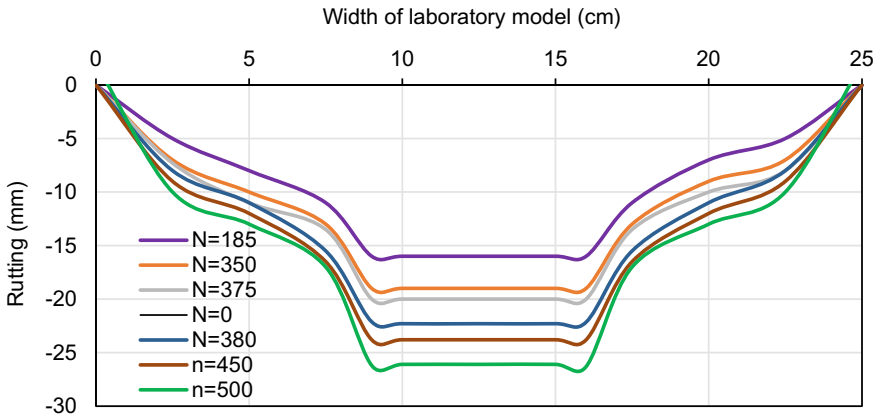


Fig. 7 Profile of deformation in asphalt layer of laboratory model

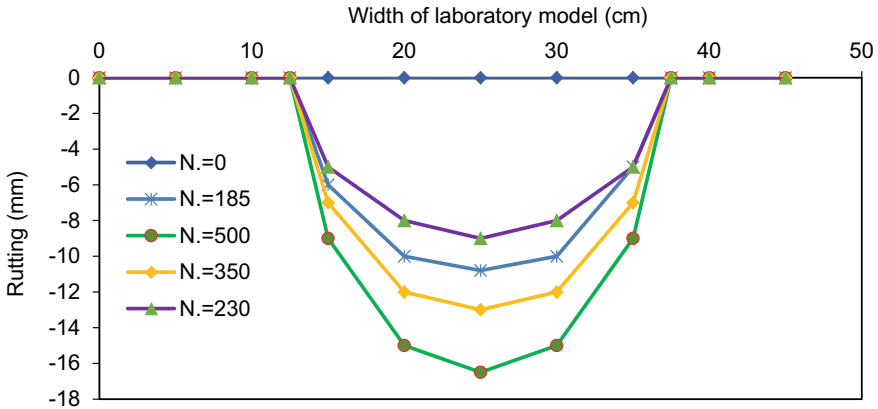


Fig. 8 Profile of deformation in subbase layer of laboratory model

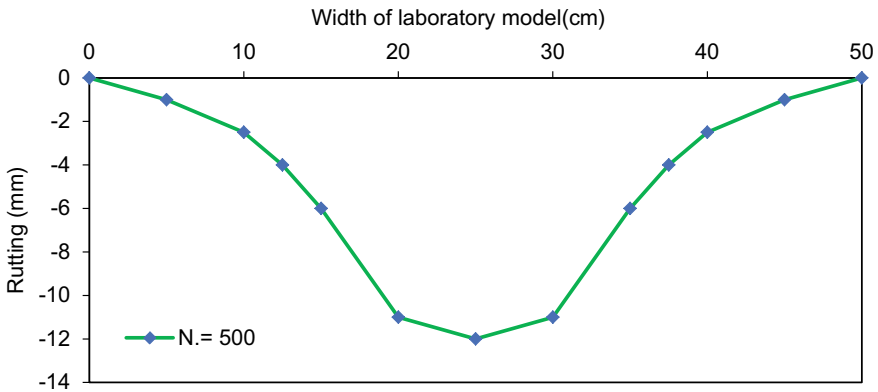


Fig. 9 Profile of deformation in sand subgrade layer of laboratory model

builds to simulate it, laboratory model, the result of the ABAQUS program demonstrated in Fig. 10, the verify of models show that laboratory and ABAQUS result was so close as shown in Fig. 11, so the ABAQUS program can be used to simulate the asphalt pavement. After verified of models, and ABAQUS program was used to simulate a real road to get comprehensive capture for strain and rutting on the entry of pavement layers and the effect of change asphalt layer thickness on strain and rutting when using sand soil as a subgrade layer in the construction of roads under constant loading condition and understand the range of effect the thickness of asphalt layer on the behavior of pavement structure. Figures 12, 13, 14 and 15, we can see the rutting distribution for each model. When the thickness of the asphalt layer increases, the pavement may behave in the same pattern, but the result of models shows that when the thickness of pavement increases, the value of rutting decreases for the same loading condition as illustrated in Fig. 16. From the ABAQUS output's

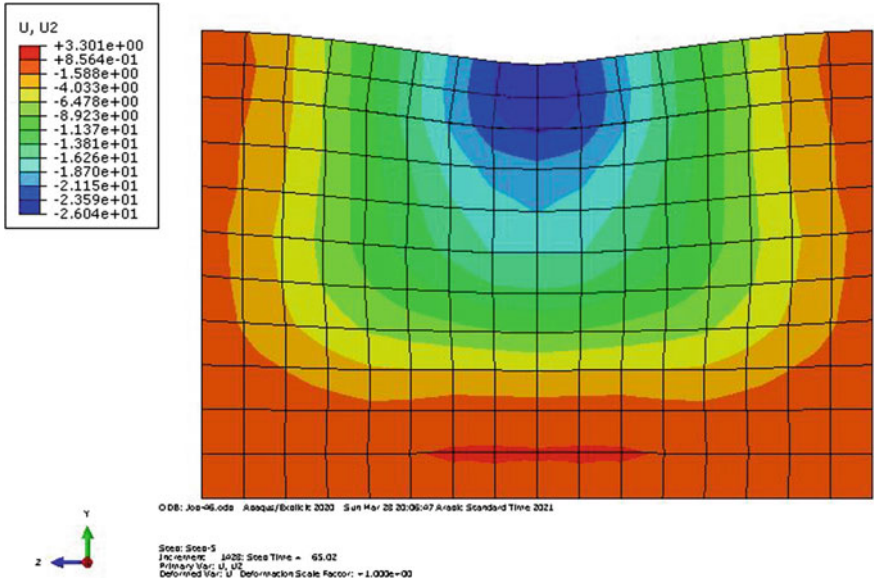


Fig. 10 ABAQUS result for rutting for laboratory model simulation

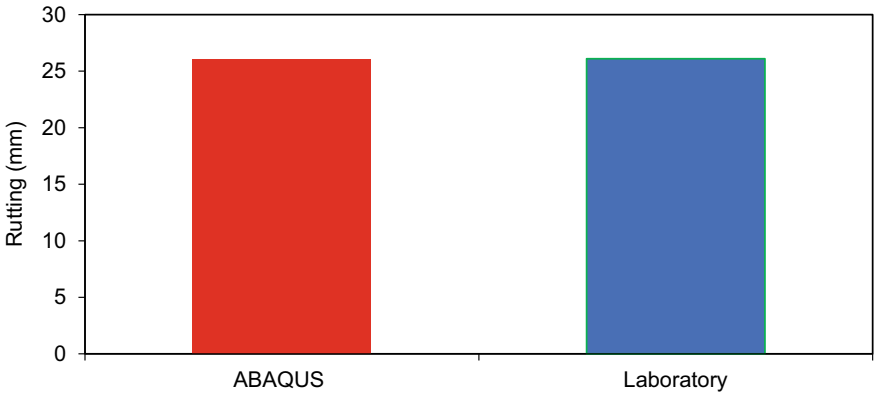


Fig. 11 Result of laboratory and ABAQUS models

strain distribution shape, we can see the difference between each one to another. The value of logarithm also strains different for each thickness of asphalt layer, as illustrated in Figs. 17, 18, 19 and 20. Figure 21 demonstrated that when asphalt thickness increases, the strain in the whole pavement structure decreases.

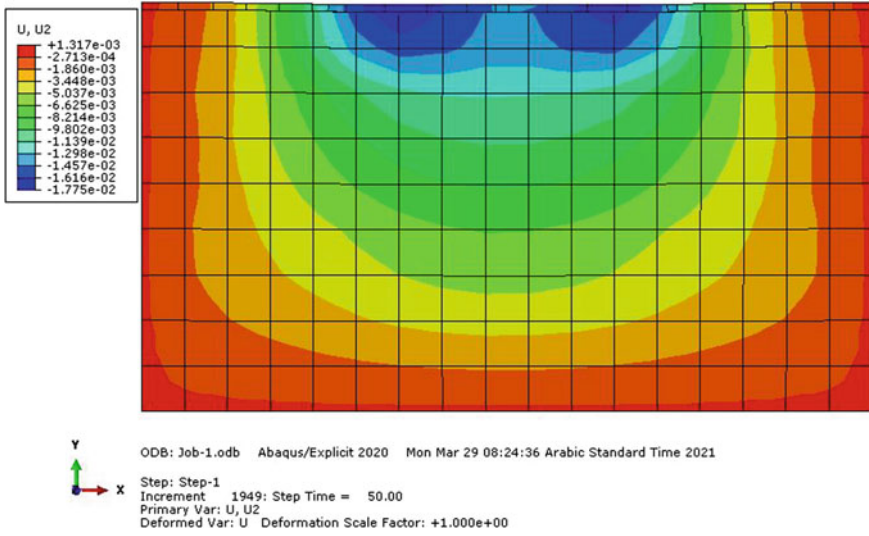


Fig. 12 Rutting for real road simulation with asphalt layer 5 cm

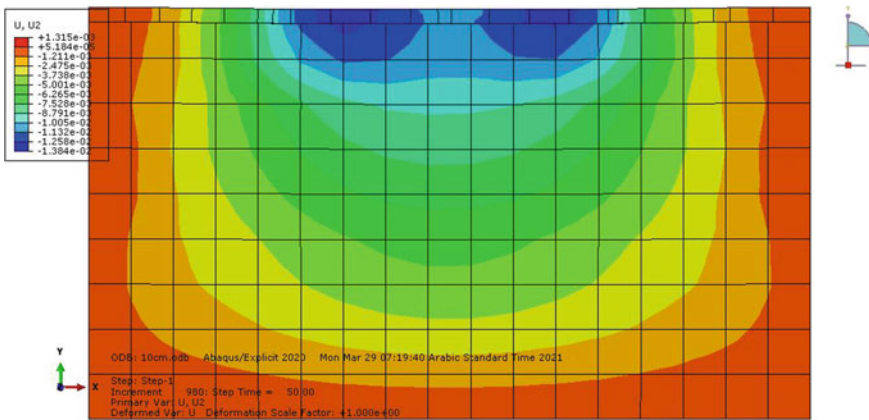


Fig. 13 Rutting for real road simulation with asphalt layer 10 cm

## 6 Conclusions

The effect of asphalt layer thicknesses over sand soil foundation have been studied through using laboratory approach through build model and theoretically approach by the utilization of ABAQUS program to investigate the behavior of road which have sandy soil as subgrade at relative density 57% and different thicknesses of an asphalt layer on the strain and rutting of roads. The following concluding notes;

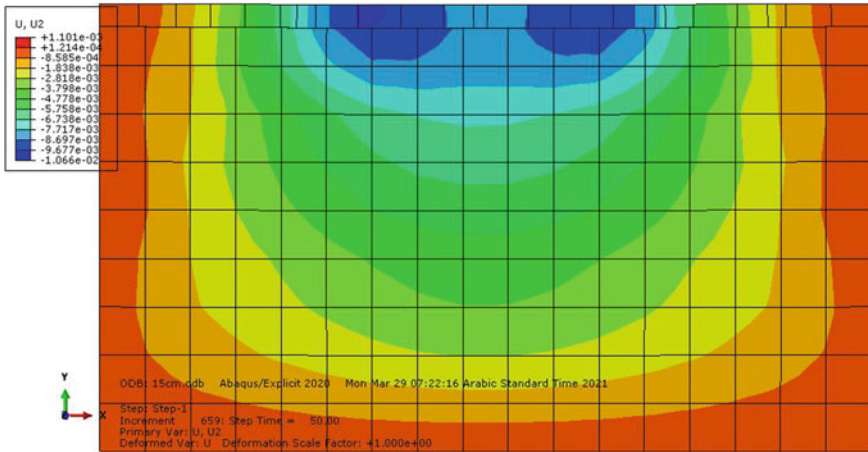


Fig. 14 Rutting for real road simulation with asphalt layer 15 cm

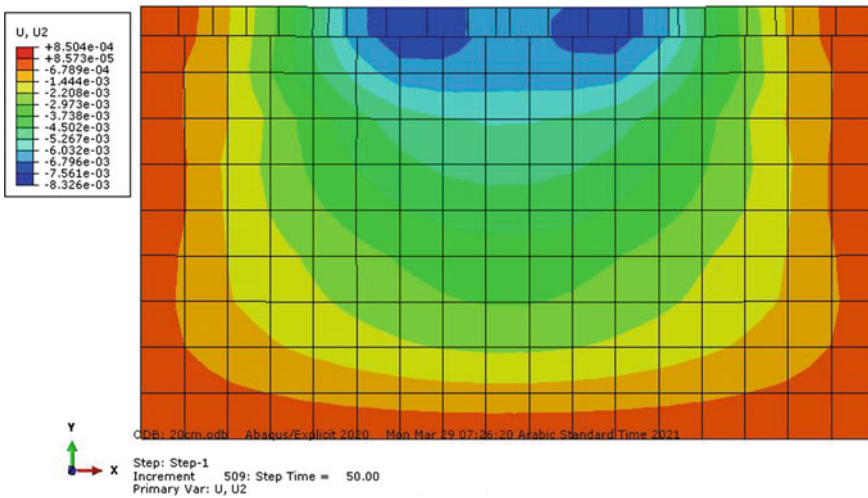
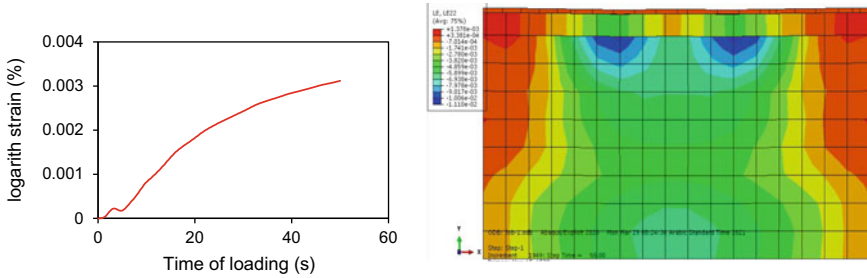
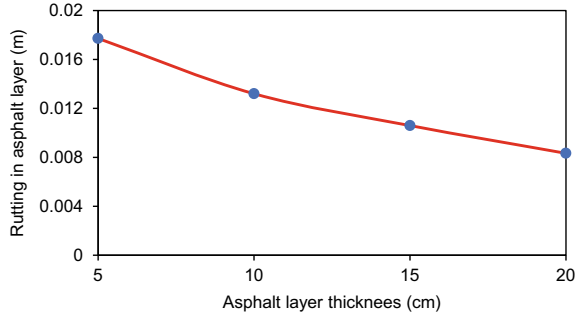


Fig. 15 Rutting for real road simulation with asphalt layer 20 cm

- The laboratory model shows that the pavement with sand soil subgrade has sustained a low number of wheel passes which means the pavement with sand subgrade at a relative density of 57% is weak.
- The ABAQUS program simulation results for the laboratory model illustrate that the ABAQUS program can be used to simulated Asphalt pavement.
- The models of ABAQUS, which simulate the real roads, shows the shape of rutting more minor each model to other which mean that the increase in thickness of

**Fig. 16** The relationship between rutting and thickens of the asphalt layer



**Fig. 17** ABAQUS logarithm strain result for real road simulation with 5 cm asphalt layer thickness

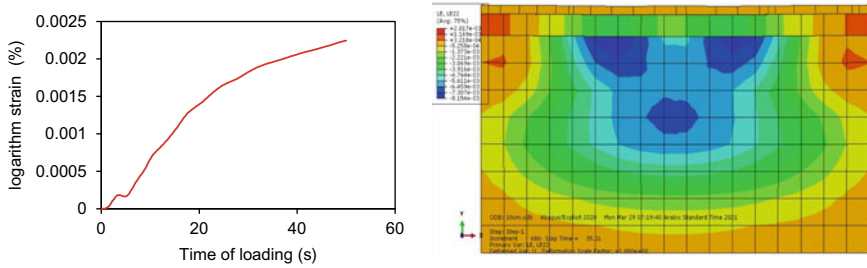


**Fig. 18** ABAQUS logarithm strain result for real road simulation with 10 cm asphalt layer thickness

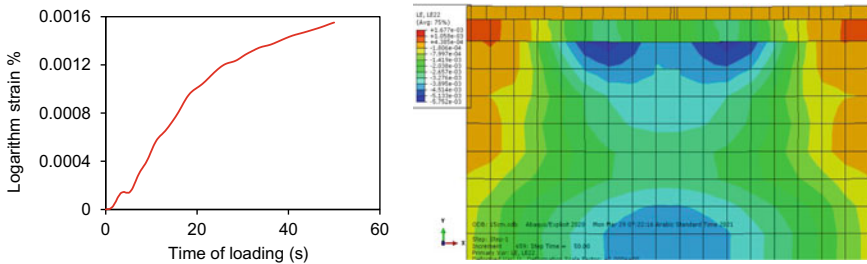


**Fig. 19** ABAQUS logarithm strain result for real road simulation with 15 cm asphalt layer thickness

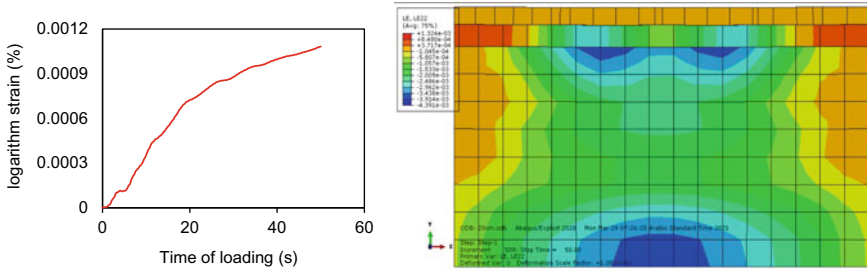


Fig. 20 ABAQUS logarithm strain result for real road simulation with 20 cm asphalt layer thickness

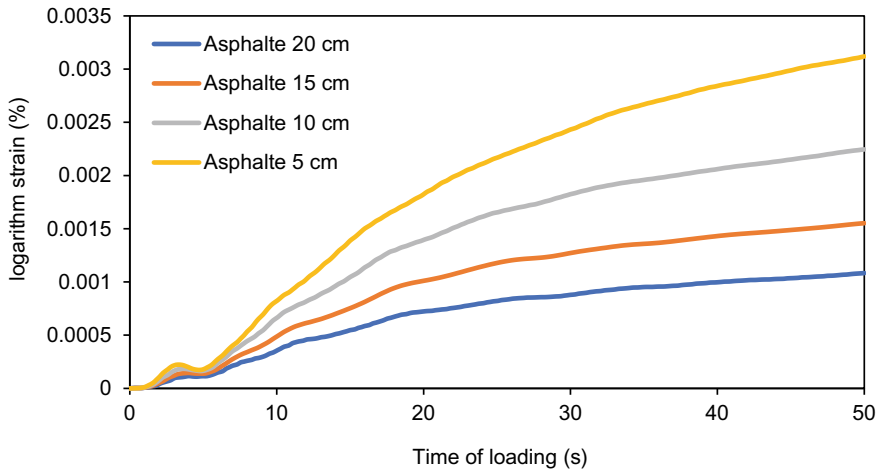


Fig. 21 Relationship between logarithm strain and time loading for different asphalt thicknesses

asphalt layer with sand subgrade don't affect in change the pattern of deformation of road, but the value of rutting decrease as thickness of asphalt increases.

- The models of ABAQUS, which simulate the real roads, shows that the pattern of logarithm strain variation from each model to another, which mean that the increase in thickness of asphalt layer with sand soil subgrade effect changes the pattern of strain for road, and the value of strain decrease as thickness of asphalt increases.
- From the conclusion above is apparently the use of sand soil at a relative density of 57% don't give stable roads so it's not an economic choice to use without more investigation and improvement.

## 7 Future Work

The result and conclusion represented in this paper show that we need more investigation before used sand soil at a relative density of 57% as a subgrade, so we suggest constructing a portion from the road as using the sand soil as subgrade and study with real traffic loads.

## References

1. Teama, Z. (2014). *Suitability of sand dunes beneath flexible pavement*. M.Sc Thesis, Highway and Transportation Department, University of Al-Mustansiriyah, Iraq
2. Al-Abdullah, S. F., Sofia, G. G., & Teama, Z. T. (2016). Evaluation of using geosynthetic material and the process of grouting to improve pavement performance over sand dunes subgrade. In *International conference on transportation and development 2016* (pp. 859–870).
3. Al-Abdullah, S. F., Sofia, G. G., & Teama, Z. T. (2017). An approach in study behavior of sand dunes to use as a subgrade in pave road under moving loads. In *congress on technical advancement 2017* (pp. 53–64).
4. AlAbdullah, S. F., & Taresh, N. S. (2017). Improvement the behavior of sand subgrade beneath flexible pavement structure using reinforcement under dynamic loads. *Imperial Journal of Interdisciplinary Research (IJIR)*, 3(1), 999–1010.
5. Masood, G. (2013). *Experimental and numerical investigation of stabilized unbounded granular pavement materials*. M.Sc. Thesis, Highway and Transportation Department, Al-Mustansiriyah University, Iraq.
6. Albayati, A., Wang, Y., Wang, Y., & Haynes, J. (2018). A sustainable pavement concrete using warm mix asphalt and hydrated lime treated recycled concrete aggregates. *Sustainable Materials and Technologies*, 18, e00081.
7. Aljubory, A., Teama, Z. T., Salman, H. T., & Abd Alkareem, H. M. (2021). Effects of cellulose fibers on the properties of asphalt mixtures. In *Materials today: proceedings*.
8. Fakhraldin, M. (2013). *Properties measurement and applications of some geogrid ds in Iraq*. Ph.D. Thesis, Nahrain University, Iraq.
9. Alkaissi, Z. A. (2020). Effect of high temperature and traffic loading on rutting performance of flexible pavement. *Journal of King Saud University-Engineering Sciences*, 32(1), 1–4.
10. Raju, S., Kolathayar, S., & Sharma, A. (2018). Strength behavior of subgrade soil mixed with sand manufacturing dust and fiber. *Journal of GeoEngineering*, 13(2), 79–84.
11. Huang, Y. (2004). *Pavement analysis and design*. Prentice-Hall.



# Large Scale Laboratory Setup for Testing Structural Performance of Slender High-Strength Concrete Columns Subjected to Axial Load and Fire: A Preliminary Study



Muyasser M. Jomaa'h, Ali I. Salahaldin, Qahtan A. Saber,  
and Aram M. Raheem

**Abstract** This study has introduced a large-scale laboratory framework to investigate the structural performance of distinctive concrete types, including reactive powder and normal strength concretes to be used in slender columns exposed to high degrees of temperature. An advanced laboratory assembly has been prepared to ensure the full control of the applied high temperature on the tested concrete samples. Two distinctive types of concretes, consisting Normal Strength Concrete “(NSC)”, and Reactive Powder Concrete “(RPC)”, have been cured for 28 days tested under extraordinary heats in the variety of 450 °C to 750 °C. It has been shown that as the temperatures increased from 450 °C to 750 °C, the compressive strengths have decreased by 93% and 81% for both NSC and RPC, respectively. In addition, a strong linear relationship has been observed between the concrete compressive strength and temperature, where a linear model has been used to predict such association with a maximum  $R^2$  of 0.9944.

**Keywords** Large-scale laboratory · Distinctive concrete · Slender column · High degree of temperature

## 1 Introduction

Reinforced concrete is a commonly used building element in Iraq and around the world. As a consequence, the behavior of these systems, as well as their failure modes, has been thoroughly researched. In recent years, the deterioration of concrete

---

M. M. Jomaa'h · Q. A. Saber  
Civil Engineering Department, Tikrit University, Salahuddin, Iraq  
e-mail: [muyasserjomaah@tu.edu.iq](mailto:muyasserjomaah@tu.edu.iq)

A. I. Salahaldin (✉) · A. M. Raheem  
Civil Engineering Department, University of Kirkuk, Kirkuk, Iraq  
e-mail: [ali.ihsan@uokirkuk.edu.iq](mailto:ali.ihsan@uokirkuk.edu.iq)

A. M. Raheem  
e-mail: [aram\\_raheem@uokirkuk.edu.iq](mailto:aram_raheem@uokirkuk.edu.iq)

strength induced by rapid-duration coverage to high temperatures (fire) has received a lot of recognition. The behavior of members exposed to fire is dictated by dynamic interactions that occur throughout the heating phase. The forms of concrete failure that arise when a building is exposed to fire vary based on the intensity of the fire, the loading mechanism, and the form of structure. Furthermore, failure may occur for a number of causes, including a defeat of shear strength, a reduction in bending or tensile strength, and a drop in compressive strength.

Several experimental and theoretical reviews on the deterioration of the strength of concrete column because of rapid-period fire coverage have been conducted in the last decade [1–7]. The following findings have been taken from these analyses of fire-damaged columns:

1. At approximately 300 °C, concrete starts to break on the floor, with deeper cracking beginning at 540 °C. Spalling happens, accompanied by the tearing away of the thin concrete cover along with the corners and sides.
2. As the temperature of concrete is raised to 300 °C, it loses almost third of its compressive strength, and once warmed to 600 °C, it loses around 70% of its compressive strength.
3. At 300 °C, the concrete elasticity modulus approaches 60% of its original value, and at 600 °C, it comes to 15% of its initial value.
4. Concrete strength reduces as the temperature rises, and this reduction in strength is followed by a decrease in concrete stiffness as the concrete strains rise.
5. Vertical cracks emerge, followed by concrete crushing, accompanied by a crackle sound and local longitudinal reinforcing buckling.
6. The fire resistance of columns with wide longitudinal bar diameters is somewhat lower than that of columns contain lesser bar diameters, besides the rise in the cover of the concrete has a beneficial impact on the fire endurance in all types of the columns.

Research reports have shown that column models and prototypes have a clear connection (with comparable manners of cracking shapes and failure), suggesting that no demand to examine the accurate impact of a large-size prototype is necessary where a instance measure feature for prototypes should stand in use [3, 4].

Any requirements for structural fire-resistance are required by design building codes to maintain building stability for a defined period of time exposed to fire circumstances. These requirements grant inhabitants to safely evacuate and firefighters to gain entry.

The principal aim of this research is to test different types of concrete samples prepared from Normal strength concrete “(NSC)” and Reactive Powder Concrete “(RPC)” subjected to a high level of temperatures. Specifically, it is required to investigate the relationship between the compressive strength of various kinds of concrete exposed to a high level of temperatures applied for a long period of time where the tested temperatures differ from 450 to 750 °C. In addition, the study has focused on using the obtained results as a preliminary characteristic on the possibility of using such types of concrete in designing slender structural concrete exposed to high temperatures.

**Table 1** Natural chemical and physical cement properties, Type I

Constituents	Substance %	Limits (Iraqi Standards, No. 5-1984)
Al <sub>2</sub> O <sub>3</sub>	4.9	–
CaO	62	–
SO <sub>3</sub>	2.2	2.8% (Max.)
Fe <sub>2</sub> O <sub>3</sub>	3	–
SiO <sub>2</sub>	20.8	–
MgO	2.2	5% (Max.)
Highest compositions		
C <sub>3</sub> S	50.62	–
C <sub>2</sub> S	21.60	–
C <sub>3</sub> A	4.30	–
C <sub>4</sub> AF	9.08	–
Limits (Iraqi Standards, No. 5-1984)	Results	Physical properties
lower limit (230 m <sup>2</sup> /kg)	346 m <sup>2</sup> /kg	Specific surface area (m <sup>2</sup> /kg)
Not less than 45 min Not more than 10 h	3:05 5:20	Setting time using vacate Initial setting in hrs:min Final setting in hrs:min
Not less than 15 MPa Not less than 23 MPa	22.7 MPa 27.7 MPa	Compressive strength in MPa 3 days 7 days

## 2 Materials and Methods

### 2.1 Cement

The used cement was the regular Portland cement “(Type I)” produced by the Mass factory in Bazian-Iraq. The natural chemical and physical properties of the cement are given in Table 1. From the test results, it was indicated that the utilized cement followed the Iraqi standards (No. 5-1984) [8].

### 2.2 Fine Aggregate

In the concrete mix, the used fine aggregate was the river sand, and it was obtained from the Kara Salem zone in Kirkuk city. Once performing the necessary evaluation,

it was shown to be in zone (2) (IQS No. 45/1984, 2/2010) [9]. The grading is shown in Table 2 whereas the physical and chemical properties are summarized in Table 3 and Fig. 1, respectively.

### **2.3 Coarse Aggregate**

The used gravel (crushed) is provided from the zone of Lailan area in Kirkuk city, and the used gravel had a maximum size of 12.5 mm. The grading is shown in Table 4, and it is following the standard requirements [9]. The chemical and physical properties for the coarse aggregate are summarized in Table 5.

### **2.4 Micro Silica**

Densified micro-silica type (MS 610) produced by CONMIX, as shown in Fig. 2, was utilized to be supplied as a mineral constituent to the mix as a fractional substitution for the cement weight. Such silica is extremely effective pozzolanic substance with tiny sphere-shaped elements. It is a silicon processing product, which reacts from hydrate to the calcium hydroxide product to create an extra binder cement. Table 6 represents the typical properties of the micro-silica used in this study, which satisfies the performance requirements of ASTM(C1240-03 2005) [12].

### **2.5 Super-Plasticizer**

The admixture MegaFlow 3000 provided by CONMIX chemical industrial company, presented in Fig. 3. In this research, a superplasticizer with an extraordinary water reducing capacity known as HRWR was applied. HRWR has the ability to enhance the workability of RPC. As the HRWR is functioned, the water amount for the same workability is reduced and the concrete strength will considerably improved for the curing ages. In addition, HRWR accelerates the cement scattering and electrostatic dispersion. It has no chloride and satisfies type (E) [13]. Its main properties are given in Table 7.

### **2.6 Polypropylene Fibers**

Monofilament fibers developed by the BASF chemical corporation, commercially known as (RHEOFIBRE®), were the polypropylene fibers that used in this analysis.

**Table 2** Fine aggregate grading

Sieve diameter-mm (IQS No. 23)	Retained (%)	Accumulative (%)	IQS (No.45-1984)
10	0	100	100
4.75	9.78	90.22	90-100
2.36	24.80	75.20	75-100
1.18	38.95	61.05	55-90
0.6	51.92	48.08	35-59
0.3	80.64	19.36	8-30
0.15	97.77	2.23	0-10

**Table 3** Mechanical properties of aggregate (fine)

Properties	Results	Standards	Limits
Sulfate-SO <sub>3</sub> (%)	0.09	IQS [9]	Max. (0.5)
Finer than 0.075 mm	1	IQS [9]	Max. (5)
Dry unit weight (kg/m <sup>3</sup> )	1495	ASTM (C29/C29M) [11]	-
Specific gravity	2.65	ASTM (C128-01) [10]	-
Absorption (%)	2.15	ASTM (C128-01) [10]	-

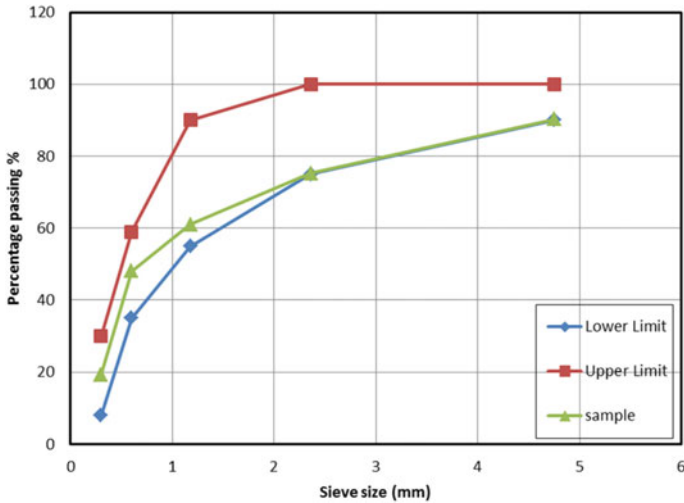


**Fig. 1** Sieve analysis of fine aggregate

**Table 4** Coarse aggregate grading

Sieve diameter-mm (IQS No. 23)	Retained (%)	Accumulative (%)	IQS (No.45-1984)
19.5	0	100	100
12.5	55.5	94.45	90-100
9.5	49.07	50.93	40-70
4.75	90.73	9.27	0-15
2.36	99.99	0.01	0-5

**Table 5** Chemical and physical properties of normal coarse aggregate

Properties	Results	Standards	Limits
Sulfate content-SO <sub>3</sub> (%)	0.029	IQS [9]	Max. (0.1)
Dry unit weight (kg/m <sup>3</sup> )	1595	ASTM (C29-C29M) [11]	-
Specific gravity	2.6	ASTM (C128-01) [10]	-
Absorption (%)	1.12	ASTM (C128-01) [10]	-

**Fig. 2** Micro Silica



**Table 6** Typical properties of Micro Silica

Defined property	Range or description
Color	Grey powder
Availability	Micro powder
Specific gravity	2.1–2.4
Density	500–700 kg/m <sup>3</sup>
Chemical requirements	Minimum 85%
Silicon Dioxide (SiO <sub>2</sub> )	Maximum 3%
Moisture Content (H <sub>2</sub> O)	Maximum 6%
Loos on Ignition (L O I)	
Physical requirements	Minimum 15 m <sup>2</sup> /g
Surface area	Maximum 105% of control
Activity index (Pozzolanic)—7 days	Maximum 10%
% retained on sieve 0.045 mm	

Each fiber is approximately 12 mm in length. Polypropylene is a synthetic hydrocarbon polymer whose fabric is immune to the cement mixture’s alkaline environment without degrading, non-magnetic, rustproof, chemical-inert water absorption (Masterfiber, Masterfiber, and Can, n.d.). The polypropylene fibers with their properties are represented in both Fig. 4 and Table 8 respectively. The main advantage of polypropylene is its melts when exposed to high temperatures and left small cavities in the structure of concrete. This feature allows for trapped water vapor to go out from reactive powder concrete as they very dense materials. the trapped water vapor destroys the concrete under high temperature due to an increase in the internal pressure of vapor.



**Fig. 3** Super-plasticizer

**Table 7** Typical properties of HRWR (MegaFlow 3000)

Defined property	Range or description	Standard
Color	Opaque	–
Form	Fluid	–
Constituent	Distinct	–
Chloride percent	0	BSEN 480–10
Air entrainment	$\geq 1\%$ (control mix)	ASTM C231
Specific weight	ASTM C494	$1.11 \pm 0.02$
pH	5 to 7	ASTM C494

## 2.7 Mix Preparation

Normal Strength Concrete (NSC).

Mixing was done in a blender cylinder with a capacity of  $0.103 \text{ m}^3$ , as shown in Fig. 5. It was important to keep the mixer clean, moist, and free of water before starting process. Coarse with fine aggregates have been placed at the beginning process, after which cement was placed and mixed in a dry state, then the water with sufficient volume has been added to the mixer where the mixing process continues inside the mixer for 5 min to obtain a homogeneous mixture.

Reactive Powder Concrete (RPC).

The route of mixing is crucial to obtain the necessary workability with uniform consistency of the prepared mixes of concrete. The labrotary process of mxing has been completed using a horizontal mixer (pan type with capacity of  $0.103 \text{ m}^3$ ). The



**Fig. 4** Polypropylene fibers**Table 8** Standard polypropylene properties

Modulus of Elasticity (Mpa)	3500–3900
Length of fiber (mm)	12
Diameter of fiber (micron)	18
Density (gm/cm <sup>3</sup> )	0.91
Surface area (m <sup>2</sup> /kg)	230 (min.)
Air entrainment	Obviously retaining air content in concrete
Alkalis %	0
Chloride %	0
Sulfate %	0
Tensile strength (MPa)	350 (min.)
Melting point (°C)	160

required weights of sand (fine particles) were measured in the condition of saturated surface dry state (SSD). The procedure is summarized as follows [14]:

- The sand is placed in the mixer.
- The fibers are slowly added to the used mixer in order not to congregate. The blending of fibers proceeds for almost five minutes.
- Both quantities of cement and micro-silica have been added and blended for five minutes.
- Fifty percent of the required mixing water is applied to the spinning blender for five minutes.
- In the remaining mixing water, the superplasticizer has been liquefied.



**Fig. 5** Mixer used for specimen mixes

- The solvent is applied subsequently and mixed for five minutes in the rotary mixer.

In this study, multiple mix ratios were checked to achieve optimum compressive power according. In the current analysis, ninth RPC mixes were performed as shown in Table 9 to investigate the fresh and hard RPC performance to optimize the best blend. Linear polynomial has been used to model the variation of concrete compressive strength with different W/P. The proposed model can be represented as follows:

$$\sigma'_c = A * (W/P) + B \quad (1)$$

where: A and B are model parameters.

**Table 9** Reactive powder concrete mixtures used for this study

Trail Mix	Cement: Sand	Cement (kg/m <sup>3</sup> )	Sand (kg/m <sup>3</sup> )	Silica fume (kg/m <sup>3</sup> )	W/P	Polypropylene Fibers (V <sub>f</sub> %)	S.P Dosage (kg/m <sup>3</sup> )	Comp. Str. For 28 day (fcu) (MPa)
1	1:1	1091.25	1091.25	121.25	0.20	0.50	18.18	104.0
2	1:1	1091.25	1091.25	121.25	0.22	0.50	18.18	97.1
3	1:1	1091.25	1091.25	121.25	0.24	0.50	12.13	96.8
4	1:1.25	970.2	1347.5	107.8	0.20	0.50	16.17	102.0
5	1:1.25	970.2	1347.5	107.8	0.22	0.50	10.78	97.8
6	1:1.25	970.2	1347.5	107.8	0.24	0.50	10.78	90.0
7	1:1.5	873.0	1455.0	97.0	0.20	0.50	14.55	112.0
8	1:1.5	873.0	1455.0	97.0	0.22	0.50	14.55	101.0
9	1:1.5	873.0	1455.0	97.0	0.24	0.50	9.70	93.0

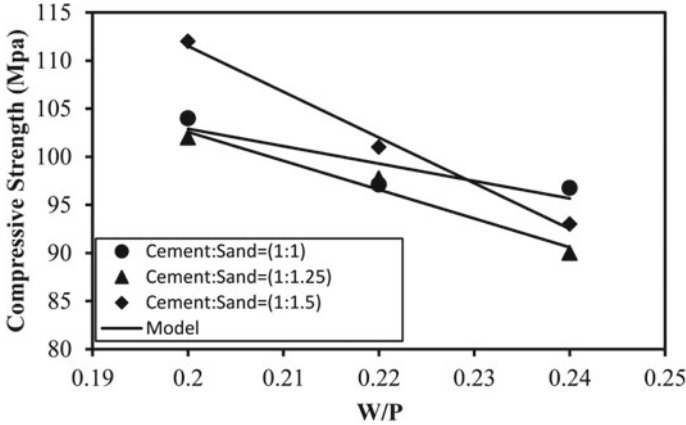


**Fig. 6** The relation of compressive strength with W/P for various ratios of cement to sand

**Table 10** Model parameters for compressive strength versus W/P

Cement: Sand	A	B	R <sup>2</sup>
1:1	-181.25	139.16	0.7871
1:1.25	-300	162.58	0.9724
1:1.5	-475	206.5	0.9918

The modeling for the correlation of concrete compressive strength using various W/P has been shown in Fig. 6. All the linear polynomial model coefficients have been summarized in Table 10. It is noticeably shown that the proposed mathematical model has a good agreement with the experimental data where the R<sup>2</sup> range was from 0.7871 to 0.9918.

The used mix design is utilized for constructing slender columns exposed to fire or high temperatures. Building such a design in the laboratory needs a careful strategy where the details have been explained thoroughly.

### 2.8 Testing Device

The concrete column inspection device consists of a steel frame with a thickness of 20 mm, a length of 2.8 m, and a width of 1.44 m, as shown in Fig. 7.

A temperature measuring device inside the oven with a thermal cable Device type: EXTECH: 4-Channel thermometer/Datalogger Model SDL 200 as shown in Fig. 8.

The dimensions of the firing furnace are 1.40 m long and 1.20 m wide, as shown in Fig. 9.

This oven consists of three basic layers:

- The outer layer is ordinary clay bricks



**Fig. 7** Steel frame



**Fig. 8** Temperature measuring device inside the oven



**Fig. 9** Steel frame and incineration oven

- Ceramic fiber blanket withstands 1260 °C.
- Fire brick withstands 1200 °C.
- A high-pressure gas flame

The bonding material for building fire bricks is gallema sicacllg withstands 1400 °C.

The furnace with the used equipment in the combustion process has been supplied with two small openings to provide sufficient air for the burners. The main objective of

the oven chamber is to continuously increase the temperature for the required period. The burner net is made of single methane gas stoves in length parallel to a single-sided column model. At the age of 28 days, the curing process will be completed, after which, samples will be left for 25 days without treatment, and on the fifty-fifth day, the column samples will undergo a burn. The portion of the concrete sample localized between the edges (middle portion) has a fair face toward the methane stoves. After achieving the burning time for 1, 1.5, and 2 h at temperatures 450, 600, and 750 °C, the gas valve will be closed. Then, the samples will be allowed to cool to an ambient temperature.

### 2.9 Reinforced Concrete Columns

Twenty reinforced concrete columns will be tested using the test rig mentioned before; half of the samples will be constructed using normal concrete and the other by high strength reactive powder concrete. All the specimens have the same cross-section and reinforcing details. The columns are 150 by 150 mm in width and 1600 mm in length. Four bars 10 mm will be used as the main reinforcement, while 6 mm bars will be used as ties.

## 3 Results

The preliminary results of this study have included investigating the effects of abnormal temperatures on the compressive strength of both NSC and RPC samples, as shown in Fig. 10. The studied temperatures varied from 450 °C to 750 °C. It is clearly indicated that the compressive strengths of both NSC and RPC have decreased with increasing temperatures. The RPC has shown greater strength compared to NSC

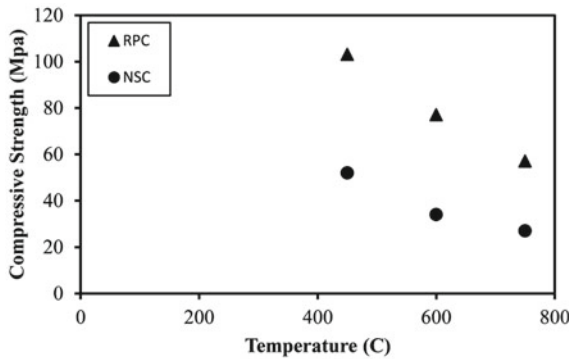


Fig. 10 The relation of the concrete compressive strength with the temperature



Fig. 11 Both tested NSC and RPC samples

at the same corresponding temperatures. As the temperatures increased from 450 °C to 750 °C, the compressive strengths have decreased by 93% and 81% for both NSC and RPC, respectively. The rate of the reduction in the compressive strength in the RPC was lower than the NSC, which makes the RPC more favorable to be used in high-temperature conditions.

Both tested samples of NSC and RPC have been shown in Fig. 11.

A linear polynomial has been used to model the correlation of concrete compressive strength with different temperatures. The proposed model can be represented as follows:

$$\sigma'_c = C * (W/P) + D \tag{2}$$

where: C and D are model parameters.

The modeling for the relation of concrete compressive strength with temperatures has been shown in Fig. 12. Both linear polynomial model coefficients have been summarized in Table 11. It is noticeably shown that the proposed mathematical model has a decent agreement with the experimental data where the R<sup>2</sup> range was from 0.7871 to 0.9918.

Fig. 12 Modeling the relation of the concrete compressive strength with the temperature

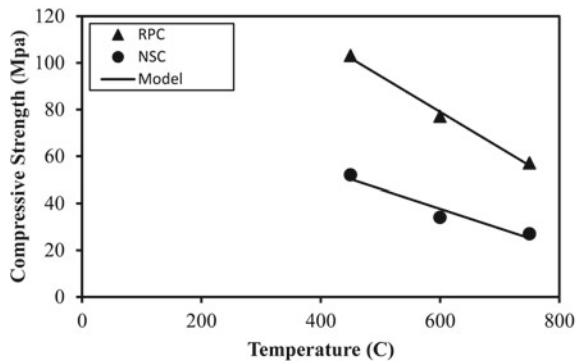


**Table 11** Model parameters for compressive strength versus temperature

Concrete types	C	D	R <sup>2</sup>
NSC	-0.1533	171	0.9944
PRC	-0.0833	87.667	0.9394

## 4 Conclusions

The results of this study have revealed the following conclusions:

1. A linear relationship has been noticed between the concrete compressive strength and W/P, where a linear model has been used to predict such variation with a maximum R<sup>2</sup> of 0.9918.
2. It is clearly showed that the compressive strengths of both NSC and RPC have reduced with increasing temperatures.
3. The RPC has shown greater strength compared to NSC at the same corresponding temperatures.
4. As the temperatures increased from 450 °C to 750 °C, the compressive strengths have decreased by 93% and 81% for both NSC and RPC, respectively.
5. The amount of the decrease in the compressive strength in the RPC was lower than the NSC, which makes the RPC more favorable to be used in high-temperature conditions.
6. A linear relationship has been observed between the concrete compressive strength and temperature, where a linear model has been used to predict such association with a maximum R<sup>2</sup> of 0.9944.

## References

1. Hosny, H., & Abo, E. (1994). *Fire of reinforced concrete structures*. Dar El Nasher For Egyptian University.
2. Cruz, C. R. (1996). Elastic properties of concrete at high temperature. *Journal of PCA Research and Development Lab*, 8(1), 37–45.
3. Dotreppe, J. C., et al. (1997). Experimental research on the determination of the main parameters affecting the behavior of reinforced concrete columns under fire conditions. *Magazine of Concrete Research*, 149, 117–127.
4. Ng Ah Book, Mirza, M. S., & Lie, T. T. (1990). Response of direct models of reinforced concrete columns subjected to fire. *ACI Structural Journal*, 87(3), 313–325.
5. Lin, W.-M., Lin, T. D., & Durrani, A. J. (1996). Microstructure of fire damaged concrete. *ACI Material Journal*, 93(3), 199–205.
6. Mohamed, B. M. (2004). *Behavior of reinforced concrete columns exposed to fire Master of Science, Cairo University, Giza, Egypt*.
7. ACI Committee 216 R,81. (1987). *Fire resistance and fire protection of structure*. American Concrete Institute.
8. Iraqi Specifications No. (5), 1984 for Portland Cement.
9. Iraqi Specification No.5/1984. (2001). *Aggregate from natural sources for concrete and construction*. Central Organization for Standardization and Quality Control, Baghdad, No.5/1984.

10. ASTM C128-15. (2015). *Standard test method for relative density (specific gravity) and absorption of fine aggregate*. ASTM International, West Conshohocken, PA. [www.astm.org](http://www.astm.org).
11. ASTM C29/C29M-17a. (2017). *Standard test method for bulk density ("Unit Weight") and voids in aggregate*. ASTM International, West Conshohocken, PA. [www.astm.org](http://www.astm.org).
12. ASTM C1240-20. (2020). *Standard specification for silica fume used in cementitious mixtures*. ASTM International, West Conshohocken, PA. [www.astm.org](http://www.astm.org).
13. ASTM C494/C494M-19. (2019). *Standard specification for chemical admixtures for concrete*. ASTM International, West Conshohocken, PA. [www.astm.org](http://www.astm.org).
14. ASTM C143/C143M-20. (2020). *Standard test method for slump of hydraulic-cement concrete*. ASTM International, West Conshohocken, PA. [www.astm.org](http://www.astm.org).



# Experimental Investigation of Masonry Arches Strengthened with Carbon Fiber Composites CFRP



Juman E. M. ALTemimi, Abdulmuttalib I. Said, and R. Al-Mahaidi

**Abstract** This study is a part of a full experimental program intended to contribute to the understanding of the structural behavior of masonry arches before and after being strengthened with FRP composite materials. The work involved constructing two sets of masonry arch models and loading them to failure by applying single-point loads at the quarter span. The research presents results and conclusions regarding the structural response, load-carrying capacity improving, and mode of failure for the un-strengthened and strengthened arches. A significant increase of load-carrying capacity was evident for the strengthened arches when compared with un-strengthened arches; the value exceeded the double. The corresponding displacements were evidently affected. The most affected displacements were the displacements corresponding with the upward zone. The upward displacement decreased about five times in the strengthened arches when compared with the displacements of the same locations in the un-strengthened arches. One of the most important results gained was the load–displacement curves which were clearly affected by CFRP applying in values and shapes.

**Keywords** Experimental · Masonry arches · Strengthened · CFRP

## 1 Introduction

Due to their structural advantage, arches were being the fundamental structural elements in the historical buildings and the most efficient to span openings. Conservation of this architectural heritage is a challenging task due to the geometrical complexity and lack of knowledge about their structural behavior. Recently, an

---

J. E. M. ALTemimi (✉) · A. I. Said  
Civil Engineering Department, University of Baghdad, Baghdad, Iraq

A. I. Said  
e-mail: [Dr.AbdulMuttalib.I.Said@coeng.uobaghdad.edu.iq](mailto:Dr.AbdulMuttalib.I.Said@coeng.uobaghdad.edu.iq)

R. Al-Mahaidi  
Swinburne University of Technology, Melbourne, Australia  
e-mail: [ralmahaidi@swin.edu.au](mailto:ralmahaidi@swin.edu.au)

increasing interest in composite fiber materials, commonly known as fiber-reinforced polymers (FRP) has been devote. These materials present several advantages, such as low specific weight, corrosion immunity, and high tensile strength. Their flexibility and ease of application allow a wide range of intervention strategies. In recent years, researches in strengthening or retrofitting of masonry building using composite polymers have evidently increased. Many experimental and theoretical studies were made on a specific element or the building as a whole, using numerous systems of FRP reinforcing [1–16]. The possibility of adopting FRP composites for the strengthening of masonry was initially investigated by Croci et al., who tested wall specimens strengthened with vertical and inclined FRP materials. Schwegler was the first to propose and study the use of carbon laminates (CFRP) as a seismic strengthening element for masonry structures. He demonstrated the effectiveness of this technique through full-scale, both in-plane and out-of-plane, cyclic testing of one-story masonry walls. He developed an analytical model for the in-plane behavior of walls strengthened with CFRP.

Luciano, in his study, investigated the effectiveness of the CFRP reinforcement by performing experimental tests on full-scale unreinforced and reinforced masonry arch made of blocks in dry contact and reinforced by FRP materials arches. All previous studies showed that strengthening arched masonry structures with fiber reinforcement polymers changes the structural behavior and significantly increases the load-bearing capacity. The line of thrust of these compression members moves outside the structure, and additional failure mechanisms would occur. Basilio investigated the effect of the strengthening of masonry with two types of FRP material; glass and carbon fibers. He investigated different locations of strengthening, and good agreement between experimental and theoretical results was obtained. This study is concerned with investigating the response of un-strengthened experimentally and strengthened masonry arches submitted to a single point load at the quarter of the span, with the emphasis on the characterization of the failure modes.

## 2 Materials and Framework

Masonry is an assemblage of two different materials, brick units and mortar. In this work, Resized Iraqi brick tiles of (240 mm × 120 mm × 60 mm) size and ordinary gypsum as mortar were used. Each arch model was built using (15) brick units with mortar joints that have an average of (10 mm) thickness. The arch model has an interior span of (873 mm) and a rise of (323 mm). The dimensions and shape of the arch are illustrated in Fig. 1. The woven SikaWrap-230 °C was used in this experimental study as a reinforcing system. It is composed of carbon fibers impregnated on-site with an epoxy resin of type SikaDur 330. The woven form was chosen because it can be easily set to the curvilinear surface of the masonry arch. On the lateral surfaces, the woven has a thin texture that safeguards the stability of the fiber during the application process, made of thermoplastic material.

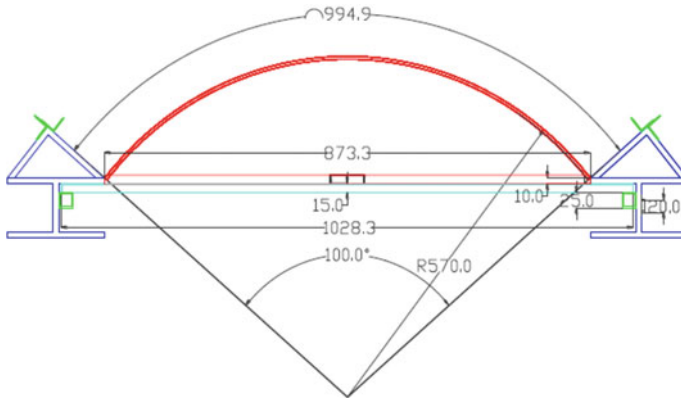


**Fig. 1** Scheme for shape and dimensions of the arch model

Suitable steel frameworks were designed and fabricated to hold the masonry arch model during construction and work as foundation supports or buttresses during testing. The steel framework consists of three main parts. Two supports have the shape of wide-flange, which made of steel plate of 10 mm thickness, with folded inclined cover having the same thickness were considered to provide the angle of slope for both ends of the masonry arch model. Each web contains two slots with two screws to move up and down in it, in order to allow the inside lateral supports to move up and down whenever it is needed. Figure 2 shows a scheme of the frame shape and dimensions.

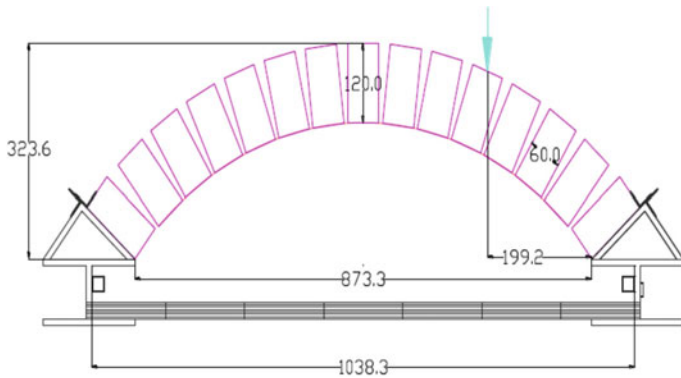


**Fig. 2** Scheme of the framework (all dimensions are in mm)

### 3 Arch Models Construction

The steel frames were cleaned and prepared a day before construction. The curved supporting parts were mapped precisely with the position of each brick unit and mortar joint. Then the curved supporting part was covered with a sheet film of nylon to prevent sticking of the arch being built with the steel frame, Fig. 3. Two arches were built at each time, Fig. 4. One of them was regarded as a controlled arch, while the other was strengthened with a Woven SikaWrap-230CCFRP sheet of (100 mm width) at the extrados using epoxy resin type SikaDur 330 after curing time passed. During the week of primary curing time, the arches were kept in the dry medium at room temperature.

**Arches Testing.** The supported ends were tied up before testing to prevent movements at the ends of the arch. Both arches were tested on the same date.

**Un-strengthened Arch Testing.** The arch was positioned on the carriage of the universal machine so that the load will be applied at the quarter span of the arch.



**Fig. 3** Preparing the supporting frames



**Fig. 4** View of two models

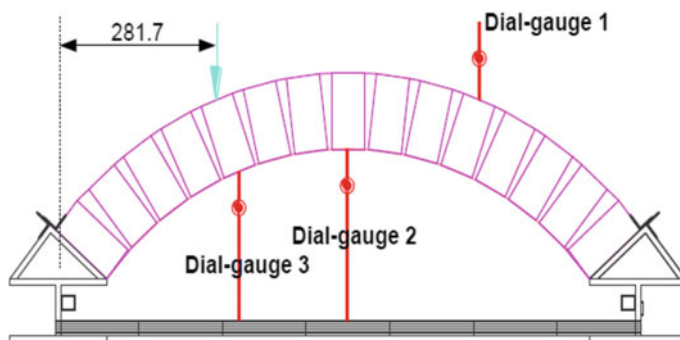


Fig. 5 Scheme of the arch and the dial-gauges positions

To measure the vertical displacements at the critical positions, three-dial gauges were positioned in three locations. One of them was positioned beneath the loaded section to measure the vertical displacement under the load location, the second was positioned under the crown of the arch, and the last was positioned on the extrados at the same distance of force application on the opposite side to determine the upward displacement. The scheme of the arch standing on its steel supports and the dial gauges positions are illustrated in Fig. 5.

## 4 Test Results

The most significant events observed were the formation of the hinge. The first crack appeared between brick No. (5), and the next mortar joint lay under the load location at the intrados to form the first hinge. Gradually the second hinge was formed when the next crack occurred between a brick unit of number (11) and the mortar joint at the extrados on the opposite side of hinge no-1. The third crack occurred between the first brick unit and the mortar joint at the far end from the load location, which was succeeded by the fourth one, which occurred at the other springs between the brick unit and the mortar joints at the nearby end. Forming of hinges was captured by means of photographs. The ultimate load was recorded, and the significant steps are illustrated in Figs. 6, 7, 8, 9, 10 and 11. The load–displacement curve measured at the point underneath the load location is presented in Fig. 12. The load–displacement curve measured at the crown of the arch is presented in Fig. 13.

**Strengthened Arch Testing.** The same procedure presented un-strengthened arch was followed in testing the strengthened arch. The most significant observed event was that there were no hinges or detaching between brick units and mortar joints at low specified load values. The brick units reached cracking and crushing stages as the loading continued to almost twice the failure load value recorded for un-strengthened arch testing. In the beginning, the recorded displacements were relatively small,

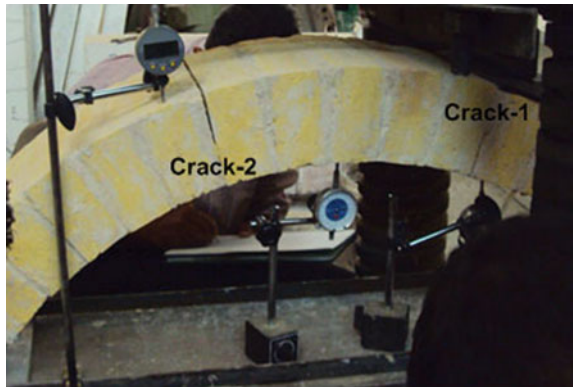


**Fig. 6** The arch model and the dial-gauges positions

**Fig. 7** First crack occurred at the nearest joint to the load location



**Fig. 8** The second crack occurred on the opposite side



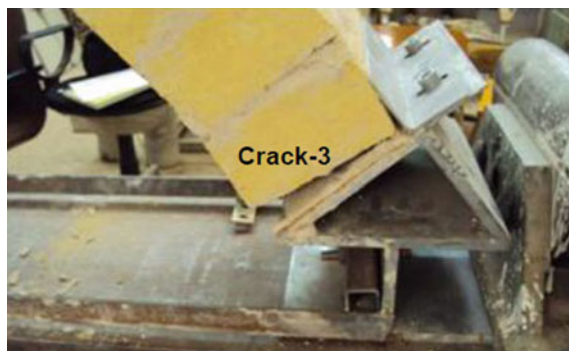


**Fig. 9** Crack 3 occurred at the far end



**Fig. 10** Crack 4 occurred at the nearest end

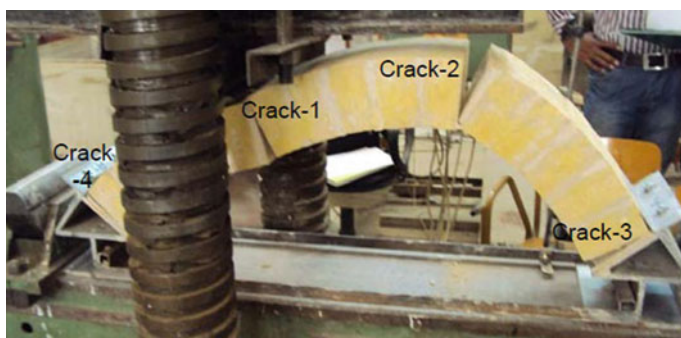


**Fig. 11** Cracks No. 1, No. 2, No. 3, and No. 4

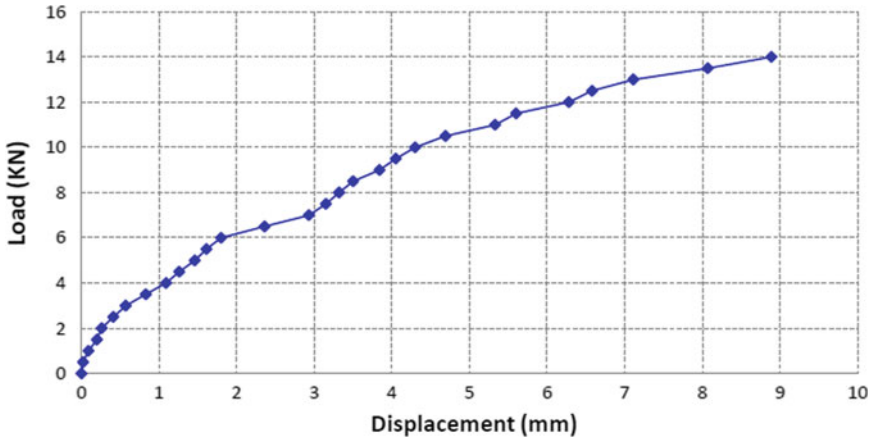


Fig. 12 Un-strengthened arch-1, load–displacement curve for vertical displacement at the point underneath the load location

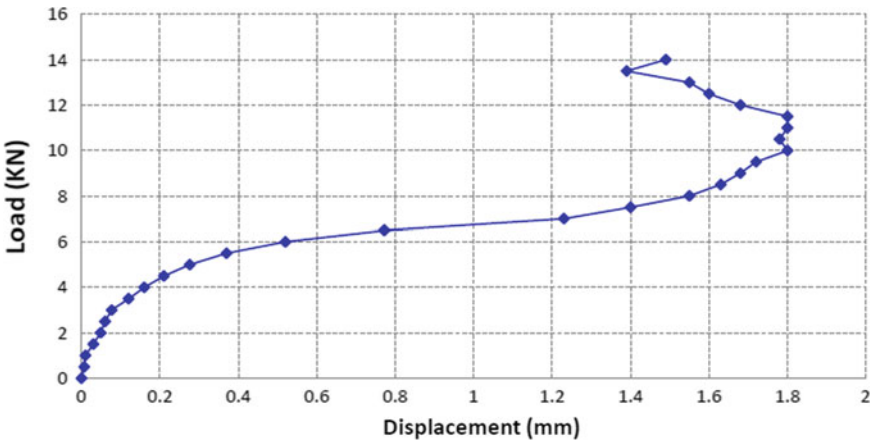


Fig. 13 Un-strengthened arch-1, load-vertical displacement curve at the crown

considering the displacements recorded in the previous test for the un-strengthened arch, especially the upward deflected side. As the load was increasing, the brick units started cracking. The cracking and crushing started in the loading zone, then the cracking spread to the other parts of the arch until it failed with the almost totally crushed model. The ultimate load had been recorded as well as the displacements corresponding to each step of loading. The procedure steps are illustrated in Figs. 14, 15, 16, 17, 18, 19, 20, 21 and 22. The load–displacement curve measured at a point underneath the load location is presented in Fig. 21. The load–displacement curve measured at the crown of the arch is presented in Fig. 22.



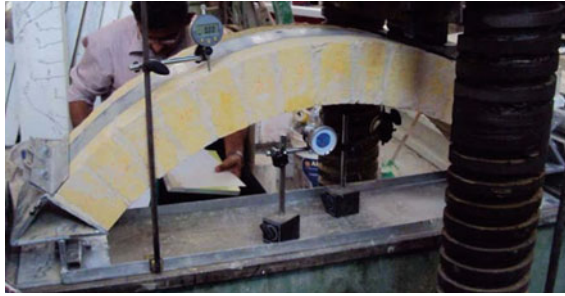


Fig. 14 The strengthened model



Fig. 15 Cracking at far end



Fig. 16 Cracking of bricks and mortar, and starting of detaching

**Collapse Mechanisms.** The behavior of a partial-circular-shaped un-strengthened masonry arch subjected to a concentrate loaded point applied at quarter span is essentially characterized by the formation of the hinges failure mechanism. Photos captured during the test show the localization and the sequence of hinges indicated by an associated number. All hinges detected and reported here were based on visual inspection, and some of them were difficult to detect at the very beginning. Hinges'

**Fig. 17** Cracking and crushing at crown



**Fig. 18** Cracking at the nearby end



**Fig. 19** Cracking and crushing in other parts



positions were the same in both tests, as well as their sequence of formation. For strengthened arches, where the reinforcing CFRP composite strip was continuously applied at extrados, a different collapse mechanism was expected since the presence



Fig. 20 Strengthened arch, material spalling

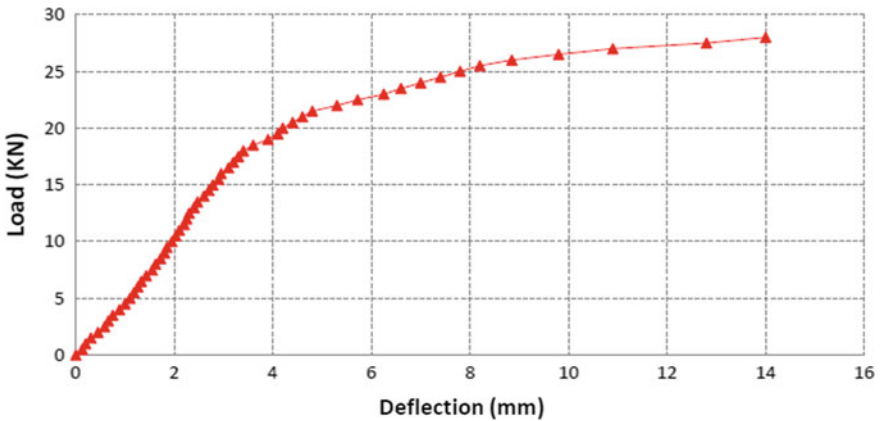
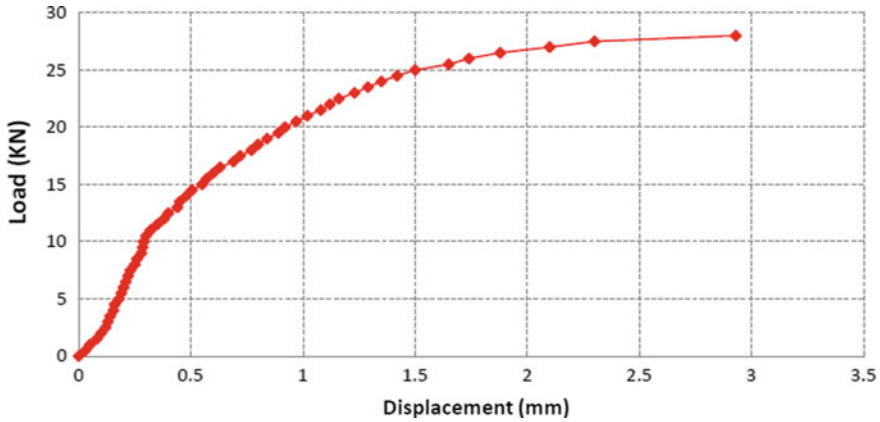


Fig. 21 Strengthened arch-2, load-vertical displacement curve at the point underneath the load location

of the strengthening material would prevent the hinges from occurring. Furthermore, the imparity was clear in terms of the stiffness increasing, deflected shapes, maximum load increasing, displacements at load location and other positions for different loading stages, and changing the failure pattern. Both strengthened arches showed the same structural behavior.

## 5 Summary and Conclusions

A summary of the tested arches results is presented in Table 1, including arch identification, ultimate load, and maximum recorded displacements at sensitive locations.



**Fig. 22** Strengthened arch-2 load-vertical displacement curve at the crown

**Table 1** Summary of tested masonry arches results

Model No	Failure mode	Ultimate load (kN)	Max. vertical displacement underneath load (mm)	Max. vertical displacement at key (mm)	Max. vertical up-ward displacement (mm)
Un-strengthened arch-1	Four hinges formations	14	8.89	1.49	13
Strengthened arch-2	Crushing of brick units and mortar	28	14	2.93	2.13

A significant increase of load-carrying capacity was evident for the strengthened arches when compared with un-strengthened arches; the value exceeded the double. The corresponding displacements were evidently affected. The most affected displacements were the displacements corresponding with the upward zone. The upward displacement decreased about five times in the strengthened arches when compared with the displacements of the same locations in the un-strengthened arches. This is because the CFRP composite strip is continuously applied at extrados, prevent the hinges from occurring, and changing the failure pattern.

One of the most important results gained was the load–displacement curves which were clearly affected by CFRP applying in values and shapes. The Load–displacement curves for position underneath line load were flattered for un-strengthened arches than the strengthened ones, more smooth for strengthened ones. The load–displacement curves of the arch key (crown) were totally different between un-strengthened and strengthened arches in shape as well as in values. Maximum displacements at key increased by (95%) for strengthened arches. These venial increments were due to a change in the whole deflected shape of the arches. The strengthened arches tend to behave as more ductile compared to un-strengthened arches.

**Acknowledgements** This project is supported by the University of Baghdad, College of Engineering, civil engineering department, Iraq, in providing advisory support and optimal research output to achieve this work. The authors gratefully acknowledge the support received from the University of Baghdad, College of Engineering, civil engineering department.

## References

1. Al-Tmimi, J. E. M. (2012). Structural behavior of clay masonry arches strengthened with fiber reinforced polymers FRP. Ph.D. Thesis, Civil Engineering, University of Baghdad.
2. Abdulhameed, A. A., & Said, A. I. (2019). Experimental investigation of the behavior of self-form segmental concrete masonry arches. *Fibers*, 7(7), 58.
3. Abdulhameed, A. A., & Said, A. I. (2020). CFRP laminates reinforcing performance of short-span wedge-blocks segmental beams. *Fibers*, 8(1), 6.
4. Abdulhameed, A. A., & Said, A. I. (2019). Behaviour of segmental concrete beams reinforced by pultruded cfrp plates: An experimental study. *Journal of Engineering*, 25(8), 62–79.
5. Abdulhameed, A. A., & Said, A. M. I. (2020). Systematic Design of Short-Span Segmental beams reinforced by CFRP plates. In *Key engineering materials* (Vol. 857, pp. 130–137). Trans Tech Publications Ltd.
6. Alshethir, A. M. (1994). Parametric study of masonry arches. M.Sc. Thesis, Al-Nahrain University.
7. Basilio, I., Oliveira, D., & Lourenco, P. (2004). Optimal FRP strengthening of masonry arches. In *13th International Brick and Block Masonry Conference Amsterdam*.
8. Basilio, I. (2007). Strengthening of arched masonry structures with composite materials. Ph.D. Thesis, Department of Civil Engineering, University of Minho.
9. Bati, S. B., & Rovero, L. (2001). Experimental validation of a proposed numerical model for the FRP consolidation of masonry arches. In *Proceedings of the 3rd Internatio*.
10. Brick Industry Association. (1995). Technical notes on brick construction: Brick masonry arches. 11490 Commerce Park Drive, Reston, Virginia 20191.
11. Croco, G., Ayala, D., & Asdia, P. (1987). Analysis on shear walls reinforced with fibers. In *IABSE Syrup on Safety and Quality Assurance of Civil Engineering Structures* (pp. 125–132). IABSE, Tokyo.
12. Foraboschi, P. (2004). Strengthening of masonry arches with fiber-reinforced polymer strips. *Journal of Composites for Construction*, 8(3), 191–202.
13. Heyman, J. (1982). The masonry arch. In *Ellis Horwood Series in Engineering Science*.
14. Huerta, S. (2005). The use of simple models in the teaching of the essentials of masonry arch behaviour. In G. Mochi (Ed.), *Theory and practice of construction: Knowledge, means, and models* (pp.747–761). Ravenna.
15. Luciano, R., Marfia, S., & Sacco, E. (2002, June). Reinforcement of masonry arches by FRP materials: Experimental tests and numerical investigations. In *Proceedings of ICCI'02 international conference on FRP composite in infrastructures*, San Francisco, USA.
16. Schwegler, G. (1994, August). Masonry construction strengthened with fiber composites in seismically endangered zones. In *The 10th European Conference on Earthquake Engineering*, Vienna, Austria.

# Mechanical Properties of Normal Strength Concrete Covered with Gypsum Layers and Exposed to High Temperatures (Fire Flame)



Raid S. Warwar and Abdulmuttalib I. Said

**Abstract** The paper presents results of exposure of normal concrete to high temperatures (400 and 700) °C covered by layers (gypsum and Plaster) with different thicknesses (10 and 20) mm. Where the casted specimens for each type of test were divided into three groups, the first was without covering the concrete surface with gypsum, while the second and third groups were covered with gypsum of the outer surface with a thickness of 10 and 20 mm respectively. From the experimental results, it was found that the compressive strength of concrete was improved by using Gypsum layers at 400 °C, the percentage of lost compressive strength was (4 and 6)% at (10 and 20) mm respectively as compared to the reference specimens. As for the temperature of 700, the reduction in compressive strength was about half. The values of modulus of rupture during firing at 400 °C, the deterioration of the concrete not covered with gypsum. The reduction rate was 46% compared to the prism covered with gypsum, where the reduction percentage was (30 and 23)% at (10 and 20) mm respectively. But at high temperatures of 700, the reduction percentage was 70% for non-gypsum-covered concrete and (64 and 46)% at (10 and 20) mm, respectively. Modulus of elasticity was lost about (16 and 11)% at (10 and 20) mm respectively compared to the cylinders not covered with gypsum was the loss rate is about 24%. As for the temperature of 700, the reduction in modulus of elasticity was about (63 and 52 and 43) % at (0, 10, and 20) mm. The results showed that the splitting tensile strength after burning at 400 and 700 °C for one hour and gradually cooled decreased.

**Keywords** Compressive strength · Temperature · Gypsum · Plaster · Fire flame

---

R. S. Warwar (✉) · A. I. Said  
Department of Civil Engineering, University of Baghdad, Baghdad, Iraq

A. I. Said  
e-mail: [Dr.AbdulMuttalib.I.Said@coeng.uobaghdad.edu.iq](mailto:Dr.AbdulMuttalib.I.Said@coeng.uobaghdad.edu.iq)

## 1 Introduction

When designing concrete structures, thermal insulation and fire resistance are taken into account during the design. Therefore, Gypsum is considered one of the construction materials used in fire resistance because it contains the percentage of water in it, which works to reduce the effects of fire in the structure, which contributes as a heat-resistant barrier. When the gypsum is exposed to fire, the water slowly dilutes as vapor, which dampens the heat production. The Gypsum is affected by several factors, the most important of which are: extreme weather conditions, poor or no ventilation, thermal shake, unusual framing or body loading, etc. Precautions shall be taken to prevent these and other adverse provisions. Umran [1] studied the effect of heat on the mechanical properties of concrete. Use three temperature levels (400, 500, and 700) °C with four burning periods (0.5, 1, 1.5, and 2) h without any loads when burning. The samples were burned and cooled under the same conditions and tested after exposure to fire at the age of (30, 60, and 90) days. It was found that the residual compressive strength ranges between (70–80)% at 400 °C, (59–78)% at 500 °C, and (43–62)% at 700 °C.

The modulus of rupture was found to be lower in compressive strength, as they ranged between (67–78) at 400 °C, (40–67) at 500 °C, and (40–45) at 700 °C. Elizzi [20] studied the influence of different temperatures on the compression strength and density of concrete. A 100 mm cubes were heated for about one hour and temperature ranging from 20 to 600 °C and the ages of concrete at heating were 14, 28, and 90 days. The test outcomes indicated that the compression strength decreased 10% from the original strength up to 400 °C, and at 600 °C the strength reduction was 50% from the original. Elizzi [20] noticed that there was a large strength reduction when the specimens heated to a temperature above 400 °C. Also, Elizzi mentioned that the small reduction in density up to 300 °C was a result of the loss of the free water from concrete specimens. At temperature above 300 °C, a large reduction in density took place because of the reduction of water in concrete.

In order to understand and predict the behavior of plaster and gypsum during a fire, it is necessary to know the properties of the materials that determine the behavior of the member at different temperatures. Plaster and gypsum were used to coat the outer surface of the concrete to slow down the heat directly to the surface of the concrete during firing. Compression strength, splitting tensile strength, the elastic modulus, and the modulus of rupture was tested to denote the true values after firing and examination and to be able to predict the fire resistance of the structural member.

## 2 Material Properties

**Mix Proportions.** The ordinary Portland cement was used in the concrete mix of a proposition by weight of (1:1.5:3) for normal strength concrete (cement: sand:

**Table 1** Mix proportions of normal strength concrete

Cement (C) (kg/m <sup>3</sup> )	Sand (S) (kg/m <sup>3</sup> )	Gravel (G) (kg/m <sup>3</sup> )	Water (W) (kg/m <sup>3</sup> )	Water/cement ratio W/C	Mix proportion by weight
400	600	1200	180	0.45	1:1.5:3

gravel). Table 1 gives details about mix proportions in this study, depending on the trial mixes and previous research [3–5].

**Cement.** Ordinary Portland cement (Type I) is used in this work. Tables 2 and 3 show the cement's chemical composition and physical properties throughout the experimental study for normal strength concrete (NSC). Many tests indicate that; the used cement conforms to the Iraqi Specification No. 5/1984 [6].

**Table 2** Chemical composition of the cement<sup>a</sup>

Mineral or property	Abbreviation	Content by weight (%)	Limit of Iraqi specification No. 5/1984 [6]
Lime	CaO	63.11	–
Silica	SiO <sub>2</sub>	20.66	–
Alumina	Al <sub>2</sub> O <sub>3</sub>	5.13	–
Iron oxide	Fe <sub>2</sub> O <sub>3</sub>	3.36	–
Magnesia	MgO	2.32	5.0 (max)
Sulfate	SO <sub>3</sub>	2.05	2.8 (max)
Loss on ignition	L.O.I	2.39	4.0 (max)
Insoluble	I.R	0.68	1.5 (max)
Lime saturation Factor	L.S.F	0.93	(0.66–1.02) %

<sup>a</sup>Chemical analysis is conducted by National Center for Construction Laboratories and Researches

**Table 3** Physical properties of cement used in this study<sup>a</sup>

Physical properties	Test results	Limits of Iraqi specification No. 5/1984 [6]
Specific surface area (Blaine method), (m <sup>2</sup> /kg)	330	230 (min)
Setting time (Vicat's apparatus)	1: 50	0:45 (min)
Initial setting time, (h: min.)	3: 40	10:00 (max)
Final setting time, (h: min.)		
Compressive strength, (MPa)	27.2	15 (min)
3 days	37.4	23 (min)
7 days		
Soundness (Autoclave method), (%)	0.22	0.8 (max)

<sup>a</sup>Physical analysis is conducted by National Center for Construction Laboratories and Researches



**Table 4** Grading of fine aggregate<sup>a</sup>

Sieve size (mm)	Natural sand (for NSC) <sup>a</sup>	
	Cumulative passing (%)	Limits of Iraqi specification No. 45/1984 [7] for Zone 3
10	100	100
4.75	100	90–100
2.36	98	75–100
1.18	88	55–90
0.600	67	35–59
0.300	42	8–30
0.150	27	0–10

<sup>a</sup>All tests were made in the National Center for Construction Laboratories and Research (NCCLR), Baghdad, Iraq

**Table 5** Grading of coarse aggregate<sup>a</sup>

Sieve size (mm)	Cumulative passing (%)	Limit of Iraq specification No. 45/1984 [7] for size 14
14	100	100
10	80	85–100
5	3	0–25
2.36	–	0–5

<sup>a</sup>All tests were made in the National Center for Construction Laboratories and Research (NCCLR), Baghdad, Iraq

**Fine Aggregate.** Natural sand is selected and used for the NSC mix. Table 4 shows details about grading. Results indicate is within the requirement of the Iraqi Standard Specification No. 45/1984 [7].

**Coarse Aggregate.** Crushed river gravel with a maximum particle size of 14 mm is prepared and used as coarse aggregate for NSC mix. The grading of the used coarse aggregate is shown in Table 5. The coarse aggregate grading excepts the Iraqi Standard Specification No. 45/21984 [7].

### 3 Concrete Mixer

The concrete is mixed by using a central fender for model molding.

**Mixing Procedure.** All quantities are weighed and packed in a clean container, and the molds are oiled one day before casting. Control specimens were prepared for obtaining the mechanical properties of the hardened concrete. Control specimens

involve 27 cubes, 27 cylinders (150 × 300) mm for splitting tensile strength, 27 cylinders (150 × 300) mm for modulus of elasticity, and 27 prisms (100 × 100 × 400) mm for modulus of rupture.

**Gypsum and Plaster Procedure.** Local Iraqi gypsum (Juss) was used in this study. The consistency and the setting time were measured following the IQS NO. 27 [8] and IQS NO.28 [9] standard. In this study, gypsum was used to make finishes of cubes, cylinders, and prisms, simulating the practical reality with thicknesses of (10 and 20) mm, as well as the use of Plaster material for the same purpose above. In addition, Gypsum and Plaster finishes were applied to the mechanical properties of concrete. Below are the stages of using gypsum and plaster in Fig. 1.

**Exposing to Fire Flam Test.** The furnace was manufactured by using a 3 mm thick steel plate just like a rectangular shape to burn one specimen each time, as shown in Fig. 2. The clear inner space was 1500 mm height by 2500 mm width and 3000 mm length. Two of each group were subjected to burning, one of them at 400 °C temperature and the second at 700 °C. This talk applies to burning cubes, cylinders, and prisms according to the gypsum’s thickness, the plaster, and the temperature. The firing stage was carried out in steps that are placing in the oven the specimens that



Fig. 1 The specimens covering with gypsum and plaster



Fig. 2 Furnace of burning test stage



**Fig. 3** Thermometer and thermocouple

are burned at 400 °C temperature with the cubes, cylinders, and prisms were placed and then subjected to burning for an hour with the oven covered to ensure that the firing uniformity was distributed evenly over the whole specimen where it was not exposed. The samples are transferred directly to the flame after that, a temperature is measured every 10 min to achieve specification ASTM-E-119 [19]. Note that the temperature was measured with a thermometer and a thermocouple.

## 4 Temperature Measurements

At the first test stage (burning stag), a thermometer K-type was available with dual inputs was used to measured temperature with respect to time. It also offers a wide range of K-type probes and data logging features across the range. A K-type device appropriate with different kinds of the thermocouple. A thermocouple is a temperature measuring instrument made up of non-identical metals. The metals are welded on the tip to form what is known as the thermocouple junction. The most common thermocouple junction is type K, providing the widest operating temperature range of 1400 °C. There is a selection of other probe kinds appropriate for various applications. The thermometer with the thermocouple is shown in Fig. 3.

## 5 Mechanical Properties Test

**Compressive Strength Test.** Standard (150 × 150) mm cube is used according to (ASTM C39-01) [10] for using a compression machine of 3000 kN capacity, as shown in Fig. 4. cube compressive strength test is performed in accordance with ASTM C39, respectively. An average of three specimens is used to determine the compressive strength.



Fig. 4 Compressive strength test



Fig. 5 Splitting tensile strength test

**Splitting Tensile Strength Test.** The splitting tensile strength test was performed according to ASTM C496-04 [11] on a (150 × 300) mm cylinder and using a 3000 kN capacity testing machine, as shown in Fig. 5. The following expression had calculated the splitting tensile strength values:

$$f_{sp} = \frac{2P}{\pi dL} \tag{1}$$

where:  $f_{sp}$  = splitting tensile strength (MPa),  $P$  = maximum applied load (N),  $d$  = diameter of the cylinder (mm),  $L$  = length of the cylinder (mm). The average of three specimens is used to determine the splitting tensile strength.

**Static Modulus of Elasticity Test.** According to ASTM C469-02 [12], the modulus of elasticity test is performed on (150 × 300) mm cylinder loaded uniaxial using a universal testing machine MFL of 3000 kN capacity with the strain-measuring equipment attached to the cylinder. The modulus of elasticity for each specimen is calculated, as follows:

$$E_c = (S_2 - S_1)/(\epsilon_2 - 0.00005) \tag{2}$$



**Fig. 6** Modulus of rupture test

where:  $E_c$  = chord modulus of elasticity (MPa),  $S_2$  = stress corresponding to 40% of the ultimate load (MPa),  $S_1$  = stress corresponding to a longitudinal strain, (0.00005) (MPa),  $\epsilon_2$  = longitudinal strain produced by stress  $S_2$ . To determine the modulus of elasticity for the mix, an average of three specimens is used.

## 6 Modulus of Rupture Test

The flexural strength (modulus of rupture) test was performed according to ASTM C 78-02 [13] on prismatic specimens of (100 × 100 × 400) mm with two-point loading by using a hydraulic testing machine (ELE) of 50 kN capacity, as shown in Fig. 6. The modulus of rupture is calculated as follows:

$$f_r = \frac{PL}{bh^2} \quad (3)$$

where:  $f_r$  = modulus of rupture (MPa),  $P$  = maximum applied load (N),  $b$  = width of prism (mm),  $h$  = depth of prism (mm),  $L$  = span length of prism (mm). An average of three specimens is used to determine the flexural strength of the NSC mixer.

## 7 Compressive Strength Results

Saad et al. [14], Koksal et al. [15], and Hager [16] revealed that the behavior of concrete that had been subjected to high temperature was affected by many factors. These include the following: time of exposure, rise rate of temperature, the maximum temperature will reach its concrete mass, the initial concrete temperature before the exposure to the high temperature (Fire Flame), the amount of water saturation of the concrete, the maturity of concrete, aggregate and cement type used, aggregate/cement ratio, and loading status at of exposure time. In general, for mature concrete, an increase in exposed temperature (Fire Flame) leads to a gradual loss in concrete mechanical strength. The control specimens (cubes of 150 mm) for compressive

strength testing were left 24 h after casting and then stored in a water tank for a few days. After 28 days, these specimens were covering by Gypsum with different thicknesses (10 and 20) mm with reference specimens. After that, the specimens were exposed to the same burning circumstances of the duration and the elevated temperature as that of the reinforced concrete members. When the target temperature was reached, the maximum temperature was kept for one hour (ASTM-E-119); after that, the specimens were gradually cooled to the ambient temperature. The residual compressive strength results after exposure to 400 and 700 °C temperatures are given in Table 6 and Fig. 7.

The results showed a simple difference when the concrete was exposed at a temperature of 400 after covering the concrete cubes using layers of gypsum of different thicknesses. A 10 and 20 mm thickness, the compressive strength loss was about 6% and 4%, respectively, compared to the cubes not covered with gypsum. The loss rate is about 22%, and this is clear evidence of the benefit of gypsum in reducing the temperature directly to concrete. As for the temperature of 700, the reduction in compressive strength was about half due to the gypsum's inability to withstand high temperatures, as it spalling after the high temperatures.

## 8 Modulus of Rupture ( $f_r$ )

The residual  $f_r$  results after exposure to 400 and 700 °C temperatures are given in Table 7 and Fig. 8. The results showed that the values of  $f_r$  decrease as the temperature increased, during firing with a temperature of 400 °C, the deterioration of the concrete not covered with Gypsum, where the reduction rate was 46% compared to the prism covered with Gypsum while the reduction percentage was 30% and 23% with thicknesses of 10 mm and 20 mm respectively. But at high temperatures of 700 showed a rapid deterioration of concrete. The reduction percentage was 70% for non-gypsum-covered concrete and (64 and 46%) for concrete covered with a thickness of 10 and 20 mm with gypsum respectively.

## 9 Modulus of Elasticity ( $E_c$ )

Test results are summarized in Table 8. This table reveals the residual ratio of  $E_c$  for each gypsum thickness compared to its unburned specimen; it can be observed that increasing temperature led to a decrease in the ratio of residual value of  $E_c$ . Figure 9 illustrates the relationship between the residual elastic modulus and the fire flame temperatures. The residual modulus of elasticity results after exposure to 400 and 700 °C temperatures; we noticed the clear difference in the results when the concrete was exposed at a temperature of 400 after covering the concrete cylinders using layers of gypsum of different thicknesses. At thickness 10 and 20 mm, the  $E_c$  loss was about 16% and 11%, respectively, compared to the cylinders not covered with gypsum. The

**Table 6** Effect of fire flame on compressive strength<sup>c</sup>

Gypsum thickness (t)	$f_c$ (MPa) <sup>c</sup>			Residual strength %			Compressive strength (MPa)	Residual strength (%) [17]
	t <sup>a</sup> = 0	t = 10	t = 20	t = 0	t = 10	t = 20		
Temperature (°C)	Ambient	24.6	24.78	100	100	100	t = 0	t = 0
	400	22.7	23.88	77.39	92.27	96.36	25	100
	700	12.1	12.44	13.66	49.28	50.56	21.34	85.36
							10.35	41.4

<sup>a</sup>Gypsum thickness, <sup>b</sup>Average of three cylinders of dimension (150 × 300) mm, <sup>c</sup>The results are taken from tasting the cubes, and the results have been divided according to European Standard 0.81

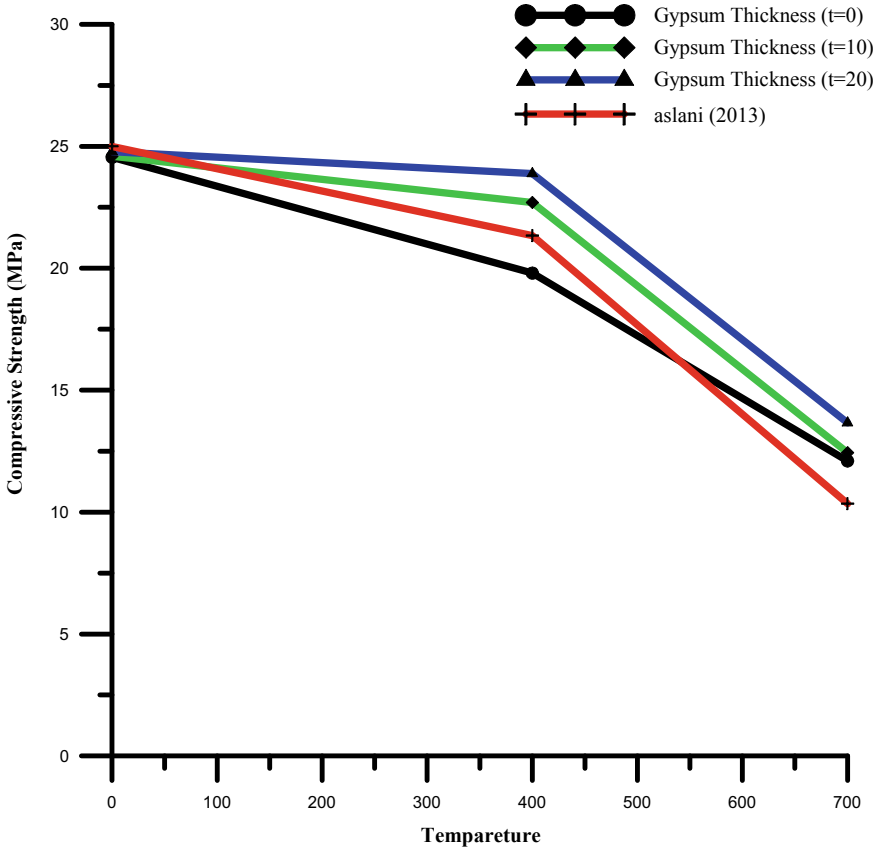


Fig. 7 Burning temperature versus compressive strength with different gypsum thickness

Table 7 Effect of fire flame on modulus of rupture<sup>b</sup>

Gypsum thickness (mm)		f <sub>r</sub> (MPa)			Residual strength %		
		t <sup>a</sup> = 0	t = 10	t = 20	t = 0	t = 10	t = 20
Temperature (°C)	Ambient	3.06	3.015	3.075	100	100	100
	400	1.65	2.1	2.22	53.9	69.6	72.1
	700	0.9	1.11	1.71	29.4	36.8	55.6

<sup>a</sup>Gypsum thickness, <sup>b</sup>Average of three cylinders of dimension (150 × 300) mm

loss rate is about 24%, and this is clear evidence of the benefit of gypsum in reducing the temperature directly to concrete. As for the temperature of 700, the reduction in E<sub>c</sub> was about 63, 52, and 43% at 0, 10, 20 mm gypsum thickness due to the gypsum’s inability to withstand high temperatures. The low modulus of concrete elasticity can



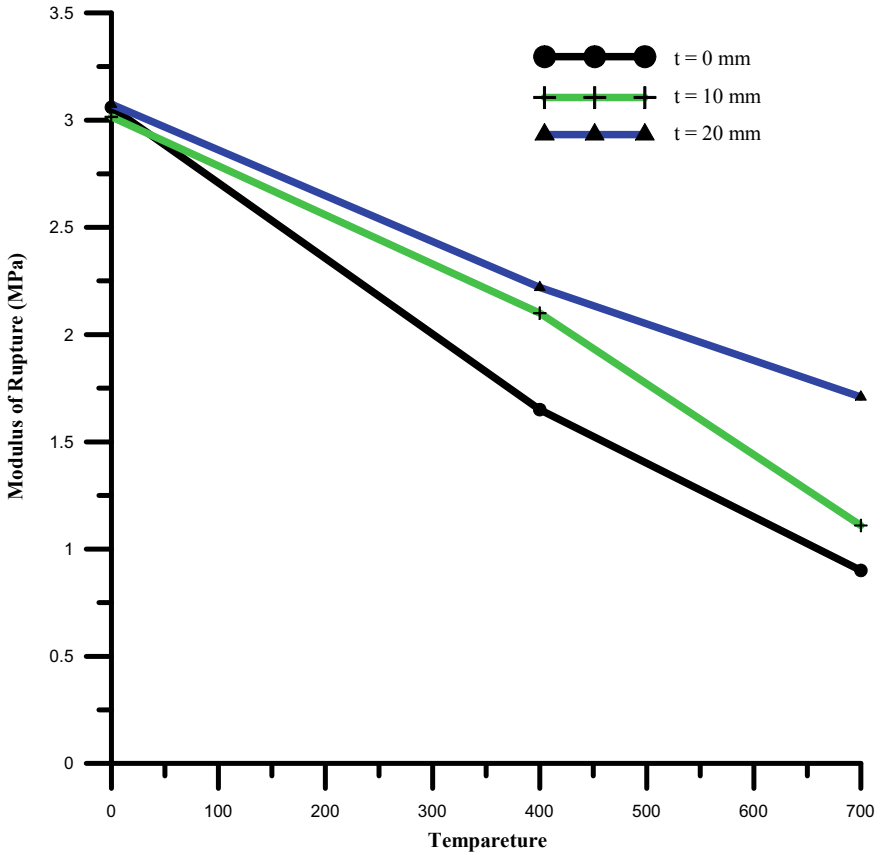


Fig. 8 Burning temperature versus flexural strength with different gypsum thickness

be referred to as the increase in the quantity of microcracks formation caused by exposure to fire, and the physical–chemical changes in concrete components during burning will result in loss of yield strength. The reduction calculations for modulus of elasticity depending on the equations proposed by Aslani [17]. The proposed reduction values are illustrated in Table 8 with that of the experimental work. It is clear that there is good agreement between them.

### 10 Splitting Tensile Strength ( $f_{sp.}$ )

The outcomes for splitting tensile strength are given in Table 9. The results showed that the splitting tensile strength after burning at 400 and 700 °C for one hour and gradually cooled decreased and the residual tensile strength was approximate. The

**Table 8** Effect of fire flame on modulus of elasticity<sup>b</sup>

Gypsum thickness (mm)	E <sub>c</sub> (MPa)				Residual strength (%)			E <sub>c</sub> (Mpa) [17]	Residual strength (%) [17]
	t <sup>a</sup> = 0	t = 10	t = 20	t = 20	t = 0	t = 10	t = 20		
Temperature (°C)	Ambient	23,175.5	23,205.2	23,321.4	100	100	100	23,500	100
	400	17,421.8	19,312.5	20,682.9	75.2	83.2	88.7	18,215.9	77.5
	700	8711.6	11,306.7	12,337.9	37.6	48.8	52.9	9594.6	40.8

<sup>a</sup>Gypsum thickness, <sup>b</sup> Average of three cylinders of dimension (150 × 300) mm

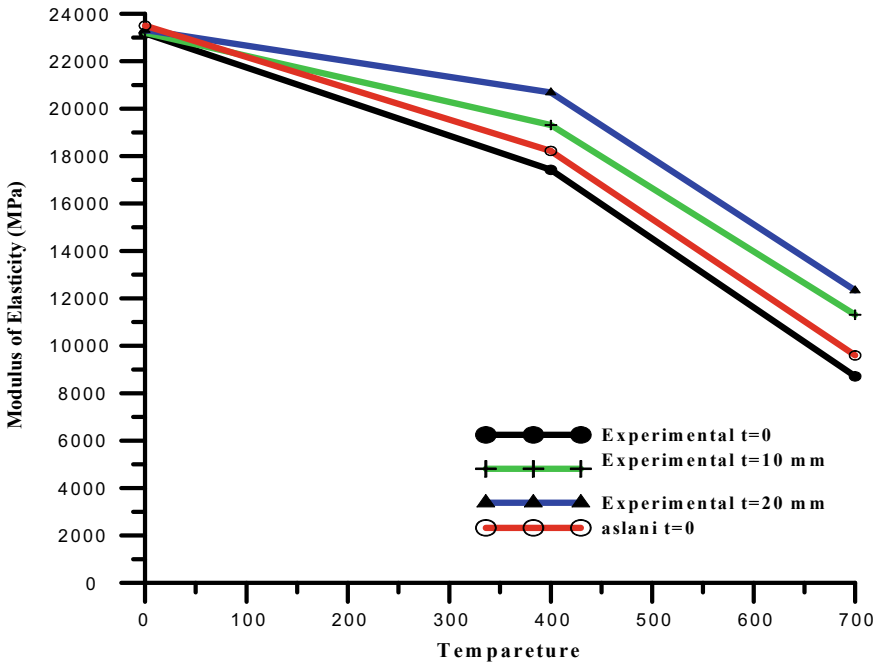


Fig. 9 Burning temperature versus modulus of elasticity with different gypsum thickness

Table 9 Effect of fire flame on splitting test<sup>b</sup>

Gypsum thickness (mm)		f <sub>sp</sub> (MPa)			Residual strength (%)		
		t <sup>a</sup> = 0	t = 10	t = 20	t = 0	t = 10	t = 20
Temperature (°C)	Ambient	3.99	4.02	4.2	100	100	100
	400	3.1	3.87	3.93	77.6	96.3	93.5
	700	1.3	2.05	2.7	32.5	50.9	64.2

<sup>a</sup>Gypsum thickness, <sup>b</sup>Average of three cylinders of dimension (150 × 300) mm

results indicate that concrete’s tensile strength was more sensitive to high temperature than compressive strength [18].

## 11 Conclusion

Through experimental results and comparison with researchers, it notes the following:

- Increasing the thickness of the concrete surface with gypsum helps reduce the direct heat transfer to the concrete and thus reduces the loss of compressive strength. Through 400 °C, the percentage of lost resistance was 6%, and 4% at 10, 20 mm respectively as compared to the reference specimens. As for the temperature of 700, the reduction in compressive strength was about half due to the gypsum's inability to withstand high temperatures, as it spalling after the high temperatures.
- The flexural strength decreases as the temperature increased. At a temperature of 400 °C, the percentage of lost resistance was 30%, and 23% at 10, 20 mm respectively as compared to the reference specimens was 46%. At high temperatures of 700, they notice a rapid deterioration of concrete. The reduction percentage was 70% for non-gypsum covered concrete and (64 and 46%) for concrete covered with a thickness of 10 and 20 mm with gypsum respectively
- Modulus of Elasticity decrease as the temperature increased, through 400 °C, the percentage of lost resistance was 16%, and 11% at 10, 20 mm respectively as compared to the reference specimens was 24% at high temperatures of 700, The reduction percentage was 63% for non-gypsum covered concrete and 52% and 43% for concrete covered with a thickness of 10, 20 mm with gypsum respectively
- The splitting tensile strength after burning at 400 and 700 °C for one hour and gradually cooled decreased and the residual tensile strength was approximately 40%.

**Acknowledgements** This project is supported by the Roads and Bridges Directorate, Ministry of Construction and Housing and Municipalities and Public Works, Iraq, in providing advisory support and optimal research output to achieve this work. The authors gratefully acknowledge the support received from the Roads and Bridges Directorate.

## References

1. Umran, M. K. (2002). Fire flame exposure effect on some mechanical properties of concrete (p. 103). M.Sc. Thesis, College of Engineering, Babylon University, October 2002.
2. Elizzi, A. (1987). Effect of different temperatures on the compressive strength and density of concrete. *Building Research Magazine*, 6(2), 1–23.
3. Sarsam, K. F., & Mohammed, M. H. (2014). Flexural strength of hybrid beams containing reactive powder concrete and conventional concrete. *Journal of Engineering and Development*, 18(5), 61–91.
4. AL- Saraj, W. K. (2013). Structural behavior of reinforced reactive powder concrete T-beams under pure torsion. Ph.D. thesis, University of Mustansiriayah, Iraq.
5. Al-Shafii, N. T. H. (2013). Shear behaviour of reactive powder concrete T-beams. Ph.D. thesis, University of Mustansiriayah, Iraq.
6. Iraqi Specification, No. 5. (1984). Portland cement. (Translator from Arabic).
7. Iraqi Specification, No. 45. (1984). Aggregate from natural sources for concrete and construction (p. 320). (Translated from Arabic).
8. Iraqi Specification. (1988). Physical examinations of Juss for construction. Central Organization for Standardization and Quality Control No. 27.

9. Iraqi Specification, No. 28. (2010). Juss for construction. Central Organization for Standardization and Quality Control.
10. ASTM C39. (2001). Standard test method for compressive strength of cylindrical concrete specimens (p. 5).
11. ASTM C496. (2004). Standard test method for splitting tensile strength of cylindrical concrete specimens (p. 5).
12. ASTM C469. (2002). Standard test method for static modulus of elasticity and Poisson's ratio of concrete in compression (p. 5).
13. ASTM C78. (2002). Standard test method for flexural strength of concrete (using simple beam with two points loading). Annual Book of ASTM Standard.
14. Thienel, K. C., & Rostasy, F. (1996). Transient creep of concrete under biaxial stress and high temperature. *Cement and Concrete Research*, 26, 1409–1422.
15. Koksai, F., Gencel, O., Brostow, W., & Lobland, H. H. (2012). Effect of high temperature on mechanical and physical properties of lightweight cement based refractory including expanded vermiculite. *Materials Research Innovations*, 16, 7–13.
16. Hager, I. (2013). Behaviour of cement concrete at high temperature. *Bulletin of the Polish Academy of Sciences: Technical Sciences*, 61, 145–154.
17. Aslani, F. (2013). Prestressed concrete thermal behaviour. *Magazine of Concrete Research*, 65(3), 158–171.
18. Obeed, A. T. (2007). Effect of exposure to fire flame on some mechanical properties of self-compacting concrete using different types of filler. M.Sc. Thesis, College of Engineering, University of Babylon.
19. ASTM E-119. (2017). Standard test methods for fire tests of building construction and materials.
20. Wang, Z. H., & Tan, K. H. (2006). Residual area method for heat transfer analysis of concrete-encased I-sections in fire. *Engineering Structures*, 28, 411–422.

# Performance of Self-compacting Geopolymer Concrete with and Without Portland Cement at Ambient Temperature



Alaa Mohammedameen, Khaleel H. Younis, Radhwan Alzebaree, Mohamed Moafak Arbili, and Talib K. Ibrahim

**Abstract** The self-compacting geopolymer concrete (SCGC) characteristics with binary and ternary binder materials were studied via experimental data research. Binary and ternary use of fly ash (FA) and ground granulated blast furnace slag (GGBFS) with and without Portland cement (PC) have been studied in the production of SCGC. Therefore, a total of seven SCGC mixes were proportioned, having binder amount of  $500 \text{ kg/m}^3$  and a constant ratio (0.5) of alkali–binder. The reference mix included 50% GGBFS and 50% FA as the binder, whereas the other mixtures having binary and ternary mixtures of Portland cement (PC), fly ash (FA). The fresh and hardened characteristics were conducted. The results demonstrated that the utilization of GGBFS affected the fresh properties of SCGC negatively. However, it has a superior influence on the compressive strength of SCGC. Also, the incorporation of PC up to 20% affected the fresh characteristic adversely; however, the use of PC up to 20% has a positive impact on the compressive strength of the SCGC specimens.

**Keywords** Self-compacting geopolymer concrete · Blast furnace slag · Fly ash · Portland cement

---

A. Mohammedameen · R. Alzebaree (✉)  
Department of Civil Engineering, Duhok Polytechnic University, Duhok, Iraq  
e-mail: [radhwan.alzebaree@dpu.edu.krd](mailto:radhwan.alzebaree@dpu.edu.krd)

A. Mohammedameen  
e-mail: [alaa.mohammedameen@dpu.edu.krd](mailto:alaa.mohammedameen@dpu.edu.krd)

Architecture Department, Nawroz University, Duhok, Iraq

K. H. Younis · M. M. Arbili  
Erbil Technology College, Erbil Polytechnic University, Erbil, Iraq  
e-mail: [khaleel.younis@epu.edu.iq](mailto:khaleel.younis@epu.edu.iq)

M. M. Arbili  
e-mail: [mohamed.arbili@epu.edu.iq](mailto:mohamed.arbili@epu.edu.iq)

K. H. Younis  
Civil Engineering Department, Tishk International University, Erbil, Iraq

T. K. Ibrahim  
Department of Environment Engineering, Knowledge University, Erbil, Iraq  
e-mail: [talib.ibrahim@knowledge.edu.krd](mailto:talib.ibrahim@knowledge.edu.krd)

## 1 Introduction

Geopolymer concrete is an eco-friendly material that performs well in hardened condition. Furthermore, it uses less energy in the manufacturing state and emits less carbon dioxide [1]. Geopolymers are an inorganic substance that has become a promising solution for OPC [2]. FA-based geopolymer concrete, in particular, can be applied as an alternative to cement and reduce the hazardous and toxic materials significantly. In the concrete industry, FA-based geopolymer concrete's performance efficiency is the main concern [3]. In addition, to fly ash, raw materials for geopolymer processing included phosphate sludge [4], waste glass powder [2], and red mud [5]. Waste materials such as silica fume and GGBFS have been used to alternate FA-based GPC in the literature [2]. According to the reports, the most commonly used geopolymer concrete is FA-based, and slag can be used as a partial substitute for GPC to replace OPC. Therefore, many types of research on geopolymer concrete are required. Self-compacting concrete (SCC) is commonly utilized in civil engineering structures, especially in structures requiring congested reinforcement and precast industries and high-rise buildings [6]. SCC's main characteristics are flowability, passing ability, and filling without segregation or bleeding. SCGC is a new development in the concrete industry. It's a kind of innovative concrete that incorporates the advantages of both SCC and geopolymer [7–9].

There have been very few studies on SCGC. As with traditional SCC, more study is essential to determine the behavior of SCGC for potential use. Mineral fillers are utilized in concrete (OPC, SCC, GC, and SCGC) to minimize costs, increase workability, and improve the hardened state's properties [10–13]. Because of the increased mechanical efficiency and benefits to the climate and economy, fly ash and GGBFS have been widely used as cementitious materials in the literature [14–16]. GGBFS and fly ash exhibits positive contributions to the mechanical characteristic of concrete, economy, and eco-friendly environment materials [17–20]. The ratio of silica/aluminum has a major effect on the strength and mechanical efficiency of GPC, and this ratio is primarily determined by the concentration of the alkali solution, curing temperature and time, and the chemical composition of the binder content [21, 22]. According to the researcher, not all of the silica and aluminum ions in the geopolymer binder are reactive. They also observed that using separate fly ashes, the mixture had a comparable percentage of silica reactive but a different percentage of aluminum reactive in the material [21, 22]. The use of GGBFS and FA in SCC has also been studied previously, and it has begun to be used more frequently as SCC efficiency has improved. The literature on the performance of GGBFS/FA-based SCGC is, however, limited. Owing to a lack of experience in geopolymer concrete substance characterization, geopolymer concretes are not found in structural construction standards or implementations. More research is required to enhance our understanding of the SCGC's fresh and mechanical properties. As a result, this research aims to see how binary and ternary blends of GGBFS and FA with a PC ratio affect the development of SCGC.

## 2 Methodology

**Materials.** To investigate the effects of GGBFS and PC together on the behavior of SCGC, seven types of SCGC mixes were manufactured, each with a different ratio of GGBFS (50%, 60%, 70%, 80%, and 100%) with and without PC (10%, and 20%). FA, Type F-based ASTM C618 was used as binder materials [23]. The mixtures were made with a PC CEM I 42.5R cement, which corresponded to ASTM C311 [24]. A total of seven different SCGC mixtures with a binder amount of  $500 \text{ kg/m}^3$  and a constant ratio of alkali/binder (0.5) were proportioned. The binder in the control mixture was 50% FA-50% GGBFS, whereas the other mixtures were a mix of GGBFS, FA, and PC. The influences of GGBFS and/or PC on SCGC properties were explored based on the test results. The PC, FA, and GGBFS were obtained from a local supplier in Erbil, Iraq. The properties of FA, GGBFS, and PC are shown in Table 1. The fine aggregate was local crushed sand brought from Harir area near Erbil City-Iraq. It had a maximum size of 4.0 mm. The crushed coarse aggregate was brought from the same area [25]. Table 2 illustrates the properties of aggregates according to the ASTM C33 [25]. The alkali activator is a mixture of sodium silicate ( $\text{Na}_2\text{SiO}_3$ ) and sodium hydroxide (NaOH) solutions. The  $\text{Na}_2\text{SiO}_3$  was gotten from a local supplier in Erbil, Iraq [26]. The NaOH had 97–98% purity and used at a 12 molar concentration, which was found to be the best concentration for SCGC mechanical efficiency [27]. A polycarboxylate was used as a superplasticizer to attain high-flowability without bleeding and/or segregation [26]. Figure 1 shows the materials used in the production of SCGC mixes.

**Mix Design.** A constant binder amount of  $500 \text{ kg/m}^3$  was used to create different series of SCGC mixtures. By weight, the mixtures binder 50% GGBFS and 50%

**Table 1** The properties of FA, GGBFS and PC

Component	CaO	SiO <sub>2</sub>	Al <sub>2</sub> O <sub>3</sub>	Fe <sub>2</sub> O <sub>3</sub>	MgO	SO <sub>3</sub>	K <sub>2</sub> O	Na <sub>2</sub> O	LOI	SG	BF (m <sup>2</sup> /kg)
PC (%)	65.58	20.825	5.31	4.04	2.82	2.73	0.92	0.22	3.02	3.15	326
FA (%)	1.59	62.34	21.13	7.16	2.39	0.11	3.38	0.37	1.57	2.29	378
GGBFS (%)	34.13	36.42	11.38	1.68	10.29	0.48	3.64	0.36	1.63	2.78	419

LOI: Loss on ignition; SG: Specific gravity ( $\text{kg/m}^3$ ); BF: Blaine fineness ( $\text{m}^2/\text{kg}$ )

**Table 2** The sieve analysis and physical properties of aggregates

Sieve size (mm)	16	8	4	2	1	0.5	0.25	Fineness modules	SG	Absorption
Fine aggregate	100	100	100	67.3	39.9	28.4	16.4	2.57	2.45	1.5
Coarse aggregate	100	31.5	1	0.5	0.5	0.5	0.4	5.66	2.72	2.4



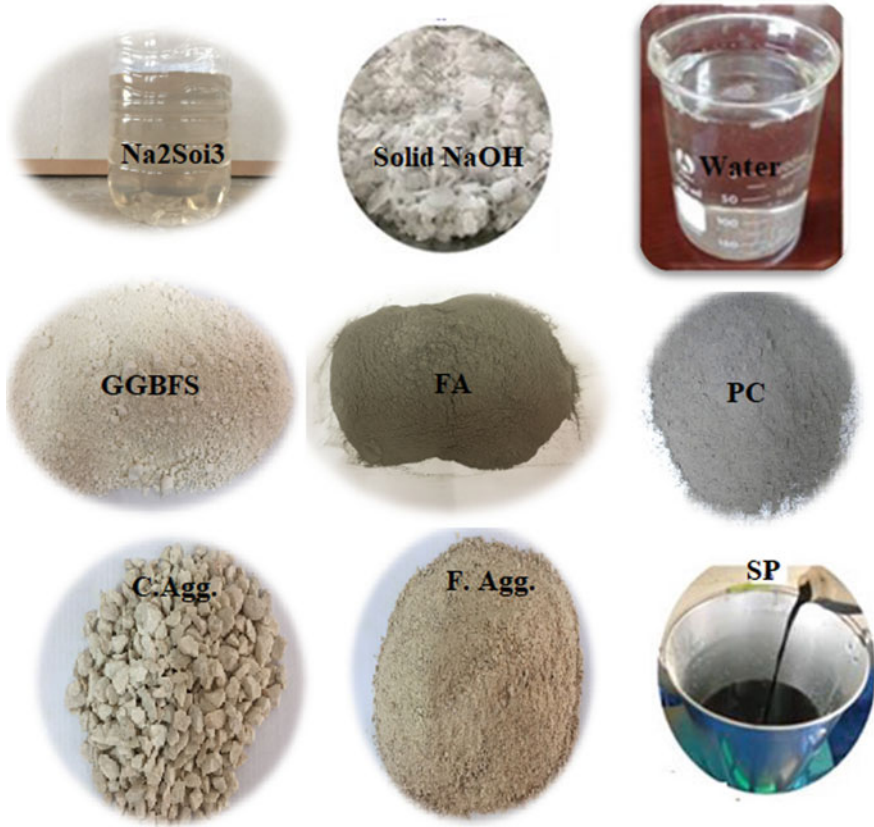


**Fig. 1** Materials used in the production of SCGC specimens

FA with different ratios (50%, 60%, 70%, 80%, and 100%) of GGBFS. The Portland cement was added at 10% and 20% by weight of the binder, respectively. The ingredients (weight per  $1 \text{ m}^3$  concrete) for the mix are shown in Table 3. SCGC specimens' fresh and mechanical efficiency are influenced by the aggregate, binder, and alkali amounts and maximum grain size ( $D_{\max}$ ). For economic purposes, the  $\text{Na}_2\text{SiO}_3/\text{NaOH}$  ratio is reduced from 1.5 to 2.5 [28], which was used in this study as 2.5. Aggregates, FA, and GGBFS with/without PC were blended for 2.5 min during the mixing process. In one minute, the alkali activator was added, and then a superplasticizer was mixed with extra water and added for two minutes. For adequate homogeneity and uniformity, the mix was mixed for additional three minutes.

**Fresh SCGC Tests.** All fresh properties tests are carried out following the EFNARC committee's European specification for SCC development [29]. A responsive test used to characterize the mixture's flow-ability in free flow situations is the slump flow value. EFNARC classifies the standard slump flow into three categories, each of which defines the purposes for which SCC is used. Figure 2 shows the slump

**Table 3** The SCGC mixture proportions

Mixture	Binder	Na <sub>2</sub> SO <sub>3</sub> + NaOH kg/m <sup>3</sup>	GGBFS kg/m <sup>3</sup>	FA kg/m <sup>3</sup>	PC kg/m <sup>3</sup>	Fine Agg kg/m <sup>3</sup>	Coarse Agg kg/m <sup>3</sup>	SH Concentration	SP %	Extra water %
	kg/m <sup>3</sup>									
S50FA50	500	250	250	250	0	865.61	742.88	12	7	7
S60FA40	500	250	300	200	0	862.65	740.34	12	7	7.5
S70FA30	500	250	350	150	0	859.69	737.80	12	7	8
S80FA20	500	250	400	100	0	865.61	742.88	12	7	9
S100FA0	500	250	500	0	0	865.61	742.88	12	7	10
S45FA45PC10	500	250	225	225	50	865.22	742.54	12	7	8
S40FA40PC20	500	250	200	200	100	864.83	742.21	12	7	9

FA; Fly ash, GGBFS (S); Ground Granulated Blast Furnace Slag, PC; Portland Cement, SH; Sodium Hydroxide, SP; Superplasticizer, Both SP and Extra water are a ratio percent of the binder weight materials

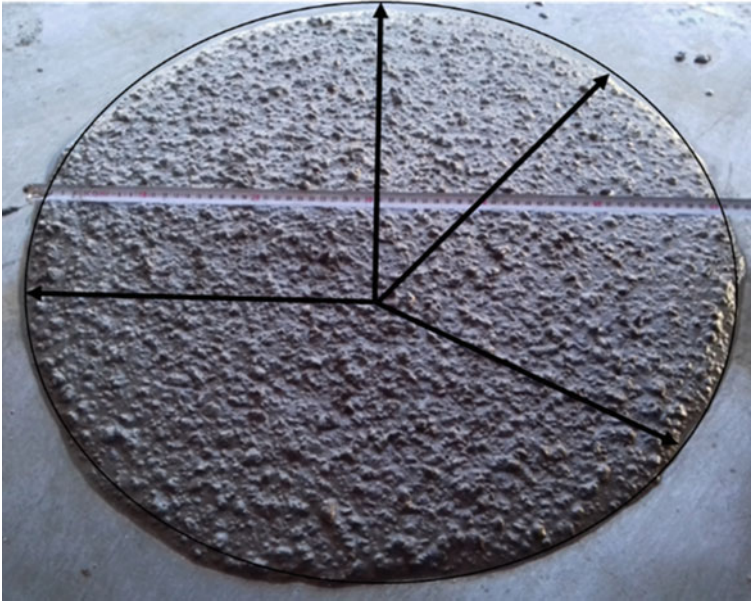


**Fig. 2** Slump flow diameter of SCGC

test for SCGC mix. On the other hand, these experiments cannot determine direct viscosity; this test determines the flow rate in terms of viscosity. Moreover, the V-funnel flow test was evaluated through the time calculated via the V-shaped funnel, which is the elapsed time almost mixed-flow through the V-funnel opening. The L-box and J-Ring measure the fresh concrete's capability to flow through narrow gaps and confined spaces, such as congested reinforcement areas, without losing homogeneity or consistency.

**Curing Method for the SCGC Specimens.** The specimens were covered for 24 h after the concrete was cast to prevent the alkaline solution from evaporating. The specimens were then stored at 22 °C in the lab until the test day. Three identical specimens were used for each experiment, and the mean value was taken.

**Hardened SCGC tests.** The hardened experiments were conducted to investigate the combined effects of GGBFS, FA, and PC on SCGC specimens' behavior. The EN 12390-3 standard was used to conduct compression intensity tests on cubic specimens (100 × 100 × 100 mm) [30].

### 3 Experimental Results

**The behavior of Fresh SCGC.** The SCGC mixes passed the EFNARC specifications in terms of flow capacity and passing ability [29]. SCGC mixes had flow diameters

that exceeded the required flow diameter of 550 mm. In the SCGC mixes, there was no evidence of separation. One of the research goals is to see how GGBFS and FA with and without PC affect the efficiency of SCGC in the fresh state. The effects of these variables on the flow-ability and passing-ability properties of SCGC were investigated in-depth for this reason.

**Effect of GGBFS on the fresh performance of SCGC.** The influence of GGBFS on the fresh state of SCGC is shown in Table 4. The combination of 50 percent GGBFS and 50 percent FA had the largest slump flow diameter (715 mm). The slump flow diameter was reduced from 715 mm (50% GGBFS) to 655 mm after GGBFS was added (100% GGBFS). According to the EFNARC specification, all of the slump flow values were in the SF2 interval, which is appropriate for a wide range of reinforced members (slab, beam, and column) [29]. It was also indicated that the GGBFS content increased both bleeding and segregation resistance, and higher GGBFS mixes were found to be more cohesive than lower GGBFS mixes. The composition and fineness of the binder compounds, the structure and concentration of alkaline activators, and the ambient temperature are all factors that have a major effect on the SCGC setting time [31, 32]. The GGBFS particles are smaller than the FA particles. GGBFS has a specific surface area of 419 m<sup>2</sup>/kg, according to research. Its higher specific surface area influences SCGC's rheological activity and flow-ability. Because of its higher specific surface area, GGBFS adsorbed a considerable amount of water on the surface, resulting in lower flow-ability of SCGC due to the reduced amount of water required for lubrication [8, 33, 34].

Similar to slump flow outcomes, the better T<sub>50</sub> time and V-funnel flow time were detected through the use of 50%-FA-50%GGBFS based SCGC and increased with the addition of GGBFS. However, all V-funnel and T<sub>50</sub> results in the current research were stated to be acceptable according to EFNARC specification [29]. The results of T<sub>50</sub> duration deduce that the amount of GGBFS ratios adversely influenced the flow-ability of SCGC; the mixtures including 100%GGBFS exhibits maximum T<sub>50</sub> duration. GGBFS decreases the slump flow value and L-Box ratio of the blend while increasing plastic viscosity. Mixes containing a higher proportion of GGBFS became more cohesive and viscous, and the flow-ability and fluidity of SCGC mixtures declined as the ratio of GGBFS increased. Since FA has a lower specific surface

**Table 4** The test result of fresh properties of SCGC

Mixture	GGBFS	FA	PC	Slump flow (mm)	V-funnel (s)	T50 (s)	L-box (%)
S50FA50	50	50	0	715	10.5	2.25	1
S60FA40	60	40	0	695	12.35	2.53	0.98
S70FA30	70	30	0	680	17.81	3.23	0.95
S80FA20	80	20	0	670	15.29	3.57	0.91
S100FA0	100	0	0	655	21.50	4.37	0.85
S45FA45PC10	45	45	10	670	19.35	3.21	0.87
S40FA40PC20	40	40	20	660	20.78	4.22	0.85

area, more free water is available for lubrication, resulting in better workability in a combination of 50%-FA and 50%-GGBFS. Workability properties were better obtained with mixes containing 50%-FA and 50%-GGBFS. Furthermore, according to EFNARC, all SCGC mixes fulfilled the SCGC characteristics.

**The Influence of PC Replacement on the Fresh Behavior of SCGC.** The combined influence of GGBFS and FA on the performance of SCGC is shown in Table 4. The addition of PC to the mixes lowered the slump flow diameter from 715 mm (0 percent PC) to 670 mm (10 percent PC) and 660 mm (10% PC) in the 20%PC mix (20% PC). The overall GGBFS replacement lowered the slump flow diameter more than the PC replacement by 20%. The EFNARC requirement [29] yielded satisfactory results. Moreover, the inclusion of PC had an effect on the other fresh properties. With the inclusion of PC, the T50 and V-funnels increased, while the L-Box values decreased. PC added viscosity and cohesiveness to the mixtures. According to the EFNARC, all mixes examined were in the VS2/VF2 class. The mixes had good segregation resistance and/or free of bleeding in addition to low formwork pressure. On the other hand, it was deduced that the mixtures' setting time improved with the addition of GGBFS. The minimum setting time was observed through the use of 100%GGBFS. Moreover, the addition of PC also increased the mixtures' setting time compared to the mixtures including 50%FA-50%GGBFS. The previous researchers reported that the use of fly ash alone with an alkaline solution, the final setting time was stated to be more than 24 h. However, replacing 10% of the fly ash with GGBFS shortened it to 9 h. Furthermore, increasing the amount of GGBFS in the mix reduced the setting time for GPC significantly [31].

**Hardened Behavior of SCGC.** GGBFS and FA's influence with and without PC on the strength of SCGC specimens exposed to ambient temperature is shown in Table 5 and Fig. 3. The specimens containing 50% FA had lower compressive strength than the specimens containing 100% GGBFS. This may be because unreacted FA particles cause severe self-dehydration, resulting in cracks and decreased compressive strength [35]. Furthermore, increasing the GGBFS ratios improved the compressive strength of SCGC. S50FA50 specimens had the lowest compressive strength due to lower fly ash activity [36] and low amount of calcium [37, 38]. The researchers examined the geopolymer concrete (GPC) with different binders, slag, slag/fly ash and fly ash

**Table 5** The compressive strength of SCGC specimens

Mix code	Compressive strength 7 days (MPa)	Compressive strength 14 days (MPa)	Compressive strength 28 days (MPa)
S50FA50	20.64	34.54	35.64
S60FA40	22.26	35.18	39.66
S70FA30	24.89	34.26	37.4
S80FA20	35.97	47.63	48.74
S100FA0	45.56	51.55	66.12
S45FA45PC10	25.23	42.85	46.43
S40FA40PC20	27.61	43.66	48.0

mixes, and discovered that compressive strengths improved in the order of FA-based GPC, FA/GGBFS mixture-based GPC, and GGBFS based GPC. The researchers then evaluated the XRD patterns of FA-based GPC (100% FA) to see the influence of low calcium fly ash. Less reactive calcium (Ca) resulted in less calcium-silicate-hydrate (C-S-H), and the lower volume of Ca in the FA did not contribute in the production of calcium-silicate-hydrate, explaining the poor mechanical strength of FA based GPC specimens. They also discovered that the key hydration agent for FA-based GPC specimens is calcium aluminum oxide hydroxide hydrate ( $\text{Ca}_6\text{Al}_2\text{O}_6(\text{OH})_6 \cdot 32\text{H}_2\text{O}$ ) [36].

It was illustrated from Table 5 and Fig. 3 that the addition of PC, also improved the compressive strength of SCGC. The compressive strength increase was found to be more than 30% and 35% for 10% and 20% PC specimens, respectively. Hence, it is possible to use the PC to improve the mechanical properties of SCGC that have been exposed at room condition. The highest compressive strength was found when 100 percent GGBFS was used, and the minimum compressive strength was found when 50% FA and 50% GGBFS were used. SCGC mixtures cured at ambient curing on the scale of normal compressive strength to high compressive strength with average values between (30 and 66) MPa can be noted. Additionally, the compressive strength values showed that the increase lasted for up to 28 days. As compared to 7 days' compressive strength test values to 14 and 28 days compressive strength test results, the average increase was around 57% and 75%, respectively.

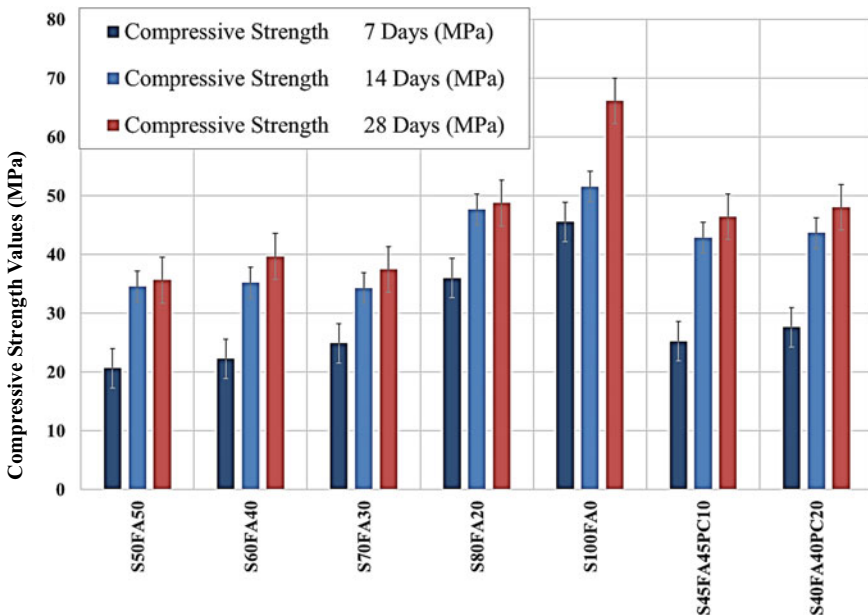


Fig. 3 The compressive strength values of SCGC specimens

## 4 Conclusions

The influence of FA and GGBFS with and without PC on the behavior of SCGC was examined in this study. The following are the outcomes;

- The use of GGBFS substantially reduced the flow-ability and passing capacity in fresh state tests. The mixes with the highest GGBFS (100%) and FA (0%) had the greatest reduction of
- Flow-ability and passing-ability requirements for all SCGC mixes have met the specifications of EFNARC and standards requirements.
- GGBFS decreases the slump flow value and L-Box ratio of the blend while increasing plastic viscosity. Mixes containing a higher proportion of GGBFS became more cohesive and viscous, and the flow-ability and fluidity of SCGC mixtures declined as the ratio of GGBFS increased and increased the resistance to bleeding and segregation.
- According to the EFNARC, all mixes examined were in the VS2/VF2 class. The mixes had good segregation resistance and/or free of bleeding in addition to low formwork pressure.
- It was discovered that using PC at a ratio between 10 and 20% decreased the fresh properties of SCGC. The use of PC, on the other hand, increased the compressive values of SCGC.
- On the other hand, it was deduced that the mixtures' setting time improved with the addition of GGBFS. The minimum setting time was observed through the use of 100%GGBFS. Moreover, the addition of PC also increased the mixtures' setting time compared to the mixtures, including 50%FA-50%GGBFS.
- The compressive strength was found to increase with time up to 28 days. Compared to 7 days compressive strength, the average increase was around 57% and 75% for 14 and 28 days test results.

## References

1. Okoye, F. N., Prakash, S., & Singh, N. B. (2017). Durability of fly ash based geopolymer concrete in the presence of silica fume. *Journal of Cleaner Production*, 149, 1062–1067.
2. Tho-In, T., Sata, V., Boonserm, K., & Chindaprasit, P. (2018). Compressive strength and microstructure analysis of geopolymer paste using waste glass powder and fly ash. *Journal of Cleaner Production*, 172, 2892–2898.
3. Zhuang, X. Y., Chen, L., Komarneni, S., Zhou, C. H., Tong, D. S., Yang, H. M., Yu, W. H., & Wang, H. (2016). Fly ash-based geopolymer: Clean production, properties and applications. *Journal of Cleaner Production*, 125, 253–267.
4. Moukannaa, S., Loutou, M., Benzaazoua, M., Vitola, L., Alami, J., & Hakkou, R. (2018). Recycling of phosphate mine tailings for the production of geopolymers. *Journal of Cleaner Production*, 185, 891–903.
5. Hu, W., Nie, Q., Huang, B., Shu, X., & He, Q. (2018). Mechanical and microstructural characterization of geopolymers derived from red mud and fly ashes. *Journal of Cleaner Production*, 186, 799–806.

6. Memon, F. A., Nuruddin, M. F., Demie, S., & Shafiq, N. (2011). Effect of curing conditions on strength of fly ash-based self-compacting geopolymer concrete. *International Journal of Civil and Environmental Engineering*, 5(8), 342–345.
7. Al-Rawi, S., & Taysi, N. (2018). Performance of self-compacting geopolymer concrete with and without GGBFS and steel fiber. *Advances in Concrete Construction*, 6(4), 323.
8. Gülşan, M. E., Alzeebaree, R., Rasheed, A. A., Niş, A., & Kurtoğlu, A. E. (2019). Development of fly ash/slag based self-compacting geopolymer concrete using nano-silica and steel fiber. *Construction and Building Materials*, 211, 271–283.
9. Noushini, A., & Castel, A. (2016). The effect of heat-curing on transport properties of low-calcium fly ash-based geopolymer concrete. *Construction and Building Materials*, 112, 464–477.
10. Koehler, E. P. (2007). *Aggregates in self-consolidating concrete*. Ph.D. Dissertation, The University of Texas at Austin.
11. Alzeebaree, R., Gulsan, M. E., Nis, A., Mohammedameen, A., & Cevik, A. (2018). Performance of FRP confined and unconfined geopolymer concrete exposed to sulfate attacks. *Steel and Composite Structures*, 29(2), 201–218.
12. Nazari, A., Torgal, F. P., Cevik, A., & Sanjayan, J. G. (2014). Compressive strength of tungsten mine waste-and metakaolin-based geopolymers. *Ceramics International*, 40(4), 6053–6062.
13. Gesoğlu, M., Güneyisi, E., Alzeebaree, R., & Mermerdaş, K. (2013). Effect of silica fume and steel fiber on the mechanical properties of the concretes produced with cold bonded fly ash aggregates. *Construction and Building Materials*, 40, 982–990.
14. Boukendakdji, O., Kenai, S., Kadri, E. H., & Rouis, F. (2009). Effect of slag on the rheology of fresh self-compacted concrete. *Construction and Building Materials*, 23(7), 2593–2598.
15. Çevik, A., Alzeebaree, R., Humur, G., Niş, A., & Gülşan, M. E. (2018). Effect of nano-silica on the chemical durability and mechanical performance of fly ash based geopolymer concrete. *Ceramics International*, 44(11), 12253–12264.
16. Güneyisi, E., Gesoğlu, M., Mohamadameen, A., Alzeebaree, R., Algin, Z., & Mermerdaş, K. (2014). Enhancement of shrinkage behavior of lightweight aggregate concretes by shrinkage reducing admixture and fiber reinforcement. *Construction and Building Materials*, 54, 91–98.
17. Khaloo, A., Raisi, E. M., Hosseini, P., & Tahsiri, H. (2014). Mechanical performance of self-compacting concrete reinforced with steel fibers. *Construction and Building Materials*, 51, 179–186.
18. Alzeebaree, R., Çevik, A., Nematollahi, B., Sanjayan, J., Mohammedameen, A., & Gülşan, M. E. (2019). Mechanical properties and durability of unconfined and confined geopolymer concrete with fiber reinforced polymers exposed to sulfuric acid. *Construction and Building Materials*, 215, 1015–1032.
19. Ling, Y., Wang, K., Li, W., Shi, G., & Lu, P. (2019). Effect of slag on the mechanical properties and bond strength of fly ash-based engineered geopolymer composites. *Composites Part B: Engineering*, 164, 747–757.
20. Mohammedameen, A., Çevik, A., Alzeebaree, R., Niş, A., & Gülşan, M. E. (2019). Performance of FRP confined and unconfined engineered cementitious composite exposed to seawater. *Journal of Composite Materials*, 53(28–30), 4285–4304.
21. Fernandez-Jimenez, A. M., Palomo, A., & Lopez-Hombrados, C. (2006). Engineering properties of alkali-activated fly ash concrete. *ACI Materials Journal*, 103(2), 106.
22. Alzeebaree, R. (2018). *Mechanical performance and durability of confined and unconfined geopolymer concrete exposed to severe environments*. Ph.D. Thesis; Gaziantep University.
23. ASTM C618. (2003). *Standard specification for coal fly ash and raw or calcined natural pozzolan for use in concrete*. West Conshohocken, PA, USA ASTM Int.
24. ASTM C311. (2002). *Standard test methods for sampling and testing fly ash or natural pozzolans for use in Portland-cement concrete*. American Society for Testing and Materials, West Conshohocken, PA ASTM Int.
25. ASTM C33-02. (2002). *Standard specification for concrete aggregates*. West Conshohocken, PA.



26. ASTM-C494-05. (2005). *Standard specification for chemical admixtures for concrete*. West Conshohocken, PA.
27. Memon, F. A., Nuruddin, M. F., Khan, S., Shafiq, N. A. S. I. R., & Ayub, T. (2013). Effect of sodium hydroxide concentration on fresh properties and compressive strength of self-compacting geopolymer concrete. *Journal of Engineering Science and Technology*, 8(1), 44–56.
28. Olivia, M., & Nikraz, H. (2012). Properties of fly ash geopolymer concrete designed by Taguchi method. *Materials & Design*, 1980–2015(36), 191–198.
29. EFNARC. (2005). *The European guidelines for self-compacting concrete: Specification, production and use*, Eur. Guidel. Self Compact. Concr., 68.
30. EN 12390-3. (2001). *Testing hardened concrete; part 3: compressive strength of test specimens*, Eur. Comm. Stand.
31. Nath, P., & Sarker, P. K. (2014). Effect of GGBFS on setting, workability and early strength properties of fly ash geopolymer concrete cured in ambient condition. *Construction and Building Materials*, 66, 163–171.
32. Deir, E., Gebregziabiher, B. S., & Peethamparan, S. (2014). Influence of starting material on the early age hydration kinetics, microstructure and composition of binding gel in alkali activated binder systems. *Cement and Concrete Composites*, 48, 108–117.
33. Sathawane, S. H., Vairagade, V. S., & Kene, K. S. (2013). Combine effect of rice husk ash and fly ash on concrete by 30% cement replacement. *Procedia Engineering*, 51, 35–44.
34. Alzebaree, R., Çevik, A., Mohammedameen, A., Niş, A., & Gülşan, M. E. (2020). Mechanical performance of FRP-confined geopolymer concrete under seawater attack. *Advances in Structural Engineering*, 23(6), 1055–1073.
35. Belkowitz, J. S., Belkowitz, W. B., Nawrocki, K., & Fisher, F. T. (2015). Impact of nanosilica size and surface area on concrete properties. *ACI Materials Journal*, 112(3).
36. Chi, M., & Huang, R. (2013). Binding mechanism and properties of alkali-activated fly ash/slag mortars. *Construction and Building Materials*, 40, 291–298.
37. Dombrowski, K., Buchwald, A., & Weil, M. (2007). The influence of calcium content on the structure and thermal performance of fly ash based geopolymers. *Journal of Materials Science*, 42(9), 3033–3043.
38. Ganesan, N., Raj, J. B., & Shashikala, A. P. (2013). Flexural fatigue behavior of self compacting rubberized concrete. *Construction and Building Materials*, 44, 7–14.

# **Construction Management and Sustainability**

# Cost Prediction of Roads Construction Projects Using OLS Regression Method



Ruqayah H. Rasheed and Sedqi E. Rezouki

**Abstract** Escalation of completed cost than contract cost of road construction project causes disputes between road agencies and contractors and lead to deserted or delay the same projects or others projects due to stealing from their budget to overlay the shortfall. Consistent occurrences cause losing credibility and reputation of road agencies in addition to political complications. Therefore, this study aims to build a model to predict the completed cost of road construction projects in the early stage of the project's life cycle to avoid cost overruns. The ordinary least square regression method (OLS) has been applied for cost prediction models based on data extracted from 52 projects that have been obtained from the Roads and Bridges Directorate of Construction and Housing Ministry in Iraq from 2011 to 2019. After projects data are divided for training and testing, then strict assumptions of the OLS method are applied, the optimal model has been developed based on the variables of contract cost (CC), contract time (CT), projects downtime (DT), road length (L) and road width (W) of the projects. The values of the assessment criteria of the optimal model are 0.96 for the coefficient of determination ( $R^2$ ), 0.95 for adjusted  $R^2$ , and 1897.8 for Schwarz's Bayesian information criterion (BIC). The mean absolute percentage error (MAPE) is 7.93%. These values are indicating that the developed model success in illustrating the pattern between predictor's parameter and project cost and well performance.

**Keywords** Road construction cost · Completed cost prediction · Ordinary least square (OLS) · Regression assumption · Best subset

## 1 Introduction

The costs are the main element of any contract for a road construction project; thus, they take over the great interest of project participants. Although cost management is an essential responsibility for the decision-makers of construction projects, costs overrunning is a common global matter [1]. So, finishing the road construction project

---

R. H. Rasheed (✉) · S. E. Rezouki  
Civil Engineering Department, University of Baghdad, Baghdad, Iraq

within contract cost has become a challenge for decision-makers because many factors can share in cost overruns of road projects cost such as; the complexity of the project, duration, the experience of the contractor, in addition to the conditions of weather, site, economic situations, social climates, and local political [2]. The parametric model of cost estimation is qualified to discover the relation between the completed cost and important factors using historical data. The model can predict the completed cost prior to the construction phase to supply information to assist highways and road agencies in taking the proper actions for the projects. When the model forecasts that the project completed cost is greater than the price of low-bid, attentive supervision is necessary during the construction of the projects [3]. The classical approach like adjusted unit price and quantity takeoff applied worldwide [4] heavily depends on estimators' sound judgment and experience to produce precise estimates. These classical approaches are not always reliable and consistent and cause estimation errors [5]. Therefore, the OLS methods have been applied in this research to develop a parametric model for road construction cost that can draw the accurate relationship between the project's cost and their main contributor's factors.

## 2 Research Methodology

The methodology that has been adopted in this research is illustrated in Fig. 1; each step of the methodology will be described in the next section.

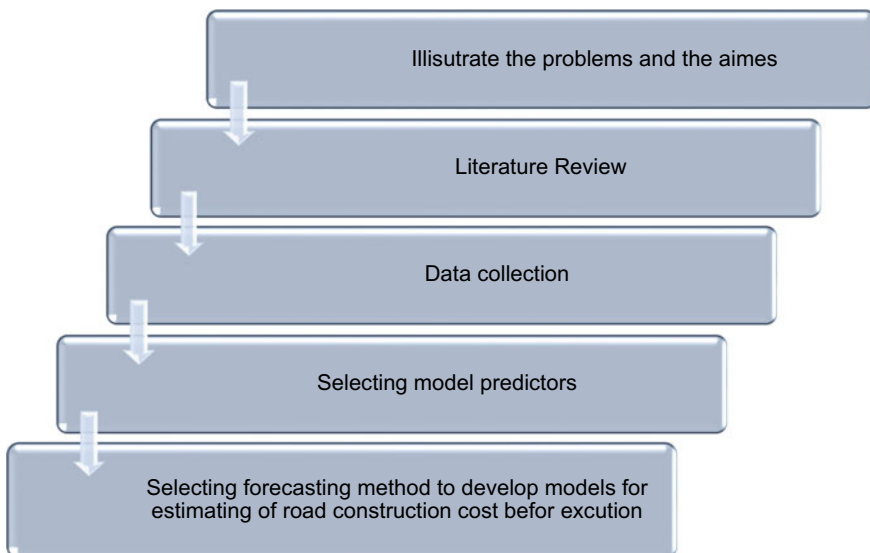


**Fig. 1** Research methodology

### 3 The Problem and Aims

Given the complexity of bidding, it is also recognized that construction projects are often completed at costs that are greater than the original estimate, so leads to disputes between the owners and contractors. It leads to delays in road construction projects resulting in severe sacrifice to the credibility and reputation of road agencies. The aims of this research are:

- Developing forecasting model via ordinary least squares (OLS) method based on the contract price, contract time, road length, road width, and downtime of projects due to weather days and holidays. A model that will predict the completed cost of road construction projects in the early stage prior to execution to avoid escalation in the final cost of road construction projects by taking necessary measures.
- Developing estimation models that can be handled easily via calculators in the early project stages.

### 4 Previous Studies

Mahamid [6] formed ten models to estimate the cost in the early stage for projects of road construction using multiple regression methods, based on about 130 sets of data gathered from Palestine. Four of developed models depending on data of bid as input variables and six depending on length and width of the road, bid data which have been used in developing the models were the quantities of earthwork, base coarse, asphalt, concrete of retaining walls, curbstone, road marking, and quantity of sidewalk concrete. According to MAPE, and  $R^2$  is the best model performance were the models which have been dependent on quantities of bid data, and the more accuracy of them the model that has MAPE equal 13%, and  $R^2$  of 0.98. Hollar et al. [7] developed a model to estimate the cost of preliminary engineering by a multiple regression method, depending on data of 461 projects of the bridge in North Carolina. The models based on 28 independent variables, 16 of them were categorical while the remaining 12 were numerical. According to  $R^2$ , MAPE the final model based on 7 predictors, four of them were numerical variables, and the other three variables were categorical variables.

Cirilovic et al. [2] built a model by multiple-regression methods to forecast the cost of road reconstruction and rehabilitation projects. The model is based on 19 predictive variables extracted from 200 projects of countries in Central Asia and Europe, the variables related to the oil price, government, and project. Williams [8] developed two simple linear regression models to predict the cost of highway projects. Bid pattern data have been applied in these models as a predictor's low bid ratio, the ratio between the low bid and maximum bid, second low bid, and mean of bid values. These data have been extracted from 1260 projects, 1000 of them applied to build the linear regression models. While the remaining data of the 260 projects have been used for testing. According to the accuracy of models which tested by

R of 0.997 and  $R^2$  of 0.995, and the performance measurement by mean square error (MSE) and the mean absolute percentage deviation (MAPD), the researcher has been concluded that the best performing models were the model that depends on the natural log of the low bid.

Zhang et al. [3] formed models using OLS regression methods to forecast the completed cost of highway construction projects. Eventually, they have been mine the data from state highway agencies (SHAs), and many other economic sources in the USA. Data collected from about 750 projects of resurfacing highways projects, about 650 projects have been selected randomly for model development, while the remaining 100 projects have been used for validation. The models are built depending on project data and economic data of the states. The project's data variables were; contract days, number of bidders, past contractor performance, number of lanes, length of the project, and low bid or contract price. While the economic variables were; consumer price index (CPI), producer price index price (PPI), prime loan rate (PLR), and construction spending (CS). According to the best subset method for performance measurement, the best OLS regression model consisted of the contract price, CS, and CPI as predictors with  $R^2$  was 0.9875, and the adjusted  $R^2$  was 0.9874. The previous research had been used detailed information about the road and highway projects (e.g., data of quantities, bid patterns, design, environmental, and geographical data) and the region's economic conditions where the project was constructed. As shown in the succeeding clause, this research has been used basic data about the projects that can be obtained at an early stage of projects like the length and width of the road. Furthermore, only one research in the previous studies has displayed and explained the strict assumption of the OLS methods and the strict process of residual diagnosis, which is the assurance of model reliability.

## 5 Data Collection

The data used to develop the OLS models were gathered from numerous departments (Legal, technical, and supervisory) of the Roads and Bridges Directorate of Construction and Housing Ministry in Iraq from 2003 to 2019. The data available in Roads and Bridges Directorate are the types of works (e.g., construction of new roads, bridge rehabilitation, and maintenance, widening, interchange, maintenance, and rehabilitation of roads, and weighing stations), lanes number, total lengths, and width of projects, engineers team of projects, original price of the contract, change orders, completed cost of projects, days of the contract, total duration of the projects, project location (governorate), downtime (weather days, and holidays), bidders number, past performance ratings of contractors, and bidding type (invitation or competitive). According to the availability of project details, the decision was to use the data of construction new roads from 2011 to 2019. The variables that were used as predictors to develop the forecasting models in the early stage of the projects were contract duration, contract price, road width, road length, and downtime (weather days and holidays). The data obtained from 52 road construction projects and from

**Table 1** Descriptive statistics of project data

Parameter	Units	Minimum	Maximum	Mean	Std. Deviation
Project price	Million (IQD)	160	42,959	9823.5	10,989
Contract price	Million (IQD)	36.4	41,188	9284.4	1068
Contract time	(Days)	148	2286	607.8	434
Downtime	(Days)	0	147	51.5	33
Projects length	(km)	2.6	70	19.4	15.3
Projects width	(m)	6	8.3	7.4	0.98

many governments in Iraq from Nineveh to Basra. According to the final price, the minimum project price was IQD 159.995 million, and the maximum was IQD 42,959 million, with a mean price escalation rate from the contract price of 4.51577%. The Descriptive Statistics of final projects price as output variable (dependent) and input variables (independent) are illustrated in Table 1.

## 6 OLS Model Development

The ordinary least-square (OLS) method minimizes the sum of the squared difference between the observed and predicted values. The best regression line guarantees that the sum of squared residuals (SSR) is the minimum, [4] which is influenced by the coefficients ( $\hat{\beta}$ ). Therefore, the strategy is to determine the regression coefficients. The mathematical formulas to determine the optimum regression coefficients are shown as Eqs. (1) and (2) [3].

$$\text{Min.}(SSR) = \text{Min.}((Y - Xb)^T(Y - Xb)) \tag{1}$$

$$\beta_{OLS} = (X'X)^{-1}X'Y \tag{2}$$

where  $X$  = predictors matrix that includes independent variables (e.g., contract time (CT), contract cost (CC), project width (W), project length (L), and downtime (DT)),  $Y$  = the dependent variable matrix (project price),  $SSR$  = the sum of the squared residuals, and  $\beta_{OLS}$  = OLS regression coefficients. The first step to develop the OLS model is checking the correlation between all the variables by Pearson’s correlation coefficient, then selecting 80% of projects to build the models by best subset selection procedure and remain 20% of projects to test the models as illustrated in succeeding paragraph and Fig. 2.

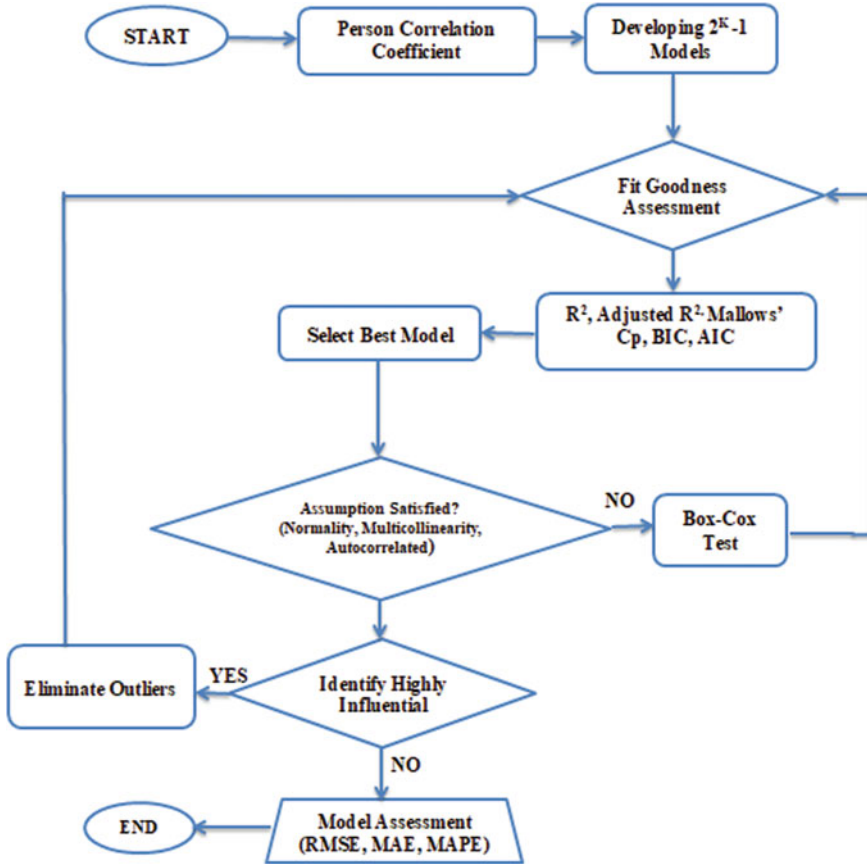


Fig. 2 OLS regressions model development

### 7 Pearson’s Correlation Factor

Pearson’s correlation factor is a strength measurement to a linear relationship between variables, scale measurement of the factor has values from  $-1$  to  $+1$ . The positive sign indicating a positive correlation between two variables while the negative values indicating a negative correlation [9]; checking variables correlations to build an OLS regression model is a standard procedure. The value of Pearson’s correlation coefficient should be more than 0.3 when checking correlations between a dependent variable and an independent variable, and it should be less than 0.7 when checking correlations between two independent variables to avoid reducing the prediction accuracy [10]. Table 2 will demonstrate the values of Pearson’s correlation coefficient between the dependent and independent variables that will use to build the models in this research.



**Table 2** Results of Pearson’s correlations coefficient

Variables	Project price	L	W	DT	CT	CC
	Pearson correlation					
Project price	1	0.712	0.632	0.469	0.511	0.863
L	0.712	1	0.507	0.243	0.340	0.598
W	0.632	0.507	1	0.402	0.479	0.598
DT	0.469	0.243	0.402	1	0.844	0.466
CT	0.511	0.340	0.479	0.844	1	0.564
CC	0.863	0.598	0.598	0.466	0.564	1

Best sub set procedure

This study chooses the best-subsets selection techniques to avoid missing the optimal model [11] compared with backward, forward, and stepwise procedures. The best-subset technique requires more computation work; however, it is no longer an important issue due to the large advancement in the science of computer programs [4] The best-subset model selection procedure includes the following steps:

1. Identifying the possible models, including all possible groups of the candidate predictors. The number of models was  $2^{K-1}$ , (K is a number of predictors variables) [12]. The possible models for this study are 31 models; see Table 3.
2. Selecting the best models from the models identified in the previous step according to the criteria of Mallows’s Cp, Schwarz’s Bayesian information criterion (BIC),  $R^2$ , and adjusted  $R^2$  [13]. This study selects the five predictors model, one best model from four predictors models, three predictors’ models, two predictors’ models, and from one predictor’s model, see Table 4.
3. Based on comparing the criteria values of the best combinations of models identified in the previous step, the final model will be:

$$\text{ProjectPrice} = -2384305410 + 0.9 \times \text{CC} - 892941 \times \text{CT} + 19181939 \times \text{DT} + 25359412 \times \text{L} + 304542686 \times \text{W} \quad (3)$$

Check normality, multicollinearity, and autocorrelated for the residuals of the optimal model to ensure that the optimal model fulfills the OLS assumptions to obtain the best estimates [14]. For this study, Shapiro–Wilk test (W) tested the normality. Although  $W = 0.85$  and  $p\text{-value} = 4.3 \times 10^{-5}$  was violated, a histogram of the residuals (Fig. 3) demonstrated a roughly normal distribution. The residuals were independent, as Durbin–Watson test proved, which was equal to 1.8. According to variance inflation factor (VIF) no multicollinearity between predictors was detected., VIF values were 3.93 for CC, 2.76 for CT, 2.23 for DT, 4.05 for L, 3.44 for W.

Identifying the points of highly influential data by checking the values of Cook’s distance [14], then detecting and eliminate outliers via the Bonferroni test. Finally, improve the fitness and linearity using the Box-Cox test to choose how to convert

**Table 3** Possible models

Predictors no	Intercept	CC	CT	DT	L	W	R <sup>2</sup>	Adjusted R <sup>2</sup>	Cp	BIC
1	x	x					0.72	0.714	2	2119.9
1	x		x				0.253	0.236	2	2166.1
1				x			0.217	0.199	2	2168.3
1	x				x		0.465	0.453	2	2150.4
1	x					x	0.424	0.412	2	2153.9
2	x	x	x				0.721	0.708	3	2123.7
2	x	x		x			0.726	0.714	3	2122.8
2	x	x			x		0.787	0.778	3	1979.2
2	x	x				x	0.747	0.735	3	2119.1
2	x		x	x			0.259	0.226	3	2169.6
2	x		x		x		0.558	0.538	3	2145.3
2	x		x			x	0.474	0.450	3	2153.5
2	X			x	x		0.575	0.556	3	2143.5
2	X			x		x	0.469	0.445	3	2153.9
2	x				x	x	0.587	0.568	3	2142.2
3	x	x	x	x			0.729	0.710	4	2126.2
3	x	x	x		x		0.788	0.774	4	2114.6
3	x	x	x			x	0.747	0.729	4	2122.9
3	x	x		x	x		0.797	0.782	4	2112.7
3	x	x		x		x	0.749	0.732	4	2122.5
3	x	x			x	x	0.797	0.782	4	1980.8
3	x		x	x	x		0.578	0.548	4	2147
3	x		x	x		x	0.477	0.441	4	2157.1
3	x		x		x	x	0.621	0.595	4	2141.9
3	x			X	x	x	0.634	0.608	4	2140.3
4	x	x	x	x	x		0.802	0.783	5	2115.2
4	x	x	x	x		x	0.753	0.729	5	2125.7
4	x	x	x		x	x	0.797	0.777	5	2116.5
4	x	x		x	x	x	0.802	0.784	5	1983.3
4	x		x	x	x	x	0.634	0.599	5	2144.1
5	x	x	x	x	x	x	0.96	0.95	6	1897.8

data for the model improvement [8]. For this research Cook’s distance test discovered the points of influential data, and one outlier was specified and eliminated by the Bonferroni test. The statistic values of the Box-Cox test show that the transformation was not required. When assessing the predictive model’s performance by testing data that are 20% of the total data, the Mean Absolute Error (MAE) is 446,951,325, and MAPE is 7.93%, which indicates the good performance of the optimal model.

**Table 4** Assessment of goodness of fit

Predictors no	Intercept	CC	CT	DT	L	W	R <sup>2</sup>	Adjusted R <sup>2</sup>	Cp	BIC
1	X	x					0.72	0.714	2	2119.9
2	X	x			X		0.787	0.778	3	1979.2
3	X	x			x	x	0.802	0.787	4	1980.8
4	X	x		x	x	x	0.808	0.788	5	1983.3
5	X	x	x	x	x	x	0.964	0.958	6	1897.8

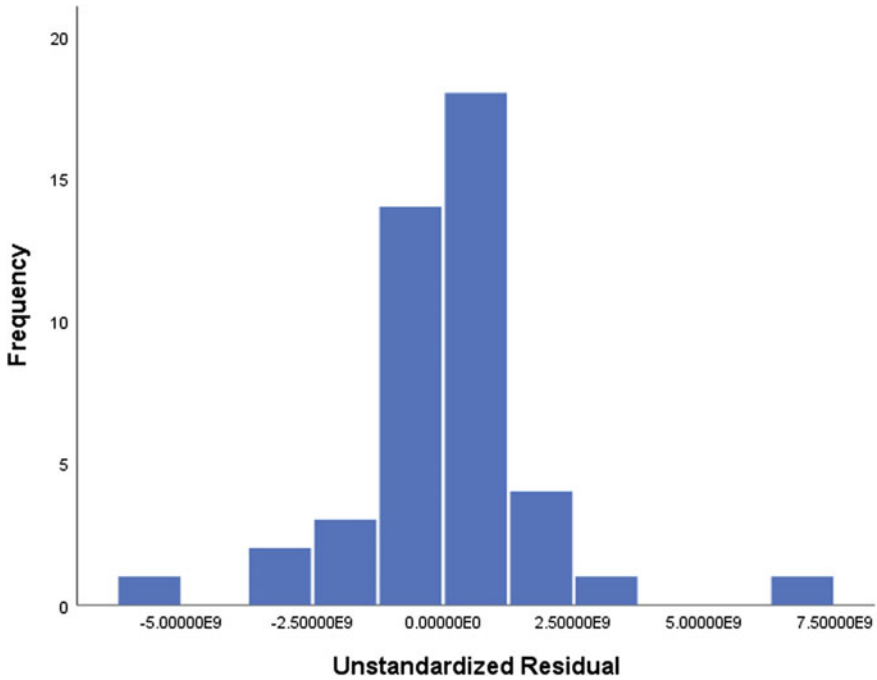


**Fig. 3** Residual histogram

## 8 Conclusions

The main objective of this study is to assist decision-makers in highways and road agencies by developing early cost estimating models and easily handled via calculators for road construction projects. The variables that were used in building the model were chosen according to previous studies and available data from 52 projects in different Iraqi governorates. The model satisfied the assumption of OLS techniques for multiple linear regression methods. In this study, 31 regression models are developed, including contract cost, contract time, downtime, road length, and width. R<sup>2</sup>

for the optimal model was 0.96. This indicates that the relationship between the independent and dependent variables of the developed models is good, and the predicted values from a forecast model fit with the real-life data. Also, the model has the best performance, as indicated by MAPE value of 7.93%. It must be noticed that the prediction model of the project cost is an opinion of potential cost is not an exact value. The reliability and accuracy of the prediction model are dependent on the definition of the project scope.

## References

1. Petrusseva, S., Zileska-Pancovska, V., Žujo, V., & Brkan-Vejzović, A. (2017). Construction costs forecasting: Comparison of the accuracy of linear regression and support vector machine models. *Technical Gazette*, 24(5), 1431–1438.
2. Cirilovic, J., Vajdic, N., Mladenovic, G., & Queiroz, C. (2014). Developing cost estimation models for road rehabilitation and reconstruction: Case study of projects in Europe and Central Asia. *Journal of Construction Engineering and Management*, 140(3), 04013065.
3. Zhang, Y., Minchin, R. E., Jr., & Agdas, D. (2017). Forecasting completed cost of highway construction projects using LASSO regularized regression. *Journal of Construction Engineering and Management*, 143(10), 04017071.
4. Si, X. S., Zhang, Z. X., & Hu, C. H. (2017). *Data-driven remaining useful life prognosis techniques*. National Defense Industry Press and Springer-Verlag GmbH.
5. Chou, J. S., Lin, C. W., Pham, A. D., & Shao, J. Y. (2015). Optimized artificial intelligence models for predicting project award price. *Automation in construction*, 54, 106–115.
6. Mahamid, I. (2011). Early cost estimating for road construction projects using multiple regression techniques. *Construction Economics and Building*, 11(4), 87–101.
7. Hollar, D. A., Rasdorf, W., Liu, M., Hummer, J. E., Arocho, I., & Hsiang, S. M. (2013). Preliminary engineering cost estimation model for bridge projects. *Journal of construction engineering and management*, 139(9), 1259–1267.
8. Shahandashti, S. M., & Ashuri, B. (2016). Highway construction cost forecasting using vector error correction models. *Journal of management in engineering*, 32(2), 04015040.
9. Sedgwick, P. (2012). Pearson's correlation coefficient. *BMJ*, 345.
10. Rawlings, J. O., Pantula, S. G., & Dickey, D. A. (2001). *Applied regression analysis: A research tool*. Springer Science & Business Media.
11. James, G., Witten, D., Hastie, T., & Tibshirani, R. (2013). *An introduction to statistical learning* (Vol. 112, P. 18). New York: Springer.
12. Brooks, G. P., & Ruengvirayudh, P. (2016). Best-subset selection criteria for multiple linear regression. *General Linear Model Journal*, 42(2), 18–25.
13. Ofori-Boadu, A. N. (2015). Exploring regression models for forecasting early cost estimates for high-rise buildings. *Journal of Technology, Management & Applied Engineering*, 31(5).
14. Jayakumar, G. S., & Sulthan, A. (2015). Exact distribution of Cook's distance and identification of influential observations. *Haceteppe Journal of Mathematics and Statistics*, 44(1), 165–178.

# Modeling of Variation Orders in Cost and Time Using System Dynamics in Iraqi Construction Projects



Wissam A. Ismaeel, Hafth I. Naji, and Raquim N. Zehawi

**Abstract** The construction industry owner quite often issues variation orders, and they can cause the contractor's work to be disrupted, impact time and cost overruns. Rework and minor changes can be qualitatively predicted and estimated during the bidding process for the most significant projects. This research explains the meaning, application, and potential application of system dynamics in assessing the impacts of variation order on cost and time. The model boundary is defined, including Exogenous and Endogenous variables. The Casual loop diagram CLD is built to explain the system structure after determining the modeling parameters fully. Using Vensim software, a system dynamics model is created, verified, and validated before being used to quantify the impact of variation orders in project scope on cost and time. The research aims to use system dynamics to simulate variation orders in Iraqi construction projects' cost and time. There are a large number of variation orders that occurred in most construction projects in Iraq.

**Keywords** Endogenous · Exogenous · Vensim · System structure · Variation orders

## 1 Introduction

Variation orders are a common occurrence in the construction industry, and they can have a negative or positive impact on the duration, cost of the project [1]. Two types of variation orders are commonly used. Owner-requested changes to, design, the project scope, or detailing are called owner-generated change directives. Field-generated variation orders are the result of issues in the field that necessitate design changes [2]. Hanna et al. [3] defined the variation orders as that due to the uniqueness of each project and the limited resources of time and money available for planning, variation is unavoidable on most construction projects, resulting in a modification of

---

W. A. Ismaeel (✉) · H. I. Naji  
Department of Civil Engineering, University of Diyala, Baqubah, Iraq

R. N. Zehawi  
Department of Airport and Transportation Engineering, University of Diyala, Baqubah, Iraq

the original scope, execution time, or cost of work. According to Gundus and Hana [4], a variation order is “a legal exchange that replaces the contracting company in the implementation of the contract’s terms that permit the amendment of the contract by the will of any party without exceeding the contract’s general scope”. According to Staiti et al. [5], variation orders can be divided into three groups based on the type of change field: Works with omissions, additions, and substitutions.

Project changes, which arise from each construction project’s unique circumstances and conditions, are a common source of concern for the construction industry these days. Because construction projects are complex, involving many participants, and take a long time to complete, they are prone to change as they progress [6]. System dynamics (SD) is a methodology for studying and managing dynamically complex systems by creating and applying simulation models [7]. System dynamics modeling can be used to properly manage and simulate processes that have two major essential characteristics: (1) they allow feedback—the transmission and reception of information (2) They involve time variation [8]. Stocks represent collected and stored quantities, characterize the system’s state, and produce the data used to make decisions. The rate at which stocks increase or decrease is referred to as the flow rate [9]. To model decisions and project management policies, information feedback loops are used [10]. Modeling decisions and project management policies are done with information feedback loops [9].

SD modeling can be used to solve problems in the construction industry. The reason for this is that construction projects include the following:

- The highly dynamic.
- Were also highly complex, with various interdependent components.
- Multiple feedback processes should be used.
- Nonlinear relationships are involved.
- Include both quantitative and qualitative data in your analysis [11].

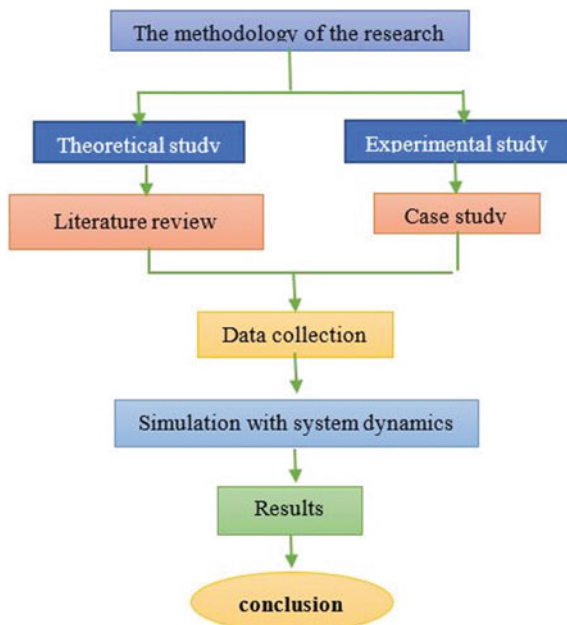
Simulation means that a system representation employs a computer’s mathematical computation execution on a model formed through the system dynamic technique [12]. The Dynamics System is an analysis of system path originated through Forrester [9] analyzed and model the behavior of complex systems of social in the context of industrial [9]. System dynamic helps analyze social, economic, physical, chemical, ecological, and biological systems. Despite broad usage of system dynamics in various business management fields, project management deems one of the most related areas for system dynamics usage [13]. In effect, SD’s critical advantage is his ability to ease conceptualization of the multi-disciplinary models by supplying the tools; the tool is a qualitative tool to supplement the quantitative simulations [14]. In the system dynamic, the causal loop diagram identifies the negative and positive feedback processes. The Causal loop diagrams shape closed loops and describe a map of cause and effect relationships among the individual system variables due to link causal loop diagrams consists of variables which are linked by the arrows indicating to influences of causal among variables [15]. The feedback is classified as either negative or positive.

The term positive and negative mention whether variation in feedback system shifts in opposite directions to output stabilizing, balancing behavior, or move in the same direction for producing compounding behavior, reinforcing [16]. The system dynamic's initial variables could be separated into two groups: Exogenous: The system and endogenous variables do not directly impact the components' values: the components' values are directly impacted by the system[17]. Behavior, the plot of the system of the variables over time, helps the system reference and understand the general system attitude [18]. Reference mode helps guide the structure's model properly for taking the historical data on the paper, and after examining the acceptability, the model is finished [9]. Exponential growth; Exponential decay; oscillations; overshoot and collapse; S-shaped growth; are common the hypothesized reference the model in the behaviors [19]. The research aims to use system dynamics to simulate variation orders in Iraqi construction projects' cost and time. There are a large number of variation orders that occurred in most construction projects in Iraq.

## 2 Methodology

The methodology is concluding two parts, the first part is the theoretical study, and the second part is Experiential study, the data collection from 27 projects in the University of Diyala in a different period from(2008–2020). The methodology is explained in Fig. 1.

Fig. 1 The methodology of the research



### 3 Case Study

For information about change orders in construction projects, a group of projects was selected within Diyala Governorate and Diyala University, specifically in case studies. All the study projects were private, governmental, and multi-story buildings and were implemented by a private and public contractor. The researcher adopted 13 construction projects in Iraq as a case study to locate the variation orders' size in Iraq's construction projects.

**Data Acquisition.** For identifying the problems, that accrued in the projects under study and the size of the variation orders, relevant data were collected on variation orders for each construction project under investigation by: (reviewing of contract for each project, meeting with the project managers and specialized engineers, study the issues of variation orders, the duration of variation orders to each project, the monthly reports). To determine the size of variation orders in the construction projects in Iraq, the researcher adopted 27 projects in Iraq, as mentioned in Table 1 summarized the actual W.A. (weighted average) of variation orders in cost and time.

$$\begin{aligned} &\text{Actual W.A.Time.V.O} \\ &= \frac{(\text{Actual time v.o\% *contract duration})\text{in the same period}}{(\text{sum .contact duration})\text{in the same period}} \end{aligned} \tag{1}$$

$$\text{Actual time V.O\%} = \left( \frac{\text{Actual time V.O}}{\text{contract duration}} \right) \text{for every period} \tag{2}$$

**Table 1** Summarize of actual W.A (weighted average) of variation orders in cost and time

No.	Year	Actual W.A T.V.O (%)	Actual W.A C.V.O (%)
1	2008	30	2
2	2009	27	2.6
3	2010	24	0.2
4	2011	18	0
5	2012	22	46.4
6	2013	30	0.2
7	2014	38	11.2
8	2015	44	1.2
9	2016	19	0.7
10	2017	26	0.0
11	2018	51	0.6
12	2019	48	2.1
13	2020	69	2.4



$$\begin{aligned} &\text{Actual W.A.Cost.V.O} \\ &= \frac{(\text{Actual cost v.o\% *contract duraton})\text{in the same period}}{(\text{sum.contract duration})\text{in the same period}} \end{aligned} \tag{3}$$

$$\text{Actual cost V.O\%} = \left( \frac{\text{Actual cost V.O}}{\text{contract duration}} \right) \text{for every period} \tag{4}$$

**System Dynamics Model Development.** The system dynamics model has been conducted to assess the owner, contractor, and legislative impact on construction projects’ performance using the free software system VENSIM PLE to visualize the model. The interconnection among variables in the conceptual model is converted into quantitative measures using the VENSIM PLE free computer system through the stock and flow diagram. This study uses two models containing a stock and flow diagram. One model impacts construction projects’ variation order cost, and the second model variation orders time on construction projects.

**The Boundaries o The Model.** In constructing the model, the first step is located scoping of the system. Exogenous and endogenous variables are scoping of the model.

Exogenous: are variables are not including the feedback. In the modeling of cost and time variation orders, legislative alteration and insurgency effect are Exogenous variables.

Endogenous variables found in the system’s feedback effect, contractor, and owner are endogenous variables in modeling cost and time variation orders.

#### 4 Description of The Modeling of System Dynamic

This part including characterization of the two modelings of variation orders as below:

**The Model of Cost Variation Orders.** The model is describing variation order cost and time in the construction project of Iraqi. The model can be represented through stocks and flows this addresses variation orders cost, contractor orders opinion on variation orders cost, owner opinion on variation orders cost, change in contractor opinion on variation orders cost, change in owner opinion on variation orders cost, and net change in variation orders cost, see Fig. 2.

**The Model of Time Variation Orders.** The model can be represented through stocks and flows this addresses variation orders time, contractor orders opinion on variation orders time, owner opinion on variation orders time, change in contractor opinion on variation orders time, change in owner opinion on variation orders time, and net change in variation orders time (Fig. 3).

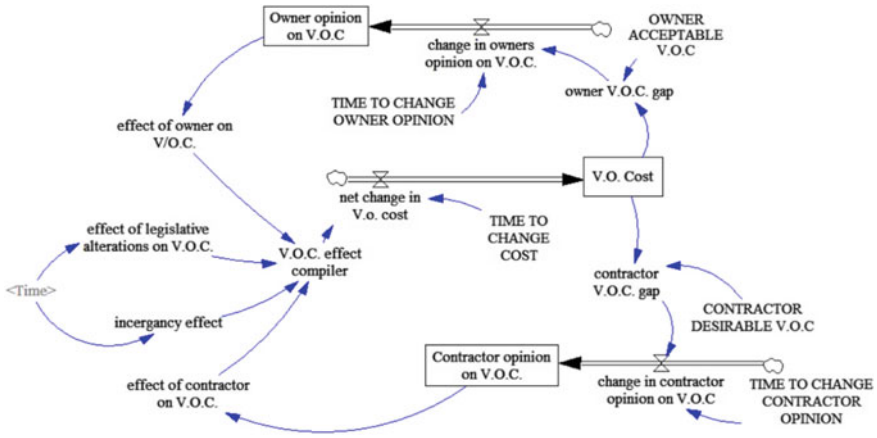


Fig. 2 Variation orders cost in a construction project

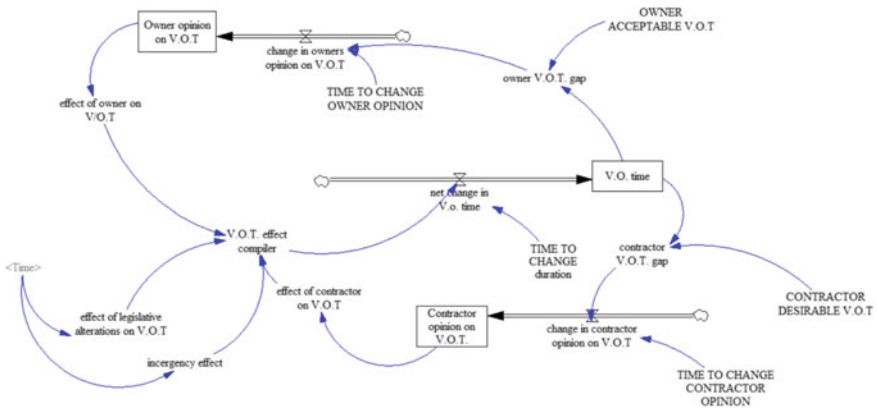


Fig. 3 Variation orders time in the construction project

## 5 The Results

Using the System Dynamics Model for the project execution data in construction projects, quantitative analysis was carried out Tables 2 and 3.

The results of SDM are explained in this section to analyze the effects of variation orders on a construction project. Various periods from 2008–2020.

**Analysis of Variation Orders Cost.** The variation orders cost in construction projects appears in different periods and is shown in Fig. 4. In the years (2008–2009–2010), the variation orders cost decreased because the Post-terror period increased in (2011) and (2012) because of the effect of laws and regulations on the variation orders. In years (2014–2016–2017), variation orders cost decreased because the

**Table 2** Validating the model of system dynamics for actual cost variation orders

Year	Actual weighted average cost (%)	Simulated weighted average cost (%)	Difference
2008	2	2	0
2009	3	3.22581	0.22581
2010	0	-0.0225952	0.0225952
2011	0	-0.0288894	0.0288894
2012	46	45.9136	0.0864
2013	0	-0.542119	0.542119
2014	11	10.391	0.609
2015	1	1.02221	0.02221
2016	0	0.522071	0.522071
2017	0	0.653568	0.653568
2018	0	0.821182	0.821182
2019	2	2.60912	0.60912
2020	2	2.14673	0.14673

**Table 3** Validating the model of system dynamics for actual time variation orders

Year	Actual weighted average time	Simulated weighted average time	Difference
2008	12	12	0
2009	2	2.62234	0.62234
2010	4	3.98289	0.01711
2011	10	10.031	0.031
2012	2	1.99973	0.00027
2013	0	0.626169	0.626169
2014	7	7.87489	0.87489
2015	8	8.39124	0.39124
2016	0	0.750232	0.750232
2017	0	-0.443413	0.443413
2018	0	0.158509	0.158509
2019	3	3.52859	0.52859
2020	5	4.46589	0.53411

impact of war and in years (2018–2019–2020), a small portion increased because completion of projects affected by 90% of standard documents.

**Analysis of Variation Orders Time.** In Fig. 5, the variation orders time increased in (2008). Projects stopped after the war and the economic crisis and decreased in (2009–2010). There was little funding for projects in that period and in (2011) increased because variation orders are affected by laws and in (2012–2013) decreased because there were restrictive instructions for the variation in (2014–2015) increased due

**Fig. 4** Variation orders actual cost on construction projects

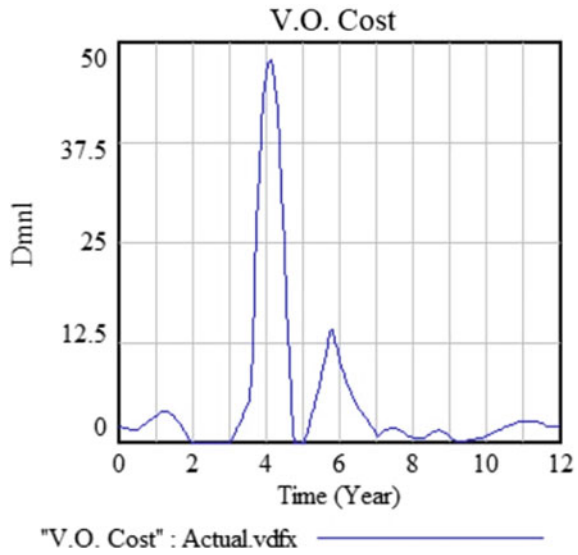
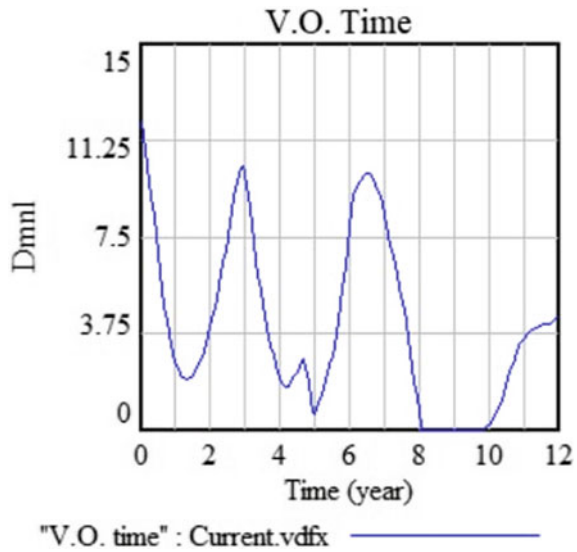
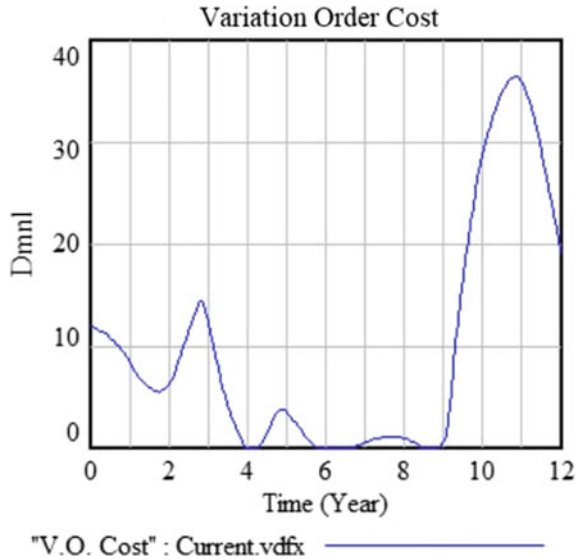


**Fig. 5** Variation orders time actual on construction projects



to financing for complementary projects orders and (2016–2017) decreased. After that, the impact of ISIS terrorism increased in (2018–2019–2020) because of stalled projects in this period and its impact on construction projects. In this study, based on general possible scenarios of contractor and owner that it is worth mentioning using system dynamics in this study to prove that the impact of variation orders in cost and time in construction projects and the related factors like insurgency and legislative effect on project performance and it helping decision-maker to control and manage

**Fig. 6** Variation orders time total on construction projects



in every stage of a project and discovering any factor that has the high of an impact on the project (Fig. 6).

## 6 Conclusion

In the system dynamic, the causal loop diagram identifies the negative and positive feedback processes.

- According to the results above, this study concluded that the variation orders impact the construction project’s time and cost to a high degree.
- There is a large number of variations orders that occurred in most construction projects in Iraq.
- In the actual time different from 12% in 2008 and decreasing to 5% in 2020.
- In actual cost additional from 2% and increasing to 46% in 2012 and dropping to 2% in 2020.

## References

1. Oyewobi, L. O., Jimoh, R., Ganiyu, B. O. & Shittu, A. A. (2016). Analysis of causes and impact of variation order on educational building projects. *Journal of Facilities Management*.
2. Gobana, A. B., & Thakur, A. S. (2017). A critical review on causes and effects of variation order on a construction project. *Critical Review*, 4(12), 1602–1606.

3. Daneshmand, P. G., Mehridehnavi, A., & Rabbani, H., (2020). Reconstruction of optical coherence tomography images using mixed low-rank approximation and second-order tensor based total variation method. *IEEE Transactions on Medical Imaging*.
4. Chen, J., Luo, Y., Li, Y., Chen, L., Wang, C., Song, Z., & Diao, P., (2020). Variation of rock mass pressure during tunnel construction in phyllite stratum. *Mathematical Problems in Engineering*.
5. Eizenga, J. M., Novak, A. M., Kobayashi, E., Villani, F., Cisar, C., Heumos, S., & Garrison, E., (2020). Efficient dynamic variation graphs. *Bioinformatics*.
6. Mohammad, N., Ani, A. C., Rakmat, R. A. O. K., & Yusof, M. A. (2010). Investigation on the causes of variation orders in the construction of building project—a study in the state of Selangor, Malaysia. *Journal of Building Performance*, 1(1).
7. Elshaikh, E., & Mahmoud, S., (2020). Variation orders in building projects in Khartoum State-Sudan: The causes and the impact on projects performance.
8. Stange, M., Barrett, R. D., & Hendry, A. P. (2020). The importance of genomic variation for biodiversity, ecosystems and people. *Nature Reviews Genetics*, 1–17.
9. Alaloul, W. S., Liew, M. S., Zawawi, N. A. W., Mohammed, B. S., Adamu, M., & Musharat, M. A. (2020). Structural equation modelling of construction project performance based on coordination factors. *Cogent engineering*, 7(1), 1726069.
10. Cui, Z., Zhao, Y., Cao, Y., Cai, X., Zhang, W., & Chen, J., (2021). Malicious code detection under 5G HetNets based on multi-objective RBM model. *IEEE Network*.
11. Siboni, S., & Cohen, A. (2020). Anomaly detection for individual sequences with applications in identifying malicious tools. *Entropy*, 22(6), 649.
12. Tayeh, B. A., Salem, T. J., Abu Aisheh, Y. I., & Alaloul, W. S. (2020). Risk factors affecting the performance of construction projects in gaza strip. *The Open Civil Engineering Journal*, 14(1).
13. Gatitu, J. N., Kabubo, C. K., & Ajwang, P. (2020). Approaches on mitigating variation orders in road construction industry in Kenya: The case of Kenya national highways authority (KeNHA). *Engineering, Technology and Applied Science Research*, 10(5), 6195–6199.
14. Ghafoor, A., & Mahmood, Y. (2020). To investigate variation order effects on building construction projects. *GSI*, 8(9).
15. Sabri, H. H. H., & Isa, C. M. M. (2020). Effects of late payments to small contractors in Malaysia. *Asian Journal of Research in Business and Management*, 2(4), 26–43.
16. Corcoran, A. W., Pezzulo, G., & Hohwy, J. (2020). From allostatic agents to counterfactual cognisers: Active inference, biological regulation, and the origins of cognition. *Biology and Philosophy*, 35(3), 1–45.
17. Odenigbo, O. G., Odusami, K. T., Okolie, K. C., & Okafor, V. C. (2020). Causes of delayed payment in construction project in Nigeria. *European Journal of Engineering and Technology Research*, 5(9), 1049–1053.
18. Malaysia, P. (2020). Risk cost analysis in malay heritage conservation project. *Journal of the Malaysian Institute of Planners*, 18(2), 59–72.
19. Hansen, S., Rostiyanti, S. F., & Rif'at, A. (2020). Causes, effects, and mitigations framework of contract change orders: Lessons learned from GBK aquatic stadium project. *Journal of Legal Affairs and Dispute Resolution in Engineering and Construction*, 12(1), 05019008.

# Evaluating the Performance of Iraq Construction Projects Using Building Information Modelling Technique



Noor H. Kadume and Hafeth I. Naji

**Abstract** Construction projects in Iraq face risks that have unique effects where it causes project stopping for long periods, sometimes for several years, and the actual cost of the project deviates from the cost of the planned project due to the weakness of the techniques used in the planning and design stage and the weakness in understanding the political, cultural and economic conditions of the country. This paper aims to evaluate the performance of construction projects in Iraq and to show the effect of these risks on the stages of project progress during the construction period through adopting an effective technique such as building information modeling and generating 4D model building to compare the between the actual work and the planned work for the project progress. The research methodology was applied in one of the completed Iraqi construction projects. The study concluded that 4D model generating is effective in evaluating the performance of construction and helps to understand the effect of risks on project activities progress and project completion time, also, the possibility of adopting this model as an evaluation program that helps the project managers to understand the performance of construction project before construction and avoiding risks. Project managers believe this model can contribute to controlling risks to a construction project and improving its performance.

**Keywords** Building information modeling · Construction risk · 4D simulation · Construction project · Construction scheduling

## 1 Introduction

The risks of the construction aor at the design phase may occur when the completed construction building does not compatible with the requirements of the owners and occupants [1]. Changing the owner requirement over time or weak communication between the design team and the owner generates this risk. However, the technique of Building Information Modelling (BIM) indicates the generating and coordinated

---

N. H. Kadume (✉) · H. I. Naji  
Civil Engineering Department, University of Diyala, Diyala, Iraq

use of a group of digital data about the project building. The project information may include schedule, cost, fabrication, energy, maintenance, and 3D models building that is used for making the design decision, production of the construction documents with high-quality performance, estimating the project cost, and construction project planning, and finally, managing and operating the project facility [2]. The building information modeling technology is an integrated and comprehensive system for all projects. It is a technology that includes procedures, applications, and policies that help enhance the projects' performance [3].

The technique of BIM considers as an effective tool in generating a virtual project environment that similar to the actual project environment of a job site that can be helping for identity and solve risk problems in the early project stages [4]. Most of the construction Companies took refuge in using the BIM technique in their projects [5]. The technique of building information modeling facilitates the design of the project and conducts modification of the 3D model and the storage of its data [6]. On another side, BIM technology can participate in information between different construction team members during the various phases of the project [7]. BIM facilitates dealing with the complexity of the construction projects, which impacts the basic objectives of construction projects [8]. Based on the previous features and characteristics of the BIM technique; it can be used as an effective technique to assess risk management process in a construction project [9], which is the important process in any construction project [10]. A number of studies were conducted to identify the risks of projects and improve the performance of construction projects. Chen and Luo [11] attempted to manage project quality using a 4D model based on the construction codes and generated a model for quality control. Mijić et al. [12] used BIM technology to develop an automated system that can improve occupational safety by linking the BIM model for the building by the developed risk databases of the construction. Chiu et al. [13] used the BIM technique to simulate a 4D model for constructing a steel bridge and conducting clash detection for it. Marzouk and Hisham [14] used the characteristic of BIM for cost estimation to generate an application that integrating BIM with Earned Value (EV) for cost controlling and schedule and identifies the project status at the specified time for infrastructure bridges. The construction sector in Iraq faces great risks due to the lack of understanding of the political, economic, cultural, and legal conditions of the construction project in a significant way, as well as the lack of evaluation of the performance of the construction project in the design stage, which affects the main objectives of the project (cost, time, quality). In this study, the researcher seeks to achieve the following goals:

- Evaluate the performance of construction projects in Iraq
- Evaluate and present the effect of risks in the construction projects in Iraq
- Shedding light on the most critical techniques used in the evaluation and management of construction projects.



## 2 Research Methodology

In this paper, the authors will use the characteristic provided by BIM to simulate and present the impact of risks in construction projects in the design stage to arrive at the best strategies to improve the performance of construction projects in the construction sector. This research methodology included two parts and can be organized as follows:

**Part One (Theoretical Side).** This part includes conducting a literature review for the previous studies concerning risk management in construction projects and the BIM technique (papers, thesis, websites, books).

**Part Two (Practical Side).** This part includes four stages as shown below:

- Stage one: identify the case study and collect related information to the construction project (2D drawing, data, project planned and actual duration, priced quantities scheduled).
- Stage two: generate a 3D model for the selected case study using Revit 2020 from Autodesk with many project details.
- Stage three: scheduling the project details (planned project start, planned project finish, actual project start, actual project finish) by Using MS Project 2010 by Microsoft project
- Stage four: this stage including of integration the output of the previous illustrated stages, which includes using Navisworks manage 2020 from Autodesk, which compatible with both Revit and MS project software and generating 4D building simulation, and Comparison the results between planned and actual project progress, and illustrate the effect of risk on actual project progress and its duration through the videos simulation results and finally conclusions that reached by the researcher.

## 3 Case Study: Internal Departments Building No. (2) at the University of Diyala

The building of internal departments at the University of Diyala No. (2) is one of the Diyala university projects. It consists of three-floor with an area (6000 m<sup>2</sup>). The University of Diyala transferred the project to a local company on 5/12/2013 with a period of (400) days at a total cost of (4,584,262,000) IQD, and the project was stopped on (9/3/2015). The work on the project was resumed on (5/2/2019) to complete the remaining works, and the project completed on (16/2/2020). Other project details summarized below:

- Type of Contract (Unit Price contract)
- Project planned start date (5/12/2013)
- Project planned finish date (8/1/2015)
- Project actual start date (5/12/2013)

- Project actual finish date (16/2/2020)
- Planned project duration (400 days)
- Actual project duration (2629 days).

The project was exposed to many risks that caused the project to stop for many years, and deviation the actual project duration about planned project duration and the actual cost exceeded the estimated cost. The author identifies these risks from many visits conducted by him with the project manager and supervisor engineer for the project; these risks are:

- Error in estimating the quantity of material
- The inability of the owner to finance the project
- Change in design
- Design difference between structural and architectural
- Effect of change order
- The difference between bill of quantity and plan
- The occurrence of risks excluded by both parties to the contract.

#### 4 Generate 3D Model for the Selected Case Study

The author used Revit software from Autodesk to generate a 3D model for the building, as shown in Fig. 1. Due to its high-quality graphics and can cause a better image significantly, and it includes many families that can be loaded to it also, it contains all the discipliners in one work environment. The Revit software interface includes many components which exactly appear when starting a new project. The collection of these components produces the tools needed to generate a 3D model for the building.



**Fig. 1** The 3D BIM model of the case study

### 5 Scheduling the Project Activities

After completing the collection of project information, the construction schedule for the 3D model components must be generating by using MS project software 2010; two types of project activity schedule are generating: planned construction schedule and actual construction schedule and taking into consideration relations between project activities. The author depends on data obtained about the case study to generate these schedules, such as bill of quantity and planned project duration, actual project duration. Figures 2 and 3 illustrate the planned and actual project Gantt chart view, respectively. The Generated schedules were imported to Navisworks manage 2020 that allows video simulation for the project activities for two cases (planned, actual).

The calendar that was adopted for the scheduling of the project activities is the internal department calendar, as shown in Fig. 4, which the local company adopted.

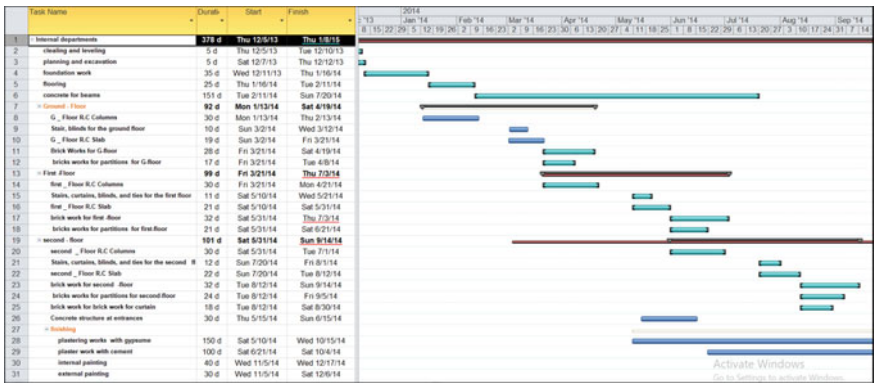


Fig. 2 Planned construction scheduling for case study

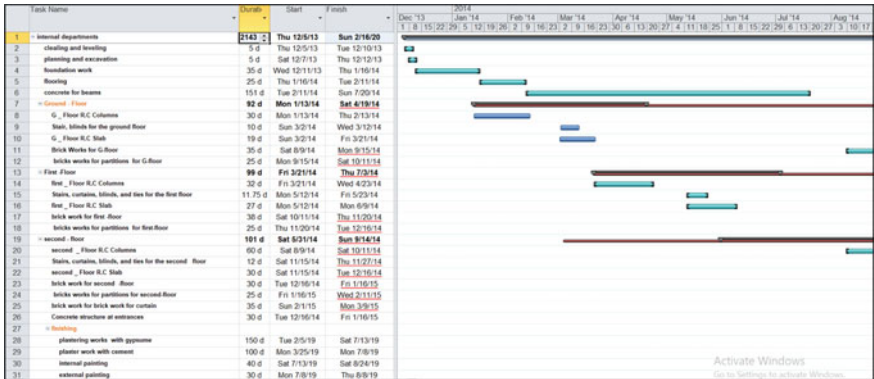


Fig. 3 Actual construction scheduling for the case study

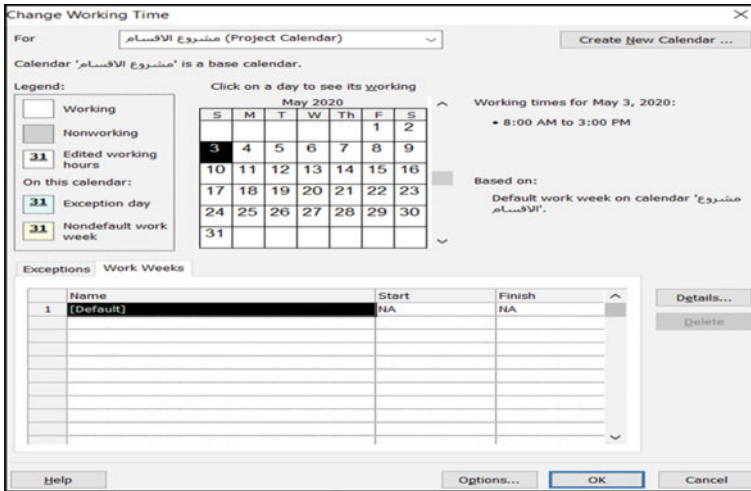


Fig. 4 The calendar adopted for scheduling

Table 1 The work time for each day

No	Day	Work time
1	Saturday	8:00 AM to 3:00 PM
2	Sunday	8:00 AM to 3:00 PM
3	Monday	8:00 AM to 12:00 PM 1:00 PM to 5:00 PM
4	Tuesday	8:00 AM to 12:00 PM 1:00 PM to 5:00 PM
5	Wednesday	8:00 AM to 12:00 PM 1:00 PM to 5:00 PM
6	Thursday	8:00 AM to 12:00 PM 1:00 PM to 5:00 PM
6	Friday	8:00 AM to 3:00 PM

All the weekdays are considered as working time, and the work time for each day is shown in Table 1.

## 6 Results and Discussion

The 3D model for the proposed case study was exported to Navisworks manage 2020. Also the construction schedule for the 3D model was imported, and generating 4D model by linking each activity in the project schedule with 3D model building, running the simulation for the project activities progress as shown in Fig. 5, which

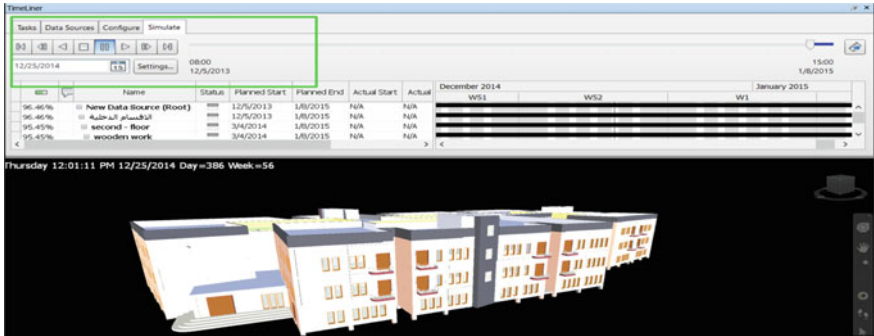


Fig. 5 Simulation running for 4D model in Navisworks software

allow identifying the effect of risks on project activities at any time from the virtual view resulted.

From the virtual view for the 4D simulation, the risks managers noted the following: For the actual construction schedule for the project activities, the 4D model simulation showed that there was a delay in completing some activities of the project, such as the brickworks for the ground floor which not completed as planned as shown in Fig. 6. Due to a number of the risks that faced the construction project,

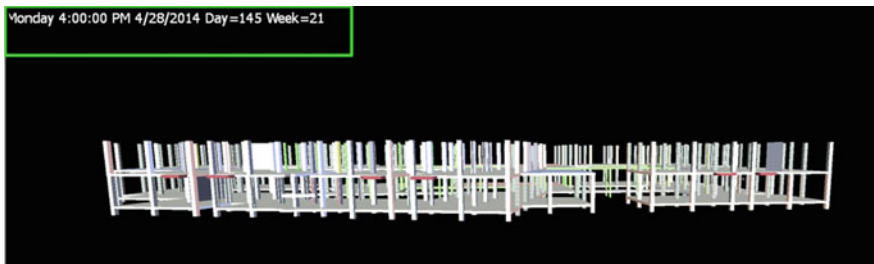


Fig. 6 Video screenshot for actual project progress

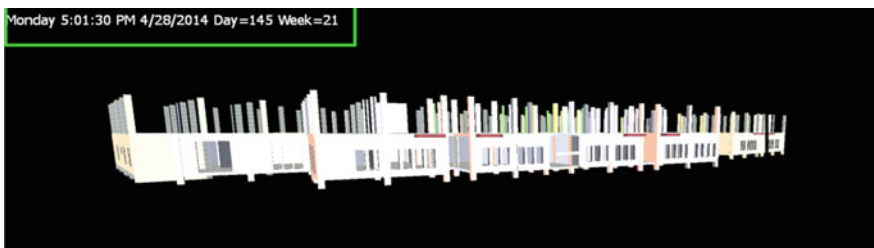
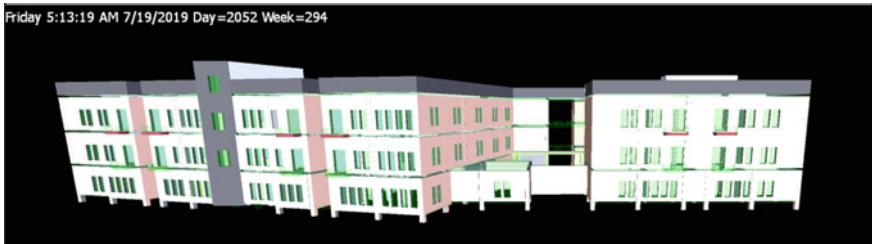


Fig. 7 Video screenshot for planned project progress



**Fig. 8** Video screenshot for actual project progress at 460 days



**Fig. 9** Video screenshot for actual project progress at 2052 days

and Fig. 7, which illustrates the planned project progress simulation for the same time.

According to the project information obtained by the author, the actual work in the project was stopped on 9/3/2015 due to the risk of the inability of the owner to finance the project. A lot of project activities were not completed, such as (window and door work, ceramic work, and brickwork for curtain); this stopping in project progress can be shown through the 4D building simulation as shown in Fig. 8.

The actual work on the project was resumed on 5/2/2019 to complete the other works that were not completed, and Fig. 9 shows a video screenshot during the simulation after resuming the work after stopping the work. The transparent green color represents the beginning of the windows and doors works for the project.

There was a difference between the planned project completion date and the actual project completion date because of the effect of project risks that were not considered in the earlier stages of the project; the simulation videos allow us to present this date difference by showing the date through simulation. The project took 400 days and 58 weeks to complete the project as planned, as shown in Fig. 10. The actual project took 2265 days and 324 weeks to complete, as shown in Fig. 11.



Fig. 10 Video screenshot for planned project progress at 400 days



Fig. 11 Video screenshot for actual project progress at 2265 days

## 7 Conclusions

Construction projects face many risks due to the uncertainty surrounding them, which in turn affects the basic objectives of the construction project (time, cost, quality). This study aims to highlight the role of BIM technology in evaluating the performance of construction projects that exposed to risks and managing these risks by generating a tool that assists project managers in understanding the impact of risks on the performance of construction projects and taking the necessary measures to control and avoid them in the later stages of construction. This goal was achieved by generating a 4D model by BIM, which allows simulating the schedule of project activities and showing the effect of risks on the time of completion of the construction project, as the proposed model helps to give a clear picture of the progress of the project activities during the construction phase, which facilitates the identification of the impact of risks on project activities. The proposed methodology can be applied in all types of construction projects. Also, video clips of the simulation model can be created in AVI format and shared among all stakeholders, which facilitates the visualization of the project clearly before its establishment, which in turn contributes to reducing the risks of the construction project.

## References

1. Albertor, D. M. (2011). *Project management for facility construction: A guide for engineers and architects*. ed.
2. Van Nederveen, S., Beheshti, R., & Gielingh, W. (2010). Modelling concepts for BIM. In *Handbook of research on building information modeling and construction informatics: Concepts and technologies* (pp. 1–18). IGI Global.
3. Hatem, W. A., Abd, A. M., & Abbas, N. N. (2018). Motivation factors for adopting building information modeling (BIM) in Iraq. *Engineering Technology and Applied Science Research*, 8(2), 2668–2672.
4. Abed, H. R., Hatem, W. A., & Jasim, N. A. (2020). Role of BIM technology in enhancing safety analysis of Iraqi oil projects. *Asian Journal of Civil Engineering*, 1–12.
5. Lam, T. T., Mahdjoubi, L., & Mason, J. (2017). A framework to assist in the analysis of risks and rewards of adopting BIM for SMEs in the UK. *Journal of Civil Engineering and Management*, 23(6), 740–752.
6. Eastman, C. M., Eastman, C., Teicholz, P., Sacks, R., & Liston, K. (2011). *BIM handbook: A guide to building information modeling for owners, managers, designers, engineers and contractors*. Wiley.
7. Jupp, J. (2017). 4D BIM for environmental planning and management. *Procedia Engineering*, 180, 190–201.
8. Bryde, D., Broquetas, M., & Volm, J. M. (2013). The project benefits of building information modelling (BIM). *International Journal of Project Management*, 31(7), 971–980.
9. Bråthen, K., & Moum, A. (2016). Bridging the gap: Bringing BIM to construction workers. *Engineering, Construction and Architectural Management*.
10. Zou, Y., Kiviniemi, A., & Jones, S. W. (2017). A review of risk management through BIM and BIM-related technologies. *Safety Science*, 97, 88–98.
11. Chen, L., & Luo, H. (2014). A BIM-based construction quality management model and its applications. *Automation in Construction*, 46, 64–73.
12. Mihić, M., Cerić, A., & Završki, I. (2018). Developing construction hazard database for automated hazard identification process. *Tehnički vjesnik*, 25(6), 1761–1769.
13. Chiu, C. T., Hsu, T. H., Wang, M. T., & Chiu, H. Y. (2011). Simulation for steel bridge erection by using BIM tools. In *Proceedings of the 28th ISARC* (pp. 560–563), Seoul, Korea.
14. Marzouk, M., & Hisham, M. (2014). Implementing earned value management using bridge information modeling. *KSCE Journal of Civil Engineering*, 18(5), 1302–1313.



# The Priorities for the Distribution of Primary School Projects According to the Spatial Gap Criterion at Baghdad/Iraq



Yaqdhan A. Kamil and Sedqi E. Rezouki

**Abstract** Baghdad governorate suffers from a lack of optimal use of resources and the problem of insufficient primary schools to accommodate the increasing number of students every year, the aging of old school buildings and the lack of construction of new schools is one of the clear examples of this. Primary education in the Republic of Iraq is mandatory. Not adhering to it. The research focused on investigating the roots of this problem and finding appropriate solutions for it in the future. The researcher relied on collecting and analyzing federal and local government data available from the Ministry of Education, the Ministry of Planning, and Baghdad Governorate. Comparisons made and compared with the standards adopted in spatial development. The main findings of the research showed that the adoption of the population standard in the distribution of school projects leads to inequality and equality between the cities that make up the city of Baghdad and creates a disparity in that service in favor of the population and not the real need for that service. It was also evident through the research that adopting the spatial gap criterion for development in the distribution of school building projects achieves justice and equality and contributes to promoting the principles of democracy and equal opportunities. The use of the spatial gap criterion for regional and local development is an effective tool in the optimal use of resources. The fair distribution of projects and creates a balance between cities according to the actual need for services and which is what has been proven in the research and has been strengthened by the results of the statistical analysis of the results.

**Keywords** Spatial · Development gap · Elementary schools · Priorities for primary school projects

## 1 Introduction

The development consists of comprehensive and continuous changes of human and material resources in various fields of living, economic, social, and others. These

---

Y. A. Kamil (✉) · S. E. Rezouki  
Civil Engineering Department, University of Baghdad, Baghdad, Iraq

changes are going in a specific direction to achieve goals for pre-drawn goals; thus, development is an intended and organized process of change, and this process throughout its course in developing countries has accompanied the development gap. Can be defined as gaps or deficiencies that occur during the comprehensive development process, whether at the sectorial or spatial level. The interest in service sectors in certain places at the expense of other places leads to a gap or defect in development in general [1]. The governorate of Baghdad, which is the capital of the Republic of Iraq, is one of the largest Iraqi cities in terms of population and the highest political and economic importance. Primary education in Iraq is one of the most important pillars of good governance, and the Iraqi systems have adopted compulsory primary education and the necessity of providing school buildings for all individuals the Iraqi people.

Baghdad suffers from a shortage of primary schools, which poses a real problem and a great challenge. What exacerbated the size of the challenge is the misuse of resources, especially in the distribution of these schools to cities in need, and the failure to set rational and real priorities for the fair and equitable distribution of these projects. The aim of the research focuses on finding the best way to use the available resources, managing them effectively to achieve the highest possible value from the optimal use of those resources, and determining the priorities for distributing school building projects for the primary stage in a fair manner. All of that among the cities of Baghdad Governorate using the spatial gap criterion for development. According to Iraqi law, the state is obligated to provide all necessary resources for primary education, and it is financed from the general budget, the development plan, and the need to properly distribute it to the population centers [2].

## 2 Spatial Development Gap

In this, section a review of the literature on the spatial development gap.

**Spatial Development.** Understandably, spatial development is those changes that occur in the state of a region (governorate) in an intended manner to improve the living conditions of the population and reduce spatial development disparities, which are the difference between one region and another in terms of the use of educational, health, social and economic services. In addition, the countryside or between the city and peripheral centers. The spatial development generally aims at achieving a balance between regions (governorates) in a way that provides convergence in average income and standard of living, reducing spontaneous trends in the field of migration, localization of industries, distribution of services, reducing unemployment, improving the level of economic activity to raise the rate of growth, Accordingly. Priorities for spatial development vary from one region to another depending on the base of natural and human resources and the development opportunities available in it [3]. The concept of spatial development means bringing about urban and regional changes. The first (urban) relates, in essence, to defining urban centers and urban

agglomerations whose regions should be developed according to specific mechanisms and periods. To achieve external savings and benefit from the elements of urban attraction and strive to achieve the highest benefit from front and backlinks from the returns of the place [4].

**Spatial Development Goals.** Spatial development goals are as follows [5]:

1. Developing national wealth sources, regions, and urban centers.
2. The integration of the territories of the parties and the organization of spatial space.
3. Improving the national system in terms of planning, management, and investment.

**The Possible Effects of The Differences in Development.** The possible effects of the differences in development, in general, can be summarized as follows [6].

1. The existence of unexploited economic resources in the less developed regions, which deprives these areas of opportunities to use them in development.
2. The high costs of investment and production in less developed regions because of the unavailability of the basic infrastructure, where the focus is on those services when establishing any of the investment projects, which constitutes additional costs on these projects.
3. Focusing on trends or theories ready for development, such as the balanced growth theory, which focuses on consumer and strategic industries that often require huge investments, which developing countries are unable to provide. The balanced growth theory is applied in the advanced stages of the development process, but the early stages. It recommended concentrating available resources in areas that make the national economy more flexible, which increases the degree of its response to market and demand expansion.
4. The lack of developmental integration between the regions of the same country as well as the lack of integration of the same region between them. This is what causes external links to the developed regions and governorates, and thus increases the external economic and trade dependency on them, and increases the degree of decline in the economic level. In addition, that strengthening the principle of economic efficiency (productivity) and social justice in the distribution of growth and development returns among the Iraqi governorates, will thus lead to limiting or reducing the deficit or disparities in the fields of development between cities.

### 3 Analysis of Spatial Development Conditions in the City of Baghdad

**Comparative Potentials and Advantages.** The city of Baghdad is located in the middle of the Iraqi lands and is the center of the governorate of Baghdad. The Tigris River divides the city into two halves: Al-Karkh on the western side of the river and

Al-Rusafa on the eastern side. There are the most popular areas and neighborhoods that the city's residents visit market Iraqi traditional products, and bridges extend along the river to connect The city's location is considered an intermediary between the two major Iraqi cities [7]. Baghdad governorate has comparative advantages and many and varied development potentials, as it owns large areas of arable land surrounding the governorate of more than 1.1 million dunums that are cultivated with all summer crops. In addition, winter, vegetables, citrus, and palm trees, and the governorate have a variety of tourism potentials (religious, archaeological, historical, and recreational).

It has more than thirty tourist sites distributed in various districts and sub-districts, as for the oil resources, there is in Baghdad governorate the Dora refinery, wax, and asphalt contains an advanced factory for manufacturing plastic cans to fill the produced oils. It produces about 11 thousand cans per month. In Baghdad, there is also an untapped oil reservoir located in the east of the province, where the reservoir reserves are estimated at 1 billion barrels. Baghdad governorate is characterized by non-oil mineral resources represented by clay and alluvial deposits, suitable for the manufacture of bricks. It has more than 10 large government factories are distributed in the governorate of Baghdad for the production of various industries and 31 medium factories and there are more than 2111 small private factories distributed in the districts and districts of the province [7].

**Administrative divisions of Baghdad governorate and population.** The Iraqi Republic is divided into governorates and governorates into districts and districts into districts, and each of them shall have a legal personality within the scope of the functions that the local administration exercise [2]. The relative importance of Baghdad Governorate is compared to the other seventeen governorates of Iraq according to the population criterion (25.02%) [8]. The population of Baghdad Governorate, according to estimates by the Central Bureau of Statistics-the Iraqi Ministry of Planning, is approximately (8,494,258) for the year 2018. The governorate of Baghdad consists of ten districts that make up the capital of the Republic of Iraq, Table 1.

**Table 1** Population estimates of Baghdad governorate depending on the Ministry of Planning-Iraq

City name	Population estimates for the year 20,018
Rusafa	1,884,250
Al-Adhamiya	1,253,379
Al-Sadr (1 + 2)	1,261,934
Al-Karkh	1,659,540
Al-Kadhimiya	938,684
Al-Mahmoudiyah	514,327
Abu Ghraib	341,126
Al-Tarmiya	154,537
Al-Madaen	486,484
Total	8,494,261

It is evident from Table 1 that Baghdad governorate is one of the big cities when compared with the nearby cities, as its population exceeds the population of some neighboring countries such as Kuwait, Qatar, Bahrain, and others. The largest districts in Baghdad governorate are the Rusafa district, followed by the district of Karkh, then Sadr City, and Adhamiya district, after which the Kadhimiya district and other relatively small districts, up to the smallest district, which is the Tarmiyah district.

#### 4 The Spatial Dimension of Primary Education Services in the City of Baghdad

**Indeed.** During the past four decades, Baghdad governorate has witnessed major developments in terms of spatial and population expansion, which has led to doubling the number of educational institutions in it and the distribution of their institutions and services independently of their indicators and planning standards, see Table 2.

From Table 2, the extent of the problem that the governorate of Baghdad suffers from, the large number of students in one school, as well as the number of students per class, with the lowest average of 39 students per class. This indicates the size of the shortage in buildings and the need to build new schools to accommodate the numbers the increasing number of students every year. Baghdad has 565 private primary schools distributed over the various districts [10].

**The Current Reality of Primary Schools According to the Local Planning Standard.** The local planning standard has specified one primary school for every (2500) inhabitant, meaning that the country needs about (13,039) schools. By comparing this standard with the actual availability of (17,235) primary schools

**Table 2** Number of primary schools, number of students, and indicators for Baghdad governorate for the year (2017–2018) based on data from the Ministry of Education in Iraq [9]

S	City name	Current elementary schools	Number of students	Number of rows	Number of teachers	Pupil/school	Pupil/class
1	Rusafa	357	297,409	6127	10,842	1/833	49/1
2	Al-Adhamiya	382	208,047	4751	11,956	1/545	44/1
3	Al-Sadr (1 + 2)	343	165,690	4955	8079	1/483	33/1
4	Al-Karkh	403	226,490	6147	16,436	1/562	37/1
5	Al-Kadhimiya	205	154,697	3583	8175	1/755	43/1
6	Al-Mahmoudiyah	243	82,736	2460	4545	1/350	34/1
7	Abu Ghraib	143	55,751	1366	2612	1/390	41/1
8	Al-Tarmiya	56	23,123	619	1128	1/413	37/1
9	Al-Madaen	159	98,782	1986	2345	1/621	50/1
	Total	2291	1,312,725	31,994	66,118		

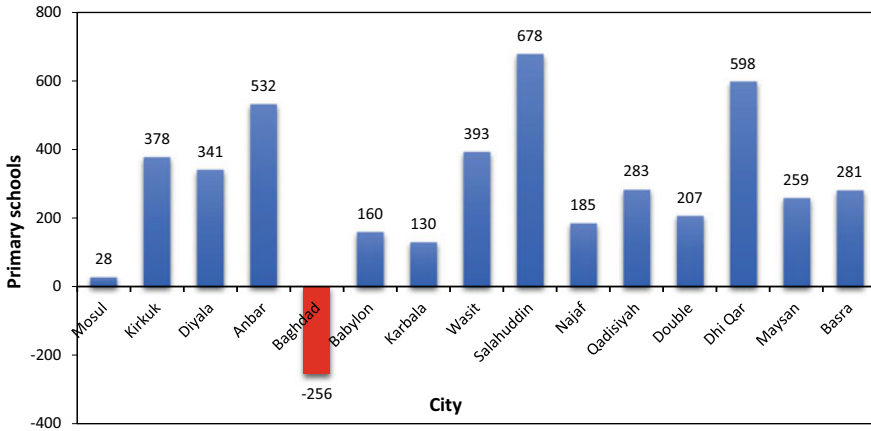


**Fig. 1** Spatial distribution of the deficit and surplus in the number of primary schools by governorates for the year 2019

(as an institution) in 2019 (see Fig. 1). On this basis, the surplus of primary schools reached (4196) schools, and when looking at the reality of the governorates, it became clear that there was a deficit found only in the governorate of Baghdad reached (256) schools [1].

Through Fig. 1, it is evident that Baghdad governorate is the only one suffering from a shortage in the number of schools according to this spatial distribution criterion, with no consideration of other criteria such as old, unqualified, and invalid schools. This supports what we have proposed regarding the necessity of studying this problem that the city of Baghdad suffers from and finding a successful solution to it.

**Calculate Spatial Need for Schools.** In this part, we calculate the number of primary schools according to the need of each district in the governorate of Baghdad. The equation that was extracted through the spatial need criterion for primary schools depending on the population, which is a local standard approved by the Ministry of Planning in Iraq and as shown in Table 3.

$$SR = (P/2500) \tag{1}$$

SR: Schools required according to the local need criterion for primary schools.  
 P: City population.

$$SPS = CS - SR \tag{2}$$

SPS: Shortage in primary schools according to the spatial need criterion.  
 CS: Current elementary schools.  
 SR: Schools required according to the local need criterion for primary schools.

**Table 3** Shortage in primary schools according to the spatial need criterion

The city name	Population estimates for the year 20,018	Required schools criterion (1/2500)	Percentage allocated to schools by population	Current elementary schools	Shortage in primary schools	Degree of development
Rusafa	1,884,250	754	22	357	-397	47
Al-Adhamiya	1,253,379	501	15	382	-119	76
Al-Sadr (1 + 2)	1,261,934	505	15	343	-162	68
Al-Karkh	1,659,540	664	20	403	-261	61
Al-Kadhimiya	938,684	375	11	205	-170	55
Al-Mahmoudiyah	514,327	206	6	243	37	118
Abu Ghraib	341,126	136	4	143	7	105
Al-Tarmiya	154,537	62	2	56	-6	91
Al-Madaen	486,484	195	6	159	-36	82
Total	8,494,261	3398	100	2291	-1107	

$$\text{PSP} = (\text{POC}/\text{PT}) \times 100 \quad (3)$$

PSP: Percentage allocated to schools by population percentage.

POC: Population by the district.

PT: The total population of the city.

$$\text{DOD} = (\text{CS}/\text{SR}) \times 100 \quad (4)$$

DOD: Degree of development.

Table 3 shows the reality of spatial development with regard to primary schools and the shortage of school buildings in the districts of Baghdad governorate. It also appears that the district of Mahmoudabad and Abu Ghraib does not suffer from a shortage of buildings, but on the contrary, there is a surplus in it equal to (37 and 7) respectively. The largest need is in the Rusafa district and the least in the Tarmiyah district.

## 5 Calculate Priority in the Distribution of Primary School Projects

The sums allocated for the reconstruction and development of projects for the Iraqi regions and governorates are distributed as follows [11]:

- According to the population of each governorate, and after it according to the population of each district.
- According to the percentage of deprivation.

**Table 4** The order of priorities according to the percentage of the population and the result of the distribution of projects according to the proportion of the population

The city name	Population estimates for the year 20,018	Percentage allocated to schools by population	priority	Distribution of new schools by population	RDP
Rusafa	1,884,250	22	1	246	-151
Al-Adhamiya	1,253,379	15	3	163	44
Al-Sadr (1 + 2)	1,261,934	15	3	166	4
Al-Karkh	1,659,540	20	2	216	-45
Al-Kadhimiya	938,684	11	4	122	-48
Al-Mahmoudiyah	514,327	6	5	67	104
Abu Ghraib	341,126	4	6	44	51
Al-Tarmiya	154,537	2	7	20	14
Al-Madaen	486,484	6	5	63	27
Total	8,494,261	100	-	-	-

**Priority According to the Population.** The districts are arranged according to the percentage of the population from most to the least and arrange in a sequence from 1 to 10. Then we will determine the relative importance of each district according to the population and as shown in Table 4.

$$RDP = SPS + NSP \quad (5)$$

RDP: The result of the distribution according to the proportions of the population.

SPS: Shortage in primary schools according to the spatial need criterion.

NSP: Distribution of new schools by population.

It has been assumed that there is a possibility of establishing 1107 new schools, which is the total value of the deficiency in primary schools in Baghdad, according to the spatial development criterion, at the rate of one school for every 2500 people. Then the new schools were distributed to the districts according to the population percentages. The result shown in Table 4, RDP indicated that the need for all districts was not covered. On the contrary, the results indicated an unfair distribution. Three districts suffered from a lack of schools compared to six districts that witnessed a surplus in the number of schools. This does not comply with the principles of social justice and the principles of rational management of resources. From the above, and because the criterion for distributing resources according to the proportions of the population does not provide a fair distribution of resources and does not achieve the required development and social justice. Another option that is more realistic and logical will be studied and will work to use the standard of spatial development in the distribution, as follows.

**Extract Relative Weight of The Districts According to the Spatial Development Criterion.** Since the distribution of resources according to the proportions of



the population did not achieve social justice and did not close the development gap for all regions in Baghdad governorate, there is no choice but to use the distribution according to the spatial criterion for development, which achieves justice in the distribution and optimal use of resources. Since the system adopted in Iraq is mainly dependent on the proportions of the population in the distribution of resources and it did not indicate how to calculate deprivation as a factor for the distribution with the factor of population. We extracted a relative weight by extracting the rate between the percentage of the population and the spatial development standard, where each factor is given a rate of 50% as shown in Table 5 that can be adopted as a medium standard, as well as taking into account the population growth of the large districts. In addition, the last field refers to determining priorities in the districts when distributing projects for schools according to the relative average of the two criteria (Fig. 2).

Negative values in the “The percentage of deficiency” column according to the spatial need indicate that the district of Mahmoudiya and Abu Ghraib has an increase in the number of schools over the spatial standard.

**Statistical Analysis of the Results.** Considering that the number of schools is the approved variable and the population is the first independent variable, and the degree of development is the second independent variable to be tested, and by applying this data statistically, we obtain the following results:

1.  $R^2$ : Its value was 0.943, meaning that more than 94% of the total changes in schools were able to explain the variables (population number and degree of development).
2. The linear relationship was confirmed by an F-test using a significance level of 5%.
3. The regression coefficients are significant for a significance level of less than 10%, and the estimated parameters are consistent with the economic starting point.
4. The index is collinearity, and through the two tests VIF and tolerance, it is clear that the model does not suffer from the problem of linear multiplicity, because the result of the test tolerance was 0.373, less than 1%, and the result of the VIF was A.81, i.e., less than 100, the summary of model results are given in Table 6.

## 6 Conclusion

Based on the results of this study, the following conclusions can be drawn out:

- It was found through the research that the governorate of Baghdad suffers from a severe shortage of primary schools, even though the law obliges them to be provided to everyone equally, as it was found that reality covers 67% of the total need.
- Baghdad governorate is the only one of the governorates of Iraq that suffers from a shortage of primary schools according to the spatial development criterion.

**Table 5** The need ratios for primary schools according to the spatial gap criterion, the rate of the development gap, and the population

The city name	Population estimates for the year 20,018	Required schools (1/2500)	Percentage allocated to schools by population	Current elementary schools	Shortage of primary schools according to the standard	Percentage of deficiency according to the spatial need	Average common relative weight	Priority order
Rusafa	1,884,250	754	22	357	-397	36	29	1
Al-Adhamiya	1,253,379	501	15	382	-119	11	13	4
Al-Sadr (1 + 2)	1,261,934	505	15	343	-162	15	15	3
Al-Karkh	1,659,540	664	20	403	-261	24	22	2
Al-Kadhimiya	938,684	375	11	205	-170	15	13	5
Al-Mahmoudiyah	514,327	206	6	243	37	-3	1	9
Abu Ghraib	341,126	136	4	143	7	-1	2	7
Al-Tarmiya	154,537	62	2	56	-6	1	1	8
Al-Madaen	486,484	195	6	159	-36	3	4	6
Total	8,494,261	3398	100	2291	-1107	100	100	

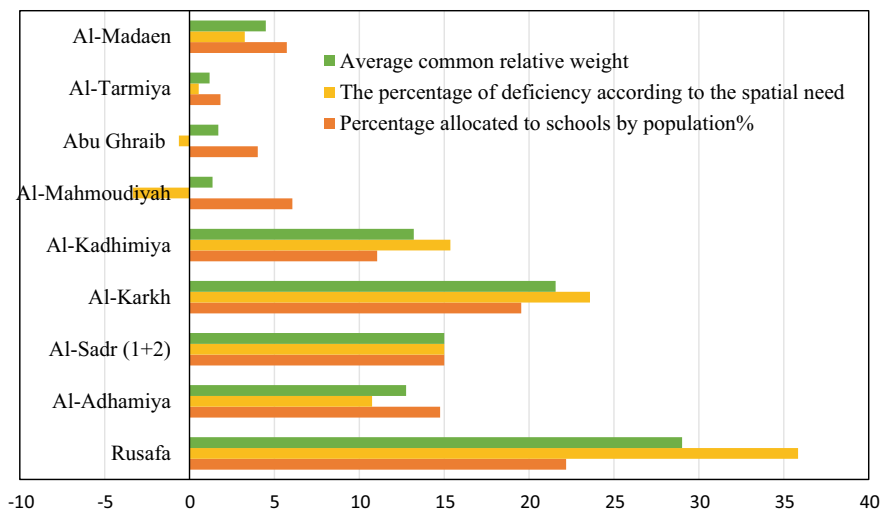


**Fig. 2** Comparing the spatial development criterion with the population criterion and the average of the two criteria

- The current reality of school buildings indicates that they are not suitable for work, as the lowest rate for students to class (1/34).
- The adoption of the criterion of distribution for projects according to the proportions of the population exacerbates the crisis and does not contribute to its condition.
- The use of the spatial development criterion greatly contributes to solving the equitable distribution of financial resources according to development priorities.
- The research suggested a compromise solution that can be adopted to reduce the development gap by adopting a population and development standard rate, which achieves a kind of balanced distribution of resources.
- Through the research, it was found that the education sector and other sectors suffer from a great lack of data necessary to make the right decisions regarding the management of their resources. It requires a general and detailed census, as it constitutes the main pillar in successful planning.
- The researcher proposes to carry out future studies that include listing the reality of the established schools, their design ages, and their validity, and linking other developmental criteria as they represent one interactive system that must be taken into consideration.

**Table 6** Summary of model results

Model	R	R <sup>2</sup>	Adjusted R <sup>2</sup>	Std. error of the estimate	R <sup>2</sup> change	Change statistics			
						F change	df1	df2	Sig. F change
1	0.971 <sup>a</sup>	0.943	0.924	39.281	0.943	49.373	2	6	0.000

<sup>a</sup> Predictors: (Constant), DOD, Population estimates for the year 20,018

## References

1. Department of Regional and Local Development. (2020). *Spatial development gaps*. Ministry of Planning.
2. Iraqi Parliament. (1969). *Provincial Law No. (159) of 1969*. Al-Waqi'a Iraqi Newspaper.
3. Shukr, A. A. A., & Youssef, B. S. (2019). Measuring the spatial development indicators among the Iraqi governorates for 2017.
4. Syed, M. M. (2007). Spatial development policy in Iraq.
5. Al-Masoudi, R. M. A. O. (2015). Spatial strategies for the development of the housing sector. *Al-Ghari Journal of Economic and Administrative Sciences*, 10, 151–167. (In Arabic).
6. Department of Regional and Local Development. (2019). *Spatial development gaps in accordance with planning standards for technical structures with economic activities in the provinces*. Ministry of Planning.
7. Department of Regional and Local Development. (2019). *Spatial development of the governorates of Iraq within the National Development Plan (2018–2022) Baghdad Governorate summary*. Ministry of Planning.
8. Central Statistical Organization and Ministry of Planning/Iraq. (2016). *Materiality by population 2016*.
9. Department of Education Planning, and Department of Statistics. (2019). *Statistics of primary education in Iraq for the academic year 2019/2018*. Ministry of Education.
10. Federal Board of Supreme Audit of Iraq. (2020). *Detailed statistics of the number of private schools inside and outside Iraq only Levels and provinces*.
11. Iraqi Parliament. (2008). *Federal supplementary budget law for the year 2008 resolution No. (25)*. Al-Waqi'a Iraqi newspaper.

# Regulation of Supplier Standards in Iraq: Through Sustainability Standards



Bariq W. Abdulmajeed and Meervat R. Altaie

**Abstract** The supply chains of construction projects in Iraq have a significant impact on the quality, cost, and time of the project, and therefore the supplier is considered of great importance in the success of the project and achieving the desired objectives. According to the Ministry of Planning publications (Standard Bid Documents Supplying of Commodities) and international standards requirements from suppliers, it found a gap between the global needs and the available requirements. The purpose of this research is to set a standard for suppliers to know the level of each supplier and to propose these standards to be combined with standard bid documents supplying commodities to fill the gap by developing it by making it a sustainable document. The standards that meet the research objectives were collected and included in a questionnaire targeting the experts from various specialties related to the research topics from academics and employees in the supplying of commodities and project departments in the various ministries to evaluate the importance of the standards in evaluating suppliers from a sustainable point of view. The RII (Relative Important Index) was adopted statistically to know the importance of the standards. The essential standards became the base standards for the rating system. The research results indicated that most economic, environmental, and social standards are important in evaluating the suppliers, thus bringing us closer to global sustainability standards. The research outputs were a rating system for suppliers on an economic, environmental, and social basis.

**Keywords** Supply chain · Sustainable supply chain management · Procurement · Suppliers selection standards

---

B. W. Abdulmajeed (✉) · M. R. Altaie  
Civil Engineering Department, University of Baghdad, Baghdad, Iraq  
e-mail: [b.wifad1101@coeng.uobaghdad.edu.iq](mailto:b.wifad1101@coeng.uobaghdad.edu.iq)

M. R. Altaie  
e-mail: [meervat.r@coeng.uobaghdad.edu.iq](mailto:meervat.r@coeng.uobaghdad.edu.iq)

## 1 Introduction

Because of the Iraqi government's orientations towards standards development and increasing awareness of its importance, the supply companies found that adopting sustainability in their system increases their competitiveness. Sustainable construction projects are affected by choice of suppliers, and that the supplier selection process is carried out through several criteria to determine the best supplier. These standards aim to cover environmental, social, and economic issues. The beginning of sustainability was on 20 March 1987 in the Brundtland Report [1] which define Sustainable Development as: "development that meets the needs of the present without compromising the ability of future generations to meet their needs" and from that point, attention and recognition of the importance of sustainable development in construction increased, and when this development is combined with construction processes to become "sustainable building".

Sustainable building is a term that describes a process that begins in the planning and design stages and continues after that. Sustainable construction is not for a period of the life of the project but for all building parts from start to finish, including recycling of these parts to reduce the environmental impact of demolition waste, where the ecological impact is seen as a fourth goal, in addition to cost, time and quality. Sustainability in construction is an integrated approach to the construction life cycle from an environmental perspective, as it adds new operating procedures and environmentally friendly maintenance methods. US Environmental Protection Agency [2] has defined sustainable construction as "the practice of creating structures and using processes that are environmentally responsible and resource-efficient throughout a building's life-cycle from siting to design, construction, operation, maintenance, renovation, and deconstruction".

Sustainable construction is defined by The Building and Construction Authority in Singapore [3] as: "the adoption of materials and products in buildings and construction that will consume fewer natural resources and increase the reusability of such materials and products for the same or similar purpose." Sustainable construction is the engine of the construction industry, which directs the construction industry towards sustainable development while trying as much as possible to take into account the environmental, social, and economic aspects [4].

## 2 Supply Chain

In general, the meaning of "supply chain" is about the information, materials, and funds flow. Supply chain defines as "the network of organizations that are involved, through upstream and downstream linkages, in the different processes and activities that produce value in the form of products and services in the hands of the ultimate customer" [5]. Simultaneously, Ganeshan and Harrison [6] defined the supply chain as a network of facilities and distribution options that perform the functions

of procurement of materials, the transformation of these materials into intermediate and finished products, and distributing these finished products to customers. Lambert et al. [7] defined the supply chain as the alignment of firms or organizations that bring products or services to market.

And with the development, the concept of management merged with the supply chain [8]. Define SCM as: “The management of a network of relationships within a firm and between interdependent organizations and business units consisting of material suppliers, purchasing, production facilities, logistics, marketing, and related systems that facilitate the forward and reverse flow of materials, services, finances, and information from the original producer to the final customer with the benefits of adding value, maximizing profitability through efficiencies, and achieving customer satisfaction”. While [9] defined Supply Chain Management (SCM) as “the management of the flow of goods and services”. And when using the supply chain in construction, where Construction Supply Chain Management (CSCM) is a specialized type of SCM that is designed for unique properties in the construction industry, and the supply chain becomes more sophisticated the more specialized or complex the building.

The SCM in construction (CSCM) is defined as “the network of facilities and activities that provide customer and economic value to the functions of design development, contract management, service, and material procurement, materials manufacture and delivery, and facilities management” [10]. It was noted that the two most important issues in recent years for the construction sector were supply chain management and sustainable construction; the integration of sustainability issues in supply chain management is referred to as sustainable supply chain management (SSCM). The SSCM defined as the strategic, transparent integration and achievement of an organization’s social, environmental, and economic goals in the systemic coordination of key inter-organizational business processes for improving the long-term economic performance of the individual company and its supply chains [11].

### **3 Construction Procurement**

The state of Procurement in Construction is a complementary part of the construction project. In addition to procurement sources, it includes activities to providing supplies, materials, construction equipment, management services, and supervision needed to achieve project goals. After increasing environmental violators’ governmental organization, it became impossible for companies to ignore the ecological issue. Simultaneously, the supply chain was integrated into the system to increase the interest, so it was necessary to develop the supply chain to meet the environmental standards. The financial performance is positively affected by the ecological purchase [12]. The ecological investment is defined as “Environmental purchasing for an individual firm is the set of purchasing policies held, actions taken, and relationships formed in response to concerns associated with the natural environment. These concerns relate to the acquisition of raw materials, including supplier selection,



evaluation and development, suppliers' operations, in-bound distribution, packaging, recycling, reuse, resource reduction and final disposal of the firm's products" [13].

## 4 Supplier Selection

Decisions are subject in the SCM standards are always different or conflicting factors, and that is why there is a need to change the standards for selecting suppliers from time to time. These factors are the general critical standards that most construction companies are looking for during materials purchasing that have a significant impact on the problem of suppliers' selection; it can also be said that the environmental and social performance of suppliers is the main condition, and the suppliers are evaluated through these standards, after reviewing the literature, many Factors for the Supplier Selection, [9]. Some of them are: Price, Payment Terms, Quality, Management, Delivery date, Proper communication, Reliability, Obligation, Financial position, Maintenance service, Test certificate, Long-term relationship, Discounts, Safety and health considerations, Customer's satisfaction.

Planning and production have many aspects, the most important of which is supply chain management (SCM), and this is what was recently considered by researchers and managers. The supply chain consists of manufacturers, producers, traders, and distributors and consultants, contractors, and suppliers, and do not forget the role of developers and researchers as well, etc. Simply, these processes and return them to the main parts that fall under product, supplier, and customer. In this sense, cooperation with suppliers with higher performance for sustainability policies always gives the best results with long-term benefits, for example, waste disposal, which in turn leads to lower costs, protection and increase reputation, increased quality development, increased flexibility to achieve customer requirements, Reduced lead times for some supply chain operations. To know the suppliers who will enter the competition to select the most appropriate supplier in terms of services and facilities provided to the customer, the supplier must fulfill specific sustainable standards. The literature outlines the supplier requirements or standards to be adhered to demonstrate the supplier's sustainability [14, 15]. And we will mention some of them, to name a few:

- Environmental supplier's activities and their management system.
- Adopting an international environmental management system (EMS) such as ISO 14001.
- Continuously developing and maintaining the ecosystem.
- Government regulations and legal compliance with environmental.

However, supplier sustainability is a complex system with many factors, and there was no global agreement among researchers on the form of supplier evaluation indicators. For that, in this study, the author will suggest a set of standards with a sustainable perspective to determine the extent of supplier sustainability. And to add knowledge about the environmental management system (EMS), which it is possible to meet

the customer's requirements, in addition to participating in environmental protection. ISO defines EMS as: "that part of the overall management system that includes organizational structure, planning activities, responsibilities, practices, procedures, processes, and resources for developing, implementing, achieving, reviewing and maintaining an environmental policy"[16, 17]. If EMS is appropriately implemented and the sustainability strategy, it will be possible to provide long-term benefits. To achieve the organization's goals in sustainability and EMS, supply chain design is an important part of this process. We can say that selecting suppliers who support the organization's EMS policies is a basis for implementing sustainability strategies effectively.

## 5 Field Survey and Statistical Analyzing

After reviewing the literature on the study subjects, the researcher extracted several standards into a questionnaire to determine the importance of each criterion in evaluating suppliers to know the best suppliers who will receive the highest evaluation score and who are qualified to compete for sustainable projects. The questionnaire aims to determine each criterion's importance in evaluating suppliers to know the best suppliers who will receive the highest evaluation score and who are qualified to compete for sustainable projects and regular projects to be more sustainable.

The questionnaire was distributed to (162) experts and specialists in research topics who have scientific and practical experience in this field, and only (79) answers were collected. After collecting the data, it was analyzed statistically using the SPSS program and Excel. The RII (Relative Important Index) was adopted statistically to know the importance of the standards. [18] The results will be used in selecting essential standards in designing a list of standards for evaluating suppliers. For this purpose, the researcher used a five-point Likert scale. Results are presented in graphical form to increase clarity. As mentioned earlier, the questionnaire was divided into major axes. The results were as follows:

**The First Axis.** This axis deals with personal information such as:

**Academic Achievement.** After reviewing 79 questionnaires, it was found that the respondents' academic achievement was: one person holding a diploma, 44 people holding a bachelor's degree, 27 people holding an M.Sc. degree, and 7 people having a Ph.D.

**Specialization.** It was found that there is 1 Business Administration, 10 Project Management, 1 Electronic and Communications, 7 Building and Construction, 2 Environmental, 3 Computers, 1 Control and Systems, 1 Electronic, 2 Chemistry, 40 Civil, 1 Survey, 2 Architecture, 1 Material, 2 Water Resources, 5 Mechanics.

**Age.** It was found that there is: 26 persons between (20–29) years old, 31 persons between (30–39) years old, 18 persons between (40–49) years old, 3 persons between (50–59) years old, 1 person between (60–69) years old.

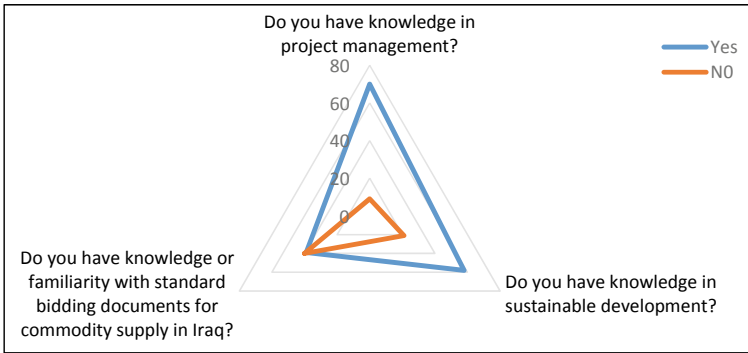


**Fig. 1** Spider chart of knowledge about basic research topics

**Years of Experience:** It was found that there is: 44 persons have between (0–9) years, 27 persons have between (10–19) years, 6 persons have between (20–29) years, 2 persons have between (30–39) years.

**The Second Axis.** Knowledge about basic research topics. This axis aims to assess respondents’ experience of project management, sustainable development, and standard bidding documents for Iraq’s commodity supply. The results were as shown in Fig. 1.

**The Third Axis-Economic Standards.** This axis consists of four parts, and the data will be analyzed; and the arithmetic mean, standard deviation, RII, and the weight of criterion will be extracted to know the level of classification for each criterion in these parts. This part aims to know the extent of the importance of the mentioned standards in evaluating the supplier in terms of cost, quality, delivery and services, and flexibility. From the 21 economic criteria that were tested, the criteria that give very high importance were chosen. The results are shown in Table 1.

**The Fourth Axis-Environmental Standards.** This axis consists of four parts, and the data will be analyzed; and the arithmetic mean, standard deviation, RII, and the weight of criterion will be extracted to know the level of classification for each criterion in these parts. This part aims to know the extent of the importance of the mentioned standards in evaluating the supplier in terms of environmental management, quality of available materials, green products, and green image. From the 29 environmental criteria that were tested, the criteria that give very high importance were chosen. The results are as shown in Table 2.

**The Fifth Axis-Social Standards.** This axis consists of four parts, and the data will be analyzed; and the arithmetic mean, standard deviation, RII, and the weight of criterion will be extracted to know the level of classification for each criterion in these parts. This part aims to know the extent of the importance of the mentioned standards in evaluating the supplier in terms of work ethics. From the 12 social

**Table 1** Economic standards

MS	Axis	SS	Details	RII (%)	Weight (%)
EC	Economical standards				
EC1	Cost	EC1.1	Disposal cost	87.85	2.77
		EC1.2	Material/Product cost	87.34	2.75
		EC1.3	Freight cost	86.58	2.73
		EC1.4	Transportation cost	85.57	2.69
		EC1.5	Cost reduction activities	85.06	2.68
		EC1.6	After-sales service cost	84.81	2.67
		EC1.7	custom duties	84.05	2.65
EC2	Quality	EC2.1	Rejection rate of the product	87.59	2.76
		EC2.2	Technology capability	86.33	2.72
EC3	Delivery and services	EC3.1	Time to solve the complaint	85.32	2.69
EC4	Flexibility	E4.1	Flexibility in discount	88.86	2.80
		E4.2	Increase of supply flexibility	84.24	2.65

criteria that were tested, the criteria that give very high importance were chosen. The results are shown in Table 3.

## 6 Economic, Environment, and Social Rating System (EES)

To achieve the best evaluation of suppliers from an economic, environmental, and social point of view to ensure the contenders' suppliers for the supplying of sustainable projects, having the highest evaluations, and determining the importance weight of the rating standards system. The EES rating system (economic, environmental, and social rating system) aims to evaluate suppliers from an economic, social, and ecological point of view in order to achieve the requirements of sustainability through several economic, environmental, and social standards that have a significant positive impact on society and the surrounding environment. The EES rating system was designed by using several economic, environmental, and social standards after it was classified as very important by experts and the field survey sample. The EES rating system included three axes:

The first axis is about the economic standards, which included 4 sections which include 7 standards in terms of cost, 2 standards in terms of quality, 1 standard in terms of delivery and services, 2 standards in terms of flexibility. The second axis is about the environmental standards, which included 4 sections which include 5 standards in terms of environmental management, 1 standard in terms of the quality of materials, 5 standards in terms of green products, 3 standards in terms of the green image provided by the supplier. The third axis is the social standards which included 10 standards in terms of work ethics.

**Table 2** Environmental standards

MS	Axis	SS	Details	RII (%)	Weight (%)
EN	Environmental standards				
EN1	Environmental management followed by the supplier	EN1.1	Supplier owning an environmental management system (ISO 14001, etc.)	88.35	2.78
		EN1.2	Supplier owning a quality management system (ISO 9001, etc. ...)	89.87	2.83
		EN1.3	Supplier commitment to periodic environmental auditing	88.10	2.77
		EN1.4	Supplier owning management of hazardous air emissions and hazardous waste	90.63	2.85
		EN1.5	Supplier owning an environmentally friendly technology	84.30	2.65
EN2	The supplier's available materials type	EN2.1	The supplier does not have material from the EPA 17 List of hazardous chemicals	84.05	2.65
EN3	The supplier's green products	EN3.1	Product designed to protect the environment	92.15	2.90
		EN3.2	Product produced in ways that protect the environment	91.65	2.88
		EN3.3	Use of environmentally friendly raw materials in the industry	90.89	2.86
		EN3.4	Recyclability of products	90.13	2.84
		EN3.5	Environmental labeling of products	84.81	2.67
EN4	Green image provided by the supplier	EN4.1	Staff training on environmental practices for green awareness	89.87	2.83
		EN4.2	The supplier controls a product storage life that does not exceed 10% of the product's total life	86.33	2.72
		EN4.3	The supplier undertakes activities to stimulate customers to consume green products	84.05	2.65

**Table 3** Social standards

MS	Axis	SS	Details	RII (%)	Weight (%)
S	Social standards				
S1	Work ethics of the supplier	S1.1	Take into account health and safety practices (ISO 45001)	94.68	2.98
		S1.2	The supplier's refuse to employ children	93.42	2.94
		S1.3	abstention the supplier about denial of financial rights and others	92.66	2.92
		S1.4	The necessity of having a contract and a work permit	92.41	2.91
		S1.5	The supplier uses local materials and encourages them	90.89	2.86
		S1.6	Suitable working hours	90.632	2.85
		S1.7	Health insurance for employees/workers	89.62	2.82
		S1.8	Abstention the supplier About Discrimination between Employees/workers	89.37	2.81
		S1.9	Recruiting local stuff	88.86	2.80
		S1.10	Providing suitable food and drink for employees/workers	85.82	2.70
Final sum				3177.14	100

## 7 Results and Conclusions

The results appear in the form of a checklist with a cumulative rate of 100%, after many environmental, economic, and social criteria were tested and the final criteria of high importance were reached in determining the best suppliers for sustainable projects. Suppliers will be identified, and their sustainable level is defined by submitting to this list to indicate the extent of conformity between the supplier's information and the standards in the system to show the supplier's result as a degree of 100% and on this basis the competition between suppliers takes place by taking the best suppliers who have achieved the highest scores.

Through reviewing the literature and studying the standard bid documents supplying commodities, we concluded some significant issues:

- (1) The construction industry suffers from a lack of studies in supply chain and supplier selection in general and sustainable suppliers in particular.
- (2) The construction supply chain management and supplier's selection are essential, so the wrong choice of supplier or lack of experience will lead to the following:

- Lower value building.
  - Harmful effects on the environment and society.
  - Higher cost to complete the work.
  - The workplace is full in a way that affects the progress of work.
- (3) Some people are trying to go towards sustainability, but they are not finding support from managers and the government.
  - (4) There are no binding legislation and laws for sustainable development in Iraq.
  - (5) There is a need to organize random efforts and direct them towards sustainable development.

## References

1. Keeble, B. R. (1988). The brundtland report: 'our common future'. *Medicine and war*, 4(1), 17–25.
2. US EPA. (2016). Basic information-green building. US EPA. Available at: <https://archive.epa.gov/greenbuilding/web/html/about.html>. Accessed: 19 June 2020.
3. Chew, K. C. (2010). Singapore's strategies towards sustainable construction. *The IES Journal Part A: Civil & Structural Engineering*, 3(3), 196–202.
4. Shafii, F., Arman Ali, Z., & Othman, M.Z. (2006). Achieving sustainable construction in the developing countries of Southeast Asia. In *Proceedings of the 6th Asia-Pacific Structural Engineering and Construction Conference*.
5. Christopher, M. (1994). Logistics and supply chain management: Strategies for reducing costs and improving services. *Journal of the Operational Research Society*, 45(11), 1341.
6. Ganeshan, R., & Harrison, T. P. (1995). An introduction to supply chain management.
7. Lambert, D. M., Cooper, M. C., & Pagh, J. D. (1998). Supply chain management: Implementation issues and research opportunities. *The international journal of logistics management*, 9(2), 1–20.
8. Stock, J. R., & Boyer, S. L. (2009). Developing a consensus definition of supply chain management: a qualitative study. *International Journal of Physical Distribution and Logistics Management*.
9. Krishnakumar, S., & Kuriakose, L. T. (2016). Supply chain management in construction industry. *International Journal of Scientific Engineering and Research (IJSER)*. ISSN (Online), pp.2347–3878.
10. Love, P. E., Irani, Z., Cheng, E., & Li, H. (2002). A model for supporting inter-organizational relations in the supply chain. *Engineering, Construction and Architectural Management*.
11. Carter, C. R., & Rogers, D. S. (2008). A framework of sustainable supply chain management: Moving toward new theory. *International Journal of Physical Distribution & Logistics Management*.
12. Carter, C. R., Kale, R., & Grimm, C. M. (2000). Environmental purchasing and firm performance: An empirical investigation. *Transportation Research Part E: Logistics and Transportation Review*, 36(3), 219–228.
13. Zsidisin, G. A., & Siferd, S. P. (2001). Environmental purchasing: A framework for theory development. *European Journal of Purchasing & Supply Management*, 7(1), 61–73.
14. Eltayeb, T. K. (2009). *Adoption of green supply chain initiatives by ISO 14001 certified manufacturing firms in Malaysia: Key drivers, outcomes, and moderating effect of relationship orientation*. Universiti Sains Malaysia.
15. Hamner, B. (2006). Effects of green purchasing strategies on supplier behaviour. In *Greening the supply chain* (pp. 25–37). Springer.

16. Darnall, N. (2006). Why firms mandate ISO 14001 certification. *Business & Society*, 45(3), 354–381.
17. Darnall, N., Jolley, G. J., & Handfield, R. (2008). Environmental management systems and green supply chain management: Complements for sustainability? *Business strategy and the environment*, 17(1), 30–45.
18. Obead, K. R., & Wali, M. R. (2020). Developing systems engineering for sustainable infrastructure projects. In *IOP conference series: Materials science and engineering* (Vol. 901, No. 1, p. 012026). IOP Publishing.



# Assessment of Standard Request for Proposal for the Selection of Consultants in Iraq



Noor A. Ramadhan and Sawsan R. Mohammed

**Abstract** Professional services are required in the construction projects starting from the pre-preparation stage reaching to project's operation. Thus, the consultant directly influences the project development and success. In Iraq, the Ministry of Planning has recently issued the standard request for a proposal for consultancy service (SRPFCS) as one of the sectorial bidding documents. The mentioned document aims to improve the consultant's selection procedures to select qualified professionals. This study is concerned with evaluating the impact of SRPFCS on Iraqi construction projects, estimating the level of experiences of the contractual entities and consultancy offices in bidding procedures, determining whether the SRPFCS are correctly implemented or not. The study was conducted using questionnaire surveys in which 130 questionnaires were distributed to participants who work in contractual entities and engineering consultancy offices in both public and private sectors. The results showed that the document positively affected the Iraqi construction project and referred that both public and private sectors don't have sufficient experience to properly implement SRPFCS. The results also identified that the participation of the private consultants' offices is very low in governmental biddings.

**Keywords** Standard request for proposal · Selection of consultants · Iraqi construction projects · Engineering consultancy offices · Impacts · Obstacles · Bidding

## 1 Introduction

A consultant is a specialist or an expert in a particular field and has professional information on the topic matter. The consultant usually works for a specific consultancy firm or is independently employed, and deals with different kinds of customers. Consequently, customers can get further degrees of help and advice that could be attainable for them to hold from in-house consultants and may buy just additional

---

N. A. Ramadhan (✉) · S. R. Mohammed  
Department of Civil Engineering, University of Baghdad, Baghdad, Iraq  
e-mail: [n.ramadhan1901m@coeng.uobaghdad.edu.iq](mailto:n.ramadhan1901m@coeng.uobaghdad.edu.iq)

assistance from the external adviser as needed [1]. The engineer (consultant) is the owner's agent who makes sure that the project is executed correctly with technical specifications and design standards and with the scheduled time and budget, offering effective value management to the project owner [2]. The construction consultancy service in the project can be described as a value creation activity. 'Value' can be conceptualized as where a consultant uses better technology, combines resources more efficiently, or aids the client to pay a lower price such that the project meets present needs without losing its ability to meet future needs [3]. The selecting of a consultant for a construction project is rather complicated. Due to the intangible nature of the provided services, the client doesn't have enough knowledge to conduct the selection process properly [4].

In Iraq, the sectorial and non-sectorial Standard Bidding Documents (SBDs) was issued by the Iraqi ministry of planning in cooperation with the World Bank. It was one of the many procedures that the Iraqi government took to improve the Public Procurement System, the SBDs has entered into the mandatory implementation since July 2016. The SRPFCS pursues to achieve transparency and fair competition in consultant selection to get high-quality service for the construction projects. It depends on the quality as the main criteria to select a qualified consultant. Three methods of consultant selection are included in the Iraqi SRPFCS: (1) selection based on quality and cost, (2) least-cost selection, (3) selection under a fixed budget. All selection methods require that the consultant's qualifications pass the degree of technical evaluation, which shouldn't be less than 60% of the total proposal evaluation, to be financially evaluated [5].

The research aimed to specify the percentage of SRPFCS application in Iraqi construction projects, identify whether the document has been appropriately implemented or not, measure the level of experience in both public and private sector, analyze if Iraqi bidding and contracting legislations need to be modified to fit the reality of contracting, and measure the impact of the SRPFCS on the Iraqi construction projects.

## **2 Roles of Consultant Engineer During the Construction Project**

In general, the project life cycle starts from the initiation stage of the project and through fulfilling its objectives- which are called the closure or project delivery. Many activities concerning the project's concept may occur in the period preceding the project's formal inception. After project fulfillment, additional activities occur relating to project delivery [6]. The consultant has multiple roles and missions during the construction project life cycle. Also, the consultant undertakes his responsibilities from the project's initiation stage to its completion. Hiring the consultant at the beginning of the construction project is extremely useful for the client. A consultant may even be involved in the pre-plan stage to help the owner with different aspects

such as project cost estimate and control, site determination, ecological studies, and his part to coordinate the relationships of stakeholders, project team, and other parties concerning the project.

During the design stage itself, the consultant decides how the project is feasible from a technical, strategic, and monetary perspective. He plans the project concept and looks for the client endorsement for it; also he seeks to obtain the permissions for the design development [7]. FIDIC [8] defined professional service by a Consulting Engineer to a Client for a project in five main stages: (1) project analysis and report, (2) creates the project full designs and specifications and bidding preparation, (3) managing the contract, (4) supervision and advice service during project execution, (5) examines and accepts the achieved work, start to operate the project, check and close the final account.

### **3 Impact of Consultant Performance on Construction Project Success**

Cost is one of the essential construction project parameters that the consultant can directly affect. The project budget overrun can occur due to several factors: lack of planning and coordination, change in plans and drawings, insufficient geotechnical investigation, additional cost due to variation works, and lack control on excessive change orders [9]. Delays are a significant issue in project development and success. The project architect, designer, and consultant should be fully realized the project requirements to translate them correctly into drawings and specifications. The project's cost analysis ensures that the project will be delivered within time. Five causes of delay linked to consultant were specified in establishing the public sector's university in the newly merged KP district. Pakistan, which is: (1) slow decision effects, (2) consultant supervisory staff size, (3) frequent changes in design documents, (4) relevant past experiences in the complex projects, and (5) inexperienced personnel in the consultant's team [10].

The design manager and resident engineer should ensure that their teams apply the design processes and implement techniques properly during the project design and construction phases. The contractual, technical and financial experiences should be considered when selecting the resident engineer. The design manager should have the ability to conduct successful collaborations and coordination between the design team during the design phase and identify the design deficiencies to improve the design and construction [11]. The group of the design was ranked as the first group, which caused a delay in Indian construction projects. The consultant group was ranked as the fourth group. The construction delay caused by consultants in India has been stated as: an improper study of design affects estimated quality, incompetent project manager/teams, insufficient inspectors [12].

The consultant should avoid any delay during design documents' reviewing and approval, which can delay the progress of the project work. Also, the consultant

should have the flexibility in evaluating the contractor works considering the comparison between the cost and the quality; A/E should focus on producing design documents and scheduling them within time. From the contractor's perspective, the causes of delay in Saudi Arabia's construction project linked to consultants were: Delays in producing design documents, late in reviewing and approving [13]. In Iraq, factors caused by a consultant that led to inaccurate executed work and delay in the construction projects are stated as: The routine official procedures in the contractual entities' communication with the consultant, the lack of drawings and design documents accuracy, and the consultative team (designers and supervisors) does not commit itself in the continuous supervising for the work and workers [14].

#### **4 Importance of Selection the Proper Consultant for the Project**

The proper selection of consultants will have a significant bearing on the project performance, overall project cost, and success and hence on the whole completed project value, including the effect on public safety and economy associated with physical infrastructure and superstructure projects. The selection of the right consultant for each particular project is of paramount importance. Project Consultancy Services cost, including design, is usually about 1–2% of the total cost of the project life cycle to save a small percentage (from the consultant's fee), perhaps 1% or less of the project cost is not worthwhile considering the potential risks, the client should realize the importance of Consultant selection on the project quality. The project operation, maintenance costs, and sustainability are identified as main factors in assessing project performance success in the long term. The impact of Consultants is critically significant in evaluating the quality of these factors [15]. The results of incompetent consultant can lead to:

1. Low quality in project design documents,
2. Low-quality in bid documents with many gaps, especially at the design stage,
3. Exceeding the budget allocated for the construction project, all these results may lead to bad budget estimation by the consultant [16].

#### **5 SBDs for Consultancy Service (SRPFCS)**

Many criteria affect the standard bidding document in the construction procurement system that can be identified as experience, legal framework, financial position, staff, contract provision not implemented, equipment, eligibility, technology [17]. Before the obligatory implementation of the standard bidding documents, the selection of consultants for the Iraqi investment project was conducted in two ways [16]:

**Table 1** Criteria used in SRPFCS [18]

Main criteria	Wight
1—Financial offer	40–20% of total
2—Technical criteria	60–80% of total
2.1—Specific experience of the consultant relevant to the task	0–10% of technical
2.2—Adequacy and quality of the proposed methodology, and work plan in responding to the terms of reference	20–50% of technical
2.3—Key experts’ qualifications and competence for the task	30–60% of technical
2.4—Suitability of the transfer of knowledge program	0–10% of technical
2.5—Participation by local consultants among key experts	0–10% of technical

- With local consultants according to a contract prepared by the Iraqi engineer’s unions called the architectural engineering contract.
- With international consultants using (FIDIC contracts for client and consultant model agreement).

In general, the process of selecting consultants goes through several stages, which are [15]:

- preparatory steps: including project cost estimation, identify the method of selection and contract type, terms of references.
- Announcement and pre-qualification (long-listing).
- Short-listing.
- Request for proposals (RFP).
- Receipt and opening of proposals.
- Evaluation of proposals.
- Selection of the consultant and negotiations.

Table 1 shows criteria used in Iraqi construction projects to select consultants according to SRPFCS.

## 6 Methodology

The following points can summarize the methodology used in this study:

1. Theoretical method: a literature review of books, papers, and theses to outline the work.
2. Study field: preliminary interviews with 14 experts of contracting and engineer consultants to outline the factors that affect SRPFCS implementation, then questionnaire was then conducted to 130 respondents in both the public and private sectors.

3. Analyzing and tabulating the answers to determine the mean, percentages, and Relative importance index of SRPFCS application's obstacles and its impact on the construction project.
4. Conclusions and recommendations were suggested according to the study results.

## 7 Questionnaire

(107) questionnaires were collected out of (130) questionnaires were distributed. The targeted societies in the questionnaire were:

1. Contractual entities/public sector.
2. Engineering consultancy offices/public sector.
3. Engineering consultancy offices/private sector.

The questionnaire was distributed in the following places, Table 2.

**Questionnaire Description.** The researcher conducted 5- Points Likert Scale questionnaire, which was classified into the following sections:

1. General information section: The participant's information including age, place of work, years of experience, position, and contact information.
2. Experience section: Focus on participant's general experience in Iraqi contract legislations and consultant selection process.

**Table 2** Questionnaire distribution

No	Target	Distributed	Collected
1	Ministry of construction and Housing (contracting department)	12	12
2	Ministry of planning (contracting directorate)	10	6
3	Ministry of transportation (contracting department, planning department)	10	8
4	Ministry of water resources (contracting department, General Authority for Dams and Reservoirs)	3	2
5	General secretariat for the council of ministers (contracting and procurements department)	3	3
6	Baghdad municipality(contracting department)	6	3
7	Mosul province (legal, contracting, and planning department)	14	14
8	Kurdistan provinces	19	19
10	University of Baghdad/engineering consultancy office	8	3
11	University of Nahrain/engineering consultancy office	1	1
12	The National Center for Engineering Consultancy (MOCH)	13	13
13	Iraqi Engineers Union/engineering consultancy office	9	4
14	Engineering consultancy offices/private sector	23	19

3. Applicability section: Evaluate the document implementation percentage and its obstacles in the targeted society.
4. Impact section: Specify the impact of implementing the SRPFCS on Iraqi construction projects.

**Questionnaire analysis.** The arithmetic means for answers calculated by Eq. 1 [14]

$$\text{Mean} = \frac{\text{Total number of iterations in the effect} \times \text{number of effects}}{\text{Size of sample}} \quad (1)$$

Equation 2 used to determine the relative importance of the document implementation impact [19].

$$\text{RII} = \frac{5(n5) + 4(n4) + 3(n3) + 2(n2) + n15n}{5N} * 100 \quad (2)$$

where N denotes the overall number of responses received, n1, n2, n3, n4, and n5 state the respondent’s number who selected 5, representing “very important” or “strongly agree”; 4, representing “fairly important” or “agree”; 3, meaning “moderately important” or “neither agree nor disagree”; respectively 2, representing “slightly important” or “disagree”; and 1, representing “not important” or “strongly disagree”. The coefficient of skewness ( $\alpha$ ) equation was used to measure the distribution of the experience answers. A positive skew indicates the most data distributed into the right, while a negative skew indicates the most data distributed in the left, the skewness coefficient calculated by using Eq. 2 [20].

$$\alpha = \frac{3(\text{Mean} - \text{Median})}{\text{Standard deviation}} \quad (3)$$

The questionnaire’s internal validity was measured by calculating the Pearson correlation coefficient between each paragraph score with the section’s total score. Pearson correlation of the first questionnaire sections ranged between (0.689–0.899) with statistical significance at level 0.01. The second section correlation coefficients ranged between (0.334–0.851) with statistical significance at level 0.01. The third section coefficients were between (0.44–0.831) with statistical significance at level 0.01. The Pearson correlation Coefficients of the last section were between (0.75–0.87) with statistical significance at level 0.01. The above results refer that all of the questionnaire sections achieved high internal validity. The total score of Cronbach’s alpha value after the questionnaire was distributed was (0.895) which means the questionnaire completed a high degree of reliability, as shown in Table 3.

**Table 3** Range of reliability and its coefficient for Cronbach's alpha

Reliability statistics			
Section	Cranach's alpha	No. of items	Degree
Experience	0.959	14	Excellent
Implementation	0.793	5	Acceptable
Impact	0.911	8	Excellent
Total	0.895	46	Good

## 8 Results and Discussion

The results analysis, as detailed below, showed medium degrees of arithmetic mean in the level of experience, 47.6% of the respondents had implemented SRPFCS, only 29.6% of them had received outsourced assistance, the application of SRPFCS improved the construction project by enhancing seven factors that were ranked according to its RII.

**Level of Experience.** Table 4 shows differences between the arithmetic means regarding the experience in contracting and consultant selection's process according to the place of work. The experience in the public sector engineering consultancy offices was higher than the private sector's offices. The ability of public sector offices to compete with lower prices led the contractual entities to prefer to contract with them. This led to the decrease of the private sector's participation in the governmental biddings, causing the low experience of the private sector's engineering consultancy offices, especially in governmental contracting legislations and SRPFCS.

Despite the experience's arithmetic means ranged between medium to high, The coefficients of skewness refer that there are numbers of participants who don't have sufficient experience in contractual legislations' and SRPFCS as shown in Table 5.

**Table 4** Results of the respondent's level of experience

Place of work	N	Mean	Std. Deviation	N% of total (%)
<i>Total general experience</i>				
Contractual entities	67	3.2761	0.75017	62.6
Engineering consultancies/public sector	17	3.5196	0.74041	15.9
Engineering consultancies/private sector	23	2.5072	1.13315	21.5
Total	107	3.1495	0.90623	100
<i>Experience in consultant selection's procedures</i>				
Contractual entities	67	3.52	0.87651	62.6
Engineering consultancies/public sector	17	3.83	0.70816	15.9
Engineering consultancies /private sector	23	2.51	1.20799	21.5
Total	107	3.3551	1.03166	100



**Table 5** Coefficients of skewness

No	Paragraphs	Skewness
<i>General experience</i>		
1	Governmental contracting legislations	-0.765
2	Sectorial SBDs	-0.610
3	Non -sectorial SBS	0.072
4	Non-governmental consulting services office’s legislations and the attached instructions (2000)	0.085
5	Legislation and instructions of the scientific and consulting services offices in the institutions of the Ministry of Higher Education (1997)	0.344
6	Engineering consultancy services office registration process	0.027
<i>Experience in consultant selection’s procedures</i>		
7	Standard bidding documents for consultancy services	-0.428
8	Terms of Reference (TOR)	-0.278
9	Method of consultant selection	-0.358
10	Consultancy services contract type	-0.303
11	Letter of interesting	-0.218
12	Short list	-0.284
13	Technical and financial proposals	-0.211
14	Evaluation report of selecting advisors	-0.150

**SRPFCS Implementation’s Percentage and Obstacles.** Figure 1 shows that the implementation of SRPFCS is less than 50% in the targeted society as the contractual entities were preferring using direct contracting with consultants, besides the successive economic crises in Iraq, which have led to a lack of financial allocation for investment projects and thus a lack of financial allocation for the consulting studies of the projects.

**Fig. 1** Implementation percentage

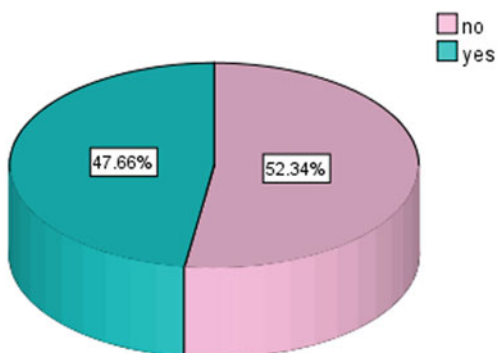


Figure 2 shows the percentage of outsourced assistance while handling the standard bidding documents, which was 29.63% of all bodies that implemented the documents. The low percentage of assistance outsourcing with a low level of experience led to the improper implementation of consultancy service bidding documents in many construction projects.

The results also refer that governmental contracting instructions need to be modified to suit the application of SRPFCS. Also, they refer that the contractual entities and engineering consultancy offices need to be trained to implement the SRPFCS, as shown in Table 6.

**Impact SRPFCS on Iraqi Construction Projects.** The analysis of the questionnaire impact section refers that the implementation of SRPFCS has a positive effect on Iraqi construction project success, and there is a relation between the percentage of SRPFCS application and construction project performance improvement. The RII of impacts is ranked in Table 7.

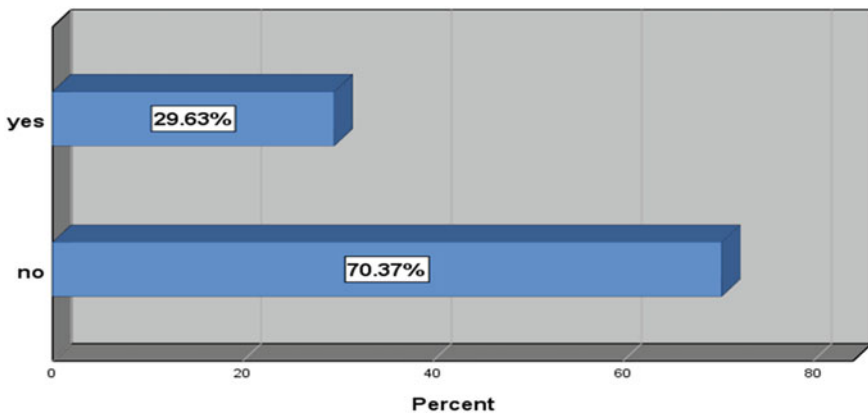


Fig. 2 Percentage of outsourcing assistance

Table 6 Implementing obstacles

No	Paragraph	Mean	Degree	Std. Deviation
1	The consultants' proposals were evaluated by specialized committee	4.06	Agree	0.728
2	Your entity staff need for training on how to deal with SRPFCS	4.11	Agree	0.793
3	Suitability of current contractual legislation	3.21	Intermediate	0.824
4	Evaluation criteria are clearly embedded in the instruction to bidder	3.78	Agree	0.756
5	Improvement rate when use SRPFCS	3.69	Agree	0.809

**Table 7** The impact of SRPFCS on Iraqi construction projects

Rank	Impact	RII
1	Developing the local consultants	0.814
2	Fair competition	0.812
3	Encourages international consultants to participate in the bidding competition	0.806
4	Increase the transparency of selection	0.802
5	Reduce complain and appeals between project parties	0.79
6	Select qualified consultant and increases the quality of service	0.784
7	Reduce delay in the execution of the project	0.774

## 9 Conclusions

The research aimed to assess the application of SRPFCS and its impacts on Iraqi construction projects. A questionnaire of 5-Points Likert Scale was conducted. The questionnaire targeted the contractual entities of the public sector and the engineering consultancy offices of both the public and private sectors. The results showed the following:

- Low level of experience and incorrect implementation process, the contractual entities and engineering consultancy offices should be trained on SRPFCS implementation.
- The are differences between the governmental contracts implementation instructions' document and the SRPFCS regarding bidding and contracting conditions. The differences led to creating confusion for the contractual entities when dealing with SRPFCS. The instructions must be unified to avoid this confusion.
- The weak participation of private sector offices in governmental biddings due to the preference of public sector offices over them and the absence of instructions that regulate the engineering consultancy work led to a decrease in the level of private sector's engineering experience consultancy offices and its deterioration.
- The application of SRPFCS by the contractual entities needs the supervision of the competent authorities represented by the Governmental Contracts Department of the Ministry of Planning to ensure the correct implementation.
- The implementation of SRPFCS affects the development of the private sector's engineering consultancy offices by providing fair opportunities for competition and encouraging the participation of international consultants in Iraqi construction projects.
- The SRPFCS gives the technical and quality criteria the most significant percentage in the consultant's evaluation process, which ensures the selection of qualified consultants for the construction projects.

**Acknowledgements** This study was conducted with the cooperation and support of the Ministry of Housing and Construction, Ministry of Planning, Ministry of Transportation, The National Center for Engineering Consultancies, and Iraqi Engineers Union.

## References

1. DiBona, F. (2014). *The consultant's Handbook*. First ed., USA.
2. Dadzie, J., Abdul-Aziz, A. R., & Kwame, A. (2012). Performance of consultants on government projects in Ghana: Client and contractor perspective. *International Journal of Business and Social Research*, 2(6), 256–267.
3. Argandoña, A. (2017). Social responsibility and ethics in organizational management.
4. Oluwatayo, A. A., & Amole, D. (2013). Ownership, structure, and performance of architectural firms. *Frontiers of Architectural Research*, 2(1), 94–106.
5. Woods, N. (2014). *The globalizers: The IMF, the World Bank, and their borrowers*. Cornell University Press.
6. Fewings, P., & Henjewe, C. (2019). *Construction project management: An integrated approach*. Routledge.
7. Musah, M. (2016). A study into the impact of the architect's site instructions on construction project delivery in Ghana-perspective of the contractor (Doctoral dissertation).
8. Baker, E., Mellors, B., Chalmers, S., & Lavers, A. (2013). *FIDIC contracts: Law and practice*. CRC Press.
9. Akinsiku, O., Akintola, A., Ameh, O., & Ige, A. (2014). Contributions of the Construction project team to cost overruns: The contractors' perspective. In *Construction Research Congress 2014: Construction in a Global Network* (pp. 1528–1536).
10. Ali, M., Iqbal, S., & Iqbal, Q. (2020). Causes of delay in the establishment of public sector University in Newly Merged District of KP. *Pakistan. International Journal of Engineering Works*, 7(05), 221–227.
11. Atout, M. M. (2016). Delays caused by project consultants and designers in construction projects. *International Journal of Structural and Civil Engineering Research*, 5(2), 102–107.
12. Arya, A., & Kansal, R. (2016). Analysing delays of construction projects in India: Causes and effects. *International Journal of Engineering, Science and Technology*, 3, 66–74.
13. Assaf, S. A., & Al-Hejji, S. (2006). Causes of delay in large construction projects. *International journal of project management*, 24(4), 349–357.
14. Shadhar, A. K., & Mahmood, B. B. (2018). Risks of design stage in Iraqi construction project. *Journal of Engineering*, 24(3), 114–121.
15. Dąbrowska, A. (2019). Analysis of the FIDIC arbitration clause in the light of international jurisprudence. *Zeszyty Naukowe Wyższej Szkoły Finansów i Prawa w Bielsku-Białej*, 23(1), 5–9.
16. Altaie, M. (2017). Optimal indicators to select the engineering consultancy office for higher education institutions in Iraq. *Journal of Engineering*, 9(23), 45–63. (In Arabic).
17. Hasan, S. A., & Mohammed, S. R. (2020, August). An evaluation of barriers obstructing the applicability of standard bidding documents (SBDs) in public procurement of Iraq. In *IOP Conference Series: Materials Science and Engineering* (Vol. 901, No. 1, p. 012027). IOP Publishing.
18. Muraina, S. A., & Dandago, K. I. (2020). Effects of implementation of International Public Sector Accounting Standards on Nigeria's financial reporting quality. *International Journal of Public Sector Management*.
19. Mohamed, S. R., & Majeed, R. A. (2016). Pre-qualification of contractors in Iraq. *Applied Research Journal*, 2(2), 77–87.
20. Information from: <https://www.statisticshowto.com/find-pearsons-coefficient-skewness-excel/>

# An Optimization Model to Estimate the Construction Costs of Highways Projects: Al-Rihab Highway as a Case Study



Abbas M. Burhan

**Abstract** Highways projects are one of the infrastructure projects with high construction costs. The decision-making process to implement such projects is one of the most important challenges that may face the relevant authorities. This study's main objective is to develop an optimization model by using linear programming to estimate the construction cost of a highway. This model may contribute by helping Al-Muthanna Governorate Board (MGB)/Projects division for decision-making related to selecting an optimum choice for implementing Al-Rihab Highway's project in Iraq. Historical data related to the cost of materials were collected from the nearest four suppliers to the job site, and many considerations had been taken to build the mathematical model. LINGO 13.0 Optimization Modeling Software was used to solve the developed model and predicting the total cost of highway materials which was 22.73 million dollars.

**Keywords** Construction costs · Highway · Optimization · Linear programming

## 1 Introduction

In the construction industry, inefficiency is one reason why projects are not completed on time [1]. The success of the project is evaluated according to the extent to which the budget, time, and quality of work match the owner's expectations. Accurate cost estimation in the preliminary stage of a project is essential for decision-makers to control the overall project [2]. In addition, the importance of early estimation from the viewpoint of owners and related project teams cannot be over-emphasized [3]. Moreover, Ma et al. [4] stated that construction cost estimation, which is normally labor-intensive and error-prone, is one of the most important works concerned by multi-participants during a project's life cycle. Previous studies have shown that the

---

A. M. Burhan (✉)  
Civil Engineering Department, University of Baghdad, Al-Jaderria, Baghdad, Iraq  
e-mail: [abbasm.burhan@coeng.uobaghdad.edu.iq](mailto:abbasm.burhan@coeng.uobaghdad.edu.iq)

combination of predictive analytics and historical data can reduce upswing cost estimation in construction projects. However, there is a challenge in accurately estimating projects' cost at the conceptual phase [5].

Forecasting cost is one of the main elements of decision-making in highway construction projects [6]. Estimators or those responsible for budgeting need techniques to assist them in forecasting costs [7]. Every project has a minimum monthly requirement for different types of materials. These requirements affect the project's progress [8]. Inadequate control and planning for the materials procurement are reported to be one of the main factors affecting cost and duration overruns of road construction projects [9]. Based on the bill of quantity for each project and the schedule of activities, these monthly requirements should be ordered to meet the project progress. This study focuses on highway projects and how the relevant authorities can take an optimal decision and estimate the construction cost of a highway project accurately. Al-Rihab highway project was taken as a case study to show the effective results of using linear programming and modern software such as LINGO software in estimating the construction costs of this type of project. Al-Muthanna Governorate Board (MGB), as well as other state authorities, is required to adopt modern techniques to plan and forecast costs of projects MGB wants to order specific amounts of pavements materials for six months as a basic element in forecasting the cost of the project with the responsibility of ordering good quality material not only at minimum cost but also to fulfill the material required for the project as well.

In this study, a linear programming model has been developed for this case study with a construction span duration of 6 months. The monthly requirements of materials for the project's four layers, which are Sub-base (gravel layer), base layer, binder layer, and the surface layer, were identified. The data related to the production capacity, prices, and shipping cost for required materials were collected from four different plants for each pavement layer. The plants have varying prices over 6 months, and the shipping prices also vary depending on the plant distance from the job site. The linear programming model was solved by using LINGO software, and the results were interpreted.

## 2 Methodology

The project of Al-Rihab Highway is located in Al-Muthanna province in Iraq with a length of 50 km. The type is A2 class highway with one lane in each direction and four layers for each lane as shown:

- Sub-base layer: 30 cm thickness with 9.24 m width.
- Base layer: 15 cm thickness with 8.44 m width.
- Binder layer: 7 cm thickness with 8.1 m width.
- Surfacing layer: 5 cm thickness with 8 m width.

MGB wanted to minimize the cost of pavement as low as possible and forecast the project's total cost. The author surveyed the nearest plants of materials needed

for the project and tested each plant by making a checklist to investigate the extent of qualification for each supplier. The checklist contained information related to:

- The quality of materials and the extent of their conformity with the standard specifications.
- The production capacity of the plant.
- The reputation of the supplier.
- The prices of materials and shipping cost.

The checklist analysis results indicated that there are four qualified plants available near the location of the project. Other plants are charging a high cost for shipping, and the asphalt will be cold if it will transport long-distance, and that will be against the limitation of the asphalt temperature (120 degrees) [10]. Therefore, MGB decided to choose the nearest four plants according to the limitation of asphalt temperature. The challenge of this project is to optimize the pavement materials purchased from different plants to minimize the cost of the pavement and satisfy the monthly requirements of materials to complete the pavement stage. This research attempts to assist MGB in forecasting the project's materials' total cost by adopting the methodology shown in Fig. 1.

### 3 Data Collection

The materials required for the total construction duration are summarized in Table 1. There are four qualified plants for each type of material required. Since practically, each plant has a production limit, as shown in Table 2. Table 3 summarizes the pricing details for each month from the plants. It can be observed that the shipping cost from the suppliers far from the site is more than the ones closer. The total cost includes the cost of material and shipping cost. Table 4 shows decision variables for each month from each plant.

### 4 Formulation

The linear programming model was developed with 96 decision variables and 120 constraints. The objective function was to minimize the total cost of the material ordered. The developed model's constraints were the monthly requirements of materials for the project's four layers to ensure a smooth construction process. Moreover, the constraints included the monthly supply limits of the suppliers. The objective function, which is represented by minimizing the project's materials' total cost, can be formulated as shown in Eq. 1.

$$Z_{min} = \text{Min.} \sum \text{Price} * (\text{G}_{ij} + \text{B}_{ij} + \text{I}_{ij} + \text{S}_{ij}) \quad (1)$$

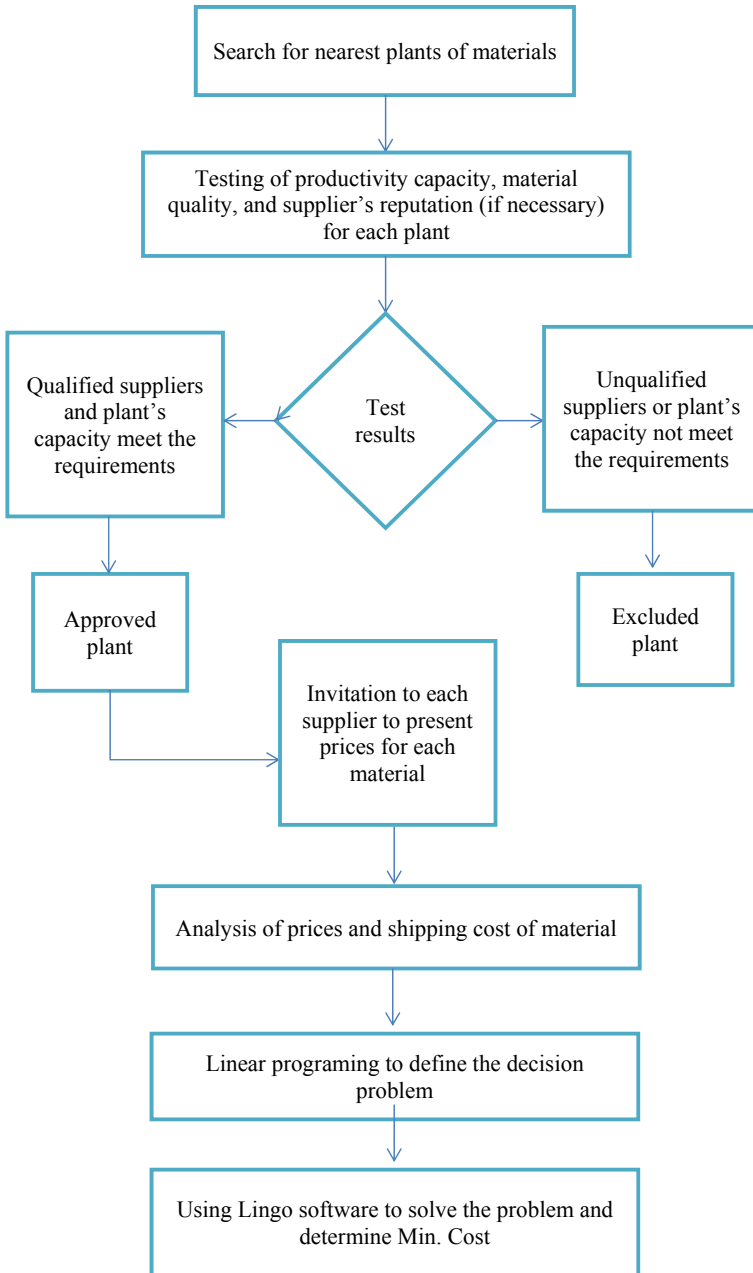


**Fig. 1** The methodology of research



**Table 1** The monthly requirements of pavement materials during six months

Quantity (m <sup>2</sup> )	Layer	Jan	Feb	Mar	Apr	May	June
	Sub-Base (Gravel)	14,160	15,576	18,408	21,240	24,072	48,144
	Base layer (Asphalt)	42,200	46,420	54,860	63,300	71,740	143,480
	Binder layer (Asphalt)	40,500	44,550	52,650	60,750	68,850	137,700
	Surface layer (Asphalt)	40,000	44,000	52,000	60,000	68,000	136,000

**Table 2** The monthly supply limits for each asphalt layer

Production (m <sup>2</sup> )	Layer	Plant	Jan	Feb	Mar	Apr	May	June
	Sub-Base layer	Plant 1	2832	3115	3682	4248	4814	9629
		Plant 2	3540	3894	4602	5310	6018	12,036
		Plant 3	4956	5452	6443	7434	8425	16,850
		Plant 4	6372	7009	8284	9558	10,832	21,665
	Base layer	Plant 1	8440	9284	10,972	12,660	14,348	28,696
		Plant 2	10,550	11,605	13,715	15,825	17,935	35,870
		Plant 3	14,770	16,247	19,201	22,155	25,109	50,218
		Plant 4	18,990	20,889	24,687	28,485	32,283	64,566
	Binder layer	Plant 1	8100	8910	10,530	12,150	13,770	27,540
		Plant 2	10,125	11,138	13,163	15,188	17,213	34,425
		Plant 3	14,175	15,593	18,428	21,263	24,098	48,195
		Plant 4	18,225	20,048	23,693	27,338	30,983	61,965
	Surfacing layer	Plant 1	8000	8800	10,400	12,000	13,600	27,200
		Plant 2	10,000	11,000	13,000	15,000	17,000	34,000
		Plant 3	14,000	15,400	18,200	21,000	23,800	47,600
		Plant 4	18,000	19,800	23,400	27,000	30,600	61,200

where

- Price vary for each plant and month (total price = material cost + shipping cost).
- G Quantity of Sub-base (gravel) in square meter to be purchased from each plant.
- i refers to the plant number, i is 1, 2, 3, & 4 respectively for each supplier.
- j refers to the month, j is 1, 2, 3, 4, 5, & 6. 1 refers to January and so forth.
- B Quantity of base layer in square meter to be purchased from each plant.
- I Quantity of Binder layer in square meter to be purchased from each plant.
- S Quantity of surfacing layer in square meter to be purchased from each plant.
- Zmin Minimum cost for ordering the materials.

**Table 3** The varying prices of pavement materials during the project duration

Layer	Plant	Cost of material for each plant and for each month (\$/m <sup>2</sup> )						Shipping Cost (\$/m <sup>2</sup> )
		Jan	Feb	Mar	Apr	May	June	
sub-Base layer	Plant 1	18.584	18.6244	18.685	18.7153	18.7355	18.7557	0.92
	Plant 2	19.32	19.362	19.425	19.4565	19.4775	19.4985	0.98
	Plant 3	20.056	20.0996	20.165	20.1977	20.2195	20.2413	1
	Plant 4	20.424	20.4684	20.535	20.5683	20.5905	20.6127	1.1
Base layer	Plant 1	22.624	22.5432	22.5735	22.725	22.3715	22.4422	1
	Plant 2	23.52	23.436	23.4675	23.625	23.2575	23.331	1.1
	Plant 3	24.416	24.3288	24.3615	24.525	24.1435	24.2198	1.18
	Plant 4	24.864	24.7752	24.8085	24.975	24.5865	24.6642	1.2
Binder layer	Plant 1	11.312	11.3625	11.3827	11.3726	11.3928	11.4029	0.85
	Plant 2	11.76	11.8125	11.8335	11.823	11.844	11.8545	0.87
	Plant 3	12.208	12.2625	12.2843	12.2734	12.2952	12.3061	0.9
	Plant 4	12.432	12.4875	12.5097	12.4986	12.5208	12.5319	1
Surfacing layer	Plant 1	9.09	9.1102	9.1405	9.1607	9.1708	9.191	0.5
	Plant 2	9.45	9.471	9.5025	9.5235	9.534	9.555	0.6
	Plant 3	9.81	9.8318	9.8645	9.8863	9.8972	9.919	0.65
	Plant 4	9.99	10.0122	10.0455	10.0677	10.0788	10.101	0.75

**Table 4** Decision variables for each month and from each plant

Layer	Plant	Jan	Feb	Mar	Apr	May	June
Sub-Base	Plant 1	G11	G12	G13	G14	G15	G16
	Plant 2	G21	G22	G23	G24	G25	G26
	Plant 3	G31	G32	G33	G34	G35	G36
	Plant 4	G41	G42	G43	G44	G45	G46
Base	Plant 1	B11	B12	B13	B14	B15	B16
	Plant 2	B21	B22	B23	B24	B25	B26
	Plant 3	B31	B32	B33	B34	B35	B36
	Plant 4	B41	B42	B43	B44	B45	B46
Binder	Plant 1	I11	I12	I13	I14	I15	I16
	Plant 2	I21	I22	I23	I24	I25	I26
	Plant 3	I31	I32	I33	I34	I35	I36
	Plant 4	I41	I42	I43	I44	I45	I46
Surfacing	Plant 1	S11	S12	S13	S14	S15	S16
	Plant 2	S21	S22	S23	S24	S25	S26
	Plant 3	S31	S32	S33	S34	S35	S36
	Plant 4	S41	S42	S43	S44	S45	S46

## 5 Monthly Requirements and Plants Limit Constraints

The monthly requirement constraints (Demand constraints) can be shown as follows:

<p><b>Sub-Base layer (Gravel):</b>  <math>G11 + G21 + G31 + G41 = 14,160</math>  <math>G12 + G22 + G32 + G42 = 15,576</math>  <math>G13 + G23 + G33 + G43 = 18,408</math>  <math>G14 + G24 + G34 + G44 = 21,240</math>  <math>G15 + G25 + G35 + G45 = 24,072</math>  <math>G16 + G26 + G36 + G46 = 48,144</math></p>	<p><b>Binder layer:</b>  <math>I11 + I21 + I31 + I41 = 40,500</math>  <math>I12 + I22 + I32 + I42 = 44,550</math>  <math>I13 + I23 + I33 + I43 = 52,650</math>  <math>I14 + I24 + I34 + I44 = 60,750</math>  <math>I15 + I25 + I35 + I45 = 68,850</math>  <math>I16 + I26 + I36 + I46 = 137,700</math></p>
<p><b>Base layer:</b>  <math>B11 + B21 + B31 + B41 = 42,200</math>  <math>B12 + B22 + B32 + B42 = 46,420</math>  <math>B13 + B23 + B33 + B43 = 54,860</math>  <math>B14 + B24 + B34 + B44 = 63,300</math>  <math>B15 + B25 + B35 + B45 = 71,740</math>  <math>B16 + B26 + B36 + B46 = 143,480</math></p>	<p><b>Surfacing layer:</b>  <math>S11 + S21 + S31 + S41 = 40,000</math>  <math>S12 + S22 + S32 + S42 = 44,000</math>  <math>S13 + S23 + S33 + S43 = 52,000</math>  <math>S14 + S24 + S34 + S44 = 60,000</math>  <math>S15 + S25 + S35 + S45 = 68,000</math>  <math>S16 + S26 + S36 + S46 = 136,000</math></p>

While Monthly Plants Limit Constraints (Supply constraints) can be summarized as follows:

$G11 \leq 2832; G12 \leq 3115; G13 \leq 3682; G14 \leq 4248; G15 \leq 4814; G16 \leq 9629;$   
 $G21 \leq 3540; G22 \leq 3894; G23 \leq 4602; G24 \leq 5310; G25 \leq 6018; G26 \leq 12,036;$   
 $G31 \leq 4956; G32 \leq 5452; G33 \leq 644; G34 \leq 7434; G35 \leq 8425; G36 \leq 16,850;$   
 $G41 \leq 6372; G42 \leq 700; G43 \leq 8284; G44 \leq 9558; G45 \leq 10,832; G46 \leq 21,665;$

$B11 \leq 8440; B12 \leq 9284; B13 \leq 10,972; B14 \leq 12,660; B15 \leq 14,348; B16 \leq 28,696;$   
 $B21 \leq 10,550; B22 \leq 11,605; B23 \leq 13,715; B24 \leq 15,825; B25 \leq 17,935;$   
 $B26 \leq 35,870; B31 \leq 14,770; B32 \leq 16,247; B33 \leq 19,201; B34 \leq 22,155; B35 \leq 25,109;$   
 $B36 \leq 50,218; B41 \leq 18,990; B42 \leq 20,889; B43 \leq 24,687; B44 \leq 28,485;$   
 $B45 \leq 32,283; B46 \leq 64,566;$

$I11 \leq 8100; I12 \leq 8910; I13 \leq 10,530; I14 \leq 12,150; I15 \leq 13,770; I16 \leq 27,540;$   
 $I21 \leq 10,125; I22 \leq 11,138; I23 \leq 13,163; I24 \leq 15,188; I25 \leq 17,213; I26 \leq 34,425;$   
 $I31 \leq 14,175; I32 \leq 15,593; I33 \leq 18,428; I34 \leq 21,263; I35 \leq 24,098;$   
 $I36 \leq 48,195; I41 \leq 18,990; I42 \leq 20,889; I43 \leq 24,687; I44 \leq 28,485; I45 \leq 32,283;$   
 $I46 \leq 64,566;$

$S11 \leq 8000; S12 \leq 8800; S13 \leq 10,400; S14 \leq 12,000; S15 \leq 13,600; S16 \leq 27,200;$   
 $S21 \leq 10,000; S22 \leq 11,000; S23 \leq 13,000; S24 \leq 15,000; S25 \leq 17,000;$   
 $S26 \leq 34,000; S31 \leq 14,000; S32 \leq 15,400; S33 \leq 18,200; S34 \leq 21,000; S35 \leq 23,800;$   
 $S36 \leq 47,600; S41 \leq 18,000; S42 \leq 19,800; S43 \leq 23,400; S44 \leq 27,000;$   
 $S45 \leq 30,600; S46 \leq 61,200.$

## 6 Non-negativity Constraints

G11, G12, G13, G14, G15, G16, G21, G22, G23, G24, G25, G26, G31, G32, G33, G34, G35, G36, G41, G42, G43, G44, G45, G46  $\geq$  zero

B11, B12, B13, B14, B15, B16, B21, B22, B23, B24, B25, B26, B31, B32, B33, B34, B35, B36, B41, B42, B43, B44, B45, B46  $\geq$  zero

I11, I12, I13, I14, I15, I16, I21, I22, I23, I24, I25, I26, I31, I32, I33, I34, I35, I36, I41, I42, I43, I44, I45, I46  $\geq$  zero

S11, S12, S13, S14, S15, S16, S21, S22, S23, S24, S25, S26, S31, S32, S33, S34, S35, S36, S41, S42, S43, S44, S45, S46  $\geq$  zero

## 7 Discussion of Results

LINGO software was used to solve the developed model. The results showed the number of pavement materials in square meters to be purchased from each plant with a total cost of 22.73 million dollars. Table 5 shows the slack values for constraints. The slack value indicates the unused quantity in square meters from each plant for a specific month. For instance, plant (4) in January will supply only (6372–3540 = 2832 square meters) for the sub-base layer; in other words, the slack of this plant for the sub-base layer (gravel) will be 3540 square meters.

## 8 Conclusions

One of the challenges facing government authorities in Iraq is an accurate estimation of project costs. This research investigates how the relevant authorities accurately estimate highway projects' construction costs, depending on the optimal preparation of materials used on the site. Many factors affect the cost of construction for this type of project, but in this research, the focus has been on the relationship of the nearest of the material plants to the worksite, the production capacity of plants, and the prices of materials. The use of modern techniques such as linear programming can facilitate the project cost estimation process. Highways projects are one of the infrastructure projects that need large money for their construction. According to this study's results, the project's owner should make a feasibility study to compare the available alternatives for implementing the project before making any decision. Optimization modeling techniques can help the owner as a case study-Al-Rihab highway, Linear programming results showed that the estimated cost for the four layers would be 22.73 million dollars. So, this estimation can be an indicator that can be used by the relevant authority when analyzing the offers presented by contractors to implement the project.

**Table 5** The slack values of constraints

Line number	Constraints	Sign	Available (m <sup>2</sup> )	Slack (m <sup>2</sup> )
[44]	G41	≤	6372	3540
[45]	G42	≤	7009	3894
[46]	G43	≤	8284	4603
[47]	G44	≤	9558	5310
[48]	G45	≤	10,832	6017
[49]	G46	≤	21,665	12,036
[58]	B23	≤	13,715	13,715
[68]	B41	≤	18,990	10,550
[69]	B42	≤	20,889	11,605
[70]	B43	≤	24,687	4602
[71]	B44	≤	28,485	15,825
[72]	B45	≤	32,283	17,935
[73]	B46	≤	64,566	35,870
[92]	I41	≤	18,990	10,890
[93]	I42	≤	20,889	11,980
[94]	I43	≤	24,687	14,158
[95]	I44	≤	28,485	16,336
[96]	I45	≤	32,283	18,514
[97]	I46	≤	64,566	37,026
[116]	S41	≤	18,000	10,000
[117]	S42	≤	19,800	11,000
[118]	S43	≤	23,400	13,000
[119]	S44	≤	27,000	15,000
[120]	S45	≤	30,600	17,000
[121]	S46	≤	61,200	34,000

**Acknowledgements** This work was supported by the University of Baghdad/College of Engineering and Al-Muthanna Governorate Board. The author gratefully acknowledges the support.

## References

1. Bayram, S. (2017). Duration prediction models for construction projects: In terms of cost or physical characteristics? *KSCE Journal of Civil Engineering*, 21, 2049–2060.
2. Magdum, S. K., & Adamuthe, A. C. (2018). Construction cost prediction using neural networks. *ICTACT Journal on Soft Computing*, 8(1), 1549–1556.
3. Kim, S., & Shim, J. H. (2014). Combining case-based reasoning with genetic algorithm optimization for preliminary cost estimation in construction industry. *Canadian Journal of Civil Engineering*, 41(1), 65–73.

4. Ma, Z., Liu, Z., & Wei, Z. (2016). Formalized representation of specifications for construction cost estimation by using ontology. *Computer-Aided Civil and Infrastructure Engineering*, 31(1), 4–17.
5. Arage S.S, & Dharwadkar, N. V. (2017). Cost estimation of civil construction projects using machine learning paradigm. In *International Conference on I-SMAC (IoT in Social, Mobile, Analytics and Cloud) (I-SMAC 2017)*, pp. 594–599.
6. Chau, A. D., Moynihan, G. P., & Vereen, S. (2018). *Design of a conceptual cost estimation decision support system for public university construction* (pp. 629–639). American Society of Civil Engineers.
7. Mayer, M., Bourassa, S. C., Hoesli, M., & Scognamiglio, D. (2019). Estimation and updating methods for hedonic valuation. *Journal of European Real Estate Research*, 12(1), 34–50.
8. Kulkarni, A., & Halder, S. (2019). A simulation-based decision-making framework for construction supply chain management (SCM), *Asian. Journal of Civil Engineering.*, 21, 229–241.
9. Kaliba, C., Muya, M., & Mumba, K. (2009). Cost escalation and schedule delays in road construction projects in Zambia. *International journal of project management*, 27(5), 522–531.
10. The State Commission for Roads and Bridges. (2003). *Standard specifications for roads and bridges*. Ministry of Construction and Housing Publication.

# Determine the Most Common Geotechnical Risks and Their Impacts on the Cost and Time Schedule for Implementing Water Treatment Plants in Iraq



Ahmed J. Kadhom and Meervat R. Altaie

**Abstract** In Iraq, geotechnical risks remain important causes of delays and cost overruns in civil engineering projects, where the geotechnical risks have been classified as damaging project threats. Engineers, decision-makers, and specialized international engineering societies have sought to find ways to analyze and manage risks in general and geotechnical risks because their impact begins early in building projects. Geotechnical conditions are a significant concern for designers when designing a project and, calculating the cost and project schedule, and it is considered one of the main problems during the project procurement phase because the accuracy and quantity of geotechnical information that is provided to bidders help them offer competitive prices without excessive contingencies to cover the risks of geotechnical uncertainty for that., A complete initial geotechnical investigation during the RFP (Request For Proposal) is often impossible. For the above, it is necessary to address potential geotechnical risk factors during the initial investigation to manage geotechnical risks. This research's main objective is to analyze geotechnical risks in the early planning stages of the project and take the appropriate decision and determine its impact on (cost, schedule) for the project. This ensures the fair distribution of responsibilities for geotechnical risks between the owner and the contractor, and this is one of the most critical matters that have a significant impact on the success of projects, especially if these projects have Significance to influence the public health of the community, such as infrastructure projects, especially central water treatment projects (CWTP).

**Keywords** CWTP · PDMS · RS · RFP · ACMS · ANN

## 1 Introduction

The attempt to create a fair balance in the distribution of responsibilities between the two parties to the construction contract to achieve the various goals of the two parties

---

A. J. Kadhom (✉) · M. R. Altaie  
Civil Engineering Department, University of Baghdad, Baghdad, Iraq  
e-mail: [a.kadhom1901m@coeng.uobaghdad.edu.iq](mailto:a.kadhom1901m@coeng.uobaghdad.edu.iq)

requires the parties to stand on the first risks that will be faced from the early start of the project. These risks are the geotechnical risks and try to identify and classify them according to the degree of their impact and find alternatives to contracting methods (ACM<sub>S</sub>). To deal with these risks and some studies showed for the past ten years, which were reviewed during this research, most of them focused on highway projects as a model for the study and defining the appropriate delivery method in light of the challenges of geotechnical risks [1, 2]. The previous studies have used various analysis methods such as AHP hierarchy [3, 4], the linear scheduling method LSM [5], and the artificial neural network ANN [6]. Despite the different methods of analysis used, these researches have reached similar results, and recommendations in some cases, such as the necessity of early investigation into geotechnical risks [7, 8], and some studies emphasized the need of adding a clause in the contract in the name of the different site conditions DSC and formulating it clearly [9, 10]. Other studies focused on identifying and analyzing the geotechnical factors affecting how the project was delivered and left the decision to the owner to determine the appropriate delivery method [11, 12]. Also, some previous studies focused on analyzing project delivery methods and knowing the level of performance and quality for them and leaving the decision to the owner to determine the appropriate method of delivery [3, 4, 13]. However, the approach followed by [14], which combines identifying the geotechnical factors of a specific type of project, analyzing and evaluating them, knowing the degree of risk and impact for each of them, and revealing the interaction relationship between them and the appropriate delivery methods, can give more reliable results for decision-makers in the construction industry to determine the appropriate decision to choose a method delivery and given that central water treatment projects are one of the most important infrastructure projects in Iraq. This paper aims, through studying the sources, reviewing previous literature, and private meetings with the specialists in these projects in 15 Iraqi cities, to find a study through which determine the most common geotechnical risks when implementing such projects and classified according to the degree of risk and impact on (cost, schedule). This method was adopted for central water treatment projects in Iraq during this research and the results were analyzed, recommendations made for decision-makers, and suggestions were made to develop the research in the future.

## 2 Materials and Data Used

The theoretical part of this research is based on references, dissertations, published research, and publications in this field inside and outside the country related to the research topic. The practical part of this research is based on.

- Create a questionnaire form and analyze the data collected using the Statistical Package for Social Sciences (SPSS).
- Using different risk management tools and techniques such as qualitative risk analysis to classify them according to the degree of risk.



**Research Justification.** Since major water treatment projects are among the important infrastructure projects that affect the health of society. These projects are considered the responsibility of the government in general and the Ministry of Construction, Housing, and Municipalities in particular. Because the researcher is one of the affiliates of this ministry, this research deals with identifying and classifying the most common geotechnical risks according to their likelihood of occurrence and their impact. Project objectives including (cost, schedule) that can be encountered when implementing this type of project.

**Research hypothesis.** There is an effect of geotechnical factors on the (cost, schedule) for central water treatment projects.

- The first sub-hypothesis: There is an effect of geotechnical factors on the costs of water treatment projects
- The second sub-hypothesis: There is an effect of geotechnical factors on the schedule of water treatment projects

**Research Methodology.** The methodology of research based on:

- (a) Adopting the interview technique to collect data about the most common geotechnical risks when implementing centralized water treatment because the questions that interest us in the research are technical and complex to the extent that face-to-face contact is required to guide people through the process of answering questions. The required information is detailed and narrative, which cannot be collected via phone or e-mail.
- (b) Determine the most common geotechnical risks when implementing central water treatment projects from the outputs of Step No. (1).
- (c) Designing a questionnaire to determine the impact of each risk on one or more of the project objectives, including (cost, schedule).
- (d) Conducting a qualitative analysis of geotechnical risks by adopting the likelihood and impact method, Eq. 1 [15]

$$RS = P \times I \quad (1)$$

where.

RS = Risk score.

P = Probability.

I = Impact.

To know the degree of risk and classify these risks from the highest impact risk to the least impactful. This analysis allows us to describe the probability and consequences of each risk to the project. Using the risk score, instead of the probability or impact alone, will ensure that the changes. The likelihood of risk, its impact, or both is disclosed and reflected in the analysis to assist decision-makers when implementing centralized water treatment projects. Arranging the risks according to the priority of attention and allocating resources to them.

**Study Area.** As seen below, the research field was divided into two domains: spatial and human.

**Spatial Field Of Study.** The study included (15) fifteen Iraqi cities starting from Ninawa through the capital Baghdad to the city of Basra. These cities are distinguished by their variation in geological nature and different sources of potable water, some of them are located on the Tigris River, and some of them are located on the Euphrates River. Also, the number of the population and its cultural fabric is varied, and on the other hand, the distribution of natural resources such as minerals and oil and gas reserves is different, and the extent of vulnerability to natural phenomena such as seismic effect on them varies, and this diversity gives more comprehensiveness and integration of the research results.

**The Human Field (Questionnaire Participants).** The engineers who specialize in the field of water treatment and who work in the water directorates of the Ministry of Construction, Housing and Municipalities participated in the questionnaire, as the ministry responsible for this sector of services in Iraq. The number of distributed questionnaire forms was 60, 48 valid forms were approved, 12 were missing, and the percentage of participants. In the questionnaire, those who hold a bachelor's degree in civil engineering (90%) and the percentage of those who hold a master's in civil engineering (10%). The percentage of participants who work in:

- Design Department (20.8%).
- Department of Planning and Follow-up (43.8%).
- Execution Department (16.7%).

These three departments are considered among the most important departments that have experience in implementing central water treatment projects in Iraq, and the years of experience of the participants in the questionnaire ranged.

- (10–15) years, with a participation rate (33.3%).
- (16–20) years, with a participation rate of (50.0%).
- (20) years and over, with a participation rate (16.7%).

It is noted from the percentages of years of experience that the participants who have more than 16 years of experience represent 66.7% of the participants. It is a good percentage that supports the validity of the questionnaire due to the accumulated experience of these participants.

**Background and Overview:** To deal with geotechnical risks, it is necessary to go through the same stages that are followed when dealing with risks in general, which are mentioned in most scientific sources, and they are as shown below:

1. Make a risk management strategy. deciding how to approach, schedule, and carry out a project's risk management activities
2. Identify Risks: Identifying and recording the risks that may affect the project.
3. Implement Qualitative Risk Analysis, which involves analyzing and factoring in the likelihood and effect of risks to prioritize them for further investigation or intervention.
4. Quantitative Risk Analysis: calculating the impact of perceived risks on the project's overall goals.

5. Develop risk-response options and activities to optimize opportunities while reducing risks to the project’s objectives.
6. Track and Manage Risks: Track defined risks, monitor residual risks, identify new risks, implement risk response plans, and evaluate their efficacy over the project life cycle.

**Geotechnical Risks.** The geotechnical risks and the way to manage them can also be understood through the definitions and the likelihood and impact technique shown below:

**Classification of Geotechnical Risks.** are the subsurface occurrences with a high degree of uncertainty that impact project expense, schedule, quality, and scope [16].

**Geotechnical Risk Management Definition.** The ability to define, understand, and assess geotechnical risks in the early stages of a project in a way that ensures reducing the probability of them occurring, preventing them, or reducing their effect on the project’s expense, schedule, and quality [16].

**Probability and Impact Matrix:** Organizations find it helpful to categorize the magnitude of many threats into some kind of a matrix. The effect and probability of a hazard occurrence are integrated into the matrix. The matrices are often divided into high, low, and minor risk areas. The related matrix entries can be colored to show which level they belong to. Low risks, for example, maybe colored green, medium risks, yellow, or high risks, red. The implementation of policies (and therefore effort and resources) according to particular risk levels is made easier with the use of this technology. Risks marked in red, for example, can necessitate action. Review at every weekly case meeting, while green risks may only be reviewed monthly or on a less frequent periodic basis [15], see Table 1.

**The Most Common Geotechnical Risks When Implementing Centralized Water Treatment Projects in Iraq.** As described in point A of the methodology, the interview approach was used to assess the most common geotechnical risks when implementing central water projects. Engineers specializing in implementing and supervising central water treatment projects were interviewed in (15) fifteen Iraqi cities. According to experts, the threats were the most common. Thirteen (13)

**Table 1** Adopted from POMBOK Guide [16]

Probability and Impact Matrix										
Probability	Threats					Opportunities				
0.9	0.05	0.09	0.18	0.36	0.72	0.72	0.36	0.18	0.09	0.05
0.7	0.04	0.07	0.14	0.28	0.56	0.56	0.28	0.14	0.07	0.04
0.5	0.03	0.05	0.10	0.20	0.40	0.40	0.20	0.10	0.05	0.03
0.3	0.02	0.03	0.06	0.12	0.24	0.24	0.12	0.06	0.03	0.02
0.1	0.01	0.01	0.02	0.04	0.08	0.08	0.04	0.02	0.01	0.01
	0.05	0.1	0.2	0.4	0.8	0.8	0.4	0.2	0.1	0.05
Impact (numerical scale) on an objective (e.g., cost, time, scope or quality)										
Each risk is rated on its probability of occurring and impact on an objective if it does occur. The organization’s thresholds for Low, Moderate, or high risks are shown in the matrix and determine whether the risk is scored as high, moderate, or low for that objective [16].										

**Table 2** The most common geotechnical risks when implementing water treatment plants in Iraq

Groups	No	The Most Common Geotechnical Risks
Soil and Rocks Risks	1	River sandy soil
	2	Loose clay soil
	3	Stony soil
	4	Gypsum soil
Underground Water Risks	5	The high level of groundwater with acceptable salinity
	6	High salinity groundwater
	7	The presence of groundwater contaminated with chemicals (fertilizers, pesticides, etc....)
Human-made Risks	8	The presence of mines or remnants of war under the soil
	9	The presence of conflicts of previous projects under the soil surface
	10	The presence of the remains of archaeological sites under the soil
Natural resources and phenomena	11	Geotechnical Slops
	12	The existence of reservoirs of natural resources below the soil, such as reservoirs (oil, gas, sulfur, etc....)
	13	The presence of a seismic effect on the project site

geotechnical risks were categorized into four categories by those interviewed, see Table 2.

### 3 Results and Discussion

The technical outputs of the interview conducted with specialists in the field of implementation and supervision of central water treatment projects provided a list of the most important geotechnical risks most common when implementing these projects. They referred to in Table 2, and for a more understanding of this list, the analysis is done for each risk identified separately. Using a differential and conquer approach. So that all risks are fully understood. Through the application of paragraph (C) of the research methodology, which includes designing a questionnaire to determine the impact of each risk on one or more of the project objectives, including (cost, schedule) and applying paragraph (D) of the research methodology, which includes conducting a qualitative analysis of geotechnical risks by adopting the probability and impact technique. After analyzing the questionnaire data mentioned in paragraph (C) of the methodology using the SPSS program and calculating the reliability coefficient to assess the accuracy of the data, its value was 0.886, which is a good indicator for its

**Table 3** The level of risk score on cost for the most common geotechnical risks when implementing centralized water treatment projects in Iraq

No	The Most Common Geotechnical Risks	Mean of risk score on cost	Evaluation
1	The presence of conflicts of previous projects under the soil surface	0.117	<i>Medium risks</i>
2	The existence of reservoirs of natural resources below the soil, such as reservoirs (oil, gas, sulfur, etc....)	0.114	
3	The presence of mines or remnants of war under the soil	0.094	
4	The presence of the remains of archaeological sites under the soil	0.084	
5	River sandy soil	0.079	
6	The presence of a seismic effect on the project site	0.077	
7	Loose clay soil	0.076	
8	Gypsum soil	0.057	<i>Low risks</i>
9	Stony soil	0.056	
10	The high level of groundwater with acceptable salinity	0.052	
11	High salinity groundwater	0.052	
12	The presence of groundwater contaminated with chemicals (fertilizers, pesticides, etc....)	0.034	
13	Geotechnical Slops	0.032	

approval. Then calculate the arithmetic average of the degree of risk on the cost and schedule, and apply the arithmetic average of the degree of risk for all risks. In the probability and impact matrix shown in Table 2, it is noted that seven of these risks had a moderate effect on the cost. In contrast, eight of them had a moderate impact on the schedule, which was represented by the yellow balloon in descending order from the highest impact to the lowest impact, as shown in Tables 3 and 4, respectively, and these are the risks Which deserve more analysis, and perhaps a quantitative analysis of risks, and the work of a response plan. The low-impact risks represented by the green color are put on the watch list and monitored.

## 4 Conclusions

The first sub-hypothesis was proven, and it became clear through the study and data analysis that seven factors have an average effect on the cost, as shown in Table 3.

**Table 4** The level of risk score on schedule time for the most common geotechnical risks when implementing centralized water treatment projects in Iraq

No	The Most Common Geotechnical Risks	Mean of risk score on time schedule	Evaluation
1	The existence of reservoirs of natural resources below the soil, such as reservoirs (oil, gas, sulfur, etc....)	0.133	<i>Medium risks</i>
2	The presence of conflicts of previous projects under the soil surface	0.123	
3	The presence of mines or remnants of war under the soil	0.111	
4	The presence of the remains of archaeological sites under the soil	0.102	
5	River sandy soil	0.071	
6	Loose clay soil	0.063	
7	The presence of a seismic effect on the project site	0.063	
8	Gypsum soil	0.061	
9	Stony soil	0.054	<i>Low</i>

The second sub-hypothesis was proven, as it was found through the study and data analysis, that eight factors have a moderate effect on the schedule, as shown in Table 4.

## 5 Recommendations and Suggestions

- The decision-makers working in the implementation of central water treatment projects, whether they are owners or contractors, must consider the findings of the research that there is a moderate effect of some geotechnical risks on the cost, schedule, and early preparation for them.
- A fair distribution of responsibility for these geotechnical risks between the contracting parties through an appropriate delivery method.
- Developing the research to include knowledge of the degree of risk to the remaining objectives of the project, which are quality and scope
- Link this effect to a relationship with appropriate delivery methods PDMS.

## References

1. Tran, D. Q., & Molenaar, K. R. (2014). Impact of risk on design-build selection for highway design and construction projects. *Journal of Management in Engineering*, 30(2), 153–162.
2. Tran, D. Q., & Molenaar, K. R. (2015). Risk-based project delivery selection model for highway design and construction. *Journal of Construction Engineering and Management*, 141(12), 04015041.
3. De Silva, A. (2002). *A model for optimizing the selection of project delivery systems using analytic hierarchy process (AHP)*.
4. Noorzai, E. (2020). Performance Analysis of Alternative Contracting Methods for Highway Construction Projects: Case Study for Iran. *Journal of Infrastructure Systems*, 26(2), 04020003.
5. Tapia, R. M. (2017). *Linear scheduling and procurement tools to manage geotechnical risk in design-build construction projects*.
6. Chen, C. H. (2004). Effect of completion level of owner's basic design in design-build projects. *Civil Hydraulic Engineering*, 30(5), 20–25.
7. Trenter, N. (2003, February). Understanding and containing geotechnical risk. In *Proceedings of the Institution of Civil Engineers-Civil Engineering* (Vol. 156, No. 1, pp. 42–48). Thomas Telford Ltd.
8. Gransberg, D. D., & Gad, G. M. (2014). Geotechnical Requirements in the Design-Build Selection Process. *Transportation Research Record*, 2408(1), 26–33.
9. Castro-Nova, I. G. (2016). *Geotechnical risk decision tools for alternative project delivery method selection*.
10. Gransberg, D. D., Loulakis, M., Touran, A., Gad, G., McLain, K., Sweitzer, S., Pittenger, D., Nova, I. C., Pereira, R. T. & Pinto-Nunez, M. (2018). *Guidelines for managing geotechnical risks in design-build projects* (No. Project 24–44).
11. van Staveren, M. T. (2009). Extending to geotechnical risk management. *Georisk*, 3(3), 174–183.
12. McLain, K., Gransberg, D., & Loulakis, M. (2014). Managing geotechnical risk on US design-build transport projects. *Australasian Journal of Construction Economics and Building*, The, 14(1), 1–19.
13. del Puerto, C. L., Gransberg, D. D., & Loulakis, M. C. (2017). Contractual approaches to address geotechnical uncertainty in design-build public transportation projects. *Journal of Legal Affairs and Dispute Resolution in Engineering and Construction*, 9(1), 04516010.
14. Tran, D. & Molenaar, K. (2012). Critical risk factors in project delivery method selection for highway projects. In *Construction Research Congress 2012: Construction Challenges in a Flat World* (pp. 331–340).
15. Řeháček, P. (2017). Risk management standards for project management.

# Mapping and Analyzing Flood Hazard Using Remote Sensing and GIS Techniques in Diyala River Basin, Iraq



Hussain Muhamed, Mustafa N. Hamoodi, and Abd Alrazzak T. Ziboon

**Abstract** Flood is defined as one of the most devastating natural events that lead to immeasurable damage in terms of human settlements and economic losses. Flooding due to extreme rainfall is a frequent hazard in the flood plains in a catchment area of Diyala River basin. In this paper, flood hazard and their impacts on residential areas, villages and agriculture areas located on both sides of Diyala River banks were mapped and analyzed. The main objective of this paper is to employ remote sensing data, including Landsat 8 and ASTER Global Digital Elevation Model, with a GIS environment for mapping and delineating the flood areas for the study area. The results revealed that the flood-prone areas were analyzed based on the final maps. The mapping and analysis of the flood-prone regions could be valuable for risk reduction.

**Keywords** Flood hazard · Diyala · LANDSAT · MNDWI · SRTM DEM

## 1 Introduction

Flood is defined as one of the most devastating natural events in the world that lead to immeasurable damage in terms of human settlements and economic losses [1]. Flood is a common and costly risk for many countries which face it frequently [2]. Three major kinds of floods, including river flooding, flash flooding, and coastal flooding, are documented. River flood usually occurs due to heavy rainfall and the melting of snow, hence leading to overflow of water to cover lands on both banks of rivers [3]. The study area of Diyala has witnessed a serious and costly risk of frequent floods that are usually resulting from heavy rain. Recently, the flood in Diyala in 2019 caused significant damage to many villages, orchards, and agricultural areas located along the Diyala river basin. Remote sensing data can provide important

---

H. Muhamed · M. N. Hamoodi (✉) · A. A. T. Ziboon  
Civil Engineering Department, University of Technology, Baghdad, Iraq  
e-mail: [40117@uotechnology.edu.iq](mailto:40117@uotechnology.edu.iq)

A. A. T. Ziboon  
e-mail: [40003@uotechnology.edu.iq](mailto:40003@uotechnology.edu.iq)



information about the earth's surface and are usually easy to obtain. Also, these data are a valuable source to detect the flood extent and determine damages and effects over rivers and land bodies [4]. However, there are some challenges related to cloud cover and distinguish flooded areas under forest cover [5]. These data have been widely used in studying many aspects, especially in hydrology. Digital elevation models were used primarily in extracting stream networks [6] and surface runoff [7]. Radar data provide important information used in studying morphometric properties of the stream-networks and flood areas [8]. Recently, Landsat data in combination with other data have been documented as an effective source for mapping and extracting flooded areas [9].

There are several methods, models, and approaches that have been employed for flood mapping and analysis. The Sponge City flood concept was designed for water resources and addressing flood risk in urban areas [10]. A linear mixture model and decision-tree approach using MODIS data were investigated to derive water fraction and flood mapping [11]. A systematic approach was employed to flood monitoring the Huaihe river basin of China using NOAA/AVHRR [12]. Spatiotemporal distribution of streamflow was analyzed using soil and water assessment tool (SWAT) [13]. In recent years, mapping and delineating floods have become a key input into flood evaluation and mitigation. The process of flood hazard mapping helps to provide information about the proposed damages for vulnerability areas that be close to the rivers. In this study, the main objective is to employ Landsat 8 images and the ASTER GDEM data with a GIS procedure to map, delineate, and analyze flood hazards along the Diyala river basin. Specifically, (1) to map surface water-based MNDWI using Landsat 8 images, (2) to delineate stream network system using GDEM data.

## 2 Study Area and Datasets

**Study Area.** The province of Diyala in Iraq (notably Hemrine Lake and Basin of Diyala River) was selected as the study area for this work. The study area lies in eastern Iraq between longitudes  $33^{\circ} 10.77'$  and  $33^{\circ} 29.26'$  and latitudes  $44^{\circ} 11.55'$  and  $44^{\circ} 34.23'$  (Fig. 1). The study area covers  $17,685 \text{ km}^2$ . The population is about 1,548,000 people, according to the Iraqi Ministry of Planning. The study area of Diyala is located in a semi-arid and subtropical desert climate type (BWh), based on the Köppen's climate classification system [14]. The average annual temperature is about  $25.3^{\circ} \text{C}$ , and the highest temperature is recorded in August. The annual rainfall of the study area is around 216 mm that mostly occurs during winter.

**Datasets.** The data used in this study included (1) Two sets of Landsat 8 images, which were acquired in January and April of 2019, downloaded from the U.S. Geological Survey as a Level-2 product (Level-1 and atmospheric corrections) [15]. (2) ASTER Global Digital Elevation Model (GDEM) data were acquired in 2019, downloaded from the Earth data website, provided in GeoTIFF format with a  $30 \text{ m} \times 30 \text{ m}$  spatial resolution [16].

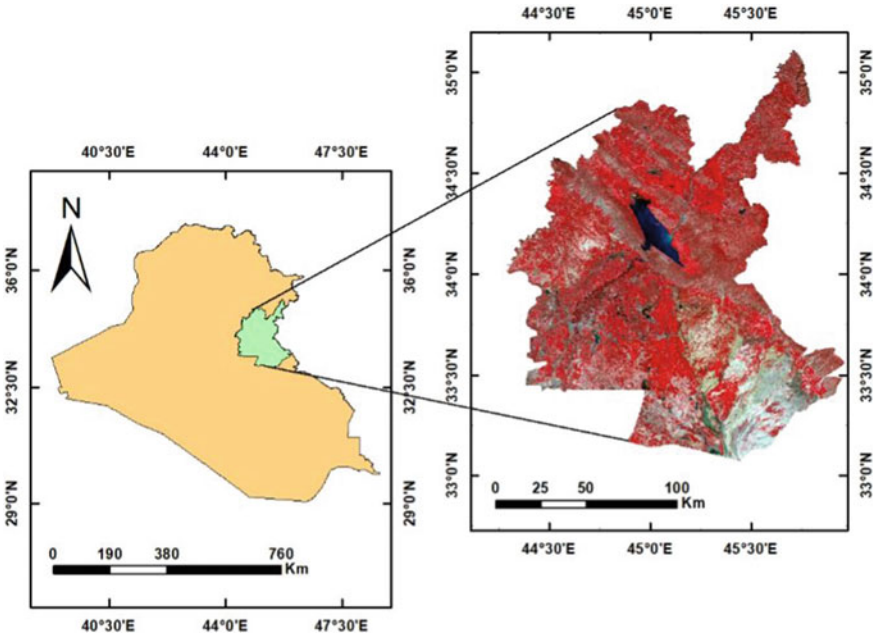


Fig. 1 Location of the study area, the province of Diyala

### 3 Methodology

The methodology adopted in this work is shown in the flowchart (Fig. 2).

**Extraction Surface Water (Landsat Images).** Two Landsat 8 images in January 2019 before the flood and in April 2019 during the flood were chosen. The pre-process of images included mosaic and clip the photos based on boundaries of the whole study area. These images were then used to map surface water and extract flood water within the study area, particularly for Hemrien Lake and the River of Diyala. The workflow for this method is shown in Fig. 2. Extraction of water bodies was conducted using modified normalized different water index indices, suggested by Xu [17]. MNDWI was computed from Landsat 8 (OLI) using Eq. (1) below:

$$MNDWI = \frac{(\rho(\text{Green band}) - (\rho(\text{SWIR}_1 \text{ band})))}{(\rho(\text{Green band}) + (\rho(\text{SWIR}_1 \text{ band})))} \tag{1}$$

Green and SWIR\_1 bands are the spectral reflectance of the green band and short-wave infrared band. Ten cross-sections were taken along the Diyala River for the two periods of January 2019 and April 2019 to compute the increase in surface water during those periods.

**Watershed Delineation (GDEM).** Two pre-processing steps were carried out for Digital Elevation Model images, including four GDEM that were mosaicked using

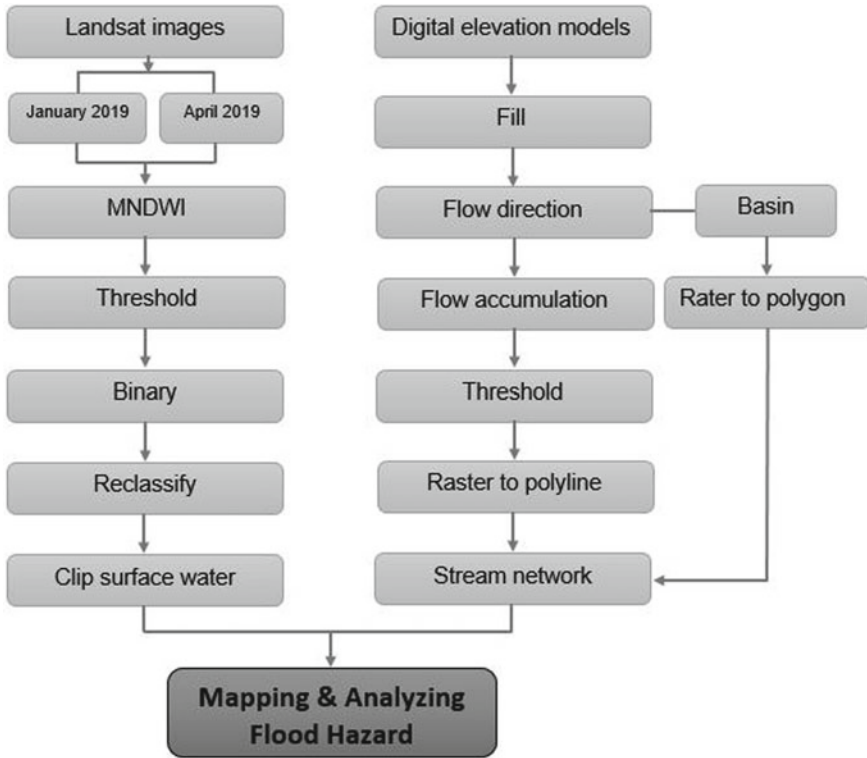


Fig. 2 Flowchart showing methods for mapping and analyzing flood hazards

ERDAS Imagine software to cover the study area. Then, clipped to the study area boundary (Fig. 3).

Delineation of the stream-networks system for the Diyala river basin was created by several processing steps using ArcGIS 10.4: (1) determine the direction in which water would flow out of each pixel. (2) Create a raster delineating all drainage basins using the basin tool. (3) Create the stream network using the flow accumulation tool. (4); finally, stream network raster for the Basin of Diyala River is delineated.

### 4 Results and Discussion

Mapping surface water for January and April of 2019 from the Landsat 8 images and delineating stream network from ASTER Global Digital Elevation Model can reveal the spatial distribution and analyze watershed behavior to determine the flood areas Diyala river basin. Figure 4 shows that the amount of water was largely increased in the River of Diyala and Hemrien Lake between January and April of 2019. It can be

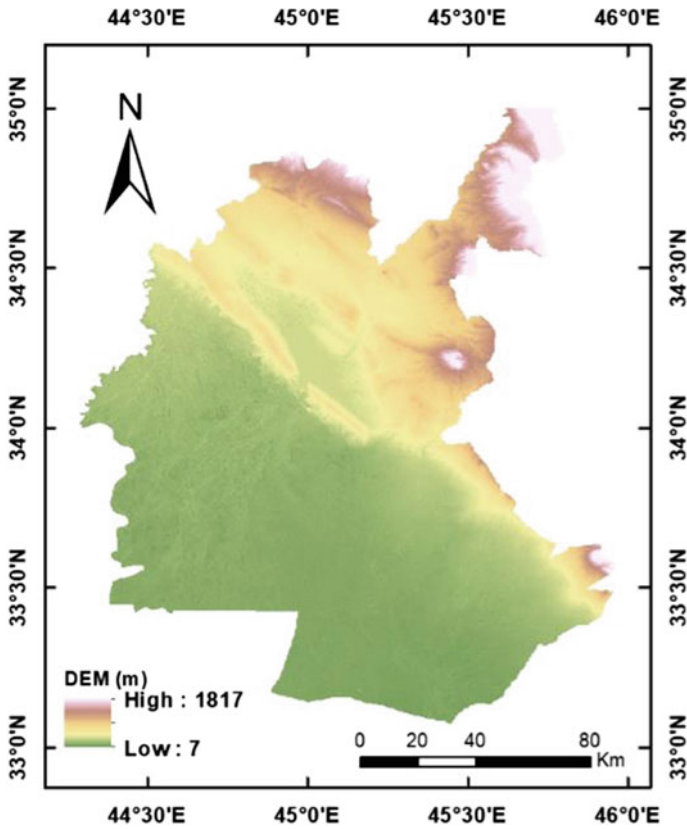


Fig. 3 ASTER global digital elevation model (GDEM)

seen that the area of surface water for Hemrien Lake was increased from 267.75 km<sup>2</sup> to 339.19 km<sup>2</sup> in January and April of 2019, respectively. This increase in water was mainly resulted from heavy rainfall in the northern and eastern regions to the study area during the season of rains. It is also related to the high outflow of Darbandikhan Dam (located in the Sulaymaniyah Governorate) toward Hemrien Lake.

This outcome agrees with data obtained from the water resources office, which recorded the highest level of water reached 105.53 m on the 26th of April 2019. In order to control the process of water storage in the Hemrien Lake, the high discharge of water was contributed to an increase in the amount of water to the river of Diyala, as the main outlet, then making river flooding. The cross sections showed the increase in surface water for the Diyala River channel between January and April of 2019 (i.e., before and during the flood). It can be clearly seen that the surface water raised and expanded in all selected cross-sections along the river from January and April of 2019, as seen in Fig. 5 and Table 1. The results obtained based on the remote sensing data and GIS processes appear to be consistent with field data that showed the level and discharge of water in the river of Diyala were 44.39 m and 720 m<sup>3</sup>/s in 2019,

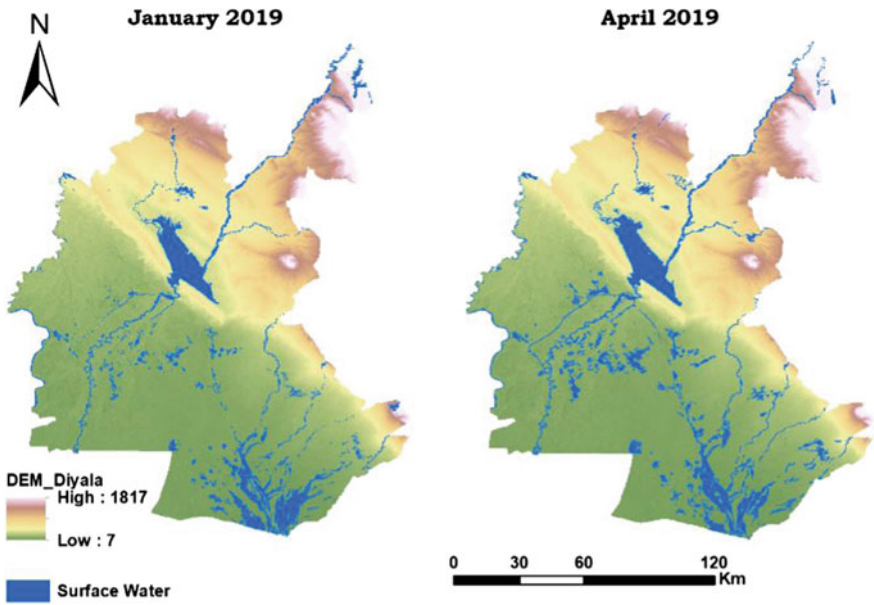


Fig. 4 Surface water during January and April of 2019, the province of Diyala

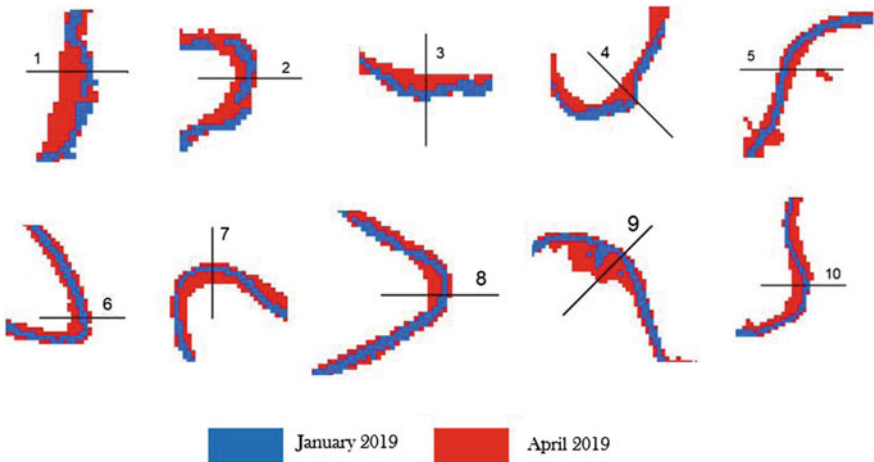


Fig. 5 Cross-sections over the Diyala River channel

respectively. It is the first time in the last three decades. The river reached this level of water. Based on the maps of surface water (Fig. 4), cross-sections taken along the river of Diyala were used to measure the width of surface water in January and April of 2019 (Fig. 5). The results revealed a significant difference in surface water between those two periods, as illustrated in Table 1.

**Table 1** Width of surface water of the Diyala River channel

Cross section	January 2019 (m)	April 2019 (m)	Cross section	January 2019 (m)	April 2019 (m)
1	28	194	6	58	142
2	32	115	7	30	150
3	52	146	8	60	120
4	84	190	9	42	240
5	60	120	10	30	150

**Fig. 6** Flood of the Diyala River in April 2019

The flood significantly influenced several villages. In addition, large agricultural areas and orchards located on both sides of river banks were destroyed (Fig. 6).

Generally, delineation flood extent areas is associated with flood mapping process. The results revealed that Landsat images were appropriate data in computing surface water and mapping the flood in the Diyala river basin. In this context, delineating the stream network-based GDEM data provided an initial investigation of morphologic features on flood and affected areas. Figure 7 shows drainage networks and catchments in Diyala river basin. Flood moves typically from the upper part, generally categorized by the terrain, toward the lower part.

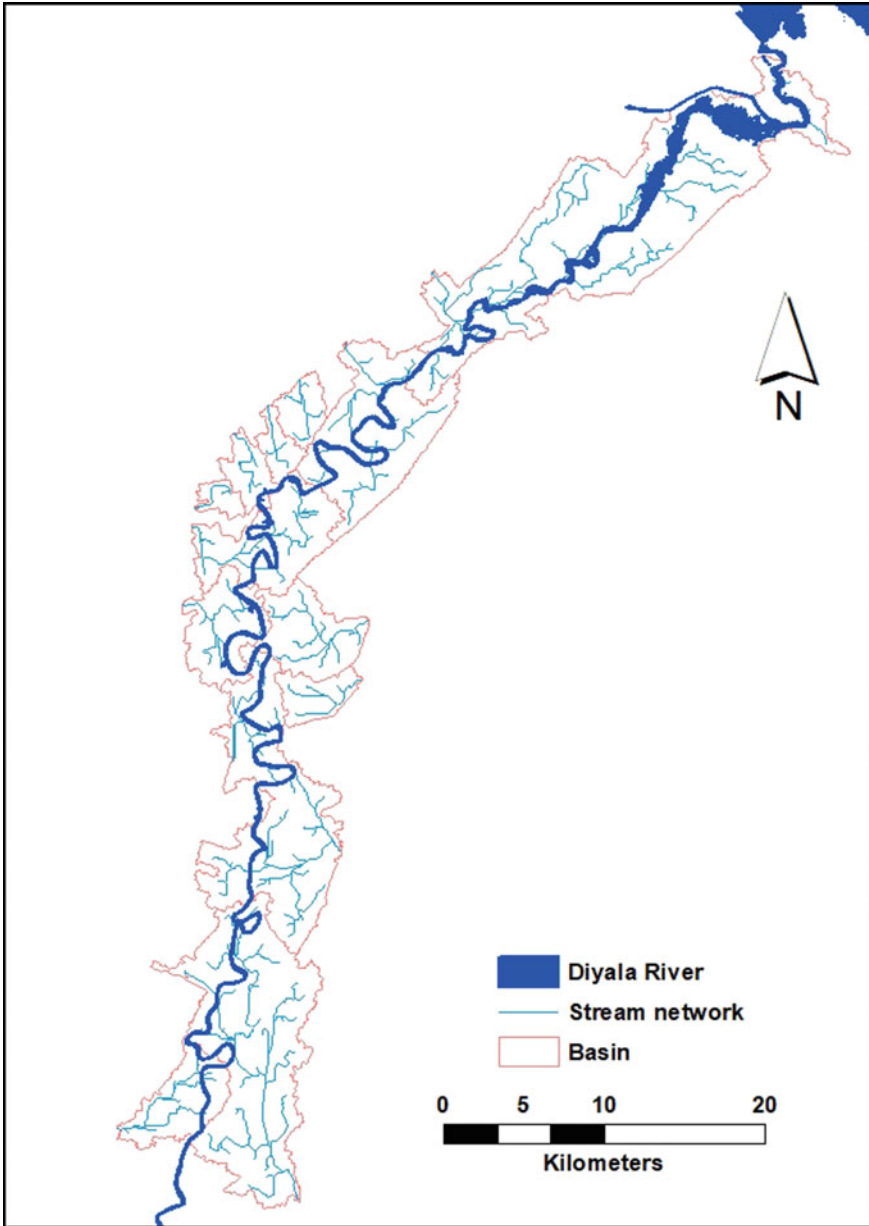


Fig. 7 Delineation stream network of Diyala river basin

## 5 Conclusion

The flood areas of the Diyala river basin were mapped and delineated using the Landsat 8 images and the ASTER GDEM data-based GIS procedure. Flood hazards on of the Diyala river basin were then analyzed. In summary, the outcomes indicate that:

- Using remotely sensed data of Landsat 8 and ASTER Global Digital Elevation Model (GDEM) and GIS provided an economical and efficient approach for mapping and analyzing flood hazard.
- Mapping and delineating the flood hazard areas can save peoples, villages, and agricultural areas from being damaged. It can also help in finding plans to avoid flood hazards in Diyala river basin.
- The obtained results could be used in determining vulnerability areas and planning flood risk management strategies.

## References

1. Rozalis, S., Morin, E., Yair, Y., & Price, C. (2010). Flash flood prediction using an uncalibrated hydrological model and radar rainfall data in a Mediterranean watershed under changing hydrological conditions. *Journal of Hydrology*, 394(1–2), 245–255.
2. Karki, S., Koirala, M., Pradhan, A. M. S., Thapa, S., Shrestha, A., & Bhattarai, M. (2011). *GIS-based flood hazard mapping and vulnerability to climate change assessment: A case study from Kankai Watershed, Eastern Nepal*. Nepal climate change Knowledge Management Center Nepal Academy of Science and Technology.
3. Kron, W. (2002). Keynote lecture: Flood risk= hazard× exposure× vulnerability. In *Flood defence* (pp.82–97).
4. Sun, D., Yu, Y., Zhang, R., Li, S., & Goldberg, M. D. (2012). Towards operational automatic flood detection using EOS/MODIS data. *Photogrammetric Engineering & Remote Sensing*, 78(6), 637–646.
5. Wang, Y., Colby, J. D., & Mulcahy, K. A. (2002). An efficient method for mapping flood extent in a coastal floodplain using Landsat TM and DEM data. *International Journal of Remote Sensing*, 23(18), 3681–3696.
6. Umitsu, M., Hiramatsu, T., & Tanavud, C. (2006). Research on the flood and micro landforms of the Hat Yai Plain, Southern Thailand with SRTM Data and GIS. *Geomorphological Union*, 27(2), 205–219.
7. Al-Khafaji, M. S., & Saeed, F. H. (2018). Effect of DEM and land cover resolutions on simulated runoff of Adhaim Watershed by SWAT model. *Engineering and Technology Journal*, 36(4 Part A), 439.
8. Jin, Y. Q. (1999). A flooding index and its regional threshold value for monitoring floods in China from SSM/I data. *International Journal of Remote Sensing*, 20(5), 1025–1030.
9. Demirkesen, A. C., Evrendilek, F., Berberoglu, S. Ü. H. A., & Kilic, S. (2007). Coastal flood risk analysis using Landsat-7 ETM+ imagery and SRTM DEM: A case study of Izmir, Turkey. *Environmental Monitoring and Assessment*, 131(1), 293–300.
10. Wang, C., Hou, J., Miller, D., Brown, I., & Jiang, Y. (2019). Flood risk management in sponge cities: The role of integrated simulation and 3D visualization. *International Journal of Disaster Risk Reduction*, 39, 101139.



11. Sun, D., Yu, Y., & Goldberg, M. D. (2011). Deriving water fraction and flood maps from MODIS images using a decision tree approach. *IEEE Journal of Selected Topics in Applied Earth Observations and Remote Sensing*, 4(4), 814–825.
12. Sheng, Y., Gong, P., & Xiao, Q. (2001). Quantitative dynamic flood monitoring with NOAA AVHRR. *International Journal of Remote Sensing*, 22(9), 1709–1724.
13. Al-Khafaji, M. S., & Al-Chalabi, R. D. (2020). Impact of climate change on the spatiotemporal distribution of stream flow and sediment yield of Darbandikhan watershed, Iraq. *Engineering and Technology Journal*, 38(2A), 265–276.
14. Peel, M. C., Finlayson, B. L., & McMahon, T. A. (2007). Updated world map of the Köppen-Geiger climate classification. *Hydrology and Earth System Sciences*, 11(5), 1633–1644.
15. Hawbaker, T. J., Vanderhoof, M. K., Schmidt, G. L., Beal, Y., Picotte, J. J., Takacs, J. D., Falgout, J. T., & Dwyer, J. L. (2020). *The Landsat Burned Area products for the conterminous US Geological Survey data release*.
16. Khal, M., Algouti, A., Algouti, A., Akdim, N., Stankevich, S. A., & Menenti, M. (2020). Evaluation of open digital elevation models: Estimation of topographic indices relevant to erosion risk in the Wadi M'Goun watershed, Morocco. *AIMS Geosci*, 6, 231–257.
17. Xu, H. (2006). Modification of normalised difference water index (NDWI) to enhance open water features in remotely sensed imagery. *International Journal of Remote Sensing*, 27(14), 3025–3033.

# Towards Sustainable Local Tourism to Conserve the Natural Environment: Foundations of Sustainable Ecologde Design



Zahraa Sabah Salih and Zaynab Radi Abaas

**Abstract** Sustainable tourism plays an essential role in achieving sustainable development goals; it reached a truly realistic representation of local, sustainable development. Sustainable tourism in natural environments represented by ecotourism, considered one of the popular types of sustainable tourism in growth and demand, helped and contributed to the conservation of the natural environment by planning an ecolodge that contributes to preserving the environment. This paper aims to create sustainable local tourism by successfully developing indicators to prepare Ecologde's conservation of the natural environment. These indicators represent a comprehensive framework and concepts to provide basic information in promoting sustainable tourism in natural environments.

**Keywords** Sustainable · Tourism · Indicators · Ecotourism · Ecologde

## 1 Introduction

The world's tourism movement increased four times after World War II; tourism has become a vital economic resource for many countries [1]. According to Cooper [2], the increasing tourism industry needs to provide accommodations, so developing ecotourism requires the main requirements. Accommodations are one of the main requirements that should be suitable for the natural environment, surroundings, local community, and tourists to enjoy their recreational activities [3]. David Weaver emphasized allowing the tourist to immerse with the environment and learn more about natural and cultural information. Hector Ceballos-Lascuráin's point of view that ecotourism creates an environmentally conscious human and contributes to preserving it [4]. Thus, the Ecologde represents the local community's identity

---

Z. S. Salih (✉)  
Muthanna Investment Commission, Samawa, Iraq  
e-mail: [z.salih1104@coeng.uobaghdad.edu.iq](mailto:z.salih1104@coeng.uobaghdad.edu.iq)

Z. R. Abaas  
Department of Architecture, University of Baghdad, Baghdad, Iraq  
e-mail: [Dr.zaynabr.a@coeng.uobaghdad.edu.iq](mailto:Dr.zaynabr.a@coeng.uobaghdad.edu.iq)

and lifestyle; it can keep, save sustainable tourism, and increase the awareness of the conservation for the local community and tourists. The international studies of successful planning ecolodge have been reviewed to produce total, comprehensive indicators and apply them to a selection global example to study their validity and potentials in achieving sustainable tourism. This paper aims to develop some primary indicator system for Ecolodge accommodations for the Iraqi case to achieve sustainable tourism. Because of the lack of these indicators and the obstacles to develop ecotourism in the right direction in the sustainable development thus, the research will present a checklist from all the relevant theories and most important practicing of accolades around the world that succeeded to represent sustainable tourism.

## 2 Sustainable Ecolodge Design

According to the Cambridge dictionary, Ecolodge is a place for tourists, designed to be softened with the natural environment and surroundings. This term is known for the first time in The International Ecotourism Society (TIES) organizational meetings in the Virgin Islands and cost Arica in 1994–1995. This organization defined Ecolodge as accommodation for holidays designed to be derived with definition, principles, and ecotourism meanings [5]. Hitesh Mehta concluded in 2005 that Ecolodge's definition is a lodge between 5 and 75, based on integration with the natural environment, sustainability in planning, designing and operation, preserving environments, provides opportunities to learn and communicate with nature and culture [6]. So, the Ecolodge can be defined as a kind of accommodation found in the natural conservation environment, built with the spirit of local culture (methods, materials) without affecting the environment, allows to learn from nature, local community culture, and also provides with cultural central to represent all the information about the surrounding environment. It's embodied the meaning of ecotourism to reserve the needs of tourists that didn't impact the environment (the researchers).

**Characteristics of Ecolodge.** World Commission on Protected Areas (WCPA) described that the Ecolodge should be simple, sensitive to the environment and local culture, suitable for tourists with low carrying capacity for the environment [7]. The International Ecotourism Society (TIES) declared in a 2002 book entitled the international ecolodge guidelines explained the characteristics of Ecolodge should embody the main philosophy of ecotourism with the other two characters as shown in Fig. 1 [5].

From the definition of Ecolodge and its characteristics, creating the Ecolodge depended on the environmental design or what is called the sustainable design, green design, or ecological design.

**Environmental Design.** The environmental design appeared in the twentieth century and developed with the emergence of sustainable development, its ideas, dimensions, applications to be real not only in theories. It's explained the integrated relationship between the human and the environment in different spatial conditions and time. So,

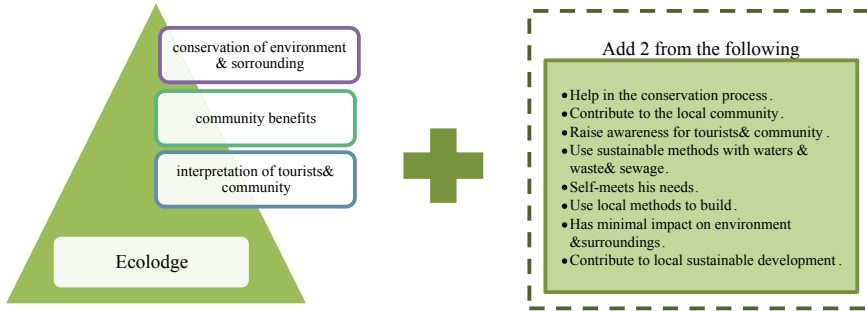


**Fig. 1** The characteristics of Ecolodge according to TIES [5]

environmental design is used in designing and practicing the consumer of the small product, even in designing housing complexes, parks, and large planning projects [8]. Environmental design aims to clarify the vision of environmental sustainability by reducing the consumption of resources and avoiding environmental damage [9]. The main principles of environmental design as following [9–11].

- Selection the suitable solutions in place, time, and climate.
- Choosing the used area to be limited to achieve for low environmental footprint.
- Using renewable energy sources to improve natural features.
- Employing an environmentally friendly building by using the theories of environmental construction.
- Minimize environmental impact to reach a sustainable urban design.
- Staying with the carrying capacity of the environment can absorb activities as long as it can.

**Types of Ecolodge.** There are four types of ecolodges according to the activities that visitors [3].

- A. Casual type: It’s built-in environments that are easy to reach, have good infrastructure services; this type tried to offer tourists a comfortable and enjoyable stay in nature.
- B. Dedicated type: This type could be in an area hard to reach, with weak infrastructure services. It is for demanding tourists, environmentalists interested in bird watching, for example.
- C. Scientific type: Tourists for this type who want to participate in exploration and educational environment.
- D. Agri-ecolodge type: This type depended on agricultural families, farms, fields. Environmentalists prefer this type because they stay beside preserved nature and enjoy the agricultural surroundings.

**Ecolodge Development Process.** Some researchers interested in the natural environment have seen that building in a natural environment abuses it because tourism development is difficult to stop [3]. On the other hand, many researchers, organizations, and commissions thought that the Ecolodge development process would

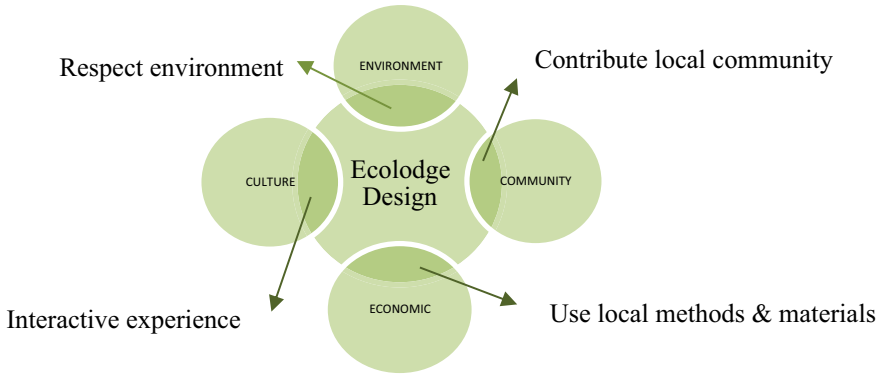


**Fig. 2** Main four pillars of Ecology development process

conserve biodiversity and develop local communities. Tourists are feeling grateful to be there and saving sustainable job opportunities [12]. So, the planners described the Ecology development process as a process of balance and synergy between subsystems of economic, cultural, environmental dimensions of sustainable development; this process can provide a good situation of lifestyle for the local community for a long time and minimize environmental impact in the surrounding [13]. Ecology’s development process depended on the four main pillars as shown in Fig. 2.

According to references [6, 14–18], the guidelines can be divided into two levels, the first level is the planning level, and the second level is the designing level.

**The Planning Level.** It can explain five main indicators to install Ecology in a specific environment. Refer to Fig. 3; every indicator has a secondary indicator. The first step is to select the site and study biological and abiotic factors in the site, create a perception of how to improve the thermal range of the Ecology [5, 14, 17], examine the suitable site ( environmental impact assessment EIA, Characteristics analysis, geo properties, hydro properties, the soil, vegetation, wildlife) is an essential factor to success the Ecology and respect the environment [15]. Site planning should respect the ecosystems, local and neighboring communities, enhancing the sense of place (climate and topography of site). Site designing based on understanding the relationship between local people and the land (zoning, the density of building, roads design, natural parks, permaculture, fence, and walls) ecology design is like

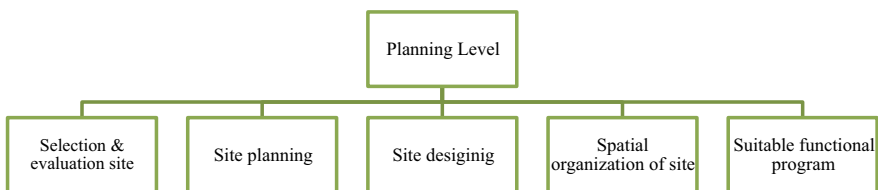


**Fig. 3** The five main indicators for planning ecology



**Fig. 4** The five main indicators in designing the Ecolodge

a balance between human needed and maintain ecosystems, so the integration with the environment is the solution to create suitable build environment with the natural environment [5, 14, 15]. The site should be organized to prevent the natural environment from damage and benefit from natural views, air movement, and solar radiation. The vegetation on the selected site and the separation of activities (day activities, night activities) will organize the site in a better way to minimize environmental impact. Functional programming should be suitable to nature and conservation at the site, conserve the local community lifestyle, provide the tourists with enjoying and learning from ecosystems, surroundings, and the indigenous people's customs [16, 17].

**The Designing Level.** Designing Ecolodge should follow sustainability principles, preserve water and reuse it, use alternative energy sources as can as possible, reduce waste, and recycle it. Another essential additional indicator is adopting local style construction (like shape and color), using environmentally friendly local materials, and selecting the appropriate technology for integration with locals' methods and materials [5–17]. Refer to Fig. 4, the five main indicators in designing the suitable Ecolodge.

In addition, the United World Tourism Organization (UNWTO) declared in 2004 a book for indicators tourism (Indicators of Sustainable Development for Tourism Destinations: A Guidebook). This book includes a wide range of type indicators and sustainable tourism's core indicators [18]. These core indicators considered brief, focused ideas of sustainable development integrated with sustainable tourism strategies as given in Table 1 [18]. From the international studies theories [5, 17–19], a checklist can be built to help planners and designers to know the Ecolodge that follows the sustainable principles to achieve sustainable tourism, that contributes to conserving the natural environment, and brings luxury for tourists, and decent living for local communities. Refer to Table 4; this checklist is considered a fully comprehensive view for planning ecolodge.

### Practical Study

Three tourism areas internationally famous in sustainable tourism have been selected to test, verify the developed checklist's effectiveness, and apply the core indicators of sustainability.

**Table 1** The core indicators of sustainable tourism according to UNWTO

No.	Indicator	Specific measure
1	Site protection	Category of site protection according to IUCN
2	Stress	Tourist number visiting site
3	Use intensity	Intensity of use peak period
4	Social impact	Ratio of tourists to locals
5	Development control	Existence of environmental review procedure or formal controls over development of site and use densities
6	Waste management	Existence of sewage from site receiving treatment
7	Planning process	Existence of organized regional plan for the tourist's destination
8	Critical ecosystems	Number of rare/endangered species
9	Consumer satisfaction	Level of satisfaction by visitors (questionnaire)
10	Local satisfaction	Level of satisfaction by locals (questionnaire)
11	Tourism contribution to the local economy	The proportion of total economic activity by tourism only

- (A) Lapa Rios Ecolodge (LR lodge) and Wildlife Reserve. This Ecolodge opened in 1994 in the Osa Peninsula in Costa Rica; this place has important biodiversity, got a higher certification in sustainable tourism in Costa Rica. Opened with 14 ecolodges and services [19]. After 2014, two ecolodges added 2 ecolodges with adding a valuable open space and expanded the restaurant with designing accommodation for staff and management offices [20]. This Ecolodge contributes significantly to the conservation of the natural environment, sustainability of the local community, environmental education to tourists and the local community [19].
- (B) AL-Maha Resort and Spa. It opened in 1999 in a UAE plan to re-green and conserve the desert from damage located in Dubai UAE. It is sited in Dubai Desert Conservation Reserve (DDCR), opened with 37 ecolodges and services. After five years, it expanded and added five ecolodges. This Ecolodge contributes to reducing the degradation of the desert, conserve the biodiversity of the desert there, established a project planted 6000 trees [21].
- (C) Hutt Lagoon (Pink Lake). It is a marine Salt Lake, rectangular lake, located beside the coast of the Indian Ocean, two kilometers (1.2 mi) north of the Hutt River in Western Australia. The lake's length is about 14 km along with it, and its width is approximately 2.3 km. It is also a wetland within the International Ramsar Convention. According to the report of the Department of Environment and Conservation in Western Australia on this lake, "Benefiting from the

**Table 3** Applying checklist of main indicators for sustainable tourism into international examples

Indicator	Example			Indicator	Example		
	A	B	C		A	B	C
Site protection	1	1	1	Planning process	1	1	1
Stress	1	1	0	Critical ecosystems	1	1	1
Use intensity	0	1	0	Consumer satisfaction	0	0	0
Social impact	0	0	0	Local satisfaction	1	0	0
Development control	1	1	1	Tourism contribution to local economy	1	1	0
Waste management	1	1	0				

natural environment is through preserving the most significant possible amount of biodiversity in it, preserving ecosystem services and scientific, educators and future uses are one of the most important conservation priorities [22]. Tourists can visit the lake for a limited time between (ten in the morning until two in the afternoon), as the lake is considered to have a distinctive and unique view because it is covered in pink [22]. Lake is conserved for scientific research.

**Measuring and testing the selected indicators.** A preliminary evaluation of the checklist was developed and after calculating the scores for each tourism site for the list of indicators for sustainable tourism, refer to Table 3, then the expanded list is given in Table 4. The standard deviation was calculated for each tourism site, and the following was obtained: the first two sites provided a perfect model for establishing a successful Ecology that achieves the goals and principles of sustainable tourism; this was confirmed by the reality of Ecology and the standard deviation test to indicators. The first two sites got eight scores, while the third site got four scores, and the results were found in Table 5. However, the third site was satisfied with preserving the natural environment and investing it in the field of science and research, and thus it did not achieve sustainable tourism despite its uniqueness with distinctive characteristics. Yet this checklist represents the starting point to develop a successful Ecology that can achieve sustainable tourism. Deduce from these values that establishing an ecology that takes into account the planning, design, and operation, the principles of sustainability, leads to achieving sustainable tourism that increases the possibility of conservation, supports local communities and their economy, increases the opportunities for environmental education and introduces the importance of natural environments.



**Table 4** Applying the developed checklist into international examples

The planning level						
Indicator	Issue		Example A	Example B	Example C	
Selection and evaluation site	Accessibility		1	1	1	
	Scale of project		1	1	1	
	EIA		0	1	1	
	Cultural identity and nearby local community		1	1	1	
	Characteristics analysis	Geo properties		0	0	1
		Hydro properties				
		The soil				
		Vegetation				
	Existence infrastructure	Wildlife		1	0	0
		Water and energy services				
		Existence highway				
Existence infrastructure	Existence highway		0	0	1	
	Medical and shopping services		1	0	0	
	Availability of environmentally friendly materials		1	0	0	
Site planning	Climate	Sun	1	1	Not measured	
		Rain				
		Wind				
		Humidity				
	Topography of site		1	1		
	Relationship of site with neighboring		1	1		
Site designing	Zoning	Building density on site	1	1	Not measured	
		Future expansion				
	Access methods	Existence way		1		0
		Creation way		1		0
		Creation Airstrip		0		1
	Determine the location of buildings		0	0		
	Road's design		1	1		
	Naturals parks		1	1		
	Fences and walls		1	0		
	Permaculture		0	0		
Inflection		1	1			

(continued)

**Table 4** (continued)

The planning level					
Spatial organization of the site	Direction of building		1	1	Not measured
	Separate activities		1	1	
	Vegetation		1	1	
Suitable functional program	–		1	1	Not measured
The designing level					
Local styles and aesthetics	Shape	Interior design	1	1	Not measured
		Exterior design	1	1	
	Color	Interior design	1	1	
		Exterior design	1	1	
	Integration with nature		1	1	
	Sustainable water management	Water conservation		1	
Water harvesting		0	0		
Water reuse		1	1		
Water treatment		0	0		
Sustainable waste management	Construction waste		0	0	
	Wastewater		1	0	
	Solid waste		0	0	
Using alternative energy	–		1	1	
Using local materials and technology	–		1	1	

**Table 5** The score results for examples

Example	Core indicator	Checklist developed	Standard deviation
Lapa Rios ecolodge	8	30	11
Al-Maha ecolodge	8	24	8
Hutt lagoon	4	6	1

### 3 Conclusions

After reviewing the international studies, specialized in successful ecotourism planning that led to the development of sustainable tourism around the world. Clear steps can be taken to develop sustainable tourism in Iraq towards achieving a local sustainable development. The first step starts from developing the checklist in which this research came out to include various tourism sites that Iraq possesses, studying what is appropriate for each region in detail, and reviewing the environmental, economic, and social-cultural requirements of each site. A study in which the multidisciplinary grouping and the local community's involvement in it, and taking essential steps to establish a reference system, this system is tested by local experts with the help of specialists. To be taken in the planning aspect of the government budget and plans to commit and implement international agreements, to keep pace with the developed world in sustainable tourism, which has proven its local success and benefits at all environmental, social-cultural, and economic levels, and to reach sustainable development. This paper aims to examine the final checklist to the one of the tourism sites in Iraq and verifying the suitability to be the beginning of design integrated system indicators of ecotourism in Iraq to achieve sustainable tourism.

### References

1. McCool, S. F., & Bosak, K. (Eds.). (2016). *Reframing sustainable tourism*. Springer.
2. Nutsugbodo, R. Y., (2016). *Tourist Accommodation*. Tourism development in Ghana's Brong-Ahafo Region: Demand and supply dynamics, pp.73–88.
3. Bulatović, D. (2017). Ecotourism and ecotourism accommodation. *ILIRIA International Review*, 7(2), 247–260.
4. Weaver, D. B. (ed.). (2001). *The encyclopedia of ecotourism*. Cabi.
5. Mehta, H., Báez, A. L., & O'Loughlin, P. (Eds.). (2002). International ecotourism guidelines. International Ecotourism Society.
6. Black, R., & Crabtree, A. (Eds.). (2007). Quality assurance and certification in ecotourism (Vol. 5). CABI.
7. Eagles, P. F., McCool, S. F., & Haynes, C. D., (2002). Sustainable tourism in protected areas: Guidelines for planning and management (No. 8). IUCN.
8. Shu-Yang, F., Freedman, B., & Cote, R. (2004). Principles and practice of ecological design. *Environmental Reviews*, 12(2), 97–112.
9. Udomiaye, E., Okon, I., Uzodimma, O. C., & Patrick, N. (2018). Eco-friendly buildings: the architect's perspectives. Department of architectural technology, *International Journal of Civil Engineering, Construction and Estate Management*, 6, p.24.
10. Lányi, E. (2007). The basic principles of sustainable architecture. *Periodica Polytechnica Architecture*, 38(2), 79–81.
11. Carmona, M. (2009). Sustainable urban design: Principles to practice. *International Journal of Sustainable Development*, 12(1), 48–77.
12. International Finance Corporation (IFC). (2004). *Ecotourism: Exploring opportunities for sustainable business*. International Finance Corporation Washington.
13. Alho, C., & Pina, J. C., (2013). In direction to sustainable eco resorts. *Green Design, Materials and Manufacturing Processes*, p. 51.

14. Mehta, H., (2005). Planning, design and construction guidelines for desert ecolodges. Kingdom of Saudi Arabia.
15. Department of National Parks, S. a. R., (2015). *Best Practice Ecotourism Development Guidelines*.
16. International Centre for Integrated Mountain Development (ICIMOD). (2017). Guidelines for Developing Ecolodges in Myanmar. Ministry of Natural Resources and Environmental Conservation (MONREC), Myanmar, p. 36.
17. Bromberek, Z. (2009). *Eco-resorts*. Routledge.
18. Guidebook, A., 2004. Indicators of Sustainable Development for Tourism Destinations.
19. Zambrano, A. M. A., Broadbent, E. N., & Durham, W. H. (2010). Social and environmental effects of ecotourism in the Osa Peninsula of Costa Rica: The Lapa Rios case. *Journal of Ecotourism*, 9(1), 62–83.
20. VIDA. (2021). *Lapa Rios Ecolodge*. VIDA Master Planning and Design. <https://www.videsignstudio.com/project/lapa-rios-ecolodge#section-6>. Accessed 11 Mar 2021.
21. Ryan, C., & Stewart, M. (2009). Eco-tourism and luxury—the case of Al Maha. *Dubai. Journal of Sustainable Tourism*, 17(3), 287–301.
22. Susac, R., Kern, S., Pinder, A., & Daniel, G., (2008). Resource condition report for a significant western australian wetland hutt Lagoon. Inland Aquatic Integrity Resource Condition Monitoring Project, Strategic Reserve Fund, Department of Environment and Conservation, p. 35.

# Using Infrared Spectroscopy to Examine the Influences of Stabilizers on the Molecular Structure of Stabilized Contaminated Clay Soils



Khitam Abdulhussein Saeed and Sabah Hassan Fartosy

**Abstract** An experimental evaluation on artificially contaminated clay soils with different amounts of heavy metals, which were then stabilized with two types of standard additives, was carried out. To examine the effect of those additives on the contaminated soils' molecular system, vibrational (infrared) spectroscopy was employed. It is well known that contaminants in soil lead to inadequate engineering properties for contaminated soils. Thus, it can change the impact of these contaminants on clayey soil's geotechnical characteristics soils over the mechanism of chemical stabilization that produces appropriate material that is preferable for construction uses. In this study, artificial polluted clay soils were prepared and then mixed with different proportions of heavy metals like (Pb and Zn) and stabilizers like quick lime CaO and ordinary Portland cement (OPC). The changes in the structure of soil molecular because of stabilizers and heavy metals were investigated based on Fourier Transform Infrared Spectroscopy (FTIR). The obtained results allow exploring the major vibrational modes in kaolin clay soil samples in which two active bands were observed at 3696.0 and 3620.0  $\text{cm}^{-1}$ . These bands were related to the octahedral (OH) stretching vibrations and identified the kaolinite minerals. The bonding mode vibration of water-molecules (H–O–H) was discovered at 1638.0  $\text{cm}^{-1}$ . It decreased with time because of the water consumption during the cement hydration and lime dissolution due to producing pozzolanic compounds, which are responsible for improving the strength properties of contaminated soils. It was also investigated that heavy metals were at the absorbance band at 1384.0  $\text{cm}^{-1}$ . So, it can be concluded from the importance of the applied FTIR test to evaluate the effect of stabilizers on the molecular structure of contaminated clay soils.

**Keywords** Contaminated soils · Portland cement · Kaolin clay · Hydrated lime · Physico-chemical behavior

---

K. A. Saeed (✉) · S. H. Fartosy  
Department of Water Resources Engineering, Mustansiriya University, Baghdad, Iraq  
e-mail: [khitamhussein@uomustansiriyah.edu.iq](mailto:khitamhussein@uomustansiriyah.edu.iq)

S. H. Fartosy  
e-mail: [dr.sabah77@uomustansiriyah.edu.iq](mailto:dr.sabah77@uomustansiriyah.edu.iq)

## 1 Introduction

This study's background problem is preventing hazardous pollutants from damaging the environment, which is related to disposal and waste production. This pays more attention to the importance of today's heavily industrialized world [1]. Therefore, the interest toward the contaminated soils grows to encourage environmental activities that depend on responsible reusable applications and avoid expensive landfill disposal. Stabilization/solidification (S/S) is among the treatment options required to consolidate the contaminants and solid wastes by adding traditional cement-based additives, such as cement, fly-ash, etc. hydrated-lime [1–4]. The mechanism of solidification/stabilization exerts a toxic chemical waste stream to a stable insoluble form (stabilization) or captures the waste through a solid cement-based structure (solidification) [5]. Hence, the quality of binder-based solidified waste elements are controlled by this mechanism [6, 7].

Nevertheless, to understand the expected effectiveness for the alteration of specific engineering characteristics of the site's polluted soil, it is essential to observe the mechanical time-dependence and the interconnection of molecular with soil stabilizers as a function of heavy metals. Infrared spectroscopy was utilized as an alternative method to describe the clay soil's interactive influence with organic matter, commonly used in soil analysis [8]. However, it can produce unique information about the mineral structure, for example; specimen set to any group of minerals which belongs to, the consistency degree inside the matrix, the uniformity level within the matrix, the nature of isomorphous substituents, also the uniqueness of molecular water from constitutional hydroxyl, and the existence of the non-crystalline and crystalline impurities [9].

The assessment and identification of different chemical reactions involved in the stabilization process of the contaminated clayey soils are the aims of this study. Therefore, the molecular structure requires examination in the expression of local bonding to evaluate the penetration extent of the crystalline structure of heavy metals and stabilizers within clay soil and its in-between layers [3]. On the other hand, the appliance FTIR technique is necessary to examine the molecular properties of polluted soil. This technology has a great history as a complementary method of X-ray diffraction (XRD.) and other clay investigation techniques, as reported in [10].

## 2 Experimental Program and Materials

**Soil and Stabilizers.** The type of soil that was used in this research was a pure brown Kaolin with a low amount of acid. A quantity of the soil was bought from the Tapah area, located in the West of Malaysia Peninsula. The physical properties and chemical ingredients for this soil are shown in Tables 1 and 2, respectively [7].

**Table 1** Physical properties for selected brown kaolin clay soil

Physical properties	Values	Physical properties	Values
Cation exchange capacity (CEC) (meq/100)	19.2	Specific gravity	2.65
pH (L/S = 2.5)	4.34	Liquid limit, LL (%)	41
ICL (%)	2.0	Plastic limit, PL (%)	23
Max. dry density (g/cm <sup>3</sup> )	1.5	Plasticity index (PI)	18
Optimum moisture content (%)	24.3	BS Classification	CL
Unconfined compressive strength (kPa)	130	–	–

**Table 2** Chemical composition for brown kaolin clay soil

Chemical compositions oxides	SiO <sub>2</sub>	Al <sub>2</sub> O <sub>3</sub>	Fe <sub>2</sub> O <sub>3</sub>	Na <sub>2</sub> O	K <sub>2</sub> O	P <sub>2</sub> O <sub>5</sub>	SO <sub>3</sub>	CO <sub>2</sub>
Value (%)	49.5	30.31	1.02	0.79	8.78	4.03	2.05	1.4

Figure 1 shows a FESEM image of natural kaolin clay. The neatly arranged, book-like kaolinite particles are a predominant characteristic of intact soil [11], while in general, kaolin owns the edge-to-edge intermittent structure and a two-faced aggregate [12].

On the other hand, the observation of Fig. 2, depicts an energy image of dispersive X-ray spectrometer (EDAX), reveals the high level of concentrations for silicon (Si) and aluminum (Al) preceded by lower concentrations of potassium (K), iron (Fe), and magnesium (Mg) were evident, with less intensity for calcium (Ca) in natural kaolin clay. The results from Fig. 2 confirm what was previously presented in Table 2.

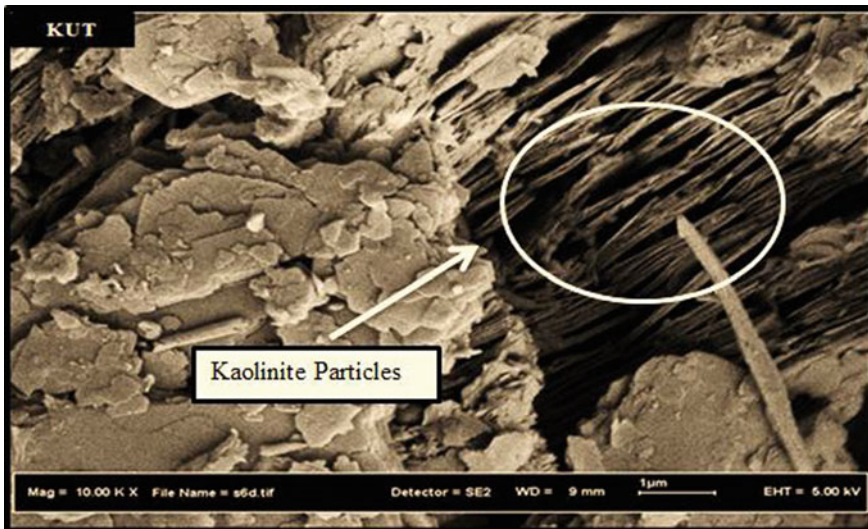


**Fig. 1** FESEM image of untreated kaolin clay soil

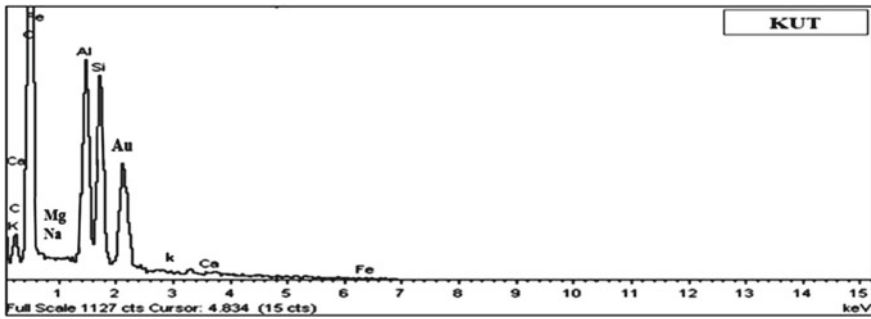


Fig. 2 EDAX spectrum of natural kaolin clay soil

To the effectiveness of the work, two kinds of traditional stabilizers were selected for comparison and detection, which are significantly more potent in treating the contaminated clay soil. The first stabilizer that used in this research was the ordinary Portland cement. It was selected because it was cost-effective, easy to obtain, and appropriate for various wastes. These factors make this type of stabilizer the most extensively used binder in the stabilization technique [13]. Cement-based stabilization produces chemical alterations that can be used for stabilization and modification applications. The second stabilizer was quick lime (calcium oxide) obtained in the form of powder brought from a lime factory located in an area known Pasir Gudang, Johor. Previous studies mentioned that lime works effectively with clayey soils, especially with soils that own plasticity index (medium to high,  $PI > 15.0$ ) [1, 7, 14]. Because of the absence of aluminates and silicates in silts and granular material pozzolanic responses, which did not occur, the lime did not interact appropriately.

Furthermore, the lime used in this study was retained in the oven under elevated temperature to prevent particles from agglomeration gradually so that the proportionate chemical composition did not change. The lime testing is implemented in compliance with the standard BS 1924.0: Part 2:1990 (Clause 5.4.60), so the lime quality is not changed. According to that standard, 5.0 g of lime was mixed with 100.0 ml distilled water free of  $CO_2$  by using a magnetic stirrer for a period (1) hour. Then, it had been placed on the suspension for 24 h in an airtight container. Its pH value should be at  $25^\circ C$  based on the following formula:

$$pH_{25^\circ C} = pH_T + 0.03(T - 25) \quad (1)$$

This test was repeated no less than three times until obtaining the average  $pH_{25.0}$  value of 12.40, that compliance with the range of 12.35–12.45 that specified in the standard. However, it is necessary to mention that cement is preferable to lime with granular material and silt [15]. According to ACI 230.1R-90 1990: cement is suitable for all types of soils, and it is preferable to stabilize any soil, except for soils contain organic content of greater than 2%. The chemical composition of Portland cement and lime is shown in Table 3.



**Table 3** Chemical composition for the Portland and quick lime

Quick lime (CaO)		Ordinary Portland cement (OPC)	
Chemical composition	Values (%)	Chemical composition	Values (%)
Calcium oxide, CaO	74.23	Calcium oxide, CaO	64.73
Phosphorus oxide, P <sub>2</sub> O <sub>5</sub>	0.08	Potassium oxide (K <sub>2</sub> O)	0.57
Magnesium oxide, MgO	0.74	Magnesium oxide, MgO	1.1
Calcium sulfate, CaSO <sub>4</sub>	0.12	Sulfur trioxide, SO <sub>3</sub>	2.01
Ferric oxide, Fe <sub>2</sub> O <sub>3</sub>	0.17	Ferric oxide, Fe <sub>2</sub> O <sub>3</sub>	3.1
Aluminum oxide	0.11	Aluminum oxide	5.2
Al <sub>2</sub> O <sub>3</sub> silica, SiO <sub>2</sub>	0.14	Al <sub>2</sub> O <sub>3</sub> silica, SiO <sub>2</sub>	21.1
Loss on ignition, LOI	24.35	Loss on ignition, LOI	0.8

The reactions of stabilizer ions in the short and long-term depending on the concentration of the stabilizer. Therefore, the stabilizer content has a significant effect on the initial cementation and alteration of the treated specimens related to the reactions that occur in the (short – long) term. Furthermore, to simulate the real field conditions, it is imperative to mix reasonable quantities of cement and lime to all design mixtures. This study compares the reaction between soil and heavy metals using two types of stabilizers. It reduces the cost of high stabilizer content, the same content for minimum and maximum concentrations for lime and cement that has been used. This research was implemented on synthetic polluted soils, which are prepared under laboratory conditions and containing 5% based on the dry soil weight for both lead (Pb<sup>+2.0</sup>), and zinc (Zn<sup>+2.0</sup>) (based on the dry soil weight. The purpose of adding these reagents was to simulate the contamination of non-organic metal, and they were selected because of their prevalence in many polluted areas [16].

**Preparation of Samples.** Under air-dried conditions which satisfied using the oven, the soil specimens were prepared. This drying condition can remarkably change soil compaction and plasticity properties, as reported in [17]. Similar amounts of cement and lime mixture (10%) were percentages based on the dry soil weight. It is necessary to mention that the synthetic soil specimens mixed with heavy metals were prepared by adding lead nitrate (Pb(NO<sub>3</sub>)<sub>2</sub>) and zinc nitrate (Zn(NO<sub>3</sub>)<sub>2</sub>) to emulate contaminant sources in intact brown kaolin clay. Furthermore, the prepared contaminated soil samples were compacted in 38.0 × 76.0 mm molds with a cylindrical cross-section. The procedure of preparation was implemented in compliance with clause 4.1.50 of BS 1924: Part 2: 1990b to obtain the designated maximum dry density and optimum water content. After curing the sample for two hours, then extracted from the mold, placed in a thin-walled PVC tube, a thin-plastic cover was used to wrap the sample, and finally, the sample was sealed using tight rubber-lids. Later, the specimens were placed in a room with a controlled temperature (27.0 ± 2 °C) for curing till conducting all experiments after a period of (7, 100, and 200 days).



**Fig. 3** Perkin Elmer spectrum 2000 instrument (FTIR)-UTM-FS-Skudi-Johor-Malaysia

### 3 Testing Program

The research project depends on the FTIR technique used to investigate the changes related to the intact specimens' molecular structure and treated with contamination. The amount of soil that dried in the oven (2 mg) was blended with 200.0 mg of potassium bromide (KBR) to obtain a homogeneous powder, then compacted into a hard disk (solid pellet) [3]. This diaphanous KBR solid pellet was then placed in a specimen holder and scanned using a Perkin Elmer Spectrum 2000 appliance to yield a beam mode moved transferred inside the  $400.0\text{--}4000.0\text{ cm}^{-1}$  specimen, Fig. 3.

### 4 Results and Discussion

The effect of two selected stabilizers on the molecular structure of the intact soil specimens and specimens treated with contamination was investigated using Infrared spectroscopy. Typical FTIR spectra of intact Brown Kaolin clayey soil near ( $400.0\text{--}4000.0\text{ cm}^{-1}$ ) are shown in Fig. 4. Two active bands near  $3696.0$  and  $3620.0\text{ cm}^{-1}$  were identified as kaolinite related to octahedral stretch vibrations from (OH). Further, sharp bands were also noticed near  $1115.0$ ,  $1031.0$  and  $1007.0\text{ cm}^{-1}$  which can be related to Si–O stretching.

The band at  $912.0\text{ cm}^{-1}$  was attributed to the deformation of OH that belongs to the hydroxyl groups. Most of the other bands, for example, the vibrations of Si–O

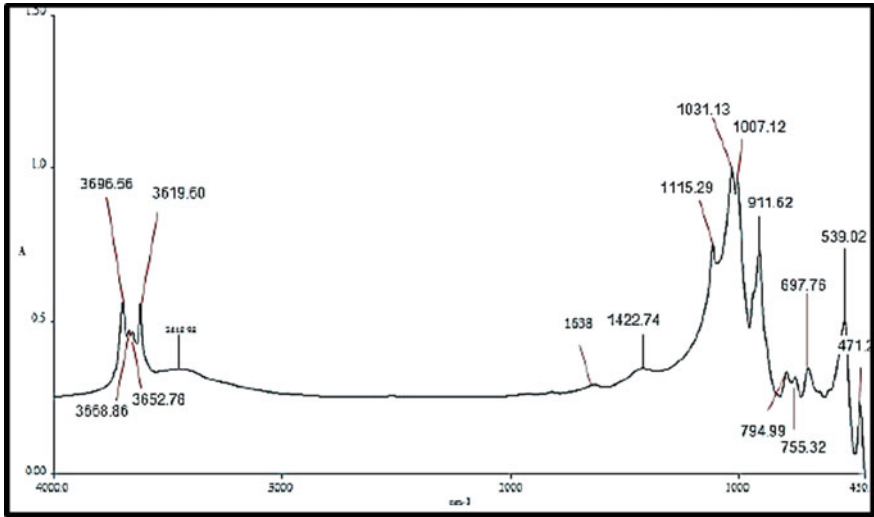


Fig. 4 FTIR spectra of intact brown kaolin clayey soil

were noticed near 794.0, 698.0, 540.0 and 470.0  $\text{cm}^{-1}$  also approved the presence of kaolinite, and another small band at 1422.0  $\text{cm}^{-1}$  highlighted the existence of calcite, while bands near 1638.0  $\text{cm}^{-1}$  pointed out the bonding vibrations of water-molecules (H-O-H). Figure 5 presents spectra of FTIR in natural vs. cement treated

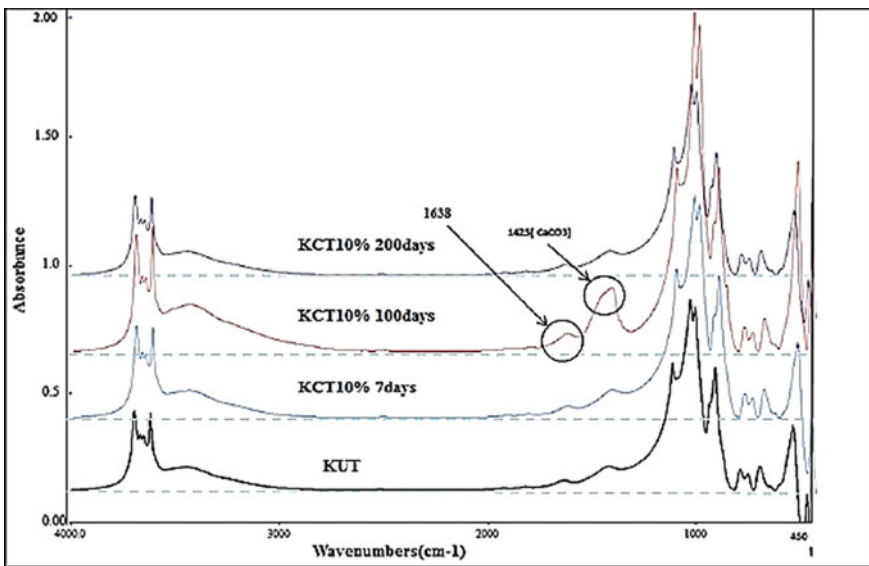
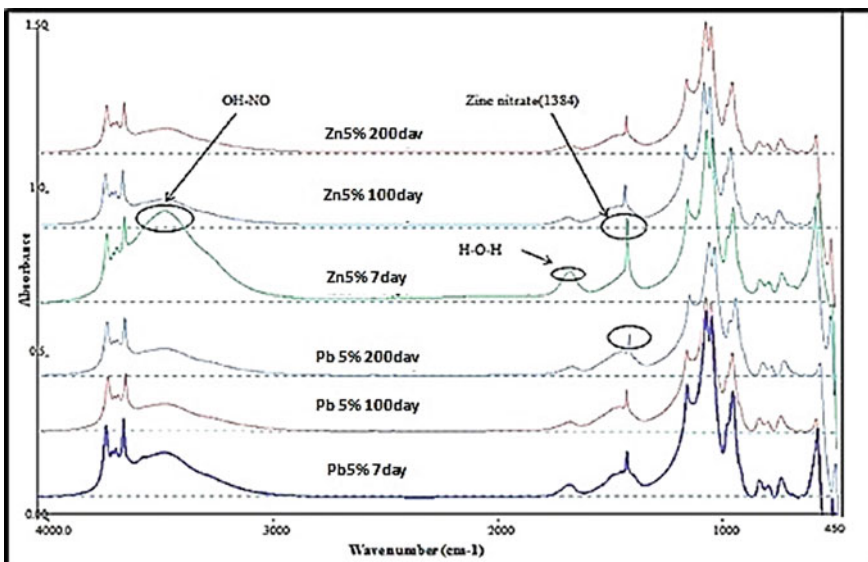


Fig. 5 FTIR spectrums of natural and cement treated kaolin clay at different time intervals

with Kaolin clay soils at different curing periods. Remarkable alterations happened in FTIR spectra for cement-treated cured Kaolin samples at one hundred days because of the increase in Si–O intensity, which is stretching at  $1031$  and  $1007\text{ cm}^{-1}$ , respectively. These may have been related to the initiation of cement hydration and the development of primary cementitious compounds, which, in turn, increased polymerized Si–O units. As indicated previously by XRD, Portland was the primary source of hydration compounds during this stage of curing.

Furthermore, the significantly increased absorption at  $1425\text{ cm}^{-1}$  and shift to higher energy was attributable to calcite, which then dropped remarkably by 200 days. The decrease was likely because of the development of the non-crystalline compound, Calcium Aluminum Oxide Carbonate Hydrate, which negatively influences the molecular structure of cured specimens, as shown in Fig. 5. Therefore, the observed decrease in FTIR spectra intensity peaks at this stage of curing; likely may attribute to the reduction of inter-layered water-molecules (H–O–H) being consumed due to the progress hydration process of cement.

Figure 6 shows spectra of FTIR from both lead and zinc contaminated cement-Kaolin cured samples. This figure reveals decreasing in intensity at  $1031$  and  $1007\text{ cm}^{-1}$ , V4 and V1; all of which reflected possible reactions of lead and zinc ions added to the cement-treated soil of reactions or adsorption of these metals that impact the polymerization phenomena of silicates. The intensity of band  $3445\text{ cm}^{-1}$  was attributed apparently to the agent OH-nitrates that increased after the addition of metallic nitrates. This decrease progressed as metallic nitrates reacted with hydroxides during cement hydration to produce new compounds, which, in turn, influenced



**Fig. 6** FTIR spectrums of lead and zinc added to the cement-treated Kaolin Clay at various time intervals

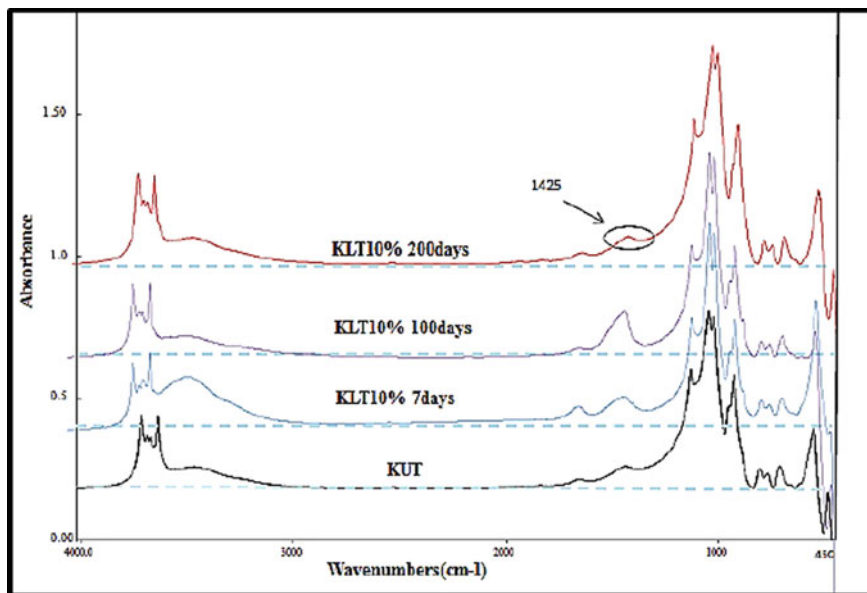
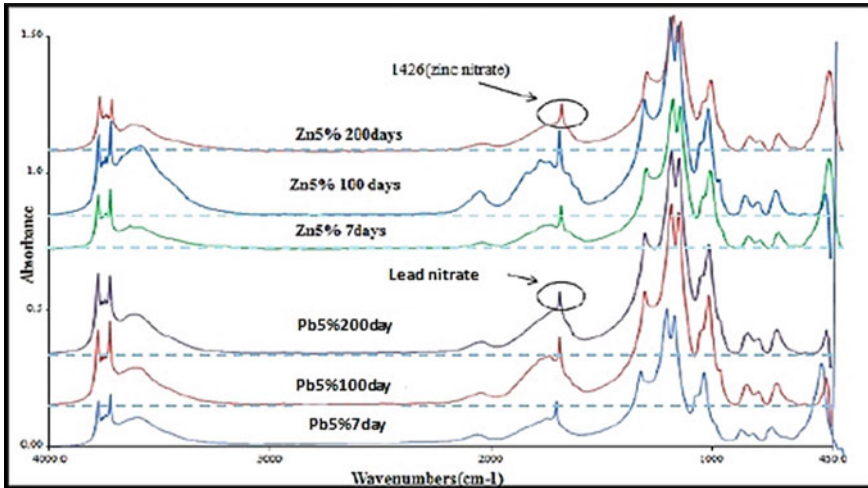


Fig. 7 FTIR spectrums of natural and lime treated kaolin clay at different various intervals

cement hydration, as stated previously. Over time, decreased intensity of lead–zinc nitrates confirmed heavy metal reactions within the cement–soil matrix that produced the new compounds observed earlier by XRD.

Also, FTIR spectroscopy was implemented on Kaolin clay specimens treated with lime, as appeared in Fig. 7. FTIR spectra were not shown any significant changes for lime in comparison to soil samples treated with cement. Nevertheless, the rise in absorption intensity at band  $1425\text{ cm}^{-1}$  is related to improving calcium sources provided by lime. Moreover, the stretching of Si–O causes a trivial increase in their intensities beyond the polymerization that progresses. Figure 8 illustrates molecular structures of interactions with lead and zinc within a lime-treated Kaolin matrix compared to FTIR spectra of the cement-treated matrix. Only minor differences, especially with zinc, were observed. As shown in Fig. 8, compared to treated uncontaminated samples, more significant percentages of decreasing Si–O intensity are observed in lime-treated samples than in cement-treated samples, especially with zinc. Otherwise, no significant alteration of functional groups in contaminated samples was noticed except for metallic nitrates' appearance for both lead and zinc at wave number  $1426\text{ cm}^{-1}$ .



**Fig. 8** FTIR spectrums of lead and zinc doped with lime treated Kaolin Clay at various time intervals

## 5 Conclusions

The mechanism of additives (cement and lime) used to treat contaminated clay soil achieved in current research depends primarily on the physico-chemical behaviors of treated-contaminated soils regarding a detailed analysis of their molecular characterizations. The molecular studies by Fourier Transform Infrared Spectroscopy (FTIR) on both lime and cement treated brown kaolin clay samples were revealed the following results. Two strong bands were observed near  $3696.0$  and  $3620.0\text{ cm}^{-1}$ , referred to the octahedral OH stretching vibrations; these bands identified the kaolinite minerals. In addition, other bands appeared because of the quartz and hematite existence.

- The existence of calcite was observed at the vibrational band at  $1422\text{ cm}^{-1}$ .
- The bonding mode vibration of water-molecules (H–O–H) was noticed near  $1638.0\text{ cm}^{-1}$ . It decreased with time because of water consumption through the hydration of cement and the dissolution of lime.
- The lead and zinc nitrates existences were investigated at the absorbance band at  $1384\text{ cm}^{-1}$ .

## References

1. Saeed, K. A., Kassim, K. A., Nur, H., & Yunus, N. Z. M. (2015). Strength of lime-cement stabilized tropical lateritic clay contaminated by heavy metals. *KSCE Journal of Civil Engineering*, 19(4), 887–892.

2. Conner, J. R. (1990). *Chemical fixation and solidification of hazardous wastes* (p. 692). Van Nostrand Reinhold.
3. Dermatas, D., & Meng, X. (2003). Utilization of fly ash for stabilization/solidification of heavy metal contaminated soils. *Engineering Geology*, 70(3–4), 377–394.
4. Arbili, M. M., Karpuzcu, M., & Khalil, F. (2020). Effect of slag on engineering properties of contaminated soil. In *Key engineering materials* (Vol. 857, pp. 253–258). Trans Tech Publications Ltd.
5. Wiles, C. C. (1987). A review of solidification/stabilization technology. *Journal of hazardous materials*, 14(1), 5–21.
6. Asavapisit, S., Naksrichum, S., & Harnwajanawong, N. (2005). Strength, leachability and microstructure characteristics of cement-based solidified plating sludge. *Cement and Concrete Research*, 35(6), 1042–1049.
7. Saeed, K. A. H., Kassim, K. A., Yunus, N. Z. M., & Nur, H. (2015). Physico-chemical characterization of lime stabilized tropical kaolin clay. *Jurnal Teknologi*, 72(3).
8. McCarty, G. W., & Reeves, J. B. (2006). Comparison of near infrared and mid infrared diffuse reflectance spectroscopy for field-scale measurement of soil fertility parameters. *Soil Science*, 171(2), 94–102.
9. Farmer, V. C. (1979). *Infrared spectroscopy: Data handbook for clay materials and other non-metallic minerals*. Pergamon Press.
10. McKelvy, M. L., Britt, T. R., Davis, B. L., Gillie, J. K., Lentz, L. A., Leugers, A., Nyquist, R. A., & Putzig, C. L. (1996). Infrared spectroscopy. *Analytical Chemistry*, 68(12), 93–160.
11. Mitchell, J. K., & Soga, K. (2005). *Fundamentals of soil behavior* (Vol. 3). John Wiley & Sons.
12. Lee, K. H., & Lee, S. (2002). Mechanical properties of weakly bonded cement stabilized kaolin. *KSCE Journal of Civil Engineering*, 6(4), 389–398.
13. U. S. Environmental Protection Agency (USEPA). (2004). Treatment technologies for site cleanup: Annual status report. 11th E., EPA542-R-03–009, Adapted from <http://www.epa.gov/>.
14. Saeed, K. A., Kassi, K. A., Nur, H., & Al-Hashimi, S.A.M. (2020). Molecular characteristics of cement-lime treated contaminated-lateritic clay soil. In *IOP Conference Series: Materials Science and Engineering* (Vol. 870, No. 1, p. 012082). IOP Publishing.
15. Chew, S. H., Kamruzzaman, A. H. M., & Lee, F. H. (2004). Physicochemical and engineering behavior of cement treated clays. *Journal of Geotechnical and Geoenvironmental Engineering*, 130(7), 696–706.
16. Saeed, K. A., & Hashim, S. A. (2020). The morphology and elemental variation for contaminated clay soil using energy dispersive X-ray spectrometry. In *IOP Conference Series: Materials Science and Engineering* (Vol. 737, No. 1, p. 012082). IOP Publishing.
17. Goswami, R. K., & Mahanta, C. (2007). Leaching characteristics of residual lateritic soils stabilised with fly ash and lime for geotechnical applications. *Waste Management*, 27(4), 466–481.

# Spatial Analysis of Archaeological and Heritage Sites Using Geographic Information System Techniques: A Case Study of Wasit Province, Iraq



Ali Hussein Alwan and Hussein Sabah Jaber

**Abstract** Wasit province contains more than 500 archaeological and heritage sites within its administrative boundaries, reflecting the long history of various cultural ages. Analysis of archaeological and heritage site patterns is critical for archaeologists to detect past human activities. This study aims to clarify the importance of using geographic information system (GIS) techniques in the spatial statistical analysis of archaeological and heritage sites in the study area. GIS tools and methods were used to create a geo-archaeology database based on archaeological surveys recorded in the antiquities and heritage inspectorate of Wasit. Spatial statistical analysis was applied to reveal the spatial patterns of archaeological sites. The results of the analyses of the average nearest neighbor and multi-distance spatial cluster showed that the sites have a cluster pattern. The central feature analysis also showed that Tal Samar in the Nu'maniyah district is the most located. The results of the directional distribution indicate the spread of most of the archaeological and heritage sites in the northwest and southeast. It also found that 301 sites are within a standard distance of 63,414.82 m. Analysis of hot and cold spots showed that the sites were densely clustered in the northwest and included 171 sites. The area of hot spots reached 1563.30 km<sup>2</sup> and constitutes 8.74% of the area of Wasit province. Spatial analysis using GIS has also been shown to provide quantitative ways in which the pattern of distribution of historical and heritage features can be understood. This study recommends using spatial statistical analysis to discover the spatial relationships of archaeological and heritage sites since this method can clarify a wide variety of theoretical and functional foundations of archaeology's behaviors.

**Keywords** Spatial statistical · Hot and cold spots · ANN · GIS · Antiquities and historical sites · Kut city

---

A. H. Alwan (✉)

Kut Technical Institute, Middle Technical University, Kut, Iraq

H. S. Jaber

Surveying Engineering Department, University of Baghdad, Baghdad, Iraq



## 1 Introduction

The significance of the spatial aspect of the archaeological record has long been known to archaeologists. Many, if not all, data that archaeologists recover are spatial contain an important spatial component. Large quantities of spatial data, varying in size from the relative positions of archaeological sites on a continental landmass to the locations of individual objects in unearthened contexts, are routinely dealt with in archaeology [1]. In essence, we see official spatial analysis not as a means of producing complete archaeological explanations but as an extension of our monitoring equipment. Although the human mind is a good explanatory tool, if presented with a series of random points, it tends to suggest patterns even if they do not exist. However, it also means that we can't rely entirely on our eyes and minds to give us an unbiased explanation of the things that show spatial embossing, and here quantum measurement can be a great help for us [1]. GIS has become an effective tool for archaeologists to organize, interpret and analyze spatial data [2]. Archaeological evidence can provide an opportunity to analyze past regional activity and record our cultural complexities through the use of spatial analysis [2, 3].

Through methodical analysis of antiquities proof, the regional singularity may lead to a greater understanding of how to direct the duty sector to provide a utility for the use of cultural heritage in related economies like tourism and to ensure that antiquities are protected and remain an intangible value for coming generations [3, 4]. The use of spatial technology in the sense of detecting urban footprint patterns about the regional dimension of land use planning is the starting point for knowing cultural heritage at the regional level [3, 5]. Analysis of patterns within site is crucial for archaeologists to detect previous human activities and, as a result, previous human behavior. It can also be used to describe how sites are formed and how they are formed after they have been sediment [6]. The primary goal of spatial analysis is to define the spatial structure inherent in the distribution of a specific point (these objects, environmental practices, or structures) to make inferences about the specific behavior that resulted in the observed pattern. The major fields of research for planning, forecasting, and measuring spatial patterns are spatial and geographical statistics [7–9].

The most recent advances in spatial statistics have resulted in several powerful tools for obtaining as much information as possible from a set of organized data. The three most important aspects of spatial statistics are spatial structure clarification, the analysis of clustering, and spatial change inspection. These three factors are related to the impact of the influence of point pattern analytical techniques, which are a collection of methods that focus on identifying key structural properties of a point process. Spatial statistical analysis and geographical statistics are two powerful tools that archaeologists have used to analyze remains of previous human activities and explain the behavior that gave birth to them [8, 10]. The use of point pattern analysis to describe, interpret, and analyze the spatial distribution of archaeological phenomena is seen as a valuable tool. In terms of the distribution of the site and the pattern of settlement, an analysis of the archaeological style of settlement is a remarkable method. In the application of analytical methods such as GIS in archaeology, this

approach has taken a special position at both the conceptual and functional levels [11]. Based on the literature review, a spatial statistical analysis of archaeological and heritage sites in the study area has not yet been studied. The objective of this study is to use spatial statistical analysis techniques to analyze the spatiality of antiquity and heritage sites.

## 2 Study Area

Wasit province is located in the eastern part of the central region of Iraq, between (31° 52'–33° 36') N latitude and (44° 30'–46° 40') E longitude as shown in Fig. 1. It has borders with many provinces, including Baghdad, Diyala, Babil, Al-Qadisiyah, Dhi Qar, and Maysan. It borders Iran state to the east. Wasit province has good natural resources, such as water and oil. Farming and trade are other important parts of its economy. Al-Kut city is the center of Wasit governorate, which lies on the River Tigris. Wasit governorate covers an area of 17889 km<sup>2</sup> and constitutes 4% of the area of Iraq. It is classified as a coastal area with a climate that is intermediate between the Mediterranean and hot and dry desert climates, with low rainfall and high temperatures [12, 13]. Water is one of the most important natural resources as it directly affects the formation of most of the components of life, and water is a necessary element for the emergence and growth of life and its development

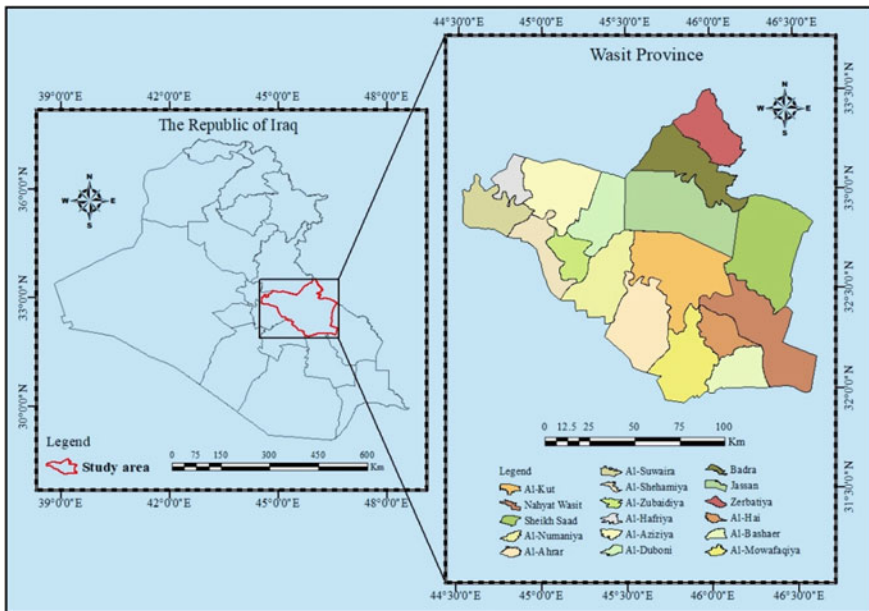


Fig. 1 Location map of the study area

on the earth. Therefore, the existence of the human race is linked to a large extent to the sources of water and that the majority of civilizations in dry and semi-arid regions have arisen around water sources and riverbanks [14–16]. The civilizations of Mesopotamia, which depended on irrigation agriculture and exploiting the waters of the Tigris and Euphrates rivers, are considered a model for that. Wasit Governorate is part of the sedimentary plain, so the governorate has a large share of the cultural legacy left by these civilizations. Wasit Governorate has more than 500 archaeological and heritage sites that date back to different roles, stretching from the ancient Stone Age until the Islamic ages. The first archaeological discovery in this province was found in 1935. Some of these sites are located above the ground, some are in the form of large or small hills, and some are buried under the ground. The height of any archaeological site means the continued residence in it for a long time and several roles of civilization [14, 17].

### 3 Materials and Methods

**Materials.** Archaeological data (non-spatial data) was provided by the Inspectorate of antiquities and Wasit heritage. Cadastro maps (raster) at a scale of 1:10,000 were provided scanned and corrected by the Wasit Agriculture Directorate, which covers the study area to extract the coordinates (X, Y) of archaeological sites. Archaeological data and its coordinates were entered into an excel table and imported into GIS to create a point feature. Shapefiles (vector) of the study area were provided by the GIS Department of Wasit Provincial Council.

**Methods.** This study used GIS tools and methods to create a geo-archaeology database. A good and structured database has been built that facilitates sustainable management and investigation of archaeological and heritage sites based on archaeological surveys recorded in the Antiquities and Heritage Inspectorate of Wasit. It is important to construct a geo-archaeology database of all archaeological and heritage sites, as well as focus on the digital system by developing digital maps with databases. ArcGIS for desktop software version 10.8 was used to perform spatial statistical analyses and GIS data processors. GIS tools aid in the compilation, preservation, processing, customization, and eventually, visual presentation of data so that the user can understand it. This study's methodology is depicted in a flowchart Fig. 2.

**Average Nearest Neighbor.** The ANN tool calculates the space between each attribute's centroid and the centroid location of its closest neighbor. It then takes the average of all of the spaces that are close neighbors. The distribution of the attributes being evaluated is called clustered if the average space is less than the average for an assumed random distribution. The attributes are called distributed if the average space exceeds an expected random distribution [18, 19]. The average closest neighbor ratio is calculated as follows [19]:

$$\text{ANN} = \frac{\bar{D}_O}{\bar{D}_E} \quad (1)$$

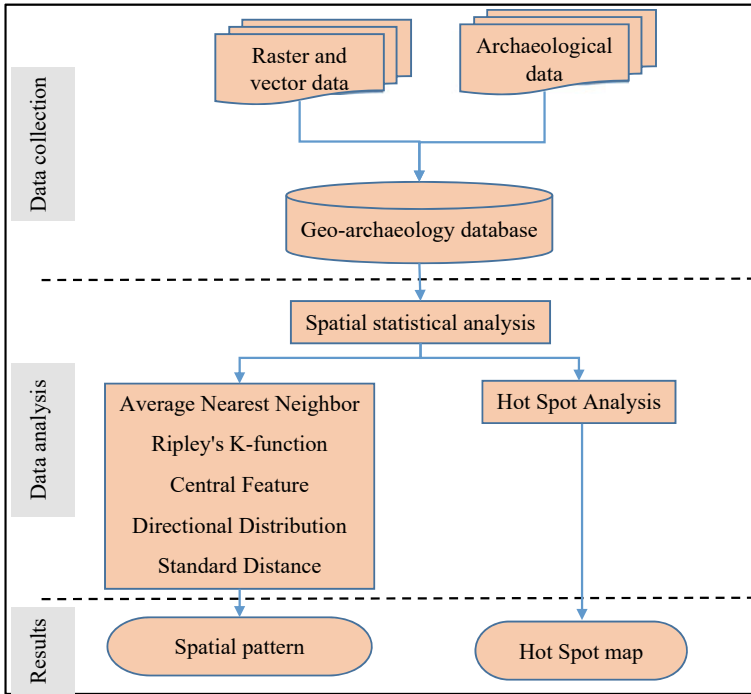


Fig. 2 Methodology flowchart depicted for the study

where  $\bar{D}_O$  denotes the observed mean space between each attribute and its close neighbor:

$$\bar{D}_O = \frac{\sum_{i=1}^n d_i}{n} \tag{2}$$

and  $\bar{D}_E$  denotes the expectant mean space for the attribute certain in a random pattern:

$$\bar{D}_E = \frac{0.5}{\sqrt{n/A}} \tag{3}$$

where  $d_i$  denotes the space between attribute  $i$  and its closest neighbor attribute,  $n$  denotes the overall number of attributes, and  $A$  denotes the area of a minimal surrounding rectangle across all attributes or a user-specified area value. The statistic's average z-score is estimated as follows [19]:

$$z = \frac{\bar{D}_O - \bar{D}_E}{SE} \tag{4}$$

where

$$SE = \frac{0.26136}{\sqrt{n^2/A}} \tag{5}$$

**Multi-Distance Spatial Cluster Analysis.** Another method for analyzing the spatial pattern of data from incident points is based on Ripley’s K-function. This method differs from others in that it sums up spatial dependency (attribute clustering or attribute dispersion) over a range of distances [18, 20]. The K-Function is defined as follows [20]:

$$L(d) = \sqrt{\frac{A \sum_{i=1}^n \sum_{j=1, j \neq i}^n K_{i,j}}{\pi n(n-1)}} \tag{6}$$

where: d denotes the space, n denotes the overall number of attributes, A denotes the total region of the attributes, and  $K_{i,j}$  denotes the weight. If no edge correction is applied, the weight will be one of the spaces between i and j is less than d and zero otherwise.  $K_{i,j}$  will be slightly modified if a given edge correction method is used.

**Central Feature.** The most central attribute identification tool in the attribute class (point, line, and polygon). Spaces from each attribute to each other attribute in the data set are calculated and collected. The attribute associated with the shortest cumulative space is then selected to all other attributes and copied to the newly created output attribute category [21, 22].

**Directional Distribution.** Separately calculating the standard space in the x and y directions is a popular method for measuring the direction for a collection of points or areas. These two scales delimit the axes of the ellipse that encompass the distribution of the attributes. An ellipse is denoted as a standard ellipse because the way measures the standard deviation of the x-coordinates and the y-coordinates from the average center to determine the ellipse’s axes [21, 23]. The standard deviational ellipse is calculated as follows [23]:

$$C = \begin{pmatrix} \text{var}(x) & \text{cov}(x,y) \\ \text{cov}(y,x) & \text{var}(y) \end{pmatrix} = \frac{1}{n} \begin{pmatrix} \sum_{i=1}^n \tilde{x}_i^2 & \sum_{i=1}^n \tilde{x}_i \tilde{y}_i \\ \sum_{i=1}^n \tilde{x}_i \tilde{y}_i & \sum_{i=1}^n \tilde{y}_i^2 \end{pmatrix} \tag{7}$$

where

$$\text{var}(x) = \frac{1}{n} \sum_{i=1}^n (x_i - \bar{x})^2 = \frac{1}{n} \sum_{i=1}^n \tilde{x}_i^2 \tag{8}$$

$$\text{cov}(x,y) = \frac{1}{n} \sum_{i=1}^n (x_i - \bar{x})(y_i - \bar{y}) = \frac{1}{n} \sum_{i=1}^n \tilde{x}_i \tilde{y}_i \tag{9}$$

$$\text{var}(y) = \frac{1}{n} \sum_{i=1}^n (y_i - \bar{y})^2 = \frac{1}{n} \sum_{i=1}^n \tilde{y}_i^2 \tag{10}$$

Where: x and y denotes the coordinates for attribute i,  $\{\bar{x}, \bar{y}\}$  denotes the average center for the attributes and n denotes the overall number of attributes. The variable matrix model is analyzed into a criterion that matrix's results being described by its eigenvalues and eigenvectors. The standard deviations for the x-axis and y-axis then [23]:

$$\sigma_{1,2} = \left( \frac{(\sum_{i=1}^n \check{x}_i^2 + \sum_{i=1}^n \check{y}_i^2) \pm \sqrt{(\sum_{i=1}^n \check{x}_i^2 - \sum_{i=1}^n \check{y}_i^2)^2 + 4(\sum_{i=1}^n \check{x}_i \check{y}_i)^2}}{2n} \right)^{1/2} \tag{11}$$

**Standard Distance.** The distribution compression measurement provides one value that represents the dispersal of the attributes about the middle. The value is a distance, so the compression of a group of attributes on the map can be described by sketch a circle with a radius same as the standard distance value. The standard distance tool makes a circular polygon. Measures the degree to which elements are concentrated or dispersed about the center of the geometric mean [21, 24]. The standard distance is given as [24]:

$$\text{SD} = \sqrt{\frac{\sum_{i=1}^n (x_i - \bar{X})^2}{n} + \frac{\sum_{i=1}^n (y_i - \bar{Y})^2}{n} + \frac{\sum_{i=1}^n (z_i - \bar{Z})^2}{n}} \tag{12}$$

where  $x_i, y_i,$  and  $z_i$  denotes the coordinates for attribute i,  $\{\bar{x}, \bar{y}, \bar{z}\}$  denotes the average center for the attributes, and n denotes the overall number of attributes. The weighted space extends to the following [24]:

$$\text{SD}_w = \sqrt{\frac{\sum_{i=1}^n w_i (x_i - \bar{X}_w)^2}{\sum_{i=1}^n w_i} + \frac{\sum_{i=1}^n w_i (y_i - \bar{Y}_w)^2}{\sum_{i=1}^n w_i} + \frac{\sum_{i=1}^n w_i (z_i - \bar{Z}_w)^2}{\sum_{i=1}^n w_i}} \tag{13}$$

where:  $w_i$  denotes the weight at attribute i and  $\{x_w, y_w, z_w\}$  denotes the weighted average center.

**Hot Spot Analysis.** The hot spot analysis method computes the Getis-Ord  $G_i^*$  statistic to every attribute in a set of data. This tool examines each attribute of its surroundings. A high-value attribute is fascinating, but it might or might not be a statistically important hot spot. An attribute should have a high-value and be surrounded by other attributes with high-values to be statistically important. The local sum of the attribute and its neighbors are comparison in proportion to the overall

number of attributes; When the local total is very dissimilar from the expected local total, and when this variance is too high to be the result of random opportunity, a statistically significant z-score results [25, 26]. The Getis-Ord local statistic is calculated as follows [27, 28]:

$$G_i^* = \frac{\sum_{j=1}^n w_{ij}x_j - \bar{X} \sum_{j=1}^n w_{ij}}{S \sqrt{\frac{[n \sum_{j=1}^n w_{ij}^2 - (\sum_{j=1}^n w_{ij})^2]}{n-1}}} \quad (14)$$

where  $x_j$  denotes the attribute value for attribute  $j$ ,  $w_{ij}$  denotes the spatial weight between attribute  $i$  and  $j$ ,  $n$  denotes the overall number of attributes [27, 28]:

$$\bar{X} = \frac{\sum_{j=1}^n x_j}{n} \quad (15)$$

$$S = \sqrt{\frac{\sum_{j=1}^n x_j^2}{n} - (\bar{X})^2} \quad (16)$$

## 4 Results and Discussion

GIS tools and methods were used to create a geo-archaeology database for more than 500 sites in this study. Based on archaeological surveys recorded in the Antiquities and Heritage Inspectorate of Wasit, a good and structured database has been built that facilitates sustainable management and investigation of archaeological and heritage sites. Next, spatial statistical analysis was applied to reveal the spatial patterns of archaeological sites. According to the results of ANN analysis that were acquired for archaeological and heritage sites revealed that the pattern of the geographical distribution of sites is clustered pattern. The z-score of  $-14.27$  denotes that the likelihood of this clustered pattern being the product of random opportunity is less than 1%, as shown in Fig. 3a. This method helps to distinguish the spatial distribution pattern of sites over a wide area. While, the results of Ripley's K-Function analysis confirm that point patterns are clustered at distances from 8977.952 m to 37940.274 m, dispersed patterns at distances from 37940.274 m to 45912.659 m Fig. 3b. Ripley's K function analysis allows for more comprehensive interpretations of the distribution of sites at varying distances.

The analysis of the central feature also showed that Tell Samar in Al-Numaniya district is the most centrally located Fig. 4a. The results of the directional distribution indicate that the spread of the most archaeological and heritage sites in the northwest and southeast Fig. 4a. The standard distance measurement also displayed that 301 sites are located at a standard distance of 63414.82 m Fig. 4b.

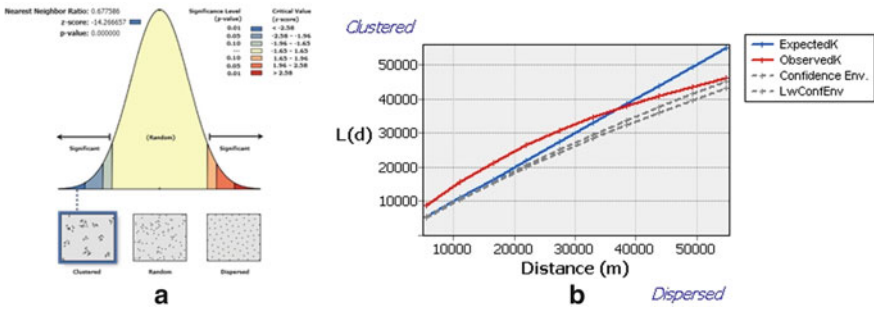


Fig. 3 a The result of ANN analysis; b The result of Ripley's K-Function analysis

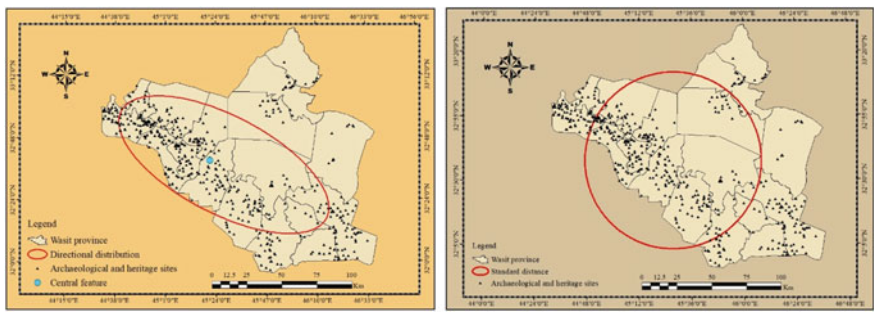
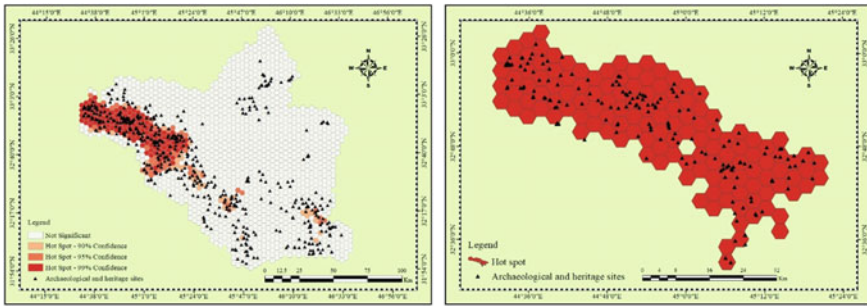


Fig. 4 a The results of central feature and directional distribution analysis; b The result of standard distance analysis

Therefore, all previous spatial analyses indicate that all archaeological and heritage sites are highly organized and assembled. It also confirms that many sites have physical evidence between antiquities from different eras. This increases the need to clarify careful planning for archaeological site protection in a multi-dimensional framework of physical evidence. According to the analysis of hot and cold spots, all hot spots are densely clustered in the northwest, and 171 sites are located in hot spots (Fig. 5a). The area of hot spots reached 1563.30 km<sup>2</sup> and constituted 8.74% of the area of Wasit province (Fig. 5b). This method highlighted sites with large spatial clusters. As a result, the use of spatial statistical analysis methods will greatly influence the archaeological interpretation of settlement distributions. It also provides the missing link between specific human actions and what remains of those actions on earth.





**Fig. 5** a The result of hot spot analysis; b hot spots are clustered in the northwest

## 5 Conclusions

The spatial statistical analysis gives a comprehensive view of ancient behavior and spatial distribution of archaeological and heritage sites. Spatial pattern analysis is a method of describing spatial patterns, and ANN analysis provides a useful way to determine the generalization sought about the distribution of archaeological and heritage sites. Spatial analysis using GIS has also been shown to provide quantitative ways in which the pattern of distribution of historical and heritage monuments can be understood. This study concludes that spatial concentrations of archaeological sites are expected for at least two main reasons: land finesse and cultural, social, and economic aspects. Land finesse can be associated with many important features of the housing area, such as the environmental characteristics of the land, height, slope, soil structure, availability, and continuity of food and water sources. The analytical results of the distribution patterns used in this study can show sufficient capacity to study the spatial characterizations of settlements from different periods in Wasit province. Since this approach will explain a wide range of theoretical and practical foundations of archaeology's behaviors, it is recommended to use spatial statistical analysis to discover the spatial relationships of archaeological and heritage sites.

**Acknowledgements** The authors appreciate the facilities provided by the Wasit Provincial Council's GIS Department, the Wasit Agriculture Directorate, and the Inspectorate of Antiquities and Wasit Heritage.

## References

1. Wheatley, D., & Gillings, M. (2002). *Spatial technology and archaeology: The archaeological applications of GIS*. CRC Press, London and New York.
2. Verhagen, P. (2018) Spatial analysis in archaeology: Moving into New Territories. In: Siart, C., Forbriger, M., Bubbenzer, O. (Eds.). *Digital Geoarchaeology: New Techniques for Interdisciplinary Human-Environmental Research* (pp. 11–25). Springer International Publishing. [https://doi.org/10.1007/978-3-319-25316-9\\_2](https://doi.org/10.1007/978-3-319-25316-9_2)

3. Vaz, E. (2020). Archaeological sites in small towns-A sustainability assessment of Northumberland county. *Sustainability*, 12, 1–13. <https://doi.org/10.3390/su12052018>
4. González Álvarez, D. (2018). Rethinking tourism narratives on the cultural landscapes of Asturias (Northern Spain) from the perspective of Landscape Archaeology: do archaeologists have anything to say?. *Landscape Research* 44, 117–133. <https://doi.org/10.1080/01426397.2017.1413174>
5. Vaz, E., Taubenböck, H., Kotha, M., & Arsanjani, J. J. (2017). Urban change in Goa, India. *Habitat International*, 68, 24–29. <https://doi.org/10.1016/j.habitatint.2017.07.010>
6. Driscoll, K., Alcaina, J., Égüez, N., Mangado, X., Fullola, J. M., & Tejero, J. M. (2015). Trampled under foot: A quartz and chert human trampling experiment at the Cova del Parco rock shelter, Spain. *Quaternary International*, 424, 130–142. <https://doi.org/10.1016/j.quaint.2015.04.054>
7. Barceló, J. A., & Maximiano, A. (2008) Some notes regarding distributional analysis of spatial data. In Proceedings of the 35th International Conference on Computer Applications and Quantitative Methods in Archaeology.
8. Lancelotti, C., Negre Pérez, J., Alcaina-Mateos, J. & Carrer, F. (2017) Intra-site Spatial Analysis in Ethnoarchaeology. *Environmental Archaeology* 22, 354–364. <https://doi.org/10.1080/14614103.2017.1299908>
9. Sabah Jaber, H. (2019) Geographic information system—based for spatial suitability mapping of groundwater for agricultural uses (Iraq), *Acta Scientific Agriculture* 3, 55–58. <https://doi.org/10.31080/asag.2019.03.0724>
10. Nicu, I. C., Mişu-Pintilie, A., & Williamson, J. (2019). GIS-based and statistical approaches in archaeological predictive modelling (NE Romania). *Sustain.*, 11, 1–13. <https://doi.org/10.3390/su11215969>
11. Vines, G., & Page, S. (2012). GIS-based spatial analysis for archaeological site prediction and evaluation. *Geospatial Sci. Res.*, 1328, 15.
12. Mahmoud, R. R., Mahmood, A. K., & Mahmoud, M. R. (2019). Maximum likelihood classification for land cover change detection utilizing lands at-8 Imagery in Wasit. *EM Int.*, 25, 72–76.
13. AL-AZZAWI, T. M. F., & AL-ZIRGANY, A. A. S. (2018) Change detection for some land cover types of Wasit Province (Eastern Iraq) using remote sensing and GIS techniques for years 1989. *Indian Journal of Natural Sciences* 9, 15359–15367.
14. Wali, N., Mushir, M., Fahad, M., & Abdul-Ridha, B. (2013). *Ancient Cities and Archaeological Sites in Wasit Province*. Republic of Iraq, Dar Al-Sadiq Foundation, Babil.
15. Abbas, Z., & Jaber, H. S. (2020) Accuracy assessment of supervised classification methods for extraction land use maps using remote sensing and GIS techniques. In *IOP Conference Series: Materials Science and Engineering* (Vol. 745). <https://doi.org/10.1088/1757-899X/745/1/012166>
16. Ali, A. H., & Jaber, H. S. (2020). Monitoring degradation of Wetland Areas using satellite imagery and geographic information system techniques. *The Iraqi Journal of Agricultural Science* 51, 1474–1485. <https://doi.org/10.36103/ijas.v51i5.1158>
17. Salman, I. (1970). *Archaeological Sites in Iraq*. Republic of Iraq, Ministry of Information, Directorate General of Antiquities, Baghdad.
18. Thompson, A. E., Meredith, C. R., & Pruffer, K. M. (2018). Comparing geostatistical analyses for the identification of neighborhoods, districts, and social communities in archaeological contexts: A case study from two ancient Maya centers in southern Belize. *Journal of Archaeological Science*, 97, 1–13. <https://doi.org/10.1016/j.jas.2018.06.012>
19. How Average Nearest Neighbor works, (n.d.). <https://pro.arcgis.com/en/pro-app/latest/tool-reference/spatial-statistics/h-how-average-nearest-neighbor-distance-spatial-st.htm>. Accessed March 8, 2021.
20. How Multi-Distance Spatial Cluster Analysis (Ripley's K-function) works, (n.d.). <https://pro.arcgis.com/en/pro-app/latest/tool-reference/spatial-statistics/h-how-multi-distance-spatial-cluster-analysis-ripl.htm>. Accessed March 8, 2021.

21. Abahre, J. S. H., & Burqan, M. (2019). Pattern of the spread of archaeological and touristic sites in the city of nablus and easily accessible analysis using geographic information systems. *Journal of Environmental Management & Tourism X*, 1906–1917. [https://doi.org/10.14505/jemt.v10.8\(40\).20](https://doi.org/10.14505/jemt.v10.8(40).20)
22. How Central Feature works, (n.d.). <https://pro.arcgis.com/en/pro-app/latest/tool-reference/spatial-statistics/h-how-central-feature-spatial-statistics-works.htm>. (Accessed March 8, 2021).
23. How Directional Distribution (Standard Deviatonal Ellipse) works, (n.d.). <https://pro.arcgis.com/en/pro-app/latest/tool-reference/spatial-statistics/h-how-directional-distribution-standard-deviationa.htm>. Accessed March 8, 2021.
24. How Standard Distance works, (n.d.). <https://pro.arcgis.com/en/pro-app/latest/tool-reference/spatial-statistics/h-how-standard-distance-spatial-statistic-works.htm>. Accessed March 8, 2021.
25. Tran, D. X., Pla, F., Latorre-Carmona, P., Myint, S. W., Caetano, M., & Kieu, H. V. (2017). Characterizing the relationship between land use land cover change and land surface temperature. *ISPRS Journal of Photogrammetry and Remote Sensing*, 124, 119–132. <https://doi.org/10.1016/j.isprsjprs.2017.01.001>
26. Ranagalage, M., Estoque, R. C., Zhang, X., & Murayama, Y. (2018). Spatial changes of urban heat island formation in the Colombo District, Sri Lanka: Implications for sustainability planning. *Sustainability* 10. <https://doi.org/10.3390/su10051367>
27. Elfadaly, A., Eldein, A. S., & Lasaponara, R. (2020). Cultural heritage management using remote sensing data and GIS techniques around the archaeological area of ancient Jeddah in Jeddah city. *Saudi Arabia, Sustain.*, 12, 1–15. <https://doi.org/10.3390/SU12010240>
28. How Hot Spot Analysis (Getis-Ord Gi\*) works, (n.d.). <https://pro.arcgis.com/en/pro-app/latest/tool-reference/spatial-statistics/h-how-hot-spot-analysis-getis-ord-gi-spatial-stati.htm>. Accessed March 8, 2021.

# Future Cities and Reality: Analytical Preview of the Different Theories from Information Cities, Smart Cities, to Liveable Cities



Hussaen Ali Hasan Kahachi

**Abstract** Although the subject of Future Cities is not new in the academic literature, it is highly controversial. While most researchers agree that planning for Future Cities is a must, there is an ongoing argument on the best approach to achieve future cities and their components and goals. This research argues that Liveable Future Cities is by far the most appropriate theory as a plan for the cities worldwide as it directly links the city with people/community needs. The research will start by briefly introducing the subject of future cities and their importance. Then it will use an analytical approach to discuss and evaluate the different theories for conceptualizing Future Cities in a chronicle framework. Based on this evaluation, the research will underline each theory's advantages and disadvantages compared to the utilization of qualitative data for validation. The research will conclude by highlighting the key differences between these theories and justifying why Liveable Cities is considered a superior theory for planning future cities.

**Keywords** Future cities · Information cities · Smart cities · Resilient cities · Sustainable cities · Eco cities

## 1 Introduction

In their physical form, cities are defined as “a context of interlocking integrated systems that consists of physical objects like buildings, houses, services, infrastructure, and relations between these physical objects, cities and their surroundings, and between cities themselves” [1, 2]. The city is a giant human-made object/machine that existed to serve the human race, and it requires continuous maintenance and development to keep up with its inhabitant's needs and requirements. It is a complex nexus of systems with many levels and layers besides the physical level/layer, such as the economic, environmental, social, cultural, technical, and relational layers. All

---

H. A. H. Kahachi (✉)

Department of Architectural Engineering, University of Technology, Baghdad, Iraq  
e-mail: [hussaen.a.hasan@uotechnology.edu.iq](mailto:hussaen.a.hasan@uotechnology.edu.iq)

of these layers are crucial for the city to function and work in tandem to serve its inhabitants and ultimately achieve overall well-being [3, 4].

However, the rapid urbanization, population growth, and other challenges have put great pressure on planners and researchers worldwide when thinking about the future city. The UN estimated the total world population to be just above 8 billion people in 2020. This number is projected to be nearly 10 billion by 2050 and as high as 13 billion by 2090 [5, 6]. Additionally, while more than half of the world population is currently residing in urban areas, specifically cities, almost all of the population growth around the world is projected to happen in urban areas [6–8]. This, cemented by the rising complexity of cities due to factors such as the increasing minimum standards of living, economic and environmental challenges, social and cultural requirements, has made planning for the future of cities an essential yet even more complex task [8–12]. Today, cities, and urban areas in general, have to withstand the rapid growth in population and economy, and at the same time, they have to be inclusive, safe, sustainable, dynamic, and resilient [1, 6, 13–17]. Finally, cities have to overcome many, sometimes overwhelming, urban challenges such as effective unemployment rates, segregation, migration, political instability, pollution [12], urban sprawl, transportation ineffectiveness, law enforcement, and any significant changes/shifts due to situations such as pandemics, like the recent COVID-19 pandemic, and large scale displacement and conflicts, such as the ISIS conflict in Iraq and Syria [18–21].

Researchers and experts around the world were concerned with thinking about the city of the future for decades. Eugène Hénard was arguably the first architect/planner to discuss the subject of future cities in 1910 in Europe. In his vision, he predicted that technology would greatly influence city planning and inhabitants' lives in the future. In 1924, Le Corbusier presented his projection of a future city, the Radiant City. His projection was of a future city that is symmetrical and highly centralized [1, 22]. Many researchers and planner/architects followed many subsequent visions. However, many of these visions were arguably considered unpractical or way too futuristic during these periods. Of those future cities theories that followed, there were some that were considered achievable or, to some extent possible. These theories were further developed or even adopted by some researchers, organizations, or even governments [2, 3, 23]. Such theories include Information Cities, Big Data Cities, Techno Cities, Eco-Friendly Cities, Sustainable Cities, Resilient Cities, Smart Cities, and Livable Cities.

This paper aims to understand and discuss several famous future cities theories. It uses the academic literature as starting point to analyze the definitions and characteristics of each theory against a number of properties and indicators. Then, the paper will highlight their relative strengths and weaknesses and ultimately recommends one of the theories as to the most suitable based on the analysis of the qualitative data. It is important to note that this paper will not discuss future cities theories that are incomplete, such as Quantum Cities, or theories that are very basic or artistic, such as Green Cities. It is difficult to yield any results or find a consensus about its definition and characteristics from the academic literature available when writing this paper respectively.

## 2 Research Methods

Although there are several theories about the future city, all theories share the same goals and objectives. Generally, future cities are cities where an understanding and management of city resources allows for an automated/semi-automated, efficient, sustainable, and dynamic management of these resources on different levels so that to serve the present inhabitants and future generations better. The city resources include physical objects and non-physical relations mentioned earlier and the many activities that occur in a city and city inhabitants themselves [1–5]. Based on this, it is possible to identify five main characteristics/criteria of future cities; data source and collection, automation level and speed, decision Making and Implementation, sustainability type and level, and the timeframe/time scope.

This research will be based on qualitative data analysis of literature around the different future cities theories; Information Cities, Big Data Cities, Techno Cities, Eco-Friendly Cities, Sustainable Cities, Resilient Cities, Smart Cities, and Liveable Cities, against the five characteristics of future cities mentioned above. Each of the five characteristics/criteria will have different levels as follows:

- A. Data source and collection: there are two parts for this indicator, data sources, and data collection. Data sources in a city could be sensors, people, organizations, and more. On the other hand, data collection could be done via census and surveys, mobile and network connections, direct input, and websites.
- B. Automation level and speed: this includes the way data analysis and results in extraction happens. This could be manual, semi-manual, semi-automatic, or automatic. It could also happen slowly, i.e., over several days to weeks, or relatively fast over a period of few hours to a couple of days.
- C. Decision Making and Implementation: The decision-making and source of decision power could be invested in experts, machines, or directly acquired from the people themselves. Additionally, the decision could be implemented through policies or dynamically through the community and specialized systems.
- D. Sustainability type and level: This ranges from no consideration to sustainability to full sustainability measures implementation. Sustainability could include measures to achieve environmental, economic, social sustainability or any combination of them.
- E. Timeframe/time scope: this is related to the time frame of the decision and planning of the decision, which could be short (days or weeks), medium (months, years), long/strategic (extend from several years). Moreover, the decisions could influence current matters only or extend to decisions that impact the city's future and its inhabitants.

Based on Tim's and Bryman's work [6, 7], the researcher used semi-structured interviews with experts and specialists. 23 city planning experts and specialists were interviewed, out of a total of 32 asked originally. They were asked to individually evaluate and rank the different theories according to the different criteria and definitions, giving each a score between 1 and 10. Following that, the resulting priorities

were discussed further with each of the interviewees to understand the justification for their choices better. Finally, the results for each theory and criterion were averaged, and the outcome mean was presented in the final results as a percentage.

### 3 Discussion of Future Cities' Theories

This section is concerned with defining each of the eight future cities theories and discussing them in some detail to understand its characteristics and enable informed evaluation of the theory against the five indicators mentioned previously. The theories will be addressed in approximately chronological order starting with the theory of information cities and ending with the theory of livable cities. As some of the future cities' theories are complex, the research will focus on the aspects related to the criteria mentioned above only.

**Information Cities.** The Information City theory is one of the first future cities theories. An information City is a virtual non-physical system that parallelly exists with the physical city and collects data from it that is not generally and appears typically to facilitate decision making. According to Schmitt [1, 9], "It is a digital representation of a city and its components where the emphasis is on information, creation, handling, storage, mining, and refinement into knowledge for the city". According to this, information cities are concerned with gathering the data through different mechanisms such as crowdsourcing and surveys. The collected data will then be analyzed in what is called 'urban observatories' to produce results that experts and planners can use in the decision-making process. This has nothing to do with the enforcement of the decisions or making it dynamic. Also, while the data could be used for achieving sustainability on some level, it is not one of its main goals.

**Big Data Cities.** The Big Data City is the next level future cities theory after Information Cities. It first appeared in the first decade of the 21st Century. According to this theory, data and information form the bases of this theory and the main focus for future cities [1, 10]. Similar to Information Cities, they also focus on data gathering, handling, mining, and refinement into results/knowledge. However, contrary to information cities, big data cities do this on a much bigger scale where all the data gathered are interconnected and interrelated in one extensive multi-relational database. Additionally, the data gathered on different aspects of the city would result in a more inclusive set, thus enabling more informed decision-making. The data include urban planning and design data, data on the economy, geographic and remote-sensing data, social data, environmental data, services, and more. The main challenge for big data cities is not data collection, instead it is the refinement of the data and benefiting from it to make decisions by planners and experts.

Furthermore, similar to information cities, big data cities theory does not propose/deal with decision enforcement mechanisms or achieve sustainability per se. It is, however, better suited to gather the data that enable planners/decision-makers to reach decisions to improve sustainability if they choose to. In that regard, a big data city model uses sensors, crowdsourcing, and existing urban masterplans/data

as bases to extract urban space readiness for urban reform, greenhouse gases and pollution levels, city heat islands effects, housing provision, and people's happiness and well-being.

**Techno Cities.** Techno Cities, so-called Technological Cities, are cities that merely focus on the advancement of technology and consider it the main factor in achieving some level of automation for the residents' happiness [11, 13]. This theory aims to give greater prominence to service delivery and simple decision-making in the cities. This type of city relies on the type and quality of data gathered, which are collected via a network of sensors covering the city. For it to function, it is crucial to be programmed and managed to clearly allocate the responsibilities of each of the technological systems in a city by deciding what inputs and outputs to expect.

In Techno-cities, most large-scale decisions will still be made through human interaction, i.e., experts and planners. However, small-scale short-sighted, and simple tasks will be managed by computers and special IT networks. This includes, for example, opening or closing specific lanes in the street according to the traffic levels or directing trash collection trucks in streets. A Techno-city does not necessarily and precisely consider achieving sustainability as one of its goals. However, it could aid in achieving sustainability, especially environmental, if it was programmed for that and the necessary data collection facilities and sensors were implemented.

**Eco-Friendly Cities.** An Eco-Friendly City, or so-called eco-city (Eco<sup>2</sup> for short), is defined as "a human settlement modeled on the self-sustaining resilient structure and function of natural ecosystems" [14]. The World Bank also defines it as "cities that enhance the well-being of citizens and society through integrated urban planning and management that harness the benefits of ecological systems and protect and nurture these assets for future generations" [15]. Eco-cities theory, therefore, considers the integration between planning and management with the environment and economy as bases for future cities success and inhabitants well-being. It aims to balance economic development without sabotaging the city's environmental sustainability, its surroundings, and the globe overall.

In eco-friendly cities, the data is collected via sensors and technologies that are available in the markets. The collected data is analyzed and used to identify projects that align with environmental sustainability and economic development. Investments are then sought out to form public-private partnerships to implement these projects. Therefore, it is a top-down approach that lacks true citizen involvement, especially as it relies on experts and planners to make the decisions. Thus, this theory neglects the third pillar of sustainability that is social sustainability. Furthermore, the mechanism used for implementing the decisions is through projects. These projects tend to have a medium timeframe in terms of their effects and could be semi-dynamic, i.e., not entirely based on rigid policies. The level of automation is relatively slow since decision-making relies mainly on projects that could take some time to be set and functional. Additionally, it is mainly reliant on human interaction to be set, making it semi-manual.

**Sustainable Cities.** Sustainable cities are one of the new theories in the context of future cities. The UN defines sustainable cities as "cities that are dedicated to achieving green sustainability, social sustainability and economic sustainability" [16,



18]. It is, therefore, often seen as an expansion of the eco-friendly cities' theory as in addition to environmental and economic sustainability, it is also concerned with social sustainability. In the sustainable city model, data is collected using sensors as well as from people. This data is then sorted and analyzed to make them into knowledge that can be used for decision making. The decision-making is still reliant on experts and planners; however, citizens have the right and the means for pitching in and being involved by commenting and sharing their perspectives through special channels. This could be through focus groups, surveys, and online systems. The final decision, nevertheless, would be made by experts. Moreover, some of the decisions are fully automated. For instance, having too much pollution in some areas will trigger a medium-term response to reduce it. Ultimately, this will affect not only on the current standards/conditions of living but also on the conditions of living for future generations.

Achieving sustainable cities involves implementing several solutions such as urban farming, sustainable buildings, regenerative architecture, sustainable and smart transportation system, diversifying economic growth sources, advanced urban planning that reduces waste and recycling. From this, sustainable cities' theory is much larger and complex compared to eco-friendly cities' theory. It is also more mature and thorough since it included mechanisms and tools for achieving its goals. Hence, many countries have adopted this theory for achieving future cities. However, they used somewhat different models that have a variant mixture of tools and mechanisms of implementation.

**Resilient Cities.** Resilient cities are “cities that have the ability to absorb, recover and prepare for future shocks including economic, environmental, social and institutional” [19]. A resilient city promotes inclusive growth, sustainable development, and well-being [19, 20]. For a city to be resilient, issues, problems, and challenges need to be identified first in order to be able to act accordingly and preserve the usual activities and flows within the city by as much as possible [21, 22]. Nevertheless, it is argued that without proper and fast data collection mechanisms, it is nearly impossible for a city to be truly resilient as identifying urban challenges and issues will be slow and inefficient [1], and it will be difficult to preserve the heritage [23].

In a resilient city, data is collected from sensors and people directly through reporting mechanisms. The data is then sorted and analyzed for the results to be used in the decision-making. The decision-making involves making predictions and projections about the consequences and results of implementing a solution and the urban problem/challenge itself. However, the decision-making is mainly reliant on experts and planners who will test different approaches and sometimes present the alternatives to the community for it to choose and send feedback. Additionally, some of the issues and challenges facing the city will be presented directly and automatically to the community to allow them to find a solution. The decision-making of a resilient city is often concerned with medium-length solutions in terms of its effects' timeframe. Moreover, although achieving sustainability is part of resilient cities theory, it is only concerned with achieving sustainability. Hence, it is not entirely concerned with the sustainability of the city's surroundings and connections. This is one of the main criticisms of this theory by some researchers, especially those

who see achieving sustainability in a city as part of a nexus of efforts regardless of the geographic location and boundaries [24, 25].

**Smart Cities.** The concept of smart cities has its origins dating back to Le Corbusier and his theory in “The City of Tomorrow” [26]. The theory of smart cities has developed since as technology, that facilitates the working and transformation to a smart city, rapidly advanced. A smart city concept today integrates “Information and Communication Technology”, ICT for short, and various other technologies and devices connected to the Internet-of-Things (IoT) network to improve the efficiency of the city, its operation, and services [10, 27, 28]. In a smart city, the collected data, which is often thorough and live, is used for managing the different assets, services, operations, and resources in the city. The data typically includes data acquired from devices, citizens, streets, sensors, buildings, and other monitoring systems. The data is sorted and analyzed automatically using special algorithms to make decisions affecting transportation and traffic, power systems and plants, utilities and water supply, waste and recycling, crime detection and reduction, other services and buildings such as libraries, schools, markets, public spaces, hospitals, firefighting, and more [10, 22, 29]. The decision-making happens relatively fast, and its implementation is often dynamic than does not rely on rigid policies only; rather, present and future modifications could be implemented through projects and systems directly. Furthermore, as the collected data is often real-time, it will provide the basis for future planning and monitoring/controlling of these projects and policies. Thus decisions could have planned long-lasting effects and implications.

The smart city theory is criticized for being largely reliant on technologies rather than people. While this could have beneficial consequences for achieving environmental sustainability, and to some extent, social and economic sustainability, it would be more likely than not to reduce the role of the people, hence making the city not very attractive to them. For instance, issues like housing needs, rapid urbanization, high unemployment rates, and capital mobility could be overlooked or its size misrepresented. Moreover, the new technologies could form a new barrier to some people, especially those with a disability, economic or technological-accessibility problems.

**Liveable Cities.** A liveable city, sometimes written livable city, is defined as “a city where people like to and can afford to live. Criteria for livability include safety, income possibilities, living options, climate, culture, private and public transportation, equality and inclusion, medical care, and city governance.” [1, 30]. The main focus of this theory is the livability of the city for its residence. Like smart cities and big data cities, livable cities use different means of collecting data from people and sensors. This data will then be sorted and analyzed with the aid of machines and experts. However, this theory differs in that it proposes the use of city/urban simulation models to generate then analyze the different alternative solutions and developments. Initially, these alternatives could be inserted/generated by the residents, experts or machines through a set of specialized channels, algorithms, mechanisms, and tools. These alternatives will be presented to the people, who have different weighting according to their role, to vote for the best alternative. The implementation of the proposed solution for each region within the city will be through the

people themselves and local authorities, and the final decision implemented might vary accordingly.

In livable cities, the people are the main force driving the decision-making for city planning and design. Experts and machines are there to provide aid and analysis to allow normal citizens to make informed choices. Although this is seen as a massive advantage for livable cities' theory over other theories, it is also the source of criticism as seen by some experts. Some experts have argued that in order for the citizens to make an informed decision, they need to have a good understanding of the problems and solutions. Otherwise, people could be misled or misdirected [31]. However, the response of other experts to this argument is that if data collection, simulation, analysis, and presentation were standardized and transparent, the livable city model could be successful in achieving its goals. Another argument against this theory is that it is tough to simulate all potential future scenarios. Therefore this model is not perfect. Understandably, this applies to all theories, and the only solution in that case to have resilience measures implemented, which is already part of livable cities' theory. In a livable city, the decision-making could influence the development of the city for periods ranging from current/short-sighted issues to strategic/long-term problems and challenges. Furthermore, a livable city works in tandem with other cities and areas within a large spatial plan/strategy to benefit all regions and cities. This includes all of the three pillars of sustainability; environmental, economic, and social.

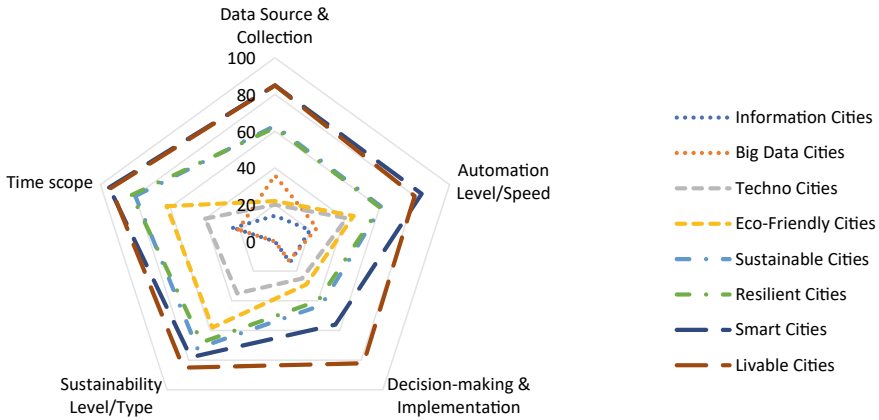
## 4 Results Summary and Discussion

Table 1 illustrates the results of the five criteria analysis of the eight future cities theories discussed in this paper. As seen, most of the early theories, such as Information Cities, Big Data Cities, and Techno-Cities, are mainly focused on data collection to facilitate decision making by experts and planners, or in the Techno-City theory machines on a small scale. The decisions are then implemented through a set of policies that are short-scoped in most cases. This is seen as a major flaw in these theories as the fast changes require fast dynamic actions that consider long-term consequences. The next tier of theories, namely Eco-Friendly cities and Sustainable Cities, is more focused on achieving urban sustainability in part or in whole. They use data inputted by people and sensors in a semi-automatic fashion to allow experts to decide that has medium timeframe effects. These theories, however, do not provide enough access to people to achieve governance and get them involved in the decision-making. Moreover, they tend to lack fast action mechanisms to respond to current/urgent problems.

The last tier of theories, namely Resilient Cities, Smart Cities, and Livable Cities, are mature. These theories have more advanced methods for data collection, probably because they encapsulated the new advancement in technologies. They all use some sort of simulation model to represent the data better and sort it out. Livable Cities, nevertheless, is the only theory that aims to use simulation models to forecast

**Table 1** Final results of future cities' theories analysis

Theory	Data source and collection	Automation level/speed	Decision-making and implementation	Sustainability level/type	Time scope
Information Cities	Sensors only—Basic	Manual—Slow	Experts-Policies	N/A	Short—Current
Big Data Cities	Sensors and People—Medium	Manual—Slow	Experts-Policies	N/A	Short—Current
Techno Cities	Sensors only—Medium	Semi-Manual—Slow Medium	Machine but mainly Experts-Policies	Minimum Environmental only	Short—Current
Eco-Friendly Cities	Sensors only—Medium	Semi-Manual—Slow Medium	Experts-Semi Dynamic	Max Environmental and Economic only	Medium—Current/Future
Sustainable Cities	Sensors and People—Medium	Semi-Automatic—Fast Medium	Experts-Dynamic	Full, Med All	Medium—Current/Future
Resilient Cities	Sensors and People—Medium	Semi-Automatic—Fast Medium	Experts-Dynamic	Full, Medium All	Medium—Current/Future
Smart Cities	Sensors and People—Thorough	Automatic—Fast	Machine and Experts-Dynamic	Full, Max Environmental, Med others	Long—Current/Future
Livable Cities	Sensors and People—Thorough	Automatic—Fast	People, Machine and Experts—Dynamic	Full, Max All	Long—Current/Future



**Fig. 1** Relative comparison of the 8 future cities' theories

future events and set a response plan on the larger intra-spatial context. It is also the only one that directly involves the people in the decision-making by incorporating an urban governance model that aims to cover all aspects of sustainability in full. Figure 1 graphically compares the eight future cities' theories using the five criteria/characteristics of future cities star diagram. It is important to note here that the Livable Cities theory appears to be the most comprehensive and complete theory only compared to other theories analyzed. This does not mean that Livable Cities theory covers all of these criteria fully. This is especially important since future cities' theories keep developing and new ones evolving, changing the balance and rating of the respective theory's characteristics/criteria.

## 5 Conclusions

Based on the previous presentation and analysis of the different future cities' theories, it is possible to conclude that the idea of future cities is an important one, especially with the rapid growth of cities/urban development and the advancement of living standards and technologies. The concept of the future city has come through a long way of development since the early 1900s to the present time, at it will surely continue developing in the future as more technologies and issues arise and others become dominant.

- This research evaluated eight of the future cities' theories against the five criteria of a future city; data source and collection, automation level and speed, decision Making and Implementation, sustainability type and level, and the timeframe/time scope. This is to understand which of the different theories are better aligned with the definition of a future city. The research used semi-structured interviews with 23 planning experts and specialists to rank and categorize each of the eight

future cities' theories against the five criteria. The use of the qualitative semi-structured interview method allowed good flexibility while giving an insight to experts/specialists' justification of their categorization and ranking of the different theories.

- Based on the results of the interviews, Livable Cities Theory is seen by many interviewees as the complete theory in terms of the five criteria discussed. This does not mean that it fully covers all of these criteria fully, rather it is better qualified to achieve the criteria fully than the other seven theories discussed in this research. This is especially important since future cities' theories keep developing and new ones evolving, changing the balance and rating of the respective theory's characteristics/criteria.
- Livable Cities is seen as a better future cities' theory as it puts the people themselves as the main driving force of city planning and design. Experts and machines provide advice and directions in livable cities and provide alternatives for implementing city planning and design. They allow the people to make an informed decision regarding their city design and planning through data collection, simulation, and analysis. Moreover, in livable cities, the full spectrum of sustainable challenges for durations reaching several decades are collected live, simulated, and analyzed. This makes livable cities better equipped to deal with unforeseen circumstances, provide resilience, deal with present issues on multiple scales, and forecast potential future scenarios to prepare for them. All this makes livable cities the best future cities' theory compared to other theories available at the time of writing this paper.
- The previous results do not necessarily mean that livable cities' theory is better in practice. This could be the subject of another future research using actual cases and statistical data. Moreover, as future cities' theories keep developing and new ones emerging, this comparison does not apply to all future theories in the context of future cities. Finally, it is worth noting that people and experts have a different understanding of the different future cities' theories, especially that this subject, as previously stated, is highly controversial amongst researchers and experts. Exploring this further could also be the subject of another research in the future.

## References

1. Schmitt, G. N. (2015). *Information cities*. ETH Zürich.
2. Dunn, N., & Cureton, P. (2020). *Future cities: New challenges mean we need to reimagine the look of urban landscapes*. Online.
3. Eremia, M., Toma, L., & Sanduleac, M. (2017). The Smart City concept in the 21st century. *Procedia Engineering*, 181, 12–19.
4. Saaty, T. L., & Sagir, M. (2015). Choosing the best city of the future. *Journal of Urban Management*, 4(1), 3–23.
5. Kiss, G., Jansen, H., Castaldo, V. L., & Orsi, L. (2015). The 2050 city. *Procedia Engineering*, 118, 326–355.
6. May, T. (2011). *Social research: Issues, methods and process* (4th edn). Maidenhead. OUP.

7. Bryman, A. (2012). *Social research methods* (4th edn). Oxford OUP.
8. Kahachi, H. A. H. (2017). The impact of the 2008 world financial crisis on homelessness in developed countries: The case study of New York city. *Dirasat Human and Social Sciencess*, 44(3), 269–280.
9. Müller Arisona, S., Zhong, C., Huang, X., & Qin, R. (2013). Increasing detail of 3D models through combined photogrammetric and procedural modelling. *Geo-spatial Information Science*, 16(1), 45–53.
10. Batty, M. (2012). Smart cities, big data. *Environment and Planning B: Planning and Design*, 39(2), 191–193.
11. Van Noorloos, F., Avianto, D., & Opiyo, R. O. (2019). New master-planned cities and local land rights: The case of Konza Techno City, Kenya. *Built Environment*, 44(4), 420–437.
12. Kahachi, H. A. H. (2020). Spatial Planning Contribution to Addressing Large Scale Multi-National Urban Problems and Challenges in Practice. 10(10), 7693–7708
13. Molella, A. P. (2009). Invented Edens: Techno-cities of the twentieth Century. *Choice Reviews Online*, 46(12), 46-6958–46-6958.
14. Ecocity Builders. (2018). *What is an Ecocity*. Online.
15. Suzuki, H., Dastur, A., Moffatt, S., Yabuki, N., & Maruyama, H. (2010). *Eco2 Cities: Ecological Cities as economic cities*. The World Bank.
16. UNDP—Human Development Reports. (n.d.). *The Human Development concept*. (22 November 2011).
17. Kahachi, H. A. H. (2020). The practice of sustainable spatial planning between an essentialist and relational conceptions. *Journal of Green Engineering*, 10(9).
18. United Nations Environment Programme. (2012). *United Nations conference on sustainable development*. In: About Rio+20, United Nations, Rio.
19. Organization for Economic Co-operation and Development (OECD). (2018). *Resilient cities*. Online.
20. Admiraal, H., & Cornaro, A. (2020). Future cities, resilient cities—The role of underground space in achieving urban resilience. *Underground Space (China)*, 5(3), 223–228.
21. Havko, J., Mitašová, V., Pavlenko, T., Titko, M., & Kováčová, J. (2017). Financing the disaster resilient city in the Slovak Republic. *Procedia Engineering*, 192, 301–306.
22. Gargiulo, M., Chiodi, A., De Miglio, R., Simoes, S., Long, G., Pollard, M., Gouveia, J. P., & Giannakidis, G. (2017). An integrated planning framework for the development of sustainable and resilient cities—The case of the InSMART project. *Procedia Engineering*, 198, 444–453.
23. Agustina, I. N. A. H. (2021). GIS approach to spatial analysis of heritage settlement: Case study of Magersari Kasepuhan Palace, Indonesia. *Journal of Engineering Science and Technology*, 16(2), 1614–1629.
24. Wakefield, S. (2020). Urban resilience as critique: Problematizing infrastructure in post-Sandy New York City. *Political Geography*, 79, 102148.
25. Rhule, J. (2017). *Resilient City critique: Resilient San Francisco*. Online.
26. Corbusier, L., & Etchells, F. (2013). *The city of tomorrow and its planning*. Dover Publications.
27. Peris-Ortiz, M., Bennett, D. R., & Yábar, D. P. B. (2016). *Sustainable Smart Cities: Creating spaces for technological*. Springer International Publishing.
28. Al-Saadi, M. K. (2021). Economic operation planning of combined heat and power smart distribution system. *Journal of Engineering Science and Technology*, 16(1), 25–43.
29. Romão, J., Kourtit, K., Neuts, B., & Nijkamp, P. (2018). The smart city as a common place for tourists and residents: A structural analysis of the determinants of urban attractiveness. *Cities*, 78, 67–75.
30. Tan, K. G., Woo, W. T., & Tan, K. Y. (2012). *Ranking the liveability of the world's major cities: The Global Liveable Cities Index (GLCI)*.
31. Yamagata, Y., & Seya, H. (2013). Simulating a future smart city: An integrated land use-energy model. *Applied Energy*, 112, 1466–1474.